

ISBN: 978-4-909106087 C3051

# GEOMATE 2022 Proceedings



**November 22–24, 2022  
Swissôtel Bangkok  
Rachada, Thailand**



**Edited by  
Zakaria Hossain  
Suksun Horpibulsuk**

GEOMATE 2022 BANGKOK, THAILAND 22-24 NOVEMBER, 2022  
GEOTECHNIQUE, CONSTRUCTION MATERIALS AND ENVIRONMENT



PROCEEDINGS OF THE TWELVETH INTERNATIONAL CONFERENCE – GEOMATE 2022  
GEOTECHNIQUE, CONSTRUCTION MATERIALS AND ENVIRONMENT, BANGKOK,  
THAILAND 22-24 NOVEMBER, 2022

# **Geotechnique, Construction Materials and Environment**

*Edited by*

**Prof. Zakaria Hossain**

*Department of Environmental Science and Technology  
Graduate School of Bioresources  
Mie University, Japan*

**Prof. Suksun Horpibulsuk**

*School of Civil Engineering,  
Faculty of Science and Engineering  
Suranaree University of Technology, Thailand*



THE GEOMATE INTERNATIONAL SOCIETY

Copyright @ 2022 by The GEOMATE International Society

All rights reserved. In principle, no part of this publication or the information contained herein may be reproduced in any form or by any means, translated in any language, stored in any data base or retrieval system, or transmitted in any form or by any means without prior permission in writing from the publisher.

Disclaimer: The editors and the publisher have tried their best effort to ensure the integrity and the quality of this publication and information herein. However, they give no warranty of any kind, expressed or implied with regard to the material contained in this book, and will not be liable in any event for the consequences of its use.

Published by:  
The GEOMATE International Society  
Tsu city, Mie, Japan  
E-mail: [society@geomate.org](mailto:society@geomate.org)  
<http://www.geomate.org/>

ISBN Number: 978-4-909106087 C3051

## Table of Contents

	Preface	xii
	Organization	xiii
<b>ID</b>	<b>Keynote Papers</b>	<b>1</b>
k1	IMPROVED MECHANISTIC PERFORMANCE OF CEMENT- NATURAL RUBBER LATEX STABILIZED SOILS AT VARIOUS TEMPERATURES Suksun Horpibulsuk	2
k2	SOIL BIO-ENGINEERING: A SUSTAINABLE GROUND IMPROVEMENT TECHNIQUE FOR STABILIZATION OF MARGINAL SOILS Bashir Ahmed Mir	3
	<b>Technical Papers</b>	<b>13</b>
<b>ID</b>	<b>Geotechnique</b>	<b>14</b>
g12105	FINITE ELEMENT ANALYSIS OF BEAM RESTING ON FOOTING Radhi Alzubaidi, Husain M Husain and Samir Shukur	15
g12106	ANALYSIS AND DESIGN ON VARYING THE OFFSET DISTANCES IN SUPERIMPOSED MECHANICALLY STABILIZED EARTH WALLS Vuttichai Chatpattananan and Vatanavongs Ratanavaraha	23
g12114	NUMERICAL ANALYSIS FOR ESTIMATING PULL-OUT RESISTANCE OF FLIP-TYPE GROUND ANCHORS IN SAND GROUNDS Shota Yoshida, Xi Xiong and Tatsunori Matsumoto	29
g12118	FIBER-BASED MEASUREMENT OF THE ACTIVATION OF GEOSYNTHETICS IN SOIL Jan Derksen, Jeanette Ortega, Kira Heins, Thomas Gries and Raul Fuentes	35
g12121	SATELLITE-BASED GROUND DEFORMATION MONITORING IN NAGA CITY, CEBU ISLAND IN THE PHILIPPINES Ryan A. Ramirez, Rajiv Eldon E. Abdullah and Christabel Jane P. Rubio	41
g12124	FINITE ELEMENT PARAMETRIC STUDY OF CONTIGUOUS PILE WALL REINFORCEMENT IN A DEEP EXCAVATION Fachrizal Naufal Indrawan, Fikri Faris and Akhmad Aminullah	47
g12126	NUMERICAL ANALYSIS OF INTERSECTING URBAN METRO TUNNELS IN ROCK MASS Isan Dey and Ramanathan Ayothiraman	55



g12130	SLOPE STABILITY DURING EXTREME DAILY RAINFALL: A COMPARATIVE STUDY USING STATIONARY AND NON-STATIONARY GENERALIZED EXTREME VALUE MODEL Thapthai Chaithong	59
g12133	ESTIMATION OF THE ALLOWABLE BEARING CAPACITY OF SOIL IN SOME MUNICIPALITIES OF THE PROVINCE OF PAMPANGA USING NEURAL NETWORKS Carmela Marie A. Lingad and Erica Elice S. Uy	65
g12138	DYNAMIC CENTRIFUGE MODEL TESTS FOR SOIL-BENTONITE VERTICAL CUTOFF WALLS WITH EARTHQUAKE-PROOF PERFORMANCE Koji Watanabe, Daisuke Ueno and Masaaki Hasegawa	72
g12140	REPRODUCTION OF DYNAMIC BEHAVIOUR AND CLASSIFICATION OF FAILURE PATTERNS OF STONEWALLS BY DISTINCT ELEMENT METHOD SIMULATION Satoshi Sugimoto, Kosuke Yamaguchi and Maho Yamaguchi	78
g12141	MPS-CAE SIMULATION FOR JET-GROUTING TECHNIQUE IN GROUND IMPROVEMENTS Sudip Shakya and Shinya Inazumi	84
g12142	PROSPECTS AND MERITS OF USING CALCIUM PHOSPHATE COMPOUNDS FOR SOIL IMPROVEMENT: A REVIEW Maksym Avramenko, Kazunori Nakashima and Satoru Kawasaki	90
g12145	ESTIMATION OF SUBSURFACE STRUCTURE OF LANDSLIDE AREA BASED ON MICROTREMOR AND SEISMIC OBSERVATION IN THE SAJI AREA, TOTTORI, JAPAN Tatsuya Noguchi, Isamu Nishimura and Takao Kagawa	96
g12148	EXPERIMENTAL STUDY ON STATE BOUNDARY SURFACE OF COMPACTED SILTY SOIL Tufail Ahmad, Riko Kato and Jiro Kuwano	102
g12150	PERFORMANCE AND BEHAVIOR OF DIAPHRAGM WALL OF UNDERGROUND AUTOMATIC CAR PARK PROJECT IN BANGKOK SUBSOIL Jirat Teparaksa	108
g12151	NATURALLY DERIVED CEMENTS FOR CONSTRUCTION AND BUILDING MATERIALS LEARNED FROM THE WISDOM OF ANCESTORS: A LITERATURE REVIEW Su Zhan, Kazunori Nakashima and Satoru Kawasaki	114
g12154	EFFECTIVENESS OF SAND COMPACTION PILE AND PREFABRICATED VERTICAL DRAINS IN IMPROVING SOFT SOIL FOR PAVEMENT SUBGRADE Tanim Shahriar and Shah Md Muniruzzaman	119
g12158	XRD PATTERNS OF TURBIDITY IN SEEPAGE WATER THROUGH TWO SOIL LAYERS Shota Takano, Motoyuki Suzuki, Taichi Ishimaru and Asahi Komori	128
g12159	ESTIMATION OF SUBSURFACE STRUCTURES AND GROUND MOTION CHARACTERISTICS OF ARTIFICIALLY IMPROVED LAND FROM MICROTREMOR OBSERVATIONS – CASE STUDY IN TOTTORI CITY, JAPAN Isamu Nishimura, Tatsuya Noguchi and Takao Kagawa	134
g12162	EVALUATION OF VERTICAL BEARING CHARACTERISTICS FOR SOIL-CEMENT COMPOSITE PILES Shohei Koga, Koji Watanabe and Tadahisa Yamamoto	140
g12169	REVIEW ON CONCEPTS, RESEARCH, AND CHALLENGES FOR THE ADOPTION OF PERMEABLE PAVEMENT SYSTEM IN VIETNAM Van Nam Pham, Hoang Giang Nguyen, Tien Dung Nguyen and Ken Kawamoto	146
g12171	INFLUENCE OF FOOTING SIZE AND RELATIVE DENSITY IN ULTIMATE BEARING CAPACITY FORMULA OF STRIP FOOTING ON SANDY SOILS Tahir Iqbal, Satoru Ohtsuka, Koichi Isobe, Yutaka Fukumoto and Kazuhiro Kaneda	152
g12177	SUSTAINABLE SOLUTION TO EXPANSIVE SUBGRADE AND EXISTING PAVEMENT USING GEOCONFINEMENT SYSTEM Lokanathan Logitharan and Umar Ali	158

g12184	EXPERIMENTAL STUDY ON DATA TRANSMISSION USED FOR CONSTRUCTION QUALITY CONFIRMATION OF EMBEDDED PILE CONSTRUCTION METHOD Yasuhide Mochida and Tatsuki Maniwa	164
g12201	NUMERICAL SIMULATION FOR SEDIMENTATION OF SAND PARTICLES IN EXCAVATION STABILIZERS Hiroya Asano, Koki Nakao, Tomotaka Morishita, Toshihiko Miura, Yasuharu Wachi, Kazuhiro Watanabe and Shinya Inazumi	170
g12205	STRENGTH PROPERTES OF BENTONITE SUBJECTED TO CYCLIC LOADING STRESS Tomoyoshi Nishimura, Seiichi Narushima, Yasunori ARAI and Yuki Sakoda	176
g12208	PROPERTIES AND PERFORMANCES OF SOIL CEMENT MODIFIED WITH CONCENTRATED PARA-RUBBER Supathinee Kowsura, Susit Chaiprakaikeow, Apiniti Jotisankasa, Suphawut Malaikrisanachalee, Supakij Nontananandh, Korakod Nosit, Auckpath Sawangsuriya and Shinya Inazumi	182
g12209	NUMERICAL STUDY OF A HYBRID COUNTERMEASURE FOR RIVER EMBANKMENT IN ACTUAL FIELD CASE Kakuta Fujiwara and Enayat Mallyar	189
g12210	A YIELD FUNCTION AND UNDRAINED BEHAVIOR OF K0 CONSOLIDATED CLAYS Yoshihito Imai, Salisa Chaipayut, Koichi Iinuma, Masaru Akaishi and Motohiro Sugiyama	195
g12211	FAILURE INITIATION AND MODES OF HOEK-BROWN ROCK MASSES SURROUNDING UNDERGROUND STORAGE WITH HIGH INTERNAL PRESSURE Apiwish Thongraksa and Pornkasem Jongpradist	202
g12212	EVALATION OF DISPLACEMENT AT GROUND SURFACE DURING GROUNDWATER RECOVERY Sutasinee Intui, Jittiphan Jindawutthiphan, Apinya Rungrueang, Choknimit Leelananthawong, Thanapatsa Srisarn Trpkovski and Kearnkeart Apisshotecawankit and Shinya Inazumi	208
g12215	A BASIC STUDY ON ESTIMATING PARTICLE-SIZE DISTRIBUTION BY AUGER EXCAVATION SOUND USING MACHINE LEARNING Keito Endo, Taizo Kobayashi and Ryoichi Fukagawa	214
g12217	MODEL TESTS ON CONCRETE BLOCKS SINKING INTO SEABED GROUND WITH UPWARD SEEPAGE FLOW GENERATED Tatsuya Matsuda, Kinya Miura, Naoto Naito and Yuki Ando	220
g12218	MODEL TESTS ON SAND BOILING AROUND SHEET PILE REGARDING PROPERIES OF GROUND MATERIAL Tatsuya MATSUDA, Naoto NAITO and Kinya MIURA	226
g12219	DISCRETE ELEMENT MODELING OF SLOPE FLOW BEHAVIORS OF DRY GRANULAR MATERIALS WITH DIFFERENT COLLAPSE CONDITIONS Naoto Naito, Tatsuya Matsuda, Kinya Miura, Yasuhiro Yamada and Takumu Omura	232
g12220	MODEL ROCK-SLOPE FAILURE TESTS ON FINAL RUNOUT DISTANCE OF DRY GRANULAR AVALANCHE WITH SECONDARY SLOPE FAILURE Naoto Naito, Tatsuya Matsuda, Kinya Miura, Takumu Omura and Arif Daniel Bin Azmi	238
g12224	INFLUENCE OF TEMPERATURE ON ELASTIC STIFFNESS AND TIME-DEPENDENT DEFORMATION BEHAVIOURS OF HOSTUN SAND IN TRIAXIAL COMPRESSION TEST Kosit Jariyatatsakorn and Warat Kongkitkul	244
g12236	NUMERICAL ANALYSIS FOR VERTICAL RESPONSE OF SHALLOW SUCTION PILE Donghyun Lee, Jaewoo Jung, Yoowon Lee, Jaehun Ahn and Jongwon Jung	254
g12237	MODELLING LIGHTWEIGHT DEFLECTOMETER BASED ON ANALYTICAL AND NUMERICAL MODELS Tram Huyen Nguyen, Yunje Lee, Hoa Phuong Thi Nguyen, Sangwook Kang and Jaehun Ahn	257
g12252	FEASIBILITY STUDY ON SOIL CLASSIFICATION FROM SOIL IMAGES USING DEEP LEARNING Tomoki Abe and Taizo Kobayashi	261

g12260	A COMPARISON BETWEEN PAVEMENT RESPONSES FROM THE FALLING WEIGHT DEFLECTOMETER AND THOSE FROM TRUCK LOADING BASED ON THE LAYERED ELASTIC ANALYSIS Thinn Thinn and Auckpath Sawangsuriya	265
g12261	PERFORMANCE OF BEARING LAYER CONSTRUCTED USING LIGHTLY CEMENTED CLAY Juan Wei Koh, Soon Hoe Chew, Yeow Chong Tan, Cheng Soon Teo, Shanyin Kee and Danette S.E. Tan	270
g12264	CORROSION OF UNDERGROUND STEEL BETWEEN SOIL AND CLAY AND ITS PREVENTION Keiyu Kawaai and Takahiro Nishida	276
g12269	PILE INSTALLATION EFFECTS ON THE STRESS AND DEFORMATION STATE OF SURROUNDING SOIL: REVIEW Worku Firomsa Kabeta	280
g12303	A CORRELATION BETWEEN ONE-DIMENSIONAL CONSOLIDATION COEFFICIENTS WITH BASALT FIBER LENGTH AND RHA-CEMENT CONTENT IN FIBER-REINFORCED STABILIZED EXPANSIVE SOILS Alex Otieno Owino and Zakaria Hossain	288
<b>ID</b>	<b><i>Construction Materials</i></b>	<b>302</b>
g12112	PARAMETRIC MODELING OF RECYCLED BRICK AGGREGATE CONCRETE (RBAC) USING ARTIFICIAL NEURAL NETWORK (ANN) AND MULTIPLE LINEAR REGRESSION (MLR) Albert Jr Griño	303
g12146	RAW MATERIAL OPTIMIZATION WITH NEURAL NETWORK METHOD IN CONCRETE PRODUCTION ON PRECAST INDUSTRY Ranti Hidayawanti and Yusuf Latief	309
g12156	EFFECT OF ADMIXED POLYPROPYLENE FIBERS ON CONCRETE PROPERTIES AND SHEAR STRENGTH OF REINFORCED CONCRETE BEAMS Osama Daoud and Reham Ibrahim Ahmed Ibrahim	316
g12157	ADDITION OF SEWAGE SLUDGE ASH TO CONCRETE AS SUBSTITUTE FOR PORTLAND CEMENT Jean-Frank Wagner	322
g12161	STUDY OF THE HEAT EQUATION AND THE EFFECT OF TEMPERATURE INSIDE AN ELECTRIC CABLE CONSISTING OF ALUMINUM AND COPPER METALS Dalal Adnan Maturi	326
g12214	ANALYSIS OF RESOURCE REQUIREMENTS IN A CONSTRUCTION SAFETY PROGRAM TO ESTIMATE COST OF ARCHITECTURAL WORK IN FLATS BUILDING Rossy Armin Machfudiyanto, Yusuf Latief, Ratih Fitriani and Amira Syifa	331
g12221	EXPERIMENTAL STUDY ON SURFACE PROTECTION OF RESTORATIVE BRICK FOR CULTURAL PROPERTIES IN AYUTTHAYA Yuko Ishida, Masaru Koemoto, Mika Yamada and Hajime Ito	338
g12223	SELECTION OF RAILWAY BALLAST BASED ON CEMENTING POTENTIAL: A CASE STUDY IN THAILAND Phitsanu Pholkainuwatra, Sitthiphat Eua-apiwatch and Siam Yimsiri	344
g12244	RECOVERY AND VALORIZATION OF DEMOLITION AND CONSTRUCTION WASTES SPREAD OVER ALL THE CITY OF CASABLANCA (MOROCCO) Mourad MORSLI, Mohamed TAHIRI, Youssef HALIMI and Mehdi MAANANE	349
g12250	THE EFFECT OF LDPE PLASTIC WASTE ON THE COMPRESSIVE STRENGTH OF PAVING BLOCKS Fauzan, Rani Fahmi Zakaria, Dyan Adhitya Nugraha M and Zev Al Jauhari	355
g12251	FRAGILITY CURVE DEVELOPMENT OF SCHOOL BUILDING IN PADANG CITY WITH AND WITHOUT RETROFITTING DUE TO EARTHQUAKE AND TSUNAMI LOADS Fauzan, Ruddy Kurniawan, Nandaria Syahdiza and Zev Al Jauhari	361



g12254	REMEDICATION OF AL-QATIF EXPANSIVE CLAY USING CEMENT KILN DUST, INITIAL ASSESSMENT Sultan Abdulaziz Almuaythir and Mohamed Farid Abbas	367
g12266	EFFECT OF MACRO-SYNTHETIC POLYPROPYLENE FIBER ON DRYING SHRINKAGE OF SELF-CONSOLIDATING CONCRETE Aris Aryanto and Andy Muliohardjo	372
g12267	ACTIVATION ENERGIES OF CHLORIDE INDUCED CORROSION OF STEEL IN CONCRETE Takahiro Nishida, Keiyu Kawaai and Nobuaki Otsuki	378
g12275	APPLICATION OF DIGITAL IMAGE CORRELATION METHOD IN RC AND FRC BEAMS UNDER BENDING TEST Messa Revolis, Aris Aryanto, Yuki Oribe and Hibino Yo	384
g12276	A STUDY ON METHODS OF SELF-HEALING ASPHALT PAVEMENT Enohmbey Chubisong Moses and Yoshitaka Kajita	390
g12302	PRODUCING VALUABLE 'SAND-LIKE' MATERIAL FROM EXCAVATED MARINE CLAY USING MID-SIZED ROTARY KILN Sathya Subramnian, Juan Wei Koh and Soon Hoe Chew, Y. C. Tan, C. S. Teo, M. Y. C. Koh, T. H. H. Cheung, H.B. G. Foo	396
<b>ID</b>	<b><i>Environment</i></b>	<b>401</b>
g12104	MATERIAL SOURCE OF MUARAJAMBI TEMPLES, INDONESIA Sondang Martini Siregar, Edy Sutriyono, Ari Siswanto and Agus Aris Munandar	402
g12109	DESALINATION BEHAVIORS FROM SEAWATER USING NATURAL ZEOLITE AND CALCINED CA-FE LAYERED DOUBLE HYDROXIDE FOR CULTIVATION Takaaki Wajima and Fumika Sekihata	409
g12116	MEASUREMENT OF CRACK DISPLACEMENT USING DIGITAL PHOTOGRAMMETRY Afia S. Boney, Satoshi Nishiyama and Teruyuki Kikuchi	415
g12120	STABILITY OF THE MUNICIPAL SOLID WASTE LANDFILL ON SLOPING LAND IN BATU CITY, EAST JAVA, INDONESIA A Rachmansyah, A P Putra, A Darmawan and Harimurti	420
g12123	FACTORS INFLUENCING ANAEROBIC DIGESTION PROCESSES OF MARKET WASTE AND COW DUNG AS RAW MATERIAL FOR RENEWABLE ENERGY Ellina Sitepu Pandebesie, Susi Agustina Wilujeng and Trifena Karunia Marbun	426
g12131	TiO <sub>2</sub> PHOTOCATALYST SUPPORTED ON FLY ASH PARTICLES USED IN WASTEWATER TREATMENT LOADED WITH FOOD DYES M. Visa and I. Visa	432
g12137	A NOVEL ROUGH FUZZY BASED DELPHI METHOD FOR HIGHWAY PROJECTS RISK ANALYSIS: THE SOE ASSIGNMENT SCHEME CASE STUDY Gilang Ardi Pratama, Yusuf Latief and Lukas Beladi Sihombing	438
g12139	RESULTS OF RECOVERY PROJECT ON WETLANDS WITH LOST BIODIVERSITY Michiko Masuda, Koichi Nagarekawa and Fumitake Nishimura	444
g12143	PREPARATION OF GEOPOLYMER CEMENT FROM LUNAR ROCK SAND USING ALKALI FUSION, AND ITS EVALUATION OF RADIATION SHIELDING ABILITY Osamu Toda and Takaaki Wajima	450
g12152	PROPOSAL OF A FLOATING OFFSHORE BASE FOR DISASTER PREVENTION AND MULTIPURPOSE USE Shinji Sato and Kai Nagatomi	454

g12153	STUDY ON THE ALLEY IN THE CITY BASED ON PEDESTRIAN'S IMAGE Shonosuke Kajita and Kazunari Tanaka	460
g12155	A STUDY ON THE RELATIONSHIP BETWEEN VISUAL STIMULI AND THERMAL SENSATION IN A TROPICAL REGION – TARGETING SHORT TERM RESIDENTS – Kenta Fukagawa, Yoshihito Kurazumi, Ariya Aruninta and Yoshiaki Yamato	464
g12165	THE RECYCLING BIOCHAR BASED-MUSHROOM GROWING MEDIA FOR SOIL ENRICHMENT IN CORN CULTIVATION Ambar Pertiwinigrum, Margaretha Arnita Wuri, Alva Edy Tontowi and Andang Widi Harto	470
g12167	STRATEGIES FOR INCREASING ACCESS TO WATER AND SANITATION IN A WATER-SENSITIVE AREA Shella Zahrawani, Ahmad Soleh Setiyawan, Prasanti Widiasih Sarli, Prayatni Soewondo and Dion Awfa	474
g12168	DETERMINATION FACTORS FOR SELLING LOCATIONS, GENDER, AND MIGRATION STATUS OF STREET VENDORS IN EAST JAKARTA IN ACHIEVING ECONOMIC RESILIENCE DURING THE COVID-19 PANDEMIC Beti Nurbaiti, Chotib, Kemas Ridwan K, Mia Siscawati and Elisabeth Ratu Rante Allo	480
g12172	ON MOVEMENT OF PEDESTRIANS IN THE STATION SQUARE Haru Kanda and Kazunari Tanaka	485
g12173	CEMENT SOLIDIFICATION CHARACTERISTICS OF COAL CINDERS-MIXED SOIL Shoji Kamao, Kentaro Ishii, Satoshi Shigemura and Yuta Murakami	489
g12175	ROAD TRAFFIC EVALUATION FORCUSHING ON VELOCITY AND FORM Shion Muramoto and Kazunari Tanaka	495
g12176	METHOD FOR EVALUATING URBAN COMFORT SPACES FOCUSING ON ENVIRONMENTAL SOUND USING EEG Shotaro Otsuji and Kazunari Tanaka	499
g12180	APPLICATION OF THREE-DIMENSIONAL POINT CLOUDS FOR RIVER MANAGEMENT USING DRONE SURVEYING Nanoka Akiyama and Satoshi Nishiyama	503
g12185	ASSESSMENT OF DOMESTIC WASTEWATER MANAGEMENT PROGRAMS IN RIVERBANK SETTLEMENTS Moch Zaelani Pebriansyah, Ahmad Soleh Setiyawan, Dyah Wulandari Putri and Ken Aryu Ruska Yuniar	509
g12186	THE IMPACT OF COVID 19 ON CHANGE OF MONTHLY INCOME IN INDONESIA Aditya Maulana Mugiraharjo and Chotib	515
g12193	MULTIMODAL GOODS TRANSPORTATION POLICY MODEL: TRANSPORTATION POLICY ENHANCEMENT IN NORTH COAST LINE OF JAVA Zony Yulfadli, Achmad Wicaksono, Ludfi Djakfar, Muhammad Zainul Arifin and Moch. Abdillah Nafis	518
g12194	SMART, INTEGRATED SUSTAINABLE AND ENVIRONMENT FRIENDLY TRANSPORTATION INFRASTRUCTURE CONNECTIVITY TO THE CAPITAL CITY OF NUSANTARA Achmad Wicaksono, Rosa Agustaniah and Ludfi Djakfar	524
g12196	EVALUATING IMPACTS OF OVER-DIMENSION AND OVERLOADING TRUCKS (CASE STUDY IN ARTERIAL ROADS) Achmad Wicaksono and Meriana Wahyu Nugroho	534
g12197	APPLICATION OF THE IDEAL FLOW NETWORK (IFN) METHOD TO EVALUATE THE LEVEL OF SERVICE ARTERIAL ROADS Susilowati, Achmad Wicaksono, Ludfi Djakfar and Solimun	540
g12203	THE EFFECT OF CHANGES IN LAND USE ON THE PREDICTION OF CRITICAL LAND DISTRIBUTION IN THE RAWAS WATERSHED (SOUTH SUMATRA PROVINCE, INDONESIA) Zainuddin Muchtar, Dinar Dwi Anugerah Putranto, Febrian Hadinata, Lawin Bastian and Julian fikri	546

g12216	COPPER RECOVERY FROM WASTE WIRE HARNESS USING POTASSIUM HIDROXIDE Koto Kagawa and Takaaki Wajima	555
g12222	INFLUENCE OF COMPOSITION ANALYSIS ON UNIT WEIGHT OF SYNTHETIC MUNICIPAL SOLID WASTE Vidit Singh and Prof.Taro Uchimura	559
g12238	SPATIAL STATISTICS AND PERCOLATION PROBABILITY OF PORE-NETWORK IN POROUS MEDIA WITH AGGREGATE STRUCTURE Junichiro Takeuchi, Yu Song, Yuto Takeuchi and Masayuki Fujihara	566
g12239	NONLINEAR TIME SERIES ANALYSIS OF IRREGULAR OSCILLATION INDUCED BY SALINE INTRUSION IN GROUNDWATER WITH LAB-SCALE EXPERIMENT Theara Seng, Junichiro Takeuchi and Masayuki Fujihara	572
g12242	MODELLING THE EFFECT OF CLIMATE CHANGES ON COASTAL AQUIFERS IN OMAN Javed Akhtar, Ahmad Sana, Syed Mohammed Tauseef and Shakila Javed	578
g12243	SIMULATION OF SMOKE DISPERSION AND TEMPERATURE DISTRIBUTION ON KEBON MELATI SUB-DISTRICT FIRE USING COMPUTATIONAL FLUID DYNAMICS Deffi Ayu Puspito Sari, Agnes Setioningrum and Dani Harmanto	584
g12277	GEOMETRIC SHAPE FOR IRRIGATION SEDIMENT TRAPS VORTEX DESILTING BASIN Muhammad Isnaeni, Muhammad Syahril Badri Kusuma, Joko Nugroho, Mohammad Farid and Muhammad Cahyono	596
g12279	PROFILING EXHALED VOLATILE ORGANIC COMPOUNDS FROM SEMERU ERUPTION REFUGEES BY USING E-NOSE Arinto Yudi Ponco Wardoyo, Eko Teguh Purwito Adi, Hari Arief Dharmawan, Susanthi Djajalaksana, Arif Budianto, Ngakan Putu Putra, Aditya Sri Listyoko, Fitri Indah Sari and Raden Dicky	605
g12280	EFFECT OF DIATOMACEOUS EARTH ON DESICCATION CRACKING OF EXPANSIVE SOILS Alemshe B. Tadesse, Y. Fukubayshi, A. Koyama and D. Suetsugu	613
g12284	URBAN HEAT HAZARD MODEL BASED ON LOCAL CLIMATE ZONE Adi Wibowo, Nadira Retno Abisha, Eko Kusratmoko and Ratna Saraswati	621
g12286	URBAN HEAT SIGNATURE AS MONITORING OF ENVIRONMENTAL HEALTH Adi Wibowo, Iqbal Putut Ash Sidiq, Mariney Binti Mohd Yusoff and Tengku Adeline Adura Binti Tengku Hamzah	627
g12288	STUDY ON THE TEMPERATURE MITIGATION EFFECT BY A CULTURAL HERITAGE IN JAPAN -TARGETING A SHRINE LOCATED NEAR THE CENTER OF FUKUOKA CITY Kenta Fukagawa, Yoshihito Kurazumi, Ariya Aruninta and Yoshiaki Yamato	633
g12297	SOME QUESTIONS ABOUT GEORGIA'S LANDSCAPES DYNAMICS (ON THE EXAMPLE OF SAMTSKHE-JAVAKHETI) Maia Tskhavadze, Dali Nikolaishvili, Lia Matchavariani, Lamzira Lagidze and Vazha Trapaidze	639
g12293	STRENGTH PARAMETERS AND THE RATE PROCESS THEORY APPLIED TO COMPACTED FADAMA SOILS Ola, Samuel Akinlabi, Fadugba, Olaolu George and Nnochiri, Emeka Segun	645
g12300	AN EMPIRICAL STUDY OF FLEXURAL STRENGTH OF BEAMS MADE OF RECYCLED AGGREGATE CONCRETE FROM CONSTRUCTION AND DEMOLITION WASTE IN HANOI, VIETNAM Ha Tan NGHIEM, Tran Viet CUONG, Nguyen Ngoc TAN, Phan Quang MINH, Nguyen Tien DUNG, Ken KAWAMOTO and Nguyen Hoang GIANG	652
g12310	LEGALIZATION OF THE USE OF MEDICAL MARIJUANA AS A TREATMENT IN THE EFFORT OF RENEWING THE NATIONAL HEALTH LAW IN INDONESIA. Siska Elvandari, Yandrizza, A. Irzal Rias, Tenofrimer and Ansiha Nur	658
g12225	FLASH CALCINATED SEDIMENT USED IN THE CEM III CEMENT PRODUCTION AND THE POTENTIAL PRODUCTION OF HYDRAULIC BINDER FOR THE ROAD CONSTRUCTION – PART I: CHARACTERIZATION OF CEM III CEMENTS Mahfoud BENZERZOUR, Duc Chinh CHU, Joelle KLEIB, Mouhamadou AMAR, Nor-Edine ABRIAK	664



	and Jaouad NADAH	
g12311	MICROSCOPIC INVESTIGATION ON ATMOSPHERIC PARTICLES IN CHELYABINSK, SOUTH URAL REGION, RUSSIA Olga V. Rakova, Tatyana G. Krupnova, Kirill A. Bondarenko, Svetlana V. Gavrilkina and Valerii N. Udachin	671
g12312	CAN TREES HELP REDUCE LEAD IN URBAN AIR? A CASE STUDY OF GREENING IN A RUSSIAN INDUSTRIAL CITY Tatyana G. Krupnova, Olga V. Rakova, Susanna V. Berentseva, Svetlana V. Gavrilkina and Valerii N. Udachin	677
g12313	FUNDAMENTAL PROPERTIES OF SOIL AND RICE HUSK ASH COMPOSITE FOR GROUND IMPROVEMENT – A REVIEW Abd Elmageed Atef, Alex Otieno Owino, Md. Yachin Islam, Md. Mahabub Alan, Md. Soybur Rahman and Zakaria Hossian	683

## **Preface**

On behalf of the GEOMATE 2022 Organizing Committee, we would like to welcome you in attending the Twelveth International Conference on Geotechnique, Construction Materials and Environment held at Swissôtel Bangkok Rachada, Thailand in conjunction with School of Civil Engineering, Suranaree University of Technology, The GEOMATE International Society, Useful Plant Spread Society, Glorious International, AOI Engineering, HOJUN, JCK, CosmoWinds and Beppu Construction, Japan.

On Friday 11 March 2011, at 14:46 Japan Standard Time, the northeast of Japan was struck and severely damaged by a series of powerful earthquakes which also caused a major tsunami. This conference was first dedicated to the tragic victims of the Tohoku-Kanto earthquake and tsunami disasters. The Geomate 2022 conference covers three major themes with 17 specific themes including:

- |   |   |
|---|---|
| • Advances in Composite Materials       | • Ecology and Land Development          |
| • Computational Mechanics               | • Water Resources Planning              |
| • Foundation and Retaining Walls        | • Environmental Management              |
| • Slope Stability                       | • Public Health and Rehabilitation      |
| • Soil Dynamics                         | • Earthquake and Tsunami Issues         |
| • Soil-Structure Interaction            | • Safety and Reliability                |
| • Pavement Technology                   | • Geo-Hazard Mitigation                 |
| • Tunnels and Anchors                   | • Case History and Practical Experience |
| • Site Investigation and Rehabilitation |   |

Even with the COVID-19, this year we have received many submissions from different countries. The participated countries are Bangladesh, Georgia, Germany, India, Indonesia, Japan, Morocco, Oman, Philippines, Romania, Saudi Arabia, Singapore, South Korea, Sudan, Thailand and United Arab Emirates. The technical papers were selected from the vast number of contributions submitted after a review of the abstracts. The final papers in the proceedings have been peer reviewed rigorously and revised as necessary by the authors. It relies on the solid cooperation of numerous people to organize a conference of this size. Hence, we appreciate everyone who supports as well as participate in this joint conference.

Last but not least, we would like to express our gratitude to all the authors, session chairs, reviewers, participants, institutions and companies for their contribution to GEOMATE 2022. We hope you enjoy the conference and find this experience inspiring and helpful in your professional field. We look forward to seeing you at our upcoming conference next year.

Best regards,

Prof. Zakaria Hossain,  
Mie University, Japan,  
Chairman (General)



Prof. Suksun Horpibulsuk,  
School of Civil Engineering,  
Suranaree University of Technology, Thailand,  
Chairman (Program)



## **Organization**

### *Conference Honorary Chairmen:*

Emeritus Professor Dr. Sohji Inoue, Mie University, Japan  
Emeritus Professor Dr. Teruo Nakai, Nagoya Institute of Technology, Japan  
Emeritus Professor Dr. Fusao Oka, Kyoto University, Japan  
Prof. Dr. Bajang B.K. Huat, UPM, Malaysia

### *Scientific Committees:*

#### Conference Chairmen:

Prof. Dr. Zakaria Hossain, Mie University, Japan (General)  
Prof. Suksun Horpibulsuk, Suranaree University of Technology, Thailand (Program)

#### *Conference Organizing Committee:*

Prof. Dr. Zakaria Hossain, Mie University, Japan (General)  
Prof. Suksun Horpibulsuk, Suranaree University of Technology, Thailand (Program)  
Prof. Dr. M Ibn Ibrahimy, Prof., Int. Islamic Univ. (Co-Chair)  
Prof. Dr. Toshinori Sakai, Mie University, Japan (Co-Chair)  
E/Prof. Dr. Takamitsu Kajisa, Mie University, Japan (Co-Chair)  
Dr. Vivi Anggraini, Lecturer, Monash Uni Malaysia (Co-Chair)  
Dr. Masaaki Kondo, Mie University, Japan (Co-Chair)

#### *National & International Advisory Committee:*

Dr. Fumio Tatsuoka, E/Prof., Tokyo University of Science, Japan  
Dr. Junichiro Takeuchi, Prof., Kyoto University, Japan  
Dr. Kingshuk Roy, Prof., Nihon University, Japan  
Dr. Sai Vanapalli, Prof., University of Ottawa, Canada  
Dr. Musharraf Zaman, Prof. Univ. of Oklahoma, USA  
Dr. Rafiqul Tarefder, Prof. University of New Mexico, USA  
Dr. M. Bouassida, Prof., National Sch. of Engg. of Tunis  
Dr. L.R. Austriaco, E/Prof., Angeles Univ. Found., Philippines  
Dr. M. Ibn Ibrahimy, Prof., Int. Islamic Univ., Malaysia  
Dr. Mohammad Shariful Islam, Prof., BUET, Bangladesh.  
Dr. Bujang B.K. Huat, Prof., Univ. Putra Malaysia  
Dr. Nemy Banthia, Prof., UBC, Canada  
Dr. Ian Jefferson, Prof., Univ. of Birmingham, UK  
Dr. John Bolander, Prof., Univ. of California, USA  
Dr. Shamsul Chowdhury, Prof., Roosevelt Univ., USA  
Dr. Isabel Pinto, Prof., University of Coimbra, Portugal  
Dr. Mark Jaksa, E/Prof., University of Adelaide, Australia Dr. Jim Shiau, A/Prof., USQ, Australia  
Dr. Hj. Ramli Bin Hj. Nazir, A/Prof., UTM, Malaysia  
Dr. H.M. Shahin, Prof., Islamic University of Technology, Bangladesh  
Dr. Md. Ariful Islam, A/Prof. Ohio State University, USA  
Dr. Md. Nurul Amin, Prof. Dhaka University, Bangladesh  
Dr. Chan Chee-Ming, Prof. Universiti Tun Hussein Onn Malaysia  
Dr. Ahmed H. A. Dabwan, A/Prof. TATI Univ. College, Malaysia



*International Technical Program Committee:*

Prof. Adolf Heinrich Horn, Geological Institute - Federa University of Minas Gerais, Brazil  
Prof. Bang-Fuh Chen, National Sun Yat-sen University, Taiwan  
Prof. Bindeshwar Singh, Kamla Nehru Institute of Technology, India  
Prof. Catherine Mulligan, Concordia Institute of Water, Energy and Sustainable Systems, Canada  
Prof. Chi-Min Liu Chienkuo Technology University, Taiwan  
Prof. Daffalla Rabih, Kenana Sugar Company, Sudan  
Prof. Essaid Bilal, Ecole Nationale Supérieure Des Mines De Saint Etienne, France  
Prof. Hakan Caliskan, Usak University, Faculty of Engineering, Turkey  
Prof. Ibrahim Maiyza, National Institute of Oceanography & Fisheries, Egypt  
Prof. Loc Nguyen, Sunflower Soft Company, Vietnam  
Prof. Marilia Hagen, Indiana University, United States  
Prof. Md Najib bin Ibrahim, Universiti Teknologi MARA, Malaysia  
Prof. Md. Abdul Baset Mia, BSMR Agri. Univ., Bangladesh  
Prof. Mihaela Popescu, University of Craiova, Romania  
Prof. Mohamed Abdou, Faculty of Education Department of Mathematics, Egypt  
Prof. Mohamed Tahiri, Présidnce de l'Université Hassan II de Casablanca, Morocco  
Prof. Nazar Oukaili, University of Baghdad, Iraq  
Prof. Radim Cajka, Technical University Ostrava, Faculty of Civil Engineering, Czech Republic  
Prof. Rajaraman Jambunathan, AMET University, India  
Prof. Saad Farhan Ibrahim Alabdullah, University of Almustansiriyah, Iraq  
Prof. Salem Alsanusi, Benghazi, Libya  
Prof. Sudhir Kumar Das, Retired Senior Project Manager of Indian Railways, India  
Prof. Zachary Senwo, Alabama A&M University, United States  
Prof. Imed Jabri, University of Tunis, Tunisia  
A/Prof. Bindeshwar Singh Kamla Nehru Institute of Technology, India  
A/Prof. Hasi Rani Barai, Yeungnam University, South Korea  
A/Prof. Jamaluddin Mahmud, Universiti Teknologi MARA, Malaysia  
A/Prof. Mohamed Ramadan, University of Hail, Saudi Arabia  
A/Prof. Najam Hasan, Dhofar University, Oman  
A/Prof. Nosina Krishna Chaitanya, Jawaharlal Nehru Technological University, India  
A/Prof. Nurbek Saparkhojayev, Almaty Management University, Kazakhstan  
A/Prof. Pandian Vasant, Universiti Teknologi Petronas, Malaysia  
A/Prof. Teodor Lucian Grigorie, University of Craiova, Romania  
A/Prof. Zawawi Daud, Universiti Tun Hussein Onn Malaysia  
A/Prof. Abdull Halim Abdul, Oil and Gas department, Malaysia  
A/Prof. Baoping Cai, China University of Petroleum, China  
A/Prof. Dariusz Jakóbczak, Koszalin University of Technology, Poland  
A/Prof. Edgar Allan Mendoza, University of the Philippines  
A/Prof. Lakhveer Singh, Universiti Malaysia Pahang (UMP) Malaysia, Malaysia  
A/Prof. Lidia Sas Paszt, Research Institute of Pomology, Poland  
A/Prof. Mahmood Barbooti, University of Yechology, Iraq  
A/Prof. Majid Mirzaei, Universiti Tunku Abdul Rahman, Malaysia  
A/Prof. Najeh Lakhoua, University of Carthage, Tunisia  
A/Prof. Ryan Joseph Calinao, Lyceum of the Philippines University-Laguna  
A/Prof. Sarawut Thepanondh, Mahidol University, Thailand  
A/Prof. Yasir Al Hussein, Jerash University, Faculty of Engineering, Jordan  
A/Prof. Grigorie Teodor Lucian, University of Craiova, Romania  
A/Prof. Hêriş Golpîra, Islamic Azad University, Sanandaj, Iran  
A/Prof. Muhammad Aslam, King Abdulaziz University, Saudi Arabia  
A/Prof. Tomasz Plech, Medical University of Lublin, Poland  
A/Prof. Fellah Mamoun, Abbes laghrour University, Algeria  
A/Prof. R. S. Ajin, GeoVin Solutions Pvt. Ltd., India  
A/Prof. Roman Szewczyk, Industrial Research Institute for Automation and Measurements, Poland  
Dr. Abolghasem Akbari, University Malaysia Pahang, Malaysia  
Dr. Ahmad Safuan A Rashid, Universiti Teknologi Malaysia, Malaysia  
Dr. Akinola Johnson Olarewaju, Federal Polytechnic Ilaro, Ogun State, Nigeria

Dr. Alexandre Costa, Federal University of the valleys of Jequitinhonha and Mucuri, Brazil  
 Dr. Angelo Gallone, Scotland's Rural College (SRUC), United Kingdom  
 Dr. Azizul Azhar Ramli, Universiti Tun Hussein Onn Malaysia  
 Dr. Bashir Dar, University of Kashmir Delina Baramulla J&K India, India  
 Dr. Bassam Abdellatif, National Authority for Remote Sensing and Space Sciences, Egypt  
 Dr. Binh Phu Nguyen, National University of Singapore, Singapore  
 Dr. Cazacu Gabriela, S.C. Geotech Dobrogea, Romania  
 Dr. Chengen Yang, Intel Corporation, United States  
 Dr. Dayang Norulfairuz Abang Zaidel, Universiti Teknologi Malaysia  
 Dr. Evgeni Starikov, KIT, Karlsruhe, Germany; Chalmers, Gothenburg Sweden, Germany  
 Dr. Fatma Khanchel, University of Tunis El Manar, Tunisia  
 Dr. Hamidreza Khataee, Griffith University, Australia  
 Dr. Hêriş Golpîra, Islamic Azad University, Iran  
 Dr. Iskhaq Iskandar, Dept. Physics, University of Sriwijaya, Indonesia  
 Dr. Jingwei Zhao, University of Wollongong, Australia  
 Dr. Jitendra Agrawal, Rajiv Gandhi Proudhyogiki Vishwavidyalaya, India  
 Dr. Liza Patacsil, Malayan Colleges Laguna, Philippines  
 Dr. Mohamed Amine, Ferrag Guelma University, Algeria  
 Dr. Mohd Afendi Rojan, Universiti Malaysia Perlis, Malaysia  
 Dr. Mohd Altaf, University of Kashmir Delina Baramulla J&K India, India  
 Dr. Mohd Hairy Ibrahim, Sultan Idris Education University, Malaysia  
 Dr. Mostafa Khater, Egypt - El Sharqia - Zagazig, Egypt Dr. Najam Hasan, Dhofar University, Oman  
 Dr. Namir Alkawaaz, University of Almustansiriyah, Iraq  
 Dr. Nashrul Fazli Mohd Nasir, Universiti Malaysia Perlis, Malaysia  
 Dr. Naufal Mansor Kampus Unicity Alam, Universiti Malaysia Perlis (UniMAP), Malaysia  
 Dr. Obed Majeed Ali, Northern Technical University, Iraq  
 Dr. Piyapong Janmaimool, King Mongkut' University of Technology, Thailand  
 Dr. Po-Sheng Chiu, National Cheng Kung University, Taiwan  
 Dr. Prabu Mohandas, Adhiyamaan College of Engineering, India  
 Dr. Raman Kumar, D A V Institute of Engineering and Technology, India  
 Dr. Riccardo Colella, University of Salento, Italy  
 Dr. Rolando Javellonar, Romblon State University, Philippines  
 Dr. Shikha Agrawal, Rajeev Gandhi Technical University, India  
 Dr. Stefania Tomasiello CORISA, University of Salerno, Italy  
 Dr. Sumiyyah Sabar, Universiti Sains Malaysia, Malaysia  
 Dr. Suphaphat Kwonpongsagoon, Mahidol University, Thailand  
 Dr. Wei Hong Tan, Universiti Malaysia Perlis, Malaysia  
 Dr. Yoshiro Fujii, Shin Kobe Dental Clinic, Japan  
 Dr. Yuk Feng Huang, Universiti Tunku Abdul Rahman (UTAR), Malaysia  
 Dr. Zongyan Zhou, Monash University, Australia  
 Dr. Purnanand Savoikar, Goa Engineering College, India  
 Dr. Ahmed Toaha Mobashsher, University of Queensland, Australia  
 Dr. Chupong Pakpum, Maejo University  
 Dr. Emanuele Quaranta, Politecnico di Torino, Italy  
 Dr. Jiangling Yin, Apple Inc., Cupertino, CA, United States  
 Dr. Khor Shing Fhan, Universiti Malaysia Perlis, Malaysia  
 Dr. Mario Chauca, Ricardo Palma University, Peru  
 Dr. Santosh Gaikwad, Model College, Ghansawangi, India  
 Dr. Tse Guan Tan, Universiti Malaysia Kelantan  
 Dr. Vikas Panthi, National Institute of Technology, India  
 Dr. Watoo Phrompittayarat, Naresuan University, Thailand  
 Dr. Hamidreza Namazi, Nanyang Technological University, Singapore  
 Dr. Parichat Phumkhachorn, Ubon Ratchathani University, Thailand  
 Dr. Subhasis Roy, University of Calcutta, India

*Conference Correspondence:*

Prof. Dr. Zakaria Hossain, Conference Chairman,  
Dept. of Env. Sci. & Tech., Mie University, Japan,  
E-mail: [conference@geomate.org](mailto:conference@geomate.org)  
Tel & Fax: +81-59-231-9578

*Editorial Committee and Executive Committee:*

Prof. Zakaria Hossain  
Prof. Suksun Horpibulsuk  
Engr. Alex Otieno Owino  
Engr. Md. Aminul Islam

## ***Keynote Papers***

# **IMPROVED MECHANISTIC PERFORMANCE OF CEMENT-NATURAL RUBBER LATEX STABILIZED SOILS AT VARIOUS TEMPERATURES**

Suksun Horpibulsuk, PhD

Suranaree University of Technology  
Nakhon Ratchasima, Thailand

## **ABSTRACT**

Thailand is an agricultural country, which is ranked the top in the world for the production and export of natural rubber. This study investigated the influence of natural rubber latex (NRL) replacement on the mechanistic performance improvement of cement stabilized soil. The mechanical strengths were investigated via unconfined compressive strength (UCS), indirect tensile strength (ITS), flexural strength (FS), and indirect tensile fatigue tests. The UCS, ITS, FS and indirect tensile fatigue life (ITFL) values were found to increase when increasing the NRL replacement ratio, up to the highest values at the optimum NRL replacement ratio. The mechanistic performance improvement was examined through the scanning electron microscopy (SEM) and energy dispersive X-ray spectroscopy (EDS) analyses. NRL replacement was found to significantly enhance the mechanistic performance of cement-NRL stabilized soil. Even though the NRL films within the soil-cement matrix improved the cohesion of the soil matrix, it was found to retard cementation bonding. As such, the excessive NRL replacement not only reduced the compactability but also retarded the cement hydration; hence the strength reduction.

The increased temperature at the early state of curing affects the fatigue properties of pavement base materials especially at high cement contents. The cement-NRL stabilized soil was found to have superior ITS, ITFL and indirect tensile resilient modulus ( $IT M_r$ ) values, as compared to cement stabilized soil for the same cement content, whereas having the same rate of reduction in ITS due to the raised temperature. For the NRL replacement ratio on the dry side of optimum, the cement-NRL stabilized soil had lower rate of  $IT M_r$  reduction than the cement stabilized soil though they had the same ITS due to the higher toughness. Therefore, the rate of ITFL reduction of cement-NRL stabilized soil was lower than that of the cement stabilized soil. It was proven in this research that the NRL replacement could reduce the thickness (superior  $IT M_r$ ) of cement-NRL stabilized base course for a given traffic volume and service life, and therefore the construction (material and operation) cost by 17.26% benchmarked to cement stabilized base course. The outcome of this research will promote the usage of NRL as a sustainable alternative to imported synthetic latexes for improving the mechanistic performance of cement stabilized soil for pavement bases.

# SOIL BIO-ENGINEERING: A SUSTAINABLE GROUND IMPROVEMENT TECHNIQUE FOR STABILIZATION OF MARGINAL SOILS

B. A. Mir, Ph. D., MASCE (USA), MISSMGE (UK), MIGS (I), C. Engg. (I)

Professor, Deptt. of Civil Engineering, National Institute of Technology Srinagar-190 006, Kashmir, J&K (India)  
E-mail: p7mir@nitsri.net, bashiriisc@yahoo.com, ORCID: 0000-0002-9360-9223

## ABSTRACT

Soil Bio-engineering is a novel technique for enhancement of stability of steep banks/slopes by means of vegetative cover and reinforced structures. This technique enables the researchers and designers to work together for sustainable management of ecosystem for the overall benefit of human beings and to safeguard the natural environment. Many researchers have developed sustainable soil additives/stabilizers for ground improvement to replace conventional traditional and non-traditional stabilizers, which are ecologically adverse and cause heavy carbon foot print. Among these soil additives, soil bio-cementation by means of carbonate precipitation has been found most suitable and eco-friendly ground improvement technique for enhancement of geotechnical properties of marginal soils. Soil improvement using bio-engineering techniques, which include vegetative covers, microbial induced carbonate precipitation (MICP) and enzyme induced carbonate precipitation (EICP) are eco-friendly and sustainable in nature. In this paper, an innovative approach of MICP has been adopted to improve the unconfined compressive strength and CBR of dredged soils. Dredged soils are dredged from water bodies and cause tremendous environmental problems if not utilized scientifically. Therefore, to avoid these problems by dredged soils, two bacteria's, *Bacillus subtilis* (B.S) and *Bacillus megaterium* (B.M), were used under controlled conditions at an optical density of 2.0 by bio-augmentation approach for improving the properties of these soils. Based on test results, it has been seen that the dredged soils can be stabilized by MICP technique. Thus, using soil bio-engineering technique reduces the cost of stabilization of marginal soils and also improves their engineering properties for safe construction of Engineering Structures.

*Keywords: Marginal soils, Soil bio-engineering; Vegetative cover; MICP; Environment; Remediation*

## INTRODUCTION

Soil is universally available as a construction material or as a foundation medium for building of various infrastructures safely. However, there is scarcity of good construction sites as well as construction materials due to huge population increase and rapid urbanization around the world. Therefore, there is lot of pressure on Geotechnical Engineers to characterize marginal soils for construction of various infrastructures. On the other hand, due to rapid industrialization, lot of solid waste materials are produced every day, which need to be disposed-off in a scientific way to avoid any environmental or health problems. Thus, there is a dire need of identification of the sources and types of solid waste materials produced for the sustainable management and eco-friendly development. There are various types of solid wastes generated such as residential, commercial, institutional, construction and demolition, municipal services, treatment plant sites, industrial, agricultural and dredging of water bodies such lakes and rivers. Among various such solid wastes, this study deals with the solid waste material generated by dredging the flood spill channel of Jhelum River, Srinagar. Jhelum River is essentially the backbone of all its economic

activities in Kashmir [1]. However, this River is also the main cause of large and small-scale flooding in the region and one of the most disastrous floods occurred in September 2014. In view of this, various flood control measures have been recommended and one among them is flood spill channel which carry excess water from Jhelum River during flooding. But unfortunately, the present capacity of the channel has decreased due to the encroachments and sediment deposition in the river and flood spill channel over the years. Therefore, the scheme for shoreline dredging of flood spill channel was carried for the eco-regeneration and sustainable development of the flood spill channel. However, the dredging of the flood spill channel generated the dredged soil in large quantity posing serious disposal and environmental problems.

The scarcity of stable soil deposits and inherent properties of dredged soils has put pressure on geotechnical engineers for characterization and stabilization of this soil as a resource for various beneficial applications for the eco-friendly and sustainable development of various infrastructures. Many researchers have reported that the dredged soil is no longer being regarded as a "spoil" or "waste" but as a resource [2]-[5]. Its mineralogy and Geotechnical properties qualify it for use in the

manufacture of high value, beneficial use products. However, in such a situation, modification/stabilization of these soils through ground strengthening is usually beneficial for eco-friendly and sustainable development [6]. Also, since few decades before, the marginal soils have been improved extensively for the construction of various infrastructural developments all over the globe due to scarcity of stable soil deposits [7]-[10]. Soft clay deposits with high water content exhibit high compressibility characteristics and low bearing capacity. Due to huge population and urbanization, there is increasing demand for more and more infrastructural developments for which very limited stable construction sites are available. Thus, there is dire need for improvement of soft soil deposits by means of various ground improvement techniques. Although, large number of conventional ground improvement techniques such as Mechanical Ground Improvement Methods, Ground Treatment Methods using Traditional/Non-Traditional admixtures and Ground Reinforcement Methods have been developed to improve poor ground conditions. However, conventional ground improvement methods are ecologically adverse and cause heavy carbon emissions [11]-[14]. Therefore, ground treatment using Soil Bio-Engineering Methods are increasingly being used for soil stabilization and are replacing the conventional methods. Soil bio-engineering is a well-recognized component of ecological engineering, defined as “the design of sustainable systems, consistent with ecological principles, which integrate human society with its natural environment for the benefit of both”. Soil bioengineering technique can also be used as reinforced structures in the construction projects to provide soil reinforcement such as living retaining walls and live reinforced earth walls. The concept of

using Bio-Chemical or Biological process in soil improvement, which is also known as bio-mediated soil improvement method has proven as an eco-friendly and a sustainable ground improvement technique for stabilization of marginal soils [15]-[18]. The processes of Soil bioengineering being investigated range from use of living plant materials to stabilize complex slopes [16], [19] to microbially induced calcite precipitation (MICP) for solidifying clays and sands to bio-film slimes generated to reduce hydraulic conductivity [20]-[22]. Soil microorganisms are broadly defined as a group of microscopic life forms that include bacteria, archaea, viruses, and eukaryotes like fungi.

Many researchers [23]-[24] have reported that the microbially induced calcite precipitation (MICP) is an eco-friendly and sustainable soil stabilization technique, which is being explored by the researchers all-over the globe. Also, Mitchell and Santamarina [25] have reported that the bio-chemical methods of soil stabilization is a novel and emerging research area in geotechnical engineering for the sustainable development of various infrastructures. Among various bio-chemical methods, MICP technique can alter/enhance the physical and mechanical properties of the marginal soils, which can support the superstructures safely [26]. Reichle [27] reported that the microbes constitute about 70% to 85% of the living component in the soil matrix/systems, which can be successfully utilized as a sustainable means of soil stabilization. However, researchers need to understand about the metabolic rate for proper forecasting and understanding of mechanism and working principle of how the microorganisms behave under different conditions [28]. The various Bio-Engineering Techniques for treatment of marginal soils are shown in Fig. 1.

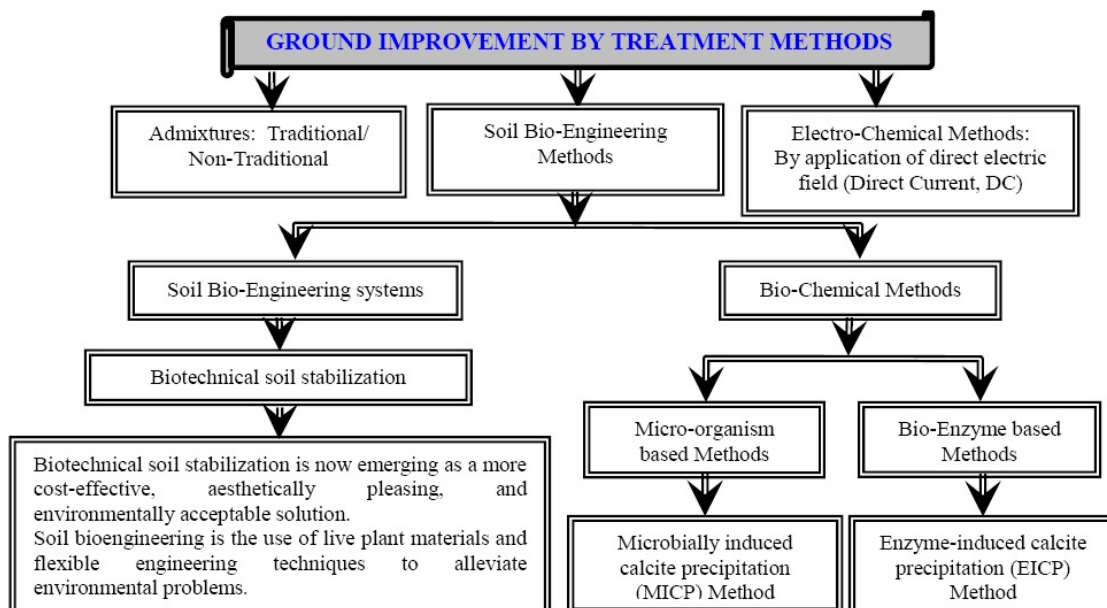


Fig. 1. Bio-Engineering Techniques for treatment of marginal soils



In the present study, two different bacteria, *Bacillus subtilis* (*B.S.*) and *Bacillus megaterium* (*B.M.*) at an optical density (OD) of 2.0 were chosen for stabilization of dredged soil. The soil specimens for UCS and CBR tests were prepared at  $0.85 \gamma_{d(max)}$  and optimum water content (OMC) to ensure that sufficient pore space is available for the bacteria and cementing solution to percolate into the soil matrix. The UCS samples were treated in both fabricated brass moulds and full contact flexible moulds (FCFM) made of non-woven geo-textiles under controlled conditions and tested as per standard codal procedures. The increase in UCS for 0.5 cementing solution molarity from 197 to 544kPa and 197 to 637 kPa for *B.S.* and *B.M.* bacteria treatment, in fabricated brass moulds and 197-603kPa and 197 to 674kPa for *B.S.* and *B.M.* bacteria in FCFMs was appreciable. The CBR values increased from 1.3% to 8.4% for *B.S.* and 9.1% for *B.M.* bacteria treatment in soaked conditions respectively. The experimental results were also supported by scanning electron microscopy (SEM) and Fourier transform infrared spectroscopy.

## MECHANISM OF BIO-CEMENTATION

The Mechanism and working principle of Bacteria for Bio-cemented weak soils have been reported by Wani and Mir [29]. Bio-cementation is a natural process that occurs over millions of years and utilizes microbes, nutrients and natural procedures to efficiently develop the engineering properties of soils. Mechanism of bio-cementation starts with mixing of a urease producing bacteria to the oven-dried soil and then treatment with external cementing solution (CS). Through hydrolysis, urea ( $CO(NH_2)_2$ ) is hydrolyzed by the enzyme into ammonium ( $NH_4^+$ ) and carbonate ions ( $CO_3^{2-}$ ). The deposition of  $CaCO_3$  crystals within the soil grains by MICP is shown in Fig. 2.

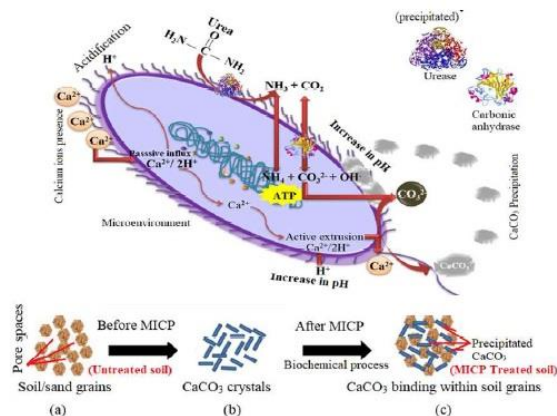
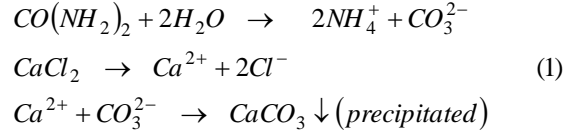


Fig. 2. Illustration of MICP technique mediated by urease and carbonic anhydride

This  $CO_3^{2-}$  combines with calcium ions ( $Ca^{2+}$ ) from the Cementing solution molarity (CSM) to form calcite ( $CaCO_3$ ) which induces strength to the soils by cementing the particles together (Eqn.1):



## MATERIALS AND METHODS OF SAMPLE PREPARATION AND TESTING

### Soil Used in this Study

Disturbed and undisturbed soil samples were collected from three distinct sites distanced 300m apart on the flood spill channel of Jhelum River (Fig. 3). The study area also falls near an internationally recognized wetland, Hokersar in the outskirts of Srinagar city, India. The process of soil sample collection is shown in Fig. 4. The undisturbed soil samples were carefully packed and transported to Geotechnical soil testing laboratory so that the in situ state of soil samples is not altered.

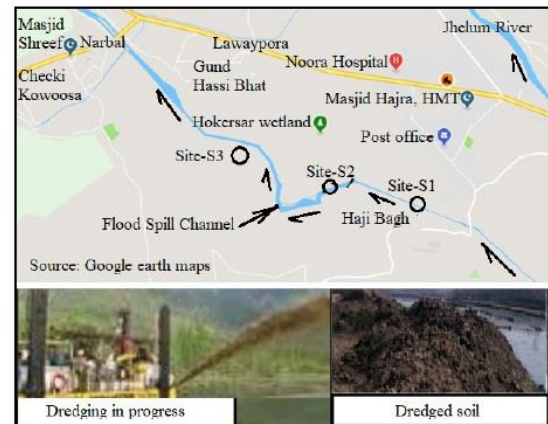


Fig. 3. Sample collection site from flood channel



Fig. 4. Process of dredging, collection of undisturbed, disturbed soil samples

The disturbed soil samples were air-dried and pulverized in the laboratory for conducting various basic tests such as soil grading, compaction, shear strength and CBR tests. All the soil samples were tested as per standard procedures [30]-[33]. The particle size distribution (PSD) curves of three sites are shown in Fig. 5 and the physical properties are given in Table 1 respectively.

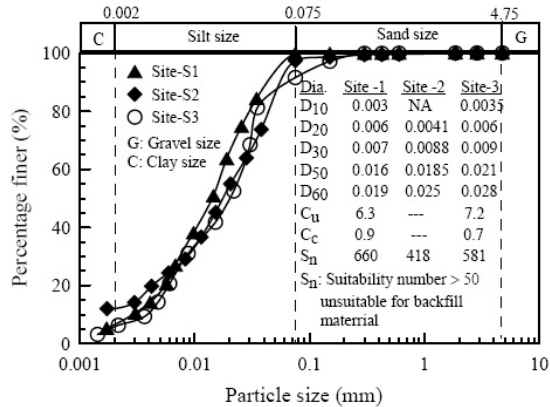


Fig. 5. PSD curves for different site samples

Table 1 Properties of soil samples used in the study

Properties	Site 1	Site 2	Site 3
In situ water content (%)	31.2	31.7	27.9
In situ dry unit weight (kN/m <sup>3</sup> )	14.3	13.6	15.6
Specific gravity (G)	2.66	2.61	2.65
Percentage finer than 75 µm	99	95	92
Clay (%)	7.5	02	04
Silt (%)	91.5	93	88
Sand (%)	01	05	08
Liquid limit (%)	36.2	33.9	29.7
Plastic limit (%)	25.1	24.6	20.1
Plasticity index (%)	11.1	9.3	9.6
P.I, A-line	11.8	10.1	7.1
P.I, U-line	25.4	23.3	19.5
Clay mineral	Kaolinite		
Classification	MI	ML	ML
Maximum dry unit weight, MDU (kN/m <sup>3</sup> )	16.2	15.7	16.5
Optimum moisture content, OMC (%)	21.4	16.3	15.7
In situ UCS, $q_u$ (kPa)	25.7	15.5	15.9
UCS at OMC, $q_u$ (kPa)	39.2	33.3	33.8
CBR, Un-Soaked (%)	6.3	5.1	6.9
CBR, Soaked (%)	3.1	1.3	3.7

The test results show that the soil is poorly graded silty soil with low to medium compressibility. Hence, the soil is not suitable in its in-situ state as a construction or foundation material.

Thus, based on basic geotechnical characterization of the soil samples, the weakest sample (S-2) out of the three chosen sample was selected for stabilization.

### Bacteria Used in this Study

In this study, two urease producing bacteria namely *Bacillus Subtilis* (B.S) and *Bacillus Megaterium* (B.M) *Bacillus* along with a cementing solution molarity (CSM) were used for improving the unconfined compressive strength (UCS) and CBR of dredged soils.

### Bacteria culture

The bacteria culture process has already been discussed in detail by Wani et al. [34]. In this study, two bacteria's *Bacillus Subtilis* (BS) and *Bacillus Megaterium* (BM) were cultivated in the laboratory as per standard procedure provided by the supplier. The stock of bacteria was revived on LB-agar Plate at 37°C overnight. Accordingly, single bacteria colonies were patched on LB agar plate and grown in a 37°C incubator. The bacteria cells were then inoculated in a 5 ml LB broth and grown with 180 rpm at 37°C overnight. Similarly, the sub-culturing process was carried out by adding 2 ml of the saturated culture in a 200 ml of LB broth and grown with 180 rpm at 37°C overnight. The bacteria cells were checked for optical density (O.D.) of 2.0 (equivalent to 2.108 cells/ml) at 600nm till the desired O.D was attained. The bacteria colony formation units were projected by the equation given by previous researchers [35]:

$$C = 8.59 * 10^7 * (D^{1.3627}) \quad (2)$$

Where:  $D$  = reading at OD<sub>600</sub> (the optical density of a sample measured at a wavelength of 600 nm, and  $C$  = concentration (cells per ml).

### Cementing solution molarity (CSM)

In this study, the urea, CaCl<sub>2</sub>·2H<sub>2</sub>O (hydrated calcium chloride) and distilled water were used for preparation of cementing solution molarity. A CSM of 0.5 for UCS tests was prepared by mixing 30 g of urea and 73.5 g of calcium chloride in a litre of distilled water to make a litre of CSM solution. Similarly, a CSM of 1.0 for CBR tests was prepared by mixing 60 g of urea and 147 g of calcium chloride to make a litre of CSM solution. The aforesaid selected CSM values were chosen based on extensive literature, which revealed that there is significant enhancement in soil properties at lower values of CSMs. However, many researchers in the past have used different concentrations of media for in-depth studies involving microbes [36]-[37].

### Fabrication of MICP setup

In this study, a customized setup was required for microbial induced carbonate precipitation (MICP). Accordingly, the MICP setup was fabricated in the Institute workshop, which consisted of unconfined compression test moulds, wooden stand, over head supply tank and control knobs. The customized setup is shown in Fig. 6a. The UCS moulds were fabricated of brass material to avoid rusting during continuous treating of soil samples up to 48 hours. The moulds had screw arrangement at the top and bottom to facilitate compaction at desired density. Provision for accommodating porous stones was provided inside the mould and the final extruded sample was of standard size, 76mm height and 38mm diameter. Also, full contact flexible mould (FCFM) (Fig. 6b) was made from non-woven geo-textiles for treatment of soil samples.

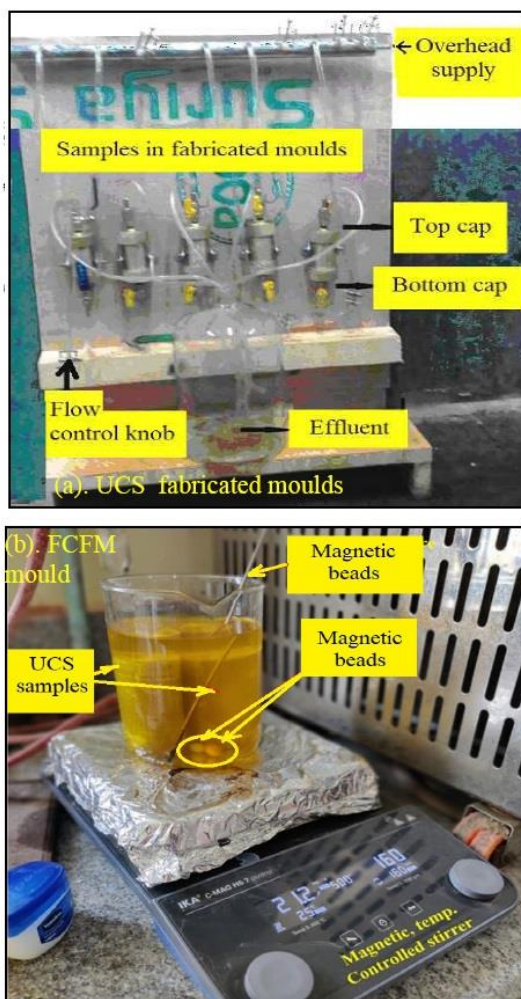


Fig. 6. MICP setup for bacterial treatment of soil samples

### Specimen preparation

The remolded soil specimens were prepared at  $0.85 \gamma_{d(max)}$  and corresponding water content for conducting UCS and CBR tests for stabilized soil. The dry unit weight ( $\gamma_{d(max)}$ ) was chosen dry of optimum to make sure that sufficient pore void space is made available for the bacteria and the cementing solution (CS) to percolate into the soil specimen. Also, the purpose of using reduced density was to ensure that there is homogeneity in the distribution of calcite in the soil specimen. Two different treatment procedures were adopted for preparation of UCS samples [32]. In the first method, the soil specimens were treated from bottom to top in fabricated brass mould for 48 hours and then tested as per standard procedure [38]. In the second method, the soil specimens were treated in full contact flexible mould (FCFM) made from non-woven geo-textiles. Both the treatment methods are shown in Fig. 6a&b respectively. Likewise, CBR tests on soil specimens were conducted for both unsoaked and soaked conditions. For unsoaked CBR tests, 48 hours treatment was given to soil specimens by keeping the soil moulds in CS buckets. These soil specimens were tested after 24h rest period. Similarly, soaked soil samples moulds were kept in CS buckets for 96h and the tested as per standard procedure [33].

## RESULTS AND DISCUSSIONS

### Effect of Biological Processes on the UCS Values of Treated Soil

To study the effect of microbial induced carbonate precipitation on the UCS values of treated soil samples for site-2, the unconfined compression tests were carried out on soils samples for different curing periods. The soil specimens were compacted at  $0.85\gamma_{dmax}$  and corresponding water contents on the dry side of optimum and treated with “BS & BM” bacteria and Cementing solution (CS) in fabricated brass and full contact flexible moulds. The stress-strain curves for “BS & BM” treated soils for both treatment methods are shown in Figs. 7 (a-b) & 8 (a-b) respectively. The test results showed that the UCS values increased from 197 to 544kPa for *B.S.* treatment at 2.0 OD and 0.5 CSM for 3 days of curing, whereas an increase from 197 to 637kPa was observed for *B.M.* treatment for the same testing condition in brass moulds. Similarly, the UCS values increased from 197 to 603kPa for *B.S.* treatment with 2.0 OD and 0.5 CSM for 7days of curing, whereas an increase from 197 to 674kPa was observed for *B.M.* treatment for the same testing condition in full contact flexible moulds (FCFM). This overall increase in UCS is attributed due to the formation of calcite which bonds the soil particles

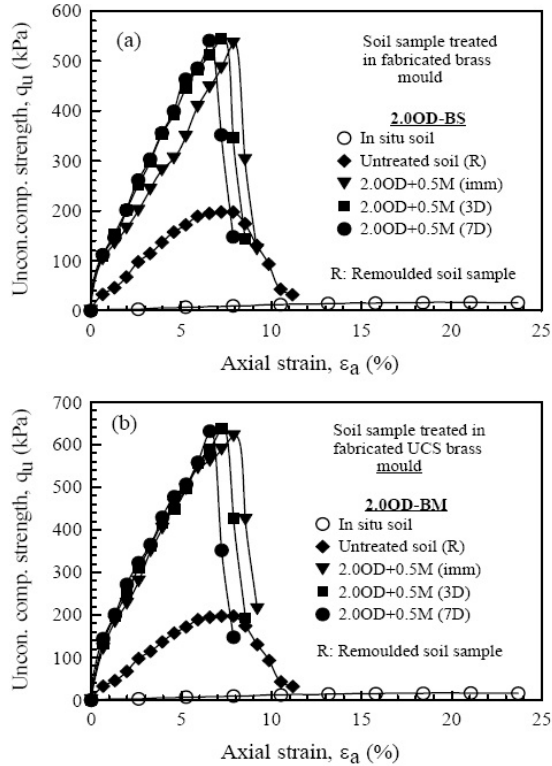


Fig. 7. Stress versus strain plots (Brass mould) for: **a** *B.S.*-treated soil; **b** *B.M.*-treated soil

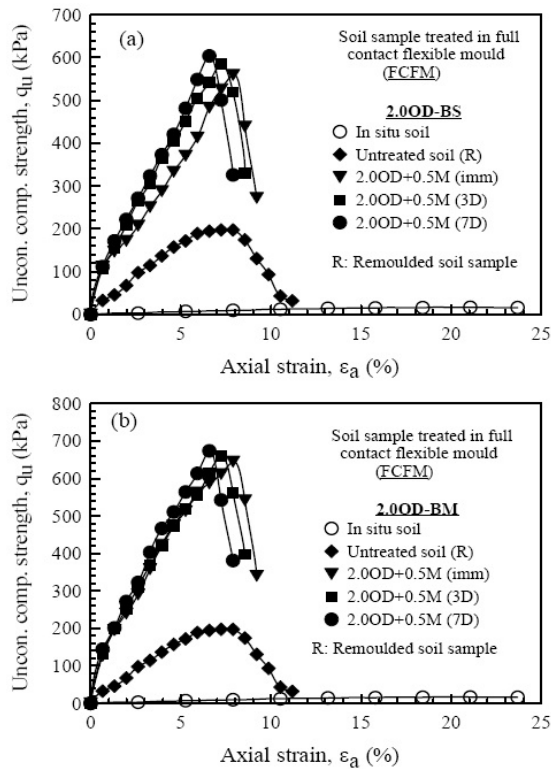


Fig. 8. Stress versus strain plots (*FCFM*) for: **a** *B.S.*-treated soil; **b** *B.M.*-treated soil

together. From Fig. 7(a-b), it can be seen that “UCS” decreased after 3 days of curing period, which can be attributed due to the access salt accumulation in brass fabricated moulds and inactive microbes in the soil matrix. Lee et al. [2013] has reported that access salt accumulation is unfavorable to bacteria growth and as such leads to uneven calcite precipitation. Therefore, in this study, to over-come this short coming, the soil samples were treated in *FCFM* moulds by means of full immersion methodology. This can also be observed from Fig. 8(a-b) that “UCS” values increased after 3 days of curing period, which can be attributed due to the fact that a uniform distribution of precipitates in *FCFM* moulds. It may be noted here that 2 days of treatment was given in brass moulds whereas continuous treatment was provided for *FCFMs*. This treatment procedure was chosen for the expulsion of bacteria from the moulds over large span of time. The test results indicate that the treated soil samples failed at lower strain compared to untreated soil, which can be attributed due to stiffer behavior of treated soil specimens. Wani and Mir [17] have also reported similar behavior or bio-cemented soils. The variation of “UCS” and modulus of elasticity with increased curing period is given in Table 2. From Table 2, it is observed that with increase in curing period, the behavior of untreated soil from ductile to brittle behavior for treated soil. The change in soil behavior can also be observed from Figs. 7(a-b) and 8(a-b), which is clearly seen that the failure strain of stabilized soil specimens is decreasing with increase in unconfined compression strength and the curing period for both treatment methods.

Table 2 Variation of “UCS” & modulus of elasticity of stabilized soils with different curing days

CSM	OD	Curing days	UCS (kPa)	Modulus of elasticity (MPa)	Bacteria used	Treatment Approach
0.5	2.0	0	534	3.429	BS	In UCS moulds
0.5	2.0	3	544	5.571		
0.5	2.0	7	541	6.143		
0.5	2.0	0	560	6.429	BS	In <i>FCFM</i>
0.5	2.0	3	585	7.000		
0.5	2.0	7	603	7.428		
0.5	2.0	0	620	8.000	BM	In UCS moulds
0.5	2.0	3	637	8.571		
0.5	2.0	7	632	9.142		
0.5	2.0	0	645	9.285	BM	In <i>FCFM</i>
0.5	2.0	3	659	9.500		
0.5	2.0	7	674	13.333		



### Effect of Biological Processes on the Microstructure of Treated Soil

SEM tests were conducted on untreated and post-test stabilized soil samples at a magnification ranging from 2 to 3k. SEM images for untreated sample (Fig. 9a) showed less interaction between soil particles and changes in soil microstructure are predominantly seen in treated samples (Fig. 9b-d). The flocculated structure and reduced pore size along with formation of new cementitious materials after treatment are also seen in bio-treated soil samples (Fig. 9b-d). Similar test results have also been reported by various researchers for the bio-cemented soils [40]-[41].

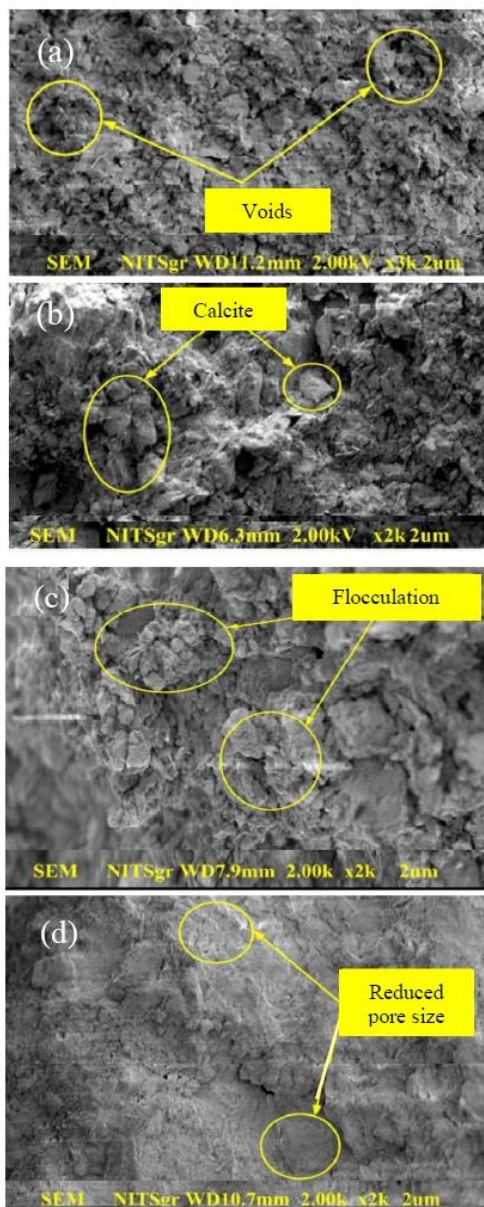


Fig. 9. SEM image for: a untreated sample, b–d bacteria- treated soil samples (Site-2)

### Effect of Biological Processes on the CBR Values of Treated Soil in both Unsoaked and Soaked Conditions

Based on previous research finding, a predetermined CSM of 1.0 for treatment of soil samples for CBR [42]. This was done in agreement with the fact that CSM is directly proportional to the amount of precipitate [43]. The load-settlement curves for CBR tests for site-2 under different treatment conditions are shown in Fig. 10. From Fig. 10, it is seen that the CBR value increased from 1.3% to 8.4% for BS treated soil and 1.3% to 9.1% for BM treated soil in soaked conditions. Likewise, CBR value increased from 5.1% to 13.1% for BS treated soil and 14.1% for BM treated soil in unsoaked conditions respectively.

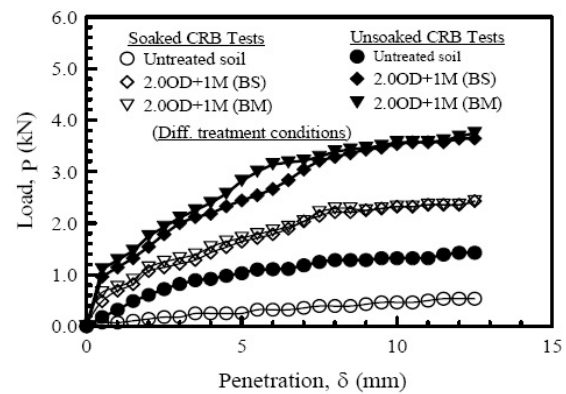


Fig. 10. CBR curves for untreated and treated soil samples (site-2)

The increase in CBR may be attributed due to the reaction of bacteria with the cementation reagent to produce calcite, which binds the soil together and fill the void spaces in the granular soil to increase its strength [44]-[45]. Dejong et al. [15] attributed increase in CBR to be due to higher relative density and increased number of contacts per particle within the dense sand, which contributed to the higher CBR value. The higher precipitation of calcite at 1 CSM must be responsible for enhanced CBR values as the precipitate fills the pores and increases cohesion amongst the grains. The effect of bio-cementation on CBR can also be correlated to the bearing capacity of the same site location as has been studied by the authors wherein the bearing capacity increased up to 2 times in the treated state [17]. The effects on CBR are comparatively low in the unsoaked state when compared to other stabilization techniques like cement, lime or use of geo-synthetics, but still in accordance with Indian Roads Congress for rural roads [46]-[47]. This decrease in CBR can be attributed due increase of

moisture content in the soil specimen, which is given 24h of rest at room temperature (20–25°C) after treatment. The post-test variation of moisture content in the soil specimen with different curing periods for both treatment methods is given in Table 3. From Table 3, it can be observed that the moisture content of “UCS” soil specimen decreases marginally with increasing curing period. However, the CBR soil specimens have higher water holding capacity due to their large area compared to “UCS” specimens. Thus, the CBR soil specimen exhibit low CBR values, which are permissible as per standard Codes, and proves beneficial for the field applications.

Table 3 Post-test variation of moisture content with different curing periods test methods

CSM	Curing days	Testing	Moisture content after testing (%)	Bacteria used	Treatment Approach
0.5	0	UCS	15.0	BS	In UCS moulds
0.5	3	UCS	14.5		
0.5	7	UCS	14.0		
0.5	0	UCS	14.5		In FCFM
0.5	3	UCS	14.5		
0.5	7	UCS	14.0		
1.0	-	CBR	28.0	BM	Bucket
0.5	0	UCS	14.5		In UCS moulds
0.5	3	UCS	14.5		
0.5	7	UCS	14.0		
0.5	0	UCS	14.5		In FCFM
0.5	3	UCS	14.5		
0.5	7	UCS	01.0		
1.0	-	CBR	27.0		Bucket

## CONCLUSIONS

Based on the test results and discussions, the following conclusions were drawn:

1. The UCS values increased from 197 to 544kPa and 197 to 637kPa for *B.S.* and *B.M.* treated samples with 0.5 CSM for 3 day curing period by Bio-cementation technique for soil samples treated in fabricated brass moulds.
2. The UCS values increased from 197 to 603kPa and 197 to 674kPa for *B.S.* and *B.M.* treated samples with 0.5 CSM for 7 days curing period by Bio-cementation for soil samples treated in FCFMs.

3. At 1.0 CSM and 2.0 OD bacterial concentrations, CBR values increased from 5.1% to 13.1% for *B.S.* treated soil and 14.1% for *B.M.* treated soil in unsoaked conditions respectively. The increase in CBR values may be attributed mainly because of the precipitate filling the void spaces and forming a thin crust of calcite over the sample.
4. As the OD, CSM and curing time is increased, the amount of precipitate in the form of calcite increases proportionally. The values for *B.M.* were considerably more in comparison with *B.S.*
5. The SEM analysis showed reduced pore size and agglomeration of particles in the stabilized soils, which supports the test results.

The above experimental procedures have scale effects, and as such, in situ response might be different as the samples used in the laboratories were small and homogeneous. The improvement in the properties of soil largely depends on calcite precipitation which is in turn dependent on many other factors like pattern of precipitation, pH, development of flow paths, temperature, mixing of bacteria with the soil, etc. Taking all the above factors into consideration, the optimization of calcite distribution is not possible by means of model testing in the laboratory. Therefore, the present results can only be taken to be qualitative in nature.

## ACKNOWLEDGMENTS

The investigation reported in this paper formed part of the research carried out in the Geotechnical Engineering Laboratory-I and II of National Institute of Technology, Srinagar, India. The Author would like to thank Institute Administration and Deptt. of Civil Engineering for providing the necessary facilities for carrying out this work and SKUAST-K, Shalimar for proper guidance on bacterial culture preparations and for providing laboratory facilities.

## REFERENCES

- [1]. Mir B. A., Shah Basit M., and Shah Faizan A., Some Model Studies on Reinforced Dredged Soil for Sustainable Environment. In Book: Recent Advances in Environmental Science from the Euro-Mediterranean and Surrounding Regions, In A. Kallel et al. (eds.), Chp No. 94, 2018, pp. 1697-1700.
- [2]. Bartos M. J. Jr., Classification and Engineering Properties of Dredged Soil. Technical Report D-77-18, U.S. Army Waterways Experiment Station, Vicksburg, MS, 1977, Corpus ID: 107373248.
- [3]. Mir B. A. and Mir F. A., Applications and geotechnical evaluation of dredged soil obtained from Dal Lake in Srinagar. Proc. National Conf.

- on Soils and their applications in Civil Engg., 2004, pp. 26-37.
- [4] Mir B. A., Some Studies on Physical and Mechanical Behavior of Dredged Soil from Flood Spill Channel of Jhelum River, Srinagar. *Acta Ingenieria Civil*, Vol. 1, No. 1, 2016, pp. 1-7.
  - [5] Wani K. M. N. S. and Mir B. A., Stabilization of Weak Dredged Soils by Employing Waste Boulder Crusher Dust-A: Laboratory Study. *International Journal of Geotechnical and Geological Engineering*, Vol. 38, No. 6, 2020, pp. 6827-6842.
  - [6] Mitchell J. K., Soil improvement – state of the art report. *Proceedings of the 10<sup>th</sup> International Conference on Soil Mechanics and Foundation Engineering*, Stockholm, Sweden, Vol. 4, 1981, pp. 509-565.
  - [7] Broms B. B., Problems and Solutions to Construction in Soft Clay. *Proceedings of the 6<sup>th</sup> Asian Regional Conference*, Singapore, SMFE, Southeast Asian Society of Soil Engineering, Vol. 2, 1979, pp. 3-38.
  - [8] Butt Wajid Ali, Mir B. A. and Jha J. N., Strength Behavior of Clayey Soil Reinforced with Human Hair as a Natural Fibre. *International Journal of Geotechnical and Geological Engineering*, Vol. 34, No. 1, 2016, pp. 411-417.
  - [9] Elias V., Welsh J., Warren J., Lukas R., Collin J.G. and Berg R.R., *Ground Improvement Methods*. FHWA NHI-06-019 (Vol. 1) and FHWA NHI-06-020 (Vol. 2), 2006, pp. 1056.
  - [10] Holtz R.D., Shang J.Q. and Bergado D. T., Soil Improvement. Chapter 15 in *Geotechnical and Geoenvironmental Engineering Handbook* edited by R.K. Rowe, Kluwer Academic Publishers, Boston, 2001, pp. 429-462.
  - [11] Karol R. H., *Chemical grouting and soil stabilization* revised and expanded. Marcel Dekker Inc., New York, 2003, pp. 1-584.
  - [12] Ho M. H. and Chan C. M., Some Mechanical Properties of Cement Stabilized Malaysian Soft Clay. *World Academy of Science, Engineering and Technology*, 74, 2011pp. 24-31.
  - [13] Mir B. A., Some Studies on the Effect of Fly Ash and Lime on Physical and Mechanical Properties of Expansive Clay. *International Journal of Civil Engineering-Transaction B: Geotechnical Engineering – Geotechnique*, Vol.13, No. 3&4B, 2015, pp. 203-212.
  - [14] Mir B. A., Some Studies on Mechanical Behaviour of Cement Stabilized Dredged Soil from Flood Spill Channel of Jhelum River Srinagar. In *International Congress and Exhibition on Sustainable Civil Infrastructures-Innovative Infrastructure Geotechnology*, 2017, pp. 386-406.
  - [15] DeJong J.T., Mortensen B., Martinez M. and Nelson D. C., Biomediated soil improvement. *Ecol Eng.*, Vol. 36, No. 2, 2010, pp. 197-210.
  - [16] Inavov V. and Chu J., Applications of Microorganisms to Geotechnical Engineering. *Environ Sci Biotechnol*: 7, 2008, pp. 139-153.
  - [17] Wani K.M.N.S. and Mir B.A. Effect of Microbial Stabilization on the Unconfined Compressive Strength and Bearing Capacity of Weak Soils. *Transp Infrastruct Geotechnol*. Vol. 8, No. 1, 2020, pp. 59-87.
  - [18] Mir B. A. and Wani K. M. N. S., Effective Use of Microbes in Waste Soil Stabilization Considering Natural Temperature Variations. *Geomechanics and Geoengineering - An International Journal*, 2021, pp. 1-21.
  - [19] Georgi N. J. and Stathakopoulos I. (2006) Bioengineering techniques for soil erosion protection and slope stabilization. Neapolis University Pafos, Cyprus.
  - [20] Ivanov V., Chu J., Stabnikov V. and Li B., Strengthening of Soft Marine Clay Using Bioencapsulation. *Mar Georesour Geotechnol.*, Vol. 33, No. 4), 2015, pp. 320-324.
  - [21] Phadnis H.S. and Santamarina J. C., Bacteria in Sediments: Pore Size Effects. *Geotech Lett.*, Vol. 1, No. 4, 2011, pp. 91-93.
  - [22] Tian Z-F, Tang X, Xiu Z-L, Xue Z-J., Effect of Different Biological Solutions on Microbially Induced Carbonate Precipitation and Reinforcement of Sand. *Mar Georesour Geotechnol.*, Vol. 38, 2019, pp. 450-460.
  - [23] Hamdan N., Kavazanjian J., Rittman B. E. and Karatas I., Carbonate mineral precipitation for soil improvement through microbial denitrification. In *Proc.of Geo-Frontiers 2011: Advances in Geotechnical Engineering*, Dallas TX, ASCE, Geotechnical Special Publication, Vol. 211, pp 3925-3934.
  - [24] Dawoud O., Chen C.Y. and Soga K., Microbial Induced Calcite Precipitation for Geotechnical and Environmental Applications. In *Proc. of New Frontiers in Geotechnical Engineering*, ASCE Geotechnical Special Publication, Vol. 234, 2014, pp. 11-18.
  - [25] Mitchell J.K. and Santamarina J.C., Biological Considerations in Geotechnical Engineering. *J Geotech Geoenviron Eng.*, Vol.131, No. 10, 2005, pp. 11222-11233.
  - [26] Sari Y.D., Soil Strength Improvement by Microbial Cementation. *Mar Georesour Geotechnol*. Vol. 33, No. 6, 2015, pp. 567-571.
  - [27] Reichle D. E., The role of soil invertebrates in nutrient cycling. *Ecol Bull* 25, 1977, pp. 145-156.
  - [28] Whiffin V., Microbial CaCO<sub>3</sub> precipitation for the production of bio-cement (Ph.D. thesis).



- Mudroch University, Perth, Western Australia, 2004, pp. 1-154.
- [29] Wani K. M. N. S. and Mir B. A. (2020). Unconfined Compressive Strength Testing of Bio-cemented Weak Soils: A Comparative Upscale Laboratory Testing. *Arabian Journal for Science and Engineering*, Vol. 45, No. 10, 2020, pp. 8145–8157.
- [30] IS: 2720-part-1., Indian Standard Code for preparation of soil samples, BIS, New Delhi, 1980.
- [31] IS: 2720-part-8., Indian Standard Code for Determination of Water Content-Dry Density Relation Using Heavy Compaction, BIS, New Delhi, 1980.
- [32]. IS: 2720-part-10., Indian Standard Code for Determination of shear strength parameter by unconfined compression test, BIS, New Delhi, 1973.
- [33]. IS: 2720-part-16., Indian Standard Code for Laboratory Determination of CBR Tests, BIS, New Delhi, 1987.
- [34]. Wani K.M.N.S., Mir B. A. and Sheikh I.R., Effect of Microbes on the Unconfined Compressive Strength of Dredged Sediments. In Book: Sustainable Development through Engineering Innovations- Vol. 113: Chp. 15, 2021, pp 163-174.
- [35] Ramachandran S. K., Ramakrishnan V. and Bang S. S., Remediation of concrete using micro-organisms. *ACI Mater J Am Concr Inst.*, Vol. 98, No. 1, 2001, pp. 3–9.
- [36] Hammes F. and Verstraete W., Key roles of pH and calcium metabolism in microbial carbonate precipitation. *Rev Environ Sci Biotechnol.*, Vol. 1, No. 1, 2002, pp. 3–7.
- [37] Cheng L., Shahin M.A., Cord-Ruwisch R., Addis M., Hartanto T. and Elms C., Soil Stabilization by Microbial-Induced Calcite Precipitation (MICP): Investigation into Some Physical and Environmental Aspects. *Proc. 7<sup>th</sup> Int. Congress on Environmental Geotechnics: ICEG2014*. Engineers Australia, 2014, pp .1-8.
- [38] Umar M., Kassim K. A. and Chiet K. T. P., Temperature Effects on the Strength Properties of Microbially Stabilized Residual Soil. *Journal Teknologi.*, Vol. 78, No.7, 2016, pp. 101-104.
- [39] Lee M. L., Ng W. S. and Tanaka Y., Stress-Deformation and Compressibility Responses of Bio-Mediated Residual Soils. *Ecol Eng.*, Vol. 60, No.1, 2013, pp. 42–149.
- [40] Xiao Y., Zhao C., Sun Y., Wang S., Wu H., Chen H. and Liu H., Compression behavior of MICP-treated sand with various gradations. *Acta Geotech.*, Vol. 16, No. 5, 2021, pp. 1391–1400.
- [41] Wani K.M.N.S. and Mir B.A., Effect of biological cementation on the mechanical behaviour of dredged soils with emphasis on micro-structural analysis. *Int J Geosynth Ground Eng.*, Vol. 5, No. 4, 2019, pp. 1-14.
- [42] Zhao Q., Li L., Li C., Li M., Amini F. and Zhang H., Factors Affecting Improvement of Engineering Properties of MICP-Treated Soil Catalyzed by Bacteria and Urease. *J Mater Civ Eng*. Vol. 26, No. 12, 2014, pp. 1-10.
- [43] Chiet KTP, Kassim KT, Chen KB, Martula U, Yah CS, Arefnia A (2016). Effect of reagents concentration on biocementation of tropical residual soil. In: IOP conference series: materials science and engineering, vol 136, p
- [44] Soon N.W., Lee M.L., Tan C.K. and Hii S. L., Factors Affecting Improvement in Engineering Properties of Residual Soil through Microbial-Induced Calcite Precipitation. *J Geotech Geoenviron Eng*. Vol. 140, No.5, 2014, pp.1-11.
- [45] Congress I. R., Guidelines for the Design of Flexible Pavements. *Indian Code of Practice, IRC:37*, 2018, pp. 1-108.
- [46] Sharma A. and Ramkrishnan R., Study on Effect of Microbial Induced Calcite Precipitates on Strength of Fine Grained Soils. *Perspect Sci.*, Vol. 8 (C), 2016, pp.198–202.
- [47] Ibrahim A. O. and Oladunni O. A., Comparative Effect of Microbial Induced Calcite Precipitate, Cement and Rice Husk Ash on the Geotechnical Properties of Soils. *SN Applied Sciences*, 2:1157, 2020, pp. 1-12.

## ***Technical Papers***

## ***Geotechnique***

## **FINITE ELEMENT ANALYSIS OF BEAM RESTING ON FOOTING**

<sup>1</sup>Radhi Alzubaidi, <sup>2</sup>Husain M Husain and <sup>3</sup>Samir Shukur

<sup>1</sup>Professor of Civil engineering, college of Engineering, University of Sharjah, Sharjah, UAE.

<sup>2</sup>Formerly professor of civil engineering, University of Baghdad, Baghdad, Iraq.

<sup>3</sup>MSc student, College of Engineering, University of Kufa, Iraq.

### **ABSTRACT**

Unreinforced concrete members used in construction projects lead to low costs and easy construction, a nonlinear three –dimension finite element technique utilized in present research to explore the load deflection of unreinforced concrete beam rest on strip footings by using the computer program(ANSYS 5.4). , the criteria used by solving the non-linear equation by conducting incremental and iterative method running load procedure. The developed Newton –Raphson method been conducted for non-linear solution algorithm and load or displacement that used as a convergence criterion. A vast Investigation been conducted to explore the effects on such parameters such as depth ,width and length of foundation. The results of the experimental and theoretical load – deflection curves showed a great agreement with those analyzed by four applications using the finite element technique. The present finite element and available experiential results showed a good agreement. the percentage of differences not exceeding 6% in the ultimate load prediction and 15.6% in deflection in case of using interface element and critical state model.

*Keyword: Strip footing, Finite element, Deflection, Depth, Length*

### **INTRODUCTION**

Design of different type of foundations has led to the concept of transmitting the load to soil through development a special member system. The foundations types are varied according to different requirements. Concrete or steel members like beams or plates rest on layered soils have attracted the attention of both structural and geotechnical engineers and merges the effect on both superstructure and substructure element.[1] presented his theory of the modulus of subgrade reaction, the basic assumption of this model is the relation between the applied surface pressure and the vertical surface deflection at every point. [2] studied interaction analysis for the design of open plane frame resting on soil, the soil has been modeled as 4-node isoparametric element, a plane strain approach is adopted for representing the soil. A comparison is made between the more realistic half-space continuum and the plane-strain approach to examine the approximation involved in the latter type of representation of the soil. They concluded sagging moments in superstructure beams as obtained using plane-strain model were always greater than those obtained from the elastic half. [3] investigated into numerical analysis of most deep excavation and stated that most designers careless about structural modelling. They modify a 3D finite element method to model in their solutions . The case study was a building project located in Bangkok .The structure models used

including diaphragm wall, diagonal braces and bored piles. They concluded that the types of elements implemented to model the structures distinctively affect the analysis of finite element.

[4] presented a finite element modeling of beam resting on a two-parameter layered soil, in their model analysis, they consider the strain energy solutions, the shear strain of the beam element and soil foundation. They concluded that the shear deformations showed crucial influence on the beam, on the structure and on the interface behaviors. [5] studied the development of a methodology for the identification of optimal design parameters for a system of beams resting on a stone

column–improved soft soil. They conducted a finite difference–based simulation model and an evolutionary multiobjective optimization model. In their study tried to minimize the settlement at the center of the beam and the maximum shear force. They concluded that the evaluation of the system showed that stiffness of the stone columns or modular ratio and flexural rigidity of the beam are the most important parameters for optimal design. [6] presented a developed method for nonlinear analysis of Euler-Bernoulli beams resting on heterogeneous multilayered soil.

They obtained the governing differential equations for beam and soils displacements using the virtual work, the equations been solved using one-dimensional finite-element and finite-difference methods, the analysis showed that beam responses with accuracy comparable with those obtained from equivalent two-dimensional finite-element analysis are obtained within seconds. [7] studied a boundary element method to analyze the elastic foundation finite beams on 2D plane-strain and 3D multilayered isotropic soils. They tried to explore the solution of multilayered elastic soils that obtained to be a kernel function of BEM analysis. They found that with the displacement and stress condition of coordination between beam and soil, the solution is acquired for beams resting on multilayered

### FOUDATION ANALYSIS METHOD

[8] established a computer program capable of analyzing combined footing and irregular with openings or notches and non –prismatic sections and resting on layered medium ,by using the finite element method . In his study used “the thin plate bending theory”. [9] analyzed the combined footings and mats foundations utilized the finite grid method and prepared nomograms which can aid the designer in rapid prediction of displacements of displacements and bending moments. The results of the study compared with those obtained by finite element and Hetebyi solution. He also studied the properties of each soil and foundation ,variation of thickness and configuration of foundation, effect of adding stone columns and probable existence of soil voids. [10] proposed a non-local viscoelastic foundation model to analyze the dynamics of beams with different boundary conditions using the finite element method. They conclude that the case study, prdicted that the finite element technique is efficient for the dynamic analysis of beams with non-local viscoelastic foundations. [11] investigate into behavior of shallow foundation resting on multi layered and homogeneous soil under dynamic loading. They used 2-dimensional finite element software Cyclic TP to modeling the soil foundation system. In their conclusion ,they compared the results to understand the effect of layered soil on dynamic load response of soil foundation system.

### INTERFACE MODEL

The use of finite element for analysis of soil structure interaction problems has been limited to some extent, however due to difficulties in represent the interface between soil and structure ,most analysis been performed using one of two limiting

assumptions concerning the characteristics of soil – structure interface :

- 1- The interface is perfectly rough ,with no possibility for slip between the soil and the structure .
  - 2- The interface is perfectly smooth ,with no possibility for shear stress that would retard relative movement between the soil and the structure ([12].
- Many types of finite elements have been developed foe representing the soil- structures interface in finite element analysis in more realistic fashion. [13] In their study to analyze the seismic of soil- structure interaction in rigid rock ,applying the finite element method ,there are many methods modified to input earthquake on the lateral boundary of finite element model. They concluded that the formulations and ABAQUS implementations of these boundaries were used . The accuracy properties of these boundaries are then compared by numerical examples including the free-field and SSI problems. The comparison studies indicate that the free and VS boundaries failed to reproduce the free-field and SSI responses when a relatively small size SSI model is employed. [14] studied the developments in the particle finite element method (PFEM) that used for analysis of many complex coupled problems in mechanics involving fluid–soil–structure interaction (FSSI). They showed some examples of application of the particle finite element method to solve fluid–soil–structure interaction problems like, the motion of rocks by water streams, the erosion of a river bed near to a bridge foundation, the stability of breakwaters and constructions sea waves and the study of landslides. [15] in their study to review the non-linear analysis of soil structure interaction problem. They discussed the coupled finite element modeling of soil structure interaction (SSI) system with soil non-linearity and interface element modeling. In their reviewing study stated that the focusing is on advantages and disadvantages of the methods discussed according to their applicability, accuracy and caliber to idealize the superstructure and soil.

### MODELLING OF MATERIAL

The most powerful representation that incorporates for concrete and soil behavior is the elastoplastic model. The model exhibits nonlinearities, failure, and residual strain upon loading to initial stress condition. Several location of yield points are introduced due to various material types , however yield is the starting point of plastic behavior and the end points of elastic behavior for the elastic- plastic material . the criteria for deciding which combination of stress will cause yielding and this called yield criterion. In present study the concrete is modeled by Willam and Warnk yield

surface, while the soil is modeled by Druker- Prager yield surface.

### MODELING OF CONCRETE MATERIAL

There are many constitutive models which have been developed to predict the response of plain and reinforced concrete under various stress states. The main constitutive models are the elasticity based models and plasticity based models. The elasticity – based models describe the concrete as a linear elastic or non-linear elastic material. The elasticity models have been used to study the non-linear response of plain and reinforced concrete beams, panels ,and shells in which the main nonlinearity is introduced by the cracking and widening of cracks in the concrete[16] . Elastic model for concrete in compression can be significantly improved by assuming a nonlinear elastic stress-strain relationship. [17] proposed a nonlinear elastic –strain relationships for concrete materials, they can generally classify into

- 1- The total stress-strain formation in the form of secant stiffness relation
- 2- The incremental stress-strain formulation in the form of tangential stiffness formulation.

### Finite element representation of interface

The present study describes a technique for solving two and three dimensional interface problems. The elements (contact 52) shown in Fig. 1 are adopted in present research

The elements (contact 52) shown in Fig. 1 are adopted in present research.

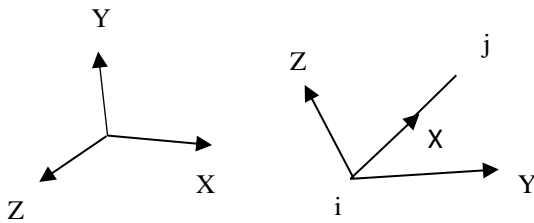


Fig. 1 CONTACT52 3-D point –to- point (ANSYS Manual 1997)

The interface element includes normal and sliding forces [18] and [19]. This element has one of two condition if the elastic COULOMB friction is used :

- 1- Stuck element (no sliding)

$$\mu |f_n| > |f_s|$$

Where:

$\mu$ = coefficient of friction

$f_n$ = normal force

$$f_n = K_n (u_{n,j} - u_{n,i} + d)$$

$K_n$  = normal stiffness

$u_{n,j}$ =displacement of node j in normal direction

$u_{n,i}$ = displacement of node i in normal direction

$d$ = distance between nodes.

Also

$$f_s = K_s (u_{s,j} - u_{s,i} - u_o)$$

$f_s$ = sliding force

$K_s$ =sticking stiffness

$u_{s,j}$ = displacement of node j in sliding direction

$u_{s,i}$ = displacement of node i in sliding direction

$u_o$ = distance that nodes i and j have slide with respect to each other

Writing:

$$\{F\} = [K] \{\Delta\} \quad (1)$$

$$\{F\} = \begin{bmatrix} f_n \\ f_{sy} \\ f_{sz} \\ f_n \\ f_{sy} \\ f_{sz} \end{bmatrix} \quad (2)$$

Where :

$f_n$  = normal force

$f_s$  = stick force (in y and z direction)

$$\{\Delta\} = \begin{bmatrix} u_i \\ v_i \\ w_i \\ u_j \\ v_j \\ w_j \end{bmatrix} \quad (3)$$

$$[K] = \begin{bmatrix} kn & 0 & 0 & -kn & 0 & 0 \\ 0 & ks & 0 & 0 & -ks & 0 \\ 0 & 0 & ks & 0 & 0 & -ks \\ -kn & 0 & 0 & kn & 0 & 0 \\ 0 & -ks & 0 & 0 & ks & 0 \\ 0 & 0 & -ks & 0 & 0 & ks \end{bmatrix} \quad (4)$$

#### 1. Sliding element

If  $\mu |f_n| = |f_s|$

Then sliding occurs in both directions, the stiffness matrix (in element coordinate) is:

$$[K] = \begin{bmatrix} kn & 0 & 0 & -kn & 0 & 0 \\ 0 & 0 & 0 & 0 & 0 & 0 \\ 0 & 0 & 0 & 0 & 0 & 0 \\ -kn & 0 & 0 & kn & 0 & 0 \\ 0 & 0 & 0 & 0 & 0 & 0 \\ 0 & 0 & 0 & 0 & 0 & 0 \end{bmatrix} \quad (5)$$

#### ANSYS Computer Program

[20]in the present study used a computer program ANSYS 5.4 to analyze plain concrete beams rested on soil. The program has the capacity to solving linear and nonlinear problems including the effect of cracking, crushing, yielding of reinforcement (if existing), creep, bond slip, temperature change, with 165 different elements conducted in the program.

#### Numerical applications

Numerical actual cases are conducted to compare the results obtained by the present method of finite elements with those obtained from experimental or analytical solutions.

A number of numerical examples have been also analyzed by the computer program ANSYS 5.4. The examples also used to check the validity of the material models used and the applicability and capability of the analysis method adopted in present research where different types of elements are employed. The theoretical study is approximate in nature due to different factors mainly:

- 1- Approximation in the material modeling of concrete and soil.
- 2- Approximation inherent in discretization in finite element technique.
- 3- Approximation in the integrations used in the numerical analysis.
- 4- Approximation introduced due to the type of procedure used in solving the nonlinear system of equations.

The main results obtained by the solution introduced through present study are the load – deflection response, crack propagation and stress distribution.

#### BEAM REST ON STRIP FOOTING

A long strip footing with uniformly distributed load of 450 MPa lies on a surface of homogeneous isotropic linear elastic half space was analyzed numerically by [21]. Table 1, showed the details of the problem. According to the symmetry, only one- half of the case considered. A mesh of 1338 elements was used to model the concrete, soil and interface. The details of geometry and the finite element mesh are shown in Fig. 1 and Fig. 2 respectively. Fig. 3 shows the load – deflection results obtained by the present study and compared with results predicted by [21] using the finite element and infinite elements for the soil, the results showed a good agreement. The cracks patterns at the bottom surface of the beam at initial cracking and at failure are shown in Fig. 4. It can be noted that first cracking appeared at a load 300 KPa, the initial cracks appeared at the bottom region of the beam. As the load increased, the value of stress in tension zone



increased and cracks extended towards the top and sides. distribution stress.

### Parametric Study

There are some parameters that affect the behavior of the plain concrete strip foundation on soil under static load been studied. These parameters include the effect of beam's dimension like length, width and depth.

#### Effect of Beam Depth

The effect of depth of beam on deflection been investigated by [20], where 6 values of depth been used while the length and width are kept constant, equal to 6 m and 0.5 m respectively. Fig. 5 showed that there is a distinctive decrease in deflection when increasing the depth of the beam, under the same load. This result seemed to be reasonable for increasing the flexural rigidity for strip footing

#### Effect of Beam Width

The investigation of beam width on deflection carried out using 8 values of beam width while keeping the length and depth constant. Fig. 6 showed that there a considerable increase in deflection of the beam with increasing the width, this may attribute to the increase of the concrete mass.

#### Effect of Beam Length

The effect of length of the beam studied by considering 7 values of length while keeping the width and depth

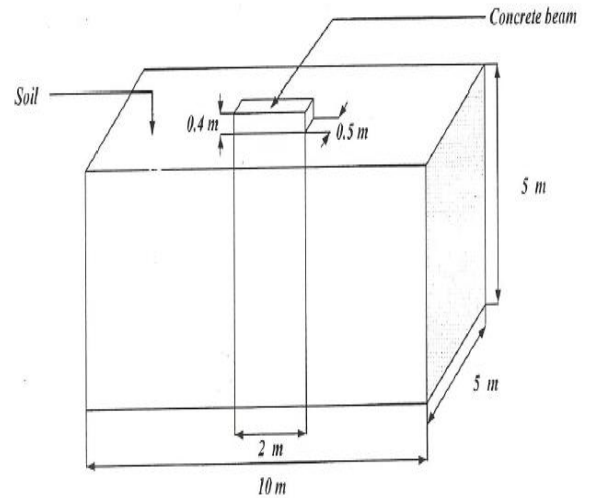


Fig.1 Geometrical details of strip footing

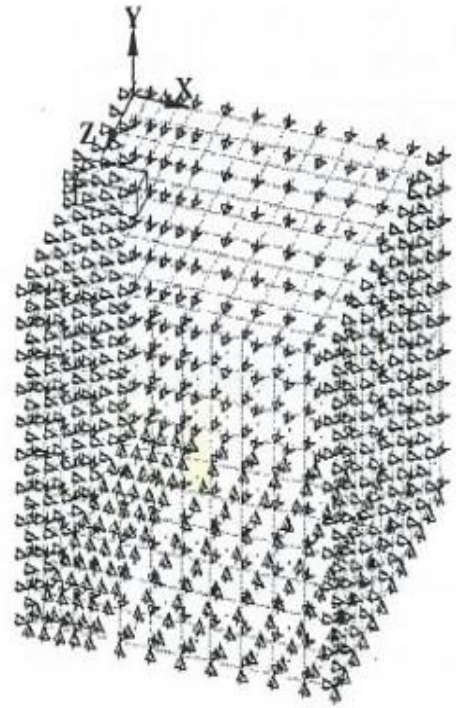


Fig. 2 Finite element mesh of strip footing

Table. 1 Material properties of strip footing

Concrete	Young's modulus	$E_c$ (/mm <sup>2</sup> )23000
	Compressive strength	$f_c$ (N/mm <sup>2</sup> )25
	Tensile strength	$f_t$ (N/mm <sup>2</sup> )2.5
	Poisson' ratio	$\nu_c$ 0.2
Soil	Young's modulus	$E_{so}$ (N/mm <sup>2</sup> )12
	Poisson' ratio	$\nu_{so}$ 0.3
	Cohesion	$C$ (N/mm <sup>2</sup> )0
	Angle of internal friction	38
Interface	Factor friction	0.3

constant, the results as shown by Fig. 7 that the deflection decreased as the length increased, this also due to increase of the mass of the concrete.

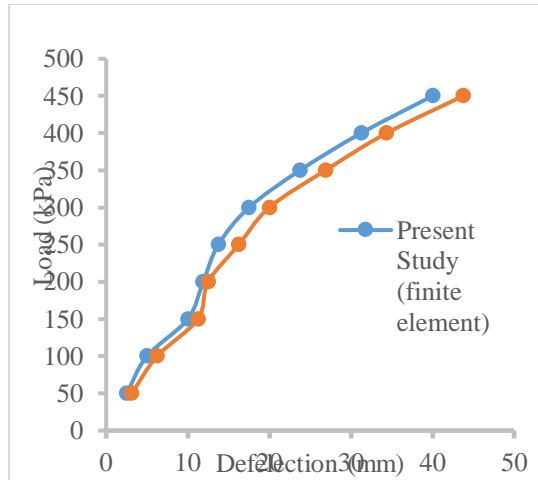
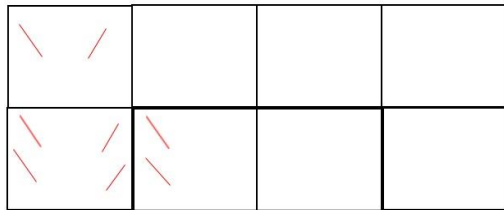


Fig.3 Load -deflection curve of strip footing



At load 300 kPa

Fig.4 Crack patterns of strip footing

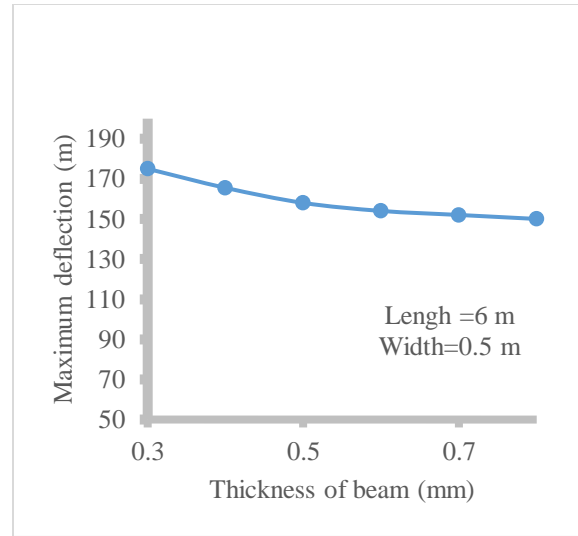


Fig.5 Effect of thickness on load-deflection curve for strip footing

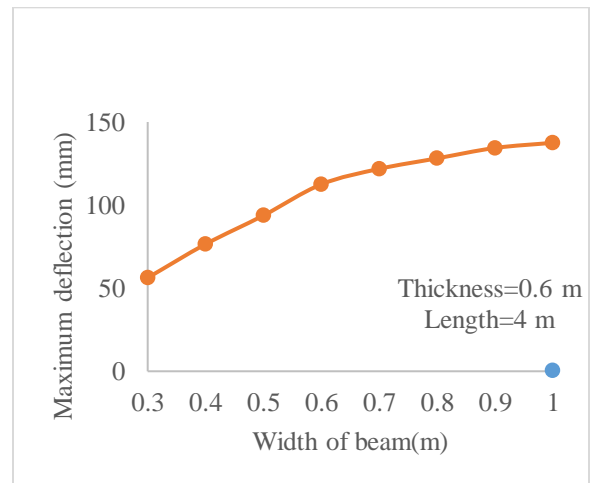


Fig.6 Effect of width on load- deflection curve for strip footing

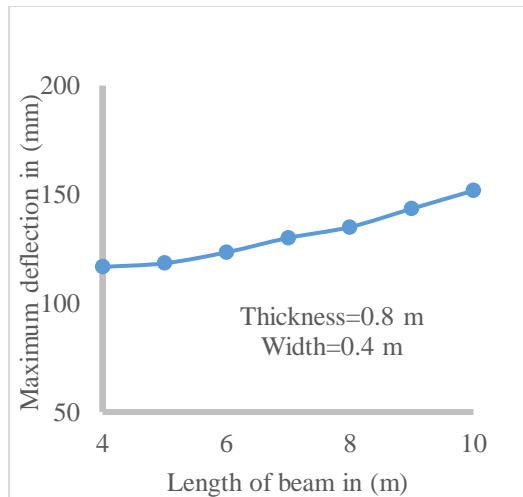


Fig.7 Effect of length on load- deflection curve

## CONCLUSIONS

A numerical method of analysis for strip beam foundation rest on soil under static load been presented. The analysis implemented 8-node brick has been used to model the concrete foundation. The soil been modelled by 8-node brick element, while the interaction between the soil and the concrete foundation is simulated by contact interface element. Based on the present finite element developed program ,which been conducted through the present work , the following conclusions can be drawn as follows:

- 1-The ability of using unreinforced concrete beams in the foundation with a good performance even after the occurrence some cracks.
- 2-The results obtained from the present finite element method showed that the computational model adopted in present research is suitable for prediction of load-deflection behavior of unreinforced concrete foundation under static load. The comparison between the numerical and the available experimental results showed a good agreement.
- 3- Increasing the depth of the strip footing leads to decreasing the deflection under the same static load. This seems reasonable due to increase in the flexural rigidity.
- 4-The depth of the strip footing when increased ,the inflection will experienced distinctive increase due to increase in concrete mass.
- 5- When increasing the length of the strip footing ,showed increase in the deflection of the beam due to decrease in stiffness of the strip footing beam.

## REFERENCES

- [1] Winkler (1967), E. "Die Lehre Von Der Elastizität und Festigkeit " Dominicus, Prague, 1976.
- [2] Rao P, Rambabu, K.V, and Allam, M.M. (1995). 'Representation of Soil Support in Analysis of Open Plan Frames'. Computers and Structures, **56**(6), 917-925
- [3] Likitlersuang, S, Chheng, and Keawsawasvong, S. (2019). 'Structural Modelling in Finite Element of Deep Excavation' , Journal of GeoEngineering, **14**(3), 121-128.
- [4] Boudaa ,S, Khalfallah, S, and Bilotta, E. (2019) 'Static interaction analysis between beam and layered soil using a two-parameter elastic foundation'. International Journal of Advanced Structural Engineering., **11**, 21–30.
- [5] Deb ,K. and Dhar, A. (2013). ' Parameter estimation for a system of beam resting on stone column-reinforced soft soil'. International Journal of Geomechanics , **13**(3).
- [6] Haldar, S and Basu , D.(2016). 'Analysis of Beams on Heterogeneous and Nonlinear Soil ' . International Journal of Geomechanics. **16**(4).
- [7] Al,Z , Li, Z, and Cheng ,Y(2014) " BEM analysis of elastic foundation beams on multilayered isotropic soils " Soils and Foundations, **54**(4):667-674.
- [8] Munther, J.(1971). 'Mats and combined Footings Analysis by Finite Element Method'. ACI Journal, **68**(12), 945-949.
- [9] Noori, F.(1990). 'Effect of Foundation Soil Rigidity on Concrete Pressure Distribution Beneath Rafts Foundations', MSc Thesis ,University of Technology ,Bagdad , Iraq.
- [10] Friswell , M, Adhikari , S and Lei,Y. (2007) . 'Vibration analysis of beams with non-local foundations using the finite element method'. International journal for numerical methods in engineering, **71**, 1365-1386
- [11] Verma,A and Mohanty ,S. (2018). 'Finite element analysis of foundation on layered and homogeneous soil deposit under dynamic loading'. Indian geotechnical conference, Bengaluru, India
- [12] Clough ,G and Duncan ,J. (1971) . 'Finite Element Analysis of Retaining Wall Behavior' , Journal of Soil Mechanics and Foundation Division ,ASCE, **97**(SM 12)
- [13] Li,Y, Zhao, M , Xu, C, Du,X, and Li,Z .(2018) . 'Earthquake input for finite element analysis of soil- structure interaction on rigid bedrock'. Tunneling and Underground Space Technology, **79**, 250-262
- [14] Oñate, E, Celiqeta, M, Idelsohn,S, Salazar,F, and Suárez,B.(2011). 'Possibilities of the particle

- finite element method for fluid–soil–structure interaction problems'. Computational Mechanics,48
- [15] Dhadse, G, Ramtekkar, G and Bhatt, G. (2021). 'Finite Element Modeling of Soil Structure Interaction System with Interface: A Review'. Archives of Computational Methods in Engineering , 28, 3415–3432.
- [16] Chen, W., and Saleeb, A . (1982) . Constitutive Equations for Engineering Material, John Willey and Sons, New York.
- [17] Yasuhiro ,C and Chen ,W. (1987). ' Hypoelastic – Perfectly Plastic Model for Concrete Material . Journal of Engineering Mechanics, ASCE, 113(12),840- 1858.
- [18] Mazurkiewicz M, and Ostachowicz, W. (1983). 'Theory at Failure Element Method for Elastic Contact Problems of Solid Bodies'.Computers and Structures,17(1),51-59.
- [19] ANSYS Manual (1997) ,Version 5.4 , Swanson Analysis System .Inc., Houston , Pennsylvania ,
- [20] Shukur, S. (2002). 'Analysis of Unreinforced Concrete Beams on Soil By Finite Elements'. MSc thesis, University of Kufa, Iraq.
- [21] Sitharm ,T and Kamar, I.(1998). 'Non-Linear Analysis of Geomechanical Problems Using Coupled Finite and Finite Element'. Geotechnical and Geological Engineering,16,129-149

# ANALYSIS AND DESIGN ON VARYING THE OFFSET DISTANCES IN SUPERIMPOSED MECHANICALLY STABILIZED EARTH WALLS

Vuttichai Chatpattananan<sup>1</sup> and Vatanavongs Ratanavaraha<sup>2</sup>.

<sup>1</sup>King Mongkut's Institute of Technology Ladkrabang, Thailand;

<sup>2</sup>Suranaree University of Technology, Thailand

## ABSTRACT

Superimposed MSE walls or multi-tier MSE walls are frequently used due to their eye-pleasing, economical, and safety requirements compared with single tall MSE walls. Designing an MSE wall requires checking the failure modes in its external stability, internal stability, and global stability. Calculating the external stability and global stability for superimposed walls is well explained. Internal stability, however, is more complicated in calculating the additional vertical stress from the upper wall as an equivalent surcharge on the lower wall with its magnitude determined by the offset distance. By varying offset distances, the additional vertical stress can be categorized into three cases. Case 1 is the maximum additional vertical from the upper wall load when the offset distance is less than  $H_1 \tan(45^\circ - \phi_r/2)$ . The additional vertical stress is zero in case 3 where the offset distance is greater than  $H_1 \tan(90^\circ - \phi_r)$ . In case 2, the additional vertical stress is a hyperbola function that can be calculated easily using the proposed equation  $\sigma_i = [(H_L - z_1) / (z_2 - z_1)] (\gamma H_L + q)$  in Eq. (7) with geometric and algebraic explanations are used through a numerical example in designing a superimposed wall.

**Keywords:** Additional vertical stress, Internal Stability, Mechanically stabilized earth walls, Multi-tier walls, Superimposed walls.

## INTRODUCTION

Mechanically stabilized earth walls or MSE walls are retaining walls consisting of facing units, reinforcements using metal strips or geogrids, and reinforced backfill soil. MSE walls can be single walls or complex geometric walls like superimposed walls. Superimposed walls or multi-tier walls are frequently used due to their eye-pleasing, economical, and safety requirements compared with single tall MSE walls. Designing an MSE wall requires checking the failure modes in its external stability, internal stability, and global stability. FHWA [1] and AASHTO [2] provide details guidelines and clear calculation examples for designing single walls. However, [1] provides only two pages as shown in Fig. in designing superimposed MSW walls.

FHWA/TX-2 [3] suggest design methods for multi-tiered MSE retaining walls by treating the upper-tier wall as an equivalent surcharge on the lower-tier wall with its magnitude determined by the offset distance. Different offset distances determine different equivalent surcharges. Figure 1 shows that there are three cases in which calculating the additional vertical stress depends on the offset distance.

FHWA/TX-1 [4] provides calculation examples but with some parts of the internal stability checking which is rather complicated and may lead to mistaken designs that are evidenced in some superimposed wall damages due to misunderstanding concepts or

designs.

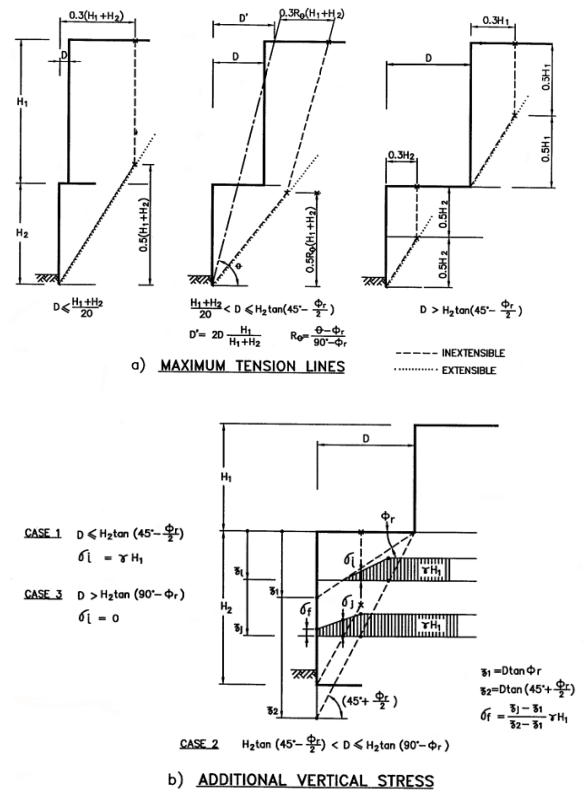


Fig. 1 Design rules for superimposed walls [1]

An example of this complicated design concept is that FHWA [1] mentions that a footing located

outside case 1 is not a surcharge on the lower wall in Fig. 1 while an upper wall in case 2, that is outside case 1, is a surcharge distributed to the lower wall. This reflects the main question in designing a superimposed wall is how much the superimposed load or the additional vertical stress in Fig. 1 is at different offset distances.

This study provides concepts and proposed an easier formula than FHWA/TX [4] for calculating the additional stress imposed on the lower wall. A numerical example is used for calculation details for the internal stability checking for 2 tiers of superimposed walls at different offsets. External stability and global stability are omitted due to space limitations.

## DESIGN CONCEPT

Let  $D$  be the offset distance shown in Fig. 2.  $H_U$  or  $H_1$  Fig. 2 is the upper wall height.  $H_L$  or  $H_2$  Fig. 2 is the lower wall height.  $\phi_r$  is the reinforced soil internal friction angle of both the upper wall and the lower wall.  $\gamma$  is the reinforced soil density of both the upper wall and the lower wall.  $q$  is the surcharge on the upper wall.

### External stability

For external stability checking, there are 3 cases as follows:

Case 1) If  $D \leq (H_U + H_L)/20$ , the wall should be designed as a single wall with a height  $H = H_U + H_L$ .

Case 2) If  $(H_U + H_L)/20 \leq D \leq H_L \tan(90 - \phi_r)$ , the upper wall in a surcharge acting upon the lower wall.

Case 3) If  $D \geq H_L \tan(90 - \phi_r)$ , there is no superimposed load from the upper wall to the lower wall.

### Internal stability

For internal stability checking, there are 3 cases as follows:

Case 1)  $D \leq H_L \tan(45 - \phi_r)$ ,  $\sigma_i = \gamma H_U$ . This case includes the external stability case 1 and some part of the external stability case 2 where  $(H_U + H_L)/20 \leq D \leq H_L \tan(45 - \phi_r)$

Case 2)  $H_L \tan(45 - \phi_r/2) \leq D \leq H_L \tan(90 - \phi_r)$ ,

$$\sigma_i = \frac{(\gamma H_U + q) - \sigma_f}{(z_2 - d_i) \tan(45 - \phi_r/2)} L_a + \sigma_f \quad (1)$$

$$\sigma_f = \frac{d_i - z_1}{z_2 - z_1} (\gamma H_U + q) \quad (2)$$

$$z_1 = D \tan \phi_r \quad (3)$$

$$z_2 = D \tan(45 + \phi_r/2) \quad (4)$$

$$L_{ai} = (H_L - d_i) \tan(45 - \phi_r/2) \quad (5)$$

$L_{ai}$  is the active zone length of the  $i^{\text{th}}$  layer of reinforcement.

$d_i$  is the depth of the  $i^{\text{th}}$  layer of reinforcement..

$\sigma_i$  is the additional stress on the  $i^{\text{th}}$  layer of reinforcement caused by the upper wall.

$\sigma_{fi}$  is the additional stress at the wall face on the  $i^{\text{th}}$  layer of reinforcement caused by the upper wall.

Equation (1) is from a similar triangle in Eq. (6). This similar triangle is also shown later in Fig 6.

$$\frac{(\gamma H_U + q) - \sigma_f}{(z_2 - d_i) \tan(45 - \phi_r/2)} = \frac{\sigma_i - \sigma_f}{L_a} \quad (6)$$

By substituting Eq. (2), Eq. (3), Eq. (4) in Eq. (5), or Eq. (6),  $\sigma_i$  shown in Eq. (7) remains constant for all reinforcement layers and does not depend on the layer depths,  $d_i$ .

$$\sigma_i = \frac{(H_L - z_1)}{(z_2 - z_1)} (\gamma H_L + q) \quad (7)$$

Case 3) If  $D \geq H_L \tan(90 - \phi_r)$ ,  $\sigma_i = 0$ . This case is the same as the external stability case 3.

### Combining external stability and internal stability

When considering both external stability and internal stability, there are four cases to calculate additional stress ( $\sigma_i$ ) as follows: case 1)  $D \leq (H_U + H_L)/20$ , case 2)  $(H_U + H_L)/20 \leq D \leq H_L \tan(45 - \phi_r)$ , case 3)  $H_L \tan(45 - \phi_r/2) \leq D \leq H_L \tan(90 - \phi_r)$  and case 4)  $D \geq H_L \tan(90 - \phi_r)$ .

Let  $D_1 = (H_U + H_L)/20$ ,  $D_2 = H_L \tan(45 - \phi_r/2)$ ,  $D_3 = H_L \tan(90 - \phi_r)$ . The offset distances  $D_1$ ,  $D_2$ ,  $D_3$  are shown in Fig. 3. In case 1,  $D$  is less than  $D_1$ , both the upper wall and lower wall will be treated as one wall. In case 4,  $D$  is greater than  $D_3$ , both the upper wall and lower wall will be treated separately as two walls. In case 2,  $D$  is between  $D_1$  and  $D_2$ , the additional stress is simply  $\sigma_i = \gamma H_U$ . In case 3,  $D$  is between  $D_2$  and  $D_3$ , the additional stress  $\sigma_i = \frac{(H_L - z_1)}{(z_2 - z_1)} (\gamma H_L + q)$  as mentioned in Eq. (7).

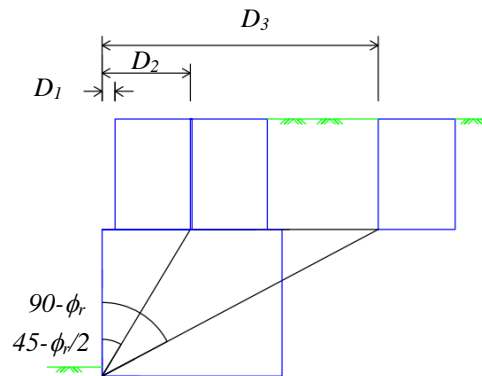


Fig. 2 Offset distances showing  $D_1$ ,  $D_2$ ,  $D_3$

## A NUMERICAL EXAMPLE

The soil parameters, surcharge, and wall geometry for this illustrated example are shown in Table 1. The



total height,  $H = H_U + H_L = 3 + 4 = 7$  meters. For the reinforcement length [1] with  $H_U = 3$  meters, the upper wall reinforcement length is  $L_U = 0.7H_U = 0.7 \times 3 = 2.1$  meters. The lower wall reinforcement length is  $L_L = 0.7(H_U + H_L) = 0.7H = 0.7 \times 7 = 4.9$  meters. The minimum lower wall reinforcement [1]  $L_L = 0.6(H_U + H_L) = 4.2$  meters is not enough that is later shown in Table 5 at layer 8 representing the top reinforcement of the lower wall that  $L_T = 4.89$  meters which is less than 4.2 meters. With  $D = 3$  meters.  $z_1 = D \tan \phi_r = 3 \tan(28) = 1.60$  meters from (3).  $z_2 = D \tan(45 + \phi_r/2) = 3 \tan(45 + 28/2) = 4.99$  meters. The dimension of this 2-tier superimposed walls is shown in Fig. 3.

Table 1 Soil parameters, surcharge, and wall geometry.

Item	Symbol	Value	Unit
Soil cohesion	$c$	0	kN/m <sup>2</sup>
Soil internal friction	$\phi_r$	28	degree
Soil density	$\gamma$	18	kN/m <sup>3</sup>
Surcharge	$q$	10	kN/m <sup>2</sup>
Upper wall height	$H_U$	3	meter
Lower wall height	$H_L$	4	meter
Offset distance	$D$	3	meter

Note: All the retained soil, reinforced backfill soil, and the foundation soil have the same properties

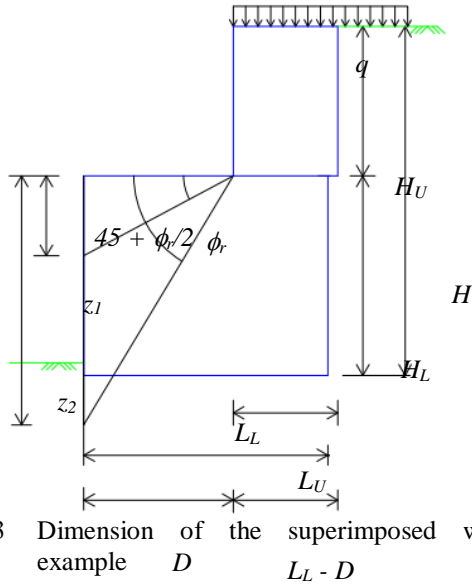


Fig. 3 Dimension of the superimposed wall example  $D$   $L_L - D$

Compared with Fig. 2,  $D_1 = (H_U + H_L)/20 = (3+4)/20 = 0.35$  meters.  $D_2 = H_L \tan(45 - \phi_r/2) = 4 \tan(45 - 28/2) = 2.4$  meters.  $D_3 = H_L \tan(90 - \phi_r) = 4 \tan(90 - 28) = 7.52$  meters.

## ADDITIONAL STRESSES

### Reinforcement layers

The reinforcement layers are shown in Fig. 4. The reinforcement spacing is 0.5 meters where the top layers at both the upper wall (layer 14) and the lower wall (layer 8) are started at 0.25 meters below their surfaces. The reinforcement layer depths are also shown as  $d_i$  in Table 4. The active zone length for each reinforcement layer is also shown in Table 4 using Eq. (5).

The reinforcement depths for 14 layers in both walls are shown in Fig. 4 denoted as  $d_1$  to  $d_{14}$  where the lower wall has layer 1 to layer 8 and the upper wall has layer 9 to layer 14.  $z_1$  from Eq. (3) and  $z_2$  from Eq. (4) are also included.

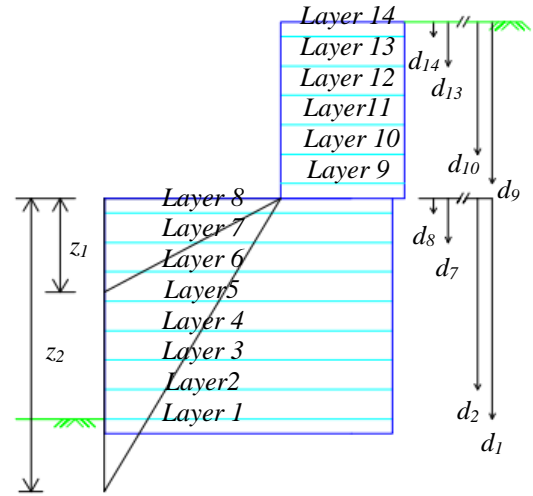


Fig. 4 Reinforcement layers for internal stability

### Calculation of the additional stresses ( $\sigma_i$ )

For the superimposed lower wall, all reinforcement layers 1 to 8 fall in to the internal stability case 2 because  $D_2 (= 2.4) \leq D (= 3.0) \leq D_3 (= 7.52)$ . The additional stresses can be calculated using either Eq. (7) or Eq. (1) in any layer. All gives the same result as shown as follows. For example,

$$\begin{aligned} \text{Using Eq. (7), } \sigma_i &= \frac{(H_L - z_1)}{(z_2 - z_1)} (\gamma H_U + q) \\ &= \frac{(4 - 1.60)}{(4.99 - 1.60)} (18 \times 3 + 10) = 45.30 \text{ kN/m}^2. \end{aligned}$$

Using Eq. (1) for layer 6 as shown in Fig. 6.

$$\begin{aligned} \text{From Eq. (2), } \sigma_f &= \frac{d_i - z_1}{z_2 - z_1} (\gamma H_U + q) \\ &= \frac{1.25 - 1.60}{4.99 - 1.60} (18 \times 4 + 10) = -6.50 \text{ kN/m}^2. \end{aligned}$$

$$\begin{aligned} \text{From Eq. (5), } L_a &= (H_L - d_i) \tan(45 - \phi_r/2) \\ &= (4 - 1.25) \tan(45 - 28/2) = 1.65 \text{ m}. \end{aligned}$$

$$\begin{aligned} \text{From Eq. (1), } \sigma_i &= \frac{(\gamma H_U + q) - \sigma_f}{(z_2 - d_i) \tan(45 - \phi_r/2)} L_a + \sigma_f \\ &= \frac{(18 \times 4 + 10) - (-6.50)}{(4.99 - 1.25) \tan(45 - 28/2)} 1.65 + (-6.50) \\ &= 45.30 \text{ kN/m}^2. \end{aligned}$$

Using Eq. (1) for layer 3 as shown in Fig. 6.

$$\text{From Eq. (2), } \sigma_f = 21.75 \text{ kN/m}^2 \text{ at } d_i = 2.75 \text{ m}.$$

$$\text{From Eq. (5), } L_a = 0.75 \text{ m}.$$



From Eq. (1),  $\sigma_i = 45.30 \text{ kN/m}^2$ .

As shown in Table 4 and in Fig. 5, the additional stress at the wall face,  $\sigma_f$ , is negative if the reinforcement depth,  $d_i$ , is less than  $z_1$ .  $\sigma_f$ , is positive if  $d_i$  is greater than  $z_1$ .

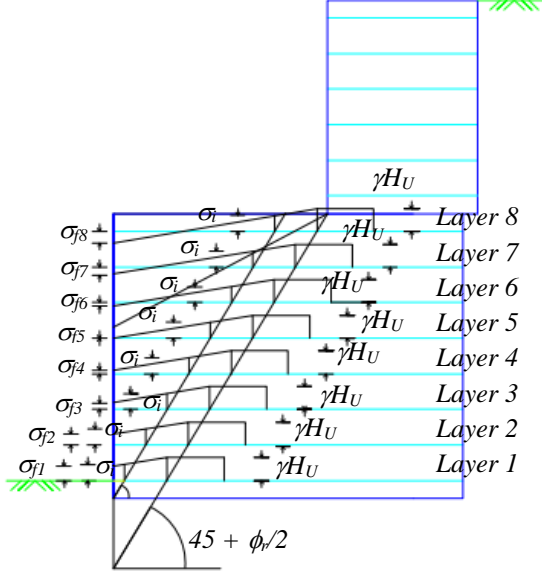


Fig. 5 Offset distances showing  $D_1, D_2, D_3$

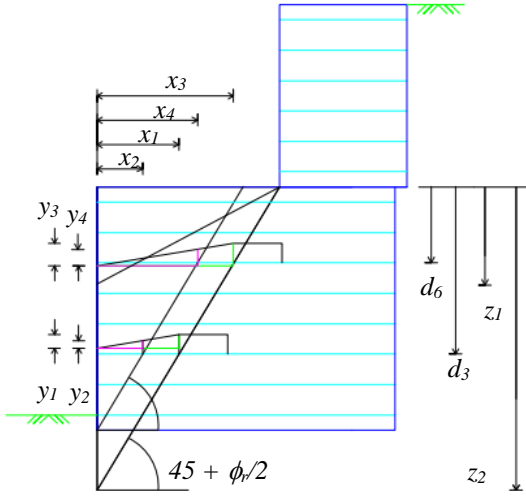


Fig. 6 Similar triangle in Eq. (6)

#### Similar triangle of the additional stresses

Figure 6 shows that the additional stresses,  $\sigma_i$ , for all the layers in the superimposed lower wall gives the same value because they all possess the same similar triangle properties. In this example,  $\sigma_i$  for layer 1 to 8 using Eq. (1) is  $45.30 \text{ kN/m}^2$ . Fig. 5 also shows that  $\sigma_i$  for layer 1 to 8 have the same magnitude.

Figure 6 also shows the similar triangle using Eq. (6) where  $\frac{(\gamma H_U + q) - \sigma_f}{(z_2 - d_i) \tan(45 - \phi_r/2)} = \frac{\sigma_i - \sigma_f}{L_a}$ .

For layer 3,  $y_1 = (\gamma H_U + q) - \sigma_{f3}$ ,  $y_2 = \sigma_i - \sigma_{f3}$ , and  $x_1 = (z_2 - d_3) \tan(45 - \phi_r/2)$ ,  $x_2 = L_{a4}$   
For layer 6,  $y_3 = (\gamma H_U + q) - \sigma_{f6}$ ,  $y_4 = \sigma_i - \sigma_{f6}$ , and  $x_3 = (z_2 - d_6) \tan(45 - \phi_r/2)$ ,  $x_4 = L_{a6}$

Figure 7 shows that this similar triangle is also held for Eq. (7) where  $\sigma_i = \frac{(H_L - z_1)}{(z_2 - z_1)} (\gamma H_L + q)$ . Additionally, similar triangle in Eq. (2) where  $\sigma_f = \frac{d_i - z_1}{z_2 - z_1} (\gamma H_U + q)$  holds true with Eq. (7) where  $\sigma_i = \frac{(H_L - z_1)}{(z_2 - z_1)} (\gamma H_L + q)$  in which  $d_i$  in Eq. (2) is  $H_L$  in Eq. (7).

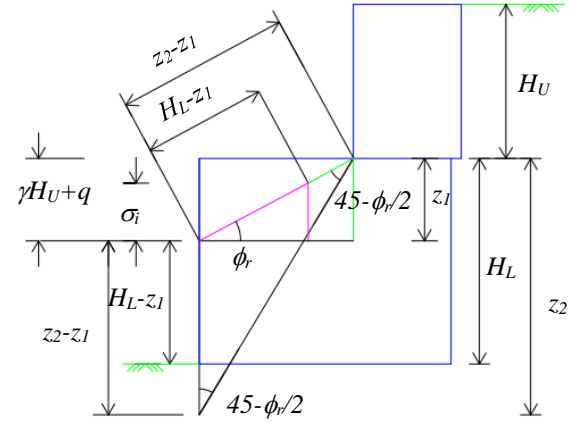


Fig. 7 Similar triangle in Eq. (7)

#### Additional stresses outside the internal stability case 2

Eq. (1) or Eq. (7) to calculate the internal stability are valid only  $D_2 \leq D \leq D_3$ . Suppose that the offset distance,  $D$ , is 2 meters, this superimposed wall falls in the internal stability case 1 where  $D \leq D_2$  at 2.4 meters. Thus,  $\sigma_i = \gamma H_U + q = 18 \times 3 + 10 = 64 \text{ kN/m}^2$ . However, if the additional stress,  $\sigma_i$ , is wrongly calculated using Eq. (1) or Eq. (7), then

Using Eq. (7),  $\sigma_i = \frac{(H_L - z_1)}{(z_2 - z_1)} (\gamma H_U + q)$

From (3),  $z_1 = D \tan \phi_r = 2 \tan(28) = 1.06$

From (4),  $z_2 = D \tan(45 + \phi_r/2) = 2 \tan(45 + 28/2) = 3.33$

From (7),  $\sigma_i = \frac{(4 - 1.06)}{(3.33 - 1.06)} (18 \times 3 + 10) = 82.97 \text{ kN/m}^2$ .

A layer can be picked to calculate  $\sigma_i$ . For example, arbitrarily pick layer 6, then

Using Eq. (1) for layer 6

From Eq. (2),  $\sigma_f = \frac{d_i - z_1}{z_2 - z_1} (\gamma H_U + q) = \frac{1.25 - 1.06}{3.33 - 1.06} (18 \times 4 + 10) = 5.27 \text{ kN/m}^2$ .

From Eq. (1),  $\sigma_i = \frac{(\gamma H_U + q) - \sigma_f}{(z_2 - d_i) \tan(45 - \phi_r/2)} L_a + \sigma_f = \frac{(18 \times 4 + 10) - (5.27)}{(3.33 - 1.25) \tan(45 - 28/2)} 1.65 + 5.27 = 82.97 \text{ kN/m}^2$ .

This value at  $82.97 \text{ N/m}^2$  is incorrect since the

similar triangle does not hold. In fact, Eq. (1) or Eq. (7) are starting to be valid when  $D$  is  $D_2$  which is 2.4.

Suppose that  $D$  is 8 meters which is in the internal stability case 3 where  $D \geq D_3$  at 7.52 meters. Using Eq. (7) or Eq. (1),  $\sigma_i = -1.79 \text{ kN/m}^2$  where the correct value is  $\sigma_i = 0$ .

In conclusion, for internal stability case 1 where  $D \leq D_2 = H_L \tan(45 - \phi_r/2)$ ,  $\sigma_i = \gamma H_U + q$ . For internal stability case 3 where  $D \geq D_3 = H_L \tan(90 - \phi_r)$ ,  $\sigma_i = 0$

### Additional stresses inside the internal stability case 2

The additional stress ( $\sigma_i$ ) by varying the values of the offset distance ( $D$ ) to be inside the internal stability case 2 or  $D_2 \leq D \leq D_3$  is shown in Fig. 8. Substitute Eq. (3) and Eq. (4) into Eq. (7) leads to

$$\sigma_i = \frac{(H_L - D \tan \phi_r)}{(D \tan(45 + \phi_r/2) - D \tan \phi_r)} (\gamma H_U + q) \quad (8)$$

in which  $\sigma_i$  is a function of  $\phi$  and  $D$  where  $D_2 \leq D \leq D_3$ ,  $\sigma_i$  is a hyperbola function.

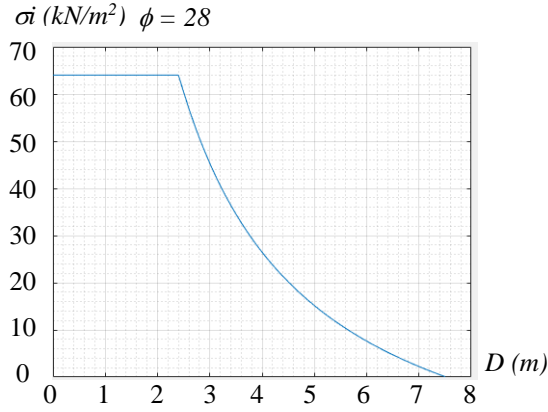


Fig. 8 Additional stresses by varying  $D$  at  $\phi = 28$

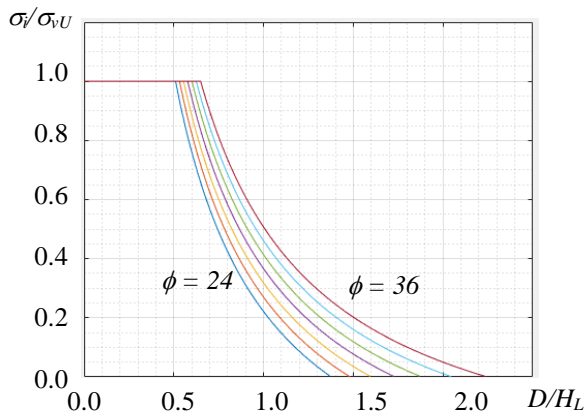


Fig. 9 Additional stresses ratio ( $\sigma_i/\sigma_{vH}$ ) by varying offset distance ratio ( $D/H_L$ ) and  $\phi$  increment by  $2^\circ$

From Eq. (8), suppose  $\sigma_{vU} = \gamma H_U + q$  is the

vertical stresses from the upper wall, then the additional stress ratio is defined as  $\sigma_i/\sigma_{vU}$ . Also, let define the offset distance ratio as  $D/H_L$ . Varying both the offset distances ( $D$ ) and the internal friction angles ( $\phi$ ) is shown in Fig. 8 where  $\phi$  is increased by 2 degrees starting from 24 degrees to 34 degrees.

Figure 9 is further clarified in Table 2 and Table 3. Table 2 shows the offset distance ratios of  $D_2/H$  and  $D_3/H$  at different  $\phi$ . At  $\phi = 28$  degrees, for example, the offset ratio of  $D_2/H_L$  at 0.60 means that if the offset distance ( $D$ ) is less than 0.6 of lower wall height, the lower wall will bear the full vertical superimposed load from the upper wall ( $\sigma_{vU}$ ). Also,  $D_3/H_L$  at 1.88 for  $\phi = 28$  degrees means that  $D$  must be more than 1.88 times the lower wall height to get away from the upper wall load.

Table 3 implies that at  $\phi = 28$  degrees, the lower wall with a typical reinforcement length from  $0.7L/H$  to  $1.1L/H$  [1] is not enough to bear the upper wall load.  $0.7L/H$  lower wall still needs to bear the additional stress at 0.79 times the upper wall load.

Table 2 Offset distance ratios of  $D_2/H$  and  $D_3/H$  at different  $\phi$ .

$\phi$	24	28	32	36
$D_2/H_L$	0.65	0.60	0.55	0.51
$D_3/H_L$	2.25	1.88	1.60	1.38

Table 3 Additional stresses ratio ( $\sigma_i/\sigma_{vH}$ ) at different  $D/H$  and different  $\phi$ .

$\phi$	24	28	32	36
$0.7D/H$	0.90	0.79	0.68	0.57
$D/H$	0.51	0.41	0.32	0.22
$1.1L/H$	0.42	0.33	0.24	0.15

### INTERNAL STABILITY

The result from the internal stability calculation is shown in Table 4 and Table 5, in which

$$\sigma_{vi} = \gamma d_i + \sigma_i \quad (8)$$

$$\sigma_{hi} = k_a \sigma_{vi} \quad (9)$$

$$k_a = \tan^2(45 - \phi_r/2) \quad (10)$$

$$T_{max-i} = \sigma_{hi} V_i \quad (11)$$

$$L_{ei} = 1.5 T_{max-i} / C \tan(\phi_r) \gamma d_i R_c \alpha \quad (12)$$

$$L_{Ti} = L_{ai} + L_{ei} \quad (13)$$

where

$\sigma_{vi}$  is the vertical stress at the  $i^{\text{th}}$  layer of reinforcement.

$\sigma_{hi}$  is the horizontal stress at the  $i^{\text{th}}$  layer of reinforcement.

$k_a$  is the active earth pressure coefficient.

$T_{max-i}$  is the maximum tension at the  $i^{\text{th}}$  layer of

reinforcement.

$V_i$  is the tributary area at the  $i^{\text{th}}$  layer of reinforcement.

$L_{ei}$  is the embedment length in the resisting zone at the  $i^{\text{th}}$  layer of reinforcement.

$C$  is 2 for geogrid.

$R_c$  is coverage ratio = 1.

$\alpha$  is scaling ration = 1.

$L_{Ti}$  is the total length at the  $i^{\text{th}}$  layer of reinforcement.

Table 4 Internal stability showing additional stresses, vertical stresses, and horizontal stresses.

Layer	$d_i$ (m)	$L_{ai}$ (m)	$\sigma_{fi}$ (kN/m <sup>2</sup> )	$\sigma_{vi}$ (kN/m <sup>2</sup> )	$\sigma_{hi}$ (kN/m <sup>2</sup> )
8	0.25	2.25	-25.34	49.80	17.98
7	0.75	1.95	-15.92	58.80	21.23
6	1.25	1.65	-6.50	67.80	24.48
5	1.75	1.35	2.91	76.80	27.73
4	2.25	1.05	12.34	85.80	30.98
3	2.75	0.75	21.75	84.80	34.23
2	3.25	0.45	31.17	103.80	37.47
1	3.75	0.15	40.59	112.80	40.72
Emb	4.0				

Note:  $d_i$  is the reinforcement layer depth.  $L_{ai}$  is the active zone length.  $\sigma_i$  is the additional stress at the wall face.  $\sigma_{fi}$  is the additional stress on the reinforcement layer. Emb is the embedment depth.

Table 5 Internal stability showing maximum reinforcement tensions and reinforcement lengths.

Layer	$d_i$ (m)	$V_i$ (m)	$T_{max-i}$ (kN/m)	$L_{ei}$ (m)	$L_{Ti}$ (m)
8	0.25	0.375	6.74	2.64	4.89
7	0.75	0.5	10.61	1.39	3.34
6	1.25	0.5	12.24	0.96	2.61
5	1.75	0.5	13.86	0.78	2.13
4	2.25	0.5	15.49	0.67	1.73
3	2.75	0.5	17.11	0.61	1.36
2	3.25	0.5	18.74	0.56	1.02
1	3.75	0.5	20.36	0.53	0.68
Emb	4.0				

Note:  $d_i$  is the reinforcement layer depth.  $V_i$  is the reinforcement tributary area active zone length of the reinforcement layer.  $T_{max-i}$  is the maximum tension of the reinforcement layer.  $L_{ei}$  is the active zone length.  $L_{Ti}$  is the minimum reinforcement length.

The calculation detail can be followed as in [1] that is not shown here. The tensile of the

reinforcement layers can be determined using Eq. (11) and the reinforcement length can be determined using Eq. (13).

The external stability needs to check the sliding, overturning, and bearing capacity. FHWA/TX-1 [4] suggests that only the part of the upper walls directly above the lower wall is treated as a surcharge. Global stability in the limit equilibrium method or finite element method is also omitted because of the space limitation.

## CONCLUSIONS

The key point for internal stability checking in designing superimposed MSE retaining walls is to treat the upper wall as an equivalent surcharge on the lower wall with its magnitude determined by the offset distance. By varying offset distances, the equivalent surcharge magnitude or the additional vertical stress can be categorized into three cases. The additional vertical stress is maximum in case 1 which is the full upper wall load where the offset distance is less than  $H_L \tan(45 - \phi_r/2)$ . The additional vertical stress is zero in case 3 where the offset distance is greater than  $H_L \tan(90 - \phi_r)$ . In case 2, the additional vertical stress is a hyperbola function that can be calculated easily using the proposed equation  $\sigma_i = [(H_L - z_1)/(z_2 - z_1)](\gamma H_L + q)$  in Eq. (7) with the geometric and algebraic explanations.

## REFERENCES

- [1] FHWA-NHI-00-043, Mechanically Stabilized Earth Walls and Reinforced Soil Slopes Design and Construction Guidelines, 2001, U.S. Department of Transportation - Federal Highway Administration.
- [2] AASHTO, Standard specifications for highway bridges, 1998, American Association of State Highway and Transportation Officials.
- [3] FHWA/TX-05/0-4485-2, Design Guidelines for Multi-Tiered MSE Walls, 2004, Texas Department of Transportation and the Federal Highway Administration.
- [4] FHWA/TX-05/0-4485-1, An Examination of Design Procedures for Single- and Multi-Tier Mechanically Stabilized Earth Walls, 2004, Texas Department of Transportation and the Federal Highway Administration.

# NUMERICAL ANALYSIS FOR ESTIMATING PULL-OUT RESISTANCE OF FLIP-TYPE GROUND ANCHORS IN SAND GROUNDS

Shota Yoshida<sup>1</sup>, Xi Xiong<sup>2</sup> and Tatsunori Matsumoto<sup>3</sup>

<sup>1</sup>Daisho Co., Ltd., Japan; <sup>2</sup> Kanazawa University, Japan; <sup>3</sup> Professor Emeritus, Kanazawa University, Japan

## ABSTRACT

Flip-type ground anchors (hereinafter referred to as “flip anchors”) are a kind of ground anchors, which do not require grouting to obtain the pull-out resistance. The flip anchors are directly driven into the ground from the ground surface with their anchor heads closed. When pull-out forces act on the anchors, their anchor heads rotate and open in the ground. Unlike ordinary pre-embedded plate anchors, there are few studies on flip anchors. Thus, to investigate the pull-out behavior of flip anchors, and to estimate their pull-out resistance in sand grounds, numerical analyses using the finite element method (FEM) were conducted. The Mohr-Coulomb model was employed to model the soil. The numerical analyses were conducted to simulate full-scale field pull-out experiments. In the field experiments, 5 sizes of actual flip anchors embedded or driven in the sand ground were pulled out vertically. Pull-out force and vertical displacement were measured while pulling the anchors. In the numerical analyses, not only the pull-out resistance but also the displacement of the ground due to the pull-out of the anchor was investigated. By comparing the experimental results under various conditions with the calculated results of the FEM analyses, a method of estimating the pull-out resistance of flip anchors by FEM was proposed.

*Keywords: Ground anchor, Flip anchor, Numerical analysis, Sand ground*

## INTRODUCTION

Anchors have been widely used for supporting structures on the ground mainly called earth anchors or ground anchors. The types of anchors can be broadly divided into those that are used with grouting or those without grouting. Among the anchors installed without grouting, there are mainly 2 types of anchors. One is pre-embedded in the ground and the other is driven or penetrated into the ground.

Figure 1 is examples of pre-embedded plate anchors. The plate anchors are expected to have pull-out resistance due to earth pressure acting on the anchor plates. The plate anchors can be used for a wide variety of purposes, such as embankment reinforcement, retaining wall reinforcement, tower support, and so on.

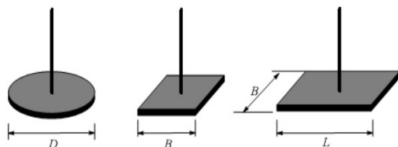


Fig. 1 Examples of pre-embedded plate anchors [1].

Among anchors that are driven or penetrated into the ground, there are commonly 2 types of anchors, which are often called “percussion anchors” and “helical anchors”. The pull-out resistance of percussion anchors is obtained by earth pressures acting on the anchor plates like the plate anchors, but it differs from the plate anchor in that it rotates to

open in the ground when tensile force acts. For this reason, percussion anchors (Figs. 2 & 3) are called “flip anchors” in this study.

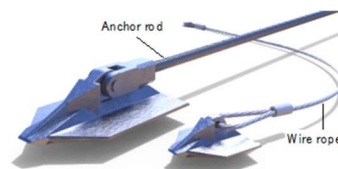


Fig. 2 Examples of flip anchors [2].

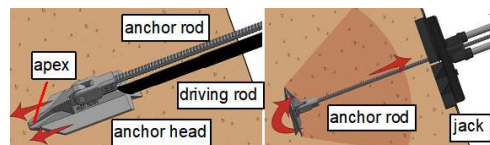


Fig. 3 Installation procedures of a flip anchor [2].

Although the flip anchors have convenient workability, estimation of the pull-out resistance according to ground conditions is more difficult compared to general pre-embedded plate anchors, due to their particular resistance mechanism. A number of previous research on empirical estimation of pull-out resistance of plate anchors were conducted so far, such as [3]–[5]; however, there are few studies on flip anchors [6].

Pull-out resistance of plate anchors has been estimated based on the ground failure models [7]–[9]. As shown in Fig. 4, the ground failure models need to

be divided into “Shallow anchor” model or “Deep anchor” model according to the embedment ratio  $H/L$  ( $H$  = embedment depth of anchor head,  $L$  = length of anchor plate). It is because the slip lines extend from edges of an anchor plate do not reach the ground surface when the anchor is installed deeper than the critical embedment ratio  $(H/L)_{cr}$ . If  $H/L$  is smaller than the  $(H/L)_{cr}$ , the failure pattern appears as a “Shallow anchor” model, and if  $H/L$  is equal or greater than  $(H/L)_{cr}$ , the pattern appears as a “Deep anchor” model. In practice,  $(H/L)_{cr}$  can be set in relation to the friction angle of soil  $\phi'$  (Table 1).

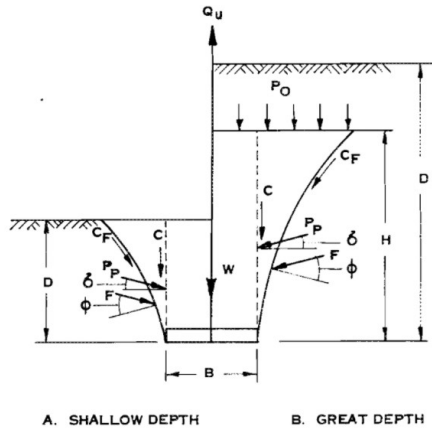


Fig. 4 Ground failure models above a plate anchor.

Table 1  $(H/L)_{cr}$  depending on  $\phi'$  [10]

$\phi'$	20°	25°	30°	35°	40°	45°	48°
$(H/L)_{cr}$	2.5	3	4	5	7	9	11

Merifield [11] estimates anchor break-out factor  $N_\gamma$  for horizontal square and circular anchors by rigorous numerical analysis for various friction angles of soil  $\phi'$ . The effectiveness of numerical analysis to estimate pull-out resistance of plate anchors has been verified.

In this study, pull-out resistance of flip anchors in sandy ground is calculated by numerical analysis using the finite element method (FEM). And the calculated values are compared with measured values of field experiments. According to the calculated results, ground failure modes are also investigated.

## FIELD PULL-OUT EXPERIMENTS OF FLIP ANCHORS EMBEDDED OR DRIVEN IN A SAND GROUND

### Experimental Conditions

A full-scale model sand ground was prepared in a test pit of 4.0 m in length, 4.0 m in width, and 2.5 m in height in a field. The peak internal friction angle  $\phi'$  of the sand, which was measured by direct shear tests, was 42 degrees. The ground was compacted using a

vibration tamper to have a relative density  $D_r$  of around 80% and a dry density  $\rho_d$  of around 1.745 t/m<sup>3</sup>. As shown in Figs. 5 & 6, five sizes of actual flip anchors made of ductile iron were used in the experiments. The length of the anchor  $L$ , the breadth of the anchor  $B$ , and the projected area of the anchor  $A$  are different for each anchor. Each anchor was buried in the ground during ground preparation at designated embedment depths  $H$  under Opened or Closed head conditions. In driven installation condition, the anchors were driven into the ground from the ground surface. After that, each anchor was vertically pulled out with a hydraulic jack, and pull-out force  $F$  and pull-out displacement  $w$  were measured.

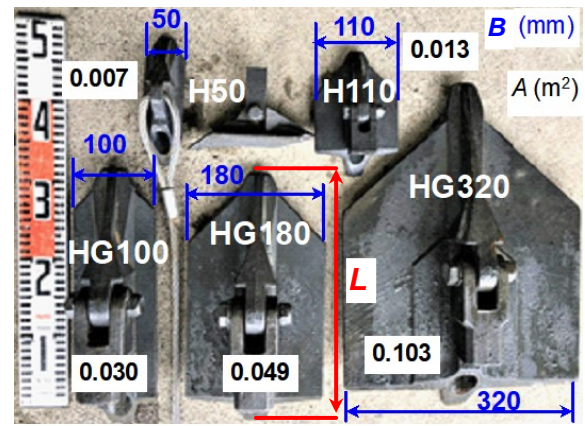


Fig. 5 Actual flip anchors used in experiments.

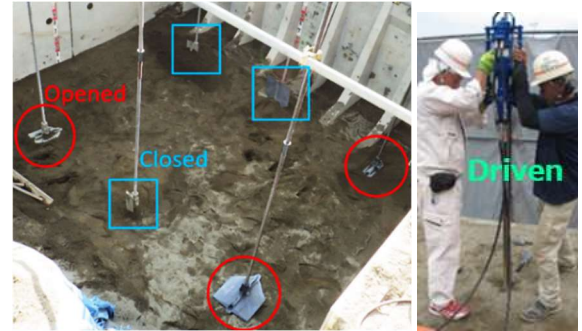


Fig. 6 Three installation conditions of flip anchors.

### Experimental Results

Maximum pull-out resistance  $F_{max}$  of flip anchors increased as the projected area of anchors  $A$  increased.  $F_{max}$  of Driven anchors were equivalent to  $F_{max}$  of Closed anchors.  $F_{max}$  of Driven anchors, which is corresponding to the practical installation condition of flip anchors, reached about 80% of  $F_{max}$  of horizontally embedded plate anchors (Opened anchors). From the results of field experiments,  $w$  required for the flip anchors to open sufficiently in the dense sand could be the same amount as plate length  $L$  or about 1.5 times  $L$ .



# CALCULATION OF $F_{\max}$ OF FLIP ANCHORS BY NUMERICAL ANALYSIS (FEM)

## Modeling of the Ground and Plate Anchors

The above field pull-out experiments were simulated by the finite element method (FEM) to examine the effectiveness of FEM for estimating pull-out resistance of flip anchors. A FEM analysis software Plaxis 3D was adopted.

As shown in Fig. 7, the ground with a length of 4.0 m, a width of 2.0 m, and a depth  $H$  of more than  $H/L = 20$  was modelled for each anchor used in the field experiments. For the calculation, because the flip anchor has a unique shape, the shape was approximated to a rectangle having the same  $A$  by adjusting the breadth of anchor  $B$  as  $B_c$  (Table 2 & Fig. 8). For simplicity, the model was split in half, where the anchor plate was halved ( $B_c/2$ ). As the displacement boundary conditions, the horizontal displacement of the side surface and the vertical displacement of the bottom surface were fixed. Mohr-Coulomb model was applied to the soil constitutive law.

Table 3 shows the parameters of the ground, based on the ground conditions of the field experiments. Residual internal friction angle  $\phi'_r$  was adopted in the FEM analysis. Modulus of elasticity  $E'$  was empirically estimated by  $E' = 2700 N$  (kPa) based on measured SPT  $N$ -values of the ground. Table 4 shows parameters of an anchor plate based on the actual flip anchors used in the experiments (Fig. 5). Interfaces were set between the bottom of the anchor plate and the sand for tension cut-off.

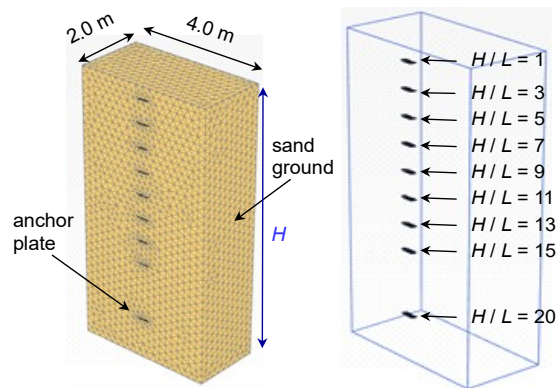


Fig. 7 Modelling of the ground and plate anchors for FEM analysis.

The following procedure were applied to simulate the pull-out experiment.

- Step 1:  $K_0$  self-weight analysis on horizontal ground was performed with  $K_0 = 1 - \sin \phi'$ .
- Step 2: An anchor plate was set.
- Step 3: Upward vertical displacement that is equal to  $L$  was applied to the anchor plates.

Table 2 Dimensions of approximated rectangular shapes of flip anchors for the calculation

Flip anchor	$L$ (m)	$*B_c$ (m)	$B$ (m)	$A$ (m <sup>2</sup> )
H50	0.160	0.043	0.050	0.007
H110	0.160	0.079	0.110	0.013
HG100	0.340	0.088	0.100	0.030
HG180	0.340	0.143	0.180	0.049
HG320	0.440	0.235	0.320	0.103

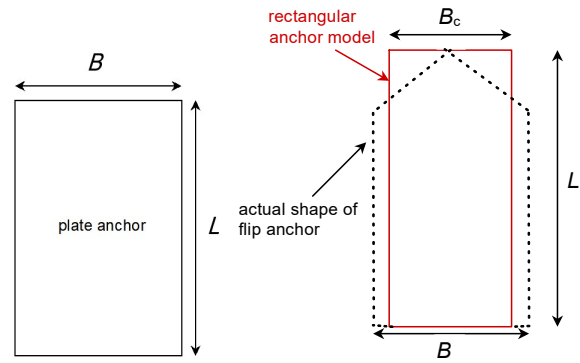


Fig. 8 An outline of an approximated rectangular shape of a flip anchor for the calculation.

Table 3 Parameters of the sand ground for FEM analysis

Item	Value
Unit weight of the unsaturated soil, $\gamma_{\text{unsat}}$ (kN/m <sup>3</sup> )	17.10
Initial void ratio, $e_{\text{init}}$	0.540
Modulus of elasticity, $E'$ (kPa)	8400
Poisson's ratio, $\nu$	0.30
Cohesion, $c$ (kPa)	0.0
Residual int. friction angle, $\phi'_r$ (deg)	35
Dilatancy angle, $\psi$ (deg)	0.0
The earth pressure coefficient at rest, $K_0$	0.43

Table 4 Parameters of the anchor plates for FEM analysis

Item	Value
Unit weight, $\gamma$ (kN/m <sup>3</sup> )	71.54
Thickness, $d$ (mm)	50.0
Young's modulus, $E$ (GPa)	176.0
Poisson's ratio, $\nu$	0.27

## Calculation of $F_{\max}$ of Flip Anchors by FEM

### Pull-out force $F$ vs. pull-out displacement $w$

Figures 9-13 show the relationships of  $F$  vs.  $w$  for each  $H/L$ .  $F$  becomes larger with an increasing  $H/L$ . The tendency of the relationship changes with increasing  $H/L$ . When  $H/L \leq 5$ ,  $F_{\max}$  was clearly appeared; whereas when  $H/L > 5$ ,  $F_{\max}$  cannot be defined because  $F$  kept increasing with increasing  $w$ .

The tendency of the relationship of  $F$  vs.  $w$  seems to shift from general shear failure to local shear failure with increasing  $H/L$ . And  $(H/L)_{cr}$  is regarded as a turning point of the tendency. Thus for Deep anchors  $[(H/L)_{cr} \leq H/L]$ , maximum allowable  $w$  is need to be defined to determine  $F_{max}$ . Some references [12] regard  $w$  where the gradient  $(\Delta F / \Delta w)$  becomes to the minimum as the maximum  $w$  at  $F_{max}$ . For flip anchors in this study, the amount of maximum allowable  $w$  for Deep anchor is defined as  $L/2$ .

Figure 14 shows  $F_{max}$  calculated by FEM vs. measured  $F_{max}$ . The calculated and measured values are in good agreement.  $F_{max}$  of each anchor in deep anchor condition was estimated from  $F$  at  $w = L/2$ .  $F_{max}$  becomes larger with increasing  $A$  or  $H/L$ . The increasing tendency of  $F_{max}$  changes from an exponential increase tendency to a linear increasing tendency at  $(H/L)_{cr}$  as the conversion point.

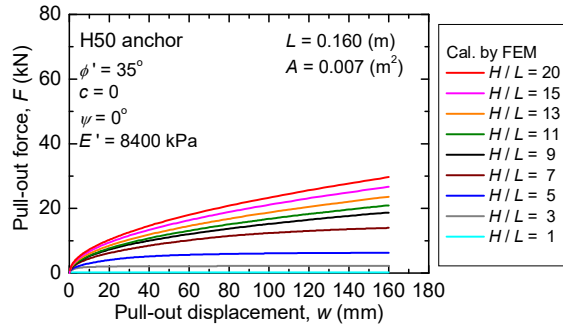


Fig. 9  $F$  vs.  $w$  by FEM simulations for H50 anchor.

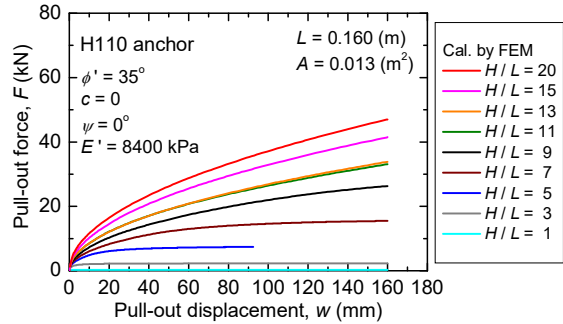


Fig. 10  $F$  vs.  $w$  by FEM simulations for H110 anchor.

#### Displacement of the Ground

Figures 15 and 16 show the results of FEM analysis on displacements of the ground when the HG180 anchor was pulled until the  $w$  at  $F_{max}$ . The anchor displacements affected the ground surface when  $H/L = 1$ ; however when  $H/L = 5$  or more, the anchor displacements did not affect the ground surface. From these results,  $H/L = 5$  can be regarded as  $(H/L)_{cr}$ . This result certainly agrees with the empirical values in Table 1.

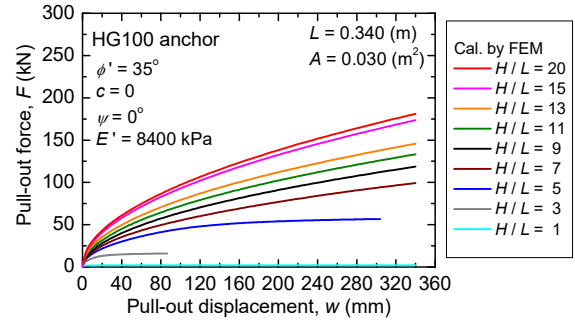


Fig. 11  $F$  vs.  $w$  by FEM simulations for HG100 anchor.

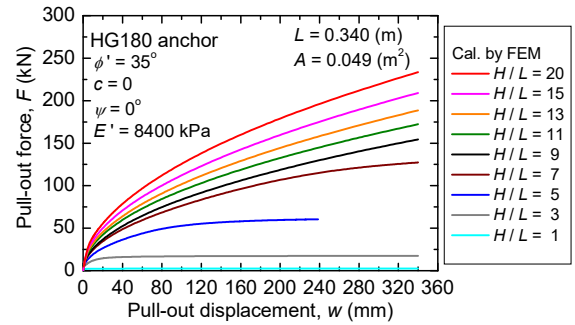


Fig. 12  $F$  vs.  $w$  by FEM simulations for HG180 anchor.

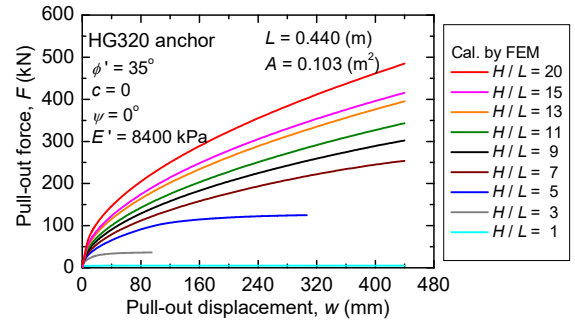


Fig. 13  $F$  vs.  $w$  by FEM simulations for HG320 anchor.

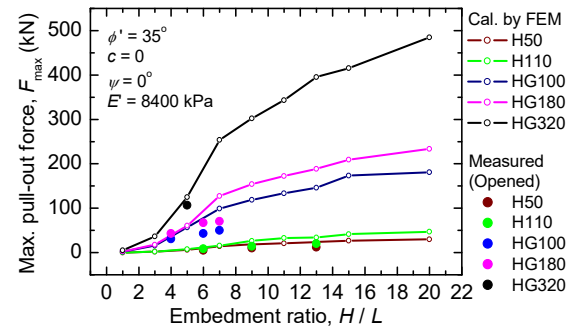


Fig. 14 Measured  $F_{max}$  vs. calculated  $F_{max}$  (by FEM).

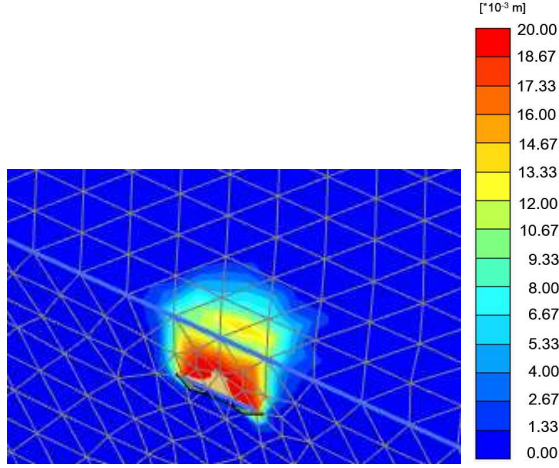


Fig. 15 Displacements of the ground at  $w = 20$  mm calculated by FEM (HG180,  $H/L = 1$ ).

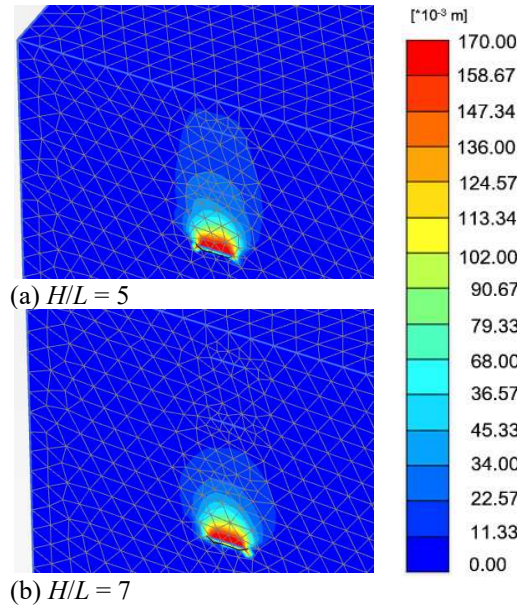


Fig. 16 Displacements of the ground at  $w = 170$  mm calculated by FEM (HG180).

### Calculation of $F_{\max}$ of Half-Opened Flip Anchors by FEM

*Pull-out force  $F$  vs. pull-out displacement  $w$*

Figure 17 shows the comparison of  $F$  vs.  $w$  of Opened (horizontal,  $\beta = 0^\circ$ ) and half-opened ( $\beta = 45^\circ$ ) anchors pulled vertically. The inclined anchor imitates the anchor in the middle of opening or the anchor half opened. As shown in Fig. 18, if the anchor half opened,  $F$  tended to be smaller than  $F$  of the horizontal (completely opened) anchor.  $F_{\max}$  of the half-opened anchor was about  $2/3$  of  $F_{\max}$  of the anchor completely opened.

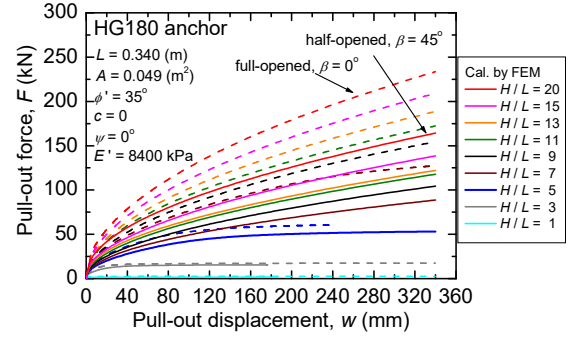


Fig. 17  $F$  vs.  $w$  by FEM simulations for full opened or half-opened HG180 anchor.

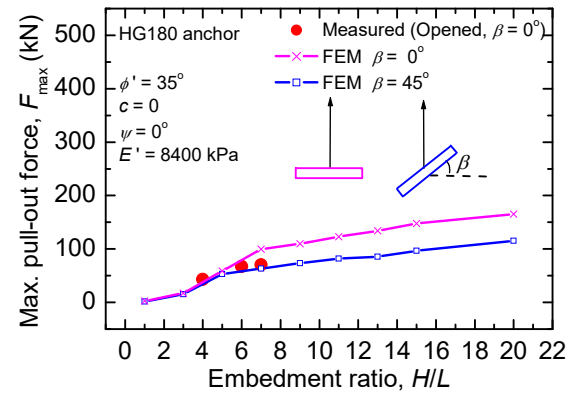


Fig. 18 Measured (full-opened) vs. calculated (full & half-opened)  $F_{\max}$  by FEM.

### Displacement of the Ground

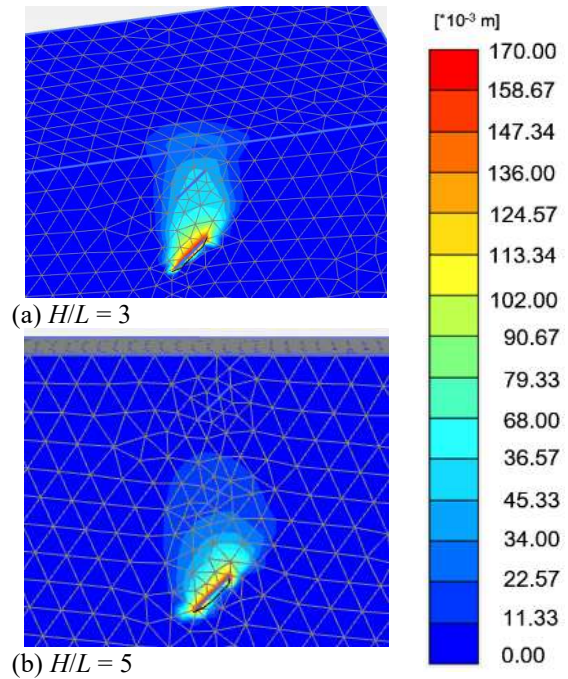


Fig. 19 Displacements of the ground calculated by FEM (at  $w = 170$  mm, HG180).



Fig. 19 shows the results of FEM analysis on displacements of the ground when pulling the half-opened anchor vertically. Although the basic tendency is not so different from that of the fully opened anchor, the displacement area seems to be distorted and slightly smaller. That might be the reason for the smaller  $F_{\max}$ . Thus, in practice, it is particularly important to ensure that the anchor can be fully opened to be perpendicular to the pull-out direction. However, even if the anchor plate is half opened, it could reach 70% of  $F_{\max}$  of the fully opened anchor.

#### What required to calculate $F_{\max}$ of a flip anchor in the same way as a plate anchor by FEM.

The above results agreed well with measured  $F_{\max}$  of flip anchors; however these simulations do not take into consideration the unique mechanism for flip anchors that rotate and open in the ground after being driven in closed state. The field pull-out experiments have shown that flip anchors can attain about 80% or more of  $F_{\max}$  of horizontal plate anchors having the same  $A$ . Thus, if the amount of  $w$  required for flip anchors to open sufficiently is taken into considerations as Fig. 20,  $F_{\max}$  of flip anchors can be estimated by FEM.

Compared to pre-embedded plate anchors at same  $H$ , flip anchors should be installed (Driven) deeper by at least  $L$ . If the anchor plate is not fully opened,  $F_{\max}$  will be about 70% as shown in Fig. 18. It is necessary to estimate  $F_{\max}$  with such possibility in mind.

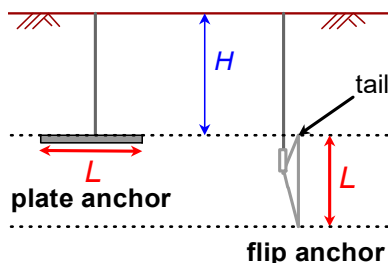


Fig. 20 Difference in  $H$  between plate anchor and flip anchor in calculation

#### CONCLUSIONS

In this study, the pull-out resistance of flip anchors in sandy ground was calculated by FEM. The ground failure modes were observed and the calculated values were compared with measured values of field experiments. Main conclusions in the paper are as follows:

- 1)  $F_{\max}$  of flip anchors can be reasonably estimated by FEM.
- 2) By FEM, the behavior of the ground affected by the pull-out of flip anchors, and relationship  $F$  vs.  $w$  can also be obtained.
- 3) The ground failure patterns calculated by FEM

analysis certainly changes from “Shallow anchor” to “Deep anchor” at  $(H/L)_{cr} = 5$ , which was in common with the value assumed empirically in [10].

- 4) In FEM analysis,  $F$  at  $w = L/2$  is defined as  $F_{\max}$  in the deep anchor condition.
- 5) When designing  $H$  of flip anchors, the amount of  $w$  equivalent to  $L$  or 1.5 times  $L$  that is required for flip anchors to open sufficiently, need to be added to designed  $H$  for the installation depth.

#### REFERENCES

- [1] Niroumand H., Kassim K. A. and Nazir R., Anchor plates in two-layered cohesion less soils, American Journal of Applied Sciences, Vol. 7, No. 10, 2010, pp. 1396-1399.
- [2] Anchoring Rope and Rigging Pty. Ltd., <https://www.arandr.com.au>, 2022.
- [3] Baker W.H. and Kondner R. L., Pullout load capacity of a circular earth anchor buried in sand, Highway Research Record, Vol. 108, 1966, pp. 1-10.
- [4] Das B.M. and Seeley G. R., Breakout resistance of shallow horizontal anchors, Journal of the Geotechnical Engineering Division, Vol. 101, No. 9, 1975, pp. 999-1003.
- [5] Dickin E.A., Uplift behavior of horizontal anchor plates in sand, Journal of Geotechnical Engineering, Vol. 114, No. 11, 1988, pp. 1300-1317.
- [6] Niroumand H. and Kassim K.A., Pullout capacity of irregular shape anchor in sand, Measurement, Vol. 46, No. 10, 2013, pp. 3876-3882.
- [7] Balla A., The resistance to breaking-out of mushroom foundations for pylons, Proceedings of the 5th international conference on Soil Mechanics and Foundation Engineering, Vol. 1, 1961, pp. 569-576.
- [8] Majer J., Zur berechnung von zugfundamenten, Österreichischer, Bauzeitschrift, Vol. 10, No. 5, 1955, pp. 85-90.
- [9] Mors H., Das Verhalten von Mastgründungen bei Zugbeanspruchung, Bautechnik, Vol. 39, No. 10, 1959, pp. 367-378.
- [10] Meyerhof G. G. and Adams J. I., The ultimate uplift capacity of foundations, Canadian Geotechnical Journal, Vol. 5, No. 4, 1968, pp. 225-244.
- [11] Merifield R.S., Lyamin A.V. and Sloan S.W., Three-dimensional lower-bound solutions for the stability of plate anchors in sand, Géotechnique, Vol. 56, No. 2, 2006, pp. 123-132.
- [12] Das B.M. and Puri V. K., Load displacement relationship for horizontal rectangular anchors in sand, Proc. 4th Int. Conf. Civil Struct. Eng. Computing, London, Civil-Comp Press, Vol. 2, 1989, pp. 207-212.

# FIBER-BASED MEASUREMENT OF THE ACTIVATION OF GEOSYNTHETICS IN SOIL

Jan Derksen<sup>1</sup>, Jeanette Ortega<sup>2</sup>, Kira Heins<sup>2</sup>, Thomas Gries<sup>2</sup> and Raul Fuentes<sup>1</sup>

<sup>1</sup>Institute of Geomechanics and Underground Technology, RWTH Aachen University, Germany;

<sup>2</sup>Institut für Textiltechnik, RWTH Aachen University, Germany

## ABSTRACT

The integration of monitoring systems in critical infrastructure is becoming increasingly important for assessing the safety and reliability of these structures. In geomechanics, a large number of these infrastructures such as dams, dikes, embankments or bridge abutments contain geosynthetics as reinforcements. This paper presents a novel approach to capture geogrid activation in terms tensile strains by using a fiber-based electrical sensor system. The electrical properties of fiber materials as well as their ability to be integrated into or on a textile justify a high potential for this fiber-based measurement concept. First, the metrological response of the fiber-based electrical sensor materials to tensile strain is determined and transferred into calibration curves. The measurement system was applied in geogrid tensile tests in air. Moreover, geogrid pullout tests are performed with different confining stresses to verify the applicability of the fiber-based electrical sensors to be used on geosynthetic-reinforced earthworks. The test results with redundant measurements of Linear Variable Differential Transformers (LVDTs) prove that the novel measurement system is generally applicable for measuring geosynthetic strains, but has to be improved in terms of reliability for monitoring purposes.

*Keywords: Geogrid, Sensor Fibers, Tensile Test, Pullout Test*

## INTRODUCTION

Geosynthetic-reinforced soil (GRS) is an important component of infrastructure as it is widely used for retaining structures for slopes, cuttings, dams, walls and abutments, to name but a few applications [1]–[3]. Typically, geogrids are used as geosynthetic reinforcements to enhance the overall stability and to improve the settlement performance of the structures by interaction mechanisms described in [4]. Once the geogrids are embedded in the soil, the GRS is a black box for the designer, as there is usually no information available about the mobilization of the reinforcement in the structure. However, the integration of monitoring systems in critical infrastructure is becoming increasingly important for assessing the safety and reliability of these structures.

In this context, this paper presents a novel fiber-based electrical sensor material to measure geosynthetic tensile strains in GRS structures. The new measuring technique was tested in tensile tests in air and in pullout tests in soil with the fiber attached to the geosynthetic.

## MATERIALS AND METHODS

### Materials

#### Fibers

The sensor fibers employed in this work are developed at the Institut für Textiltechnik of the

RWTH Aachen University in Aachen, Germany. In order to avoid measurement disturbance through moisture in the soil or environment, bicomponent thermoplastic filaments are spun, with a conductive core and insulating sheath. The melt spinning parameters and the materials used are described in [5]. The characteristic properties of the employed filaments are shown in Table 1 as well as a cross-sectional microscopy image in Fig. 1.

Table 1 Properties of the sensor filament

Property	Units	Value
Fineness	dtex	1280 ( $\pm$ 83)
Diameter	$\mu\text{m}$	408.82 ( $\pm$ 6.55)
Linear resistivity	$\text{M}\Omega/\text{m}$	3.9 ( $\pm$ 0.5)
Tensile strength	cN/tex	5.37 ( $\pm$ 0.34)
Max. Elongation	%	697.89 ( $\pm$ 44.11)
Elastic limit	%	1.805 ( $\pm$ 0.043)

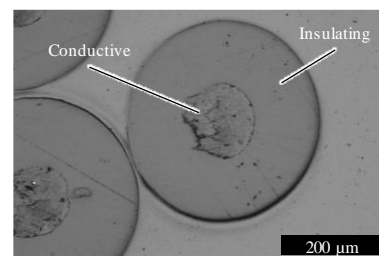


Fig. 1 Cross-sectional microscopy image of the sensor filament.

## Geogrid

In this study, a biaxial geogrid made from polyester (PET) was used. The general specifications are summarized in Table 2 for machine direction (MD) and cross-machine direction (CMD).

Table 2 Characteristic properties of the geogrid

Property	Units	Value
Polymer	-	PET
Aperture size, $d_A$	mm	25×25
Mass per unit area	g/cm <sup>3</sup>	160
Ultimate tensile strength, $T_{ult}$ in MD/CMD	kN/m	≥ 20/20
Strain at ultimate tensile strength, $\varepsilon$ in MD/CMD	%	≤ 10/10
Tensile stiffness, $J_{0-1\%}$	kN/m	357

## Soil

A dry sand was used as fill material. According to the Unified Soil Classification System (USCS) [6], the soil is classified as a poorly graded sand (SP). The characteristic properties of the sand are given in Table 3 for a relative density of  $D_r = 89\%$ , which was used in the subsequent pullout tests.

Table 3 Characteristic properties of the soil

Property	Units	Value
Grain density, $\rho_s$	g/cm <sup>3</sup>	2.65
Mean particle size, $d_{50}$	mm	0.5
Void ratio, $e_{min}/e_{max}$	-	0.482/0.842
Friction angle, $\phi'_{c'=0}$	°	43.9
Stiffness, $E_{oed}$	MN/m <sup>2</sup>	52.9

## Testing methods

### Calibration curves

In order to understand the sensor response of the filament, calibration curves are produced, which are then used for the data interpretation of the trials in soil. The filament is first contacted, in order to receive the electrical signal from the core of the filament. To do this silver paint was applied to the end of the filament. This increases the accessible conductive area. This silver-tipped filament is then connected to a standard copper wire with a mechanical crimp.

To record the change in resistance during straining, a digital multimeter is used (Keithley 2100 Series: 6,5 Digit USB Multimeter, Tektronix, Inc., Oregon, USA). The strain is induced using a tensile tester, zwickiLine Z2.5, ZwickRoell GmbH & Co. KG, Ulm, Germany. The strain rate for the calibration curves was held at 1 mm/min, in order to match the

strain rate of the later measurements. The experimental set up for the calibration curve generation can be seen in Fig. 2.

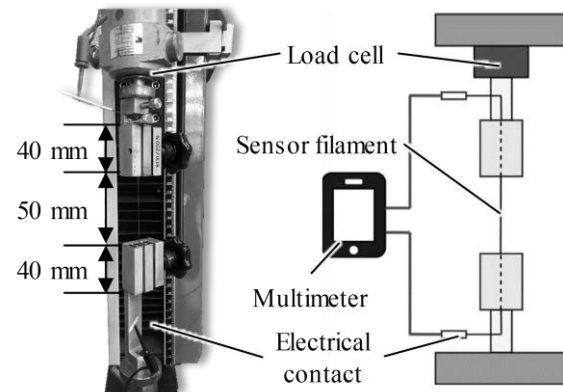


Fig. 2 Experimental setup for the calibration

### Application of fiber on geogrid

The application of the fiber-based sensor technology on the geotextile is an essential issue for ensuring the functionality of the system. The application must ensure the transmission of the forces and strains to the sensor fiber without influencing the properties of the sensor fiber at the connection points. In addition, the application method must be able to withstand the stresses that occur during handling, installation and operation. Regardless of the application method, the sensor fiber must be applied in a stretched state, so that stretching of the substrate results in immediate stretching of the sensor fiber.

Bonding by means of individual clamps or textile bonding methods such as sewing or embroidery are ruled out because of the effort involved and the lack of reliability of the bond. In addition, these methods involve an increased risk of premature damage to the sensor fiber due to mechanical clamping loads. In comparison, the utilized adhesive bond is uncomplicated to apply and avoids any additional mechanical stress on the sensor fiber.

### Tensile tests in air

In order to investigate possible changes in the sensor response due to the application process, the filaments applied the geogrid are also tested in air before performing pullout tests in soil. For these tests the tensile tester ZMART.PRO, ZwickRoell GmbH & Co. KG, Ulm, Germany is employed. The maximum tensile force of this device is 20 kN, which is needed to apply strain to the geogrid. The strain rate is held at 1 mm/min and the clamping length is 250 mm. The test setup for the tensile test in air of the sensor filament applied to the geogrid can be seen in Fig. 3.

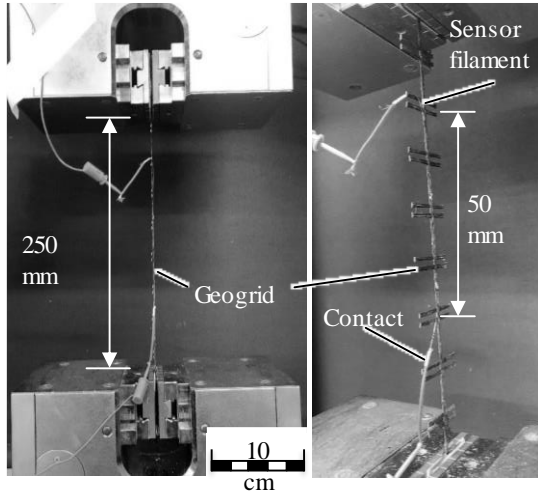


Fig. 3 Test setup for tensile test of applied filament on the geogrid in air

#### Pullout tests in soil

Pullout tests are typically used to quantify the interfacial efficiency of geosynthetic reinforcements with the fill. Its wide application is due to the ease of experimental realization and the standardized framework [7]–[8]. The experimental setup of the pullout tests of this study is shown in Fig. 4.

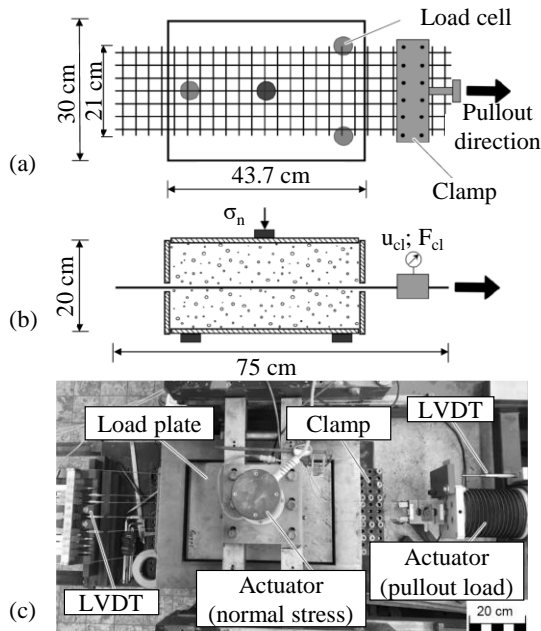


Fig. 4 Experimental setup for pullout tests: (a) top view, (b) side view, (c) final setup

In the tests, geogrids with dimensions of  $750 \times 210$  mm in length and width were used. The mid-section of the geogrid was embedded in the test box filled with soil and the rear ends were led out of the box. On top of the specimen, a constant normal

stress was applied with an actuator loading the top plate. Then, the geogrid specimen was pulled out of the confined soil at the right end by a clamp moving displacement controlled with 1 mm/min. The test series comprises three tests with varying normal stresses of  $\sigma_n = 7.5, 15$  and  $30$  kN/m<sup>2</sup>. At each test, the pullout load and displacement of the clamp were recorded. Additionally, the fiber-based measurement system was tested in the measurement section (A – B), shown in Fig. 5. At the neighboring longitudinal member conventional steel wires connected to LVDTs outside the box were used as a redundant control measurement.

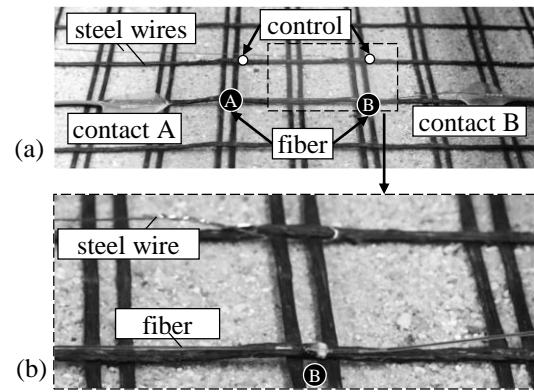


Fig. 5 Detail of measurement section

## RESULTS AND DISCUSSION

First, calibration curves of the fiber material are developed that relate the electric resistance to the tensile strain. Second, the performance of the sensor fiber is evaluated in geogrid tensile tests in air. Third, the novel measuring system is tested for geogrids in soil subjected to pullout.

#### Calibration curves

In Fig. 6, the electrical response of the filament alone is shown for 7 repetitions.

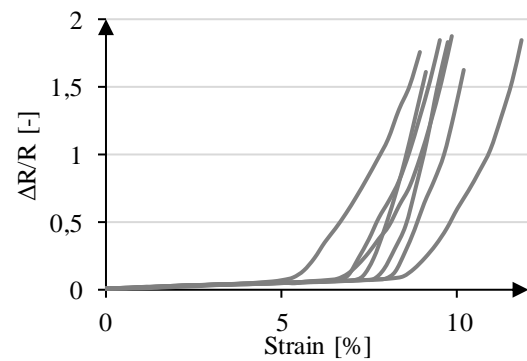


Fig. 6 Initial calibration of the filaments alone

It is clear that the filaments have a slight increase until 5%, then a rapid increase after this point. The filaments are relatively homogenous at low strains (0–5%), but deviate after this point. The focused region of 0–5% can be seen in Fig. 7. The sensor response can be considered linear at the lower strains and homogeneous. This is only partially relevant for the application at hand, since strains up to 10% can be experienced by the geogrid as stated in Tab. 2.

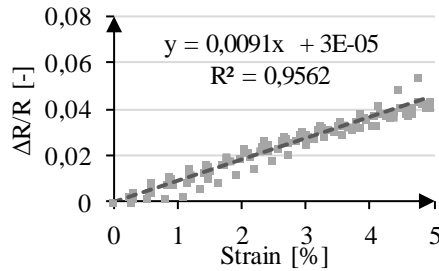


Fig. 7 Sensor response 0–5%

#### Performance evaluation in air

The sensor response is then repeated for the filaments which are applied to the geogrid to investigate possible changes due to application. In order to ensure reproducible results, the filaments are applied in a pretensioned state. This is evaluated for a pretension to reach a specific strain (10%) and specific resistance (1 MΩ). The resulting graphs of the electrical response of the filaments in both states can be seen in Fig. 8 and 9 (zoomed in to 0–5%).

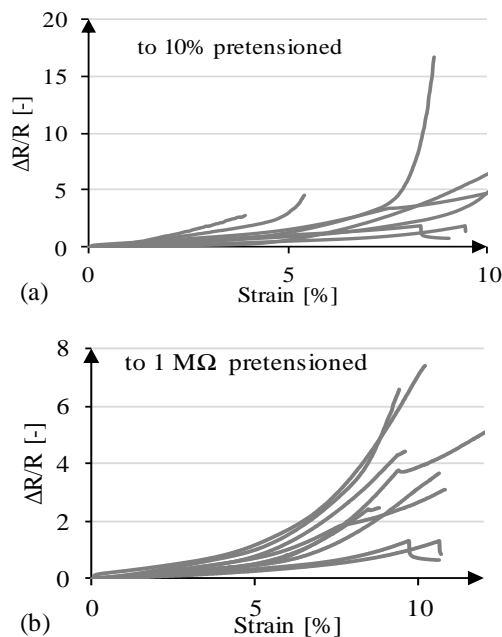


Fig. 8 Sensor response for applied filaments, (a) to 10%, (b) to 1 MΩ

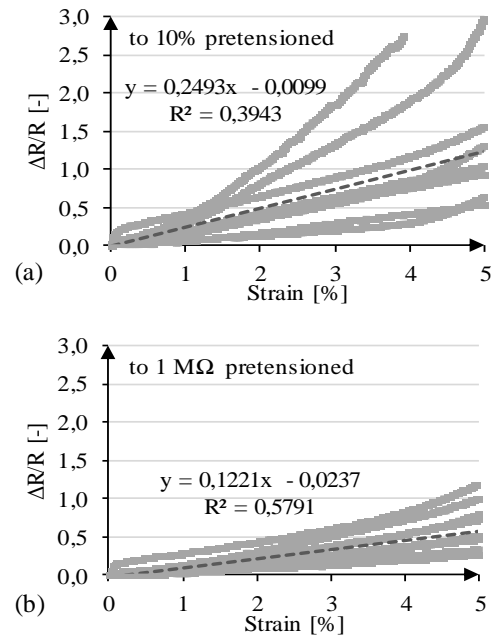


Fig. 9 Sensor response for applied filaments only 0–5%, (a) to 10%, (b) to 1 MΩ

It is clear to see that the sensor response is stronger for the 10% pretensioned (larger slope), but that the response is more homogenous for the 1 MΩ pretensioned samples (larger R²). When comparing the response of the single filament with the applied filament, it can be seen that the response is much lower for the single filament, but very homogenous. These differences are compared in Fig. 10.

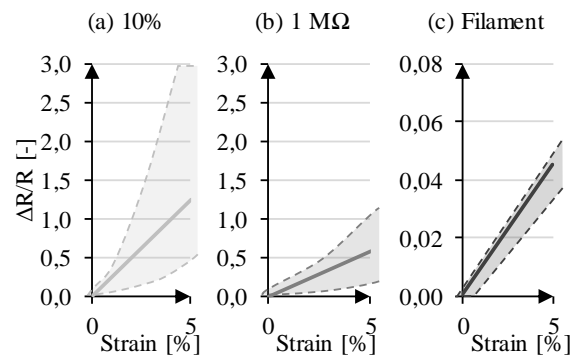


Fig. 10 Comparison of the homogeneity and sensitivity, (a) prestrained to 10%, (b) prestrained to 1 MΩ, (c) not prestrained single filament

#### Performance evaluation in soil

Fig. 11 shows the tensile force-displacement curves of the clamp, pulling out the geosynthetic from the soil for the three confining stresses. Each test was repeated (Test-1 and -2) and the good agreement of the response curves confirmed the tests. Geogrid pullout occurred for normal stresses up to 15 kN/m².

Contrary, rupture at the clamp was observed at 30 kN/m<sup>2</sup>, because the pullout resistance exceeded the ultimate tensile strength of the geogrid. The rupture is evident from the rapid decrease of tensile load at a displacement of about  $u_{cl} = 17$  mm.

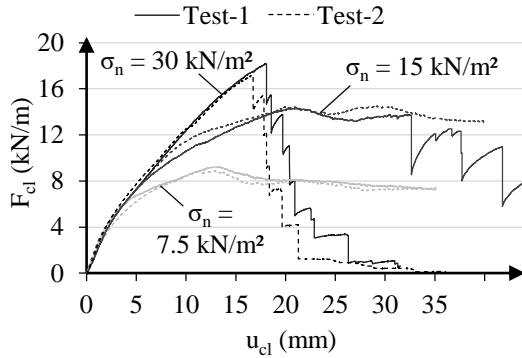


Fig. 11 Results pullout tests

The interface coefficients were calculated for normal stresses up to 15 kN/m<sup>2</sup> according to the total area method, which assumes an average shear stress along the full anchorage length on the top and bottom of the geogrid. This assumption applies for the present tests since pullout failure of the entire geogrid was observed. In Fig. 12, the internal shear strength of the soil and the maximum mobilized shear stresses at the geosynthetic-soil interface from pullout tests are plotted. By relating the interfacial shear stress to the shear strength of the soil, the interface efficiency  $\lambda$  was determined to 0.95 and 0.91 for normal stresses of 7.5 and 15 kN/m<sup>2</sup>, proving a high interaction efficiency of the geosynthetic with the soil.

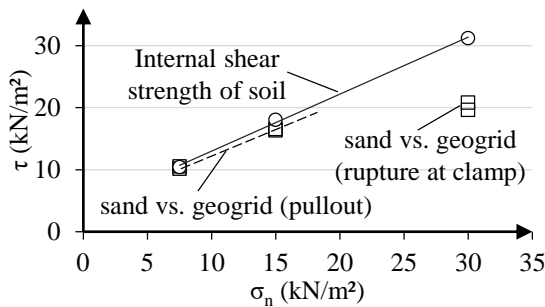


Fig. 12 Interface efficiency from pullout tests

The fiber-based measurement of the geogrid strains was tested in the measurement section as shown in Fig. 5. The results of the measured geogrid strains are summarized in Fig. 13 for the three confining stresses, where the dotted lines represent the control measurement with wires connected to LVDTs and the continuous lines represent the fiber measurement. For the control measurements with LVDT, the measured geosynthetic strains increases as the pullout resistance was mobilized.

Once the geogrid was pulled out of the soil, the geogrid strain remained relatively constant, even though a slight decrease was found at 7.5 kN/m<sup>2</sup> and an increase was detected for 15 kN/m<sup>2</sup>. Overall, the geosynthetic strains were found between 2–7%, where no clear tendency of strain magnitude was found for different confining stresses.

As can be seen from Fig. 13, the fiber measurement technique resulted in geosynthetic strains that were reasonably consistent (a, c) with the control measurement, or significantly deviate from the strains determined with LVDTs (b). For a normal stress of 7.5 kN/m<sup>2</sup>, both measurements represent similar tensile strains up to clamp displacement of 15 mm. Then, the fiber recorded a rapid increase in tensile strain, which was not detected by the LVDTs. The reason can be explained with a local stretching of the fiber, which will be discussed in detail in the chapter “limitations”. For a normal stress of 30 kN/m<sup>2</sup>, the fiber measurement represented the tensile strain of the LVDT measurement accurately during the mobilization of the pullout resistance (up to  $u_{cl} = 15$  mm). From there, a constant tensile strain was measured, which was, about 100% higher than recorded by the LVDTs. For a normal stress of 15 kN/m<sup>2</sup>, the fiber measurement did not correspond to the geosynthetic strain at any clamp displacements.

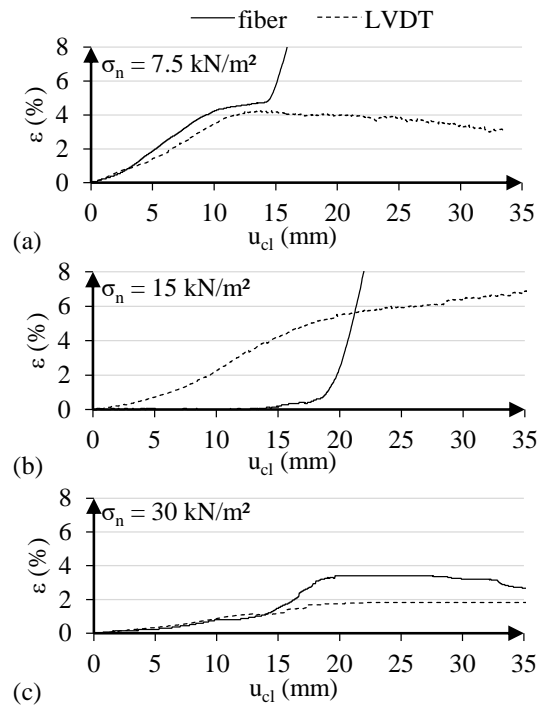


Fig. 13 Results pullout tests for normal stress of (a) 7.5 kN/m<sup>2</sup>, (b) 15 kN/m<sup>2</sup>, (c) 30 kN/m<sup>2</sup>

In conclusion, the pullout tests revealed that the fiber measurement technique is generally applicable for measuring geosynthetic strains (Fig. 13 a, c).



However, it should be emphasized that at the fiber used in this study, was not reliable enough to represent the tensile strain in all tests and significant deviations were detected during one of the three tests.

## LIMITATIONS

The test results of the previous section have clearly revealed that current development stage of the fiber measurement technique is not reliable enough to be used in geotechnical structures as monitoring system. The limitations of the system can be summarized as follows:

- Inhomogeneous cross section of fiber resulting in deviating electrical resistance due to not optimized spinning process
- Difficult contacting of the filament to cable and geogrid due to small dimensions
- Sensitivity of the filament to mechanical strains outside of the testing area (Fig. 14)
- Filament relaxation from application to testing
- Sensitivity of the filament to mechanical impact of the surrounding soil.

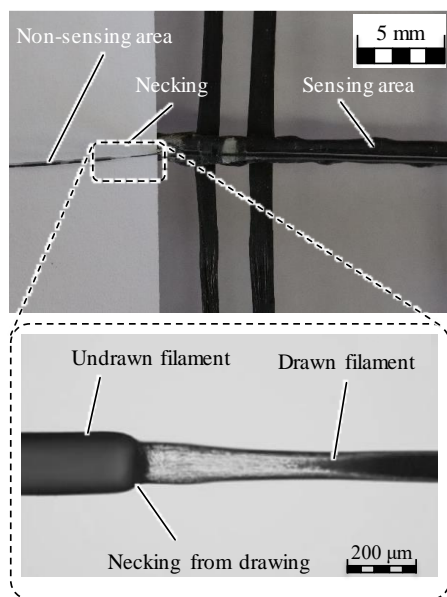


Fig. 14 Deformation of the filament

## CONCLUSIONS & OUTLOOK

The results of this work are promising in showing that the measurement of strains in geostructures is principally possible when employing filament-based sensors. However, the need for process optimization has been demonstrated. In the next steps, the processing parameters of the spinning trials for the filament production will be further investigated and improved. Afterwards, it is expected that the sensor

response is not only more accurate but more sensitive. Furthermore, the material used can be modified, as a lower resistivity can actually contribute to a higher sensitivity of the sensor. For this, the particle concentration can be lowered in order to find the maximum sensitivity of the sensor filament.

Additional work must also be carried out in the sensor calibration. Possible other environmental changes, such as pressure, moisture or temperature can alter the electrical properties and must be compensated. The sensors should be tested in cyclic stress as well as relaxation, in order to understand the long-term changes of the electrical resistance when the filament is pretensioned during application.

## ACKNOWLEDGMENTS

The authors would like to thank Huesker Synthetic GmbH for providing geogrids for this study.

## REFERENCES

- [1] Tatsuoka, F., Tateyama, M., Koseki, J. and Yonezawa, T. 2014. Geosynthetic-Reinforced Soil Structures for Railways in Japan. *Transportation Infrastructure Geotechnology*, 1, 3–53.
- [2] Allen, T. M., Bathurst, R. J. and Berg, R. R. 2002. Global Level of Safety and Performance of Geosynthetic Walls: An Historical Perspective. *Geosynthetics International*, 9, 395–450.
- [3] Skinner, G. D. and Rowe R. K. 2005a. Design and behaviour of a geosynthetic reinforced retaining wall and bridge abutment on a yielding foundation. *Geotextiles and Geomembranes*, 23, 234–260.
- [4] Derksen, J., Ziegler, M. and Fuentes, R. 2021. Geogrid-soil interaction: A new conceptual model and testing apparatus. *Geotextiles and Geomembranes*, 49, 1393–1406.
- [5] Ortega, J., & Gries, T. 2022. Investigation of production influences on the properties of resistive based filament sensors. *Fiber Society Spring Conference*, 30 May – 1 June, 2022, Leuven, Belgium.
- [6] ASTM D 2487. Standard Practice for Classification of Soils for Engineering Purposes (Unified Soil Classification System), American Society for Testing and Materials, West Conshohocken, USA.
- [7] ASTM D6706 (2013): Standard Test Method for Measuring Geosynthetic Pullout Resistance in Soil. ASTM Standards, West Conshohocken, USA.
- [8] DIN 60009 (2017): Geosynthetics - Determination and testing of the interaction coefficient to the soil using pullout test, Beuth, Berlin, Germany



# SATELLITE-BASED GROUND DEFORMATION MONITORING IN NAGA CITY, CEBU ISLAND IN THE PHILIPPINES

Ryan A. Ramirez<sup>1,2</sup>, Rajiv Eldon E. Abdullah<sup>1</sup> and Christabel Jane P. Rubio<sup>1,2</sup>

<sup>1</sup>Faculty of Engineering, University of Santo Tomas, Manila 1015, Philippines; <sup>2</sup>National Research Council of the Philippines, Taguig 1631, Philippines

## ABSTRACT

Human activities are increasingly altering subsurface conditions leading to unwanted ground deformations. Excessive ground deformations endanger buildings, linear systems, underground facilities, and ultimately, people's safety. Thus, mapping and monitoring ground deformation are critical in managing disaster risk and mitigating socio-economic damage from possible geohazards. Accessible and archived satellite data and the continual development of advanced remote sensing technologies can now provide valuable information about the earth's surface for various applications. This study applied the descending Sentinel-1 Persistent Scatterer Interferometric Synthetic Aperture Radar (PSInSAR) technique for long-term remote ground deformation monitoring over the coastal city of Naga in Cebu Island in the Philippines. The Sentinel-1 PSInSAR technique provided relatively dense ground monitoring points, specifically over built-up areas. The maximum ground subsidence along the radar line-of-sight (LOS) estimated throughout the monitoring period from October 2014 to September 2018 exceeds -50 mm, whereas the LOS mean displacement velocity exceeds -15 mm/yr. The two-parameter hyperbolic model well fitted the PSInSAR results to describe the nonlinear behavior of ground deformation. Ground deformation over the coastal city continues to evolve, and stabilization is yet to occur. This study suggests that the Sentinel-1 PSInSAR technique can provide technical support in mapping and monitoring ground deformation over vast areas with less human labor and efficient cost.

*Keywords: Sentinel-1 PSInSAR, Ground deformation monitoring, Hyperbolic model, Coastal city, Cebu Island*

## INTRODUCTION

Reclamation projects along coastal cities for industrial, residential, and commercial use have allowed land expansions. Human activities aiding continual urban sprawl over reclaimed lands are increasingly altering subsurface conditions resulting in unwanted ground deformations. Excessive ground deformations endanger structures, linear systems, underground facilities, and ultimately, people's safety. Thus, ground deformation mapping and long-term monitoring over coastal cities are critical to prevent disaster risk and mitigate socio-economic damage from such geohazards [1].

Ground-based geodetic methods such as precise leveling and terrestrial measurements such as Global Positioning System (GPS) are standard monitoring methods providing accurate and reliable ground deformation [2]–[3]. However, these methods are inefficient to deploy over vast areas and long term because of the workforce needed and the high cost associated. Meanwhile, accessible and archived satellite Synthetic Aperture Radar (SAR) data and the continual development of advanced remote sensing techniques have emerged as viable solutions for geohazard mitigation. The launch of the Sentinel-1 (S1) mission under the Copernicus Program of the European Space Agency (ESA) and European Commission (EC) has provided accessible SAR data

since 2014, which the scientific community is enjoying for various earth and geoinformation applications. Specifically, the Persistent Scatterer Interferometric SAR (PSInSAR) has been successfully applied in various geohazard applications [4]. Theoretical and technical reviews of different PSInSAR algorithms are available in the literature [5]–[6]. PSInSAR provided the opportunity to detect, map, and monitor ground deformations along the coasts caused or enhanced by natural and anthropic activities [7]–[12]. In low-lying coastal urban areas in Metro Manila, Philippines, ground deformation from 1993-to-2010 has been investigated using differential InSAR (DInSAR) [13]. Nevertheless, limited studies are available in the literature exploiting the S1-PSInSAR technique in other coastal cities in the Philippines experiencing short- to long-term nonlinear ground deformations reflecting the complex interaction among different natural and anthropic processes.

This study applied the PSInSAR technique for long-term remote ground deformation monitoring over the coastal city of Naga in Cebu Island in the Philippines using descending S1 SAR dataset acquired between October 2014 and September 2018. The cumulative line-of-sight (LOS) displacement acquired from the S1-PSInSAR analysis was modeled using a two-parameter hyperbolic model to describe the nonlinear ground deformation process over a

multipurpose complex zone built over reclaimed land in Naga city.

## STUDY AREA AND SAR DATASET

### Study Area

Cebu Island's geological structure comprises a Jurassic-Cretaceous igneous and metamorphic basement complex and Cenozoic sedimentary and volcanic rock units [14]–[15]. The island is classified as a tropical rainforest [16]. The Philippine Atmospheric, Geophysical and Astronomical Services Administration (PAGASA 2022) reported a mean annual rainfall of 1,565 mm for Cebu Island. Naga city is located on the southeastern coast of Cebu Island, characterized by karst terrain. Ridges and valleys converged to a coastal plain in the southeastern part of the city. Land use is predominantly cultivated lands with quarry zones. Small villages are located inland, whereas built-up areas are concentrated mainly along the coastal plain. The nearest potentially active faults are the South and Central Cebu faults; the latter passes through Naga city. Between October 2014 and September 2018, the Philippine Institute of Volcanology and Seismology (PHIVOLCS 2018) recorded one earthquake of magnitude 5.2, 7 earthquakes of magnitude between 4 and 5, 45 earthquakes of magnitude between 3 and 4, and 173 earthquakes of magnitude between 2 and 3 that shook Cebu Island. There were also 14 earthquakes with a magnitude below 2.

### SAR Dataset

The SAR dataset exploited in this study was acquired by the S1 mission operated jointly by ESA and EC under the Copernicus Program. The S1 mission consists of two right-side looking satellites: S1-A, which was launched in 2014, and S1-B, which was launched in 2016. S1 sensors operate at a wavelength  $\lambda$  equal to 5.6 cm (C-band). The twin constellation has a near-polar sun-synchronous orbit with a 6–12 days repeat cycle over the exact location. S1 SAR products acquired in the interferometric wide swath mode have a ground range coverage of approximately 250 km, thanks to the Terrain Observation by Progressive Scans (TOPS) mode [17]. The geometric resolution in the range and azimuth directions is  $5\text{ m} \times 20\text{ m}$ , respectively.

This study collected 139 S1 single look complex SAR images from October 21, 2014, to September 18, 2018. The images were acquired by the S1 descending satellite (track 61), whose flight is from north to south direction. The minimum and maximum time gap between each successive image are 6 and 48 days, respectively, as shown in Fig. 1. All interferometric pairs have a perpendicular baseline of less than 150 m, thanks to the improved S1's orbital

tube. The image acquired on July 31, 2017, was set as the master image to mitigate the decorrelation effect.

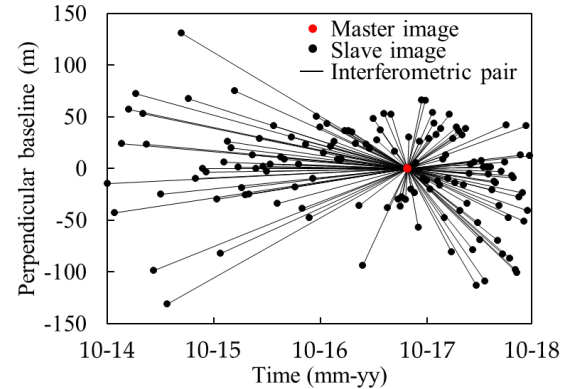


Fig. 1 S1 SAR dataset. The vertical and horizontal axes represent the perpendicular and temporal baselines of interferometric pairs.

## METHODS

### Advanced Time Series InSAR Analysis

The S1 SAR images were processed following a two-staged processing workflow, namely (1) multiple differential interferogram formation and (2) time series InSAR analysis. In Stage 1, the SeNtinel Application Platform (SNAP), freely distributed by ESA, was utilized, whereas, in Stage 2, the open-source software package of Stanford Method for Persistent Scatterers (StaMPS) was used [18].

#### Stage 1: SNAP pre-processing

First, a master image from the S1 SAR dataset is selected under good weather conditions. To this aim, the InSAR Stack Overview tool in SNAP was used. Then, the open-source snap2stamps package tool automated the pre-processing steps [19]. The area of interest (AOI) was selected during the image splitting and orbit file correction to reduce the computational effort. Subsequently, the interferogram formation followed immediately after the coregistration of slave images to the geometry of the master image using back-geocoding with Enhanced Spectral Diversity (ESD). Afterward, the Shuttle Radar Topography Mission digital elevation model (SRTM DEM) 1 arcsec data in the SNAP library allowed topographic phase removal. Then, debursting of the coregistered images and differential interferograms followed to produce seamless image products. These products are then exported in Stage 2.

#### Stage 2: StaMPS processing

After exporting the SNAP pre-processed image products into the format supported for StaMPS

processing in Matlab, an amplitude dispersion index (ADI) of 0.42 was used to select and load initial PS candidates (PSCs). Then, the phase noise value for each PSC in every differential interferogram was estimated iteratively. Based on the estimated phase noise characteristics, final PSs were selected, and those PSs deemed noisy were weeded afterward. The final PSs in the wrapped phase were then corrected for DEM error. The corrected phase information is then unwrapped using the open-source software, Statistical-Cost, Network-Flow Algorithm for Phase Unwrapping (SNAPHU) [20]. Then, the spatially correlated look angle (SCLA) error is estimated and removed from the unwrapped data. Finally, phase errors attributed to atmospheric perturbations are mitigated using spatiotemporal filters.

The immediate results after Stage 2, such as the LOS mean displacement velocity map and time series, are relative measures concerning a selected reference area. For this purpose, a preliminary S1-PSInSAR analysis with an ADI of 0.60 was performed, introducing more PSCs corrupted with noise. Then, the AOI was inspected for a stable reference area by evaluating the LOS mean displacement velocity and time series of PSs groups within a moving window with a 20-m radius. The mean velocity within the selected reference area must be between  $\pm 1$  mm/yr with a nearly horizontal displacement time series.

### Hyperbolic Modeling

Due to the success of applying and validating advanced time series InSAR using various archived SAR datasets, modeling the long-term temporal evolution of ground deformation has been possible with several mathematical functions [21]–[22]. The fitted model describing the settlement curve obtained from advanced time series InSAR is typically the hyperbolic function. Advanced time series InSAR results from existing literature utilized distributed scatterers (DSs), whose phase behavior are different from those of PSs. Generally, DS-based time series InSAR techniques are preferred for non-urban areas with considerable vegetation cover or when few SAR images are available. On the one hand, the PSInSAR technique is more suitable for ground deformation monitoring in urban areas. Therefore, in this study, a two-parameter hyperbolic model was fitted to our S1-PSInSAR results to describe the nonlinear deformation phenomenon over Naga city, specifically on the reclaimed land where a multipurpose complex zone is built. The displacement  $d$  at a specific time  $t$  described by the hyperbolic model is expressed in Eq. (1), as shown below [23].

$$d = t / (\alpha + \beta t) \quad (1)$$

where  $\alpha$  and  $\beta$  are the PS point-specific constants

derived using regression analysis. The root-mean-squared error (RMSE) and coefficient of determination ( $R^2$ ) were optimized to constraint the two constants.

## RESULTS AND DISCUSSION

### Spatial Distribution of Measurement Points

After the S1-PSInSAR processing, 5,767 quality PSs were recognized over the AOI. Figure 2 shows the LOS mean displacement velocity map. PSs were plotted relative to the selected reference stable area (i.e., negligible ground deformation). Warm colors represent a movement away from the radar (i.e., subsidence), and cold colors indicate a movement towards the radar (i.e., uplift). Most PSs were detected over built-up areas, characterized by houses, buildings, and roads. On the one hand, there is the complete absence of PSs over vegetated areas and water bodies, which are normally subjected to rapid changes between two S1 SAR image acquisitions. These rapid surface changes lead to temporal decorrelation.

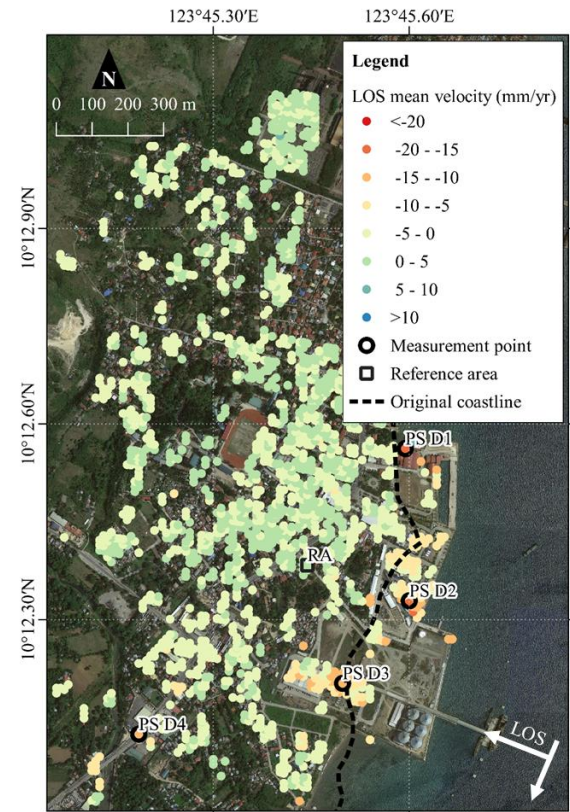


Fig. 2 LOS mean displacement velocity map over the coastal area in Naga city, Cebu Island, Philippines.

Subsiding areas were detected and mapped during the analysis period over the reclaimed land, the

eastside of the coastline in Fig. 2, where a multipurpose complex zone is built. However, groundworks on the east side of the reclaimed land during the monitoring period resulted in a lack of PSs. The maximum subsidence rate exceeded  $-15$  mm/yr. The inland, located west side of the coastline, was generally stable, with most of the PSs having a LOS mean displacement velocity between  $\pm 5$  mm/yr. The distribution of PSs concerning the ground movement type is shown in Fig. 3.

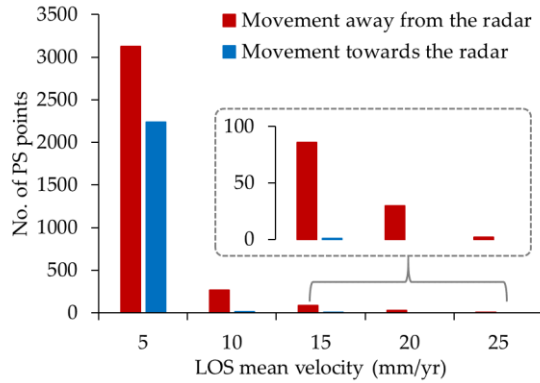


Fig. 3 Distribution of LOS mean displacement velocity for PSs over the AOI. The inset shows the number of PSs with subsidence rate  $\leq -15$  mm/yr.

### Temporal Evolution of Ground Deformation

Four representative PSs or measurement points were selected within the subsiding zone near the coastline over the AOI. These four points are labeled as PSs D1–D4 in Fig. 2. PSs D1, D2, D3, and D4 are located over the sports arena, public market, industrial flour milling company, and national road. The subsidence rate of these points exceeds  $-10$  mm/yr. The cumulative LOS displacement time series of the PSs are plotted in Figs. 4a–d. Accumulated subsidence of the PSs varies depending on their location over the AOI. At the end of the monitoring period in September 2018, the subsidence values of PSs D1, D2, D3, and D4 were  $-86.807$  mm,  $-70.193$  mm,  $-53.146$  mm, and  $-45.074$  mm, respectively. The maximum subsidence was recorded for PS D1, located over the reclaimed land. On the one hand, PSs recognized over the inland (i.e., PS D4) record lower subsidence values than PS D1.

The hyperbolic curve fitted to the S1-PSInSAR displacement time series of PSs D1–D4 is also plotted in Figs. 4a–d. Table 1 summarizes the optimized hyperbolic model constants. The constant  $\alpha$  is highly dependent on the spatial location of the PSs than that of the constant  $\beta$ . The modeled cumulative LOS displacements are in excellent agreement with the S1-PSInSAR results with low RMSE ( $<4$  mm) and

relatively high  $R^2$  ( $>0.90$ ).

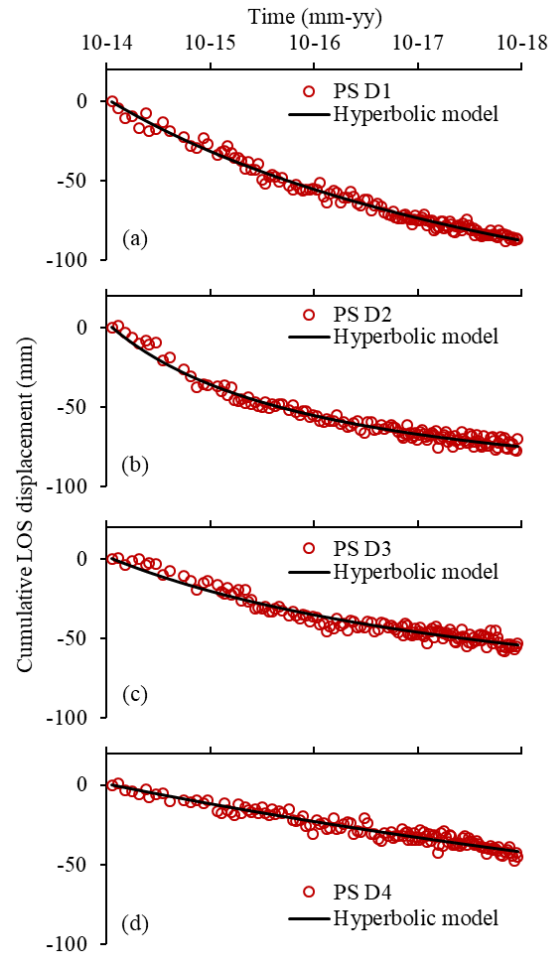


Fig. 4 Cumulative LOS displacement time series of PSs D1–D4, including the fitted hyperbolic curve.

Table 1 Optimized hyperbolic model constants

PS No.	Model constants		RMSE	$R^2$
	$\alpha$	$\beta$		
D1	-9.367	-0.0049	2.691	0.99
D2	-6.634	-0.0088	2.847	0.98
D3	-13.965	-0.0087	3.222	0.95
D4	-27.809	-0.0045	2.747	0.94

The modeled displacement time series of the four PSs implies that subsidence may have occurred before the start of the satellite-based monitoring period. However, the hyperbolic function might not have captured the commencement stage of the subsidence phenomenon [23]. Nevertheless, the modeled results suggest that subsidence slowly decelerates faster over time for PSs D2 and D3. For PSs D1 and D4, the modeled results suggest that stabilization is yet to occur over the coastal area. Using the Google Earth Street View function, a



walkthrough over the AOI showed signs of active subsidence, such as hairline cracks on buildings, road pavements, and masonry fences.

### Potential Contributory Factors of Subsidence

The modeled cumulative LOS displacement time series of PSs D1–D4 was plotted with the monthly average precipitation from October 2014 to September 2018 in Fig. 5 to verify the cause of nonlinear subsidence over the coastal area. The weather monitoring station of PAGASA in Cebu Island is located at Mactan Station (10°19'18.15"N, 123°58'33.7"E). The collected precipitation data shows good relation with the modeled displacement time series.

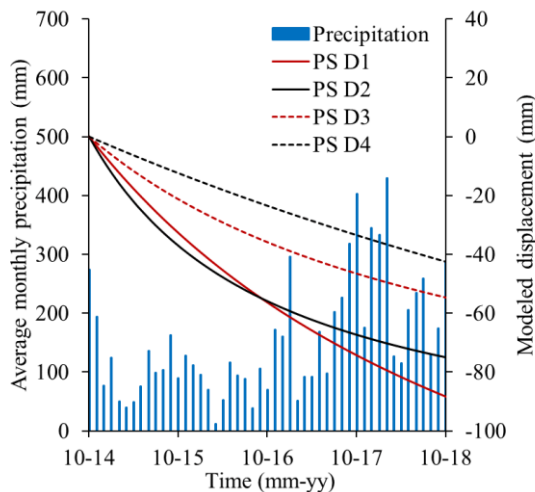


Fig. 5 Relation of modeled cumulative LOS displacement of PSs D1–D4 with average monthly precipitation from October 2014 to September 2018.

Most of the highest monthly average precipitations (>200 mm) were recorded between January 2017 and July 2018. In the case of PSs D2 and D3, subsidence may have decelerated after precipitation has recharged the groundwater [24]–[25]. In the case of PSs D1 and D4, subsidence may be related to precipitation and other contributory natural factors, including the geology of Naga city, the thickness of compressible soil layers along the coastal area, and the swarm of seismic activities during the monitoring period. Anthropogenic processes or human interventions such as excessive groundwater exploitation, continual urbanization, industrialization, and quarrying may have also contributed to the different ground deformations over the AOI. However, detailed analyses were not possible due to the lack of available ancillary data collected during the study period. Further investigation, including in-situ measurements to

validate our observations, is indispensable.

Nevertheless, the S1-PSInSAR results reported here recommend that continuous ground deformation monitoring is needed until the ground has been stabilized completely.

### CONCLUSIONS

This study demonstrated the S1-PSInSAR technique for long-term ground deformation monitoring over the coastal city of Naga in Cebu Island in the Philippines. The satellite-based SAR data and advanced remote sensing technique detected, mapped, and monitored the nonlinear ground deformation in the multipurpose complex zone built over reclaimed land. The two-parameter hyperbolic model was fitted to the S1-PSInSAR displacement time series to describe the nonlinear ground deformation behavior. Overall, the modeled results show excellent agreement with the S1-PSInSAR results, suggesting maximum ground subsidence over –50 mm and subsidence rate over –15 mm/yr. Ground deformation over the reclaimed land continues to evolve related to natural and anthropogenic processes, and stabilization is yet to occur. This study suggests that the S1-PSInSAR technique can provide technical support in mapping and monitoring ground deformation over vast areas under different meteorological conditions with less human labor and efficient cost.

### ACKNOWLEDGMENTS

The authors would like to thank the National Research Council of the Philippines (NRCP) for the financial assistance provided through the Support to Research Dissemination in Local and International Platforms (RDLIP) component of the Basic Research Information Translation for Empowerment in the Regions (BRITER) Program.

### REFERENCES

- [1] Galloway D.L., and Burbey T.J., Review: Regional Land Subsidence Accompanying Groundwater Extraction. *Hydrogeology Journal*, Vol. 19, 2011, pp.1459–1486.
- [2] Abidin H.Z., Andreas H., Djaja R., Darmawan D., and Gamal M., Land Subsidence Characteristics of Jakarta Between 1997 and 2005, as Estimated using GPS Surveys. *GPS Solutions*, Vol. 12, Issue 1, 2008, pp.23–32.
- [3] Pecoraro G., Calvello M., and Piciullo L., Monitoring Strategies for Local Landslide Early Warning Systems. *Landslides*, Vol. 16, 2019, pp.213–231.
- [4] Ferretti A., Prati C., and Rocca F., Permanent Scatterers in SAR Interferometry. *IEEE Transaction on Geoscience and Remote Sensing*,

- Vol. 39, 2001, pp.8–20.
- [5] Crosetto M., Monserrat O., Cuevas-González M., Devanthery N., and Crippa B., Persistent Scatterer Interferometry: A Review. *ISPRS Journal of Photogrammetry and Remote Sensing*, Vol. 115, 2016, pp.78–89.
- [6] Jia H., and Liu L., A Technical Review on Persistent Scatterer Interferometry. *Journal of Modern Transportation*, Vol 24, Issue 2, 2016, pp.153–158.
- [7] Peyret M., Dominguez S., Cattin R., Champenois J., Leroy M., and Zajac A., Present-day Interseismic Surface Deformation Along the Longitudinal Valley, Eastern Taiwan, from a PS-InSAR Analysis of the ERS Satellite Archives. *Journal of Geophysical Research: Solid Earth*, Vol. 116, Issue B3, 2011, pp.1–21.
- [8] Aucelli P.P.C., Di Paola G., Incontri P., Rizzo A., Vilardo G., Benassai G., Buonocore B., and Pappone G., Coastal Inundation Risk Assessment due to Subsidence and Sea Level Rise in a Mediterranean Alluvial Plain (Volturno Coastal Plain-Southern Italy). *Estuarine, Coastal and Shelf Science*, Vol. 198, 2017, pp.597–609.
- [9] Liu P., Chen X., Li Z., Zhang Z., Xu J., Feng W., Wang C., Hu Z., Tu W., and Li H., Resolving Surface Displacements in Shenzhen of China from Time Series InSAR, Vol. 10, Issue 7, 2018, pp.1162.
- [10] Polcari M., Albano M., Montuori A., Bignami C., Tolomei C., Pezzo G., Falcone S., La Piana C., Doumaz F., Salvi S., and Stramondo S., InSAR Monitoring of Italian Coastline Revealing Natural and Anthropogenic Ground Deformation Phenomena and Future Perspectives, Vol. 10, Issue 9, 2018, pp.3152.
- [11] Hu B., Chen J., and Zhang X., Monitoring the Land Subsidence Area in a Coastal Urban Area with InSAR and GNSS. *Sensors*, Vol. 19, Issue 14, 2019, pp.3181.
- [12] Altintas F., and Gokalp E., Monitoring Surface Deformations of the Reclamation Site using PS Interferometry: Senol Gunes Sports Complex (Turkey). *Geocarto International*, 2021, pp.1–14.
- [13] Raucoules D., Le Cozannet G., Wöppelmann G., de Michele M., Gravelle M., Daag A., and Marcos M., High Nonlinear Urban Ground Motion in Manila (Philippines) from 1993–2010 observed by DInSAR: Implication for Sea-level Measurement. *Remote Sensing of Environment*, Vol. 139, 2013, pp.386–397.
- [14] Dimalanta C., Suerte L., Yumul G., Tamayo R., and Ramos E., A Cretaceous Supra-Subduction Oceanic Basin Source for Central Philippine Ophiolitic Basement Complexes: Geological and Geophysical Constraints. *Geosciences Journal*, Vol. 10, Issue 3, 2006, pp.305–320.
- [15] Deng J., Yang X., Zhang Z.F., and Santosh M., Early Cretaceous Arc Volcanic Suite in Cebu Island, Central Philippines and Its Implications on Paleo-Pacific Plate Subduction: Constraints from Geochemistry, Zircon U-Pb Geomorphology and Lu-Hf Isotopes. *Lithos*, Vol. 230, 2015, pp.166–179.
- [16] Beck H.E., Zimmermann N.E., McVicar T.R., Vergopolan N., Berg A., and Wood E.F., Present and Future Köppen-Geiger Climate Classification Maps at 1-km Resolution. *Scientific Data*, Vol. 5, 2018, pp.108214.
- [17] Torres R., Snoeijs P., Geudtner D., Bibby D., Davidson M., Attema E., Potin P., Rommen B., Floury N., Brown M., Traver I.N., Deghaye P., Duesmann B., Rosich B., Miranda N., Bruno C., L'Abbate M., Croci R., Pietropaolo A., Huchler M., and Rostan F., GMES Sentinel-1 Mission. *Remote Sensing of Environment*, Vol. 120, 2012, pp.9–24.
- [18] Hooper A., Bekaert D., Spaans K., and Arikian M., Recent Advances in SAR Interferometry Time Series Analysis for Measuring Crustal Deformation. *Tectonophysics*, Vol. 514–514, 2012, pp.1–13.
- [19] Fomelis M., Delgado Blasco J.M., Desnos Y.L., Engdahl M., Fernández D., Veci L., Lu L., and Wong C., ESA SNAP-StaMPS Integrated Processing for Sentinel-1 Persistent Scatterer Interferometry. In *Proceedings of the 2018 IEEE International Geoscience and Remote Sensing Symposium*, 2018, pp.1364–1367.
- [20] Chen C.W., and Zebker H.A., Two-dimensional Phase Unwrapping with Use of Statistical Models for Cost Functions in Nonlinear Optimization. *Journal of the Optical Society of America A*, Vol. 18, Issue 2, 2001, pp.338–351.
- [21] Kim S.W., and Won J.S., Measurements of Soil Compaction Rate by using JERS-1 SAR and a Prediction Model. *IEEE Transactions on Geoscience and Remote Sensing*, Vol. 41, Issue 11, 2003, pp.2683–2686.
- [22] Park S.W., and Hong S.H., Nonlinear Modeling of Subsidence from a Decade of InSAR Time Series. *Geophysical Research Letters*, Vol. 48, Issue 3, 2021, pp.1–10.
- [23] Tan T.S., Inoue T., and Lee S.L., Hyperbolic Method for Consolidation Analysis. *ASCE Journal of Geotechnical Engineering*, Vol. 117, Issue 11, 1991, pp.1723–1737.
- [24] Zhang Y., Liu Y., Jin M., Jing Y., Liu Y., Sun W., Wei J., and Chen Y., Monitoring Land Subsidence in Wuhan City (China) using the SBAS-InSAR Method with Radarsat-2 Imagery Data. *Sensors*, Vol. 19, 2019, pp.743.
- [25] Zhou L., Guo J., Hu J., Li J., Xu Y., Pan Y., Shi M., Wuhan Surface Subsidence Analysis in 2015–2016 based on Sentinel-1A Data by SBAS-InSAR. *Remote Sensing*, Vol. 9, 2017, pp.982.



# FINITE ELEMENT PARAMETRIC STUDY OF CONTIGUOUS PILE WALL REINFORCEMENT IN A DEEP EXCAVATION

Fachrizal Naufal Indrawan<sup>1</sup>, Fikri Faris<sup>2</sup> and Akhmad Aminullah<sup>3</sup>

<sup>1</sup>Department of Civil and Environmental Engineering, Universitas Gadjah Mada, Indonesia

## ABSTRACT

Deep excavation for underground structures has become a common practice in the world. This study discusses the parametric study of contiguous pile wall (CPW) reinforcement in a deep excavation in dry medium dense sand soils. The parametric study focuses on studying the effect of excavation dimension ratio, pile diameter (d), and cap beam dimensions on lateral displacement and bending moment behaviour of CPW reinforcement. The research model is set as an example case of a square excavation in dry medium dense sand with a depth of excavation (he) 7.50 m, and the pile length is 18.50 m, with 11.00 m penetration depth (D). 3-D and 2-D finite elements are used to support this research. Rocscience RS3 was used for 3-D analysis and RS2 for 2-D analysis. The result showed that 3-D analysis is effective in a square excavation with a small dimension ratio ( $B/L \leq 2$ ), while 2-D analysis is more suitable for a square excavation with a large dimension ratio ( $B/L \geq 3$ ). Increasing the pile diameter reduces the lateral displacement of the pile, although it increases the bending moment. The cap beam on the pile head reduced the lateral displacement on the pile by 45% and the bending moment by 54% compared to the pile without the cap beam. Increasing the cap beam dimensions also reduced the lateral displacement of the pile but increased the bending moment, although not significantly.

*Keywords: Parametric study, Contiguous pile wall, Deep excavation, Finite element*

## INTRODUCTION

The main problem in deep excavation work and sub-structure of high-rise buildings in dense urban areas is the narrow space and adjacent buildings. If forced, it will result in excessive ground movement, deformation, subsidence, and even damage to existing structures around the excavation site [1]. An alternative solution to the problem of deep excavation and sub-structure of high-rise buildings in narrow land and adjacent buildings is contiguous pile walls (CPW) reinforcement. CPW is an expensive reinforcement, but it can save space and time, especially in dense urban areas.

The study of deep excavation with CPW reinforcement is a popular topic, especially in the geotechnical field. Several researchers used two-dimensional (2-D) and three-dimensional (3-D) finite elements (FE) to analyze the complexity of deep excavation problems. The 2-D analysis has proven more economical and relevant in continuous modeling (plane strain), fast modeling, and calculation. 2-D FE also does not require a high-specs computer as required in 3-D. A 3-D analysis is the most realistic analysis and approaches the actual conditions in the field compared to the 2-D analysis [2]. Many studies have explored the behavior of soil and reinforcement in deep excavations using FE, including [2-17], advantages of 3-D analysis over 2-D [18-23], and soil-structure interaction behavior: [24-26]. In these previous studies, the effect of

excavation dimension ratio and cap beam on lateral displacement and bending moment of the CPW reinforcement were less studied.

This study focused on studying the lateral displacement and bending moment behavior of CPW reinforcement based on variations in several parameters such as excavation dimension ratio, pile diameter, and cap beam dimensions in 3-D and 2-D models using Rocscience RS3 and RS2. In 3-D analysis, this study assumed the pile and the cap beam model as a beam element to approach the actual condition of the reinforcement configuration in the field. The 2-D analysis was used to verify variations in the ratio of excavation dimensions in the 3-D analysis.

## NUMERICAL SIMULATION AND PARAMETERS USED

Deep excavation design requires careful consideration of the strength and stability of various structural elements at all stages during the construction process [25]. Excavated wall deformation is crucial in selecting a stabilization system [9]. In this study, deep excavation modeling with CPW reinforcement in homogenous dry medium dense sand was carried out to represent the construction sequences, the excavation and reinforcement behavior, soil-structure interaction, and conditions in the field. The Mohr-Coulomb (MC)

constitutive model and the reinforcement parameters used were determined based on the existing literature. Figure 1 illustrates the model of a deep excavation case in sandy soil with a square geometry used in this study. It shows a model with an excavation depth ( $h_e$ ) of 7.50 m, and the pile length is 18.50 m, with 11.00 m pile penetration depth ( $D$ ). A surcharge load of 10.00 kN/m<sup>2</sup> with a width of 10.00 m was applied to each side of the excavation. The equation for determining the pile distance ( $s$ ) is:

$$s = d + 0.10 \quad (1)$$

where:  $s$  = Pile distance (m),  $d$  = Pile diameter (m).

Since the excavation did not consider the wall impermeability, the pile distance ( $s$ ) was determined by Eq. (1). Hence, the optimal pile configuration can be obtained while still being easy and realistic to implement in the field. The excavation dimensions will be varied on the primary side ( $L$ ) while the complementary side ( $B$ ) is fixed. Variations were also made on the diameter of the pile ( $d$ ) and the dimensions of the cap beam. Rocscience RS3 and RS2 simulated all execution sequences, such as reinforcement installation, excavation, and surcharge loading in 3-D and 2-D models.

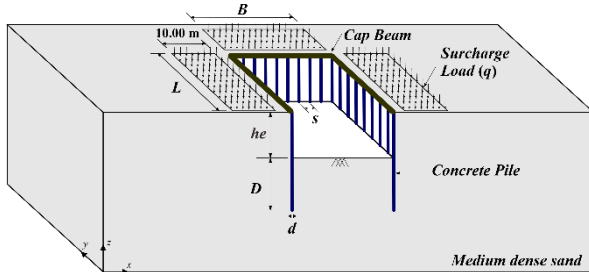


Fig. 1 Excavation layout modelling with FE

### Soil Constitutive Model and Material Properties

Medium dense sand soil analysis was carried out under drained conditions using effective stress. Mohr-Coulomb (MC) constitutive models in RS3 and RS2 were applied for sand idealization. A linear-elastic perfectly plastic Mohr-Coulomb (MC) idealization for sandy soil was adopted from several previous studies such as those [2, 6, 11, 26]. Some properties of medium dense sand, such as unit weight, Poisson's ratio, friction angle, and Young's modulus, were chosen as suggested by [27]. The determination of the cohesion and the dilation angle of sandy soil using [11]. The analyses used a low cohesion value ( $c = 1.00 \text{ kN/m}^2$ ) for sandy soil to avoid numerical instability and errors during calculations. The

physical and mechanical properties of medium-dense sand are shown in Table 1.

Table 1 Physical and mechanical properties of soil

Parameter	Value
Unsaturated unit weight (kN/m <sup>3</sup> )	17.00
Saturated unit weight (kN/m <sup>3</sup> )	20.00
Young's modulus (kN/m <sup>2</sup> )	$25 \times 10^3$
Poisson's ratio	0.30
Cohesion (kN/m <sup>2</sup> )	1.00
Friction angle (degree)	35.00
Dilatancy angle (degree)	5.00
Material behaviour	drained

The excavation support system in this study consists of a contiguous pile wall and a cap beam at the head of the pile, which were modeled in 3-D and 2-D conditions. Reinforced concrete piles used in deep excavation analysis with 3-D and 2-D FE would apply four types of diameters ( $d$ ) variations, including  $d_1 = 0.60 \text{ m}$ ,  $d_2 = 0.80 \text{ m}$ ,  $d_3 = 1.00 \text{ m}$ , and  $d_4 = 1.20 \text{ m}$ . The distance between the piles ( $s$ ) is determined by Eq. (1).

The pile length was 18.50 m with 11.00 pile penetration depth ( $D$ ), and the excavation height ( $h_e$ ) was 7.50 m. Piles in the 3-D analysis were modelled as circular vertical beam elements with linear elastic behaviour.

In the 2-D analysis (plane strain), the configuration of the CPW reinforcement must be equivalent due to the limitations of the 2-D model. Equivalence was carried out by modeling the pile rows as a continuous structure (liner/plate). It was assumed that the moment of inertia of the pile rows in the 3-D model would equal the moment of inertia of continuous structure (liner/plate) in the 2-D model.

Cap beam (CB) modeling on the pile head in the 3-D analysis was assumed to be a horizontal beam element. Cap beam was only used for 3-D analysis because, in the 2-D plane strain model, the reinforcement is supposed to be a continuous structure (liner/plate). The dimensions of the cap beam are adjusted to the diameter of the pile ( $d$ ). Fig. 2 shows the typical cap beam dimensioning as suggested by [28]. Several variations of the dimensions are used including: CB1: 0.825 x 0.90 m, CB2: 1.025 x 1.10 m, CB3: 1.225 x 1.30 m, and CB4: 1.425 x 1.50 m.

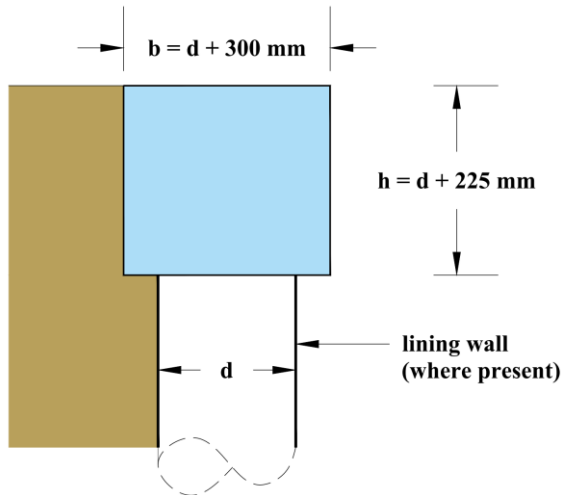


Fig. 2 Cap Beam (CB) typical design (Wells, 2009)

At the surface level, a surcharge load ( $q$ ) of 10.00 kN/m<sup>2</sup> with 10.00 m width was applied to each excavation side. The application of surcharge load to the model is shown in Fig. 1. Surcharge loads represent external loads such as heavy equipment, excavated soil, and other loads (SNI 8460:2017).

## PARAMETRIC STUDY VARIABLES

The parametric study focused on studying the effect of excavation dimension ratio ( $B/L$ ), pile diameter ( $d$ ), and cap beam dimensions on lateral displacement ( $U_{tot}$ ) and bending moment ( $M_x$ ) behavior of CPW reinforcement. The variation excavation dimension of 3-D models are model A (15 x 15 m<sup>2</sup>), model B (15 x 30 m<sup>2</sup>), model C (15 x 45 m<sup>2</sup>), model D (15 x 60 m<sup>2</sup>), while model E is two dimensional. Each model was run by variation of pile diameter which are  $d_1$  (0.60 m),  $d_2$  (0.80 m),  $d_3$  (1.00 m) and  $d_4$  (1.20 m). Cap beam effect analysis was only carried out on the pile with  $d_1 = 0.60$  m and excavation ( $B$ ): 15.00 x 30.00 m<sup>2</sup>.

## NUMERICAL SIMULATION

Numerical simulations were conducted using 3-D and 2-D models, as discussed before. The first step was applying the surcharge load at the ground level on each excavation side, and then the second step was installing the pile and cap beam. Step-by-step excavation was carried out after the installation of the reinforcement. The result of lateral displacement and bending moment used in the output graph is the maximum value for the pile located at the middle of the excavation in each analysis (critical pile).

The boundary conditions in the 3-D model varied depending on the dimensions of the excavation to be analyzed. The meshing configuration used was a 10-noded tetrahedron graded with high-quality mesh around the excavation area where the stress is high

and medium-quality mesh for the boundaries area where the stress is low. The 3-D excavation model is shown in Fig. 3.

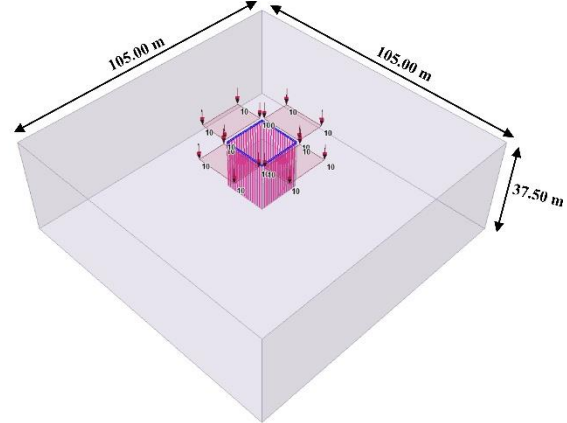


Fig. 3 Finite element model in 3-D

The boundary conditions for the 2-D model were set at 105.00 m x 37.50 m, with a surcharge load applied to each side of the excavation. The 6-noded triangular grade was used as a meshing configuration in the 2-D.

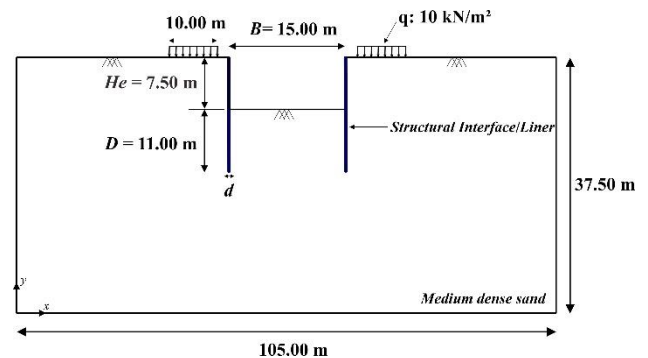


Fig. 4 Finite element model in 3-D

## RESULTS AND DISCUSSION

The analyses results in Fig. 5 consistently show that with the more significant excavation dimensions ratio ( $B/L$ ), the lateral displacement ( $U_{tot}$ ) occurs in all variations of pile diameters ( $d_1$ ,  $d_2$ ,  $d_3$ , and  $d_4$ ) also increases. The 3-D analysis has proven to be more effective for a square excavation with small dimension ratios ( $B/L \leq 1:2$ ), such as excavation in conditions (A) and (B). The 2-D analysis is more suitable for a square excavation with large dimension ratios ( $B/L \geq 1:3$ ), such as excavation in conditions (C) and (D).

Lateral displacement ( $U_{tot}$ ) value in 3-D analysis for excavation (C), on pile  $d_1 = 0.60$  m was 0.0743 m,  $d_2 = 0.80$  m was 0.0550 m,  $d_3 = 1.00$  m was 0.0455 m, and for  $d_4 = 1.20$  m was 0.0396 m. For excavation (D), lateral displacement ( $U_{tot}$ ) on pile  $d_1 = 0.60$  m was 0.0783 m,  $d_2 = 0.80$  m was 0.0583 m,  $d_3 = 1.00$  m was 0.0489 m, and for  $d_4 = 1.20$  m was 0.0436 m.

In the 2-D analysis, the lateral displacement ( $U_{tot}$ ) that occurs on pile  $d_1=0.60$  m was 0.0789 m,  $d_2=0.80$  m was 0.0597 m,  $d_3=1.00$  m was 0.0518 m, and for  $d_4=1.20$  m was 0.0479 m. This shows that the value of lateral displacement ( $U_{tot}$ ) in 3-D analysis for a

square excavation with large dimension ratios ( $B/L \geq 1:3$ ), such as excavations (C) and (D), is close to the result of lateral displacement ( $U_{tot}$ ) of excavation (E) or 2-D (plane strain).

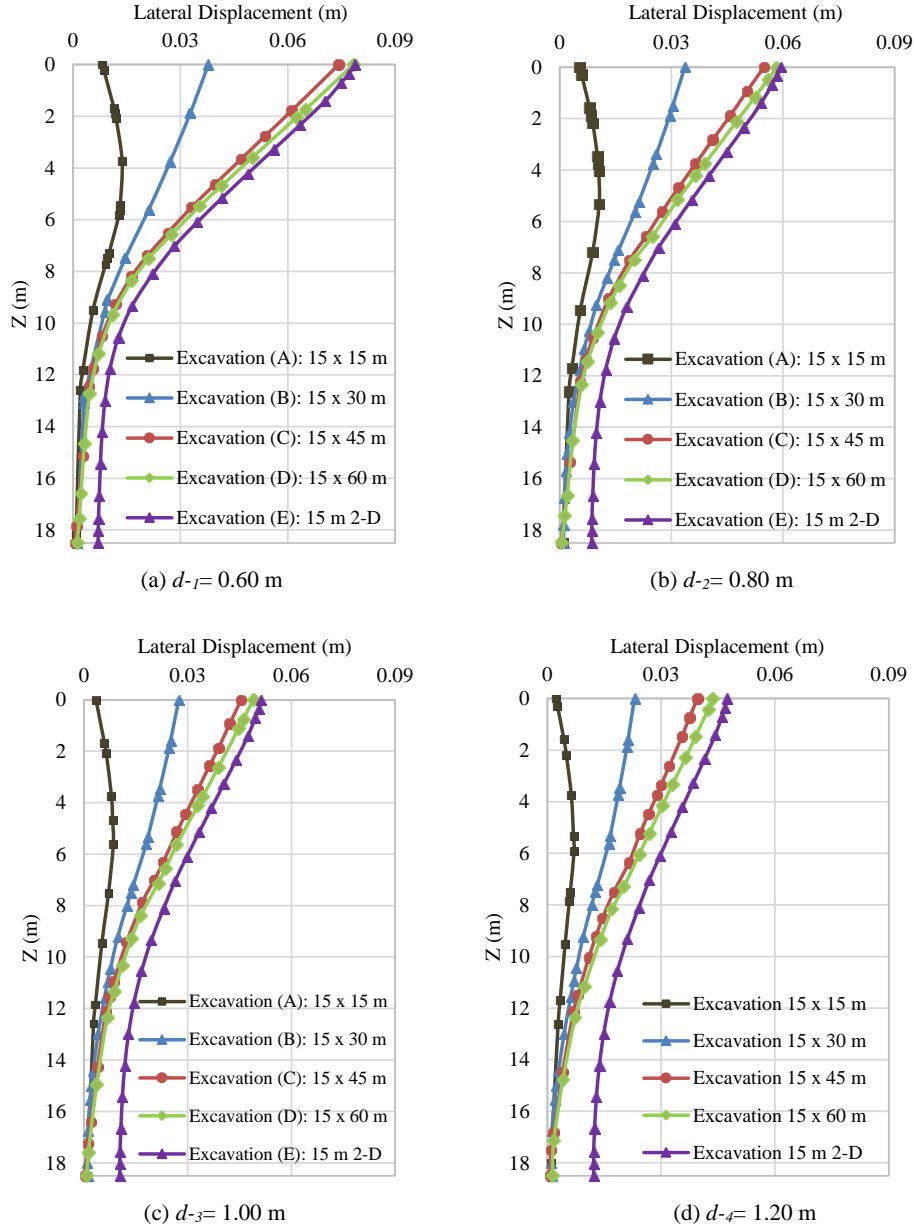


Fig. 5 Lateral displacement of CPW reinforcement in medium dense sand ( $H_e=7.50$  m,  $q=10.00$  kN/m<sup>2</sup>).

The cap beam at the pile head significantly affects the lateral displacement ( $U_{tot}$ ) and bending moment ( $M_x$ ) that occurs in a pile. It shows that the value of lateral displacement ( $U_{tot}$ ) for piles without cap beam (NO-CB) yielded lateral displacement ( $U_{tot}$ ) of 0.0698 m and bending moment ( $M_x$ ) of -181.26 kN.m. In contrast, the cap beam dimension ( $CB_I$ ) reduced the lateral displacement ( $U_{tot}$ ) significantly by 45% to 0.0378 m. The bending moment ( $M_x$ ) was decreased

by 54% to 83.240 kN.m. Figure 6 shows that increasing the cap beam dimensions also reduced the lateral displacement ( $U_{tot}$ ). However, it showed an increased bending moment ( $M_x$ ), although it is not significant.

These results show the effectiveness of cap beam as CWP reinforcement and stiffener. Enlarging inertial stiffness of the cap beam ability in therefore can potentially replace the use of invasive ground

anchor or a space consuming battered pile. However, the use of large cap beam should still consider the specific environmental and architectural constraints.

The use of a cap beam on the pile head also changes the displacement pattern that occurs in the CPW reinforcement.

Fig. . shows the displacement pattern of CPW reinforcement without a cap beam, the piles tend to work individually while the use of a cap beam with the minimum dimensions ( $CB_I$ ) in

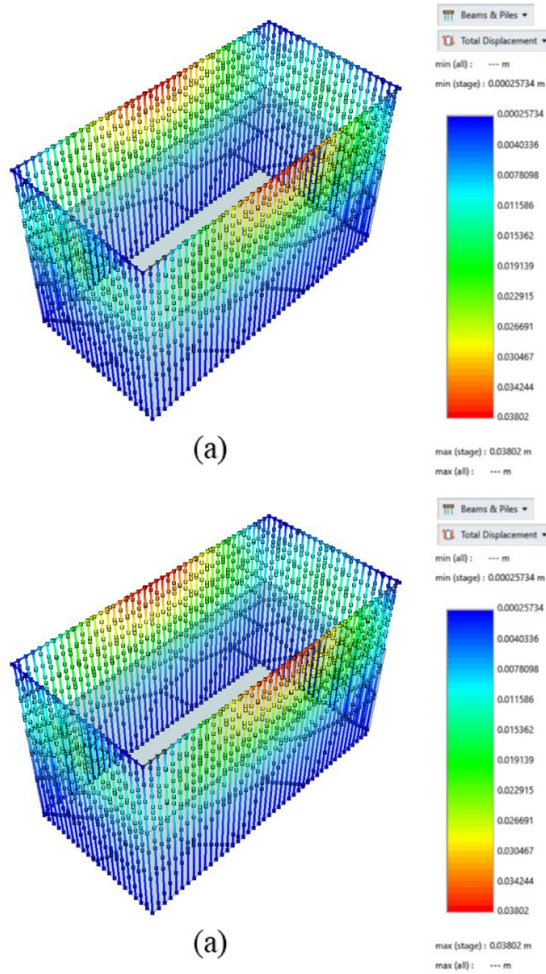


Fig. . shows a more concentrated displacement pattern on the primary side ( $L$ ) of the excavation which indicates the reinforcement works in monolith.

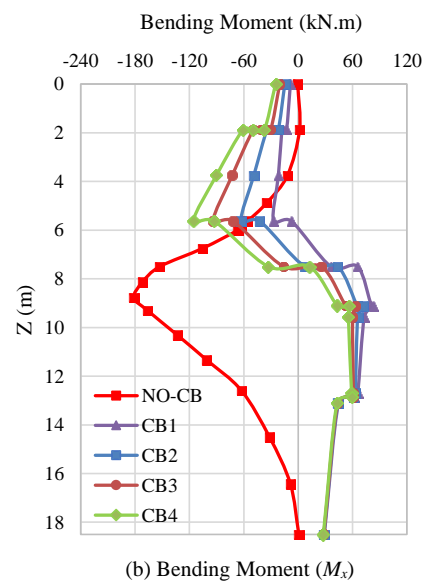
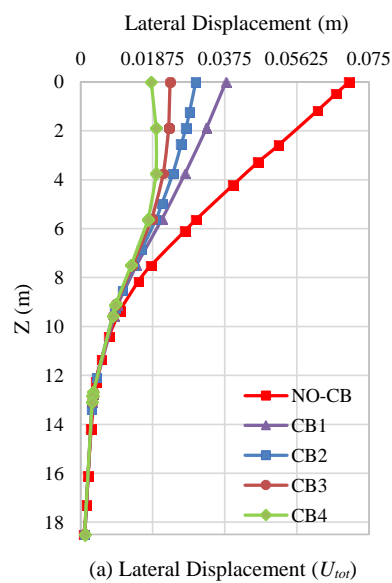




Fig. 6 Lateral displacement and bending moment of CPW reinforcement in medium dense sand (Excavation (B): 15.00 x 30.00 m,  $d_I=0.60$  m,  $H_e=7.50$  m, and  $q=10.00$  kN/m<sup>2</sup>).

## CONCLUSION

In excavations with a square geometry in medium dense sands, the ratio of excavation dimensions ( $B/L$ ) in the 3-D analysis proved to be very influential for the lateral displacement ( $U_{tot}$ ). 3-D FE has proven to be very effective in square excavations with dimension ratios ( $B/L \leq 2$ ), such as excavations (A) and (B). 2-D FE (plane strain) is more suitable for use in the case of excavations with a dimension ratio ( $B/L \geq 3$ ), such as excavations (C) dan (D).

Using a cap beam on the pile head in 3-D analysis significantly reduced lateral displacement ( $U_{tot}$ ) and bending moment ( $M_x$ ) of the pile. Based on the 3-D analysis, a cap beam is proven to reduce lateral displacement ( $U_{tot}$ ) in a pile by 45% and bending moment ( $M_x$ ) by 54% compared to without a cap

beam. Increasing the dimensions of the cap beam also reduces the lateral displacement ( $U_{tot}$ ) that occurs, but it shows an increase in the bending moment ( $M_x$ ), although it is not significant.

Based on the results of deep excavation parametric studies with several parameters such as excavation dimension ratio ( $B/L$ ), pile diameter ( $d$ ), and cap beam dimensions, it shows FE 3-D and 2-D have their respective advantages in the analysis. Therefore, it is necessary to be careful in considering the method of deep excavation analysis with 3-D or 2-D FE to achieve an efficient design.

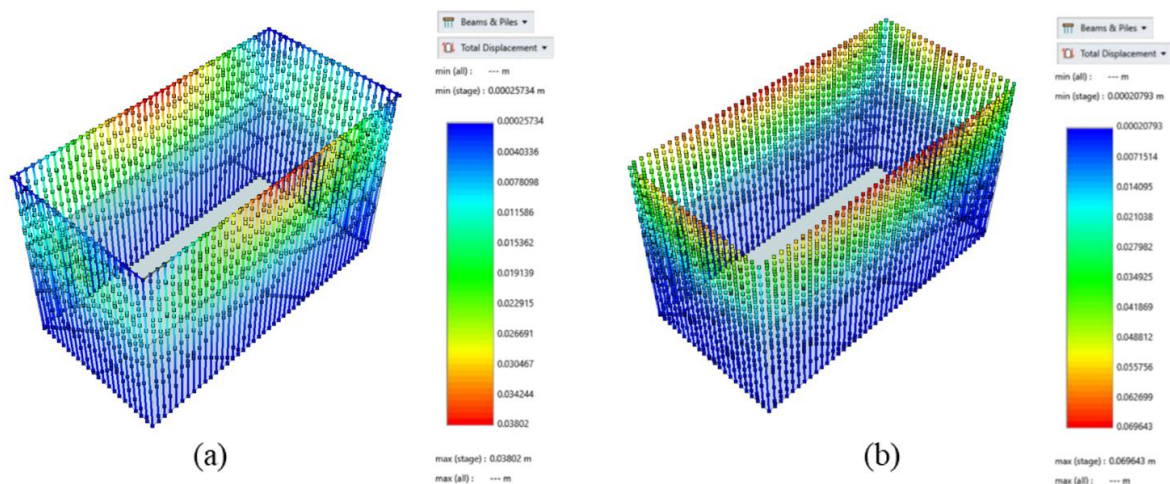


Fig. 7 CPW reinforcement lateral displacement pattern: (a) without a cap beam; (b) with cap beam  $CB_1$

## ACKNOWLEDGMENTS

The authors are very grateful for the facilities and support from the Department of Civil and Environmental Engineering, Universitas Gadjah Mada, Yogyakarta, which has supported this research.

## REFERENCES

- [1] Faris, F., M.A. P., & A., M. (2019). Pemodelan Numeris Dua Dimensi dan Tiga Dimensi pada Konstruksi Galian Basement (Studi Kasus Pembangunan Rumah Susun di Sleman). Civil Engineering and Environmental Symposium, 1–7.
- [2] Ahmadi, A., & Ahmadi, M. M. (2019). Three-Dimensional Numerical Analysis of Corner Effect of an Excavation Supported by Ground Anchors. International Journal of Geotechnical Engineering, 1–13. <https://doi.org/10.1080/19386362.2019.1682349>
- [3] Ramadan, M. I., & Meguid, M. (2020). Behavior of Cantilever Secant Pile Wall Supporting Excavation in Sandy Soil Considering Pile-Pile Interaction. Arabian Journal of Geosciences, 13(12), 1–13.
- [4] Pratama, A. P., Hardyatmo, H. C., & Faris, F. (2020). Parametric Study of the Effect of Ground Anchor on Deep Excavation Stability. Journal of the Civil Engineering Forum, 6(1), 19.
- [5] Likitlersuang, S., Chheng, C., & Keawsawasvong, S. (2019). Structural Modelling in Finite Element Analysis of Deep Excavation. Journal of GeoEngineering, 14(3),



- 121–128.  
[https://doi.org/10.6310/jog.201909\\_14\(3\).1](https://doi.org/10.6310/jog.201909_14(3).1)
- [6] Bahrami, M., Khodakarami, M. I., & Haddad, A. (2018). 3D Numerical Investigation of the Effect of Wall Penetration Depth on Excavations Behavior in Sand. *Computers and Geotechnics*, 98, 82–92.
- [7] Dong, Y. P., Burd, H., Houlsby, G., & Hou, Y. (2014). Advanced Finite Element Analysis of a Complex Deep Excavation Case History in Shanghai. *Frontiers of Structural and Civil Engineering*, 8(1), 93–100.  
<https://doi.org/10.1007/s11709-014-0232-3>
- [8] Emuriat, J. E. (2017). Parametric Study on Analysis and Design of Permanently Anchored Secant Pile Wall for Earthquake Loading. *International Journal of Computational Engineering Research*, 07(05).  
<https://doi.org/10.4172/2168-9717.1000181>
- [9] Rashidi, F., & Shahir, H. (2017). Numerical investigation of anchored soldier pile wall performance in the presence of surcharge. *International Journal of Geotechnical Engineering*, 6362(May), 1–10.  
<https://doi.org/10.1080/19386362.2017.1329258>
- [10] Bhatkar, T., Barman, D., Mandal, A., & Usmani, A. (2016). Prediction of Behaviour of a Deep Excavation in Soft Soil: a Case Study. *International Journal of Geotechnical Engineering*, 6362(May).  
<https://doi.org/10.1080/19386362.2016.1177309>
- [11] Hsiung, B. C. B., Yang, K. H., Aila, W., & Hung, C. (2016). Three-dimensional effects of a deep excavation on wall deflections in loose to medium dense sands. *Computers and Geotechnics*, 80, 138–151.
- [12] Abdou, M., El-Naiem, A., Towfeek, A. R., Hassan, W., & El-Samea, A. (2016). Numerical Analysis of Concrete Solider Pile With Steel Sheet Pile Lagging Supporting System in Sandy Soil. *International Journal of Scientific & Engineering Research*, 7(5), 1643–1660.  
<http://www.ijser.org>
- [13] Schwamb, T., & Soga, K. (2015). Numerical Modelling of a Deep Circular Excavation at Abbey Mills in London. *Geotechnique*, 65(7), 604–619. <https://doi.org/10.1680/geot.14.P.251>
- [14] Khoiri, M., & Ou, C. (2013). Evaluation of Deformation Parameter for Deep Excavation in Sand through Case Histories. *Computers and Geotechnics*, 47, 57–67.
- [15] Ramadan, E. H., Ramadan, M., Khashila, M. M., & Kenawi, M. A. (2013). Analysis of Piles Supporting Excavation Adjacent to Existing Buildings. 18th International Conference on Soil Mechanics and Geotechnical Engineering: Challenges and Innovations in Geotechnics, ICSMGE 2013, 4, 2835–2838.
- [16] Finno, R. J., Blackburn, J. T., & Roboski, J. F. (2007). Three-Dimensional Effects for Supported Excavations in Clay. *Journal of Geotechnical and Geoenvironmental Engineering*, 133(1), 30–36.
- [17] Lin, D. G., & Woo, S. M. (2007). Three dimensional Analyses of Deep Excavation in Taipei 101 Construction Project. *Journal of GeoEngineering*, 2(1), 29–42.  
[https://doi.org/10.6310/jog.2007.2\(1\).4](https://doi.org/10.6310/jog.2007.2(1).4)
- [18] Chheng, C., & Likitlersuang, S. (2018). Underground Excavation Behaviour in Bangkok using Three-Dimensional Finite Element Method. *Computers and Geotechnics*, 95(July 2017), 68–81.  
<https://doi.org/10.1016/j.compgeo.2017.09.016>
- [19] Lee, F. H., Hong, S. H., Gu, Q., & Zhao, P. (2011). Application of Large Three-Dimensional Finite Element Analyses to Practical Problems. 12th International Conference on Computer Methods and Advances in Geomechanics 2011, 11(6), 529–539.  
[https://doi.org/10.1061/\(asce\)gm.1943-5622.0000049](https://doi.org/10.1061/(asce)gm.1943-5622.0000049)
- [20] Iwata, N., Nakai, T., Zhang, F., Inoue, T., & Takei, H. (2007). Influences of 3D effects, Wall Deflection Process and Wall Deflection Mode in Retaining Wall Problems. *Soils and Foundations*, 47(4), 685–699.  
<https://doi.org/10.3208/sandf.47.685>
- [21] Zdravkovic, L., Potts, D. M., & St. John, H. D. (2005). Modelling of a 3D Excavation in Finite Element Analysis. *Geotechnique*, 55(7), 497–513. <https://doi.org/10.1680/geot.2005.55.7.497>
- [22] Hong, S. H., Lee, F. H., & Yong, K. Y. (2003). Three-dimensional pile-soil interaction in soldier-piled excavations. *Computers and Geotechnics*, 30(1), 81–107.  
[https://doi.org/10.1016/S0266-352X\(02\)00028-9](https://doi.org/10.1016/S0266-352X(02)00028-9)
- [23] Yu Ou, C., Dar Chang, C., & Tzong-Shiann, W. (1996). Three-Dimensional Finite Element Analysis of Deep Excavations. *Journal of Geotechnical Engineering*, 122(May), 337–345.  
[https://doi.org/https://doi.org/10.1061/\(ASCE\)0733-9410\(1996\)122:5\(337\)](https://doi.org/https://doi.org/10.1061/(ASCE)0733-9410(1996)122:5(337))

- [24] Dong, Y. P., Burd, H. J., & Houlsby, G. T. (2018). Finite Element Parametric Study of The Performance of a Deep Excavation. *Soils and Foundations*, 58(3), 729–743.
- [25] Dong, Y. P., Burd, H. J., & Houlsby, G. T. (2016). Finite-element analysis of a deep excavation case history. *Géotechnique*, 66(1), 1–15. <https://doi.org/10.1680/geot.14.p.234>
- [26] Hsiung, B. C. B. (2009). A Case Study on the Behaviour of a Deep Excavation in Sand. *Computers and Geotechnics*, 36(4), 665–675.
- [27] Look, B. G. (2014). *Handbook of Geotechnical Investigation and Design Tables* (2nd ed.). CRC Press. <https://doi.org/10.1201/b16520>
- [28] Wells, J. (2009). Design of Capping Beams. *The Institution of Structural Engineers*, 87(23), 23–26.

# NUMERICAL ANALYSIS OF INTERSECTING URBAN METRO TUNNELS IN ROCK MASS

Isan Dey<sup>1</sup>, Ramanathan Ayoythiraman<sup>2</sup>

<sup>1</sup>M.Tech. Student, Department of Civil Engineering, IIT Delhi, India;

<sup>2</sup>Professor, Department of Civil Engineering, IIT Delhi, India

## ABSTRACT

Underground excavation for urban tunnels is one of the most important areas of study as it poses a great challenge with respect to variation in geology, surface conditions and alignment of the tunnels. Due to spiderweb network of metros undergoing in almost every major city across the world, it is seen that tunnels of different metro lines could intersect at different heights and also at different angles. The urban tunnels are generally twin tunnels having 6 m diameter each, with different pillar widths. 3D FEM models are prepared for shallow depth tunnel at 10 m, 15 m, 20 m and 25 m i.e., incremental depths of every 5m for the shallow tunnel while deeper tunnel depth at 40 m with angles of intersection at 30°, 60° and 90° to understand the effect of settlements on the surface, and deformations of the shallow tunnel with respect to progression of deeper tunnel. It is found that the construction sequence, separation distance with respect to depth between tunnels and angle of intersection have profound effects on the existing tunnel response.

*Keywords: Metro Tunnel, Rock, Intersecting Tunnels, Numerical Analysis.*

## INTRODUCTION

The necessity for tunnels and the benefits they bring can be visualized in the modern-day very vividly. Tunnels improve connections and shorten lifelines. The utilization of underground space for continuous traffic, storage, power and water treatment plants, civil defense, and other activities is often a must give limited space, safe operation, environmental protection, and energy-saving. Of course, the construction of tunnels is risky and expensive and requires a high level of technical skills.

For urban metro tunnels it is seen that the shallower tunnel is generally constructed earlier due to the availability of space, but the deeper tunnel is excavated at a later stage to cater to the proposed requirement at a later stage. As a result of this, it is expected that there would be change in the stresses, deformations and settlements of the shallow tunnel as well on the surface due to the effect of the construction of the deeper tunnel. Henceforth, it shows that the intersection of the tunnels at various depths is the major area of concern in the present scenario of a spiderweb network of tunnels in most areas worldwide. As a result of this, it is very important to study the effect of tunneling due to varying depths, and angles of intersection between the tunnels. Though there are studies reported on interaction of twin tunnels and tunnel-pipeline interaction [1 – 8], studies on intersecting tunnel are limited.

In the present study, the effect of angle of intersection and depth of the tunnels are investigated through three-dimensional analysis. The shallower tunnel shall be excavated for different tunnel depths starting from 10 m and incremented by every 5 m

until a depth of 25 m while the deeper tunnel shall be at a depth of 40 m. The settlement and deformation results are required to be obtained from twin intersecting tunnels for different angles of intersection of 30°, 60° and 90°.

## GEOTECHNICAL DATA

Lithological data pertaining to one of metros in India are considered. Top layers are mainly comprised of backfilled soils followed by Silty/ Sandy clay for about 4 to 5 m. Below this, highly to moderately weathered rock formations are observed. Major rock types occurring in the area are fine-grained, greenish basalt to black colored associated with acidic and basic tuffs, volcanic breccia.

The rock is identified as highly weathered Volcanic Breccia to slightly weathered/ Fresh Volcanic Breccia with core recovery varying from 13 to 100 % and Rock Quality Designation (RQD) is varying from 13 to 100 %. Bulk rock density is varying from 22 to 26 kN/m<sup>3</sup>. The design parameters of the soil adopted in the analysis are shown in Table 1.

Table 1: Soil shear strength parameters

Thickness layer	Density (kN/m <sup>3</sup> )	$c$ (kN/m <sup>2</sup> )	$\phi$ (°)	E (MPa)
0-2m	19	10	28	14

The design parameters of the different grades of Breccia rocks as per the weathering grades which have been obtained from Rock lab software [9] and summarized in Table 2.

Table 2: Rock shear strength parameters

Grade	Density (kN/m <sup>3</sup> )	$c$ (kN/m <sup>2</sup> )	$\phi$ (°)	E (MPa)
IV(2-6m)	22	26	25	111
III (6-56m)	22	108	51	912
II (56-100m)	24	262	59	3310

### MODELLING OF TUNNELS

The tunnels having 6 m diameter have been excavated in FEM analyses followed by installation of liners which have a thickness of 400 mm and a modulus of elasticity of 31622 MPa. The surcharge loads have been applied on the surface with an average load of 10 kPa per floor. The in-situ stress condition has been considered as unity for the analyses in FEM.

The construction methodology of the analyses has been considered such that the tunnel on left is excavated followed by application of liner. Correspondingly the same approach is used for the right-hand side tunnel. Along the length of tunnel, excavation length of 10 m is adopted with corresponding application of liner.

The typical geometry of the problem analyzed for intersecting twin tunnels is shown in Fig. 1 for different angles of intersection of 30°, 60° and 90°.

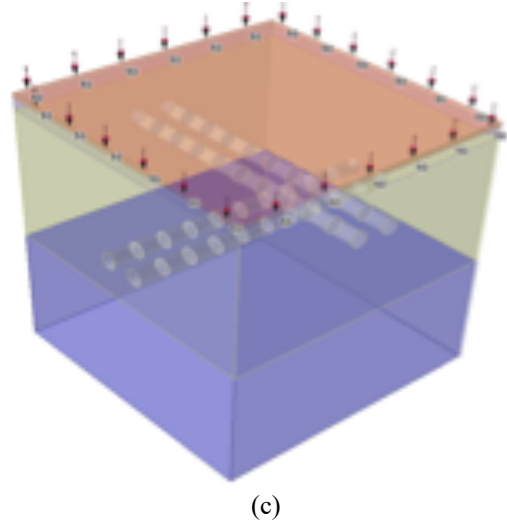
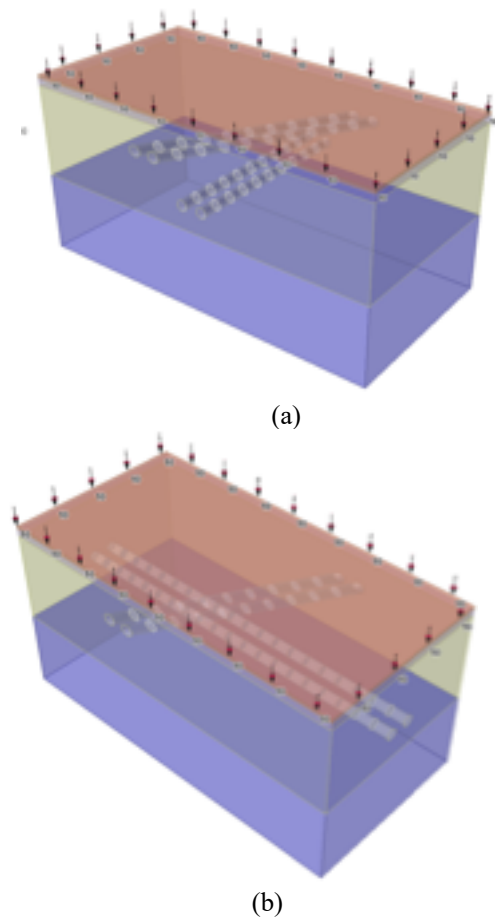


Fig. 1. The typical layout of the problem analyzed for different intersecting tunnels at (a) 30°, (b) 60°, and (c) 90°.

### RESULTS AND DISCUSSION

#### Surface Settlement

The surface settlement results have been derived from the FEM models and the same have been plotted in Fig. 3. In Fig. 2, the maximum surface settlement is shown in Y-axis and  $E_z/D$  is plotted in X-axis where  $E_z$  is the vertical clear distance between the tunnels at the intersecting location and  $D$  is the diameter of tunnel for different angles of intersection. It is inferred from the figure that the settlement decreases as the depth increases, i.e., as the clear distance between the tunnel increases. The percentage increase in settlement due to intersecting tunnels is calculated and is shown in Fig. 3. From Fig. 4, it is seen that the maximum settlement increases by almost 85 to 250% with the excavation of deeper tunnel. Such a trend of settlement increase is reported for existing pipeline and tunnel interaction in [1] and [5].

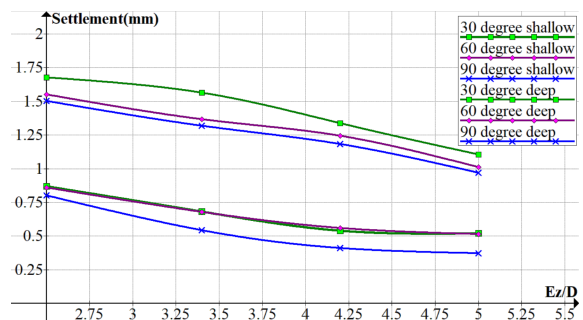


Fig. 3. Variation of maximum surface settlement with normalized clear distance between the intersecting tunnels.

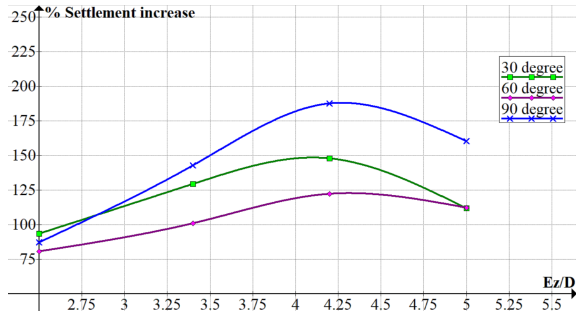


Fig. 4. Variation of increase in settlement (%) with normalized clear distance between the intersecting tunnels.

The variation of maximum surface settlement with angle of intersection for different depths of tunnel is shown in Fig. 4. From Fig. 5, it is observed that as the angle of intersection increases the maximum settlement decreases, and the average decrease of settlement is around 10 to 15% with increase of the angle of intersection. The trend of decrease is similar for tunnels located at all depths analyzed.

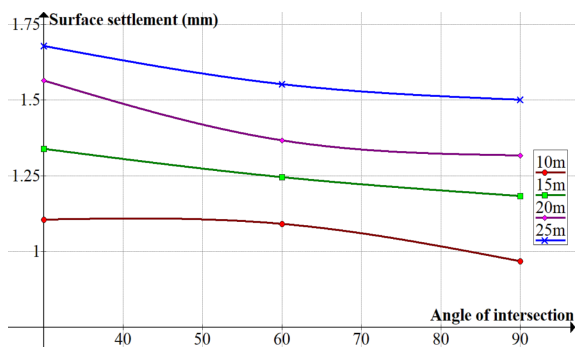


Fig. 5. Variation of maximum surface settlement with angle of intersection.

The surface settlement troughs obtained from the analyses are plotted in Fig. 5. It is evident from Fig. 6 that with an increase of the degree of intersection, the influence area of the settlement trough also increases for different angle of intersections (30°, 60° and 90°).

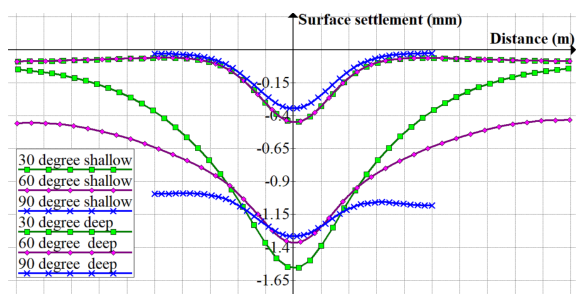


Fig. 6. Settlement troughs obtained for the different cases.

It can also be deduced from Fig. 5 that the maximum settlement decreases with the overall increase in the angle of intersection with a corresponding increase in the influence area. Also, for 90° intersecting tunnel, the influence area is more gradual than the 60° intersecting tunnel. But the settlement increases after a certain point because of the settlement occurring due to excavation of the deeper tunnel.

#### Deformation of existing tunnel

The existing shallow tunnel would undergo deformation due to the construction of deeper new tunnel. The deformation of crown of shallow tunnel with the normalized clear distance is shown in Fig. 6. From Fig. 7, it is noticed that the maximum tunnel crown deformation increases by almost 10-80 % with the excavation of the deeper tunnel.

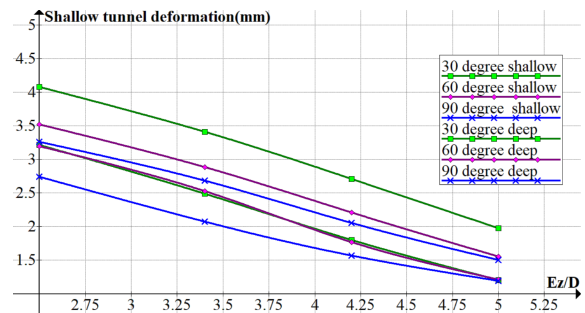


Fig. 7. Variation of shallow tunnel deformation with normalized clear distance between the intersecting tunnels.

The variation of deformation at crown of shallow existing tunnel with angle of intersection is shown in Fig. 7. It is clearly evident from Fig. that the angle of intersection has considerable effect on the deformation of shallow existing tunnel which could not have been captured in two-dimensional finite element analysis. It is also interpreted from the figure that there is about 15% to 20% reduction in tunnel deformation occurs with an increase of angle of intersection.

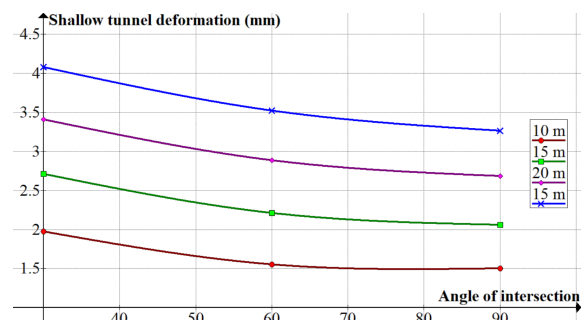


Fig. 7. Variation of deformation of tunnel crown with angle of intersection.

## SUMMARY AND CONCLUSIONS

The effect of construction of new and deeper tunnel intersecting the shallow existing tunnel is investigated using three-dimensional finite element analysis. The angle of intersection and depth of shallow and deeper tunnels have been varied in the analysis. Based on the results of numerical analysis the following conclusions are drawn:

1. The construction of deeper tunnel is found to have considerable deformation of existing shallow tunnel as well as surface settlement.
2. The angle of intersection of two tunnels and the clear distance between the two tunnels are having pronounced effect on both surface settlement as well as existing tunnel deformation.
3. Three-dimensional analysis could capture the effect of angle of intersection efficiently. The settlement trough at surface and the zone of influence/point of inflection of trough are significantly affected by the angle of intersection of tunnels of different lines.
4. It showed that the maximum surface settlement was encountered for 30° while the minimum settlement was encountered for 90°.

The study considered limited geotechnical data and further detailed parametric study is required for different rock mass conditions so that generalized guidelines can be arrived at for quantifying the effect of intersecting tunnels.

## REFERENCES

- [1] Sheng-Wu Zhao, Xiao-Li Li, Xin Li, Li-Guang Chen, Tong Li, Suo-Hui Li, Yu Bail, Analysis of Pipeline Deformation Caused by Shield Tunnel Excavation that Obliquely Crosses Existing Pipelines, *Arabian Journal of Geosciences*, (IF1.827), Pub Date: 2022-01-22.
- [2] Xiaolu Gan, Jianlin Yu, Xiaonan Gong, Nianwu Liu, Dongzhu Zheng, Behaviors of existing shield tunnels due to tunnelling underneath considering asymmetric ground settlements, *Underground Space Technology*, <https://doi.org/10.1016/j.undsp.2021.12.011>.
- [3] Rui Zhanga, Yao Xiaob, Minghua Zhaob, Heng Zhaob, Stability of dual circular tunnels in a rock mass subjected to surcharge loading, *Computers and geotechnics*, 108 (2019) 257–268.
- [4] Luo-bin Lin, Yan-ping Lu, Fu-quan Chen , Da-yong Li , Analytic study of stress and displacement for shallow twin tunnels subjected to surcharge loads, *Applied Mathematical Modelling*, 93 (2021) 485–508.
- [5] Xinrong Liu, Linfeng Wang, Xiaohan Zhou, Jiming Wang, Zuliang Zhong, Peng Liu, Fei Xiong, Chunmei He, E-M calculation model and its application of calculating deformation in a new tunnel orthogonally undercrossing an existing tunnel, *Tunnelling and Underground Space Technology*, 123 (2022) 104418.
- [6] Zhiyong Liu, Jianfeng Xue, Jianzhong Ye, Jiangu Qian, A simplified two-stage method to estimate the settlement and bending moment of upper tunnel considering the interaction of undercrossing twin tunnels, *Transportation Geotechnics* 29 (2021) 100558.
- [7] Mingfeng Lei, Jiyao Liu, Yuexiang, Shallow Tunnel Excavated in Soft Clay with High Plasticity, *Hindawi Advances in Civil Engineering*, Volume 2019, Article ID 7483628, 14 pages.
- [8] Lianyang Zhang, *Engineering Properties of Rocks*, Butterworth-Heinemann (2016).
- [9] Hoek-Brown and Generalized Hoek-Brown Material Models, <https://static.rockscloud.com>.



# SLOPE STABILITY DURING EXTREME DAILY RAINFALL: A COMPARATIVE STUDY USING STATIONARY AND NON- STATIONARY GENERALIZED EXTREME VALUE MODEL

Thapthai Chaithong<sup>1</sup>

<sup>1</sup>Faculty of Social Sciences, Kasetsart University, Thailand

## ABSTRACT

Extreme rainfall data are valuable for assessing an area's susceptibility to landslides. Previous research generated an Intensity–Duration–Frequency (IDF) curve of extreme rainfall by using a generalized extreme value (GEV) distribution. The stationary generalized extreme value model is the most common method for generating an extreme rainfall dataset; however, extreme rainfall may also occur under non-stationary conditions, requiring the trend to be analyzed from past to present. Therefore, the non-stationary generalized extreme value model may be an alternative method for analyzing extreme rainfall data. This study compares the stability of residual soil slopes under extreme daily rainfall using stationary and non-stationary generalized extreme values. The study analyzes the daily rainfall at the Chiang Mai meteorological station from 1952 to 2021. The three return periods explored were 5-, 100-, and 1000-year. The residual soil slope is analyzed using the analytical framework for the stability of infinite slopes under steady unsaturated seepage conditions. The results show that an increasing annual maximum of daily rainfall has been found in Chiang Mai. The study finds that the safety factor differs for slopes under stationary and non-stationary conditions based on the amount of rainfall. The safety factor is lower for the residual soil slope under non-stationary conditions than in stationary conditions. Moreover, the safety factor gap between stationary and non-stationary conditions increases over time.

*Keywords: Slope stability, Extreme rainfall, Generalized extreme value, Landslide*

## INTRODUCTION

Extreme rainfall is a significant triggering factor in natural and man-made slope failure [1]. Historically, disastrous landslides have occurred in many parts of Thailand as a result of heavy monsoon rains. Nowadays, Thailand has experienced an increment of heavy or extreme rainfall events due to climate change and climate variability. IPCC 2021 reported an increase in heavy rainfall in the South-East Asia region [2]. This may increase the occurrence of landslides in Thailand.

Considering extreme value theory, a generalized extreme value (GEV) distribution is widely used to fit the distribution of extreme rainfall. The GEV is based on the block maxima method of extreme value theory. The block maxima method considers and extracts the maximum value from periods of equal length. The assumption of GEV can be divided into two forms of analysis: stationary and non-stationary conditions. For a non-stationary assumption, the parameters of the GEV distribution function are time-dependent in contrast to the parameters for a stationary assumption, which are time-independent. [3]–[5]

Given this context, this study aims to compare the stability of residual soil slopes under both the stationary and non-stationary assumptions of GEV distribution. The method of slope stability analysis is based on the analytical framework for the stability of infinite slopes under vertical steady seepage

conditions.

## METHOD AND DATA

There are three main steps in this study. First, the historical rainfall data at Chiang Mai meteorological station from 1952 to 2021 are analyzed using stationary and non-stationary GEV distributions. Second, the pore water pressure is generated based on the vertical steady seepage conditions. Finally, the stability of the residual soil slope is analyzed using an infinite slope stability model.

### Extreme Daily Rainfall Analysis

In the first step of the analysis, the study used a generalized extreme value (GEV) distribution. The historical daily rainfall data were measured from 1952 to 2021 at Chiang Mai meteorological station. The annual daily maximum rainfall data were extracted and fitted using a generalized extreme value (GEV) distribution. The GEV distribution consists of three types: (1) Gumbel distribution ( $\xi = 0$ ), Fréchet distribution ( $\xi < 0$ ) and the Weibull distribution ( $\xi > 0$ ). The GEV distribution function is given by [5]

$$F(x) = \exp \left\{ - \left[ 1 + \xi \left( \frac{x - \mu}{\sigma} \right) \right]^{-\frac{1}{\xi}} \right\} \quad (1)$$

where  $\mu$ ,  $\sigma$ , and  $\xi$  are the location, scale, and shape parameters,

Used to estimate the Intensity–Duration–Frequency (IDF) curve of extreme daily rainfall, the quantiles of the GEV distribution are given by

$$x_T = \mu - \frac{\sigma}{\xi} \left[ 1 - \left\{ -\log \left( 1 - \frac{1}{T} \right) \right\}^{-\xi} \right] \quad (2)$$

where  $T$  is return level.

For stationary model, the location ( $\mu$ ), scale ( $\sigma$ ), and shape ( $\xi$ ) parameters are constant. In order to investigate the non-stationary model, the scale ( $\sigma$ ) and shape ( $\xi$ ) parameters are remained constant. The location ( $\mu$ ) varies linearly over the time.

$$\mu(t) = \beta_0 + \beta_1 t \quad (3)$$

where  $\beta_0, \beta_1$  are parameters to be estimate using a simple linear regression.

### Vertical Steady Seepage Analysis

The pore water pressure profile under the steady-state condition can be written as [6]

$$\frac{du_w}{dy} = \gamma_w [(q/k) - 1] \quad (4)$$

where  $u_w$  is pore water pressure,  $k$  is the unsaturated hydraulic conductivity dependent on matric suction,  $q$  is ground surface flux,  $\gamma_w$  is the unit weight of water. To describe the unsaturated hydraulic conductivity, it can be expressed as [7]

$$k = k_s e^{-\alpha(u_a - u_w)} \quad (5)$$

where  $u_a - u_w$  is the matric suction,  $k_s$  is the saturated hydraulic conductivity,  $\alpha$  is inverse of the air entry pressure.

With the combined equation (4), equation (5), and the boundary condition of zero suction at the water table and a steady-state flow rate, a one-dimensional steady-state matric suction profile can be expressed as [7]

$$u_a - u_w = \frac{-1}{\alpha} \ln \left[ (1 + q/k_s) e^{-\gamma_w \alpha z} - q/k_s \right] \quad (6)$$

Considering the suction stress, the profile of suction stress under the surface flux conditions can be shown as [8]:

$$\sigma^s = -(u_a - u_w) \quad ; u_a - u_w \leq 0 \quad (7)$$

$$\sigma^s = \frac{1}{\alpha} \frac{\ln \left[ (1 + q/k_s) e^{-\gamma_w \alpha z} - q/k_s \right]}{\left( 1 + \left\{ -\ln \left[ (1 + q/k_s) e^{-\gamma_w \alpha z} - q/k_s \right] \right\}^n \right)^{(n-1)/n}} \quad (8)$$

$$; u_a - u_w > 0$$

where  $\sigma^s$  is the suction stress.

### Infinite Slope Stability Model

Based on the extended Mohr-Coulomb failure criterion for an unsaturated soil slope [6], the safety factor for infinite slopes under steady vertical seepage, for both saturated and unsaturated conditions, is given by

$$F_s = \frac{c'}{\gamma_{sat} H \sin \theta \cos \theta} + \frac{\tan \phi'}{\tan \theta} - \frac{\sigma^s \tan \phi'}{\gamma_{sat} H} (\tan \theta + \cot \theta) \quad (9)$$

where  $F_s$  is the factor of safety,  $c'$  is the effective cohesion,  $\phi'$  is the effective friction angle,  $\gamma_{sat}$  is the saturated unit weight of soil and  $\theta$  is the slope angle.

### Data

The study area located in Chiang Mai province in the northern region of Thailand. The daily rainfall data from 1952 to 2021 were measured by the Thai Meteorological Department at Chiang Mai meteorological station. The selected return period for both stationary and non-stationary models in the study is 5-, 100-, and 1000-year. Moreover, to estimate the GEV distribution parameters, the maximum likelihood estimation (MLE) method is used to fit the data. Table 1 shows the soil parameters in this study.

Table 1 Summary of soil properties

Parameter	Value	Unit
$k_s$	0.0231	mm/sec
$\alpha$	0.2	kPa <sup>-1</sup>
$\gamma_w$	9.81	kN/m <sup>3</sup>
$n$	5	-
$c'$	10.29	kPa
$\phi'$	40.13	Degree
$\gamma_{sat}$	18.53	kN/m <sup>3</sup>
$\theta$	30	Degree

## RESULTS AND DISCUSSION

### Trend of Extreme Daily Rainfall

Figure 1 shows a plot of the annual maximum

daily rainfall: the trend is to increase slightly over time. The average annual maximum daily rainfall from 1952 to 2021 is approximately 80.97 ( $\pm 26.59$ ) mm.

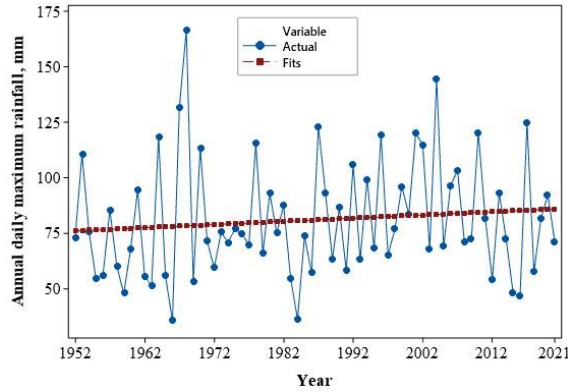


Fig. 1 Trend of annual maximum daily rainfall from 1952 to 2021 at Chiang Mai meteorological station.

To analyze the changing annual maximum daily rainfall, the study separated the rainfall data into two periods: 1952 to 1986 and 1987 to 2021. According to the analysis, the curves of the probability density function of rainfall data shifted as shown in Fig 2.

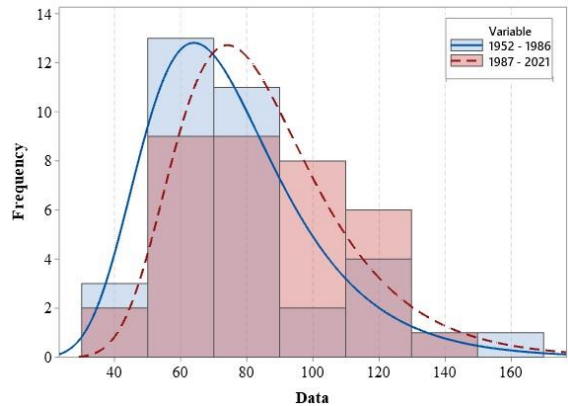


Fig. 2 Probability density function and histogram for two periods of analysis.

To estimate the parameters of GEV distribution using a maximum likelihood estimation method, the parameters for the stationary model are shown in Table 2.

Table 2 Parameters for stationary GEV distribution

Parameter	Value
Location	68.85
Scale	20.90
Shape	0.00

In addition, to estimate the location parameter for non-stationary GEV distribution using the simple linear regression, the equation of location parameter can be written:

$$\mu(t) = 75.90 + 0.143t \quad (10)$$

where  $t$  is  $(t_{\text{year}} - t_0 + 1)$ ;  $t_0$  is 1952

For the scale and shape parameters, the stationary and non-stationary have the same values.

The IDF plots of annual maximum daily rainfall in both stationary and non-stationary GEV distribution conditions are shown in Fig 3 and Fig 4.

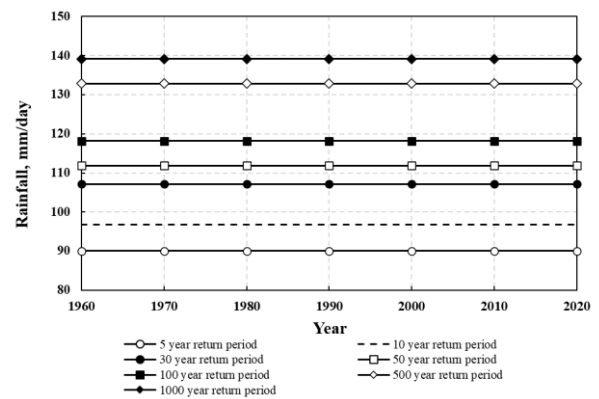


Fig. 3 IDF curve for annual maximum daily rainfall in stationary condition.

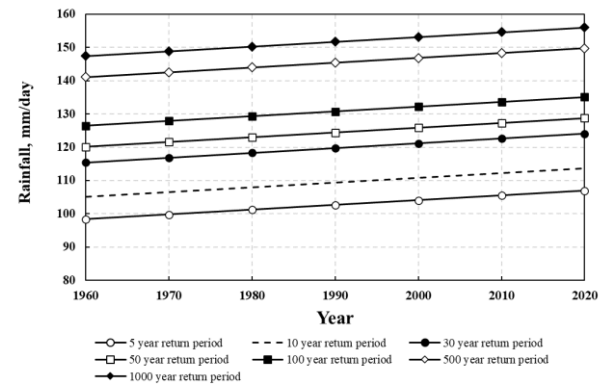


Fig. 4 IDF curve for annual maximum daily rainfall in non-stationary condition.

Consider to Fig 3 and Fig 4, the graphs present the difference in the amount of rainfall in the same return period, in which the amount of rain in the non-stationary condition is higher than in the stationary condition. It also shows that the amount of rain or IDF precipitation under non-stationary conditions varies over time.

### Pore Water Pressure Profiles under Vertical Seepage Condition

The pore water pressure profile for stationary and non-stationary conditions can be predicted using Equation 6. The pore water pressure profile is shown for 1960 in Fig. 5, for 1990 in Fig. 6, and 2020 in Fig. 7.

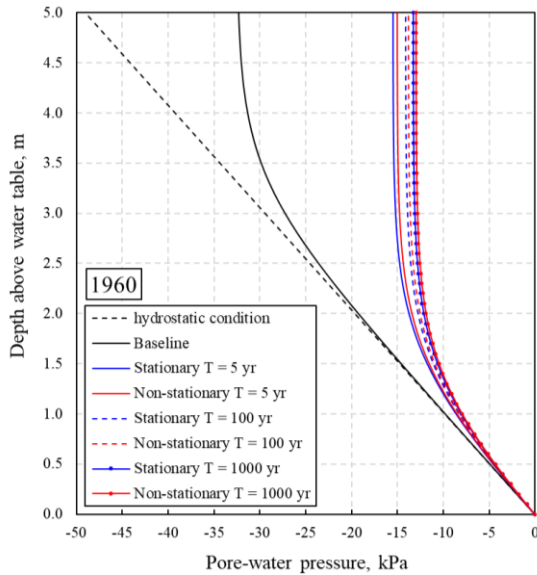


Fig. 5 Pore water pressure profile for 1960.

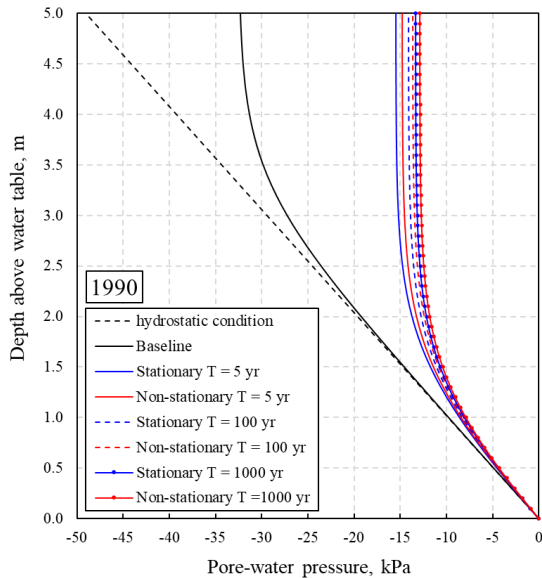


Fig. 6 Pore water pressure profile for 1960.

According to the difference in rainfall between stationary and non-stationary conditions, the pore water pressure profile of non-stationary conditions is less negative than the stationary condition. In addition, the pore water pressure profile for non-stationary varies over time at the same return period. The pore water pressure of non-stationary is a shift into the

saturated state because the amount of rain in the IDF curve increases over time, as shown in Fig. 4. In contrast, the pore water pressure profile of the stationary condition is constant because the amount of rain in the IDF curve is fixed over time, as shown in Fig.3.

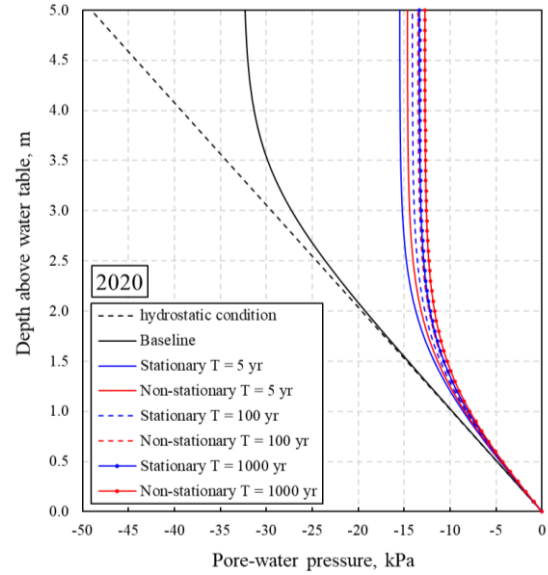


Fig. 7 Pore water pressure profile for 2020.

Fig. 8 presents a comparison of the pore water pressure profile for a 5-year return period. Fig. 9 presents a comparison of the pore water pressure profile for a 100-year return period. Fig. 10 presents a comparison of the pore water pressure profile for a 1000-year return period.

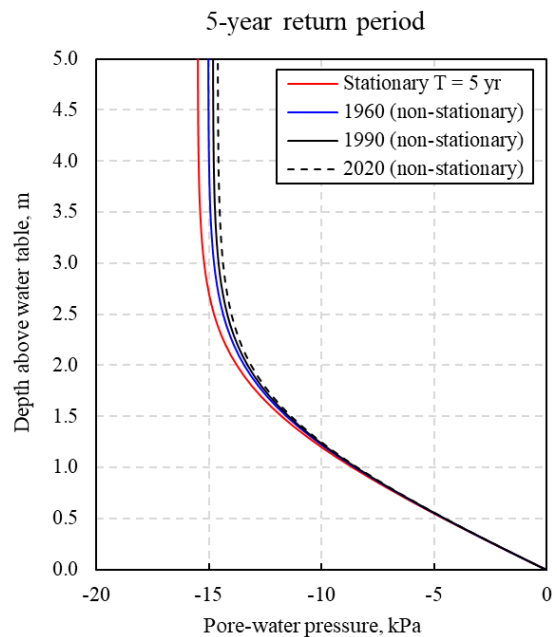


Fig. 8 Comparison of pore water pressure profile for return period 5-year.

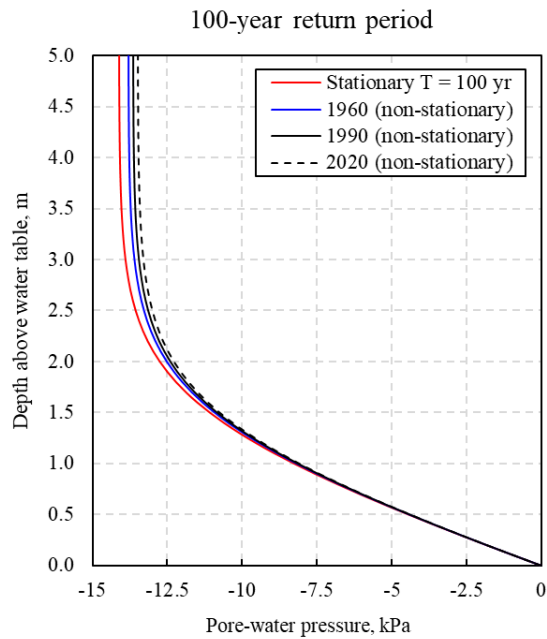


Fig. 9 Comparison of pore water pressure profile for return period 100-year.

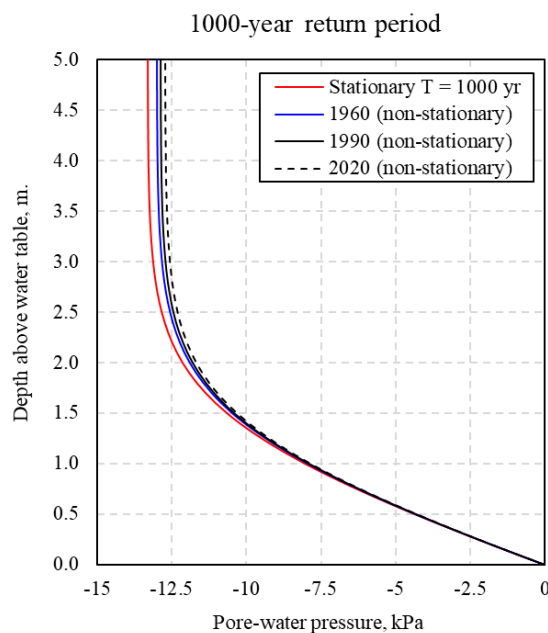


Fig. 10 Comparison of pore water pressure profile for return period 1000-year.

### Slope Stability Analysis

Slope stability analysis in the study is based on an infinite slope stability model: the depth of failure plane is shallow, and the failure plane is parallel to the surface. According to the slope stability analysis, the results show that the safety factor of residual soil slopes decreases when the return period increases. Moreover, the safety factor is constant in the

stationary condition. In contrast, the safety factor decreases in the non-stationary condition when the amount of rain increases. When comparing the safety factor in both stationary and non-stationary conditions of GEV distribution, the results show that the safety factor of non-stationary conditions is lower than in stationary conditions. Moreover, the safety factor gap between both stationary and non-stationary conditions of GEV distribution is increasing over time. Fig.11 presents the plots of the safety factor in this study.

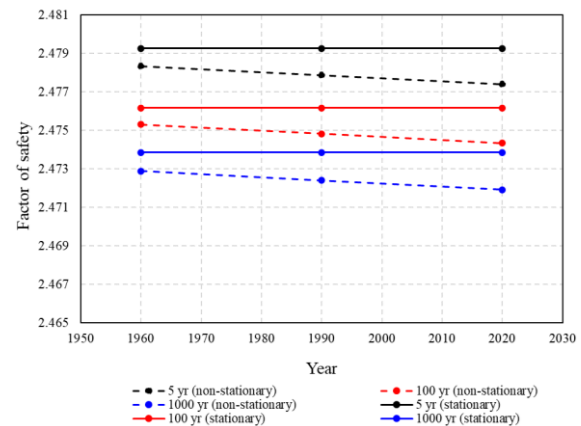


Fig. 11 Comparison of factor of safety.

### CONCLUSIONS

The amount of rainfall is a key controller of the stability of the soil slope. Comparing the stationary and non-stationary conditions of GEV distribution, this study found that the selection of historical data to generate IDF curves is the essential step for slope stability modelling because, if the modeller selects the low rainfall period to generate IDF curves, the results of the slope stability are high, and the susceptibility of slope failure is low. It may lead to neglecting the prevention of soil slope failure. In addition, changes in extreme rainfall are important issues of imperative concern for landslide or slope failure risk management.

### ACKNOWLEDGMENTS

The authors gratefully acknowledge the rainfall data provided by the Thai Meteorological Department (TMD).

### REFERENCES

- [1] Chaithong T., Influence of changes in extreme daily rainfall distribution on the stability of residual soil slopes. Big Earth Data, 2022. DOI: 10.1080/20964471.2022.2046306
- [2] IPCC., Summary for policymakers. In Climate change 2021: The physical science basis.

- Contribution of working group I to the Sixth assessment report of the intergovernmental panel on climate change. Cambridge, United Kingdom: Cambridge University Press. (In Press).
- [3] Martins E.S. and Stedinger J.R., Generalized maximum-likelihood generalized extreme-value quantile estimators for hydrologic data. *WATER RESOURCES RESEARCH*, Vol. 36 NO. 3, 2000, pp.737-744.
- [4] Xavier A.C.F, Rudke A.P, Fujita T, Blain G.C, Morais M.V.B, Almeida D.S, Rafee S.A.A, Martins L.D, Souza R.A.F, Freitas E.D, and Martins J.A., Stationary and non-stationary detection of extreme precipitation events and trends of average precipitation from 1980 to 2010 in the Paraná River basin, Brazil. *International Journal of Climatology*, 2019, pp.1–16. DOI: 10.1002/joc.6265
- [5] Wi S, Valdes J.B, Steinschneider S, and Kim T.W., Non-stationary frequency analysis of extreme precipitation in South Korea using peaks-over-threshold and annual maxima. *Stoch Environ Res Risk Assess*, 2015. DOI 10.1007/s00477-015-1180-8
- [6] Zhang L.L, Zhang J, Zhang L.M, and Tang W.H., Stability analysis of rainfall-induced slope failure: a review. *Proceedings of the Institution of Civil Engineering: Geotechnical Engineering*, Vol. 164, Issue GE5, 2011, pp.299-316.
- [7] Lu N, and Griffiths D.V., Profiles of steady-state suction stress in Unsaturated soils. *Journal of Geotechnical and Geoenvironmental Engineering*, Vol. 130, No. 10, 2004, pp.1063-1076.
- [8] Lu N, and Godt J., Infinite slope stability under steady unsaturated seepage conditions. *WATER RESOURCES RESEARCH*, Vol. 44, 2008. doi:10.1029/2008WR006976



# ESTIMATION OF THE ALLOWABLE BEARING CAPACITY OF SOIL IN SOME MUNICIPALITIES OF THE PROVINCE OF PAMPANGA USING ARTIFICIAL NEURAL NETWORK

Carmela Marie A. Lingad<sup>1</sup>, Erica Elice S. Uy<sup>2</sup>

<sup>1</sup>Graduate Student, De La Salle University, Philippines; <sup>2</sup>Faculty, De La Salle University, Philippines

## ABSTRACT

Urbanization is evident in some municipalities of Pampanga specifically in San Fernando and Santo Tomas. Those municipalities being developed, requires an information of the load-bearing capacity of soil. Predicting the soil bearing capacity provides an estimation of how much loads can the soil carry. The bearing capacity was calculated using the local shear failure equation of the Terzaghi's bearing capacity formula. Also, the bearing capacity was predicted using Artificial Neural Network for those locations which has available data with the  $N_{60}$  value, friction angle, unit weight, and footing width as dependent parameters. The results show a coefficient of correlation of approximately equal to 1 and a mean squared error of at least 0 for a hidden layer of 10 which proves that ANN is an efficient way in predicting the bearing capacity. Based on the sensitivity analysis, it was found out that the unit weight is the most significant parameter affecting the value of the bearing capacity. A relationship between the  $N_{60}$  value, soil classification, and the bearing capacity was observed. It was concluded that the  $N_{60}$  value and soil classification are the two determining factors on how the value of the bearing capacity will be, because it affects the consistency of the soil and most of the parameters are dependent on those two variables. The value of the bearing capacity ranges from a minimum of 20 kPa to a maximum of 630 kPa for a specific area.

*Keywords: Allowable Bearing Capacity, Artificial Neural Networks, Geographic Information System, SPT-N*

## INTRODUCTION

Urbanization starts to arise in the Philippines. Also, some of the provinces being near to Metro Manila start to get urbanized and be developed. One of the provinces that are starting to get urbanized is the province of Pampanga.

According to Das and Sobhan [6], bearing capacity are usually analyzed when it comes to designing foundations. Bearing capacity is the load-carrying capacity with respect to the shear failure of soil of shallow foundations. A wrong estimation of the bearing capacity often leads to a wrong design of the foundation.

Chao, Zhang, Zhu, and Hu [2] stated that artificial Neural Network (ANN) is the duplication of the physiological structure and mechanics of human brain. They stated that ANN is mostly used in computing some geotechnical engineering problems. It was also said that using ANN for solving is beneficial because of the following factors: a) it has high speed when it comes to calculation; b) it has strong ability when it comes to fault-tolerance; and, c) it has dexterous capability when it comes with dealing with convoluted solving rules [2].

The determination of the allowable bearing capacity allows the easier design of the proper dimension of a footing that can carry such loadings. In addition, the use of artificial neural network for the estimation of the bearing capacity provides a more accurate value because it also provides a validation

value in the means of the mean square error and the coefficient of correlation.

This paper used artificial neural network to simulate an estimation of the allowable bearing capacity of soil in the municipality of San Fernando and Santo Tomas, Pampanga.

## METHODOLOGY

For the study, 52 borehole data was used to estimate the bearing capacity. The borehole data was obtained from the municipalities of San Fernando and Santo Tomas, Pampanga. Most areas in the said location are sand. 52 borehole data was obtained because of the availability of the borehole data. The borehole data was plotted to provide an estimation of the bearing capacity of the area within 1 km radius. The standard penetration test – N (SPT – N) value was obtained in the borehole data provided by the local government units and some private testing companies. The SPT–N value was corrected using Eq. 1 which was provided by Das and Sobhan [6].

$$N_{60} = \frac{N_{H\eta B\eta S\eta R}}{60} \quad (1)$$

## Input Parameters/Independent Parameters

The input parameters for the calculation of the bearing capacity are the following: SPT-N values, friction angle, unit weight of soil, and footing width.

The friction angle and unit weight of soil was calculated according to the corresponding corrected SPT-N value. The value of the friction angle was interpolated using Table 1 which was proposed by Kulhawy and Mayne [10]. The value of the footing width was considered as 1 m for all embedment depths considering the limitations of the Terzaghi's bearing capacity equation [6].

Table 1. SPT-N value vs. Friction angle relationship from Kulhawy and Mayne [10]

SPT – N value	Friction angle
0 – 4	< 28
4 – 10	28 – 30
10 – 30	30 – 36
30 – 50	36 – 41
> 50	> 41

A study done by Puri, Prasad, and Jain [15] provided a prediction of the geotechnical parameters using machine learning, one of which is the density of soil using SPT-N value. The following equations (Eq's 2-a to 2-e) were used for the calculation of the density of soil which is then multiplied to the acceleration due to gravity to obtain the unit weight of the soil which will be used for Eq. 3.

a) For Coarse Grained soil,

a.1) Dry Density with  $1 \leq N \leq 50$ ,

$$\rho_d = 0.0068(N) + 1.5554 \quad (2-a)$$

a.2) Bulk Density with  $1 \leq N \leq 39$ ,

$$\rho_b = 0.0096(N) + 1.5001 \quad (2-b)$$

a.3) Bulk Density with  $40 \leq N \leq 50$ ,

$$\rho_b = 0.0141(N) + 1.3726 \quad (2-c)$$

b) For Fine Grained soil,

b.1) Dry Density with  $1 \leq N \leq 50$ ,

$$\rho_d = 0.0114(N) + 1.2488 \quad (2-d)$$

b.2) Bulk Density with  $1 \leq N \leq 50$ ,

$$\rho_b = 0.0080(N) + 1.7202 \quad (2-e)$$

#### Output Parameter/Dependent Parameter

The ultimate bearing capacity was calculated using the Terzaghi's bearing capacity equation (Equation 3) considering local shear failure [6].

$$q_{u(GS)} = 1.3cN_c + qN_q + 0.4\gamma BN_\gamma \quad (3)$$

where  $B$  is the width or diameter of the base of the footing,  $L$  is the length of the footing,  $q$  is the vertical effective stress from the natural ground level to the bottom of the footing,  $\gamma B$  is the effective vertical stress from the bottom of the footing to the 'B' projection,  $N_c$ ,  $N_q$ , and  $N_\gamma$  are the Terzaghi's bearing capacity coefficient, and  $c$  is the cohesion in which according to Kulhawy and Mayne [10] can be expressed as  $c = \frac{1}{2} [0.06(N)(P_a)]$ , where  $N$  is the SPT-N value, and  $P_a$  is the atmospheric pressure.

The allowable bearing capacity was computed using a factor of safety of 3.

#### Artificial Neural Network

Artificial Neural Network was used to predict the allowable bearing capacity with the independent parameters (SPT-N value, friction angle, unit weight, footing width) as input values and the dependent parameter (allowable bearing capacity computed using Terzaghi's bearing capacity equation) as output value. For the simulation of training of artificial neural network, the dataset was trained using a different number of hidden layers such as 5, 10, 15, and 20. The value of the coefficient of correlation and the mean square error was obtained to validate the efficiency of ANN in predicting the dependent parameter.

A sensitivity analysis was done to determine which independent parameter is highly significant and greatly affects the accuracy of the dependent parameter. According to Mrzyglod, Hawryluk, Janik, and Olejarczyk-Wozenska [13] to know the significance of one parameter to the desired output, a sensitivity analysis should be done. Sensitivity analysis can be computed by obtaining the error of the measured and predicted outputs. The equation of the error is presented in Eq. 4 and can be denoted as,

$$Error = \frac{1}{n} \sum_{i=1}^n (y_i - \hat{y}_i)^2 \quad (4)$$

$$W = \frac{Error_i}{Error} \quad (5)$$

where  $n$  is the number of output values,  $y_i$  is the measured/computed values,  $\hat{y}_i$  is the predicted values from ANN. Eq. 5 represent the value of  $W$ .  $W$  is the ratio (sensitivity of the parameter),  $Error_i$  is the computed error without the specific parameter, and  $Error$  is the total error including all parameters. If the value of  $W$  is less than or equal to 1, hence, the parameter is insignificant; in other words, it does not affect the value of the output.

#### Artificial Neural Network Validation

According to Rezaei, Nazir, and Momeni [18] to validate the predicted values for ANN, the coefficient of correlation and the mean square error should be

obtained. Both the coefficient of correlation and mean square error are displayed upon the ANN simulation. An article written by Elcicek, Akdogan, and Karagoz [8] provided an equation for the mean square error and coefficient of correlation. It can be computed as,

$$MSE = \frac{1}{N} \sum_{i=1}^N (x_{ob} - x_{pr})^2 \quad (6)$$

$$R^2 = \frac{\left[ \sum_{i=1}^N (x_{ob} - \bar{x}_{ob})^2 - \sum_{i=1}^N (x_{ob} - \bar{x}_{pr})^2 \right] \times \left[ \sum_{i=1}^N (x_{ob} - \bar{x}_{ob})^2 \right]^{-1}}{\quad} \quad (7)$$

where  $MSE$  is the mean square error,  $R^2$  is the coefficient of correlation,  $N$  is the total number of data,  $x_{ob}$  are the actual computed values,  $x_{pr}$  are the predicted values using ANN,  $\bar{x}_{ob}$  is the mean of the actual computed values, and  $\bar{x}_{pr}$  is the mean of the predicted values using ANN.

## RESULTS AND DISCUSSION

From the borehole data, refer to Table 2 for the data in one of the borehole logs obtained from a bridge in Bulaon, San Fernando City. Table 3 represents the values of the input parameters.

Table 2. Sample borehole analysis of a bridge in barangay Bulaon, San Fernando City

Depth		SPT	$N_{60}$	Soil Classification
1st	2nd	N-value		
0	1	22	12.375	SM
1	2	22	12.375	SM
2	3	15	8.4375	SM
3	4	21	11.8125	SM
4	5	21	11.8125	SM
5	6	18	10.125	SM

Table 3. Input parameters for the calculation of the bearing capacity

Depth		$N_{60}$	$\phi'$ (°)	$\delta$ (kN/m <sup>3</sup> )	B width
1st	2nd				
0	1	12.375	21.61	16.08	1
1	2	12.375	21.61	16.08	1
2	3	8.4375	20.65	15.82	1
3	4	11.8125	21.47	16.05	1
4	5	11.8125	21.47	16.05	1
5	6	10.125	21.08	15.93	1

### Bearing Capacity Calculation

From the obtained data, refer to Table 3 for the calculated ultimate bearing capacity equation using

Eq. 3 and the allowable bearing capacity using a factor of safety of 3 [7]. All the values of the parameters required for the ultimate bearing capacity equation was computed first such as the cohesion, unit weight,  $q$ , and  $N_c$ ,  $N_q$ ,  $N_{\gamma}$ .

Table 4. Sample Calculation of the Bearing Capacity in a school in Bulaon, San Fernando City

Depth (m)		$N_{60}$	Soil Class	Ultimate Capacity (kPa)	Allow Capacity (kPa)
1st	2nd				
0	1	12.38	SM	171.04	51.65
1	2	12.38	SM	312.30	93.38
2	3	8.44	SM	406.89	119.63
3	4	11.81	SM	585.04	173.67
4	5	11.81	SM	724.28	214.73
5	6	10.13	SM		

To validate the results of the computed allowable bearing capacity, the computed values were compared to the allowable foundation pressure provided in the National Structural Code of the Philippines 2015 [14]. Observing all the computed allowable bearing capacity for different embedment depths, it satisfies all the limitations within the code. Hence, the values computed are acceptable.

### ANN Validation

Since different values of hidden layers were used, the values of the coefficient of correlation were obtained for all hidden layers (HL) (5, 10, 15, 20) in both locations.

The lowest value of the mean square is found when there are 10 hidden layers. Though all the other 3 returns a value of mean square error of approximately 0, yet the lowest value of MSE is found at 10 hidden layers. Table 5 represents the value of the MSE and R of all the hidden layers with their corresponding embedment depths.

Figure 1 shows the regression fit graph of the training, validation, and testing of the data in both locations with their corresponding coefficient of correlation with a hidden layer of 10. As it can be seen in Figure 1, the regression fit line and data lies on the fitting line which explains the accuracy of the output values predicted using ANN with 10 hidden layers. The regression fit line also provided the values of the coefficient of correlation which shows that it is approximately equal to 1.

There are 52 available borehole data. The dataset was divided into a 70% – 15% – 15% distribution for the training, validation, and testing, respectively; hence, 36 data was used for the training, 8 data for validation and testing.

Table 5. Summary of validation results in ANN with 10 hidden layers

Df	HL = 10		HL = 5	
	MSE	R	MSE	R
1	0	1	0.067	1
2	0.0003	0.986	0.001	0.997
3	0.002	0.991	0.009	0.994
4	0.0017	0.98	0.0018	0.995
5	0.003	0.995	0.011	0.956

Df	HL = 15		HL = 20	
	MSE	R	MSE	R
1	0.069	0.98	0.051	1
2	0.002	0.995	0.013	0.991
3	0.009	0.954	0.004	0.996
4	0.023	0.994	0.0021	0.943
5	0.003	0.985	0.003	0.977

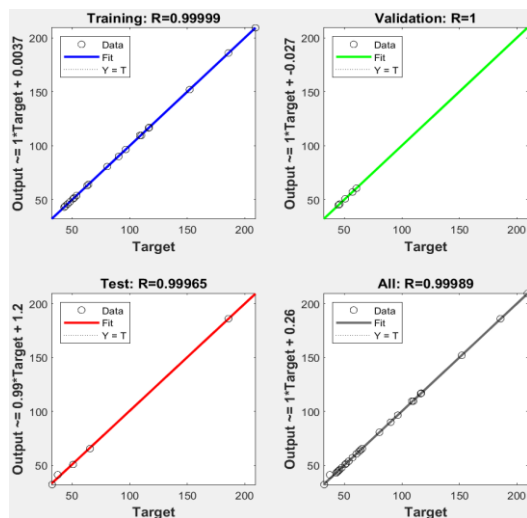


Figure 1. Regression fit curve for the training, validation, and testing of both municipalities for Df = 1 m with 10 hidden layers

Figure 2 shows the comparison of the computed values of the allowable bearing capacity using the Terzaghi's bearing capacity equation and the estimated allowable bearing capacity using Artificial Neural Network. It shows how close the values are from each other. The figure also proves that the estimated values using ANN are close enough to the computed values/

### Sensitivity Analysis

A summary of the weights for both locations is provided in Table 6. The sensitivity analysis provided an idea of whose the most significant parameter amongst the independent parameters such as the SPT-N value, friction angle, unit weight, and the footing width. As it can be seen, the unit weight is the most significant parameter as it returns the highest value of

the weight, second is the SPT-N value, and the third is the friction angle. For the footing width, two embedment depth returns a value of weight of less than 1, but the rest provides a value of more than 1. In conclusion, it can then be said that the footing width is still a significant parameter. In contradiction, it can also be concluded that it is the least significant because it has the lowest value of the weight.

Table 6. Summary of the dependent parameters' weights for both locations

Df (m)	Weights			
	SPT – N value	Friction angle	Unit weight	Footing Width
1	25.464	2.057	748.984	0.929
2	21.452	1.306	224.052	0.794
3	4.863	4.236	209.623	2.307
4	29.043	18.131	382.678	9.210
5	61.387	9.709	158.060	7.500

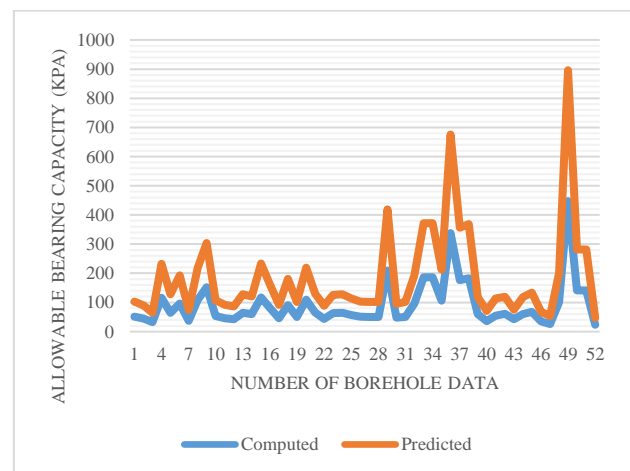


Figure 2. Comparison of results of the computed and predicted allowable bearing capacity at Df = 1 m

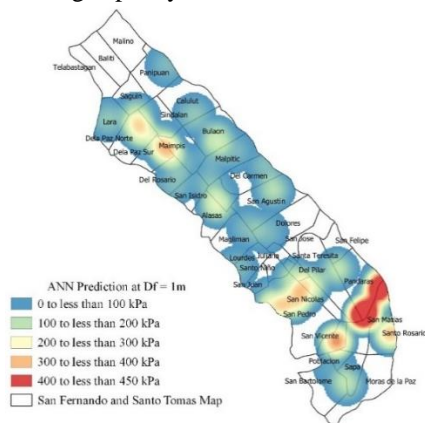
### Allowable Bearing Capacity Map

The allowable bearing capacity distribution map for the municipalities of San Fernando and Santo Tomas are shown in Figure 3a to Figure 3e. The values of the bearing capacity were mapped using Geographic Information System (GIS). The values of the allowable bearing capacity are within a range of minimum of 20 kPa to a maximum of at least 635 kPa.

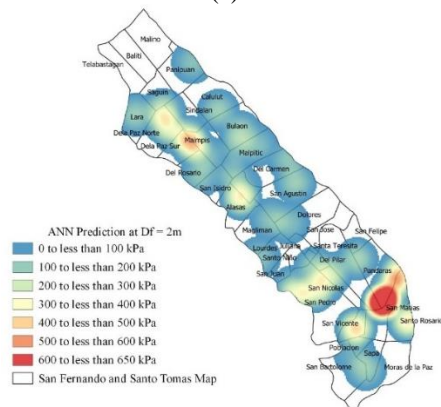
### Relationship between the allowable bearing capacity, $N_{60}$ value, and the soil classification

Relating the two parameters and the allowable bearing capacity, it can be observed that both  $N_{60}$  value and soil classification are directly related to the value of the allowable bearing capacity. It is notable

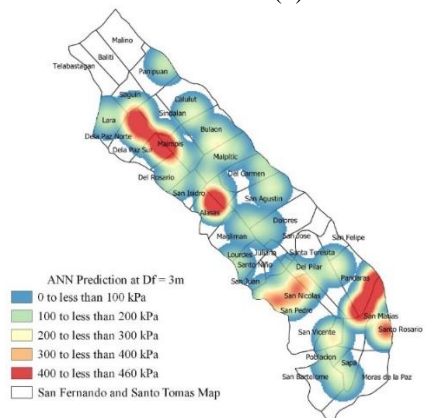
that the  $N_{60}$  value and soil classification affects the consistency of the soil. It can be observed that even if the soil is classified as coarse-grained, if the  $N_{60}$  value is greater than 11, the soil is already considered as dense; hence, it can have a greater value of the bearing capacity. In contradiction, if the soil is considered as fine-grained, yet the  $N_{60}$  value is within 0 – 4, the soil has a very soft to soft consistency. Therefore, even if the soil is cohesive, it does not possess a higher value of bearing capacity. Hence, it can be concluded that both the  $N_{60}$  value and soil classification should be considered as the greatest contributing factor in the value of the allowable bearing capacity.



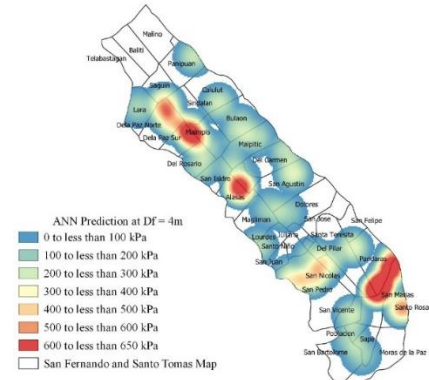
(a)



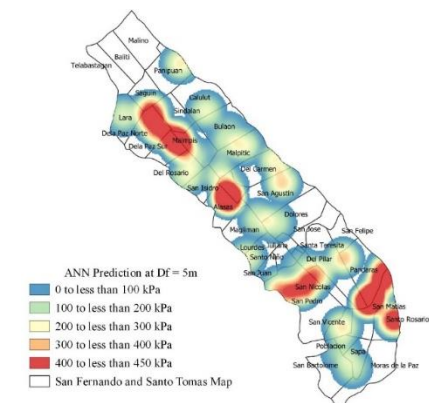
(b)



(c)



(d)



(e)

Figure 3. Allowable Bearing Capacity Map at (a) Df = 1m; (b) Df = 2m; (c) Df = 3m; (d) Df = 4m; and, (e) Df = 5m

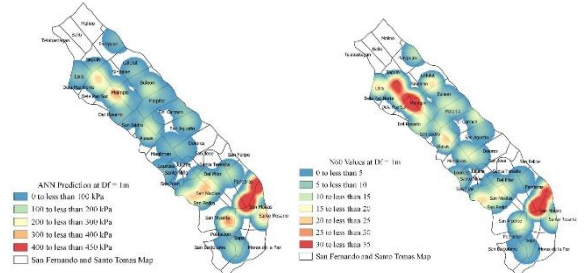


Figure 3. Side-by-side allowable bearing capacity map and  $N_{60}$  value map for Df = 1m

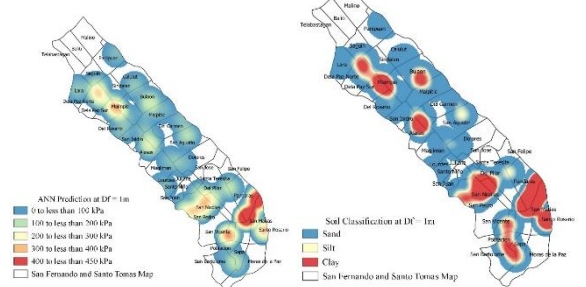


Figure 4. Side-by-side allowable bearing capacity map and soil classification map for Df = 1m

## CONCLUSIONS

Urbanization starts to arise in most of the provinces in the country and one of which is the province of Pampanga. Pampanga is one of the provinces that is just a few hours away from Manila; hence, developments are evident there. Some of the highly urbanized municipalities in the province of Pampanga is San Fernando (the province's capital) and Santo Tomas just below San Fernando. An estimation of the allowable bearing capacity was provided for both locations using artificial neural network.

The SPT-N value and soil classification was obtained from the borehole data and those data were used to obtain the bearing capacity using the Terzaghi's bearing capacity equation. The values of the allowable bearing capacity are within a range of a minimum of 20 kPa to a maximum of at least 635 kPa. It is notable as well that as the value of the embedment depth of footing increases, the values of the bearing capacity increase, respectively.

Upon obtaining the actual values of the bearing capacity, the values were trained using the artificial neural network where the  $N_{60}$  value, friction angle, unit weight, and footing width are the input values, and the bearing capacity is the output value. 10 hidden layers was used because it yields to a more acceptable value of the allowable bearing capacity. The results were validated by obtaining the mean square error and coefficient of correlation. It is observed that all the values of the coefficient of correlation for all embedment depths yields to a value of approximately equal to 1, which proves the efficiency of the artificial neural network in predicting the values of the bearing capacity. After training the data using ANN, the independent parameters have undergone a sensitivity analysis to determine its significance in the prediction of the bearing capacity. The sensitivity analysis has provided an observation that the most significant parameter is the unit weight, followed by the  $N_{60}$  value, and lastly is the friction angle.

## ACKNOWLEDGMENTS

The author would like to thank the Department of Science and Technology-Engineering Research and Development for Technology (DOST-ERDT) for funding the research.

## REFERENCES

- [1] Budhu, M. (2010). Soil Mechanics and Foundation. Hamilton Printing Company, John & Wiley Sons, Inc., USA. 3<sup>rd</sup> Ed.
- [2] Chao, Z., Ma, G., Zhang, Ye., Zhu, Y. & Hu, H. (2018). The Application of Artificial Neural Network in Geotechnical Engineering. 2018 *International Conference on Civil and Hydraulic Engineering*.
- [3] Chen, W. F. & McCarron, W. (1991). Bearing Capacity of Shallow Foundations.
- [4] Das, B. M. (2009). Shallow Foundations – Bearing Capacity and Settlement. CRC Press, Taylor & Francis Group, USA. 2<sup>nd</sup> Ed.
- [5] Das, B. M., & Larbi-Cherif, S. (1983). Soils and Foundations: Bearing Capacity of Two Closely-Spaced Shallow Foundations on Sand. *Japanese Society of Soil Mechanics and Foundation Engineering*. 23(1).
- [6] Das, B. M., & Sobhan, K. (2014). Principles of Geotechnical Engineering. Cengage Learning, Stamford, USA. 8th Ed.
- [7] Dungca, J. (2019). A Reference for the Allowable Soil Bearing Capacities in Quezon City, Philippines. *International Journal of GEOMATE*. 19 (71), 42 – 47.
- [8] Elcicek, H., Akdogan, E. & Karagoz, S. (2014). The Use of Artificial Neural Network for Prediction of Dissolution Kinetics: Research Article. *The Scientific World Journal*.
- [9] Fatehnia, M. & Amirinia, G. (2018). A Review of Genetic Programming and Artificial Neural Network Applications in Pile Foundations. *International Journal of Geo-Engineering*.
- [10] Kulhawy, F. H. & Mayne, P. W. (1990). Manual on Estimating Soil Properties for Foundation Design. *Research Project*. 4 – 13.
- [11] Moayed, H., Kalantar, B., Dounis, A., Bui, D. T. & Foong, L. K. (2019). Development of Two Novel Hybrid Prediction Models Estimating Ultimate Bearing Capacity of the Shallow Circular Footing. *Applied Sciences*.
- [12] More, J. J. (2006). The Levenberg-Marquardt Algorithm: Implementation and Theory. *U.S. Energy Research and Development Administration*. 105 – 106.
- [13] Mrzyglod, B., Hawryluk, M., Janik, M. & Olejarczyk-Wozenska, I. (2020). Sensitivity Analysis of the Artificial Neural Networks in a System for Durability Prediction of Forging Tools to Forgings Made of C45 Steel. *The International Journal of Advanced Manufacturing Technology*. 109, 1385 – 1395.
- [14] National Structural Code of the Philippines (NSCP) 2015. Association of Structural Engineers of the Philippines, Inc. Volume 1, 7<sup>th</sup> Edition, 1<sup>st</sup> Printing.
- [15] Puri, N., Prasad, H. D. & Jain, A. (2017). Prediction of Geotechnical Parameters Using Machine Learning Techniques. 6<sup>th</sup> *International Conference on Smart Computing and Communications*. 509 – 517.
- [16] Quoc, V. N. (2008). Numerical Modeling of the Undrained Vertical Bearing Capacity of Shallow Foundations. A Thesis. University of Southern Queensland.



- [17] Ramesh, S., Suman, R. V., Yashwanth, M. & Prasad, S. K. (2019). Evaluation of Bearing Capacity of Ground in Transition Zone. *Proceedings of the Indian Geotechnical Conference 2019*. IGC – 2019, 1 (451).
- [18] Rezaei, H., Nazir, Rm. & Momeni, E. (2016). Bearing Capacity of Thin-Walled Shallow Foundations: An Experimental and Artificial Intelligence-Based study. *Journal of Zhejiang University-SCIENCE A (Applied Physics & Engineering)*.
- [19] Sharma, S. (2017). Epoch vs. Batch Size vs. Iterations. Retrieved September 23, 2017, from <https://towardsdatascience.com/epoch-vs-iterations-vs-batch-size-4dfb9c7ce9c9>.
- [20] Skempton, A. W. (1986). Standard penetration test procedures and the effects in sands of overburden pressure, relative density, particle size, ageing and overconsolidation. *Geotechnique*, 36(3), 425-447.

# DYNAMIC CENTRIFUGE MODEL TESTS FOR SOIL-BENTONITE VERTICAL CUTOFF WALLS WITH EARTHQUAKE-PROOF PERFORMANCE

Koji Watanabe<sup>1</sup>, Daisuke Ueno<sup>2</sup> and Masaaki Hasegawa<sup>2</sup>

<sup>1</sup>Department of Civil Engineering, Aichi Institute of Technology, Japan; <sup>2</sup>Seikotone Co. Ltd., Japan

## ABSTRACT

Vertical cutoff walls using low permeable materials are often constructed at contaminated sites to contain the contaminants and to prevent their migration in the aquifer. The purpose of this study is to develop the soil-bentonite vertical cutoff walls with earthquake-proof performance. The soil-bentonite vertical cutoff wall which is developed in this study is a rather flexible material compared with other typical barrier materials such as soil-cement mixing material. In this study, dynamic centrifuge model tests were performed to confirm the earthquake-proof performance and the impermeable performance of cutoff wall. Four kinds of step-wise shaking using sine wave were conducted for the soil-bentonite vertical cutoff wall and the soil-cement mixing vertical cutoff wall. The following findings were obtained from this study.

1) It is concluded that the soil-bentonite vertical cutoff wall which was developed in this study has the high earthquake-proof performance because the deformation of soil-bentonite vertical cutoff wall follows the model ground deformation during the shaking.

2) According to the observation after the dynamic centrifuge model tests, the failure of soil-bentonite cutoff wall does not occur although the collapse of soil-cement mixing vertical cutoff wall due to the shaking is confirmed. Therefore, this fact implies that the soil-bentonite vertical cutoff wall has the high earthquake-proof performance.

*Keywords: Soil-bentonite Cutoff Wall, Dynamic Centrifuge Model Test, Earthquake-proof Performance*

## INTRODUCTION

Vertical cutoff walls using low permeable materials are often constructed at contaminated sites to contain the contaminants and to prevent their migration in the aquifer. It is also needed to the leakage control of river embankment and regulating pond. Figure 1 summarizes the concept of applicability on vertical cutoff walls. The usual countermeasure for the migration and the leakage control is to construct the soil-cement cutoff wall. However, it is pointed out that the soil-cement cutoff wall is damaged when the earthquake happens. Moreover, the barrier performance of cutoff wall decreases as the crack of cutoff wall occurs.

The purpose of this study is to develop the soil-bentonite vertical cutoff walls with earthquake-proof performance. The soil-bentonite vertical cutoff wall which is developed in this study is a rather flexible material compared with other typical barrier materials such as soil-cement mixing material. There are some previous researches to examine the performance of soil-bentonite cutoff walls [1]–[3]. These researches are subjected to construct the vertical cutoff walls by mixing powdered bentonite and in-situ soil. The results of previous researches are reported as follows;

1. It is possible to construct the low permeable

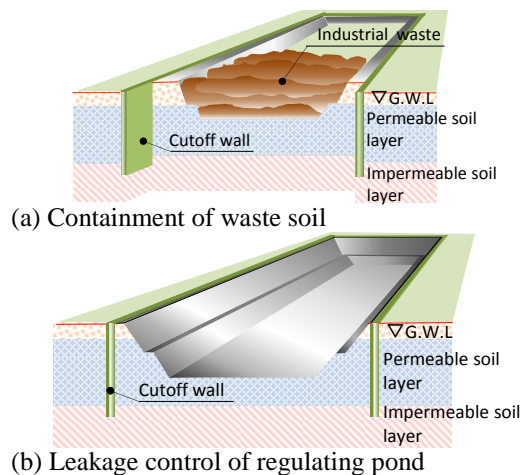


Fig. 1 Concept of vertical cutoff walls.

cutoff walls as bentonite and in-situ soil are mixed.

2. The damage of cutoff walls does not occur when the large deformation happens in the ground.

3. Corrosion and degradation does not occur because it is stable that the major component of bentonite is inorganic substance such as montmorillonite

4. Sludge amount due to the construction of cutoff walls decreases as bentonite and in-situ soil are mixed in the construction process.

Watanabe et al. [4] developed the soil-bentonite vertical cutoff walls with earthquake-proof performance. The following findings obtained from literature [4];

1) The hydraulic conductivity showed the high value and decreased with the confining pressure from the triaxial hydraulic conductivity tests.

2) According to the in-situ full scale test, it is confirmed from the results of CPT that the soil-bentonite vertical cutoff wall can be constructed the constant quality along to the depth direction by using TRD (Trench cutting Re-mixing Deep wall) method.

3) It is examined that the soil-bentonite vertical cutoff wall has the high hydraulic conductivity from hydraulic conductivity test for the core sampling specimen of in-situ full scale test.

In this study, the dynamic centrifuge model tests were performed to confirm the earthquake-proof performance and the impermeable performance of cutoff wall. Four kinds of step-wise shaking using sine wave were conducted for the soil-bentonite vertical cutoff wall and the soil-cement mixing vertical cutoff wall.

## CONSTRUCTION METHOD OF SOIL-BENTONITE CUTOFF WALLS

The vertical cutoff wall with earthquake-proof performance is constructed by TRD (Trench cutting Re-mixing Deep wall) method as shown in Fig. 2. Figure 3 also indicates the construction machinery which is applied the construction of vertical cutoff wall. The construction process is described as follows;

1. The agitated auger which is chainsaw type shape connects the base machinery and this auger inserts into in-situ ground.

2. The specialty bentonite slurry injects into the in-situ ground and the chainsaw type auger agitates in-situ ground as the chainsaw type auger moves to horizontal direction.

It may be suggested that the homogeneous cutoff wall is constructed by using TRD method.

## DYNAMIC CENTORIFUGE MODEL TESTS

### Centrifuge Apparatus

The beam type centrifuge apparatus was used to the model test as described in this paper. This beam type centrifuge has a pair of parallel arms that hold platforms on which the model container and a weight for counterbalance are mounted as shown in Fig. 4. Radius of rotation is 7.01m, which is the distance from the rotating shaft to the platform base. The surface of swinging platform is always normal to the resultant acceleration of the centrifuge acceleration,  $nG$ , and earth's gravity. The shaking

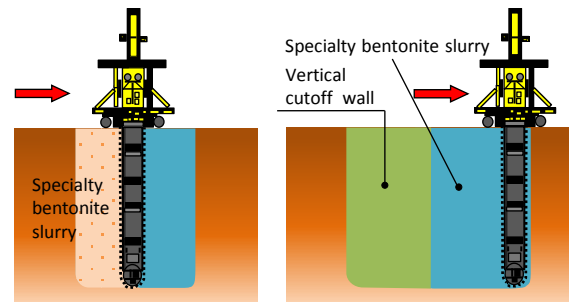


Fig. 2 Concept of vertical cutoff walls.



Fig. 3 Construction machinery for TRD method.

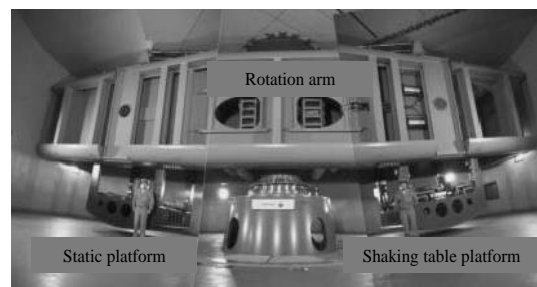


Fig. 4 Centrifuge apparatus.

Table 1 Specifications of centrifuge apparatus.

Outer diameter of arm	16.67m
Height of arm	3.00m
Radius of platform	7.01m
Maximum payload	700g-t
Payload weight	7t
Platform space	2.2m*2.2m
Test model height	2.5m

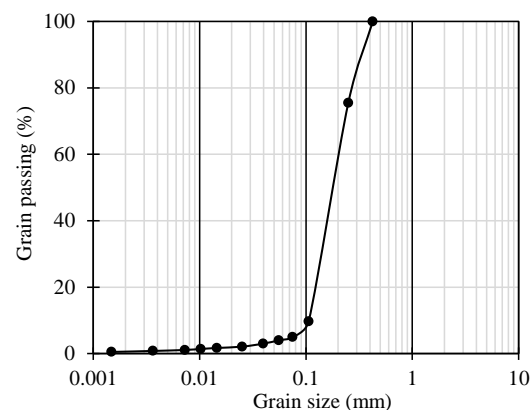


Fig. 5 Grain size distribution of silica sand No. 7.

Table 2 Physical properties of silica sand No. 7.

Soil particle density $\rho_s$ (g/cm <sup>3</sup> )	2.654
Mean diameter $D_{50}$ (mm)	0.185
Maximum void ratio $e_{max}$	1.193
Minimum void ratio $e_{min}$	0.698

Table 3 Compounding condition.

	Soil type	Sand (g)	Kaolin clay (g)	Water (g)	Ca-bentonite (g)	Ion-exchange material (g)
Case 1	Sandy soil	1713	-	480.4	122.6	4.4
Case 2	Composite soil	1486.6	165.2	541.6	122.6	4.4

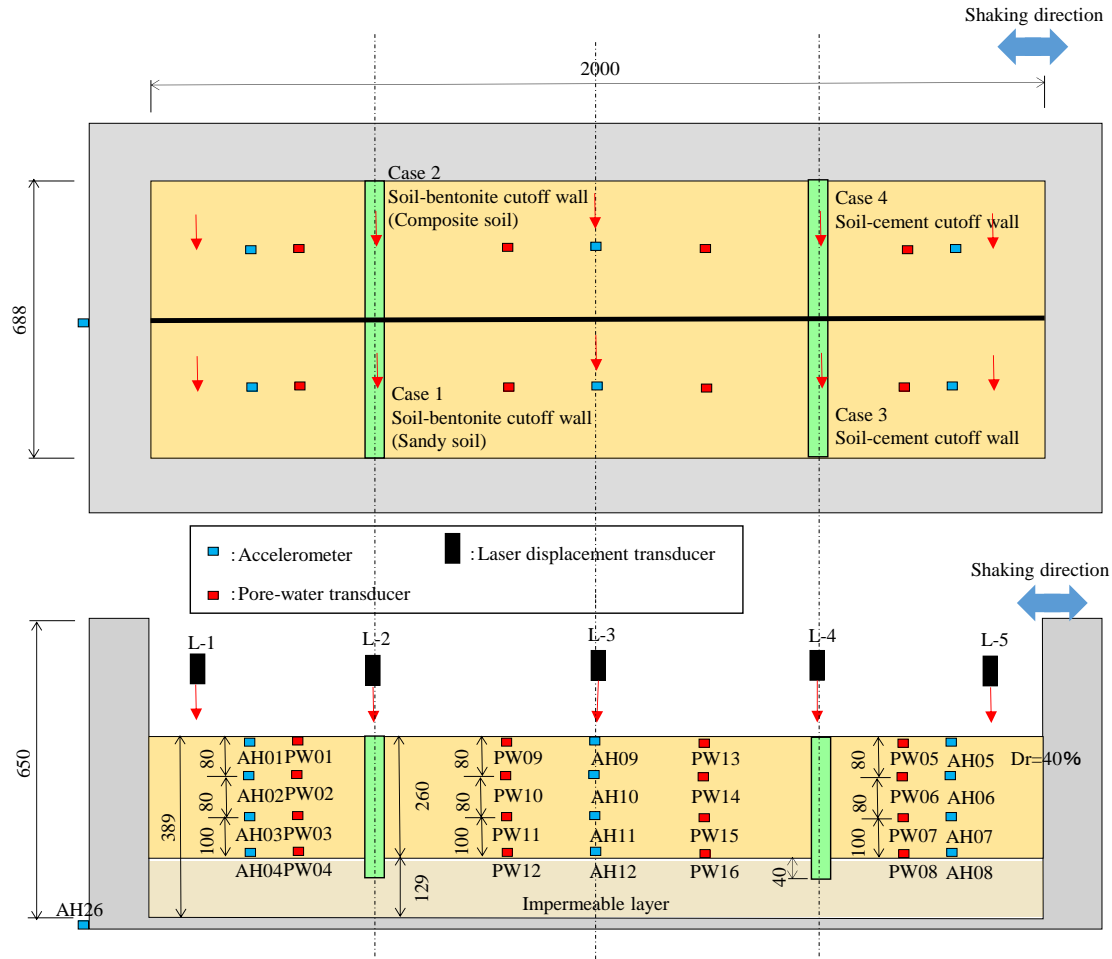


Fig. 6 Schematic view of centrifuge shaking table test.

table platform as shown in Fig. 4 was used in dynamic centrifuge model tests. The specifications of beam type centrifuge which was used in this study are summarized in Table 1.

### Material Used in Centrifuge Model Tests

Figure 5 indicates the grain distribution curve of Silica sand No. 7, and the physical properties of that are also shown in Table 2. The model ground is prepared by air-pluviation method using Silica sand No. 7.

The compounding conditions of model soil-bentonite cutoff wall are proposed in Table 3. The constitutional materials are sand (Silica sand No. 5), Kaolin clay (only Case 2), Ca-bentonite, water and ion-exchange material. The making process of model soil-bentonite cutoff wall is described as

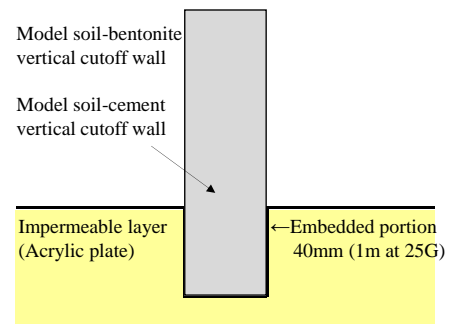
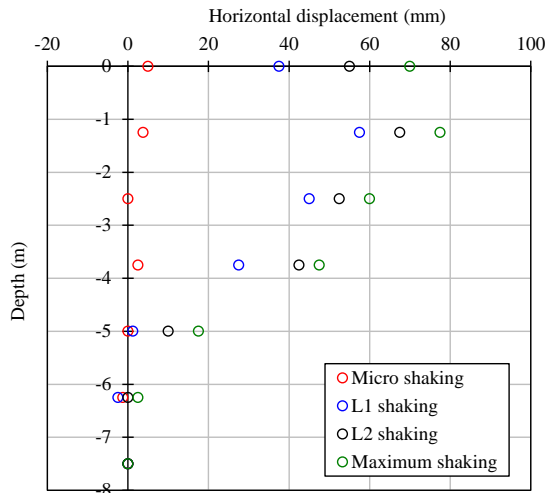


Fig. 7 Detail of embedded portion for model vertical cutoff wall

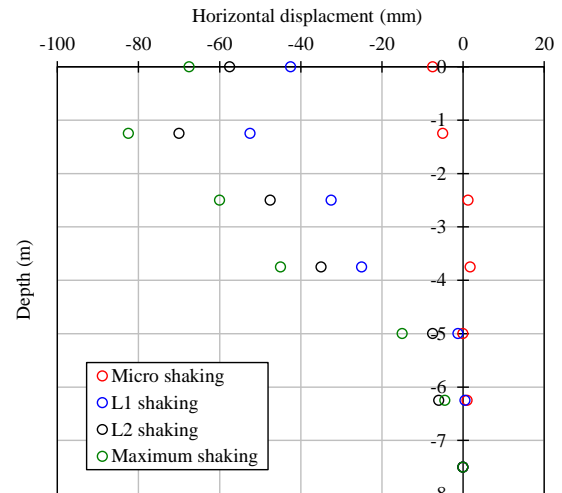
follows;

1. The predetermined sand and water are mixed homogeneously by the rotary-type mixer. (i.e. model ground material) Here, the predetermined Kaolin clay is added in the Case 2.

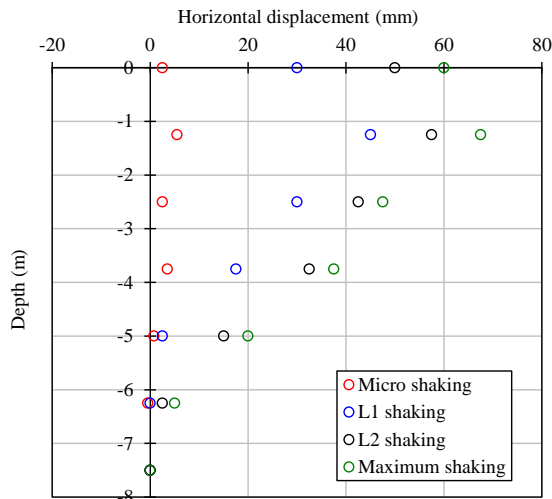
2. The predetermined Ca-bentonite and water are



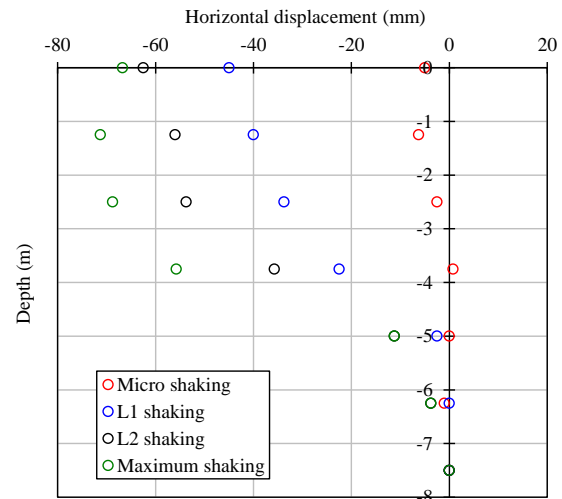
(a) Sine wave (2.4Hz).



(a) Sine wave (2.4Hz).



(a) Sine wave (4.8Hz).



(a) Sine wave (4.8Hz).

Fig. 8 Depth distribution of horizontal displacement for Case 1.

Fig. 9 Depth distribution of horizontal displacement for Case 2.

mixed homogeneously. (i.e. injection liquid)

3. The predetermined ion-exchange material and water are mixed homogeneously. (i.e. injection activating agent)

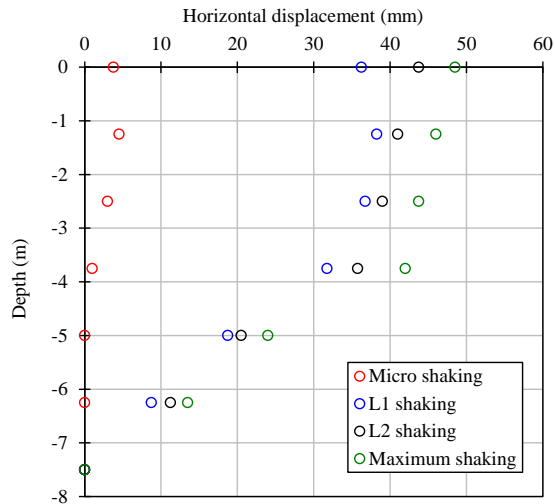
4. The injection liquid and injection activating agent are added to the model ground material.

5. The model soil-bentonite cutoff wall is made by injecting the model ground.

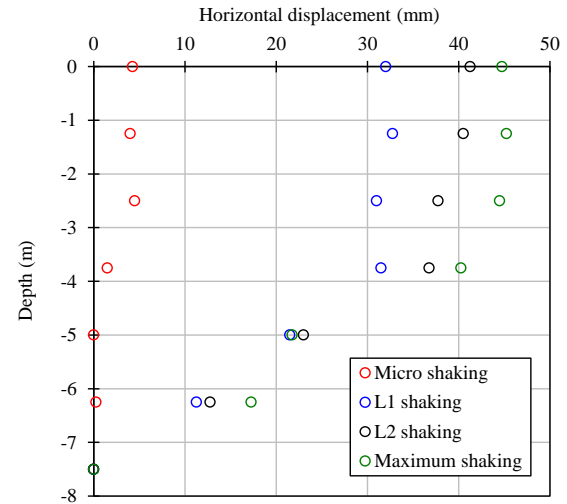
## Experimental Method

Figure 6 shows the schematic view of centrifuge shaking table test. A rigid soil container was used in the shaking table test, and the model ground was created using air-pluviation method such that the relative density of the  $D_r$  was 40%. Silica sand No. 7 (Specific gravity of soil,  $G_s=2.645$ ) was used in preparing the model ground. The bottom layer was the impermeable layer which was made by the

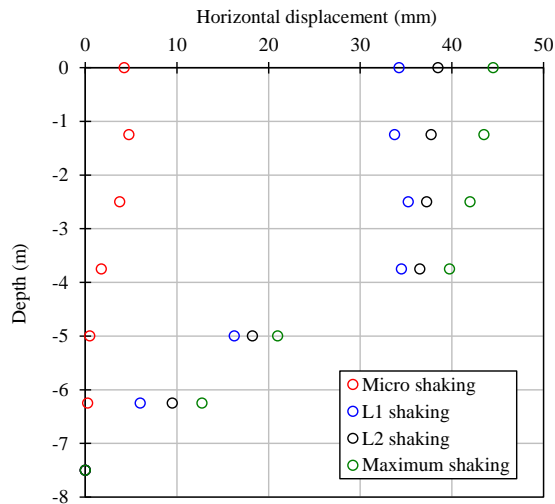
acrylic plate. The detail of embedded portion for the model vertical cutoff wall is shown in Fig. 7. For the vertical cutoff wall, the sandy soil-bentonite cutoff walls was simulated using compounding condition of Case 1 as described in Table 3, whereas composite soil-bentonite cutoff wall was simulated using compounding condition of Case 2 as described in Table 3. The model soil-cement mixing walls (Cases 3 and 4) are made by Silica sand No. 5 and cement. The target strength of soil-cement mixing walls are unconfined strength  $q_u=500\text{kN/m}^2$ . It is confirmed that the strength of soil-cement is almost  $q_u=500\text{kN/m}^2$  from the unconfined compression test. The dimension of model cutoff wall are width 20mm, depth 340mm and length 300mm. As the model scale ratio was 1:25, a centrifuge acceleration of 25G was used in the shaking table tests. The model ground is saturated after preparing the dry sand ground by using the metolose water which has 25



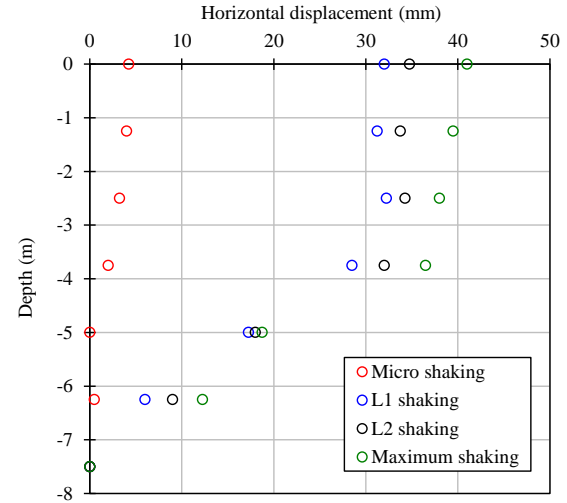
(a) Sine wave (2.4Hz).



(a) Sine wave (2.4Hz).



(a) Sine wave (4.8Hz).



(a) Sine wave (4.8Hz).

Fig. 10 Depth distribution of horizontal displacement for Case 3.

Fig. 11 Depth distribution of horizontal displacement for Case 4.

times larger viscosity than water. All the tests were conducted to the saturated sand conditions under 25G centrifuge acceleration field.

The frequency and amplitude of acceleration were varied using sine wave as input to generate stepwise shaking. The frequencies of sine wave used in this experiment are 60Hz and 120Hz to examine the dynamic behavior due to the different frequency. Thus, the prototype frequencies were 2.4Hz and 4.8Hz respectively. Parameters measured in the experiment include acceleration at various depths of the model ground, displacement of the model cutoff wall surface at ground level, and the pore water pressure at depth of model ground. Moreover, the analysis such as PIV (Particle Image Velocimetry) to obtain the deformation of model cutoff wall and model ground was carried out after the experiment by tracking the model ground movement

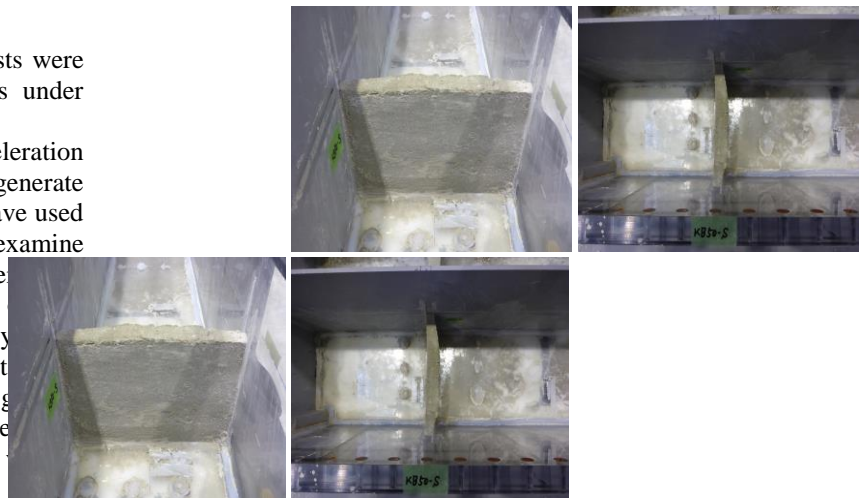


Fig. 12 Soil-bentonite cutoff wall after shaking.

sequentially. It is possible to examine the failure mode of model cutoff wall and model ground from



the results of image analysis.

## RESULTS OF CENTRIFUGE MODEL TESTS

The results of centrifuge model tests present the prototype scale values in this chapter. The depth distributions of horizontal displacement are shown in Fig. 8~Fig. 11. Here, the input acceleration levels are described as follows;

Micro shaking: Lower than 100gal

L1 shaking: 200~300gal

L2 shaking: 600~700gal

Maximum shaking: Higher than 1000gal

It is important to estimate the horizontal displacement of cutoff wall to obtain the earthquake-proof performance. Therefore, the horizontal displacement of cutoff wall is calculated by PIV analysis during the shaking. It is confirmed that the horizontal displacement of soil-bentonite cutoff wall as shown in Figs. 8 and 9 indicates the large value at the shallow depth of model ground. This fact implies that the horizontal displacement of model cutoff wall dominates at the shallow depth of model ground because the large horizontal force is acted to the model cutoff wall at the shallow depth of model ground. The deformation behavior of model soil-bentonite cutoff wall as described above shows the same trend regardless of the input wave frequency.

On the other hand, the horizontal displacement of soil-cement cutoff wall as shown in Fig. 10 and Fig. 11 presents that the difference of horizontal displacement at the shallow depth of model ground indicates the small value. It is said that the failure such as the cracks of cutoff wall occurs in the small shaking level. Thus, the soil-cement cutoff wall cannot follow the ground deformation during the shaking. The deformation behavior indicates the same trend regardless of the input wave frequency.

Figure 12 and 13 presents the model cutoff wall after the shaking. The soil-bentonite cutoff wall as shown in Fig. 12 does not occur the failure such as the cracks of model cutoff wall. It is concluded that the soil-bentonite cutoff wall can follow the ground deformation in the large earthquake. Moreover, it is said that the impermeable performance can be kept after the large earthquake because the large failure is not examined. Figure 13 indicates the soil-cement cutoff wall after the shaking tests. Here, the red lines in Fig. 13 mean the dominant cracks. From Figure 13, the many cracks of model cutoff wall are observed. This fact implies that the soil-cement cutoff wall cannot follow the ground deformation.

## CONCLUSIONS

In this study, the dynamic centrifuge model tests were performed to confirm the earthquake-



Fig. 13 Soil-cement cutoff wall after shaking.

proof performance and the impermeable performance of cutoff wall. Four kinds of step-wise shaking using sine wave were conducted for the soil-bentonite vertical cutoff wall and the soil-cement mixing vertical cutoff wall. The following findings were obtained from this study.

1) It is concluded that the soil-bentonite vertical cutoff wall which was developed in this study has the high earthquake-proof performance because the deformation of soil-bentonite vertical cutoff wall follows the model ground deformation during the shaking.

2) According to the observation after the dynamic centrifuge model tests, the failure of soil-bentonite cutoff wall does not occur although the collapse of soil-cement mixing vertical cutoff wall due to the shaking is confirmed. Therefore, this fact implies that the soil-bentonite vertical cutoff wall has the high earthquake-proof performance.

## REFERENCES

- [1] Evans J. C., Shacklford C. D., Yeo S. S. and Henning J., Membrane Behavior of Soil-bentonite Slurry-trench Cutoff Walls. *Soils and Foundations*, Vol. 17, No. 4, 2008, pp. 316-322.
- [2] Yeo S.S., Shacklford C. D. and Evans J. C., Hydraulic Conductivity and Compressibility of Soil-bentonite Back-fill Amended with Activated Carbon, *Journal of Geotechnical and Geoenvironmental Engineering*, ASCE, Vol. 135, No. 5, 2009, pp. 664-672.
- [3] Takai A., Inui T., Katsumi T., Kamon M. and Araki S., Factors Affected The Hydraulic Barrier Performance of Soil-bentonite Mixture Cut-off Wall, *Journal of Japan Society of Civil Engineers*, Ser. C (Geosphere Engineering), Vol. 68, No. 1, 2012, pp. 1-14.
- [4] Koji W., Shinya M., Daisuke U and Masaaki H., Study on Soil-bentonite Vertical Cutoff Walls with Earthquake-proof Performance, *Proceedings of International Conference of GEOMATE*, 2020, pp. 241-246.

# REPRODUCTION OF DYNAMIC BEHAVIOUR AND CLASSIFICATION OF FAILURE PATTERNS OF STONEWALLS BY DISTINCT ELEMENT METHOD SIMULATION

Satoshi Sugimoto<sup>1</sup>, Kosuke Yamaguchi<sup>1</sup> and Maho Yamaguchi<sup>2</sup>

<sup>1</sup>Graduate School of Engineering, Nagasaki University, Japan; <sup>2</sup> Nagasaki City Office, Japan

## ABSTRACT

While large earthquakes are predicted to occur in the near future, there is no established method for evaluating the stability of castle stonewalls from an engineering perspective. Therefore, there is an urgent need to elucidate the mechanism of dynamic stability of castle stonewalls. In this study, we measured the angle of repose, clarified the relationship between the measurement results and input physical properties, and reproduced the collapse behavior of stone base types and half-stone base types to investigate the factors affecting the stability of stonewalls. As a result, the deformation and collapse patterns of stonewalls were classified according to the shear resistance angle of the block surface and the width of the cobblestone layer.

*Keywords: Stonewall, DEM analysis, Dynamic behavior, Displacement*

## 1. INTRODUCTION

The 2016 Kumamoto earthquake caused enormous damage to ground structures such as buildings and stonewalls at Kumamoto Castle. Besides, many stonewalls in Kumamoto Castle collapsed and overturned, and tensile cracks occurred in the back of the embankment. The 2016 Kumamoto earthquake is characterized by the fact that Kumamoto Castle was damaged by a foreshock with a seismic intensity of 5+ and the main shock of 6+. Although the stonewalls of Kumamoto Castle escaped deformation during the foreshock, many cases were found to have been deformed or collapsed due to the mainshock.

However, despite the fact that large earthquakes are predicted to occur in the future, a method for evaluating the stability of castle stonewalls as civil engineering structures has not yet been established. Therefore, there is an urgent need to elucidate the mechanism of dynamic stability of castle stonewalls.

Studies have been conducted to follow the dynamic behavior of stonewalls using various numerical analysis methods. Hashimoto et al. [1] conducted a dynamic analysis using the finite element method (FEM) and focused on the response acceleration and response velocity obtained from FEM at the stonewall location to clarify the relationship with damage. However, since FEM treats a stonewall as a continuum, it is difficult to represent local collapse behavior. Therefore, in this study, the distinct element method (DEM: analysis code UDEC) was used [2], which can analyze local deformation in discontinuous structures. The distinct element method usually models the analysis target as a set of rigid elements and traces the movement of individual blocks down to their very shape [3] [4] [5]. The UDEC used in this analysis can treat elements not only as rigid bodies

but also as deformable bodies, and nonlinear models such as elasticity and elasto-plasticity can be considered for the deformable bodies. Failure mode and crack propagation simulations can also be performed.

In a past report [6], we reproduced the collapse behavior of a stone base type wall under various conditions. However, the validity of the input physical property values has not been clarified. In this study, the angle of repose was measured and the relationship between the measurement results and the input physical property values was clarified. In addition to the stone base type, the collapse behavior of the half stone base type was reproduced, and the factors affecting the stability of the stonewall were examined.

## 2. OVERVIEW OF ANALYSIS MODEL

### 2.1 Selection of The Stonewall Model

According to past research [7] [8] [9], the stonewalls of Kumamoto Castle can be roughly divided into three types according to their internal composition. The stonewall model handled in this study was divided into three types based on the literature: the "stone base type" consisting of only stonewall blocks and cobblestones, the "half stone base type" consisting of stonewall blocks, cobblestones, and the embankment, and the "stone-less base type" consisting of only stonewall blocks and the embankment. In this study, we focused on the stone base type and the half stone base type that have cobblestone. Fig.1 shows the internal composition, shape characteristics, and constituent materials.

## 2.2 Conditions of The Analysis Model

Figure 2 shows the model outline and Table 1 shows the model conditions. Table 2 shows the seismic waveforms used in the analysis. In this study, the distinct element method (analysis code: UDEC), which is an analytical method for solving the motion of a discontinuity model, was used to model the individual movements of the stonewall blocks and cobblestones. Based on past studies, for the stone base type, comparisons are made by the magnitude of the shear resistance angle of the block surface and by the height of the stonewall. For the half stone base type, only the slope angle of the stonewall was changed to 60° and 80° without changing the conditions of the physical properties of each block, and the comparison was made. Next, to make a comparison by the width of the cobblestone zone, we compare the width of the cobblestone zone in the depth direction of 3m and 7m without changing the physical property values and stonewall slope angle of each block. Considering that the physical properties of the stonewall block and cobblestone surfaces contribute significantly to the generation of earth pressure, the shear resistance angle values of the stonewall block and cobblestone surfaces were set to the cases shown in Table 3.

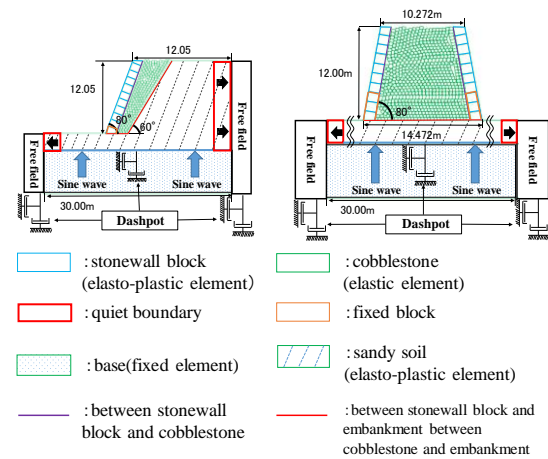


Fig. 2 Cross-section of the analysis model

Table 3 Conditions for shear resistance angle of surface

Stonewall block (°)	10	20	30	40
Cobblestone (°)	10	20	30	40

## 3. RESULTS OF DYNAMIC BEHAVIOR ANALYSIS

### 3.1 Measurement of Angle of Repose

The angle of repose was measured on the simulation to estimate the shear resistance angle as a block aggregate. According to the Geotechnical Engineering Dictionary, the angle of repose is the angle of the soil slope when uncohesive soil such as sand or gravel is dropped from a certain height and is stable without collapsing. Theoretically, the angle of repose should coincide with the shear resistance angle (internal friction angle) of loosely packed sand or gravel under low pressure. The shear resistance angles of the block surface were set to 10°, 20°, 30°, 40°, and 50° when the parameter "round" was set to 0.05, 0.10, and 0.15 on the UDEC to represent the roundness of the block, angle of repose were measured, respectively. The analytical model was made to drop a disturbed specimen from a height of 15 meters by applying gravitational acceleration. Figure 3 shows the results of the comparison of angle of repose and angle of shear resistance. From these results, it was found that the angle of shear resistance  $\phi_s$  on the block surface and the angle of repose  $\theta$  are generally related to  $\phi_s \pm 5 = \theta$ . Based on these results, the shear resistance angle of cobblestones behind the stonewall can be set as  $\theta \approx \phi_m$ .

Type name	Stone base type	Half stone base type
Style	 Stonewall block Cobblestone	 Stonewall block Cobblestone Embankment
State at the time of collapse		
Materials	Stonewall block, Cobblestone	Stonewall block, Cobblestone, Embankment
Characteristic	Height : low Slope : steep	Height : high Slope : gentle

Fig. 1 Characteristics of each stonewall type

Table 1 Physical properties of each block

Vertical rigidity(N/mm)	3000
Shear rigidity(N/mm)	3000

Table 2 Seismic waveforms used in the analysis

Waveform	Period	Amplitude	Excitation time
sine wave	10Hz	1.0m/s	2.0 sec

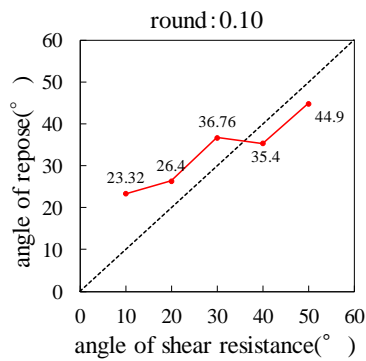


Fig. 3 Comparison results of angle of repose and angle of shear resistance

### 3.2 Creation of Analysis Model

Figure 4 shows how the models were created for the stone base type and half stone base type with a stonewall slope of  $70^\circ$ . Figure 3 shows the model after cutting the cobblestones. In the stone base type, two blocks were made inside the stonewall and one block was made at the top of the stonewall, and the blocks were cut into 40 cm squares. Blocks were made separately because it is more difficult to create gaps when blocks are dropped separately than when a single block is made and dropped. To approximate the actual construction procedure, cobblestones were made at a certain height, and then free-fallen to fill the inside of the stonewall. In a past study, free-fall alone caused gaps in the corners of the stonewall. Based on this reflection, this time gravity was applied to the left, right, and vertically downward while the stonewall blocks and base were fixed. In the half stone base type, a large block was created at the top of the stonewall and cut into 40 cm squares. After that, only the left portion of the cobblestone block was removed and allowed to fall freely in order to allow it to fall smoothly. Then, with the stonewall blocks and the base fixed, gravity was applied to the left and right and vertically downward. As a result of this procedure, it can be confirmed that the cobblestones are sufficiently packed, as shown in the Fig. 4.

### 3.3 Analysis Results and Consideration of Stone Bases Type

#### 3.3.1 Stonewall height

Based on past studies, analytical models were developed to compare different heights of stonewalls, with heights of 12 m and 6 m, a stonewall slope angle of  $70^\circ$ , and surface shear resistance angles of  $10^\circ$ ,  $30^\circ$ , and  $50^\circ$ . The deformation diagrams are shown in Fig.5. Even under the same conditions, there were differences in the collapse behavior as the height of the stonewall was lowered. The inclination of the slip surface differs depending on the height of the

stonewall. When the height of the stonewall is 12m, the overburden pressure is relatively large due to the high height of the stonewall. Therefore, the horizontal force acting due to the inertia force of earthquake motion is larger than the soil overburden pressure, and the slope of the slip surface is considered to be steeper. In the case of the 6 m high stonewall, the lower height of the stonewall causes the cobblestones to collapse in the form of horizontal lateral slip, resulting in a gentle slope of the slip surface.

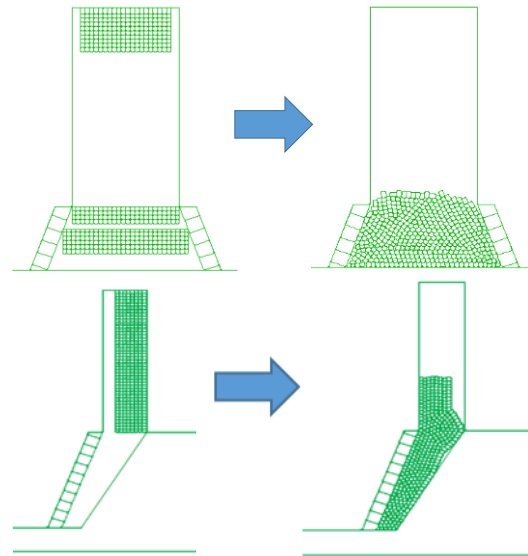


Fig. 4 Schematic diagram of the model construction of stone base type and half stone base type

	Height:12m	Height:6m
	Maximum displacement:5.348m	Maximum displacement:2.192m
$10^\circ$		
$30^\circ$	Maximum displacement:4.948m	Maximum displacement:1.908m
$50^\circ$	Maximum displacement:4.547m	Maximum displacement:0.2262m

Fig. 5 Displacement vectors for 12m and 6m height of stonewall



### 3.3.2 Surface shear resistance angles

In order to compare the shear resistance angle of the stonewall surface, an analytical model was created for a height of 12 m, a stonewall slope angle of  $70^\circ$ , and shear resistance angles of  $10^\circ$ ,  $30^\circ$ , and  $50^\circ$  on the surface of the stonewall. Figure 6 shows the analytical results. For the 12m height, collapse was observed for all shear resistance angles from  $10^\circ$  to  $50^\circ$ . As the angle of shear resistance increased, the maximum displacement decreased, indicating that the collapse was less likely to occur.

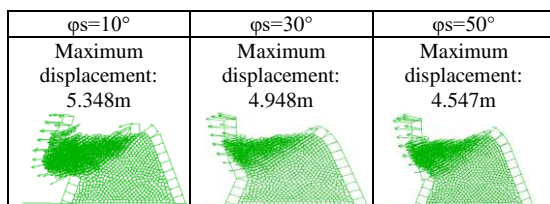


Fig. 6 Displacement vector for stonewall height of 12m and stonewall slope angle of  $70^\circ$

## 3.4 Analysis Results and Consideration of Half Stone Bases Type

### 3.4.1 Stonewall slope angle

Figure 7 shows the deformation when the shear resistance angle between the stonewall face and the cobblestone face is  $20^\circ$  for two cases of stonewall slope angle of  $60^\circ$  and  $80^\circ$ . Based on past studies and actual damage, the larger the stonewall slope angle, the more likely it was to collapse. However, in the present results, no collapse was observed in all cases where the shear resistance angle of the block surface was between  $10^\circ$  and  $40^\circ$ , indicating that the block was in a stable condition.

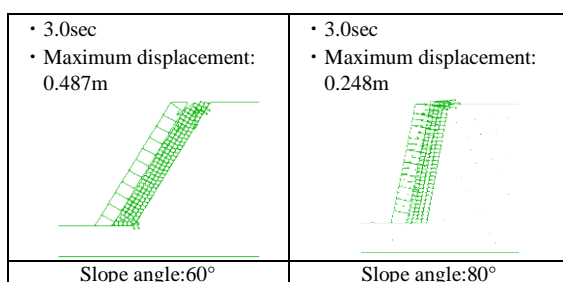


Fig. 7 Comparison of deformation caused by different stonewall slope angle

### 3.4.2 Width of cobblestone zone

Figure 8 shows a deformation diagram of a stonewall with a slope angle of  $80^\circ$  and cobblestone zone with width of 3 m and 7 m. The shear resistance angles of the stonewall and cobblestone surfaces are both  $20^\circ$ . From figure 8, the 3m-width cobblestone

did not collapse. However, the vector diagram shows that force was applied to the entire stonewall block, causing impregnation in the horizontal direction. Collapse was observed when the width of the cobblestone was 7 m. This may be due to the fact that the wider the cobblestone is, the greater the force that pushes out the stonewall block as a whole, causing it to collapse.

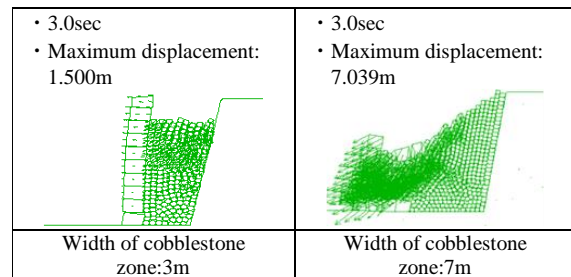


Fig. 8 Comparison of different width of cobblestone zone

### 3.4.3 Surface shear resistance angles

Figure 9 shows the deformation of a stonewall with a slope of  $80^\circ$ , cobblestone zone 3m width, and surface shear resistance angles of  $10^\circ$ ,  $20^\circ$ ,  $30^\circ$ , and  $40^\circ$ . When the surface shear resistance angle was  $10^\circ$ , the entire stonewall was deformed as if it was pushed out. When the surface shear resistance angle was  $20^\circ$ , the stone did not collapse, but the upper part of the stone was deformed as if pushed out. When the surface shear resistance angle was  $30^\circ$  and  $40^\circ$ , there was almost no deformation of the entire stonewall, and the stonewall was stable. Figure 10 shows the deformation of the stonewall with a slope of  $80^\circ$ , cobblestone zone 7m width, and surface shear resistance angles of  $10^\circ$  and  $40^\circ$ . The results show that both cases collapsed, but the higher the value of the shear resistance angle, the less likely it was to collapse. The difference in deformation is also apparent. The smaller the value of shear resistance angle on the surface, the more easily the cobblestones slide against each other and collapse occurs. The larger the value of the shear resistance angle, the greater the static frictional force of the stonewall blocks than the magnitude of the cobblestones' sliding down, resulting in a difference in collapse. The angle of repose changes with the value of the shear resistance angle on the block surface, and the range in which the cobblestones can stand on their own may also change. Figure 11 compares the horizontal displacement of the top of the stonewall under different conditions. The horizontal axis represents elapsed time, and the vertical axis represents horizontal displacement. The input seismic wave is indicated by a dotted line. The graph shows that when the shear resistance angles of the block surfaces are  $10^\circ$  and  $20^\circ$ , the displacement is greatly affected by the seismic

waves as time passes. However, when the shear resistance angles of the block surfaces are  $30^\circ$  and  $40^\circ$ , little change is observed.

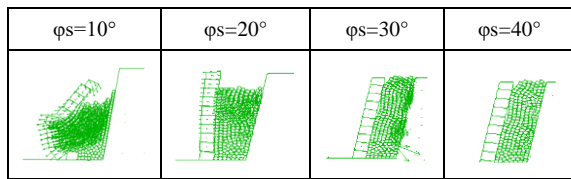


Fig. 9 Comparison of different surface shear resistance angles no.1

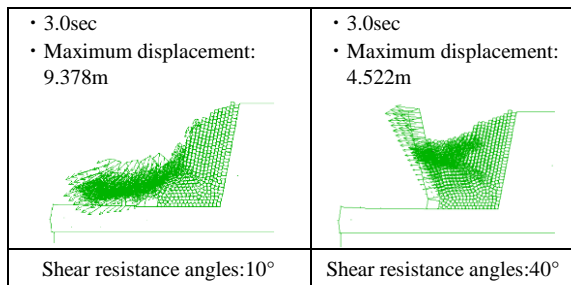


Fig. 10 Comparison of different surface shear resistance angles no.2

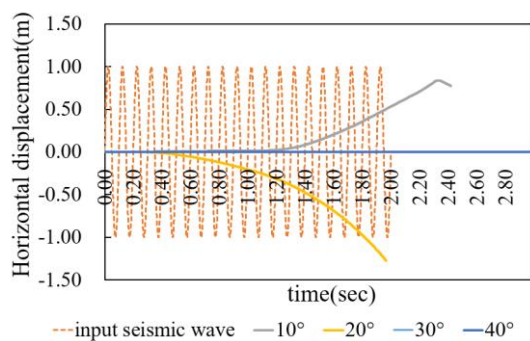


Fig. 11 Horizontal displacement of stonewall stone tops under various conditions

#### 3.4.4 Embankment slope angle

Figure 12 shows deformation diagrams for a stonewall slope angle of  $80^\circ$ , a surface shear resistance angle of  $30^\circ$ , and embankment slopes of

$60^\circ$  and  $80^\circ$ . Even with the same values of stonewall slope angle and surface shear resistance angle, collapse was observed when the slope angle of the embankment was  $60^\circ$  and no collapse was observed when the slope angle of the embankment was  $80^\circ$ . This may be due to the fact that the overburden pressure of the upper cobblestones is greater than the static friction force between the stonewall blocks.

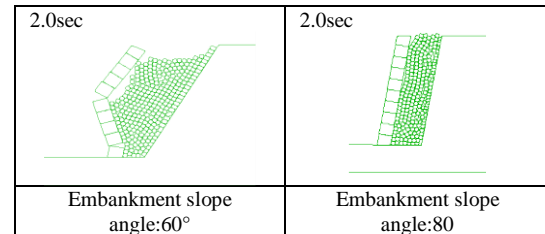


Fig. 12 Comparison of different embankment slope angle

#### 3.4.5 Comparison of all analysis results for the half stone base type

Figure 13 shows the analysis results of the half stone base type. In particular, the deformed stonewalls that did not collapse but were deformed are the types that are often found in actual damaged stonewalls. Therefore, it is necessary to elucidate the conditions for the occurrence of this type of deformation behavior through this analysis in the future.

## 4. CONCLUSION

In this study, we focused on a half stone base type stonewall, modeled its collapse, and compared various conditions. Although the slope of the stonewall was considered to be a factor in the collapse in past studies, no collapse was observed even if the slope was steep, depending on the width of the cobblestones. It was found that the wider the cobblestones zone, the more likely it was to collapse. The same model also showed a change in the collapse rate by changing the magnitude of the shear resistance

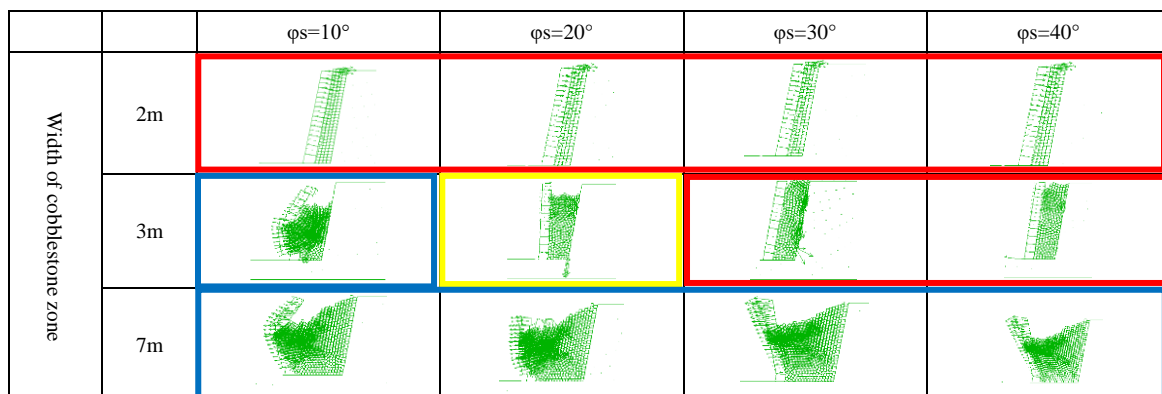


Fig. 13 Comparison of all analysis results for the half stone base type



angle. These results indicate that the dynamic behavior of the half stone base type and stone base type stone structures is characterized by their mechanical stability based on the relationship between the slope of the stonewall blocks, the wider of the cobblestone zone, and the roughness of the block surface.

## 5. ACKNOWLEDGMENTS

The authors gratefully appreciate a lot of support and understanding for this investigation from all officers of Kumamoto Castle Survey and Research Center after shortly after the 2016 Kumamoto earthquake. And our gratitude extends to all cooperators of this study with several information.

## 6. REFERENCES

- [1] Hashimoto T., Isobe Y., Matsuo T., Ishizukuri K.: 3D geological modeling and 2D seismic response analysis of Ishigaki in Kumamoto Castle, Department of Science and Engineering, National College of Science and Engineering Abstract No. 14, 2021, pp.113-119. (in Japanese)
- [2] Fujii I., Yang L., Jiang Y., Li S., Tanahashi T.: Evaluation of the dynamic behaviors of the bedrock containing discontinuities under important buildings based on numerical simulations, Proceeding of 2011 JSCE west conference (CD-ROM), 2011, pp.411-422(in Japanese)
- [3] Noma Y., Yamamoto H., Nishimura T., Kasa H., Nishigata T., Nishida K.: Study on seismic deformation prediction and dynamic stability evaluation of castle masonry wall, Civil Engineering Society Proceedings C (Geomatics), Vol. 64, No. 4, 2013, pp.444-456. (in Japanese)
- [4] Kasa H., Nishida K., Nishigata T., Morimoto H., Awatani Y., Yamamoto H.: A study on stability analysis of castle masonry walls by using the distinct element method, Civil History Research Papers, Vol.27, 2008, pp.45-51. (in Japanese)
- [5] Nishimura T., Noma Y., Kasa H., Yamamoto H., Nishigata T.: Examination of deformation behavior of shaking table test by stability analysis of castle wall using distinct element method, Proceedings of 66th JSCE Conference (CD-ROM), 2011, pp.325-326. (in Japanese)
- [6] Sugimoto S., Yamaguchi M., Yamanaka M.: Surface shape measurement and evaluation of mechanical stability by DEM simulation for damaged traditional stonewalls, International Journal of GEOMATE, Vol.20, Issue 80, 2021, pp.121-127.
- [7] Sugimoto S., Yamanaka M.: Reports of damaged earth structures in Kumamoto Castle, Proceedings of 54th Natural disaster and science symposium, 2017, pp.45-51. (in Japanese)
- [8] Katsuda Y., Jiang Y., Omine K., Sugimoto S.: Research of damaged stone structures in Kumamoto Castle by the 2016 Kumamoto Earthquake, Proceedings of 72th JSCE Conference (CD-ROM), 2017, pp.479-480. (in Japanese)
- [9] Katsuda Y., Sugimoto S., Yamanaka M.: Reports of a survey on damaged stonewalls in Kumamoto Castle by the 2016 Kumamoto Earthquake, Proceedings of the Japan National Conference on Geotechnical Engineering, 2018. (in Japanese)

# MPS-CAE SIMULATION FOR JET-GROUTING TECHNIQUE IN GROUND IMPROVEMENTS

Sudip Shakya<sup>1</sup> and Shinya Inazumi<sup>2</sup>

<sup>1</sup> Graduate School of Engineering and Science, Shibaura Institute of Technology, Japan;

<sup>2</sup> College of Engineering, Shibaura Institute of Technology, Japan

## ABSTRACT

This study focuses on the recreation of the jet grouting construction simulation by MPS-CAE method. Jet grouting method is one of the innovative ground improvement techniques in which the ground improvement procedure is conducted at grout injection. In this study, the simulation ground model is created by computer-aided engineering (CAE) system and the construction simulation is recreated by the MPS method. Since the actual construction procedure is surrounded by various uncertainties due to the lack of visibility in development progress; it is the objective of this study to solve those uncertainties involved in the construction. The ground model was designed while making comparison to the existing ground condition and development of soil-improvement body was visualized. After confirming the successful construction of the soil-improvement body, the construction simulation is verified by calculating the mud discharge quantity and its density. It is expected that the result obtained from this simulation can be used as guideline for the future jet grouting construction.

*Keywords: Cement slurry, Computer-aided engineering, Jet-grouting technique, Moving particle semi-implicit*

## INTRODUCTION

Technology for the columnar soil-improved body using high-pressure jets to spray cement slurry was first developed in 1970 in Japan as a single-pipe type of high-pressure jet grouting method [1],[2],[3]. Since then, this technology has been widely used for the improvement of social infrastructures, such as rivers, ports, roads, railways, and water and sewer systems [4],[5]. The single-pipe type of high-pressure jet grouting method [1],[2] is one of the ground-improvement methods for developing a columnar soil-improved body. In this method, the ground is cut with cement slurry sprayed at high pressure and, at the same time, the cut ground (soft soil) is mixed with the cement slurry. In recent years, by applying this technology and using silica sand or mechanical agitation and mixing in combination with jets that spray cement slurry, it is possible to develop a higher quality columnar soil-improved body even with relatively low-pressure jets of cement slurry. One of the problems generally encountered in ground-improvement methods is the sophistication of the design and performance evaluation methods of the ground-improvement method itself. Since this improved body construction mechanism is a complicated and "invisible" phenomenon as the development of it is conducted in an in-situ ground, it has been put into practical use by making speculations experimentally and empirically for constructions and finally checking the quality after construction. Thus, not only the inability of confirming the construction status visually but also

the difficulty in proving the validity of design. Only if the improved body formation phenomenon by high-pressure injection could be analytically verified based on the mechanical theory, it would contribute to the explanation of the construction mechanism, the optimization of the construction method, and the improvement of the visualization technology for the improved body construction.

This study focuses on the application of a computer-aided engineering (CAE) system that simulates the performance of the middle-pressure jet grouting method. Specifically, as one of the CAE systems, the moving particle semi-implicit (MPS)-CAE method [6],[7],[8], which can handle ground failure phenomena and high-velocity fluids, is used. Employing the MPS-CAE with the "Particleworks" software [6], an attempt is made to visualize and evaluate the development situation of the columnar soil-improved body by the middle-pressure jet grouting method.

## CAE WITH MPS METHOD

Computer-aided engineering (CAE) is a technology that simulates and analyzes prototypes on a computer created by CAD (computer-aided design) and so on, considering the site conditions [9]. In the field of geotechnical engineering, CAE can be used to visualize the inside of the ground and the stress acting on the inside of the ground, and to understand experiments that would require huge costs and/or phenomena that would be difficult to reproduce. In addition, by performing appropriate post-processing,

it is possible to communicate with other people in a visually easy-to-understand manner. In this study, the authors attempt to apply CAE using 3D-CAD and MPS, one of particle methods, as an elemental technology for the visualization of the inside of the ground during soil-improvement construction and the reproduction of a series of constructions. Specifically, based on the reproduction of the middle-pressure jet grouting method by MPS-CAE with the “Particleworks” software [6] the construction specifications can be examined according to the ground conditions.

In this study, the authors apply MPS method [6],[7],[8] to analyze the behaviour of fluid particles. The governing equations for the incompressible flow used in the analysis are the mass conservation law of Eq. (1) and the Navier’s stroke law of Eq. (2) considering surface tension.

$$\frac{D\rho}{Dt} = 0 \quad (1)$$

$$\frac{D\mathbf{u}}{Dt} = -\frac{1}{\rho}\nabla P + \vartheta\nabla^2\mathbf{u} + \mathbf{g} + \frac{1}{\rho}\sigma\mathbf{k}\delta\mathbf{n} \quad (2)$$

Where,  $\rho$  is the density of the fluid,  $\mathbf{u}$  is the velocity vector,  $P$  is the pressure,  $\vartheta$  is the kinematic viscosity coefficient,  $\mathbf{g}$  is the gravity vector,  $\sigma$  is the surface tension coefficient,  $\mathbf{k}$  is the curvature,  $\delta$  is the delta function for the surface tension to act on the surface, and  $\mathbf{n}$  is the unit vector in the direction perpendicular to the surface.

In the MPS method, each differential operator (slope, divergence, and Laplacian) of the governing equation, as shown in Eq. (2), is discretized by a weighting function [6],[7],[8]. The weighting function depends on the interparticle distance  $r$  and the influence radius ( $R$ : 2.1 to 4.1 times the interparticle distance) in each particle interaction model.

The weighting function ( $w$ ) is expressed by Eq. (3), and it is a function of the distance ( $r$ ) between particles and the influence radius ( $R$ ) of the support domain.

$$w(r) = \begin{cases} \frac{R}{r} - 1 & (0 < r \leq R) \\ 0 & (R \leq r) \end{cases} \quad (3)$$

The sum of the weight functions in the support domain is commonly known as the particle number density ( $n_i$ ) and it is defined as Eq. (4).

$$n_i = \sum_{j \neq i} w_{ij} \quad (4)$$

Where,  $w_{ij} = w(r_{ij}, R)$  is the weight function between particle ( $i$ ) and ( $j$ ). The particle number density when particles are located on a regular grid

whose grid size is the same with the diameter of the particles is called the criterion of particle number density ( $n^*$ ).

## OUTLINE OF MIDDLE-PRESSURE JET GROUTING METHOD

The middle-pressure jet grouting method, which is a cement slurry jet grouting method [4],[5] that uses middle-pressure jets of 20 MPa or less. The first one is a method using a single-tube type of rod equipped with a jet nozzle to loosen the ground by a horizontal water jet during the penetration of the rod. Next, the rod with the jet nozzle is pulled up and rotated, spraying the cement slurry at middle-pressure to develop a columnar soil-improved body with a maximum diameter of 1.0 m.

Meanwhile the latter one uses a special mixing blade attached with an escape prevention plate at the end to combine the soil and cement slurry sprayed at middle pressure mechanically. The middle-pressure jet grouting method is a ground-improvement method that allows the selection of both of the above-mentioned construction methods. Up to now, the full-length confirmation of the columnar soil-improved body sampled by boring after full-scale experiments and construction has been performed. Although the quality of the construction has been verified by unconfined compression test and so on, it has yet to be verified analytically. Therefore, in this study, the authors apply the MPS-CAE to the middle-pressure method and verify it analytically.

## METHODOLOGY

### Ground Modelling and Analysis Condition

Figure 1 shows the actual scale models for the jet grouting method. They were created as the analytical models by three-dimensional AutoCAD. In the jet grouting method, the jet material was sprayed in one horizontal direction from the jet nozzle in a cylindrical ground with a diameter of 2 m and a height of 1.5 m.

Table 1 shows the analysis condition for the jet grouting construction. The water will be sprayed for first 20 s while digging until it will reach the desired depth. Then, the injection fluid is switch to the cement grout and the jet grouting string is pulled upward while rotating. The total time of cement grout spraying is 58 s and the height retracted upward is 0.5 m only and not up to the surface level.

### Material Parameters

Table 2 shows the material parameters of the water, cement slurry, and ground particles that comprised the target materials of the analysis.

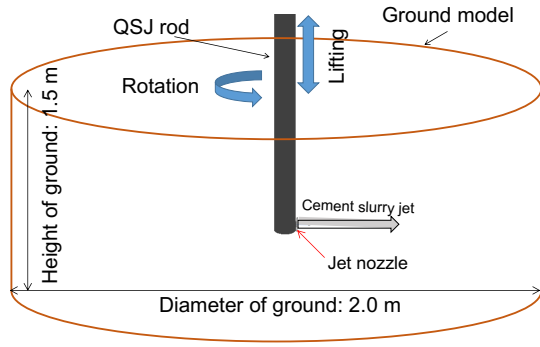


Fig. 1 Jet grouting method model

Table 1 Analysis condition

Dimension of the ground model	2m diameter	1.5m height
Material of jet	Water <sup>*1</sup>	Cement slurry <sup>*2</sup>
Time of spraying	20 s	58 s
Length of penetration while blanking (m)	0.5	0 <sup>*2</sup>
Length of penetration while improving soil (m)	0.5	0.5
Amount of jet (L/min)	80	90
Pressure of jet (MPa)	9.4	18.0
Velocity of jet (m/s)	137.5	155.0
Velocity of penetration while blanking (m/min)	3.0	-
Velocity of penetration while improving soil (m/min)	3.0	-
Velocity of lifting while improving soil (m/min)	-	0.52 <sup>*2</sup>
Velocity of rotation (rpm)	20 <sup>*1</sup>	20

<sup>\*1</sup> while penetrating <sup>\*2</sup> while pulling up

Table 2 Material parameter

Parameters	Water	Cement Slurry	Ground
Density (kg/m <sup>3</sup> )	1000	1500	1600
w/c	-	1	-
Yield value (Pa)	-	10	60000
Plastic viscosity (Pa·s)	-	0.28	17000
Yield parameter (-)	-	0.0001	0.0001
Surface tension (N/m)	0.1	0.1	0.002
Fluid model	Newton fluid	Bingham fluid	Bingham fluid

Water is the Newtonian fluid meanwhile cement slurry and ground are assumed to be Bingham fluid. The water particles used the general value of a Newtonian fluid, and the cement slurry particles used the value of a Bingham fluid with the plastic viscosity being measured by a B-type viscometer.

For cement slurry, other values can be measured by the standard test. Since the cement slurry is assumed to be the Bingham Fluid, it should possess certain value of yield point at which it finally starts to flow from the stationary state. But, since the water-cement ratio is taken as 1, the cement slurry will flow before applying any kind of additional stress. Meaning the yield point for the sample cement slurry is very low and equivalent to the zero.

For the ground particles, the material parameters were set using the value of a Bingham fluid by a

reproducible analysis of an unconfined compression test [10],[11]. Bingham fluid has a property whereby it begins to flow when the shear stress exceeds the yield stress. Therefore, until the shear stress exceeds the yield stress value, it is regarded as being in an immobile state, but if the strain ratio is 0, an analysis becomes impossible. In this study, as a coping method, a bi-viscosity model is adopted; it treats the fluid as a highly viscous fluid when it is less than the yield stress value. The constitutive equations when flowing and when immobile are expressed by Eqs. (5) and (6), respectively:

$$T_{ij} = -P\delta_{ij} + 2\left(\eta_p + \frac{\tau_y}{\sqrt{n}}\right)\dot{\epsilon}_{ij}^{vp} \quad \Pi > \Pi_c \quad (5)$$

$$T_{ij} = -P\delta_{ij} + 2\left(\eta_p + \frac{\tau_y}{\sqrt{n_c}}\right)\dot{\epsilon}_{ij}^v \quad \Pi < \Pi_c \quad (6)$$

where  $P$  is the pressure,  $\eta_p$  is the plastic viscosity,  $\tau_y$  is the yield value,  $\dot{\epsilon}_{ij}^{vp}$  is the strain ratio when flowing,  $\dot{\epsilon}_{ij}^v$  is the strain ratio when immobile, and  $\Pi_c$  is the yield reference value for the fluid state and the immobile state. It should be noted that  $\Pi_c$  is expressed by Eqs. (7) and (8), respectively, using the flow limit strain rate:

$$\Pi = 2\dot{\epsilon}_{ij}\dot{\epsilon}_{ij} \quad (7)$$

$$\Pi_c = (2\pi_c)^2 \quad (8)$$

where,  $\pi_c$  is the flow limit strain ratio.

### Setting Probe Region and Boundary

The probe boundaries are set at the top of the ground model to calculate the quantity of mud discharge during the simulation at the beginning and at the end from the top view and front view respectively. The total three different dimension probe boundary is placed at the top. The cylindrical disc of 1.8 m, 1.6 m and 1.4 m diameter and height 0.1 m and width 0.1 m each are set at the just above the top of ground model and the number of cement particles, water particles and soil particles collected at the end of the simulation is computed. The 1.8m, 1.6m and 1.4m diameter probe region is indicated by red, green and black color respectively.

## RESULTS AND DISCUSSION

### Validation of Analytical Ground Model

Figure 2 shows the result of stress-strain curve obtained by the simulation of the unconfined compression test for the material parameter from Table 2 and is compared with the two real unconfined compression test data. The result shows that the soil yielded at the compression strength of 61.24 kN/m<sup>2</sup> and 12.59 % strain value. The graph indicated by the

triangular plot point is the result of the unconfined compression test for the soil sample from Aomori prefecture, Tsugaru city. It is extracted from the depth of 7 to 7.85 m below the ground and is silty soil with the average soil diameter of 0.0036 mm which yielded at the 64.69 kN/m<sup>2</sup> and strain of 4.73 %. The graph plotted with the square plot point represents the result obtained for the unconfined compression test result of soil sample from Mikawa town, Yamagata prefecture. The core sample was taken from the depth of 4 to 4.7 m below the ground. The soil sample is sandy soil with the average soil diameter of 0.034 mm which yielded at 61.55 kN/m<sup>2</sup> and strain of 0.55 %.

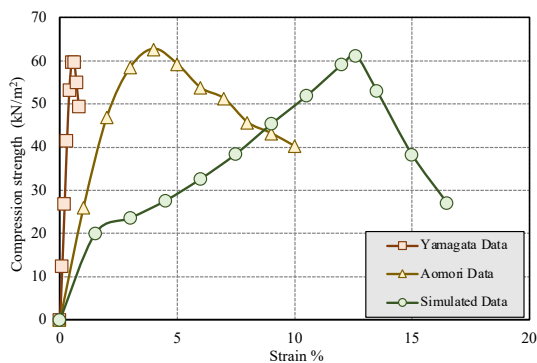


Fig. 2 Simulation result compared to known data

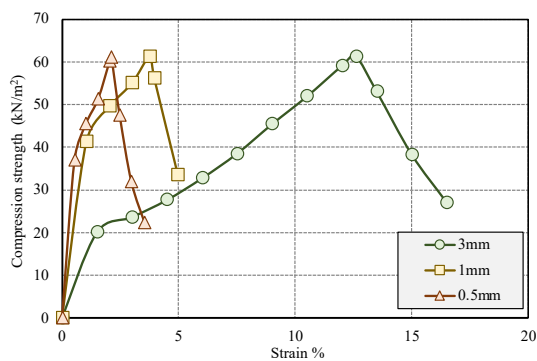


Fig. 3 Simulation result for different soil size

It is found that the densities of soil have no influence on the ground modelling but the size of soil considered during simulation does influence. Figure 3 shows the stress-strain relation generated for the two different soil size and compared to the model adopted in this study. For 0.5 mm soil sample, yield value of 61.07 kN/m<sup>2</sup> is obtained when input plasticity viscosity is 5500 Pa·s and it yield at 2.11 % strain value. For 1 mm soil sample, yield value of 61.03 kN/m<sup>2</sup> is obtained at 3.8 % strain value when input plasticity viscosity value is 9000 Pa·s. For 2 mm soil sample, the ground modelling parameter did not change much but the time of calculation is increased by 1.5 times that for 3 mm soil sample. Meanwhile for 1 mm and 0.5 mm, it was 2 and 42 times more respectively. Thus, if these models are adopted the simulation might have been failed due to high calculation load so despite being comparatively less accurate, this study is conducted for 3 mm soil particles.

### Reproduction of Development Situation of Columnar Soil-Improved Body

Figure 4 shows the development progress of the columnar soil-improved body. Ground particles are shown in transparent yellow color, water particles in light blue color and slurry particles in red color. About 2 s after the start of the construction water starts spraying and continues till it reaches the maximum depth of 1 m. The time required to reach this depth is set to be 20 s. Water particles are seen to be moving to the surface as mud discharge and some particles are even seen to scatter into the open space. When the jet grouting string reaches the desired maximum depth of 1m, then it starts rotating in counter-clockwise direction and the rod starts pulling upward while spraying cement grout. It can be seen that the water particles have scoured the ground model below the desired depth; although it is not the intention of forming soil-improvement body below the lowest tip of jet grouting string. The velocity of

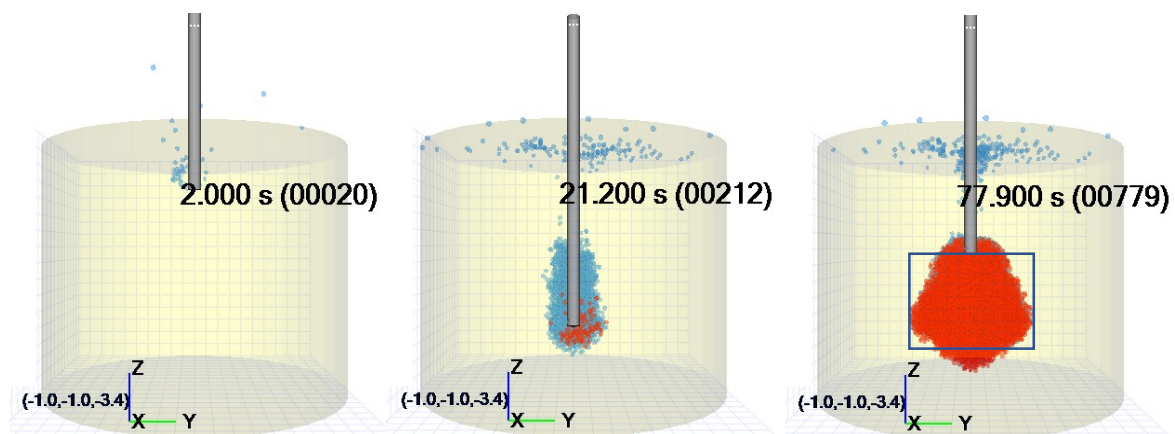


Fig. 4 Reproduction of the development condition of soil-improvement body

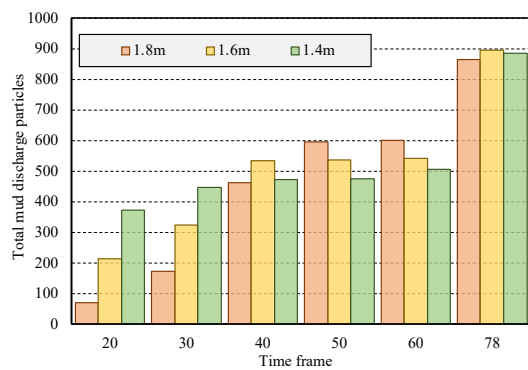


Fig. 5 Total mud discharge particles comparison

pulling the rod while spraying cement grout is much slower compared to the time during digging. At 78 s, the rod reaches the desired height of 0.5 m from the lowest point of digging and the construction procedure is completed. The cement grout is sprayed for the total height of 0.5 m only but it can be seen that the cement grout has spread beyond the sprayed area and is distributed unevenly throughout the target area and outside. Almost all of the water particles sprayed during digging at the beginning within the ground have been removed as mud discharge. The mud discharge is mostly water particles that had been replaced by the higher density cement grout particles.

The overall simulation can be said to be successful as it has been able to recreate the realistic phenomenon of mud discharge and formation of the soil improved body. In real case scenario, the status of the jet grouting construction is determined by the mud discharge phenomenon and by confirming the diameter of the soil improved body formed at the end. In this simulation, both phenomena can be confirmed at each stage without waiting for the completion of the construction. Mud discharge in real case scenario contains the soil particles and certain amount of cement grout carried to the surface by the upstream water particles; same is confirmed in the simulation too.

The ideal shape of the soil improved body is geometrically accurate cylindrical shape but it can be observed that the shape is cylindrical in nature with different diameter at each level. The target design shape is shown by the blue rectangular frame in Fig. 4. The maximum diameter is observed at the lowest drilled level and is measured to be 0.9 m in diameter. Then it starts decreasing gradually in both upward and downward direction. The diameter at the target top surface is measured to be 0.6 m. The total height of the soil improved body formation is 0.86m but the objective was to form only of 0.5 m height. The height of 0.1 m and average diameter of 0.5 m soil improvement body is formed above the target area meanwhile the height of 0.26 m and average diameter of 0.5 m soil improved body is formed below the target area. It is expected that more geometrically

accurate shaped soil improved body can be formed by making amendment in the construction specifications.

### Computation of the mud discharge quantity

Figure 5 shows the total mud discharge particles accumulating pattern at each time frame in different probe region. It is seen that the total number of particles keeping accumulating throughout the process and attains maximum value at the end of the process. However, it is expected that the largest probe region would automatically attains maximum number of the discharged mud particles at every time frame as the lower probe region already is within the boundary of it. There are cases where each probe region contains highest number of particles at certain time frame. The number is highest for the probe region of 1.8 m diameter at 50 s and 60 s, for the probe region of 1.6 m diameter at 40 s and 78 s and for the probe region of 1.4 m diameter at 20 s and 30 s.

The water was injected at 80 L/min for 20 s and cement grout at 90 L/min for 58 s so, total injected amount is about 0.113 m<sup>3</sup>. However, from the maximum number of particles at 78s if converted into volume results only to 0.000024 m<sup>3</sup> and as for the density it is equivalent to 1600kg/m<sup>3</sup> because 99% of the ejected mud is composed of ground particles. The main reason for the low mud discharge volume can be as follows:

- 1) The data suggests the number of particles present at the given instant rather than the total accumulated quantity.
- 2) Mud discharge particles are scattering throughout the whole process instead of remaining stationary and few found its way out of the boundary of probe region too.
- 3) Calculation of water particles are either not included or being overlapped with the soil particles.

In future, it is necessary to develop the efficient method of counting total mud discharge particles for more relatable comparison.

### CONCLUSIONS

This simulation has been successful to recreate the realistic jet grouting construction phenomenon and can be used as the guideline for future research but there are still certain limitations that this research paper failed to address properly. The major conclusions that can be drawn from this research is listed below.

- (1) Ground modelling for the 60 kPa soil is successful in this simulation as indicated by the validation test. Hence, unconfined compression test simulation can be used for checking the validity of the ground model and also changing the perspective; the reverse can be used to find the correct parameters of the ground.



- (2) Real case scenario like mud discharge phenomenon is recreated so the jet grouting construction simulation is also successful.
- (3) The ability of making visual assessment during and after the construction simulation makes it easier to make correct speculation about the probable events and action that might be undergoing or likely to take place. Thus, it will be helpful in formulating future guidelines and make correction to achieve the better result.

This simulation is carried out with making assumption and parameter setting such that the calculation load is low. This might have been the reason for occurring certain conflict during simulation such as difference in soil particles and water particles ejection as mud discharge in visual data and computational data. This simulation also tried to calculate the total amount of mud discharge occurring during the construction. However, it has failed to compute the accurate result. The immediate reason for it is the inability to predict the range of the probe region that need to be set and the unpredictable scattering trajectory of the ejected mud discharge particles. The degree of accuracy for the construction can be calculated by comparing the data from empirical rules and computational data. Since this simulation failed to compute the exact volume of mud discharge, this subject need to be studied further.

## REFERENCES

- [1] Modoni G., Croce P., and Mongiovì, L., Theoretical modelling of jet grouting. *Géotechnique*, Vol. 56, Issue 5, 2006, pp. 335-347.
- [2] Nakanishi W., and Nakazawa J., The process of development on jet grouting methods and their future. *Soil Mechanics and Foundation Engineering*, Vol. 54, 2006, pp. 10-12.
- [3] Shen S. L., Wang Z. F., Yang J., and Ho C. E., Generalized approach for prediction of jet grout column diameter. *Journal of Geotechnical Geoenvironment Engineering*, Vol. 139, Issue 12, 2013.
- [4] Harada K., Ohbayashi J., Matsumoto J., Kubo Y., and Akima T., New ground improvement technologies under restricted conditions in Japan. *Japanese Geotechnical Society Special Publication*, Vol. 2, Issue 32, 2016, pp. 1165-1170.
- [5] Pinto A., Tomásio R., and Marques G., Ground improvement with jet grouting solutions at the new cruise terminal in Lisbon, Portugal. *Procedia Engineering*, Vol. 143, 2016, pp. 1495-1502.
- [6] Hattori M., An attempt to apply mathematical foundation of Moving Particle Simulation to the MPS software "Particleworks". *Proc. Symp. Educ. Appl. Inf. Technol.* 2015, 9, 59-62.
- [7] Shakibaeini A., and Jin Y. C., MPS mesh-free particle method for multiphase flows. *Computer Methods in Applied Mechanics and Engineering*, Vol. 229-232, 2012, pp. 13-26.
- [8] Tanaka M., Cardoso R., and Bahai H., Multi-resolution MPS method. *Journal of Computational Physics*, Vol. 359, 2018, pp. 106-136.
- [9] Inazumi S., Kuwahara S., Jotisankasa A., and Chaiprakaikeow S., MPS-CAE simulation on dynamic interaction between steel casing and existing pile when pulling out existing piles, *International Journal of GEOMATE: Geotechnique. Construction Material and Environment*, Vol. 18, 2020, pp. 68-73.
- [10] Güllü H., A new prediction method to rheological behavior of grout with bottom ash for jet grouting columns. *Soils and Foundation*, Vol. 57, Issue 3, 2017, pp. 384-396.
- [11] Güllü H., Cevik A., Al-Ezzi K. M., and Gülsan M. E., On the rheology of using geopolymers for grouting: A comparative study with cement-based grout included fly ash and cold bonded fly ash. *Construction and Building Material*, Vol. 196, 2019, pp. 594-610.

## PROSPECTS AND MERITS OF USING CALCIUM PHOSPHATE COMPOUNDS FOR SOIL IMPROVEMENT: A REVIEW

Maksym Avramenko<sup>1</sup>, Kazunori Nakashima<sup>2</sup> and Satoru Kawasaki<sup>2</sup>

<sup>1</sup>Graduate School of Engineering, Hokkaido University, Sapporo, Japan

<sup>2</sup>Faculty of Engineering, Hokkaido University, Sapporo, Japan

### ABSTRACT

Many new soil reinforcement techniques have recently emerged, the most popular of which are microbial-induced carbonate precipitation (MICP) and enzyme-induced carbonate precipitation (EICP). They are environmentally friendly and more sustainable than conventional methods, but during carbonate (e.g., calcite) precipitation occurs ammonia ( $\text{NH}_3$ ) and ammonium ( $\text{NH}_4^+$ ) emissions into air and groundwater, which are hazardous. There are techniques for removing  $\text{NH}_4^+$  from the soil, but in the case of calcium phosphate compounds (CPCs) emissions of ammonium can be eliminated by over than 90%. Calcium phosphate precipitation occurs when urea and acid urease or acidic bacteria interact with a source of calcium and phosphorus. Precipitation takes place in between sand particles enhancing their contact and, therefore, strengthens the soil. Properties rely on type of CPCs, which is sensitive to the pH of the medium and the concentration of calcium and phosphorus. Given the relatively low strength of CPCs, this review paper aims to look at ways to increase their durability. In addition, it will also show differences in products when using different methods of obtaining CPCs. Ultimately, prospects for the use of CPCs for soil reinforcement will be provided.

*Keywords: Soil improvement, Calcium Phosphate Compounds (CPCs), Morphology, pH dependency, Ground improvement.*

### INTRODUCTION

Soil is a porous natural material that needs to be compacted or strengthened before it can be used for engineering purposes. It is a critical, non-renewable material for humanity's future existence. Therefore, it is vital to understand how to use it in environmental and sustainable conditions [1], [2]. There are many kinds of soils in nature. According to [3], soils for engineering applications can be divided into: Gravels, Sands, Silts and Clays and Highly Organic Soils. For each type of soil, there are appropriate techniques to strengthen it. In general, soil stabilization methods can be divided into (I) Chemical methods, (II) Biological methods and (III) Mechanical methods.

Chemical stabilization involves adding additives to the soil to obtain the desired physical and mechanical characteristics. Chemical methods of soil stabilization consist of on-site work and mixing the soil with cement, asphalt, silicates, bentonite, ash, polymers, fly ash, silica fume, blast furnace slag, gypsum, calcium-based chemicals and lime, acids, salts, petroleum emulsions, resins and lignosulfonates. Biological methods are a mixture of environmental practices and engineering techniques and include the use of bio-organisms and/or their byproducts as a structural component. Mechanical stabilization involves methods and techniques by which air voids can be removed from the ground with a nominal change in water content to strengthen it. Mechanical

methods are the oldest, most common techniques and include synthetic reinforcement application. Displacement and replacement, soil nailing, stage constructions, stone columns method and preloading, reinforcing bars, fibers, grids, strips are the most commonly used techniques [4] - [6].

Because of the rapid growth of Earth's population, there is a need to find alternative, environmentally friendly and harmless methods to strengthen the soil or improve existing ones. Sustainable engineering practices rank first worldwide in encouraging and incentivizing use. The construction industry alone accounts for 23% of the global carbon dioxide ( $\text{CO}_2$ ) emissions, with Portland cement production responsible for 6% of those emissions. This motivates for the need to discover new environmentally friendly methods and these techniques must be implemented in the field of engineering, including geotechnical engineering [7].

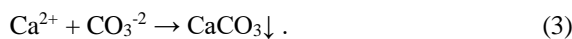
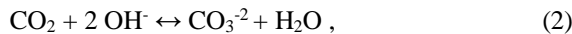
A relatively new method that is rapidly gaining popularity is biocementation. Biocementation is a geotechnical process that utilizes microorganisms to bind the soil particles, which significantly increases the strength of soil [8]. Mainly, this process used in two major biochemical methods: microbial-induced carbonate precipitation (MICP) and enzyme-induced carbonate precipitation (EICP).

MICP is a process where the bacterium produces a urease enzyme that reacts with urea ( $\text{CH}_4\text{N}_2\text{O}$ ), converting it into ammonium ( $\text{NH}_4^+$ ) and carbonate

ions ( $\text{CO}_3^{2-}$ ) Eqs. (1) - (2). This process raises the pH of the environment, resulting in higher emissions of ammonia ( $\text{NH}_3$ ) into the atmosphere and ammonium into the water. Calcium ions ( $\text{Ca}^{+2}$ ), in turn, react with  $\text{CO}_3^{2-}$  to produce calcium carbonate ( $\text{CaCO}_3$ ) at the nucleation sites provided by the bacteria cells Eq. (3). Precipitation of calcium carbonate can be achieved by urease produced bacteria (MICP) or by using a urease enzyme directly (EICP). With urease source being the different factor between the two methods, the reaction pathways are similar [6], [9].

Although MICP and EICP are significantly more environmentally friendly than conventional soil-reinforcement methods, they have their limitations.

(I) a byproduct produced during urea hydrolysis is ammonia (which release to atmosphere) and ammonium and hydroxide ions (which pollute ground water). This occurs according to the following equations Eqs. (1) - (3):



(II) relatively fragile bonding of soil particles

(III) the use of calcium reagents is less cost effective when compared to convention cement [8], [10].

## DRAWBACKS OF CONVENTIONAL METHODS OF BIOCEMENTATION

Ammonia ( $\text{NH}_3$ ) is a colorless gas with a density similar to air,  $0.73 \text{ kg/m}^3$ . During MICP/EICP, large amounts of  $\text{NH}_3$  and  $\text{NH}_4^+$  are released into atmosphere and water, respectively. In small quantities, these substances are not harmful to humans or animals, but large quantities of  $\text{NH}_3$  can cause severe illness and even death in animals [11]. This has resulted in the legislation in Japan where the maximum concentration of ammonium in industrial wastewater  $<100 \text{ g/L}$  [12]. This has led to only a handful of studies conducted in large-scale applications [13]. During conventional MICP/EICP, the pH of the medium increases to 8.8-9.0, resulting in the precipitation of calcium carbonate [14]. Figure 1 shows that up to pH 7.3, the formed nitrogen is in its  $\text{NH}_4^+$  form, and after 7.5 it is almost completely converted into gaseous form, releasing a large amount of gas into the atmosphere, which prevent these methods from being applied in the field. During urease hydrolysis, 1 mol of urea produces 1 mol of carbon dioxide ( $\text{CO}_2$ ) and 2 mol of ammonia ( $\text{NH}_3$ ). One part of  $\text{NH}_3$  turns into  $\text{NH}_4^+$  in the solution, the part goes into gaseous phase and pollutes the air, and the other part remains in the solution as  $\text{NH}_3 \cdot \text{H}_2\text{O}$ . Therefore, most of the  $\text{NH}_3$  gas produced during the biocementation process is uncontrollable and gets

released into the environment, resulting in pollution [11].

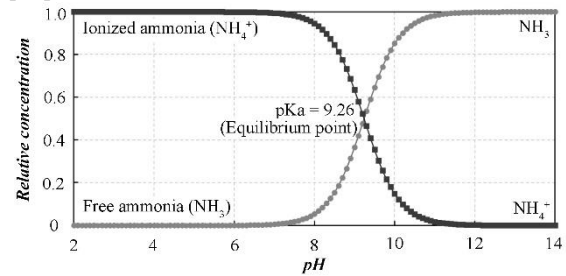


Fig. 1 Dependence of ammonium and ammonia relative concentration and pH (modified from [15]).

Scientists from all over the world are trying to solve the problem of  $\text{NH}_3$  gas and  $\text{NH}_4^+$  produced during the MICP/EICP process. If their formation is inevitable, it is necessary to control the course of the reactions. Among the effective techniques are rinsing technique (with  $\text{NH}_4^+$  removals exceeding 97.9%) [16], electro-biocementation [17], the addition of zeolite [18], absorbance of released  $\text{NH}_3$  by sulphuric acid [10], [19], precipitation  $\text{NH}_4^+$  as struvite [11], [20].

## CALCIUM PHOSPHATES COMPAUNDS

A potential, alternative method to reduce emissions of toxic  $\text{NH}_3$  gas to the environment is biogrouting. First type of biogrouting occurs due to CPCs precipitation using phosphate and calcium stock solutions [21]. Second – due to CPCs precipitation obtained via reaction between bacteria, urea and phosphate source [22], [23]. CPCs has an adequate physical strength (unconfined compressive strength (UCS)  $0.1\text{-}2.0 \text{ MPa}$ ) [21], [22], [24] - [31], and are promising geotechnical material.

Calcium phosphates are currently widely used for dental applications [1], [32], [33], bone tissue engineering [34], coating of implants, drug delivery and encapsulation [35], bioceramics [36] - [39] and strengthen the soil [21], [25] - [31], [40], [41]. The benefits of using this family of compounds for strengthening soils are the following:

- CPCs are environmentally friendly and non-toxic materials. The basic mineral HA [ $\text{Ca}_5(\text{PO}_4)_3\text{OH}$ ] with a Ca-to-P molar ratio of 1.55 is the most documented and investigated calcium phosphate and is the mineral that makes up bones and teeth [42].

- CPCs become stronger over time through a self-setting mechanism. Amorphous or gel-like calcium phosphate turns into a stable form, HA (Fig. 2).

- The solubility of CPCs depends directly on the pH of the medium, so by controlling the pH solution you can control the minerals that will form (Table 1, Fig. 3).

- CPCs are recyclable. CPCs, that remain in the soil after applying various precipitation techniques

can be removed and used as agricultural fertilizer [22], [21].

Along with its advantages, CPCs also have its disadvantages. They have low strength, and it is challenging to control the reaction and precipitation. Compared to UCS soil reinforced with CPC and MICP/EICP, the strength of the soil is several times lower (0.1-2.0 MPa and 0.31-14.0 MPa respectively) [6]. Because of the relatively low precipitation of CPCs ( $\sim 28 \text{ kg/m}^3$ ), more calcium-phosphate resources are required to achieve a measurable strength in soils ( $\sim 60 \text{ kg/m}^3$ ), resulting in a more expensive method [22].

Some researchers have used pure chemicals [21], [25] - [30]; and urease hydrolyses [12], [22], [24], [31], [40], [41] to improve soil with CPCs. The reaction of formation of CPCs during urease hydrolysis takes place at from weakly acidic to neutral pH, causing formation of almost all ammonium in ionic form, rather than in the most dangerous gaseous form. However, methods should be used to control and evacuate ammonium ions in the soil after treatment.

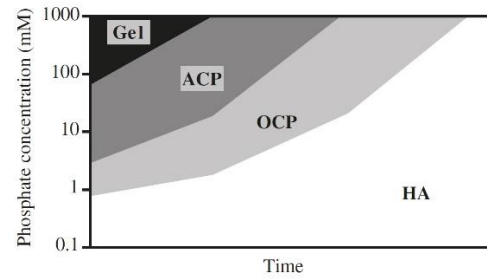


Fig. 2 The dependence of calcium phosphate presence [21].

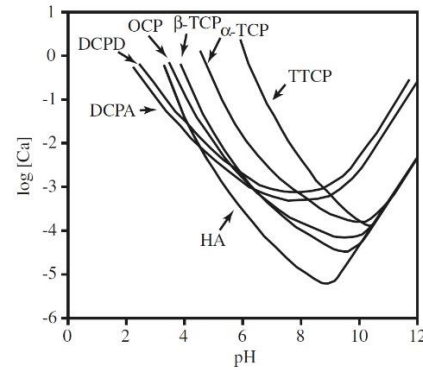


Fig. 3 Solubility of each calcium phosphate compound as a function of pH [21].

Table 1 List of calcium phosphate compounds [29].

Ca/P ratio	Compound	Abbreviation	Formula
0.5	Monocalcium phosphate monohydrate	MCPM (MCP)	$\text{Ca}(\text{H}_2\text{PO}_4)_2 \cdot \text{H}_2\text{O}$
0.5	Monocalcium phosphate anhydrate	MCPA (MCP)	$\text{Ca}(\text{H}_2\text{PO}_4)_2$
1.0	Dicalcium phosphate dihydrate	DCPD (DCP)	$\text{CaHPO}_4 \cdot 2\text{H}_2\text{O}$
1.0	Dicalcium phosphate anhydrate	DCPA (DCP)	$\text{CaHPO}_4$
1.33	Octacalcium phosphate	OCP	$\text{Ca}_8(\text{HPO}_4)_2(\text{PO}_4)_4 \cdot 5\text{H}_2\text{O}$
1.5	$\alpha$ -tricalcium phosphate	$\alpha$ -TCP	$\alpha\text{-Ca}_3(\text{PO}_4)_2$
1.5	$\beta$ -tricalcium phosphate	$\beta$ -TCP	$\beta\text{-Ca}_3(\text{PO}_4)_2$
1.2-2.2	Amorphous calcium phosphate	ACP	$\text{Ca}_x(\text{PO}_4)_y \cdot n\text{H}_2\text{O}$
1.5-1.67	Calcium-deficient hydroxyapatite	CDHA	$\text{Ca}_{10-x}(\text{HPO}_4)_x(\text{PO}_4)_{6-x}(\text{OH})_{2-x} \quad (0 < x < 1)$
1.67	Hydroxyapatite	HA	$\text{Ca}_{10}(\text{PO}_4)_6(\text{OH})_2$
2.0	Tetracalcium phosphate	TTCP	$\text{Ca}_4(\text{PO}_4)_2\text{O}$

## WAYS TO INCREASE STRENGTH OF CPCS

CPCs are weaker in strength than conventional methods for soil improving, which in turn limits their use for soil enhancement. Solving this problem will increase the capabilities and variability of CPCs implementation.

The following methods can be used to increase soil strength by applying CPCs:

- ammonia and ammonium can be turned into struvite, which not only solves the problem of contamination of the environment after the reaction of CPCs deposition, but also increases the strength of the soil [11], [43]. Using this practice together with the CPC solves two challenges at once: low strength of soil and ammonium pollution.

- the most common method of strengthening building materials is the use of reinforcement. There are a wide variety of investigated fibrous materials - fibers. Both synthetic, such as glass fiber, plastic fiber, metal fiber, and natural fiber, such as plant fiber, fiber from animal components and mineral fiber, are used [4]. In CPCs, ceramic nanofibers are widely used for reinforcement [44].

- adding some powders, such as tricalcium phosphate; magnesium phosphate; calcium carbonate and magnesium carbonate, and scallop shell powders [27], [28], [30].

- in the case of microbial/enzymatic CPC precipitation, pure chemical reagents can be used to improve the physical characteristics of the compounds. The other way to improve soil properties

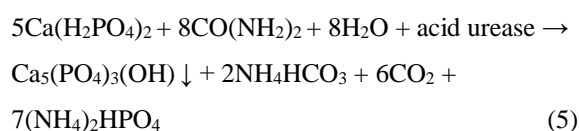
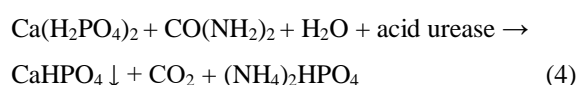
is to use bacteria with high urease activity or pure urease with calcium and phosphate chemicals. UCS of soil can be increased by modifying the way the chemicals are applied to the soil, such as injection frequency or volume.

### DIFFERENCES IN PRODUCTS WHEN USING DIFFERENT METHODOLOGY FOR OBTAINING CPCs

The formation of CPCs depends on various factors, such as the pH of the medium, time, and the Ca/P ratio in the system.

The reactions leading to the formation of CPCs are divided into 2 types, the acid-base reaction or the hydrolysis reaction. Only one CaP precursor compound is involved in the hydrolysis reaction, which interacts with the liquid phase and transforms into the hydrate phase. During the acid-base reaction, the acid base and other bases interact with several CaP precursor compounds, with the formation of the final end-product with neutral pH [34], [45].

CPCs can be formed due to acid tolerant urease-producing microorganisms by the following DCPA and HA precipitation reaction Eq. (4) and Eq. (5) respectively [8].



The application of bacteria can control the pH of the environment, which will control the products that will eventually be formed. CPCs can be divided into two groups: apatitic and brushite CPCs. The final product, apatitic and brushite, can be predicted depending on the solubility of CaP precursor and the pH of setting reaction. The final products of apatitic CPCs are either CDHA or HA. Apatitic CPCs can be formed either by acid-base interactions or by hydrolysis reactions. Brushite CPCs are acidic, and reactions can also occur at pH < 2.5. Thus, this type of CPC can only be formed due to the reactions of the acid base with DCPD as the final product. Apatitic CPCs are less soluble than brushite CPCs. Brushite has a short setting time, so it is more porous and non-strength. For this reason, most CPCs are apatite CPCs [34], [45].

### CONCLUSIONS

The application of CPCs for soil reinforcement is a novel, environmentally safe method in civil and

environmental engineering. These compounds will help to solve the issue of toxic emissions in a wide range of applications. Because of size of enzyme or chemicals, CPCs can be applied for compact soils with a small space between particles. Applying different fibers at different levels, from micro to nano levels, can significantly increase soil strength and facilitate the process of soil injection. By changing the ratio of chemicals or using natural sources of calcium or phosphorus, it is possible to make these methods more cost effective. Phosphorus is a limited resource that decreases every year [46], but using CPCs for soil strengthening, there is an opportunity to reuse phosphorus from soil. It is also possible to apply acid bacteria from food and by modifying the urease activity to improve results. Since these bacteria are harmless to humans, it greatly accelerates the waiting period before application to the open field.

The application of CPC for soil strengthening is a promising methodology that requires further research and improvement.

### REFERENCES

- [1] Zhao J., Liu Y., Sun W., Zhang H., Amorphous calcium phosphate and its application in dentistry, *Chemistry Central Journal*, Vol. 5, Issue 1, 2011, pp. 40-46.
- [2] Clunes J., Valle S., Dörner J., Martínez O., Pinochet D., Zúñiga F., Blum W. E. H., Soil fragility: A concept to ensure a sustainable use of soils, *Ecological Indicators*, Vol. 139, 2022, p. 108969.
- [3] Standard Practice for Classification of Soils of Engineering Purposes (Unified Soil Classification System).
- [4] Gowthaman S., Nakashima K., Kawasaki S., A State-of-the-Art Review on Soil Reinforcement Technology Using Natural Plant Fiber Materials: Past Findings, Present Trends and Future Directions, *Materials*, Vol. 11, Issue 4, 2018, p. 553.
- [5] Verma H., Ray A., Rai R., Gupta T., Mehta N., Ground improvement using chemical methods: A review, *Heliyon*, Vol. 7, Issue 7, 2021, p. e07678.
- [6] Almajed A., Lateef M. A., Moghal A. A. B., Lemboye K., State-of-the-Art Review of the Applicability and Challenges of Microbial-Induced Calcite Precipitation (MICP) and Enzyme-Induced Calcite Precipitation (EICP) Techniques for Geotechnical and Geoenvironmental Applications, *Crystals*, Vol. 11, Issue 4, 2021, p. 370.
- [7] Saif A., Cuccurullo A., Gallipoli D., Perlot C., Bruno A. W., *Advances in Enzyme*

- Induced Carbonate Precipitation and Application to Soil Improvement: A Review, Vol. 15, Issue 3, 2022, p. 950.
- [8] Ivanov V., Chu J., Stabnikov V., Chapter 2 Basics of Construction Microbial Biotechnology, Springer International Publishing, 2015, pp. 21-56.
- [9] Gowthaman S., Iki T., Nakashima K., Ebina K., Kawasaki S., Feasibility study for slope soil stabilization by microbial induced carbonate precipitation (MICP) using indigenous bacteria isolated from cold subarctic region, SN Applied Sciences, Vol. 1, Issue 11, pp. 1-16.
- [10] Ivanov V., Stabnikov V., Kawasaki S., Ecofriendly calcium phosphate and calcium bicarbonate biogrouts, Journal of Cleaner Production, Vol. 218, 2019, pp. 328-334.
- [11] Yu X., Chu J., Yang Y., Qian C., Reduction of ammonia production in the biocementation process for sand using a new biocement, Journal of Cleaner Production, Vol. 286, 2021, p. 124928.
- [12] Ministry of the Environment of Japan. National Effluent Standards.
- [13] Haouzi F. Z., Courcelles B., Major applications of MICP sand treatment at multi-scale levels: A review, Conference proceedings, in GeoEdmonton, 2018.
- [14] Dharmakeerthi R. S., Thenabadu M. W., Urease activity in soils: A Review, Journal of the National Science Foundation of Sri Lanka, Vol. 24, Issue 3, 2013, pp. 159-195.
- [15] Whiffin V. S., Microbial  $\text{CaCO}_3$  Precipitation for the Production of Biocement. PhD Dissertation, West. Aust. Murdoch Univ. Perth., 2004.
- [16] Lee M., Gomez M. G., San Pablo A., Kolbus C. M., Graddy C. M., DeJong J. T., Nelson D. C., Investigating Ammonium By-product Removal for Ureolytic Bio-cementation Using Meter-scale Experiments, Scientific Reports, Vol. 9, Issue 1, 2019, pp. 1-15.
- [17] Keykha H. A., Asadi A., Solar Powered Electro-Bio-Stabilization of Soil with Ammonium Pollution Prevention System, Advances in Civil Engineering Materials, Vol. 6, Issue 1, 2017, pp. 360-371.
- [18] Keykha H. A., Mohamadzadeh H., Asadi A., Kawasaki S., Ammonium-Free Carbonate-Producing Bacteria as an Ecofriendly Soil Biostabilizer, Geotechnical Testing Journal, Vol. 42, Issue 1, 2018.
- [19] Stabnikov V., Ivanov V., Chu J., Construction Biotechnology: a new area of biotechnological research and applications, World Journal of Microbiology and Biotechnology, Vol. 31, Issue 9, 2015, pp. 1303-1314.
- [20] Mohsenzadeh A., Aflaki E., Gowthaman S., Nakashima K., Kawasaki S., Ebadi T., A two-stage treatment process for the management of produced ammonium by-products in ureolytic bio-cementation process, International Journal of Environmental Science and Technology, Vol. 19, Issue 1, 2022, pp. 449-462.
- [21] Akiyama M., Kawasaki S., Novel grout material comprised of calcium phosphate compounds: In vitro evaluation of crystal precipitation and strength reinforcement, Engineering Geology, Vol. 125, 2012, pp. 119-128.
- [22] Gowthaman S., Yamamoto M., Nakashima K., Ivanov V., Kawasaki S., Calcium phosphate biocement using bone meal and acid urease: An eco-friendly approach for soil improvement, Journal of Cleaner Production, Vol. 319, 2021, p. 128782.
- [23] Yu X., Jiang J., Mineralization and cementing properties of bio-carbonate cement, bio-phosphate cement, and bio-carbonate/phosphate cement: a review, Environmental Science and Pollution Research, Vol. 25, Issue 22, 2018, pp. 21483-21497.
- [24] Yamamoto M., Precipitation of calcium phosphate compounds using urease and bone meal for soil improvement, Graduation Thesis, Department of Environmental and Social Engineering, Faculty of Engineering, Hokkaido University. 2021, pp. 1-80 (in Japanese with English abstract).
- [25] Akiyama M., Kawasaki S., New grouting materials using calcium phosphate compounds, Conference proceedings, in 12th ISRM Congress. OnePetro, 2011.
- [26] Akiyama M., Kawasaki S., Improvement in the unconfined compressive strength of sand test pieces cemented with calcium phosphate compound by addition of calcium carbonate, Ecological Engineering, Vol. 47, 2012, pp. 264-267.
- [27] Kawasaki S., Akiyama M., Effect of Addition of Phosphate Powder on Unconfined Compressive Strength of Sand Cemented with Calcium Phosphate Compound, Materials Transactions, 2013, pp. M-M2013827.
- [28] Kawasaki S., Akiyama M., Enhancement of unconfined compressive strength of sand test pieces cemented with calcium phosphate compound by addition of various powders, Soils and Foundations, Vol. 53, Issue 6, 2013, pp. 966-976.
- [29] Kawasaki S., Akiyama M., Unique Grout Material Composed of Calcium Phosphate Compounds, International Journal of



- GEOMATE, Vol. 4, Issue 7, 2013, pp. 429-435.
- [30] GGNN. A., Koreeda T., Kawasaki S., Improvement in the Unconfined Compressive Strength of Sand Test Pieces Cemented with Calcium Phosphate Compound by Addition of Calcium Carbonate Powders, *Materials Transactions*, Vol. 55, Issue 9, 2014, pp. 1391-1399.
- [31] Kumamoto Y., Precipitation of calcium phosphate compounds using acid urease and bone meal, Graduation Thesis, Department of Environmental and Social Engineering, Faculty of Engineering, Hokkaido University. 2022, pp. 1-51 (in Japanese with English abstract).
- [32] Al-Sanabani J. S., Madfa A. A., Al-Sanabani F. A., Application of Calcium Phosphate Materials in Dentistry, *International Journal of Biomaterials*, Vol. 2013, 2013.
- [33] LeGeros R. Z., Calcium Phosphate Materials in Restorative Dentistry: a Review, *Advances in Dental Research*, Vol. 2, Issue 1, 1988, pp.164-180.
- [34] Graça M. P. F., Gavinho S. R., Chapter Calcium Phosphate Cements in Tissue Engineering, *Contemporary Topics about Phosphorus in Biology and Materials*, 2020.
- [35] Salama A., Recent progress in preparation and applications of chitosan/calcium phosphate composite materials, *International Journal of Biological Macromolecules*, Vol. 178, 2021, pp. 240-252.
- [36] Balázs C., Wéber F., Kövér Z., Horváth E., Németh C., Preparation of calcium-phosphate bioceramics from natural resources, *Journal of the European Ceramic Society*, Vol. 27, Issues 2–3, 2007, pp. 1601-1606.
- [37] Pietak A. M., Reid J. W., Stott M. J., Sayer M., Silicon substitution in the calcium phosphate bioceramics, *Biomaterials*, Vol. 28, Issue 28, 2007, pp. 4023-4032.
- [38] Xin R., Leng Y., Chen J., Zhang Q., A comparative study of calcium phosphate formation on bioceramics in vitro and in vivo, *Biomaterials*, Vol. 26, Issue 33, 2005, pp. 6477-6486.
- [39] LeGeros R. Z., Biodegradation and bioresorption of calcium phosphate ceramics, *Clinical Materials*, Vol. 14, Issue 1, 1993, pp. 65-88.
- [40] Roeselers G., Van Loosdrecht M. C. M., Microbial Phytase-Induced Calcium-phosphate Precipitation - a Potential Soil Stabilization Method, *Folia microbiologica*, Vol. 55, Issue 6, 2010, pp 621-624.
- [41] Dilrukshi R. A. N., Watanabe J., Kawasaki S., Strengthening of Sand Cemented With Calcium Phosphate Compounds Using Plant-Derived Urease, *International Journal of GEOMATE*, Vol. 11, Issue 25, 2016, pp 2461-2467.
- [42] Al-Sanabani J. S., Madfa A. A., Al-Sanabani F. A., Application of Calcium Phosphate Materials in Dentistry, *International Journal of Biomaterials*, Vol. 2013, 2013.
- [43] Yu X., Yang H., Wang H., A cleaner biocementation method of soil via microbially induced struvite precipitation: A experimental and numerical analysis, *Journal of Environmental Management*, Vol. 316, 2022, p. 115280.
- [44] Sun L., Guo D., Study on the improvement of compressive strength and fracture toughness of calcium phosphate cement, *Ceramics International*, Vol. 48, Issue 13, 2022, pp. 18579-18587.
- [45] Lodoso-Torrecilla I., van den Beucken J. J., Jansen J. A., Calcium Phosphate Cements: Optimization toward Biodegradability, *Acta biomaterialia*, Vol. 119, 2021, pp. 1-12.
- [46] Sattari S. Z., Bouwman A. E., Giller K. E., van Ittersum M. K., Residual soil phosphorus as the missing piece in the global phosphorus crisis puzzle, *Proceedings of the National Academy of Sciences*, Vol. 109, Issue 16, 2012, pp. 6348-6353.

# ESTIMATION OF SUBSURFACE STRUCTURE OF LANDSLIDE AREA BASED ON MICROTREMOR AND SEISMIC OBSERVATION IN THE SAJI AREA, TOTTORI, JAPAN

Tatsuya Noguchi<sup>1</sup>, Isamu Nishimura<sup>1</sup> and Takao Kagawa<sup>1</sup>

<sup>1</sup>Faculty of Engineering, Tottori University, Japan

## ABSTRACT

It is important to investigate the subsurface structure to consider seismic strong ground motions in landslide areas. In this study, microtremor and seismic observations were conducted in the Saji area, Tottori City, Japan, based on the landslide topographic distribution map. The seismic ground motion characteristics were determined, and the ground structure was estimated from the analysis of the observation data. H/V and its predominant period were obtained from three-component single-point microtremor observations. The predominant period was in the range of 0.1 - 0.4 seconds, indicating that areas with similar periods were concentrated and distributed regardless of topographic cliffs or moving mass. S-wave velocity structure of the sedimentary layer of the moving mass was obtained from the array observation of microtremors. The S-wave velocity of the sedimentary layer of the mobile mass was found to be between 150m/s - 400m/s, with a maximum layer thickness of about 30m. The shape of the H/V and its predominant period corresponds to the thickness of the sedimentary layer of the moving mass of the landslide. The H/V of seismic records were obtained from seismic observation, and their characteristics suggested the influence of the deep structure below the moving mass.

**Keywords:** *Landslide area, Subsurface structure, Microtremor observation, Seismic observation*

## INTRODUCTION

In areas where rocks have become brittle due to volcanic deposition and weathering, repeated landslides may have occurred in the past due to earthquakes and heavy rainfall. The 2009 Sumatra earthquake caused a large seismic landslide [1], and microtremor surveys of the area [2] suggest that the

strong ground motion characteristics and subsurface structure of the target area were related to the occurrence of the landslide. In such a landslide area, it is very important to understand the strong ground motion characteristics and subsurface structure to consider the risk of slope disasters caused by earthquakes. In this study, microtremor and seismic observations were conducted in the Saji area, Tottori

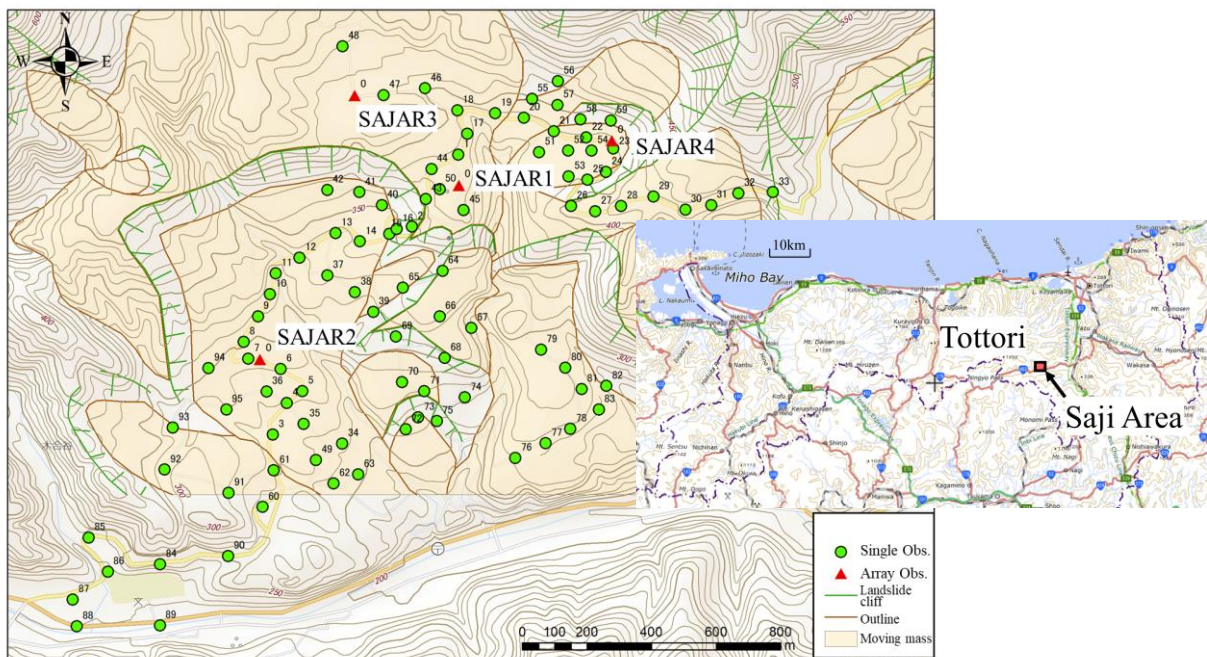


Fig. 1 Location of the observation area (upper map) and microtremor observation point (lower map)

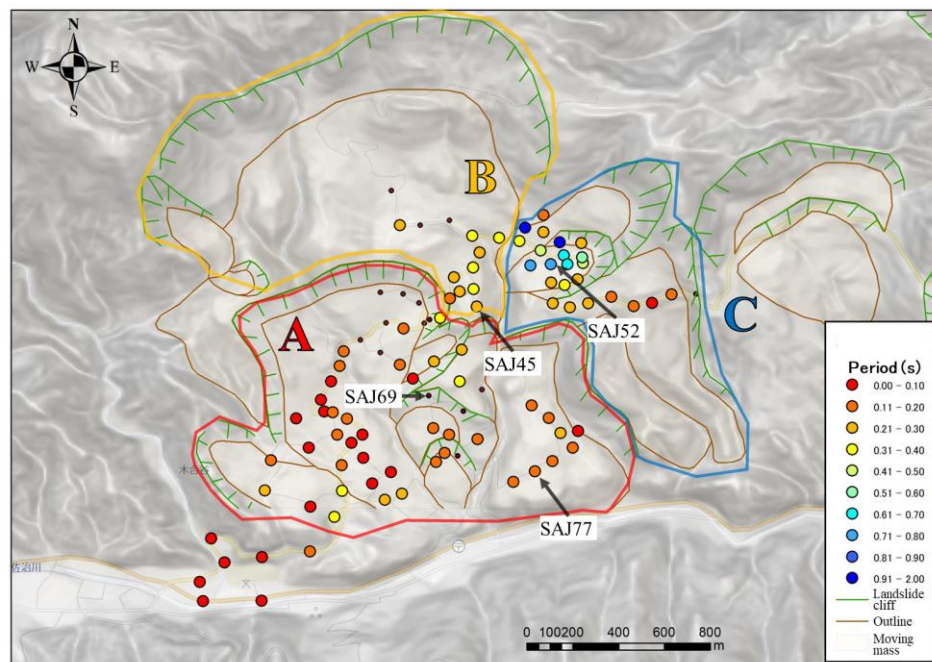


Fig. 2 Distribution map of predominant period

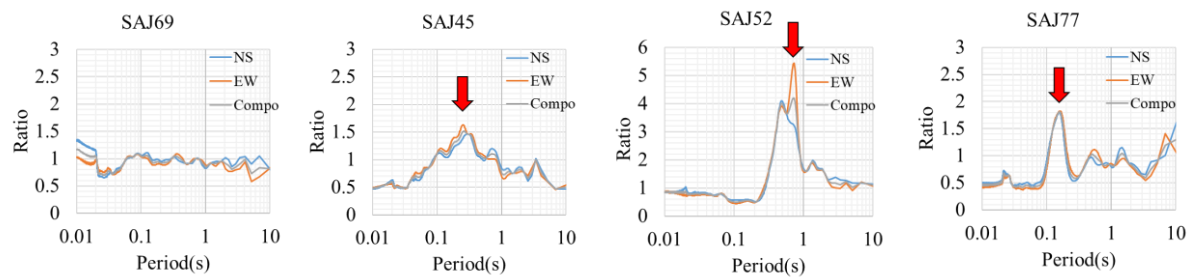


Fig. 3 H/V of microtremors

City, Tottori Prefecture, Japan, based on the landslide topographic distribution map [3], [4] to determine strong ground motion characteristics and estimation of subsurface structure.

## OBSERVATION

### Microtremor observations

As microtremor observations, three-component single-point observations were conducted to determine the predominant period and amplification characteristics of the subsurface structure, and array observations were conducted to estimate the S-wave velocity structure. Three-component single-point observations were made at 95 points on the road at 100 m intervals. Array observations were conducted at four points (SAJAR 1, SAJAR 2, SAJAR 3, and SAJAR 4). Array observation points were selected based on the assumption that the subsurface structure differs according to the distribution of the predominant period based on three-component

single-point observations. SAJAR1 was conducted on the site of the institution where the seismic stations are located, as described below. Fig. 1 shows the locations of the observation points.

A three-component acceleration seismograph, JU410, was used as the observation equipment. The array consisted of one at the center of the circle and three at equal intervals along the circumference of the circle. The distance between the center point and the seismometers on the circumference ranged from 1 to 15 meters. Because the power of the microtremors was expected to be low, three to four adults jumped at a position about 5 m from the outer seismograph to artificially induce vibrations, and their waveforms were also observed.

### Seismic observation

As for seismic observation, a seismograph has been installed on the foundation in the Saji Astro Park in Tottori City (same location as SAJAR1) since July 1, 2021 (observation is ongoing). The instruments used were a three-component integrated velocity

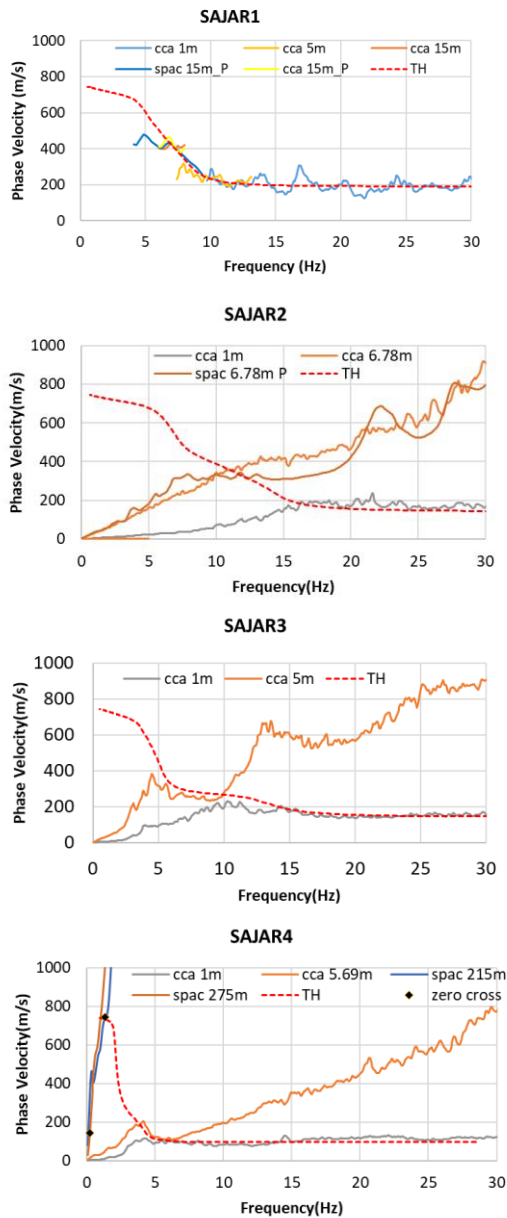


Fig. 4 phase velocity dispersion curve

seismometer CV-374V, a three-component velocity seismometer KVS-300, and a data logger HKS-9700. The specifications of the observations were as follows: sampling frequency of 100 Hz, time calibration using a GPS clock, and continuous observation.

## ANALYSIS

### Microtremor observation data

For the three-component single-point observation data, at least 10 stable 20.48 s intervals were selected visually, excluding non-stationary portions, and the Fourier spectrum of each component was obtained by FFT, and the average spectrum was obtained. A log

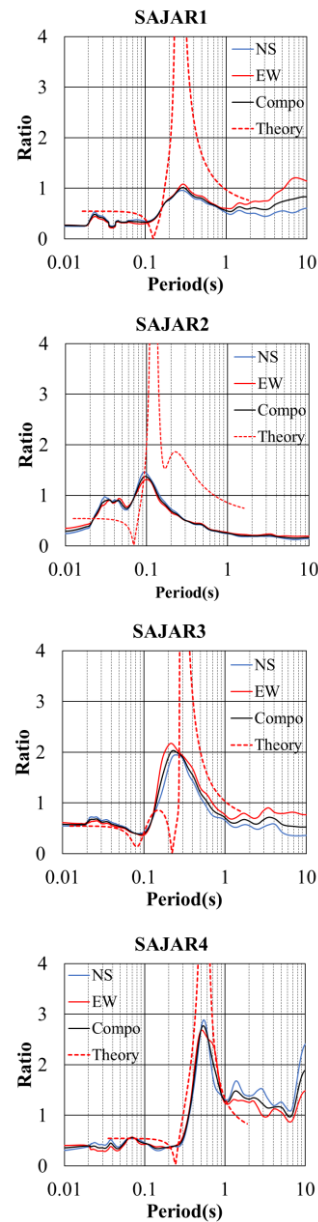


Fig. 5 H/V at the center of the array

window [5] with a coefficient of 20 was used to smooth the spectra. The ratio of the spectra of the horizontal and vertical components (H/V) was obtained from the obtained Fourier spectra of the three components. The predominant period was read from the H/V obtained at each location. The distribution of the predominant period is shown in Fig. 2 and some examples of H/V are shown in Fig. 3.

For the simultaneous data of array observations of microtremors, the phase velocity was estimated based on the CCA method [6] and SPAC method [7] using the microtremor analysis package tool BIDO2.0 [8]. More than 10 segments were automatically selected from the RMS values of the observation recordings with a segment length of 10.24 s. The power spectra of these segments were smoothed by Parzen window



Table 1 Subsurface structural models (microtremor)

Thickness (m)	$\rho$ (g/cm <sup>3</sup> )	Vp (m/s)	Vs (m/s)
11	1.8	1510	200
25	1.9	1790	450
$\infty$	2.2	2180	800

Thickness (m)	$\rho$ (g/cm <sup>3</sup> )	Vp (m/s)	Vs (m/s)
5	1.8	1460	150
25	1.9	1790	450
$\infty$	2.2	2180	800

Thickness (m)	$\rho$ (g/cm <sup>3</sup> )	Vp (m/s)	Vs (m/s)
5	1.8	1460	150
24	1.9	1620	300
$\infty$	2.2	2070	700

Thickness (m)	$\rho$ (g/cm <sup>3</sup> )	Vp (m/s)	Vs (m/s)
12	1.8	1400	100
25	1.9	1790	450
$\infty$	2.2	2180	800

with a bandwidth of 0.3 Hz, and then averaged. Phase velocity dispersion curves were obtained using these spectra. Using the phase velocity dispersion curve and the H/V of the array center, we estimated the subsurface structure by forward analysis based on the borehole data. Density was obtained from previous studies [9], and P-wave velocity was obtained using the S-wave velocity conversion formula [10]. At each array observation point, the phase velocity dispersion curve in Fig. 4 and the H/V obtained at the center of the array is shown in Fig. 5. In Fig. 4 and Fig. 5, the observed values (solid lines) and the theoretical values of Rayleigh wave fundamental modes obtained from the estimated model (dotted lines) are overlaid. The colors of the solid lines in Fig. 4 indicate blue: NS/UD, orange: EW/UD, and black: horizontal composite/UD. The solid colors in Fig. 5 show the dispersion curves obtained for each radius. The obtained parameters of the subsurface structure model by this analysis are shown in Table 1.

### Seismic observation data

Seismic observation data were analyzed for 21 earthquakes of intensity 2 or greater that occurred within 200 km of the seismic stations between August 11 and December 11, 2021. For data processing, 10.24 seconds of the S-wave portion of each

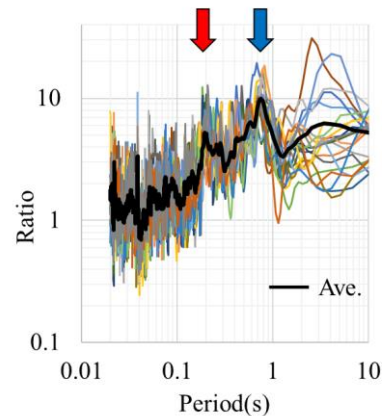


Fig.6 H/V of the earthquakes

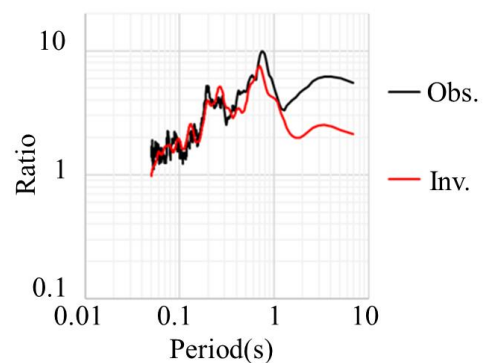


Fig.7 Comparison of H/V observed (black) and theoretical values of inversion (red).

component was selected from the seismic record, and a cosine taper with a half-period time rising by 0.5 s was applied to the outside of both ends, and then zero data was added to obtain a time of 20.48 s. From this data, the Fourier spectrum was calculated by using FFT and smoothing these by the Parzen window with a bandwidth of 0.2 Hz, and H/V was obtained. H/V of the earthquakes is shown in Fig. 6. From the mean H/V of all earthquakes, a subsurface structural model was determined by inverse analysis using the diffusion wavefield theory [11] and the hybrid heuristic method [12]. Microtremor array observations were made for the shallow layers smaller than  $V_s = 800$  m/s, and the initial model for the deeper layers above  $V_s = 800$  m/s was based on the previous subsurface structure model [9]. The inverse analysis was searched for S-wave velocity:  $V_s$ , P-wave velocity:  $V_p$ , layer thickness, and damping constant:  $h$ . In the uppermost and lowermost layers, the initial model values were fixed for modeling. Fig. 7 is the graph of H/V overlaid with observed and theoretical values from inversion. The obtained parameters of the subsurface structure model by this analysis are shown in Table 2.

The frequency characteristics H/V of the earthquake (Fig.6, Fig7) show peaks around 0.2 s (blue arrows) and 0.8 s (red arrows). The peak around 0.2 s is also seen in the H/V of the microtremor

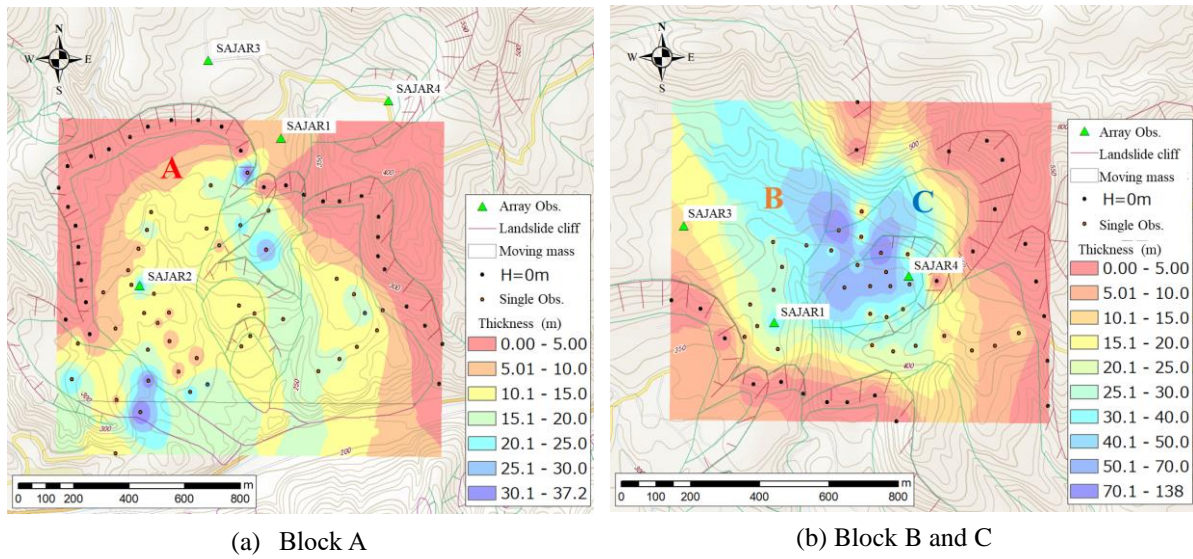


Fig.8 Distribution of thickness of sediment layer

(SAJAR1 in Fig. 4); the peak around 0.8 s is not seen in the H/V of the microtremor and appears to be influenced by the deeper ground beneath the sedimentary layer of the moving mass.

## PREDOMINANT PERIOD AND SUBSURFACE STRUCTURE

### Results from microtremor data analysis

The distribution of the predominant period of microtremors (Fig. 2) is not so much related to the topographic areas of sliding cliffs and cliff cone deposits (moving masses). For each block, Block A has a short period of less than 0.3 s, Block B has a slightly longer period of 0.2-0.4 s, and Block C has a long period of 0.4 s or longer. The distribution of the time periods in Blocks A and B did not change much, while those in Block C varied greatly.

According to the subsurface structure model in Table 1, the S-wave velocity of the sedimentary layer of the moving mass is small (150m/s~400m/s), and the layer thickness is about 30m for SAJAR1 and SAJAR3, and about 4m for SAJAR2. These results suggest that the predominant period corresponds to the thickness of the sedimentary layer of the moving mass with respect to the subsurface structure.

To investigate the areal thickness distribution of the moving mass, layer thickness:  $H$  was determined based on the 1/4 wavelength law using the predominant period of H/V:  $T$  and the average S-wave velocity:  $V$  up to the second layer of the subsurface structure model at the array points in the block. The equation is as follows.

$$H = T \cdot V / 4 \quad (1)$$

Table 2 Subsurface structural models (earthquake)

SAJAR1 (Seismic Analysis Model)				
Thickness (m)	$\rho$ (g/cm <sup>3</sup> )	Vp (m/s)	Vs (m/s)	h
11.0	1.70	1524	200	0.038
26.8	1.94	2015	655	0.090
36.4	1.94	2404	659	0.038
60.6	2.02	2644	854	0.038
1640.3	2.40	4716	2241	0.030
$\infty$	2.56	5500	3000	0.010

The average S-wave velocities are 400 m/s for block A, 370 m/s for block B, and 350 m/s for block C. Fig. 8 shows the layer thickness distribution. The layer thicknesses of the surrounding cliffs in these distribution maps are spatially complemented by assuming that the thicknesses are 0 m (black dots in the figures).

In block A, the layer is thicker in the center of several small landslide areas, with the maximum thickness exceeding 20 m in some areas. In blocks B and C, the layer thickness is thicker in general, with areas exceeding 50 m at the center of the moving mass in block C and the surrounding cliffs. The geology of the area consists of Neogene sedimentary rocks, andesitic lava and metamorphic rocks, and these strata are thought to exist beneath the layers of cliff cone deposits.

### Results from seismic data analysis

From the estimation of subsurface structure model (Table 2), the correspondence between geology and S-wave velocity is as follows. The first layer is a cliff cone deposit at 200 m/s, the second to fourth layers are Neogene sedimentary rocks or andesite lava at Vs



= 650-850 m/s, and the fifth to sixth layers are metamorphic rocks at  $V_s = 2200-3000$  m/s. In other areas where moving masses are present, the stratigraphy is assumed to be similar to that at this site.

## CONCLUSIONS

In this study, microtremor and seismic observations were conducted in the Saji area, Tottori City, Japan, based on the landslide topographic distribution map, to understand strong ground motion characteristics and estimate of subsurface structure.

The predominant period of H/V distribution was obtained from single-point microtremor observations, and the S-wave velocity structure of moving masses was obtained from array microtremor observations. The layer thickness distribution was found to be thicker near the center of the moving mass, with a maximum thickness of 50 meters. Furthermore, the H/V of the earthquake was obtained from seismic observation records, and the estimation of the subsurface structure of the deep subsurface structure below the cliff cone sediments was also obtained.

## ACKNOWLEDGMENTS

Part of this research is based on the results of the graduation thesis by Ms. Rino Sasaki, who belonged to the Faculty of Engineering, Tottori University. This work was supported by JSPS Grant-in-Aid for Scientific Research JP20K05028 (Principal Investigator: Tatsuya Noguchi). We also used a seismograph borrowed from the Earthquake Research Institute of the University of Tokyo with the support of the Ministry of Education, Culture, Sports, Science and Technology (MEXT) of Japan, under its Earthquake and Volcano Hazards Observation and Research Program (Phase 2). We would like to thank Atsushi Miyamoto, former director of the Saji Astro Park in Tottori City, and all the staff for providing us with the installation site and the use of a power supply.

## REFERENCES

- [1] Faris F. and Fawu W., Investigation of the initiation mechanism of an earthquake- induced landslide during rainfall: a case study of the Tandikat landslide, West Sumatra, Indonesia, *Geoenvironmental Disasters* 2014 1:4., doi:10.1186/s40677-014-0004-3, 2014.
- [2] Nishimura I., Noguchi T., Ono Y. and Kohno M.: Subsurface structures based on Microtremor observations in landslide area of Tandikat, West Sumatra, Indonesia, *International Journal of GEOMATE*, Vol.22, Issue 90, pp.57-62, DOI: <https://doi.org/10.21660/2022.90.gxi282>, 2022.
- [3] National Research Institute for Earth Science and Disaster Prevention, *Landslide Maps, Series 21 "The Miyazu and Tottori Region"*, *Explanations of Landslide Distribution Maps*, Vol.260, 2005 (in Japanese).
- [4] National Research Institute for Earth Science and Disaster Prevention, *Landslide Maps, Series 25 "The Matsue and Takahashi Region"*, *Explanations of Landslide Distribution Maps*, Vol.278, 2005 (in Japanese).
- [5] Konno K. and Ohmachi T., A smoothing function suitable for estimation of amplification factor of the surface ground from microtremor and its application, *Journal of JSCE*, No.524/1-33, 1995, pp.247-259 (in Japanese with English abstract).
- [6] Cho I., Tada T. and Shinozaki Y., Centerless circular array method: Inferring phase velocities of Rayleigh waves in broad wavelength ranges using microtremor records, *Journal of Geophysical Research*, 2006, Vol.111, B09315.
- [7] Aki, K., Space and time spectra of stationary stochastic waves, with special reference to microtremors, *Bull. Earthq. Res. Inst.*, 1957, 35, pp.415-456.
- [8] Cho I., Tada T. and Shinozaki Y., Possibility of microtremor array opened up by general theory: Release of analysis tool BIDO, *Seismological Society of Japan Fall Meeting in 2009*, 2009 (in Japanese).
- [9] Noguchi T., Nishikawa H., Yoshida S. and Kagawa T., Estimation of subsurface structure and characteristics of ground vibration based on microtremor and seismic observation in the central Tottori Prefecture, Japan, *Journal of Japan Association for Earthquake Engineering*, Vol. 19, Issue 6, 2019, pp. 258-271. (in Japanese with English abstract)
- [10] Kitsunezaki C., Goto N., Kobayashi Y., Ikawa, T., Horike M., Saito T., Kurota T., Yamane K., Okuzumi K., Estimation of P- and S- wave velocities in deep soil deposits for evaluating ground vibrations in earthquake, *Natural disaster science*, 1990, 9-3, 1-17. (in Japanese with English abstract)
- [11] Kawase, H., Sanchez-Seama, F. J. and Matsushima, S., The optimal use of horizontal-to-vertical spectral ratios of earth-quake motions for plane waves, *Bull. Seism. Soc. Am.*, Vol. 101, No. 5, pp. 2001-2014, 2011.
- [12] Yamanaka, H., Inversion of surface-wave phase velocity using hybrid heuristic search method, *geophysical Exploration*, Butsuri-Tansa, Vol.60, No.3, pp. 265-275, 2007. (in Japanese with English abstract).

## EXPERIMENTAL STUDY ON STATE BOUNDARY SURFACE OF COMPACTED SILTY SOIL

Tufail Ahmad<sup>1</sup>, Riko Kato<sup>1</sup> and Jiro Kuwano<sup>1</sup>

<sup>1</sup>Department of Civil & Environmental Engineering, Saitama University, Japan

### ABSTRACT

To understand the behavior of unsaturated soil, considerable research has already been done. However, there is limited research to model the behavior of unsaturated soil in a generalized state boundary surface (SBS). SBS is the surface outside which a soil stress state can never exist. It is an envelope surface of all the possible soil stress paths in the  $p'$ - $q$ - $e$  space. In order to investigate the SBS of unsaturated soils, a series of triaxial compression tests were performed in this study under constant water content conditions using a double cell triaxial test apparatus. The samples were prepared with 80%, 83% and 86% degree of compaction and water contents of 20% (Optimum water content) and 25%. All the soil specimens were consolidated isotropically under 500kPa confining pressure before being sheared with constant void ratio under monotonic loading. The results show that constant void ratio tests depict contour like lines which can help in defining the SBS of unsaturated soil.

**Keywords:** *Unsaturated soil, State Boundary Surface (SBS), Constant water content, Constant void ratio, Contours*

### INTRODUCTION

The soil near the surface of the earth ground is usually unsaturated by nature. The processes of excavation, compaction and soil reshaping used in various civil engineering structures such as highways, earth fill dams, embankments and runways result in unsaturated soils. There are only two phases in saturated soil that are soil and water while for unsaturated soil there are three phases: namely, soil, air, and water [1].

A novel approach to soil mechanics was developed in the 1950s and 1960s based on the concepts of critical state. It establishes a framework for relating a saturated soil's shear distortion during yielding to its stress and volume condition [2]-[3]. For saturated soils, the critical state theory is a three-dimensional (3D) approach that is defined by three state variables: effective mean stress ( $p'$ ), deviatoric stress ( $q$ ), and specific volume ( $v$ ). When the soil is sheared, it eventually reaches a critical state condition, which is located on a unique line in the  $p'$ ,  $q$  and  $v$  space. This surface contains both sets of stress paths. This is known as the Roscoe surface or state boundary surface. All drained and un-drained stress paths appear to lie on a 3D surface for normally consolidated soil, bordered at the top by the critical state line (CSL) and at the bottom by the normal consolidation line (NCL). Another state boundary surface that connects to the Roscoe surface at the CSL is the Hvorslev surface. The significance of this surface is that a sample's shear strength is a function of the specific volume and the mean net stress ( $p'$ ). Marto [4] and Moradi [5] demonstrated the Roscoe

and Hvorslev surfaces using compression and extension triaxial tests on soil samples. The Roscoe-Hvorslev model, based on elastic-perfectly plastic behavior, was presented by Houlsby et al. [6]. The critical state framework for saturated soils is built around the concepts of yielding and critical state. Sasitharan et al. [7] found that very loose saturated sand is loaded slowly under drained conditions can collapse undrained following a certain stress path. It was observed that for a particular void ratio and consolidation stress, the post-peak component of an undrained stress path specifies the state boundary above which a stress state cannot exist. Several researchers have attempted to extend the critical state concept to unsaturated soils [8]-[13]. The mechanical behavior of unsaturated compacted soil has already been thoroughly researched [8], [14]-[16]. However, due to the complexity and time-consuming nature of testing unsaturated soils, there is limited experimental study to determine the state boundary surface for unsaturated soils.

Estabragh and Javadi [17] performed controlled suction triaxial tests with constant confining pressure under drained conditions on samples of unsaturated compacted silty soil to investigate the existence and features of Roscoe and Hvorslev boundary surfaces for unsaturated soil. The findings reveal that the Roscoe and Hvorslev surfaces exist for unsaturated silty soil as well. With the increase and decrease of suction, the Roscoe surface expands and shrinks, while the Hvorslev surfaces are almost parallel for different suctions.

This study presents experimental data from triaxial compression tests performed on samples of

unsaturated compacted silty soil under constant volume and constant water content conditions. The findings are being utilized to investigate the existence, shape and the features of the state boundary surface of unsaturated soil.

## EXPERIMENTAL PROGRAMME

The physical properties of soil, sample preparation, experimental setup and procedure will be discussed in this part.

### Soil Properties

The commercial term for the soil utilized in this study is DL Clay; it is a fine soil with negligible plasticity. Freshly and freely deposited DL clay has a yellowish-brown color. According to the Japanese Geotechnical Society (JGS), it has Medium-Low compressibility (ML) and is made of 10% clay and 90% silt, indicating that the grain size is larger than ordinary clay. The grain size distribution of this soil is relatively uniform, with a mean grain size D50 of about 0.03 mm [18]. The physical properties of DL Clay are shown in Table 1.

Table 1 Physical Properties of DL Clay

Properties	Unit	Value
Density of soil particle, $\rho_s$	g/cm <sup>3</sup>	2.635
Maximum dry density, $\rho_{dmax}$	g/cm <sup>3</sup>	1.55
Optimum water content	%	20
Consistency	-	Non-Plastic

### Sample Preparation

A static compaction machine with a hydraulic jack was used to prepare homogenous specimens by compacting the soil in 5 layers in a cylindrical mold having diameter of 5cm, each layer being 2 cm thick [19]. The low energy of static compaction can provide a homogeneous density in the specimen, preventing the formation of a weaker zone [16]. Water was mixed with dry DL clay prior to compaction to make specimens at water contents of 20% and 25% i.e., to wet side of optimum water content. Specimens were compacted to degree of compaction of 80%, 83% and 86%. Specimens prepared with an 80% degree of compaction represent the loose state of soil with a void ratio of 1.13, an 83% degree of compaction represents the medium dense state of soil with a void ratio of 1.05, and an 86% degree of compaction represents the dense state of soil with a void ratio of

0.98. For specimens prepared with 80% and 83% degree of compaction, the pressure exerted to the soil during sample preparation was less than the confining pressure during the test phase, hence the samples are known to be normally consolidated. Similarly for sample compacted with 86% degree of compaction and 20% water content, the pressure exerted during sample preparation is higher than the applied stress during the test phase, so the sample is deemed to be slightly over-consolidated ( $OCR \approx 2$ ). All prepared specimens were 10 cm in height and 5 cm in diameter. The features of the specimens used in this study are shown in Table 2.

Table 2 Specimen Properties

Properties	Value					
$D_c$ (%)	80	80	83	83	86	86
$\rho_d$ (g/cm <sup>3</sup> )	1.24	1.24	1.29	1.29	1.33	1.33
$w$ (%)	20	25	20	25	20	25
$S_r$ (%)	46.2	57.8	49.5	62.6	53.6	67.5
$e$	1.13	1.13	1.05	1.05	0.98	0.98
Compaction Pressure, (kPa) $\approx$	200	100	300	210	850	375
Initial Suction, kPa $\approx$	20	15	20	15	20	15

Initial matric suction of soil samples prepared with 20% and 25% water content and degrees of compaction of 80%, 83%, and 86% was around 20kPa and 15kPa, respectively. This is consistent with the findings of Yang et al. [20], who found that compaction energy has a lower impact on soil suction in soils having a lower clay content. The soil-water characteristic curve (SWCC) is a representation of the relationship between matric suction and water content. For determining SWCC of DL-clay, the initial suction was measured for several specimens prepared with variable water content (or initial degree of saturation) after they were placed on top of a saturated pedestal having a thin membrane filter. The results are shown in Fig. 1, which show that when the saturation ratio rises, the suction falls [19].

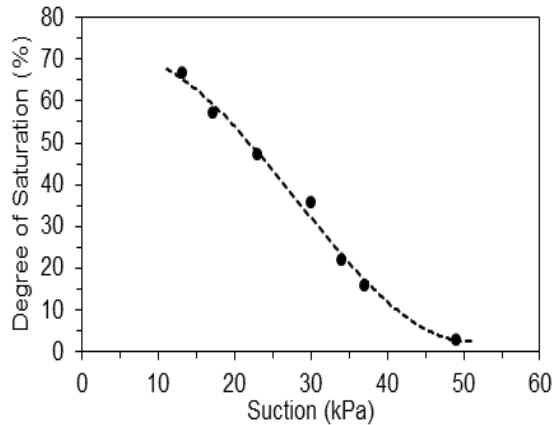


Fig. 1 SWCC for the studied soil [19]

### Experimental Setup

Figure 2 shows a schematic of the double cell triaxial apparatus utilized in current research, which includes a pore water pressure transducer, pore air pressure transducer, cell pressure transducers and loading system for exerting axial load. The device could measure both pore air and pore water pressures at the same time. The pore air pressure transducer is installed in the top cap and connected to an air regulator for continuous air supply to the specimen. A Low-Capacity Differential Pressure Transducer (LCDPT) measured the volume change in the soil sample as a function of the fluctuation in water level in the inner cell, while an external Linear Variable Displacement Transducer (LVDT) measured the vertical deformation of the specimens.

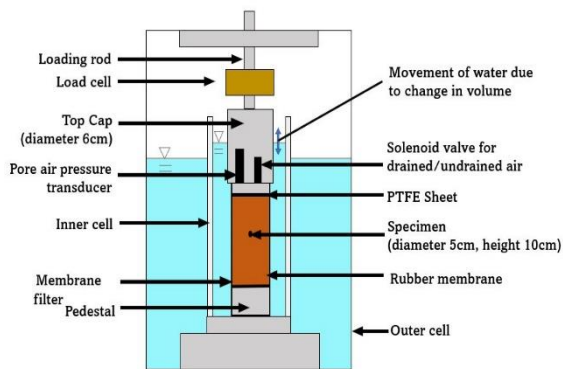


Fig. 2 Schematic of Double Cell Triaxial

For effective control and measurement of pore water and pore air, a thin membrane "Supor 450" and a Polytetrafluoroethylene (PTFE) sheet were utilized. The thin membrane having a pore size of 0.45  $\mu\text{m}$ , thickness of 140  $\mu\text{m}$ , and air entry value of 250 kPa was mounted on the bottom pedestal to allow water to flow while blocking the air passage [21]. To oppose the flow of water, the PTFE sheet was pasted to the bottom of the top cap. A solenoid-controlled

exhaust air valve was also fitted inside the top cap to reduce the volume of air in the pore air drainage line. A balance with external load cell is also connected to the triaxial apparatus to measure the amount of water drained or infiltrated into the specimen.

### Test Procedure

Before the start of each experiment the bottom pedestal is fully saturated so that no air bubble remains inside the porous stone of the pedestal. During the testing, de-aired water was utilized to reduce inaccuracies caused by air entrapment in the soil. The water in the external upper and lower tanks was de-aired for at least 24 hours by applying vacuum pressure using the suction pump.

After the specimen preparation, the sample was wrapped in a rubber membrane using a membrane holder and placed over the pedestal having a thin membrane, in order to note the value of initial suction. The Axis translation technique (ATT) was carried out after measuring the initial suction and setting all necessary connections. The main purpose of ATT was to prevent formation of cavities or voids inside the pedestal, which would ultimately influence the reading of pore-water pressure. To make pore water pressure zero, the confining pressure and pore air pressure were both increased simultaneously, leaving the specimen volume unaltered [22]. During ATT, volumetric strain should theoretically be zero.

Following ATT, the specimen was isotropically consolidated by applying the required net confining pressure of 500kPa, to get the sample to the desired state before start of shearing. To dissipate the excess pore water pressure, the drain valve was opened throughout the consolidation. The axial stress was automatically controlled by the load control system to keep deviatoric stress ( $q$ ) equal to zero.

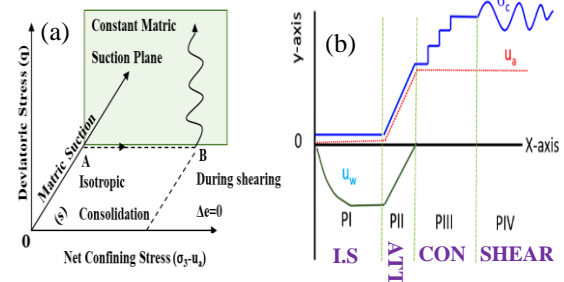


Fig. 3 (a) Stress path followed in constant void ratio test; (b) Test phases involved

The test phases and stress path followed during current research is illustrated in Fig. 3. The soil specimens were sheared with constant void ratio (constant volume) at a strain rate of 0.05 mm/min under constant water content condition, by keeping the drainage valve for pore water pressure closed, while the pore air pressure was constantly drained and

controlled. The constant water content test simulates the state of compacted soil in an embankment or slope. The sample volume was maintained constant by varying the confining pressure in response to the volume change (i.e., reading of the LCDPT value) of the specimen. According to the standards of Japan Geotechnical Society “JGS 0527-2009”, the shearing phase was automatically stopped when the axial strain reached 15%.

## EXPERIMENTAL RESULTS

The initial matric suction has a significant impact on the mechanical behavior of unsaturated soils. It can be seen from Fig. 4 that specimen prepared with 20% and 25% water contents has different values of initial matric suction. For samples with lower water content, the matric suction is high, and it takes more time to stabilize the matric suction as compared to sample with high water content.

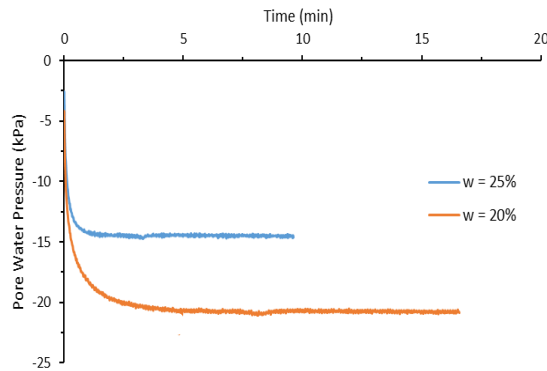


Fig. 4 Variation in initial matric suction over time.

The sample was sheared at a rate of 0.05% per minute up to an axial strain of 15%. The shearing was performed under constant water conditions, i.e., water drain valve was closed while the air drain valve was open. As the samples were to be sheared with constant void ratio or zero volumetric strain, therefore the cell pressure was increased or decreased corresponding to the LCDPT value to keep the sample void ratio constant.

Figure 5 shows the void ratio against mean effective stress during consolidation and shearing for samples prepared with 20% and 25% water content. It can be observed from Fig. 5 that as the degree of compaction increases from 80% to 86%, the decrease in void ratio becomes less during the consolidation for both 20% and 25% water content samples. Similarly for samples with same degree of compaction e.g. (80%, 83% or 86%), the decrease in void ratio during consolidation is slightly less for samples with 20% water content as compared to 25% water content samples. The void ratio is kept constant throughout the shearing.

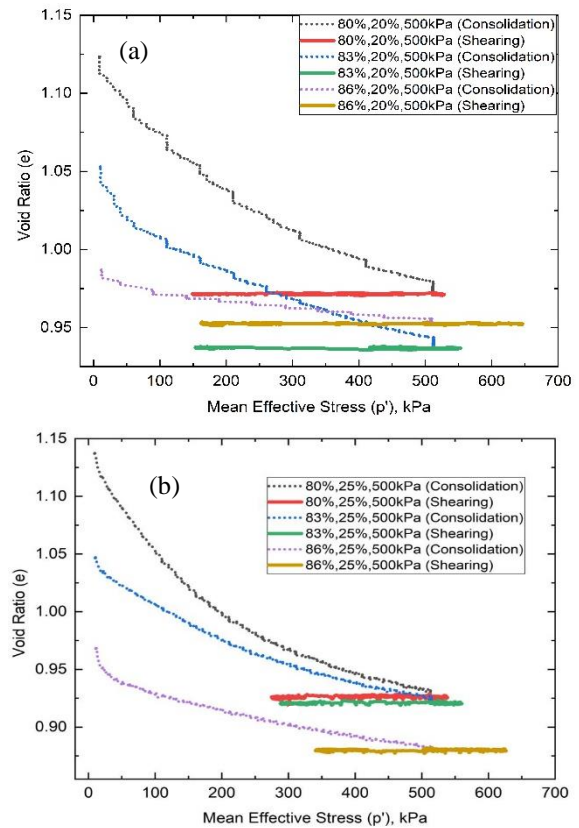


Fig. 5 Void ratio Vs Mean effective stress for samples prepared with (a) 20% water content (b) 25% water content

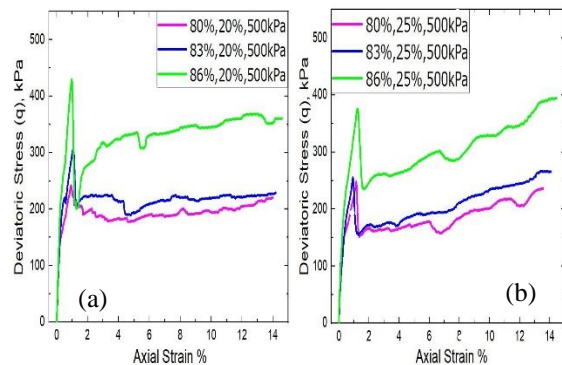


Fig. 6 Deviatoric stress during shearing for samples prepared with (a) 20% water content (b) 25% water content

It can be seen from Fig. 6 that the peak deviatoric stress was slightly more towards the optimum moisture content than the wet side of optimum moisture content. This is because of matric suction in unsaturated soil. When water content in a specimen increase, the deviatoric stress decrease accordingly. When there is less water content, water will not be sufficient to act as a lubricant between soil particles so they can slide and reorient when stress is increased. Hence the internal friction between soil particles is



increased which increases the deviatoric stress. Also, the deviatoric stress is more for samples prepared with high degree of compaction. The effective stress plotted against the axial strain is shown in Fig. 7. The effective stress value is more for dense samples as compared to the semi dense and loose samples.

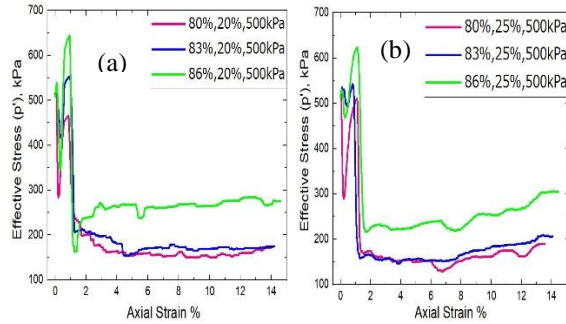


Fig. 7 Mean effective stress during shearing for samples prepared with (a) 20% water content (b) 25% water content

It can be noted from Fig. 7, there is some unusual behavior for axial strain range of 0-2%. The effective stress initially increases slightly followed by a sudden decrease and then again increases and decreases continuously until the specimen reaches the critical state. This phenomenon may be due to the sudden loading impact under high confining pressure of 500 kPa during shearing which may cause the soil particles held together by suction to collapse suddenly to fill in the gaps and then reorient.

Both pore water and pore air pressure decreased throughout the shearing phase, as illustrated in Fig. 8 and Fig. 9. However, the decrease in pore water pressure was more than the pore air pressure. As a result, the matric suction also increased slightly. The degree of saturation of samples did not alter throughout shearing as the water drainage valve was closed and the tests were performed with constant void ratio.

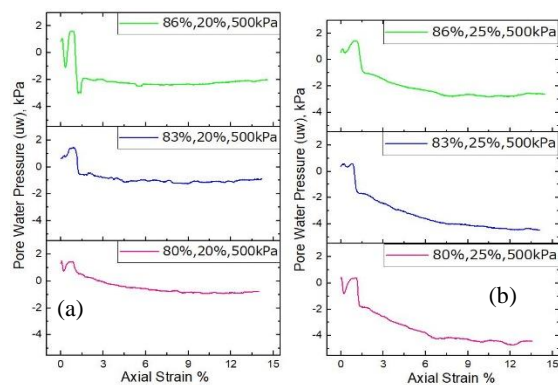


Fig. 8 Pore water pressure during shearing for samples prepared with (a) 20% water content (b) 25% water content

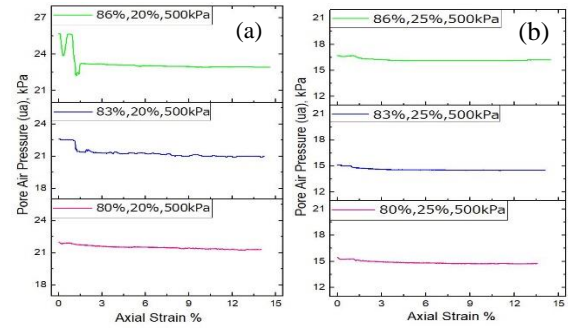


Fig. 9 Pore air pressure during shearing for samples prepared with (a) 20% water content (b) 25% water content

The void ratio ( $e$ ), net mean effective stress ( $p'$ ), and deviator stress ( $q$ ) is plotted in a 3D space as shown in Fig. 10. All the stress paths lie on the same failure plane forming the state boundary surface. SBS separates the possible and impossible stress states. It can be observed that the constant void ratio test provides contour like lines which helps in identifying the shape of state boundary surface. With increase in matric suction, the SBS extends outwards.

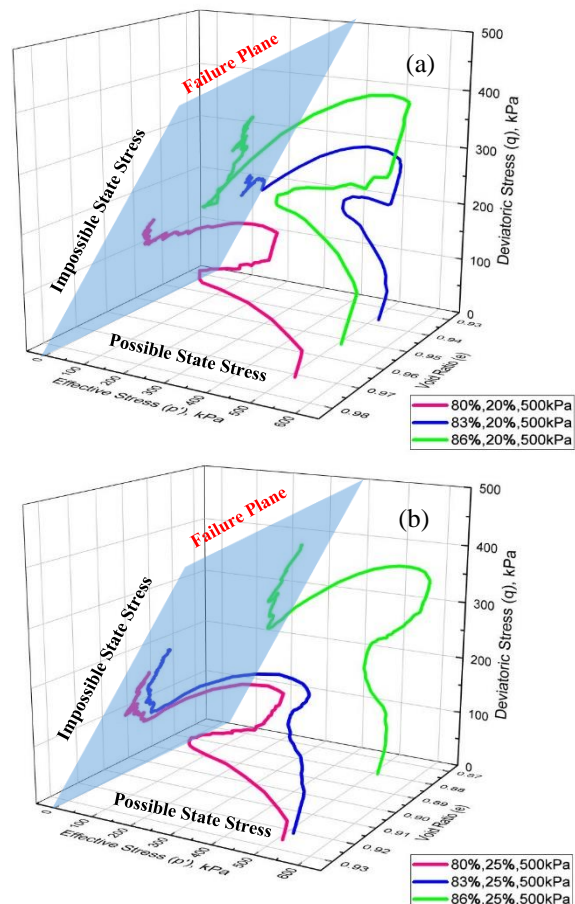


Fig. 10 State Boundary Surface for samples prepared with (a) 20% water content (b) 25% water content tested under constant void ratio



## CONCLUSIONS

A series of laboratory element tests were carried out to investigate the state boundary surface of unsaturated soil under constant void ratio and constant water content conditions. It was found that for soil samples with higher water content, initial suction values stabilize in a shorter time interval, while lower water content soil samples take longer to stabilize. The soil samples prepared at optimum water content shows higher shear strength than those prepared at wet side of optimum water content. Also, the shear strength of soil increased with increase in degree of compaction. The effective stress increased and decreased multiple times within axial strain range of 0-2%. The matric suction of samples slightly increased during shearing due to decrease in pore water pressure. The SBS was set up by contour like lines obtained with constant void ratio tests which separates the possible and impossible stress states.

## ACKNOWLEDGEMENTS

The Japanese Ministry of Education, Culture, Sports, Science and Technology (MEXT) is gratefully acknowledged for research facilities and financial assistance.

## REFERENCES

- [1] Fredlund DG, Rahardjo H, Soil Mechanics for Unsaturated Soils. New York: John Wiley and Sons Inc., Soil Dynamics and Earthquake Engineering, Vol. 12, No. 7, 1993, pp. 449–450.
- [2] Roscoe, K. H., Schofield, A. W., and Worth, C. P., On the yielding of soils. *Géotechnique*, Vol. 8, No. 1, 1958, pp. 22-53.
- [3] Schofield, A. W., and Worth, C. P., Critical State Soil Mechanics. *Engineer*, Vol. 16, No. 3-4, 1968, pp. 53-66.
- [4] Marto, A., Volumetric compression of a silt under periodic loading. Ph.D. thesis, Univ. of Bradford, Bradford, U.K, 1996.
- [5] Moradi, G., Symmetric and non-symmetrical cyclic triaxial loading of silt. Ph.D. thesis, Univ. of Bradford, Bradford, U.K, 1998.
- [6] Houlby, G. T., Wroth, C. P., and Wood, D. M., Predictions of the results of laboratory test on a clay using a critical state model. *Proc., Int. Workshop on Constitutive Behavior of Soil*, Balkema, Rotterdam, Netherlands, 1982, pp. 99–121.
- [7] S. Sasitharan, P.K. Robertson, D.C. Sego, and N.R. Morgenstern., Collapse behavior of sand. *Canadian Geotechnical Journal*. Vol. 30, No. 4, 1993, pp. 569-577.
- [8] Wheeler, S. J., and V. Sivakumar, An Elasto-Plastic Critical State Framework for Unsaturated Soil. *Geotechnique*, Vol. 45, No. 1, 1995, pp. 35-53.
- [9] Maâtouk, A., Leroueil, S. and La Rochelle, P., Yielding and critical state of a collapsible unsaturated silty soil. *Géotechnique*, Vol. 45, No. 3, 1995, pp. 465-477.
- [10] Loret, B., and Khalili, N., An effective stress elasto-plastic model for unsaturated porous media. *Mech. Mater.*, Vol. 34, No. 2002, pp. 97-116.
- [11] Toll, D. G., and B H. Ong, Critical-State Parameters for an Unsaturated Residual Sandy Clay. *Géotechnique*, Vol. 53, No. 1, 2003, pp. 93-103.
- [12] Tarantino, A., A possible critical state framework for unsaturated compacted soils.” *Géotechnique*, Vol. 57, No. 4, 2007, pp. 385-389.
- [13] Estabragh, A. R., & Javadi, A. A., Critical State for Over-consolidated Unsaturated Silty Soil. *Canadian Geotechnical Journal*, Vol. 45, No. 3, 2008, pp. 408-420.
- [14] Cui, Y. J., and Delage, P., Yielding and plastic behaviour of an unsaturated compacted silt. *Géotechnique*, Vol. 46, No. 2, 1996, pp. 291-311.
- [15] Jotisankasa A, Coop M, Ridley A, The mechanical behavior of an unsaturated compacted silty clay. *Géotechnique*, Vol. 59, No. 5, 2009, pp. 415-428.
- [16] Melinda F, Rahardjo H, Han KK, Leong EC, Shear strength of compacted soil under infiltration conditions, *Journal of Geotechnical Eng. Div. ASCE*, Vol. 130, No. 8, 2004, pp. 807–817.
- [17] Estabragh, A. R., & Javadi, A. A., Roscoe and Hvorslev Surfaces for Unsaturated Silty Soil. *International Journal of Geomechanics*, Vol. 14, No. 2, 2014, pp. 230-238.
- [18] Chae, Jonggil, Byeongsu Kim, Seong-wan Park, and Shoji Kato., Effect of suction on unconfined compressive strength in partly saturated soils. *KSCE Journal of Civil Engineering*, Vol. 14, No. 3, 2010, pp. 281-290.
- [19] Rasool AM, Kuwano J, Influence of matric suction on instability of unsaturated silty soil in unconfined conditions. *International Journal of GEOMATE*, Vol. 14, No. 42, 2018, pp. 1–7.
- [20] Yang S-R, Lin H-D, Huang W-H, Variation of initial soil suction with compaction conditions for clayey soils. *Journal of Mechanics*, Vol. 28, No. 3, 2012, pp. 431-437.
- [21] Habasimbi P, Nishimura T, Soil water characteristic curve of an unsaturated soil under low matric suction ranges and different stress conditions. *International Journal of Geosciences*, Vol. 10, No. 1, 2019, pp. 39-56.
- [22] Hilf JW, “An investigation of pore water pressure in compacted cohesive soils” U.S. Department of Interior Bureau Reclamation Technical Memo. no. 654, 1956.

# PERFORMANCE AND BEHAVIOR OF DIAPHRAGM WALL OF UNDERGROUND AUTOMATIC CAR PARK PROJECT IN BANGKOK SUBSOIL

Jirat Teparaksa<sup>1</sup>

<sup>1</sup>Faculty of Engineering, Kasetsart University, Thailand

## ABSTRACT

Currently, in Bangkok, the underground automatic car park becomes more popular since it can provide maximum usage space without ramp. However, the automatic system requires large openings of the basement slab resulting in possible insufficient axial capacity of the slab which must be rechecked. This paper focuses on one of the latest underground construction projects in Bangkok city center, True Digital park. There were in total four basement stories with 13.20m-maximum depth of excavation including mat foundation. The 800mm-thick diaphragm wall (D-wall) was proposed to be a soil retaining structure with 3-layers of full temporary bracing. Finite Element Method (FEM) with Mohr-Coulomb soil model was employed for the D-wall design and horizontal movement prediction. To date, the construction of basement was completed and the superstructure is being constructed. The field performance of D-wall construction was evaluated by means of horizontal movement using installed inclinometers. During construction, every sequence, such as soil excavation and bracing installation was carefully monitored and strictly controlled to minimize the D-wall movement. The monitoring result shows good agreement with FEM analysis. This paper describes the project construction and monitoring together with field performance results.

*Keywords: Deep excavation, Field monitoring, Diaphragm wall, Underground automatic car park*

## INTRODUCTION

Currently, in Bangkok, as one of the largest developing cities, there are many underground construction projects including government infrastructures and private skyscrapers to optimum land usage. The most widely designed for private underground structures is intended to be underground car parking especially an automated car park as it provides maximum usage space without car ramp. However, the automatic system requires many large openings for vehicle elevators resulting in possible insufficient axial capacity or stiffness of underground slab.

High-rise mixed-used building with four basement stories of substructure is being constructed. The basement floors are desired to be an underground automatic carpark as it helps maximizing parking space eliminating driving path and ramps.

Four basement includes B1 – B4 at elevation EL.-10.50 m., -7.65 m., -5.10 m. and -2.00 m. with the maximum excavation depth of -13.20 m. from ground surface. Diaphragm wall (D-wall) of 0.80 m. thick with 21.0 m. length penetrated in stiff clay layer was employed as a soil retaining structure. During excavation, the 3 layers of temporary steel bracing strut was used at EL. -1.50 m., -4.50 m. and -9.00 m.

Typical section of temporary bracing and basement floor are presented in Fig 1 and Fig 2. In this project, there are a few openings for both car elevators and mechanical system works in basement

floor B2 and B3 as shown in Fig 3. It can be seen that there are large number of openings closed to the D-wall for the mechanical system and five openings in the middle for car transferring lifts. This paper presents soil retaining structural design and its behavior during construction.

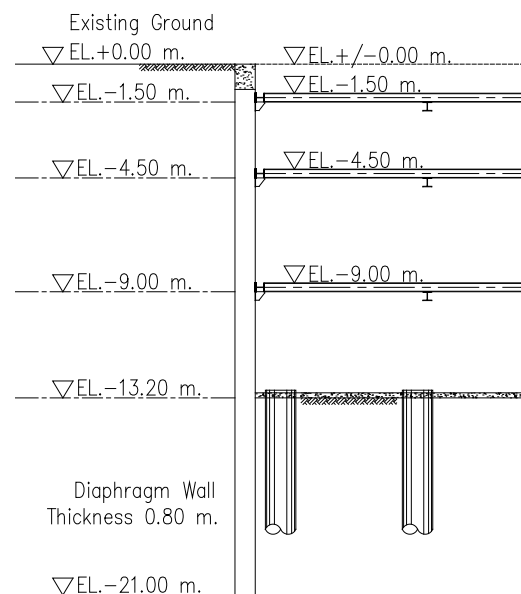


Fig. 1 Typical section of temporary bracing.

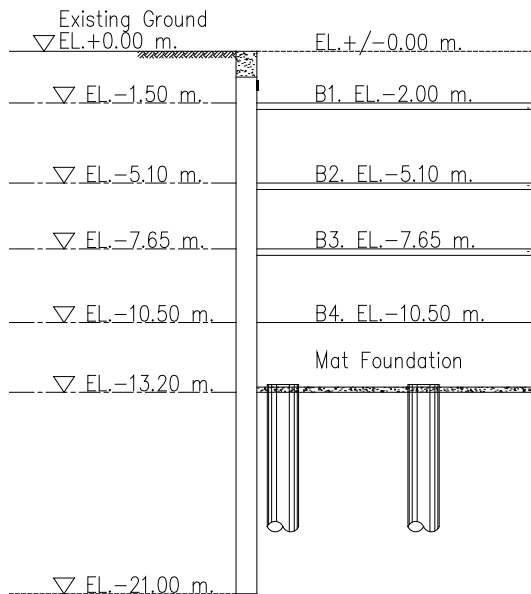


Fig. 2 Typical section of basement.

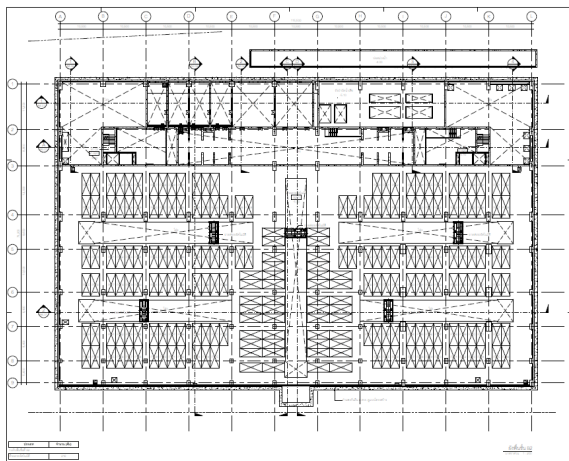


Fig. 3a B2 floor plan

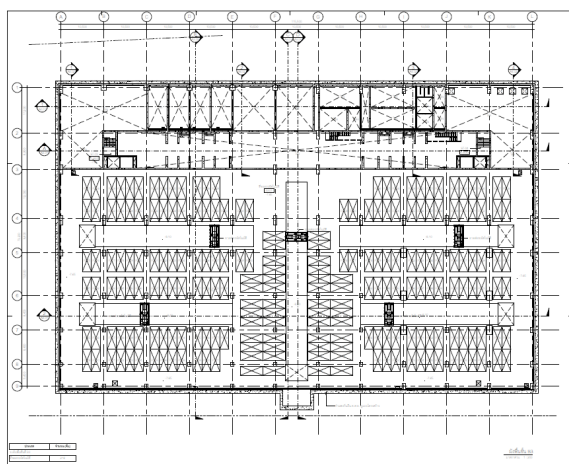


Fig. 3b B3 floor plan

## SOIL CONDITIONS

Six boreholes of 75 m. deep were conducted to investigate soil condition in the site. It consisted of a 12 m. thick soft clay layer followed by 3 m. of medium clay. There was a stiff clay layer up to approximately EL.-35.00 m. from ground surface. It should be noted that there was a variation between EL.-19.00 m. to EL.-23.00 m. where four boreholes revealed very stiff silty clay while the other two boreholes showed medium silty sand. Soil profile and soil properties are presented in Fig 4.

Groundwater condition of Bangkok soft clay is in hydrostatic condition starting from -1.0 m. Deep well pumping in the past had promoted drawdown of the soft, medium and the first stiff clay. The piezometric level of Bangkok aquifer was reduced and was constant at EL.-23.0 m [1]. This is beneficial to practicing geotechnical engineers in terms of higher effective stress and dry condition during underground construction. However, as the Thailand's government has been enforced deep well pumping prohibition law for about 20 years to solve the problem of land subsidence, the current piezometric level is increasing up to -13.0 m. as illustrated in Fig 5 [2].

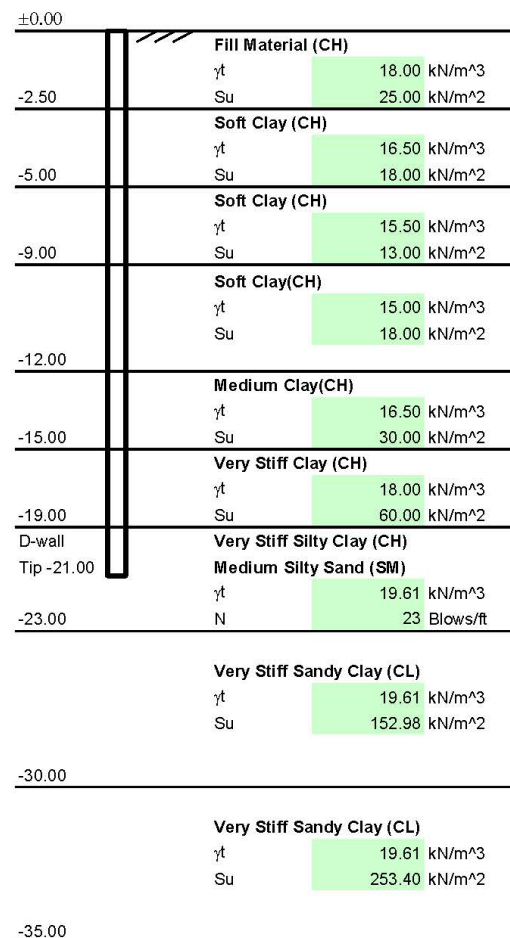


Fig. 4 Soil profile and soil properties.

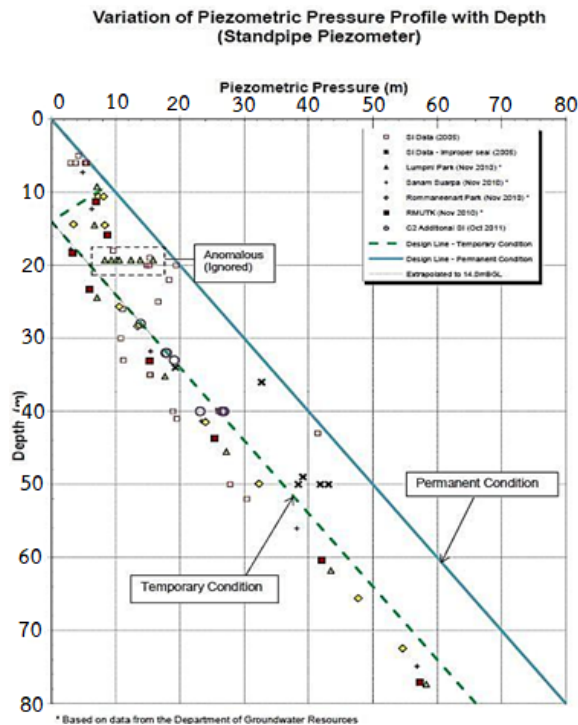


Fig. 5 Recent Bangkok groundwater conditions data [2].

Although the sand layer was encountered at EL.-19.00 m., the maximum depth of excavation was just 13.20 m. This scenario gives safety factor against uplift of approximately 1.75, therefore, the excavation is safe in respect of uplift pressure.

## ANALYSIS OF DIAPHRAGM WALL BEHAVIOR BY FINITE ELEMENT METHOD

### Design Criteria of Diaphragm Wall

The behavior of diaphragm wall can be predicted by numerical analysis by mean of Finite Element Method (FEM). The diaphragm wall behavior, result of FEM, is presented in terms of bending moment and shear force induced in the diaphragm wall as well as lateral displacement. The step of soil excavation, bracing installation, as well as preloading in the strut system is simulated in the FEM analysis. The casting of base slab, basement floor and the step of removal of strut system are also combined in the FEM analysis of diaphragm wall. In this project, the PLAXIS 2D [3] program was used as the FEM program to predict the diaphragm wall behavior.

The Mohr-Coulomb soil modeling was employed. The Undrained Young's modulus ( $E_u$ ) of layer was correlated with undrained shear strength ( $S_u$ ) while in the sand layer, the drained modulus ( $E'$ ) was correlated with the Standard penetration SPT N-value.

The correlation of  $E_u$  and  $S_u$  as well as  $E'$  and N-value can be conducted as follows.

- For soft to medium clay layer, Undrained

Young's modulus

( $E_u$ ) = 500 – 700  $S_u$  (Undrained Shear Strength)

- Stiff to very stiff silty clay layer  
 $E_u = 1000 S_u$
- Sand layer  
 $E' = 2000(N)$  SPT-N-Value ( $kN/m^2$ )

The above correlation between  $E_u$ - $S_u$ , and  $E'$ -N(value) is based on the back analysis from various basement excavation project by means of FEM analysis compared with field measurement proposed by [4].

### Surcharge on the diaphragm wall

The ground surface surcharge behind the diaphragm wall during construction was assumed at 10  $kN/m^2$  for 6 m. wide to simulate the machinery load. This ground surface was applied during excavation, basement casting and completion of the basement work.

### Groundwater table

The ground water of Bangkok subsoil condition is in the draw down condition due to deep well pumping. Recently, as the deep well pumping is not allowed, the recent ground water table has been increasing to EL.-13.00 m. below ground surface. This groundwater level was used in the model during excavation.

## FEM ANALYSIS RESULTS

All the construction sequences starting from the first excavation to the final stage after construction were modelled in the FEM analysis, using Mohr-Coulomb as a failure criterion. The first sequence was initial excavation to install the first strut layer. The second was after the first strut installation which was excavation to the second strut layer level. The process continued until reaching the final depth as shown in terms of deformed mesh in Fig 6. It should be noted that since there was variation in soil investigation, two models with stiff clay and medium sand layer between -19.00 to -23.00 m. were developed.

For the upward construction, it was started by casting the mat foundation and removal of strut layer 3. The second strut layer was removed in the next stage after casting basement B2 and B3 floor. Then, B1 was casted followed by removal of strut layer 1. The FEM model was completed at the construction step of that ground water table was at -1.00 m. and consolidation was taken place for long-term simulation as presented in Fig. 7.

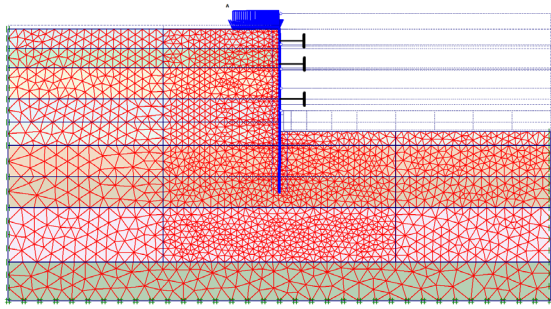


Fig. 6 Deformed mesh at the final depth excavation.

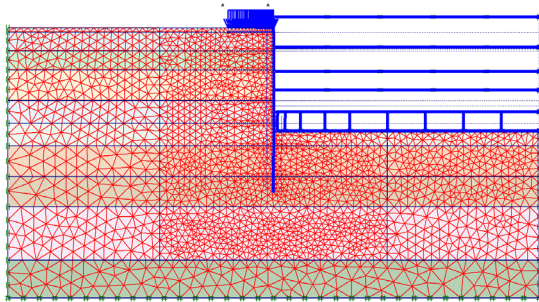


Fig. 7 Deformed mesh at the final stage.

All the basement floors were modelled to obtain the axial forces at every step for the structural engineer to recheck the reinforcement especially at the openings closed to the D-wall. The moment and shear envelopes, of both stiff clay and medium sand layer, were then employed to design the D-wall reinforcement as illustrated in Fig. 8. In addition, the presented moment envelope was summarized from all construction stages including final stage where consolidation occurred. It can be seen that the reinforcement covered the predicted maximum moment in both cases with safety factor of 1.5.

#### DIAPHRAGM WALL DIAPLACEMENT AND SAFETY CONTROL

Not only bending moment and shear force that were obtained from the FEM analysis but also horizontal D-wall movement at every construction step. The maximum horizontal displacement was used to set the trigger level for safety control during construction as shown in Table 1. There were four inclinometers installed at each side as illustrated in Fig 9. The inclinometers were read after completion of every construction step. The final reading showed horizontal displacement of 40.64 mm., 37.71 mm., 41.31 mm. and 58.65 mm. for IW1 to IW4 respectively. IW4 started to exceed maximum value after removal of strut layer 2.

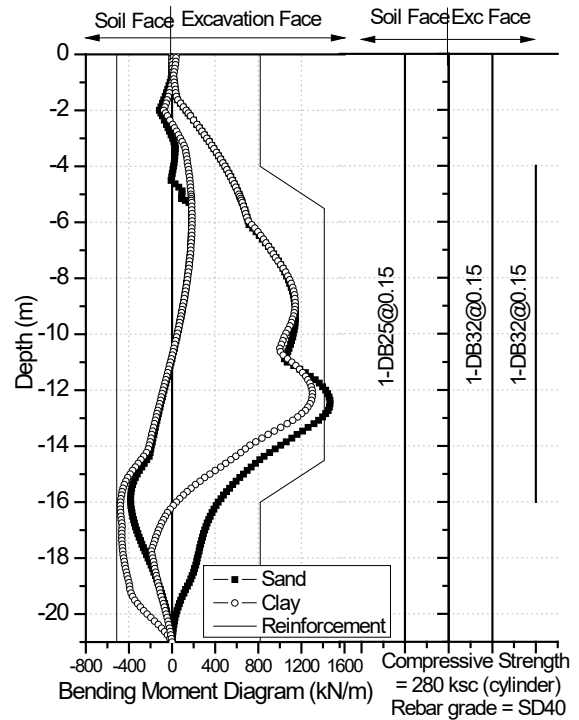


Fig. 8 Bending moment envelope and D-wall reinforcement.

Table 1 Trigger level and safety control

Trigger Level	Disp. (mm.)	Safety Criteria
Alarm Level (70 % of DV)	37.43	Inform designer to review CS
Alert Level (80 % of DV)	42.78	Inform all parties to review CS
Action Level (90 % of DV)	48.12	Stop construction and revise the CS
Maximum	53.47	

Note: Disp. = Displacement, DV = Design Value, CS = construction sequence.

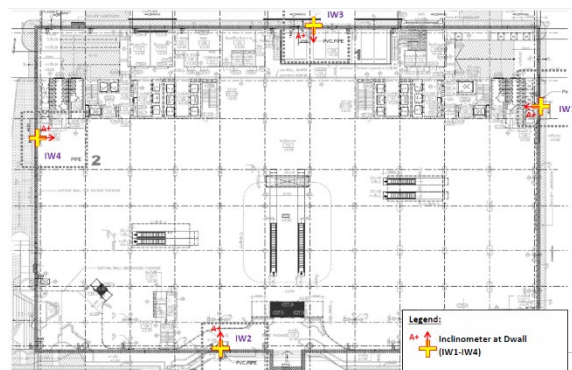


Fig. 9 Inclinometer location.



The inclinometer reading of IW4 is shown in Fig 10 together with trigger level and basement levels. There was large movement at the very initial stages where the inclinometer reading showed cantilever behavior. The movement firstly touched the alarm level during excavation to the final depth at -13.20 m. The horizontal movement continued during upward construction until the completion of basement construction at 58.65 mm. which was more than the predicted maximum value.

It can be noticed that after casting the basement floor B2, B3 and B4, there was movement at those elevations which can be implied that the basement slab might be weak. Similar horizontal movement but larger was also obviously found at Inclinometer IW2 as shown in Fig 11 despite the fact that the overall movement did still not exceed the alert level. At first, it was thought that it might be because the basement slabs B2 and B3 at IW2 location are closed to the opening. However, the movement continued further at basement B1 even the B1 has no opening.

It was, then, suggested to do visual investigation of all the basement floor but no crack was observed. Several photograph of basement B2 and B3 are shown in Fig 12 and Fig 13 respectively.

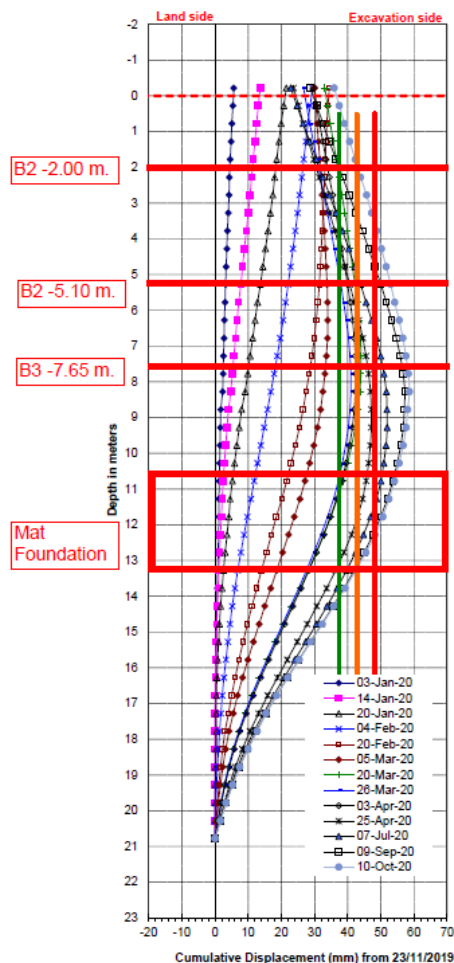


Fig. 10 Inclinometer reading IW4

All of the inclinometer readings (IW1 – IW4) are compared to the FEM prediction as presented in Fig. 13. The movement of IW1, IW2 and IW3 agreed well with the FEM analysis with larger movement at top of D-wall observed at IW2 as discussed previously. The IW4 reading seemed to be different from the others and FEM prediction. This might be because of very large movement at the initial stages due to weak local strut together with described horizontal movement during upward construction.

The construction continued to the super-structure as there was no observed damage to the substructure. Currently, at the time of this paper, the whole building is almost completed.

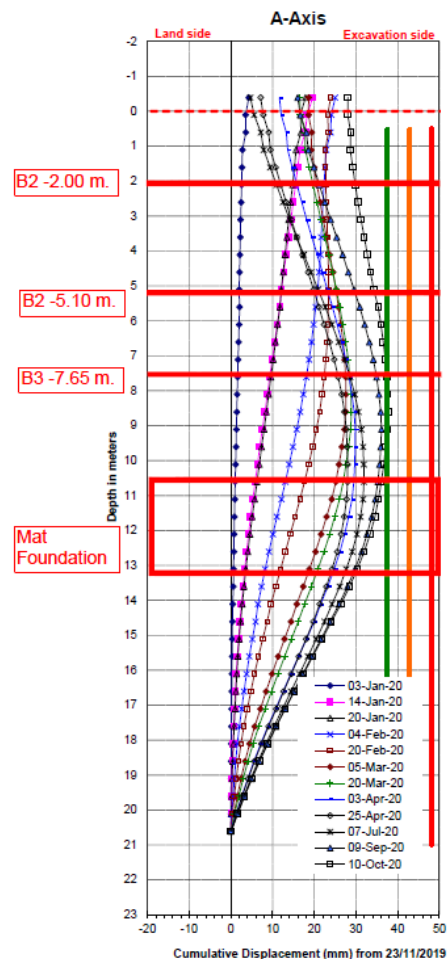


Fig. 11 Inclinometer reading IW2



Fig. 12 Photo of B3 after removal of bracing layer 2.





Fig. 13 Photo of B2 after removal of bracing layer 2.

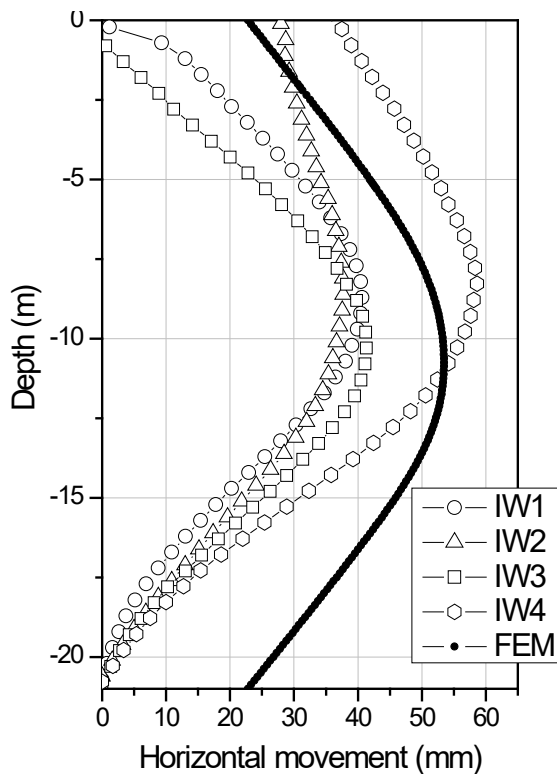


Fig. 14 Comparison of Inclinator readings and FEM prediction.

## CONCLUSIONS

The underground basement construction was designed to be underground automatic carpark of the high-rise mixed-use building. There were many openings in the sub-structure floors for car elevator and mechanical systems. The diaphragm wall, designed using FEM analysis with Mohr-Coulomb failure criteria, was employed as a soil retaining structure. All the construction sequences were simulated in the FEM. The diaphragm wall behavior and displacement were predicted and compared with the field inclinometer monitoring data. The FEM result agreed well with the field performance. However, the unusual horizontal movements at basement slab and mat foundation level were detected during the upward construction.

## REFERENCES

- [1] Teparaksa W., Principal and application of instrumentation for the first MRTA subway project in Bangkok, 5th International Symposium on Field Measurement in Geomechanics, Singapore, 1999.
- [2] Teparaksa W., and Teparaksa J., Comparison of Diaphragm Wall Movement Prediction and Field Performance for Different Construction Techniques. Underground Space, 2019.
- [3] Brinkgreve, R.B.J., PLAXIS 2D Version 8 Manual, A.A. Balkema Publishers, 2002.
- [4] Teparaksa W., Displacement analysis of diaphragm wall for subway construction, The 7th National convention in the Civil Engineering Bangkok, 2001

# NATURALLY DERIVED CEMENTS FOR CONSTRUCTION AND BUILDING MATERIALS LEARNED FROM THE WISDOM OF ANCESTORS: A LITERATURE REVIEW

Su Zhan<sup>1</sup>, Kazunori Nakashima<sup>2</sup> and Satoru Kawasaki<sup>3</sup>

<sup>1</sup>Graduate School of Engineering, Hokkaido University, Sapporo, Japan

<sup>2</sup>Faculty of Engineering, Hokkaido University, Sapporo, Japan

## ABSTRACT

For over a thousand years, many ancient lime mortars have remained durable despite long-term exposure to atmospheric or humid agents. This review paper summarizes technologies of worldwide ancient architectures which vest remarkable durability to maintain them over thousands of years of constant erosion. It aims to identify the influence of organic and inorganic additions in altering mortar properties and take the lost and forgotten technologies to the production frontline. The types of additions are usually decided based on the local environment and use purpose. The ancient Romans built magnificent structures by making hydraulic cement using volcanic ash. The old Chinese introduced sticky rice and other local materials in addition to improving the properties of pure lime mortar. A variety of organic and inorganic additions used in traditional lime mortar not only changes the properties but also improves its durability for centuries. The benefits they bring to lime mortar may also be useful in Enzyme Induced Carbonate Precipitation (EICP) and Microbially Induced Carbonate Precipitation (MICP) fields. For instance, sticky rice has been confirmed to play a crucial role in regulating calcite crystal growth and providing interior hydrophobic conditions which contributed to its reserve, which may improve the strength and durability of EICP and MICP treated samples as well.

*Keywords: naturally derived cement, lime mortar, sticky rice, enzyme induced carbonate precipitation (EICP), microbially induced carbonate precipitation (MICP), ground improvement*

## INTRODUCTION

Lime has a long history of being used as a building material. Thousands of years ago, ancient engineers around the world began to utilize lime to produce mortar for architecture construction. To satisfy the demand for different use purposes, the properties of lime mortar were constantly modified by various organic or inorganic additions. Some of these give lime mortar the remarkable strength and durability that allowed ancient architecture to be well preserved even over thousands of years of environmental erosion. This review paper aims to summarize the types and influence of various organic and inorganic additions used in ancient architecture and take those lost and forgotten technologies to the production frontline.

## DISCOVERED ADDITIONS

Use the Republican period, perhaps in the third but certainly by the second century B.C., ancient Romans discovered how to create hydraulic mortar, a kind of building material with enormous performance [1], [2], which was more durable than other building materials they used. The Pantheon in Rome, which

was built by Agrippa in about 118–125 AD, has stood for nearly two thousand years with only several minor repairs. Hydraulic mortar used a pozzolanic additive to replace the pure silica sand in previous lime mortar [3].



Fig. 1 The Pantheon, Roma. [4].

The history of utilization of lime mortar was much older, and evidence of its use for binding stones seems to have first appeared in Egypt in the third

millennium B.C. [5]. Lime is obtained by the calcination of limestone at around 1,000°C, and the final product calcium oxide, quicklime, is its main ingredient. Another ingredient of lime mortar is sand [6]. Vitruvius, a Roman architect and engineer writing around 30 B.C., suggested several different formulations for lime mortar and specifications of sands in his book. In addition, he outlined the types of sands. River sand makes mortar dry more slowly, which leads to delays in construction, and sea sand could lead to a salty efflorescence when used in stucco. Vitruvius preferred pit sand to river or sea sand, which, he explains, can crackle when rubbed in the hand. Later, as conventional mortared rubble construction became more common in the third century B.C., builders may simply have found that the replacement of local volcanic ash for sea sand resulted in a stronger mortar that could set under seawater. When Vitruvius was writing, hydraulic mortar and concrete were still being used sparingly and tentatively as they were relatively recent innovations [8]. He described volcanic ash is a kind of powdery sand, which, by its nature, produces wonderful results. It is found in the neighborhood of Baiae and in the lands of the municipalities around Mount Vesuvius. Not only does this material furnish strength to other buildings when mixed with lime and rubble, but also, when piers are built in the sea, they set under water, and neither the waves nor the force of water can dissolve them.

Not long after, Roman engineers quickly realized the remarkable potential of this new material in view of its special suitability for the construction of hydraulic installations, bridge footings, and harbor structures. Roman engineers could construct harbors anywhere political, economic, or military considerations dictated and not simply where advantageous physical features existed. The resulting changes in Roman architectural construction have been termed a “revolution” [7].

Approximately a century later, the development of hydraulic mortar reached its peak [8]. The use of hydraulic concrete for the construction of harbors and other maritime structures in Italy and in some other regions of the Mediterranean had virtually become routine. Pliny the Elder specified that pozzolana should be taken from the hills around Puteoli, and a series of investigations into the ancient port confirmed his record. The crushed ceramics represent an artificial pozzolanic additive that was used to supplement non-pozzolanic sand, producing a mortar particularly suitable for waterproofing cisterns.

The remarkable durability of Roman mortar results from crystalline, calcium-aluminum silicate-hydrate (C-A-S-H binder) in the cementing matrix of the mortar, which was produced through reaction of seawater, lime, and volcanic ash [9], [10], [12]. C-A-S-H is the poorly crystalline analog of Al - tobermorite—a rare, layered, calcium-silicate hydrate mineral composed of aluminosilicate chains bounded by an interlayer region and a calcium oxide sheet [11]. In Portland cement, the inert aggregate particles tend to lead the expand and growth of crack; however, in the Roman concrete, tobermorite (Al-tobermorite) is formed between the aggregate and the mortar, preventing the cracks from extending further [10]. Al- tobermorite forms crystals with platy shapes that interlock to reinforce the cementing matrix and thus increase the concrete’s resistance to brittle fracture.

A long time ago, the ancient Chinese began to use lime and lime-based gelled materials. Archeological evidence shows that the application of lime started long before the prehistoric period. By the mid to late West Zhou (1046–771 B.C.) [15], lime materials were widely used in the reinforcement of pill, ground improvement, and roofing. After the Qin and Han dynasties, lime material was more widely adopted. Pig blood was used on the floor of the Xianyang Palace site during the Qin Dynasty (221–206 B.C.) [16], mixing with lime and ginger stone into a dark red, smooth surface with moisture-proof effect.



Fig. 2 The Great Wall, China. [17].

It is worth noting that at least during the Han Dynasty, inorganic hybrid gelled material commonly referred to as “tabia” (composed of lime, loess, and sand) was invented and applied. In the Sixteen States and the Empire of the Eastern Jin Dynasty (317–420 A.D.) [18], the use of tabia was more widespread, and a tomb constructed by tabia was found in North Yan. Tongwan city—the capital of the state of Helian—

was also found to be built with *tabia*. After seeing Tongwan by himself, Shen Kuo, a scientist of the North Song Dynasty, described the city as “hard like stone” in his book, *The Dream Rivulet Diary*. A reference in *General History of China* also said that the city was “hard enough to sharpen knife and axe.” These records show the toughness of *tabia* [19] – [21].

With the latest analytical technology, researchers [13] found that crystals of aluminium tobermorite were growing from a silicate mineral called phillipsite, which is frequently found in volcanic rocks. The reason that tobermorite had grown from the phillipsite is the reaction of seawater between the concrete, which increased its degree of alkalinity. Such kinds of crystallisation are highly unusual and indeed are only found in such places as the volcanic island of Surtsey [13], which is located in the Vestmannaeyjar archipelago off the southern coast of Iceland. It is thought that as the tobermorite grows throughout the concrete, it may provide strength due to its long, plate-like crystals, which allow the concrete to flex—and not shatter—when stressed.

At least no later than the South-North Dynasty (386–589 A.D.) [22], sticky rice lime mortar was already a mature technology. The appearance of organic/inorganic hybrid mortar such as sticky rice lime mortar was great progress. The building work *Tian Gong Kai Wu*, written during the Ming Dynasty, recorded the composition, method of making, and performance of it in detail: “Sticky rice soup and *Actinidia chinensis* cane juice is added to the mixture of 1/3 of lime and 2/3 of loess and river sand and well stirred, and the mortar is produced. The buildings constructed by it are very strong and permanent, and this kind of material is named *tabia*.” This kind of *tabia* with added sticky rice is the sticky rice lime mortar mentioned above. The addition of natural organic compounds such as sticky rice soup greatly improved the performance of building gelled material. Due to its excellent properties and performance, such as high adhesive strength, good toughness, waterproofness, and durability [23], [24], traditional organic mortar such as sticky lime mortar was valued by many people after its invention. However, due to low levels of production, it was not available in large quantities. Until the Yuan and Ming Dynasties, pure lime mortar could be found in brickwork; then, sticky rice mortar became the most mature and widely used technology in construction [25].

Modern evaluation shows that the bonding properties of sticky rice mortar were good enough to match modern cement. In addition to its high strength,

sticky rice mortar was characterized by amazing durability [24], and it was used to build important architecture such as city walls, palaces, stone bridges, dams, and so on. After hundreds or even thousands of years, such architecture is still well preserved. Further research found that sticky rice pulp plays the role of biological template, regulating and coordinating the carbonation of mortar so that it will generate nano-sized calcium carbonate crystal with fine structure and improve its toughness, impermeability, and compressive strength [25]. The reason why sticky rice can endure in mortar for a long time in the natural is the anticorrosion effect of lime. The organic and inorganic compositions wrap and pad each other, similarly to the formation process of products of biomineralization, such as bones, teeth, and shells. The incompletely reactive calcium hydroxide, which is wrapped in sticky rice pulp, inhibits the growth of bacteria and thus protects glutinous rice from decay for a long time [26] – [28].

In addition to sticky rice soup, blood mortar was also common in ancient China, and it was mainly used for building painted floors [29]. According to relevant record, Qin Xianyang Palace is paved with blood mortar. Zhejiang University found that animal blood plays an important role in the mortar as it adds air, reduces water, prevents freezing and thawing, resists cracking, and increases bond strength. The underlying mechanism is as follows. Firstly, the protein in the blood is expected to have a foaming ability; thus, the small bubbles can improve the mortar’s workability. Secondly, anions and hydrophilic groups in blood protein can generate electrostatic repulsion between mortar particles and improve their dispersion. Thirdly, blood protein is decomposed in an alkaline environment, connects with calcium ions in mortar and enhances bond strength. Fourthly, the amino and carboxyl groups in blood protein provide waterproof ability.

Tung oil mortar is mainly composed of boiled tung oil and lime mortar [30] because it has good water resistance, anti-codling, and bond strength. Thus, in ancient China, it was widely used in water wells’ hooks, wooden boats’ greasy seams, hole filling, housing grounds, and where buildings had special requirements in waterproof ability and durability. The main components of tung oil mortar are calcium carbonate and calcium carboxylate, which give it better mechanical properties, waterproof properties, and weathering resistance.

The following admixtures which are listed in Table 1 are used to modify the properties of lime mortar. The superscript “C” in the table indicates that

the type of additive was used in China, and the superscript “R” in the table indicates that the type of additive was used in Roma.

Table 1 Additions and their purposes used in ancient architecture.

The name of additions	The purpose of use
Raw Sugar <sup>C</sup>	Bonding agent
Sugar <sup>C</sup>	Prevent shrinkage
Egg white <sup>C, R</sup>	Improve strength
Soybean milk <sup>C</sup>	Better bonding
Animal Blood <sup>C, R</sup>	Better Viscosity
Tong oil <sup>C</sup>	Waterproof
Straw fiber <sup>C, R</sup>	Better bonding
Jute fiber <sup>C, R</sup>	Better bonding
Bean dregs <sup>C</sup>	Better bonding
Paste(wheat) <sup>C</sup>	Better bonding
Sand <sup>C, R</sup>	Improve strength
Ceramic chip <sup>R</sup>	Improve strength
Brick bat <sup>R</sup>	Improve strength
Gypsum <sup>C, R</sup>	Work ability

## CONCLUSIONS

Historical records have proved the efficiency of additives used in lime mortars, especially in terms of improving durability for hundreds/thousands of years with construction quality.

Further research is needed on the performance of these additives not only for restoring and preserving existing old buildings but also for their application in modern and future construction. In recent research, sticky rice has been proved to play a crucial role in regulating calcite crystal growth and improving its endurance. The same mechanism may be used in MICP/EICP technologies and improve the effect of treated samples as well.

## REFERENCES

- [1] Blackman, D. J. (1982) Ancient harbours in the Mediterranean, *IJNA* 11: 79–104, 185–211.
- [2] Gazda, E. K. (2001) Cosa's Contribution to the Study of Roman Hydraulic Concrete: An Historiographic Commentary, in N. W. Goldman (ed.), *Classical Studies in Honor of Cleo Rickman Fitch*, 145–77. New York.
- [3] Delatte, N. (2001). "Lessons from Roman Cement and Concrete." *J. Prof. Issues Eng. Educ. Pract.*, 127(3), 109–115.
- [4] <https://www.dreamstime.com/pantheon-rome-ancient-pantheon-rome-cloudy-sunrise-italy-image141378165>
- [5] Adam, J-P. (1994). *Roman building: Materials and techniques*, Indiana University Press, Bloomington, Ind.
- [6] Vitruvius, M. (1960). *The ten books on architecture*, M. H. Morgan, translator Dover, New York.
- [7] White, K. D. (1984). *Greek and Roman technology*, Cornell University Press, Ithaca, New York.
- [8] Gianfrotta, P. A., 1996, Harbour structures of the Augustan Age in Italy, in A. Raban and K. G. Holum (eds), *Caesarea Maritima: a Restrospective after Two Millennia*, 65–76. Leiden.
- [9] Jackson, M.D., Vola, G., Všíanský, D., et al. (2012) Cement microstructures and durability in ancient Roman seawater concretes. In: Válek, J., Groot, C. and Hughes, J. (eds), *Historic mortars, characterisation, assessment and repair*, pp. 49–76. Springer, Berlin.
- [10] University of Utah (2017) How seawater strengthens ancient Roman concrete. <https://unews.utah.edu/roman-concrete/> [accessed 11 December 2017].
- [11] Jackson, M.D. (2014) Seawater concretes and their material characteristics. In: Oleson, J.P. (ed.), *Building for eternity: the history and technology of Roman concrete engineering in the sea*, pp. 141–187. Oxbow Books, Oxford.
- [12] Dean, A.M. (2017) Rock solid history of concrete – how limestone, rocks, and volcanic ash built the modern world. <https://www.concretepavements.org/2017/10/18/rock-solid-historyof-concrete-how-limestone-rocks-and-volcanic-ash-built-the-modern-world/> [accessed 11 December 2017].
- [13] Jackson, M.D., Mulcahy, S.R., Chen, H., et al. (2017) *Am. Mineral.*, 102, 1435–1450.
- [14] Witze, A. (2017) *Nature News*. 3 July. <https://www.nature.com/news/seawater-is-the-secret-to-long-lasting-roman-concrete-1.22231> [accessed 11 December 2017].
- [15] Yao Y. *The History of Xi'an in Han Dynasty (Science and Technology) (in Chinese)*. Xi'an: Shanxi People's Publishing House, 1993. 477–478.
- [16] Zuo Q M (Spring and Autumn Period). *Zuo Zhuan (in Chinese)*. Changsha: Yuelu Press, 2001. 289.
- [17] <https://www.dreamstime.com/stock-images-great-wall-china-image21049254>.
- [18] Pu S. North Yan tomb in Yuantaizi village, Chaoyang country, Liaoning province (in Chinese). *Cul Rel*, 1994, 11: 43–47.
- [19] Yao Q Z, Lv Da. On historical evolution of the ancient Tongwan City & its architecture (in Chinese). *J Yan'an Univ (Social Science Edition)*, 2004, 26 (2): 126–128.
- [20] Shen Kuo (Song Dynasty). *The Dream Rivulet Diary (in Chinese)*. Changchun: Times Wenyi

- Press, 2001. 110.
- [21] Tang C R. References of Chinese General History (in Chinese). Beijing: Zhong Hua Press, 1983.
- [22] Archeology crew of Henan province. A Stick Tomb with Colorized Portrait in Deng Country, Henan Province (in Chinese). Beijing: Cultural Relic Press, 1958.
- [23] Alexandra Olga Pintea. New types of mortars obtained by adding traditional mortars with natural polymers to increase physico-mechanical performances. *Procedia Manufacturing*, 32 (2019)201–207
- [24] Wu Q Z. The experience and implication for the flooding control in the ancient towns in China (continued) (in Chinese). *City Plan Rev*, 2002, 26 (5): 76—84
- [25] Vintilă-Bolchiș, O. The Great Wall of China has overcome a century due to rice. *The Diary.ro*. [Publication Date] 05 06 2010. [Quote: 18 03 2018.] <http://jurnalul.ro/afla-ce-e-nou/marele-zid-chinezesc-a-rezistat-sutelor-de-ani-datorita-orezului-545810.html>.
- [26] Yang F, Zhang B, Ma Q. Study of sticky rice lime mortar technology for the restoration of historical masonry construction. *Acc Chem Res* 2010; 43:936–44.
- [27] Yuyao Zeng, Zhang Bingjian, Xiaolin Liang. Study on characteristics and consolidation mechanism of historical mortar materials. *Sci Conserv Archaeol* 2008; 2:1–7 (in Chinese).
- [28] Zeng Yuyao, Zhang Bingjian, Liang Xiaolin. A case study and mechanism investigation of typical mortars used on ancient architecture in China. *Thermochim Acta* 2008; 473:1–6.
- [29] Li Hongming. Studies on properties and formula of traditional lime mortar. Taiwan: National Cheng Kung University; 2005.
- [30] Ma Tao, Chong-bin Bai, Yang Qi. Studies on the traditional techniques and the conservation method of polychrome paintings on wooden structures of Chinese traditional buildings. *Wen Bo* 2009; 6:412–2



# EFFECTIVENESS OF SAND COMPACTION PILE AND PREFABRICATED VERTICAL DRAINS IN IMPROVING SOFT SOIL FOR PAVEMENT SUBGRADE

Tanim Shahriar<sup>1</sup> and Shah Md Muniruzzaman<sup>1</sup>

<sup>1</sup>Faculty of Civil Engineering, Military Institute of Science and Technology, Bangladesh

## ABSTRACT

The study examines the effectiveness of Sand Compaction Pile (SCP) and Prefabricated Vertical Drains (PVD) in improving properties of soft soil underlying road pavement. Subgrade improvement techniques are often used to reinforce the subsoil properties with regards to its bearing capacity, shear strength, settlement etc.

This research scrutinized two interconnecting roads at Jolshiri outskirts of Dhaka city. Physical soil properties were measured at four different locations, two locations each from both the roads. Average SPT-N values were found around 3 to 4 before subgrade improvement. Basing on soil properties and SPT-N values, suitable dimensions and parameters of SCP and PVD were designed. SCP was installed in one of the road mainly due to constrain of time of construction. PVD was conducted at another road as there was flexibility of time. SPT test was executed again and average SPT-N values were found around 14 to 18 in all four locations. Dynamic Cone Penetration (DCP) test was performed to check the suitability between SCP and PVD. DCP test results shows that PVD provides slightly more compacted ground surface than SCP at shallow depth. An economic analysis was also carried out to check the cost effectiveness. SCP found considerably cheaper when compared to PVD which needs geotextile and other imported materials.

All soil properties and test results were analyzed to determine the impact of subgrade improvement and compare the effectiveness. It is found that, SCP and PVD are two technically viable and cost-effective solutions for soils which are weak in strength and needed treatment.

*Keywords: Sand Compaction Pile, Prefabricated Vertical Drain, Dynamic Cone Penetration*

## 1. INTRODUCTION

The performance of road pavement depends largely on its subgrade layer that provides support to a whole pavement system. As such, subgrade layer plays a key role in mitigating the detrimental effects of geotechnical, environmental and dynamic stresses generated by the traffic load, and building a stable subgrade is vital for constructing an effective and sustainable pavement system.

## 2. BACKGROUND OF THE STUDY

Many subgrade improvement techniques are practiced around the globe. Out of these subgrade improvement techniques, some of them are widely practiced in our country. Among these, SCP is one of the potential methods for improving ground stability. This method was originally developed in order to increase the density of loose sandy ground and to increase the uniformity of sandy ground, to improve its stability or compressibility and to prevent liquefaction failure. It has also been applied to soft clay ground to assure stability and to reduce ground settlement [1]. The principal concept of the SCP method for application in sandy ground is to increase the ground density by placing a certain amount of granular material (usually sand) in the

ground [2].

In road construction on compressible, saturated soils like loose and soft clay, excessive settlement is a common problem to deal with. The subgrade improvement technique using Prefabricated Vertical Drains (PVD) are one of the most appropriate methods to overcome this problem. Vertical draining of fine-grained soils for ground improvement purposes was first advised and applied in the US in the late 1920's [3]. In the early days of the method, there was some pioneer work done by a Swedish engineer, Walter Kjellman, who patented a type of prefabricated cardboard drain and equipment for its installation. Later on, methods for designing vertical drains were developed by Barron in 1948. However, the design of vertical drains today is based mainly on the subsequent and more practical, simplifications and additions to the theory [4].

In Bangladesh SCP and PVD have been used in few highway projects in subgrade improvement recently. In this research a venture is taken to look over the effect of subgrade improvement using SCP and PVD methods.

## 3. DESCRIPTION OF THE STUDY AREA

Dhaka, one of the fastest growing megacities of the world experiences huge pressure of mass

population and traffic congestion. Two east bound roads Purbachal Expressway and Madani Avenue traversed to connect Dhaka city with its Eastern region. Considering inter connectivity, it had been decided to construct two roads of 3.25 km (Purbachal 300 feet Expressway to Madani Avenue) and 3.79 km (Madani Avenue extension up to Shittalakha River) in this area. But both these future roads situated on the reclaimed area with soft clay soil underground. These two roads would require substantial subgrade improvement to withstand future designed traffic load. The study area was located at this reclaimed land of Purbachal commonly known as Jolshiri Abashon. The area was basically a low-lying paddy field which was later sand filled for housing project about 10 years ago. The surface of the ground seems to be settled and hard enough. But underlying ground were still comprising very loose, soft clay or sandy layer of soil. The main features of this area are two inter-connecting under construction roads from Jolshiri to Shittalakha River and Jolshiri to Purbachal 300 feet Expressway. Locations of the study area are represented in Fig 1.

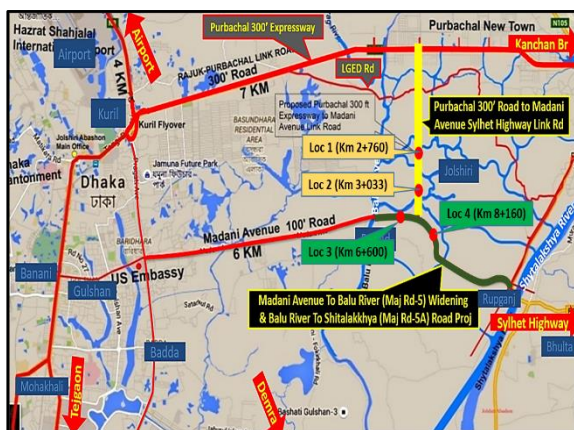


Fig. 1 Locations of study area (marked as dots).

Table 1 SCP and PVD test locations

Location	Chainage (km)	Description
1	2+760	300 feet expressway to Madani Avenue link road
2	3+033	Same as location 1
3	6+600	Madani Avenue to Shitalakkhya river road
4	8+160	Same as location 3

Table 1 shows the description of four locations of the study area and the chainages are mentioned in km.

## 4. METHODOLOGY

### 4.1 Standard Penetration Test (SPT)

The Standard Penetration Test, commonly known as SPT, was forwarded to provide subgrade properties for highway design basis. The test was brought out in this study area to ascertain the soil properties of the study area [5]. The results can be used to determine soil properties like specific gravity, Atterberg limit test, particle size distribution etc.

Typical components of a SPT set up used in this study are shown in the picture of Fig. 2.



Fig. 2 Standard Penetration Test (SPT) setup

### 4.2 Soil Properties before Ground Improvement

The condition of the soils at the four different locations are almost similar based on tests. Inside each of the boreholes at different layers loose silty sand, lean clay and fat clay type soil was found in all the four sampling locations.

According to soil properties, it was found that the value of specific gravity varied in between 2.65 and 2.75 in all the sampling boreholes. Atterberg Limit Test assured that, till depth of 3m Silty sand was identified and the next advancing layers had lean clay, fat clay at the 4 different locations. The laboratory test depicted that the liquid limit and the plasticity index of the soils were almost same.

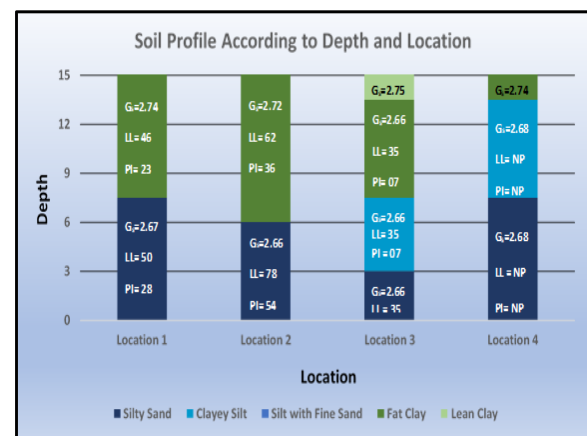


Fig. 3 Soil condition at four different locations

### 4.3 Sand Compaction Pile (SCP)

Sand Compaction Pile (SCP) method was used in this study area to build up loose and soft clay ground by installing sand or a similar material into the soft ground via a casing pipe manually to assemble strongly compacted sand piles in the ground.

#### 4.3.1 General specification

Table 2 Design of SCP

Diameter of pile	300 mm
Length of pile	8 meter
Spacing	1.4 meter
SCP Arrangement	Triangular Arrangement

A 1500 rpm traditional rig machine and a two-end open casing pipe 8 mm thickness and 300 mm in diameter and 8 m long with a vibro-hammer of weight 1000 kg. The vibro-hammer was 250 mm in diameter and 3.00 m long. The construction sequences are described in the following statements.

A two-end open casing pipe, 300 mm in diameter and 8 m long was placed vertically at the designed point on the natural ground surface for sand pile construction. The casing Pipe was then inserted vertically into the ground about 300 mm to 450 mm depth at its own weight just by applying some pressure manually.

At first a plug is made by the designated sand up to 750 mm of casing pipe at bottom level. The vibro-hammer 250 mm in diameter and 3.0 m long, weighting 1000 kg was placed inside the casing pipe. The vibro-hammer displaced the soil from beneath the casing pipe hence the casing pipe was driven by its own weight till reached the designated position (depth) into the ground. Here one casing pipe of 7 m long was driven inside the ground.

After reaching the designated depth, the sand plug is broken by providing excess energy then the vibro-hammer is withdrawn from the casing pipe. Casing pipe was then lifted up by about 1m from its original bottom position. The designated granular materials were poured into the hole about 1m layer thickness measured from the bottom. The poured granular materials were densified by vibro-hammer till the required compactness achieved. Casing pipe was then withdrawn from inside the ground that left the bottom portion of hole unsupported and the top portion supported by the casing pipe. It was observed that the bottom portion of the hole standing safely without any lateral support. Then hole was poured by the selected granular materials in layers and hence 10~15 drops compacted each layer was densified by vibro-hammer till the designated compactness was reached. After the top of granular piles were reached about 1.0~1.5 m below the

ground surface the casing pipe was withdrawn and left the remaining hole unsupported. The process was continued until the granular piles were constructed up to the ground level [6].



Fig. 4 Sand Compaction Pile (SCP) installation

### 4.4 Prefabricated Vertical Drain (PVD)

Prefabricated Vertical Drains (PVDs) or Wick Drains are formulated of a plastic core confined by a geotextile for the basis of accelerating consolidation of slow draining soils. They are typically coupled with surcharging to expedite preconstruction soil consolidation.

#### 4.4.1 General specification

Table 3 Design of PVD

Average length	15 meter
Average Spacing	1.5 meter
Sand blanket height	0.6 meter (FM >2.5)
Surcharge height	1 meter (FM >1)



Fig. 5 Installation of Prefabricated Vertical Drain

The spacing and pattern of the drains are now

fairly well standardized. In most situations, triangular or square grid spacing of 1-4 m is used with 1.5-2.5 m being most commonly adopted.

A number of sections was defined and each section was indicated by a letter code. For each section a predefined installation depth for the drains was required. This depth was selected according to the design parameters. A section was set out based on the information from the detail survey as per site condition. The four corners of each section were marked with pegs. The grid, which defined the actual positions of the drains, had a triangular or square spacing as specified by the design specification. The individual drain position was marked by pulling a nylon string, marked with the required drain spacing along the alignment of the drain positions. The anchor plate was used to mark the position of the drain. The drain was placed in position in the grid, with a tolerance of 150 mm.

The leader was aligned on top the drain location. The drain was wrapped around the fixture on the anchor plate (dimensions: 140x80x1 mm), dimensions might vary depending on soil conditions and the folded end of the wrapped drain was pulled back into the mandrel, until the plate rested against the base of the mandrel. The hydraulic motors of the machine pushed the mandrel to the design depth. The drains were installed to the depth as defined above, with a tolerance of 150 mm. The operator saw on the display of the drain logger, if the mandrel had been inserted till the required depth. This actual depth varied due to irregularities in the layer profile.

On reaching the depth of the drains, the operation was reversed and the mandrel was withdrawn from the PVD. The anchor plate locked itself at the driven depth such that the drain was fixed as the mandrel rises. The drain roll was mounted on the side of leader allowing the drain to be fed into the mandrel through a series of rollers, which prevent damage and minimize friction. Once the mandrel cleared the ground surface, the drain was cut off approximately 250 mm above ground level and the drain was installed. The leader was aligned onto the next drain position and the above procedure was repeated [7].

#### 4.5 Dynamic Cone Penetration (DCP)

Dynamic Cone Penetration (DCP) testing is operated to evaluate subgrade's strength and the thickness and location of subgrade soil layers. In this study, DCP test was also conducted to check the suitability of SCP and PVD through average CBR percentage. Figure 5 represents Dynamic Cone Penetration test in the study area.

After assembly, the zero reading of the apparatus was recorded. This was done by standing the DCP on a hard surface, such as concrete, checking that it was vertical and then entering the zero reading in the

appropriate place on the data sheet. The instrument was held vertical and the weight carefully raised to the handle. It was carefully ensured that the weight was touching the handle, but not lifting the instrument, before it was allowed to drop and that the operator let it fall freely and did not lower it with his hands. It is recommended that a reading should be taken at increments of penetration of about 10 mm. However, it is usually easier to take a scale reading after a set number of blows.

Therefore, it was necessary to change the number of blows between readings according to the strength of the layer being penetrated. For good quality granular bases readings every 5 or 10 blows are normally satisfactory but for weaker sub-base layers and sub-grades readings every 1 or 2 blows may be appropriate. After completing the test, the DCP was removed by gently tapping the weight upwards against the handle [8].



Fig. 6 Implementation of Dynamic Cone Penetration (DCP) test

## 5. RESULTS AND ANALYSIS

### 5.1 Soil Properties (up to 8 meter depth)

Table 4 Soil properties after SCP installation at location 1 and location 2

Properties	Location 1	Location 2
Specific Gravity	2.56	2.68
Liquid Limit	0	0
Plastic Limit	NP	NP
Plasticity Index	NP	NP

Table 5 Soil properties after PVD installation at location 3 and location 4

Properties	Location 3	Location 4
Specific Gravity	2.69	2.67
Liquid Limit	0	0



Plastic Limit	NP	NP
Plasticity Index	NP	NP

## 5.2 Results of Sand Compaction Pile

Then columns were installed, the area replacement ratio is defined as,

$$a_s = C \times (d_c \div s)^2$$

Where,  $a_s$  = area replacement ratio

$d_c$  = diameter of the column

$s$  = Center to center spacing of columns in a square or equilateral triangular pattern

$C$  = Constant (0.907 for an equilateral triangular pattern)

Kensetsu Kikai Chosa suggested the average weighted SPT-N value including the sand compaction column and the surrounding soil as follows [9]:

$$N_{eq} = a_s \times N_2 + (1 - a_s) \times N_1$$

Where,

$N_{eq}$  = average weighted (equivalent) SPT N value

$N_1$  = SPT N value in the surrounding soil

$N_2$  = SPT N value in the sand compaction column.

For 1st Location: SPT-N value at 3-meter depth;

SPT-N Value midway between sand compaction columns,  $N_1 = 21$

SPT-N Value in the center of sand compaction columns,  $N_2 = 22$

Area Replacement Ratio,

$$a_s = C \times (d_c \div s)^2 = 0.907 (0.3 \div 1.4)^2 = 0.04165$$

Now for example at 3 meter depth, the average weighted SPT-N value including the sand compaction column and the surrounding soil,

$$N_{eq} = a_s \times N_2 + (1 - a_s) \times N_1 = 0.04165 \times 22 + (1 - 0.04165) \times 21 = 21$$

Table 6 Comparison between SPT-N values before and after execution of SCP at location 1

Depth	SPT-N (before SCP)	Average SPT-N (before SCP)	SPT-N (after SCP)	Average SPT-N (after SCP)
1	-	4.20 $\approx$ 4	18	18.25 $\approx$
1.5	4		-	18
2	-		18	
3	4		21	
4	-		19	
4.5	3		-	
5	-		17	
6	5		18	

7	-	19
7.5	5	-
8	-	16
9	4	8
10	-	8

From Table 6, it can be seen that at 3 meter depth before installation of SCP the SPT-N value was very low and the value was 4. The soil condition was not suitable for highway construction and soils were mostly loose and very soft fat clay. Average SPT-N value was identified around 4 up to 10 meter depth. After installation of sand column, subgrade conditions improved and become silty fine sand. SPT-N values were also increased after execution of SCP and average SPT-N value was found 18 up to 10 meter depth.

Table 7 Comparison between SPT-N values before and after execution of SCP at location 2

Depth	SPT-N (before SCP)	Average SPT-N (before SCP)	SPT-N (after SCP)	Average SPT-N (after SCP)
1	-	3.20 $\approx$ 3	18	18
1.5	7		-	
2	-		16	
3	4		17	
4	-		19	
4.5	2		-	
5	-		17	
6	1		19	
7	-		21	
7.5	2		-	
8	-		17	
9	1		7	
10	-		8	

From Table 7, it is observed that at 6 meter depth before installation of sand compaction pile SPT-N value was as 1. Average SPT-N value was obtained 3 up to 10 meter depth. After installation of SCP, Subgrade conditions become Silty Fine Sand. SPT-N values were also increased after execution of SCP and average SPT-N value was found around 18 up to 10 meter depth.

### 5.2.1 Findings

a. After the installation of SCP, the loose to very loose clay soil becomes Silty Fine Sand.

b. At location 1, SPT-N value was found around 4 before the installation of SCP. After the installation of SCP, the SPT-N value was investigated around 18 up to 10 meter depth.

c. At location 2, SPT-N value was found around 3 before the installation of SCP. After the installation of SCP, SPT-N values was found around 18 up to 10 meter depth.

d. The SPT-N value after execution of SCP was found 18 at two different locations which is sufficient enough for pavement subgrade.

e. SCP can be installed isolate for a smaller area.

f. By the installation of SCP, soil becomes Silty Fine Sand.

### 5.3 Results of Prefabricated Vertical Drain

Table 8 Comparison between SPT-N values before and after execution of PVD at location 3

Depth	SPT-N (before SCP)	Average SPT-N (before SCP)	SPT-N (after SCP)	Average SPT-N (after SCP)
1	-	3.40 $\approx$ 3	13	13.87 $\approx$
1.5	3		-	14
2	-		14	
3	4		18	
4	-		14	
4.5	4		-	
5	-		13	
6	3		12	
7	-		16	
7.5	3		-	
8	-		11	
9	4		12	
10	-		10	

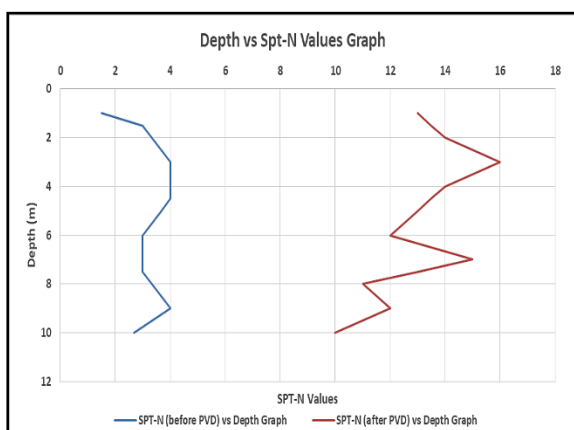


Fig. 7 SPT-N values of before and after execution of PVD at Location 3

SPT-N value was increased and soil condition was also improved after installation of PVD in these

locations. Very loose Silty Sand, Yellowish Gray and Lean Clay became mostly Sand after subgrade improvement at location 3. Average SPT-N value was found 14 up to 10 meter depth. The recommended SPT-N value for highway construction is around 10. Installation Reduced Level (RL) was 7.770 meter on June 22, 2020. Plate Pipe Top RL was found 7.578 meter on Jan 21, 2021. Soil settlement was found 192 mm (7.56 inch) after seven months. A graphical representation of cumulative settlement of soil (in mm) with time after installation of Prefabricated Vertical Drain (PVD) is shown below in Figure 8.

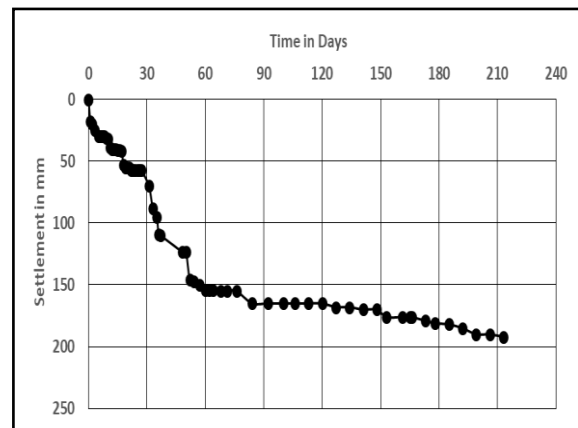


Fig. 8 Cumulative Settlement after Installation of PVD at location 3

Table 9 Comparison between SPT-N values before and after execution of PVD at location 4

Depth	SPT-N (before SCP)	Average SPT-N (before SCP)	SPT-N (after SCP)	Average SPT-N (after SCP)
1	-	3.40 $\approx$ 3	13	13.87 $\approx$
1.5	3		-	14
2	-		14	
3	4		18	
4	-		14	
4.5	4		-	
5	-		13	
6	3		12	
7	-		16	
7.5	3		-	
8	-		11	
9	4		12	
10	-		10	



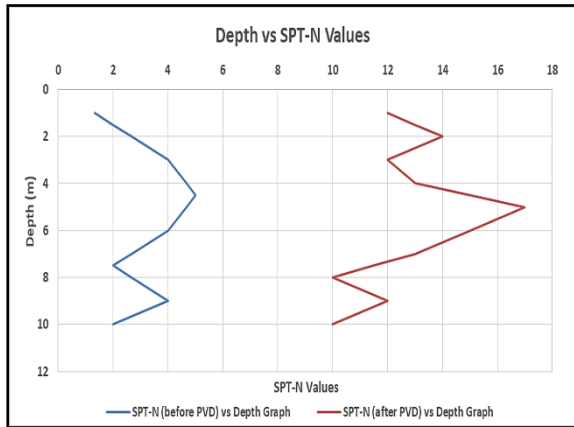


Fig. 9 SPT-N values of before and after execution of PVD at location 4

At location 4, very loose Silty Sand, Yellowish Gray and Lean Clay became mostly Silty Sand after subgrade improvement. Average SPT-N value was found also 14. Installation Reduced Level (RL) was 7.759 meter on June 22, 2020. Plate Pipe Top RL was found 7.595 meter on Jan 21, 2021. Soil settlement was found 164 mm (6.45 inch) after seven months.

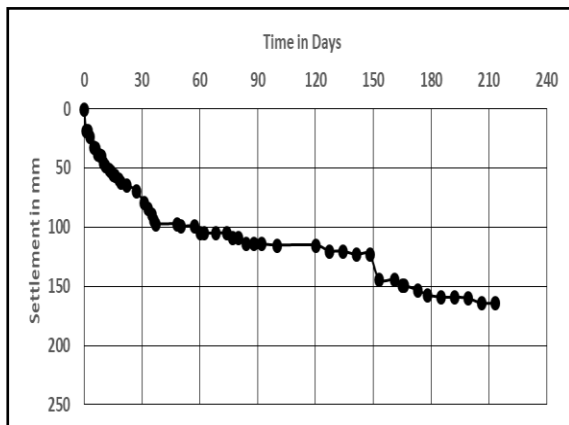


Fig. 10 Cumulative settlement after installation of PVD at location 4

#### 5.4 Results of Dynamic Cone Penetration

DCP was done at location 1, 2 and location 3, 4 where SCP and PVD were done before. DCP test was done to show the comparison between SCP and PVD, which is suitable for subgrade improvement.

After installation of SCP at location 1, soil becomes Silty Sand. The penetration reading were taken at 90 mm to 390 mm (total depth 300 mm) and 28 blows were counted. The 1st Layer thickness was 135 mm (8 no blows) and the average CBR percentage was found 14.94. Next layer thickness was 165 mm (20 no blows). Here CBR percentage was found 31.3. DCP termination depth was taken -

0.3 meter. Average CBR percentage for the full depth can be taken 24%.

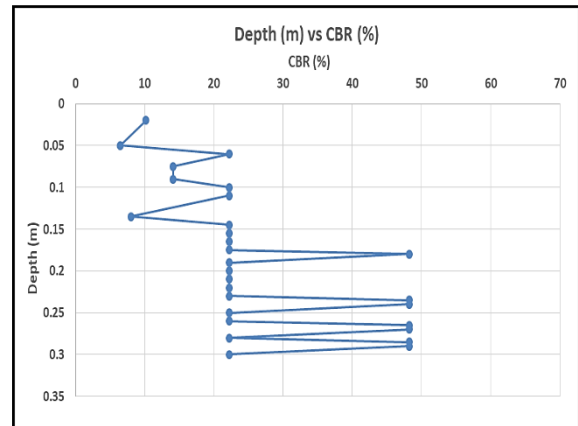


Fig. 11 Graphical representation of depth (m) vs CBR (%) at location 1

After installation of SCP at location 2, soil becomes Silty Sand. Penetration reading of DCP was taken from 100 mm to 415 mm (total depth 315 mm). The 1st layer thickness was 110 mm (4 no blows) and the average CBR percentage was found 7.73. Next layer thickness was 205 mm (17 no blows) and CBR percentage was found 19.11. The DCP termination depth was taken 0.315 meter. Average CBR percentage for the full depth can be taken 15%.

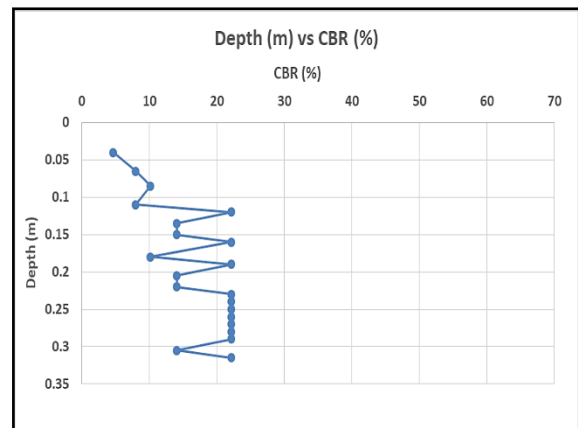


Fig. 12 Graphical representation of depth (m) vs CBR (%) at location 2

After installation of PVD at location 3, The DCP penetration reading were taken from 140 mm to 365 mm (total depth 225 mm). The 1st layer thickness was 95 mm up to 235 mm depth (3 no blows) and the average CBR percentage was found 6.73. The 2nd layer thickness was 45 mm (4 no blows) and CBR percentage was found 20.18. Next layer thickness was 85 mm (13 no blows) and CBR percentage was found 40.2. The DCP termination

depth was taken as 0.225 meter. Average CBR percentage for the full depth can be taken 22%.

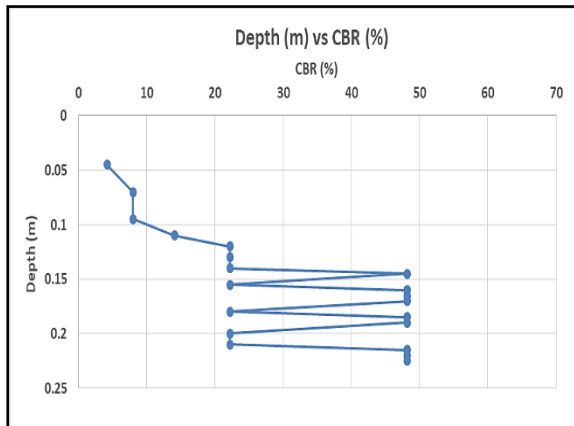


Fig. 13 Graphical representation of depth (m) vs CBR (%) at location 3

After installation of PVD at location 4, the DCP penetration reading was taken from 125 mm to 420 mm (total depth 295 mm). 26 number of blows were counted. The layer thickness was 295 mm (26 no blows). Average CBR percentage was 20.87. The DCP termination depth was taken as 0.295 meter. The average CBR percentage for the full depth can be taken 21%.

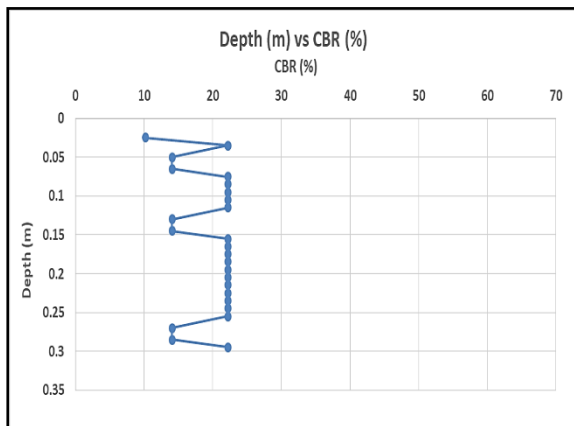


Fig. 14 Graphical representation of depth (m) vs CBR (%) at location 4

#### 5.4.1 Findings

The results of DCP test were used to estimate the CBR of subgrade soil of both types of sites (improved by SCP and PVD) using the procedures suggested by ASTM D6951 (2018). The following observations obtained from DCP test are given below:

a. The DCP test was performed in shallow depth (only up to 0.4 meter) to assess the strength of subgrade at top surface. The DCP test was

conducted after ground improvement only to compare effectiveness of SCP and PVD.

b. From Figs. 4.7 to 4.10, the average CBR (%) was found 19.5% and 21.5% respectively subgrade improvement done by SCP and PVD respectively. The average CBR as such was slightly higher where ground improvement was conducted through PVD than that of SCP. Therefore, it is understood that SCP and PVD provide comparable CBR at shallow depth.

c. One of the probable causes of higher CBR due to PVD might be that DCP test was done at shallow depth after the removal of surcharge and thus soil was under compression.

## 6. ECONOMIC ANALYSIS BETWEEN SCP AND PVD

There are multitude of factors which are required to be considered for economic analysis between SCP and PVD such as: diameter of the pile, spacing, length of pile, fineness modulus (FM) are estimated in subgrade improvement for SCP whereas Prefabricated Vertical Drain depends upon composite drain properties, filter fabric properties, average spacing, length, sand blanket height, surcharge height etc. This economic analysis is specific to this area and particular to this design of SCP and PVD.

### 6.1 Cost for Sand Compaction Pile (SCP)

The following specification has been considered for SCP at site:

Diameter of pile :	300 mm
Length (Depth) of pile :	8 meter
Spacing :	1.4 meter
FM of filled sand :	2.5
Volume of Sand :	0.25 cum/meter

Considering 100 square meter area:

Quantity of SCP in 100 sqm area

= Total No of Borehole x Depth of Pile = 60 x 8

= 480 RM

Rate of SCP per RM = 930.49 BDT (11 USD) [10]

Total Cost = 480 x 930.49 BDT

= 4,46,635.20 BDT (5207.33 USD)

### 6.2 Cost for Prefabricated Vertical Drain (PVD)

The following specification has been considered for SCP at site:

Average Spacing =	1.5 meter
Average length =	15.0 meter
No of PVD in 100 sqm area =	42
Sand Blanket height =	0.6 meter (FM >2.5)
Surcharge height =	as per filling height say 1 meter (FM >1.0)

Considering 100 square meter area:

Quantity of PVD requires in 100 sqm area

= Number of PVD x Length of PVD  
 = 630 RM  
 Rate of PVD per RM=268.56 BDT (3.18 USD) [10]  
 Sand Blanket required in 100 sqm area = 60 cum  
 Rate of Sand Blanket per cum = 2830 BDT (33.46 USD) [10]  
 Surcharge required in 100 sqm area = 100 cum  
 Rate of Surcharge per cum = 420 BDT (4.97 USD) [10]  
 Soil Settlement required in 100 sqm area =  $100 \times 0.18 = 18$  cum  
 Rate of Soil Settlement per cum = 181.44 BDT [10]  
 So, Total cost of PVD in 100 sqm area  
 =  $(630 \times 268.56) + (60 \times 2830) + (100 \times 420) + (18 \times 181.44)$  BDT  
 = 6,10,641.92 BDT (7119.49 USD)

### 6.3 Findings from Economic Analysis

Total cost of PVD = 6,10,641.92 BDT (7119 USD)  
 Total cost of SCP = 4,46,635.20 BDT (5207 USD)  
 Therefore, difference of cost is  $(6,10,641 - 4,46,635)$   
 = 1,64,006 BDT (1912 USD) per 100 sqm area  
 The result evidently shows that SCP cost is 1.37 times (37%) higher/costly than PVD cost.

## 7. SUITABILITY COMPARISON

Both SCP and PVD are suitable for improving subgrade strength at soft soil. However, when both these two methods were applied on ground some advantages and disadvantages were observed between these two. According to survey data analysis and observation, following comparison between SCP and PVD may be brought out:

a. With the installation of SCP at location 1 and 2, subgrade soil condition was improved and SPT-N values also increased significantly. The SPT-N value raised around 18 from 4 at location 1 and raised around 18 from 3 at location 2 up to the depth (8 meter) where sand piles are driven.

b. With the installation of PVD at location 3 and 4, subgrade soil condition was improved and SPT-N values also increased sharply. The SPT-N value raised around 14 from 3 at location 3 and raised around 14 from 3 at location 4 up to the depth examined (8 meter).

c. Average CBR (%) was found around 19.5% where subgrade improvement has been done through SCP and 21.5% where subgrade improvement was conducted through PVD. Average CBR (%) is slightly higher where ground improvement was conducted through PVD than that of SCP.

d. The primary advantage of SCP is that the sand used is considerably cheaper when compared to PVD which needs geotextile and other imported materials. In comparison to Prefabricated Vertical Drains, SCP is more economic. In this case, PVD cost is 1.37 times (37%) higher/costly than SCP cost.

e. Construction of the sand columns is extremely fast. Several SCP can be constructed very easily within a day whereas PVD takes around seven months due to soil settlement.

## 8. CONCLUSION

SCP method is one of the typical ground improvement methods to densify the ground by installing compacted sand piles into ground. PVDs are a type of geo-composites which has got application in highway construction. It slacks time requirement and amount of surcharge required in a given time. It also augments the rate of strength gain due to consolidation of soft soils when stability is of major concern. In the context of Bangladesh both SCP and PVD are much efficacious for ameliorating subgrade improvement techniques. SCP can be constructed very easily where as PVD takes a long time due to soil settlement. Both are excellent techniques in context of Bangladesh.

## 9. REFERENCES

- [1] Hossain, M. Z., “Effectiveness of Sand Compaction Piles in Improving Soil Bed Formed of Alluvial Deposits of Bangladesh”, M. Sc. Engg. Thesis, Department of Civil Engineering, BUET, Bangladesh, pp. 1, 2015.
- [2] Kitazume, M., “The Sand Compaction Pile Method”, A.A. Balkema Publishers, London, UK, 2005.
- [3] Hansbo, S., “Band Drains”, Ground Improvement (Second Edition), Blackie Academic Professional, U.K, pp. 4-6, 1993.
- [4] Hansbo, S., “Consolidation of clay by band-shaped prefabricated drains.” Ground Engineering, 12(5), pp. 16-25, 1979.
- [5] ASTM: D1586-11, “Standard Test Method for Standard Penetration Test (SPT) and Split-Barrel Sampling of Soils”, American Society for Testing and Materials (ASTM), USA, 2017.
- [6] Samanta, M., Sawant, V.A. and Ramasamy, G. (2010), Ground Improvement using Displacement Type Sand Piles, Proc. Indian Geotechnical Conference, IGS Mumbai Chapter and IIT Mumbai, Dec.16-18, 2010, pp. 629-632.
- [7] Sakleshpur, V. A., Prezzi, M. and Salgado, R., “Ground Engineering Using Prefabricated Vertical Drains: A Review”, Geotechnical Engineering Journal of the SEAGS & AGSSEA, vol. 49, no. 1, March 2018.
- [8] Sharif, G., Standard Test Procedures, Ministry of Communications Roads and Highways Department, Bangladesh, pp 5.21-5.23, May 2001.
- [9] Han, J., “Principles and Practices of Ground Improvement”, New Jersey: Wiley-Sons, 2015.
- [10] “Item of Works and Schedule of Rates”, Dhaka Zone, LGED, 2019-20.

## XRD PATTERNS OF TURBIDITY IN SEEPAGE WATER THROUGH TWO SOIL LAYERS

Shota Takano<sup>1</sup>, Motoyuki Suzuki<sup>1</sup>, Taichi Ishimaru<sup>1</sup> and Asahi Komori<sup>1</sup>

<sup>1</sup>Graduate School of Sciences and Technology for Innovation, Yamaguchi University, Japan

### ABSTRACT

To detect the internal erosion associated with groundwater seepage, it is important to estimate the path of the seepage water flowing under the ground. The authors thought that if the mineral species of the turbidities in the seepage water could be identified by XRD (X-ray diffraction), the flow path of the seepage water could be estimated. It is expected that the XRD patterns of turbidity in seepage water flowing through multi-layered ground, which is composed of various mineral species, will be complex. However, the characterization of XRD patterns of mineral species in seepage water that has passed through multi-layered ground is not always well understood. Thus, the authors analyzed the diffraction patterns by XRD using turbidities composed of multiple minerals discharged by the seepage water passing through two soil layers. In the present study, a model experiment was conducted in which two layers of soil were placed in a cylindrical container and water flowed from the top. Four cases of XRD analysis were performed on the turbidities in the drained water. In each case, the type of soil in the upper and lower layers and the density of each layer were changed. The results showed that the diffraction pattern of the turbidities changed significantly when the upper and lower soil layers had replaced each other. They also showed that the diffraction pattern changed with time in each case.

*Keywords: Suffusion, Internal erosion, XRD, Seepage*

### INTRODUCTION

The loss of fine particles due to internal erosion (suffusion) is believed to affect the deformation and strength properties of the soil [1], [2], [3]. Therefore, it is important to estimate the path of the seepage flow in order to estimate where suffusion may occur in the ground.

The authors thought that by analyzing the fine soil particles contained in seepage water by XRD (X-ray diffraction) and examining their crystal structure, it would be possible to determine which point in the ground these particles are passing and to estimate the path of the seepage flow. However, when the turbidities contained in the seepage water passing in an actual ground are analyzed by XRD, the XRD pattern becomes complicated. The reason for the complexity of the XRD pattern may be that the seepage flow in the ground passes through various soil layers, each time incorporating fine grains of different mineral species. Figure 1 shows an illustration of the mixing of fine grains.

Although studies have been conducted to trace the source of the turbidities in seepage water [4], the discharge behavior of fine grains, when different types of fine grains are simultaneously discharged by seepage, has not been fully clarified. Therefore, in order to investigate the temporal variation of the diffraction patterns of turbidities composed of multiple fine grains discharged by internal erosion, a constant water head one-dimensional infiltration experiment was conducted in this study using two

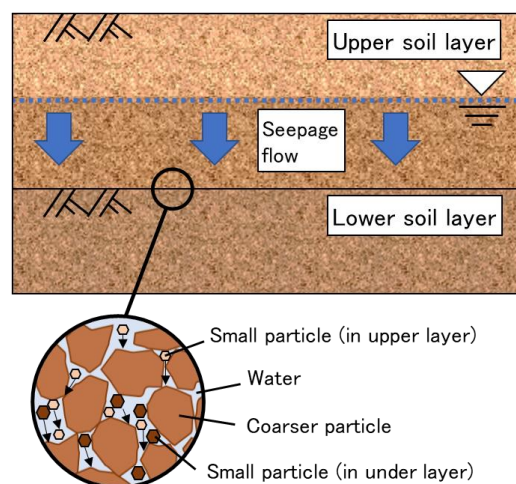


Fig. 1 Mixing of fine grains

types of soil samples to reproduce two layers of the ground, which were vertically drained. The flow rates and effluent concentration obtained from the experiment were then measured, and the turbidities in the effluent were extracted. XRD analysis was then performed to analyze the temporal changes in the crystal structure of the turbidities.

### TEST METHOD

#### Test apparatus

In this study, two types of soil were placed in two layers (upper and lower) in a cylindrical column

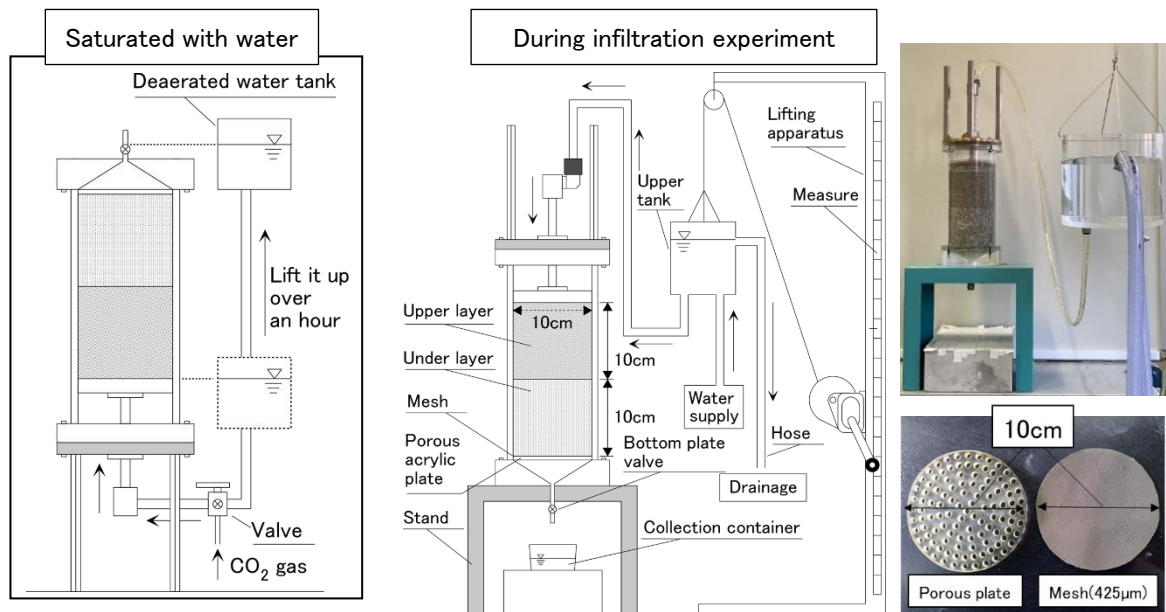


Fig. 2 Schematic of cylindrical column infiltration apparatus

infiltration vessel made of acrylic to reproduce a two-layer ground, and water flowed through the vessel in the vertical direction. Figure 2 shows a schematic diagram of the apparatus.

The inner diameter of the specimen inside the column was 10 cm, and the height of both the upper and lower layers was 10 cm. A porous acrylic plate, with 108 perforations, each with a diameter of 5 mm, and a replaceable mesh were installed at the bottom of the specimen to adjust the particle size of the discharged soil particles. In this study, a 425 µm-diameter mesh was used, thereby allowing only fine sand to flow out. A funnel-shaped depression in the bottom plate of the specimen facilitated the discharge of soil particles.

#### Tested material

The soil samples were composed of host silica sand, which is a mixture of several silica sands of different grain sizes, and kaolin or DL clay mixed to achieve a fine-grain content of 5 %. Table 1 shows the physical properties of kaolin and DL clay. Kaolin and DL clay were used as the fine-grain fraction because of the difference in grain size and the plasticity of the fine fractions, which would result in different discharge behavior during infiltration experiments. The host silica sand was composed of six different grain sizes of silica sand No. 1, No. 3, No. 4, No. 5, No. 6, and No. 7 in the proportions shown in Table 2. The soil sample with the host silica sand and kaolin was named "QK" (quartz sand and kaolin), and the soil sample with the host silica sand and DL clay was named "QDL" (quartz sand and DL clay). Water contents of 11.5 % and 10.6 % were prepared in the cases of QK and QDL, respectively.

Table 1 Physical properties of kaolin and DL clay

	Kaolin	DL clay
Density of soil particles $\rho_s$ (g/cm <sup>3</sup> )	2.675	2.741
Liquid limit $w_L$ (%)	59.9	NP
Plastic limit $w_p$ (%)	35.6	NP
Plasticity index $I_p$	24.3	—

Table 2 Proportion of host silica sand

Silica sand	Grain size (mm)	Proportion (%)
No. 1	4.8~1.7	9
No. 3	3.3~0.8	41
No. 4	2.4~0.3	16
No. 5	1.7~0.2	22
No. 6	0.6~0.07	2
No. 7	0.2~	10
Total	—	100

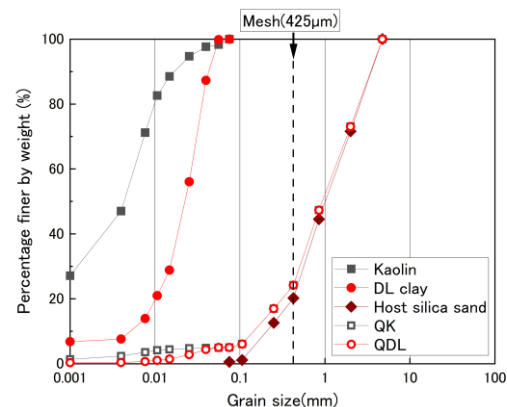


Fig. 3 Percentage finer by weight



### Definition of skeleton relative density $D_{rg}$

The composition of the mixed soil is composed of the void ratio, fines, and sand, as shown in Figure 4. In this study, kaolin and DL clay are the fines, and the host silica sand is the sand. Void ratio  $e$  is obtained by the following equation:

$$e = \frac{V_v}{V_{ss} + V_{sf}} \quad (1)$$

However, based on the idea that the fines are regarded as part of the leakable component, skeleton void ratio  $e_g$ , devised by Mitchell et al. [5], was adopted in this study.  $e_g$  is obtained by the following equation:

$$e_g = \frac{V_v + V_{sf}}{V_{ss}} \quad (2)$$

The maximum void ratio of the host silica sand is defined as maximum skeleton void ratio  $e_{gmax}$  and the minimum void ratio is defined as minimum skeleton void ratio  $e_{gmin}$ . The relative density is defined by  $e_{gmax}$ ,  $e_{gmin}$  and  $e_g$  is defined as skeleton relative density  $D_{rg}$ , as in the following equation:

$$D_{rg} = \frac{e_{gmax} - e_g}{e_{gmax} - e_{gmin}} \times 100 \text{ [\%]} \quad (3)$$

In this study, the soil layer was prepared with  $D_{rg} = 60 \%$  as the relatively dense condition and  $D_{rg} = 30 \%$  as the relatively loose condition.

### Saturation process

Once the two soil layers have been placed in the column infiltration vessel, a lid with legs is attached and the vessel is sealed. The vessel is positioned so that the upper soil layer side is down, and  $\text{CO}_2$  gas is injected upward from the upper soil layer side, as shown on the left side of Figure 2. The specimen is filled with  $\text{CO}_2$  gas for approximately one hour. Deaerated water is then injected upward through the tubes of the deaerated water tank. The deaerated water tank is raised up for approximately one hour until the height of the water surface of the tank is the same as the height of the bottom plate valve. The tank

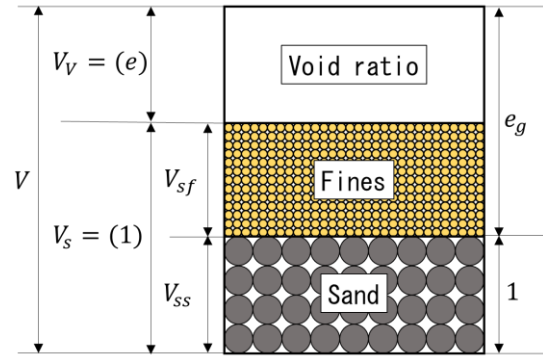


Fig. 4 Schematic of mixed soil

is then allowed to stand for approximately one day to saturate the specimens with deaerated water.

### Infiltration procedure

In this study, the infiltration procedure of Ishimaru et al. [6] is employed. Water is injected into the cylindrical column vessel and a vertical downward seepage flow is applied to the specimens while the water level is kept constant by overflow. In all cases, the height of the water surface in the upper tank of the infiltration device is set to the top of the upper soil layer of the specimen, and the hydraulic gradient is kept constant at  $i = 1$ . As soon as the water starts to flow, the bottom plate valve at the bottom of the device is opened, and 100 mL of seepage water is collected 20 times using a collection vessel, for a total of 2,000 mL of seepage water. The time required to collect 100 mL is measured. After infiltration is completed, soil particles are extracted from the effluent to determine the amount of soil particles discharged.

### TEST CASE







Table 3 shows the details of the test cases in this study. In total, four cases of infiltration experiments were conducted, employing two different fine-grained and two skeleton relative density conditions. The thickness of both soil layers in the specimens was 10 cm. The case name means [Upper soil layer type (QK or QDL) + Lower soil layer type (QK or QDL) –  $D_{rg}$  (30 % and 60 %.)].

Table 3 Specimen preparation conditions

	Case name	Fines (upper layer)	Fines (lower layer)	$D_{rg}$ (%)
Case 1	UQK+LQDL-30	Kaolin	DL clay	30
Case 2	UQDL+LQK-30	DL clay	Kaolin	30
Case 3	UQK+LQDL-60	Kaolin	DL clay	60
Case 4	UQDL+LQK-60	DL clay	Kaolin	60



Table 4 Examples of seepage water samples (Upper : QDL, Lower : QK,  $D_{rg} = 30\%$ )

Container No.	Purified water	①	⑤	⑩	⑮	⑳
Pictures of seepage water						
Time taken to collect (s)		13.20	12.35	11.98	11.45	11.53
Amount of turbidity material (g)		0.693	0.344	0.053	0.015	0.008
Concentration (g/L)		7.33	3.69	0.55	0.16	0.09

## TEST RESULTS

### Visual observation of seepage water

Table 4 shows examples of the effluent samples obtained from Case 2 (upper soil layer: QDL, lower soil layer: QK,  $D_{rg} = 30\%$ ). 20 samples of the effluent are shown with sampling numbers ①, ⑤, ⑩, ⑮, and ⑳. Picture of purified water without fine particles is also given to compare the turbidity of the seepage water. The seepage water of Number ① is so turbid that the other side of the container cannot be seen at all, indicating that it contains a lot of turbid soil particles. From ⑤ to ⑳, it is found that the amount of turbid matter in the water has decreased, although the turbidity of the drainage can be seen from ⑤ to ⑳.

### Emissions of soil particles

Figure 5 shows the flow rates of the seepage water over time. It can be seen that there is a clear difference in the flow rates of the seepage water between the cases with  $D_{rg} = 30\%$  and  $60\%$ . However, when comparing the cases with different soil layer arrangements under the same skeleton relative density condition, there is no significant difference in the flow rates. In other words, in the case of two-layered soil, even if the order of the soil layers through which the water passes is changed, there is no significant difference in the amount of seepage that is ultimately discharged.

### Accumulated emissions of soil particles

Focusing on the discharge rate per container, in all cases, the discharge rates were greater between container numbers ① to ③, while the discharge rate of the soil particles after that decreased rapidly with the water flow and almost disappeared after container number ⑩.

When focusing on the cumulative discharge, it can be seen that  $D_{rg} = 30\%$  yields a larger value of cumulative discharge than  $D_{rg} = 60\%$  as well as the

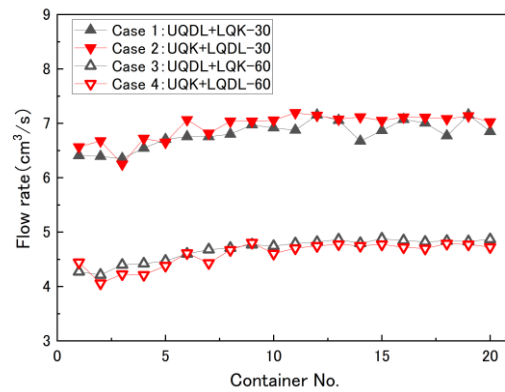


Fig. 5 Flow rates of turbid water

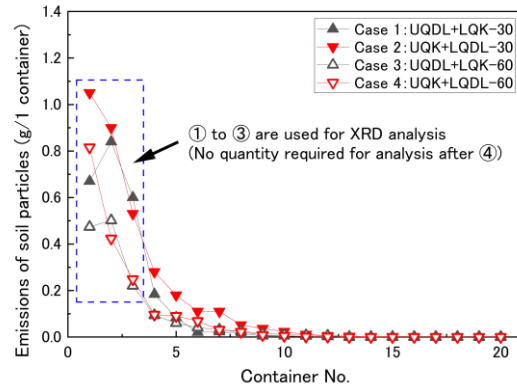


Fig. 6 Emissions of soil particles

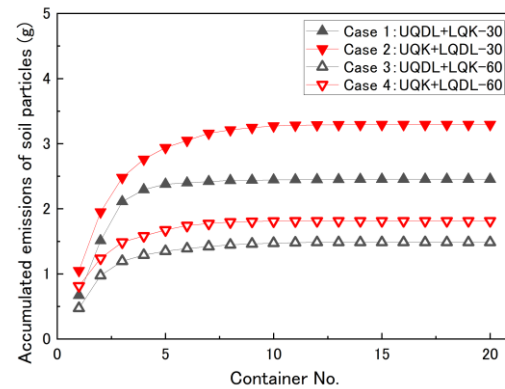


Fig. 7 Accumulated emissions of soil particles

time variation of the flow rate of the seepage water. However, the effect of the difference in the soil layer arrangements was also observed, and the discharge was larger in the percolation case where the fine grains in the upper layer were kaolin and the fine grains in the lower layer were DL clay. The smaller particle size and higher plasticity index of kaolin may have allowed it to flow more easily in the pore spaces than DL clay and to pass through the soil layer below, even if it was contained in the upper layer. Therefore, the final discharge was probably larger for the upper layer than for the DL clay and for the lower layer than for the kaolin.

### XRD analysis of turbidites

In the XRD analysis, the turbidites in the seepage water, obtained in the four water flow cases, were analyzed for their respective XRD patterns using XRD to examine the temporal changes in the patterns in each water flow case. The samples to be analyzed were container numbers ① to ③ immediately after the start of the water flow in all cases. The samples of discharged sediment after ④ were not included in the analysis because the amount necessary for XRD analysis could not be collected. However, since approximately 75-80 % of the total final discharge

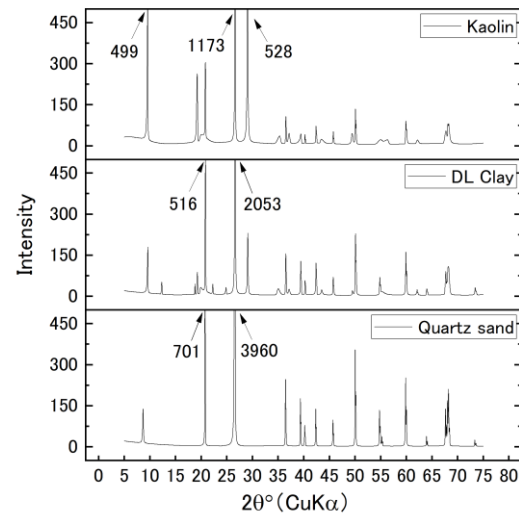


Fig. 8 XRD patterns of basic samples of soil

volume of turbid material was discharged up to ③, it can be assumed that most of the dischargeable soil particles had been discharged by the time of ③.

The turbidites collected from the seepage water by filtration were dried, then thoroughly ground in an agate bowl to a powder form for analysis. Under the conditions of the analysis, CuKα X-rays were

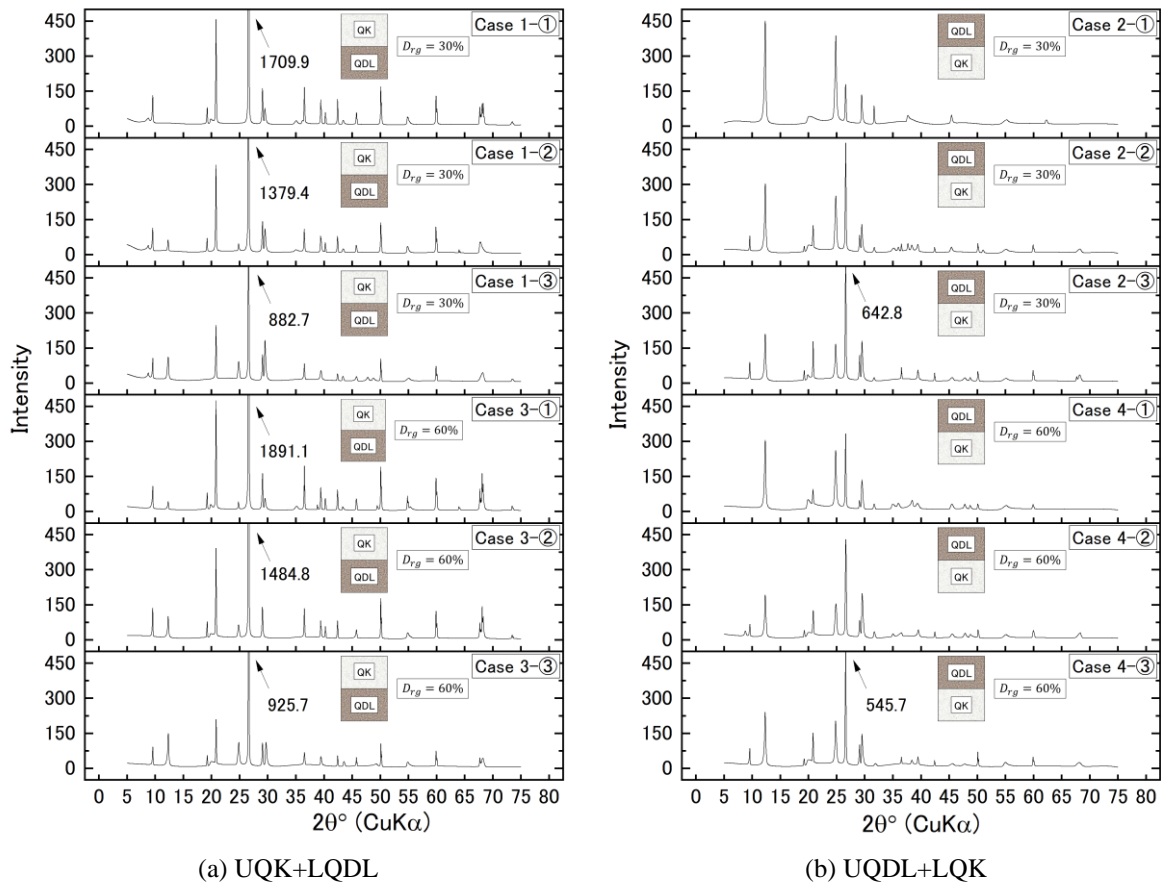


Fig. 9 Results of XRD analysis

irradiated at diffraction angles from  $5^\circ$  to  $75^\circ$ .

### Diffraction patterns of basic samples

Figure 8 shows the diffraction patterns of the kaolin, DL clay, and silica sand powder that may have been discharged by the fine-grained runoff. Although kaolin and DL clay were used as the fine-grained components in this study, the maximum particle size of the outflowable component was  $425\ \mu\text{m}$ . Strictly speaking, this means that fine silica sand particles in the host silica sand were also discharged in addition to the two types of fine-grained components. These three diffraction patterns were used as reference when analyzing the samples obtained from the flow-through experiment.

### XRD pattern analysis of two soil layers

Figures 9 (a) and (b) show the results of the UQDL+LQK and UQK+LQDL analyses, respectively. The maximum value of the Y-axis scale is set to 500 in each result so that the maximum diffraction intensities can be compared, and values are shown in Figure 9 for the peaks exceeding 500. A comparison of these figures shows that the XRD diffraction patterns were clearly different depending on the arrangement of the soil layers. When comparing the diffraction intensity of the largest peak near  $26.6^\circ$ , the diffraction intensity values were larger when the lower soil layer was QDL. Comparing the diffraction patterns of the basic sample of kaolin and DL clay, the diffraction pattern of UQK+LQDL is closer to that of DL clay and the diffraction pattern of UQDL+LQK is closer to that of kaolin because DL clay has a larger peak near  $26.6^\circ$ . In other words, the diffraction pattern of the turbidites in the seepage water that has passed through the two-layer ground is characterized by the fine grains contained in the lower layer near the outlet.

In terms of the difference in skeleton relative density, the XRD patterns for  $D_{rg} = 30\%$  and  $D_{rg} = 60\%$  were not completely identical; there were some differences in the diffraction intensity values. In the case of  $D_{rg} = 30\%$ , the peaks appeared and disappeared more frequently. In other words, the XRD patterns were more likely to change from ① to ③ when the relative density was loose. It is thought that a loose relative density will cause the fine grains in the upper layer to be more easily discharged and to become mixed with the fine grains

in the lower layer, resulting in a larger change in the XRD pattern.

### CONCLUSIONS

In this study, the temporal variation in the XRD patterns of the turbidites in seepage water, that passed through a two-layer ground, was investigated. The main results of the study are summarized as follows:

1. The flow rate of seepage water through two layers of soil is not affected by the arrangement of the soil layers, but only by the density.
2. The discharge of soil particles is greater when the density is loose. In this study, the discharge was greater when the soil in the lower layer was QDL.
3. The XRD patterns of the turbidites varied greatly depending on the soil layer arrangement, and it was clear that the two-layer soil was more likely to produce a special number of fine grains in the subsoil. In addition, peaks tended to disappear or appear more frequently in the flow-through case where the relative density of the soil was smaller.

### REFERENCES

- [1] Sato M., and Kuwano R., Laboratory testing for evaluation of the influence of a small degree of internal erosion on deformation and stiffness, *Soils and Foundations*, Vol. 58, Issue 3, 2018, pp. 547-562.
- [2] Ke, L., and Takahashi, A., Triaxial erosion test for evaluation of mechanical consequences of internal erosion, *Geotechnical Testing Journal*, Vol. 37, Issue 2, 2014, pp. 347-364.
- [3] Prasomsri, J., Takahashi, A., The role of fines on internal instability and its impact on undrained mechanical response of gap-graded soils, *Soils and Foundations*, Vol. 60, Issue 6, 2020, pp. 1468-1488.
- [4] Murakami T., Suzuki Y., Oishi H., Kenichi I. and Nakao T., Tracing the source of difficult to settle fine particles which cause turbidity in the Hitotsuse reservoir, Japan, *Journal of Environmental Management*, Vol. 129, 2013, pp. 37-47.
- [5] Mitchell, J.K., *Fundamentals of Soil Behaviors*, John Wiley Interscience New York, 1976, pp. 172-189.
- [6] Ishimaru T., Suzuki M., and Takano S., Particle size composition of migrating soil particles and the time change in water-passing experiments for reproducing suffusion using turbidity, *Journal of Geotechnical Engineering*, Vol. 17, Issue 1, 2022, pp. 47-60 (in Japanese).

# ESTIMATION OF SUBSURFACE STRUCTURES AND GROUND MOTION CHARACTERISTICS OF ARTIFICIALLY IMPROVED LAND FROM MICROTREMOR OBSERVATIONS – CASE STUDY IN TOTTORI CITY, JAPAN

Isamu Nishimura<sup>1</sup>, Tatsuya Noguchi<sup>1</sup> and Takao Kagawa<sup>1</sup>

<sup>1</sup>Graduate school of Engineering, Tottori University, Japan

## ABSTRACT

In recent earthquakes, a large number of houses on artificially filled valleys were damaged due to large ground motions. It is because lower S-wave velocities in the filled valleys than that in earth cut section amplify ground motions. In this study microtremor observations were carried out at two areas in Tottori City, Japan that are designated as large-scale artificially improved lands, in order to understand distribution of ground motion characteristics. The results show that in both areas, the predominant periods tend to be longer and the peak values of H/V spectra are larger in the filled valley sections than in the each cut sections. Furthermore, it was found that the peak value of the H/V spectrum of microtremors had a certain correlation with the thicknesses of the embankment regardless of the presence or absence of soft layer before the improvement. Estimated S-wave velocities based on microtremor array observations and predominant periods from H/V spectra were used to estimate thicknesses of sediments from the quarter-wavelength law. It is found that the estimated layer thicknesses agree well with the elevation change of topography between present and before the improvements.

*Keywords: Microtremor observation, Subsurface structure, Artificially improved land*

## INTRODUCTION

Artificially improved lands such as filled valleys have been constructed on hills and foothills continuously after 1970's, the economic grow period in Japan, and they concern about earthquake damage in the areas. In the recent series of earthquake disasters, damage caused by soft embankment ground has become remarkable, and it has been reported that the damage was more severe in the area than that of the surrounding cut ground in each large earthquake [e.g., 1]. This is because the different characteristics of the ground in the filled valley and earth cut section, such as the fact that S-wave velocity in valley filled part is lower than that in cut part, and it tends to amplify ground motions. In the suburbs of cities, large-scale residential land development has been

carried out to build new towns, etc., and there are large areas with flat terrain that have been artificially created. Cuts and embankments are intricately distributed in these areas, and it is assumed that the ground motion characteristics and potential of housing damages due to an earthquake differ greatly from point to point.

The Ministry of Land, Infrastructure, Transport and Tourism (MLIT) is promoting earthquake resistance improvement for such large-scale artificially improved lands by investigating the prediction of fluctuations and preventing landslides and collapses. As a part of the project, the local government is preparing cut-and-fill maps in hillside landform to identify large-scale development sites. This cut-and-fill map is based on a comparison of the old topographic map and the current topographic map,

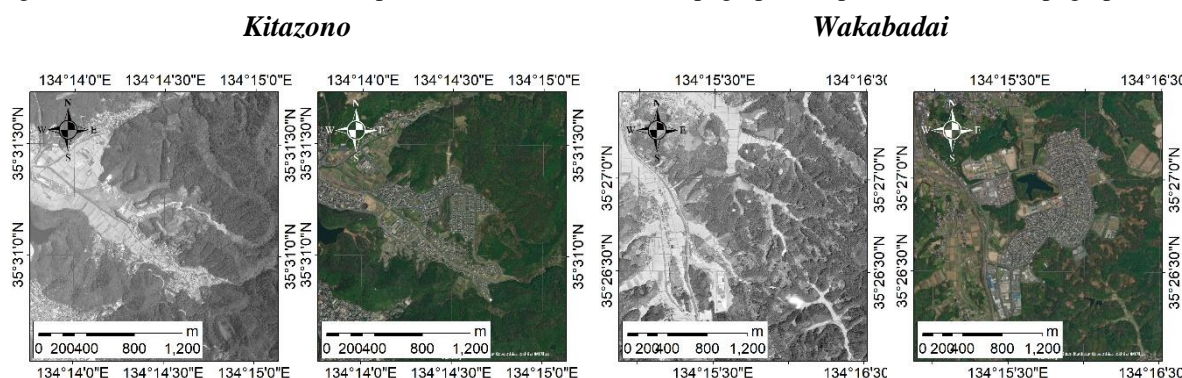


Fig.1 Aerial photographs before and after the development in both areas



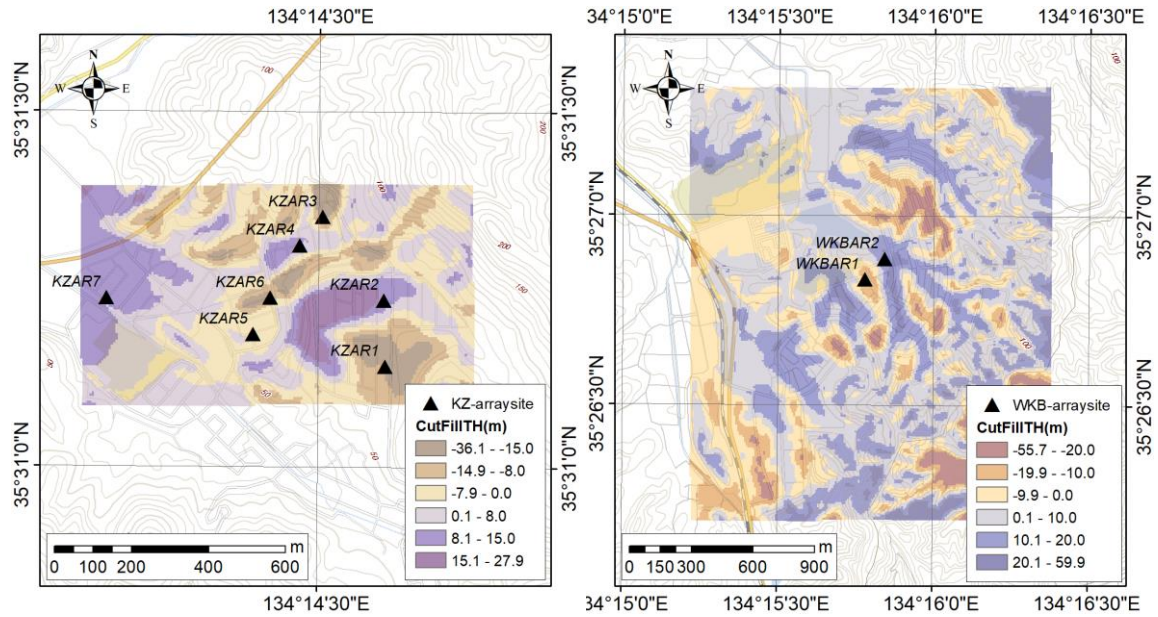


Fig. 2 Distribution of cut-and-fill thicknesses based on topographic maps and microtremor array sites (left: Kitazono, right: Wakabadai)

and is published on the websites of local governments as "Large-scale Embankment Landform Map." In some areas, the secondary investigation was conducted, not only borings but also detailed investigations such as surface wave surveys, to evaluate stiffness of the embankments.

In this study, microtremor observations were carried out at two areas - Kitazono and Wakabadai - in Tottori City, Japan that are designated as large-scale artificially improved lands as shown Figure 1., in order to understand ground motion characteristics.

### ESTIMATING THICKNESSES OF ARTIFICIALLY IMPROVED LAND BY USING GIS

Figure 1 shows aerial photographs of the site before and after the development at Kitazono and Wakabadai regions. In this study, by taking elevation difference between the old and the current topographic maps, cut-and-filled thicknesses were estimated. For the old topographic maps, a 1/25,000 scale topographic map issued in 1984 [2] was used for Kitazono and a 1/25,000 scale topographic map issued in 1975 [3] was used for Wakabadai. ArcGIS by ESRI was employed to obtain the cut-and-fill thicknesses in each region. The method for estimating the cutting thicknesses is as follows.

- 1) Scan and digitize the old topographic maps.
- 2) Match the digitized data to the current topographic map using geo-referencing function of GIS.
- 3) Obtain elevation values for each contour line on the old topographic map.

- 4) Create a rasterized elevation distribution before the development by interpolation based on ANUDEM [4].
- 5) Digital elevation data (DEM) of 5m mesh issued by Geospatial Information Authority of Japan [5] is used for the current map, and it is interpolated by the reverse distance load method (IDW) to make a raster data.
- 6) The difference between the old and current elevations was calculated spatially using raster operations, and the value was used as thicknesses of cut-and-filled.

The distribution of cut-and-fill thicknesses at Kitazono and Wakabadai are shown in Fig. 2.

### OBSERVATIONS

Single-point microtremor observations were conducted at 53 sites in Kitazono and 94 sites in Wakabadai for a total of 147 sites. A JU410 three-components accelerometer with a 24-bit recorder was used for data acquisition. We used the following specifications: an amplification factor of 100 for 4G maximum output from the sensor, a sampling frequency of 200 Hz, and a recording time of 10–15 min. Seismographs were placed at about 50 m intervals in cut and fill sections based on the cut-and-fill thickness distribution.

We also conducted microtremor array observations at 7 sites (KZAR1-7) at Kitazono and 2 sites (WKBAR1-2) at Wakabadai as shown in Fig. 2. Four JU410s synchronized by GPS clocks were used to conduct the measurements. One seismometer was placed at the center of a circle, and other three were

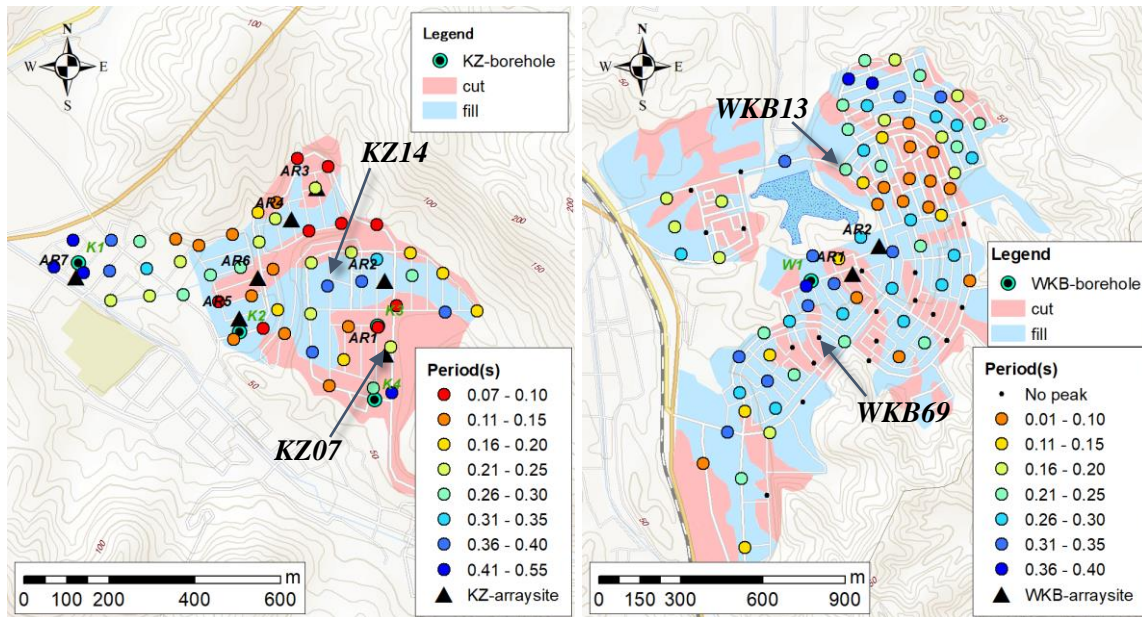


Fig. 3 Predominant period distributions (left: Kitazono, right: Wakabadai)

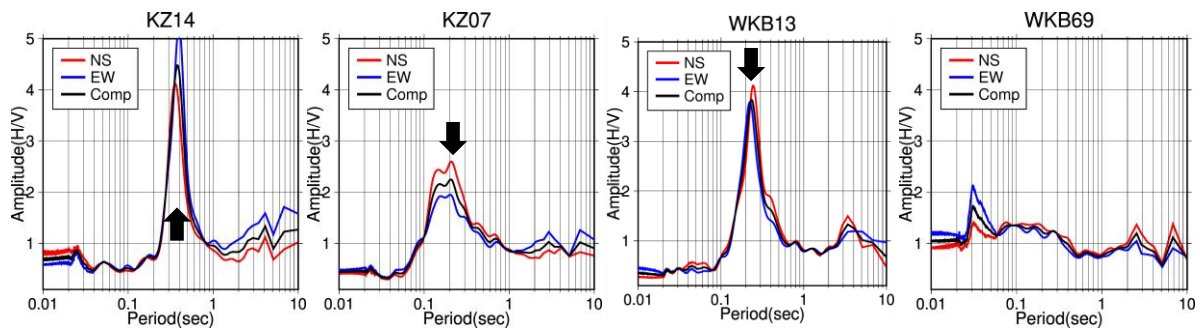


Fig. 4 H/V spectral ratios

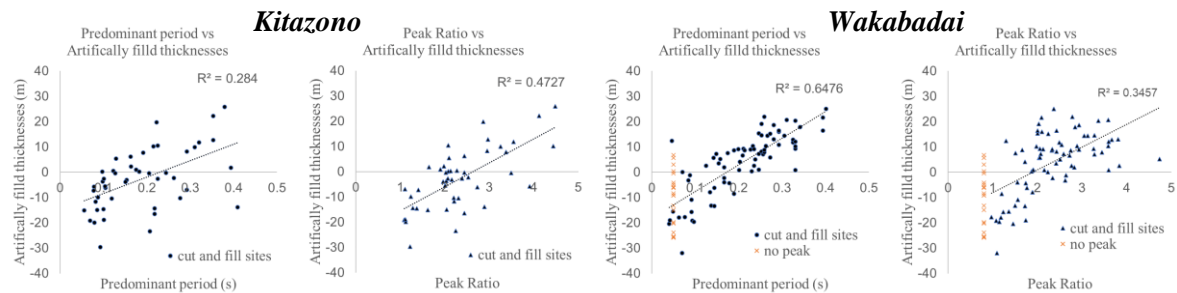


Fig. 5 relationships between difference in elevation before and after land development and the predominant periods and peak values

set in an equilateral triangle around the circumference. Linear arrays with two seismographs were additionally conducted at the 4 sites at Kitazono (KZAR3-6) with the equilateral triangular arrays. The specifications were as follows: an amplification factor of 100, a 200-Hz sampling frequency, 1–30-m radius of the array, and a 15-min recording duration.

## DISCUSSIONS

### Results of microtremor single-point analysis

The analyzing procedure for microtremor single-point observation is as follows. Fourier spectra were calculated from 20.48 s length segments and they were smoothed using a log window with a coefficient of 20 [6]. Average spectra were evaluated from at



least 10 different stable sections. Horizontal to vertical (H/V) spectral ratios were calculated from the averaged Fourier spectra, and the predominant periods were visually estimated. The predominant period distributions at Kitazono and Wakabadai are shown in Fig. 3.

As results, predominant periods in Kitazono region were from 0.07 to 0.55 s, while Wakabadai region were between 0.01 and 0.40 s. Figure 4 shows typical microtremor H/V spectra of embankment and cut land sites in both regions. The H/V spectra of embankment sites have clear peak in a range of 0.1–0.4 seconds. On the other hand, the H/V spectra of the cut sites have a period of about 0.1 seconds or less, and the peaks are unclear at many points. Particularly at Wakabadai, the shape of H/V spectra at cut-off lands are almost flat, and there is a remarkable tendency that no peaks are recognized.

Figure 5 shows the relationship between difference in elevation before and after land development and the predominant periods and peak values of the microtremor H/V spectra at Kitazono and Wakabadai observation sites. At Wakabadai without clear peak, the predominant period is marked as 0.05 s, and the peak value as 0.8. In addition, the natural ground sites at Kitazono that did not correspond to cut-and-fill operations were excluded. At Kitazono, there is not a strong correlation between the predominant periods and the elevation difference before and after construction, but there is a

remarkable correlation with the peak values. On the other hand, a certain correlation is observed between the predominant periods and the elevation difference at Wakabadai. It is considered that Wakabadai has almost no soft layers near the mountains, and the correlation is particularly high with the predominant periods. On the other hand, Kitazono has weathered and cultivated lands on natural ground even near the mountains.

### Estimation of Subsurface Structures

Analysis of the array observations was conducted with the following procedure: the phase velocity dispersion curves were estimated from vertical component records based on the SPAC [7] or CCA methods [8]. Using the published analysis tool [9], at least ten sections with 10.24 s length were selected by automatic extraction using the root mean square values of microtremor recordings. Then, the power spectra of those sections were smoothed by a Parzen window with 0.3-Hz bandwidth and the average was estimated. Finally, the phase velocity dispersion curves were determined, and those obtained at each radius were integrated at each observation site, with respect to their continuity.

Assuming that microtremors are mainly composed from Rayleigh waves, their propagation characteristics allow us to estimate subsurface structures. The subsurface structure models were

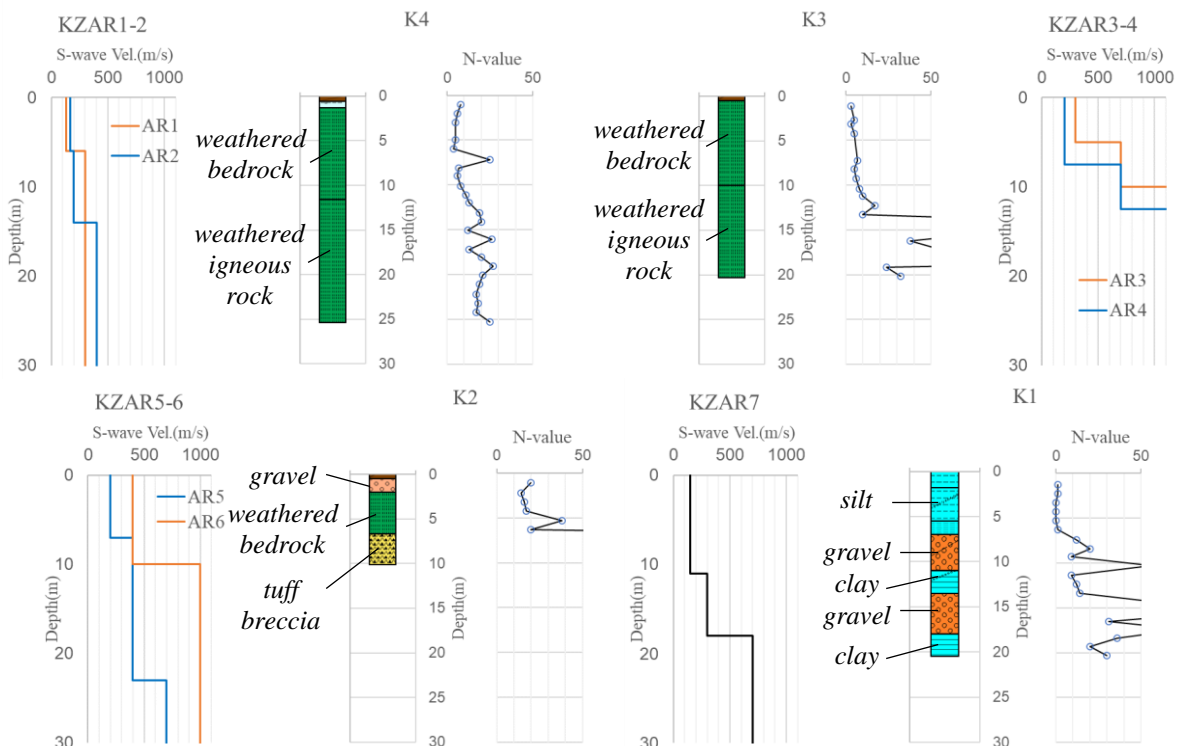


Fig. 6a S-wave velocity structures based on array observations and borehole data at Kitazono (Red line: cut sites, blue line: fill sites)

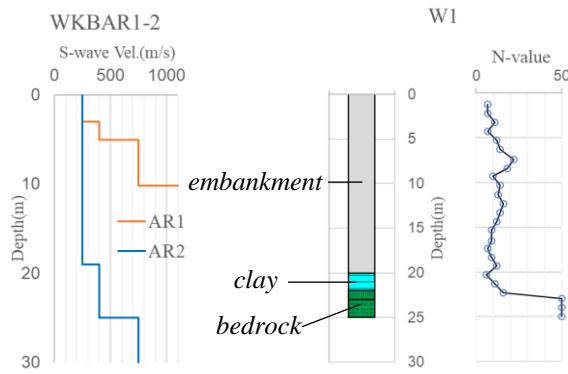


Table 1 Converted S-wave velocities

	Site	Converted Vs(m/s)
Kitazono	KZAR1(cut)	267.1
	KZAR2(fill)	339.2
	KZAR3(cut)	300.0
	KZAR4(fill)	200.0
	KZAR5(fill)	336.4
	KZAR6(cut)	400.0
	KZAR7	208.3
Wakabadai	WKBAR1(cut)	534.3
	WKBAR2(fill)	365.9

Fig. 6b Same as Fig. 6a but for Wakabadai

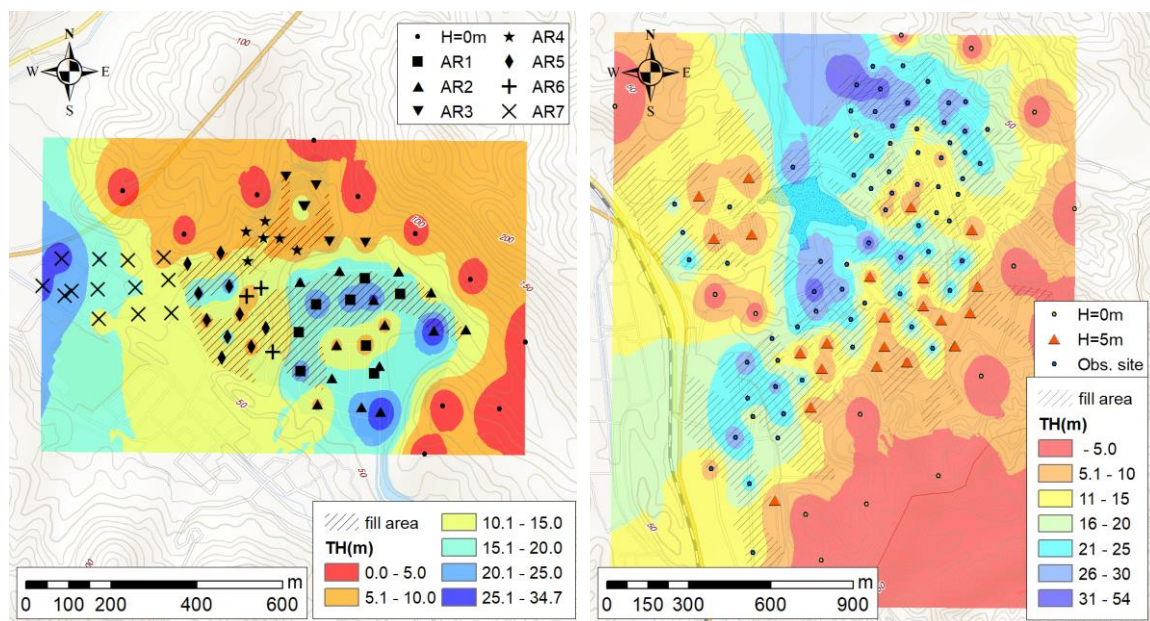


Fig. 7 Layer thicknesses in Kitazono and Wakabadai regions

estimated through trial and error to ensure that these phase velocity dispersion curves and the microtremor H/V spectral ratios obtained at the center of the array, to match the theoretical phase velocity dispersion curves and H/V spectral ratios based on the Rayleigh wave fundamental mode, respectively. The total numbers of sedimentary layers were determined with reference to the borehole data around the observation sites.

The resulting S-wave velocity structure models and borehole data are presented in Fig. 6a and 6b. Please note that the borehole data of Kitazono were acquired before the development. The thickness of embankment near K2 at Kitazono is considered to be several meters from Fig. 2. The S-wave velocity of the embankment layer was estimated as 200 m/s based on KZAR5. The S-wave velocity at the surface layer at KZAR6 was 400 m/s. It confirms that the cut sites have higher S-wave velocities than the fill sites. However, KZAR1 and KZAR2 have several meters

of layers with S-wave velocities of 150 m/s on the surface layer regardless whether cut or fill sites, and they have over 30m depth layers with S-wave velocities of 400 m/s or less. Therefore, the ground motion characteristics of this area are affected not only by the thicknesses of embankment but also by the weathered layers under the embankment layers.

The thickness of embankment near W1 at Wakabadai is about 22 m. The S-wave velocity of the embankment layer was estimated to be 250 m/s based on WKBAR2. At the cut-off site WKBAR1, a layer of  $V_s=500$  m/s or more is estimated at a depth of 5m or deeper. It suggests that the site has very hard ground.

#### Estimation of artificially improved land thickness based on microtremor results

The S-wave velocities and the predominant periods were used to estimate the layer thicknesses

from the quarter-wavelength law. S-wave velocities were calculated by weighted average using down to the top surface of  $V_s = 500$  m/s of the estimated model at Kitazono and the top surface of  $V_s = 1000$  m/s at Wakabadai as sediments. Table 1 shows the converted S-wave velocities at each location used to estimate the layer thicknesses hereafter. The layer thicknesses at the cut-off sites with no clear peak at Wakabadai is set to be 5 m. In both regions, dummy data with a layer thickness of 0 m were added at several points in stiff mountainous areas. After obtaining the estimated layer thicknesses at each site, the distribution was rasterized by interpolation based on the reverse distance load method (IDW).

The distributions of layer thicknesses are shown in Figure 7. It is clear that the points with thick sediment layers in both areas generally correspond to the embankment areas. The thicknesses of the layers were confirmed to be about 20 m at the deepest point at Kitazono and about 30 m at Wakabadai. Thicker layers are observed in the cut areas at Kitazono. This is because the microtremor H/V spectra in the areas are considered to reflect velocity contrasts of the structures due to deeper part of the embankment layers.

## CONCLUSIONS

This study conducted microtremor observations in the areas - Kitazono and Wakabadai in Tottori City, Japan - designated as large-scale artificially improved land. The subsurface structures of the cut-and-fill areas were estimated from the microtremor records, and the characteristics of ground motion were examined. Consequently, the following findings are noted.

The predominant periods of microtremor H/V spectra on embankment ground shows a high correlation with the thicknesses of the embankment where no soft layer deposited before land improvement, such as in Wakabadai.

The peak values of the H/V spectra of microtremors show a certain correlation with the thicknesses of the embankment regardless of the presence or absence of soft layers before the improvement.

The estimated ground structure indicates that soft sediments are deposited mainly in the fill area but not in the cut area. It is considered to be an important index for predicting the risk of future earthquake disasters.

Comparison between the estimated surface thickness distribution and the cut distribution in both regions showed similar trends. We would like to increase the number of case studies in other improved lands.

## ACKNOWLEDGMENTS

Part of this research is based on the results of the graduation thesis by Ms. Nazuna Nishimura who belonged to the Faculty of Engineering, Tottori University. We used seismographs provided by the Earthquake Research Institute of the University of Tokyo with the support of the "Research Plan for Earthquake and Volcano Observation to Contribute to Disaster Mitigation (2nd)" by the Ministry of Education, Culture, Sports, Science and Technology of Japan.

## REFERENCES

- [1] Mori T. and Kazama T., The damage research of filled-valley residential area in Sendai City Izumi ward about the 2011 off the Pacific coast of Tohoku Earthquake, Japanese Geotechnical Journal, Vol.7, No.1, pp.163-173, 2012. (in Japanese with English abstract)
- [2] National Institute of Geography, Topographic map at 1/25,000 scale Tottori Kita, 1984.
- [3] National Institute of Geography, Topographic map at 1/25,000 scale Inabayama, 1975.
- [4] Hutchinson, M.F., Optimising the degree of data smoothing for locally adaptive finite element bivariate smoothing splines. Australian & New Zealand Industrial and Applied Mathematics Journal 42(E): C774-C796, 2000.
- [5] Geospatial Information Authority of Japan, Digital Elevation Model (DEM), <https://www.gsi.go.jp/kiban/index.html> (view on 2022.6.14)
- [6] Konno K. and Ohmachi T., A smoothing function suitable for estimation of amplification factor of the surface ground from microtremor and its application, Journal of the Japan Society of Civil Engineers, No525/I-33, 1995, pp247-259. (in Japanese with English abstract).
- [7] Aki K., Space and time spectra of stationary stochastic waves, with special reference to microtremors, Bull.Earthq.Res.Inst., 35, pp415-456, 1957.
- [8] Cho I., Tada T. and Shinozaki Y., Centerless circular array method: Inferring phase velocities of Rayleigh waves in broad wavelength ranges using microtremor records, J. Geophys. Res., 111, B09315, 2006.
- [9] Cho I., Tada T. and Shinozaki Y., Possibility of microtremor array opened up by general theory: Release of analysis tool BIDO, Seismological Society of Japan Fall Meeting in 2009. (in Japanese)

## EVALUATION OF VERTICAL BEARING CHARACTERISTICS FOR SOIL-CEMENT COMPOSITE PILES

Shohei Koga<sup>1</sup>, Koji Watanabe<sup>2</sup> and Tadahisa Yamamoto<sup>3</sup>

<sup>1</sup>Obayashi Corporation, Japan; <sup>2</sup> Department of Civil Engineering, Aichi Institute of Technology, Japan

### ABSTRACT

There are several pile construction methods with relatively small construction machinery that are suitable for construction in narrow urban spaces and areas with low overhead clearance. The Top-drive Boring Hole (TBH) method, which has a machine height of 4.5m, is often used. The Boring Hole (BH) pile method can handle narrow spaces and low overhead clearances better than the TBH method. However, because the BH pile method is a direct circulation method, mud cakes easily form on the hole walls, and slime tends to accumulate at the pile tip. Such challenges related to the construction method, bearing capacity and settlement need to be resolved for pile construction in narrow urban spaces. Pile construction in narrow urban spaces and for existing structures to strengthen the seismic resistance is subjected to constraints on the construction site and process. Therefore, a method for soil-cement composite pile construction was developed that uses a compact mechanical agitator for pile foundations of lightweight structures. In this study, static compression load tests on soil-cement composite piles that were constructed with the developed ground improvement construction method were carried out to evaluate the vertical bearing characteristics. Furthermore, it was evaluated the performance of vertical bearing characteristics on the soil-cement composite piles to compare the evaluation method as shown in the design specifications in Japan.

*Keywords: Soil-cement composite pile, Compression load test, Bearing capacity, Evaluation method*

### INTRODUCTION

There are several pile construction methods with relatively small construction machinery that are suitable for construction in narrow urban spaces and areas with low overhead clearance. The Top-drive Boring Hole (TBH) method, which has a machine height of 4.5m, is often used. However, there are many cases where even these construction machines are interfered with by architectural limitations and existing structures. In particular, piles near railway tracks or on rail platforms are currently constructed after temporary construction is carried out to ensure construction space. The Boring Hole (BH) pile method can handle narrow spaces and low overhead clearances better than the TBH method. However, because the BH pile method is a direct circulation method, mud cakes easily form on the hole walls, and slime tends to accumulate at the pile tip. This lowers the bearing capacity of the piles, so subsidence is more likely to occur. Such challenges related to the construction method, bearing capacity and settlement need to be resolved for pile construction in narrow urban spaces.

Pile construction in narrow urban spaces and for existing structures to strengthen the seismic resistance is subjected to constraints on the construction site and process. Especially, this pile is subjected to the lack of bearing capacity due to the increase of superstructure weight by strengthening the superstructure. Furthermore, noise and industrial



Fig. 1 Construction machine of soil-cement composite pile.

waste need to be considered with regard to their effects on the surrounding environment. Therefore, a method for soil-cement composite pile construction combined with soil cement ground improvement was developed that uses a compact mechanical agitator for pile foundations of lightweight structures. The construction machine is a mechanical agitator with an attached vibrating mechanism and improved drilling capacity. This developed machine can be used to realize pile construction in narrow spaces where construction is usually difficult. This method is characterized by having no need to drill up to a fixed depth as in the pre boring pile construction method. Instead, soil is agitated along with the cement milk at the original position. This greatly reduces the spoil generated by pile construction. In this method, the



drilling rod of the developed machine is sent down to the bearing stratum; after agitating and mixing, the pile is composed of segmental steel pipes that are connected with bolts on flanges.

In this study, static compression load tests on the soil-cement composite pile (i.e. H-section steel piles with soil-cement ground improvement) that were constructed with mechanical agitator ground improvement method were carried out to evaluate the vertical bearing capacity. Furthermore, it was evaluated the performance of vertical bearing capacity on the soil-cement composite pile to compare the evaluation method as shown in the design specifications in Japan.

### SUMMARY OF SOIL-CEMENT COMPOSITE PILE CONSTRUCTION

In this construction method, strength of the soil cement is in the ranges of  $1000 \sim 5000 \text{ kN/m}^2$ . The H section steel piles were used to be fabricated from JIS standard steel piles to ensure a low cost and certain level of quality. The typical construction process with this method is described as follows;

1) Excavate to the bearing stratum, carry out agitation and mixing, and lay the soil cement as the ground improvement structure. During this time, carry out drilling so that the rod will reach a predetermined depth.

2) Build H section steel pile joints in the ground improvement structure, which is in loose and poorly lithified soil.

3) After the pile construction is completed, fix the pile head before the soil-cement hardens.

The above construction can be carried out using only the developed construction machine shown in Fig. 1. The planar dimensions of the construction machine are extremely compact: a 1.55m width and 2.32m length. In addition, the construction machine is 3.0m tall, including the leader. Thus, construction is possible even with low overhead clearances. The machine has a vibration mechanism to improve the agitation and mixing capability. The results of construction test showed that even strong sandy stratum with an N value of about 40–50 can be agitated and mixed [1].

In order to increase the end bearing capacity, two plates were attached to the tip of the H section steel pile. Fig. 2 and Fig. 3 shows the tip shape of the H section steel pile. As shown in Fig. 2 and Fig. 3, two plates were attached to the tip of the H section steel pile with an inclination of  $135^\circ$  from the horizontal direction.

### IN-SITU FULL SCALE COMPRESSION LOAD TEST



Fig. 2 Pile tip shape of soil-cement composite pile.

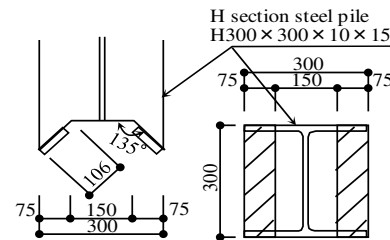


Fig. 3 Scale of soil-cement composite pile tip.

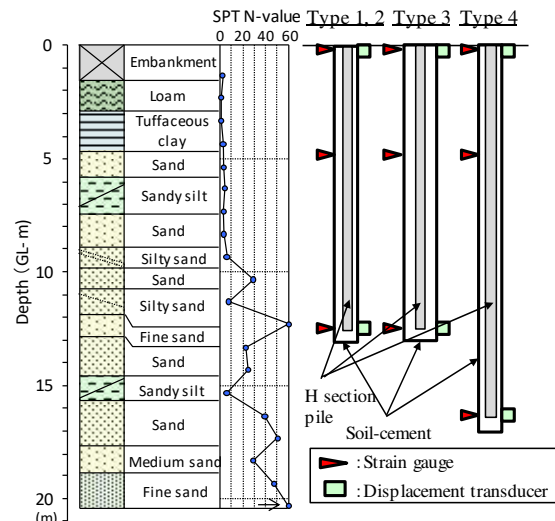


Fig. 4 Soil profile and test piles.

Table 1. Specifications of test piles.

	Pile diameter (mm)	Pile length (m)	Strength of soil-cement ( $\text{kN/m}^2$ )
Type 1	600	14.0	1000
Type 2	600	14.0	3000
Type 3	800	14.0	1000
Type 4	600	17.0	1000

The soil profile and test piles indicates in Fig. 4. The test ground was composed of loam and tuffaceous clay up to about GL -5.0 m and sandy silt and medium sand, fine sand below that. Four piles were constructed for the static load test with the soil cement diameter, pile length, and soil cement strength as parameters.

Table 1 presents the specifications of the test piles. The bearing stratum was adopted to be  $N=20$  and 40

from the results of ground investigation; the test piles were embedded in the bearing stratum. The test piles were pre-drilling soil-cement column diameter of 600mm and 800mm, H section steel shape of H-300×300×10×15. The target strength of the pre-drilled soil cement as the improved ground structure was 1000kN/m<sup>2</sup> with the test pile of Type 1, 3, 4 and 3000kN/m<sup>2</sup> with the test pile of Type 2. In the core strength test carried out after the load test, the average strengths with the all of the test piles were over the target strength, respectively.

The arrangement of test piles and reaction piles presents in Fig. 5. Four test piles and six reaction piles were constructed. Similar to the test piles, six reaction piles were also constructed as the H section steel pile with soil cement by the same construction method as the test piles. The distance between the test piles and the reaction piles were set based on the influence range as described in the Japanese Geotechnical Society (“Methods for vertical load test of piles”) [2], the distance are  $3D=1800, 2400$  (mm). Here,  $D$  means the pile diameter such as soil cement diameter.

The static load test was carried out based on the standards of the Japanese Geotechnical Society (“Methods for vertical load test of piles”) [2]. A stepwise multi cycle loading system was employed with a new load holding period of 30min, hysteretic load holding duration of 2min, and zero load holding duration of 15min. The measured parameters were the pile head load, pile head and pile tip displacements, and strain of the H section steel. The pile tip displacement was measured with the pipe-in pipe method (i.e. double steel tube method). In order to evaluate the shaft friction of each stratum and the end bearing capacity, the strain were measured at the tip of pile, the boundary of each soil stratum and top of pile.

## RESULTS OF IN-SITU FULL SCALE COMPRESSION LOAD TEST

Figure 6 shows the relationships between the load and displacement at the pile head. The maximum loads were 2500kN for Type 1 and 2700kN for Type 2~Type 4. For all of the piles, the curve was steep from the initial of loading; and all of the piles possessed a large initial stiffness. The gradient of the curve then changed with the loading and reached the maximum load. For the test piles of Type 2~Type 4, a larger  $N$  value for the bearing stratum, a larger pile diameter and a longer pile length meant a higher stiffness.

The axial force was calculated by considering

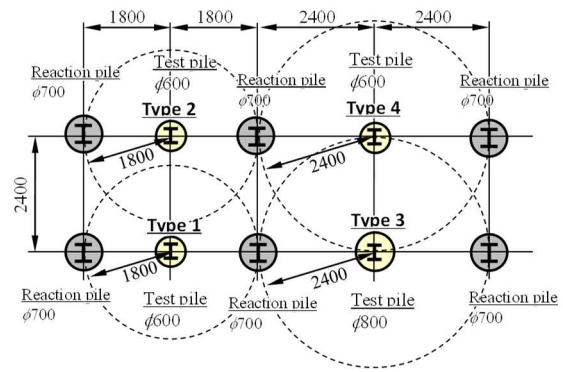


Fig. 5 Arrangement of test piles and reaction piles.

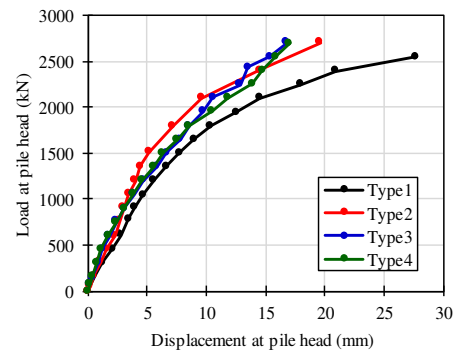
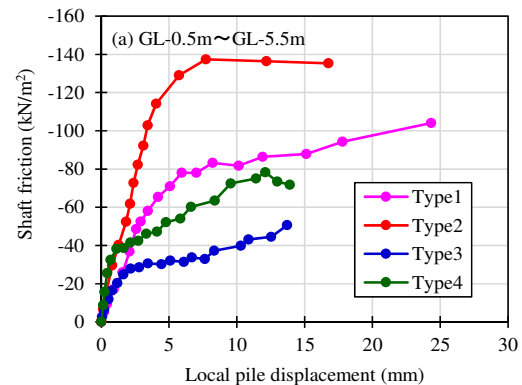
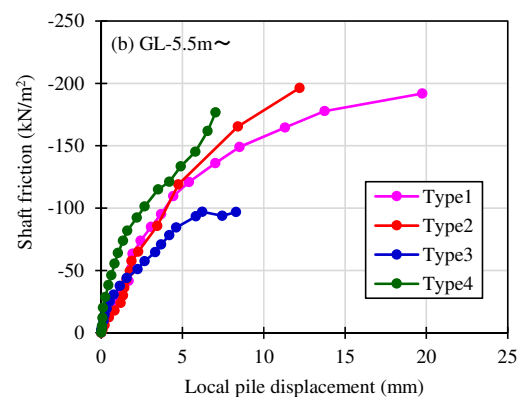


Fig. 6 Relationships between load and displacement at pile head.



(a) Clayey soil: GL-0.5m~GL-5.5m.



(b) Sandy soil: GL-5.5m~.

Fig. 7 Relationships between shaft friction and local pile displacement.



only the H section steel. The strain of the H section steel obtained from the load test was multiplied with the Young's modulus and cross-sectional area of the H section steel. The relationships between the shaft friction and local pile displacement which was obtained by dividing this axial force difference by the circumferential area are shown in Fig. 7. The improved diameter of the soil cement (i.e. outer diameter of soil cement column) was used when calculating the circumferential area of the pile. Figure 7(a) shows that a maximum shaft friction of 50 ~ 140kN/m<sup>2</sup> was reached in clayey soil stratum. In comparison, the average value for the unconfined compressive strength of the corresponding section of the ground was 57kN/m<sup>2</sup>. Thus, it can be concluded that the shaft friction was more than the undrained shear strength of the ground (=28kN/m<sup>2</sup>). In the sandy ground stratum, it is observed that the maximum shear strength is 100~200kN/m<sup>2</sup>. Therefore, it is said that the shaft friction of the corresponding section shows the large value.

The end bearing capacity was calculated by dividing the axial force reaching the pile tip by the envelope area of the H-section steel ( $B \times H$ ) as shown in Fig. 8. The relationships between the end bearing capacity and displacement at pile tip indicates in Fig. 9. The reference displacement of pile tip is 10% of the diameter of the equivalent circle area which is equal to the envelope area of H-section steel pile when the end bearing capacity is evaluated. However, the maximum displacement at pile tip does not reach the reference displacement in this load test. Thus, the end bearing capacity is evaluated at the maximum displacement at pile tip. The end capacity of 3000~6600kN/m<sup>2</sup> is examined in this load test. The trend indicates that the end bearing capacity is gradually increasing because the displacement at pile tip is small and does not reach the reference displacement to evaluate the end bearing capacity. In addition, the end bearing capacity of the test pile Type 3 indicates the largest value of four test piles. This means that the large end bearing capacity is mobilized due to the large diameter of the pile.

## EVALUATION OF VERTICAL BEARING CAPACITY

The end bearing capacity which was obtained from the developed soil-cement composite pile is compared to the calculated end bearing capacity as shown in the design specification of Japan. In this study, the calculated value is estimated by the Design Standards for Railway Structures and Commentary (Railway Technical Research Institute, 2012) [3] because the developed soil-cement composite pile is

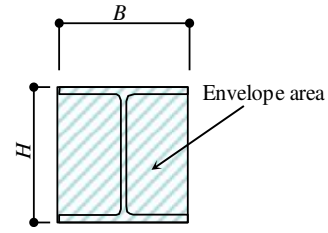


Fig. 8 Pile tip area (Envelope area).

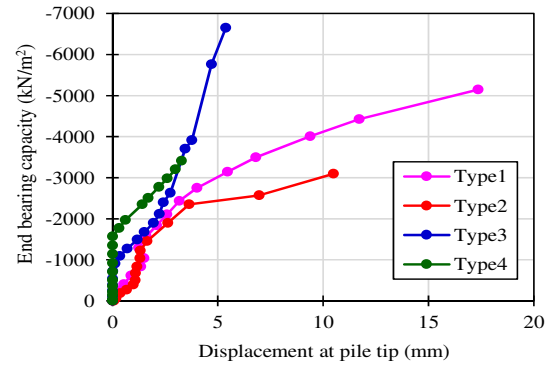


Fig. 9 Relationships between end bearing capacity and displacement at pile tip.

applied to the railway structure. The estimation equations of bearing capacity for the steel pipe soil-cement pile and cast in-situ pile are used in this study. The estimation equations are described as follows;

1) Steel pipe soil-cement pile  
Shaft friction for sandy soil:

$$\gamma_{fk} = 7N \leq 200(\text{kN/m}^2) \quad (1)$$

Shaft friction for clayey soil:

$$\gamma_{fk} = 10N \leq 200(\text{kN/m}^2) \quad (2)$$

End bearing capacity for sandy soil:

$$q_{fk} = 150N \leq 10000(\text{kN/m}^2) \quad (3)$$

2) Cast in-situ pile  
Shaft friction for sandy soil:

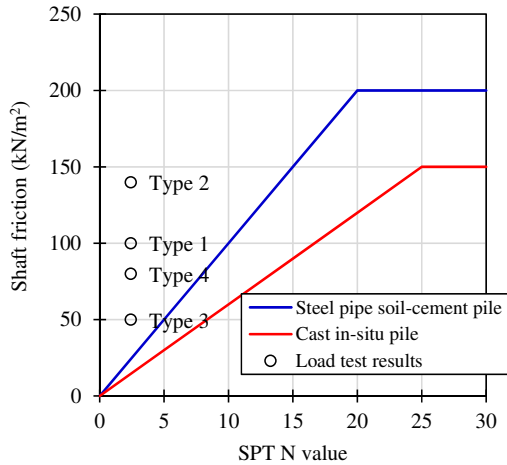
$$\gamma_{fk} = 3N \leq 150(\text{kN/m}^2) \quad (4)$$

Shaft friction for clayey soil:

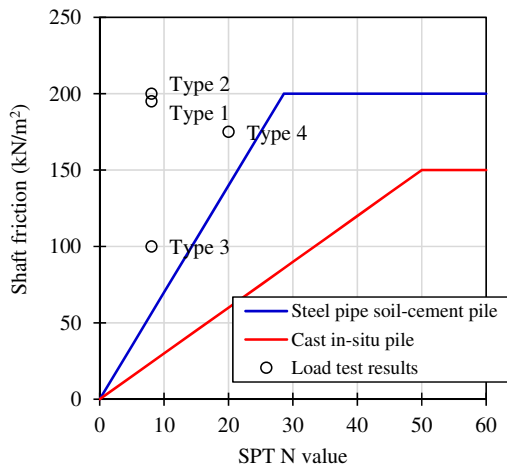
$$\gamma_{fk} = 6N \leq 150(\text{kN/m}^2) \quad (5)$$

End bearing capacity for sandy soil:

$$q_{fk} = 60N \leq 3500(\text{kN/m}^2) \quad (6)$$



(a) Clayey soil.



(b) Sandy soil.

Fig. 10 Relationships between shaft friction and SPT N value.

Where,

$N$ : SPT (Standard Penetration Test) N value

The relationships between shaft friction and SPT N value for clayey soil and sandy soil indicate in Fig. 10. The estimated values from Eqs. (1), (2), (4) and (5) are also plotted in Fig. 10. According to Fig. 10(a), the shaft friction which is obtained from the load test is larger than the estimated value from the design specification. It is said that the developed soil-cement composite pile has the enough shaft friction for the clayey soil. From Fig. 10(b), compared to the shaft friction from the load test and that from the design specification, the shaft friction of load test shows the large value. Therefore, it is also said that the shaft friction of the developed soil-cement composite pile has the enough shaft friction for the sandy soil.

The relationships between end bearing capacity and SPT N value for sandy soil are plotted in Fig. 11. The estimated values from Eqs. (3) and (6) are also plotted in Fig. 11. It is seen that the end bearing capacity of Type 1 and Type 3 from the load test is larger than that of the estimated value. However, the end bearing capacity of Type 2 and Type 4 from the

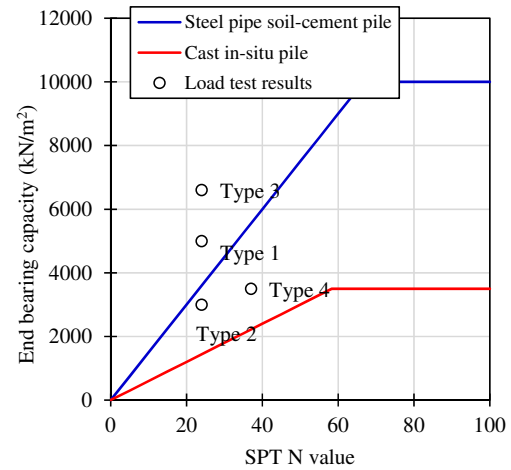


Fig. 11 Relationships between end bearing capacity and displacement at pile tip.

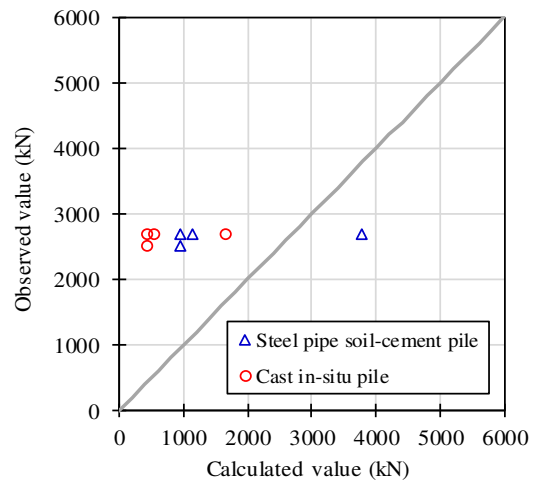


Fig. 12 Relationships between observed bearing capacity and calculated bearing capacity.

load tests is lower than that of estimated value for the steel pipe soil-cement pile although the end bearing capacity of load test shows the large value for the cast in-situ pile. This means that the end bearing capacity does not mobilize because the displacement at the pile tip is too small.

The relationships between observed bearing capacity and calculated bearing capacity are plotted in Fig. 12. Here, the calculated bearing capacity is evaluated by Eqs. (1)~(6). The trend indicates that the bearing capacity which was obtained from the load test is larger than the calculated value.

## CONCLUSIONS

The static compression load tests on the soil-cement composite pile (i.e. H-section steel piles with soil-cement ground improvement) that were constructed with the mechanical agitator ground improvement method were carried out to evaluate the vertical bearing capacity in this study. Furthermore, it

was evaluated the performance of vertical bearing capacity on the developed soil-cement composite pile to compare the evaluation method as shown in the design specifications in Japan. The following findings were obtained from this study.

1) According to the compression load test, both the shaft friction and the end bearing capacity has the enough performance on the vertical bearing capacity.

2) It is concluded that the shaft friction of the load test is larger than the estimated shaft friction which is calculated by the design specification in Japan.

3) Compared to the end bearing capacity which is obtained from the load test and that of estimated value from the design specification in Japan, the end bearing capacity of the load test shows the large value. However, the partial results is lower than the estimated value. This means that the end bearing capacity is gradually increasing because the displacement at the pile tip is too small.

There are some research issues to address in the future. More vertical load tests to examine the vertical bearing behavior will be carried out. Moreover, it is

needed to confirm the performance of pile body such as the bond strength and the effect of reinforcing pile tip. We will tackle the research issues described as the above sentence in the future.

## REFERENCES

- [1] Kitade, K., Watanabe K., Yamamoto T. and Kubo T., Verification of The Improvement Effect of The Ground Improvement Structure Constructed Using a Low-overhead Clearance Ground Improvement Method. Proceedings of the 67<sup>th</sup> Annual Conference of the Japan Society for Civil Engineers, 2012, pp.799-800.
- [2] Japanese Geotechnical Society, Standards of the Japanese Geotechnical Society (Method for Vertical Load Test of Piles), Japanese Geotechnical Society, 2001.
- [3] Railway Technical Research Institute., Design Standard for Railway Structures and Commentary (Foundation Structures), Railway Technical Research Institute, 2012.

# REVIEW ON CONCEPTS, RESEARCH, AND CHALLENGES FOR THE ADOPTION OF PERMEABLE PAVEMENT SYSTEM IN VIETNAM

Van Nam Pham<sup>1</sup>, Hoang Giang Nguyen<sup>2</sup>, Tien Dung Nguyen<sup>2</sup>, and Ken Kawamoto<sup>1,2</sup>

<sup>1</sup>Graduate School of Science and Engineering, Saitama University, Japan, <sup>2</sup> Hanoi University of Civil Engineering, Vietnam

## ABSTRACT

To make flood control and to mitigate urban heat islands, numerous studies of permeable pavement systems (PPS) have been carried out, especially in the fields of road, material, geotechnical, and environmental engineering. In developed countries, PPS has been mostly applied to roadways with light traffic load, parking lots, and sidewalks. Additionally, several PPS have been used with heavy loads. Previous studies have also repeated that PPS contributed to improving stormwater quality and driving safety, and reducing stormwater runoff and volume. Despite its popularity, the application of PPS is currently not receiving mainstream use throughout much of developing countries such as Vietnam. This study, therefore, investigated structural design, performance, water drainage control, operation and maintenance, case studies, and challenges necessary to examine suitable and applicable PPS in Vietnam based on the literature survey of previously published research papers and reports, fully considering technical standards/requirements and case studies in developed countries. This literature survey found that some of the most important constraints and corresponding challenges/requirements include site-specific, technical/engineered, sustainability, economic, environmentally friendly, existing associated facilities, current policies, and social when applying PPS in Vietnam.

*Keywords: Permeable Pavement System (PPS), Flood control, Monitoring, Barriers, Challenges.*

## INTRODUCTION

In developing countries, climate change and urban concretization contribute to the increased risk of urban flooding [1]. Traditional systems capture the storm runoff, and subsequently delivered it to nearby receiving rivers or sewage systems, however, they have become inefficient and expensive [2]. In that context, PPS which allows the rainwater to infiltrate in to the permeable surface and base layers, as well as the soil subgrade, have been deployed in many developed countries [3]. Previous studies have constantly demonstrated the beneficial performance of PPS in reducing the surface runoff rate and volume, improving groundwater quality, and providing smooth driving conditions [4-5]. Despite its widespread use in developed countries, it has not received adequate attention in developing countries. Many studies have focused on examining the technical design and engineering performances, however, have not yet shown the barriers and challenges that need to be overcome for PPS adoption in developing countries such as Vietnam. This study, therefore, examined existing research in developed countries with a particular focus on design concepts, materials, performances, and economic aspects, and to potentially assess barriers and challenges to PPS adoption considering various specific factors in Vietnam.

## METHODOLOGY

This review work searched database includes

publications by US and Japan Road Association, Google Scholar, and Web of Science<sup>TM</sup> with several keywords including permeable pavement system (PPS), permeable asphalt pavement (PAP), pervious concrete pavement (PCP), permeable interlocking concrete pavement (PICP), and grid pavement (GP) with combination of design, hydrologic, hydraulic, water quality performance, and cost. Based on this research process, the previously published research papers, reports, technical standards, and case studies in developed countries were selected for review. The present review comprises a summary graphical representation of results, and a table listing barriers and challenges/requirements.

## EXISTING PPS IN DEVELOPED COUNTRIES

### Permeable pavement system

In addition to the benefits of stormwater management, PPS also provides pavement for pedestrians and vehicles[5]. PPS are often suitable for light duty such as parking lots and sidewalks [6-8], but case studies also have confirmed the applicable use of PAP and PCP for roadways [9, 10].

### Design concepts

The typical structures of PPS were summarized in Fig. 1. PPS systems can be designed and constructed to accommodate three drainage conditions including infiltration, partial infiltration, and no infiltration pavement [11, 12] and one PPS with a water storage

tank [2] as shown in Fig.1. Depending on the site conditions, and target concepts and setting of PPS such as stormwater control, pollution control, groundwater recharge, and UHI mitigation their designs vary greatly. For example, when exfiltration is not desired or when there is any concern about the possible migration of pollutants into groundwater (i.e., pollution control) the PPS with an impermeable liner

should be constructed (Fig.1c and d).

When targeting the UHI mitigation, PICP and PCP might be considered due to their lower surface temperature in the same weather condition instead of PAP [13-14]. The reservoir thickness is mainly determined by hydrological design (i.e., rainwater control). The design process of PPS has been well documented by several guidelines [2, 5].

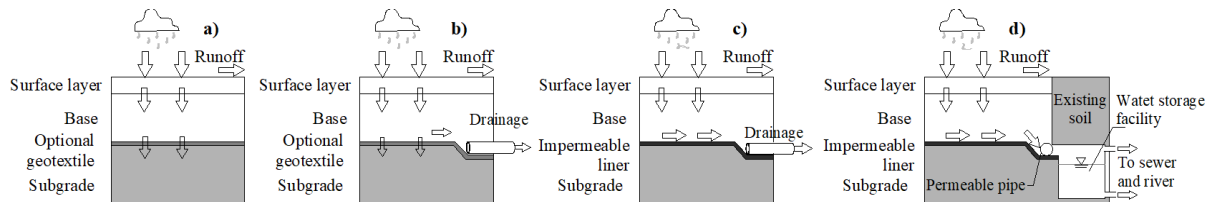


Fig. 1 Typical structure of PPS [2, 11]. (a) Full infiltration, (b) Partial infiltration, (c) No infiltration, (d) No infiltration with a water storage facility.

## Materials

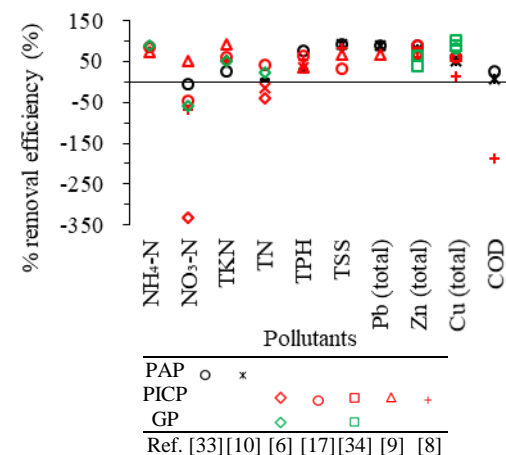
Generally, materials used for roadbed and surface layers must have appropriate engineering properties and environmental safety [2]. Granular roadbed applies to the roadbed structure of roadway, parking lot, and sidewalk, while stabilized materials such as asphalt and cement-based can be considered to use for the upper roadbed of the roadway due to their high strength [2]. Using recycled materials and industrial by-products has received much attention recently [15]. Pham et al. [16] used recycled concrete (RC) and autoclaved aerated concrete (AAC) which is an industrial by-product for roadbed materials. The results showed a significant improvement in water retention capacity was found by blending AAC grains and the saturated volumetric water contents for 20 and 40% AAC blended RC samples increased approximately 1.8 to 2.2 times compared to that of RC 100% while still satisfying the minimum bearing capacity for road base material.

## Performances

### Water quality

PPS reduces the total pollutant mass discharged to receiving systems by diminishing runoff and outflow volumes and removing pollutants from stormwater [17]. Pollutants of interest include suspended solids, metals, nutrients, and hydrocarbons [18]. The pollution removal efficiency of PPS was showed in Fig.2. In general, PPS contributes to reducing pollutants concentration, but the removal rate varies greatly, even with the same type of pavement. This might be attributed to not only the pavement structure itself but also local sources of pollution [18]. It also can be seen that PPS has been effective to remove heavy metals such as Pb, Zn, and, and **TSS** by at least

20 % [9-10] while the removal rate of nutrients (i.e., nitrogen species) is somehow less effective (negative and positive removal efficiency). Collins et al [6] examined the transformation and fate of N through PPS. He concluded that PPS provides suitable conditions for nitrification  $\text{NH}_4^+$  to  $\text{NO}_3^-$  based on the observation that PPS exfiltration had consistently lower TKN and  $\text{NH}_4^+$  concentrations and consistently higher  $\text{NO}_3^-$  concentrations than asphalt runoff. Collins et al [6] and Yong et al [19] observed that TN concentrations can be higher in PPS effluent than in asphalt runoff and atmospheric deposition. The pH from exfiltration of PPS has been demonstrated to be basic ranging from 7.7 to 10 [6, 8], while that of rainfall and asphalt runoff tend to be acidic ranging from 6.5 to 7.6 [20-21]. Limited studies examined the potential for decreasing pollutant removal with age after new construction.



NH<sub>4</sub>-N: Ammonia nitrogen, NO<sub>3</sub>-N: Nitrate as nitrogen, TKN: Total Kjeldahl nitrogen TPH: Total petroleum hydrocarbons, TSS: total suspended solids, TN: total nitrogen, and COD: Chemical oxygen demand.

Fig.2 Pollution removal efficiency of PPS.

### Hydrologic and hydraulic performance

Climatic conditions (i.e., cumulative rainfall) is one of the factors that affect hydrologic performance [22]. Figure 3 showed the relationship between runoff and cumulative rainfall at an event. Generally, PPS is more effective in reducing runoff rate (ranging between no runoff and 4/3:1 line) than asphalt conventional pavement (ranging between no runoff and 4/3:1 and 4:1 line). Most technical standards indicated that PPS is restricted in places with high water tables or low soil permeability [4-5]. Few studies, however, have investigated the hydrologic performance under these conditions.

One of the concerns of PPS is clogging and loss of hydraulic function over time. Fig.4 describes the in-situ infiltration rate as a function of the age of pavement. The age, in this study, is the year of PPS since new construction at the time of the in-situ surface infiltration test. It can be seen that the infiltration rate decreases rapidly over time although the minimum permeability requirement is still satisfied many years after new construction. However, without regular maintenance, a complete loss of hydraulic capacity can occur rapidly. For example, Boogaard et al. [23] examined the effect of the age of 55 PPS which was installed in the Netherlands and Australia with the age ranging from 1 to 12 years on their infiltration function. There is some PPS loss their hydraulic function only after an age of 1 to 4 years. Measuring in-situ infiltration rate is the only common method used to access clogging. Therefore, developing a suitable monitoring system is essential to access long-term hydraulic performance, but not much information in the literature discusses this system.

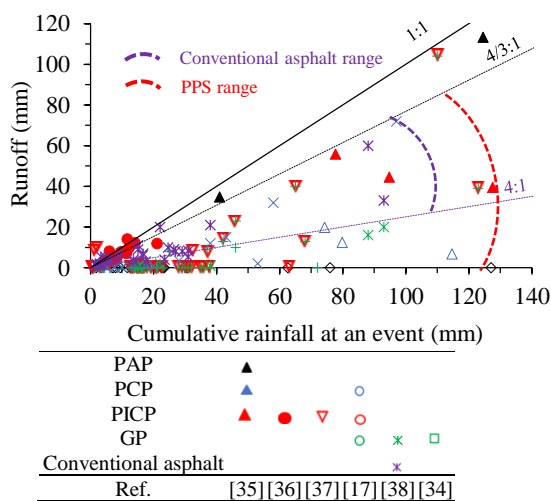


Fig.3 Runoff as a function of cumulative rainfall at an event of PPS.

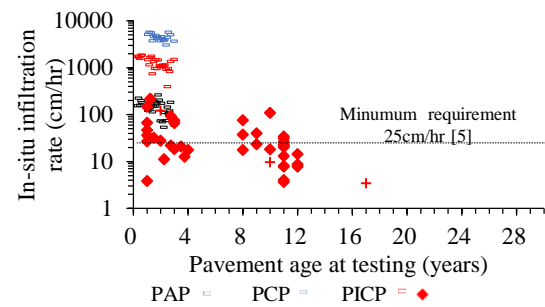


Fig.4 In-situ infiltration rate as a function of age of PPS [23, 39].

### Cost

The economic efficiency of PPS remains a challenge. There are limited reports on initial construction costs. A report by ASCE (2015) [11] collects the estimated costs for conventional asphalt pavement and PAP from projects in San Diego County in 2007. The result showed that the square foot costs of PAP are almost 2 times higher than that of conventional asphalt pavements, mainly due to the higher cost of excavation and installation of the subbase of PPS. The PPS is expected to have a lower overall price based on the hypothesis of reducing the need for stormwater infrastructure, and surface water treatment [4]. However, there are no reports to assess the efficiency of these costs.

### POTENTIAL ADOPTION OF PPS IN VIETNAM

#### Barriers and challenges/requirements for the adoption of PPS in Vietnam

Experience from developed countries shows that PPS still has limitations such as the applicability of PPS under unfavorable conditions (i.e., poorly draining soil and high water table), the potential risks of contaminating groundwater, and loss of long-term hydraulic function due to clogging. A suitable monitoring system for clogging assessment has not yet been established. Besides, the construction of PPS often requires highly qualified human resources [5]. The cost uncertainty remains a concern. Although designed to have a lifespan as conventional pavement, PPS is generally expected to be shorter [24].

All these limitations will become barriers to the adoption of PPS in Vietnam. Even in developed countries, although widely acknowledged, the above limitations still exist somewhere. For example, Cote et al [25] assessed the social and economic barriers to use in residential driveways in Kitchener, Canada, and showed that social perception, price, and



technological acceptance are barriers to overcome. Monroe et al. [22] had an overview of PPS for applying in Small Island Developing States and also pointed out limitations of PPS, aggregate choice and availability, and support from policymakers as important parameters when considering PPS adoption. All the above experiences on the barriers, requirements/challenges that need to be overcome to be able to apply PPS in Vietnam have been carefully reviewed and summarized in Table 1. These barriers include site-specific, technical/engineered, sustainability, economic, environmentally friendly, existing associated facilities, current policies, and social. It is clear that, whether these barriers are natural factors, such as site-specific (i.e., poorly draining soil, high water table, and climate) occurring unpredictably, or other factors that can be controlled by individuals/communities, the geographic and geologically, and social factors of Vietnam present unique parameters for considering the PPS system.

#### **Specific factors to be considered in Vietnam**

Vietnam is incorporated by large fertile, low-lying, and densely populated deltas of the Mekong and the Red Rivers [1]. Vietnam would be classified as a region physically vulnerable to present day climate extremes and potentially to changes in the typhoon regime and sea-level rise [1,26]. The annual average rainfall is 2050 mm in the rainy season and the lowest is 1600 mm in summer [27]. Many areas in the Mekong delta are under sea level with a mean elevation of only 80 cm above sea level. According to Asian Development Bank, the population is approximately 85.8 million in 2009, with an urban population of 25.4 million (nearly 30% of the total population). The rate of urbanization has averaged 3.4% per annum since 2000 and is expected to remain at the same level [28]. Most urban growth is in the metropolises of Hanoi and Ho Chi Minh city [28].

Regarding site-specific barriers, the high water table is a factor that needs to be fully considered. As discussed above, some areas of Vietnam are below sea level, with the average elevation being just 80 cm above sea level. Moreover, Vietnam is also strongly influenced by high tides. One of the presented requirements is the design of the PPS as a detention system [29]. Although hydrologic has performed well in developed countries, however, the climate factor is different. Vietnam tends to suffer more annual rainfall than the reviewed areas. For example, New Jersey (USA), New Hampshire (USA), Toronto (Canada), and South Australia have an average

annual rainfall of 1260, 1200, 834, and 538 mm, respectively [30], while that of Vietnam the lowest of 1600 mm in the summer, and the rainy season is up to 2050 mm. To reduce investment costs, using locally available materials is proven to be economically viable, especially recycled materials, and these materials are very abundant and safe in Vietnam [15].

There are concerns about groundwater contamination and clogging, however many, case studies still demonstrate perform well for many after new construction. But, in the long term, it is necessary to establish a suitable system for assessing clogging. In Vietnam, the planning of traditional drainage systems and infrastructure facilities is not synchronized with the speed of urbanization and does not take into account the effects of extreme weather conditions ( i.e., climate change, sea level rise) leads to many consequences [31], despite the promulgation of current policies on strengthening solutions to deal with the problems above, taking advantage of natural conditions [32]. For example, a decision no.35/1999/QĐ-TTg dated 1999 on ratifying the orientation for the development of urban drainage in Vietnam up to the year 2020 considered the urban flood reduction as a top priority, and it is necessary to have solutions to take advantage of natural factors such as soil infiltration. PPS meets this requirement and can be a premise to adopt PPS in Vietnam. But it is necessary to make policymakers recognize this benefit.

#### **CONCLUSIONS**

PPS are suitable for a wide variety of parking lot, sidewalks, and roadways. They have exhibited beneficial performance in reducing the surface runoff rate (i.e., from 25-100% with the cumulative rainfall less than about 120 mm), improving groundwater quality (e.g., at least of 20% removal efficiency for Pb, Zn, Cu, and TSS). Despite its popularity, there are still concerns regarding environmental, and hydrologic performances in the long-term and under adverse conditions, and cost uncertainty. The social and policy factors have not been discussed in guidelines and case studies in developed countries. A suitable monitoring system for accessing clogging has not been established. The above concerns are barriers to PPS adoption in developing countries. To adopt PPP in Vietnam, all must be carefully considered in the conditions of Vietnam. This needs the cooperation of all individuals, scientists, the whole community, and policymakers.

Table 1. Barriers and challenges/requirements for the adoption of PPS in Vietnam.

No	Item	Barriers	Challenges/requirements	Refs
1	Site specific	Poorly draining soil and high water table	Design a pavement as a detention system	[26, 29, 40]
		Climate	Establish guidance that fully considers the suitable intensity -duration – frequency curve	[2]
		Aggregate selection and availability	Practice sustainable methods to obtain construction aggregates. Local construction materials are easily available	[22]
2	Technical/Engineered	Groundwater contamination	Treated stormwater should subsequently be discharged into a suitable drainage system.	[41]
		Clogging/maintenance	Establish an applicable and suitable monitoring system to assess clogging and sign of distress	[42]
		Ease of construction, maintenance	Proposed a system is simple to construct and maintain with locally available human resources and expertise	[11]
3	Sustainable	Durable and long-term performance	Perform lifespan as traditional pavement and have a capacity to absorb dissolved pollutant in a manner that outlasts the useful life of PPS	[11]
4	Economical	Less investment	Reduce initial cost by use of available construction materials	[22]
5	Environmentally friendly	Use of safe PPS	PPS and its construction materials used do not harm the environment	[2]
7	Associated facilities	Asynchronous	Demand should be transferred to the natural renewed solution to cope with impervious surface expansion and overload drainage facility	[31, 43]
8	Policy and law	Policy on flood control	Promote the implementation of current policies on strengthening flood prevention and water pollution by taking advantage of available natural conditions such as the infiltration capacity of soil	[32]
9	Social	Awareness	Policymakers easily recognize PPS practice as being beneficial	[25]

## ACKNOWLEDGEMENTS

This research was supported by JST-JICA Science and Technology Research Partnership for Sustainable Development (SATREPS) project (No. JPMJSA1701).

## REFERENCES

- [1] W. N. Adger, “Social Vulnerability to Climate Change and Extremes in Coastal Vietnam,” *World Dev.*, vol. 27, no. 2, pp. 249–269, 1999.
- [2] Japan Road Association, “Permeable Pavement Handbook,” 2007, in Japanese.
- [3] M. E. Dietz, “Low impact development practices: A review of current research and recommendations for future directions,” *Water. Air. Soil Pollut.*, vol. 186, no. 1–4, pp. 351–363, 2007,
- [4] NAPA, “Porous Asphalt Management for Stormwater Pavements, Design, Construction and Maintenance Guide,” Series 131, 2008.
- [5] American Society of Civil Engineers (ASCE), “Permeable Interlocking Concrete Pavement”, 2018.
- [6] A. Collins et al, “Side-by-Side Comparison of Nitrogen Species Removal for Four Types of Permeable Pavement and Standard Asphalt in Eastern North Carolina,” *J. Hydrol. Eng.*, vol. 15, no. 6, pp. 512–521, 2010.
- [7] M. Legret and V. Colandini, “Effects of a porous pavement with reservoir structure on runoff water: Water quality and fate of heavy metals,” *Water Sci. Technol.*, vol. 39, no. 2, pp. 111–117, 1999.
- [8] T. and R. Conservation, “Performance Evaluation of Permeable Pavement and a Bioretention Swale Seneca College, King City, Ontario,” 2007.
- [9] J. K. Gilbert and J. C. Clausen, “Stormwater runoff quality and quantity from asphalt, paver, and crushed stone driveways in Connecticut,” *Water Res.*, vol. 40, no. 4, pp. 826–832, 2006.
- [10] M. E. Barrett, “Effects of a Permeable Friction Course on Highway Runoff,” *J. Irrig. Drain. Eng.*, vol. 134, no. 5, pp. 646–651, 2008.
- [11] S. D. Eisenberg B, Lindow KC, “Permeable pavements,”(ASCE), 1801 Alexander Bell Drive Reston, Virginia, 20191-4382, 2015.
- [12] W. Lin, S. W. Ryu, and Y. H. Cho, “A case study of flow characteristics of permeable pavements by time and space model,” *Can. J. Civ. Eng.*, vol. 41, no. 7, pp. 660–666, 2014.
- [13] T. Asaeda and V. T. Ca, “Characteristics of permeable pavement during hot summer weather and impact on the thermal environment,” *Build. Environ.*, vol. 35, no. 4, pp. 363–375, 2000.
- [14] H. Li, J. T. Harvey, T. J. Holland, and M. Kayhanian, “The use of reflective and permeable pavements as a potential practice for heat island mitigation and

- stormwater management,” *Environ. Res. Lett.*, vol. 8, 2013.
- [15] N.V Tuan *et al.*, “Current status of construction and demolition waste management in Vietnam: Challenges and opportunities,” *Int. J. GEOMATE*, vol. 15, no. 52, pp. 23–29, 2018.
- [16] P. Van Nam, A. Kato, N. H. Giang, N. Van Tuan, and P. Q. Minh, “Evaluating effects of mixing proportion on water retention curve and pore size distribution of recycled concrete aggregates blended with autoclaved aerated concrete grains,” *GEOMATE*, 2020.
- [17] B. Bean, “Evaluation of Four Permeable Pavement Sites in Eastern North Carolina for Runoff Reduction and Water Quality Impacts,” *J. Irrig. Drain. Eng.*, vol. 133, no. 6, pp. 583–592, 2007.
- [18] J. A. P. Drake, A. Bradford, and J. Marsalek, “Review of environmental performance of permeable pavement systems: State of the knowledge,” *Water Qual. Res. J. Canada*, vol. 48, no. 3, pp. 203–222, 2013.
- [19] C. F. Yong, A. Deletic, T. D. Fletcher, and M. R. Grace, “Hydraulic and treatment performance of pervious pavements under variable drying and wetting regimes,” *Water Sci. Technol.*, vol. 64, no. 8, pp. 1692–1699, 2011.
- [20] J. A. P. Drake, A. Bradford, and J. Marsalek, “Review of environmental performance of permeable pavement systems: State of the knowledge,” *Water Qual. Res. J. Canada*, vol. 32, no. 1, pp. 49–56, 2013.
- [21] E. A. Fassman and S. D. Blackburn, “Road Runoff Water-Quality Mitigation by Permeable Modular Concrete Pavers,” *J. Irrig. Drain. Eng.*, vol. 137, no. 11, pp. 720–729, 2011.
- [22] K. T.-M. John Monrose, “Technological Review of Permeable Pavement Systems for Applications in Small Island Developing States (SIDS),” 2018.
- [23] F. Boogaard, T. Lucke, and S. Beecham, “Effect of age of permeable pavements on their infiltration function,” *Clean - Soil, Air, Water*, vol. 42, no. 2, pp. 146–152, 2014.
- [24] M. Scholz and P. Grabowiecki, “Review of permeable pavement systems,” *Build. Environ.*, vol. 42, no. 11, pp. 3830–3836, 2007.
- [25] S. A. Cote and S. E. Wolfe, “Research article: Assessing the social and economic barriers to permeable surface utilization for residential driveways in Kitchener, Canada,” *Environ. Pract.*, vol. 16, no. 1, pp. 6–18, 2014.
- [26] P. S. J. Minderhoud *et al.*, “Mekong delta much lower than previously assumed in sea-level rise impact assessments,” *Nat. Commun.*, vol. 10, no. 1, pp. 1–13, 2019.
- [27] T. Thriveni, N. Lee, G. Nam, and A. J. Whan, “Impacts of Climate Change on Water Crisis and Formation of Green Algal Blooms in Vietnam,” *J. Energy Eng.*, vol. 26, no. 1, pp. 68–75, 2017.
- [28] Asian Development Bank, *Viet Nam Urban Sector Assessment, Strategy and Road Map*. 2012.
- [29] E. A. Fassman and S. Blackburn, “Urban runoff mitigation by a permeable pavement system over impermeable soils,” *J. Hydrol. Eng.*, vol. 15, no. 6, pp. 475–485, 2010.
- [30] M. Razzaghamanesh and S. Beecham, “A review of permeable pavement clogging investigations and recommended maintenance regimes,” *Water (Switzerland)*, vol. 10, no. 3, 2018.
- [31] N. V. Giang and N. T. Dat, “Solutions to deal with flooding by using green buildings in Vietnamese urban areas from Japanese experience,” *IOP Conf. Ser. Mater. Sci. Eng.*, vol. 869, no. 7, 2020.
- [32] “Decision no.35/1999/QĐ-TTg dated 1999. Ratifying the orientation for the development of urban drainage in Vietnam up to the year 2020. Issued by the Prime Minister,” 1999.
- [33] B. J. Eck, R. J. Winston, W. F. Hunt, and M. E. Barrett, “Water Quality of Drainage from Permeable Friction Course,” *J. Environ. Eng.*, vol. 138, no. 2, pp. 174–181, 2012.
- [34] B. O. Brattebo and D. B. Booth, “Long-term stormwater quantity and quality performance of permeable pavement systems,” *Water Res.*, vol. 37, no. 18, pp. 4369–4376, 2003.
- [35] I. A. Muhammed Mustafa, Jianpeng Zhou, “Effect of Rainfall Intensity on Stormwater Reduction in Combined Sewers from the Impact of Permeable Pavements,” *World Environ. Water Resour. Congr. 2017*, pp. 383–390, 2017.
- [36] C. L. Abbott and L. Comino-Mateos, “In-situ hydraulic performance of a permeable pavement sustainable urban drainage system,” *Water Environ. J.*, vol. 17, no. 3, pp. 187–190, 2003.
- [37] B. Hunt, S. Stevens, and D. Mayes, “Permeable pavement use and research at two sites in Eastern North Carolina,” *Glob. Solut. Urban Drain.*, 2002.
- [38] E. A. Dreelin, L. Fowler, and C. Ronald Carroll, “A test of porous pavement effectiveness on clay soils during natural storm events,” *Water Res.*, vol. 40, no. 4, pp. 799–805, 2006.
- [39] R. A. Brown and M. Borst, “Evaluation of Surface Infiltration Testing Procedures in Permeable Pavement Systems,” *J. Environ. Eng.*, vol. 140, no. 3, p. 04014001, 2014.
- [40] Q. T. Nguyen, “The main causes of land subsidence in Ho Chi Minh City,” *Procedia Eng.*, vol. 142, pp. 334–341, 2016.
- [41] S. Wilson, A. P. Newman, T. Puehmeier, and A. Shuttleworth, “Performance of an oil interceptor incorporated into a pervious pavement,” *Eng. Sustain.*, vol. 156, no. 1, pp. 51–58, 2003.
- [42] M. B. Robert A. Brown, “Assessment of Clogging Dynamics in Permeable Pavement Systems with Time Domain Reflectometers,” *J. Environ. Eng.*, vol. 139, pp. 1255–1265, 2013.
- [43] L. T. Dung *et al.*, “Sustainable Urban Drainage System Model for the Nhieu Loc - Thi Nghe Basin, Ho Chi Minh City,” *IOP Conf. Ser. Earth Environ. Sci.*, vol. 652, no. 1, 2021.

# INFLUENCE OF FOOTING SIZE AND RELATIVE DENSITY IN ULTIMATE BEARING CAPACITY FORMULA OF STRIP FOOTING ON SANDY SOILS

Tahir Iqbal<sup>1</sup>, Satoru Ohtsuka<sup>2</sup>, Koichi Isobe<sup>3</sup>, Yutaka Fukumoto<sup>4</sup>, Kazuhiro Kaneda<sup>5</sup>

<sup>1</sup>Department of Energy and Environment Engineering, Nagaoka University of Technology, Japan

<sup>2,4</sup>Department of Civil and Environmental Engineering, Nagaoka University of Technology, Japan

<sup>3</sup>Division of Field Engineering for Environment, Hokkaido University, Japan

<sup>5</sup>Department of Civil and Environmental Engineering, Chiba Institute of Technology, Japan

## ABSTRACT

For the estimation of the ultimate bearing capacity (UBC) of footings, most contemporary formulas employ a linear yield function in the shear stress-normal stress space. However, it is well known that the general property in the failure envelopes of sandy soils manifests the non-linear effect of the stress level on the peak friction angle. Moreover, the effect of relative density on bearing capacity is often not well considered by the conventional UBC formulas. The focus of this research study is the assessment of the UBC of surface strip footings ascribed to the effect of confining stress level and relative density ( $D_r$ ) on the shear strength of sandy soils. The rigid plastic finite element method (RPFEM), using the confining stress dependence property of Toyoura sand, is utilized in non-linear finite element analyses. The ground failure domains in the case of the non-linear shear strength model are gleaned smaller than those in the case of the linear shear strength one. The results of the UBC analyses are ascertained to be consistent with those of the centrifuge experiments in the published references. The analysis results are compared with prevailing guidelines, for instance, the Architectural Institute of Japan (AIJ) and the Japan Road Association (JRA), which are developed for the mean shear strength property of sandy soils. The precision of the UBC formula is examined by considering the effect of relative density. The applicability of the UBC formula to effective stress analysis is also discussed, and the modified formula is developed.

*Keywords: Ultimate bearing capacity, Strip footing, Size effect with footing width, Relative density, Sandy soils*

## INTRODUCTION

Most of the formerly developed well known bearing capacity formulas, for instance, Terzaghi, do not appraise the effect of footing size and relative density on the shear strength property of sandy soils. On the other hand, numerous experimental studies have now ratified that the typical yielding phenomenon of sandy soils is non-linear in shear stress-normal stress space. The UBC formulas being commonly used in Japan are those recommended by AIJ [1] and JRA [2], which consider the same effect of footing size on UBC in the absence of surcharge load. The simplified AIJ bearing capacity formula is indicated in Eq. (1) in the case of surface strip footing under centric vertical load only.

$$q = \frac{1}{2} \gamma B \eta N_\gamma \quad \text{where} \quad \eta = \left( \frac{B}{B_o} \right)^{-\frac{1}{3}}, \quad B_o = 1 \text{ m} \quad (1)$$

Here,  $N_\gamma$  depicts the well known bearing capacity factor,  $\gamma$  denotes the soil unit weight,  $B$  and  $B_o$  account for the footing size and reference value in it, respectively, and  $\eta$  symbolizes the size effect modification factor for  $N_\gamma$ .

In both AIJ and JRA formulas, the stress level

effect is estimated in terms of footing size only; for the centric vertical load without surcharge. Nonetheless, prominent experimental studies, for instance, Zhu [3], have highlighted the significance of soil unit weight ( $\gamma$ ) in determining the stress level effect on UBC in terms of product  $\gamma B$ . Similarly, the size effect mechanism has also been attributed to the effect of relative density in the eminent experimental studies [4]–[6]. Therefore, this study is focused on the estimation of the size effect of footing on UBC under centric vertical load in the case of total and effective stress analysis conditions. RPFEM, using non-linear shear strength characteristics of Toyoura sand, is utilized in finite element analysis. A modified UBC formula is put forward, rendering consistency with the centrifuge experiments in the published references. Moreover, the efficacy of the proposed formula is examined through UBC analysis in the case of various relative densities of Toyoura sand and other granular soils existing in the European region.

## CONSTITUTIVE EQUATION FOR RPFEM

The typical non-linear yield function employed for numerical analysis in this research investigation is indicated in Eq. (2).

$$f(\sigma) = aI_1 + (J_2)^n = b \quad (2)$$

Here,  $a$  and  $b$  express the material shear strength characteristics, i.e., internal friction and cohesion, respectively, while  $n$  denotes the non-linearity of the yield function in relation to the first stress invariant,  $I_1$ , and the second invariant of deviator stress,  $J_2$ . The non-linear rigid plastic constitutive equation, as proposed by Nguyen [7], is used for numerical computations.

## NON-LINEAR SHEAR STRENGTH OF SANDY SOILS

In this study, Toyoura sand is used to model the non-linear shear strength property of sandy soils. The physical characteristics of Toyoura sand are listed in Table 1 after Tatsuoka [8].

Table 1 Physical characteristics of Toyoura sand

Property	Value
Specific gravity of solids, $G_s$	2.64
Max. void ratio, $e_{\max}$	0.977
Min. void ratio, $e_{\min}$	0.605
Mean grain size, $d_{50}$	0.16 mm
Uniformity coefficient, $C_u$	1.46
Grain shape	angular to sub-angular
Minerology	quartz (90%), chert (4%)

Figure 1 manifests the influence of confining pressure on the shear strength of Toyoura sand based on the experimental study of Tatsuoka [9]. It demonstrates that the internal friction angle,  $\phi$ , decreases with the increase in confining pressure for a given void ratio,  $e$ . In this study, triaxial compression test results are used to arrange the correlation between  $\phi$  and  $I_1$  (Fig. 2) with the aim of estimating the influence of pressure level on  $\phi$ . Figure 2 specifies the reduction in internal friction angle with the increase in the first stress invariant. Moreover, the experimental data is extrapolated to estimate the y-intercept, i.e., internal friction angle,  $\phi_0$ , against each relative density,  $D_r$ , as indicated through dashed lines in Fig. 2, to normalize the internal friction angle corresponding to the various stress levels. By using the least squares method, normalized relationships are established between  $\phi/\phi_0$  and  $I_1$  corresponding to each relative density as well as the mean trendline (Fig. 3). Due to the similarity in soil response having different  $D_r$  under various stress levels, it is meaningful to establish a simplified relation based on the mean property of Toyoura sand.

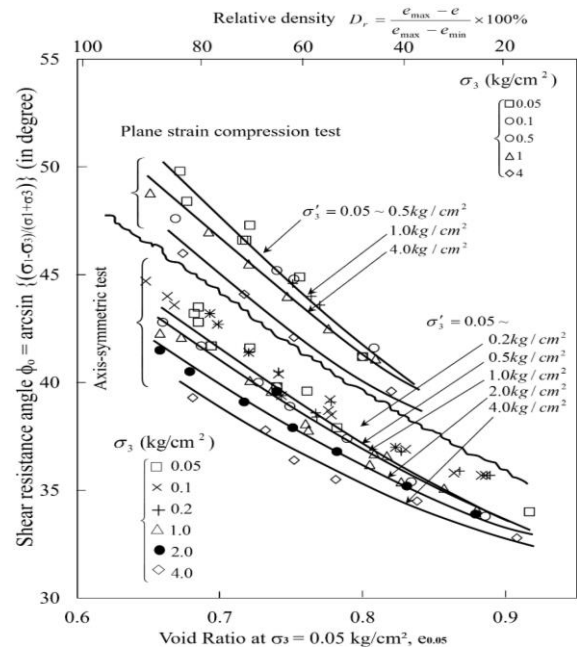


Fig. 1 Strength test results of air-pluviated Toyoura sand<sup>[9]</sup>

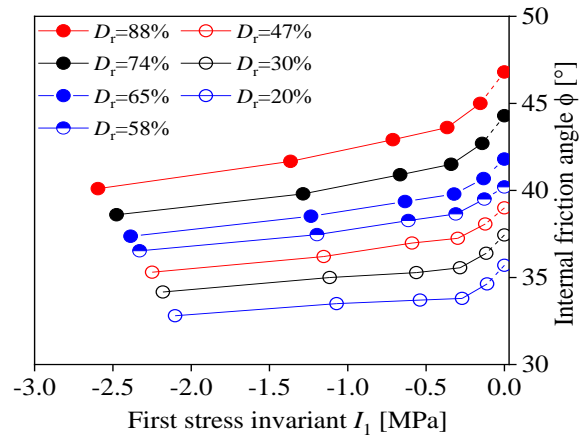


Fig. 2 Relation between  $\phi$  and  $I_1$  for Toyoura sand (after Tatsuoka<sup>[9]</sup>)

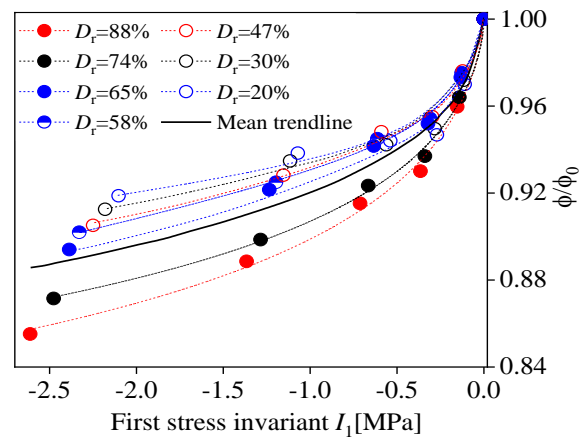


Fig. 3 Normalized relation between  $\phi/\phi_0$  and  $I_1$



Based on the relationships plotted in Fig. 3, the non-linear shear strength parameters are set corresponding to each relative density and the mean trendline in Tables 2 and 3, respectively, in the case of Toyoura sand.

Table 2 Shear strength parameters for Toyoura sand

$D_r$ (%)	$\phi_0$ (°)	$\gamma$ (kN/m <sup>3</sup> )	$a$	$b$	$n$
20	35.7	13.6	0.217		0.522
65	41.8	15.0	0.262	1	0.526
88	46.8	15.7	0.280		0.528

Table 3 Parameters based on the mean property

$\phi$ (°)	$a$	$b$	$n$
30	0.175		
35	0.216	1	0.526
40	0.257		

## ULTIMATE BEARING CAPACITY ANALYSIS

### Drucker-Prager Criteria and Conventional UBC Estimation

This section analyzes the bearing capacity of strip footing under plane strain condition by employing the RPFEM Drucker-Prager (DP) using the shear strength parameters identical to those gleaned from conventional triaxial compression tests. The bearing capacity is estimated for a wide range of footing sizes (1 m to 30 m) and soil shear strength parameters to properly investigate the correctness of the applied method. The footing is considered as a perfectly rigid mass, while the boundary conditions are defined to be large enough so as not to have any influence of rigidity on the collapse mechanism. The analysis results are plotted in comparison with the AIJ, JRA, and one of the conventional UBC formulas, i.e., Terzaghi [10], in the case of centric vertical load only (Fig. 4). As the Drucker-Prager criterion is a simplified Mohr-Coulomb criterion; thereby, the RPFEM(DP) results are in good agreement with the Terzaghi [10]; however, there is a marked difference with those from the AIJ and JRA formulas. This distinction is primarily because both AIJ and JRA formulas consider the size effect of footing in UBC estimation in contrast with the Mohr-Coulomb yield criterion. Numerous experimental studies have also pointed out the stress level effect on UBC [11]–[14]. However, the correctness of the semi-experimental AIJ and JRA formulas needs to be well investigated based on the shear strength property of real sandy soils, such as Toyoura sand, thereby endorsing the necessity of this research study.

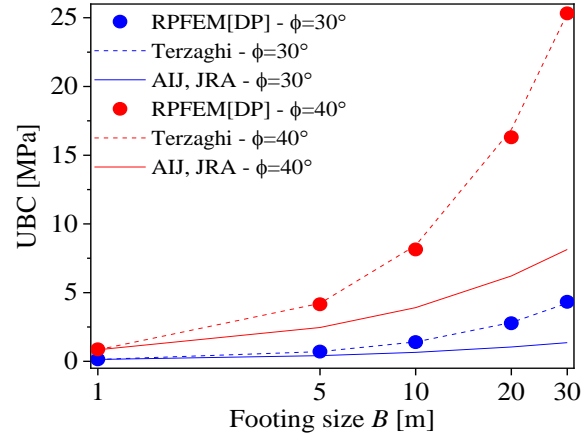


Fig. 4 Comparison of UBC results ( $\gamma=18$  kN/m<sup>3</sup>)

### Bearing Capacity Analysis Using Non-Linear Shear Strength Property

In this section, UBC analysis is conducted using the non-linear shear strength parameters set in Table 3. The UBC results through the non-linear (NL) RPFEM are arranged in Fig. 5 for the given range of footing sizes and shear strength parameters. Figure 5 illustrates that the UBC analysis based on the mean confining stress property of Toyoura sand well estimates the size effect. Experimental studies [3] have indicated the stress level effect as a function of  $\gamma B$ . Moreover, often practical situations involving frequent variations in the ground water table come across, ultimately affecting the soil strength characteristics. Therefore, it is necessary to broadly investigate the effect of  $\gamma$  on UBC. The typical ground failure domain in the case of NL analysis is smaller than that of the DP criterion (Fig. 6) due to the reduction in  $\phi$  at higher stress levels. Moreover, the failure mode at  $\gamma=8$  kN/m<sup>3</sup> is obtained larger than at  $\gamma=18$  kN/m<sup>3</sup> in the case of NL shear strength, mainly because of the difference in the mean effective stress in both cases, in contrast with the DP criterion.

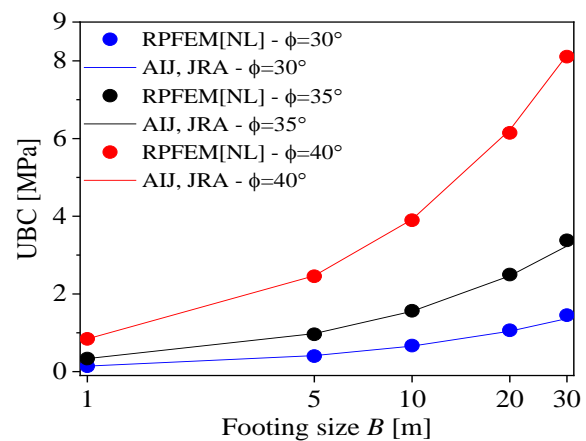


Fig. 5 Comparison of UBC results ( $\gamma=18$  kN/m<sup>3</sup>)



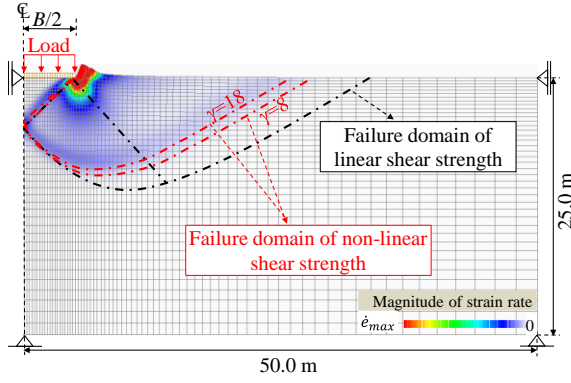


Fig. 6 Ground deformation domains in the case of  $\phi=35^\circ$ ,  $B=10$  m and variation in  $\gamma$  (kN/m<sup>3</sup>)

## ULTIMATE BEARING CAPACITY FORMULA FOR SANDY SOILS

### Modification Coefficient for $N_\gamma$

In this study, the size effect modification coefficient is defined as Eq. (3):

$$\eta_\gamma = \frac{2q}{\gamma B N_\gamma} \quad (3)$$

The analysis results are arranged in Fig. 7 in terms of normalization variable  $\gamma B/p_a$  against  $2q/\gamma B N_\gamma$  in the case of  $\phi=35^\circ$  for variation in  $\gamma$ . Here,  $p_a$  symbolizes the normalization factor i.e., standard atmospheric pressure,  $p_a=101.325$  kPa. Figure 7 manifests the decrease in normalized UBC with the higher stress levels by increasing  $\gamma$  with the mean property of Toyoura sand, while the AIJ and JRA formulas do not consider such an effect of  $\gamma$ . Likewise, previous studies such as Loukidis [15] have also corroborated that the bearing capacity factor  $N_\gamma$  decreases with the increase in  $\gamma$ . Considering the effect of soil unit weight and the findings of experimental studies, it is pertinent to figure out the modification coefficient for  $N_\gamma$ . The RPFEM analysis results are plotted in Fig. 8 for an extensive range of shear strength parameters, i.e.,  $\phi$ , footing sizes, and soil unit weights with the mean property of Toyoura sand to perfectly grasp the influence of stress level and to propose a relationship for the modification coefficient  $\eta_\gamma$  (Eq. (4)) by setting the mean trendline using the least squares method. Although, the range in  $\gamma B/p_a$  encountered in practice lies between 0.1 and 0.6 [15]; however, in this study, results are investigated for a comparatively wide range to broadly fathom out the confining stress dependency of shear strength parameters. The efficacy of the proposed UBC formula (Eq. (5)) is assessed against RPFEM in Fig. 9 for the wide range of  $B$  and shear strength parameters. The newly proposed formula estimates the UBC within  $\pm 5\%$ .

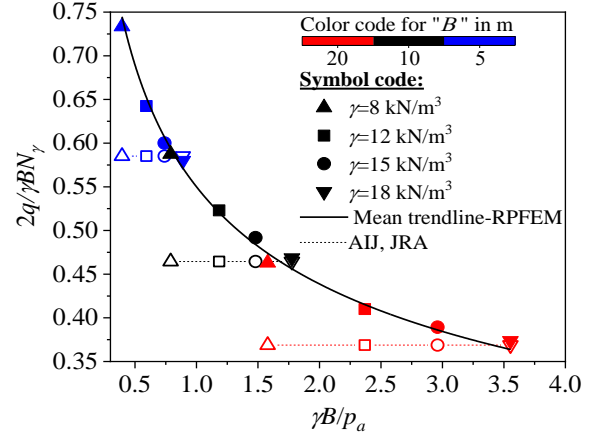


Fig. 7 Effect of  $\gamma$  on  $2q/\gamma B N_\gamma$  in case of  $\phi=35^\circ$

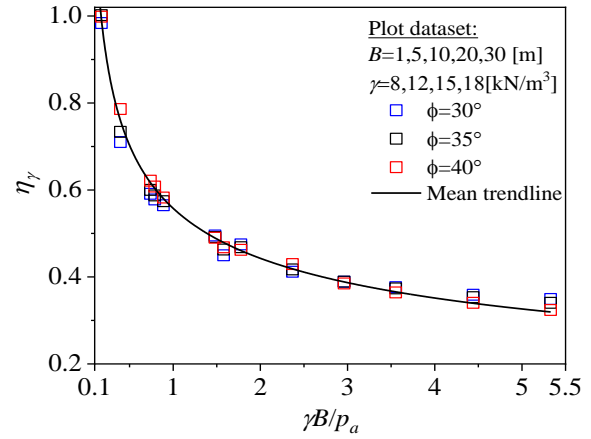


Fig. 8 Relation between  $\eta_\gamma$  and  $\gamma B/p_a$  for mean property in case of Toyoura sand

$$\eta_\gamma = 0.55 \left( \frac{\gamma B}{p_a} \right)^{-\frac{1}{3}} \quad \text{where} \quad 0 \leq \eta_\gamma \leq 1 \quad (4)$$

$$q = \frac{1}{2} \gamma B N_\gamma \eta_\gamma \quad (5)$$

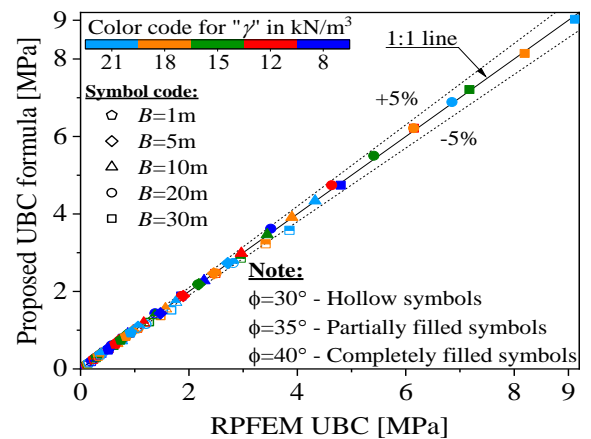


Fig. 9 Performance of the proposed UBC formula

### Effect of Relative Density on UBC

It is pertinent to estimate the UBC for the various compactness levels of Toyoura sand and corresponding  $\gamma$ , i.e.,  $\gamma$  changes with  $D_r$  to check the aptness of the proposed UBC formula ascribed to the size effect. The UBC analysis is conducted based on the non-linear shear strength parameters set in Table 2, and results are arranged in terms of  $\gamma B/p_a$  against  $\eta_\gamma$  for various relative densities and the mean trendline in Fig. 10. Interestingly, the change in  $\eta_\gamma$  with the mean trendline corresponds to the  $D_r=65\%$  in the case of Toyoura sand. Moreover, it can be noticed that the size effect becomes less marked with a decrease in the relative density of Toyoura sand and vice versa. This observation is consistent with the experimental studies [4]–[6]. The proposed formula estimates the size effect within  $\pm 20\%$  for the broad variation in relative density of Toyoura sand (Fig. 11). Moreover, it also estimates the size effect within  $\pm 10\%$  in the case of other granular soils [5] having similar mineralogy as that of Toyoura sand (Fig. 12).

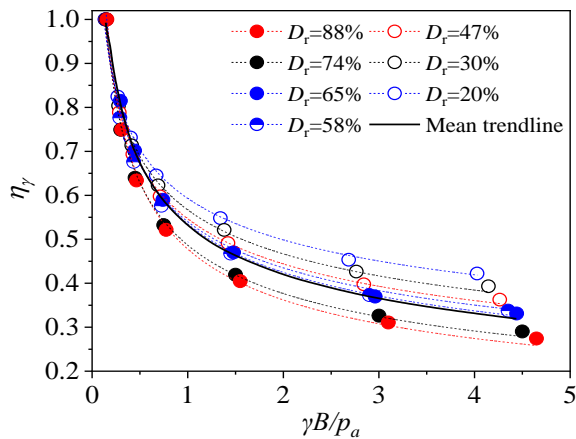


Fig. 10 Relationship between  $\eta_\gamma$  and  $\gamma B/p_a$  in the case of Toyoura sand

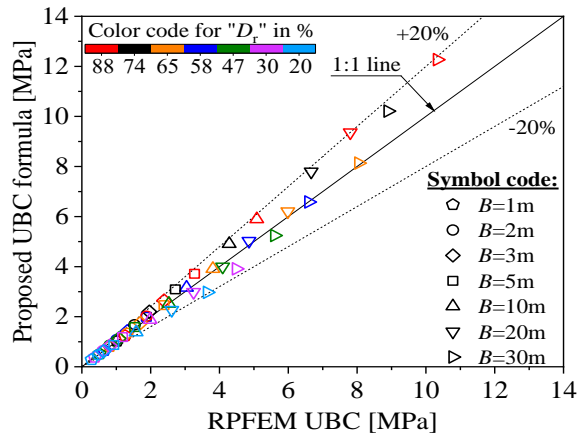


Fig. 11 Performance of the proposed UBC formula for various relative densities of Toyoura sand

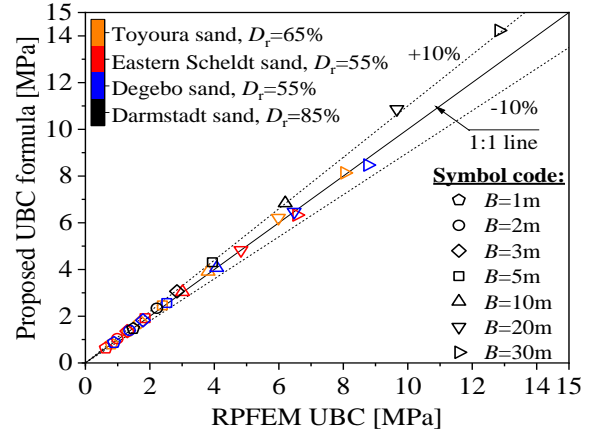


Fig. 12 Performance of the proposed UBC formula in the case of various sands

### Experimental Validation

The estimated bearing capacity based on the RPFEM analysis is compared with the centrifuge model loading tests on surface strip footings by Okahara [16] in Fig. 13 for three different relative densities of 58%, 74%, and 88%. In Fig. 13, RPFEM analysis results indicate fairly good agreement with the experimental findings and a similar effect of footing size can be witnessed. Moreover, bearing capacity results through the proposed UBC formula are also compared with the centrifuge tests by Zhu [3] in the case of silica sand of  $D_r=90\%$  and other conventional UBC formulas (Fig. 14). The unit weight of the Silica sand used for the centrifuge experimentation was  $15.4 \text{ kN/m}^3$  and the confining stress in the triaxial compression tests ranged from 25 to 2500 kPa. As Toyoura sand is also a kind of Silica sand; therefore, a good agreement with the proposed UBC formula is evident from Fig. 14. On the other hand, formulas by Eurocode and the US Army Corps of Engineers (USACE) significantly overestimate the UBC.

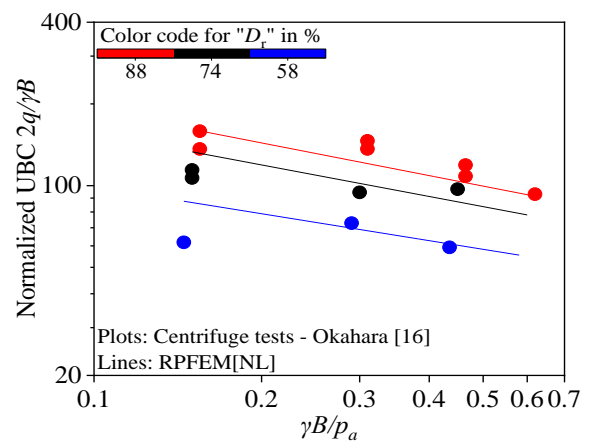


Fig. 13 Comparison of the analysis results with the centrifuge experiments in the case of Toyoura sand

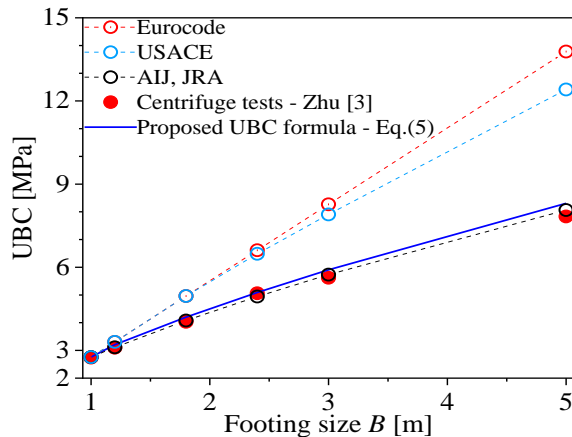


Fig. 14 Experimental validation of proposed UBC formula in the case of  $\phi=46.7^\circ$  and  $\gamma=15.4 \text{ kN/m}^3$

## CONCLUSIONS

A UBC formula was examined in detail and modified based on the mechanical property of Toyoura sand. The applicability of the analysis technique for UBC estimations was corroborated through the centrifuge experiments in the published references. Based on the numerical survey, the effect of soil unit weight was clarified to be well expressed by normalized variable  $\gamma B/p_a$  regarding size effect; therefore, the correction factor for  $N_\gamma$  was newly proposed. Moreover, the applicability of international guidelines such as Eurocode and USACE is found to be limited, ascribed to the size effect of footing on UBC. The proposed formula estimates the size effect on UBC within  $\pm 20\%$  in the case of the wide variation in the relative density of Toyoura sand. Moreover, the performance of the proposed UBC formula was also assessed by analyzing the bearing capacity of other granular soils such as Eastern Scheldt sand, Degebo sand, and Darmstadt sand; and found to estimate the size effect within  $\pm 10\%$ .

## ACKNOWLEDGEMENTS

This work was supported by JSPS KAKENHI Grant Number JP18H01533. The authors deeply acknowledge the financial support of Grant-in-Aid for Scientific Research (B) in Japan.

## REFERENCES

[1] AIJ, Recommendations for Design of Building Foundations, Architectural Institute of Japan, 1988, 2001, pp. 430.  
 [2] JRA, Road Bridge Specifications (Substructure), Japan Road Association, 2017, pp. 205-206.

[3] Zhu B. F., Clark J. I., and Phillips R., Scale Effect of Strip and Circular Footings Resting on Dense Sand, *J. Geotech. Geoenviron. Eng.*, Vol. 127, Issue 7, 2001, pp.613-621.  
 [4] Kimura T., Kusakabe O., and Saitoh K., Geotechnical Model Tests of Bearing Capacity Problems in a Centrifuge, *Géotechnique*, Vol. 35, Issue 1, 1985, pp.33-45.  
 [5] Hettler A., and Gudehus G., Influence of the Foundation Width on the Bearing Capacity Factor, *Soils Found.*, Vol. 28, Issue 4, 1988, pp.81-92.  
 [6] Cerato A. B., and Lutenecker A. J., Scale Effects of Shallow Foundation Bearing Capacity on Granular Material, *J. Geotech. Geoenviron. Eng.*, Vol. 133, Issue 10, 2007, pp.1192-1202.  
 [7] Nguyen D. L., Ohtsuka S., Hoshina T., and Isobe K., Discussion on Size Effect of Footing in Ultimate Bearing Capacity Using Rigid Plastic Finite Element Method, *Soils Found.*, Vol. 56, Issue 1, 2016, pp.93-103.  
 [8] Tatsuoka F., Goto S., and Sakamoto M., Effects of Some Factors on Strength and Deformation Characteristics of Sand at Low Pressures, *Soils Found.*, Vol. 26, Issue 1, 1986a, pp.105-114.  
 [9] Tatsuoka F., Sakamoto M., Kawamura T., and Fukushima S., Strength and Deformation Characteristics of Sand in Plane Strain Compression at Extremely Low Pressures, *Soils Found.*, Vol. 26, Issue 1, 1986b, pp.65-84.  
 [10] Terzaghi K., *Theoretical Soil Mechanics*, John Wiley and Sons Ltd., 1943, pp. 510.  
 [11] De Beer E. E., Bearing capacity and settlement of shallow foundations on sand, *Proc. Symposium on Bearing Capacity and Settlement of Foundations* Duke Univ., 1965.  
 [12] Shiraishi S., Variation in Ultimate Bearing Capacity Factors of Dense Sand Assessed by Model Loading Tests, *Soils Found.*, Vol. 30, Issue 1, 1990, pp.17-26.  
 [13] Ueno K., Miura K., and Maeda Y., Prediction of Ultimate Bearing Capacity of Surface Footings with Regard to Size Effects, *Soils Found.*, Vol. 38, Issue 3, 1998, pp.165-178.  
 [14] Kumar J., and Khatri V. N., Effect of Footing Width on  $N_\gamma$ , *Can. Geotech. J.*, Vol. 45, Issue 12, 2008, pp.1673-1684.  
 [15] Loukidis D., and Salgado R., Effect of Relative Density and Stress Level on the Bearing Capacity of Footings on Sand, *Géotechnique*, Vol. 61, Issue 2, 2011, pp.107-119.  
 [16] Okahara M., Takagi S., Obata H., Mori K., and Tatsuta M., Centrifuge Tests on Scale Effect of Bearing Capacity, 42<sup>nd</sup> Japan Annual Conf. of Civil Engineers, Vol. 3, 1988, pp. 250-251 (in Japanese).

# **SUSTAINABLE SOLUTION TO EXPANSIVE SUBGRADE AND EXISTING PAVEMENT USING GEOCONFINEMENT SYSTEM**

Lokanantham Logitharan<sup>1</sup> and Umar Ali<sup>2</sup>

<sup>1</sup>Faculty of Health, Engineering and Sciences, University of Southern Queensland, Australia; <sup>2</sup> Department of Transport and Main Roads, Australia

## **ABSTRACT**

The Darling Downs region, located over 100kms west of Brisbane, comprises predominately fertile black soil. Black soil found across the region has characteristics which are extremely problematic to civil engineers and have caused significant damage to the road infrastructure in the region. The black soil in the region has a high shrink/swell characteristic which has caused substantial pavement damage through rutting, shoving, wash outs and settlement issues. Many pavement rehabilitation techniques such as lime stabilisation and foamed bitumen have been used to minimise the damage caused by moisture infiltration, however, the issues remain. The Department of Transport and Main Roads developed 10 innovative rehabilitation methods as a trial using geocells and geosynthetics along a 1km section of the main highway in the region. The Gore Highway had been identified as the ideal location as previous rehabilitation methods achieved limited benefits in reducing pavement failures, which posed safety concerns.

*Keywords: Expansive soil, Geocells, Geocomposite and Geogrid*

## **INTRODUCTION**

The Darling Downs region consist of roads that link the national highways which predominately are used by the tourism and the transport industry for transporting goods across the nation. The characteristics of the soils pose a greater threat as the region is also susceptible to large scale flooding

Most of the area in Toowoomba, soils are formed from basalt rock and weathered rock. There are two types of soils that can be found around the region which are 'red soil and 'black soil'[11]. Most of the roads are built on the black soil, which is sensitive to water. Black soil comprises both alluvial and residual soils, which formed across the low laying areas around the region [3]. The black soils around the region are highly fertile, comprising high water-absorption, liquid limits, and plasticity. These characteristics pose significant concerns for engineers as the black soils absorb significant water content, resulting in high expansive properties whilst also shrinking significant when drying out.

This creates serious issues for engineers when designing and building roads and major infrastructure in the region. The expansive soils around the Darling Downs have caused significant damage to the road networks mainly causing large cracking, shoving, and rutting along throughout roads across the region.

Over the years, various trials have been used by the Department of Transport and Main Roads (TMR) to counter the properties of the soils. Some of these techniques include lime stabilisation and foam bitumen.

## **BACKGROUND**

The Department of Transport and Main Roads (TMR) undertook an innovative rehabilitation trial along the Gore Highway 28A. The trial comprised of 10 various trials over a 1km section of the Gore highway. Each trial was undertaken over a 100m section using different innovative techniques, most of which had never been used in Queensland.

The 1km section chosen for the trial posed a safety concern for traffic because of the degradation of the existing pavement. Significant rutting, shoving, wash outs and cracking were observed over the selected area.

The project site was located 57 km west of Toowoomba between the suburbs of Pampas to Brookstead.

The section was previously stabilised using foamed bitumen and lime stabilisation, however, because of the significant rainfall and flooding events the region had experienced, significant pavement damage had occurred.

## **Expansive Soil Property**

Black soil is a cohesive soil, which is sometimes referred to as black cotton soil. The typical characteristics of black soil include its colour, which is typically black or dark grey [12]. The soil is usually soft to very soft when wet and has high plasticity and liquid limits, which may cause significant swelling as it has a high-water retention capability. Its ability to retain water results from the high clay content present within the soil.

When drying the soil experiences significant shrinkage, resulting in cracking as the water molecules evaporate from the bonding matrix. Black soils have low bearing capacity and low shear strength [7].

Black soils make up about one third of the area of the state of Queensland [13]. There are three types of black soils found in the Darling Downs region, all of which have similar qualities, however, were formed geologically differently. Black soil from alluvial origin, was derived from weathering produced from the Rolling Downs Group, which was transported along with sediments from the Tertiary age [3].

Residual black soil was formed directly over the weathered sedimentary rock of the Rolling Downs group during the Cretaceous age. The third black soil type found in the region was formed on the Tertiary basalt deposits [3]. The engineering properties of these soils are summarised below.

Table 1: Engineering properties for black soils [3]

Property	Alluvial	Residual on Cretaceous	Residual on Basalt
Liquid Limit	40 – 60	40 -70	60 -90
Plastic Index	25 – 35	25 - 35	40 – 60
Linear Shrinkage	12 -18	15 - 20	15 – 25
USC	CL -CH	CL - CH	CH

### Geogrids and geosynthetics

Geogrids and geosynthetics have been used across the world for many years with various engineering applications. TMR were required to find alternative solutions to the ever-growing problem of pavement rehabilitation in the region. Various trials and stabilisation techniques, such as lime and foamed bitumen, were used across the region with various degrees of success.

TMR began investigating alternative solutions and began trialing geocells and geosynthetics on a section of the Gore Highway. Using geo-cells on the Gore Highway was a first for the state of Queensland, as these had only been trailed in other states in Australia with different soil conditions.

The trial involved stabilising a 1km length of road along the Gore Highway 28A, between Pampas and Brookstead approximately 57km west of Toowoomba. The trial involved using 10 different geogrids each over a 100m length.

The project, along with the procedures, was developed between consultation with technical experts and TMR.

### Geocells and Geosynthetics.

Geosynthetic reinforcement has been used for subgrade improvement as well base reinforcement for over 40 years around the world [6]. However, in Queensland, geocells had not been used despite the vast areas of weak expansive soils.

Geocells and geosynthetics are used to achieve five functions which assist with improving the durability of a road. The five key functions they are designed for include providing reinforcement, stiffness, improved drainage, filtration, and separation [2].

Because of the above, geocells and geosynthetics help with mitigating reflective cracking in asphalt, separate, lateral restraints. Geosynthetics can be used both as a subbase treatment and a subgrade treatment.

Some other benefits of using geocells include limiting the use of lime or foam bitumen and using recycled material, thus significantly reducing the cost of construction and maintenance and as well as providing an environmentally friendly alternative solution.

The diagram below shows the benefits of using geogrids. Load distribution of the axle force and shear stresses are distributed over a larger area therefore resulting in reducing the impact on the pavement. The geosynthetic absorb the forces and remain in tensile stress [2].

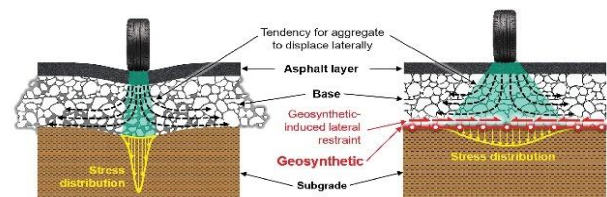


Figure 1: Stress distribution with and without geogrid in stabilised roads [2].

Research was carried out at the University of Kansas to investigate the vertical stresses and impact of permanent deformation because of using geocells in recycled asphalt pavement (RAP) with weak subgrade material under cyclic plate loading. The experiment involved using test samples with and without geocells in a geotechnical test box applying cyclic loading replicating a single wheel load force of 40kN. The subgrade material used in the experiment had a CBR value of 2%, a plastic limit of 22% and a liquid limit of 30%. During the cyclic loading, the surface deformation and vertical stresses and strains were monitored, and the results indicated using geocells improved the life of the pavement by a factor of up to 19% compared with not using geocells. The data also indicated using geocells improved the resilient deformation whilst reducing plasticity properties [5].

Other research using geocells in unpaved roads with fill material also indicated a reduction in



permanent deformation and an increase in stress distribution angles when using geocells compared [6].

Research into the benefits of using geocells over planar geosynthetics indicated using geocells was more effective in increasing the strength, bearing capacity, and reducing settlements in various engineering applications [8].

### Trial

The trial involved using different geocells and geosynthetics in various ways to treat the subgrade and base along the Gore Highway. The figure below shows how each trial was undertaken.

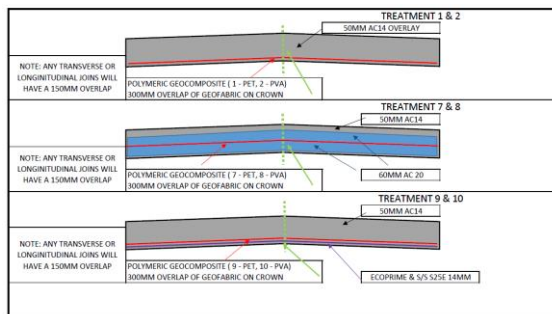


Figure 2: Trial techniques used on Gore Highway.

### Trial 1 and 2

Trials 1 involved adding the polymeric-PET (HaTelit C) geosynthetic over the full 10m width. The process involved brooming and cleaning the existing pavement surface before adding a tack coat to assist with binding the existing layer with the Hatelitic C. The Hatelitic C polymer was laid using a forklift with a modified frame to lay the product. Once the product was laid over the subgrade, AC20 was laid over it.



Figure 3: Trial 1 using Hatelitic C

HaTelit C is made from reinforced mesh comprising of high-modulus polyester yarn. It is made by combining ultra-light non-woven fabric with the polyester yarn. Some advantages of using this product include minimal loss of strength, high

resistance to pavement damage and resistance to permanent dynamic traffic loads by absorbing and distributing tensile stress. [4, 10].

In Trial 2, a HaTelit XP geosynthetic was used. This product is made from polyvinyl alcohol (PVA), which is known for having good resistance to reflection cracking, high resistance to pavement damage and traffic loads and can be used on asphalt surfaces [9].

### Trial 3 and 4.

These trials were focused on treating the base layers. The trials involved cleaning the existing surface to remove dust and loose stones, allowing the tack coat to bind better with the surface. Once the tack coat was placed, the geotextile was laid respectively over the trial areas.

Geocomposite chip seal grids were used as they are easy to use, durable, provide high resistance, through flexibility and rupture resistance which helps prevent crack propagation [4]. Once the geotextiles were laid, hot bitumen crack treatment and HSS2 seal were placed over a 10m width.



Figure 4: Geotextile on tack coat



Figure 5: HSS2 Seal



### Trial 5

The rest of the trials comprised subgrade treatment trials. Trial 5 involved profiling/ milling out approximately 400mm of unsuitable material. Class A MRTS04 material was used to replace soft areas, allowing for the Hilf test to achieve a minimum of 97% compaction. A basetrac duo geocomposite (Basetrac Duo PET 50 B15) was placed over the layer to prevent penetration of moisture to the subgrade. Basetrac Duo was another geocomposite used made from polypropylene, polyester, or polyvinyl alcohol. The manufacturer states the product has a biaxial tensile strength of up to 75kN/m whilst providing the ability to interlock with granular material to prevent fine soil particles from segregation [4].

The geocells Fortrac 80MDT was placed over the geocomposite and stretched out and nailed to the edges of the existing pavement surrounding the trial area. This allowed the geocells to remain in a state of tension. Fortrac geogrids were also used as they are easy to use because of the flexibility of the product. This product also provides high tensile strength made from low-creep synthetic materials [4].

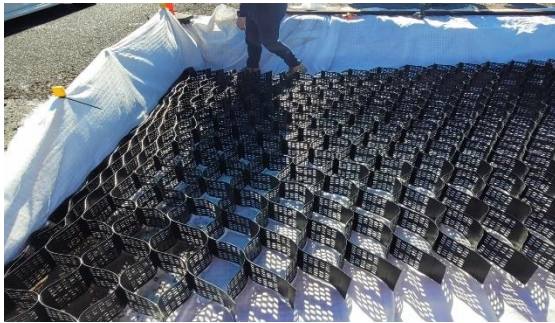


Figure 6: Placing Geogrids on Geofabric

Type 4.1 material was used to fill in around the geocells before being compacted using a smooth drum, before being sealed off using spray seal



Figure 7: Placing material and fill voids

### Trial 6

This trial involved removing 250mm of existing material before the Bastrac Duo PET 50 B15 layer was placed over 5m X 100m area. Type 4.1 was then laid over the geocomposite before the Fortrac 80 MDT was laid. Type 2.1 material was laid and compacted to 250mm before the primar10mm seal was placed.



Figure 8: Trial 6

### Trial 7 and 8

These trials involved milling 150mm of the existing surface and placing a geosynthetic material (HaTelit XP and C respectively). A tack coat was placed over the geosynthetic before AC20 was placed and compacted.



Figure 9: Trial 7 and 8

### Trials 9 and 10

These trials involved milling out approximately 60mm of the existing pavement before being primed and then the geocomposites were placed.

Trail 9 had a polymeric-PET HaTelit C geosynthetic placed and trial 10 had a polymeric-PVA HaTelit XP placed. Once these were laid, A/C 20mm was placed and compacted.



Figure 3: Trial 9 & 10

### LIMITATIONS:

Although research has been undertaken using geocells and geosynthetics as reinforcements by subgrades and bases, the research is limited to laboratory testing trying to simulate real world scenarios.

Due to time, weather and budget constraints, the trials were limited to 100m length sections, which may limit the true reflection of performance of each geocell and geosynthetic product. Prior pavement rehabilitation techniques, such as subgrade treatment (lime and foamed bitumen) may also hinder the true performance of the products. Likewise, any prior water infiltration or subgrade damage may not have been identified at the time of construction and may influence the performance of the products.

### CONCLUSIONS

The trials undertaken along the Gore Highway provided a much needed alternative to a problem that has caused a significant impact to the road network in the Southern Downs region. Finding a long-term solution to countering the highly expansive soils in a region suffering both from severe drought and largescale flooding could have substantial economic impacts for not only the region but also for the state of Queensland.

Geocells and geosynthetics provide an alternative engineering solution to a widespread problem in the Southern Downs region.

Although limited research is available on the impacts of these products on black soils, the research suggests these products could solve a problem that has plagued the region.

Some of the expected benefits of using these products include minimizing the ability for moisture to penetrate through to the subgrade whilst also improving and increase the strength of the pavement.

Geocells can transfer the shear stresses caused by axle loading to a larger area of the base and subgrade, therefore reducing the impact and stress on those areas. As a result, reducing the potential for damaging the structural integrity of the pavement.

To better understand the true impact on the performance of these products, further analysis is required of the trialed section of the Gore Highway.

### ACKNOWLEDGMENTS

Authors would like to acknowledge the work done by Murray Peacock and Department of Transport and staff involved in developing scope and assisting during construction. The authors are also grateful to the Department of Transport and Main Roads for providing an opportunity to carry out the research and present the paper to the international forum.

### REFERENCES

- [1] Patil, D., 2022. Black Cotton Soil | Black Cotton Soil Properties | Types of Foundation In Black Cotton Soil | Black Cotton Soil Definition. [online] Civiconcepts. Available at: <[https://civiconcepts.com/blog/black-cotton-soil#Black\\_Cotton\\_Soil\\_Properties](https://civiconcepts.com/blog/black-cotton-soil#Black_Cotton_Soil_Properties)> [Accessed 11 June 2022].
- [2] Geosynthetics Magazine. 2022. PART 2 Functions and applications of geosynthetics in roadways - Geosynthetics Magazine. [online] Available at: <<https://geosyntheticsmagazine.com/2017/04/01/part-2-functions-and-applications-of-geosynthetics-in-roadways/>> [Accessed 11 June 2022].
- [3] Vanderstaay, L. and Reeves, I., 2000. Soils of Western Queensland. Technical Notes - Department of Transport and Main Roads, (WQ32), pp.1-8.
- [4] ITM design Werbeagentur, G., 2022. HaTelit. [online] Huesker.com.au. Available at: <<https://www.huesker.com.au/geosynthetics/products/geogrids/hatelit/>> [Accessed 10 June 2022].
- [5] Thakur, J., Han, J., Pokharel, S. and Parsons, R., 2012. Performance of geocell-reinforced recycled asphalt pavement (RAP) bases over weak subgrade under cyclic plate loading. Geotextiles and Geomembranes, 35, pp.14-24.
- [6] Thakur, J., Han, J., Pokharel, S. and Parsons, R., 2012. Performance of geocell-reinforced recycled asphalt pavement (RAP) bases over weak subgrade under cyclic plate loading. Geotextiles and Geomembranes, 35, pp.14-24.
- [7] Toll, D., 2009. Unsaturated soils. London: Taylor & Francis.
- [8] Tafreshi, S. and Dawson, A., 2010. Behaviour of footings on reinforced sand subjected to repeated loading – Comparing use of 3D and planar

- geotextile. Geotextiles and Geomembranes, 28(5), pp.430-450.
- [9] Leite-Gembus, F., Hilpert, D. and Bakrac, M., 2002. Theory and practical experiences in pavement rehabilitation using asphalt reinforcement grids. Doctoral. Technological Institute of Aeronautics, São José dos Campos, Brazil.
- [10] Kaya, Z., 2020. Asphalt Reinforcement with HaTelit and Sami Grid Technology
- [11] Thompson C.H., and Beckmann G.G., 1959, Soils and Land use in Toowoomba area, Darling Downs, Queensland, Soil and Land Use Series No.28, 1959.
- [12] Sivapullaiah, P.V., Sridharan, A., and Bhaskar Raju, K.V., 2000, Role of amount and type of clay in the lime stabilisation of soils, proceedings of the institution of civil engineers, ground improvements
- [13] [www.tmr.qld.gov.au](http://www.tmr.qld.gov.au)

# EXPERIMENTAL STUDY ON DATA TRANSMISSION USED FOR CONSTRUCTION QUALITY CONFIRMATION OF EMBEDDED PILE CONSTRUCTION METHOD

Yasuhide Mochida<sup>1</sup>, Tatsuki Maniwa<sup>1</sup>

<sup>1</sup>Ritsumeikan University, Japan <sup>2</sup>Graduate School of Science and Engineering, Ritsumeikan University, Japan

## ABSTRACT

Maintaining the construction quality of foundation work in construction is an important construction management act to prevent major defects that occur during building operation such as uneven settlement. In Japan, in 2016, a defect in the foundation work of an embedded pile in a building caused the reinforced concrete condominium to tilt, and it had to be rebuilt. In the embedded pile construction method using preboring, poor quality in construction caused by insufficient bearing capacity at the tips of piles is a significant problem. To solve this problem, it is necessary to ensure the quality immediately after construction in the soil, the interior of which is invisible. To do so, a method of measuring the electrical resistivity of the soil cement between the ready-made pile and the hole wall in real time and monitoring the construction can be considered. An attempt was made in this study to clarify the possibility of wireless data transmission in the soil of the measured resistivity value associated with pile construction. The aim was to help promote quality confirmation immediately after construction in the soil at the actual construction site.

*Keywords: Wireless communication, Data transmission, Pile construction method, Construction quality*

## 1. INTRODUCTION

During the construction of a foundation, most of the work in the ground cannot be seen directly, which makes it difficult to control the construction quality. To solve this problem, a method of measuring management data (electric resistivity) immediately after construction in the soil in real time and monitoring the construction would be effective. However, in current foundation work, the available communication technology has not been established. Wired communication is not suitable because of bad weather, impacts, rotation, and connection work, and an important technical issue to be addressed is underground wireless communication technology. In this study, an experiment was conducted on the possibility of wireless communication under the condition that the cavity is filled with a medium (water, soil, cement, etc.) in which radio waves are easily attenuated in the soil.

## 2. ICT OUTLINE OF THIS RESEARCH

The goal of this research is to enable the excavation with an excavation auger, measure the electrical resistivity while injecting the root hardening liquid and the fixing liquid around the pile, and monitor the construction. To implement partial wireless features for radio wave transmission in the soil, an experiment was conducted using water and soil cement as an attenuation medium.

An attempt was made to clarify the possibility of using a coaxial leakage cable (hereinafter referred to as a “coaxial cable”) for wireless communication in the final wireless communication. In a coaxial cable, the entire cable becomes an antenna by leaking radio waves to the outside through a slit made inside. As shown in Fig. 1, a coaxial cable was placed along the shaft of the earth auger, and a simulated experiment was attempted assuming wireless transmission with the measurement electrode attached to the tips of the wings of the auger.

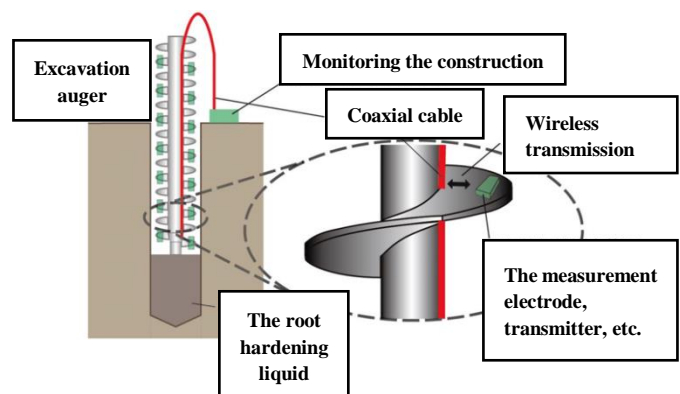


Fig.1 Detailed drawing of wireless transmission

## 3. WIRELESS COMMUNICATION EXPERIMENT USING WATER IN THE SOIL AS AN ATTENUATION MEDIUM



### 3.1 OUTLINE OF THE EXPERIMENT

To investigate the possibility of wireless communication using water in the soil as an attenuation medium, the following three types of experiment were conducted to clarify the difference between frequency in water and radio communication distance, difference between radio output and radio communication distance, and possibility of wireless communication using the transmission cable (coaxial cable).

Experiment 1: Communication limit between transmitter GTR-920F and GSU-7000 (1 W)

Experiment 2: Radio field strength of transmitter GSU-7000 output 1, 3, and 5 W

Experiment 3: Transmitter GSU-7000 (1 W) + coaxial cable communication limit

Fig. 2 shows the measurement electrode and the outline of the experimental device on the transmitting side, and Fig. 3 shows the outline of the experiment. Assuming a drilling hole for pile foundation work, a device was created that incorporates tools such as a transmitter, battery, well pack (electrical resistivity measuring device), and electrodes. into one set in a waterproof case in a well (Agano City, Niigata Prefecture, depth of approximately 90 m, diameter of 200 mm, PVC pipe protection) for observation. An experiment was conducted by submerging it in the depth direction and receiving it on the ground to understand the wireless communication properties using water as the attenuation medium. The equipment used was a 920-MHz band, 20-mW specified low-power radio station GTR-920F (using an ancillary antenna), a UHF band (351-MHz band) digital simple radio station, a data communication dedicated module (GSU-7000; antenna AZ350S), which is common; a waterproof case with a diameter of 140 mm and height of 700 mm, a battery (GBL-1275; lithium ferrite), a coaxial cable (5D-2V), an electrical logging device (Well Pack10), and an electrical resistivity electrode (four-pole method).

### 3.2 EXPERIMENTAL RESULTS

Fig. 4 shows the relationship between the depth of the GTR-920F and radio wave attenuation in Experiment 1. The depth is 210 cm from the water surface. From 0 to 210 cm, communication is through the air, and the total attenuation is 0.43 dBm per 10 cm; after this depth, the communication limit reached (1) at approximately 50 cm in deep water. When calculating the propagation loss in water, it can be estimated that the attenuation coefficient is 54 dB/m from the total attenuation of 76 dBm at a depth of 210 cm and 103 dBm at 260 cm. Fig. 5 shows the relationship between the depth of GSU-7000 (1 W)

and the signal strength level. The radio field intensity level changed from 9 to 8 at a depth of 340–350 cm,

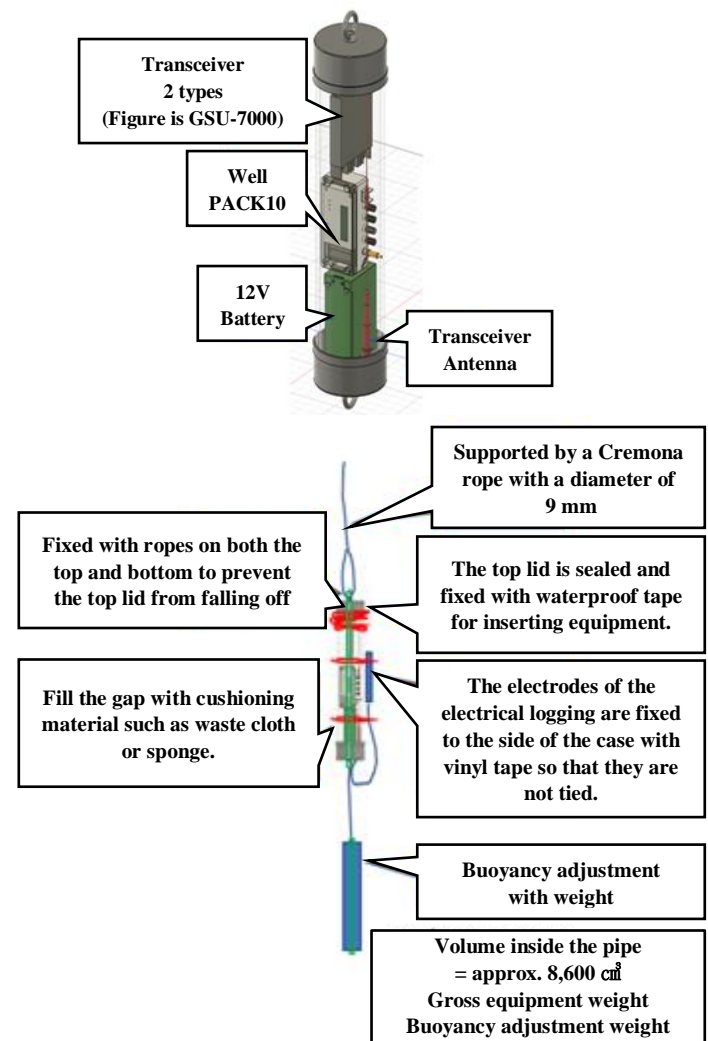


Fig. 2 Outline of the experimental device

and it changed from level 3 to 2 at a depth of 500–510 cm. From the level conversion table (2), the fields show  $-88$  and  $-113$  dBm. Based on this value, the attenuation constant is 15.6 dB/m. The maximum underwater communication distance increased seven times with the change from 920 to 350 MHz.

Fig. 6 shows the relationship between 1, 3, and 5 W of GSU-7000 and the radio field intensity level in Experiment 2. The depth of change from level 9 to level 8 and the depth of level 0 increased to 345 and 570 cm at 1 W, 445 and 620 cm at 2 W, and 485 and 680 cm at 3 W. The differences were 225, 175, and 195 cm, respectively, and the attenuation constants can be calculated as 15.6, 20.0, and 17.9 dB/m.

Fig. 7 shows a comparison of radio field intensity levels up to a depth of 20m with and without a coaxial cable using GSU-7000 (1 W) in Experiment 3. In the



experiment of (1), it decreased to level 4 at a depth of approximately 4 m without the coaxial cable; however, with the coaxial cable, it became level 9 in the entire measurement at a depth of 20 m, and almost no propagation attenuation was observed.

### 3.3 EXPERIMENTAL CONSIDERATION

#### 3.3.1 RADIO ATTENUATION IN WATER

Fig. 8 shows the relationship between the frequency of electromagnetic waves in water and the attenuation coefficient (3). In general, when electromagnetic waves are transmitted in water, absorption attenuation is larger because of the difference in density, and the communicable distance is shorter when electromagnetic waves are transmitted in water. The shorter the frequency, the less the susceptibility to attenuation. Furthermore, the propagation loss in water can be considered as follows.

The electric field  $E$  of a plane wave propagating in the  $x$ -direction in a loss medium is

$$E = E_0 e^{-\gamma x} \quad (1)$$

where  $\gamma = \alpha + j\beta = \sqrt{j\omega\mu(\sigma + j\omega\epsilon)}$ ,  $\gamma$  is the propagation constant,  $\alpha$  is the attenuation constant,  $\beta$  is the phase constant,  $\omega$  is the plane wave angular frequency,  $\sigma$  is the medium conductivity,  $\epsilon$  is the dielectric constant, and  $\mu$  is the magnetic permeability.

When the frequency is extremely low,  $\sigma \gg \omega\epsilon$ , and the displacement current can be ignored, so the propagation constant can be approximately expressed as  $\gamma = \sqrt{j\omega\mu\sigma}$ , and  $\alpha = \beta = \sqrt{(\omega\mu\sigma / 2)}$ . Here, the average salinity is approximately 76 mg/l, and the conductivity at 18°C is considered to be about 11.15 mS/m. This conductivity value is treated as the freshwater conductivity value. The attenuation constant of fresh water is  $\alpha = 2.098 \times 10^{-4} \sqrt{f} \text{ [Np/m]} = 1.822 \times 10^{-3} \sqrt{f} \text{ [dB/m]}$ .

The following evaluations can be made as a result: (GTR-920F)  $\alpha = 1.822 \times 10^{-3} \times \sqrt{(920 \times 1000000)} \doteq 55 \text{ dB/m}$ , and (GSU-7000(1W))  $\alpha = 1.822 \times 10^{-3} \times \sqrt{(351.2 \times 1000000)} \doteq 34 \text{ dB/m}$ .

#### 3.3.2 FREQUENCY AND COMMUNICATION

In underwater communication, a short frequency band leads to a decrease in data transmission speed and capacity. Among the underground communication technologies currently in practical use, there are communication devices in the range of 10–1000 Hz that use magnetic field lines at extremely low frequencies. In this experiment, where the objective is to obtain construction results in real time, inexpensive and easy-to-use frequency equipment was used instead of low frequencies.

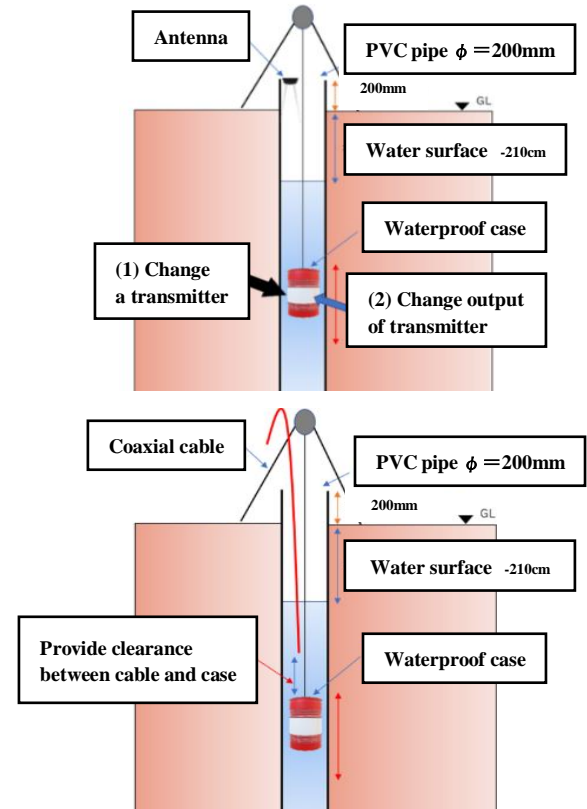


Fig. 3 Outline of the experiment

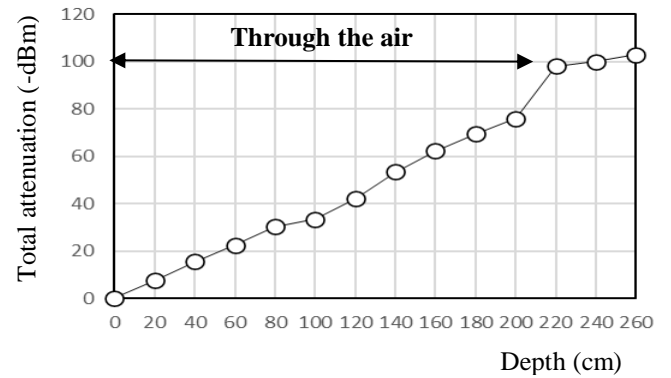


Fig. 4 Relationship between the depth of the GTR-920F and radio wave attenuation

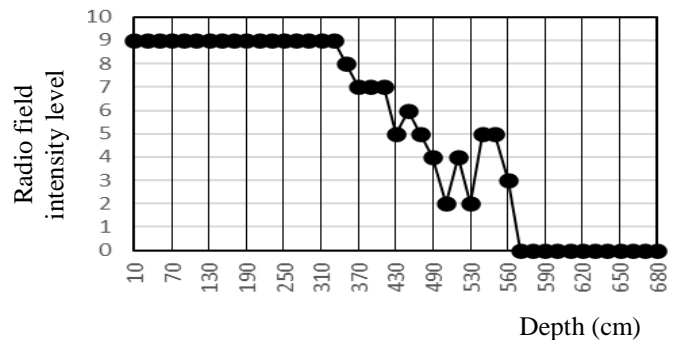


Fig. 5 Relationship between the depth of GSU-7000 (1W) and the radio field intensity level

### 3.3.3 RADIO OUTPUT AND TRANSMISSION DISTANCE

From the Friis formula, the output of the radio is greatly related to the transmission distance. In this experiment, the difference in transmission power was investigated, and it was confirmed that the larger the output, the longer the communication distance.

$$Pr = Gt \cdot Gr \cdot Pt \cdot (\lambda / 4 \cdot \pi \cdot r)^2 \quad (2)$$

Here,  $Gt$  is the transmission gain,  $Gr$  is the reception gain,  $Pt$  is the transmission power (W),  $Pr$  is the reception power (W),  $\lambda$  is the wavelength (m), and  $r$  is the distance (m).

## 4. WIRELESS COMMUNICATION EXPERIMENT USING SOIL CEMENT IN THE SOIL AS AN ATTENUATION MEDIUM

In this experiment, it was assumed that there was soil cement at the root of the pile tip, and the effect of the composition and degree of mixing on radio wave attenuation when sandy soil or cohesive soil is mixed in a cement slurry of a certain W/C was clarified. Furthermore, it was clarified whether radio communication in soil cement is possible at a distance of 500 mm between the tips of the auger wings and the core of the auger.

### 4.1 OUTLINE OF THE EXPERIMENT

As shown in Fig. 9, a cubic hole of  $B \times D \times H = 500 \times 500 \times 500$  mm was excavated on the ground surface, and a cavity with a depth of 500 mm was created by using a PVC pipe with a diameter of 120 mm facing the surface. A transmission radio was installed at a position 250 mm from the surface of the earth. Assuming the ground of the construction site, two types of soil cement, sand and clay, were created. First, as mentioned above, excavation was done to create an underground space. Next, water was poured into the space to make it a water tank. After draining, the blended cement slurry was injected. Fifty percent of cement slurry was replaced with muddy water to make soil cement. A predetermined amount of silica sand No. 7 was added to the soil cement (Kasaoka clay was not added because it was highly viscous, and it became difficult to stir). After 24h, it was confirmed that the soil cement had hardened. The electrical resistivity was continuously measured in each of the above-mentioned experimental procedures. In each experimental procedure, it was measured step by step with a portable resistivity meter in the Well Pack 10. Two types of muddy water with a specific density of  $1.6 \text{ (kg/cm}^3\text{)}$  were used with silica sand No. 7 and two types of muddy water with a specific density of  $1.6 \text{ (kg/cm}^3\text{)}$  with Kasaoka clay. The radio field intensity and resistivity at each procedure and age were measured. In addition, Table 1 and Table 2 show the

performance and usage of radios, etc., and the composition table of the materials used, respectively.

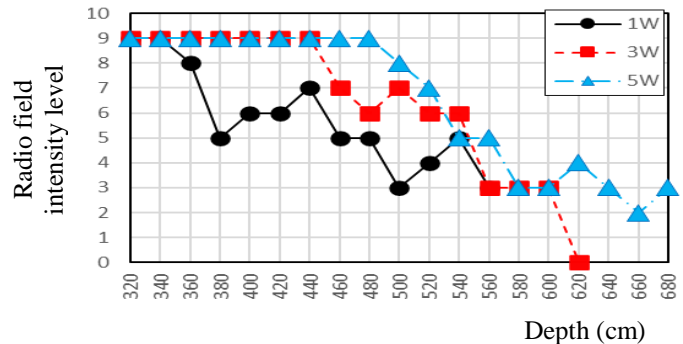


Fig. 6 Relationship between 1, 3, and 5 W of GSU-7000 and the radio field intensity level

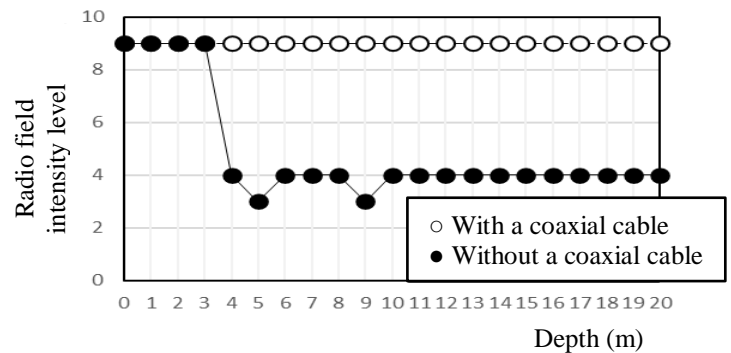


Fig. 7 Comparison of radio field intensity levels up to a depth of 20m with and without a coaxial cable using GSU-7000 (1W)

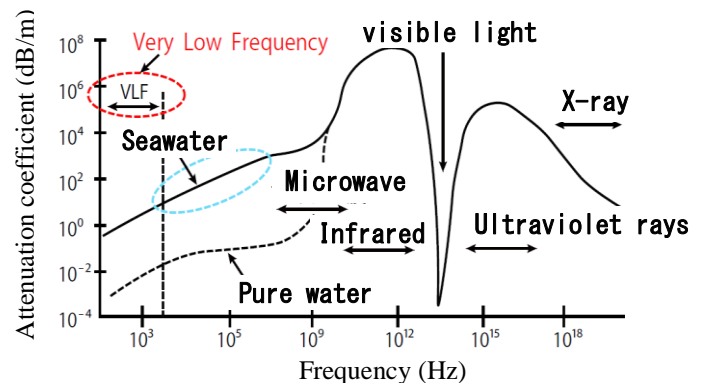


Fig.8 Relationship between the frequency of electromagnetic waves in water and the attenuation coefficient

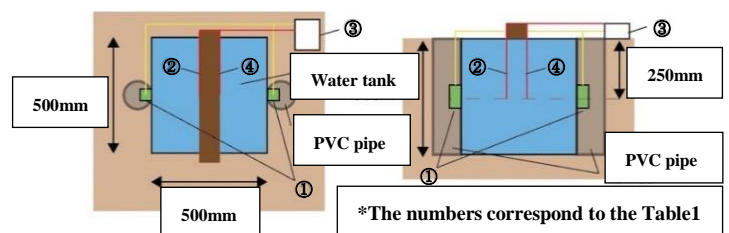


Fig. 9 Plan view and cross-sectional view of the experimental device

## 4.2 EXPERIMENTAL RESULTS

Fig. 10 and Fig. 11 summarize the resistivity and radio wave attenuation derived from the relationship between the resistance value of the Well Pack 10 and the output of the GTR-24H over time. From these figures, the transition of the resistivity measured by the electrode for measuring resistivity and the portable agrees with the transition of radio wave attenuation to some extent, and there is a correlation between the specific resistance and the radio wave attenuation.

## 4.3 EXPERIMENTAL CONSIDERATION

Table 3 summarizes the evaluation of radio field strength for each experimental procedure. Although there are some areas where communication is unstable, radio communication is possible within the soil cement at intervals of 500 mm.

In addition, based on the radio wave attenuation constant of water,

$$\alpha = \sqrt{\omega \cdot \mu \cdot \sigma / 2} \quad (3)$$

where  $\omega$  is the angular frequency of plane wave,  $\mu$  is the magnetic permeability, and  $\sigma$  is the conductivity of water. Here,  $\sigma$  was replaced with the conductivity of soil cement to derive the theoretical value of soil cement in this study. For the damping constant of soil cement,

when transforming Eq. (1), this becomes

$$\beta = \sqrt{\omega \cdot \mu \cdot \sigma / 2} = \sqrt{\pi \cdot f \cdot \mu / \rho} \quad (4)$$

where  $F$  is the plane wave frequency,  $\mu$  is the magnetic permeability, and  $\rho$  is the specific resistance of soil cement. The damping constant of muddy water 2 in (6) can be evaluated as  $\beta_1 = 0.674 \times 10^{-3} \times \sqrt{f[\text{Np/m}]} = 5.85 \times 10^{-3} \times \sqrt{f[\text{dB/m}]} = 5.85 \times 10^{-3} \times \sqrt{920 \times 10^{-6}[\text{dB/m}]} \div 178[\text{dB/m}]$ . In addition, the total attenuation of muddy water 2 in (6) is  $97 \text{ dBm} - 28 \text{ dBm} = 69 \text{ dB}$ , so when the attenuation constant of the measured value is obtained,  $\beta_2 = 69 \text{ dB} / 0.5 \text{ m} = 138 \text{ dB/m}$ .

## 5. CONCLUSION

In an experiment on the possibility of wireless communication using water as an attenuation medium, the maximum underwater communication distance was seven times higher at the difference between the frequencies of 920 and 351 MHz of the equipment used. As the radio output increased from 1 to 5 W, the communicable depth increased from 570 to 680 cm. It was confirmed that there was no propagation attenuation up to a depth of 20 m with a coaxial cable. In an experiment on the possibility of wireless communication using soil cement as an attenuation

Table 1 Performance and usage of radios

The numbers in Fig. 9	Name of radios and measurement electrodes
①	GTR-920F
It is a radio device for data transmission. It measures the radio wave strength between two GTR-920F and transmits data for GTR-24H.	
②	Electrical resistivity measuring device
It accurately measures the resistivity and transmits data for GTR-24H.	
③	GTR-24H
Device to continuously receive and store measured data in ①②. Converting radio wave strength to radio wave attenuation.	
④	Well PACK10
It accurately measures the resistivity. Electrical tester with digital display of the resistance values	
⑤	Portable resistivity meter
It simply measures the resistivity, humidity, and pH.	

Table 2 Composition table of the materials used

Experimental material and Composition
Muddy water 1 [1.6 (kg/cm <sup>3</sup> )]
<b>Silica sand No. 7</b> [2.6 (g/cm <sup>3</sup> )] + water
Muddy water 2 [1.6 (kg/cm <sup>3</sup> )]
<b>Kasaoka clay</b> [2.5 (g/cm <sup>3</sup> )] + water
Cement slurry [W/C 60(%)]
Ordinary portland cement [3.15 (g/cm <sup>3</sup> )] + water
Soil cement [Volume ratio 1:1]
Cement slurry + Muddy water 1or 2

medium, radio communication was possible within an interval of 500 mm, although communication was unstable in some areas. A coaxial cable was placed along the shaft of the earth auger, and it was assumed that wireless transmission would be performed with the measurement electrode attached to the tips of the wings of the auger. From this, it became clear that transmission is possible at 500 mm and that wireless

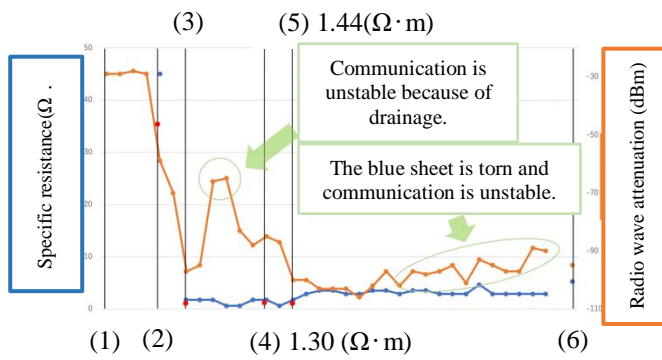


Fig. 10 Relationship between the specific resistance and the radio wave attenuation (Muddy water 1)

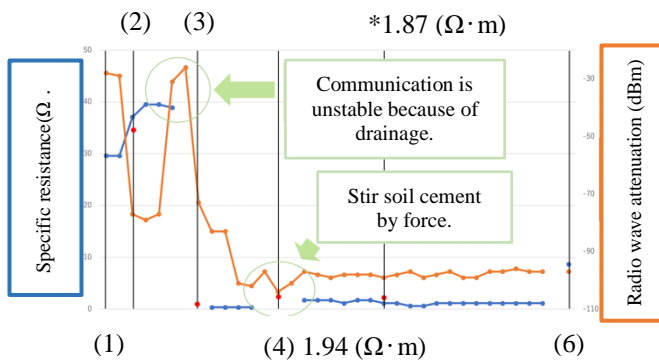


Fig. 11 Relationship between the specific resistance and the radio wave attenuation (Muddy water 2)

communication is possible. The radio wave attenuation was smaller in the experiment than in the evaluation, and it became necessary to predict the attenuation to be slightly larger. In planned future research, efforts will be made to derive more accurate theoretical values by investigating such physical properties as the magnetic permeability of soil cement in consideration of the attenuation of free space and closed space.

This research was carried out as part of the "Study on quality confirmation method immediately after pile construction using electrical resistivity": Grant-in-Aid for Scientific Research (KAKENHI) (C), 20K04782.

Table 3 Evaluation of radio field strength

Evaluation		
	Muddy water 1	Muddy water 2
(2)	Stable	Relatively stable
(3)	Performance Limitations of Radios	Relatively stable
(4)	Performance Limitations of Radios	Communication is possible, but unstable
(5)	Performance Limitations of Radios	-
(6)	Performance Limitations of Radios	Performance Limitations of Radios

\*Numbers correspond to experimental procedures

## REFERENCES

- [1]GTR920F, Materials related to electrolytic strength and communication distance
- [2]GSU7000, digital simple radio (351 Hz)  
Electrolytic strength test value and communication status guideline
- [3]Absorption and attenuation of electromagnetic waves in water (JAMSTEC 2020 data)
- [4]G. Komatsu, M. Fujii, et al., Quality Evaluation for the Foot Protection part of the Bored Precast Pile using the Electric Resistivity, Summaries of Technical Papers of Annual Meeting of Architectural Institute of Japan, pp. 621–622, 1998/9
- [5]Y. Mochida, T. Maniwa, et al., Experimental study on data transmission for confirming pile construction quality (wireless communication properties using water as an attenuation medium), Summaries of Technical Papers of Annual Meeting of Architectural Institute of Japan, pp. 747–748, 2021/9
- [6]Procedure manual for radio field strength test of wireless modem GTR-920F (2019/05/23 Geotech Service Co., Ltd.)

## NUMERICAL SIMULATION FOR SEDIMENTATION OF SAND PARTICLES IN EXCAVATION STABILIZERS

Hiroya Asano<sup>1</sup>, Koki Nakao<sup>1</sup>, Tomotaka Morishita<sup>2</sup>, Toshihiko Miura<sup>2</sup>,  
Yasuharu Wachi<sup>2</sup>, Kazuhiro Watanabe<sup>2</sup> and Shinya Inazumi<sup>3</sup>

<sup>1</sup> Graduate School of Engineering and Science, Shibaura Institute of Technology, Tokyo, Japan;

<sup>2</sup> Obayashi Corporation, Tokyo, Japan;

<sup>3</sup> College of Engineering, Shibaura Institute of Technology, Japan

### ABSTRACT

This study focuses on the behavioral pattern of sand particles in the excavation stabilizers used during construction of the cast-in-place piles. Sand particles get mixed as an impurity in the excavation stabilizer, which will cause a detrimental effect while driving cast-in-place piles. That's why sand particles should be removed from the excavation stabilizer. However, it is difficult to confirm the behavior of sand particles in excavation stabilizer visually. This study attempts to reproduce the sedimentation behavior of sand particles in the excavation stabilizer by numerical simulation using the CAE coupled with MPS-DEM analysis during the construction of cast-in-place concrete pile. The simulation cylindrical column model is created by computer-aided engineering (CAE) system and the excavation stabilizer and sand particles are modeled by MPS and DEM, respectively. After confirming the simulation behavior of sand particles in excavation stabilizer by reproducing cylindrical column test for sedimentation test and reproduction of CAE coupled with MPS-DEM analysis simulation, it is expected that the result obtained from this simulation will contribute to more efficient and economic construction of cast-in-concrete piles.

*Keywords: Excavation stabilizer, Numerical simulation, Sand particle, Sedimentation, Viscosity*

### INTRODUCTION

Most of urban areas in Japan are located on soft ground, and geo-disasters such as land subsidence and liquefaction occur frequently. In the construction of infrastructures, it is indispensable to apply the foundation structure in the ground. In the construction of cast-in-place concrete piles, the stabilizer is filled into the excavated hole which at the same time will act as medium to prevent the falling of surrounding sand, and it will be replaced by concrete [1,2]. This study focuses on the excavation stabilizer used in the cast-in-place concrete pile method for constructing reinforced concrete piles at the on-site among the foundation structures. Figure 1 shows the process of substitution process of the excavation stabilizer that has been initially filled into the excavated hole as it will get mixed with the surrounding sands. Since it is undesirable to have mixing of sand as it will change the original property of excavation stabilizer. In order to protect the quality of pile formation by use of this reclaimed excavation stabilizer, it is important to control properties like specific gravity, viscosity, wall building capacity, and sand ratio contained within it. Since the high concentration of sand will reduce the quality of concrete, it is desired to understand the behavioral pattern of sand present in excavation stabilizer before making substitution.

However not only it is difficult to confirm the construction status visually but also to prove the validity of design.

This study focuses on the application of a computer-aided engineering (CAE) [3-5] system that simulates the sedimentation of sand particles in excavation stabilizers. During construction of cast-in-place- concrete method, sedimentation behavior of sand within the excavation stabilizer is studied/trailed by CAE coupled with DEM-MPS analysis method, sedimentation behavior vs time is visualized and evaluated. This study, using cylindrical column test only for sedimentation test, reproduction accuracy checking of the simulation.

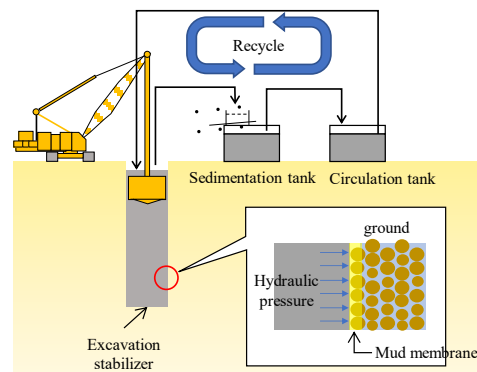


Fig. 1 The good excavation stabilizer substitution



## CAE WITH DEM-MPS METHOD COUPLED ANALYSIS (MPS-DEM-CAE)

### MPS (Moving Particle Simulation) Method

MPS (Moving Particle Simulation) method is an analytical method dealing with incompressible flow, which discretizes continuum mechanics using particles.

In this study, the authors apply MPS method [3-5] to analyze the behavior of fluid particles. The governing equations for the incompressible flow used in the analysis are the mass conservation law of Eq. (1) and the Navier's stroke law of Eq. (2).

$$\frac{D\rho}{Dt} = 0 \quad (1)$$

$$\frac{D\vec{u}}{Dt} = -\frac{\nabla P}{\rho} + \nu \nabla^2 \vec{u} + \vec{g} \quad (2)$$

Where,  $D/Dt$  expresses a Lagrangian derivation,  $\rho$  is density of the fluid,  $\vec{u}$  is the velocity vector,  $P$  is the pressure,  $\nu$  is kinematic viscosity coefficient, and  $\vec{g}$  is the gravity acceleration.

In the MPS method, the Navier-Stokes equations are divided into two stages, and all terms are solved explicitly, except for the pressure term, which is solved implicitly.

Explicit calculations of terms except the pressure term is expressed by Eq. (3).

$$\frac{\vec{u}^* - \vec{u}^k}{\Delta t} = \nu \nabla^2 \vec{u}^k + \vec{g} \quad (3)$$

Implicit calculation of pressure is expressed by Eq. (4).

$$\nabla^2 P^{k+1} = \frac{\rho}{\Delta t^2} \frac{n^* - n^0}{n^0} \quad (4)$$

Velocity and position correction by the pressure gradient is expressed by Eq. (5).

$$\frac{\vec{u}^{k+1} - \vec{u}^*}{\Delta t} = -\frac{\nabla P^{k+1}}{\rho} \quad (5)$$

Where,  $n$  is the particle number density, and  $n^0$  is the particle number density at the initial state, both of which are explained later. Superscript  $k$  expresses the time step. Superscript  $*$  expresses a physical quantity at the stage where the explicit calculation has been completed. Figure 2 shows the calculation algorithm of the MPS method.

### DEM (Discrete Element Method) Method

DEM (The Discrete Element Method) is a technique for analyzing the behavior of powders by following each individual particles through their

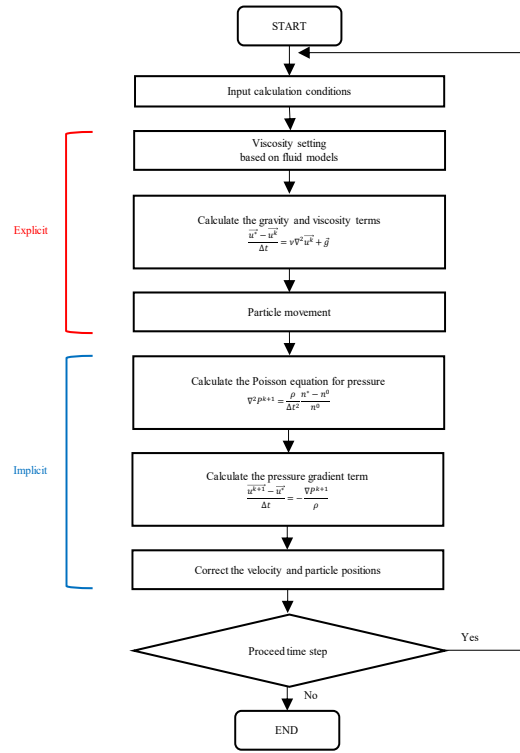


Fig. 2 The calculation algorithm of the MPS

equations of motion. DEM calculates the dynamics of each individual particles by solving Newton's equation of motion. Equations of motion for translational and rotational motion of DEM particles are expressed by Eq. (6) and (7).

$$m \frac{d}{dt} \vec{v} = \vec{F} \quad (6)$$

$$I \frac{d}{dt} \vec{\omega} = \vec{M} \quad (7)$$

Where,  $m$  is the mass,  $\vec{v}$  is the velocity,  $\vec{F}$  is the contact force,  $I$  is the inertia moment,  $\vec{\omega}$  is angular velocity, and  $\vec{M}$  is the torque

For a spherical particle, the inertia moment is expressed by Eq. (8).

$$I = \frac{2}{5} m r^2 \quad (8)$$

Where,  $r$  is the radius of the particle. DEM handles particles as rigid particles that do not deform, but it allows overlapping of particles to accelerate calculation.

The contact forces (repulsive force, energy damping/decay, and slide due to friction) of a powder particle are expressed by a rigid-body spring model, viscous damper model, and slider model, respectively, as shown in Fig. 3.

The contact force of normal and tangential are defined as in Eq. (9) and (10).

$$\vec{F}^n = -k^n \vec{\delta}^n - \eta^n (\vec{v}_i^n - \vec{v}_j^n) \quad (9)$$

$$\vec{F}^t = -k^t \vec{\delta}^t - \eta^t \left( (\vec{v}_i^t - \vec{v}_j^t) + (\vec{r}_i \times \vec{\omega}_i) + (\vec{r}_j \times \vec{\omega}_j) \right) \quad (10)$$

Where,  $k$  is the spring constant,  $\vec{\delta}$  is the overlap,  $\eta$  is

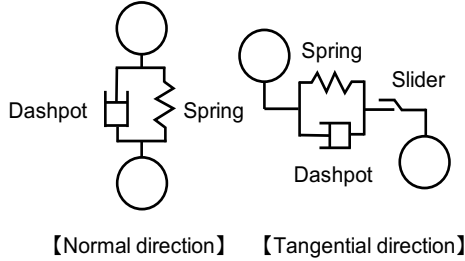


Fig. 3 The contact model of DEM (Voigt model)

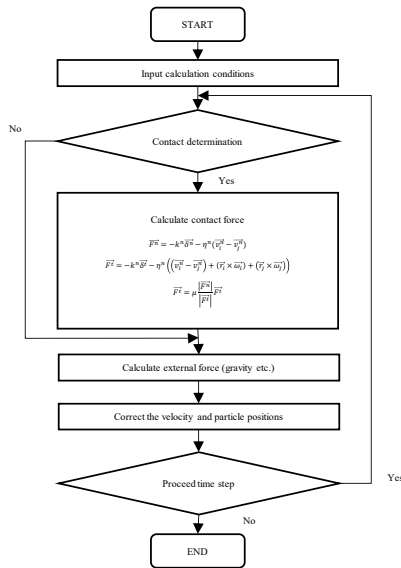


Fig. 4 The calculation algorithm of the DEM

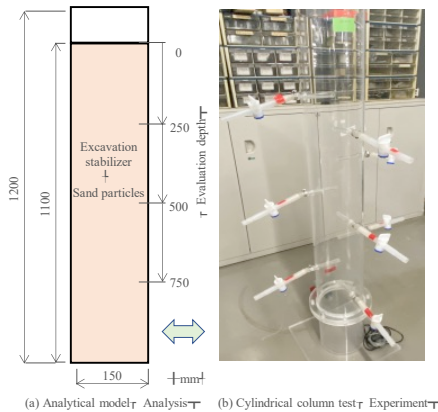


Fig. 5 Analytical model simulating a cylindrical column

the damping coefficient,  $\vec{v}$  is the velocity,  $\vec{r}$  is the distance from center of gravity to point of contact, and  $\vec{\omega}$  is angular velocity. The upper subscripts n represents the normal direction component, t is the tangential direction component, and the lower subscripts i and j represent each particle. The calculation algorithm for DEM is shown in Fig. 4.

### CAE Coupled with DEM-MPS Method Analysis (MPS-DEM-CAE)

A computer aided engineering (CAE) is an alternative technology for large-scale tests, conducted in a room-situ, using prototypes that have been prepared in a study as part of the development process of “manufacturing”. In other words, CAE is a general term for technology that simulates and analyzes prototypes on a computer created by a computer-aided design (CAD) and so on, considering the site conditions [3-5]. At the same time, CAE may refer to computer-aided engineering work or its tools for the prior examination, design, manufacturing, and products. In the field of geotechnical engineering, CAE can be used not only to visualize the inside of the ground and the stress loading on the inside of the ground, but also to estimate the results of tests that would require huge costs and/or phenomena that would be difficult to reproduce. In addition, by performing appropriate post-processing, it is possible to communicate with other people in a visually easy-to-understand manner. In the MPS-DEM coupled system, the motion of viscous fluid and powder is expressed by Eq. (12) and (13). Here, for simplification, it is assumed that there is no external force.

$$\rho \frac{D\vec{v}_l}{Dt} = -\nabla \epsilon \mathbf{P} + \nu \nabla^2 \epsilon \vec{v}_l - \frac{\epsilon}{\tau_0} \vec{F}_D \quad (12)$$

$$\mathbf{m} \frac{D\vec{v}_s}{Dt} = \vec{F}_{DEM} + \vec{F}_D + \vec{F}_{VP} \quad (13)$$

Where,  $\rho$  is fluid density,  $\epsilon$  is volume fraction of the fluid,  $\vec{v}_l$  is fluid velocity,  $\mathbf{P}$  is fluid pressure,  $\nu$  is viscosity of the fluid,  $\mathbf{m}$  is powder mass,  $\vec{v}_s$  is powder velocity,  $\vec{F}_{DEM}$  is contact force,  $\vec{F}_D$  is fluid resistance, and  $\vec{F}_{VP}$  is buoyancy.

### CYLINDRICAL COLUMN TEST FOR SEDIMENTATION TEST

This study was conducted for checking the accuracy of simulation. In this study using the cylindrical column shown in Fig. 5, the sedimentation behavior of sand particles in high viscous excavation stabilizer (CASE-1), medium viscous excavation stabilizer (CASE-2), and water (CASE-3) as shown in Table 1 are measured as sand particle concentration changes over time at each

Table 1 MPS parameters for excavation stabilizers particles

Parameters	MPS		
	Excavation stabilizer		
	CASE 1	CASE 2	CASE 3
Particle size (mm)	10		
Density (kg/m <sup>3</sup> )	1200	1200	1000
Plastic viscosity (Pa·s)	0.306	0.0082	-
Yield value (Pa)	0.042	0.0028	-
Rheology model	Bingham		Newton

Table 2 DEM parameters for sand particles

Parameters	DEM
	Soil particles
Particle size (mm)	2
Density (kg/m <sup>3</sup> )	1800
Spring constant	$1 \times 10^8$
Damping coefficient	0.7

depth. The viscosity and yield value of each excavation stabilizers were measured by a B-type viscometer.

The procedure of the test is described below.

- 1) Add 10 g/L of 75 to 150µm sand to the sample (excavation stabilizers or water) and homogenize it well.
- 2) Put the sample in the cylindrical column and collect 1L of sample including sand from the collection hole of the column at regular intervals.
- 3) Measure the specific gravity, viscosity, API wall building capacity, and sand concentration of the collected sample.

## ANALYSIS MODEL AND CONDITIONS

In this study, as shown in Fig. 5, a cylindrical column (height 120 cm, inner diameter 15 cm) is used as the analytical model, where excavation stabilizer and sand particles up to 110 cm in height are mixed in the initial state. After modeling the excavation stabilizer using the MPS method and the sand particles using the DEM method, we will use MPS-DEM-CAE analysis to qualitatively evaluate the changes over time in the sedimentation of sand particles of the stable solution. This study also focuses on changes over time in the settling behavior of DEM sand particles in each MPS fluid with three cases of viscosity: high viscosity stable fluid (CASE-1), medium viscosity stable fluid (CASE-2), and water (CASE-3).

Table 1 shows the MPS parameters for the excavation stabilizers and water. Table 2 shows the DEM parameters for the sand particle.

As for the rheological models for MPS excavation stabilizers, the Bingham fluid model, a non-Newtonian fluid, is defined for the excavation stabilizers in (CASE-1) and (CASE-2), and a Newtonian fluid for the water in (CASE-3). All these physical property parameters refer to and cite previous tested values. Attention should be paid to the DEM parameters for sand particles as shown in Table 2, especially the setting of sand particle diameter and density. The particle diameter and density of the sand used in the cylindrical column test were 75µm and 2650kg/cm<sup>3</sup>.

In this study, diameters and densities of sand particles modeled in the DEM were set while making consideration of analysis accuracy and computational load; so that the particle settling velocities of typical sand particles and sand particles modeled in the DEM becomes equal for the Stokes fluid.

## RESULTS AND DISCUSSION

### Result of DEM-MPS Simulation for Sedimentation of Sand Particles

Figure 6 shows a longitudinal section of the model showing changes of sand particle sedimentation. In addition, in Fig. 6, only sand particles are shown after processing the MPS particles transparently to visually evaluate the sedimentation of sand particles, and the red particles correspond to sand particles.

Figure 6(a) shows the settling behavior of sand particles in a highly viscous excavation stabilizer for 90 seconds at 10-second intervals.

However, due to the long time required for the analysis, it was not possible to show the sedimentation of sand particles until they converged. Figure 6(b) shows the settling behavior of sand particles in a medium viscous excavation stabilizer for 45 seconds at 5 second intervals. From Fig. 6(b), the settling of sand particles is completely converged after 45 seconds.

Figure 6(c) shows the settling behavior of sand particles in water for 6 seconds at intervals of 1 second. Figure 6(c) shows that the settling of sand particles in water is completely converged after 6 seconds. From these results, it is clear that the behavior of sand particle sedimentation and the settling velocity vary depending on the viscosity of the liquid. Here, focusing on the results of CASE-2 shown in Fig. 6(b), it can be seen that the settling velocity of sand particles gradually decreased from the middle to the lower of the column. This may be due to the influence of pressure differences between the upper, middle, and lower parts of the column, as well as collisions of sand particles or sand particles with each other and with stable liquid particles. In addition, the top of the sand particles settles with

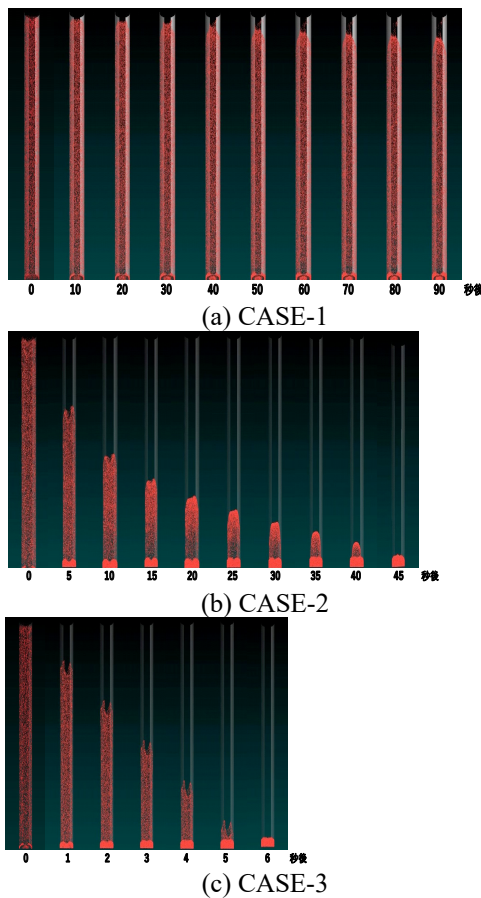


Fig. 6 Change over time of sedimentation of sand particles in each MPS fluid of different viscosity

Table 3 Stokes' settling velocity of sand particles calculated from conditions of MPS-DEM-CAE analysis and column test

CASE	Cylindrical column test (m/s)	MPS-DEM-CAE (m/s)
1	$1.45 \times 10^{-5}$	$4.27 \times 10^{-3}$
2	$5.42 \times 10^{-4}$	$1.59 \times 10^{-1}$
3	$5.05 \times 10^{-3}$	$1.74 \times 10^{-0}$

concave shape for 15 seconds, but after 20 seconds they settle with convex shape. This is thought to be due to friction between the wall of the cylindrical column and the sand particles. The convex settling of sand particles observed after 20 seconds is considered to be due to an array substitution between excavation stabilizer particles and sand particles, in which stable solution particles spread outward like ripples from the center at the bottom of the cylindrical column and move upward along the wall surface while sand particles move downward along the wall surface.

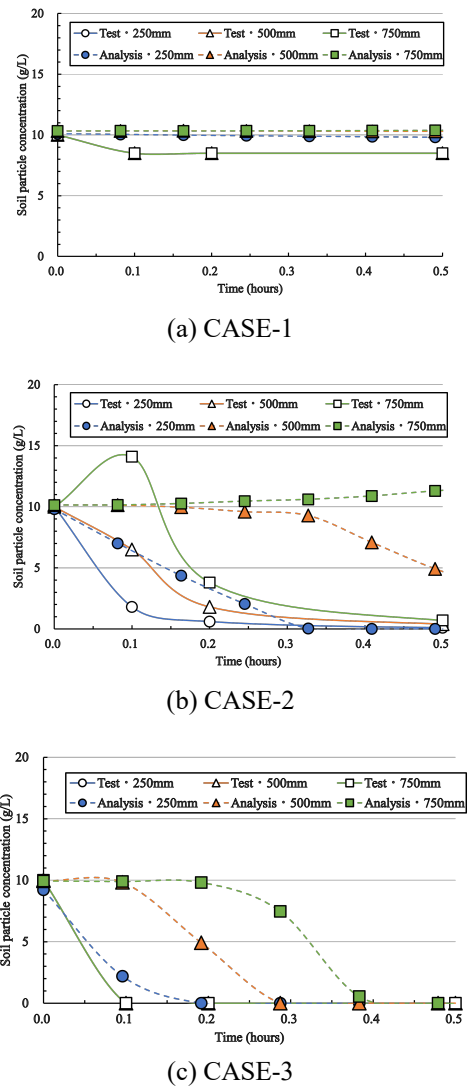


Fig. 7 Sedimentation behavior vs time by MPS-DEM-CAE analysis and column test

### Comparison of the cylindrical column test and analytical results

The Stokes' law has been commonly used in the evaluation of sand particle sedimentation in fluids such as water and stable liquids. The Stokes law represents the terminal velocity of particles as they settle in a fluid. The average particle diameter and density of the sand particles used in the cylinder test were 75  $\mu\text{m}$  and 2650  $\text{kg/m}^3$ , respectively, while for the DEM sand particle parameters used in the CAE coupled with MPS-DEM analysis it was 0.002 m and 1800  $\text{kg/m}^3$  respectively. The Stokes settling velocity of sand particles calculated from the cylinder test conditions and the CAE coupled with MPS-DEM analysis conditions is shown in Table 3.

The Stokes settling velocity obtained from the MPS-DEM-CAE analysis is approximately from 295

to 345 times larger than the Stokes settling velocity obtained from the cylindrical column test conditions. Therefore, in order to treat the Stokes settling velocity obtained from both as equivalent, the elapsed time in the MPS-DEM-CAE analysis must be corrected by a factor of 295 to 345.

Figure 7 shows the changes in sand particle concentration over time in highly viscous excavation stabilizer, medium viscous excavation stabilizer, and water at each depth, obtained from the cylindrical column test and MPS-DEM-CAE analysis. The elapsed time for the MPS-DEM-CAE analysis was corrected according to the above. Comparison between test and analysis in Fig. 7, suggests that the settling time and settling trend of sand particles in excavation stabilizer may be reproduced (assuming actual behavior), although there are slight discrepancies in the settling behavior of sand particles. The reason for the discrepancies in the settling behavior of the sand particles between the two is that the elapsed time in the MPS-DEM-CAE analysis was assumed to be the Stokes settling velocity. Stokes' settling velocity is the one-dimensional settling velocity of a single particle. On the other hand, the cylinder test and MPS-DEM-CAE analysis show a large number of sand particles of varied sizes mixed together, and phenomenon like collision, repulsion, and rotation of sand grains occur during the settling process, that is, the settling of sand particles is three-dimensional. Therefore, the results of the cylinder test and the MPS-DEM-CAE analysis are considered not to be in strict match with Stokes' law.

## CONCLUSIONS

The sedimentation behavior sand particles in excavation stabilizer were evaluated using MPS-DEM coupled CAE analysis in this study. An attempt to reproduce a cylindrical column test using the CAE coupled with MPS-DEM analysis was made, and qualitatively evaluated the sedimentation behavior of soil particles in the excavation stabilizing solution with respect to time.

The results and findings obtained in this study are shown below.

- (1) CAE coupled with MPS-DEM analysis succeeded in visualizing the sedimentation behavior of sand particles in excavation

stabilizer by applying Stokes' law (one-dimensional).

- (2) By CAE coupled with DEM-MPS analysis, sedimentation behavior vs time was visualized and evaluated.
- (3) By reproducing cylindrical column test for sedimentation test, reproduction accuracy of CAE coupled with MPS-DEM analysis simulation was confirmed.
- (4) By visualizing the behavior of sand particles, it can be expected to contribute to efficient and economical pile driving during construction of cast-in-concrete piles.

The results of the numerical simulation using the CAE coupled with MPS-DEM analysis proposed and implemented in this research will greatly contribute to the establishment of ICT with higher precisions and the promotion of DX at construction sites those will surely be required in the future.

## REFERENCES

- [1] Morishita, T., Miura, T., Wachi, Y. and Yoshimoto, K. (2019): Development of Automatic Measuring Apparatus for Stabilization Slurry, Report of the Engineering Research Laboratory, Obayashi-Gumi, Ltd, No.83.
- [2] Otsuka, Y. and Matsuda, S. (1965): Problems and Considerations for Excavation Stabilizer Method, Reports of the Research Institute of Shimizu Construction Co., Vol.6.
- [3] Chang, K.H. (2014): Product Design Modeling using CAD/CAE: The Computer Aided Engineering Design Series, Elsevier.
- [4] Pan, Z., Wang, X., Teng, R. and Cao, X. (2016): Computer-aided design-while-engineering technology in top-down modeling of mechanical product, Computers in Industry, Vol. 75, pp. 151-161, doi: 10.1016/j.compind.2015.05.004.
- [5] Inazumi, S., Kuwahara, S., Jotisankasa, A. and Chaiprakaikeow, S. (2020b): MPS-CAE simulation on dynamic interaction between steel casing and existing pile when pulling out existing piles, International Journal of GEOMATE: Geotechnique, Construction Materials and Environment, Vol. 18, Issue 70, pp. 68-73, doi: 10.21660/2020.70.9166.



# STRENGTH PROPERTIES OF BENTONITE SUBJECTED TO CYCLIC LOADING STRESS

Tomoyoshi Nishimura<sup>1</sup>, Seiichi Narushima<sup>2</sup>, Yasunori ARAI<sup>2</sup> and Yuki Sakoda<sup>2</sup>

<sup>1</sup>Department of Civil Engineering, Ashikaga University, Japan; <sup>2</sup>Natural Blanket Institute, Japan

## ABSTRACT

Further research works have identified shear characteristic before decade ago, and it is successful to improve testing in GCL strength testing are suggested. It is provided that an approach for comparing the effectiveness of geosynthetic clay liners (GCLs) and compacted clay liners (CCLs) associated with association with geomembranes. Geomembrane has some activity, which are similar to equivalency demonstrations with barrier system consist of bentonite, and extremely low hydraulic conductivity and high expansive deformation are delegate components. This study presented that unsaturated-saturated bentonite indicated stress-strain properties in monotonic loading and cyclic mobility using cyclic triaxial test for various dry densities. Static triaxial compression test was conducted to determine strength parameters for establishing safety number. Also, dynamic triaxial test performed under undrained conditions under various initial stress ratios and loading frequencies. Three different dry densities are prepared, which are determined using maximum dry density from Proctor compaction method in soil mechanics theory. Dynamic strength properties have significant effort on depending of dry density.

*Keywords: Bentonite, Monotonic loading test, Cyclic loading test, Liquefaction*

## INTRODUCTION

Various clay liners such as Geosynthetic clay liners (GCLs) are placed at the bottom of waste disposal facilities where they hydrate from the subsoil and eventually from a hydraulic head on geomembranes (GMs) defects [1][2]. Bentonites consist of Geosynthetic clay liners (GCLs) which have further low permeability and enough expansive activity. Predicting hydration behavior of bentonite requires knowledge of hydraulic conductivity, swelling properties and mechanical properties. Hydraulic conductivity and swelling properties for bentonite have been conducted out in decade ago. It is verified that dry density and chemical components such as salinity influenced on couple phenomena. Then, Seiphoori et al., (2016) [3] investigated the water retention properties of the Geosynthetic clay liners (GCLs) subjected to different ranges of vertical stresses along wetting paths (i.e., reduction of suction) in laboratory test. To do so, conventional controlled suction oedometer was used in osmotic suction control technique. It is successful to compare results between experimental laboratory test measurement and modelling simulations in results. A geosynthetic clay liner (GCL) is a composite geosynthetic material. It commonly consists of a thin bentonite clay liner (typically of the order of 5-10 mm thick) that is either bound by needle-punched geotextiles or bounded to a geomembrane with an adhesive [4].

In order for a clay liner composed by expansive bentonite to act as an efficient hydraulic barrier, the expansive bentonite component of the clay liner must

be sufficiently hydrated. The hydration behavior has been clearly demonstrated in the laboratory through the investigation of advective flow of various permeants regard to unsaturated clay liner. Mechanical properties such as strength properties, compression properties and cyclic loading resistance are one of some couple phenomena such as hydration, and it is effectively to determine the safety code. Despite the importance of hydration to the overall effectiveness of the clay liner system, surprisingly little research has addressed this aspect of clay line cyclic loading properties.

Further research works have identified shear characteristic before decade ago, and it is successful to improve testing in GCL strength testing are suggested. It is provided that an approach for comparing the effectiveness of geosynthetic clay liners (GCLs) and compacted clay liners (CCLs) associated with association with geomembranes. Geomembrane used for waste disposal system has some activity, which are similar to equivalency demonstrations with barrier system consist of bentonite, and extremely low hydraulic conductivity and high expansive deformation are delegate components. The contribution of bentonite is to remaining low permeability without advective leachate flow. Shear strength for a compacted clay liner including bentonite is of great importance for landfill stability analysis and safety design on construction waste disposal in practice.

## PREVIOUS WORKS ON CLAY LINER

To interpret aspect of strength properties to clay

liner (GCL) in a municipal solid waste (MSW) landfill liner system lead to evaluate safety concept clay liner system in mechanical properties. Fox and Stark (2015) [5] appears that some identified factors such as the slope inclination, slope height, physical characteristic are significant important for remaining safety situation. Shear strengths of geosynthetic clay liners (GCLs) and soil liner are necessary for static and seismic stability analyses in the design of waste containment facilities and other waste disposal facilities, which incorporate these materials as hydraulic barriers. The aspect corresponds to establish safety design for various disposal system such as the context of landfill bottom liner, cover systems and high-level radioactive waste disposal at deeply repository barrier system [6][7][8].

Further research works have identified shear characteristic before decade ago, and it is successful to improve testing in GCL strength testing are suggested. The contribution of bentonite is to remaining low permeability without advective leachate flow. Shear strength or shear resistance for a compacted clay liner including bentonite is of great importance for landfill stability analysis and safety design on construction waste disposal. Other hands, it is few to appear the cyclic behavior of bentonite that it is possible to refer the like liquefaction behavior either loose sand or soil having much fine components.

Yamamuro and Lade (1997) [9] presented some experimental results on two different instability soils with performing both drained and undrained triaxial compression tests, and all tests were produced under monotonic loading. It is obviously that complete static liquefaction phenomena were exhibited for instability soil. In generally, liquefaction phenomena have been appeared on cyclic loading triaxial test with completely full saturation situation that Yamamuro and Lade (1997) [9] verified static liquefaction phenomena due to performing monotonic triaxial compression test associated to expression effective stress paths. Lade et al. (2009) [10] moderated shear strength and static liquefaction under undrained conditions for non-plastic fine particles that some efforts such as minimum and maximum void ratios, compressibility. Prepared non-plastic soil material had a range from 0 % to 100 % in fine components. While liquefaction is determined, observations applied comparison between liquefaction behavior and stable behavior on void ratio and fine components scales. Monkul and Yamamuro (2011) [11] studied investigates the fines contents influence on liquefaction potential of a single base sand mixed with three different essentially non-plastic silts through strain-controlled monotonic undrained triaxial compression test. Test results also revealed that commonly used comparison bases (i.e., void ratio, intergranular void ratio, relative density) are not sufficient for assessing the influence of fines

on liquefaction potential of silty sands. Then, they represented that current geotechnical engineering practice mostly considered that the influence of fines contents on mechanical properties may be significantly affected by the natural of the fines.

## POURPOSE OF THIS STUDY

This study presented that unsaturated-saturated bentonite indicated monotonic loading properties and cyclic stress-strain behavior such as cyclic mobility on static-cyclic triaxial test for various dry densities. Monotonic static triaxial compression test was conducted to determine strength parameters such as coefficient of friction, angle of shear resistance and apparent cohesion that it possible to evaluate mechanical properties. The monotonic static triaxial compression test performed under undrained conditions in order to simulate effective stress paths using principal stress and excess pore-water pressure. It can be seen effective stress paths with/without instability paths including two effective principal stress. Also, dynamic triaxial test conducted out under undrained conditions that various initial stress ratios and loading frequencies were controlled in order to observe the influence of assigned cyclic mobility components on stress-strain behavior. It seemed to indicate slightly liquefaction phenomena according to initial cyclic stress ratio.

## TEST PROCUDER

### Soil material

This study used bentonite with maximum grain size of 4.0 mm that grain size distribution test results 47.6 % of gravel, 52.3 % of sand and clay of 0.1 % in gradations.  $D_{50}$  is 1.80 mm,  $D_{30}$  is 0.988 mm and  $D_{10}$  is 0.43. Therefore, uniformity coefficient is 0.43 and coefficient of curvature is 0.919. Compaction properties determined through in A-c part in Test method for soil compaction using a rammer (JIS Code: JIS A 1210:2009) that maximum dry density was 1.357 Mg/m<sup>3</sup> and optimum water content was 27.7 %. Three difference dry densities such as physical factor was required that were 1.357 Mg/m<sup>3</sup>, 1.221 Mg/m<sup>3</sup> and 1.153 Mg/m<sup>3</sup>, respectively. Each dry density corresponds to 100 %, 90 % and 85 % of maximum dry density. Compaction water content takes coincident as 27.7 % that is optimum water content. As one of physical properties for used bentonite, previously swelling pressures have determined under constant volume, and were 300.2 kPa, 153.6 kPa and 109.6 kPa corresponding to 1.357 Mg/m<sup>3</sup>, 1.221 Mg/m<sup>3</sup> and 1.153 Mg/m<sup>3</sup>, respectively for dry density. Then, specimen was prepared in static compaction method using stiffness steel mold and a hydraulic jack, which had a height of 76 mm and a diameter of 38 mm, respectively.

## Testing Apparatus

Both unsaturated and saturated bentonite with various dry densities were tested on the one triaxial apparatus, while extra components was added to the apparatus for the measurement of cyclic strength-strain behavior. It is possible to control the vertical cyclic loading, and had sinusoidal loading with frequency of 0.5 Hz and 0.05 Hz. Regulator contribute to remain lateral confining pressure constant, and had 100 kPa duration cyclic loading test. It is often that the total mean principal stress constant test was conducted out, and reported in liquefaction resistance researches. Wang, et al., (2016) [12] sufficiently explain composing of modified apparatus for cyclic loading triaxial test, which is possible to apply accurately to unsaturated-saturated specimen phenomena in order to observe liquefaction resistance while the total mean principal stress constant test. Cyclic loading triaxial test performed without remaining the total mean principal stress ( $p$ ), the influence of changing the total mean principal stress is not clear to the obtained results regard to stress-strain behavior duration cyclic loading. The apparatus is possible to measure excess pore-water pressures by the pressure transducer connected with triaxial basement, which used for static triaxial compression test and cyclic loading test.

## Testing Program

This testing programs consist of main two triaxial tests that one is static triaxial test, another one is cyclic loading test. Static triaxial compression test (i.e. monotonic loading test) performed for saturated specimens that effective stress paths had determination under undrained conditions due to various lateral confining pressures. Applied lateral confining pressure had a range from 25 kPa to 100 kPa, and required compression speed correspond to create 20 % in axial strain duration 24 hours. Excess pore water pressures measured and evaluated the changing effective stresses including the influence of two lateral confining pressures. Then, effective mean principal stress was verified to three difference dry densities for determination of failure criterion, and it leads to estimate coefficient of friction and strength parameters such as shear resistance angle and apparent cohesion. While cyclic loading triaxial test under lateral confining pressure of 100 kPa constant, unsaturated-saturated specimens were used for comparison of delete suction in specimen. Controlled initial cyclic stress ration was a range from 0.24 to 1.24, and required external loading frequencies were 0.5 Hz and 0.05 Hz. Observing that deviator stress, axial strain, excess pore-water pressure were

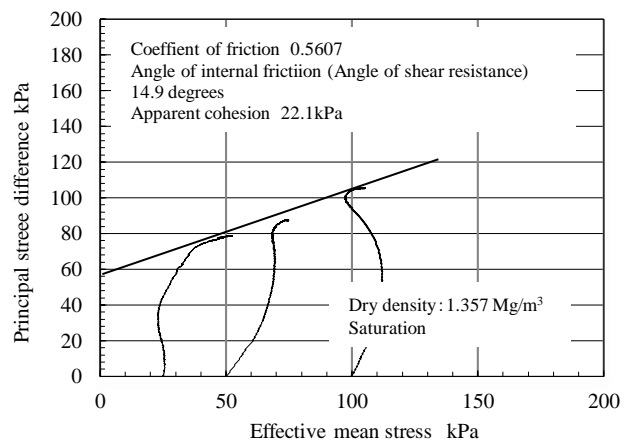


Fig. 1 Effective stress paths.

significant factors in cyclic behavior.

## STRENGTH PARAMETERS

Within a range of low lateral confining pressures, undrained triaxial compression test on saturated bentonite with three difference dry densities conducted out previously to cyclic loading triaxial test. These results from a series of saturated monotonic tests are shown in Fig 1 that effective stress paths defined as effective mean principal stress of varying initial lateral confining pressures fall onto a unique line, which called “instability line” by Yamamuro et al. (1997) [9]. These lines intersect the stress origin, and meant failure criterion (i.e., failure envelope). Also, it possible to be characterize three strength parameters such as coefficient of friction, shear resistance angle and apparent cohesion. Yamamuro et al., (1997) [9] demonstrated undrained soil instability on instability line comparison with effective stress failure line, and evidenced expansion of instability region according to increment confining pressure for loose Scaramnto River sand. As shown in Figs 1 to 3, observed saturated bentonite behavior with various dry densities was seemed to be slightly instability line. Strength parameters was exhibited from failure criterions as followings; coefficient of friction indicated a range from 0.42 to 0.56, shear resistance angle had a range from 11.6 degrees to 14.9 degrees, and apparent cohesion result a range from 12.9 kPa to 22.1 kPa. Shear resistance angles were namely coincident, apparent cohesion dropped with reduction of dry density.

## CYCLIC MOBILITY FOR UNSATURATED BENTONITE

The cyclic triaxial test apparatus performed well when measuring the axial strain of unsaturated bentonite having a dry density of 1.153 Mg/m<sup>3</sup> corresponding to 85 % of maximum dry density

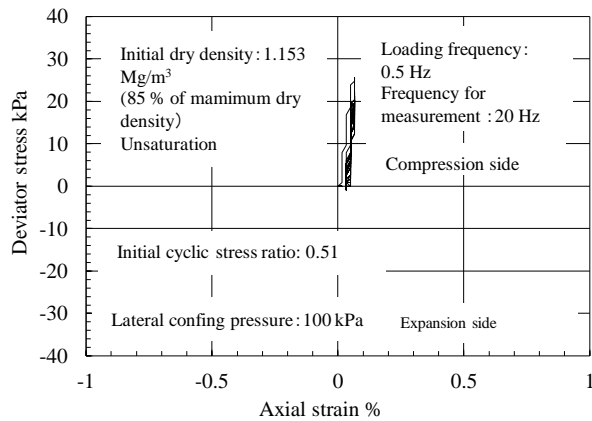


Fig. 2 Cyclic mobility at loading frequency of 0.51.

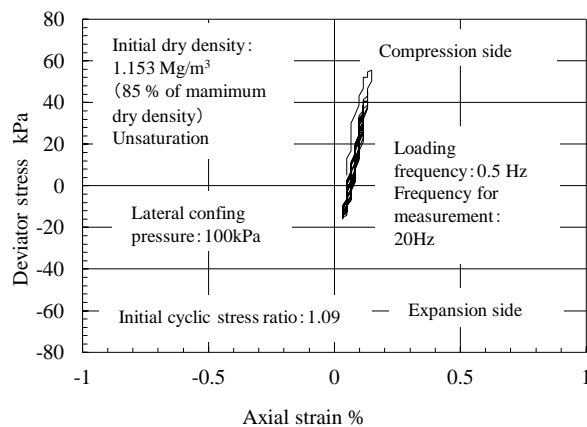


Fig. 3 Cyclic mobility at loading frequency of 1.09.

as described in Figs. 2 and 3. With two external loading frequencies of 0.51 and 1.09, deviator stress (i.e. amplitude stress) was measured with axial strain during cyclic loading. It would be appropriate to grow axial strain in compression side, and growing of axial strain is relatively small value. Then, axial strain increased over two times due to increase initial cyclic stress ratio, and it was typical small hysteric loop. It seemed to be extremely small for plastically deformations than elastic behavior. The specimen was not approached to liquefaction failure mode. Compress stress comparisons to expansion stress, and it surpass during cyclic loading.

#### CYCLIC MOBILITY WITH LOADING FREQUENCY OF 0.5 Hz FOR SATURATED BENTONITE

Saturated specimens were prepared that had dry density of 1.221 Mg/m<sup>3</sup> and 1.153 Mg/m<sup>3</sup>, respectively. Each dry density corresponds to 90 % and 85 % to maximum dry density. Applied initial cyclic stress ratio had a range from 0.57 to 1.32 that external loading frequency was common, and it was 0.5 Hz. Figs 4 and 5 show the typical cyclic stress strain relationships of saturated bentonite, respectively. For the sake of comparison in dry

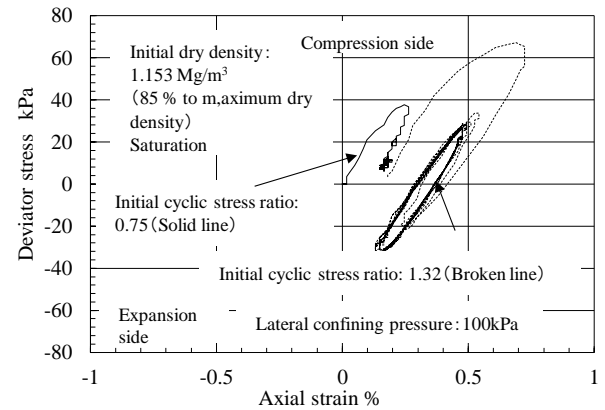


Fig. 4 Reduction amplitude stress (Dry density of 1.153 Mg/m<sup>3</sup>)

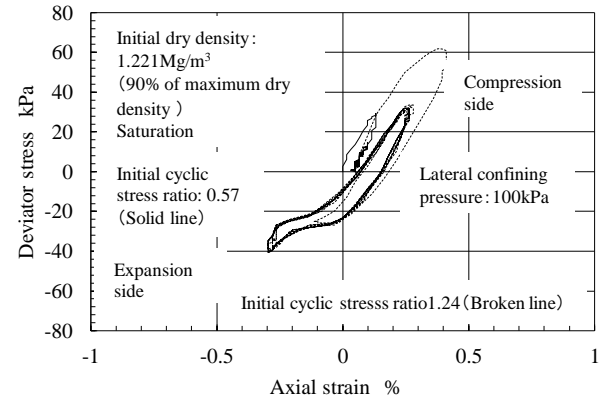


Fig. 5 Reduction amplitude stress (Dry density of 1.221 Mg/m<sup>3</sup>)

density, two figures were prepared, and reported the much growing of axial strain when dry density was 1.153 Mg/m<sup>3</sup>. In addition, axial deformation reached sufficiently to compression side. Therefore, it was observed that saturated bentonite with low dry density described compression deformation due to first cyclic loading.

#### CYCLIC MOBILITY WITH LOADING FREQUENCY OF 0.5 HZ FOR SATURATED BENTONITE

For saturated bentonite with dry density of 1.357 Mg/m<sup>3</sup> cyclic behaviors due to the assigned deviator stress amplitude were investigated on cyclic stress amplitude, excess pore water pressure against to cyclic number. Required external loading frequency was 0.5 Hz. The obtained relationships were shown in Figs 6 to 8. Produced axial deformation not achieved to failure condition due to cyclic loading, because saturated specimen had relatively dense, and cyclic mobility seemed to be not typed flow (i.e. no liquefaction) as shown in Fig. 6. It proved that excess pore water pressure during cyclic loading was not much, and measured excess pore water pressure ratio was less than 0.05 as shown in Fig. 8.

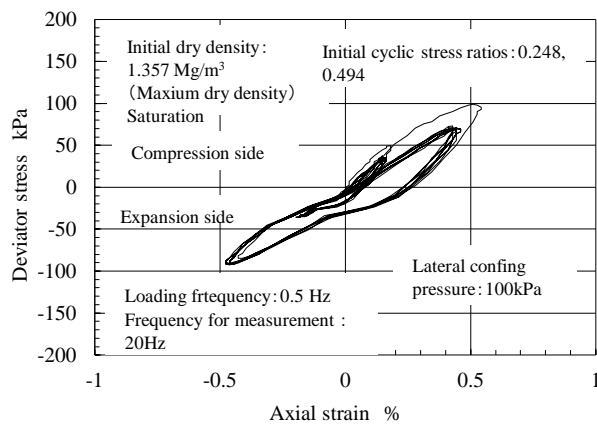


Fig. 6 Reduction amplitude stress (Dry density of 1.357 Mg/m<sup>3</sup>)

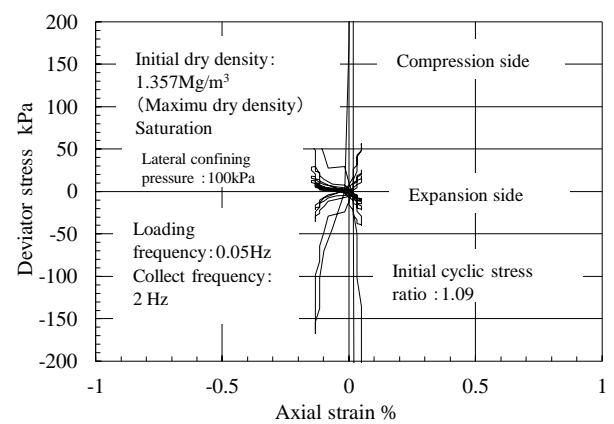


Fig. 9 Stress-strain behavior (Dry density of 1.357 Mg/m<sup>3</sup>)

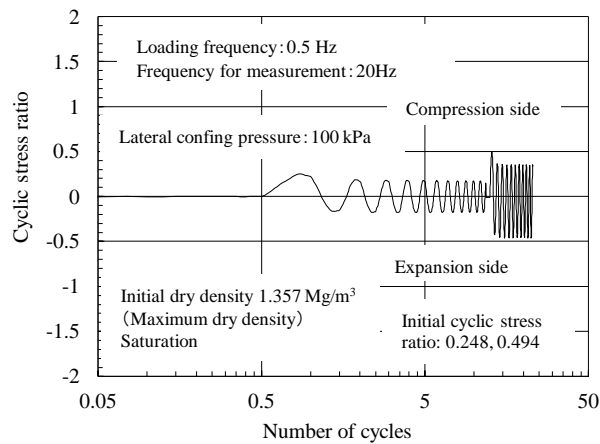


Fig. 7 Observation of amplitude stress (Dry density of 1.357 Mg/m<sup>3</sup>)

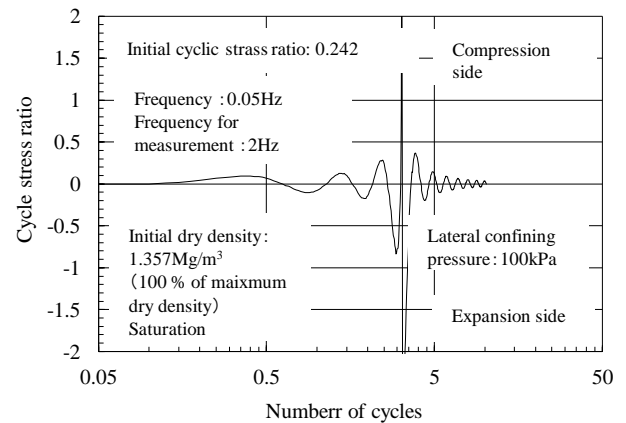


Fig. 10 Decreasing of amplitude stress

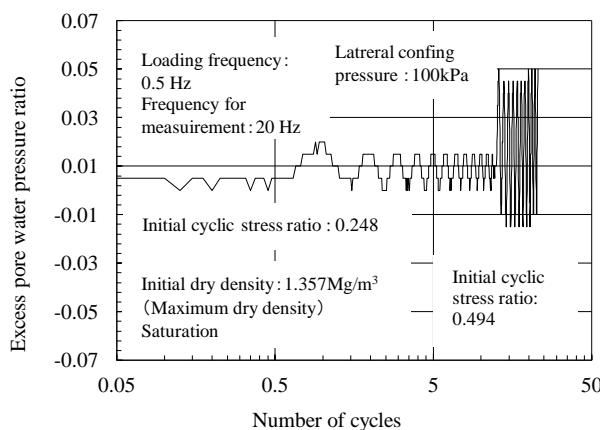


Fig. 8 Growing of excess pore water pressure (Dry density of 1.357 Mg/m<sup>3</sup>)

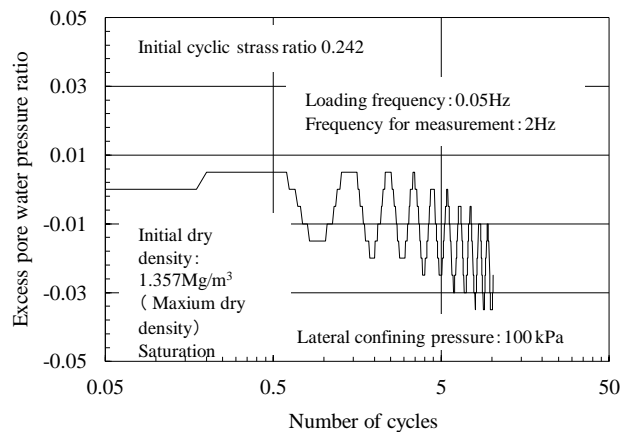


Fig. 11 Measurement of excess pore water pressure.

Excess pore water pressure was namely zero, when initial cyclic stress ratio was 0.248. Beyond the assigned cyclic stress ratio was 0.484, occurrence of excess pore water pressure was obviously and remained same value duration of cyclic loading. Certainly, excess pore-water pressure

behavior under undrained condition corresponding to cyclic loading amplitude ratio as shown in Fig. 7.

# **CYCLIC MOBILITY WITH LOADING FREQUENCY OF 0.05 Hz FOR UATURATED BENTONITE**



The difference external loading frequency was attempted to saturated bentonite with dry density of  $1.357 \text{ Mg/m}^3$  which was 0.05 Hz. Similar factors to frequency of 0.5 Hz as shown in Figs. 8 to 10 were observed, and the obtained results were provide as shown in Figs. 9 to 11. It seemed to be extremely different cyclic mobility associated to cyclic stress, and it was worth mentioning that brittle failure at the small external loading frequency at initial stress ratio of 1.09. From the cyclic number and stress relationships, it can be seen that further growing of stress was observed. Other hands, excess pore water pressures seemed to be not accumulated. The external loading frequency compare that the difference frequency induced further difference cyclic mobility phenomena for saturated bentonite. Dense saturated bentonite had the resistance against liquefaction. Note that excess pore water pressure was certain small, and not achieve to zero duration cyclic triaxial test. your native language is not English and if you feel that you need to go through, please get a native English-speaking colleague to proofread your paper.

## CONCLUSIONS

This study conducted out monotonic-cyclicmobility triaxial test under undrained condition for bentonite used for geosynthetic clay liners, which had appeared shear strength parameters and ewxplained interpetation of cyclic strength strain properties with the influemce of various dry densities. The obtained results are summary as following.

Determined effective stress paths composite two total principal stresses and pore-water pressure descibed typical failure criterion line without instabiolity point mentioned by Yamamuro et al. (1997). Estimated angle of internal friction (i.e. shear resistance angle) was certainly, and the influence of dry denmsity was not so much. Other hands, apparenly cohesion increased according to dense.

For unsaturated bentonite it can be seen that growing of axial strain was silightly in cyclic mobility. Beyound saturation, increement of initial cyclic stress ratio enmphased to produce large deformaions toward compression side. It was however to measure samll excess pore-water pressure duration cyclic amplitud stress, and achieveing of liquefaction can be not seen in this testing coditions.

## REFERENCES

- [1] Kavazanjian Jr. E., Dixon N., Katsumi T., Kortegast A., Legg P. and Zanzinger H., Geosynthetic barriers for environmental protection at landfills, In Geosynthetics, 8th International Conference on Geosynthetics, 2006, pp. 121-152.
- [2] Bannour H., Stoltz G., Delage P. and Touze-Foltz N., Effect of stress on water retention of needle punched geosynthetic clay liners, *Geotextiles and Geomembranes*, 42(6), 2014, pp. 629-640.
- [3] Seiphoori A., Laloui L., Ferrari A., Hassan M. and Khushfati W. H., Water retention and swelling behaviour of granular bentonites for application in Geosynthetic Clay Liner (GCL) systems, *Soils and Foundations*, 56(3), 2016, pp. 449-459.
- [4] Beddoe R. A., Take W. A. and Rowe R. K., Development of suction measurement techniques to quantify the water retention behaviour of GCLs, *Geosynthetics International*, 17(5), 2010, pp. 301-312.
- [5] Fox P. J. and Stark T. D., State-of-the-art report: GCL shear strength and its measurement—ten-year update, *Geosynthetics International*, 22(1), 2015, pp. 3-47.
- [6] Giroud J. P., Badu-Tweneboah K. and Soderman K. L., Comparison of leachate flow through compacted clay liners in landfill liner systems. *Geosynthetics International*, 4(3-4), 1997, pp. 391-431.
- [7] Giroud J. P., Rad N. S. and McKelvey J. A., Evaluation of the surface area of a GCL hydrated by leachate migrating through geomembrane defects. *Geosynthetics International*, 4(3-4), 1997, pp. 433-462.
- [8] Giroud J. P. and Soderman K. L., Criterion for acceptable bentonite loss from a GCL incorporated into a liner system, *Geosynthetics International*, 7(4-6), 2000, pp. 529-581.
- [9] Yamamuro J. A. and Lade P. V., Static liquefaction of very loose sands, *Canadian Geotechnical Journal*, 34(6), 1997, pp. 905-917.
- [10] Lade P. V., Yamamuro J. A. and Liggio Jr, C. D., Effects of fines content on void ratio, compressibility, and static liquefaction of silty sand, *Geomechanics and Engineering*, 1(1), 2009, pp. 1-15.
- [11] Monkul M. M. and Yamamuro J. A., Influence of silt size and content on liquefaction behavior of sands, *Canadian Geotechnical Journal*, 48(6), 2011, pp. 931-942.
- [12] Wang H., Koseki J., Sato T., Chiaro, G. and Tian J. T., Effect of saturation on liquefaction resistance of iron ore fines and two sandy soils, *Soils and Foundations*, 56(4), 2016, pp. 732-744.

## PROPERTIES AND PERFORMANCES OF SOIL CEMENT MODIFIED WITH CONCENTRATED PARA-RUBBER

Supathinee Kowsura<sup>1</sup>, \*Susit Chaiprakaikeow<sup>1</sup>, Apiniti Jotisankasa<sup>1</sup>, Suphawut Malaikrisanachalee<sup>1</sup>,  
Supakij Nontananandh<sup>1</sup>, Korakod Nusit<sup>2</sup>, Auckpath Sawangsuriya<sup>3</sup> and Shinya Inazumi<sup>4</sup>

<sup>1</sup>Department of Civil Engineering, Kasetsart University, Thailand;

<sup>2</sup>Department of Civil Engineering, Naresuan University, Thailand;

<sup>3</sup>Bureau of Road Research and Development, Department of Highways, Thailand;

<sup>4</sup>Department of Civil Engineering, Shibaura Institute of Technology, Japan

### ABSTRACT

Due to the slump of the price of Para-rubber, the Department of Highways of Thailand has adopted the rubber to be used in the quality improvement of cement stabilized materials. Hence, this research aims to study the changes of properties of soil cement modified with concentrated Para-rubber. Lateritic soils were mixed with cement, at the ratio of 1, 3 and 5%, and Para-rubber, at the ratio of 1 and 2% of dry soil weight. The shear wave velocity ( $V_s$ ), unconfined compressive strength ( $UCS$ ), strain at failure, indirect tensile strength ( $IDT$ ), resilient modulus ( $MR$ ), fatigue resistance ( $FR$ ) and soil permeability ( $k$ ) were tested after 7 days of curing. The results indicated that  $UCS$  increased with the increasing of cement ratio but tended to decrease with the increasing of Para-rubber which were consistent with the results of  $V_s$ . For the performance tests,  $IDT$  and  $MR$  tended to decrease while  $FR$  and  $k$  tended to increase with the increasing of Para-rubber. It was expected that Para-rubber affected the compaction quality and, probably, the creation of hydration reaction. Conclusively, the addition of cement increased the brittleness of the material resulting in higher strength. On the other hand, the addition of Para-rubber increased the ductility resulting in lower strength but higher deformation and higher fatigue crack resistance.

*Keywords: Para-rubber, Cement, Strength, Shear Wave Velocity, Performance*

### INTRODUCTION

The Department of Highways of Thailand (DOH) has been using cement to improve road structure quality for a long time. By mixing cement with soil and water, the compressive strength of soil cement (SC) is increased due to the hydration reaction resulting in its ability to carry higher load [1]-[4]. However, due to the slump of the price of Para-rubber, DOH has been assigned to use Para-rubber in their missions with the intention to increase the consumption of Para-rubber in the country. One of them is the use of Para-rubber to improve the properties of SC. Hopefully, adding more amount of Para-rubber into the mix will help the rubber plantation farmers to be able to sell their product more. However, a mixture of natural rubber latex may affect strength and properties of the materials [5]-[7]. Though, most of the studies used natural latex that has dry rubber content (DRC) of around 30% by mass, hence, the use of more Para-rubber is preferable as it can enhance the consumption rate. With the purpose of doing that, the study of the effects of mixing higher amount of Para-rubber into SC is necessary.

The objective of this study is to study the effects of Para-rubber on properties and performances of soil cement modified with concentrated Para-rubber (SCP). The tests comprise of shear wave velocity

( $V_s$ ), unconfined compressive strength ( $UCS$ ), strain at failure, indirect tensile strength ( $IDT$ ), resilient modulus ( $MR$ ), fatigue resistance ( $FR$ ) and soil permeability ( $k$ ).

### BASIC PROPERTIES OF MATERIALS

The soils used in this study were lateritic soils from 2 sources, Chainat province and Chonburi province. The soils were tested for their basic properties according to [8]-[13]. The results of the basic properties and the soil classifications are shown in Table 1. The grain size distributions are shown in Fig. 1. The results showed that the lateritic soils from both sources met the requirements of [14]-[15]. However, the lateritic soil from Chainat was a more suitable material for road structure as it has lower plasticity, lower fine content, higher compacted dry density, higher California bearing ratio (CBR) value, and lower percent loss by Los Angeles abrasion compared to the lateritic soil from Chonburi.

The cement used was Portland cement type 1. The Para-rubber latex used was concentrated latex type HA (High Ammonia) that contains no less than 60% of DRC. Nonionic surfactant NP9 (Nonylphenol Ethoxylate 9 MOLES) was also used to help preventing the rubber particles from clumping before mixing with the aggregates.

Table 1 Basic properties of lateritic soils

Basic properties	Chainat	Chonburi
Liquid Limit	Non-Plastic	26.00
Plasticity Index	Non-Plastic	9.51
Maximum Dry Density (kN/m <sup>3</sup> )	22.86	20.40
Optimum Water Content (%)	5.30	10.00
Percent Loss (%)	39.14	49.64
CBR (%)	46.2	14.4
USCS*	SM	SC
AASHTO**	A-1-b	A-2-4

\*Unified Soil Classification System

\*\*American Association of State Highway and Transportation

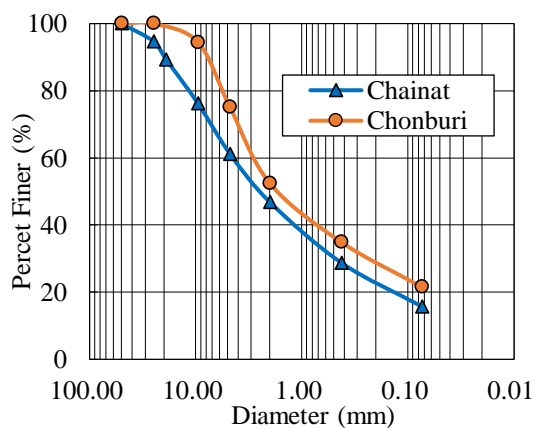


Fig. 1 Grain size distribution curves of lateritic soils from Chainat and Chonburi

## METHODOLOGY

### Shear Wave Velocity and Unconfined Compressive Strength Determinations

#### Sample preparation for shear wave velocity and unconfined compressive strength determinations

Samples from both sources were compacted with modified Proctor test in the mold with an inner diameter of 101.6 mm and a height of 116.43 mm by considering the use of cement content of 1, 3 and 5% and the use of Para-rubber of 0 (SC), 1 and 2% of dry soil weight. The surfactant used was 5% of cement weight. To be noted that the amount of added water for compaction was calculated from the optimum water content subtracted the amount of Para-rubber and surfactant. Five samples per mixture ratio were prepared to study the effect of cement and Para-rubber contents on  $V_s$  and  $UCS$  as shown in Table 2. After the compaction, the samples were wrapped in a plastic sheet and cured for 7 days. Then, the samples were immersed in water for 2 hours before conducting the free-free resonance (FFR) test and then  $UCS$  test.

Table 2 Number of samples for FFR and UCS tests

Cement (% by weight)	Para-rubber (% by weight)	Chainat (Sample)	Chonburi (Sample)
1	0	5	5
1	1	5	5
1	2	5	5
3	0	5	5
3	1	5	5
3	2	5	5
5	0	5	5
5	1	5	5
5	2	5	5

#### Free-free resonance (FFR) test

FFR test is a low strain, undisturbed, dynamic test that is simple, reliable and has been widely used to determine the resonant frequency and shear velocity of materials [16]-[19]. In this study, the sample was placed on the sponge to create a free-boundary condition. An accelerometer was attached horizontally at the side of one end, perpendicularly to the long side, of the sample. Shear waves were generated by vertically tapping the sample at the side of the other end, perpendicularly to the orientation of the accelerometer, using a small impact hammer as shown in Fig. 2a. The resonant, maximum peak amplitude, frequency was recorded, then shear wave velocity was analyzed using the following equation,

$$V_s = f \lambda = 2fL \quad (1)$$

where  $f$  is resonant frequency,  $\lambda$  is wavelength and  $L$  is sample length.

#### Unconfined compressive strength (UCS) test

After a completion of FFR test, the same sample was put into the universal testing machine (UTM) for  $UCS$  test according to [20]. The shearing rate was 2 mm/min. The  $UCS$  and strain at failure of the samples were recorded for further analysis. An example of the test is illustrated in Fig. 2b.

## Laboratory Performance Tests

#### Admixture design and sample preparation for laboratory performance tests

After the  $UCS$ -cement content analysis, the mixing ratio was determined for laboratory performance tests, including  $IDT$ ,  $MR$ ,  $FR$ ,  $k$ . The designed cement content, normally, is determined to satisfy the required  $UCS$ , 1724 kPa after 7 days of curing time, according to [the DOH standard], of SC. However, in this study, the amount of cement content

was depended on the 125% of normal designed strength to avoid the potential loss of performance during the field construction in the future. The targeted *UCS* then became 2155 kPa instead. This criterion was applied for the soils from both sources, Chainat and Chonburi.

Three samples of SC and 3 samples of SCP from 2 lateritic sources, a total of 12 samples, were used for each test to study the performance of these materials. The soils were compacted and cured for 7 days before the tests. Details of each test are mentioned in the following topics.

#### Indirect tensile strength (*IDT*) test

*IDT* tests were performed in accordance with [21]. Samples were compacted, following a modified compaction, to a diameter of 100 mm and a height of 50 mm. The sample was arranged for testing, as shown in Fig. 2c, and was pressed until failure using a pressing rate of  $50 \pm 5$  mm/min. The maximum force at failure (*P*, in N) was recorded. The *IDT* (in kPa), then, was calculated using Eq. 2

$$IDT = \frac{2,000 \times P}{\pi \times T \times D} \quad (2)$$

where *T* is the height of the tested sample (in mm), and *D* is the diameter of the tested sample (in mm).

#### Resilient modulus (*MR*) test

*MR* tests were conducted in accordance with [22]. The size of the samples and the apparatus were as same as the *IDT* tests. To measure *MR*, the sample was subjected to 5 cycles of constant load repetitions, each cycle was subjected to a Haversine force for 0.1 s and was allowed to recover for 0.9 s before the second cycle begins. The standard recommends that the optimum loading force in the test should be no more than 20% of the *IDT* measured from the same mixture to ensure that the material still responds elastically in every cycle of repetitions. The lateral swelling of the sample was also measured with Linear Variable Differential Transformer (LVDT). After the sample had been subjected to 5 repeated load cycles, the resilient modulus was calculated based on the repetitive force and lateral swelling of the sample according to the equation and procedure specified in the standard.

#### Fatigue resistance (*FR*) test

*FR*, or also called fatigue life, tests were performed according to [23]. *FR* is a value that indicates the strength of a material against repetitive loads, typically represents as the number of cycles that cause the failure of the sample. *FR* tests also use the same apparatus and sample size as the *IDT* tests.

The tested sample was subjected to constant repetition of force until the specimen underwent rupture and failure. Coincide to the *MR* test, the sample was subjected to a Haversine force for 0.1 s and was allowed to recover for 0.9 s. In this study, the tested sample was subjected to constant repetition loads, which equaled to 30-40% and 60-70% of *IDT* for soil samples from Chainat and Chonburi, respectively, until failure. Number of cycles to failure was recorded and used to compare the *FR* of materials.

#### Soil permeability (*k*) test

*K* tests were carried out by constant head tests in accordance with [24]. The tested soil was compacted, following the mix design, in the molds with a diameter of 101.6 mm and a height of 116.43 mm. The amount of water over the measured time was recorded, then the *k* of each sample was calculated. Examples of *k* tests are shown in Fig. 2d.



Fig. 2 Examples of (a) free-free resonance test (b) unconfined compressive strength test (c) indirect tensile strength, resilient modulus and fatigue resistance tests (d) soil permeability test

## ANALYSIS AND TEST RESULTS

### Effect of Cement and Para-rubber Contents on Shear Wave Velocity

The effect of cement and Para-rubber contents on *V<sub>s</sub>* of SC and SCP from Chainat and Chonburi are shown in Fig. 3 and Fig. 4, respectively. It was found out that *V<sub>s</sub>* increased with the increasing of the cement content which agreed well with [25]-[26]. However, once Para-rubber was added into the mixture, *V<sub>s</sub>* tended to decrease with an increasing of Para-rubber content instead. This could be that Para-rubber affected the compaction quality and only partially bound the soil particles, as shown in Fig. 5, resulting in higher void ratio. The amount of water replaced by the Para-rubber could also affect the

cement hydration reaction, however, the microstructure analysis is required for further investigation.

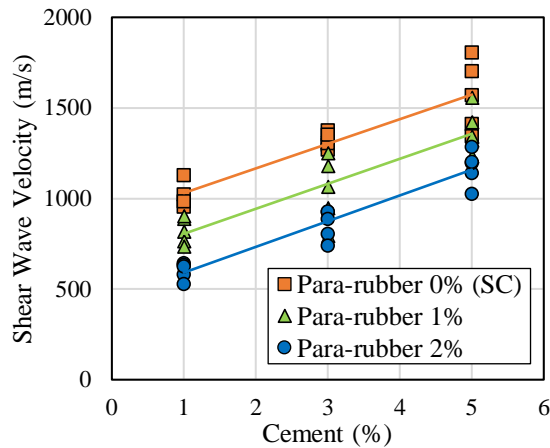


Fig. 3 Vs of treated soils from Chainat

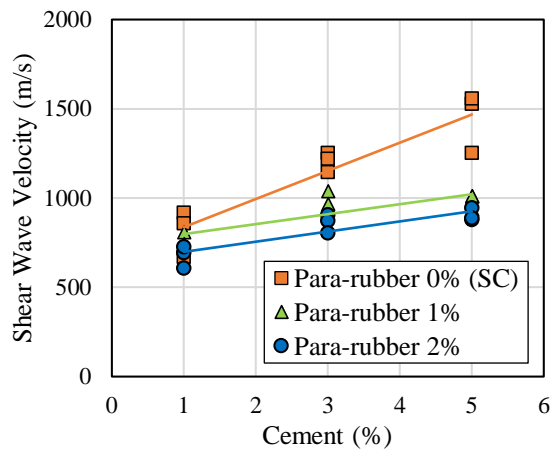


Fig. 4 Vs of treated soils from Chonburi



Fig. 5 Bond of Para-rubber of SCP.

### Effect of Cement and Para-rubber Contents on the Unconfined Compressive Strength

The effect of cement content and Para-rubber contents on *UCS* of SC and SCP from Chainat and Chonburi are shown in Fig. 6 and Fig. 7, respectively. The results presented that at the same amount of Para-rubber, the *UCS* of all materials increases as the cement content increases, which was consistent with [27]-[30] and the results of FFR tests. The results also showed that at the same amount of cement content, the SC and SCP from Chainat had higher *UCS* than the SC and SCP from Chonburi which could be due to the soil basic properties.

In a similar way to *Vs*, when considering the samples that had the same amount of cement content, it was found out that the addition of Para-rubber into the mixture tended to lower *UCS* which agreed well with [31]. The loss of *UCS* could also come from the poorer compaction quality and, probably, the hydration reaction generation. It is worth noting that the amount of Para-rubber had a greater impact on strength of SCP from Chainat than Chonburi province. Expecting that the lateritic soil from Chainat is non-plastic while lateritic soils from Chonburi has higher plasticity, resulting in a higher cohesion between soil particles.

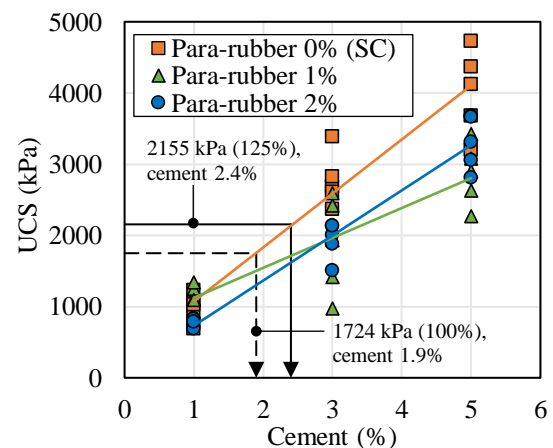


Fig. 6 *UCS* of treated soils from Chainat

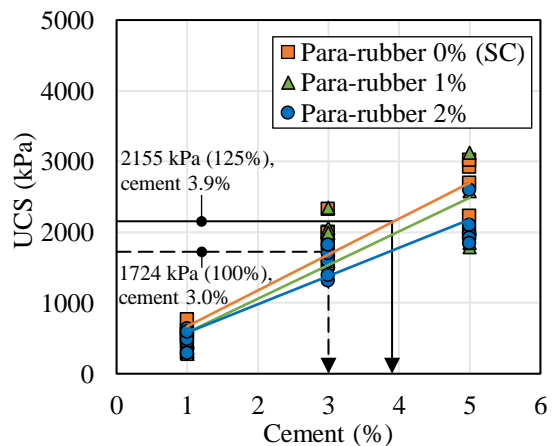


Fig. 7 *UCS* of treated soils from Chonburi



### Effect of Cement and Para-rubber Contents on Strain at Failure

The strain at failure also measured from the *UCS* tests as shown in Fig. 8 and Fig. 9 for the samples from Chainat and Chonburi, respectively. The results showed that the strain decreased with the increasing of cement content suggesting that cement tended to increase the brittleness of the samples. Considering at the low amount of cement content, the samples from Chonburi had slightly higher strain than the samples from Chainat due to the higher plasticity of the soil from Chonburi. However, when considering at the high amount of cement content, there was not much different between 2 material sources as the hydration reaction may govern their behaviors. Though, the microstructure analysis is preferred.

When Para-rubber was added into the mixture, it was found that the strain at failure increased, the change was clearly seen for the addition of 2% of Para-rubber indicating that Para-rubber tended to increase the ductility of the samples [32]. This could be the consequence of the high flexibility of Para-rubber. An addition of 1% of Para-rubber, however, provided slightly change on the strain at failure, expecting that the rubber created interparticle bonds only at some portions of the samples. The microstructure analysis is, again, preferred to confirm the notion.

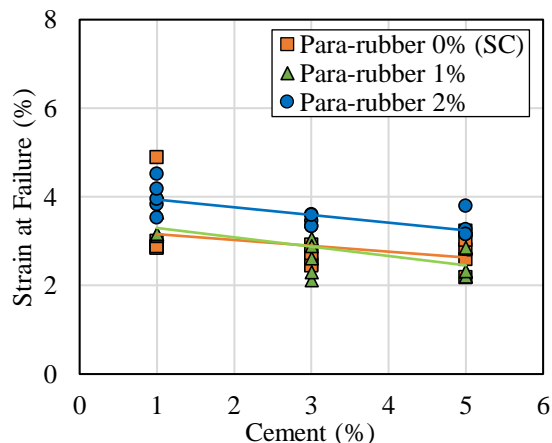


Fig. 8 Strain at failure of treated soils from Chainat

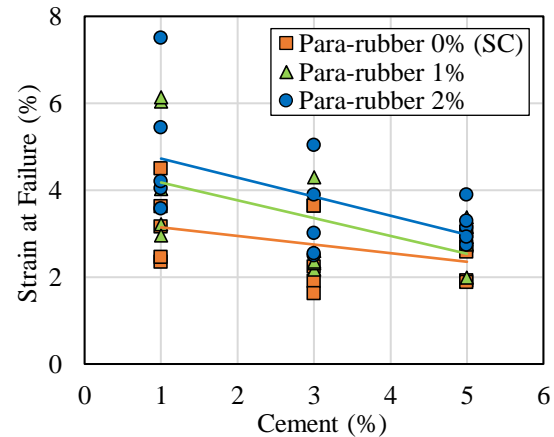


Fig. 9 Strain at failure of treated soils from Chonburi

### The Admixture Ratio for Laboratory Performance Tests

The results of *UCS* of SC were used to determine the most appropriate admixture ratio for the laboratory performance tests as shown in Fig. 6 and Fig. 7. For the soil from Chainat, the soil required cement content of only 1.9% of dry soil weight to satisfy the required *UCS*, 1724 kPa after 7 days of curing time. On the other hand, the soil from Chonburi required higher cement content, 3.0% of dry soil weight to satisfy the same required *UCS*. Though, due to the reason mentioned prior, the target designed strength in this study was higher than the minimum requirement, at 2155 kPa. Hence, the optimum cement content for the soils from Chainat and Chonburi became 2.4% and 3.9% of dry soil weight, respectively.

The amount of Para-rubber used for the performance test was selected at 2% of dry soil weight for both sources as it tended to increase the ductility of the samples and, also, to satisfy the objective of using high amount of Para-rubber.

### Effect of Cement and Para-rubber Contents on Indirect Tensile Strength

The summary of the performance test results is shown in Table 3, noted that the numbers represent the mean of 3 samples. The result indicated that the mean *IDT* of SC were generally higher than SCP. The samples using lateritic soil from Chonburi had higher *IDT* than the lateritic soil sample from Chainat. Expecting that cement content was an important factor for the increasing of the *IDT* of the samples. In contrast, Para-rubber resulted in a decrease in the *IDT* of the samples.

Table 3 Summary of the performance test results

Test	Chainat	Chonburi
------	---------	----------

	SC	SCP	SC	SCP
<i>IDT</i> (kPa)	424	234	513	428
<i>MR</i> (MPa)	15,234	10,103	7,435	6,547
<i>FR</i> (No. of cycle to failure)	64	964	28	458
<i>k</i> (cm/sec)	4.3x10 <sup>-7</sup>	3.0x10 <sup>-6</sup>	1.4x10 <sup>-8</sup>	1.3x10 <sup>-8</sup>

#### Effect of Cement and Para-rubber Contents on Resilient Modulus

The test results of *MR* are also shown in Table 3. An average *MR* of SC was generally higher than SCP. It was also found that *MR* measured from the samples from Chonburi was lower than the samples from Chainat which was in contrast with the results of *IDT*. Expecting that the quality of lateritic soils is an important factor to the increasing of *MR* of compacted samples. Para-rubber, again, resulted in a decrease in *MR* of the samples.

#### Effect of Cement and Para-rubber Contents on Fatigue Resistance

The results, shown in Table 3, indicated that SC had lower *FR* than SCP when considering at the same amount of applied stress ratio. However, it is noteworthy that the test that uses equivalent applied stress ratio is the test that many researchers have been used to compare the performance of studied materials assuming that those materials have similar response under the same repetitive load. However, the applied stress ratio clearly depends on the *IDT* of each material. In this study, the applied stress ratio was 40% for the soil from both sources, however, the applied loads were different, 170 kPa and 94 kPa for the soil from Chainat and Chonburi, respectively. This study also only limited to the laboratory condition as the samples were cured under controlled conditions, wrapped in room temperature. However, the materials on the construction sites are normally exposed so there might be some deterioration due to the environment, temperature, humidity etc. which could affect the performance of the materials.

#### Effect of Cement and Para-rubber Contents on Soil Permeability

The results of *k* test, presented in Table 3, indicated that the *k* of SC prepared from the lateritic soil from Chainat was lower than SCP, suggesting that the SCP had higher void ratio than SC. This could also specify that the Para-rubber affected the quality of compaction or even the generation of hydration reaction. However, when using the lateritic

soil from Chonburi, it was found out that the *k* of both SC and SCP were not much different. It is expected that the soil from Chonburi had more fine particles leading to a less effect on *k*. Also, as a result, the samples from Chonburi had lower *k* than the samples from Chainat because it had higher fine content and higher plasticity.

## CONCLUSIONS AND RECOMMENDATIONS

The study showed the effect of cement (1, 3 and 5% of dry weight) and Para-rubber (60% DRC at 1 and 2% of dry weight) contents on the properties and performances of SC and SCP from 2 lateritic soils that have different basic properties. The results of the study showed that the increase of cement content resulted in higher *UCS* and *Vs*. However, the addition of Para-rubber tended to decrease both properties. On the contrary, the strain at failure increased with the increasing of Para-rubber. This suggested that the Para-rubber might affect the compaction quality due to the partial bonds of Para-rubber and, probably, affected the creation of hydration reaction due to the substitution of water to Para-rubber. Nonetheless, microstructure analysis is recommended for further study.

The performances of the materials were also affected by the addition of Para-rubber. The *IDT* and *MR* tended to decrease, while *FR* and *k* tended to increase after adding 2% of Para-rubber into the mixture. It can be concluded that the use of cement increased the brittleness of the material, resulting in higher strength, while the use of Para-rubber increased the ductility, resulting in lower strength but could be benefited from higher deformation and higher fatigue crack resistance.

However, this study did not cover the durability against wet-dry cycles which is important for the pavement structure design of tropical countries. Hence, further study on the test is also recommended.

## ACKNOWLEDGEMENTS

The authors would like to thank DOH for the funding support. The kind supports from the staff of DOH and Kasetsart University during the course of this study are also appreciated.

## 7. REFERENCES

- [1] Terashi M., Theme Lecture: Deep Mixing Method-Brief State of the Art, In Proceeding of the 14th International Conference on Soil Mechanics and Foundation Engineering, Vol. 4, 1997, pp. 2475-2478
- [2] Horpibulsuk S., Katkan W., Sirilerdwattana W., and Rachan R., Strength Development in Cement Stabilized Low Plasticity and Coarse Grained Soil: Laboratory and Field Study, Soil and Foundation, Vol. 46, No. 3, 2006, pp. 351-366

- [3] Cortez E. R., Moisture effects on the mechanical behavior of flexible pavement subgrades, Ph.D. Dissertation, University of New Hampshire, Durham, NH, USA, 2007
- [4] Ribeiro D., Neri R., and Cardoso, R., Influence of Water Content in the UCS of Soil-Cement Mixtures for Different Cement Dosages, *Procedia Engineering*, Vol. 143, 2016, pp. 59-66
- [5] Kantatham K., Horpibulsuk S., Suddeepong A., Buritatum A., Hoy M., and Takaikaew T., Effect of Natural Rubber Latex on the Compressive Strength and Durability of Cement Stabilized Soil, *Suranaree J. Sci. Technol.*, 28(3):030054(1-5), 2020
- [6] Paotong P., Jaritngam S., and Taneerananon P., Use of Natural Rubber Latex (NRL) in Improving Properties of Reclaimed Asphalt Pavement (RAP), *Engineering Journal*, Volume 24 Issue 2, 2020, DOI:10.4186/ej.2020.24.2.53
- [7] Jose A., and Kasthurba A.K., Laterite soil-cement blocks modified using natural rubber latex: Assessment of its properties and performance, *Construction and Building Materials*, Volume 273, 2021, 121991
- [8] Department of Highways of Thailand, Standard Test No. DH-T. 102/ 1972, Method of Test for Determining the Liquid Limit (LL) of Soils (in Thai)
- [9] Department of Highways of Thailand, Standard Test No. DH-T. 103/ 1972, Method of Test for Determining the Plastic Limit (PL) and Plasticity Index (PI) of Soils (in Thai)
- [10] Department of Highways of Thailand, Standard Test No. DH-T. 205/1974, Method of Test for Wet Sieve Analysis (in Thai)
- [11] Department of Highways of Thailand, Standard Test No. DH-T. 108/ 1974, Method of Test for Modified Compaction Test (in Thai)
- [12] Department of Highways of Thailand, Standard Test No. DH-T. 202/ 1972, Method of Test for Resistance to Degradation of Coarse Aggregate by Los Angeles Abrasion Machine (in Thai)
- [13] Department of Highways of Thailand, Standard Test No. DH-T. 109/ 1974, Method of Test for Determining the CBR (in Thai)
- [14] Department of Highways of Thailand, Standard No. DH-S. 204/2021, Standard for Soil Cement Base (in Thai)
- [15] Department of Highways of Thailand, Specification for Natural Rubber Modified Soil Cement Base Course, 2017 (in Thai)
- [16] Ryden N., and Ekdahl U., Quality control of cement stabilized soil using non-destructive seismic tests, *Advanced Testing of Fresh Cementitious Materials*, Stuttgart, Germany, 2006
- [17] Guimond Barrett A., Nauleau E., Le Kouby A., Pantet A., Reiffsteck P., and Martineau F., Free free resonance testing of in situ deep mixed soils, *Geotechnical Testing Journal*, vol. 36, no. 2, 2012
- [18] Verastegui-Flores R.D., Di Emidio G., Bezuijen A., Vanwelleghem J., and Kersemans M., Evaluation of the free-free resonant frequency method to determine stiffness moduli of cement-treated soil, *Soils and Foundations*, 55(5), 2015, pp. 943-950
- [19] Barus, R.M.N., Jotisankasa A., Chaiprakaikeow S., and Sawangsuriya A., Laboratory and field evaluation of modulus-suction-moisture relationship for a silty sand subgrade, *Transportation Geotechnics*, 19, 2019, pp. 126–134
- [20] Department of Highways of Thailand, Standard Test No. DH-T. 105/1972, Method of Test for Determining the Unconfined Compressive Strength of Soils (in Thai)
- [21] American Society for Testing and Materials, ASTM D6931-17, Standard Test Method for Indirect Tensile (IDT) Strength of Asphalt Mixtures
- [22] American Society for Testing and Materials, ASTM D7369-11, Standard Test Method for Determining the Resilient Modulus of Bituminous Mixtures by Indirect Tension Test
- [23] British Standard Institution, Method for determination of the fatigue characteristics of bituminous mixtures using indirect tensile fatigue, DD AFB, 1995.
- [24] American Society for Testing and Materials, ASTM D2434, Standard Test Method for Permeability of Granular Soils (Constant Head)
- [25] Chaiprakaikeow S., Soponpong C., and Sukolrat J., Development of a quality control index of cement stabilized road structures using shear wave velocity, In: *Proceedings of the 2nd World congress on civil, structural, and environmental engineering (CSEE'17)*, ICGRE 113, April 2 – 4, 2017, Barcelona, Spain
- [26] Lindh P., and Lemenkova P., Resonant Frequency Ultrasonic P-Waves for Evaluating Uniaxial Compressive Strength of the Stabilized Slag–Cement Sediments. *Nordic Concrete Research*, 65(2), 2021, pp. 39-62
- [27] Kamdee S., Thongmune S., and Jitsangiam P., Effects of Fine Content and Cement Content on Unconfined Compressive Strength of Lateritic Soil-Cement, *The 25th National Convention on Civil Engineering*, July 15-17, 2020, Chonburi, Thailand (in Thai)
- [28] Saroglou H., Compressive Strength of Soil Improved with Cement, *International Foundation Congress and Equipment Expo*, March 15-19, 2009, Orlando, Florida, United States
- [29] Horpibulsuk S., Rachan R., Chinkulkijniwat A., Raksachon Y., and Suddeepong A., Analysis of strength development in cement-stabilized silty clay from microstructural consideration, *Construction and Building Materials* 24, 2010, 2011-2021
- [30] Jaritngam S., Yandell W.O., and Taneerananon P., Development of Strength Model of Lateritic Soil-Cement, *Engineering Journal* Vol 17, Issue 1, 2013
- [31] Pinwiset K., Raksuntorn W., and Witchayangkoon B., An Investigation and Test of Natural Rubber Latex Soil Cement Road, *International Transaction Journal of Engineering, Management, & Applied Sciences & Technologies*, Vol. 9, No. 2, 2018, pp. 67-74
- [32] Veena U., and James N., Natural Rubber Latex for Improving Ductility Characteristics of Soil: A Preliminary Experimental Investigation, *Geotech Geol Eng*, 2022, <https://doi.org/10.1007/s10706-022-02162-1>

## NUMERICAL STUDY OF A HYBRID COUNTERMEASURE FOR RIVER EMBANKMENT IN ACTUAL FIELD CASE

Kakuta Fujiwara<sup>1</sup>, Enayat Mallyar<sup>1</sup>

<sup>1</sup> Dept. of Civil Eng., Tokai University, Japan

### ABSTRACT

In this study, a hybrid countermeasure for river embankments is proposed consisting of a wall of sheet-piles installed on one side of the toe of embankment and partial floating sheet-piles (PFS) installed on the other. Previous studies show that the PFS method is effective against embankment settlement caused by liquefaction of loose sand and consolidation of soft clay. However, such previous studies were carried out on simple model cases, and hybrid countermeasures on actual embankments have not been thoroughly studied. In this study, the authors have performed numerical analyses to verify the effectiveness of the hybrid countermeasure applied to actual field cases. It was concluded that the settlement of embankment was reduced by the hybrid countermeasure in the actual field case. Additionally, authors obtained a result for design that the maximum bending stress among the different length of the sheet-piles were almost same after consolidation.

*Keywords: Numerical analysis, Liquefaction, Countermeasure, PFS, Three-dimension*

### INTRODUCTION

Loose sand layers along river embankments are continuously damaged and settled due to liquefaction caused by earthquakes. As a conventional countermeasure, sheet-piles are installed at both toes of the embankment to potentially prevent damage to the embankment as well as settlement along the embankment, according to Fujiwara et al [1]. There are several examples of river embankments in Japan that demonstrate the effectiveness of sheet-piles against settlement due to earthquakes (Fig. 1(a)).

However, a layer of soft clay on the ground near the river embankment settles due to consolidation caused by the weight of the embankment. Otani [2] studied the partial floating sheet-pile (PFS), which consists of partially floating sheet-piles and end-bearing sheet-piles (Fig. 2), applied to one side of the toe of the embankment in a residential area (Fig. 1 (b)).

Nowadays, a “hybrid countermeasure” (a term coined by the authors in this paper) is in use (Fig.1 (c)), where an embankment having clay and sand layers has sheet-piles installed in river areas and the PFS installed in residential areas along both toes of the embankment. Yamamoto et al [3] investigated certain examples where the damage to a river embankment, due to consolidation and liquefaction during long-term including an earth-quake event was reduced through the use of hybrid countermeasures. Such hybrid countermeasures could be effective against soil deformation due to liquefaction and consolidation. However, the behavior and effectiveness of these hybrid countermeasures are not fully understood.

As a first step, Fujiwara et al [4] carried out

numerical analysis to verify the effectiveness of the PFS method for a river embankment under liquefaction. They concluded that the PFS could inhibit settlement of the embankment under liquefaction. Furthermore, the relationship between the parameters of the sheet-pile, such as the distance between the end-bearing sheet-piles and the length of the floating sheet-piles, as well as their effectiveness against embankment settlement was quantitatively verified.

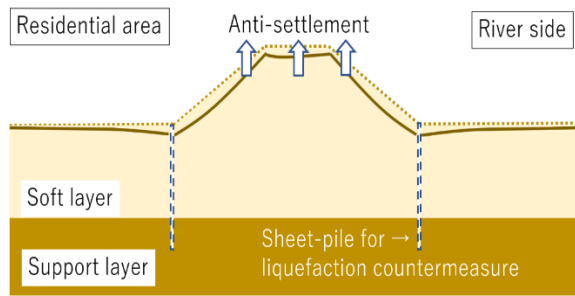
However, these analyses were carried out under several simple assumptions as follows:

- Vertical load was applied to the surface ground instead of modelling of an embankment.
- The ground had only two sand layers.
- A sinusoidal wave with enormous acceleration was given as an input.
- Bending stress of sheet-piles were not discussed for making a design method

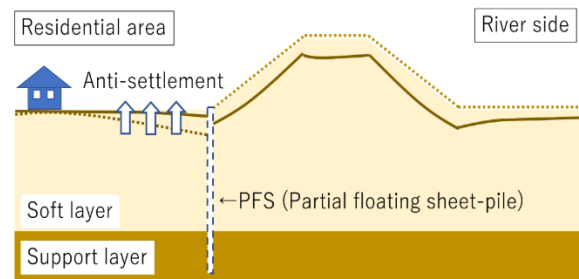
Therefore, in this study, the authors carried out numerical analyses to investigate the effectiveness of the hybrid countermeasure against settlement in an actual field case. Additionally, the authors discuss the bending stress of the sheet-piles in the PFS for the purpose of designing this countermeasure.

### NUMERICAL CONDITION

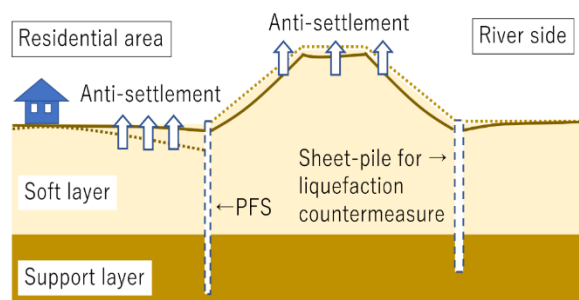
The numerical analyses were conducted using LIQCA3D20. The target embankment is constructed on six horizontal layers of ground shown as Fig.3. The width and depth of this model was relatively small for reduction of calculation time. Model size should be considered in the future. To perform the numerical analysis, parameters such as dimensions,



(a) Sheet-piles as a liquefaction countermeasure



(b) PFS to prevent settlement by consolidation



(c) Hybrid countermeasure

Fig. 1 Countermeasures for the river embankment

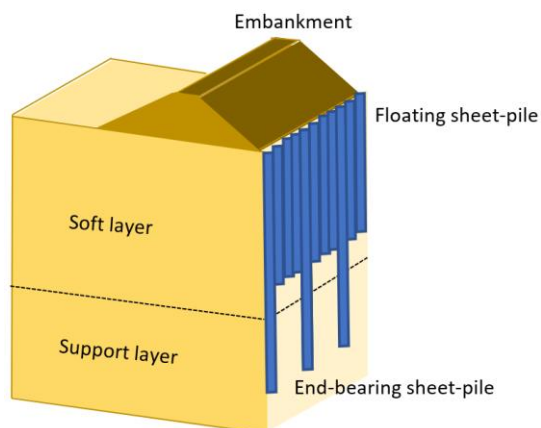


Fig. 2 The PFS structure

soil parameters, and countermeasures needed to be specified. The following sub-sections describe the ground condition and these parameters and their corresponding values.

## Soils

The soil parameters used in the numerical model are shown in Table 1. Some pieces of information (soil species, N value, water level) could be gained by a ground survey. Detail information (stress-strain relationship, liquefaction curve, consolidation test result, and so on) were not gained. Therefore, these parameter values were inferred and determined from the survey results referring to the manual of LIQCA by Liquefaction Geo Research Institute [5] and the academic paper by Fujiwara et al [6].

The embankment and basement (Dg) are modeled as elastic-perfectly plastic models. The sand layers (As1 and As2) were modeled as elasto-plastic models created by Oka et al [7], which is often used to model a loose sand layer. This model represents sand behavior resulting from an increase in excess pore water pressure which causes motion, making the sand soft, and finally causing liquefaction. An elasto-viscoplastic model proposed by Adachi [8], which can represent an increase in excess pore water pressure by the load, making the clay soft and causing consolidation.

## Countermeasures

The sheet-piles were installed along the toe of the embankment, shown as Fig. 3, in residential area. The PFS has three floating sheet-piles and one end-bearing sheet-pile per one set shown in Fig. 4. The sheet-piles were modeled by cuboid meshes with linear elastic material having no yield. The PFS sheet-piles in the residential area were modeled with a flexural rigidity of  $8.0 \times 10^4 \text{ kN} \cdot \text{m}^2$  (per unit width of 1 m) and a thickness of 210 mm, such that the flexural rigidity was equivalent to that of a IVw steel sheet-pile, considering corrosion allowance. The sheet-piles on the river side were modeled with a flexural rigidity of  $4.0 \times 10^4 \text{ kN} \cdot \text{m}^2$  (per unit width of 1 m) and a thickness of 300 mm, such that the flexural rigidity was equivalent to that of a 25H steel sheet-pile, considering corrosion allowance. As the values of flexural rigidity and the section modulus cannot be the same as the actual values of the sheet-piles, the section modulus of the cuboid sheet-piles was higher than the actual value of the sheet-piles. Therefore, the bending stress (discussed herein later) of the cuboid sheet-piles was lower than the actual value of the sheet-piles.

## Numerical cases

For Case 1, no sheet-piles were set in the numerical model. For Case 2, the target field with the hybrid countermeasure was modeled, as explained herein above. As a further study, the length of the end-bearing sheet-piles was changed for making a design method. For Case 3, the length of the end-bearing



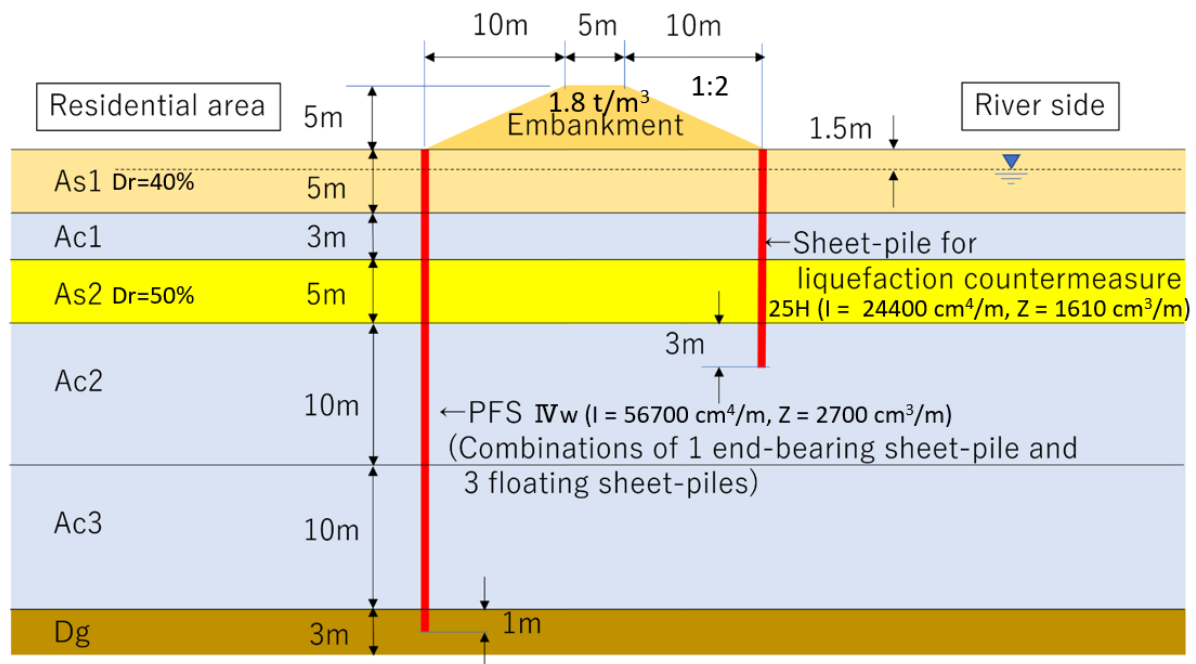


Fig. 3 Target embankment

Table 1 Soil parameters

Layer			Embankment	As1	Ac1	As2	Ac2	Ac3	Dg
Model			Elastic-perfectly plastic	Elasto-plastic	Elasto-viscoplastic	Elasto-plastic	Elasto-viscoplastic	Elasto-viscoplastic	Elastic-perfectly plastic
Density	$\rho$	t/m <sup>3</sup>	1.8	1.8	1.7	1.9	1.7	1.7	2.1
Young's moduls	$E_0$	kN/m <sup>2</sup>	14000	9810	5730	30000	7040	7040	140000
Poisson's ratio	$\nu$		0.33	0.33	0.33	0.33	0.33	0.33	0.33
Cohesion	$C$	kN/m <sup>2</sup>	0	0	20	0	50	70	0
Friction angle	$\phi$	degree	30	30	0	30	0	0	40
Coefficient of permeability	$k$	m/s		$1.0 \times 10^{-5}$	$1.0 \times 10^{-8}$	$1.0 \times 10^{-5}$	$1.0 \times 10^{-8}$	$1.0 \times 10^{-8}$	$1.0 \times 10^{-4}$
Initial void ratio	$e_0$			0.821	1.25	0.856	1.25	1.25	
Compression index	$\lambda$			0.015	0.341	0.018	0.341	0.341	
Swelling index	$\kappa$			0.002	0.019	0.0055	0.019	0.019	
	OCR*			1.0	1.0	1.0	1.0	1.0	
Initial elastic shear modulus ratio	$G_0/\sigma'_m$			1000	75.2	851	75.2	75.2	
Stress ratio at critical state	$M^*_m$			0.909	1.24	0.909	1.24	1.24	
Stress ratio at failure	$M^*_f$			1.122	1.24	1.122	1.24	1.24	
	$B^*_0$			7000	100	2200	100	100	
Hardening parameter	$B^*_1$			50	40	30	40	40	
	$C_f$			2000	10	2000	10	10	
	$C_1$	1/s			$1.0 \times 10^{-5}$		$1.0 \times 10^{-5}$	$1.0 \times 10^{-5}$	
Viscoplastic parameter	$C_2$	1/s			$3.83 \times 10^{-6}$		$3.83 \times 10^{-6}$	$3.83 \times 10^{-6}$	
	$m'$				24.68		24.68	24.68	
Structural parameters	$\beta$				3.6		3.6	3.6	
Scalar hardening parameter	$A^*_2$				5.9		5.9	5.9	
	$B^*_2$				1.8		1.8	1.8	
Dilantancy parameter	$D_0$			3		5			
	$n$			3		1.5			
Reference strain parameter	$\gamma^{p*}$			0.02		0.1			
	$\gamma^{E*}$			0.01		0.015			

sheet-pile was 27 m. For Case 4, the length of the end-bearing sheet-pile was 16 m, which was the same as that of the floating sheet-piles.

### Input motion

The dynamic analyses were carried out from the results of the initial analyses, using the input motion, which was observed in the Kumamoto Earthquake in 2016 in Japan, as represented by the plot (Fig. 5). The Japan Meteorological Agency provided the data [9]. This wave had a maximum acceleration of  $3.24 \text{ m/s}^2$ , and a duration of 43 s. The long-term analyses were carried out after shaking, using input data of no acceleration up to  $t = 3.0\text{E}+07 \text{ s}$ , which is approximately one year.

### Target points

The locations of target points D, P1, P2, and P3 (discussed herein later) are selected for discussion indicated in Fig. 6. These points are located in the center of this model. The point D indicates vertical displacement located at top of the embankment, whereas the points P1, P2, and P3 indicate the excess pore water pressure located at 33m, 25m and 13m from bottom of the model, respectively.

## RESULT AND DISCUSSION

### Deformation of ground

The ground deformation with volume strain at  $t = 3.0\text{E}+07 \text{ s}$  is shown in Fig. 7 (Cases 1 and 2). Time histories of the settlement at D are shown in Fig. 8. The horizontal displacements of the soil and sheet-piles at the toe of the embankment along z-direction at  $t = 3.0\text{E}+07 \text{ s}$  in residential area is shown in Fig. 9. The time histories of the excess pore water pressure at P1, P2, and P3 are shown in Fig. 10 (Case 1).

For Case 1, the liquefied sand layers laterally moved outwards, due to the weight of the embankment (Fig. 7(a)). After the shaking, although the void water drained out from the surface (as seen from the data at P1), the excess pore water pressure at P3 increased in the clay layers (Fig. 10). This is because the shear force from the weight of the embankment applied to the clay layers generated the water pressure at P3. Therefore, the excess pore water pressure layers remained. The settlement of the embankment was 1.33 m. The settlement would continue to raise after  $t = 3.0\text{E}+07 \text{ s}$ .

For Case 2, the sheet-piles prevented the settlement up to 1.16 m, this was 13% lesser than that in Case 1 at  $t = 3.0\text{E}+07 \text{ s}$  shown in Fig. 8. The volume strain near the left sheet-pile of the PFS reduced, which means that the friction of the sheet-piles reduced the ground settlement (Fig. 7(b)). For Cases 3 and 4, the settlements were almost same. In this analysis, the

elements of the sheet-pile were connected directly to the soil elements without any joining elements. Therefore, soil didn't pass through between the gap between end-bearing sheet-piles. Accordingly, there was little difference of settlements among Cases 2, 3 and 4 shown in Fig. 8.

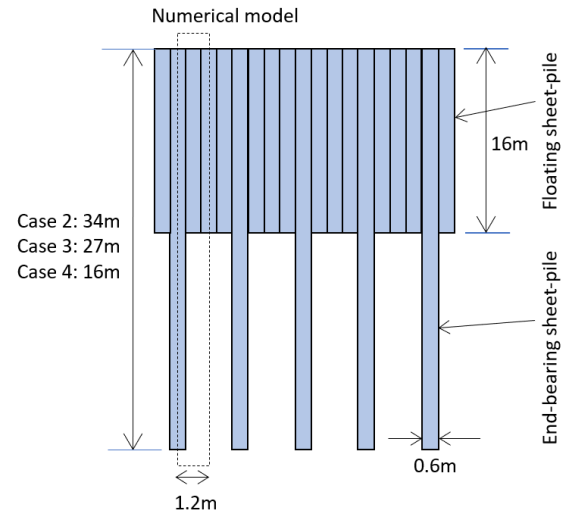


Fig. 4 The PFS structure

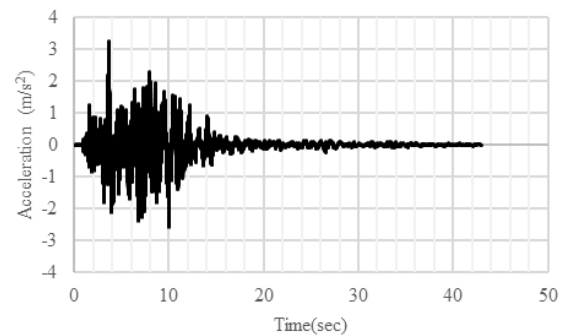


Fig. 5 Input motion

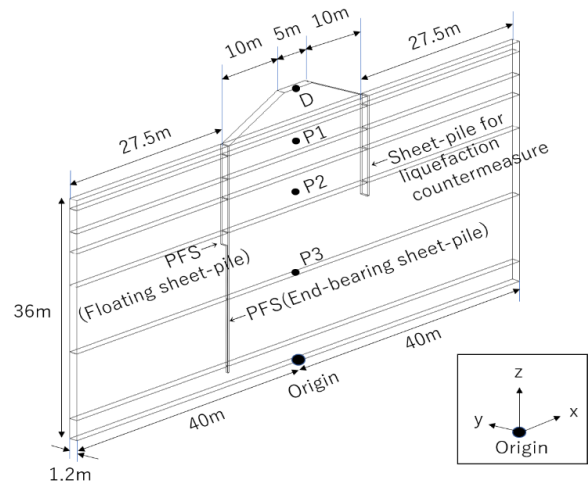


Fig. 6 Target point

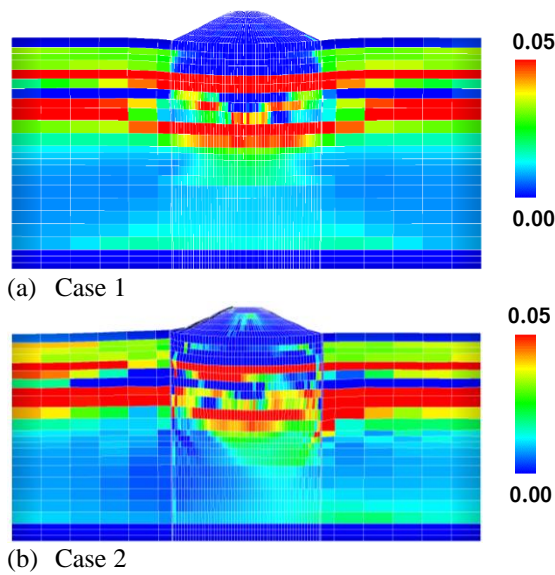


Fig. 7 The ground deformation with volume strain

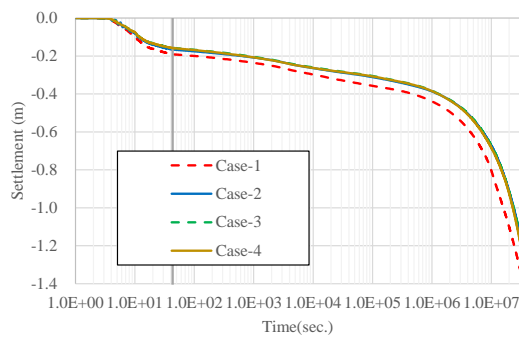


Fig. 8 Time histories for settlement at D

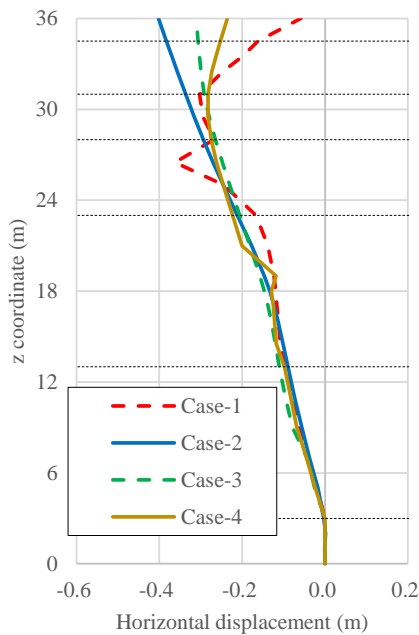


Fig. 9 Horizontal displacement for the PFS sheet-pile in residential area

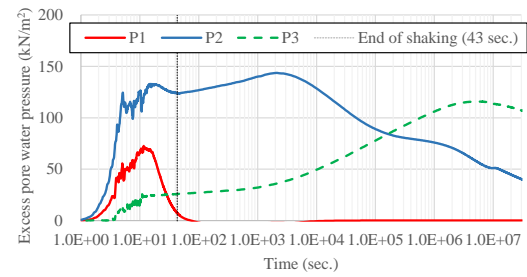


Fig. 10 Time histories for excess pore water pressure at P1, P2 and P3 (Case 1)

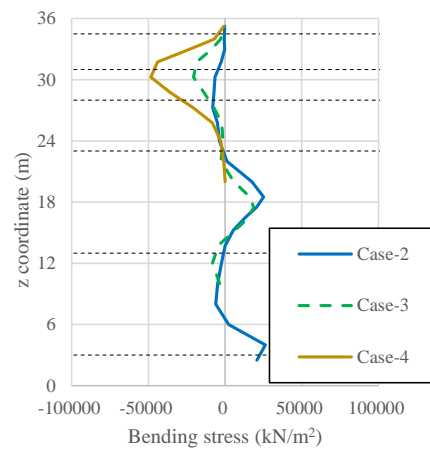


Fig. 11 Bending stress for the sheet-pile in depth direction

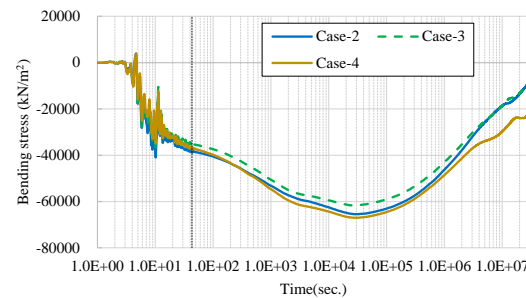


Fig. 12 Time histories for bending stress at  $z = 30$  m

### Bending stress of sheet-piles

Fig 11 shows the bending stress of the end-bearing sheet-pile obtained from Fig. 9 at  $t = 3.0E+07$  s. For Case 2, that is long end-bearing sheet-piles case, the maximum bending stress was generated in the lower layer. For Case 4, that is short end-bearing sheet-piles case, the maximum bending stress was generated in upper layer. For Case 3, the medium result between Cases 2 and 4 was obtained.

From Fig. 9, a difference in the displacements for Cases 2, 3 and 4, could be seen near the top of the sheet-pile. The top of the short end-bearing sheet-pile was moved to the right side by the motion of the

ground, indicated in Case 1. There were minor differences of bending stress in the clay layers among Cases 2, 3 and 4, which was the same as the result of horizontal displacements. The clear differences along the upper side of the sheet-pile were caused by the deformation of soil, as mentioned earlier in the explanation of horizontal displacement. For Case 4, the lower side of the sheet-pile was inclined towards the left side by the deformation of the clay layers and the upper side was pushed to the right side, generating large bending stress around  $z = 30$  m. As the longer the sheet-pile became, the smaller the bending stress became at  $z = 30$  m. Above all, Case 4 had the highest bending stress among Cases 2, 3 and 4.

The time histories of the peak bending stress at  $z = 30$  m are shown in Fig. 12. The bending stress for Cases 2, 3, and 4 were nearly the same during and after shaking. As the excess pore water pressure at P2 and bending stress at  $z = 30$  m are in same layer (As2), these values are strongly correlated, shown in Fig. 10 and Fig. 12. Since all the excess pore water pressure did not dissipate in this analysis, the bending stress would continue to change after  $t = 3.0E+07$  s.

## CONCLUSIONS

A hybrid countermeasure for river embankment comprising sheet-piles on the river side and the PFS in the residential area is proposed. Numerical analysis was carried out using LIQCA3D20 to investigate the performance of this countermeasure, applied in the actual field, for a period of one year from an earthquake event. The clay layers were modeled by elasto-viscoplastic model. Furthermore, the behavior of an end-bearing sheet-pile in PFS was investigated by changing the length of the end-bearing sheet-pile. The following conclusions were reached:

1) During the shaking that accompanied the quake, the sheet-piles prevented the settlement by 13% compared to no countermeasure case, even in the actual field case.

2) The maximum bending stress was generated in the sand layers near surface for short end-bearing sheet-piles case, and that was in the clay layers deep underground for long end-bearing sheet-piles case. Above all, short end-bearing sheet-pile had the highest bending stress in the numerical condition.

3) Soil and sheet-piles are connected directly without joint elements. Therefore, soil didn't pass through between the gap of end-bearing sheet-piles under floating sheet-piles. Accordingly, there was little difference of settlements for countermeasure cases. That should be discussed in a future work.

## ACKNOWLEDGMENT

We are grateful to International Press-in Association TC3 Design WG members (Hidetoshi Nishioka, Hiroaki Akutagawa, Jun Otani, Kiyonobu

Kasama, Shinji Taenaka, Shin Oikawa, Yukihiro Ishihara) for helpful discussions.

## REFERENCES

- [1] Fujiwara, K., Koseki, J., Otsushi, K. and Nakayama, H., Study on reinforcement method of levees using steel sheet-piles, Foundation and Soft Ground Engineering Conference, Thu Dau Mot University ICTDMU-1, 2013, pp. 281-289.
- [2] Otani, J., A new sheet-pile method for countermeasures against the settlement of embankment on soft ground (Development of PFS Method), IPA News Letter, Vol. 2, Issue 3, 2017, pp. 8-10.
- [3] Yamamoto, S., Kasama, K., Ohno, M. and Tanabe, Y., Seismic behavior of the river embankment improved with steel sheet piling method, proceedings of the First International Conference on Press-in Engineering, Kochi, 2018, pp. 227-232.
- [4] Fujiwara, K., Ogawa, N. and Nakai, K., 3-D numerical analysis of partial floating sheet-pile method as countermeasure for liquefaction, Journal of JSCE, Vol. 9, 2021, pp. 138-147.
- [5] Oka, F., Yashima, A., Shibata, T., Kato, M. and Uzuoka, R., FEM-FDM coupled liquefaction analysis of a porous soil using an elasto-plastic model, Applied Scientific Research, Vol. 52, 1994, pp. 209-245.
- [6] Fujiwara, K., Ogawa, N. and Nakai, K., Quantitative evaluation of PFS (Partial floating Sheet-pile) method under liquefaction. Geotechnics for Sustainable Infrastructure Development, 2020, pp. 467-472.
- [7] Oka, F., Yashima, A., Tateishi, A., Taguchi, Y. and Yamashita, A., A cyclic elasto-plastic constitutive model for sand considering a plastic-strain dependence of the shear modulus, Geotechnique, 1999, Vol. 49(5).
- [8] Adachi, T. and Oka, F., Constitutive equations for normally consolidated clay based on elasto viscoplasticity, Journal of Soils and Foundations, Vol. 2, Issue 4, 1982, pp. 57-70.
- [9] Japan Meteorological Agency (<http://www.data.jma.go.jp/svd/eqev/data/>)

## A YIELD FUNCTION AND UNDRAINED BEHAVIOR OF $K_0$ CONSOLIDATED CLAYS

\*Yoshihito Imai<sup>1</sup>, Salisa Chaiyaput<sup>2</sup>, Koichi Iinuma<sup>3</sup>, Masaru Akaishi<sup>4</sup> and Motohiro Sugiyama<sup>4</sup>

<sup>1</sup>ONODA CHEMICO Co.,Ltd., Japan, <sup>2</sup>Department of Civil Engineering, King Mongkut's Institute of Technology Ladkrabang, Thailand, <sup>3</sup>OHBA Co.,Ltd., Japan, <sup>4</sup>Department of Civil Engineering, Tokai University, Japan

### ABSTRACT

The Cam Clay model is one of the typical elastoplastic soil models based on the critical state concept and its yield function is derived from an assumption regarding the dissipation of energy during the plastic deformation. The constant line of minimum principal effective stress for normally consolidated clay lies inside the yield surface of Cam Clay. An anisotropic critical state model with a yield function is formulated to represent the undrained path of normally consolidated clays. The parameters required for the model are easy to decide from the conventional test except of one parameter, which makes the soil model practicable. It has been demonstrated that the calculated and observed undrained paths of normally consolidated clays are satisfactory for small strain softening case. In addition, an anisotropic yield function is shown to give a reliable estimation of the elastoplastic stress boundary surface that can reproduce experimental results.

*Keywords: Anisotropic yield function, Earth pressure at rest, Triaxial test, Clay, Cam Clay model*

### INTRODUCTION

The greatest pressure under which clays had been consolidated during its past geological history, is the so-called pre-consolidation pressure and called the consolidation yield stress in Japan [1]-[2]. The yield stress in multidimensional consolidation analysis is defined by the yield function which means the limit of the stress space for the elastic behavior of clays. The useful mathematical constitutive model for clays is based on the theories of elasticity and plasticity. The Cam Clay model developed by Roscoe et al. [3] is one of typical elastoplastic soil models based on the critical state concept and its yield function is derived from an assumption regarding the dissipation of energy during the plastic deformation. However, for the validity of its yield function there are not still enough for the experimental evidence, because a line of the minimum principal effective stress for  $K_0$  normally consolidated clays lie in the yield surface of Cam Clay. So long as the stress state stays in the yield surface, its behavior must be purely elastic, even if the applied minimum principal effective stress exceeds the maximum value to which the clay was ever subjected in the past.

The purpose of this study is to present a yield function for  $K_0$  normally consolidated clays, and to examine experimentally its reliability in the viewpoint of the relations of the yield stress and the minimum principal effective stress. The validity of the yield function will be evaluated by the undrained triaxial test result since the undrained path depends on the yield function only and independent of the plastic potential. And also from the drained triaxial

test results it is clarified that the plastic strain actually occurs due to the stress change into the yield surface of Cam Clay model.

### YIELD FUNCTION AND UNDRAINED PATH

#### Yield function

In order to define the yield function of Cam Clay model, it has been postulated that the external work acting on a clay element is equal to the dissipation energy due to the plastic deformation and that the Eq. (1) is expressed as follow [3].

$$p * dv_p + q * d\epsilon_p = M * p * d\epsilon_p \quad (1)$$

where  $p$  is the effective mean stress,  $q$  is the deviator stress,  $M$  is the slope of Critical State Line (CSL),  $dv_p$  and  $d\epsilon_p$  are the increments of the plastic volumetric and the deviator strain. By assuming that normality rule exists and substituting Eq. (2) in Eq. (1) it is possible to drive the yield function  $F$ . Yielding of the clay occurs whenever the stress satisfies the yield function, i.e., Eq. (3).

$$\frac{dq}{dp} * \frac{d\epsilon_p}{dv_p} = -1 \quad (2)$$

$$F = \eta - M * \log\left(\frac{p_c}{p}\right) = 0 \quad (3)$$

where  $\eta(=q/p)$  is the stress ratio and  $p_c$  is a hardening parameter and analogous to a pre-consolidation pressure.

Dafalias et. al. [4] postulated the following plastic

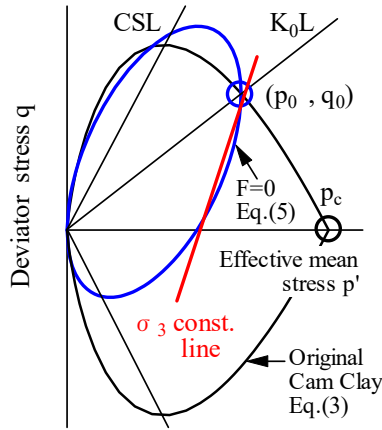


Fig.1 The yield surfaces of normally isotropic and  $K_0$  consolidated clay

work dissipation equation to derive the yield function for normally  $K_0$  consolidated clays.

$$p * dv_p + q * d\varepsilon_p = p \sqrt{(dv_p)^2 + (N * d\varepsilon_p)^2 + 2 * \beta * dv_p * d\varepsilon_p} \quad (4)$$

$$F = q^2 - 2 * \beta * p * q + \beta^2 * p^2 + N^2 * (p^2 - p * p_0) = 0 \quad (5)$$

where  $N$  and  $\beta$  are a material constant related to the shape of yield surface,  $p_0$  is the effective mean stress in the particular case of  $K_0$  consolidated clays.

The yield surfaces of normally isotropic and  $K_0$  consolidated clay is shown in Fig. 1 [4]. The yield surface of Original Cam Clay by Eq. (3) is well known and widely used, and its shape looks like a leaf. If  $N=M$  and  $\beta=\eta_0=0$ , Eq. (5) corresponds to that of Modified Cam Clay. An anisotropic surface with a blue line is the transformed and rotated ellipse of Modified Cam Clay. A red line shown in Fig. 1 has an incline of 3 in 1 in which the minimum principal effective stress of a normally consolidated clay is held constant. The red line is located inside of the yield surface given by Eq. (3) although Eq. (5) with a blue line close enough to a red line. Even if the stress state for the over consolidated clay moves to the right side of the red line, only elastic strains will be predicted by means of the yield function, i.e., Eq. (3). Plastic strain never occurs even if the minimum principal effective stress exceeds the past maximum value. As logical consequence the definition on the yield function is ambiguous.

Although the yield criterion should be noted in determining the stress level at which plastic deformation begins, it is not clear whether the shape of the yield surface depends on the consolidated stress state. It is difficult to obtain a yield function that can strictly define the stress space in which the clay

behaves elastically. However, the validity for these yield functions should be examined by the experimental evidence.

### Undrained path

The volumetric strain increment  $dv$  of a soil element is expressed by Eq. (6), as the sum of elastic and plastic strain components both with superscripts  $e$  and  $p$  respectively. Using yield function  $F$  and plastic potential  $Q$ , the hardening parameter  $H$  is given by Eq. (7).

$$dv = dv^p + dv^e = \left( \frac{1}{H} \frac{\partial F}{\partial p} \frac{\partial Q}{\partial p} + \frac{1}{K} \right) dp + \frac{1}{H} \frac{\partial F}{\partial q} \frac{\partial Q}{\partial q} dq \quad (6)$$

$$H = - \frac{\partial F}{\partial v^p} \frac{\partial Q}{\partial p} \quad (7)$$

where  $K$  is the elastic bulk modulus. It is possible to calculate the undrained path in the consolidated undrained triaxial test by making the volumetric strain increment in Eq. (6) to be equal zero.

With the above condition  $dv=0$ , Eq. (8) and Eq. (9) yields the  $p$ - $q$  relation derived from Eq. (3) and Eq. (5) respectively. It should be emphasized that the undrained path is not affected by the plastic potential  $Q$ , as  $\partial Q / \partial p$  in the volumetric strain is eliminated in this derivation.

$$\eta = \frac{M}{\Lambda} * \ln \left( \frac{p_c}{p} \right) \quad (8)$$

$$p = p_0 \left[ \frac{\eta_0^2 - 2 * \beta * \eta_0 + N^2}{\eta^2 - 2 * \beta * \eta + N^2} \right]^\Lambda \quad (9)$$

where  $\Lambda = 1 - \kappa/\lambda$ ,  $\kappa$  and  $\lambda$  are the swelling and compression index,  $N$  is stress ratio at the maximum deviator stress in the undrained triaxial test,  $\beta$  is equal to the stress ratio  $\eta_0 (= q_0/p_0)$  at  $K_0$  consolidation.

Proposed model expressed by Eq. (9) can explain the strain softening behavior if  $N$  is less than  $M$ . The yield surface shown by the blue line in Fig. 1, is expressed by using  $M=1.57$  and  $N=1.35$ .

An example of the undrained path affected by  $\beta$  value with  $N=M$  is shown in Fig. 2. Fig. 3 shows the effect of  $N$  value on the undrained path. When  $\eta < M$ , the deviator stress  $q$  shows the maximum value, and then  $q$  decreases until  $\eta=M$ . Reduction of deviation stress, i.e. the peak drop can be calculated.

### EXPERIMENTAL PROCEDURE AND CLAYS TESTED

Undisturbed saturated normally consolidated alluvial clays were taken by the thin wall sampling for the residential development in the suburbs of Tokyo.



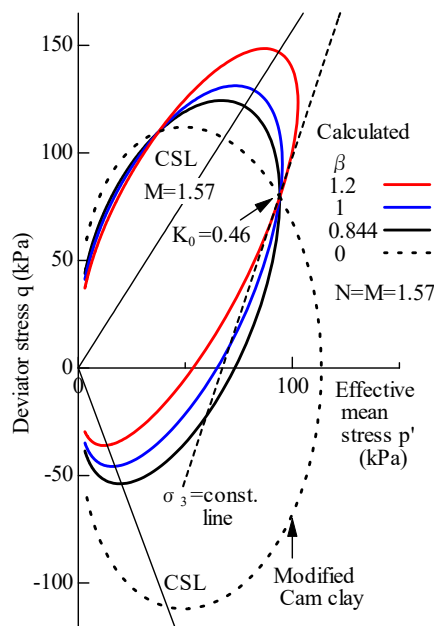


Fig.2 Effect of  $\beta$  value on undrained paths

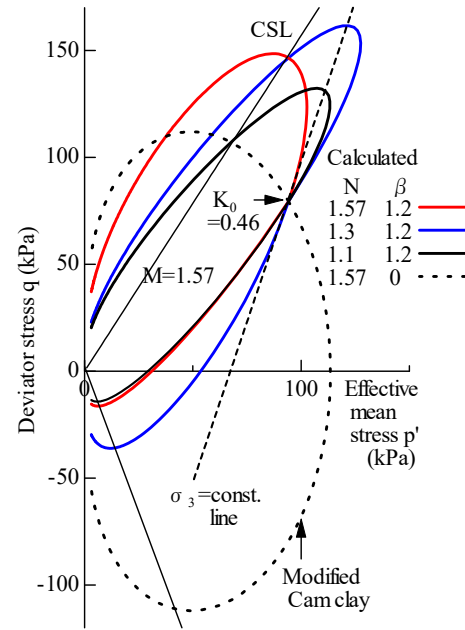


Fig.3 Effect of  $N$  value on undrained paths

Table 1 Physical and mechanical properties of clay samples

Site	$G_s$	$w_L$ (%)	$I_p$ (%)	$\lambda$	$\kappa$	$M$	$K_0$
Kashiwa	2.643	112	50	0.200	0.030	1.48	0.40
Soka	2.672	83	39	0.182	0.041	1.54	0.43
Hitachi	2.657	121	69	0.460	0.120	1.57	0.46

The physical and mechanical properties of the clay sample and soil constants used in the calculation are shown in Table 1.

### Consolidated Undrained (CU) Triaxial Test

In order to examine the effects of secondary compression and the stress state in the anisotropic consolidation on the yield surface, consolidated undrained triaxial compression and extension tests are performed by the strain control with the strain rate of 0.1 %/min.

The specimens with a diameter of 5 cm and a height of 12 cm wrapped with the drain paper are consolidated under  $K_0$  condition before the undrained shear test and the pore water pressure during undrained shearing is measured at the bottom of the specimen. The influence of the secondary consolidation period on the undrained path, that is, the yield function was investigated as remarkable secondary compression was observed during  $K_0$  consolidation.

The lateral pressure of some specimens was increased after  $K_0$  consolidation, and anisotropically consolidated under constant axial stress for one day. This stress change is occurred inside of the initial yield surfaces of Cam Clay. The effect for the

increase of the lateral pressure is investigated by the undrained path. And the constants  $M$  and  $N$  were determined using the maximum stress ratio  $\eta_{max}$  and the peak deviator stress  $q_p$ , respectively in CU tests.

### Consolidated Drained (CD) Triaxial Test

The void ratio change for the over consolidated clay was measured in order to examine the effects of dilatancy on the initial yield surface. Over consolidated clays ought to exhibit the elastic behavior. No volumetric strain is observed without the change of the effective mean stress as it is clear from Eq. (6).

For CD tests, the saturated clay specimens are first subjected to  $K_0$  normally consolidated condition. Each stress increment duration of one day is used for complete drainage so that the excess pore water pressure becomes equal to zero. The conditions for the axial and radial stress increment with the experimental results are shown in the latter discussion.

Back pressure is applied of 98.1 kPa in both triaxial tests during consolidation and shearing.

## TEST RESULTS AND DISCUSSIONS

### $p_c$ in the isotropic consolidation test

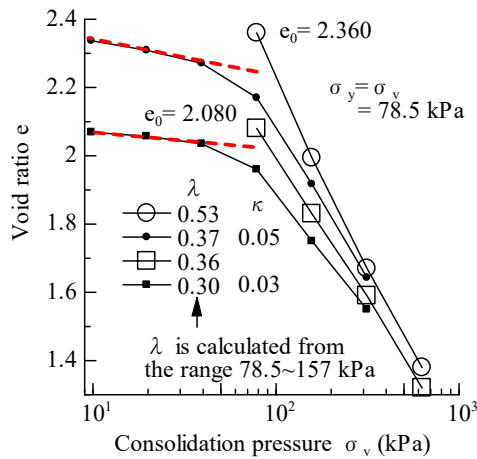


Fig.4  $e$ -log  $p$  curves of one-dimensional consolidation test with Hitachi clay

To investigate the relationship between the hardening parameter  $p_c$  of the Cam Clay model and the consolidation yield stress  $\sigma_y$  ( $p_y$ ), a one-dimensional and isotropic consolidation test was performed on Hitachi clay. The results are shown in Figs. 4 and 5. In the one-dimensional consolidation test, two sets with similar sampling depths, a total of four specimens, were pre-consolidated at an overburden pressure of  $\sigma_v = 80$  kPa. Each one of the clays was then consolidated by incremental loading (white symbols in Fig. 4), and the other clays were unloaded to 10 kPa and then reloaded by incremental loading (black symbols in Fig. 4).

In the isotropic consolidation test, initial consolidation pressures of 10 kPa and 20 kPa were applied to two cylindrical specimens, each 5 cm in diameter and 10 cm high, and then 20 kPa load increments were applied in stages.

Fig. 4 shows the  $e$ -log  $p$  relation in one-dimensional consolidation test. From the  $e$ -log  $p$  curve as shown black symbols obtained by reloading after the release of consolidation pressure, the void ratio and compression index decrease but the vertical yield stress hardly change. Therefore, the settlement prediction by the compression index obtained from the laboratory consolidation test may lead to the underestimation. So, it is difficult to infer the actual behavior in the field by using the relationship measured from the laboratory sample released the overburden pressure. The effective mean stress as the consolidation yield stress obtained from one-dimensional consolidation test is equal to 50 kPa since  $K_0 = 0.46$ .

According to the results of isotropic consolidation test in Fig. 5 it is possible to confirm the value of the hardening parameter,  $p_c$  because the deviator stress is kept to zero. The value of  $p_c$  as Original Cam Clay becomes 86 kPa. As shown in Fig. 5, it is clearly understood that the yield stress is approximately

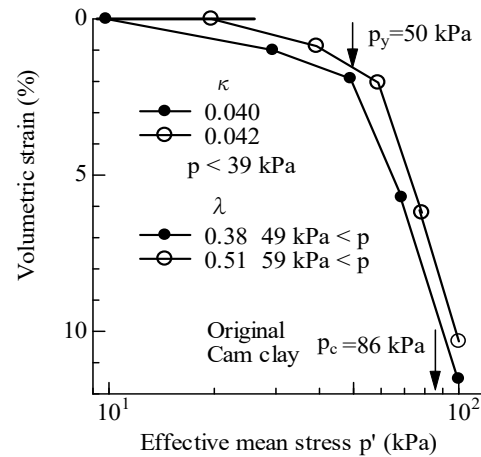


Fig.5  $e$ -log  $p$  curves of isotropically consolidation test with Hitachi clay

equal to the effective mean stress obtained from of the one-dimensional consolidation test and is much smaller than the hardening parameter  $p_c$  in the case of Original Cam Clay. Therefore, plastic strains are occurred by the stress change inside of the yield surface. This leads to a doubt about the assumption of the yield function.

### Effects of quasi-overconsolidation

Before the undrained compression test, the consolidation settlement seems to continue almost infinitely under the sustained load as shown in Fig. 6. No method has been proposed to determine the appropriate time for the transition to the undrained shear test, though the undrained strength increases due to secondary compression.

Figs. 7 and 8 show that the undrained path is affected by the duration of quasi-over consolidation. The calculated undrained paths are approachable to the experimental results according to the value of constants  $\beta$  in Eq. (9). Therefore, it can be considered that the yield surface is also influenced by secondary compression during  $K_0$  consolidation.

The effective stress path traverses along the path  $A \Rightarrow B \Rightarrow C \Rightarrow D$  as shown in Fig. 9, if the lateral stress during  $K_0$  consolidation increases with secondary compression. This stress change is equivalent to a kind of quasi-over-consolidation because the vertical stress is kept constant. And after  $K_0$  consolidation the effective stress is located in the inside of the yield surface of Cam Clay.

It is clear that the undrained path is influenced by such stress history. It can be considered that there is a possibility of enlargement/deformation of the yield surface due to secondary compression.

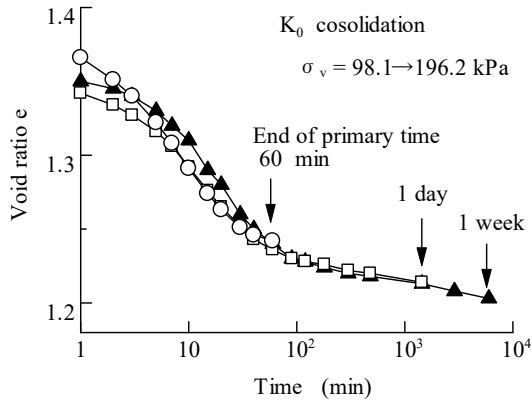


Fig.6 Consolidation time curves

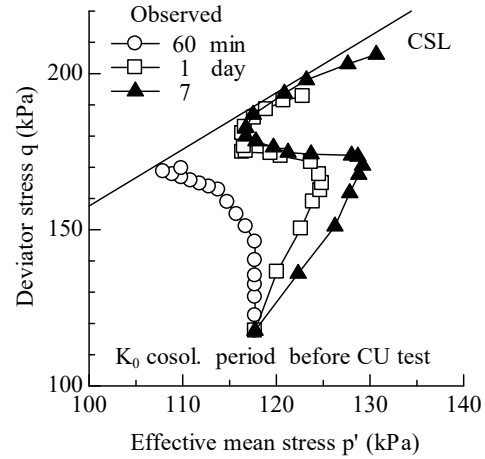


Fig.7 Observed undrained paths

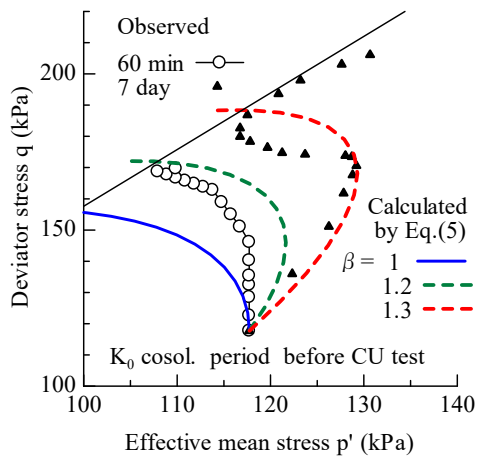
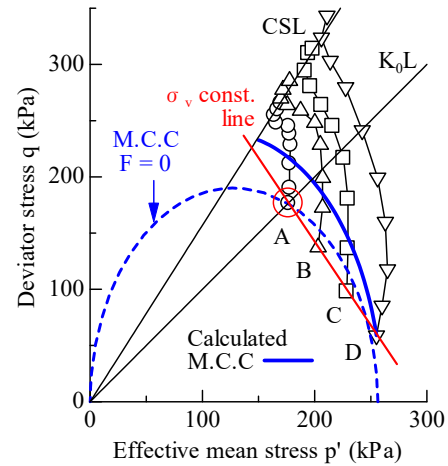

 Fig.8 Undrained paths calculated with different  $\beta$  values


Fig.9 Undrained paths and quasi-overconsolidation

### Undrained path in the extension side

Fig. 10 show the calculated and observed undrained paths in the triaxial compression and extension tests. The subscripts C and E in the figure for  $N$  and  $\beta$  mean compression and extension, respectively. As seen from these figures, the observed undrained path lies inside of the yield surface of Cam clay. The undrained path in the extension side should be located in a little bit outside of the yield surface as it can be known from the comparison between Eq. (3) and Eq. (8).

As the undrained path based on Eq. (9) depends on the constant  $\beta$  described in the figures. The constant  $\beta$  was varied so that the result of the calculation was close to the measured one. The undrained path on the compression side can be calculated close to the observed one though the calculation is greatly affected by the set value of the constant  $\beta$ .

### Void Ratio Change inside of the Yield Surface

Fig. 11 show the yield surface and the change of the void ratio caused by the loading and unloading along those stress paths ( $A \Rightarrow B \Rightarrow C$ ,  $B \Rightarrow D$ ,  $B \Rightarrow E$  and  $1 \Rightarrow 2 \Rightarrow 3 \Rightarrow 4$ ). If the stress at a point A in Fig. 11(a) lie on the yield surface and then is loaded beyond A to B, the clay will yield and cause the elastic and plastic strains corresponding to the normal consolidation line. The void ratio changes along the path  $A \Rightarrow B \Rightarrow C$  of Hitachi clay in Fig. 11(b) represent  $e$ -log  $p$  relation under  $K_0$  compression and swelling.

On the other hand, when a clay sample brought to B is subjected to unloading paths such as  $B \Rightarrow D$  and  $B \Rightarrow E$ , their paths have to cause purely elastic strain. The change of the void ratio due to the unloading path  $B \Rightarrow E$  must be zero. As the effective mean stress increment is equal zero ( $dp=0$ ) inside of the yield surface, the elastic strain increment must be zero. However, the experimental results of two clays in Fig. 11(b) show the reduction of the void ratio. If these reductions are caused by plastic strains, the loading path  $B \Rightarrow E$  must lie outside of the initial yield surface. For the loading path  $B \Rightarrow D$ , the change of the void

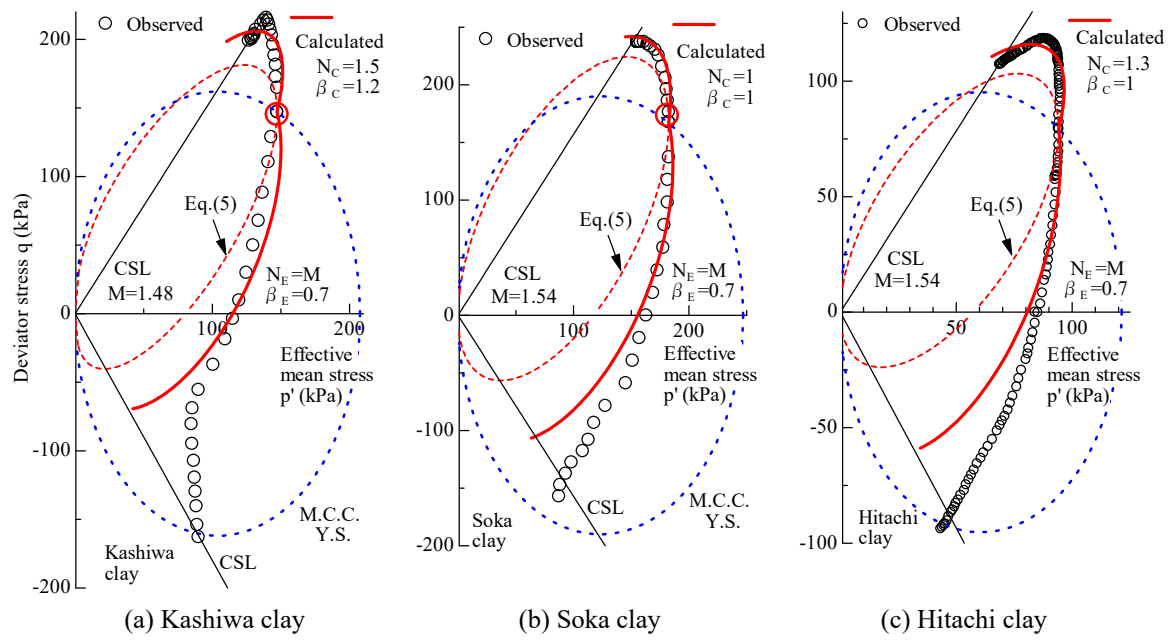


Fig.10 Yield function and undrained paths

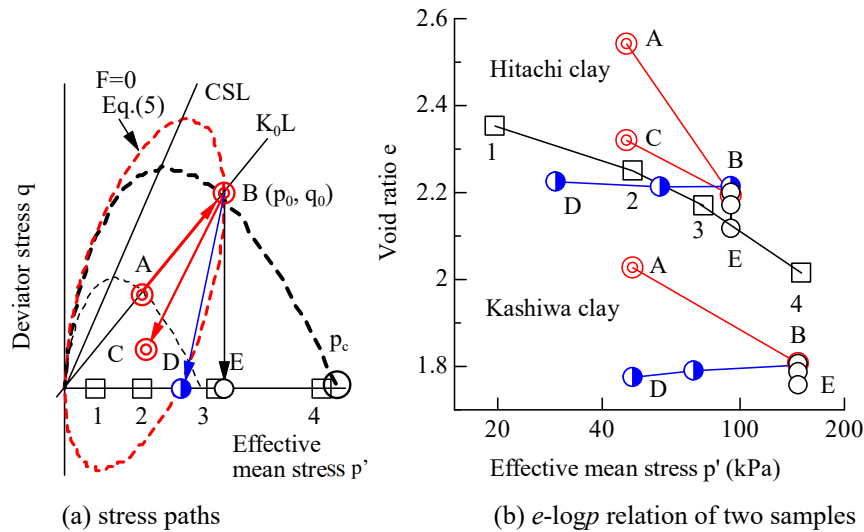


Fig.11 Stress paths and  $e$ - $\log p$  relation under  $K_0$  compression and swelling

ratio is very small. As the loading path  $B \Rightarrow D$  is located near the constant line of the past minimum principal effective stress, it can be considered to be equivalent to the yield surface.

The stress path such as  $1 \Rightarrow 2 \Rightarrow 3 \Rightarrow 4$  of Hitachi clay corresponds to the isotropic compression. The void ratio decreases rapidly when the mean stress exceeds the past maximum mean stress ( $p_0$ ). This means that the yield surface may cross the  $p$  axis on the left side of  $p_0$ .

These experimental results signify that the assumption for the yield function of Cam Clay is doubtful and does not define strictly the limit of the elastic behavior. It can be considered that there is a limit in ability of elasto plastic soil models.

## CONCLUSIONS

This paper presents a yield function exhibiting strain softening behavior for  $K_0$  normally consolidated clays and evaluates the simulative capability using the undrained and drained triaxial test results. Proposed yield function is equivalent to that of Modified Cam Clay if the constant  $N=M$  and the initial stress ratio  $\eta_0 (=q_0/p_0) = 0$  in the isotropic consolidated clay. The following conclusion can be drawn from the comparison of the calculated and observed triaxial test results.

1) The calculated undrained paths using an anisotropic yield function agree well with observed

ones of  $K_0$  normally consolidated clays. The strain softening behavior can be approximated by the proposed yield function if the degree of the strain softening is small.

2) Results of the consolidated drained triaxial test show that the plastic strains are occurred when the applied minimum principal stress exceeds the past maximum pressure. It has been shown by the experimental results that the yield surface for  $K_0$  consolidated clays is located near the constant line of the minimum principal effective stress.

3) The void ratio and volume of the clay decreased despite the unloading test into the yield surface of Cam Clay, which exhibits elastic behavior. This experimental result can emphasize that the stress change into the yield surface causes plastic strain in the clay, indicating that the existence of a yield planes is questionable.

## REFERENCES

- [1] Tschebotarioff, G.P., Soil Mechanics, Foundations and Earth Structures, McGraw Hill Book Company, Inc., 1951, 102-104.
- [2] A. Casagrande, The Determination of the Pre-Consolidation Load and Its Practical Significance, Proceedings of the 1st International Conference on Soil Mechanics, Harvard, Vol. 3, 1936.
- [3] Roscoe, K. H. and Burland, J. B., On the Generalized Stress-Strain Behavior of 'Wet' Clay, Engineering Plasticity, Cambridge Univ. Press, 1968, pp. 535-609.
- [4] Dafalias, F.Y., Manzari, M.T. and Akaishi, M., A Simple Anisotropic Clay Plasticity Model, Mechanical Research Communication, Vol.29, 2002, pp.241-245.

# FAILURE INITIATION AND MODES OF HOEK-BROWN ROCK MASSES SURROUNDING UNDERGROUND STORAGE WITH HIGH INTERNAL PRESSURE

Apiwish Thongraksa, Pornkasem Jongpradist\*

Construction Innovations and Future Infrastructures Research Center, Department of Civil Engineering, Faculty  
of Engineering, King Mongkut's University of Technology Thonburi, Bangkok 10140, Thailand \*

Corresponding author: [pornkasem.jon@kmutt.ac.th](mailto:pornkasem.jon@kmutt.ac.th)

## ABSTRACT

The critical issue for the design of highly pressurized caverns is the uplift failure. A reasonable evaluation of the failure path including the initial failure location and direction of the crack propagation is needed. A series of numerical analyses based on the finite element method was conducted in the framework of the 2D axisymmetric model by considering the variety of rock mass properties, cavern depth, and in-situ stress ratio. The wide range of the natural rock mass properties (rock strength) and initial stress conditions surrounding the cavern, which include in-situ stress ratio and depth of tunnel were considered in this investigation. To detect and distinguish the location of failure initiation and failure modes between tensile and shear failure, the tensile criterion and Hoek-Brown failure criterion are utilized, respectively. The numerical results indicated that the rock strength has a strong effect on the initial failure mode while the initial failure location strongly depends on the in-situ stress ratio and rock strength. The charts of failure mode and initial failure location were created by using the relationship between unconfined compressive strength and tensile strength of rock mass and initial stress condition, respectively.

*Keywords: Failure mode, Uplift failure pattern, Rock failure, High pressurized cavern.*

## INTRODUCTION

The large renewable energy storage with lined rock caverns (LRC) is becoming the popular alternative solution to provide stable energy sources of base load electricity [1]. When the power demand period is low, the high-pressure nature of air or gas is absorbed by the driving compressor with excess electric energy. The high-pressure air or gas is stored underground. During the peak period, the high-pressure air or gas can be released into the generator to generate electrical energy for supplying the increase in the power demand. With the high internal pressure storage and relatively small underground cavern depth, the stability of rock mass above the underground cavern can fail caused by the uplift, which is a critical issue that needs to be considered [2].

In the decade, many researchers have performed analyses to suggest a reasonable uplift failure pattern [3–6]. According to their study, the initial failure point along the cavern periphery depends on the in-situ stress ratio that can lead to the different uplift failure patterns [2,4]. However, the linear failure criterion model, Mohr-Coulomb, is mainly used in numerical analysis due to its simple form. To investigate the rock behavior with a wide range of stress, the nonlinear behavior is exhibited. Thus, the linear Mohr-Coulomb may present unrealistic behavior, which can affect the factor of safety during

the analysis.

To gain a better understanding of the failure behavior of rock and rock mass materials, intact rock is commonly chosen. Many failure criteria have been proposed to understand the rock behavior. The popular nonlinear failure model based on the Hoek-Brown (H-B) criterion [7] was developed. In recent years, the H-B criterion has been proved to be able to better describe the nonlinear rock mass behavior and is widely utilized in engineering practices [8], road cuts and cliff face stability analysis [9]. However, the H-B failure criterion was developed to capture only the shear failure mode. Generally, the rock mass can fail both tensile and shear failures [10], which may lead to different uplift failure path evaluations.

The failure behavior of rock mass around a pressurized cavern is investigated by considering the initial failure mode and location. A series of numerical analyses are conducted by taking to account the variety of rock mass properties, cavern depth, and in-situ stress ratio. The H-B criterion and tensile criterion are used to determine the rock failure. A conceptual guideline for predicting the failure mode of rock mass and the possible location of a failure initiation along the cavern periphery with considering the rock strength and initial stress state is established in this study.



## FAILURE MECHANISM

The failure mode of rock material, the tension or shear can be obtained. For tensile failure, when the value of tensile stress reaches the critical value of the material, the failure occurs. The simple equation can be written as

$$\sigma_1 - \sigma_T = 0 \quad (1)$$

When  $\sigma_1$  and  $\sigma_3$  are the major and minor principal stress, and  $\sigma_T$  is the tensile strength of the material (tension is positive).

For the shear failure criterion, the Hoek and Brown (H-B) model was developed. The general form of H-B failure criterion can be mathematically expressed in terms of the major and minor principal stress as

$$\sigma_{3HB} = \sigma_1 + (-m_i \sigma_c \sigma_1 + s \sigma_c^2)^{0.5} \quad (2)$$

The  $m_i$  and  $s$  are the constant value that depends on the properties of the rock mass. The unconfined compressive strength (UCS) of rock represents by the  $\sigma_c$  in the equation. For intact rock material,  $s = 1.0$ . The shear failure occurs when the stress state which is represented by the Mohr circle reaches the shear failure envelope determined by the H-B model as displayed in Fig. 1. The minor principal stress calculated from the H-B model in Eq. 2 ( $\sigma_{3HB}$ ) can be determined using the stress state and rock strength. According to Fig.1, the shear failure occurred under the condition of  $\sigma_{3HB}/\sigma_3$  equal to 1. The failure ratio used in this investigation can be expressed as

$$\frac{\sigma_{3HB}}{\sigma_3} = \frac{\sigma_1 + (-m_i \sigma_c \sigma_1 + s \sigma_c^2)^{0.5}}{\sigma_3} = 1.0 \quad (3)$$

## NUMERICAL ANALYSIS

### Problem Characteristic

In this investigation, the 2D axisymmetric problem is considered. The analytical model and loading condition are demonstrated in Fig. 2. The silo cavern has a diameter of 22.2 m. and 33.3 m in high. The depth of cavern storage is located at a depth in the range of 60 – 150 m. The bottom boundary was constrained in both lateral and vertical directions. Boundaries on both vertical sides were fixed in only one direction, which does not allow to move in the lateral direction. The properties of rock mass used in the numerical model can be divided into 2 groups including the control properties and varying properties. The unit weight of rock ( $\gamma$ ), Young's modulus ( $E$ ), and Poisson's ratio ( $\nu$ ) are fixed as shown in Table 1. Regarding the literature review, [11] collected the properties of rock mass of 28

different types of rock from many researchers. The range of the unconfined compressive strength and  $m$  value of rock exhibited in the range of 37.2 – 264.8 MPa and 3.2 – 54.6. Therefore, in the sensitivity analyses, the range of unconfined compressive strength of rock and the  $m$  value are considered between 1 to 300 MPa and 5 – 25, respectively. Moreover, the influencing factor that strongly affects the initial failure location as discussed in the work of [2], the in-situ stress ratio ( $k$ ) is taken into account in the range of 0.3 – 3.0.

### Procedures for Detection of Initial Failure

A series of stress analyses by using the continuum finite element program ABAQUS (2016) of the cavern under increasing internal pressure is performed to determine the failure initiation location. The analysis procedures can be divided into 3 steps from the initial to operation stages which are the generate the in-situ stress state, the silo cavern excavation, and applied the internal pressure to simulate the underground cavern storage state. The level of internal pressure increases until the deviator stress along the cavern storage achieves the shear failure criterion, the value of the maximum major principal stress and the location of maximum  $\sigma_1$  and minimum of  $\sigma_{3HB}/\sigma_3$  are captured.

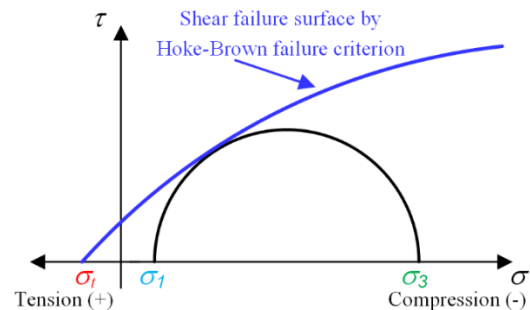


Fig. 1 Shear failure proposed by Hoek-Brown.

Table 1 Controlled rock properties

Quantity	Symbol	Value	Unit
Unit weight	$\gamma$	26	kN/m <sup>3</sup>
Young modulus	$E$	6.66	GPa
Poisson's ratio	$\nu$	0.2	-

### The Notion of the Failure Mode Identification

Due to the underground storage with internal pressure inside, the stress state in the rock mass surrounding the silo chamber gradually changes both principal and deviatoric stresses as the internal pressure increases. The stress along the cavern wall, radial stress, becomes compression while the stress in the perpendicular direction, tangential stress,

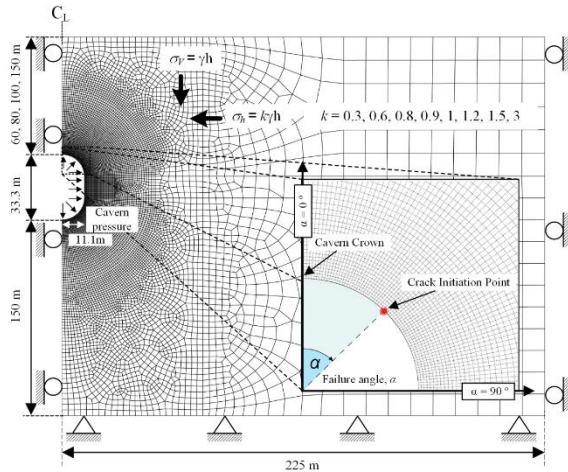


Fig.2 The loading and boundary conditions of the analytical model.

becomes tension as represented as  $\sigma_3$  and  $\sigma_1$ , respectively. Therefore, the radius of the Mohr circle increases with the increase of internal pressure. When the Mohr circle reaches the failure envelope surface which is determined by the H-B model of  $\sigma_{3HB}/\sigma_3 = 1.0$ , the shear failure occurred. If the tensile strength of rock mass is equal to the maximum major principal stress at  $\sigma_{3HB}/\sigma_3 = 1.0$ , the failure initiation occurs under shear and tension simultaneously. For rocks that have greater tensile strength, the shear failure mode can be obtained while the rock with a lower tensile strength than the value of  $\sigma_1$  at  $\sigma_{3HB}/\sigma_3 = 1.0$ , the failure initiation caused by tensile mode is induced.

## NUMERICAL RESULTS

### Influence of the Rock Properties on Initial Failure Mode for Underground Cavern Storage

The effect of the rock strength and types of rock mass, which are the ultimate compressive strength and types of rock, are described in this section. Fig. 3 presents the major principal stress distribution at shear failure occurs under operation state for various cases of ultimate compressive strength of rock. It can be noticed that the location of a minimum of  $\sigma_{3HB}/\sigma_3$  and maximum major principal stress are the same location for the example case, which is the case having the cavern depth of 60 m. and  $k$  of 1. With the rock having greater ultimate compressive strength, the required level of pressure inside the cavern storage ( $P_{cav}$ ) is increased. The location of the initial failure tends to move from cavern crown to cavern sidewall while the location of maximum  $\sigma_1$  and minimum  $\sigma_{3HB}/\sigma_3$  are still the same locations. If the ultimate tensile strength of rock is equal to maximum  $\sigma_1$ , the initial failure is induced under shear and tensile mode simultaneously. From the simulation results in

the case of cavern depth of 60 m. and  $k = 1$ , the data points which are the relationship between ultimate compressive strength and tensile strength under shear and tensile failure occurs simultaneously, are plotted as shown in Fig. 4. The further investigations were conducted to get a better understanding of the effect of rock strength by considering rock strength in compressive of 1 to 300 MPa and  $m$ -value of 5, 10, and 25. By collecting all the relationships between the unconfined compressive strength of rock and maximum major principal stress (indicated the tensile strength) at the shear and tensile failure occurs simultaneously in all analysis cases, the boundary line to distinguish the mode of failure can be obtained as shown in Fig. 5. According to the results, it can be seen that the influence of the rock mass strength has a strong effect on the initial failure mode. The rock with the relationship properties between shear and tensile strength locates above the boundary line, the tensile failure is dominated at the initial failure while

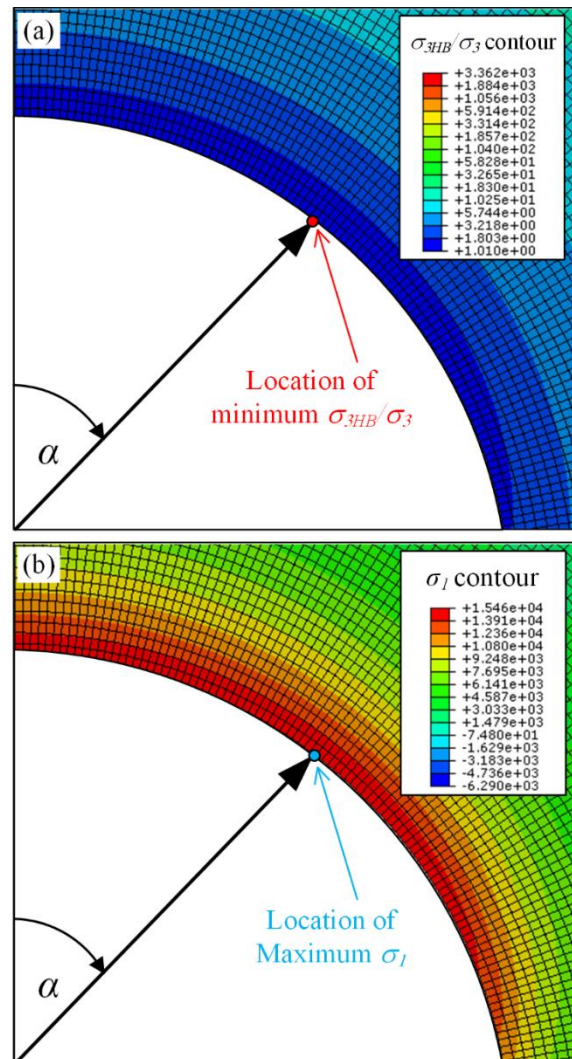


Fig. 3 The location of (a) the minimum value of  $\sigma_{3HB}/\sigma_3$  and (b) the maximum  $\sigma_1$  with internal pressure of 32.6 MPa.

the strength of rock mass both shear and tensile locate under the boundary line, the initial failure mode is governed by shear. To improve the reliability of the analysis results, the information on rock mass used in the physical model test for the underground storage cavern with high internal pressure was conducted by Thongraksa et al.[4] is plotted in the figure by considering the scaling factor. In their work, the triaxial tests were performed to determine the synthetic rock properties used for the experiment in the laboratory by reducing the scale by 200 times. By using the Hoek-Brown failure criterion to determine the shear failure envelope, the  $m$ -value and UCS can be calculated, which are equal to 17.78 and 43.95 kPa. In addition, it can be seen that the expected initial failure mode is a shear failure, which is shown a good agreement with the previous study. Therefore, the chart of initial failure mode with nonlinear criterion has been proven to predict the failure of rock mass in underground cavern storage with high pressure inside problem.

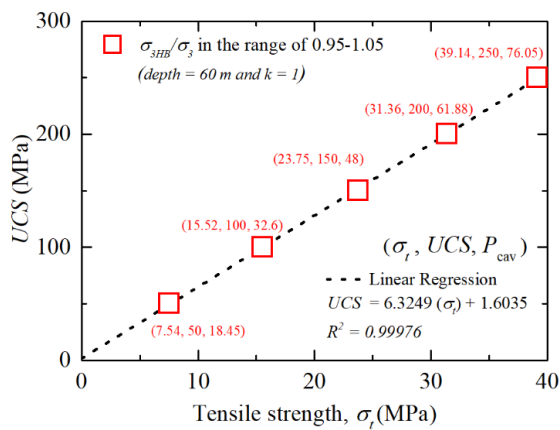


Fig. 4 The relationship between shear strength and tensile strength at both shear and tension occur simultaneously.

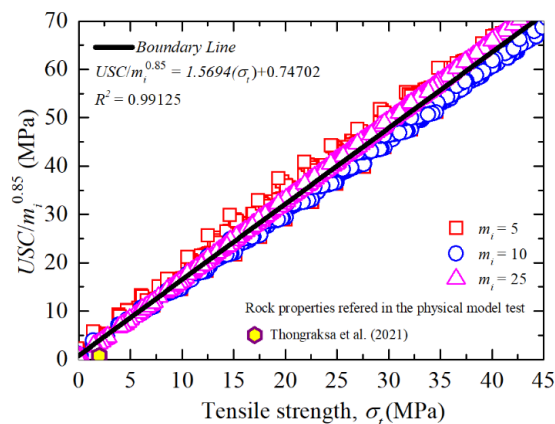


Fig. 5 The chart for classifying the initial failure mode.

## The Initial Failure Location Assessment of Underground High-Pressure Storage

To determine the initial failure location, the depth of the cavern, in-situ stress ratio, and rock strength are taken into account in the analysis. According to Fig. 4, it can be seen that with the rock strength increase the required cavern pressure increase. Fig. 6 shows the initial failure location in the case of cavern depth of 60 m and  $k$  of 0.3, 1, and 3, which represent the in-situ stress ratio of less and more than 1 and equal to 1 by varying the UCS in the range of 50 to 250 MPa. In the case of  $k$  less than 1, the initial failure occurs at the cavern roof while for the  $k$  larger than 1, the initial failure is located at the cavern sidewall. In case of  $k$  become unity, the initial failure location can be captured between cavern roof and sidewall which has a failure angle in the range of 30° and 40°. In addition, the required pressure level also increases with the rock having greater strength. It can be seen that the initial failure location depends on the rock mass strength. Similar results can be obtained in previous studies [4,12].

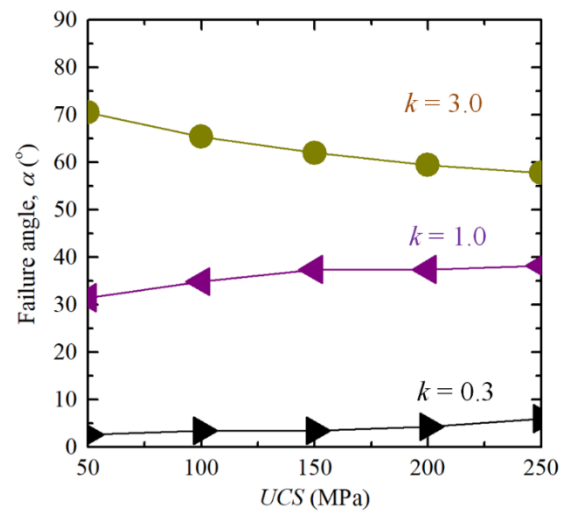


Fig. 6 The relationship between unconfined compressive strength (UCS) and failure angle ( $\alpha$ ) at depth of craven of 60 m.

To get a better understanding of the initial failure location of the rock, the in-situ stress in a range of 0.3 to 3.0 and the depth of the cavern in the range of 60 to 150 m. are chosen to perform the further investigation. The analysis data in the initial failure location are plotted in a radial space concerning the rock mass strength along the X-axis and Y-axis for tensile strength and shear strength, respectively, while the initial failure angle is exhibited on the radial axis as illustrated in Fig. 7. To eliminate the influence of cavern depth, both terms shear strength and tensile



strength are normalized by the vertical stress. From the results in Fig. 7, it is seen that the rock strengths have a strong effect on the initial failure location for cases with  $k$  in the range of 0.8 – 1 for the low rock strength. Moreover, for cases of  $k$  less than 0.8, the initial failure locations are located at the cavern roof while in cases of  $k$  larger than 1, the locations of initial failure occur at the cavern side wall. With increasing the rock strength, the location of the initial failure tends to approach the cavern shoulder which has a failure angle of approximately 40°. After all the influencing factors on the initial failure location are investigated, the uncomplicated chart for determining the initial failure location is proposed as demonstrated in Fig 8. By knowing the mode of failure from the chart of the mode of failure as presented in Fig 5, the expected failure location can start with the horizontal and vertical axis for the tensile failure and shear failure, respectively. Then, move in the circumferential direction to the line which represents the in-situ stress ratio, and determine the initial failure angle by moving in the radial direction to the value of the failure angle.

To validate the proposed chart, the scale-down model tests for the case of underground storage with internal pressure were conducted by Thongraksa et al.[4] are chosen. In their work, the initial failure occurred under shear failure both  $k$  of 1 and 3 with a depth of 40 m for full-scale. The initial failure angle for  $k$  of 1 and 3 are 45° and 75°, respectively. In Fig. 8, the failure initiation points for both cases are added to the chart by plotting the relationships between the term of shear strength and initial failure angle. In the case of  $k$  larger than 1, a good agreement between the physical model test and the proposed chart can be obtained. The small discrepancy between the failure angle captured in the experiment and the prediction chart is exhibited in the case of  $k$  equal to 1 because the failure angle is very sensitive to low rock strength for  $k$  become unity. It can be concluded that the proposed chart for determining the failure location shows reasonable agreement with the experimental.

## CONCLUSION

This investigation presents the initial failure behavior of rock mass surrounding the underground cavern storage with high internal pressure inside via the numerical analysis. The effect of the depth of cavern, in-situ stress ratio, and rock mass strength (ultimate compressive strength) on the initial failure and mode of failure by using nonlinear failure criterion, Hoke-Brown failure are conducted. The main finding of this investigation can be summarized as follows;

1. The initial failure mode strongly depends on

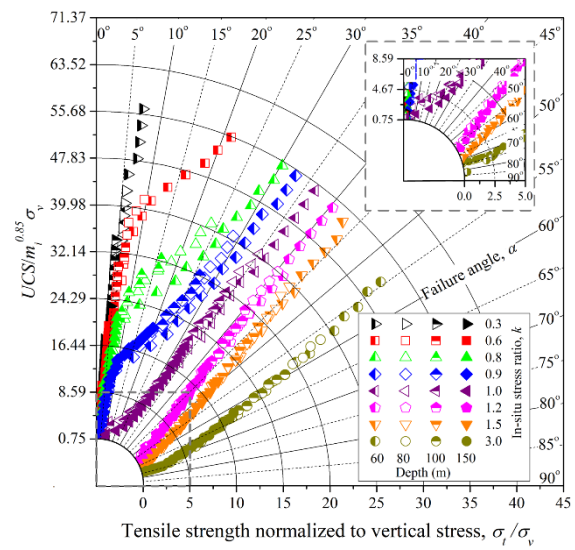


Fig. 7 Effect of the rock strength and stress state on the initial failure location.

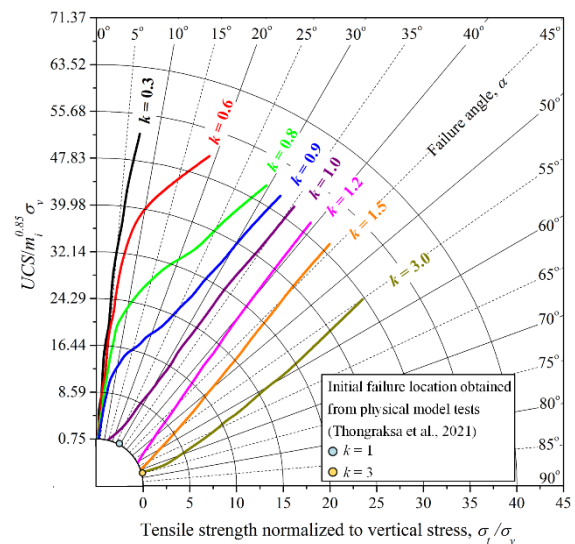


Fig. 8 Chart for predicting the location of initial failure, accounting for the rock mass strength, cavern depth, and in-situ stress ratio.

rock mass strength which is the relationship between shear strength and tensile strength. By considering the range of the natural rock properties in terms of rock strength between shear and tensile strength, the boundary line to separate tensile and shear failure modes can be obtained. The initial failure mode can be expected by knowing the rock mass strength.

2. The influencing factors consist of rock strength, depth of cavern, and initial in-situ stress ratio that have influenced the initial failure location. The depth of the cavern has a slight effect on the

initial failure point. In low rock strength, the in-situ stress ratio has a strong effect on the initial failure location. For high rock strength, the initial failure location seems to locate in the zone between the cavern roof and sidewall.

## ACKNOWLEDGMENT

This research work was supported by King Mongkut's University of Technology Thonburi (KMUTT) under The Petchra Pra Jom Klao scholarship contract No. 29/2558 and the financial support provided by the National Research Council of Thailand (NRCT) through grant No. NRCT5-RSA63006 and Thailand Science Research and Innovation (TSRI) under Fundamental Fund 2023 (Project: Advanced Construction Towards Thailand 4.0).

## REFERENCES

- [1] Salgi G., Lund H., System behaviour of compressed-air energy-storage in Denmark with a high penetration of renewable energy sources, *Appl. Energy*, Vol. 85, No. 4, 2008, pp. 182–189.
- [2] Tunsakul J., Jongpradist P., Kongkitkul W., Wonglert A., Youwai S., Investigation of failure behavior of continuous rock mass around cavern under high internal pressure, *Tunn. Undergr. Sp. Technol.*, Vol. 34, 2013, pp. 110–123.
- [3] Kim HM., Park D., Ryu DW., Song WK., Parametric sensitivity analysis of ground uplift above pressurized underground rock caverns, *Eng. Geol.*, Vol. 135-136, 2012, pp. 60–5.
- [4] Thongraksa A., Punya-in Y., Jongpradist P., Kim H-M, Jamsawang P. Failure behaviors of rock masses around highly pressurized cavern: Initiation and modes of failure. *Tunn. Undergr. Sp. Technol.*, Vol. 115, 2021, p. 104058.
- [5] Tunsakul J., Jongpradist P., Kim HM., Nanakorn P., Evaluation of rock fracture patterns based on the element-free Galerkin method for stability assessment of a highly pressurized gas storage cavern, *Acta. Geotech.*, Vol. 13, 2018, pp. 817–832.
- [6] Wang H-T., Liu P., Li S-C., Li X-J., Zhang X., Limit analysis of uplift failure mechanisms for a high-pressure gas storage tunnel in layered Hoek-Brown rock masses, *Eng. Fail. Anal.*, Vol. 138, 2022, p. 106274.
- [7] Hoek E., Brown E., *Underground excavations in rock* The Institution of Mining and Metallurgy, 1980.
- [8] Zhao J., Applicability of Mohr-Coulomb and Hoek-Brown strength criteria to the dynamic strength of brittle rock, *Int J. Rock Mech. Min. Sci.*, 2000;37:1115–21.
- [9] Lindsay P., Campbell RN., Fergusson DA., Gillard GR., Moore TA., Slope stability probability classification, Waikato Coal Measures, New Zealand. *Int. J. Coal. Geol.*, Vol. 45, 2001, pp. 127–45.
- [10] Paterson MS., Wong T., *Experimental rock deformation — the brittle field*, Springer, 2005.
- [11] He M., Zhang Z., Zheng J., Chen F., Li N., A New Perspective on the Constant  $m$  of the Hoek–Brown Failure Criterion and a New Model for Determining the Residual Strength of Rock, *Rock Mech. Rock Eng.*, Vol. 53, 2020, pp. 3953–3967.
- [12] Perazzelli P., Anagnostou G., Upper bound limit analysis of uplift failure in pressurized sealed rock tunnels, *Int J Numer Anal. Methods Geomech.*, Vol. 42, 2018, pp. 719–735.

## EVALUATION OF DISPLACEMENT AT GROUND SURFACE DURING GROUNDWATER RECOVERY

Sutasinee Intui<sup>1</sup>, Jittiphan Jindawutthiphan<sup>2</sup>, Apinya Rungrueang<sup>2</sup>, Choknimit Leelananthawong<sup>2</sup>,  
Thanapatsa Srisarn Trpkovski<sup>2</sup> and Kearkkeart Apischotecawankit<sup>2</sup> and Shinya Inazumi<sup>3</sup>

<sup>1</sup>Graduate School of Engineering and Science, Shibaura Institute of Technology, Japan;

<sup>2</sup>Faculty of Engineering, Bangkok Thonburi University, Thailand;

<sup>3</sup>College of Engineering, Shibaura Institute of Technology, Japan

### ABSTRACT

Chao Phraya River basin is located in the central area of Thailand which has a lot of land subsidence issues due to groundwater pumping. Following the recording data of Department of Groundwater Resources (DGR), the groundwater level change due to water pumping from 1960 until the present time. In 1997, DGR has issued law regulating the use of groundwater effect to the characteristic of groundwater level changing. Therefore, the characteristic of groundwater level changing was separated into two periods. First period, high groundwater pumping ratio led to rapidly decrease of groundwater level at about 27 meters from ground surface. After DGR issued the law, pumping ratio decrease and groundwater level was increase or recovery close to the ground surface. The groundwater level recovery had an effect to both settlement and rebound of ground surface. This study focuses on the evaluation and prediction of soil displacement during groundwater level recovery in the future based on Terzaghi's theory. The research area considers only zone D (10 to 14 meters soft clay thickness) in Bangkok clay area. The soil profile and the soil boring log were gathered from Department of Public Works and Town & Country Planning. This study research the displacement behavior of clay layer during groundwater level recovery. All data will be used to make a 3D soil profile and calculate to predict surface displacement in the future of soil layer. The results found that the settlement has rebound to ground surface every bored hole during the groundwater recovery.

*Keywords: Soil displacement, Bangkok clay, Groundwater recovery, Terzaghi's theory*

### INTRODUCTION

Before 1997, the groundwater level decrease continuously due to groundwater pumping in center part of Thailand. The high demand of groundwater pumping has affected to land subsidence especially in the soft soil area or center part of Thailand. After Department of groundwater resource issued the law to control the amount of groundwater pumping for industry, the groundwater level tends to increased or recovered to nearly ground surface. This is the interesting point to evaluate the soil surface displacement refer to the instrument data of some areas still settlement down and some areas occur lift up of soil surface or called rebound in this research. The soil displacement during groundwater level recovery has affect to the soil surface displacement in term of civil engineering structure issues such as road crack, building damage especially the old building which design at lowest the groundwater level.

The land subsidence is a global problem included Thailand. Many researchers try to analyze and explain the soil surface displacement behavior in soft soil area. Land subsidence occurs around the world in soft soil area. The reason depends on the usage of that area such as groundwater pumping, [2] and [3]. Jakarta city in Indonesia located on the lowest sea

water level. The groundwater is rapidly decrease during groundwater pumping. The land subsidence is continuously increase during that period. Thailand also occurs land subsidence due to groundwater pumping same as Jakarta. [4] showed the evaluation of soil surface displacement after groundwater pumping was controlled. After 1997 to present, both researches were predicted that the soil surface displacement at ground surface, has rebound by using ABAQUS software. The recovery ratio is approximately 0.26 to 0.32 centimeters per year [5] studied the soil surface behavior during groundwater recovery. In period of 1997 to 2037, the soil surface has rebound around 35 percentage of maximum displacement.

This research tries to evaluate the soil surface displacement during groundwater recovery or the behavior after 1997 in Thailand. The Bangkok clay have wide area along Chao Phraya River basin, central area of Thailand. Following the previous study, summarized the soft soil area follow by the soft clay thickness in each zone. So, this study chooses only zone D of soft soil thickness to consider the soil displacement in Soft clay and Stiff clay layer base on Terzaghi's theory of consolidation in both saturated soil and unsaturated soil.



## BANGKOK SOFT SOIL PROFILE

Bangkok soft soil area located along Chao Phraya River basin covering many provinces, Bangkok and urban area. In the past, this area has been the sea. The soil was deposited to be clay layer alternate with sand layer alternately. The subsoil layer consists of very soft clay to soft clay, very stiff to stiff clay, first sand, hard clay, second sand respectively. Department of Groundwater Resource (DRG), Department of Public Works and Town & Country Planning and many researchers have studied the characteristics of subsoil layer in Chao Phraya River basin area found that the subsoil layer have variance. However, overall soil layer still be the clay layer alternates with sand layer.

## GROUNDWATER LEVEL SITUATION

Characteristics of groundwater level situation in Bangkok area depends on the behavior of groundwater pumping. After 1997, groundwater level in Bangkok area tend to recover to ground surface after groundwater pumping was controlled. Following the Fig.1, showed the behavior of groundwater level and land subsidence during groundwater consumption changing [6]. The graph represented groundwater level increase from 1997 and tend to reach ground surface in the future. In contrast, Land subsidence still occurs and gradually stable after 2008.

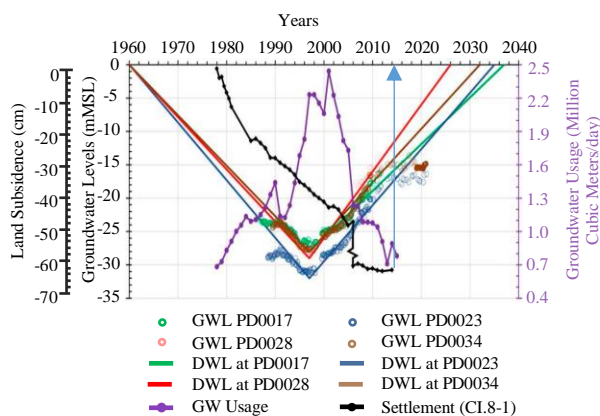


Fig. 1 Groundwater level change and land subsidence due to groundwater pumping

In present, DGR measures the groundwater level by using piezometer measurements. The groundwater level situation showed the groundwater level increasing ratio in each province in Table 1. All of the provinces that located along the Chao Phraya River

basin have groundwater level increasing ratio about 0.57 m/yr. to 2.74 m/yr.

## METHODOLOGY

This study focuses to collect the data of the soil boring log from Department of Public Works and Town & Country Planning to evaluate the displacement from each subsoil layer. The subsoil layer characteristic was compared and verified by the groundwater level data from Department of Groundwater Resource. All data was drawn and presented subsoil layer in 3D layout. The soil parameters from 3D layout were used to calculate the soil surface displacement during groundwater level change.

### Subsoil profile of zone D

Following the soft soil thickness of Bangkok clay as Fig. 2, Bangkok clay was separate to 6 zone with different colors [1]. Each zone was divided by the soft clay thickness. The dark red (F) area has soft clay layer thicker more than 18 m. The red (E) area has soft clay thickness from 14 m to 18 m. The yellow (D) area has soft clay thickness from 10 m to 14 m. The blue (C) area has soft clay thickness from 6 m to 10 m. The green (B) area has soft clay thickness from 3 m to 6 m and the grey (A) area has soft clay thickness less than 3 m. The red marks show the data from boring log by Department of Public Works and Town & Country Planning. The green marks show the investigated holes of DGR. The name of each hole show as Table 2. This study considers only zone D because this area is a developed area and have data to evaluate the behavior of soil surface displacement by using Terzaghi's theory of consolidation by conducting the data from Department of Groundwater Resource and Department of Public Works and Town & Country Planning [7]. Finally, the calculation results will be used to evaluate in other areas.

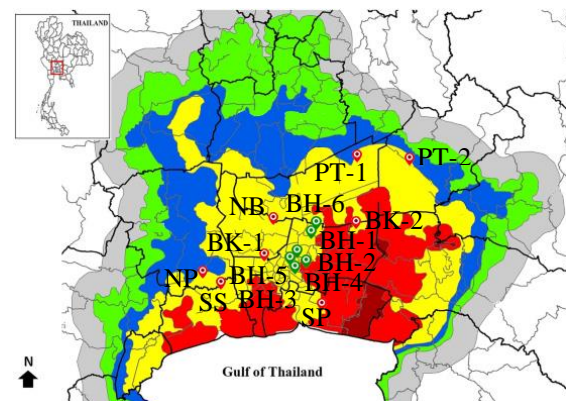


Fig. 2 Location of the studied hole (Modified [1])

Table 1 Groundwater level situation each hole

Province	Groundwater Level Recovery Rate (2009)		
	Elevation (m)	Minimum Rate (m/yr)	Maximum Rate (m/yr)
Bangkok	32.86	0.57	2.74
Samutprakan	29.47	1.07	2.45
Pathumthani	19.3	0.48	2.41
Nonthaburi	12.7	0.27	1.06
Ayutthaya	16.3	0.61	1.23
Nakhonpathom	19.18	0.60	1.59
Samutsakhon	32.75	1.94	2.34

Table 2 Location of the marks on the map

Name	Description
NP	NahonPathom
SS	SamutSakhon
BK-1	Bangkok (Taling Chan)
BK-2	Bangkok (Klong Sam Wa)
NB	Nonthaburi
SP	SamutPrakon
PT-1	PathumThani (KlongLuang)
PT-2	PathumThani(Thanya)
BH-1	Chatuchak Park
BH-2	Lumphini Park
BH-3	Suea Pa Park
BH-4	Rommaninath Park
BH-5	Rajamangala University
BH-6	Kasetsart University

Table 3 Soil parameters for calculation

Soil layers	Soil parameters	Description	Bored holes							
			NP	SS	NB	BK-1	BK-2	SP	PT-1	PT-2
Very soft to Medium Clay (2m. to 13m.)	W <sub>n</sub> (%)	Water content	52	38	88	69	72	62	78	65
	LL (%)	Liquid Limit	41	43	87	64	48	46	50	38
	PL (%)	Plastic Limit	23	25	67	27	25	37	25	20
	$\gamma_t$ (t/m <sup>3</sup> )	Total density	1.70	1.84	1.50	1.59	1.58	1.64	1.55	1.62
	e <sub>o</sub>	Initial void ratio	1.40	1.03	2.37	1.86	1.94	1.67	2.10	1.75
Stiff to Very stiff clay (13m. to 25m.)	W <sub>n</sub> (%)	Water content	19	17	-	22	37	34	25	25
	LL (%)	Liquid Limit	31	35	-	51	50	51	60	40
	PL (%)	Plastic Limit	18	17	-	2.06	1.85	1.88	2.01	2.01
	$\gamma_t$ (t/m <sup>3</sup> )	Total density	2.12	2.16	-	2.06	1.85	1.88	2.01	2.01
	e <sub>o</sub>	Initial void ratio	0.51	0.46	-	0.59	0.99	0.92	0.68	0.68

## Soil parameters

The soil parameters in this research were adopted from the boring log data of 8 bore holes which located in zone D. Soil parameters such as water content, liquid limit, plastic limit, total density, undrained shear strength and standard penetration test (SPT) were gathered from each bore hole. Initial void ratio was calculated by using phase relationship equation from bore hole parameters. The soil parameters and thickness of soil layer were calibrated with the data from DGR. This study chooses 8 bore holes to evaluate the soil surface displacement. The soil parameters of each soil layer shown in Table 3. Some parameters cannot be interpreted by using only boring log data. So, many parameters were adopted from previous studies such as the soil specific gravity equal to 2.7 [6], over consolidation ratio (OCR) [8], effective stress parameter as matric of suction coefficient ( $\chi$ ) [9] by referred from soil parameters from previous study [10].

## Theoretical calculation

The soil surface displacement calculation is very important to evaluate stability of building in each period of time. This study tries to simplify the equation to evaluate the soil surface displacement during groundwater level change based on timing of DGR during groundwater level increase. Consolidation settlement equation calculate in case of over-consolidation clay because the maximum vertical effective stress is more than the final vertical effective stress, as in Eq. (1). Many parameters were calculated such as the recompression index  $C_r$ , the initial void ratio  $e_o$ , the maximum vertical effective stress  $\sigma'_{vm}$ , the final vertical effective stress  $\sigma'_{vf}$

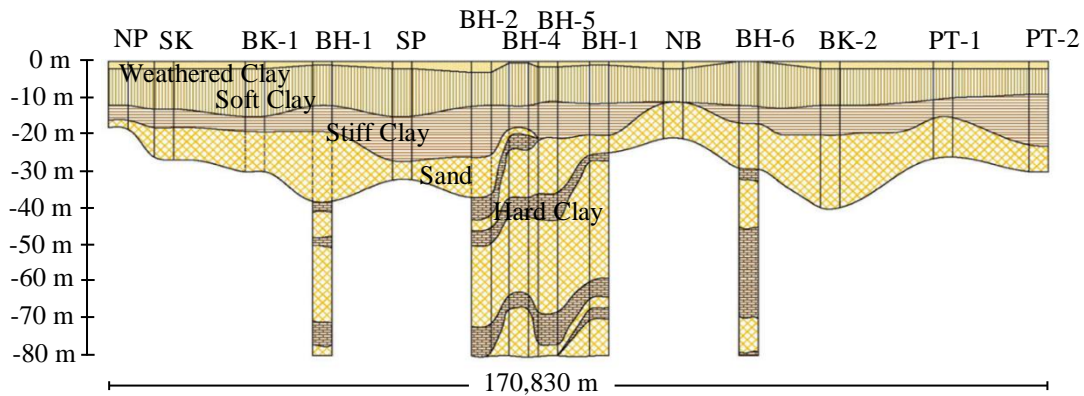


Fig. 3 Soil profile layout of zone D

and the thickness of soil or drainage path. High groundwater level was considered as a saturated soil refer to Eq. )2( based on Terzaghi theory )11[ and low groundwater level was considered as an unsaturated soil refer to Eq. )3( following the expression of Bishop equation )12]. The total vertical effective stress ) $\sigma$ (, an effective stress parameter ) $s$ (, pore-air pressure ) $u_a$ (, pore water pressure ) $u_w$ ( and suction ) $S$ ( as in Eq. )4(.

$$\Delta H = \frac{c_r}{1+e_o} \log \frac{\sigma'_{vf}}{\sigma'_{vm}} H_o \quad (1)$$

$$\sigma' = \sigma - u_w \quad (2)$$

$$\sigma' = [(\sigma - u_a) + \chi(u_a - u_w)] ; 1 > \chi > 0 \quad (3)$$

$$S = \frac{u_a - u_w}{u_a} \quad (4)$$

## RESULTS AND DISCUSSIONS

This part shows the results of soil surface displacement after estimation and interpretation of the soil parameters, soil profile and groundwater level recovery.

### 3D soil profile

The 8 bored holes was located on the zone D, yellow area. All bored holes are distributed around the area for evaluate the soil parameters and soil profiles. The soil layers were specified from soil parameters in boring log data. The data in boring log is not enough to determine the soil layer. So, some parameter such as  $C_c$  and  $C_r$  were adopted from the previous research and DGR data, [13] – [17]. The data in this research were adopted only the value which has the R square more than 0.9. Then, this study drew the 2D soil profile by the AutoCAD software as the Fig. 3 and drew the 3D layout by 3ds Max software.

The variation of each soil layer was interpreted from soil boring log that verified by DGR. (BH-1 to BH-6) again. After verification of 2D soil profile, the 3D soil profile was prepared as shown in Fig. 4 to Fig. 6. This study has considered only upper 3 subsoil layers which have affected to groundwater level change covering the area of 1334 square meters. All of soil profile found that each soil layer has different soil thickness. So, this is the gap to evaluate the surface settlement in the future.

### Soil surface displacement

This study focuses on the soil surface displacement of the soft Bangkok clay and stiff to very stiff clay by using theoretical calculation. This result shows the total displacement at ground surface and displacement ratio during groundwater increase or recovery to ground surface. The methodology of theoretical calculation was considered the time period of DGR.

So, this study estimates the total displacement every 5 meters of groundwater level increase. It represents the groundwater level equal to -25 m. in 2001 then groundwater level increase to ground surface in 2032. The 8 bored holes have similar total displacement trend and displacement ratio from 2001 to 2032 as in Table 4. The Fig.7 show the relationship between the total displacement and time of all bored hole in zone D. There is the rebound displacement trend due to groundwater recovery. In the same study area, the results of this study have the characteristic of soil surface behavior similar to other results such as the measurement of DGR have displacement ratio equal to 0.25 cm/yr., the results of the ABAQUS software have the rebound ratio from 1997 to 2016 equal to 0.26 to 0.32 cm/yr. And the result of PLAXIS2D evaluate the soil displacement ratio equal to 0.35 cm/yr. from 1997 to 2037. By the way, the result of this study was evaluated by using the

prediction of groundwater level from previous studies. In present, no one know that when the groundwater level will increase to ground surface and how about the soil surface displacement during groundwater rise up. So, this research tries to simplify the calculation method. Therefore, the results from simplified theoretical calculation can be conducted to evaluate or predict soil surface displacement due to groundwater recovery in the future.

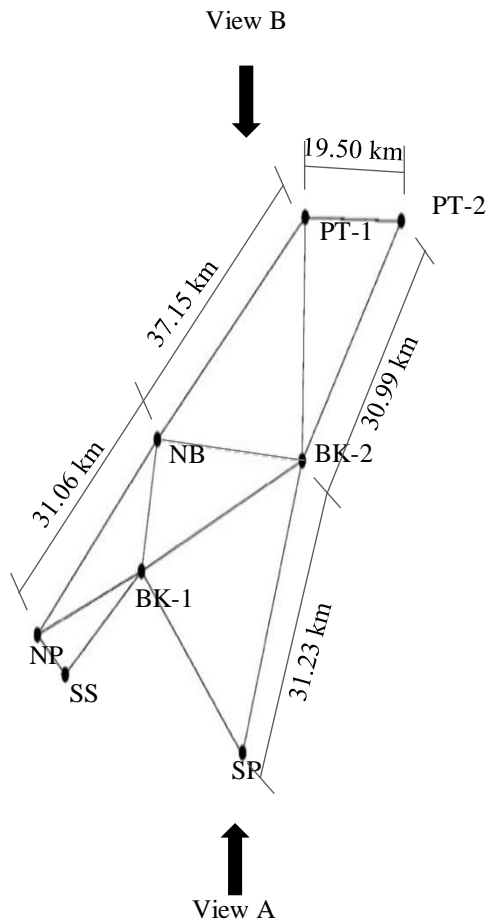


Fig. 4 Soil profile layout of zone D

Table 4 Total displacement and displacement ratio

Bored hole	Total displacement (cm)		Displacement Rate (cm/year)
	At 2001	At 2032	
NP	-9.07	-17.68	-0.28
SS	-7.29	-13.64	-0.20
BK1	-12.30	-23.50	-0.36
BK2	-17.41	-33.31	-0.51
NB	-18.92	-35.03	-0.52
SP	-17.05	-28.52	-0.37
PT1	-12.63	-25.90	-0.43
PT2	-11.48	-20.44	-0.29

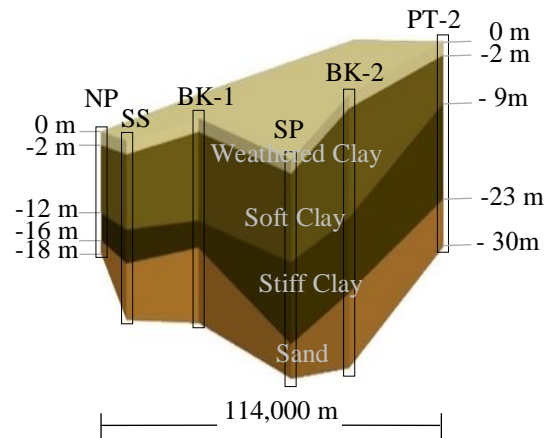


Fig. 5 3D of view A

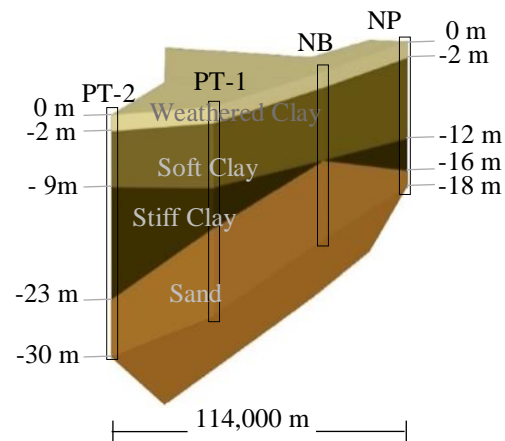


Fig. 6 3D of view B

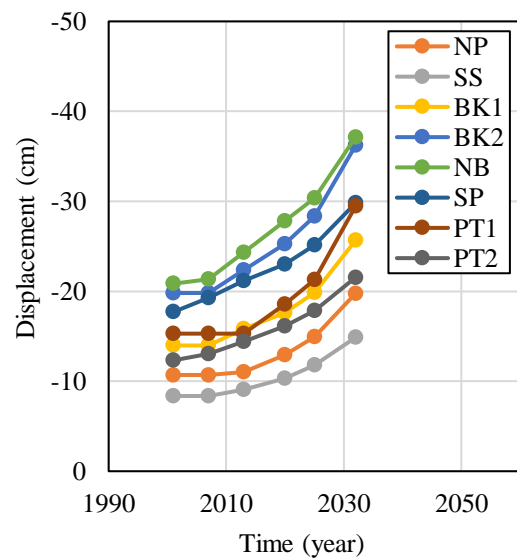


Fig. 7 Displacement of each bored hole

## CONCLUSIONS

This study summarizes the subsoil layer characteristic and soil properties to evaluate the soil surface displacement during groundwater level changing. The results were calculated base on the Terzaghi's theory of consolidation. This research tries to simplified the soil layer characteristic and other data from Department of Public Works and Town & Country Planning and Department of Groundwater Resource (DGR). The results of this study were separated in to two parts. The first part is simplified the subsoil layers of zone D. The soil schematics have verified by the subsoil data of DGR. The second part is evaluation of soil surface displacement during groundwater level recovery by theoretical calculation. The soil surface displacement has rebound to ground surface every bored hole was considered. All result of this calculation shows that the soil surface displacement characteristic trend similar to the previous studies which evaluation by another software such as ABAQUS and PLAXIS2D.

## ACKNOWLEDGMENTS

All authors would like to thank Department of Groundwater Resource to support the instrument data and Department of Public Works and Town & Country Planning to support the soil boring log data. That is the necessary data to help this research to get the result to evaluate the soil surface displacement.

## REFERENCES

- [1] Amornkul C., Engineering Subsoil Database of Lower Central Plain, Thailand, Master of Engineering, 2010, pp. 3-161.
- [2] Intachai K., Assessment on pile capacity in view of Effects of groundwater drawdown and rebound Associated with deep well pumping in Bangkok, Asian Institute of Technology, 2018.
- [3] Phien-Wej N., Giao P.H., and Nutalaya P., Land Subsidence in Bangkok, Thailand., *Geology*, Vol. 82(4), 2006, pp. 187–201.
- [4] Saowiang K., and Giao P. H., Numerical analysis of subsurface deformation induced by groundwater level changes in the Bangkok aquifer system, *Acta Geotechnica*, 2021, pp. 1265–1279.
- [5] Phoban H., Seeboonruang U., and Lueprasert P., Numerical Modeling of Single Pile Behaviors Due to Groundwater Level Rising, *Appl. Sci.*, 2021.
- [6] Department of Groundwater Resources., The study of the effect of underground structures due to the recovery of water pressure in the groundwater layer in Bangkok and its vicinity, Ministry of Natural Resources and Environment, 2012, pp. 17-62.
- [7] Department of Public Works and Town & Country Planning, Soil GIS DPT, [online], Available from: <http://soilgis.dpt.go.th/login.php>, 2020, April.
- [8] Giao P. H., Paveechana T., and Saowiang K., Consolidation Settlement Analysis with Reference to Groundwater Recovery in The Bangkok Multi-Aquifer System, *Advances in Geotechnical Infrastructure*, 2013, pp. 567-573.
- [9] Zhou A.N., Sheng D., Scott W. Sloan., and Gens A., Interpretation of unsaturated soil behavior in the stress – Saturation space, I: Volume change and water retention behavior, *Computers and Geotechnics* 43, 2012, pp. 178–187.
- [10] Surarak C., Likitlersuang S., Wanatowski D., Balasubramaniam A., Oh E., and Guan H., Stiffness and strength parameters for hardening soil model of soft and stiff Bangkok clays, *The Japanese Geotechnical Society*, 2012.
- [11] Terzaghi K., The shearing resistance of saturated soils and the angle between the planes of shear, in *The First International Conference on Soil Mechanics and Foundation Engineering*, A. Casagrande, P. C. Rutledge, and J. D. Watson, Eds., 1936, pp. 54–56.
- [12] Bishop A. W., The principle of effective stress. *Teknisk Ukeblad* 106(39), 1959, pp. 859–863.
- [13] Adikari, G.S.N., Statistical Evaluations of Strength and Deformation Characteristics of Bangkok Clays, MSc Thesis, Asian Institute of Technology, Bangkok, Thailand, 1977.
- [14] Suthamnatpong S., Engineering Properties and Behaviour of Bangkok Clay Soils, M.Eng. Thesis Chulalongkorn University, 1977.
- [15] Tsai, C.Y., A Monograph on the Engineering Properties of Bangkok Subsoils. M.Eng. Thesis, Asian Institute of Technology, Bangkok, 1982.
- [16] Kusuwan K., Statistical Evaluation of Engineering Properties of Bangkok Subsoil, Chulalongkorn University, 1988.
- [17] Chuenwattana R., Evaluation of engineering properties of soft Bangkok clay, M.Thesis, Kasetsart university, 2002.

## A BASIC STUDY ON ESTIMATING PARTICLE-SIZE DISTRIBUTION BY AUGER EXCAVATION SOUND USING MACHINE LEARNING

Keito Endo<sup>1</sup>, Taizo Kobayashi<sup>2</sup> and Ryoichi Fukagawa<sup>2</sup>

<sup>1</sup> Graduate School of Science and Engineering, Ritsumeikan University Graduate school, Japan;

<sup>2</sup> College of Science and Engineering, Ritsumeikan University, Japan

### ABSTRACT

The construction industry is due for a digital renovation. This paper have focused on ground excavation technology using screw drills, thereby, developing a technology that can evaluate geotechnical properties and classification in real time using AI based on sound generated around the tip of the drill. In this paper, as a fundamental study, the mass ratio of beads of each particle sizes was estimated from excavation sound of a model ground mixed with artificial beads of different particle sizes. First, we prepared a model ground involving alumina beads in a circular container and drilled it using an auger with a microphone built into the tip and compared the excavation sound waveforms and FFT results for each grain size. Second, we estimated the mass ratio of beads of each grain size in the model ground using AI from the excavation sound of the model ground mixed with beads of different grain sizes, showing the feasibility of grain size distribution from excavation sound.

*Keywords: Particle-size distribution, Machine learning, Excavation, Auger, FFT*

### INTRODUCTION

In recent years, digital technology has been developed in construction business, and technology using various types information of construction has been developed, such as to evaluate strata from the electric current of the drive unit during auger excavation [1] and to measure ground stiffness and soil density from acceleration of vibratory roller under compaction [2].

We are developing a technology for ground excavation with auger drill, that evaluate soil properties and strata in real time using AI based on excavation sound generated by the tip of the auger drill. There have been studies on using sound and vibration for geotechnical investigations, such as soil classification by the sound of friction between the screw point and soil particles during SWS test (screw weight penetration test) [3] and assessment of soil on the sound of cutting prosses by boring machine [4]. However, modeling approach to determining the relationship between sound and vibration characteristics (explanatory variables) and particle size distribution (objective variable) is difficult and has not put into practical use. On the other hand, because AI derives the correlation between explanatory variables and objective variables, there is a possibility to realize measuring particle size distribution without the process of modeling. In this paper, as a feasibility study, laboratory experiments using a small excavation machine were conducted to measure particle size distribution by auger excavation sound.

### EXAMINATION OF EXCAVATION SOUND USING MODEL EXPERIMENT WITH ALUMINA BEADS

In this study, we performed excavation experiments using artificial beads (alumina beads) as a simulated soil because of their easily managed grain size. We prepared a model ground filled with three types of beads of different particle sizes ( $D = 1, 3$ , and  $5$  mm) in a cylindrical container. The model ground was 120 mm in inside diameter and 100 mm in height (Fig. 1). We created a 3D(three dimensions)-printed auger made of plastic (material: PLA (Poly-Lactic Acid)) (shaft diameter: 20 mm, blade width: 20 mm), which has a small microphone built into its tip to record sounds generated near the auger tip during excavation (Fig. 2). The excavation conditions were set at a excavation speed of 5 mm/s and a rotation speed of 0.5 r.p.s., that means 30 r.p.m., and the sound

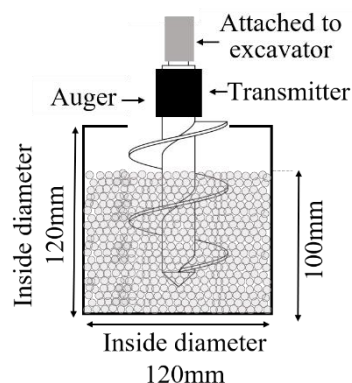


Fig. 1 Specimen



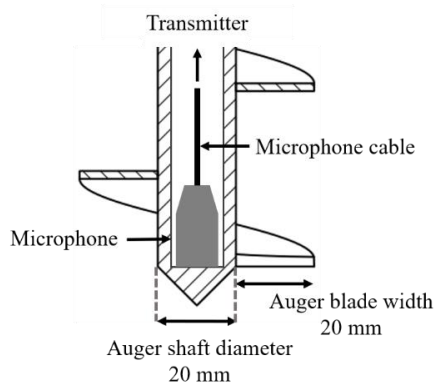


Fig. 2 Cross section of auger tip

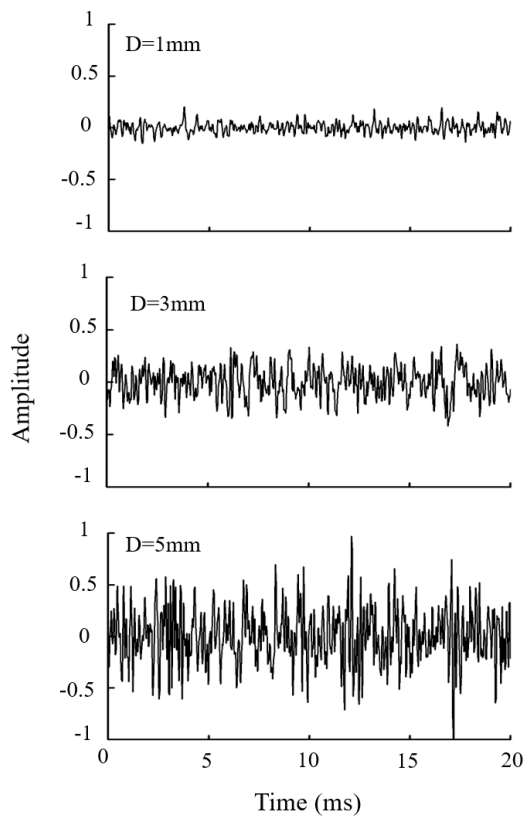


Fig. 3 Sound wave

was recorded for 10 s from the time the auger tip reached a depth of 80 mm (sampling frequency: 48 kHz).

Fig. 3 and Fig. 4 show the sound signal, when beads of each grain size were excavated, and amplitude spectra obtained by FFT analysis. The larger grain size, the larger sound signal and the different frequency characteristics.

### ESTIMATION OF MASS MIXING RATIO OF BEADS USING MACHINE LEARNING

In this section, the mass mix ratio of artificial beads of each grain size is estimated using AI from the excavation sound of a model ground mixed with

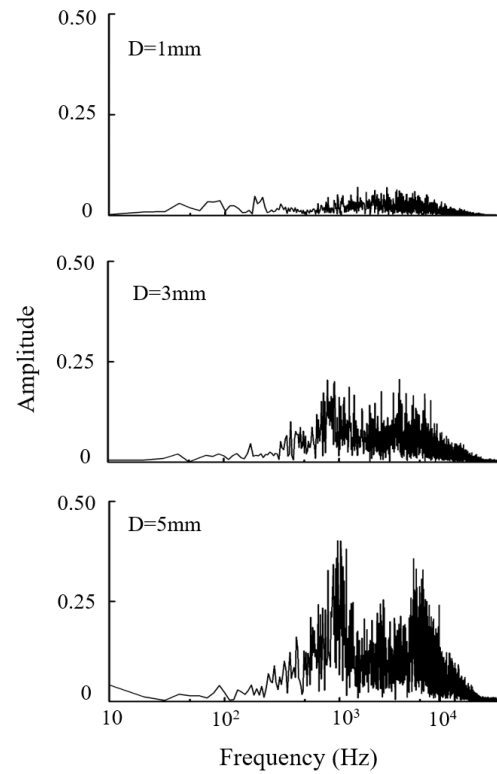


Fig. 4 FFT analysis

Table 1 Mass ratio of beads of each grain size in the model ground

No	mass content by percentage (%)		
	1mm	3mm	5mm
1	100	0	0
2	0	100	0
3	0	0	100
4	75	25	0
5	75	0	25
6	50	50	0
7	50	25	25
8	50	0	50
9	25	75	0
10	25	50	25
11	25	25	50
12	25	0	75
13	0	75	25
14	0	50	50
15	0	25	75

different grain size beads. A total of 15 model ground patterns with different mass mix ratios were prepared using alumina beads of different grain sizes ( $D = 1, 3$ , and  $5$  mm). The mass mix ratios of the model grounds prepared are shown in Table-1. The excavation conditions were the same as in the section2.

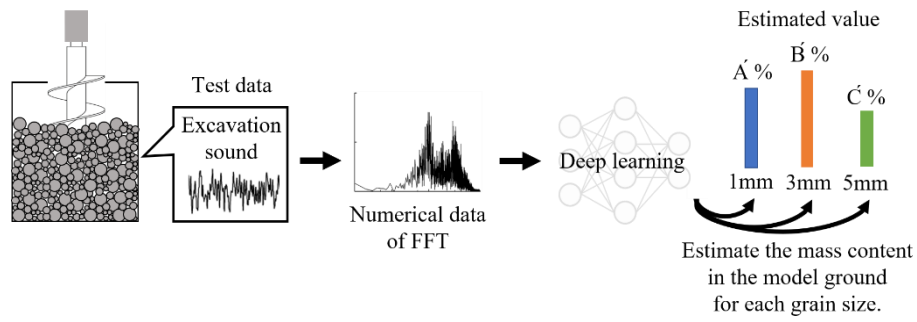


Fig. 5 Flow chart of estimation

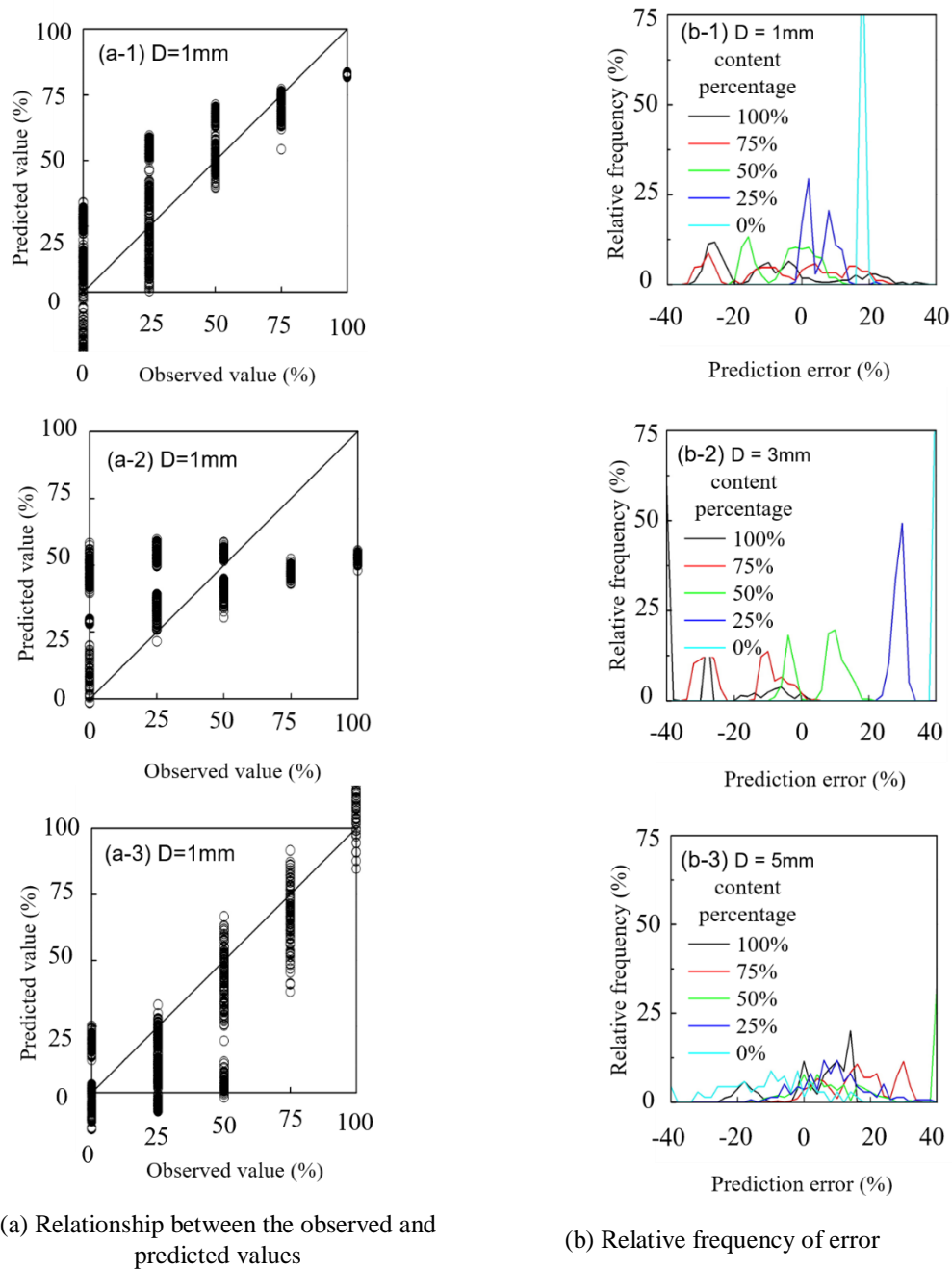
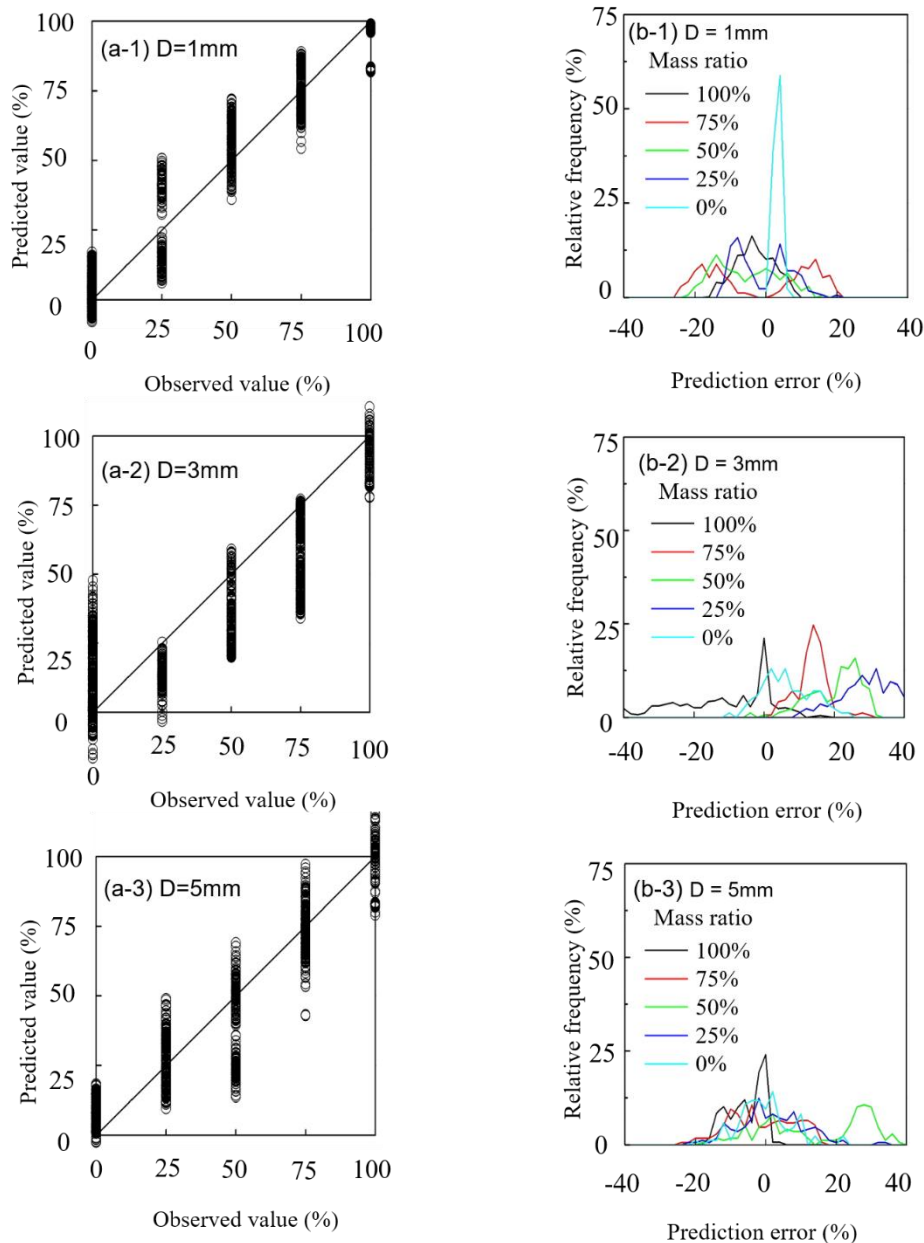


Fig. 6 Estimation results from FFT numerical data  
(Training data: Excavation sound of a single grain size)

### Develop An AI Model Based on Time History Numerical Data

We focused on FFT to extract grain size features from sound and developed a one-dimensional convolutional neural network (1D CNN) that regressively estimates the mass ratio of each bead ( $D = 1, 3, \text{ and } 5 \text{ mm}$ ) that makes up the ground given FFT-processed numerical data from the recorded excavation sound (Fig. 5). First, we provided training data involving excavation sounds of three model soils

with a single grain size: (100:0:0), (0:100:0), and (0:0:100). A time data of 11 s obtained during one drilling cycle was shifted every 12.5 ms and separated by 100 ms to create 800 training data (total number of training data: 800 data \* 3 model soils = 2400 data). For the validation data, we used the drilling sound from the mixed-model ground. To maintain the ratio of training data to validation data at 8:2–7:2 (training data: validation data), 68 data points were prepared for each type of model ground (number of test data: 68 data points, 15 types of model ground = 1020 data).



(a) Relationship between the observed and predicted values

(b) Relative frequency of error

Fig. 7 Estimation results from FFT numerical data  
(Training data: Excavation sound of single grain size and 3types mixed grain size )

Additionally, for test data, 50 data points were used for each type of model ground (training data: validation data: test data = 2400:1020:750).

When we input the test data into the constructed learning model, the outputs were the beads mass ratio for  $D = 1, 3$ , and  $5$  mm. Fig. 6 shows the relationship between the predicted and observed values of the mass ratio for each grain size output for the 750 test data and the frequency distribution of the prediction error (correct value (%) – prediction value (%)) for each

mass content of grain size (correct value). From Fig. 6(a), it can be observed that there is no positive correlation for the grain size of  $3$  mm and that the estimated values for other grain sizes also exhibit large errors.

Next, to improve the accuracy of the machine learning estimation, we input the excavation sounds of the mixed model ground into the training data in addition to the excavation sounds of the single grain size model ground. The excavation sounds added to

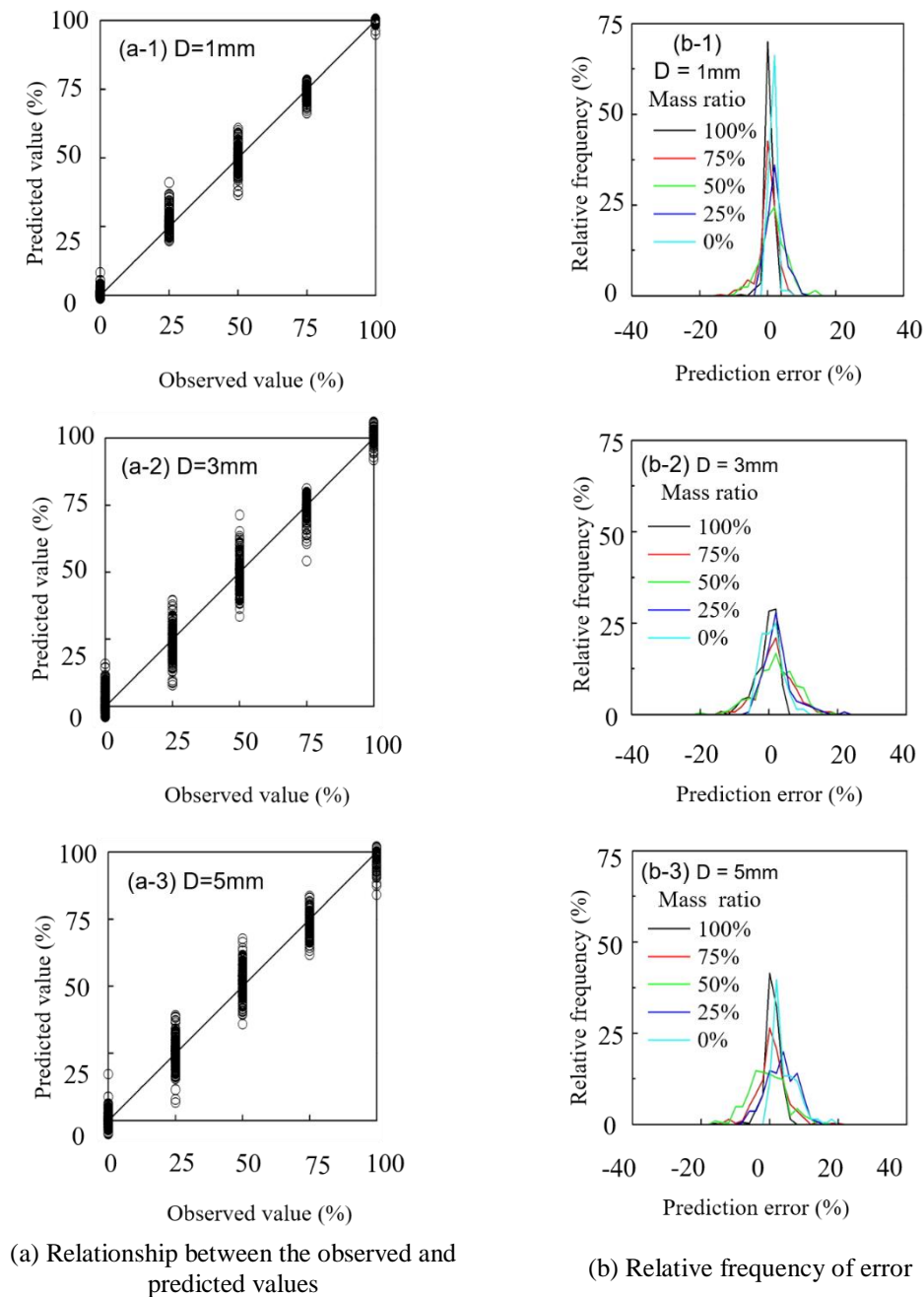


Fig. 8 Estimation results from sound numerical data  
(Training data: Excavation sound of a single grain size)

the training data were (50:25:25), (25:50:25), and (25:25:50) bead mass ratios (%) with  $D = 1, 3$ , and  $5$  mm. We selected these three model grounds as training data because all three types of beads with different grain sizes were present in these three types of model grounds. The numbers of training data and validation data were the same as in the previous training condition (number of training data:2376, number of validation data:1020). The estimation results are shown in Fig. 7. As shown in the figure, there was a positive correlation for all grain sizes, and the errors were smaller. However, as shown in Figure 7(b), the estimation accuracy is not sufficient, with errors of about 30% for some mass mixing ratios.

### Develop An AI Model Based on Time History Numerical Data

In this section, the unprocessed waveform data recorded as the teacher data for this study is used to estimate the mass ratio of beads of each particle size. The excavation sound sources used in the previous section were used to develop the AI model. We also used data from a single grain-size ground model as the training data. The estimation results of the training model are shown in Fig. 8. Fig. 8(b) shows that the error is within 20%, indicating that the estimation accuracy has improved compared to the FFT results (corresponding to a maximum 95% confidence interval of 6.0 %). Interestingly, the ratio of each grain size bead in the mixed model can be estimated by learning the excavation sound of a single grain size model ground.

### CONCLUSION

In this study, we estimated the bead mass ratio of each particle size in the model ground from excavation sound of a model ground filled with alumina beads of different particle sizes using machine learning. The main conclusions are as follows.

- (1) First, we compared the waveform data and FFT results from the drilling beads of different grain sizes. Consequently, we confirmed the difference in the sound pressure and frequency response according to the grain size.
- (2) We constructed a learning model using FFT-processed numerical data of the recorded excavation sounds as input values. The learning model using a single grain size model for training data demonstrated low estimation accuracy; however, when the number of excavation sound types used for training data was increased, the estimation accuracy was improved.
- (3) Finally, we have built a AI model using the excavation sound of a single grain size model ground as the training data and the excavation sound data as the input values, which gave the best estimation accuracy.

### REFERENCES

- [1] Japan Federation of Construction Contractors and Concrete Pile and Pole Industrial Technology Association, *Kui no sekoukanri niokeru sizisoutoutatsu no kakunin-nhouhou*, pp. 4-13, 2017.
- [2] FUJIYAMA, T and TATEYAMA, K, The evaluation of compacting ground stiffness by the acceleration of vibratory roller, *Japan society of civil engineers*, No. 652, pp. 115-123, 2000.
- [3] Yukihiro TSUKADA, Noriaki AOYAMA and Tadayoshi YAMAKI, Study of a soil assessment method based on sounds generated by rotary sounding, *Japan Society of Civil Engineers*, No.638, pp.1-10, 1999.
- [4] Noriaki SAKO, Shuichi SHIMOMURA, Masashi KAWAMURA, Hiroyoshi SHIOKAWA, and Shouta KATAOKA, Soil classification method using screw point-soil fricative sound by swedish weight sounding. *J. Struct. Constr. Eng. AIJ*, Vol. 83, No743, pp.111-121, 2018.

## MODEL TESTS ON CONCRETE BLOCKS SINKING INTO SEABED GROUND WITH UPWARD SEEPAGE FLOW GENERATED

Tatsuya Matsuda<sup>1</sup>, Kinya Miura<sup>1</sup>, Naoto Naito<sup>1</sup> and Yuki Ando<sup>1</sup>

<sup>1</sup>Department of Architecture and Civil Engineering, Toyohashi University of Technology, Japan

### ABSTRACT

Under stormy weather condition structures on shore and offshore have been severely damaged by heavy sea wave loading. Many researchers have conducted investigations on the damaged structures and revealed that the damage of the structures is emphasized by the disintegration of the seabed, caused by sea wave loading on the seafloor. The study has conducted model sea wave loading tests on sand ground and revealed that the disintegration of seabed and associated scouring are caused by the upward seepage flow as a response to sea wave loading, which reduces the effective stress in the seabed. The breakwaters which consist of concrete blocks have been monitored for years, and as a result it is reported that they are sinking every year by a fraction of a meter in accordance with stormy wave condition. This study conducted a series of model tests on a block which is equipped with three-axial accelerometer to detect its attitude and is rested on the seabed with upward seepage flow generated. The sinking behavior of the block in the seabed during the gradual increase in hydraulic gradient of seepage flow was carefully observed to clarify the fundamental mechanism of the sinking of the block. Consequently, this study found that the critical condition of the hydraulic gradient under which the sinking of the block is initiated is rather independent of the density of seabed material. In the scheme of the model tests the applicability of the three-axis accelerometer to the detection of the block even under the critical hydraulic gradient attained was demonstrated.

*Keywords: Model Test, Upward Seepage flow, Seabed, Concrete Block, Bearing Capacity*

### INTRODUCTION

Under stormy weather condition structures on shore and offshore have been severely damaged by heavy sea wave loading. The breakwaters which consist of concrete blocks have been monitored for years, and as a result it is reported that they are sinking every year by a fraction of a meter in accordance with stormy wave condition. Many researchers have conducted investigations on the damaged structures and revealed that the damage of the structures is emphasized by the disintegration of seabed, caused by sea wave loading on the seabed [1].

The fluctuation of effective stress in the seabed is caused by the upward and downward seepage flow during cyclic sea wave loading. This mechanism has been studied theoretically or experimentally. For example, Yamamoto et al. (1978) [2] has shown the analytical solution that effective stress response in seabed induced ocean wave. Miura et al. (2004) [3] qualitatively examined the relationship between the effective stress response of the seabed ground and sediment transport in response to progressive, steady and irregular waves. Zen and Yamazaki (1990) [4] have shown clarify to mechanism of the wave-induced liquefaction and densification in permeable seabed using model tests. They also showed that the heavy structures may submerge into the seabed and light-weight structures may rise up from the seabed.

Baldock and Holme (1998) [5] discussed the effects of seepage on sediment transport by waves

and currents. The results showed that upward seepage increased wave-induced erosion, while downward seepage stabilized bottom sediments. Matsuda et al. (2019) [6] have conducted model sea wave loading tests on sand ground and revealed that the disintegration of seabed and associated scouring are caused by the upward seepage flow as a response to sea wave loading, which reduces the effective stress in the seabed. The wave response of rectangular blocks on a sandy substrate was also examined. Accelerometers installed on the blocks showed that the blocks on the sandy bottom tended to tilt offshore under the action of the waves. However, it became necessary to discuss in more detail the response of blocks on sand-bed subjected to wave-induced seepage forces.

In this study, a series of model tests were conducted for clarify to behavior a block on seabed that is acting an upward seepage flow. To clarify the fundamental mechanism of block settling, the behavior of the block settling into the seafloor as the hydrodynamic gradient of the seepage flow gradually increased was carefully observed using the sensors for acceleration and displacement.

### INTRODUCTION OF MODEL TESTS

#### Experimental and Measurement Device

Fig. 1 shows a schematic diagram of the one-dimensional seepage experimental apparatus system.



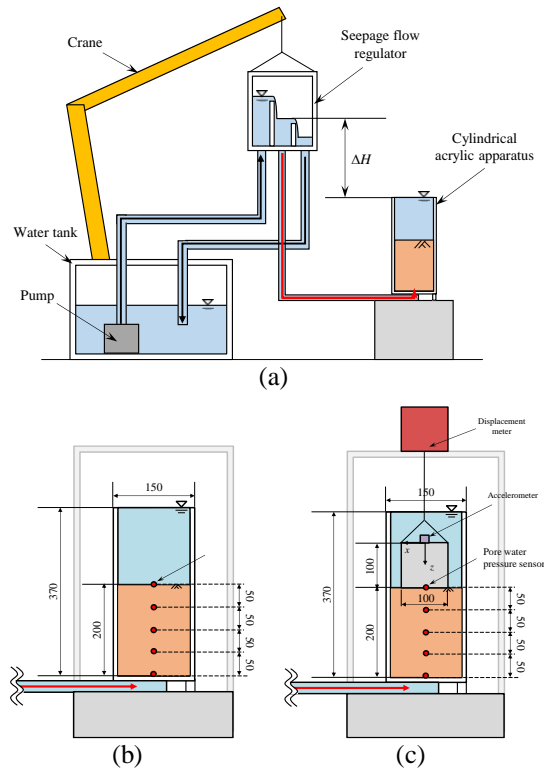


Fig. 1 Schematic of experimental apparatus system (a): Case of ground only condition (b) and Case of rectangular block placed on the Ground condition (c)

Table 1 Physical properties of geomaterials

Properties	Toyoura sand	Silica #8
$D_{50}$ (mm)	0.189	0.109
$e_{\max}$	0.999	1.218
$e_{\min}$	0.632	0.670
$G_s$	2.668	2.681

In this tests, a cylindrical acrylic apparatus with a height of 370 mm and a diameter of 150 mm was used. A drainage valve is installed at the bottom of the apparatus, which is connected to the seepage flow regulator by a hose. The seepage flow regulator is equipped with a drainage weir so that the water level is always maintained at a constant level in the device. The height of the apparatus was adjusted by a crane to change the water level difference  $\Delta H$  between the apparatus and the experimental apparatus. In all experiments, a 200 mm thick layer of soil was prepared to achieve a given density. For measure the pore water pressure in the ground, five sensors of pore water pressure were installed in the soil at on the interior wall of the apparatus at intervals of 50 mm from the bottom of the apparatus. In addition, a three-axis accelerometer and a displacement transducer were installed in the center of the top of the block to measure the behavior of the block.

Table 2 Experimental cases

Cases	Geomaterial	Relative density, $D_r$ (%)	Block
Case-T40	Toyoura sand	40	None
Case-T70	Toyoura sand	70	None
Case-S40	Silica sand #8	40	None
Case-S70	Silica sand #8	70	None
Case-T40B	Toyoura sand	40	Exist
Case-T70B	Toyoura sand	70	Exist
Case-S40B	Silica sand #8	40	Exist
Case-S70B	Silica sand #8	70	Exist

## Experimental Conditions

Toyoura sand and silica sand No. 8 (hereinafter referred to as silica sand #8) were used as the geomaterials in this test. Table 1 shows the properties of the soil materials. The ground was deposited by the underwater dropping method using a specified amount of soil measured to obtain target relative densities of  $D_r = 40\%$  and  $70\%$ . In the tests, two cases were considered: a ground only case with no blocks and a case with rectangular blocks placed on the ground surface. Table 2 shows the experimental conditions for each case. The rectangular block used was a cube 100 mm long, 100 mm wide, and 100 mm high, weighing 2.2 kg.

## External Conditions

The loading conditions for the seepage force were the same for all experimental cases. The seepage flow regulator was kept stationary with a zero-water level difference for up to 60 s after the start of the experiment, after which the seepage flow regulator was raised at a rate of 0.05 mm/s and the seepage force was applied. Thereafter, while maintaining the critical dynamic hydraulic gradient, the seepage force was applied until the ground collapsed in the case of the ground only and until 1200 s in the case of the rectangular block.

## EXPERIMENTAL RESULTS

### Case of Soil Ground Only

This section discusses the seepage failure phenomenon of the ground in the absence of blocks. Fig. 2 shows the time histories of the excess pore water pressure for each case. The pore water pressure sensor at  $z = 0.02$  m, the lowest point of the ground, is lower than the increment of pore water pressure caused by the difference in hydraulic head. This is due to the influence of the boundary. The same trend

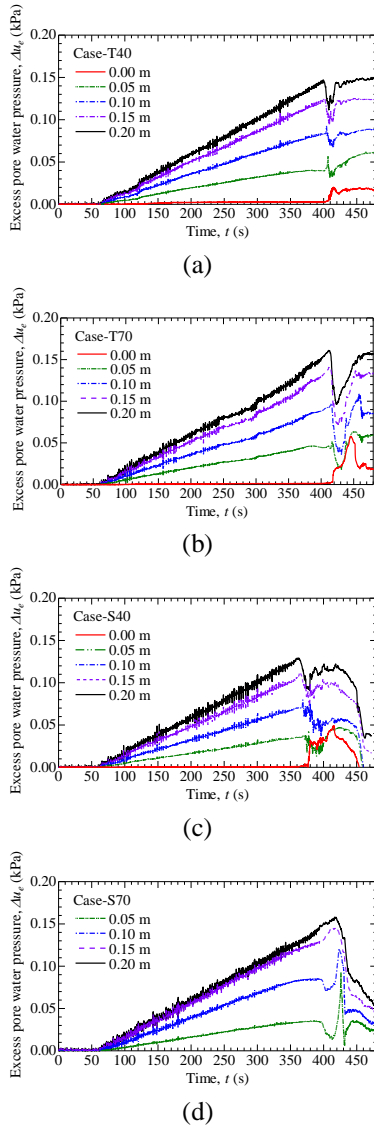


Fig. 2 Time histories of excess pore water pressure in case of soil ground only: Case-T40 (a); Case-T70 (b); Case-S40(c) and Case-S70

was observed in all cases. In Case S70, the pore water pressure at  $z = 0.00$  m at the ground surface could not be measured accurately. Therefore, the following hydrodynamic gradient values are calculated using the measured values at  $z = 0.05$  m and  $0.15$  m, where the values are stable, in order to consider spatial variations in the ground. The hydraulic gradient  $i$  and critical hydraulic gradient  $i_{cr}$  are calculated by the following equations;

$$i = \frac{(\Delta u_e|_{z=0.15} - \Delta u_e|_{z=0.05}) / \gamma_w}{0.15 - 0.05} \quad (1)$$

$$i_{cr} = \frac{G_s - 1}{1 + e} \quad (2)$$

here,  $\Delta u_e$  is excess pore water pressure,  $\gamma_w$  is unit

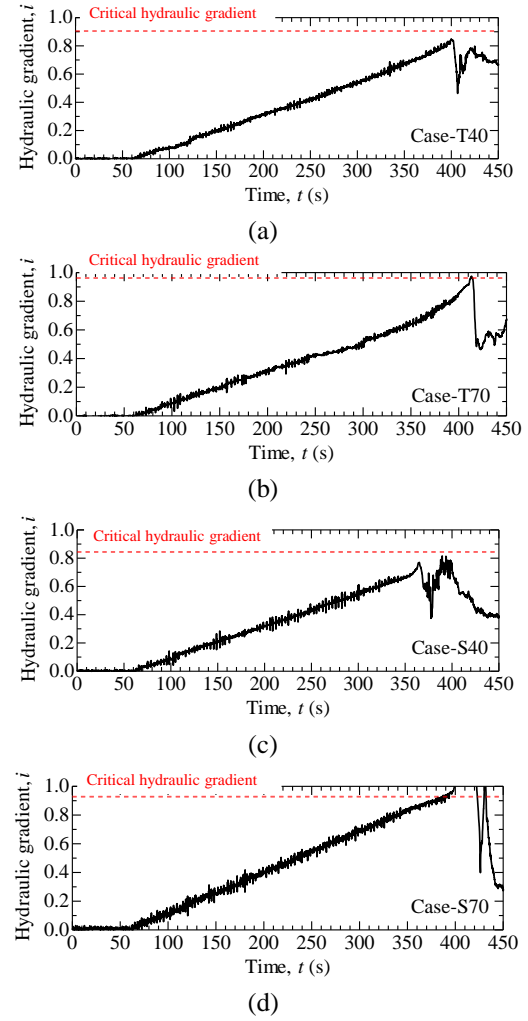


Fig. 3 Time histories of hydraulic gradient in case of soil ground only: Case-T40 (a); Case-T70 (b); Case-S40(c) and Case-S70

weight of water,  $G_s$  is specific gravity weight of soil particle, and  $e$  is void ratio, respectively.

Fig. 3 shows the change of hydraulic gradient in the ground over time. Hydraulic gradient was no differentiated depending on the geomaterials, but it was differences around the critical hydraulic gradient with the soil density. For example, in the loose ground of 40 % relative density, the hydraulic gradient changed significantly when it reached about 90% of the critical hydraulic gradient (Fig. 2(a) and (c)). On the other hand, in the case of the middle dense ground of 70 % relative density, the hydraulic gradient changed after the critical hydraulic gradient was reached (Fig. 2(b) and (d)). In both cases, there was no significant difference in the hydraulic gradient depending on the geomaterials, suggesting that the seepage failure occurred when the hydraulic gradient value changed significantly.

Fig. 4 shows the ground conditions at initial condition ( $t = 0$  s), in the region where the hydraulic

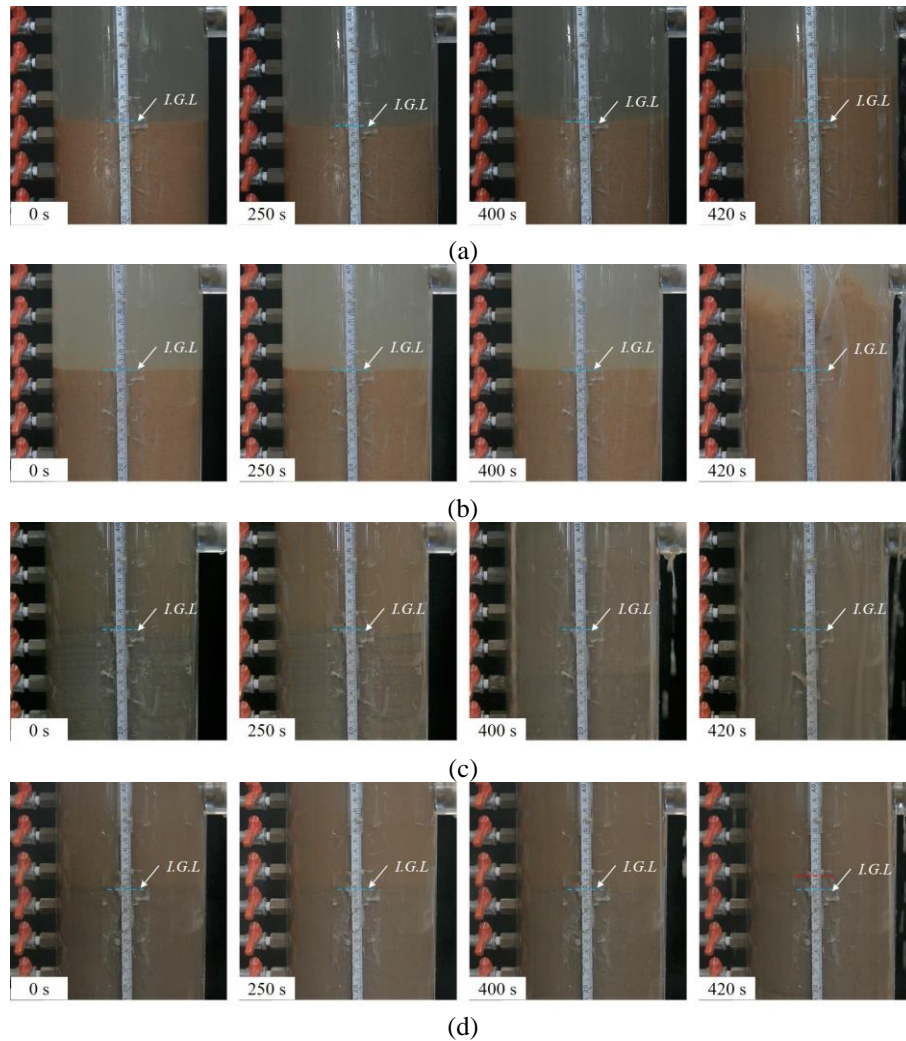


Fig. 4 Time histories of soil ground change due to upward seepage flow in case of soil ground only: Case-T40 (a); Case-T70 (b); Case-S40(c) and Case-S70

gradient reached 0.5 ( $t = 250$  s), and the near the critical hydraulic gradient at  $t = 400$  s and 420 s, respectively. The ground elevation was no changed at a hydraulic gradient of 0.5 in each case. Although the location of the ground surface cannot be determined because Case S40 failed at 400 s. In the other cases, no change from the initial ground surface was observed. In Case T40, Case T70, and Case S70, where the hydraulic gradient changed significantly near the critical hydraulic gradient and failure occurred with boiling. This suggests that the deformation of the ground when seepage forces cause seepage failure is not gradual, but rather occurs rapidly when the critical hydrodynamic gradient is reached. This is consistent with the experimental results of Yoshimi et al. (1973) [7].

#### Case of Rectangular Block Placed on the Ground

This section investigates the behavior of the ground and blocks subjected to seepage forces. Fig. 5

shows the time histories of the hydraulic gradient in the ground, the amount of settlement of the block measured by the displacement meter, and the tilt angle of a block from the initial state, which is calculated from the change in the acceleration sensor in each case. Fig. 6 shows the changes in the block conditions and sand surface level due to upward seepage flow for each case at 300 s (around hydraulic gradient  $i = 0.5$ ), 420 s (around the critical hydraulic gradient  $i_{cr}$ ), and 1,200 s (at the end of the test).

The hydraulic gradient in the ground increased as the hydraulic head difference increased in each case, and reached the critical hydraulic gradient at a given time (approximately 420 s). The critical hydraulic gradient is the same as the hydraulic gradient in the ground only, and does not take into account the effect of the over-load due to the blocks. After the critical hydraulic gradient was reached, the hydraulic head difference was kept constant, but seepage failure did not occur as in the soil-only case. The reason for this

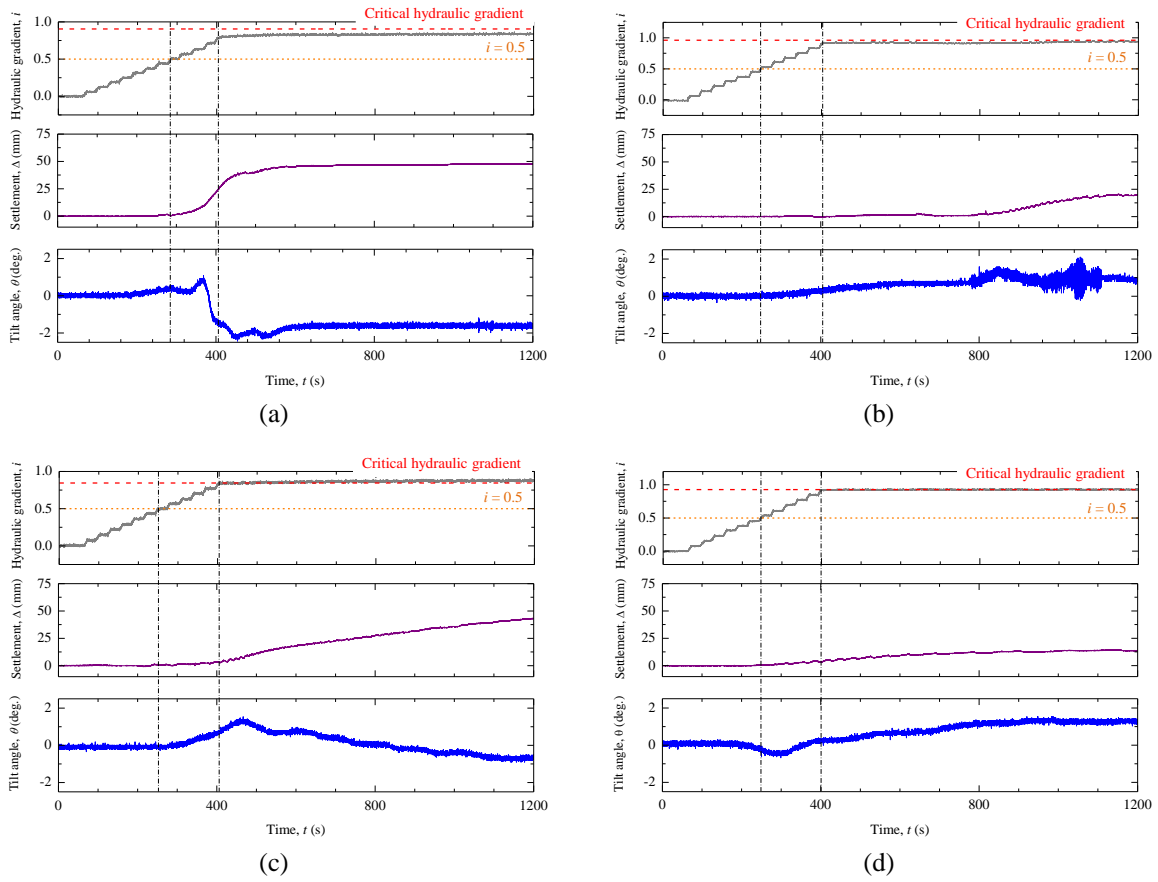


Fig. 5 Time histories of the hydraulic gradient in the ground (top), the amount of settlement of the block (middle), and the tilt angle of a block (low): Case-T40B (a); Case-T70B (b); Case-S40B (c) and Case-S70B (d)

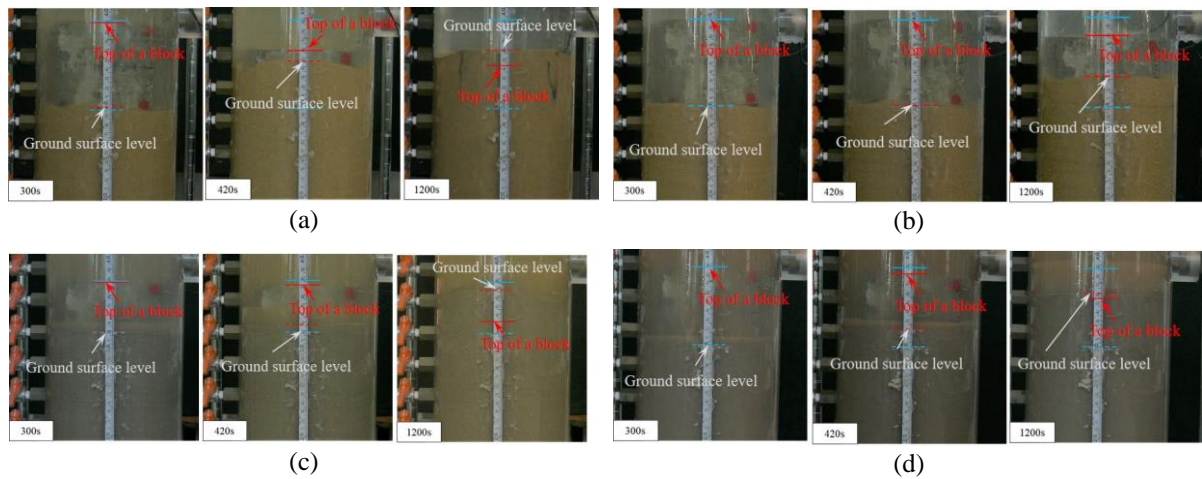


Fig. 6 Time histories of the changes in the block conditions and ground surface level due to upward seepage flow at 300 s, 420 s and 1,200 s: Case-T40B (a); Case-T70B (b); Case-S40B (c) and Case-S70B (d)

is considered to be that the ground resisted the seepage force because the rectangular blocks increased the effective stress due to the overlying load. It is also possible that the area where the ground can flow away was limited between the block and the

experimental apparatus, and therefore, the ground resisted the flow away to some extent.

In the case of 40 % relative density using Toyoura sand (Case-T40), settlement began at a hydraulic gradient of  $i = 0.5$ , and the gradient of the settlement

curve became steeper at the point where the maximum hydraulic head difference was reached around 400 s, the gradient of settlement curve of the block is maximum. On the other hand, in the other cases, the settlement tended to increase slowly. In all cases, however, the settlement of the blocks ceased to a certain degree despite the continuous application of a seepage force equivalent to the critical dynamic hydraulic gradient.

The tilt angle of the block from the time of its initial installation increased or decreased with settlement, suggesting that the block settled with a rocking behavior starting around the y-axis. This change in tilt angle was observed at the same time as or even before the response of the block displacement meter, and is considered to capture the fine behavior of the block.

## CONCLUSIONS

In this study we conducted a series of model tests on the behavior of concrete blocks resting on seafloor, where the seabed was subjected to upward seepage flow under different conditions of geomaterials and relative density of the ground using model tests. The following conclusions were drawn from the careful observation of the behavior of the concrete blocks sinking.

- (1) The critical hydraulic gradient at which effective stress diminishes due to upward seepage force was rather dependent on the relative density of seabed material, and however independent of the type of seabed material with different grain size distribution. In the case of the seabed consisted with medium loose sand ( $D_r = 40\%$ ), the concrete blocks started to sink at the hydraulic gradient of 40 % of critical value. In the case of dense sand ( $D_r = 70\%$ ), the concrete block sank near the critical hydraulic gradient.
- (2) While the concrete block resting on seafloor of loose Toyoura sand sank quickly into the seabed in the manner of progressive failure, in the other cases the concrete block sank gradually. It was found that the settlement of concrete block was capped at a certain level even when the hydraulic gradient is reaching the critical value.
- (3) The monitoring of displacement and acceleration by using sensors installed on the blocks showed that the concrete blocks started to move around the hydraulic gradient of 50 % of the critical value, regardless of the geomaterial type and relative density.

- (4) The tilting angle of the concrete block increased or decreased with settlement progressed, indicating that the block settled with a rocking behavior around horizontal axis.

## ACKNOWLEDGMENTS

This work was supported by JSPS Grant-in-Aid for Scientific Research (C) 17K06553, JSPS Grant-in-Aid for Young Scientists 20K14824. The authors would like to thank Yudai Fuji for the help with the model tests.

## REFERENCES

- [1] Oka F., Yashima A., Miura K., Ohmaki S., and Kamata A., Settlement of Breakwater on Submarine Soil Due to Wave-induced Liquefaction, in Proc. 5th International Society of Offshore and Polar. Engineers, Vol.2, 1995, pp.237-242.
- [2] Yamamoto T., Koning H. S. L., and Van Hijum E., On the Response of a Pore-elastic Bed to Water Waves, Journal of Fluid Mechanics, Vol. 87, Part 1, 1978, pp.193-206.
- [3] Miura K., Asahara S., Otsuka N., and Ueno K., Formulation of ground for coupled analysis of seabed response to wave loading, Proceedings of Geotechnical Engineering symposium, Vol.49, 2004, pp. 233-240. (in Japanese)
- [4] Zen K., and Yamazaki H., Mechanism of wave-induced liquefaction and densification in seabed, Soils and Foundations, Vol.30, No.4, 1990, pp. 90-104.
- [5] Baldock T. E., and Holmes P., Seepage effects on sediment transport by wave and currents, Coastal Engineering, 1998, pp.3601-3614.
- [6] Matsuda T., Miura K., Takayanagi R., and Anai K., Wave flume experiment on wave response of a rectangle block under different seabed characteristics, Journal of Japan Society of Civil Engineers, Ser. B2 (Coastal Engineering), Vol.75, Issue 2, 2019, pp.I\_955-I\_960. (in Japanese)
- [7] Yoshimi Y., Kuwabara F., and Tokimatsu K. One-dimensional volume change characteristics of sands under very low confining stresses, Soils and Foundations, Vol.15, No.3, 1975, pp.51-60.



## MODEL TESTS ON SAND BOILING AROUND SHEET PILE REGARDING PROPERTIES OF GROUND MATERIAL

Tatsuya MATSUDA<sup>1</sup>, Naoto NAITO<sup>1</sup> and Kinya MIURA<sup>1</sup>

<sup>1</sup>Department of Architecture and Civil Engineering, Toyohashi University of Technology, Japan

### ABSTRACT

Cofferdams have been widely employed for the construction of structures in rivers or under groundwater tables. The cofferdams constructed with sheet piles are sometimes destabilized due to sand boiling, which is caused by the upward seepage force inside the cofferdams in the vicinity of the sheet piles. A rational design method of cofferdam is indispensable for ensuring the soundness of the structures resting on integrated foundation ground even in the water. The integrity of the foundation ground inside the cofferdam is examined usually by assessing exclusively the balance between the weight of ground material and upward seepage force, where the mechanical properties of the ground material or the scale effect of soil particle are not sufficiently taken into consideration. In this study we conducted a series of model tests on the occurrence of sand boiling inside the cofferdam, in which two cofferdam models of different size are prepared, and several ground materials with different grainsize distribution and different relative densities were employed. We carefully observed the process of seepage flow until the sand boiling occurred in every model test and recorded not only the condition of seepage flow for the occurrence of sand boiling, but also the formation of ground after failure. As a consequence we found perceptible effects of mechanical properties of ground material and scale of model cofferdam on the critical seepage condition for the occurrence of boiling.

*Keywords: Cofferdams, Seepage failure, Scaling model test, Scale effect*

### INTRODUCTION

Cofferdams have been widely employed for the construction of structure foundations in river or under groundwater table. The cofferdams constructed with sheet piles are sometimes damaged due to sand boiling and the ground inside the cofferdams are disintegrated, which is caused by the upward seepage force inside the cofferdams around the sheet piles. The disintegration of ground inside cofferdam probably makes it impossible for the ground to provide load bearing capacity for structures.

Many researchers have investigated the stability of cofferdams regarding seepage force and the associated sand boiling. The primary design of cofferdam constructed with sheet piles is conducted based on the method proposed by Terzaghi and Peck (1948) [1], where the critical hydraulic head difference between outside and inside the cofferdam which triggers the occurrence of sand boiling is simply estimated by using from two-dimensional static seepage analysis where the cofferdam is implicitly modeled as a strip-shaped structure. In the method mechanical properties of ground material except its density were not considered in the calculation of critical hydraulic head difference.

Miura, et al. (1999 [2], 2001 [3]) investigated some cases where the cofferdams were severely damaged due to sand boiling during the construction of bridge piers in river, and they conducted some series of three-dimensional seepage analysis by using

FEM. As a result of the investigation it was found that the seepage force is largely dependent on the plane shape of cofferdam as well as that in vertical section, the critical hydraulic head difference for rectangular and round-shaped cofferdams is approximately two-third of that for strip-shaped cofferdam.

Tanaka and Verruijt (1999) [4] carried out the model tests on medium dense sand ground under two-dimensional condition to investigate seepage failure of the ground behind sheet piles, and the mechanism of local seepage failure. From the results of the model tests, they showed that the prismatic failure concept is effective for evaluating critical hydraulic head difference for occurrence of sand boiling, where a certain soil prism loses the equilibrium. They also clarified that the hydraulic head difference for prismatic sand model has approximately 10% free board between compared with that for total failure.

Asaoka and Kodaka (1992) [5] classified saturated soil failure problems into four types; Type I: The failure of loose and/or normally consolidated soils under fully drained loading conditions. Type II: The same soils but under perfectly undrained conditions. Type III: The failure of dense and/or overconsolidated soils under fully drained conditions. Type IV: The same soils but under perfectly undrained conditions. Based on this classification, they conducted a series of model tests for the failure problem due to seepage, and soil-water coupled limit equilibrium analyses with critical state concept combined. Their findings for the relationship between



failure load and failure mode were summarized: (1) the smallest failure load in loose sand under undrained condition, (2) the largest failure load with the largest failure region in dense sand under undrained condition, and (3) the observed no global deformation before failure with in the soil under fully drained condition that suggests the development of very localized shear deformation in the sand.

Benmebarek et al. (2005) [6] used the FLAC-2D code to analyze seepage failure of sandy soil in a cofferdam subjected to upward seepage flow. The results showed that the soil dilation angle has a significant effect on the shape of the failure mechanism. In particular, it was found that a dilating material, the failure occurs as a triangular prism due to heaving, whereas in other cases, the failure occurs as a rectangular prism and the obtained widths of the rectangular prisms were smaller than those obtained by Terzaghi's method (Terzaghi and Peck, 1948).

Okajima et al. (2009) [7] carried out the model tests which were designed for studying the seepage failure of soil behind fixed sheet piles and our elasto-plastic finite element method was applied to verify the effectiveness. The model tests and FE analysis were conducted the different relative density of the ground. Terzaghi's method also investigated by tests data. The results reaffirm the effectiveness of Terzaghi's method for calculating failure head differences in loose density ground. It was also shown that in densely density soils, the shape of the soil differs from the rectangular shape assumed by Terzaghi.

Numerical methods have been actively developed to reproduce seepage failure with large-scale ground deformation. Maeda and Sakai (1994) [8] developed Smoothed Particle Hydrodynamics (SPH) method, a discrete and continuous analysis that considers the interaction of the three phases of soil, water, and air. There were successes to simulate seepage failure around sheet piles and river embankments. Maeda and Sakai (2010) [9] also investigated a process of generating air bubbles and their effect on seepage failure using the SPH method and model test.

Fukumoto et al. (2021) [10] coupled the lattice Boltzmann and distinct element methods for both seepage flow and soil particle motion to perform two-dimensional direct simulations at the scale of a model experiment using soil particles of a size equivalent to actual sand. The results of the analysis showed that the typical series of seepage failure behaviors where boiling and heaving at downstream in the vicinity of the sheet pile and finally leading to quicksand, could be reproduced seamlessly.

At present, the stability of the foundation soil inside cofferdam is usually evaluated only from the balancing weight of soil material and upward seepage force, and the mechanical properties of soil material and the scale effect of soil particles have not been sufficiently considered. In addition, it is unclear

whether the shape of water channel observed during sand boiling model cofferdams can be useful to predict the real-scale scour shape. The prediction of failure mode and scale is rather important for evaluating the performance of cofferdams, especially if numerical analysis methods that can simulate large deformation problems can be made more accurate. In order to validate the accuracy of the numerical analysis method, it is essential to collect a series of experimental data for the evaluation of seepage failure modes and following erosion process associated being dependent on geomaterial properties.

In this study we conducted a series of model tests on the occurrence of sand boiling inside cofferdam, in which two cofferdam models of different size are used, and the model ground was formed with several ground materials with different grainsize distribution and different relative densities. In all model tests, the seepage flow and the behavior of ground up to the onset of sand boiling was carefully observed.

## INTRODUCTION OF MODEL TESTS

### Experimental and Measurement Device

A schematic diagram of the experimental device is shown in Fig. 1. Two different scales were used in this model test. The dimensions of the apparatus are shown in Table 1. Each scale experiment is referred to as a standard model test and a small model test, with the small model being 1/4 the scale of the standard model. However, the depth of the small model experiment was not 1/4 because the apparatus used in the small model test was a pre-made one. Therefore, the water injection volume was adjusted to satisfy the similarity described in the next section.

The experimental apparatus was set up with a divider in the center that simulated a sheet pile in a cofferdam. This divider is fixed to both side walls. Drainage outlets were provided on both sides of the apparatus. During the experiment, the downstream of the apparatus was opened and drained to maintain a constant water level at the downstream side. On the other hand, the upstream drain was closed, and a pump was used to inject water at a constant flow rate.

A high-speed camera and a video camera were used to capture the phenomena during the experiment. In addition, pore pressure gauges were used in the standard model test to take measurements pore water pressure change at a total of seven locations along the sheet pile perimeter.

### Experimental condition

Three types of geomaterials were used in this model tests: silica sand No. 8, silica sand No. 7, and Toyoura sand. The grain size distribution of the

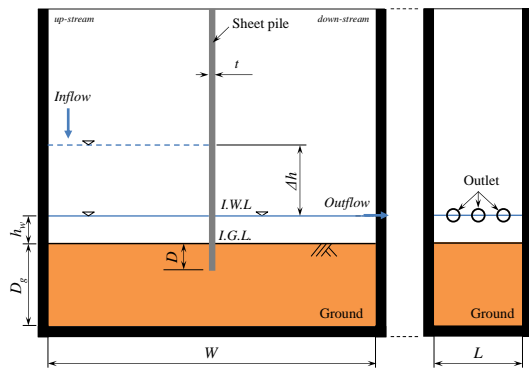


Fig. 1 Schematic of model test apparatus: (left) front view; (right) side view

Table 1 The scales of model devices

Model Size	Small	Standard
$H$ (mm)	145	600
$W$ (mm)	150	600
$L$ (mm)	39	200
$t$ (mm)	3	10
$D$ (mm)	13	50
$D_g$ (mm)	38	150
$H$ (mm)	15	50

Fig. 2 Particle size distribution curve of geomaterials

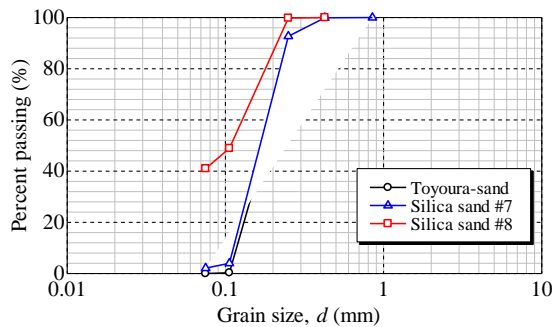


Table 2 Physical properties of geomaterials

Properties	Silica #8	Silica #7	Toyourea sand
$D_{50}$ (mm)	0.109	0.168	0.189
$e_{max}$	1.218	1.057	0.999
$e_{min}$	0.670	0.650	0.632
$k_{40}$ (m/s)	$3.02 \times 10^{-5}$	$1.16 \times 10^{-4}$	$1.96 \times 10^{-4}$
$k_{80}$ (m/s)	$1.41 \times 10^{-5}$	$6.96 \times 10^{-5}$	$1.18 \times 10^{-4}$

geomaterials is shown in Fig. 2, and the main physical properties of the geomaterials are shown in Table 2.

The model tests were conducted at relative densities

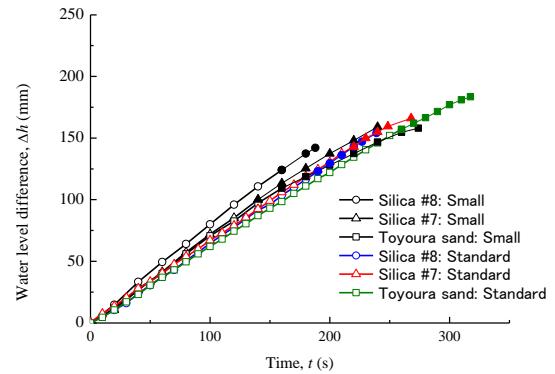


Fig. 3 Time history of water level difference at relative density  $D_r = 40\%$

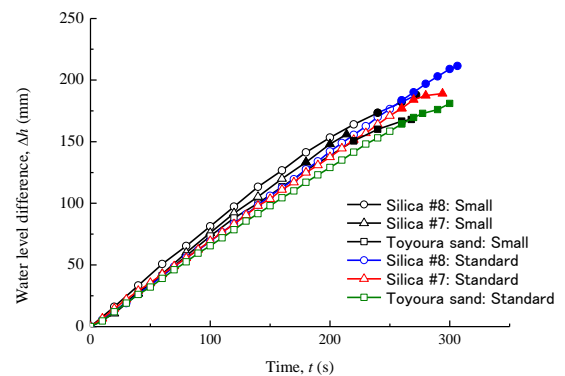


Fig. 4 Time history of water level difference at relative density  $D_r = 80\%$

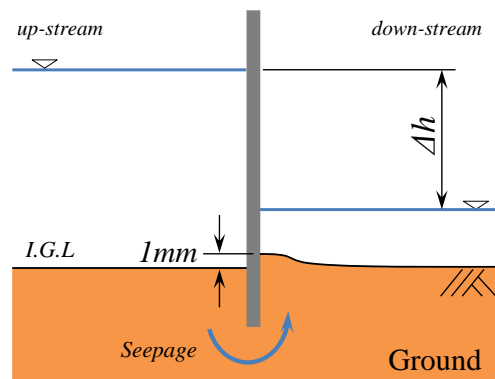


Fig. 5 Schematic diagram of the condition with displacement head difference

of  $D_r = 40\%$  and  $D_r = 80\%$  for all sedimental ground conditions in order to examine differences in seepage failure phenomena due to density. Properties  $k_{40}$  and  $k_{80}$  mean the permeability at 40 % and 80 % relative density  $D_r$ , respectively. The soil ground was deposited to a given density by the underwater drop method. In the case of relative density  $D_r = 80\%$ , the

Table 3 Displacement head difference

Head difference (mm)	Displacement head difference	
	$D_r = 40\%$	$D_r = 80\%$
Silica #8	154 (142)	212 (188)
Silica #7	159 (160)	189 (156)
Toyoura sand	184 (160)	188 (170)

Table 4 The time to reach failure head difference

Head difference (mm)	failure head difference	
	$D_r = 40\%$	$D_r = 80\%$
Silica #8	154 (142)	212 (188)
Silica #7	159 (160)	189 (156)
Toyoura sand	184 (160)	188 (170)

Table 5 The time to reach displacement head difference

Time (s)	Displacement head difference	
	$D_r = 40\%$	$D_r = 80\%$
Silica #8	190 (153)	260 (228)
Silica #7	225 (140)	260 (184)
Toyoura sand	255 (162)	265 (212)

Table 6 The time to reach failure head difference

Time (s)	Failure head difference	
	$D_r = 40\%$	$D_r = 80\%$
Silica #8	239 (188)	307 (272)
Silica #7	268 (242)	294 (214)
Toyoura sand	318 (275)	292 (268)

sedimental ground was compacted to construct the dense ground.

Water was injected upstream by a pump. The pump flow rates were  $1.29 \text{ cm}^3/\text{s}$  and  $42.9 \text{ cm}^3/\text{s}$  for the small and medium models, respectively, according to Froude's law.

## EXPERIMENTAL RESULTS

To investigate the similarity, the experimental data for the small model tests were examined in conjunction with the standard scale, doubling the time and quadrupling the length. In Tables 3 to 8 the values in parentheses indicate the experimental results for the small model and those outside the parentheses for the standard model.

### Fluctuation of hydraulic head difference

Figs. 3 and 4 shows the time histories of the

hydraulic head difference across the sheet pile between upstream and downstream. Fig. 3 shows at relative density  $D_r = 40\%$  and Fig. 4 shows at relative density  $D_r = 80\%$ . The trend of the hydraulic head difference is similar regardless of the experimental scale, confirming that the external force conditions given by the water injection rate are similar. The trend over time shows that the gradient changes after a certain amount of time has elapsed from the initial gradient. The phenomena at the time of the slope change were visually confirmed to indicate that deformation had occurred in the sedimental ground.

The head difference at that point is summarized in Tables 3 and 4, and each time to reach each head difference is summarized in Tables 5 and 6. The time when the sedimental ground at downstream was uplifted by 1 mm was defined as the displacement head difference (Fig. 5), and the time when a major failure occurred was defined as the failure head difference. The values outside the parentheses in the table indicate the values obtained in the standard model test, and the values inside the parentheses are the values obtained by converting the results of the small model test to scale and adjusting them to the standard model. In Figs. 3 and 4, the markers are filled in after the transformed hydraulic head difference is reached.

Tables 3 and 4 shows that the sedimental ground in small model tends to undergo deformation at a lower hydraulic head difference than the sedimental ground in standard model, leading to seepage failure. In terms of relative density, in the case of the loosely packed ground with  $D_r = 40\%$  in the standard model test, the displacement and failure head differences tended to increase as the grain size of the material increased, while in the case of the tightly packed ground with  $D_r = 80\%$ , each head difference increased as the grain size of the material decreased. On the other hand, the small model test did not show a uniform trend as well as each arrival time.

Tables 5 and 6 shows that for all geomaterials, regardless of the density, the sedimental ground in the small model tends to deform and reach failure earlier than the sedimental ground in standard model. In order to relative density, the arrival times of the loosely packed ground with  $D_r = 40\%$  in the standard model tests tended to increase with increasing grain size, while the arrival times of the densely packed ground with  $D_r = 80\%$  were almost the same regardless of the material. On the other hand, no such trend was observed in the small model tests.

### Scour shape of sediment ground

Figs. 6 and 7 shows the scour shapes at the time when the maximum scour depth under the sheet pile was reached for each material with a relative density of  $D_r = 40\%$  and  $D_r = 80\%$ , respectively. The maximum scour depth is defined as the depth at which

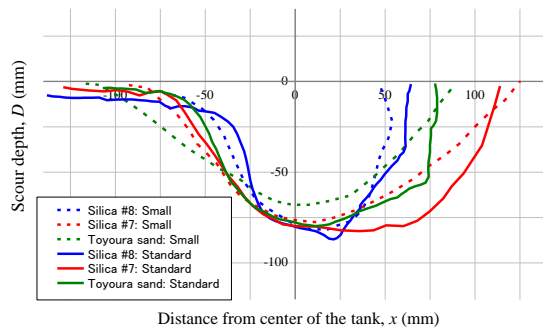


Fig. 6 Scour shape when maximum scour depth is reached at relative density  $D_r = 40\%$

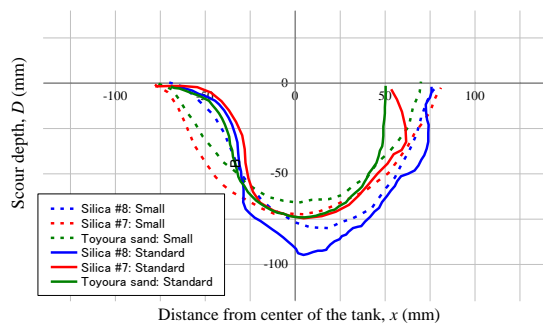


Fig. 7 Scour shape when maximum scour depth is reached at relative density  $D_r = 60\%$

the scour depth around the sheet pile reaches its maximum during the seepage failure process, and the maximum scour width is defined as the horizontal distance between the upstream and downstream sides of the sheet pile at that time. Table 5 shows the values of maximum scour depth and maximum scour width for the standard model test and the small model test, respectively. Fig. 8 shows the schematic diagram defining maximum scour depth and maximum scour width.

The maximum scour depth of each material is similar regardless of the relative density. On the other hand, the maximum scouring width varies depending on the relative density, and the loosely packed soil with a relative density of  $D_r = 40\%$  tends to have a wider scouring width, indicating that the scouring area is wider. In addition, the scour profile of the loose soil with  $D_r = 40\%$  is different from that of the dense soil with  $D_r = 80\%$ , indicating that the scour shape varies depending on the geomaterial.

Focus on the scale effects of model test, the results of the small model were similar to or slightly underestimated compared to the results of the standard model in terms of maximum scour depth and scour shape in Table 7. On the other hand, the small model overestimated the maximum scour width compared to the standard model in Table 8.

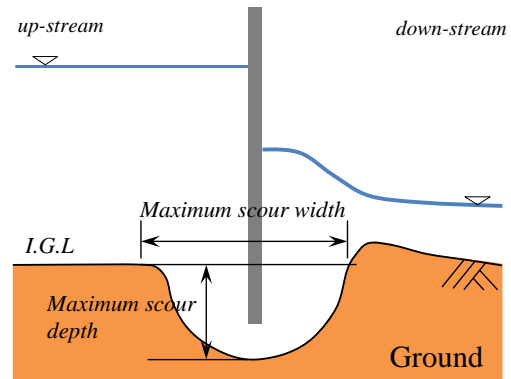


Fig. 8 Schematic diagram defining maximum scour depth and maximum scour width

Table 7 Maximum scour depth

(mm)	Maximum scour depth	
	$D_r = 40\%$	$D_r = 80\%$
Silica #8	87 (80)	95 (80)
Silica #7	83 (76)	75 (72)
Toyouura sand	80 (68)	74 (64)

Table 8 Maximum scour width

Head difference (mm)	Maximum scour width	
	$D_r = 40\%$	$D_r = 80\%$
Silica #8	64 (56)	76 (80)
Silica #7	114 (124)	62 (80)
Toyouura sand	79 (88)	50 (68)

## CONCLUSIONS

This study we conducted seepage flow tests on the model cofferdams to observing the behavior of seepage flow and ground deformation, in which two model cofferdam with different model scale and several ground materials with different grainsize distribution and different relative densities were employed. The conclusions of this study can be summarized as follows:

- The perceptive effect of the model scale was observed on the critical hydraulic head difference between inside and outside cofferdam. The critical hydraulic head difference for small-scaled model was smaller than that for standard-scaled model.
- We found that the shape of water channel from outside to inside cofferdam during sand boiling was rather influenced by the grainsize of ground material and relative density. The shape of the channel was scarcely influenced

by the model scale of cofferdam.

## ACKNOWLEDGMENTS

This work were supported by JSPS Grant-in-Aid for Scientific Research (C) 17K06553, JSPS Grant-in-Aid for Young Scientists 20K14824, The Geoscience Center Foundation, and Research Funding Granted by Toyohashi University of Technology President. We would like to thanks Erika Yagami, Yuki Ando and Nur Atiqah Syazrina Binti Aziz for their help to conduct the model tests.

## REFERENCES

- [1] Terzaghi K., and Peck R. B., Soil Mechanics in Engineering Practice, John Wiley and Sone, 1948, pp.218-233.
- [2] Miura K., Imafuku M., Furukawa N., and Nagasawa M., Ground failure due to seepage flow in a river cofferdam, Soil mechanics and foundation engineering, Vol.47 (4), 1999, pp.7-10. (in Japanese)
- [3] Miura K., Supachawarote C., Phien-Wej N., and Lin D. G., Boiling Resistant Design of Cofferdams Regarding the 3-D Effects of Seepage, The 15th International Conference on Soil Mechanics and Geotechnical Engineering (15ISSMGE), 2001, pp.2151-2154.
- [4] Tanaka T., and Verruijt A., Seepage failure of sand behind sheet piles -The mechanism and practical approach to analyze-, Soils and Foundations, Vol. 39, Issue 2, 1999, pp. 27-35.
- [5] Asaoka A., and Kodaka T., Seepage failure experiment and their analysis of loose and medium dense sands. Soils and Foundations, Vol. 32, Issue 3, 1992, pp.117-129.
- [6] Benmebarek N., Benmebarek S., and Kastner R., Numerical studies of seepage failure of sand within a cofferdam, Computers and Geotechnics, Vol. 32, 2005, pp. 264-273.
- [7] Okajima K., Tanaka T., Zhang S., and Komatsu T., Model experiments and elasto-plastic finite element analysis about seepage failure of sand behind fixed sheet pile, Transaction of the JSIDRE, Vol.260, 2009, pp.107-112.
- [8] Maeda K., and Sakai M., Development of seepage failure analysis procedure of granular ground with Smoothed Particle Hydrodynamics (SPH) method, Journal of Applied Mechanics, JSCE, Vol.7, 2004, pp.775-786.
- [9] Maeda K., and Sakai M., Seepage failure and erosion of ground with air bubble dynamics, ASCE, Geoenvironmental Engineering and Geotechnics, 2010, pp.261-266.
- [10] Fukumoto Y., Yang H., Hosoyamada T., and Ohtsuka S., 2-D coupled fluid-particle numerical analysis of seepage failure of saturated granular soils around an embedded sheet pile with no macroscopic assumptions, Computers and Geotechnics, 2021, Vol.136.

# DISCRETE ELEMENT MODELING OF SLOPE FLOW BEHAVIORS OF DRY GRANULAR MATERIALS WITH DIFFERENT COLLAPSE CONDITIONS

Naoto Naito<sup>1</sup>, Tatsuya Matsuda<sup>1</sup>, Kinya Miura<sup>1</sup>, Yasuhiro Yamada<sup>1</sup> and Takumu Omura<sup>1</sup>

<sup>1</sup>Department of Architecture and Civil Engineering, Toyohashi University of Technology, Japan

## ABSTRACT

There has been a need to improve the accuracy of predicting the arrival distance of granular avalanches generated by rock slope failures. However, it has not been entirely clarified how the flow behavior depends on properties of slope and granular material. Although many researchers have conducted the analytical investigation using discrete element simulation, the numerical models employed were merely confirmed by comparing only the final deposition shapes between experiments and simulations. When analyzing the flow behavior of granular materials, we are required as well to reproduce the velocity distribution of granular materials during slope flow. In this study was proposed a discrete element modeling method which is based on the results of particle shape measurements, restitution tests, and sliding tests, for more reliable the DEM simulation of the flow behavior of failed debris on slope. As consequence it was found that the proposed discrete element modeling is capable of reproducing the final deposition and velocity distribution of granular materials during slope flow with practical accuracies.

*Keywords: rock slope failure, granular avalanche, runout distance, discrete element method*

## INTRODUCTION

These days the restoration of aged social infrastructures is a national-wide pressing issue in Japan. The failure of aged cut slopes are involved to the issue, and the prevention of slope failure is inevitable problem for the extension service life of the social infrastructures. This study aims to propose a rational prediction method for evaluation of the degree of potential of slope failures and the range and intensity of the associated damages.

Numerical simulation by means of discrete element method (DEM) [1] has been developed as one of the most promising methods for predicting the runout distance of rock debris during rock slope failures [2] [3]. It has been reported that the deposition range can be predicted through the simulation by using DEM based on the comparison with in-situ observation and laboratory experiments. Some investigations have compared the velocity at the tip of flowing granular materials [4] [5], but their validity is often confirmed only by the final deposition shape [6] [7]. In the investigations the granular avalanche experiments that were used for comparison with the numerical simulations had constant slope angles and slope heights. However, to predict the runout distance of granular materials due to rock slope failure with high accuracy, a combination of parameters such as slope angle, slope height, granular diameter, and amount of collapse should be considered. Therefore, not only the final deposition shape but also the flow velocity distribution during slope flow must be used as a

comparison item to validate the numerical method.

In this study we presents an example of a discrete element modeling method that reproduces not only the final deposition shape of granular materials, but also the velocity distribution of the granular materials from downslope flow to deposition. The validity of the modeling method was confirmed by comparison with the results of slope flow experiments with different slope angles, slope heights, and collapse volumes.

## OVERVIEW OF EXPERIMENTAL AND NUMERICAL SIMULATION METHODS

### Outline of model tests

For the slope flow model experiment of granular material, we used the apparatus shown in Fig. 1, which consists of a slope model with a horizontal surface length of 3 m and a slope length of 2 m with a variable slope angle and a hinge type trigger gate in a soil tank with a depth length of 0.4 m. The granular materials used in the experiment were crushed rocks with grain sizes ranging from 19.0 to 37.5 mm, as shown in Fig. 2. The granular materials were collapsed by instantaneously opening the gate using a hinge placed above the initial accumulation position of the granular materials as the rotation center. During the experiment, the slope flow behavior was photographed from the side of the soil tank at 500 fps using a high-speed camera. After the experiment, photographs were taken from the side and top of the



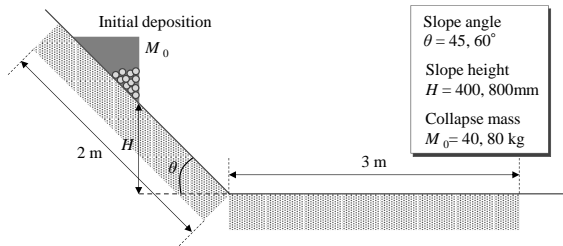


Fig.1 Outline of slope and initial deposition



Fig. 2 Photo of granular material

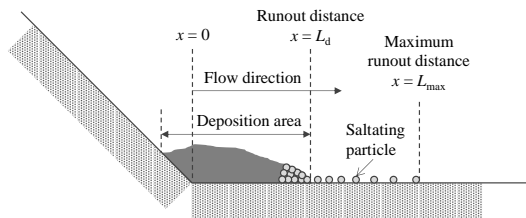


Fig. 3 Definition of runout distance

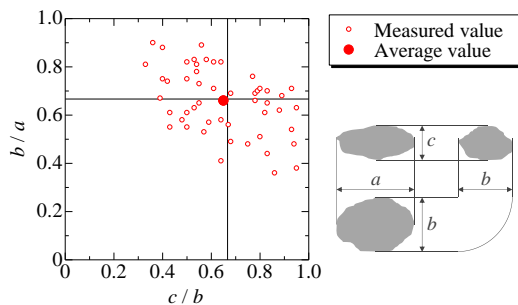


Fig. 4 Shape classification of granular materials

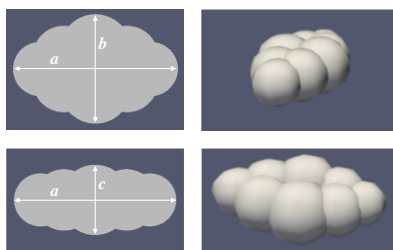


Fig. 5 Rock particle model in DEM

soil tank to confirm the runout distance of the granular materials and the deposition.

In this study, the final deposition of the granular avalanche has been divided into depositional area where the rock particle is stacked in two or more levels and saltating particles as shown in Fig. 3. The distance  $x$  in the flow direction was defined as the distance to the depositional area starting from the toe of the slope as the runout distance  $L_d$ , and the tip of

the saltating particles as the maximum runout distance  $L_{max}$ . Since the total mass of saltating particles was less than 1% of the collapse mass, the present study focused on the runout distance  $L_d$  to evaluate the area where the granular materials collide as a group with a large mass.

## Outline of numerical simulations

The DEM simulations presented here are performed using the open-source LIGGGHTS® [8], adopting Hertz contact model where Young's modulus, Poisson ratio, the coefficient of friction and the coefficient of restitution are the major parameters specified in material properties. There have been several studies of granular materials using LIGGGHTS, including studies of the shear behavior of granular materials [9] and studies of the behavior of granular materials impinging on rigid barriers [10].

## GRANULAR PROPERTIES AND ITS DISCRETE ELEMENT MODELING METHOD

### Particle shape

From the granular materials used in the experiment, 50 rock blocks were randomly selected and measured for major axis diameter  $a$ , medium axis diameter  $b$ , and minor axis diameter  $c$  to classify the particle shape [11]. Fig. 4 shows the results of the 50 measurements, and the filled plots show the average values. The particle shape is generally close to a lump shape.

In these simulations, we used clumped particles whose size ratios are the average of those of the granular materials used in the experiment, shown in Fig. 5.

### Particle mass

Fifty granular materials were randomly selected from the granular materials used in the experiment and the particle masses were measured, resulting in the distribution shown in Fig. 6.

In the simulation, five different sizes of particles were used to obtain the same conditions as the five levels of weight distribution shown in Fig. 6. The particle dimensions at each mass were set to the average size ratio shown in Fig. 5, assuming that the particles were ellipsoids with a unit volume mass of  $2700 \text{ kg/m}^3$ .

### Restitution coefficient

To investigate the restitution coefficient of particles, 50 randomly selected rock particles were impacted with the slope model and the particle fixed on the slope model from a height of 500 mm, as shown in Fig. 7, and the rebound heights were

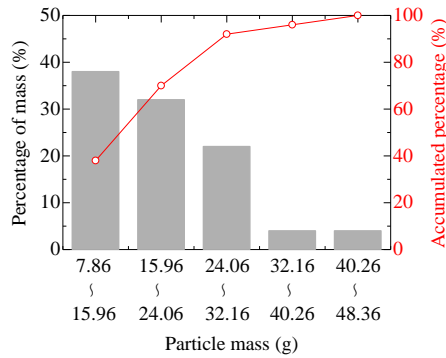


Fig. 6 Particle mass distribution

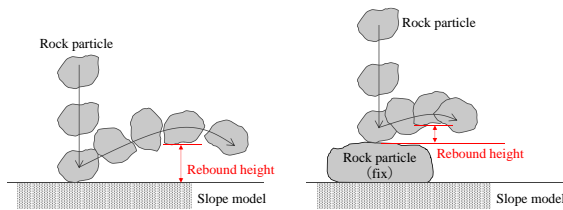


Fig. 7 Outline of rebound test

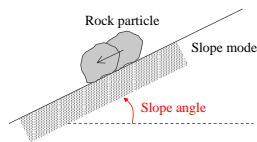


Fig. 8 Outline of sliding test

Table 1 DEM input parameters

	Unit	Basic setting
Young's modulus	Pa	$5.0 \times 10^7$
Poisson's ratio		0.32
Restitution coefficient particle-particle		0.26
Restitution coefficient particle-wall		0.64
Friction coefficient particle-particle		0.466
Friction coefficient particle-wall		0.325
Timestep	s	$1.0 \times 10^{-6}$

measured from images. The median rebound height between the rock particle and the slope model was 4 mm, and the median rebound height between the rock particles was 26 mm.

In the simulation, the restitution coefficients were set such that the median rebound height agreed with the experiment. In the simulation of the rebound test, the rock particle model in Fig. 5 was used to measure the rebound height by dropping the rock particle from a height of 500 mm onto a flat surface. Since one rock particle geometry was used in the simulation, rebound

simulation was performed for a total of 20 cases of initial postures, each rotated 18 degrees around the x-axis and y-axis. The results of the rebound simulation set the restitution coefficient between the rock particle and the slope model to 0.64 and the restitution coefficient between the rock particles to 0.26.

#### Friction coefficient

The friction coefficient between the rock particle and the slope model was measured using the sliding test shown in Fig. 8. The static friction coefficient was measured on 50 randomly selected rock particles from the angle at which the slope was inclined to start sliding. The coefficient of static friction was 0.60.

Since this study is concerned with slope flow phenomena, it was decided to use the dynamic friction coefficient in the simulation. Referring to the previous literature [12], where the dynamic friction coefficient is approximately 52% of the static friction coefficient, 0.32 was selected as a candidate friction coefficient to be used in the simulation. For the friction coefficient between rock particles, 0.47, which corresponds to a friction angle of  $25^\circ$  between particles, was selected as a candidate for the simulation based on previous measurements of the friction angle between particles [13], which ranges from about  $22$ - $30^\circ$ . The validity of the friction coefficient setting method was confirmed through sensitivity analysis of the parameters and comparison with experimental results, as described below.

#### Poisson's ratio and Young's modulus

Poisson's ratio was set to 0.32 in the analysis, referring to the values of 0.29-0.34 given in the literature of limestone association of Japan [14].

Young's modulus was set to a value that considers the computational cost, based on previous research showing that its contribution to slope flow behavior is relatively small compared to other parameters [15]. The validity of the set values was confirmed by sensitivity analysis of the parameters and comparison with experimental results, as described below.

#### PARAMETER SENSITIVITY ANALYSIS FOR SLOPE FLOW SIMULATION

In this study, sensitivity analyses of the parameters Young's modulus, computation time increments, coefficient of friction between particles, and coefficient of friction between particles and slope were conducted. The purpose was to set values for Young's modulus and computation time increments that consider computational cost, and to validate the setting method for the friction coefficient. The effects of various analytical parameters on the final deposition shape were investigated and compared with experimental results. The experimental conditions for comparison were a slope angle of  $45^\circ$ ,

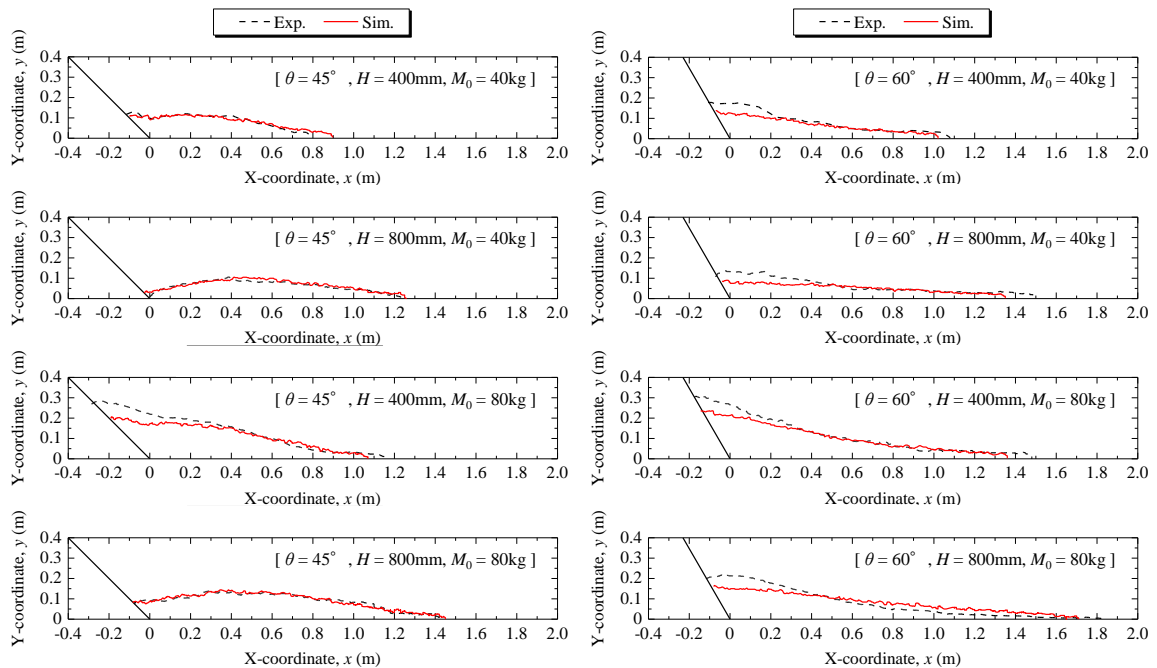
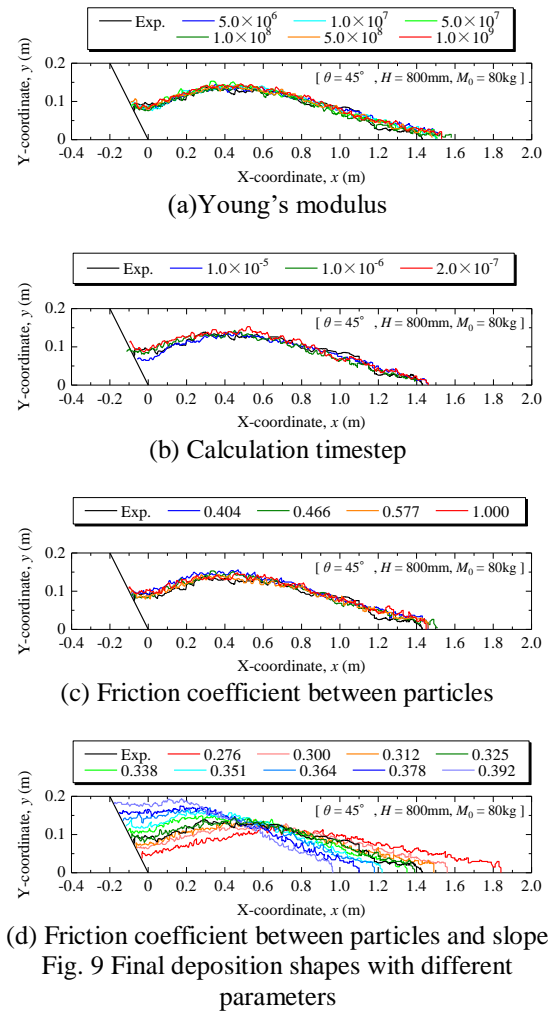
a drop height of 800 mm, and a collapse mass of 80 kg. Table 1 shows the basic setting value of parameters.

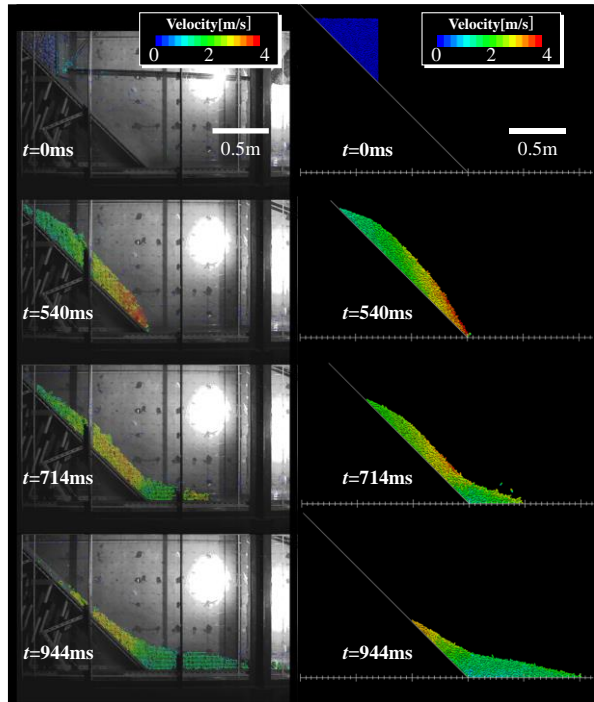
Fig. 9(a) shows the simulation result of final deposition shape with different Young's modulus and its experimental results. As in a previous study [15], Young's modulus was found to have little effect on the deposition shape, so a Young's modulus of  $5.0 \times 10^7$  Pa was set for this simulation.

Fig. 9(b) shows the simulation result of final deposition shape with different calculation timestep and its experimental results. Since the calculation timestep has little effect on the runout distance in the range of  $1.0 \times 10^{-5}$  s or less, the calculation timestep was set to  $1.0 \times 10^{-6}$  s in this simulation, referring also to the values in previous studies [10] [16].

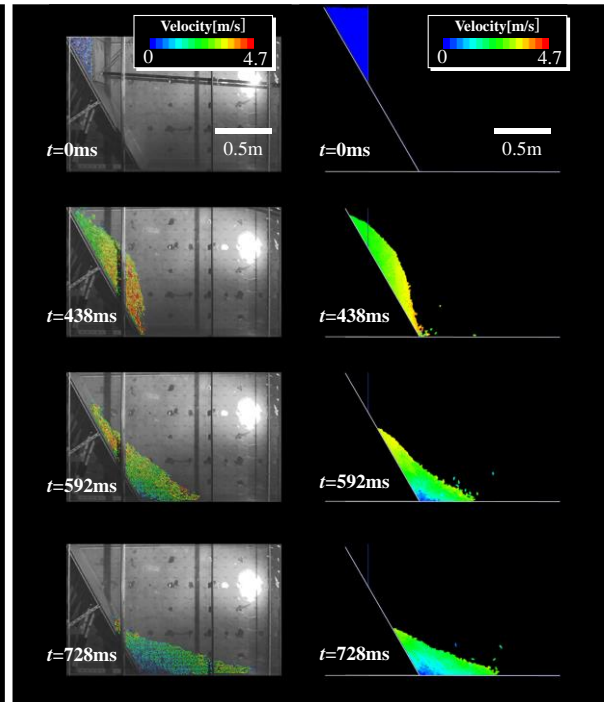
Fig. 9(c) shows the simulation result of final deposition shape with different friction coefficient between particles and its experimental results. Since the friction coefficient between particles was found to have little effect on the deposition shape, it was set to 0.466, which corresponds to an inter-particle friction angle of  $25^\circ$ , referring to a previous study [13].

Fig. 9(d) shows the simulation result of final deposition shape with different friction coefficient between the particles and the slope and its experimental results. The effect of the friction coefficient between the particles and the slope on the deposition shape is very significant. The value most consistent with the experimental results is a friction coefficient of 0.325, and we decided to use a setting method that uses a value of 52% of the static friction coefficient, based on previous research [12].





(a)Experiment (b)DEM simulation  
Fig. 11 Flow velocity distribution in the case of  $\theta = 45^\circ$ ,  $H = 800\text{mm}$ ,  $M_0 = 80\text{ kg}$



(a)Experiment (b)DEM simulation  
Fig. 12 Flow velocity distribution in the case of  $\theta = 60^\circ$ ,  $H = 800\text{mm}$ ,  $M_0 = 80\text{ kg}$

## COMPARISON OF SLOPE FLOW EXPERIMENTS AND SIMULATION RESULTS

### Final deposition shape

To confirm the validity of the discrete element modeling method based on rock particle shape measurements, rebound and sliding tests, and parameter sensitivity analysis, we compared the experimental and analytical results for a total of eight cases with different slope angles  $\theta = 45$  and  $60^\circ$ , slope heights  $H = 400$  and  $800\text{ mm}$ , and collapse masses  $M_0 = 40$  and  $80\text{ kg}$ . Fig. 10 shows the final deposition shapes obtained from the experiments and analyses for a total of 8 cases. By setting parameters based on the discrete element modeling method presented in this paper, the DEM simulation accurately reproduces the final deposition shapes obtained from the experiments.

### Granular flow velocity

Fig. 11 and Fig. 12 show experimental and analytical flow velocity distributions for slope angles  $\theta = 45$  and  $60^\circ$ , slope height  $H = 800\text{ mm}$ , and collapse mass  $M_0 = 80\text{ kg}$ . Time  $t$  is given in Fig. with  $t = 0\text{ ms}$  as the start of slope flow. In the experiment with a slope angle of  $\theta = 45^\circ$ , the flow mode was that the following granular materials pushes out the preceding granular materials. For the experiment with a slope angle of  $\theta = 60^\circ$ , the flow mode was that the following granular materials get over the preceding granular materials and the velocity of granular materials becomes zero around the slope toe. The

simulation results were consistent with the experimental results and reproduced the difference in the flow mode at the toe of slope, which varied with different slope angles.

The discrete element modeling method based on shape measurements of granular materials, rebound and sliding tests, and parameter sensitivity analysis can reproduce not only the final deposition shape of granular materials, but also the velocity distribution during slope flow. Although it is sometimes difficult to judge whether the slope flow process is reproduced by comparing only the final deposition shape because there are conditions in which the flow modes differ, at least the modeling method in this study can reproduce differences in flow modes.

## CONCLUSIONS

This study presented an example of a parameter setting method based on rock particle shape measurements, rebound tests, sliding tests, and parameter sensitivity analysis, so that the modeling of rock debris grains in DEM reproduces not only the final deposition shape of granular materials, but also the velocity distribution of the granular materials from downslope flow to deposition. It was shown that this numerical modeling can reproduce the final deposition shape observed in the experiments on rock debris flow experiments induced by slope failure with different slope angle, slope height, and collapse volume, as well as the velocity distribution during slope flow and different flow mode at the toe of slope.

We are planning to conduct numerical experiments using this modeling method in combination with various parameters such as rock particle shape, amount of collapse, and slope angle, and to clarify the relationship between internal behavior of granular materials and runout distance.

## ACKNOWLEDGMENTS

The authors are grateful for the financial support provided by the Japan Society for the Promotion of Science (Grant-in-Aid for Young Scientists 21K14239) and Toyohashi University of Technology (Grant-in-Aid for activating education and research).

## REFERENCES

- [1] Cundall, P. A. and O. D. L. Stack.: A Discrete Models for Granular Assemblies, *Geotechnique*, Vol.29, No.1, pp.47-65, 1979.
- [2] Nakase, H., Cao, G., Tochigi, H., Tabei, K.: A method to access collision hazard of falling rock due to slope collapse application of DEM on modeling of earthquake triggered slope failure for nuclear power plants, *JSCE Journal of Earthquake Engineering*, Vol.71, No.4, I\_476-I\_492, 2015.
- [3] Nakase, H., Iwamoto, T., Cao, G., Tabei, K., Sakaguchi, H., Matsushima, T.: Reproduction analysis of actual slope collapse and parametric study for evaluation of the deposit volume by a simple model of distinct element method, *JSCE Journal of Earthquake Engineering*, Vol.73, No.4, I\_694-I\_703, 2017.
- [4] Richefeu, V., Mollon, G., Daudon, D., Villard, P.: Dissipative contacts and realistic block shapes for modeling rock avalanches, *Engineering Geology* 149-150(1), pp.78-92, 2012.
- [5] Zhou, G.G.D., Sun, Q.C.: Three-dimensional numerical study on flow regimes of dry granular flows by DEM, *Powder Technol*, Vol.239, pp.115–127, 2013.
- [6] Mead, S.R., Cleary, P.W.: Validation of DEM prediction for granular avalanches on irregular terrain, *Journal of Geophysical Research: Earth Surface*, 120 (9), 1724–1742, 2015.
- [7] Gong, S., Zhao, T., Dai, F., Zhou, G.G.D.: Discrete element analysis of dry granular flow impact on slit dams, *Landslides*, Vol.18, pp.1143-1152, 2021.
- [8] Kloss, C., and Goniva, C. 2010. LIGGGHTS – a new open source discrete element simulation software. In *Proceedings of the 5th International Conference on Discrete Element Methods*. pp. 25–26.
- [9] Louati, H., Bednarek, X., Martin, S., Ndiaye, A., Bonnefoy, O., 2019. Qualitative and quantitative DEM analysis of cohesive granular material behaviour in FT4 shear tester. *Chem. Eng. Res. Des.* 148, 155–163, <http://dx.doi.org/10.1016/j.cherd.2019.05.059>
- [10] Ng, C.W.W., Choi, C.E., Goodwin, G.R.: Froude characterisation for single-surge unsteady dry granular flows: impact pressure and runup height, *Canadian Geotechnical Journal*, Vol.56, No.12, p.1968-1978, 2019.
- [11] Zingg, T.: Beitrag zur Schotteranalyse, *Schweizerische Mineralogische und Petrographische Mitteilungen*, Vol.15, pp.39-140, 1935.
- [12] Nakamura, s., Abe, K., Watanabe, K., Nakajima, S.: Analysis of flow and impulsive behavior based on existing cascading experiment of collapsed soil and reproduction analysis by MPM, *JSCE Journal of Geosphere Engineering*, vol.74, No.3, 259-274, 2018.
- [13] Rowe, P.W.: *Proc. of the Royal Society of London. Series A, Mathematical and Physical Sciences*, Vol. 269, Issue 1339, pp. 500-527, 1962.
- [14] Limestone Association of Japan: *Limestone Aggregate and Concrete*, Revised and Expanded Edition, 2005.
- [15] Moriguchi, S., Okuyama, H., Terada, K., Otake, Y., Aoki, T.: Quantification of parameter contribution in granular flow simulations using the discrete element method, *Journal of JSCE (Applied Mechanics)*, vol.76, No.2, I\_369-I\_377, 2020.
- [16] El Kassem, B.; Salloum, N.; Brinz, T.; Heider, Y.; Markert, B. A semi-automated DEM parameter calibration technique of powders based on different bulk responses extracted from Auger Dosing experiments. *KONA Powder Part. J.* 2021, 38, 235–250.

## MODEL ROCK-SLOPE FAILURE TESTS ON FINAL RUNOUT DISTANCE OF DRY GRANULAR AVALANCHE WITH SECONDARY SLOPE FAILURE

Naoto Naito<sup>1</sup>, Tatsuya Matsuda<sup>1</sup>, Kinya Miura<sup>1</sup>, Takumu Omura<sup>1</sup> and Arif Daniel Bin Azmi<sup>1</sup>

<sup>1</sup>Department of Architecture and Civil Engineering, Toyohashi University of Technology, Japan

### ABSTRACT

To rationalize the evaluation method for the runout distance of rock-slope failure debris, it is necessary to clarify the relationship between the runout distance of granular materials and their flow behavior. In this study, we conducted a series of model tests of dry granular avalanches with test parameters of slope angle, flow height, and granular diameter comprehensively changed. Thus, we investigated the effect of granular diameter on the runout distance from the comparative examination of the test results. The test results showed that the runout distance is dependent on the behavior of granular materials. If the following granular materials pushes out the preceding granular materials, the increase in particle diameter produces the longer runout distance. On the other hand, if the following granular materials get over the preceding granular materials and the velocity of granular materials becomes zero around the slope toe, the runout distance of the largest granular diameter may not be the maximum. To investigate the runout distance by the secondary slope failure, we conducted an additional series of model tests of dry granular avalanches, in which the rock masses generated by the primary slope failure were deposited at the toe of slope. The test results showed that the runout distance of the secondary slope failure was the same as that of the primary slope failure, regardless of the particle size.

*Keywords: rock slope failure, dry granular material, granular avalanche, runout distance, model test*

### INTRODUCTION

To rationalize the evaluation method for the runout distance of rock-slope failure debris, we need to clarify the relationship between the runout distance of granular materials and their flow behavior. These years Discrete Element Method (DEM) [1] has been widely used in Japan as one of the most promising numerical analysis methods to predict the runout distance of rock debris in rock slope failures [2]. The DEM has been employed to evaluate the safety of critical structures such as nuclear power plants [3]. This study aims to clarify the slope flow behavior of the rock masses and obtain fundamental dates for validating the results of DEM analyses.

Many researchers have focused on the granular diameter as one of the primary parameters that affects the runout distance of rock debris. Tochigi et al. [4] conducted a series of experiments parametrically with different grain diameter and different collapse volume, and reported that rock debris with larger grain diameter runout through longer distance. Bartali et al. [5] conducted a series of model tests on the runout distance with rock debris mixture of coarse grains and fine grains, and reported that the observed runout distance reaches maximum value when the volume ratio of coarse grains exceeds 50 percent.

Mollon et al. [6] conducted numerical analysis by means of DEM to examine the runout distance and energy attenuation mechanism with granular diameter, particle shape, and slope undulation as

parameters. Watanabe et al. [7] conducted also an numerical analysis by means of DEM to clarify the effects of the grain size distribution and grain shape on the runout distance, and suggested the relationship between segregation during granular avalanche and the runout distance has been reported. However, these researcher investigated the runout distance under a certain slope angle conditions. Almost all the investigations on the flow behavior of rock debris have focused only on the flow on slopes [8] [9], and discussed the behavior from the viewpoint of energy attenuation [6]. There have been few studies on flow modes around the toe of slope.

In this study we conducted a series of model tests on rock-slope failure and carefully observed the runout behavior of rock debris, and comparatively examined the effects of slope angle, flow height, and granular diameter on the runout distance.

### CONDITIONS OF MODEL ROCK-SLOPE FAILURE TESTS

#### Outline of model tests

Model tests have been conducted using the apparatus shown in Fig. 1, which consists of a slope model with a horizontal surface length of 3 m and a slope length of 2 m with a variable slope angle and a trigger gate installed in a 0.4 m wide earthen tank. Shutter-type gate has been used for the  $M_0 = 40$  kg



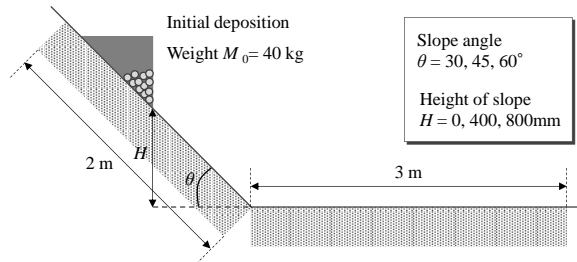


Fig. 1 Outline of slope and initial deposition

Table 1 Conditions of model tests

Case No.	Type of trigger gate	$\theta$ (°)	$H$ (mm)	$M_0$ (kg)	Granular diameter
1	Shutter type gate	30	0	40	Small
2					Medium
3					Large
4			400		Small
5					Medium
6					Large
7			800		Small
8					Medium
9					Large
10		45	0		Small
11					Medium
12					Large
13			400		Small
14					Medium
15					Large
16			800		Small
17					Medium
18					Large
19		60	0		Small
20					Medium
21					Large
22			400		Small
23					Medium
24					Large
25			800		Small
26					Medium
27					Large
28	Hinge type gate	45	800	80	Small
29					Medium
30					Large
31			40×2 (total 80)	Small	
32				Medium	
33				Large	

condition, and hinge-type gate has been used for the 80 kg case. Crushed rocks with grain sizes ranging from 4.75 to 9.50 mm (Small), 9.50 to 19.0 mm (Medium), and 19.0 to 37.5 mm (Large) were used as the granular material. Details of the granular shape and other characteristics are described below.



Fig. 2 Photo of granular materials

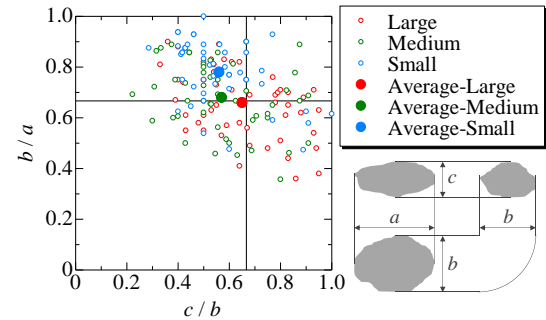


Fig. 3 Shape classification of granular materials

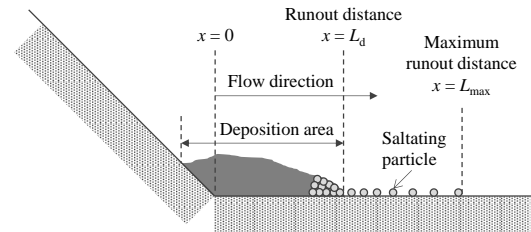


Fig. 4 Definition of runout distance

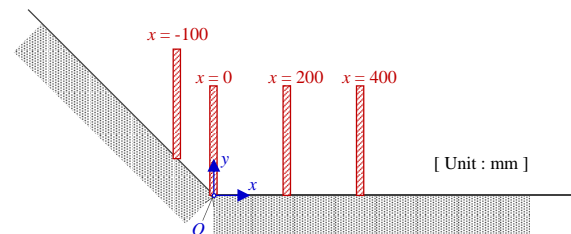


Fig. 5 Time history velocity measurement area

In the model tests, granular materials have been deposited in a storage container on the slope, and the trigger gate has been opened to collapse the granular materials. In the case of the shutter-type gate, the shutter has been pulled vertically upward at a velocity of about 1.6 m/s to collapse the granular materials. In the case of the hinge-type gate, the hinge placed above the initial deposition of the granular materials has been used as the center of rotation to instantly release the sedimentary soil pressure, causing the granular materials to collapse. During the model tests, the slope flow behaviors have been photographed at 500 fps using a high-speed camera from the orthogonal direction of the flow direction. After the experiment, photographs have been taken orthogonally to the flow direction and from the top of the soil tank to confirm the runout distance of the granular avalanche and the final deposition shapes.

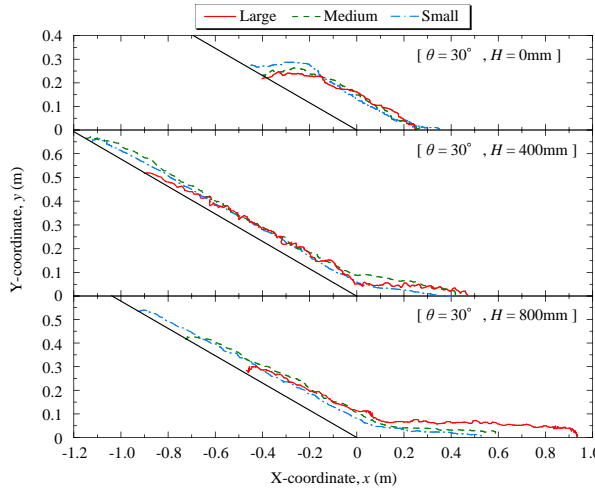


Fig. 6 Final deposition shapes;  $\theta = 30^\circ$  (case1-9)

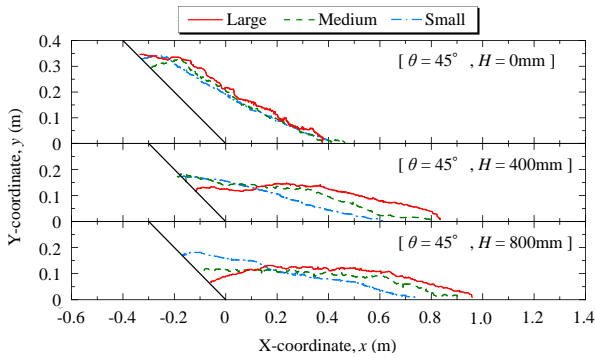


Fig. 7 Final deposition shapes;  $\theta = 45^\circ$  (case10-18)

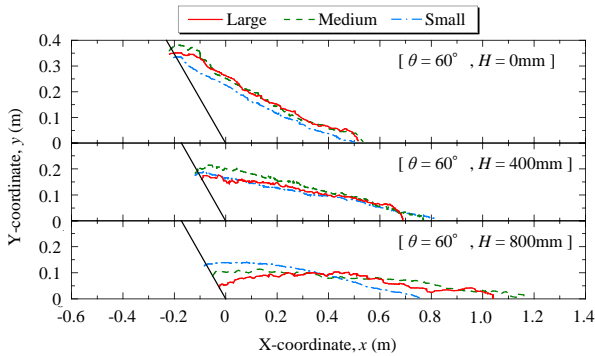
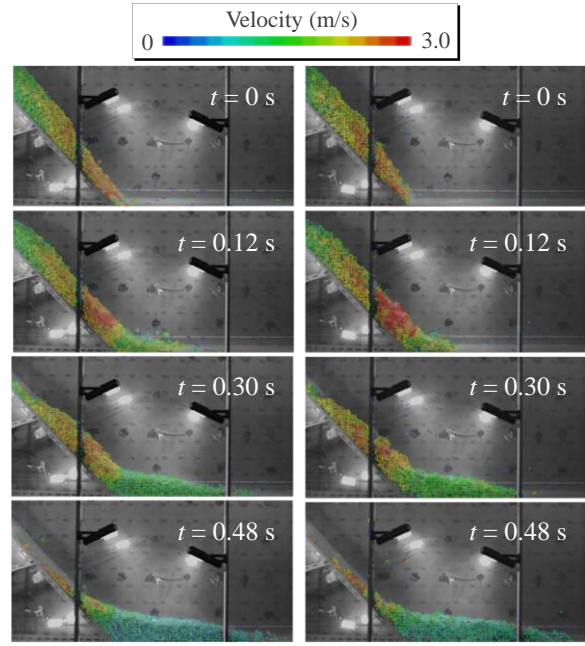


Fig. 8 Final deposition shapes;  $\theta = 60^\circ$  (case19-27)

### Model test case

In this model tests, a total of 27 cases of rock-slope failure tests have been conducted using shutter-type open devices with a combination of parameters of granular diameter (small, medium, and large granular materials), slope angle  $\theta$  ( $30^\circ$ ,  $45^\circ$ ,  $60^\circ$ ), and height of slope  $H$  (0, 400, 800 mm). Model tests have been also conducted under the conditions of a firstly failure followed by a secondary slope failure and its total collapse volume at one time. Table 1 lists the conditions of model tests.



(a) Medium(case14)

(b) Large(case15)

Fig. 9 Velocity distribution;  $\theta = 45^\circ$ ,  $H = 400$  mm

### Granular diameter and shape classification

Fig. 2 shows examples of small, medium, and large granular material, with the mean mass of each particle diameter being 0.36 g, 4.03 g, and 19.85 g, respectively. Fig. 3 shows the shape classification obtained from 50 randomly selected major axis diameter  $a$ , medium axis diameter  $b$ , and minor axis diameter  $c$  from each particle, and the filled plots show their mean values. All of the granular diameters are generally close to massive in shape.

### Data organization methods

#### Runout distance

In this study, the final deposition of the granular avalanche has been divided into depositional area where the rock particle is stacked in two or more levels and saltating particles as shown in Fig. 4. The distance  $x$  in the flow direction was defined as the distance to the depositional area starting from the toe of the slope as the runout distance  $L_d$ , and the tip of the saltating particles as the maximum runout distance  $L_{max}$ . Since the total mass of saltating particles was less than 1% of the collapse weight, the present study focused on the runout distance  $L_d$  to evaluate the area where the granular materials collide as a group with a large mass.

#### Granular flow velocity

The velocity vector of the granular avalanche has been calculated from the image taken by the high-speed camera using PIV analysis. Then, time

waveforms of the velocity in the measurement area shown by the red frame in Fig. 5 were output.

## EFFECT OF GRANULAR DIAMETER ON RUNOUT DISTANCE

### Final deposition shape

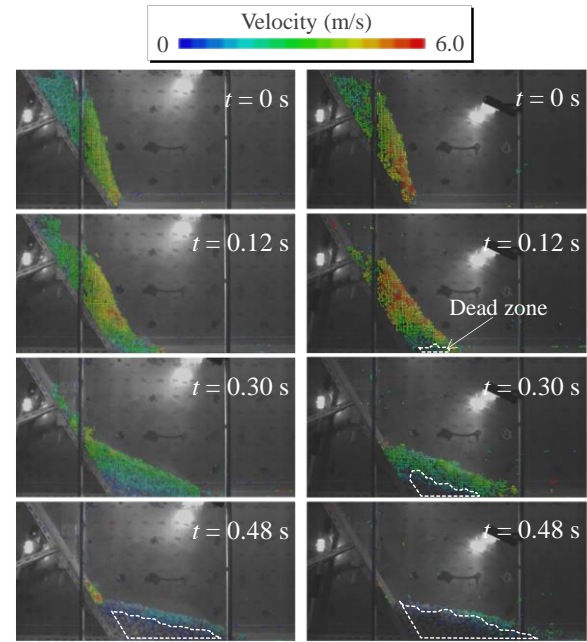
Fig. 6, Fig. 7, and Fig. 8 show the final deposition shapes summarized for each slope angle  $\theta = 30, 45$ , and  $60^\circ$ , respectively. There is no significant difference in the depositional shape at a slope height of  $H = 0$  mm. A possible reason for the small effect of granular diameter is that the flow height  $H = 0$  mm is a test condition that only collapses as in the dam-break type angle of repose test, and the short flow distance reduces the number of collisions between granular materials. At the slope height  $H = 400$  and  $800$  mm, the larger granular diameter tends to increase the runout distance under the conditions of slope angle  $\theta = 30$  and  $45^\circ$ . This trend is consistent with the results of previous studies [4] that the larger the granular diameter, the longer the distance attained. However, under the condition of slope  $\theta = 60^\circ$ , the runout distance of the large rock mass is not maximum, which is different from the previous result [4] that the larger the granular diameter, the longer the runout distance.

### Distribution of flow velocity

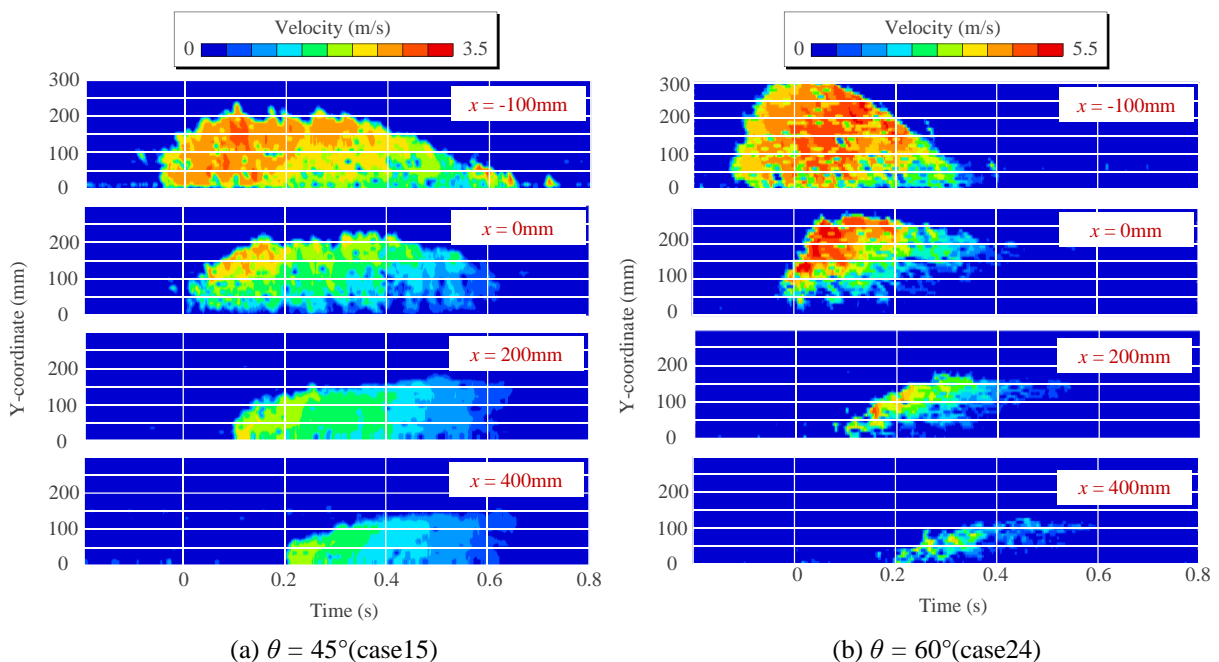
In contrast to the previous finding that the larger the granular diameter, the longer the runout distance [4], the flow velocity distribution of granular avalanche was investigated in this study to clarify

why the condition with the largest granular diameter does not maximize the runout distance under the condition with the slope angle  $\theta = 60^\circ$ .

First, we focus on the case  $\theta = 45^\circ$ ,  $H = 400$  mm as the flow behavior under the conditions that resulted in a longer runout distance for larger granular diameters. Fig. 9 shows the distribution of flow velocity for medium and large granular material. It is found that the thickness of the flow layer tends to become thicker as the granular diameter increases. The reason for the longer runout distance for larger



(a) Medium (case23) (b) Large (case24)  
Fig. 10 Velocity distribution;  $\theta = 60^\circ$ ,  $H = 400$  mm



(a)  $\theta = 45^\circ$  (case15) (b)  $\theta = 60^\circ$  (case24)  
Fig. 11 time contours of flow velocity;  $H = 400$  mm, Large granular material

granular material may be that the momentum of the following granular materials pushing the preceding granular materials is greater and the velocity is less likely to decrease as the layer thickness increases, in addition to the fewer collisions per particle as previously found [10].

We then turn our attention to the case  $\theta = 60^\circ$ ,  $H = 400$  mm, where the large granular material did not have the maximum runout distance. Fig. 10 shows the flow velocity distribution for medium and large granular material. Under the condition of large granular material, a dead zone occurs immediately after the granular avalanche impact on the horizontal plane, where the velocity near the toe of slope becomes almost zero. In particular, the dead zones of large granular material occur earlier than those of medium granular material, indicating that the dead zones have a wider developmental area than those of medium granular material.

Fig. 11 shows time contours of flow velocity for medium and large granular materials at  $\theta = 60^\circ$ . The vertical axis is the vertical layer thickness, and the horizontal axis is the time. In the figures,  $t = 0$  s is the moment when the leading edge of the granular avalanche impacts the horizontal plane. These figures indicate that the occurrence of the dead zone is not instantaneous but is a continuous phenomenon that occurs immediately after the impact of the granular avalanche on the horizontal plane.

Comparing Fig. 9 and Fig. 10, at  $\theta = 45^\circ$ , where no dead zone develops, the granular materials on the horizontal plane  $x \geq 0$  have a small velocity gradient from the bottom to the surface, indicating that the sliding mode is such that the preceding granular materials are pushed out by the following granular materials. On the other hand, at  $\theta = 60^\circ$ , where the dead zone develops significantly, the granular materials on the horizontal plane have a large velocity slope angle from the bottom to the surface, and the mode is such that the following granular materials overtakes the preceding granular materials in the vicinity of the toe of slope.

## EFFECT OF GRANULAR DIAMETER ON RUNOUT DISTANCE WITH SECONDARY SLOPE FAILURE

Fig. 12 shows the final depositional shape of the experimental case in which a 40 kg granular material was collapsed at a slope angle of  $\theta = 45^\circ$  and a slope height of  $H = 800$  mm, followed by another 40 kg granular material. The first slope failure resulted in a longer runout distance for larger granular diameters, like the condition of Fig. 7 for slope height  $H = 800$  mm. On the other hand, in the second slope failure, the runout distance was not longer than in the first failure, regardless of the granular diameter. This may be because the granular materials deposited in the first collapse increased the roughness of the toe of

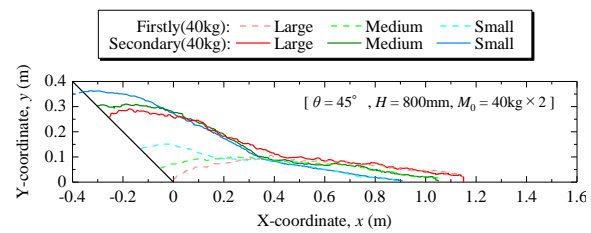


Fig. 12 Final deposition shapes;  
 $\theta = 45^\circ$ ,  $H = 800$  mm,  $M_0 = 40 \text{ kg} \times 2$  (case31-33)

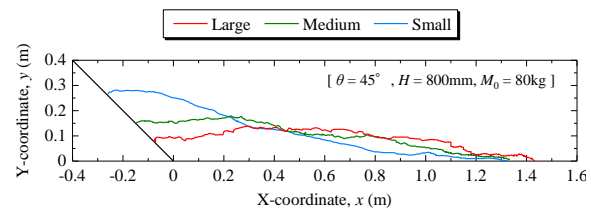


Fig. 13 Final deposition shapes;  
 $\theta = 45^\circ$ ,  $H = 800$  mm,  $M_0 = 80 \text{ kg}$  (case28-30)

slope and thus increased the frictional resistance.

Fig. 13 shows the final depositional shape for a slope angle  $\theta = 45^\circ$ , slope height  $H = 800$  mm, and collapse mass  $M_0 = 80$  kg. Both experimental conditions in Fig. 12 and Fig. 13 are for a total collapse mass of 80 kg. It can be seen from this that an 80 kg collapse at one time has a greater runout distance than a collapse divided into primary and secondary slope failures. As discussed in Fig. 9, this may be due to the possibility that the runout distance is greater under the condition where the slope failure occurs all at once due to the greater thickness of the flow layer.

Fig. 12 and Fig. 13 show the final depositional shape for a slope angle  $\theta = 45^\circ$ , slope height  $H = 800$  mm, and collapse mass  $M_0 = 80$  kg. Both experimental conditions have been for a total collapse mass of 80 kg. It can be seen from this that an 80 kg collapse at one time, in Fig. 13, has a greater runout distance than a collapse divided into primary and secondary slope failures, in Fig. 12. As discussed in Fig. 9, this may be due to the possibility that the runout distance is greater under the condition where the slope failure occurs all at once due to the greater thickness of the flow layer.

## CONCLUSIONS

In this study we investigated the effect of granular diameter on the runout distance from the comparative examination of the test results. The observed behavior can be summarized as follows:

- 1) The observed runout behavior of rock debris is accordance with previous findings that the rock debris with larger grain diameter runout through the greater runout distance.
- 2) In the case of sliding mode in which the flowing

rock debris push out the preceding ones at the toe of slope, the change in the flow layer thickness of the rock debris with different grain diameter contributes to the velocity decay on the horizontal plane and may be an important parameter in the prediction of runout distance.

- 3) The runout distance does not increase with increasing granular diameter under the condition that a dead zone develops at the toe of slope, which is a mode where the preceding granular materials are surmounted by the following ones.
- 4) In the slope failure in which the same rock debris volumes flow separately in the two steps, primary and secondary slope failures, the runout distance of the secondary slope failure is not larger than that of the primary slope failure, regardless of the granular diameter.
- 5) Even if the total collapsing volume is same, the runout distance became greater in the case where the entire mass collapsed quickly, compared with the case where the rock mass collapsed in the double process of primary and secondary slope failures.

## ACKNOWLEDGMENTS

The authors are grateful for the financial support provided by the Japan Society for the Promotion of Science (Grant-in-Aid for Young Scientists 21K14239) and Toyohashi University of Technology (Grant-in-Aid for activating education and research).

## REFERENCES

- [1] Cundall, P. A. and O. D. L. Stack.: A Discrete Models for Granular Assemblies, *Geotechnique*, Vol.29, No.1, pp.47-65, 1979.
- [2] Nakase, H., Iwamoto, T., Cao, G., Tabei, K., Sakaguchi, H., Matsushima, T.: Reproduction analysis of actual slope collapse and parametric study for evaluation of the deposit volume by a simple model of distinct element method, *JSCE Journal of Earthquake Engineering*, Vol.73, No.4, I\_694-I\_703, 2017.
- [3] Nakase, H., Cao, G., Tochigi, H., Tabei, K.: A method to access collision hazard of falling rock due to slope collapse application of DEM on modeling of earthquake triggered slope failure for nuclear power plants, *JSCE Journal of Earthquake Engineering*, Vol.71, No.4, I\_476-I\_492, 2015.
- [4] Tochigi, H.: Investigation of Influence of Falling Rock Size and Shape on Traveling Distance due to Earthquake, N09021, 2010.
- [5] Bartali, R., Rodríguez Liñán, G.M., Torres-Cisneros, L., Pérez-Ángel, G., Nahmad-Molinari, Y.: Runout transition and clustering instability observed in binary-mixture avalanche deposits, *Granular Matter*, Vol.22, No.30, 2020.
- [6] Mollon, G., Richefeu, V., Villard, P., Daudon, D.: Discrete modelling of rock avalanches: sensitivity to block and slope geometries, *Granular Matter*, Vol.17, No.5, pp.645–666, 2015.
- [7] Watanabe, D, Moriguchi, S., Terada, S.: Effect of particle size distributions on granular flow simulations using discrete element method, *JSCE Journal of Geosphere Engineering*, Vol.77, No.4, I\_392-I\_402, 2021.
- [8] Bryant, S.K., Take, W.A., Bowman, E.T.: Observations of grain-scale interactions and simulation of dry granular flows in a large-scale flume, *Canadian Geotechnical Journal*, Vol.52, pp.638-655, 2015.
- [9] Zhou, G.G.D., Sun, Q.C.: Three-dimensional numerical study on flow regimes of dry granular flows by DEM, *Powder Technology*, Vol.239, pp.115-127, 2013.
- [10] Naito, N., Yoshida, I., Nakase, H., Tochigi, H.: Probability Distribution of Falling Rock by Experiments and a Method to Assess Collision Hazard, 6th International Conference on Earthquake Geotechnical Engineering Paper, No.279, 2015.



# INFLUENCE OF TEMPERATURE ON ELASTIC STIFFNESS AND TIME-DEPENDENT DEFORMATION BEHAVIOURS OF HOSTUN SAND IN TRIAXIAL COMPRESSION TEST

Kosit Jariyatatsakorn<sup>1</sup> and Warat Kongkitkul<sup>2</sup>

<sup>1,2</sup>Department of Civil Engineering, Faculty of Engineering,  
King Mongkut's University of Technology Thonburi, Thailand

## ABSTRACT

Elastic stiffness and creep deformation of Hostun sand, at different shear stress levels and temperatures, were investigated in this study. Hostun sand is widely treated as a standard sand used in geotechnical engineering research. A comprehensive series of temperature-controlled triaxial compression tests were performed on air-dried samples. During the drained heating stage, the sand sample was heated to different target temperatures (i.e., 30, 45 and 60°C), after which the temperature is held constant. In the shearing stages, the small strain-amplitude cyclic loading (CL) was applied for evaluating the equivalent elastic Young's modulus ( $E_{eq}$ ) at different shear stress levels. Sustained loading (SL) was also applied to investigate the creep behaviour. The results from the experiment are as follows. Shear strengths, both at the peak and residual stages, decrease with increasing temperature. The  $E_{eq}$  increases with increasing shear stress level, but at the same shear stress level, it decreases with increasing temperature. The  $E_{eq}$  can be expressed as a function of the shear stress level and temperature. The axial creep strain increases with increasing shear stress level and temperature.

*Keywords: Creep, Elasticity, Hostun sand, Temperature, Triaxial compression test*

## INTRODUCTION

Nowadays, the geotechnical engineering projects tend to be more related to the temperature, for example, energy piles [1]-[4], the energy-efficient techniques for space heating and cooling via borehole heat exchangers (BHE) [5]. Thermally-active MSE wall with additional plumbing for heat exchange [6], and nuclear waste disposal [7]. Therefore, soil and geogrid are likely subjected to non-isothermal conditions because of cyclical change in temperature. From previous studies, number of research on thermo-mechanical behaviour of clay soil under various temperature-controlled tests has gradually increased over the years, for instance, triaxial compression (TC) test, one-dimensional compression, and isotropic compression [8]-[11]. Conversely, the thermal effect on the behaviour of granular materials, especially sand, has been rarely reported, for example, the stress-strain behaviour of densely compacted sand at high pressure and temperature to fill containers of waste nuclear fuel, thermal effect on the shear strength and volume change behaviour of saturated sand [12]-[14]. Particularly, the temperature effect combined with the time effect (e.g., creep behaviour) has rarely been comprehensively investigated.

For long-term settlement, known as secondary consolidation, the classical consolidation theory is commonly applied to determine the settlement of soils. In fact, the deformation of the soils has occurred as not only the elastic deformation but also inelastic

deformation. The increment of inelastic strain is developed by plastic yielding that is controlled by the viscous effect and inviscid cyclic loading effect [15]. Therefore, to precisely predict the long-term deformation of soils, Both elastic and viscous properties should be concerned.

The elastic properties of geomaterials were investigated with various aspects by plenty of studies. For example, Hoque and Tatsuoka [16] performed a series of the large triaxial specimen on various granular materials (e.g., Toyoura sand, Hostun sand, Ticino sand) and found that elasticity is a stress-dependent property. This result is corresponding to the study of Kohata et al. [17], in which the tests on small triaxial apparatuses with air-dried Hostun sand were performed. Moreover, a pair of local deformation transducers (LDTs) was attached to the surface of the specimen for precise measurement of axial strain to compare with the elastic modulus obtained from an external measurement. Duttine et al. [18] studied anisotropic small strain elastic properties on Hostun and Toyoura sands in triaxial compression test. The elastic properties were measured by both static and dynamic methods (i.e., small cyclic loadings and shear, and compression wave propagations). The test results showed that the elastic properties are non-linearly related with stress state for both Hostun and Toyoura sands. Thus, the elastic property from numerous previous studies is stress state-dependent or it can be understood that the elastic property exhibited a hypo-elastic manner. Nevertheless, the study of elastic property with the



temperature effect are rarely limited. Mitchell [19] showed that the elastic modulus of most engineering materials is temperature dependent. Therefore, the elastic characteristics of geomaterials are likely temperature-dependent too. Punya-in and Kongkitkul [20] performed a series of triaxial compression test on a clean sand. The elastic property was evaluated in terms of  $E_{eq}$  by performing small unload-reload cycles after SL test. The results revealed that the  $E_{eq}$  decreased with increasing temperature. However, in the past studies, the thermal effect on the elastic modulus of geomaterials is still ambiguous because of different experimental conditions (e.g., the studies of Cekerevac and Laloui, Liu et al., and Murayama [9], [13], [21])

Moreover, when geomaterials are subjected to SL, the developing deformation is called creep. There are several factors which affect to the creep deformation. Enomoto et al. [22] revealed that the creep deformation depends on loading rate, particle shape, stress level and so on. These factors can be explained by the viscous properties of geomaterials. Tatsuoka et al. [23] explained the creep deformation as a response by the viscous properties of geomaterials with an aid of non-linear three-component (NTC) model.

However, the studies of thermal effect on creep behaviour of geomaterials are limited. For example, Tsutsumi and Tanaka [11] investigated the combined effects of temperature and strain rate of clayey soils and found that the clay specimen exhibited peculiar viscous behaviour (i.e., non-isotach viscosity type) of clay when the temperature is high, and the strain rate is low. In addition, Kaddouri et al. [24] performed a series of creep test by using the temperature-controlled oedometer on a saturated compacted clayey soil. The test results showed that the creep deformation increases with stress level and temperature.

In this study, the creep deformation and elastic Young's modulus of Hostun sand were investigated in temperature-controlled triaxial compression test. Air-dried sand specimens were used in this study to eliminate the difference of thermal expansion between the solid and liquid in the specimen, and to avoid the pore pressure induced by the heating, consolidation, and shearing stages. The elastic properties were presented in terms of  $E_{eq}$  by performing the CL test, while the creep strain was obtained by performing SL test at different stress levels and temperatures.

## EXPERIMENTAL SETUP

### Test material

Hostun sand is widely used in the geotechnical engineering research in France. The particle shape is sub-angular to angular. It has specific gravity ( $G_s$ ) of

2.584, an effective particle size ( $D_{50}$ ) of 0.302 mm, and a coefficient of uniformity ( $C_u$ ) of 1.999. The maximum and minimum void ratios are 0.854 and 0.522, respectively, which are determined in accordance with JIS A 1224:2009 [25]. Its gradation curve, index properties, and particle shape are shown in Fig. 1.

### Test apparatus

A temperature-controlled triaxial compression test apparatus (Fig. 2), used in this study was developed by Punya-in and Kongkitkul [20]. The temperature was measured by two sets of the k-type thermocouple. One of them was installed inside the triaxial cell for measuring the temperature surrounding the specimen (No.⑥ in Fig. 2), and the other (No.⑤ in Fig. 2) at the outflow of thermal controller for the feedback control of the circulating water. The temperature value of No.⑤ was recorded by a computer. The cell water temperature was elevated to the target temperature by using a heater and a pair of diaphragm pumps, which were used to circulate the water. The cell pressure is automatically controlled by an electro-pneumatic (E/P) transducer. The complicated shear loading type (e.g., small-strain cyclic loading, sustained loading) can be achieved by the precise gear loading system, which is displacement-controlled. It can respond sharply to control the loading directions and speed [26].

In this study, some parts of this apparatus were improved. A pair of diaphragm pumps were used to solve the durability problem due to the long-term operation during SL test. And the heat insulator (No.② in Fig. 2) was installed below the outside load cell to eliminate the effect of heat transferred from the inside of the cell chamber.

### Specimen preparation

The specimen was basically cylindrical in shape (150 mm in height and 70 mm in diameter). Hostun sand sample was prepared by pluviating the sand particles through the air into a split mould, adhered which a rubber membrane to the inner surface by suction around 20 kPa. The multiple-sieving apparatus was used to achieve high uniformity. At the top cap and pedestal, one layer of silicone grease having a thickness of 50  $\mu\text{m}$  is placed to reduce friction at the ends of sample [28]. After sealing the membrane with the top cap, a partial vacuuming with 20 kPa was applied to the specimen. Then, the split mould was dissembled. The specimen was left for reaching an equilibrium stage for 30 minutes (see Fig. 3). Note that the dummy load cell was installed inside the triaxial chamber to extend the length of piston. Then, the thermocouple was installed. Next, after sealing the triaxial chamber, the partial vacuuming was replaced

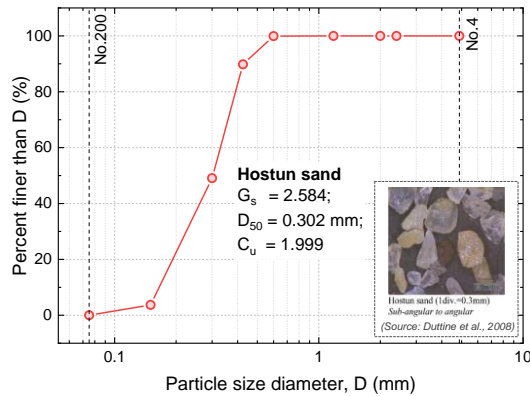


Fig. 1 Gradation curve and particle shape of Hostun sand used in present study (modified from Duttine et al. [27]).

by the cell water pressure until the cell water pressure reached 20 kPa. Then, the specimen was isotropically consolidated until the confining pressure achieved 30 kPa. The next stage is drained heating stage. In this stage, the cell pressure was maintained constant at 30 kPa, while the cell water was circulated to the heater by a pair of diaphragm pumps until reaching the target temperature. After that, the waiting period was required for allowing the specimen to achieve an equilibrium. The time spent for this period was one hour (60 mins), which is verified by the measured axial strain during drained heating as shown in Fig. 4. Even though the cell water temperature had been kept

constant at the target temperature since the first 40 minutes, the axial strain of the specimen continued to expand until reaching equilibrium.

### Test program

In this study, a comprehensive series of shear loading histories were employed to examine the elastic and creep deformation behaviours of Hostun sand. The loading type consists of two types, which can be described as follows.

Loading type a) is continuous monotonic loading (ML) at a constant strain rate. The basic strain rate is 0.075 %/min for each target temperature.

Loading type b) is sustained loading and cyclic loading (SL-CL) test. It starts from ML at the basic strain rate until reaching the target stress ratio ( $R$ ), which is defined as the ratio of the major to minor principal effective stress (i.e.,  $R = \sigma'_1 / \sigma'_3$ ). At the target stress ratio, SL is hold for three hours to observe the creep deformation. Then, the CL with a double amplitude ( $\Delta q$ ) of 25 kPa is applied for 10 cycles to evaluate the  $E_{eq}$ . After finishing in CL, ML is restarted to the next target  $R$  value. The target  $R$  value in this loading type consists of 2.0, 2.5, 3.0, 3.5, 4.0, and 5.0. To avoid the diaphragm pump overloading, this loading type was divided into two sets using two different specimens. SL-CL tests were performed at three different  $R$  values in a single specimen as shown in Fig. 5 and listed in Table 1.

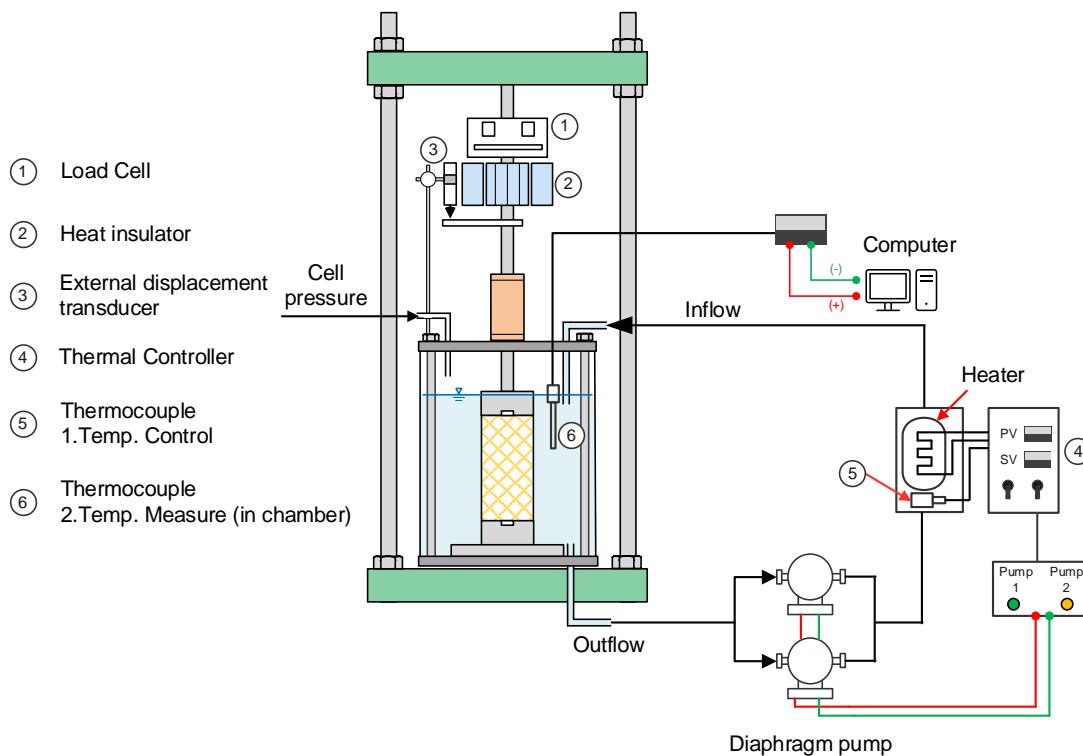


Fig. 2 Temperature-controlled triaxial compression test apparatus developed by Punya-in and Kongkitkul [20]

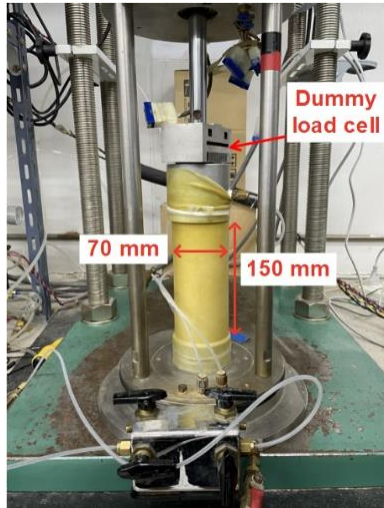


Fig. 3 Preparation of a Hostun sand sample for triaxial compression test during applying partial vacuuming of 20 kPa.

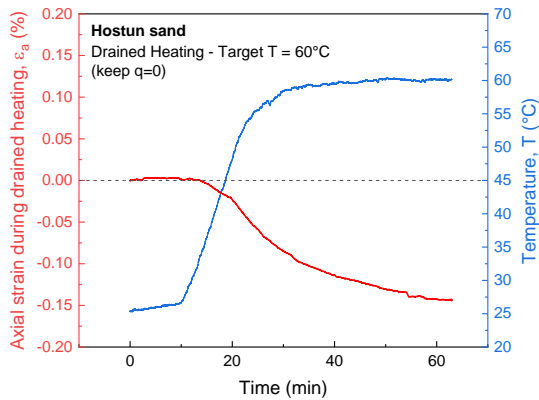


Fig. 4 Time histories of axial strain and cell water temperature during drained heating stage.

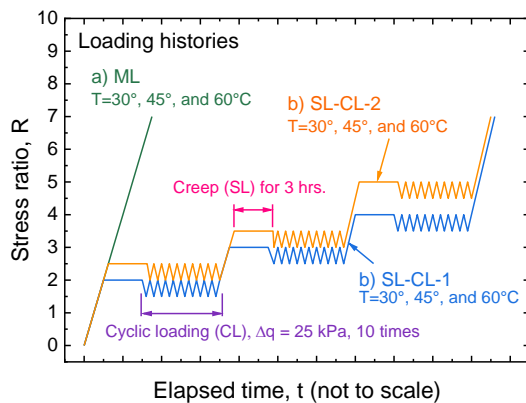


Fig. 5 Illustration of time histories of stress ratio ( $R$ ) for loading types a) and b) according to the test program.

Table 1 Test program and details of Hostun sand in present study

Test No.	Loading type	$T$ (°C)	Target $R$	$e_0$ (-)	$D_r$ (%)
1	a) ML	30	-	0.6371	86.00
2		45		0.6232	89.82
3		60		0.6503	82.37
4	b) SL-CL-1	30	2, 3, 4	0.6403	85.13
5		45		0.6395	85.35
6		60		0.6391	85.45
7	b) SL-CL-2	30	2.5, 3.5, 5	0.6426	84.49
8		45		0.6373	85.94
9		60		0.6462	83.52

For each loading type mentioned above, the cell water temperature is kept constant at either 30°C, 45°C, or 60°C throughout the shearing process. This range of temperature is consistent with the value used in the previous studies with sands by Liu et al. [13], [14], He et al. [29], and Punya-in and Kongkitkul [20]. Moreover, there are also limitation of the temperature-controlled triaxial testing in present study in that: i) the cell pressure was only 30 kPa for avoiding any damage to the heater and diaphragm pumps, ii) there was no system to cool down the cell water temperature to achieve the value below the room temperature, and iii) the maximum temperature was not exceeded 60°C for avoiding any damage to the measuring devices such as pressure transducer.

## TEST RESULTS AND DISCUSSION

### Influence of temperature on shear strength

Figure 6 shows the relationship between stress ratio ( $R$ ) and axial strain ( $\epsilon_a$ ) obtained by continuous monotonic loading (ML) (i.e., loading type a)) at constant strain rate for different temperatures. It can be readily seen that the specimens were degraded by the increasing of temperature. The shear strength of specimen can be expressed in terms of internal friction angle ( $\phi$ ), which is shown in Table 2. The  $\phi$  values can be determined in Eq. (1) because the sand sample in experiment was clean without any fines and the cohesion was assumed null. The  $\phi_{peak}$  value was the internal friction angle at the peak state, while the  $\phi_{res}$  value the internal friction angle at the axial strain of 14%.

$$\phi = \sin^{-1} \left( \frac{R-1}{R+1} \right) \quad (1)$$

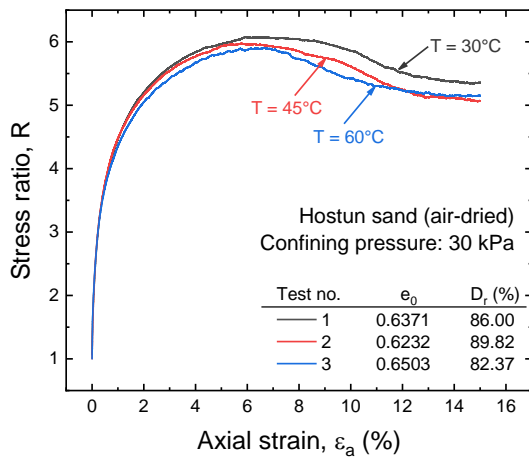


Fig. 6  $R - \varepsilon_a$  relationships by ML tests for different constant temperatures.

Table 2 The internal friction angle of Hostun sand from continuous ML test with different constant temperature

$T$ (°C)	$R_{peak}$	$R_{res}$	$\phi_{peak}$	$\phi_{res}$
30	6.068	5.378	45.81	43.35
45	5.969	5.110	45.48	42.27
60	5.888	5.149	45.20	42.43

### Influence of thermal expansion during drained heating stage

#### Determination of final void ratio after drained heating

Thermal expansion is obviously related to the change in temperature. Therefore, the thermal expansion of sand solids should partially be responsible to the temperature effects. During drained heating, the thermal expansion can occur from the solid skeleton and the air in the specimen. Due to the specimens were air-dried, the volume change could not be directly measured during drained heating. Thus, the measured axial strain was used to determine the specimen volume change. The volumetric strain ( $\Delta \varepsilon_{vol}$ ) can be estimated from the axial strain ( $\Delta \varepsilon_a$ ) as expressed in Eq. (2)

$$\Delta \varepsilon_{vol} \approx 3\Delta \varepsilon_a \quad (2)$$

Benjelloun et al. [30] showed that silicon dioxide (Silica,  $\text{SiO}_2$ ) is the main chemical composition of Hostun sand by using the X-ray fluorescence spectrometry. Therefore, the linear thermal expansion ( $\alpha$ ) of silica sand, which is equal to  $10.4 \times 10^{-6} / ^\circ\text{C}$

[31], was used to calculate the volumetric thermal expansion.

During the drained heating, the volumetric thermal expansion ( $\Delta V_s$ ) of the sand solids can be defined as follows:

$$\Delta V_s = \beta_s (T - T_0) V_s \quad (3)$$

where  $\beta_s$  is the volumetric coefficient of thermal expansion of solid skeleton,  $V_s$  is the volume of the solid skeleton,  $T$  is the target temperature, and  $T_0$  is the reference temperature, which was  $30^\circ\text{C}$  in this study. The  $\beta_s$  value can be estimated from linear thermal expansion ( $\alpha$ ) as  $\beta_s \approx 3\alpha$ . Thus, the  $\beta_s$  equal to  $3.12 \times 10^{-5} / ^\circ\text{C}$  was used in this study. This value is nearly the same as the one reported in Liu et al. [14], Campanella and Mitchell [32]. From Eqs. (2) and (3), the void ratio after drained heating can be determined by the phase calculation.

#### Internal friction angle decreased as the initial void ratio decreased

As mentioned above, the thermal expansion induced the decreasing of void ratio during drained heating prior to the shearing stage. From the studies in the past, it is known that the peak internal friction angle decrease with increasing initial void ratio ( $e_0$ ) (with decreasing relative density,  $D_r$ ) at the start of shearing as shown in Fig. 7. From the collected data from many studies of several sand, a regression line of the  $\phi_{peak} - D_r$  relationship can be proposed to estimate the reduction of  $\phi_{peak}$  value by the decreasing of relative density.

Figure 8 shows the relationship between the axial strain at the equilibrium stage after drained heating and temperature. The reference temperature was equal to  $30^\circ\text{C}$ . It can be found that the specimens were dilated by thermal expansion as a rate of  $-0.00656\% / ^\circ\text{C}$ . From this information, the reduction of peak internal friction angle at any temperature ( $\phi_{peak,T}$ ), can be calculated, and then the reduction of peak stress ratio ( $R_{peak}$ ) can be realised. To consider the effects of temperature increase on the reduction of strength on sand, the temperature effect ( $A^f$ ) was proposed in this study, which was modified from Chantachot et al. [33], as expressed in Eq. (4)

$$A^f = f(T) = \frac{R_{peak} - 1}{R_{peak,0} - 1} = 1 - a \left( \frac{T - T_0}{T_0} \right)^b \quad (4)$$

where  $R_{peak}$  is the peak stress ratio at given temperature,  $R_{peak,0}$  is the peak stress ratio at the reference temperature, and  $a$  and  $b$  are constant. The values of  $A^f$  obtained from i) the reduction of peak

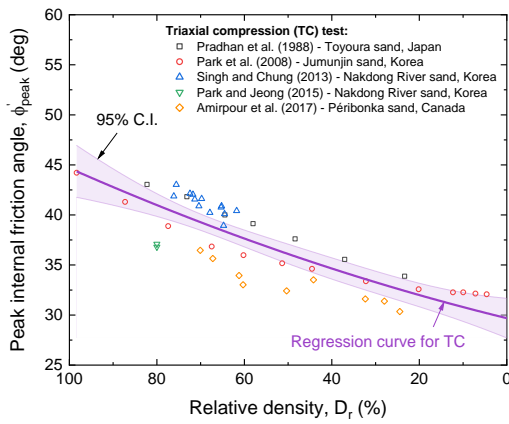


Fig. 7 Variation of peak internal friction angle with relative density of various sands collected from the literature.

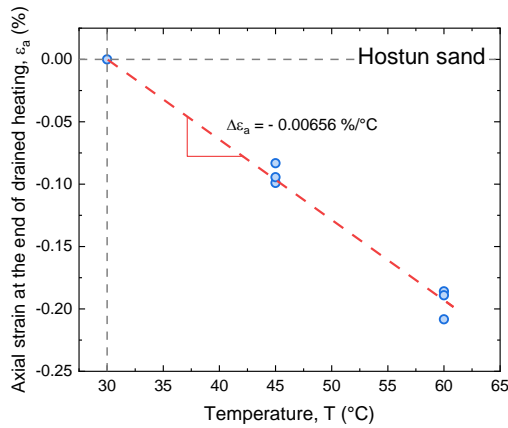


Fig. 8 Relationship between the axial strain at the end of drained heating and temperature.

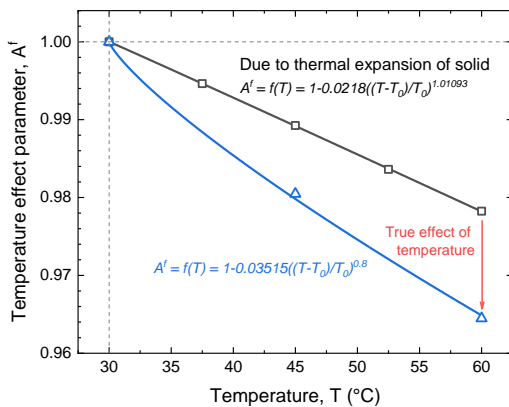


Fig. 9 Temperature effect parameter ( $A^f$ ) as a function of temperature.

stress ratio due to the thermal expansion by the computation of changing void ratio; and ii) the peak stress ratio at given temperature by the experiment

(loading type a) ML), were plotted together against the temperature as shown in Fig. 9. The thermal expansion is only a part of temperature effects. That is, the effect of temperature on the reduction of shear strength of Hostun sand cannot just simply be explained by the effect of thermal expansion. There is still true effect of temperature existing as depicted in Fig. 9.

### Stress-strain relationship during cyclic loading

Figure 10 shows the relationships between stress ratio,  $R$ , and axial strain,  $\epsilon_a$ , for loading type b) SL-CL compared with the continuous ML at temperature ( $T$ ) is equal to 30°C. SLs were performed for three hours and then, CLs were performed by unloading-reloading for 10 cycles with  $\Delta q$  of 25 kPa at different target  $R$  values. It can be found that the  $R - \epsilon_a$  relationships exhibited a high stiffness zone when the ML was restarted after the finishing of CL for each stress ratio. The stiffness value in this zone is very close to the elastic stiffness. Moreover, the  $R - \epsilon_a$  relationship shows a tendency to re-join the respective ones that could be obtained by continuous ML tests. Therefore, it can be interpreted that the peak shear strength is maintained, or in others word, independent of loading historied applied before reaching the peak. Similar trend of behaviours can also be observed for the tests performed with the other temperatures

### Determination of elastic stiffness

To determine  $E_{eq}$ , the stress-strain during CL was plotted in the relationship of major principal stress ( $\sigma_1$ ) against with axial strain ( $\epsilon_a$ ), which the unloading for the last five loops for the respective CL stages were selected as shown in Fig. 11. From Fig. 11, it can be found that the unloading branch of  $\sigma_1 - \epsilon_a$  relationship is quite linear, which exhibits a highly linear-elastic behaviour. The slope of this linear relation for each CL loop is the  $E_{eq}$ . The  $E_{eq}$  value is quite constant during the last five unload-reload cycles. Moreover, the R-square values obtained by linear regression were presented for respective  $\sigma_1 - \epsilon_a$  relationships. This fact shows that the deformation during these unloading branches is essential elastic. The  $E_{eq}$  values from each loop were averaged for respective stress ratios, and then it was plotted in the full-log scale against the vertical stress ratio ( $\sigma_1 / \sigma_0$ ) for respective temperatures as shown in Fig. 12. Note that  $\sigma_0$  is the reference stress equal to 100 kPa. It can be readily seen that the  $E_{eq}$  is not constant but increases with an increase in stress level, which the dependency of elasticity with the stress level can be expressed in Eq. (5).



$$E_{eq} = E_0 (\sigma_1 / \sigma_0)^m \quad (5)$$

where  $m$  is constant.

*Comparison the elastic stiffness to the previous studies*

Elastic Young's modulus of standard sands at small-strain level obtained from the static method are compared as shown in Fig. 13. Punya-in and Kongkitkul [20] investigated the elastic stiffness of a riverbed sand in Thailand by performing the temperature-controlled triaxial compression tests with varying temperatures, which are the same as the ones in this study. The increasing temperature decreases the elastic stiffness of granular materials. Hoque and Tatsuoka [16] performed TC tests on Toyoura and Hostun sands at room temperature (25°C) to evaluate the anisotropic elasticity of granular materials. The axial strain was measured by using a pair of local deformation transducers (LDTs). LDTs measure the axial deformation locally, and thus the measured value is free from bedding errors and system compliance [17]. However, due to the increasing of temperature in the chamber, it is inevitable to evaluate the axial strain by the external measurement (e.g., a linearly variable differential transformer, LVDT) for avoiding the measuring errors by the fact that the temperature alters the LDT's strain measured by the attached strain gauges. In summary, the trend of variation of  $E_{eq}$  with the stress level of Hostun sand determined in this study agree well with the one reported in Hoque and Tatsuoka [16]. However, at the same stress level, the  $E_{eq}$  determined in this study is lower because an LVDT was used to externally measure the axial deformation, while there was no LDTs installed. Although different experimental devices were used for measuring the axial strain, the elastic properties obtained from all the collected data show that the elasticity of different granular materials is of hypo-elasticity.

### Creep deformation with temperature changes

Figure 14 shows the time histories of axial strain during creep for 3 hours at different stress ratio values for the temperature of 30°C. It can be obviously seen that the creep strain increase with increasing stress level. Moreover, Fig. 15 presents the axial strain at the end of SL (3 hours) for different stress ratio values and different temperatures together with its cumulative. It can be found that not only the stress level but also the temperature result in an increase in the creep strain. However, the influence of stress level is much more than that of temperature.

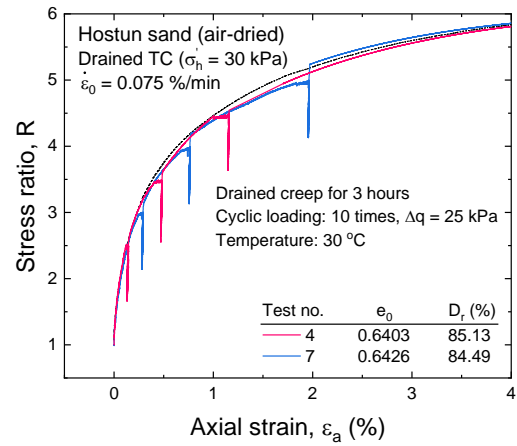


Fig. 10  $R - \varepsilon_a$  relationships with loading type b) SL-CL with  $T = 30^\circ\text{C}$ .

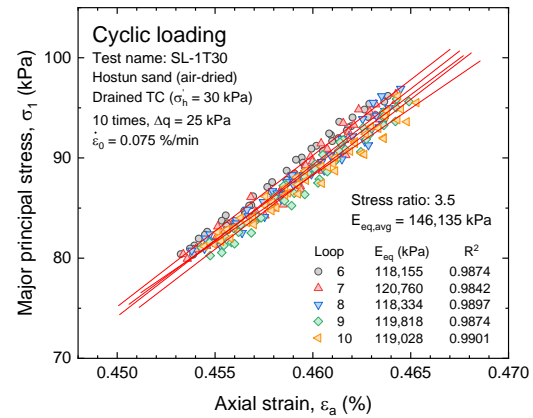


Fig. 11  $R - \varepsilon_a$  relationships during the last five unloading branches in the CL course at  $R = 3.5$  and  $T = 30^\circ\text{C}$ .

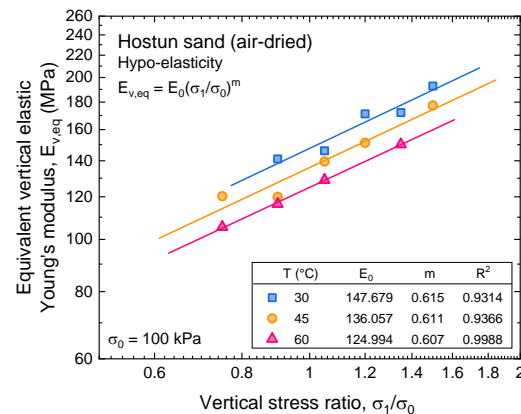


Fig. 12 Dependency of  $E_{eq}$  on the stress level and temperature with respectively fitted lines.



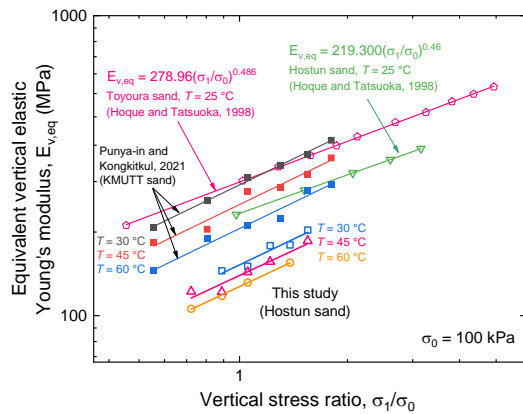


Fig. 13 Comparison of variation of  $E_{eq}$  of granular materials with the stress level and temperature.

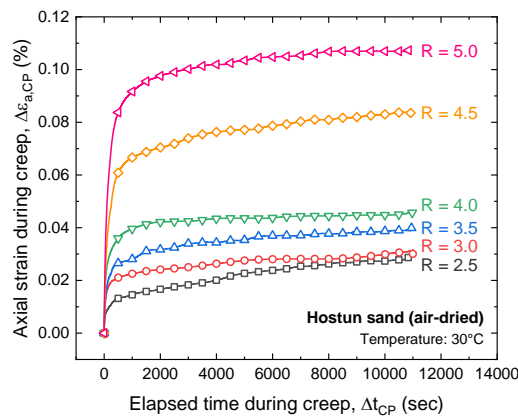


Fig. 14 Time histories of axial strain during creep by 3-hr SL at different stress ratio values with  $T = 30^\circ\text{C}$ .

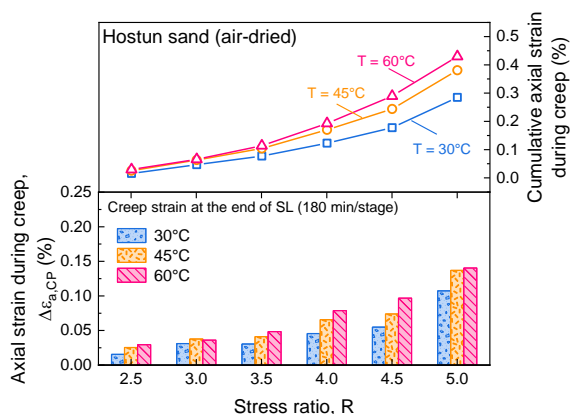


Fig. 15 Axial strain at the end of 3-hr creep and its cumulative for respective stress ratio values and different target temperatures.

## CONCLUSIONS

The following conclusions can be derived from the results of temperature-controlled triaxial compression test on Hostun sand performed in this study.

1. The peak internal friction angle decreases with increasing temperature.
2. Thermal expansion induces the dilation of sand solids when drained heating, which results in an increase in initial void ratio before shearing, and thus a reduction of the shear strength. However, its influence is only a part of temperature effects on the reduction of shear strength.
3. Elastic stiffness of Hostun sand clearly increases with the stress level, which is of hypo-elastic. Moreover, at the same stress level, the elastic stiffness decreases with increasing temperature.
4. Creep strain increases with increasing stress level and temperature. However, the influence of stress level on the creep strain development seems to be more dominant than that of temperature.

## ACKNOWLEDGMENTS

The authors are grateful to King Mongkut's University of Technology Thonburi (KMUTT) for the financial support granted to this research via The Petchra Pra Jom Klao PhD scholarship under contract Grant No. 7/2563. The authors would like to extend the appreciation to the Prof. Fumio Tatsuoka and Prof. Yoshiaki Kikuchi, Tokyo University of Science (TUS), Japan and Prof. Reiko Kuwano, Institute of Industrial Science (IIS), University of Tokyo, Japan for supporting the Hostun sand and others granular materials.

## REFERENCES

- [1] Brandl, H., Energy foundations and other thermo-active ground structures. *Geotechnique*, Vol.56, No. 2, 2006, pp. 81-122.
- [2] Knellwolf, C., Peron H., and Laloui L., Geotechnical Analysis of Heat Exchanger Piles. *Journal of Geotechnical and Geoenvironmental Engineering*, Vol.137, No.10, 2011, pp. 890-902.
- [3] Olgun, C. G., Ozudogru T. Y., and Arson C. F., Thermo-mechanical radial expansion of heat exchanger piles and possible effects on contact pressures at pile-soil interface. *Geotechnique Letters*, Vol.4, 2014, pp. 170-178.
- [4] Moradshahi, A., Faizal M., Bouazza A., and McCartney J. S., Effect of nearby piles and soil properties on thermal behaviour of a field-scale

- energy pile. *Canadian Geotechnical Journal*, Vol.58, No.9, 2021, pp. 1351-1364.
- [5] Zymnis, D. M. and Whittle A. J., Geotechnical considerations in the design of borehole heat exchangers. *Canadian Geotechnical Journal*, Vol.58, No.9, 2021, pp. 1247-1262.
- [6] Stewart, M. A., Coccia C. J., and McCartney J. S. Issues in the implementation of sustainable heat exchange technologies in reinforced, unsaturated soil structures. in *Geo-Congress 2014: Geo-characterization and Modeling for Sustainability*. 2014.
- [7] Gens, A., Sanchez M., Guimaraes L. D., Alonso E. E., Lloret A., Olivella S., Villar M. V., and Huertas F., A full-scale in situ heating test for high-level nuclear waste disposal: observations, analysis and interpretation. *Geotechnique*, Vol.59, No.4, 2009, pp. 377-399.
- [8] De Bruyn, D. and Thimus J.-F., The influence of temperature on mechanical characteristics of Boom clay: the results of an initial laboratory programme. *Engineering Geology*, Vol.41, No.1, 1996, pp. 117-126.
- [9] Cekerevac, C. and Laloui L., Experimental study of thermal effects on the mechanical behaviour of a clay. *International Journal for Numerical and Analytical Methods in Geomechanics*, Vol.28, No.3, 2004, pp. 209-228.
- [10] Abuel-Naga, H., Bergado D., Ramana G., Grino L., Rujivipat P., and Thet Y., Experimental evaluation of engineering behavior of soft Bangkok clay under elevated temperature. *Journal of geotechnical and geoenvironmental engineering*, Vol.132, No.7, 2006, pp. 902-910.
- [11] Tsutsumi, A. and Tanaka H., Combined effects of strain rate and temperature on consolidation behavior of clayey soils. *Soils and Foundations*, Vol.52 No.2, 2012, pp. 207-215.
- [12] Graham, J., Alfaro M., and Ferris G., Compression and strength of dense sand at high pressures and elevated temperatures. *Canadian Geotechnical Journal*, Vol.41, No.6, 2004, pp. 1206-1212.
- [13] Liu, H., Liu H., Xiao Y., and McCartney J. S., Effects of temperature on the shear strength of saturated sand. *Soils and Foundations*, 2018. Vol.58, No.6, 2018, pp. 1326-1338.
- [14] Liu, H., Liu H., Xiao Y., and McCartney J. S., Influence of Temperature on the Volume Change Behavior of Saturated Sand. *Geotechnical Testing Journal*, 2018. Vol.41, No.4, 2018, pp. 747-758.
- [15] Tatsuoka, F., Inelastic deformation characteristics of geomaterial, in *Soil stress-strain behavior: measurement, modeling and analysis*, Springer, 2007, pp. 1-108.
- [16] Hoque, E. and Tatsuoka F., Anisotropy in Elastic Deformation of Granular Materials. *Soils and Foundations*, Vol.38, No.1, 1998, pp. 163-179.
- [17] Kohata, Y., Tatsuoka F., Wang L., Jiang G., Hoque E., and Kodaka T., Modelling the non-linear deformation properties of stiff geomaterials. *Geotechnique*, Vol.47, No.3, 1997, pp. 563-580.
- [18] Duttine, A., Di Benedetto H., Pham Van Bang D., and Ezaoui A., Anisotropic Small Strain Elastic Properties of Sands and Mixture of Sand-clay Measured by Dynamic and Static Methods. *Soils and Foundations*, Vol.47, No.3, 2007, pp. 457-472.
- [19] Mitchell, J. K., Temperature effects on the engineering properties and behavior of soils. *Highway Research Board Special Report*, Vol.103, 1969, pp. 9-28.
- [20] Punya-in, Y. and Kongkitkul W. An experimental study on temperature effects on elastic and creep deformation behaviours of a sand. in *11th International Conference on Geotechnique, Construction Materials & Environment*, 2021, pp. 156-163
- [21] Murayama, S., Effect of temperature on elasticity of clays. *Highway research board special report*, Issue.103, 1969.
- [22] Enomoto, T., Kawabe S., Tatsuoka F., Di Benedetto H., Hayashi T., and Duttine A., Effects of particle characteristics on the viscous properties of granular materials in shear. *Soils and Foundations*, 2009. Vol.49, No.1, 2009, pp. 25-49.
- [23] Tatsuoka, F., Di Benedetto H., Enomoto T., Kawabe S., and Kongkitkul W., Various viscosity types of geomaterials in shear and their mathematical expression. *Soils and Foundations*, Vol.48, No.1, 2008, pp. 41-60.
- [24] Kaddouri, Z., Cuisinier O., and Masrouri F., Influence of effective stress and temperature on the creep behavior of a saturated compacted clayey soil. *Geomechanics for Energy and the Environment*, Vol.17, 2019, pp. 106-114.
- [25] Japanese Standards Association, Test method for minimum and maximum densities of sands (JIS A 1224: 2009). *Japanese Industrial Standards (in Japanese)*, 2009.
- [26] Santucci de Magistris, F., Koseki J., Amaya M., Hamaya S., Sato T., and Tatsuoka F., A triaxial testing system to evaluate stress-strain behavior of soils for wide range of strain and strain rate. *Geotechnical Testing Journal*, Vol.22, No.1, 1999, pp. 44-60.
- [27] Duttine, A., Tatsuoka F., Kongkitkul W., and Hirakawa D., Viscous behaviour of unbound granular materials in direct shear. *Soils and Foundations*, Vol.48, No.3, 2008, pp. 297-318.
- [28] Tatsuoka, F. and Haibara O., Shear resistance between sand and smooth or lubricated surfaces.

- Soils and Foundations, Vol.25, No.1, 1985, pp. 89-98.
- [29] He, S. H., Shan H. F., Xia T. D., Liu Z. J., Ding Z., and Xia F., The effect of temperature on the drained shear behavior of calcareous sand. *Acta Geotechnica*, Vol.16. No.2, 2021, pp. 613-633.
- [30] Benjelloun, M., Bouferra R., Ibouh H., Jamin F., Benessalah I., and Arab A., Mechanical Behavior of Sand Mixed with Rubber Aggregates. *Applied Sciences*, Vol.11, No.23, 2021, pp. 1-19.
- [31] Amonamarittakul, S., Choktaweekarn P., Sancharoen P., and Tangtermsirikul S., A Study of the Coefficient of Thermal Expansion of Paste, Mortar and Concrete. *Engineering Journal of Research and Development*, Vol.22, No.4, 2011, pp. 1-8.
- [32] Campanella, R. G. and Mitchell J. K., Influence of temperature variations on soil behavior. *Journal of the Soil Mechanics and Foundations Division*, Vol.94, No.3, 1968, pp. 709-734.
- [33] Chantachot, T., Kongkitkul W., and Tatsuoka F., Effects of temperature rise on load-strain-time behaviour of geogrids and simulations. *Geosynthetics International*, Vol.25, No.3, 2018, pp. 287-303.

# NUMERICAL ANALYSIS FOR VERTICAL RESPONSE OF SHALLOW SUCTION PILE

Donghyun Lee<sup>1</sup>, Jaewoo Jung<sup>1</sup>, Yoowon Lee<sup>1</sup>, Jaehun Ahn<sup>2</sup> and Jongwon Jung<sup>3</sup>

<sup>1</sup> Graduate Student, Department of Civil and Environmental Engineering, Pusan National University, Busan 46241, Republic of South Korea;

<sup>2</sup> Prof, Department of Civil and Environmental Engineering, Pusan National University, Busan 46241, Republic of South Korea, Tel: +82-51-510-7627, Fax: +82-51-513-9596, jahn@pusan.ac.kr, Corresponding author)

<sup>3</sup> Associate Prof, School of Civil Engineering, Chungbuk National University, Cheongju 28644, Republic of South Korea;

## ABSTRACT

Territory of human has been evolving and being expanded as technology and need for space grows. In civil engineering, the use of tunnel and underground spaces has a long history and now it is a vital component of life especially in urban area. Space travel and space terminal may become reality in a future, and the industry is trying to make it happen soon. Subsea space can also be an alternative to expansion of human territory. If engineers can develop and use underground space, why not underwater base. Recently, a project to build an underwater base has been initiated in Korea. As there is very few examples and application of underwater space, there is no well-developed guideline for design of underwater base. This study discusses a preliminary analysis of a shallow suction pile which may be used for the foundation system of underwater bases. The vertical response of a shallow suction caisson embedded in clay soils is mainly discussed here. Wider ranges of foundation types and dimensions will be investigated for fulfillment of the project.

*Keywords: Subsea space, Underground space, Underwater base, Offshore structure, Foundation*

## INTRODUCTION

While the development of space such as space exploration, the development of the space shuttle, and the construction of a space station is active, the development of the subsea space has not progressed relatively. Recently, as the need for securing future living spaces and developing deep-sea resources has been raised, technologies for subsea structures are being studied in developed countries. Currently, representative examples of subsea structures include offshore plant facilities for oil and gas production, and it consists of a platform exposed to the sea and various production and processing facilities installed below the sea level (Fig. 1). Unlike onshore structures, this subsea structure has a relatively small load due to their own weight, and repeated loads such as waves, tidal waves, earthquakes, currents, and currents act as the main loads, so considerable moments should be considered.

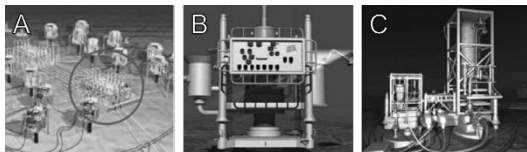


Fig. 1. Subsea structure: A. Manifold, B. Subsea tree, C. Subsea separator [1]

Here, most of the subsea structures fixed to the subsea ground use suction piles. Suction piles have been mainly used as the basis of platforms for deep-sea oil extraction in Northern Europe, such as the Netherlands and Norway, and are now widely used in offshore platforms and gravity infrastructure [2], and deep-sea subsea structure [3]. The suction pile is a cylinder-shaped structure with the upper part closed and the lower part open. It is a type of foundation that penetrates the ground using the difference of pressure. Since the foundation is penetrated using the pressure difference, the deeper the water depth, the greater the penetration force can be secured, and it is known as an excellent construction method for offshore workability and economy compared to other foundations because excavation and driving equipment are unnecessary. In this study, the vertical bearing capacity of the suction pile according to the undrained shear strength of the cohesive soil was investigated by performing a three-dimensional finite element analysis to investigate the bearing capacity of the suction pile in various clay soils.

## FINITE ELEMENT MODEL

In this study, Abaqus software [4] was used for the finite element analysis. The analysis target is as shown in Fig. 2, which is composed of the ground

and a cylindrical suction pile penetrated into the ground. In Fig. 2,  $D$  is the diameter of suction pile,  $L$  is the length of suction pile,  $W$  is the width of element model, and  $H$  is the depth of element model.

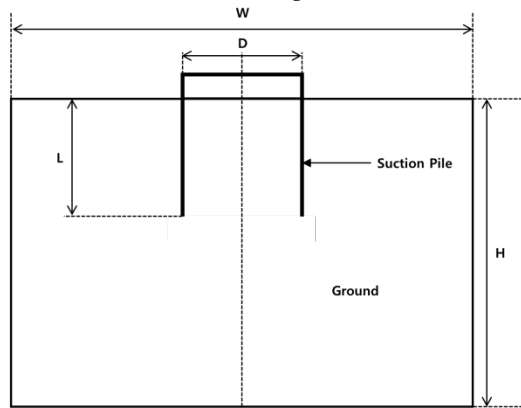


Fig. 2. Dimensions of finite element model

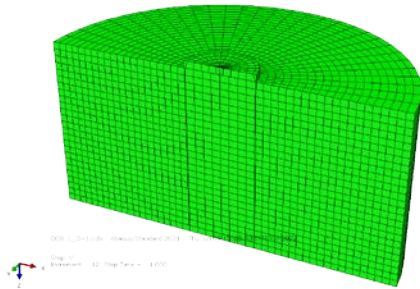


Fig. 3. Finite element model ( $L/D = 1$ )

For the overall size of the analysis model, the width was 5 times the pile penetration depth, that is,  $W = 5L$  was used, and the depth was used  $H = 2.5D$ . Based on the symmetry of the analysis target and load conditions, the finite element analysis used only the half-section of the 3D (3-dimensional) model. The finite element model used for the analysis is shown in Fig. 3 is given. The material properties of the suction pile model applied to the analysis were assumed to be linear elasticity and a circular cross-section with a diameter ( $D$ ) of 5 m, and a length ( $L$ ) to diameter ratio  $L/D = 1$  was used as a basic condition.

The ground for the installation of the suction pile was assumed to be undrained clay, and as shown in the von Mises fracture criteria and Table 1, undrained shear strength  $S_u$  corresponding to soft, medium, and hard clay, elastic modulus  $E = 20,000$  kPa, poisson ratio  $\nu = 0.45$  was applied. There is a relationship of  $\sigma_y = \sqrt{3} \times S_u$  between the Von Mises yield stresses  $\sigma_y$  and  $S_u$ . Therefore, in the actual analysis, yield stresses of 86 kPa, 173 kPa, 346 kPa were used to simulate the undrained shear strengths of 50 kPa, 100 kPa, 200 kPa. The elastic modulus of the ground is 20,000 kPa and the elastic modulus of the suction pile is much larger ( $10^7$  times), but in this research,

the analysis target is the bearing capacity of the suction pile, not the deformation of the ground. Since the modulus of elasticity of the ground is sufficiently smaller than the modulus of elasticity of the pile, this modulus of elasticity is not significant.

Table 1. Soil parameters used for numerical analysis

Parameter	Value		
	Soft Clay	Medium Clay	Stiff Clay
$\gamma_{sat}$ (kN/m <sup>2</sup> )	20		
$E$ (kPa)	20,000		
$\nu$	0.45		
$s_u$ (kPa)	50	100	200

## VERTICAL RESPONSE OF SUCTION PILE

In order to investigate the difference in vertical bearing capacity of the suction pile according to the undrained shear strength of the clay soil, a certain displacement was given to the upper part of the foundation to obtain a reaction force-displacement curve for the foundation. Based on this, the vertical bearing capacity of the foundation was calculated. Fig. 4 is the reaction force-displacement curve according to the undrained shear strength. Fig. As shown in Fig. 4, it can be seen that the bearing capacity of the foundation also increases as the undrained shear strength of the ground increases. This shows that when an additional load is applied to the foundation, the clay ground is consolidated, increasing the strength of the ground and affecting the vertical bearing capacity of the foundation.

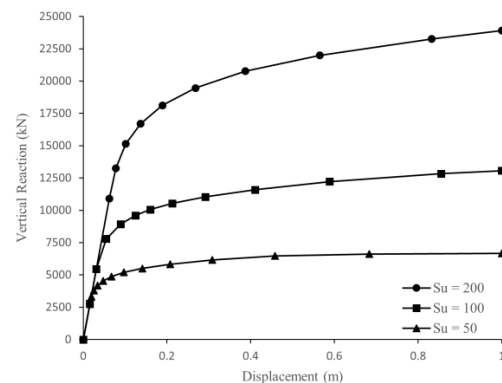


Fig. 4. Vertical displacement and reaction

## CONCLUSIONS

In this study, the vertical bearing capacity of the suction pile was calculated according to the undrained shear strength in the undrained clay ground using the finite element analysis program. The length ( $L$ ) to diameter ( $D$ ) ratio of the suction pile was used under the condition of  $L/D = 1$ , and the vertical bearing capacity of the foundation was

compared using the undrained shear strength of 50 kPa, 100 kPa, and 200 kPa.

The vertical bearing capacity of the suction pile is affected by the undrained shear strength of the surrounding ground, and as the undrained shear strength increases, the vertical bearing capacity of the foundation increases.

In order to calculate bearing capacity in more diverse environments, finite element analysis according to various variables such as depth of penetration of the foundation and drainage conditions of the ground is additionally needed.

#### ACKNOWLEDGMENTS

This research was a part of the project titled 'Development of Underwater Space Resource Creation Technologies' (No. 20220364) funded by the Ministry of Oceans and Fisheries, Korea, and the National Research Foundation of Korea (NRF) grant

funded by the Korea government (MSIT, No. 2020R1A2C1012072).

#### REFERENCES

- [1] Ji, S.-H., et al. "Development of Marine Plant Trends and Subsea Foundation Technology", *Geotechnical Engineering*, 2014, 30.11: 12-17.
- [2] Tjelta, T., et al. "The Skirt Piled Gullfaks C Platform Installation", *Proceedings, Offshore Technology Conference*, 1990, Houston, USA, OTC 6473, pp.452-462.
- [3] Hefer, P. "Oil and Gas Floating Facility to be Anchored in 390 m Deep Timor Sea", *Civil Engineers Australia*, December 1998.
- [4] Abaqus. <https://www.simuleon.com/simulia-abacus/>, Accessed in June 2021.



## MODELLING LIGHTWEIGHT DEFLECTOMETER BASED ON ANALYTICAL AND NUMERICAL MODELS

Tram Huyen Nguyen<sup>1</sup>, Yunje Lee<sup>2</sup>, Hoa Phuong Thi Nguyen<sup>3</sup>, Sangwook Kang<sup>4</sup>, Jaehun Ahn<sup>5</sup>

<sup>1,2,3,4</sup> Graduate and Bachelor Student, Department of Civil and Environmental Engineering, Pusan National University, Busan 46241, Republic of South Korea;

<sup>5</sup> Professor, Department of Civil and Environmental Engineering, Pusan National University, Busan 46241, Republic of South Korea, Tel: +82-51-510-7627, Fax: +82-51-513-9596, jahn@pusan.ac.kr, Corresponding author

### ABSTRACT

Lightweight Deflectometer (LWD) is a novel device which can determine the elastic moduli of soils. This can make a valuable tool for quality control of soil compaction enabling modulus-based control. There are a number of manufacturers and models of LWD with difference specifications out there, but then the devices do not give consistent results with sometimes high level of variations. As such, at this point, the quality control based on LWD has limitations in practice. In general, the modulus is evaluated from a simple equation based on statics. It may be necessary to consider dynamics involved in LWD operation to estimate better the modulus of soil hopefully reducing inconsistency among different LWDs. This study aims at simulating LWD, considering its dynamic behavior and investigating the results from it.

*Keywords: LWD, Elastic modulus, Dynamic, Simulating*

### INTRODUCTION

The Lightweight Deflectometer (LWD) is known as a Portable or Light Falling Weight Deflectometer and is widely used as a portable device for quality control of soil compaction enabling modulus-based control. LWDs provide reasonable results and are gradually being accepted all over the world in earthwork construction. In the LWD test, a dynamic force is imparted via a drop mass to a plate resting on the ground, which is assumed as an elastic half-space. The estimation of elastic modulus ( $E_{LWD}$ ) is often based on the Boussinesq solution in Eq. (1) [1].

$$E_{LWD} = \frac{A(1-\mu^2)P_{peak}}{\pi r U_{peak}} \quad (1)$$

where  $A$  is stress distribution factor (Zorn LWD software assumes  $A = \pi/2$ ),  $\mu$  is Poisson's ratio,  $r$  is plate radius,  $P_{peak}$  is peak impact force, and  $U_{peak}$  is peak deflection.

However, the results of LWD testing are used to calculate a dynamic modulus of the soil based on static Boussinesq theory for plate loading of an elastic half-space, while the operation of LWD involves dynamic behavior with a very high loading rate; statics may not be the most dependable theory for analysis. The study is an attempt to implement performance-based assessments of designed for properties such as the resilient modulus and stiffness.

This study presents the results of an investigation into the influence of evaluation methods on measured modulus based on the LWD test and shows the

feasibility of implementing dynamics solutions in calculating soil's young modulus.

### ANALYTICAL MODELS

#### Model Based on Elastic Half-Space

Veletsos and Verbic [2] provide solutions for vibrating massless disks resting in an elastic half-space as a model of LWD dynamic behavior (Fig.1). The LWD tests dynamic response can be calculated in the frequency domain and transformed into the time domain by applying the Fourier Transform algorithms:

$$U(\omega) = H(\omega) * P(\omega) \quad (2)$$

where  $H(\omega)$ ,  $P(\omega)$  are detailed in Veletsos and Verbic [2]. The deflection evaluated in this way is referred to  $U_v$  here.

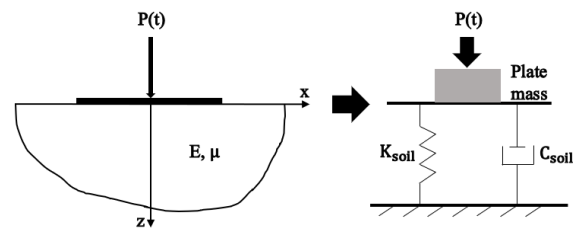


Fig. 1 Schematic of LWD resting on elastic half-space.

The impact force in the model is simulated as a haversine curve with a time step value of 0.05 ms, and its maximum amplitude value of 7.07 kN is taken (by Zorn LWD datasheet). The impacted force time history is numerically simulated, as shown in Fig. 2.

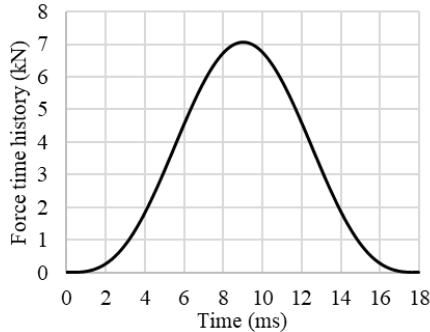


Fig. 2 Force time history applied by LWD

### Model Based on 2DOF (Two Degree of Freedom)

The mechanical system of LWD can be modeled as a 2DOF system and evaluated in the time domain by using a state-space solution, which consists of plate mass  $m_1 = 30$  kg and drop mass  $m_2 = 10$  kg connected with soil and spring [3]. Values of soil stiffness are  $K_{soil} = 30.94; 14.67; 38.63$  kN/m and values of soil damping are  $C_{soil} = 30.32; 20.88; 33.88$  kNs/m respectively, for three tests. The spring is designed as buffer with value of stiffness  $K_{buffer} = 35.384$  kN/m and damping coefficient  $C_{buffer} = 33.65$  Ns/m. The system performs linear motion in the vertical direction of springs and dampers axes. Figure 3 illustrated the LWD dynamic model as the 2DOF system. The impacted variable force as Fig. 2, is used for the model excitation.

The solution was implemented in Matlab by using Simulink. The deflection calculated by convolution integral is referred to  $U_{2DOF}$  in this article.

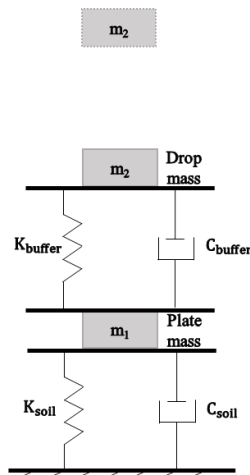


Fig. 3 LWD modeling as 2DOF system.

### FINITE ELEMENT MODEL

To investigate the influence of different calculation methods on resulting elastic moduli, frequency domain-based finite element method (FEM) analysis was performed by using Abaqus. The FEM in Abaqus is axisymmetric with a radius of sufficient size in 5 m to prevent wave reflections from effect results. An alternative parametric was implemented to ensure that the mesh size, soil dimension, and a number of input data sample points did not affect the analyzed model. In the study, the FEM model is simplified as the circular plate resting on the soil. This is a reasonable model for simulating the dynamic operation of the LWD, but not the realistic one.

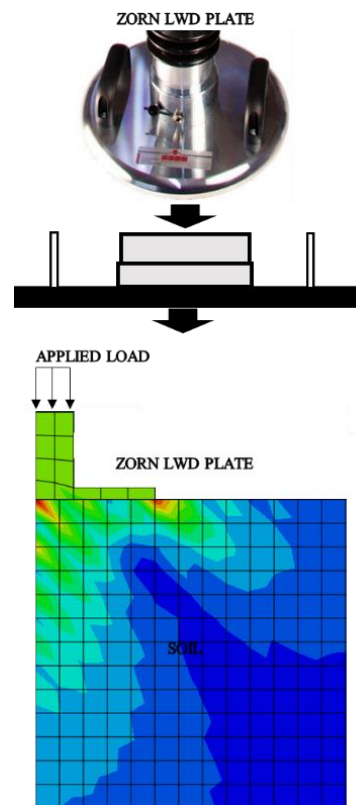


Fig. 4 Schematic of FEM for LWD in Abaqus.

All materials used in the study are assumed to be linear elastic, with their properties shown in Table 1. The LWD (Zorn) load plate is 15 mm thick, 150 mm radius, and it houses a 36 mm in diameter and 32 mm tall on-board accelerometer at the central [1]. The time history of response displacement was measured underneath the center of the plate and along the soil surface with the time step value of 0.05 ms and the impacted variable force as Fig. 2, is also used for the model.

Table 1 Summary of material properties assigned in the models [1].

Material Property	Soil	LWD Plate
Density, $\text{kg/m}^3$	2400	7850
LWD mass, kg	--	15
Poisson's ratio ( $\mu$ )	0.35	0.28
Modulus of elasticity, MPa	95.3, 46.7, 118.4	205,000
Damping factor ( $\xi$ )	0.05	0

A comparison of the analytical model response in Abaqus, three different numerical model responses with test results were implemented. These test data for three different soil specimens were taken on a vertically homogeneous granular base material; therefore, the model is assumed as an elastic homogeneous elastic half-space [4].

### CALCULATIONS OF DEFLECTION

Field test data were taken on three soil specimens for analysis. Results summarized in Table 2 show the peak deflection of each method.

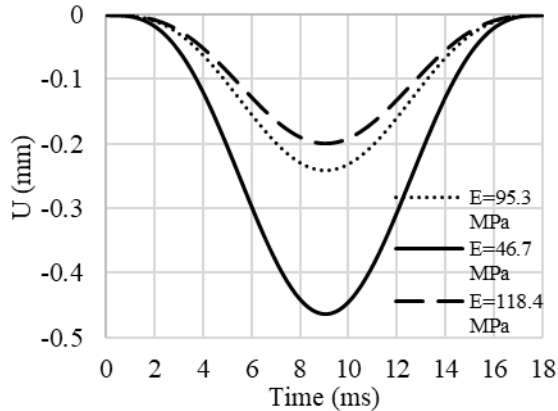


Fig. 5 Deflection time histories from Abaqus

Figure 5 shows the deflections of the point at the center of the LWD plate and soil base interface with different values of soil elastic moduli implemented by FEM method in Abaqus, which are used as a baseline for an assessment.

### Comparison of presented models

A comparison of the FEM model's responses and the other three different models' responses is shown in Fig. 6.

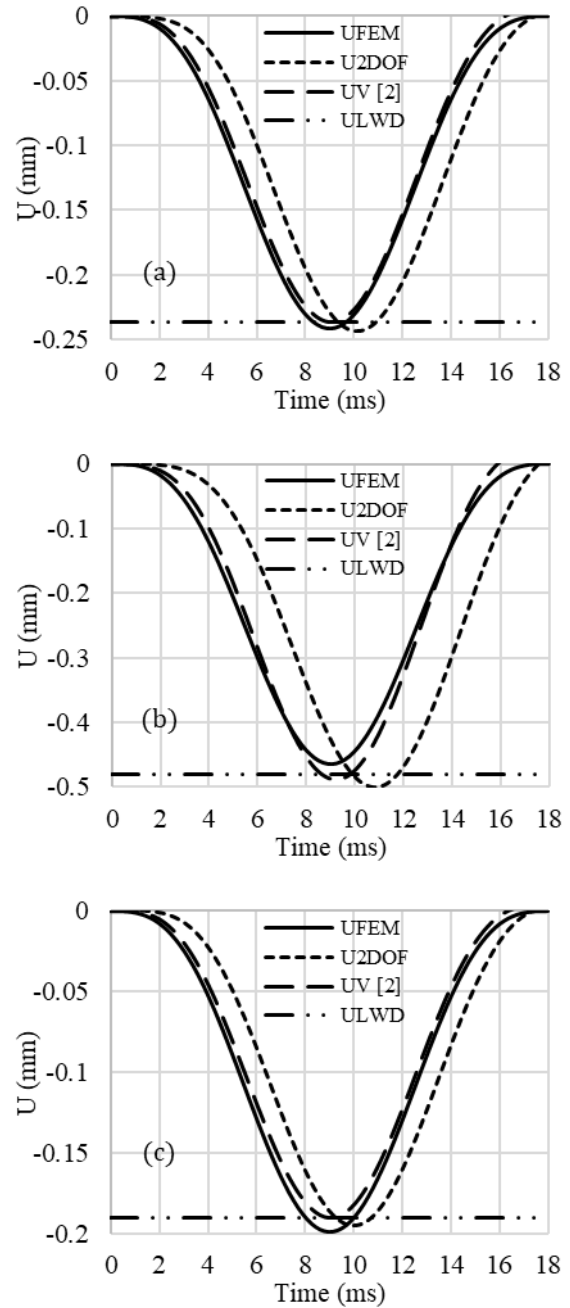


Fig. 6 The deflection time histories from different methods. (a)  $E = 95.3 \text{ MPa}$ , (b)  $E = 46.7 \text{ MPa}$ , (c)  $E = 118.4 \text{ MPa}$ .

As it is shown, there are discrepancy and inconsistency among deflection evaluated by different LWD calculation models for the same soil specimen. The peak deflection values of each method are summarized in Table 2.

Table 2 Deflection.

Case No.	$U_{FEM}$ (mm)	$U_{2DOF}$ (mm)	$U_V$ (mm)	$U_{LWD}$ (mm)
1	0.241	0.244	0.217	0.236
2	0.464	0.500	0.443	0.418
3	0.199	0.195	0.175	0.190

### BACK CALCULATION OF MODULUS

The back calculation was conducted to determine the moduli of three specimens with the three measurement deflection values of  $U_1 = 0.236$  mm,  $U_2 = 0.481$  mm,  $U_3 = 0.190$  mm respectively were inversely calculated based on one static and three dynamic models, and FEM model is addressed. Results are summarized in Table 3.

Table 3 Elastic modulus.

Case No.	$E_{FEM}$ (MPa)	$E_{2DOF}$ (MPa)	$E_V$ (MPa)	$E_{LWD}$ (MPa)
1	97.8	98.3	87.7	95.3
2	44.9	48.7	43.0	46.7
3	125.0	123.0	109.0	118.4

### CONCLUSIONS

An investigation was conducted on several dynamic solutions to compute the deflection of compacted soil under the impacted load caused by LWD based on impact force and displacement. The

results of this investigation illustrate that each of the calculations will always produce different deflection values for the same ground conditions.

Employment of a more realistic analytical model would help minimize the issue of incorrect moduli estimation. More realistic modelling based on Abaqus is planned to test the viabilities of different analytical solutions, which will help to make LWD a more reliable tool for compaction control.

### ACKNOWLEDGMENTS

This research was supported by Basic Science Research Program through the National Research Foundation of Korea (NRF) funded by the Ministry of Education (No. 2022R1I1A3069043).

### REFERENCES

- [1] Stamp, Dave and Michael A. Mooney. "Influence of Lightweight Deflectometer Characteristics on Deflection Measurement." *Geotechnical Testing Journal* 36 (2013): 216-226.
- [2] Veletsos, Anestis S. and Branislav Verbic. "Basic Response Functions for Elastic Foundations." *Journal of Engineering Mechanics-asce* 100 (1974): 189-202.
- [3] Das, Braja M., and Zhe Luo. "Principles of soil dynamics. Cengage Learning." (2016).
- [4] Tirado, Cesar, Mehran Mazari, César Carrasco and Soheil Nazarian. "Simulating Response of Different Lightweight Deflectometer Testing Using Finite Element Modeling." (2015).

# FEASIBILITY STUDY ON SOIL CLASSIFICATION FROM SOIL IMAGES USING DEEP LEARNING

Tomoki Abe<sup>1</sup> and Taizo Kobayashi<sup>2</sup>

<sup>1</sup> Graduate School of Science and Engineering, Ritsumeikan University Graduate school, Japan;

<sup>2</sup> College of Science and Engineering, Ritsumeikan University, Japan

## ABSTRACT

Although a large amount of training data is required for deep learning, it is difficult to obtain sufficient data by manually capturing pictures. Therefore, we have devised a method for estimating real soil particle images using a deep learning model trained using virtual soil particle images created on a computer. The particle shapes of V-image are circular, square, and equilateral triangle. We also created a data set that mixes images of all shapes. As a result of verifying real images, we obtained a maximum accuracy rate of 78%.

*Keywords: Deep Learning, classification of geomaterials for engineering*

## INTRODUCTION

The classification of geomaterials for engineering requires numerous soil tests and expertise, including sedimentation analyses. We wondered if it would be possible to realize a method for instantaneous classification of geomaterials for engineering using deep learning (AI) from images of soil. This study reports the results of a feasibility examination conducted on a trial basis.

## VALIDATION

### Method of Classification of Geomaterials for Engineering

As a basic trial study, we attempted to estimate the grain size from images of crushed stones with a maximum grain size of 15 mm and classify geomaterials for engineering purposes. Figure 1 shows a breakdown of the classification of geomaterials used in this study. In the sieve analysis, the grain size was defined as the smallest particle

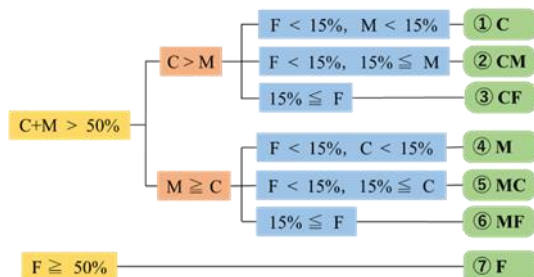


Fig.1 Classification criteria of geomaterials defined in this study

diameter. In this study, grain size was defined by the area in the image. Particles within 250 px in area were defined as fine (F) particles, and those within approximately 251–500 and 501–750 px were defined as medium (M) particles and coarse (C) particles, respectively. The soil classification of was based on the F, M, and C particle contents. The soil classification uses mass content; however, in this study, machine learning was used to estimate the number of particles in the image and content based on the number of particles.

### Image Photograph Method

As a feasibility study, we photographed a type of crushed stones under the condition that they did not overlap. Using a general digital camera, we captured

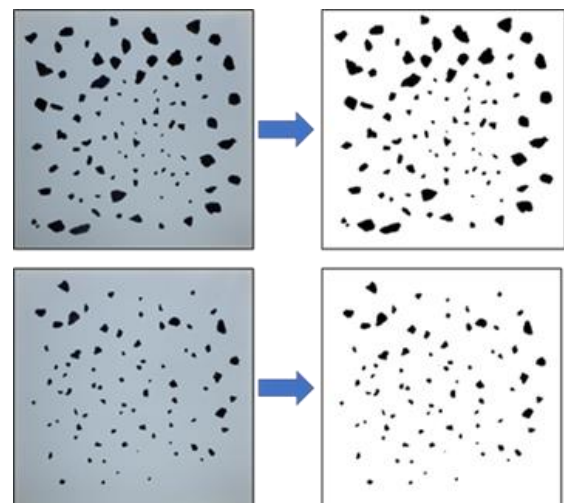


Fig.2 Acquired image and the R-image

images on a light table within a range of 250 mm  $\times$  250 mm. The image size was 512 px $\times$ 512 px. Subsequently, we binarized the images by ImageJ[1]. The processed image is called a real image (R-image) in this study. Figure 2 shows an acquired image and the R-image. Left image is acquired image. Right image is R-image.

### Method of Making Teaching Data

Machine learning generally requires a large amount training datasets to achieve high accuracy. However, it requires considerable time to manually collect a large amount several datasets. In this study, we devised a method for collecting numerous datasets. We programmed and created a virtual soil-particle image (V-image) using a PC. Currently, tens of thousands of images can be created within a few minutes. Figure 3 shows the V-image. We used the programming language Processing [2] for visual design. The grain shapes are circle, equilateral triangle, and square. The V-image was a binary image comprising a white background and black particles. The positions and contents of the particles are randomly set. We considered that learning cannot be performed efficiently if the total number of particles

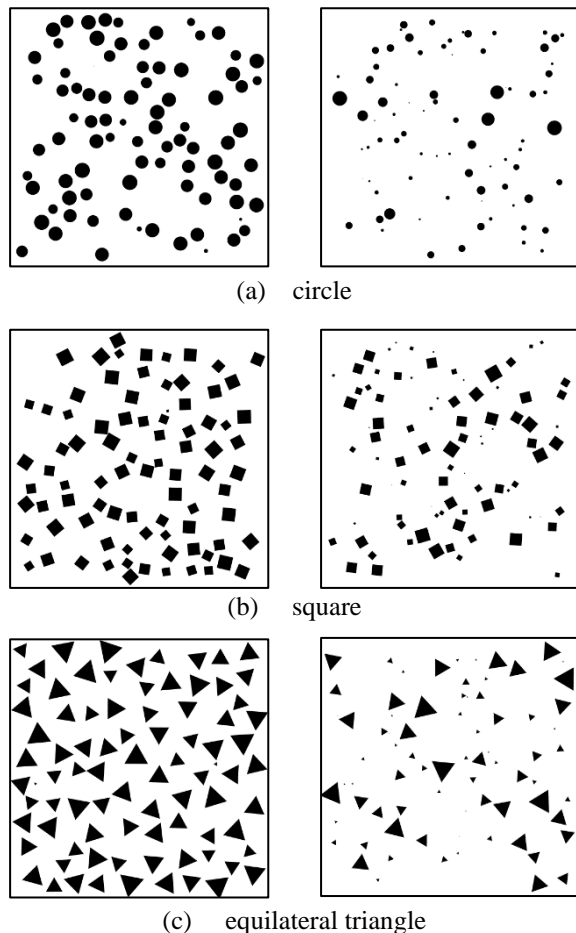


Fig.3 Virtual soil particle images (V-image)

in the image is too small.; therefore, we set the total number of particles in the V-image to 70–100.

### Deep learning network

We used a neural network console (NNC) [3] to create a deep learning model. The NNC is an application provided by the SONY Corporation. We can easily build machine learning network using drag-and-drop in the NNC. From the various types of machine learning processes, we selected convolutional neural network (CNN). CNN are frequently used in image and video recognition. We used a network that connects three units with two convolution layers, two batch normalization layers, two rectified linear unit (ReLU) layers, and a max pooling layer as one unit. We used the squared error as the loss function. Figure 4 shows the deep learning network. The role of each layer is described as follows. In the convolutional layer, layer plays the role of reacting to a specific shape called a filter. When it reacts to a particular shape, it is weighted and passed to the next layer. The content of the filter is optimized as learning progressed. In the batch normalization layer, this effect prevents vanishing gradient [4]. ReLU is an activation function. When the input value is zero or less, the output value becomes zero. When the input value is one or more, the output value is the same. ReLU has good calculation efficiency. In the max-pooling layer, the maximum value among the input values obtained within a range of  $2 \times 2$  is used as the output value. This has the effect of dealing with positional deviations in the image and reducing the number of calculations required. In the affine layer, the output value is obtained by multiplying the input value by the weight parameter. The weight parameters were optimized using repeated learning. For the squared error, the square of the difference between the correct answer and the predicted values is calculated using machine learning. The smaller the obtained numerical value is, the higher is the accuracy of deep learning.

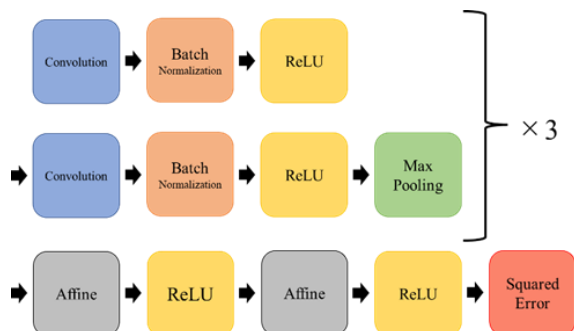


Fig.4 Deep learning network used in this study

### Results

The deep learning network that trained the V-image verified the V- and R-images. The number of



training data points was 20,000. The number of test data points the V-image was 5,000 and the number of test data points in the R-image was 100. We created a mixed dataset in addition to circular, equilateral triangle, and square datasets; it contained 1/3 of each shape. We used a deep learning model shape dataset to validate the V and R-images. We used the accuracy rate for indicator of the accuracy of the deep-learning model. We defined the accuracy rate as the percentage of correct answers that matched the estimate of the correct answer of the deep-learning model. Tables 1 and 2 present the validation results obtained using deep learning.

Table 1 Accuracy rate of deep learning model 1

accuracy rate (%)		Validation data		
		●	■	▲
Training data	●	88.9	21.2	55.2
	■	68.5	88.4	63.1
	▲	53.5	50.6	89.3
	Mix	86.2	83.0	89.7

Table 2 Accuracy rate of deep learning model 2

accuracy rate (%)		Validation data	
		Mix	R-image
Training data	●	54.8	56.0
	■	68.5	75.0
	▲	62.8	77.0
	Mix	86.4	78.0

Table 1 shows that when the grain shapes learned by the deep learning model and the verified grain shape were the same, a high accuracy rate of over 88% could be obtained. However, when the learned grain shape of the deep learning model differed from the verified grain shape, only a 63.1% accuracy could be obtained. The details of the validation results of the deep learning model learned by the circles are provided below. Figure 5 shows the results when the model trained on the circle dataset validated the circle dataset. Figure 6 shows the results when the model trained on the circle dataset validated the square dataset. Figure 7 depicts the results when the model trained on the circle dataset validated the equilateral triangle dataset. The vertical axis in the graphs represents the estimated particle count. The

horizontal axis of the graph represents the number of particles in the image. The red, blue, and green plots show the F, M, and C particles. The line drawn at 45° indicates that the estimated and real counts have the same value; the better the accuracy, the closer the plot approaches this line. When a deep learning model trained on a circle validates a circle dataset, it obtains a high accuracy rate. However, when the deep learning model trained on a circle validates the square and equilateral triangle datasets, the accuracy rate is extremely low. Fine particles tend to be estimated in greater numbers than the actual count, and coarse particles tend to be estimated fewer than the actual count. We considered that this is due to the fact that the learning process is circle-specific and does not allow for different shapes. The particles in the R-image have a variety of shapes, we assumed that a circle-specific model would be unable to correctly

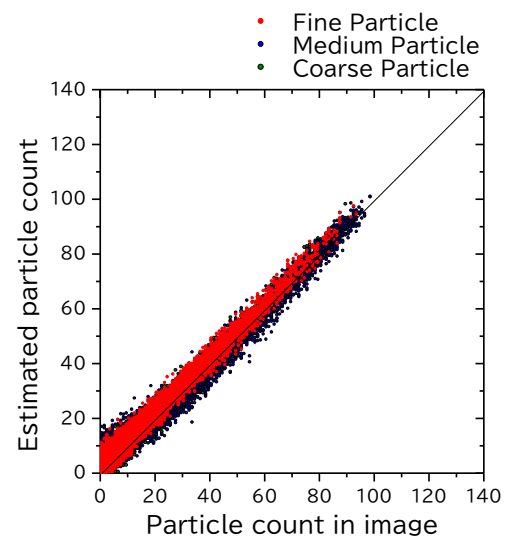


Fig. 5 Verification result for circle grain shape

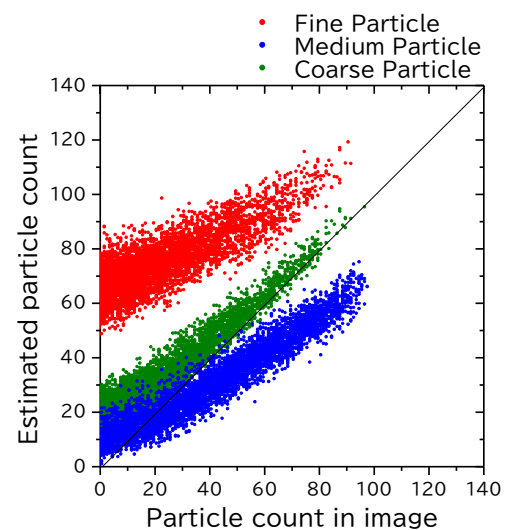


Fig. 6 Verification result for square grain shape

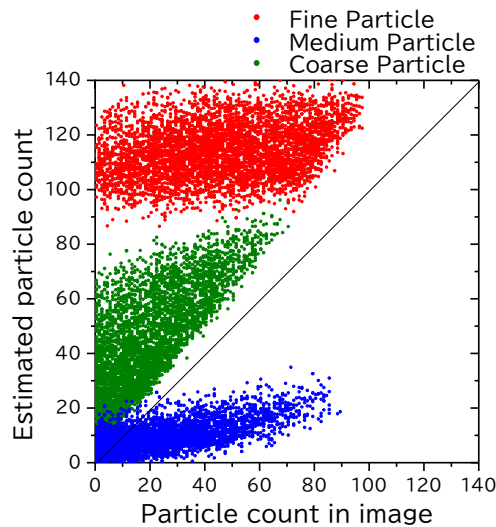


Fig. 7 Verification result for equilateral triangle grain shape

estimate the R-image. Therefore, we reviewed the mixed datasets in detail. Figure 8 shows the results when the model trained on the mixed dataset validated the mixed dataset. The deep learning model trained with the mixed dataset could validate the mixed dataset with high accuracy. As shown in Table 2, the accuracy rate was high (86.4 %). Thus, we considered that it is possible to deal with various shapes and obtain a high accuracy rate. Figure 9 shows the results when the model trained on the mixed dataset validates the R-image dataset. As can be observed from the graph, the plot approached the 45° line. In Table 2, the accuracy rate when the R-image dataset was validated using a model trained with a mixed dataset was 78%, which is higher than the deep-learning models trained on other datasets.

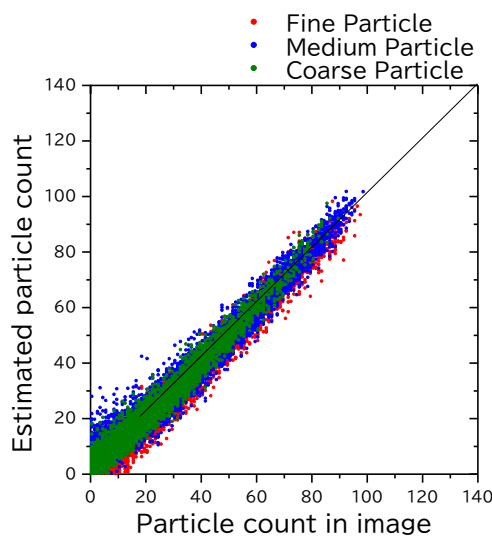


Fig. 8 Verification result for mixed dataset

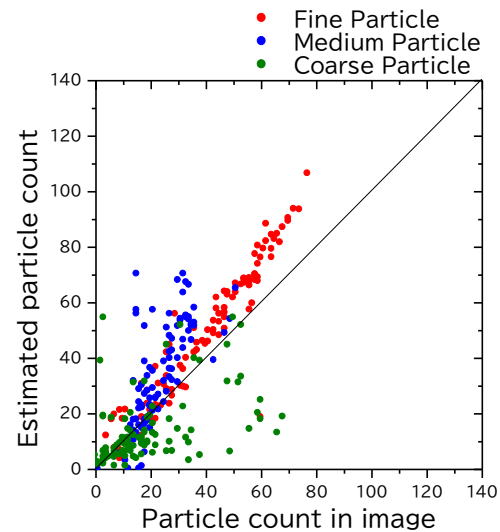


Fig. 9 Verification result for R-image dataset

Thus, the mixed dataset is considered effective for validating the R-image. However, an accuracy rate of 78% is not sufficient for practical use. Therefore, it is necessary to further improve the accuracy rate in the future.

## CONCLUSION

In this study, we proposed a method for the classification of geomaterials for engineering using deep learning of particle images. Considering the difficulty of creating a large amount of teaching data, we attempted to learn using virtual soil-particle images created on a PC. The model trained with the circle dataset was specialized for the circle, and the accuracy rate for the R-image was only 56%. However, the deep learning model trained with the mixed dataset was versatile, and the accuracy rate of the R-image improved to 78%. In the future, we would like to study teaching data with higher estimation accuracies.

## references

- [1] ImageJ HP <https://imagej.nih.gov/ij/> 08/13/2022
- [2] Processing HP <https://processing.org> 06/10/2022
- [3] NeuralNetworkConsole HP <https://dl.sony.com/ja/> 06/10/2022
- [4] Sergey Ioffe and Christian Szegedy, Batch Normalization: Accelerating Deep Network Training by Reducing Internal Covariate Shift, arXiv:1052.03167, 02/11/2015

# A COMPARISON BETWEEN PAVEMENT RESPONSES FROM THE FALLING WEIGHT DEFLECTOMETER AND THOSE FROM TRUCK LOADING BASED ON THE LAYERED ELASTIC ANALYSIS

Thinn Thinn<sup>1</sup> and Auckpath Sawangsuriya<sup>2</sup>

<sup>1</sup>Department of Transportation Engineering, Asian Institute of Technology, Thailand.

<sup>2</sup>Bureau of Road Research and Development, Department of Highways, Thailand.

## ABSTRACT

Pavement responses e.g., surface deflections, tensile strains, and compressive strains etc. were determined from the multi-layered elastic analysis (LEA). The LEA has been widely accepted in most mechanistic design and performance analysis of the road pavements, where their structures were assumed to be homogenous, isotropic, linear-elastic, and finite thickness with modulus of elasticity and Poisson's ratio. The falling weight deflectometer (FWD) is a traditional tool for the structural condition evaluation of road pavements. According to the FWD testing procedure, three magnitudes of load: 40, 53, 70 kN (e.g., 575, 750, 1,000 kPa) were applied on the road pavements. In Thailand, a typical loading stress of 700-800 kPa was practically adopted by the Department of Highways, while a tandem axle-dual wheel having a 690 kPa (100 psi) tire pressure and a 100 kN (10 metric tons) single axle load generated by the standard 10-wheel Thai truck (e.g., legal load permit of 25-ton gross weight) was considered in the pavement design and analysis. The objective of this paper is therefore to compare the pavement responses from the FWD and the standard Thai truck loads based on the LEA. Comparison results indicated that the average error was about 10% for 800 kPa FWD-standard Thai truck deflections, while 21% for 700 kPa FWD-standard Thai truck deflections. In case of tensile strain at the bottom of thin asphalt surface, the average error was respectively 2% and 14% for 800 kPa FWD-standard Thai truck and 700 kPa FWD-standard Thai truck. However, for thick asphalt surface, the average error was respectively 38% and 21% for 800 kPa FWD-standard Thai truck and 700 kPa FWD-standard Thai truck. In case of the compressive strain above the subgrade, the average error ranged from 7 to 11% for 800 kPa FWD-standard Thai truck and 8 to 12% for 700 kPa FWD-standard Thai truck.

*Keywords: pavement response, layered elastic analysis, falling weight deflectometer, truck loading*

## INTRODUCTION

In recent years, the road pavement design has evolved from a purely empirical approach to mechanistic-empirical methods, which require comprehensive knowledge of material behavior and their responses e.g., stress, strain, and deflection, under traffic loads [1]. The newly evolved mechanistic-empirical design method involved the physical relationship between causes (wheel loads, material properties) and effects (stress, strains, deflections) and developed mathematical models to relate these effects to failure modes [2]. The main structural response models used in pavement analysis and design are the finite element and layered elastic analysis (LEA). KENLAYER computer program was originally developed by Professor Yang H. Huang at the University of Kentucky [3]. KENLAYER relied on the mathematical models to predict road pavement structural responses using the layered elastic theory. This theory is based on Burmister's [4] equations for the solutions of stresses, strains, and deflections in layered systems under traffic loads. Certain general assumptions and generalizations were incorporated into the layered elastic theory, including material isotropy and homogeneity.

In Thailand, the Department of Highways (DOH) adopted both empirical and mechanistic (analytical) methods for the pavement analysis and design. A 10-wheel 25-ton truck was typically considered as the standard traffic load application in the design procedure. Recently, the deflection-based design approach has been comprehensively reviewed by the DOH for the possible adoption of local design standard and practice. One of the main reasons was that Thailand road authorities e.g., DOH and the Department of Rural Roads (DRR), consider the falling weight deflectometer (FWD) for the new construction and rehabilitation of road pavement. In addition, such the FWD has been globally accepted as the non-destructive test for deflection measurement and structural capacity evaluation [5]. Ultimately, the implication of FWD deflections for localized pavement analysis and design shall be developed and proposed to Thailand road authorities. Due to the aforementioned reasons, it was important that such a load magnitude of FWD shall be determined and verified with the 25-ton 10-wheel standard Thai truck. Therefore, this study presents the comparison of pavement responses from the FWD and those from the standard Thai truck based on the LEA.

## LAYERED ELASTIC ANALYSIS

A flexible pavement has been considered an ideal elastic body due to its relatively ease of calculation of stresses, strains, and deflections. The elastic theory has been used extensively in the computation of stresses, strains, and deflections. This involved the stresses in a homogeneous, isotropic linearly elastic solid of semi-infinite extent when subjected to a load applied normally to the surface. The assumptions of homogeneity and isotropy specify that the elastic properties in any part of a material were identical in all directions, regardless of location within the material. In this context, elasticity referred to a relationship between stress and strain that had no relationship with time, loading path, or other factors. The linearly elastic solid was the most convenient to handle, and superposition can be employed [6]. Elastic solutions were developed from Boussinesq's [7] one-layer system to Burmister's two [8] and three-layer system [4] to multi-layered elastic theories [3], to finite element techniques for the pavement performance prediction based on material properties and traffic conditions.

### Pavement Responses

Pavement responses are results of the combined effects of loading, environment condition, subgrade, and pavement material characteristics. With respect to flexible pavements, the current failure criteria are the tensile strain at the bottom of the asphalt surface and the compressive strain at the top of the subgrade. Tensile strain at the bottom of asphalt surface is used to predict and control fatigue cracking of the asphalt surface. The compressive strain at the top of the subgrade is used to predict and control the permanent deformation of the pavement structure due to shear deformation in the upper subgrade. Surface deflection is an indicator of the strength and stiffness of the entire pavement structure, which can be also related to the pavement design life.

Sawangsurriya et al. [9] utilized three-dimensional (3-D) finite-element analysis (FEA) model and LEA to examine the structural responses of flexible pavement under different types of axle group loads, e.g., single axle-dual wheel, tandem axle-dual wheel, and tridem axle-dual wheel and compared with the field measurement data. The results indicated that both FEA and LEA were in good agreement with the field measurement results with some exceptions for strains under the asphalt surface. The structural responses in terms of vertical stresses, vertical strains, and horizontal strains from LEA were identical with the FEA results. Thus, both FEA and LEA approaches could be applied for estimating the pavement structural responses.

Srikanth [10] conducted linear and nonlinear analysis for pavement layers using a finite element

software tool named Michigan Flexible Pavement Design software (MFPDS) and KENLAYER computer program to evaluate the pavement response. Results obtained from both programs appeared to be equivalent for linear analysis, but there was a significant difference in tensile strain when the surface thickness was less than 75 mm. In case of nonlinear analysis, the results did not correspond well.

Based on the past studies, the LEA was suitable for analyzing pavement responses because it gave equivalent pavement responses to FEA, but less analysis time.

## METHODOLOGY

### Material Properties and Layer Thicknesses

Flexible pavement structure in this study were comprised of different layer materials, e.g., asphalt surface, crushed rock base, soil-aggregate subbase, selected material, above natural subgrade. According to AASHTO [11], a minimum thickness of the asphalt surface and aggregate base shall be 2.54 cm (1 inch) and 10 cm (4 inches), respectively. Thus, the minimum thicknesses of asphalt surface and aggregate base were considered to be 50 mm (2 inches) and 100 mm (4 inches), respectively.

A total of 625 pavement sections was selected in this study. Five asphalt surface thicknesses included 50, 100, 150, 200, and 250 mm. Five crushed rock base thicknesses included 100, 150, 200, 250, and 300 mm. Five soil-aggregate subbase thicknesses included 100, 200, 300, 400, and 500 mm. Four selected material thicknesses included 100, 200, 300, and 400 mm as it was not existed in some sections. Table 1 summarized the elastic moduli and Poisson's ratio for pavement layer materials according to the DOH's pavement design practice [5].

Table 1 Pavement Material Properties

Pavement Materials	Elastic Modulus (MPa)	Poisson's Ratio
Asphalt Surface	2,500	0.35
Crushed Rock Base	350	0.35
Soil-aggregate Subbase	150	0.35
Selected Material	100	0.35
Subgrade	40	0.40

### Load Applications

The study considered two load applications, FWD and standard Thai truck. According to the FWD testing protocol by the DOH, a loading pressure ranging from 700 to 800 kPa was typically adopted along with a plate radius of 0.15 m. The standard 10-

wheel 25-ton truck was adopted for Thailand pavement design and analysis. Having a tandem axle-dual wheel configuration, this standard Thai truck had a tire pressure of 690 kPa (100 psi) and a single axle load of 100 kN (10 metric tons). A tire contact radius of 0.11 m was determined by dividing a wheel load of 2.5 tons (approximately 25 kN) by a tire pressure of 690 kPa. Table 2 summarized the pressure and radius of contact for the FWD and the standard Thai truck.

Table 2 Pressure and Radius of Contact for the FWD and the Standard Thai Truck

Description	Pressure (kPa)	Radius of Contact (m)
FWD	700, 800	0.15
Truck	690	0.11

### KENLAYER Analysis

The LEA by KENLAYER computer program was used to determine the pavement responses under FWD and standard Thai truck load applications. A layered elastic model required a minimum number of inputs to adequately characterize a pavement structure and its response to loading. The essential input parameters were the material properties for each layer (e.g., elastic modulus and Poisson's ratio), layer thicknesses, load configurations, numbers of load groups, x, y, and z coordinates for loads and responses.

Pavement responses under the FWD load application was determined right at the center of loading plate, while the pavement responses under the standard Thai truck were determined at four positions, e.g., under the wheel load, between the dual-wheel load, between the tandem-axle load, and between the dual-wheel and tandem-axle load etc. The standard Thai truck had a center-to-center spacing of 1,300 mm between the axles and 330 mm between the wheels. Figure 1 illustrates the location of four pavement responses as well as axle and wheel configurations of standard Thai truck.

The outputs from KENLAYER computer program were surface deflection, tensile strain at the bottom of the asphalt surface, and compressive strain at the top of the subgrade.

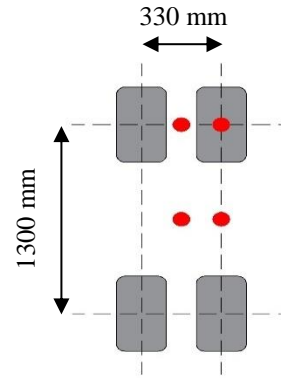


Fig. 1 Positions of pavement responses and axle/wheel load configurations of standard Thai truck

## RESULTS AND DISCUSSION

Pavement responses e.g., surface deflections, tensile strains, and compressive strains of flexible pavement under 700 kPa FWD, 800 kPa FWD, and 690 kPa standard Thai truck loads were presented herein. Only responses under the applied loading pressure were reported for the FWD, while the maximum responses were reported for the standard Thai truck.

### Comparison between FWD and standard Thai Truck -Deflections

Comparison between the FWD and the standard Thai truck deflections is shown in Fig. 2. Based on the comparison, 800 kPa FWD-standard Thai truck deflections yielded smaller error than 700 kPa FWD-standard Thai truck deflections. An average error of 10% was obtained for 800 kPa FWD-standard Thai truck deflections, whereas an average error of 21% was obtained for 700 kPa FWD-standard Thai truck deflections. As a consequence, 800 kPa FWD deflection was closer to 690 kPa standard Thai truck deflection than 700 kPa FWD deflection.

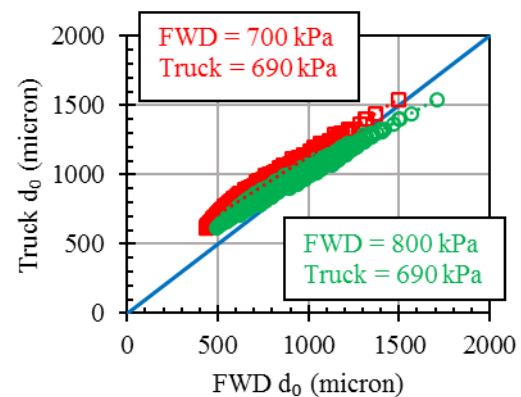


Fig. 2 Comparison between FWD and standard Thai truck deflections

### -Tensile Strains at the Bottom of Asphalt Surface

Comparison between the FWD and the standard Thai truck tensile strain at the bottom of asphalt surface is shown in Fig. 3. In cases of thin asphalt surfaces with thickness less than 100 mm, 800 kPa FWD-standard Thai truck tensile strains yielded smaller error than 700 kPa FWD-standard Thai truck tensile strains. An average error of 2% was obtained for 800 kPa FWD-standard Thai truck tensile strains, whereas an average error of 14% was obtained for 700 kPa FWD-standard Thai truck tensile strains. As a consequence, for thin asphalt surface with thickness less than 100 mm, 800 kPa FWD tensile strain was closer to 690 kPa standard Thai truck tensile strain than 700 kPa FWD tensile strain.

However, in cases of thick asphalt surfaces with thickness greater than or equal to 100 mm, 700 kPa FWD-standard Thai truck tensile strains yielded smaller error than 800 kPa FWD-standard Thai truck tensile strains. An average error of 21% was obtained for 700 kPa FWD-standard Thai truck tensile strains, whereas an average error of 38% was obtained for 800 kPa FWD-standard Thai truck tensile strains. As a consequence, for thick asphalt surfaces with thickness greater than or equal to 100 mm, 700 kPa FWD tensile strain was closer to 690 kPa standard Thai truck tensile strain than 800 kPa FWD tensile strain.

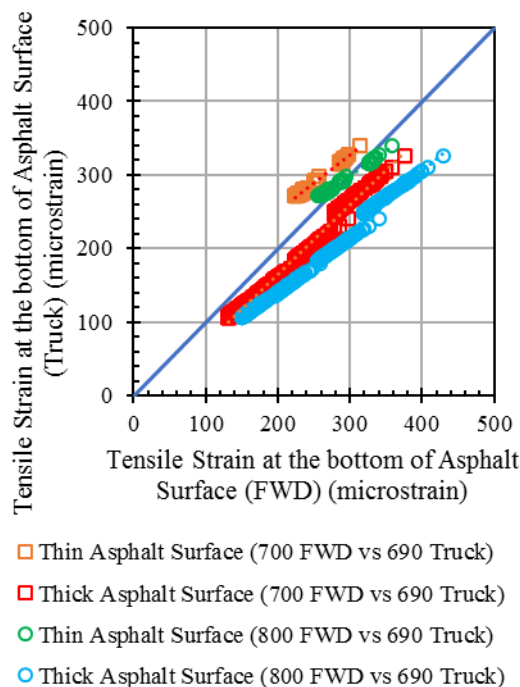


Fig. 3 Comparison between FWD and standard Thai truck tensile strain at the bottom of asphalt surface

### -Compressive Strain above Subgrade

Comparison between the FWD and the standard Thai truck compressive strain above the subgrade is shown in Fig. 4. In cases of compressive strains less than 400 microstrains, 800 kPa FWD-standard Thai truck compressive strains yielded smaller error than 700 kPa FWD-standard Thai truck compressive strains. An average error of 7% was obtained for 800 kPa FWD-standard Thai truck compressive strains, whereas an average error of 12% was obtained for 700 kPa FWD-standard Thai truck compressive strains. As a consequence, for small compressive strains less than 400 microstrains, 800 kPa FWD compressive strain was closer to 690 kPa standard Thai truck compressive strain than 700 kPa FWD compressive strain.

However, in cases of compressive strains between 400 and 2,900 microstrains, 700 kPa FWD-standard Thai truck compressive strains yielded smaller error than 800 kPa FWD-standard Thai truck compressive strains. An average error of 8% was obtained for 700 kPa FWD-standard Thai truck compressive strains, whereas an average error of 11% was obtained for 800 kPa FWD-standard Thai truck compressive strains. As a consequence, for the compressive strains between 400 and 2,900 microstrains, 700 kPa FWD compressive strain was closer to 690 kPa standard Thai truck compressive strain than 800 kPa FWD compressive strain.

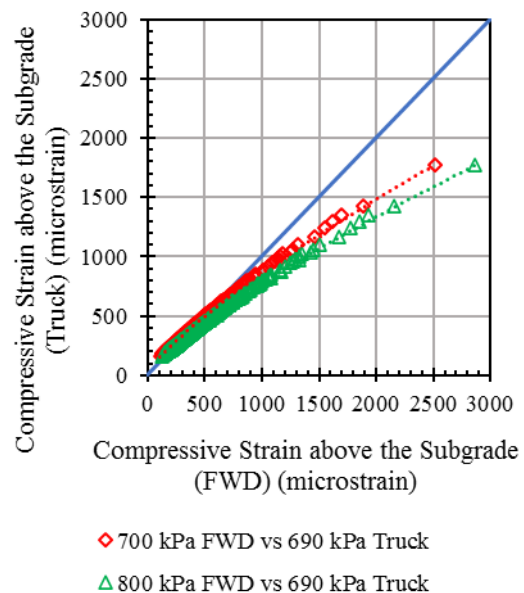


Fig. 4 Comparison between FWD and standard Thai truck compressive strain above subgrade



## CONCLUSION AND RECOMMENDATIONS

This study examined the structural responses of 625 flexible pavements under 700 kPa FWD, 800 kPa FWD, and 690 kPa standard Thai truck loads. A total of 625 LEA cases was performed to investigate the pavement structural responses. The responses from both 700 kPa and 800 kPa FWD were compared with standard Thai truck in order to determine the most suitable loading pressure of FWD.

The comparison results indicated that the average error was about 10% for 800 kPa FWD-standard Thai truck deflections, while 21% for 700 kPa FWD-standard Thai truck deflections. The average error was respectively 2% and 14% for 800 kPa FWD-standard Thai truck and 700 kPa FWD-standard Thai truck tensile strain at the bottom of thin asphalt surface. The average error was respectively 38% and 21% for 800 kPa FWD-standard Thai truck and 700 kPa FWD-standard Thai truck tensile strain at the bottom of thick asphalt surface. The average error ranged from 7% to 11% for 800 kPa FWD-standard Thai truck and 8% to 12% for 700 kPa FWD-standard Thai truck compressive strain above the subgrade.

Based on the LEA, this study suggested that 800 kPa FWD deflection was closer to 690 kPa standard Thai truck deflection than 700 kPa FWD deflection. Therefore, it is recommended that 800 kPa FWD could be considered in the development of future deflection-based design approach in Thailand. The nonlinear analysis could be further investigated to verify with the linear analysis.

## REFERENCES

- [1] Ekwulo E.O., and Eme D.B., Fatigue and Rutting Strain Analysis of Flexible Pavements Design using CBR Methods, *African Journal of Environmental Science and Technology*, Vol. 3, Issue 12, 2009, pp.412-421.
- [2] Mathew T.V., and Rao. K.V.K., Introduction to Transportation Engineering, *Civil Engineering-Transportation Engineering*, IIT Bombay, NPTEL, 2006, pp. 1-8.
- [3] Haung Y.H., *Pavement Analysis and Design*, 2nd Edition, Upper Saddle River, Pearson Prentice Hall, New Jersey, USA, 2004, pp.57-76, pp.94-143.
- [4] Burmister D.M., The General Theory of Stresses and Displacement in Layered Soil Systems, *Journal of Applied Physics*, Vol.16, Issue 2,1945, pp. 89.
- [5] Sawangsuriya A., Sirirattanachat, T., Taworn, D., and Yuayong, S., Application of Falling Weight Deflectometer to Access Road Structural Condition for Thailand Pavement Management System, *Engineering Journal of Research and Development*, The Engineering Institute of

- Thailand under H.M. The King's Patronage (EIT), Vol.31, Issue 3, 2019, pp.51-54
- [6] Morgan J.R., *Flexible Pavement Behaviour and Application of Elastic Theory – A Review*, Part of the Australian Road Research Board's Research Programme, Vol. 4, Issue 2, 1968, pp.1201-1205
- [7] Boussinesq J., *Application Des Potentiels À L'étude De L'équilibre Et Du Mouvement Des Solides Élastiques*, Gauthier-Villars, Paris, 1885.
- [8] Burmister D.M., *The Theory of Stresses and Displacements in Layered Systems and Applications to the Design of Airport Runways*, Highway Research Board, National Research Council, Washington, DC, USA, Vol. 23, 1944, pp. 126-144.
- [9] Sawangsuriya A., Imjai T., and Malaikrisanachalee S., Structural Responses of Flexible Pavement Subjected to Different Axle Group Loads, *Walailak Journal of Science and Technology*, Vol. 17, Issue 12, 2020, pp.1356-1366.
- [10] Srikanth M. R., Study on Analysis of Flexible Pavement using Finite Element based Software Tool, *International Journal of Engineering Research and Technology*, Vol. 4, Issue 9, 2015, pp.912-916.
- [11] Official, T., *AASHTO Guide for Design of Pavement Structures*. The American Association of State Highway and Transportation Officials, Washington, DC, USA, 1986.

## PERFORMANCE OF BEARING LAYER CONSTRUCTED USING LIGHTLY CEMENTED CLAY

Juan Wei Koh<sup>1</sup>, Soon Hoe Chew<sup>1</sup>, Yeow Chong Tan<sup>2</sup>, Cheng Soon Teo<sup>2</sup>, Shanyin Kee<sup>2</sup> and Danette S.E. Tan<sup>2</sup>

<sup>1</sup> Department of Civil and Environmental Engineering, National University of Singapore, Singapore,

<sup>2</sup> Housing & Development Board, Singapore

### ABSTRACT

Tons of excess clayey soils are excavated yearly from Singapore's underground construction activities. This clayey soil is often repurposed as infill material in land reclamation projects. The issue with using clayey soil as infill material is that ground improvement works, such as surcharge preloading with prefabricated vertical drains, are required to treat the clayey infill material due to its highly compressible and low-strength properties. Traditionally for this treatment, a bearing layer made from sandy soil must be laid on top of the infill material to support the machinery for the subsequent ground improvement work. In a Singapore land reclamation project, it is proposed to partially replace this sandy soil layer with lightly cemented clay layer. The performance of this lightly cemented clay layer was evaluated based on the unconfined compressive strength (UCS) of undisturbed samples and the ultimate bearing capacity estimated from the plate load test. In addition, the coefficient of permeability determined from the double-ring infiltration test was assessed. It was found that the average UCS was about 55 kPa, the ultimate bearing capacity was about 280 kPa, and the in-situ permeability was in the order of  $1 \times 10^{-7}$  m/s. Finally, the lightly cemented clay-based bearing layer was proved to be robust when loaded with a real partition bund of 6m high with a base width of around 15 m.

*Keywords: Clayey soil, Land reclamation, Bearing layer, Lightly cemented clay*

### INTRODUCTION

Numerous underground construction activities, such as basement excavations and tunnelling works, take place in Singapore every year. These underground construction works produce tons of excess excavated clayey soil. This clayey soil is repurposed as fill material in land reclamation projects. The problem with using clayey soil as an infill material is that it will undergo excessive settlement and is highly unstable when loaded due to its highly compressible and low-strength properties. Thus, ground improvement works, such as surcharge preloading with prefabricated vertical drains, are required to treat the clayey infill material. Traditionally for this treatment, a load-bearing layer made from sandy soil must be laid on top of the infill material to support the weights of machinery, material and workforce during ground improvement work. However, it was proposed to research further to partially replace this sandy soil with lightly cemented clay to form the load-bearing layer.

A 0.5 m thick lightly cemented clay layer was constructed in this project. Fig. 1 shows the schematic diagram of the constructed cemented clay layer laid on the clayey infill soil. After completing the cemented clay layer, in-situ and laboratory tests, including unconfined compression test of cored samples and laboratory cured samples, plate load test and double-ring infiltration test, were carried out to

check its quality and performance. Eventually, the cemented clay layer was loaded with a trapezoidal shape partition bund, which is 6 m high, and base width of about 15 m. This partition bund was made of stacking geotextile tubes filled with cemented clayey soil. The detail of this partition bund can be found in [1, 2]. The function of this bund is to form a partition for the infilling process for a large reclaimed area. In addition, this bund serves as the "loading test" for the cemented clay-bearing layer and enables the realistic evaluation of the overall stability and soundness of the constructed cemented clay-bearing layer.

Introducing cement into in-situ clayey soil would improve its strength and stiffness. In this project, only the top layer shallow portion of the clayey soil is required to be improved with cement to form the load-bearing layer. Thus, the conventional deep mixing method, which is for greater depth, is unsuitable for this application. Instead, a shallow soil mixing technique was explored in this application.

The early strength development of the cemented soil is the crucial criterion for field implementation. The factors that affect the early strength development of the cemented soil such as type of cement, cement dosage [3], cement dosing method [4], mixing loops/passes [5], mixing blade design [4] and others, have been discussed. Based on a field pilot trial conducted prior to this project, it was concluded that the soil mixed with CEM 1 cement ( $C=7\%$  by

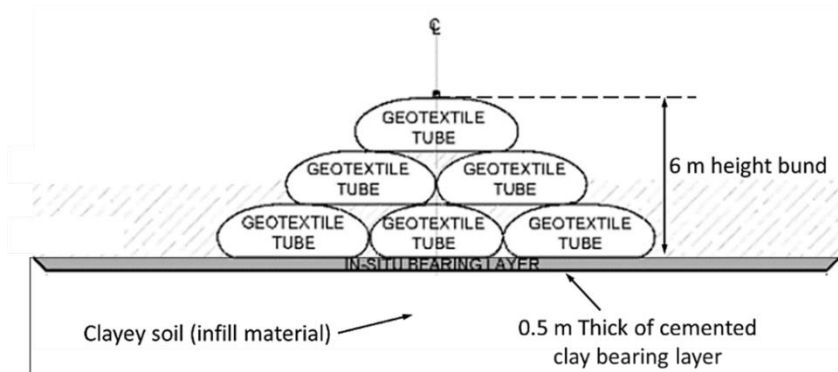


Fig. 1 Schematic diagram of the 0.5 m thick cemented clay layer and the 6 m height bund.

weight) in 3-passes is an optimised operation for this project, and the final product can provide adequate stability for subsequent construction work [5]. Early study also shows that 3-passes of mixing are needed to achieve a satisfactory uniformity of the cemented clay layer.

Before the field pilot trial, a laboratory test that simulates the shallow mixing operation was carried out and established that a 2-layer dosing method and an overlapping mixing blade design would produce a more uniform cemented clay layer [4]. These findings were then applied on-site.

In actual field work, 7 % of CEM 1 cement dosage by weight and 3-passes of mixing were employed to construct the bearing layer. Fig. 2 shows the construction of the bearing layer using a mixing bucket attached to an amphibious excavator.

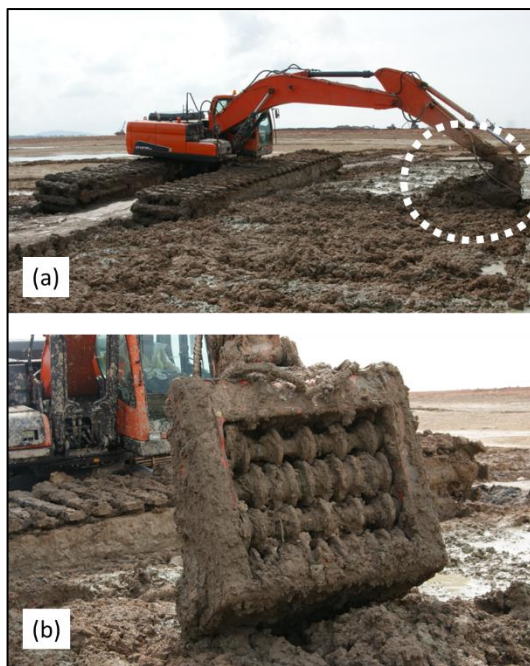


Fig. 2 (a) The amphibious excavator with soil mixing bucket; (b) The close-up view of the soil mixing bucket.

## PERFORMANCE OF THE CEMENTED CLAY LAYER

In order to ensure the quality of the load-bearing layer, a series of QA/QC tests, which comprise unconfined compression tests (UCT), plate load tests and double-ring infiltration tests, were conducted at designated locations.

### Unconfined Compressive Strength (UCS)

The unconfined compressive strength (UCS) of the cemented clay bearing layer was determined through three types of samples. First is the in-situ cored sample, where the cemented clay was mixed in-situ and cured in the ground; and was cored on the 3<sup>rd</sup>, 7<sup>th</sup>, and 28<sup>th</sup> Days of curing for the UCS test. The second type of sample was mixed on-site using the in-situ mixing bucket; the slurry state cemented clay was then poured into a UCS mould of 50 mm in diameter and 100 mm in height. Subsequently, these samples were cured in a controlled laboratory condition for wet curing. The third sample type is the same as the second type, except it used dry curing. Wet curing means the sample is submerged in water until the testing date, while dry curing means leaving the sample cured in air. Comparing the UCS under the different curing methods would assist in determining which laboratory curing method would more represent the in-situ curing conditions of the cemented clay for UCS determination.

The UCS result of the cemented clay layer is shown in Fig. 3. All the samples show an increase in strength from the 3<sup>rd</sup> to the 28<sup>th</sup> Day. On the 28<sup>th</sup> Day, the in-situ samples' UCS range from 27 – 90 kPa, where the mean and standard deviation is 55 kPa and 16.4 kPa, respectively. The high standard deviation shows some non-uniformity within the in-situ cemented clay layer. In addition, the laboratory wet curing samples show a lower UCS than the laboratory dry curing samples. The wet curing condition made the samples saturated as there was excess water available during hydration, while the dry curing condition resulted in the sample being partially

saturated as the water added during the initial mix was used for hydration. This difference in the degree of saturation would induce a different strength of cementitious products [6].

Comparing the in-situ samples with the laboratory cured samples revealed that the laboratory wet curing method would get a closer UCS value to the in-situ sample at an average of 61 kPa (28<sup>th</sup> Day), while laboratory dry curing produced a higher UCS value at an average of 99 kPa (28<sup>th</sup> Day). This result concluded that the in-situ cemented clay condition was very likely to be watery, which could be due to the exposure to rainwater.

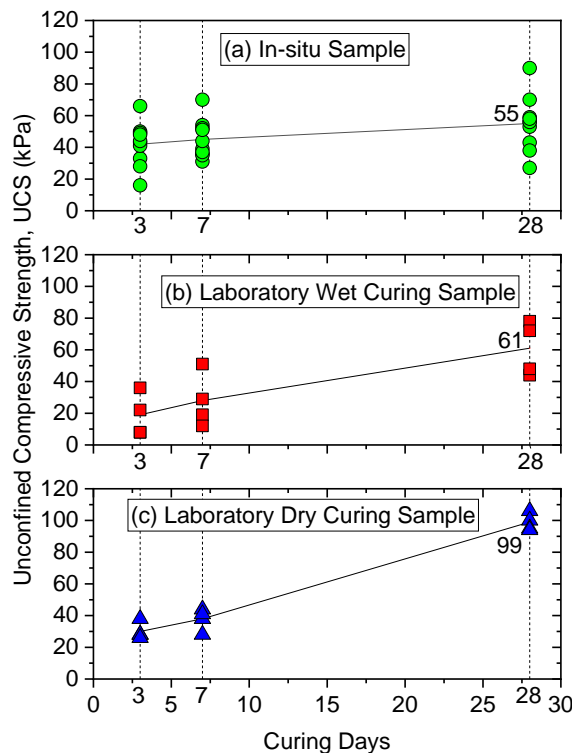


Fig. 3 Unconfined compressive strength (UCS) of the cemented clay: (a) In-situ Sample; (b) Laboratory Wet Curing Sample; and (c) Laboratory Dry Curing Sample.

### Ultimate Bearing Capacity

As the UCS strength checks via cored samples can only capture a particular localised area of the cemented clay bearing layer, plate load tests at two different locations were planned and conducted to examine the bearing capacity of the cemented clay layer on a broader area.

The designed allowable bearing capacity of the bearing layer to support the bund is 71 kPa, which is also called the working load (WL). The plate load test was designed to determine the settlement of the bearing layer under this working load (71 kPa) and up

to three times the working load (213 kPa). The plate size is 300 mm in diameter, and 25 mm in thickness, the influence zone underneath the plate is up to three (3) times the plate diameter, which is 900 mm, which is larger than the thickness of the bearing layer. The plate load test setup is shown in Fig. 4. The counterweight for the test was provided by two (2) water tanks, and (3) three LVDT (linear variation displacement transducers) were installed to monitor settlement.

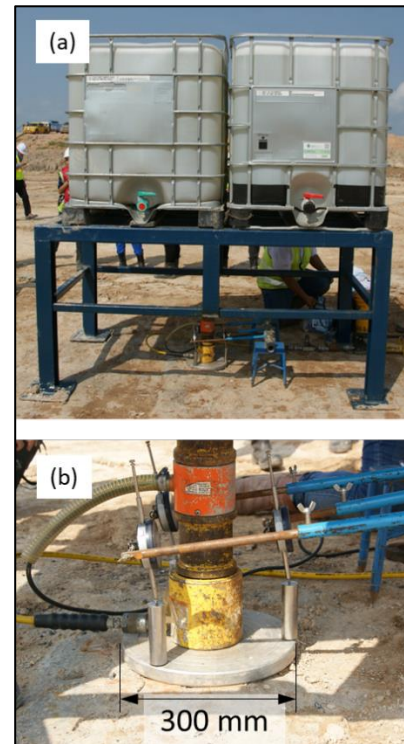


Fig. 4 (a) Plate load test setup; and (b) Close-up look at the 300 mm diameter plate.

The pressure-settlement curve for plate load tests is shown in Fig. 5. Based on the figure, the measured settlement was 3.033 mm at  $3 \times$  working load for Test 1, and 2.79 mm at  $2.5 \times$  working load for Test 2. Both maximum settlements are considered minimal and satisfying for serviceability criteria.

In addition, hyperbolic method was used to estimate the ultimate bearing capacity of the bearing layer from the load-settlement data of the plate load tests. In this method, the graph of settlement over pressure ( $x/q$ ) against settlement ( $x$ ) was plotted, as shown in Fig. 6. The ultimate bearing capacity,  $q_{ult}$ , which is the inversed gradient of the graph, was found to be 270 kPa and 285 kPa for Plate Load Test 1 and 2, respectively.

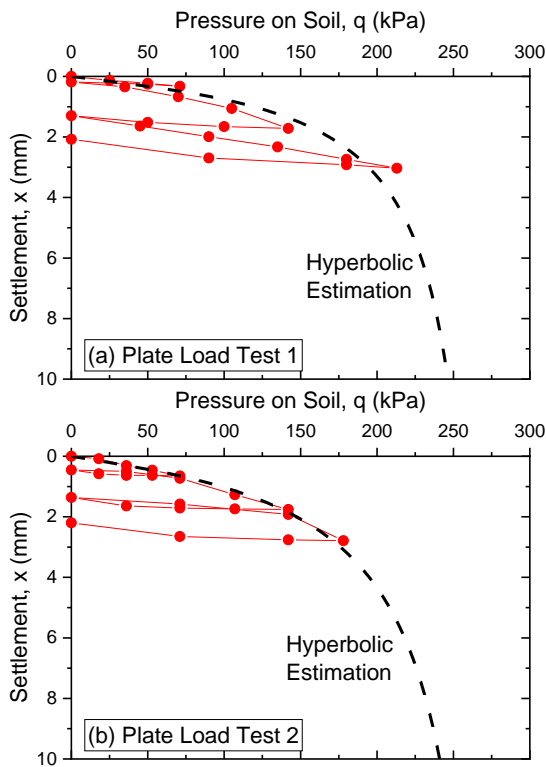


Fig. 5 Pressure-settlement curves: (a) Plate load test 1; and (b) Plate load test 2.

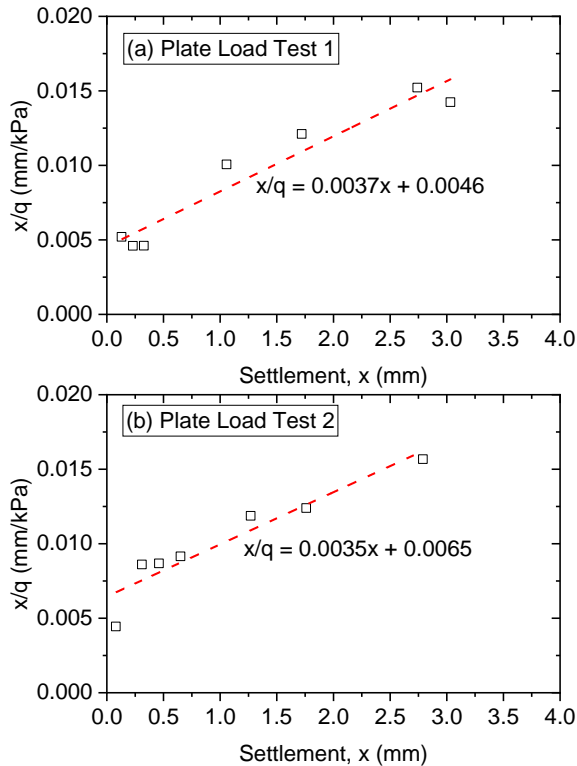


Fig. 6 Settlement over pressure against settlement plots: (a) Plate load test 1; and (b) Plate load test 2.

Conservatively, the estimated ultimate bearing capacity of 270 kPa was used for the bearing layer's safety factor check against the 6 m high bund. Three-layer of geotextile tubes were stacked together to form the 6 m height bund. Thus, the surcharge pressure on the bearing layer due to the weight of the bund is 102 kPa. Based on this bund's pressure and the calculated ultimate bearing capacity, the factor of safety of the bearing layer is found to be 2.6. Therefore, the bearing layer is safe and adequate for constructing the 6 m high bund.

### Undrained Shear Strength

The undrained shear strength of the cemented clay layer bearing layer can be calculated from UCS strength. The undrained shear strength can also be estimated by back-analysing the ultimate bearing capacity value.

In this application, the stronger cemented clay-bearing layer is laid above the weaker infilling clay layer to form a two-layered system. Two failure modes during the plate load test may occur in this system, depending on the depth of this bearing layer.

Based on Meyerhof and Hanna's [7] descriptions, it was found that the failure mode of this cemented clay layer during the plate load test was located in the top layer. Hence, the ultimate bearing capacity ( $q_{ult}$ ) of the bearing layer, which is considered undrained saturated clay, can be estimated via the equation below:

$$q_{ult} = 1.3c_u N_c \quad (\text{circular base})$$

where,  $c_u$  is the undrained shear strength, and  $N_c$  is the undrained shear strength coefficient ( $N_c = 5.14$ ).

Fig. 7 shows the undrained shear strength of the cemented clay bearing layer obtained by these two methods. As the UCS of the cemented clay has a wide range between samples, the undrained shear strength estimated via UCS is also scatter, where the upper bound value is 45 kPa and the lower bound value is 14 kPa. Nevertheless, most of the samples' undrained shear strength falls around 25 – 30 kPa, which is the firm clay category [8]. Meanwhile, from the two ultimate bearing capacity values obtained from the test, the undrained shear strength was back-calculated to be 40 kPa and 42 kPa. Hence, a reasonable undrained shear strength should be in the range of 25 – 40 kPa.



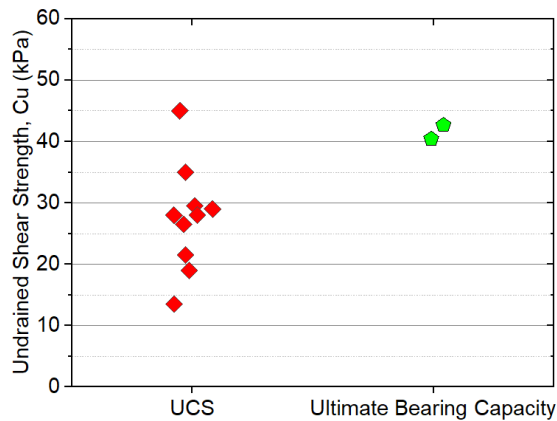


Fig. 7 Undrained shear strength of the cemented clay layer.

### Permeability

Besides the strength check, the in-situ permeability of the bearing layer at two random locations was determined using the double-ring infiltrometer. The double ring infiltrometer is a simple instrument used for determining water infiltration of the soil (Measurements according to ASTM D3385 standard test method). The rings are 500 mm in height, 300 mm (inner ring) and 600 mm (outer ring) in diameter. The infiltration rate is expressed in the volume of water per ground surface and per unit of time (L/T). The infiltration rate will reduce with time. The stable infiltration rate at a fully saturated state can be taken as permeability. The permeability of the bearing layer was found to be at  $1 - 2 \times 10^{-7} \text{ m/s}$ , which can be considered as silty soil permeability.

### Stability and Structural Soundness of Cemented Clay Layer

After assessing the quality of the cemented clay layer through the various tests, it was deemed to be safe to construct the 6 m partition bund on top of it. Fig. 8 shows the photo of the cemented clay layer with half of the partition bund constructed. Visual observation during and after the partition bund was constructed revealed that the lightly cemented clay layer was stable and did not have any damage. After completing the containment bund construction, no apparent settlement or crack was found on the bearing layer.

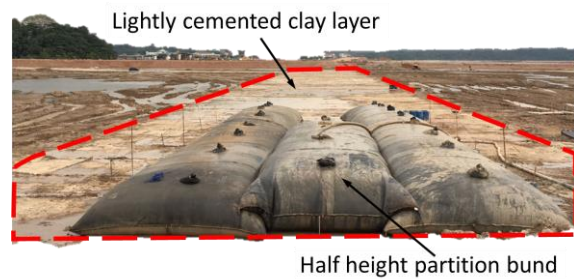


Fig. 8 Lightly cemented clay layer loaded with the half-height of partition bund.

### CONCLUSIONS

This project proposed the replacement of the conventional top-sandy soil layer with a layer of lightly cemented clayey soil layer. This layer functions as a weight-bearing layer to support the machinery and human weight during ground treatment works. The lightly cemented clay was constructed using 7 % CEM I cement dosage and 3-passes mixing sequence. Its unconfined compressive strength, bearing capacity, undrained shear strength and permeability were evaluated through in-situ and laboratory tests. Afterwards, the layer was loaded with the 6 m height partition bund construction using geotextile tubes. The key findings and conclusions are summarised as follows:

- Unconfined compressive strength (UCS) of the in-situ cored samples showed a wide range of scattering between 27 kPa to 90 kPa on the 28<sup>th</sup> Day. This result implies the non-uniformity of the mixed in-situ cemented clay layer. It also showed that the wet cured laboratory samples were close to field data, indicating that the in-situ cemented clay layer curing was continuously exposed to moisture conditions.
- The ultimate bearing capacity of the cemented clay layer was 270 – 285 kPa. Based on the lower bound of the ultimate bearing capacity, the safety factor of the bearing layer to support the partition bund is 2.6.
- The undrained shear strength of the cemented clay layer ranged from 14 – 45 kPa, while the majority was at 25 – 30 kPa. This undrained shear strength is classified as firm clay.
- The permeability of the cemented clay was on the order of  $10^{-7} \text{ m/s}$ , which is close to silty soil permeability.

Based on the results and visual inspection during and after the construction partition bund, the cemented clay layer is verified to be firm enough to support the weight of the partition bund.



## ACKNOWLEDGMENTS

The authors would like to thank Housing and Development Board (HDB), Singapore, for funding the “Joint Study on the Reuse of Excavated Soft Clay Material for Land Reclamation Works” research project. In addition, the authors gratefully acknowledge the support of Hyundai Engineering & Construction Co., Ltd. and Geoharbour Co., Ltd. for coordinating and carrying out the field tests reported here.

## REFERENCES

- [1] Chew S. H., Yim H. M. A., Koh J. W., Eng Z. X., Chua K. E., and Tan S. E. D., Performance of Pilot Test of Geotextile Tube Filled with Lightly Cemented Clay, in Proceedings of the 11th International Conference on Geosynthetics, 2018.
- [2] Koh J. W., Chew S. H., Chua K. E., Yim H. M. A., and Eng Z. X., Effect of Construction Sequence on the Performance of Geotextile Tubes in a Containment Bund. *International Journal of GEOMATE*, Vol. 19, Issue 74, 2020, pp. 1–7.
- [3] Kamruzzaman A. H., Chew S. H., and Lee F. H., Structuration and Destructuration Behavior of Cement-Treated Singapore Marine Clay. *Journal of Geotechnical and Geoenvironmental Engineering*, Vol. 135, Issue 4, 2009, pp. 573–589.
- [4] Yim H. M. A., Koh J. W., Chew S. H., Chua K. E., and Tan S. E. D., Study on the Performance of Shallow Soil Mixing with Cement. *International Journal of GEOMATE*, Vol. 19, Issue 74, 2020, pp. 15–21.
- [5] Chew S. H., Eng Z. X., Chua K. E., Lim T. Y., and Tan S. E. D., Pilot Field Test on Shallow Mixing of Lightly-Cemented-Clay, in Proceedings of the 70th Canadian Geotechnical Conference, 2017.
- [6] Subramanian S., Khan Q., and Ku T., Strength Development and Prediction of Calcium Sulfoaluminate Treated Sand with Optimised Gypsum for Replacing OPC in Ground Improvement. *Construction and Building Materials*, Vol. 202, 2019, pp. 308-318.
- [7] Meyerhof G. G., and Hanna A. M. Ultimate Bearing Capacity of Foundations on Layered Soils under Inclined Load. *Canadian Geotechnical Journal*, Vol. 15, 1978, pp. 565–572.
- [8] Look BG, Handbook of Geotechnical Investigation and Design Table, 2007, pp. 54.

# CORROSION OF UNDERGROUND STEEL BETWEEN SOIL AND CLAY AND ITS PREVENTION

Keiyu Kawai<sup>1</sup> and Takahiro Nishida<sup>2</sup>

<sup>1</sup>Civil and Environmental Engineering, Ehime University, Japan;

<sup>2</sup>Civil Engineering, Shizuoka Institute of Science and Technology, Japan

## ABSTRACT

This study reports on the corrosion of underground steel such as pipelines located especially between soil and clay. Macro-cell corrosion tended to occur at the steel in the clay owing to the variations of oxygen permeability. This led to localized corrosion thus suggesting that higher corrosion rate tended to occur in the clay regions with reduction of oxygen in the sand regions. This can be explained by the electro-chemical measurements such as half-cell potentials and cathodic polarization curves. To prevent such corrosion of underground steel between sand and clay, this study explored techniques to prevent the localized corrosion taking place in underground steel. Based on the results obtained, the use of oxygen reducing materials could be effective in preventing those localized corrosion by inhibiting cathodic reactions in the sand regions. This provides insights into the anti-corrosive techniques in enhancing corrosion resistance of underground steel such as pipelines by reducing oxygen concentrations in the sand regions.

*Keywords: Oxygen diffusion, Cathodic inhibitor, Macro-cell corrosion, Underground steel*

## INTRODUCTION

Recently, it has been reported that deteriorating pipelines have increased owing to corrosion of steel. This led to water leakage from cracking of steel and rupture of pipelines if severe. On the other hand, the visual inspection is often difficult on the buried pipelines in soil. It is widely known that deterioration of underground steel associated with corrosion is caused by electrolytic corrosion and macro-cell corrosion leading to localized corrosion. Especially, steel located between soil and clay tends to suffer from the localized corrosion owing to differences of oxygen permeability in which steel in clay leads to anodic region owing to the lower permeability of clay compared to that of sand as illustrated in Fig. 1 [1]. In order to prevent such localized corrosion, anti-corrosive techniques in preventing cathodic reactions as cathodic inhibitor in macro-cell corrosion formation was explored in this study.

For steel bars in concrete structures, macro-cell corrosion tended to occur leading to re-deterioration after patch repair method is carried out, which is caused by the chloride ions left remained in the existing regions of concrete [2]. Our recent study showed that the reduction of oxygen concentration in repaired parts of concrete is highly effective to prevent the macro-cell corrosion, which can be obtained by bio-based repair materials using *Bacillus Subtilis* [3]. Macro-cell corrosion which is often controlled by diffusion of oxygen could be inhibited by reduction of oxygen concentration leading to enhancement of corrosion resistance pertaining to the cathodic reactions by the consumption of water and oxygen.

Based on the research, this study explored the application of oxygen reducing materials including the bio-based materials to underground steel in soil and clay with respect to prevention of localised corrosion.

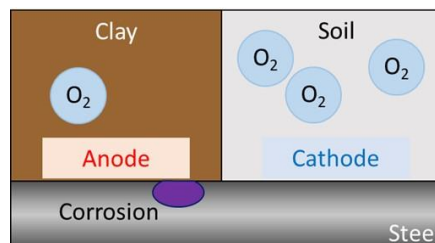


Fig. 1 Schematic of corrosion of underground steel by differences of oxygen concentration

## METHODOLOGY

This study explored the anti-corrosive techniques using oxygen reducing materials including blast furnace slag powder and *Bacillus Subtilis*. The former is advantageous in adsorption of heavy metals in addition to reduction of oxygen concentration and the latter could be possibly available in soil. In this study, the *Bacillus Subtilis* natto is specified as the micro-organism mixed in soil. And segmented steel bars are prepared to investigate the localized corrosion by electro-chemical measurements.

## Materials

This section reports on the materials properties of clay and soil used in this study. And specimen details

comprised of segmented steel bars in soil are described.

#### Soil and clay

The sand used in this study is silica sand (No.5) with apparent density of  $1.50 \text{ g/cm}^3$  obtained from Tohoku region in Japan. And the specific gravity of clay is  $2.45 \text{ g/cm}^3$  obtained from Okayama prefecture in Japan.

#### Blast furnace slag (BFS)

Blast furnace slag powder, a by-product of steelmaking, has been used as construction materials especially in corrosive environment, which is attributed to the enhanced resistance against ingress of chloride ions in concrete. This material is produced under reducible environment and could reduce oxygen concentration when contacted with water. The specific gravity of BFS is  $2.91 \text{ g/cm}^3$ .

#### *Bacillus subtilis natto* (N)

The rod-shaped ( $1 \mu\text{m}$  width and  $2\text{--}3 \mu\text{m}$  length) *Bacillus Subtilis* natto is resistant to unfavorable environmental conditions including salinity and extreme pH through the formation of an endospore at times of nutritional stress until conditions become favorable. The aerobic respiration essentially consumes oxygen in water in which oxygen concentration is significantly decreased. The culture solution containing  $5.96 \times 10^4 \text{ CFU/mL}$  is prepared and mixed in distilled water.

#### Specimens and experimental cases

Specimens are of cross section  $100 \times 125 \text{ mm}$ , and the length of  $200 \text{ mm}$  in acrylic container as shown in

Fig. 2. The sand parts are fully saturated with tap water or culture solution of *Bacillus Subtilis* natto, and clay is consolidated up to  $40 \text{ kPa}$  before the accelerated corrosion test started. For the cases of SCS specimens, the center part is comprised of clay and the both sides are comprised of silica sand with/without BFS and N. Segmented steel bars comprised of three steel elements were embedded in the specimens as shown in Fig. 2. The steel bar with  $\phi 13$  and length of  $20 \text{ mm}$  were connected by epoxy resin and lead wires were attached with each steel element to measure the electrical reactions on the steel bars.

The experimental cases are summarized in Table 1. Two types of specimens are tested such as SS specimens and SCS specimens. SS specimens are monolithic specimens consisted of silica sand tested under chloride environment. BFS and N are testing parameters for oxygen reducing materials in sand parts. On the other hand, the SCS specimens are comprised of clay (center part) and sand (side parts) in simulating the sandwich underground environment. Totally, 6 cases were tested for accelerated corrosion monitoring.

Table 1 Experimental cases

Cases	Specimen details
SS-Cl	Silica sand with $\text{Cl}^-$
SS-BFS	Silica sand with BFS and $\text{Cl}^-$
SS-N	Silica sand with N and $\text{Cl}^-$
SCS	Clay (center), Silica sand (sides)
SCS-BFS	Clay (center), BFS (sides)
SCS-N	Clay (center), N (sides)

Note: BFS is mixed in silica sand with a partial replacement ratio of 1.5%. *Bacillus Subtilis* natto is mixed in tap water and poured into the sand parts.

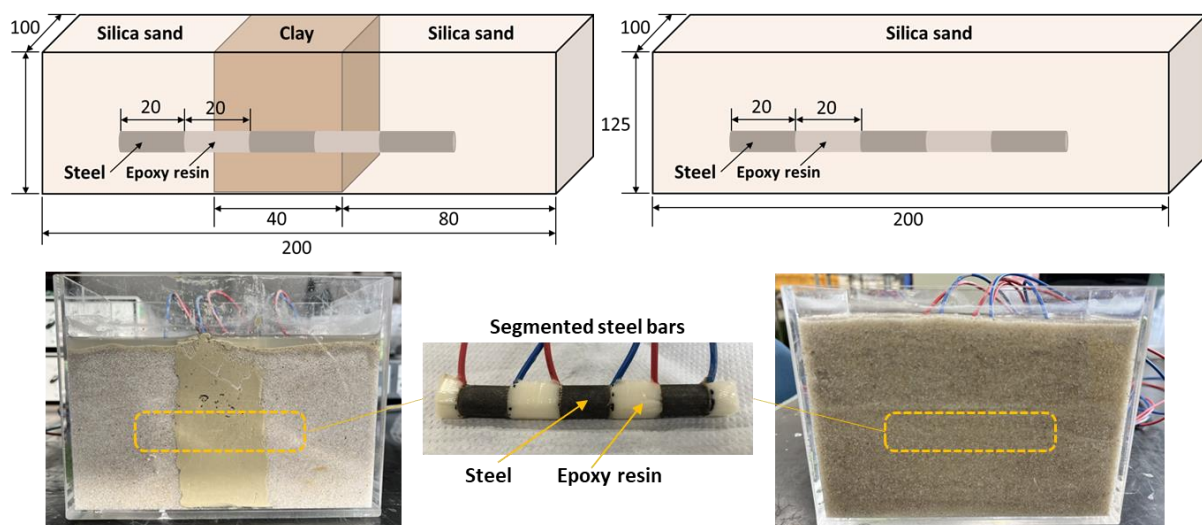


Fig. 2 Schematic of specimens and segmented steel bars in clay and sand

## Electro-chemical measurements

This section describes the electro-chemical measurements for determining the corrosion properties of steel in soil. In particular, the rate of oxygen permeability in soil was examined by cathodic polarization techniques in this study.

### Macro-cell corrosion

Macro-cell corrosion current density is determined by the current flows measured by ammeters connected with each segmented steel. The current flowing through steel A to B and B to C was simultaneously recorded by data logger and current density was calculated by dividing the current flows with surface area of a steel element. The measurements were carried out for three weeks at most for all the testing cases.

### Polarization measurements

Polarization tests were carried out on each steel element in clay or sand. The rate of polarization was specified as 1 mV/s and Ag/AgCl reference electrode was used for the measurements. The counter electrode was stainless steel located on the clay or sand. In this study, anodic and cathodic polarization curves are depicted based on the results and the integrity of passive films and oxygen permeability in cathodic regions were evaluated.

## RESULTS AND DISCUSSION

### SCS without oxygen reducing materials

Figure 3 shows the results of macro-cell corrosion current density measured in the case of SCS specimen. As can be seen in the figure, the anodic regions were formed in the clay parts. On the other hand, the steel bars located in the sand tended to form

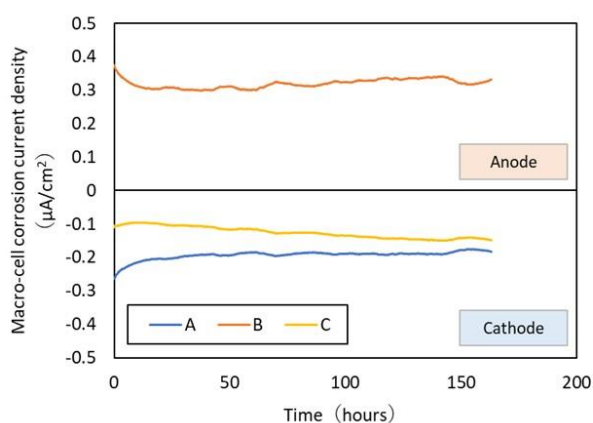


Fig. 3 Macro-cell corrosion current density in the case of SCS specimen

the cathodic region, thus macro-cell corrosion took place between clay and sand owing to the differences in oxygen permeability as reported by past research [1]. This can be explained by the changes of anodic polarization curves in Fig. 4. In particular, the current density in anodic region is likely to increase as illustrated by the curve measured on the steel B compared to that of steel C. This led to localized corrosion especially taking place in the steel B.

### SS specimens (SS-Cl, SS-BFS and SS-N)

This section reports on the effect of oxygen reducing materials in preventing corrosion of steel in soil. First, the corrosion properties under chloride environment were examined in the case of SS-Cl. Fig. 5 shows the results of macro-cell corrosion on average in each steel bar. As can be seen in the figure, macro-cell corrosion took place in the steel A with respect to anodic current density, which was increased up to  $0.15 \mu\text{A}/\text{cm}^2$ . And the steel bars B and C formed cathodic regions in the macro-cell corrosion. This is attributed to the variations of chloride ions around the steel bars in the sand.

For the case of SS-N specimen, the macro-cell corrosion current density was further increased up to about  $0.5 \mu\text{A}/\text{cm}^2$  although the oxygen concentrations in the soil could be reduced owing to the metabolic activity of *Bacillus subtilis* natto. This could be possibly attributed to the pH drop in the soil environment. In general, the cathodic reactions take place by the reduction of oxygen in the neutral to alkaline environment. However, the reactions are varied especially in acidic environment. In addition to the reduction of oxygen, generation of hydrogen could occur in the acidic environment, which is caused by the metabolic products such as organic acid.

As can be seen in the figure, the macro-cell corrosion current density is marginal in the case of SS-BFS. It is worth to note that the addition of BFS

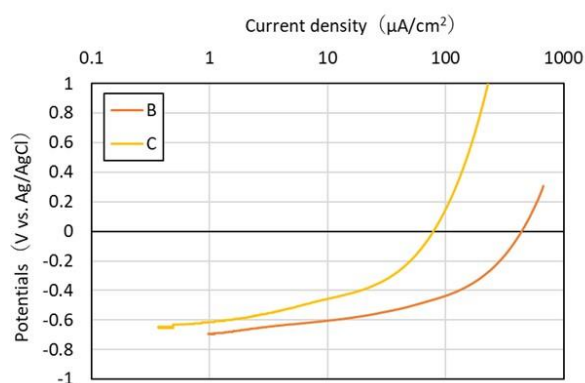


Fig. 4 Anodic polarization curves in the case of SCS specimen

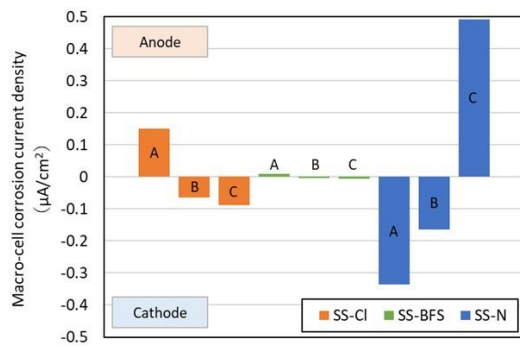


Fig. 5 Macro-cell corrosion current density in the cases of SS-Cl, SS-BFS and SS-N

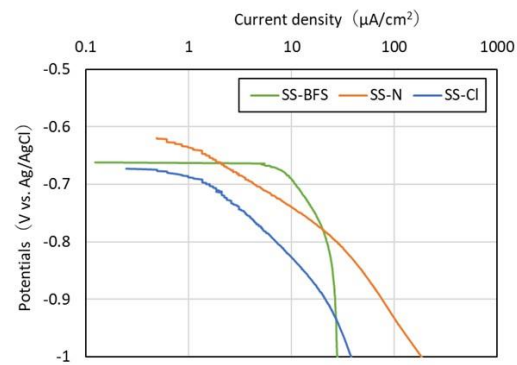


Fig. 6 Cathodic polarization curves in the cases of SS-Cl, SS-BFS and SS-N

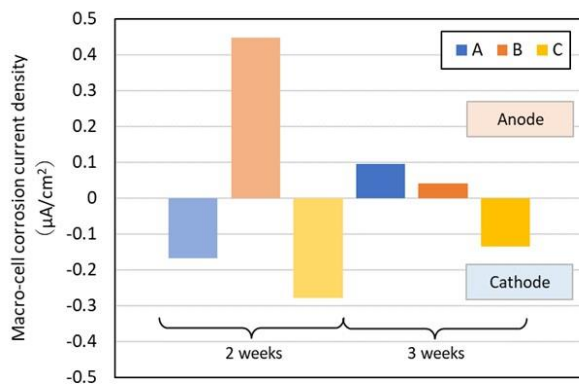


Fig. 7 Macro-cell corrosion current density in the cases of SCS-BFS up to 3 weeks

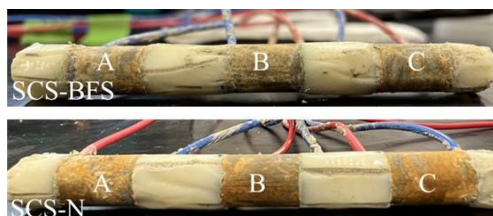


Fig. 8 Corrosion products of steel bars in the cases of SCS-BFS and SCS-N

is highly effective in preventing the macro-cell corrosion formation. This can be explained by the fact that the rate of oxygen permeability is significantly controlled by the availability of oxygen i.e. oxygen - diffusion controlled condition as illustrated by the cathodic polarization curve as shown in Fig. 6. The effect of oxygen reducing materials in preventing corrosion observed in SCS specimen is further examined in subsequent section.

### SCS with oxygen reducing materials

As mentioned in the previous section, macro-cell corrosion occurred in the SCS specimens owing to variations of oxygen permeability between clay and

sand in which cathodic reactions took place in the sand parts. If the oxygen concentration in sand parts is reduced, the cathodic reaction associated with reduction of oxygen could be decreased. The reduction of macro-cell corrosion current density in the SCS-BFS is significant until 3 weeks after tested as shown in Fig. 7. And the corrosion products generated in anodic region i.e., steel B is evidently distributed in smaller area in the case of SCS-BFS compared to those of SCS-N as shown in Fig. 8.

### CONCLUSIONS

The use of oxygen reducing materials could be effective in preventing localized corrosion by inhibiting cathodic reactions in the soil. This provides insights into the anti-corrosive techniques in enhancing corrosion resistance of underground steel such as pipelines by reducing oxygen concentrations in the soil.

### ACKNOWLEDGMENTS

This study is financially supported by JSPS KAKENHI Grant No.20K04657.

### REFERENCES

- [1] Ito, H., Suzuki, T., Kohno, E., and Aoki, M., Characteristic Evaluation of Macrocell Corrosion based on Concrete Soil relations in Service Steel Pipeline System, *Journal of Environmental Information Science*, Vol.23, 2009, pp.505-510.
- [2] Kawaai et al., Application of bio-based materials to crack and patch repair methods in concrete, *Construction and Building Materials*, 340(7), 2022, 127718.
- [3] Kawaai et al., Corrosion resistance of steel bars in mortar mixtures mixed with organic matter, microbial or other, *Cement and Concrete Research*, 124, 2019, 105822.



## PILE INSTALLATION EFFECTS ON THE STRESS AND DEFORMATION STATE OF SURROUNDING SOIL: REVIEW

Worku Firomsa Kabeta

Department of Geotechnical and Hydraulic Engineering, Faculty of Civil and Environmental Engineering,  
Gdańsk University of Technology, G. Narutowicza 11/12, 80-233 Gdańsk, Poland

### ABSTRACT

To investigate the impact of pile installation on bearing capacity, several field and model tests were conducted. However, little is known about how piles behave during installation, how they interact with the surrounding soil, and how this affects soil properties. This review paper, investigates the effect of pile driving on surrounding soil as its compact surrounding sandy soil was investigated. For this purpose, various related literature was studied based on the observation of the pile installation effect on earth pressure or lateral stress, relative density, and pore water pressure in the soil. A change in the deformation and stress state of surrounding soil due to pile driving was presented. The installation of fully displacement piles can lead to significant stresses and deformations in the surrounding soil. This is one of the main causes of uncertainty in the design and analysis of pile foundations. According to this study, the soil around the pile is compacted during pile driving, resulting in lateral and upward displacement. This leads to the densification effect of pile driving on loose sandy soil. Soil improvement with driven piles depends on pile shape, installation method, and pile driving sequences. Therefore, the driven pile can be used as a new method to improve the loose to medium-density subsoil.

*Keywords: Driven pile; Soil improvement; Pore water pressure; Lateral stress; Bearing capacity*

### INTRODUCTION

Loose sandy deposits should be improved to meet the subsoil requirements of large infrastructural projects, reducing soil settlements and structural deformations. Soil densification may also result in a reduction of liquefaction risk in saturated sandy soils [1]. There are many methods of deep soil compaction, including dynamic compaction, vibro-flotation or vibro-driving, sand pile compaction, compaction grouting, compaction by blasting, and the pile compaction method. Steel, concrete, timber, or composite piles arranged in a grid can be used for the latter. The piles with different shapes, either constant with depth or tapered, can be installed in loose sand by driving, vibro-driving, cyclic jacking, or statically pushing in. Pile driving has unquestionably been favored among the various forms of pile installation due to its numerous advantages, including high bearing capacity, rapid construction speed, and suitability for a wide range of soil conditions [2]. Due to noise and vibrations, their use in urban areas or near existing structures is, however, limited. Vibro-driving can reduce the force needed for installation decreasing the shaft friction. The pile base resistance could, however, increase during the vibro-driving process [3]. Recently developed technologies of cyclic jacking and pushed-in piles can overcome the difficulties related to noise and vibration level of previously described installation methods. The current knowledge about the effect of pile driving on the surrounding soil is reviewed and presented in this

study, which takes into account changes in stress state and displacement field, soil density, and pore water pressure

### Effect of pile driving on the surrounding soil

The full displacement pile installation process can cause significant stress and deformation in the surrounding soil. This is a key source of uncertainty in pile foundation analysis and design. A drive or jacking operation used to install a displacement pile generates changes in the soil characteristics and stress-strain states that affect pile settlement and bearing capacity [4].

### *Effect on the stress and deformation state*

During pile driving, the soil is vertically and radially pushed out to allow the pile penetration. As a result, the final lateral stress will be quite different from the in-situ stress in the free field (Figure 1). The pile installation method has a significant impact on the vertical capacity of the soil due to the high level of energy induced on it during pile driving. The entire stress field around the piles must be established to understand and model pile soil-structure interaction, load-displacement response, group action, and time-dependent behavior. In comparison to bored piles, driven piles produce a pre-stressed soil mass around the pile base, resulting in a stiffer pile base response. The mechanism of pile base penetration is similar to



that of a cone penetration test, and the cone resistance is related to the ultimate base capacity [5].

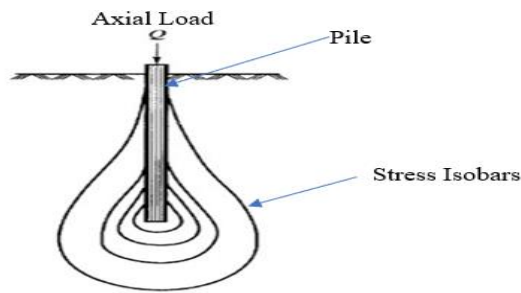


Fig. 1. Stress distribution near single pile.

As a result of the installation process, the soil properties at the pile-soil interface have also been observed to change. The particle size distribution near the pile can change, with fines reducing the interface friction angle at large deformations, according to laboratory experiments [6]. The behavior of the soil surrounding the pile during the pile installation is complex, and different laboratory tests on soil properties, interface parameters, and experiments, including calibration chamber or centrifuge test, should be used to model the entire system [7].

The effects of different installation methods, jacking and impact driving, are investigated for three different initial relative densities of sand [8]. According to their findings, the soil state after several method of installation (impact driving and pile jacking) varies significantly, according to their findings, and is also dependent on the sand initial density. The horizontal stress surrounding the pile increases with both impact driving and pile jacking. In jacked piles, however, the increase in horizontal stress is much greater than in impact-driven piles. Henke and Grabe [9] found that in a moderate-density sample of sand having relative density of 51–55%, the external horizontal stress in the vicinity of the pile tip is much lower after impact driving than jacking. Higher vertical stress near the pile tip is expected after jacking than after impact driving.

However, the degree of soil densification is higher after impact driving than after jacking, especially near the top of the pile. As a result of impact driving, the horizontal stress in the area below the pile tip increases. Improved soil strength is the result of the combined effects of increased stress and decreased void ratio (soil compaction). The magnitude of the peak horizontal stress increases as the initial relative density of sand increases. Jacked piles are also prone to soil arching more than impact-driven piles. During pile jacking, stress changes in the soil are significant near the pile, but they also extend a significant radial distance. Model tests and field measurements have been conducted during pile installation with pressure cells in the soil mass [3], [10].

Stress measurements are frequently taken in the field using a neighboring pile in which stiffness alters the stress field beneath the soil. To quantify this inaccuracy, precise stresses measurements caused by a single pile installation in laboratory conditions are required. Jacked pile experimental results [7] for sand show that with increasing  $h/R$ , the radial effective stress decreases, where  $h$  is the distance above the pile tip and  $R$  is the pile radius. During the jacked installation of a cylindrical pile in dry sand in a centrifuge, D'Arezzo *et al.* [11] used null gauges to measure horizontal stress changes. Stress is measured using both an adjacent pre-installed square pile and in-soil sensors. The normalized depth of the pile tip ( $h/R$ ) and the ratio of the increment of horizontal stress ( $\Delta\sigma_h$ ) to the pile base stress ( $q_b$ ) were calculated. As a result, the maximum horizontal stress increment at  $9D$  from the pile is 0.5 percent of the base resistance, indicating that horizontal stress decreases with increasing distance from the pile. The maximum changes in horizontal pressure occur when the pile tip is slightly above sensor level; the distance below the pile tip at which the maximum stress is detected is greater for shallower depths of penetration. Jardine *et al.* [12] obtained similar results at the same distance during the installation of a cylindrical pile in a calibration chamber.

Hughes and Robertson *et al.* [13] discovered that when a cone penetration test (CPT) probe penetrates sand, a highly stressed, rigid ring of sand forms around the tip. During pile penetration, a friction of loose sand forms around the pile. A thick cylinder of sand encircles the loosened sands and prevents the formation of complete lateral earth pressure on the pile through arching [14]. Arching is as a result of the sand compressibility relative to the piles, which causes friction between the soil and the piles (Figure 2). They also use information from the cone resistance data and the shape of the pressure expansion curve to determine in-situ stress conditions. Physical model of driven displacement piles can also be created using the full-displacement probe. After installation, the radial stress,  $\sigma'_{rc}$ , acting around the pile at any depth ( $z$ ), was found to varies with cone penetration test resistance, which reflects stiffness of sand and conditions, and to decrease as the pile installed and the relative depth above the tip increased. There was also a small reliance on the effective stress,  $\sigma'_{zo}$ .

Bond and Jardine *et al.* [16] proposed the equation (1) for radial stress expression for the design of cylindrical piles driven in sands.

$$\sigma'_{rc} = f(z) = 0.029q_c(\sigma'_{zo}/P_A)^{0.13}(h/R)^{-0.38} \quad (1)$$

In which  $P_A$  is the atmospheric pressure. The  $h/R$  and  $q_c$  variables have significant effects, but a change in  $\sigma'_{zo}$  only results in a 35 % change in  $\sigma'_{rc}$ .

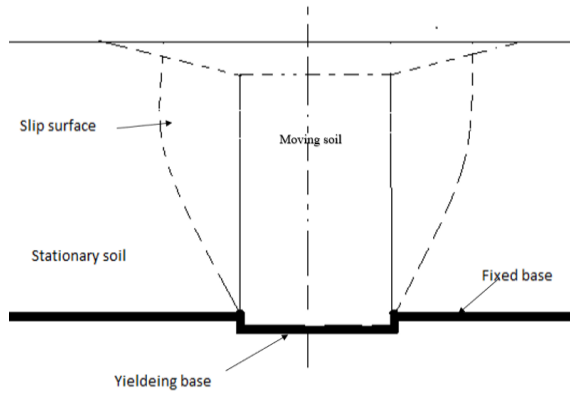


Figure 2. Stress redistribution caused by arching [15].

The stresses in the pile vicinity fluctuate dramatically as the distance between the pile axis and the radial distance increases, and as the distance between the pile tip and the top of the pile, according to all of the trials. When these data are combined with the field trends captured in the above equation (1), it appears that  $\sigma'_u$ , and  $\sigma'_r$  may be stabilized for fluctuations in free-field vertical stress  $\sigma'_{rz}$  and local  $q_c$ , and represented by 2D functions of the form.

$$\frac{(\sigma'/q_c)}{(\sigma'_{zo}/P_A)^{0.13}} = f\left(\frac{h}{R}, \frac{r}{H}\right) \quad (2)$$

Yang et al. [6] performed experimental investigations and three computational evaluations of stresses created around piles penetrating into sand. The cylindrical stresses surrounding piles intruding into normally consolidated quartz sand were investigated using a combination of three experimental studies and three numerical analyses. The interpretation summarizes predicted and measurement made at points between 10 and 550 kPa of the actual initial stress and between the relaxed and stressed states, which are related to stresses with Cone penetration test and dimensionless ratio of vertical stress  $(\sigma'_{zo}/P_A)^{0.13}$  and dimensionless spatial coordinates  $(h=R, r=R)$ , where the top of the pile is the origin of the coordinates, represent the final states and  $(h=R_p, r=R_p)$  represent the stresses around the exposed pile at moderate radial distances. Jardine et al. [12] interpreted stress measurements and presented the distribution of circumferential or vertical stress and radial stress as a function of distance to the penetrating pile in dense sand. They jacked up instrumented model piles in the calibration chamber with soil mass equipped with stress sensors. Emphasis was placed on the effective radial stresses occurring around the axes of the columns, but circumferential and vertical stresses were also taken into account. They interpreted detailed stress measurements taken on and around closed-ended model displacement piles in pressurized silica sand. The stresses that develop at any point are primarily

determined by CPT tip resistance and spatial position relative to the pile tip ( $h/R$  and  $r/R$ ), as expressed by:

$$\frac{\sigma'}{q_c} = f\left(\frac{h}{R}, \frac{r}{H}\right) \quad (3)$$

Where  $h/R$  is the (positive) relative height above or (negative) relative depth below the pile tip, and  $r/R$  is the relative radius from the pile axis.

The soil stresses vary spatially in relation to the pile tip location. The stress measurements performed by Jardine et al. [12] revealed that soil stresses developed during installation were directly correlated with local  $q_c$  values; normalization by  $q_c$  reduced the impact of test arrangement variations. Although the datasets have similar initial  $\sigma'_{rs}/q_c$  maxima as the pile tip passes and fall to similar final low  $\sigma'_{rs}/q_c$  ratios, the decay curves applied between these limits converge better when plotted against  $h/R$  than when plotted against the number of cycles ( $N$ ), indicating a closer correlation with relative pile tip depth than with the number of cycles. On-pile measurements show that doubling  $N$  did not result in steeper radial stress reductions for fixed  $h/R$  ratios. Soil mass stresses were unaffected by the number of jacking cycles. These characteristics, on the other hand, may be more important at the pile/soil interface, during dynamic installation, and over extended periods of time.

During both the penetration and pause stages, stress distributions established in the soil below and to either side of the tip level stress are roughly spherically symmetrical, though there are minor differences between the stress decay curves established on vertically and horizontally projected distributions.

Close to the pile tip, very steep stress gradients apply, with triaxial test dominating directly under the tip, where  $\sigma'_z = \sigma'_1 \approx q_c$  and  $\sigma'_{rm} = \sigma'_{\theta m} \approx q_c/Kp$ , in which  $Kp$  is Rankine coefficient of passive earth pressure.

After installation, the radial stress level reach peaks at normalized around significant radial distances  $r/R = 3$ , which are roughly double those operating on the shaft ( $r/R = 1$ ). At  $r/R > 3$ ,  $\sigma'_{rm}/q_c$  declines consistently with  $h/R$  for any given  $r/R$  and all radial stresses decompose with radius. Circumferential stresses vary at  $1 < r/R < 5$  range, according to the radial equations of equilibrium and  $\sigma'_{rs} < \sigma'_{\theta m}$  at  $1 < r/R < 3$  once installed. Here, one should notice that the maximum radial stress is not on the pile shaft, but at some distance. In low to medium density quartz sand, Lehane et al. [7] took extensive measurements of the effective stresses generated during installation, equalization, and load testing of displacement piles. They demonstrated that the stresses that develop at any given soil horizon are strongly influenced by the horizon's distance from the pile tip as well as the soil's initial state. As each jacking stage was started, the effective radial stresses

( $\sigma'_r$ ) risen by 5 to 20 kPa, causing the stationary profiles of  $\sigma'_r$ , known as  $\sigma'_{rs}$ , to separate from those recorded during the pile was moving. The long-term, fully equalized values ( $\sigma'_{rc}$ ) for a pile that has penetrated to the same tip depth but no further are the same as the stationary radial stresses recorded during installation pause periods ( $\sigma'_{rs}$ ), where  $\sigma'_{rc}$  is the radial effective stress after equalization and  $\sigma'_{rs}$  is the stationary radial effective stress.

Another study on the change in horizontal stress during pile driving were conducted by D'Arezzo et al. [17]. Null-gauges were used to measure horizontal stress changes during the jacked installation of a cylindrical pile in dry sand. They used an adjacent pre-installed square pile and in-soil sensors to measure stress, and then compared the centrifuge results to the radial stress distribution estimated using traditional methods. Their findings show that when the pile is at an equal distance between the pile null gauges and the soil null gauges, the pile experiences higher stresses due to its stiffness. For the determination of stress state near pile base [18] conducted field tests on piles equipped with surface stress transducers and discovered that severe stress fluctuations occur during sand penetration, particularly around the tips.

Beijer Lundberg et al. [19] conducted a series of geotechnical centrifuge tests of displacement pile installation in sand with various initial relative densities. The stress measurements included horizontal and axial contact stresses. The deformation measurements were displayed as displacement trajectories, with incremental stresses and soil displacements analyzed. The effect of load cycles and the influence of initial relative density were the focus of the measurement's interpretation. During pile installation and removal, the initial relative density was shown to have a significant impact on the horizontal contact stress. The horizontal displacement measurements revealed a similar impact, with denser soil samples exhibiting higher horizontal displacement. It was discovered that the soil compaction during cyclic loading shows in decreased horizontal contact stress. Dense, medium dense and loose sand with initial relative densities 0.4, 0.6 and 0.8 respectively were tested. The installation effects are strongly influenced by the relative density of the soil at the start of the experiment, according to the results. The measurements were compared to numerical models that produced similar results.

Lehane et al. [18] also used a drum centrifuge to test model piles in normally consolidated sand to see how the method of pile installation, level of stress, and aspect ratio of pile affected the increase in lateral stress on the pile while load testing. They consider pile aspect ratio (elongation) in the model tests as 1 for 14 model piles, 2 for two model piles and 6 for other two model piles. The ratios of lateral stress increases (the ratio of lateral stress in pseudo-

dynamic mode to jacked mode) measured during installation for  $h/D=3$  is higher than for  $h/D=6$ , where  $D$  is pile breadth. The difference between pseudo-dynamic and jacking installation mode is that piles are installed in a sequence of jacking strokes during jacked installation. For each stroke, the piles were pushed at 0.2 mm/s for 2 mm, then extracted at 0.005 mm/s until the pile head load was zero. During pseudo-dynamic installation, the piles were installed in a series of 2 mm downward jacking increments at 0.2 mm/s, followed by 1.5 mm extraction at 0.2 mm/s. Furthermore, due to soil compaction near the pile toe, base resistance increases with the number of cycles applied, whereas shaft load decreases with the number of cycles applied due to soil densification next to the pile shaft [17].

Figure 3 describes the effect of pile installation mode on lateral stress for both stationary and moving pile conditions. Accordingly, stationary lateral pile stresses ( $\sigma_{hc}$ ) are reduced as the distance above the pile tip ( $h$ ) increases. For the same type of installation method, lateral stresses when the pile is moving are greater than the lateral stresses when the pile is stationary [18]. They also discovered that the magnitude of lateral stress decreases as the distance between the pile tip and the pile diameter ( $h/D$ ) increases for both methods of installation.

Different measurement techniques are used to measure the deformation field around installed model piles. Otani et al. [20] investigated the deformation of sand surrounding a laterally loaded pile using X-ray computed tomography. Due to the high cost of CT scanners, it has limited application in geotechnical engineering. Particle image velocimetry (PIV), a cost-effective, full-field image correlation approach, and accurate has been employed in geotechnical engineering since the invention of digital image process [21]. In geotechnical research laboratories, PIV techniques have been used to measure soil deformations around a driven pile in sand in geotechnical models [22], [23]. According to study by White et al. [22], PIV is a velocimetry method that tracks textured particles in a series of images. Image processing algorithms have been written to apply the PIV principle to surface images. The resulting software is capable of tracking the movement of natural sand or soil to an accuracy of 1/15 pixel. The combination of digital imaging and PIV analysis makes it possible to calculate strain fields consisting of thousands of displacement vectors with greater accuracy than the averaging method.

Figure 4 shows the displacement contours after installation and displacement paths. Figure 4 (a) shows the boundary where there are no displacements as a thick dark line. These influence zones show where the soil is moved during the installation. According to the measurements, a pile model should at the very least include the boundaries of no displacements. The soil sample container should also

be wider, according to these measurements. Figure 4 (b) also shows the displacement path for loose soil and dense soil, showing that the initial density of the soil sample has a relatively large effect, with the dense soil sample experiencing more heaving vertical displacement than the loose soil sample.

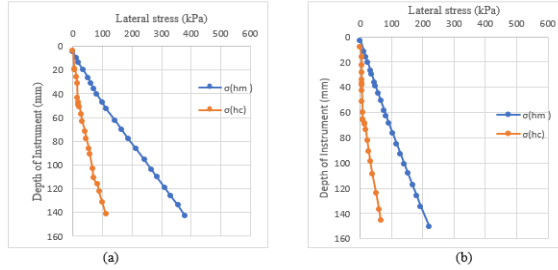


Figure 3. Lateral stresses (a) jacking installation; (b) installation by pseudo-dynamic [18],  $\sigma_{hc}$  is lateral stresses when pile is stationary and  $\sigma_{hm}$  is lateral stresses when pile is moving.

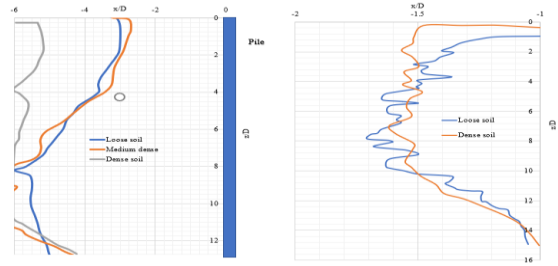


Figure 4. Displacement contours and paths (a) displacement contours and (b) vertical arrays of displacement path for typical location [24]

#### Effect on Pore water pressure

Because of soil compaction, pore water pressure rises during pile driving in loose sands and sandy silts, causing a reduction in effective soil strength. Numerous studies have tried to model the pore water response to pile installation or even other construction vibrations in the near-field analytically [4]. The initial stresses in the soil before the pile is driven are the horizontal effective stress ( $\sigma'_3$ ), the vertical effective stress ( $\sigma'_1$ ), and the pore pressure ( $u_0$ ).

The horizontal effective stress ( $\sigma'_3$ ), vertical effective stress ( $\sigma'_1$ ), and pore pressure ( $u_0$ ) are the initial stresses in the soil before the pile is driven. Vertical and horizontal stresses are also the major stresses. Because the horizontal strain in a natural deposit is zero,  $\sigma'_3$  equals  $K_0\sigma'_1$  where  $K_0$  is the coefficient at rest earth pressure [25].

Radial stress becomes the most critical stress within the failure zone during pile driving. The maximum excess pore pressure ( $\Delta u_m$ ) that results will be made up of two parts, one from the change in total ambient pressure ( $\Delta\sigma_3$ ), and the other from shearing, as follows [25]:

$$\Delta u_a = (1 - K_0)\sigma'_1 \quad (4)$$

$$\Delta u_s = (\Delta u/p)_m \sigma'_1 \quad (5)$$

Where  $p$  is the consolidation pressure,  $\Delta u_a$  is the change in pore water pressure from total ambient pressure,  $\Delta u_s$  the change in porewater pressure from shearing and  $(\Delta u/p)_m$  the maximum pore pressure ratio. Hence,

$$\Delta u_m = \Delta u_a + \Delta u_s = [(1 - K_0) + (\Delta u/p)_m] \sigma'_1 \quad (6)$$

The pore-pressure ratio  $(\Delta u/p)$  rises with the applied stress differential, reaches its maximum  $(\Delta u/p)_m$ , and then remains constant when a specific strain is reached [25].

The extra pore water pressure generated below the pile toe while driving in fine sandy soil was monitored [26], and the magnitude level of applied force and the strength level of soil material are the conditions affecting the level of excess pore water pressure. If these two parameters are at high level, the excess pore water pressure is considered to increase to the point of destruction of soil texture, and then produce the liquefaction phenomenon. A high-pressure zone of excess pore water was forming under the pile toe. This high-pressure zone operated as a barrier to pile driving, making further pile insertion impossible. The pile toe generated excessive pore water pressure, which spread throughout the surrounding area, with this pressure being transferred to the pile toe of the pre-driven pile.

At various distances from driven piles, variations in pore water pressures were measured in sandy and clayey soil layers by Hwang et al. [27]. To control the response of soil pore water pressure caused by pile driving, they used electrical piezometers. The pore water pressure of soil positioned at a radial distance of 3D from the center of the pile began to climb when the pile tip advanced to an elevation of 4 to 7D (D is the pile diameter) above the piezometer site, and reached its maximum value when the pile tip passed 4D below the piezometer location. At a distance of 3D from the pile's center, the extra pore water pressure in a sandy layer at 6 m below ground reached 1.5 times the effective overburden pressure, resulting in liquefaction conditions.

According to Fattah and Mustafa [28], twelve experiments with piles installed by overdriving were carried out on a fine sandy soil of medium density with a relative density of 60%. The changes in excess pore water pressure were measured at both the pile tip and the pile middle. The study reveals that pile slenderness ratio, machine operation frequency, and soil permeability are the parameters that influence the formation of extra pore water pressure. The excess pore water pressure generated during operation,

however, was found to be less than 20% of the initial hydrostatic pressure in all cases.

As the pile group installation is considered [25], the pore pressures due to the driving of each pile are quite easily discernible. For piezometers placed close to the pile, the maximum pore pressure is recorded about 20 minutes after the pile reaches the level of the piezometer tip. There is a slight effect of pore pressure redistribution from regions of high pressures to regions of low pressures for piezometers located further away from the pile.

Pore-water pressures were measured by inserting two piezometers at 9 and 18 meters below the ground surface during the inspection of piling activities [29]. Prior to the piling operations, readings from all piezometer were taken on a regular basis, at least once a day. As pile driving got closer, the piezometers readings were taken before and after each pile was driven. A significant increase in pore water pressure was generated at both the shallow and deep piezometers during pile section drive into very dense sand and gravel.

The amount of excess pore water induced during pile driving can be reduced by applying additional drains installed in the timber piles [30]. The extra pore pressure generated by 48 test piles with drains and 13 test piles without drains was measured. When the drain was used, the data showed that excess pore pressure was reduced by at least 50%. Furthermore, the procedure proved much less expensive than other methods for dealing with dangerously high pore water pressures caused by piling in similar soils. Pestana et al. [31] performed a geotechnical site investigation and a site control testing to measure horizontal loads and pore water pressure at three radial distances from large closed piles. Their findings show that pile driving causes significant excess pore pressures, which are related to the distance from the pile wall. Due to the excessive pore pressure generated by the pile installation, the initial effective vertical stress of the soil is slightly exceeded within one pile diameter. The generated excess pore pressure decreased as distance from the pile–soil interface ( $1/R^2$ , where  $R$  is the distance from the pile's center) increased. These pore pressures dissipate over time, and soils more than one diameter away from the pile wall achieve 80% consolidation between 50 and 80 days. Initial inclinometer measurements of outward radial deformations were very close to predictions based on cylindrical cavity expansion theory. Lateral deflection measurements show a return to the pile as the excess pore pressure dissipates, with a decreasing magnitude as the distance from the pile wall increases.

#### Effect of pile driving on the surrounding soil

There is the densification due driving pile on sandy soil. As a result, soil around the pile is

compacted, and lateral and upward displacement will occur. Several scholars and practicing engineers [2], [27], [32]–[34] have described the improved conditions that resulted from pile driving. The volume and shape of the pile, as well as the method of drive, determine the amount of this compacted area and the characteristics of the soil within it.

Depending on the grain size characteristics of the soil, on-site soil density, pile spacing, and pile diameter, the installation process can cause visible compaction and an increase in lateral stress [33]. It is well known that loose, clean, granular soils contract when displacement piles are installed [14]. When piles are installed in loose sand, some compaction occurs up to 3.5 to 6 pile diameters away from the pile shaft [35]. Szechy [36] also found that the void ratio decreased by around 5% near the lower half of driven piles. Unfortunately, few studies have been conducted since then on the extent and distribution of compaction around displacement piles.

The development of displacements around a full displacement pile causes loose sand to compact. The degree of sand compaction induced by driving has been related to bearing capacity improvement for pile [35]. Previous bearing capacity theories were mainly founded on the assumption that the soil conditions did not change as the pile was driven. However, pile driving not only increases the relative density of loose sand but also the horizontal stress, and the influence of compaction on the soil parameters cannot be ignored. The compaction increase caused by pile driving in loose sands can be related to the shift in the internal friction angle of sand and factored into pile ultimate bearing capacity estimates.

Meyerhof [35] examined the installation of a driven pile, resulting in compaction and a rise in the major stress ratio. He measured the width of the compacted zone around a single driven pile, and found that it was around 6 to 8 times the pile width. In model pile testing, Kishida [37] discovered that the distribution of displacement stresses caused by sand displacement as a result of pile driving was proportional to the width of the compacted zone. Based on their findings, the author determined that the width of this zone as  $b = 7D$ , as shown in figure 5.

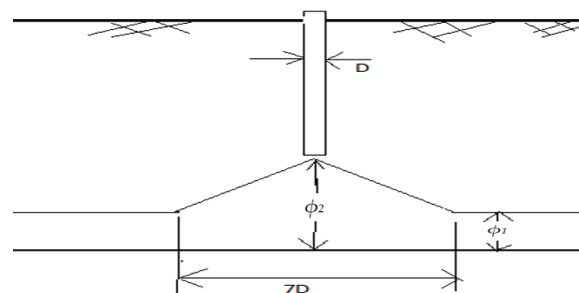


Figure 5. Effect on friction angle ( $\phi$ ) [37]



Kishida [37] assumed that the internal friction angle changes linearly with distance from the pile (where  $\phi = \phi_2$ ) to a radius of around 3.5 times the pile diameter (where  $\phi = \phi_1$ ) in the compacted zone thus established. In the sand, the link between  $\phi_1$  and  $\phi_2$  can be stated [35], [37] as:

$$\phi_2 = \frac{\phi_1 + 40^\circ}{2} \quad (1)$$

where  $\phi_1$  = Initial value friction angle.  
 $\phi_2$  = frictional angle after pile driving.

## CONCLUSIONS

Fully displacement piles can cause significant stresses and deformations in the soil surrounding them. This is one of the main causes of uncertainty in the design and analysis of pile foundations. During driving pile in loose sands and sandy silts, pore water pressure rises due to soil compaction. High compressive stresses arise in the adjacent soils during the driving of high displacement piles, resulting in a buildup of large effective lateral stresses. The compaction of the soil mass surrounding a pile increases its bearing capacity. As a result, the driven pile can be utilized as a soil compactor to enhance the soil surrounding the pile. The degree of sand compaction caused by driving the pile was related to the increase in bearing capacity of the driven pile in sand. The shape of driven piles has a significant impact on the degree of ground improvement achieved, revealing that driven tapered piles are more effective in densifying the ground than straight cylindrical ones. The spacing of displacement piles and the installation sequence affect their drivability. Unfortunately, few studies have been conducted since then on the extent and distribution of compaction around displacement piles. As the effect of pile shape on stress and deformation state is not well known in the case of tapered piles, the soil deformation and stress fields around constant diameter piles and tapered piles will be studied in a series of tests planned in the centrifuge at Gustave Eiffel University in Nantes within the Geolab project. The bearing capacity of constant diameter piles and tapered piles will be compared for the installation mode with driving and jacking. The soil deformation fields will be estimated using the PIV technique.

## REFERENCES

- [1] A. Janalizadeh and A. Zahmatkesh, "Lateral response of pile foundations in liquefiable soils," *J. Rock Mech. Geotech. Eng.*, vol. 7, no. 5, pp. 532–539, 2015, doi: 10.1016/j.jrmge.2015.05.001.
- [2] A. F. Homayoun Rooz and A. Hamidi, "A numerical model for continuous impact pile driving using ALE adaptive mesh method," *Soil Dyn. Earthq. Eng.*, vol. 118, no. January, pp. 134–143, 2019, doi: 10.1016/j.soildyn.2018.12.014.
- [3] S. Moriyasu, S. ichi Kobayashi, and T. Matsumoto, "Experimental study on friction fatigue of vibratory driven piles by in situ model tests," *Soils Found.*, vol. 58, no. 4, pp. 853–865, 2018, doi: 10.1016/j.sandf.2018.03.010.
- [4] M. F. Randolph, J. P. Carter, and C. P. Wroth, "Driven Piles in clay—The Effects of Installation and Subsequent Consolidation," *Geotechnique*, vol. 29, no. 4, pp. 361–393, 1979, doi: 10.1680/geot.1979.29.4.361.
- [5] J. H. Lee and R. Salgado, "Determination of Pile Base Resistance in Sands," *J. Geotech. Geoenvironmental Eng.*, vol. 125, no. 8, pp. 673–683, 1999, doi: 10.1061/(asce)1090-0241(1999)125:8(673).
- [6] Z. X. Yang, R. J. Jardine, B. T. Zhu, and S. Rimoy, "Stresses Developed around Displacement Piles Penetration in Sand," *J. Geotech. Geoenvironmental Eng.*, vol. 140, no. 3, p. 04013027, 2014, doi: 10.1061/(asce)gt.1943-5606.0001022.
- [7] B. M. Lehane, R. J. Jardine, A. J. Bond, and R. Frank, "Mechanisms of shaft friction in sand from instrumented pile tests," *J. Geotech. Eng.*, vol. 120, no. 8, pp. 1450–1452, 1994, doi: 10.1061/(ASCE)0733-9410(1994)120:8(1450).
- [8] S. Fan, B. Bienen, and M. F. Randolph, "Effects of Monopile Installation on Subsequent Lateral Response in Sand. II: Lateral Loading," *J. Geotech. Geoenvironmental Eng.*, vol. 147, no. 5, p. 04021022, 2021, doi: 10.1061/(asce)gt.1943-5606.0002504.
- [9] S. Henke and J. Grabe, "Numerical investigation of soil plugging inside open-ended piles with respect to the installation method," *Acta Geotech.*, vol. 3, no. 3, pp. 215–223, 2008, doi: 10.1007/s11440-008-0079-7.
- [10] K. Żarkiewicz and W. Qatrameez, "Assessment of stress in the soil surrounding the axially loaded model pile by thin, flexible sensors," *Sensors*, vol. 21, no. 21, 2021, doi: 10.3390/s21217214.
- [11] F. B. d'Arezzo, S. Haigh, M. Talesnick, and Y. Ishihara, "Measuring horizontal stresses during jacked pile installation," *Proc. Inst. Civ. Eng. Geotech. Eng.*, vol. 168, no. 4, pp. 306–318, 2015, doi: 10.1680/geng.14.00069.
- [12] R. J. Jardine, B. T. Zhu, P. Foray, and Z. X. Yang, "Measurement of stresses around closed-ended displacement piles in sand," *Geotechnique*, vol. 63, no. 1, pp. 1–17, 2013, doi: 10.1680/geot.9.P.137.
- [13] J. M. O. Hughes and P. K. Robertson, "Full-displacement pressuremeter testing in sand," *Can. Geotech. J.*, vol. 22, no. 3, pp. 298–307, 1985, doi: 10.1139/t85-043.
- [14] E. I. Robinsky and C. F. Morrison, "Sand



- Displacement and Compaction around Model Friction Piles,” *Can. Geotech. J.*, vol. 1, no. 2, pp. 81–93, 1964, doi: 10.1139/t64-002.
- [15] A. Shelke and N. R. Patra, “Effect of arching on uplift capacity of single piles,” *Geotech. Geol. Eng.*, vol. 27, no. 3, pp. 365–377, 2009, doi: 10.1007/s10706-008-9236-x.
- [16] A. J. Bond and R. J. Jardine, “Effects of installing displacement piles in a high OCR clay,” *Geotechnique*, vol. 41, no. 3, pp. 341–363, 1991, doi: 10.1680/geot.1991.41.3.341.
- [17] F. B. D’Arezzo, S. Haigh, M. Talesnick, and Y. Ishihara, “Measuring horizontal stresses during jacked pile installation,” *Proc. Inst. Civ. Eng. Geotech. Eng.*, vol. 168, no. 4, pp. 306–318, 2015, doi: 10.1680/jeng.14.00069.
- [18] B. M. Lehané and D. J. White, “Lateral stress changes and shaft friction for model displacement piles in sand,” *Can. Geotech. J.*, vol. 42, no. 4, pp. 1039–1052, 2005, doi: 10.1139/t05-023.
- [19] F. van T. A. Beijer Lundberg, J. Dijkstra, “On the modelling of piles in sand in the small geotechnical centrifuge,” *Clim. Chang. 2013 - Phys. Sci. Basis, Univ. Technol. Delft*, vol. 53, no. November, pp. 1–30, 2001, [Online]. Available: [https://www.cambridge.org/core/product/identifier/CBO9781107415324A009/type/book\\_part](https://www.cambridge.org/core/product/identifier/CBO9781107415324A009/type/book_part).
- [20] J. Otani, K. D. Pham, and J. Sano, “Investigation of failure patterns in sand due to laterally loaded pile using X-ray CT,” *Soils Found.*, vol. 46, no. 4, pp. 529–535, 2006, doi: 10.3208/sandf.46.529.
- [21] B. Yuan, R. Chen, J. Teng, T. Peng, and Z. Feng, “Investigation on 3D ground deformation and response of active and passive piles in loose sand,” *Environ. Earth Sci.*, vol. 73, no. 11, pp. 7641–7649, 2015, doi: 10.1007/s12665-014-3935-9.
- [22] D. White, A. Take, and M. Bolton, “Measuring soil deformation in geotechnical models using digital images and PIV analysis,” *10th Int. Conf. Comput. Methods Adv. Geomech.*, no. June 2014, pp. 997–1002, 2001, [Online]. Available: [http://www-civ.eng.cam.ac.uk/geotech\\_new/people/bolton/mdb\\_pub/99\\_IACMAG\\_2001\\_Proc\\_997\\_1002.pdf](http://www-civ.eng.cam.ac.uk/geotech_new/people/bolton/mdb_pub/99_IACMAG_2001_Proc_997_1002.pdf).
- [23] Z. H. Cao, G. Q. Kong, H. L. Liu, and H. Zhou, “Model test on deformation characteristic of pile driving in sand using piv technique,” *Gongcheng Lixue/Engineering Mech.*, vol. 31, no. 8, pp. 168–174, 2014, doi: 10.6052/j.issn.1000-4750.2013.03.0217.
- [24] A. Beijer Lundberg, J. Dijkstra, and A. F. Van Tol, “Displacement pile installation effects in sand,” *Install. Eff. Geotech. Eng. - Proc. Int. Conf. Install. Eff. Geotech. Eng. ICIEGE 2013*, pp. 79–85, 2013.
- [25] K. Y. Lo and A. G. Stermac, “Induced pore pressures during pile-driving operations,” 1965.
- [26] A. Wada, “Excess pore water pressure and its impact,” *15th Asian Reg. Conf. Soil Mech. Geotech. Eng. ARC 2015 New Innov. Sustain.*, pp. 335–339, 2015, doi: 10.3208/jgssp.SEA-16.
- [27] J.-H. Hwang, N. Liang, and C.-H. Chen, “Ground Response during Pile Driving,” *J. Geotech. Geoenvironmental Eng.*, vol. 127, no. 11, pp. 939–949, 2001, doi: 10.1061/(asce)1090-0241(2001)127:11(939).
- [28] M. Y. Fattah and F. S. Mustafa, “Development of Excess Pore Water Pressure around Piles Excited by Pure Vertical Vibration,” *Int. J. Civ. Eng.*, vol. 15, no. 6, pp. 907–920, 2017, doi: 10.1007/s40999-016-0073-7.
- [29] and T. I. Eigenbrod, K. D., “Pore-water pressures in soft Can., to firm clay during driving of piles into underlying dense sand,” *Geotech. J.*, vol. 33, no. 2, pp. 209–218, 1996, [Online]. Available: <https://doi.org/10.1139/t96-001>.
- [30] R. Holtz and P. Boman, “A New Technique for Reduction of Excess Pore Pressures During Pile Driving,” *Can. Geotech. J.*, vol. 11, pp. 423–430, Jan. 2011, doi: 10.1139/t74-043.
- [31] J. M. Pestana, C. E. Hunt, and J. D. Bray, “Soil Deformation and Excess Pore Pressure Field around a Closed-Ended Pile,” *J. Geotech. Geoenvironmental Eng.*, vol. 128, no. 1, pp. 1–12, 2002, doi: 10.1061/(asce)1090-0241(2002)128:1(1).
- [32] M. S. Nataraja and B. E. Cook, “Increase in SPT N-values due to displacement piles,” *J. Geotech. Eng.*, vol. 112, no. 10, pp. 969–971, 1986, doi: 10.1061/(ASCE)0733-9410(1986)112:10(969).
- [33] T. C. Siegel, W. M. NeSmith, W. M. NeSmith, and P. E. Cargill, “Ground improvement resulting from installation of drilled displacement piles,” *Proc. DFI’s 32nd Annu. Conf. Deep Found.*, pp. 129–138, 2007.
- [34] A. W. Stuedlein, T. N. Gianella, and G. Canivan, “Densification of Granular Soils Using Conventional and Drained Timber Displacement Piles,” *J. Geotech. Geoenvironmental Eng.*, vol. 142, no. 12, p. 04016075, 2016, doi: 10.1061/(asce)gt.1943-5606.0001554.
- [35] G. G. Meyerhof, “Compaction of Sands and Bearing Capacity of Piles,” *J. Soil Mech. Found. Div.*, vol. 85, no. 6, pp. 1–29, Dec. 1959, doi: 10.1061/jsfeaq.0000231.
- [36] C. Szechy, “The Effects of Vibration and Driving Upon the Voids in Granular Soil Surrounding a Pile,” in *Proc. 5th Int. Conf. of Soil Mechanics and Foundation Engineering vol. 2*, pp., 1961, pp. 161–164.
- [37] H. Kishida, “Stress Distribution by Model Piles in Sand,” *Soils Found.*, vol. 4, no. 1, pp. 1–23, 1963, doi: 10.3208/SANF1960.4.1.

# A CORRELATION BETWEEN ONE-DIMENSIONAL CONSOLIDATION COEFFICIENTS WITH BASALT FIBER LENGTH, RHA-CEMENT CONTENT IN FIBER-REINFORCED STABILIZED EXPANSIVE SOILS

Alex Otieno Owino<sup>1</sup>, and Zakaria Hossain<sup>1</sup>

<sup>1</sup>Graduate School of Bioresources, Mie University, Japan

## ABSTRACT

The consolidation behavior of reinforced and stabilized soils is essential in geotechnical engineering applications. Recently, environmentally friendly soil reinforcement and stabilization techniques to reconstitute weak expansive soils are on the rise, calling for an in-depth analysis of the consolidation projections on the engineering structures built on them. This study investigated the one-dimensional consolidation coefficients by conducting a series of odometer tests on expansive soil reinforced with different basalt fibers lengths and stabilized with rice husk ash (RHA)-cement mixtures in their specified combinations. A correlation between the coefficient of consolidation ( $c_v$ ), coefficient of volume change ( $m_v$ ), and permeability coefficient ( $k$ ) with the length of the basalt fibers and RHA-cement contents in the ultimate soil composite material was quantified using equations and graphical forms. Furthermore, scanning electron microscopic imagery (SEM) was conducted to examine the structural modifications within the reinforced and stabilized soil composite upon one-dimensional consolidation. The results showed that basalt fiber reinforced specimens with 5%RHA-3% cement mixtures showed the lowest one-dimensional consolidation coefficients with a notable reduction at high-stress states than the control specimen. Additionally, the coefficient of volume change ( $m_v$ ) and permeability coefficient ( $k$ ) decreased with increased compactive effort, with a significant reduction evident on the basalt fiber reinforced stabilized soil composites. The study demonstrated that basalt fiber, RHA, and cement could enhance the consolidation characteristics of weak expansive soils. This study also proposed analytical equations for evaluating  $c_v$ ,  $m_v$ , and  $k$  considering basalt fiber lengths. The resulting soil composites had superior properties and can be used as a fill or subbase material for engineering structures such as embankments, pavements, and foundations.

*Keywords: Soil consolidation, Basalt fiber, RHA, Coefficient of consolidation, Coefficient of volume change, Permeability coefficient, SEM*

## INTRODUCTION

With the increase in built environment due to urbanization and industrialization, the demand for infrastructure development in marginalized areas with weak expansive soils, which were considered unsuitable, is rising. Expansive soils have been analyzed to possess weak shear strength and high compressibility and pose numerous challenges to civil and geotechnical engineers while constructing any engineering structures. This instability of the expansive soil is due to the high clay contents, which tend to shrink or expand when subjected to moisture content variation. Building on expansive soils can lead to considerable damage to foundations, embankments, and pavements, raising the construction costs to construct durable and safe structures.

Stabilizing and reinforcing the expansive soils to improve their geotechnical properties is vital to curb these challenges. Conventionally, the addition of additives such as cement, lime, and lime-cement mixtures has been practiced extensively [1][2][3][4][5][6]. However, the over-dependence on cement and lime has proven to degrade the

environment, raising environmental concerns such as CO<sub>2</sub> emission, global warming, natural resources depletion, and dust generation from their manufacturing processes [7]. In addition to the environmental drawbacks, cement and lime are susceptible to high plastic shrinkage and cracking, affecting the stabilized soil's mechanical strength [8]. To reduce these environmental concerns and enhance the geotechnical properties of expansive soils, the partial replacement of cement and lime with pozzolanic materials such as rice husk ash (RHA) is gaining research attention. The potential use of RHA is due to the abundance of rice husks generated worldwide from rice processing [9] and particularly the presence of highly active amorphous silica SiO<sub>2</sub> produced during the ash production process [10]. However, the pozzolanic reactions when the amorphous silica-rich RHA is used to stabilize expansive soils form cementitious systems that need further reinforcements to avoid cracking and excessive settlement problems when subjected to extensive loads. Recently, natural fibers such as basalt fibers are being used together with the pozzolanic additives to arrest the formation of weak planes in the stabilized soil and control the

consolidation rate while improving the strength when built upon [11].

To validate the reinforcement and stabilization techniques using basalt fiber and RHA, understanding the consolidation parameters such as the coefficient of consolidation, coefficient of volume change, and the ultimate permeability coefficient is critical. The consolidation rate is related to the coefficient of consolidation ( $c_v$ ), while the settlement amount is related to the coefficient of volume change ( $m_v$ ). Based on experimental tests, researchers have realized that stabilization and fiber reinforcement techniques have increased strength, enhanced stability, and substantially reduced the rate of consolidation settlements. While working on fiber-reinforced soil, Abdi (2008) found that increasing the fiber content and length significantly reduced the consolidation settlements, swelling, and crack formation [12]. Das and Pal (2012) investigated the consolidation responses on silty clayey stabilized with fly ash in another study. They noted that the coefficient of consolidation ( $c_v$ ) increased with an increase in the fly ash content [13].

Regarding the coefficient of volume change ( $m_v$ ), Kar and Pradhan (2011) studied the compressibility trends of polypropylene and coir fiber reinforced local cohesive soils and noted that the  $m_v$  decreased significantly with an increase in fiber content. In addition, they concluded that the coefficient of consolidation increased with the fiber content [14]. Eberemu and Sada (2013), in their study on one-dimensional consolidation of expansive soils treated with RHA only, found out that the coefficient of volume change ( $m_v$ ) and coefficient of consolidation ( $c_v$ ) generally decreased with increased loading pressure and RHA treatment for up to 8%. Also, in the same study, the permeability coefficient decreased with increased RHA content for up to 8% [15].

The use of RHA as a stabilizing agent and fibers as a reinforcing agent has attracted the attention of researchers who have found out that they have an advantageous effect in developing the geotechnical properties of the soils under study [16] [17] [18] [19] [20]. However, in literature, most of the available research is limited to the reinforcement material used, the soil tested and the type of stabilizing agent used. Moreover, the testing procedures have been limited to unconfined compression, triaxial, direct shear, and CBR tests. To date, few pieces of research have been carried out on expansive soils with no scientific studies on the combined action of RHA and basalt fiber, particularly its effect on consolidation settlement, volume change, and permeability.

In this context, the present study aims to investigate a correlation between the consolidation coefficients (coefficient of consolidation, coefficient of volume change, permeability coefficient) and the addition of different basalt fiber lengths and RHA-

cement mixtures to expansive soils as the reinforcing and stabilizing agents respectively. A series of odometer tests were conducted on expansive soil reinforced with different basalt fiber lengths (3mm, 6mm, and 12mm) and stabilized with RHA(5%,10%, and 15%)-cement (3%) mixtures in their specified combinations. A correlation between the coefficient of consolidation ( $c_v$ ), coefficient of volume change ( $m_v$ ), and permeability coefficient ( $k$ ) with the length of the basalt fibers and RHA-cement mixtures in the ultimate soil composite material was determined. Furthermore, scanning electron microscopic imagery (SEM) was conducted to examine the structural modifications within the stabilized and reinforced soil composite upon complete one-dimensional consolidation. The results were presented graphically with correlation equations and pictorial forms to solve design challenges encountered by civil, geotechnical, and geo-environmental engineers working with the new composite material.

## MATERIALS

### Soil

The soil used in this study was obtained from the Handa area, Mie prefecture, Japan. The index properties of the soil are shown in Table 1. Additionally, the particle size distribution is illustrated in Fig. 1. Based on the American Association of State Highway and Transportation Officials (AASHTO), the soil was classified as A-7–5(2) clayey soils.

Table 1 Properties of soil

Property	Value
Specific gravity	2.74
Sand (75 $\mu$ m - 2 mm), (%)	6.14
Silt (5 $\mu$ m -75 $\mu$ m), (%)	51.24
Sand (<5 $\mu$ m), (%)	38.86
Liquid limit, LL, (%)	58.21
Plastic limit, PL, (%)	31.05
Plasticity index, PI, (%)	27.16
Optimum water content, (%)	26.02
Maximum dry density, (g/cm <sup>3</sup> )	1.65
AASHTO classification	A-7–5(2)

### Rice husk ash (RHA)

Rice husk ash is obtained from burning rice husks, a byproduct of rice milling. The ash was prepared by burning rice husks at temperatures between 650~700°C for 27 hours. The RHA production temperatures and time produced high levels of amorphous silica (91.10%), a valuable element for pozzolanic reactions. Make Integrated Technology Co., Ltd, Osaka, Japan, provided the controlled burnt

RHA in this study. The properties of the RHA and the particle size distribution are shown in Table 2 and Fig. 1, respectively.

Table 2 Physical and chemical properties of RHA

Physical properties	Values
Specific gravity	1.47
Average Particle Size, (mm)	0.001 to 0.30
Loss of Ignition	4.00-6.00
Chemical properties	
Oxide compounds	Values (%)
Silica (SiO <sub>2</sub> ),	91.10
Carbon dioxide (CO <sub>2</sub> )	4.35
Potassium Oxide (K <sub>2</sub> O)	2.40
Calcium Oxide (CaO)	0.57
Iron Oxide (Fe <sub>2</sub> O <sub>3</sub> )	0.05
Alumina (Al <sub>2</sub> O <sub>3</sub> )	0.03
Others	1.50

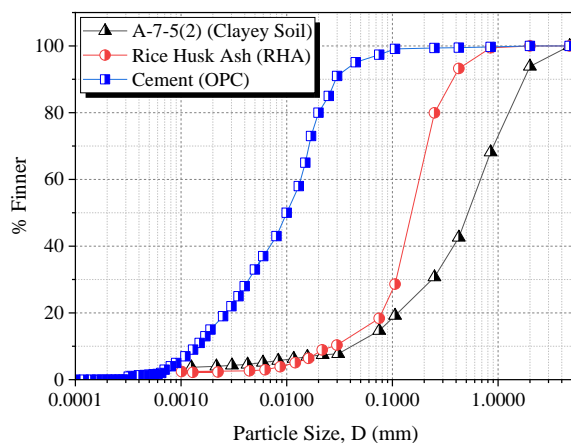


Fig. 1 Particle size distribution for soil, RHA, and OPC

### Basalt fibers (BF)

Basalt fiber is a material made from fine fibers of natural basalt rock. The production of BF is a one-stage process involving: the melting and homogenization of basalt rock and extrusion through small nozzles to produce continuous filaments of basalt fiber [21] [22]. Basalt fibers were used as the primary reinforcing material in this study. The superiority of BF compared to the other conventional fibers is derived from the high tensile strength (4100~4840MPa), high elastic modulus (93.1~111.0GPa), long-term durability, thermal stability, and alkali resistance [23]. A detailed physical, thermal and chemical properties of the BF used in this study are shown in Table 3.

Table 3 Properties of basalt fibers

Physical Properties	
Fiber diameter, (μm)	6~30
Fiber length, (mm)	3, 6 & 12

Density	2.63~2.8
Tensile strength, (MPa)	4100~4840
Elastic modulus, (GPa)	93.1~110
Fracture elongation rate, (%)	3.1
Thermal properties	
Heat resistant temperature, (°C)	-269~650
Melting temperature, (°C)	1450
Softening temperature, (°C)	1050
Chemical properties	
Oxides composition	Value (%)
Silicon oxide (SiO <sub>2</sub> )	51.6 ~ 59.3
Aluminum oxide (Al <sub>2</sub> O <sub>3</sub> )	14.6 ~ 18.3
Iron oxides	9.0 ~ 14.0
Calcium oxide (CaO)	5.9 ~ 9.4
Magnesium oxide (MgO)	3.0 ~ 5.3
Others	0.09 ~ 0.13

### Ordinary Portland Cement (OPC)

The properties of OPC are shown in Table 4. Also, a detailed particle size distribution is shown in Fig. 1. Minimal dosages if OPC was used as the pozzolanic reaction activator by providing the calcium oxide ions and as a binder element.

Table 4 Properties of OPC

Physical properties	
Initial setting time, (minutes)	170
Final setting time, (minutes)	225
Specific gravity, (g/cm <sup>3</sup> )	3.15
Specific surface area, (m <sup>2</sup> /kg)	340
28-day compressive strength, (MPa)	33~53
Loss of ignition, (%)	<4
Chemical properties	
Oxides composition	Values (%)
Calcium Oxide (CaO)	63.40
Silicon dioxide (SiO <sub>2</sub> )	21.60
Iron Oxide (Fe <sub>2</sub> O <sub>3</sub> )	5.35
Alumina (Al <sub>2</sub> O <sub>3</sub> )	4.45
Magnesium oxide (MgO)	1.65
Others	3.55

## EXPERIMENTAL APPARATUS AND TECHNIQUES

### Oedometric cell apparatus

The experimental equipment used in this study is presented in Figure 2. It consisted of an oedometric cell on a rigid base, a loading lever arm, and a dial gauge combined with LVDT (Linear Variable Differential Transformer). The oedometric cell included a water container, a pressurizing ring fitted with a porous plate at the bottom, a guide ring, a consolidation ring, and a bottom plate equipped with a porous media. The guide ring and the consolidation rings were made of stainless steel with a uniform

diameter of 60 mm and a height of 20 mm. They were inserted into the bottom plate to ensure high rigidity, capable of minimizing the expansions in the radial direction during loading. The porous media on the pressurizing plate and the bottom plates allowed proper drainage through the specimens during one-dimensional consolidation.

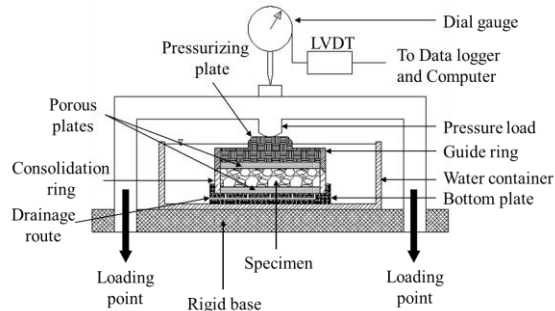


Fig. 2 Components of the oedometric cell apparatus

### Specimen preparation procedure

During specimen preparation, one of the primary considerations was achieving the maximum effects of the fibers and ensuring their random installation in the soil composite. The dry materials were mixed manually before adding water. Each specimen was prepared using soil (200g), RHA (5%, 10%, or 15% dry weight of soil), cement (3% dry weight of soil), and basalt fiber (3, 6, or 12mm length) in their specified combination schemes as shown in Table 5. Water was added to an initial water content of 45%, 50%, and 55% for 5%RHA, 10%RHA, and 15% RHA, respectively. The difference in the initial water contents was due to the high-water affinity for the higher percentages of RHA. The added water increased the water content of the dry soil to slightly above the liquid limit hence simulating pore water pressures similar to clay in its natural state [11] [24]. The materials were mixed for 10 minutes using a spatula to obtain a homogeneous mix, trimmed then transferred to the soil consolidation rings. Filter papers with similar dimensions to the consolidation rings were placed at the top and bottom of the specimen to prevent the soil composite from clogging the porous plates during the loading and drainage processes.

Table 5 Specimen combination schemes

No	Combinations	Code
1	100% Soil	S
2	100% S	
3	+5%RHA+3%C+1%BF3	S:5R:3C:1BF3
4	+10%RHA+3%C+1%BF3	S:10R:3C:1BF3
5	+15%RHA+3%C+1%BF3	S:15R:3C:1BF3
6	+5%RHA+3%C+1%BF6	S:5R:3C:1BF6
7	+10%RHA+3%C+1%BF6	S:10R:3C:1BF6
8	+15%RHA+3%C+1%BF6	S:15R:3C:1BF6

7	100% S	
8	+15%RHA+3%C+1%BF6	S:15R:3C:1BF6
9	100% S	
10	+5%RHA+3%C+1%BF12	S:5R:3C:1BF12
	+10%RHA+3%C+1%BF12	S:10R:3C:1BF12
	100% S	
	+15%RHA+3%C+1%BF12	S:15R:3C:1BF12

Note: S=Soil, RHA=Rice husk ash, C=Cement, BF3=Basalt fiber 3mm, BF6=Basalt fiber 6mm, BF12=Basalt fiber 12mm

### Experimental procedure

The general experimental procedure is explained in this subsection. After transferring the specimen into the consolidation rings, the initial weight and dimensions were determined, and the oedometric cell was assembled and filled with water. Afterward, the mechanical loading-unloading cycles were performed in steps with incremental loads of 9.8, 19.6, 39.2, 78.5, 157, 314, 628, and 1256 kN/ m<sup>2</sup> during the loading cycle and 628, 314, 157, 78.5, 39.2, 19.6 and 9.8 kN/m<sup>2</sup> during the unloading cycle. All the load increments/reductions were kept constant for 24 hours until the primary consolidation had seized and the excess pore water pressure dissipated completely [25]. Meanwhile, the settlement of the specimen with time was measured using an electronic dial gauge connected to a data logger to maintain accuracy in the data sets obtained. Each specimen was consolidated for 16 days, after which it was weighed and oven-dried to calculate the ultimate water content. Finally, a piece of each specimen was collected for SEM analysis. The testing procedures followed the Japan Industrial Standards [26,27].

### RESULTS AND DISCUSSION

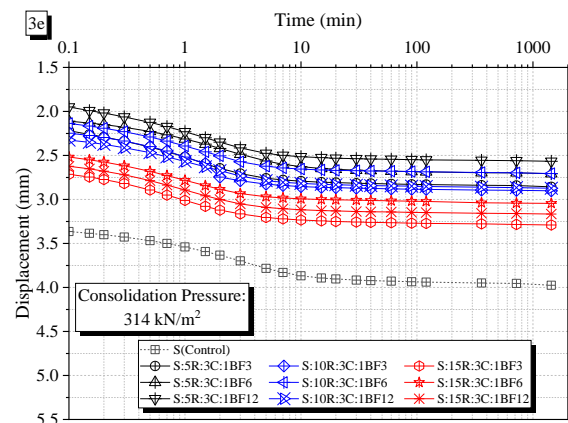
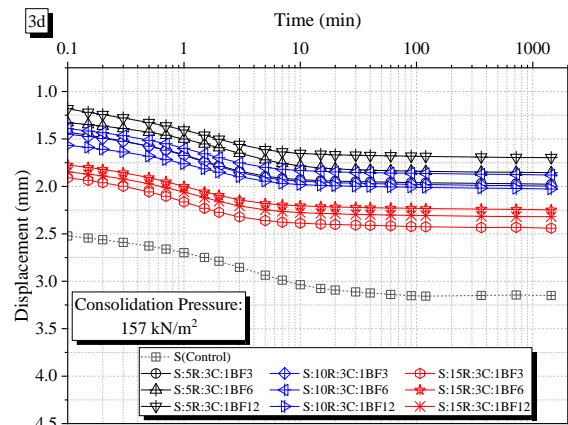
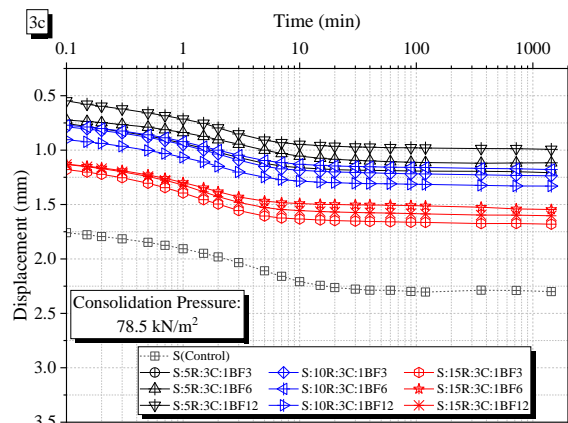
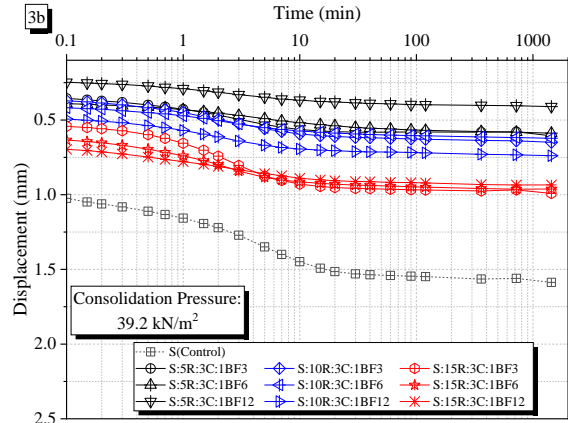
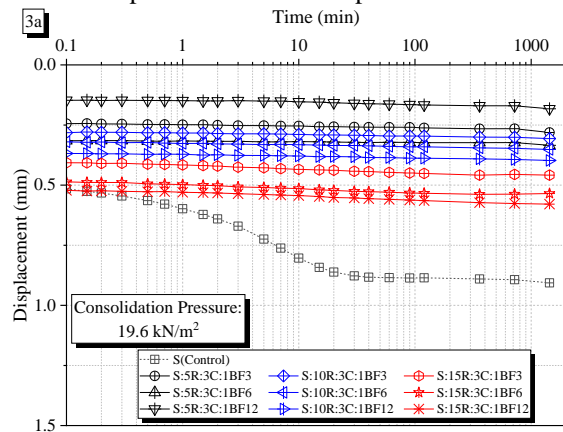
Firstly, the effects of basalt fiber reinforcements and RHA-cement stabilization on the one-dimensional consolidation coefficients of expansive soils were evaluated using the time-compression curves from the oedometer test. The curves were used to assess the coefficient of consolidation ( $c_v$ ), followed by a series of equations applied to determine the coefficient of volume change ( $m_v$ ) and the permeability coefficient ( $k$ ). Subsequently, a correlation analysis was done between the one-dimensional consolidation coefficients, basalt fibers' length, and the RHA-cement content. Additionally, SEM analyses quantified the structural modifications in the specimen upon consolidation, considering the soil structure, fiber orientation, and the porosity of the specimen combination under study, as discussed in the next section.

#### Time-compression curves

According to the theory of one-dimensional consolidation, soil undergoes a time-dependent displacement/deformation when acted upon by an

external load. These deformations can lead to the draining of excess pore water pressure due to the gradual transition of the applied loads from the pore water to the soil particles under steady pressure. The notable assumptions in this theory include; (1) soil grains and water are incompressible, (2) the load is applied in the vertical direction only, (3) the drainage of the pore water is one-dimensional in the direction of the load, (4) the coefficient of consolidation, the coefficient of volume change and the permeability coefficients are constant, (5) the time lag of consolidation is dependent on the low permeability of expansive soils [28] [29].

Based on this theory, the time-displacement plots of all the ten specimen combinations for the load increments in the present study are shown in Fig. 3(a-g). Notably, there was no clear distinction between the primary and secondary consolidation phases at low compression pressures, as shown in Fig. 3a. However, as the consolidation pressures increased, a clear contrast between the primary and secondary consolidation phases in the time-displacement curves was evident, owing to the generated exponential curve forms. From these plots, the time  $T_{50}$  required to reach 50% primary consolidation was evaluated by defining the 0% primary consolidation stage from the early portion of the curve and 100% primary consolidation stage from the point of intersection between primary and secondary consolidation segments using the logarithm of time method [30]. It was noteworthy that the time  $T_{50}$  was highly dependent on the RHA-cement content, as illustrated in Fig. 3h. Increasing the RHA content from 5% to 15% decreased the time required to achieve a certain degree of consolidation under the same effective stress. Similar results were also recorded by Jain and Puri (2013) [31]. It was also apparent that for basalt fiber reinforced and RHA- cement stabilized expansive soils, the  $T_{50}$  reduced significantly with an increase in consolidation pressure. This decrease prompted a uniform secondary consolidation phase, preventing structural failures from prolonged primary consolidation. Moreover, the addition of different lengths of basalt fibers significantly reduced the  $T_{50}$  values compared to the control specimen.





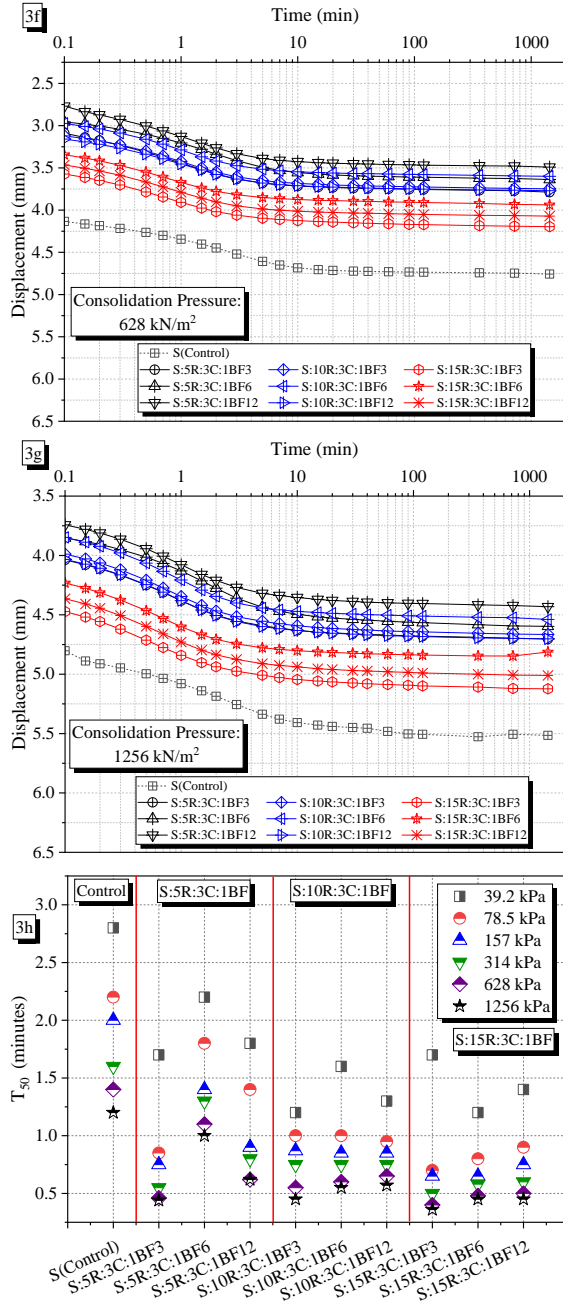


Fig. 3 (a) to (g) Time-displacement curves, (h) Relationship between  $T_{50}$  and specimen combinations schemes.

#### Coefficient of consolidation ( $c_v$ )

The coefficient of consolidation ( $c_v$ ) measures the rate at which the soil consolidation process proceeds, a basic differential equation developed by Terzaghi (1943). A presentation of the  $c_v$  as a function of the average vertical consolidation pressure ( $\bar{p}$ ) is shown in Fig. 4a. The vertical axis ( $c_v$ ) was on a logarithmic scale against the horizontal axis, plotted as the geometric mean average consolidation pressure ( $\bar{p}$ ) (with values 14, 28, 55, 111, 222, 444, 888 kN/m<sup>2</sup>) calculated by Eq. (1). All the analytical equations followed the Japanese Industrial Standards 1217 and 1227.

$$\bar{p} = \sqrt{(p \cdot p')} \quad (1)$$

Where:  $p$  is the pressure increment and  $p'$ , the consolidation pressure at the previous loading stage in kN/m<sup>2</sup>. The data points corresponding to 14kN/m<sup>2</sup> were omitted in Fig. 4 owing to the non-uniform vertical stress-time responses at low consolidation pressure. The  $c_v$  data points were defined by Eq. (2) in cm<sup>2</sup>/day for all the ten oedometer tests.

$$c_v = 0.197 \left( \frac{H}{2} \right)^2 \left( \frac{1440}{T_{50}} \right) \quad (2)$$

Where;  $c_v$  is the coefficient of consolidation in cm<sup>2</sup>/day,  $H$  is the average height of specimen, 0.197 is the value of the time coefficient at 50% consolidation, and 1440 is the unit conversion factor to cm<sup>2</sup>/day. For the ten oedometer tests, the variation of  $c_v$  with  $\bar{p}$  for the fiber-RHA-cement specimen showed a similar trend to that observed for the control specimen (soil only), as shown in Fig. 4a. During the first loading phase, it was observed that the  $c_v$  increased as the  $\bar{p}$  approached the yield stress, whereas afterward, the value remained approximately constant in the post-yield phase. The observed approximate constant values of  $c_v$  revealed that creep effects should be carefully considered while working with basalt fiber reinforced and RHA stabilized expansive soils. This trend agreed with the results Ferrari (2016) observed while working on the one-dimensional consolidation of shales [32].

Additionally, the increasing  $c_v$  trend with  $\bar{p}$  was attributed to the enhanced chemical and mechanical properties derived from RHA stabilization and basalt fiber reinforcements. Robinson and Allam (1998) and Sridharan and Nagaraj (2004) also recorded a similar trend of increasing  $c_v$  with consolidation pressure) when analyzing the role of mechanical and physio-chemical factors on the  $c_v$  trend with  $\bar{p}$ . It was also evident that the RHA content played a major role in influencing the trend of the consolidation rate. For example, specimen S:5R:3C:1BF12 with 5% RHA content produced the lowest  $c_v$  values compared to specimen S:15R:3C:1BF3 (15%RHA content) that had the highest  $c_v$  values. This increase in the  $c_v$  values at 15% RHA was due to the increased hydraulic conductivity associated with the porous structure of RHA and the additional voids created by random fiber intersections. A comparable increase in  $c_v$  value with increasing hydraulic conductivity was also recorded by Yeo (2005) [35]. It is also noteworthy that the RHA content influenced the  $c_v$  value depending on the degree of pozzolanic activity in the specimen. The complete utilization of RHA during pozzolanic reactions for specimens with 5% and 10% RHA developed the mechanical properties of the specimens by improving the compressibility behavior hence the low  $c_v$  values. Moreover, as observed for all the specimens tested, the  $c_v$  value varied at the same  $\bar{p}$  depending on the RHA content.

Furthermore, to correlate coefficient of consolidation ( $c_v$ ) and basalt fiber reinforcements, all

the values of  $c_v$  were plotted against the lengths of basalt fibers, as shown in Fig. 4b-d. In general, the length of basalt fibers significantly influenced the  $c_v$  value. The longer fibers reduced the coefficient of consolidation for the different RHA contents, as shown in the correlation plots. This reduction in  $c_v$  was more significant in the specimen containing 12mm basalt fibers, as shown in Fig. 4b and Fig. 4c, representing RHA compositions of 5% and 10%, respectively. For example, considering the maximum  $\bar{p}$  of 888kPa, with the basalt fiber length increased from 3mm to 12mm, the  $c_v$  values for the 5%RHA specimen reduced from 321.02cm<sup>2</sup>/d to 147cm<sup>2</sup>/d. A similar reduction in the  $c_v$  with increasing basalt fiber length was further reported for the 10%RHA specimens with excerpptions in the 15%RHA specimens at 12mm basalt fiber length, as revealed in Fig. 4d. Also, it was evident that the coefficient of consolidation was dependent on average consolidation pressure during the loading stage, with an apparent inverse proportionality.

Further, using the  $c_v$  versus length of basalt fiber plots, the curve fitting correlation equations for predicting  $c_v$  showed better correlation coefficients ( $R^2=1.00$ ). Hence can be used as design charts for predicting the  $c_v$  if the length of basalt fiber and the consolidation pressure is known. It can be concluded that the longer basalt fibers provided sufficient reinforcements in the specimen by resisting excessive compression during the loading phase, resulting in the reduced c:onsolidation rate.

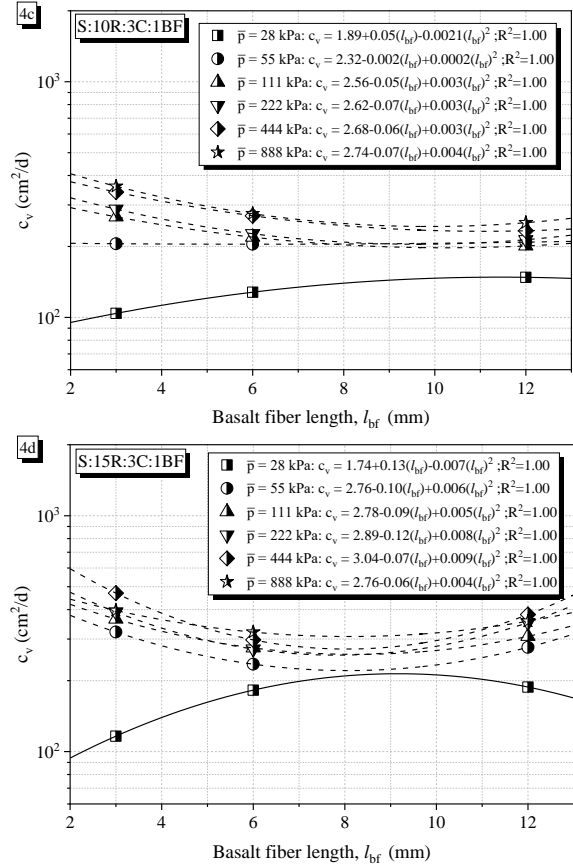
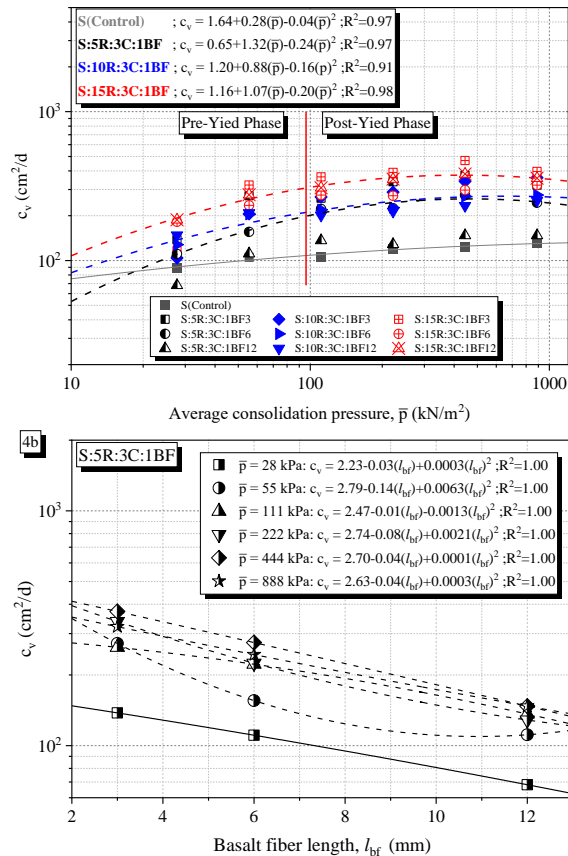


Fig. 4 (a) Relationship between  $c_v$  and  $\bar{p}$ , (b) Correlation between  $c_v$  and  $l_{bf}$  for 5%RHA specimens, (c) Correlation between  $c_v$  and  $l_{bf}$  for 10%RHA specimens, (d) Correlation between  $c_v$  and  $l_{bf}$  for 15%RHA specimens.

### Coefficient of volume change ( $m_v$ )

In the construction industry, foundation settlement is one of the safety considerations used in the geotechnical assessment of engineering structures. Excessive settlement can result in structural damage or significantly reduce the structure's durability. Evaluating the coefficient of volume change ( $m_v$ ) has been demonstrated to be a suitable parameter in calculating the consolidation settlement, providing essential measures to counter the projected soil settlement. Coefficient of volume change can be defined as the change in volume of a soil mass per unit of initial volume when subjected to an effective pressure increase. According to the Japan Industrial Standards 1217 and 1227,  $m_v$  is the ratio of the volume change of soil to the difference in the effective pressure and is calculated using Eq. (3).

$$m_v = \frac{\Delta \varepsilon / 100}{\Delta p} \quad (3)$$

Where;  $\Delta \varepsilon$  is the compression strain generated at each loading stage [the ratio of the consolidation amount ( $\Delta H$ ) to average specimen height ( $\bar{H}$ )], and  $\Delta p$  is the consolidation pressure increment. The variation of  $m_v$  at different compactive efforts for specimens

with different basalt fiber lengths and various RHA contents is shown in Fig. 5a. The coefficient of volume change could not be evaluated at low consolidation pressures (14kPa) due to the high swelling pressures in the expansive soil compared to the applied load. Eberemu (2016) reported a similar response to low consolidation loads [36]. In general, irrespective of the fiber reinforcement length, and RHA stabilization, the  $m_v$  value showed a reducing trend as the average consolidation pressure increased. This reduction was induced by the compressive forces rearranging and closely packing the composite materials, increasing the bonding forces and yield stress in the specimen, thereby reducing the  $m_v$  considerably. A relatable reduction in  $m_v$  with increasing pressure was also realized by Santagata (2008) [37].

Additionally, it was noteworthy that the  $m_v$  value was dependent on the specimen composition in the pre-yield and post-yield phases. For instance, considering the basalt fiber reinforcement and RHA-cement content, specimen S:5R:3C:1BF3 showed the lowest  $m_v$  values of  $1.20 \times 10^{-4} \text{ m}^2/\text{kN}$  compared to specimen S:15R:3C:1BF3 with  $1.07 \times 10^{-3} \text{ m}^2/\text{kN}$  during the pre-yield phase. This difference was probably due to the enhanced stiffness and resistance to compressive forces obtained from the complete pozzolanic reactions at 5%RHA than at 15%RHA. Moreover, the study showed that basalt fiber reinforcement length's effects differed for each RHA content. Fiber-reinforced specimen with 5%RHA portrayed a direct relationship, with the coefficient of volume change increasing from  $1.20 \times 10^{-4} \text{ m}^2/\text{kN}$  to  $1.41 \times 10^{-4} \text{ m}^2/\text{kN}$  to  $2.19 \times 10^{-4} \text{ m}^2/\text{kN}$  for basalt fiber lengths 3mm, 6mm and 12mm respectively. On the other hand, an inverse relationship was observed for higher RHA-cement contents.

It was also observed that RHA and basalt fiber reinforcements increased the  $m_v$  with compactive force across all specimens during the pre-yield phase. This slight increase was due to the additional displacements required to reduce the voids created by the porous RHA and the random distribution of basalt fibers. However, in the post-yield state, the ultimate compact structure in the specimen provided the resistance to compressive forces leading to the significant reduction in  $m_v$  with average consolidation pressure. Similar responses have also been observed by Xu (2020) [38], Eberemu (2011) [39], Eberemu (2016) [36], and Laskar and Pal (2013) [40].

Besides, a plot of  $m_v$  on the log scale against basalt fiber length ( $l_{bf}$ ) was considered to correlate the relationship between the  $m_v$  and the length of basalt fiber, as illustrated in Fig. 5b, 5c, and 5d for specimen S:5R:3C:1BF, S:10R:3C:1BF, and S:15R:3C:1BF respectively. It was evident that increasing the length of basalt fibers in specimens had minimal effects on  $m_v$  with increasing consolidation pressures from 55 to

888 kPa.

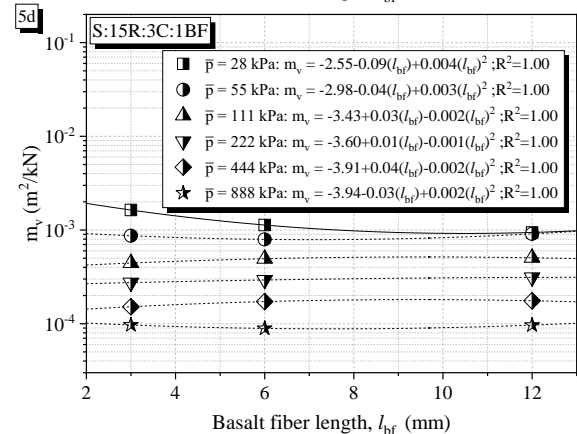
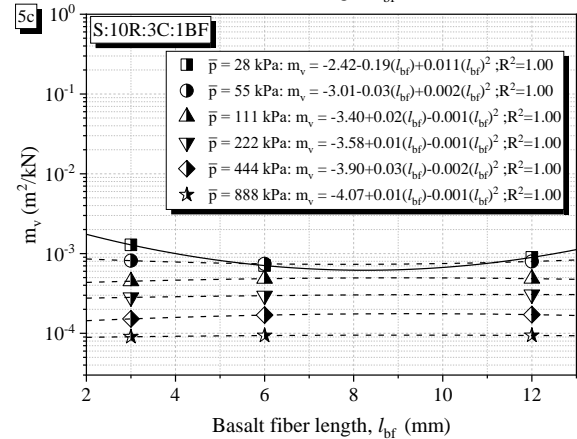
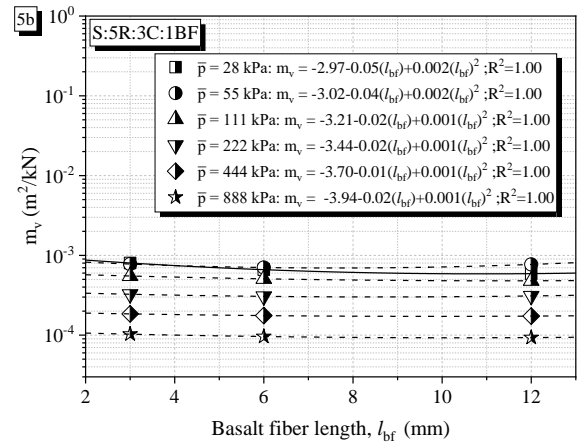
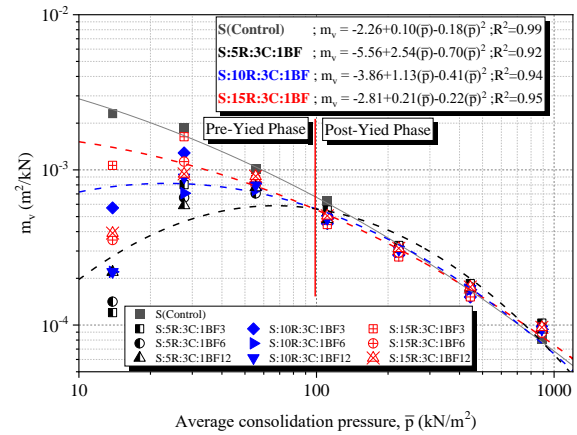


Fig. 5 (a) Relationship between  $m_v$  and  $\bar{p}$ , (b) Correlation between  $m_v$  and  $l_{bf}$  for 5%RHA specimens, (c) Correlation between  $m_v$  and  $l_{bf}$  for 10%RHA specimens, (d) Correlation between  $m_v$  and  $l_{bf}$  for 15%RHA specimens.

However, it was observed that  $m_v$  values were slightly higher for the specimen containing 15%RHA due to the extra volume changes initiated by the high void ratios. Additionally, from the  $m_v$  versus length of basalt fiber ( $l_{bf}$ ) plots, the curve fitting correlation equations to predict  $m_v$  showed better correlation coefficients ( $R^2=1.00$ ) across all specimens. Hence can be used to predict the coefficient of volume change ( $m_v$ ) if the length of basalt fiber ( $l_{bf}$ ) and the average consolidation pressures are provided.

### Permeability coefficient (k)

This section highlights the effects of basalt fiber length and RHA-cement contents on the permeability coefficient (k) of stabilized expansive soils undergoing one-dimensional consolidation. Permeability describes the rate at which water can move through the pores within a soil medium and has proven to be an essential parameter influencing soil's consolidation and strength. Following the Japan Industrial Standards 1217 and 1227, the permeability coefficient can be calculated using Eq. (4).

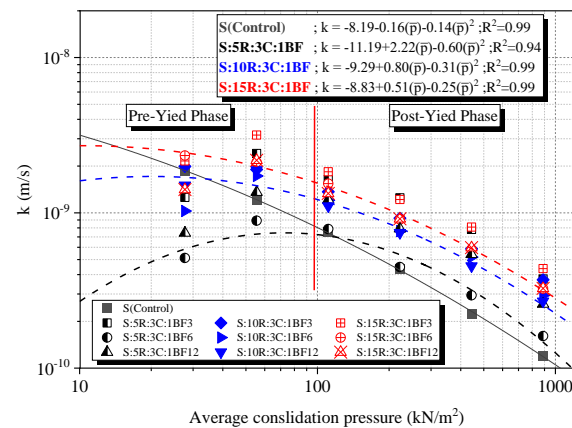
$$k = \frac{c_v m_v \gamma_w}{8.64 \times 10^8} \quad (4)$$

Where k is the permeability coefficient in m/s,  $c_v$  is the coefficient of consolidation,  $m_v$  is the coefficient of volume change,  $\gamma_w$  is the unit volume weight of water ( $9.81 \text{ kN/m}^3$ ), and  $8.64 \times 10^8$  is the conversion parameter of k to m/s. Fig. 6a compared the pressure dependence of permeability coefficient of the reinforced and stabilized expansive soil, taking into consideration the following factors; length of basalt fibers, RHA-cement content, and the average consolidation pressure. It was found that the permeability coefficient varied in the order of  $10^{-10}$  to  $10^{-9}$  and was greatly influenced by the average consolidation pressure. Also, the value of k increased during the pre-yield phase and decreased significantly in the post-yield phase for all the specimens tested. However, the value of k in the observed trend depended on the specimen composition.

For instance, the permeability coefficient increased with RHA content for all the individual average consolidation pressures, as shown in Fig. 6a. This increase was due to the high porosity caused by the excess RHA particles and the voids networks created by basalt fibers in the composite specimen. Additionally, the pozzolanic compounds due to RHA and cement precipitation enhanced cementation at low RHA-cement contents hence the low k values at 5%RHA. A similar reduction in the permeability

coefficient due to pozzolanic reaction has also been recorded by other studies, such as Onyelowe (2021)[41], Jamil (2013)[42], Gupta and Kumar (2017)[43], and Nshimiyimana (2018)[44]. However, as the average consolidation pressure increased, the k value reduced to an almost constant value of order  $10^{-10}$  for all the tested specimens due to the complete removal of the voids and sufficient rearrangement of soil-RHA-cement and fibers. This relationship between voids and permeability indicated that voids played the dominant role in affecting the permeability coefficient. Cheng (2020) also observed a similar relationship while experimenting on the consolidation properties of reconstituted clay soils [45].

Supplementary to the analyses discussed, a correlation plot was considered regarding the influence of the basalt fiber length on the permeability coefficient, as shown in Fig. 6b-d. In Fig. 6b representing basalt fiber reinforced specimen with 5%RHA and 3%cement, the permeability coefficient reduced with increasing fiber length, whereas in the case of 10%RHA-3C and 15%RHA-3C, shown in Fig. 6c and Fig. 6d, respectively, a very minimal reduction in the k value was recorded for all the average consolidation pressure increments. The notable reducing trend of k with the length of basalt fiber for the 5%RHA-3C specimens can be attributed to the well-defined structural development due to cementation from adequate pozzolanic reaction and the enhanced reinforcement. However, a further increase in the basalt fiber length to 12mm increased the permeability due to the longer paths for water to drain quicker through the specimen. The rise in permeability coefficient with the length of fiber reinforcements was also observed by Abdi (2008) while investigating the effects of fiber inclusion on the permeability in clay soils [46]. From these correlation plots, curve fitting equations with an  $R^2=1.00$  were formulated to assist design engineers in predicting the projected permeability coefficients for RHA-basalt fiber stabilized soils for a given average consolidation pressure and length of basalt fiber.





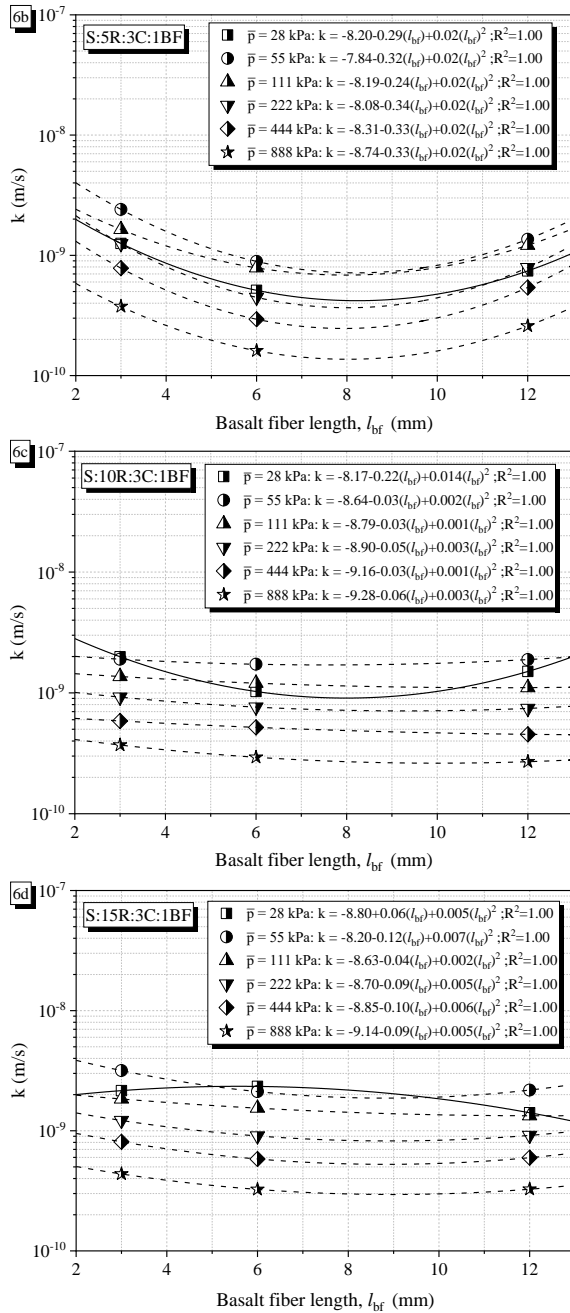


Fig. 6 (a) Relationship between  $k$  and  $\bar{p}$ , (b) Correlation between  $k$  and  $l_{bf}$  for 5% RHA specimens, (c) Correlation between  $k$  and  $l_{bf}$  for 10% RHA specimens, (d) Correlation between  $k$  and  $l_{bf}$  for 15% RHA specimens.

### Microstructural analyses

The effect of basalt fibers reinforcements and stabilization using RHA-cement mixtures on the consolidation coefficients of reconstituted expansive soils can be explained by capturing the microstructural development through a scanning electron microscope (SEM). SEM micrographs showing the coupling effect of the basalt fibers with the compact cementitious composite soil matrix for

the tested specimen combinations are shown in Fig. 7-9. These SEM images represented the corresponding specimen states at the end of the consolidation process (Average consolidation pressure = 888kPa). In this study, a detailed analysis to justify the trends of the coefficient of consolidation ( $c_v$ ) and the permeability coefficient ( $k$ ) were discussed, as explained in this section.

It can be observed from Fig. 7a, 8a, and 9a that the mobilization of basalt fiber reinforcements was driven by the interfacial contacts developed during the physical connection between the cementitious soil matrix and the fiber surface. The interfacial contacts were more significant when the length of basalt fibers increased from 3mm to 12mm due to the interconnectivity arising from the intense fiber network. Additionally, a clear indication of a cemented compact structure was evident due to the complete utilization of 5%RHA and cement during the pozzolanic reactions. The two states described above (i.e., fiber-soil interfacial contacts and the cementitious structure) reduced the coefficient of consolidation ( $c_v$ ) and the permeability ( $k$ ) significantly by resisting compressibility and eliminating excess voids, respectively, as shown in Fig. 4a and 6a. The tendency of fiber reinforcements to improve the bonding strength of expansive soil was also observed by Syed (2020) when stabilizing expansive clays using geo-polymerization and fiber reinforcement [47].

Contrarily, the rising trends of  $c_v$  and  $k$  for the fiber-reinforced specimen containing 10%RHA and 3%C were justified by the occurrence of planes of weakness and voids in the specimens as displayed in Fig. 7b, 8b, and 9b. However, the discrete distributions of high tensile strength basalt fibers in the specimen structure interlocked the separate cemented blocks, restricting further cracks during consolidation. The interlocking mechanism was more significant with increasing basalt fiber length.

It was also noteworthy that the developments of voids in the specimens were more significant in specimens containing 15%RHA and basalt fiber reinforcements, as illustrated in Fig. 7c, 8c, and 9c. The more notably porous structure developed due to the reduced pozzolanic activity that led to the balling of RHA and soil particles around the basalt fibers. This balling effect developed a highly compressible and porous specimen structure, increasing the  $c_v$  and  $k$  values.

### CONCLUSIONS

This paper presented an experimental analysis based on a series of oedometer tests to study the correlation between the one-dimensional consolidation coefficients and the length of basalt fiber, RHA-cement content in fiber-reinforced RHA-treated expansive soils. An effort has been made to explain more rationally the influence basalt fiber

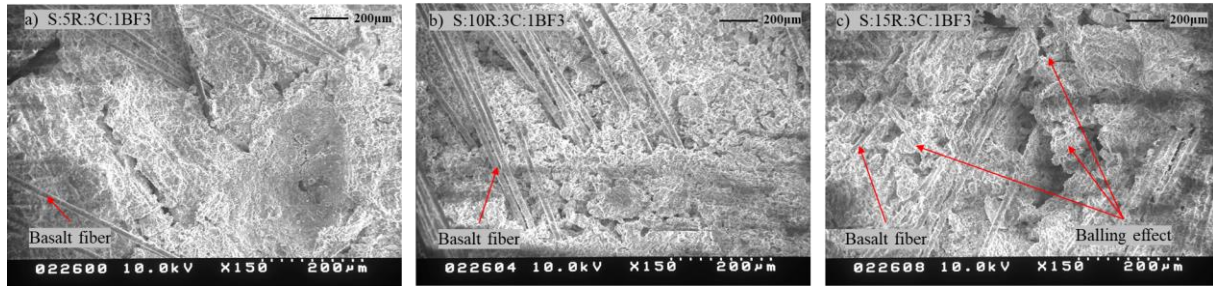


Fig. 7: SEM imagery (a) Specimen S:5R:3C:1BF3, (b) Specimen S:10R:3C:1BF3, (c) Specimen S:15R:3C:1BF3

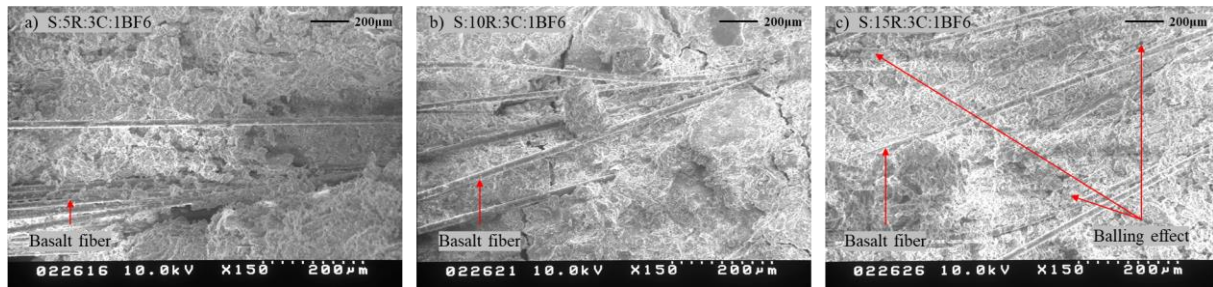


Fig. 8: (a) SEM imagery (a) Specimen S:5R:3C:1BF6, (b) Specimen S:10R:3C:1BF6, (c) Specimen S:15R:3C:1BF6

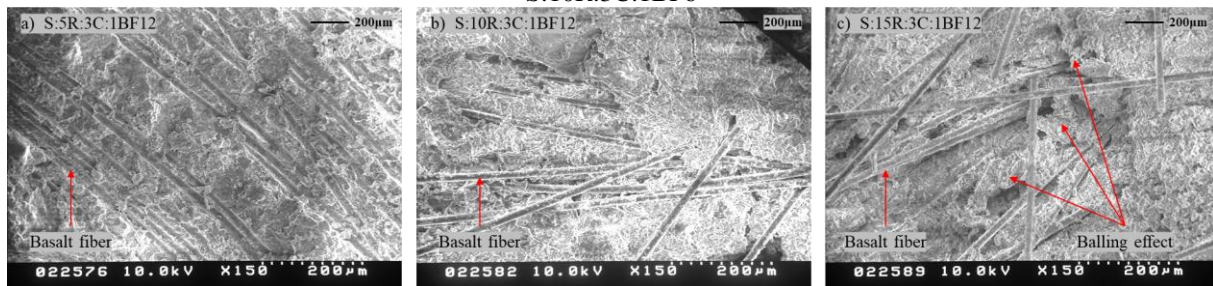


Fig. 9: (a) SEM imagery (a) Specimen S:5R:3C:1BF12, (b) Specimen S:10R:3C:1BF12, (c) Specimen S:15R:3C:1BF12

length and RHA-cement content have on the coefficient of consolidation ( $c_v$ ), coefficient of volume change ( $m_v$ ), and the permeability coefficient ( $k$ ), drawing further justifications through SEM imagery. The following conclusions can be made:

1. Increasing the length of basalt fibers for each RHA content reduced the coefficient of consolidation ( $c_v$ ). This reduction was more significant for fiber-reinforced specimens constituting 5%RHA and 10%RHA, with reduction percentages of 54.21% and 30% at the end of consolidation. This response indicated that the degree of consolidation depended on the specimen composition and the degree of reinforcement.
2. The coefficient of volume change ( $m_v$ ) was greatly influenced by the average consolidation pressure rather than the specimen composition (fiber length and RHA content). However, at low consolidation pressures during the pre-yield stage, fiber-RHA reinforced specimens depicted lower volume changes than the control specimen. Also, a slight increase of  $m_v$  with average consolidation pressure was evident compared to the control specimen.

3. The permeability coefficient ( $k$ ) of the fiber-reinforced specimen with 5%RHA-3%C reduced with increasing fiber length, whereas, in the case of 10%RHA-3C and 15%RHA-3C, very minimal reduction in the  $k$  value was recorded with increased fiber length.
4. The curve fitting methods shown in Figures 4a, 5a, and 6a, were used to propose analytical equations for evaluating  $c_v$ ,  $m_v$ , and  $k$  for all known basalt fiber lengths, as indicated in equations 5, 6 and 7.

$$c_v = 0.31 + 1.64(l_{bf}) - 0.30(l_{bf})^2; R^2 = 0.96$$

$$m_v = -3.85 + 1.13(l_{bf}) - 0.41(l_{bf})^2; R^2 = 0.93$$

$$k = -11.41 + 2.57(l_{bf}) - 0.66(l_{bf})^2; R^2 = 0.96$$

5. The SEM imagery showed that the random distribution of basalt fibers in the stabilized composite enhanced the reinforcing network within the specimens. Increasing the basalt fiber length from 3mm to 12mm provided a more robust reinforcing phenomenon in the stabilized composite, thereby controlling the interfacial strength. This strength enhancement contributed significantly to the trend of the consolidation coefficients.



6. The relationships discussed demonstrated that reinforcing expansive soils with 12mm basalt fibers, 5%RHA and 3% cement, can be considered the optimal value for use in engineering practice to avoid the over-settlement of engineering structures.
7. The experimental and analytical methodologies presented in this paper are thus believed to be of great significance for quantifying and interpreting one-dimensional consolidation coefficients and their correlation to fiber reinforcement and RHA stabilization techniques. Also, the correlation equation provided in this study can be used as design charts regarding the consolidation and settlement trends of basalt fiber-RHA-cement stabilized expansive soils.

## ACKNOWLEDGMENTS

The authors would like to acknowledge the Japan Ministry of Education, Culture, Sports, Science and Technology for providing the MEXT scholarship through Mie University, where this study was conducted. This research was also supported by Make Integrated Technology Limited, which provided experimental materials.

## REFERENCES

- [1] Yi, Y., Gu, L. and Liu, S., Microstructural and mechanical properties of marine soft clay stabilized by lime-activated ground granulated blast furnace slag. *Applied Clay Science*, 103, 2015, pp.71-76. <https://doi.org/10.1016/j.clay.2014.11.005>
- [2] Firoozi, A.A., Taha, M.R., Firoozi, A.A. and Khan, T.A., Assessment of nano-zeolite on soil properties. *Australian Journal of Basic and Applied Sciences*, 8(19), 2014, pp.292-8.
- [3] Wang, L., Cementitious stabilization of soils in the presence of sulfate. Louisiana State University and Agricultural & Mechanical College, 2002.
- [4] Prusinski, J.R. and Bhattacharja, S., Effectiveness of Portland cement and lime in stabilizing clay soils. *Transportation research record*, 1652(1), 1999, pp.215-227. <https://doi.org/10.3141/1652-28>
- [5] Cuisinier, O., Le Borgne, T., Deneele, D. and Masrouri, F., Quantification of the effects of nitrates, phosphates and chlorides on soil stabilization with lime and cement. *Engineering Geology*, 117(3-4), 2011, pp.229-235. <https://doi.org/10.1016/j.enggeo.2010.11.002>
- [6] James, J. and Pandian, P.K., Industrial wastes as auxiliary additives to cement/lime stabilization of soils. *Advances in Civil Engineering*, vol. 2016, Article ID 1267391, 17 pages, 2016. <https://doi.org/10.1155/2016/1267391>
- [7] Ghadir, P. and Ranjbar, N., Clayey soil stabilization using geopolymer and Portland cement. *Construction and Building Materials*, 188, 2018, pp.361-371. <https://doi.org/10.1016/j.conbuildmat.2018.07.207>
- [8] Biswal, D.R., Sahoo, U.C. and Dash, S.R., Durability and shrinkage studies of cement stabilized granular lateritic soils. *International Journal of Pavement Engineering*, 20(12), 2019, pp.1451-1462. <https://doi.org/10.1080/10298436.2018.1433830>
- [9] Sandhu, R.K. and Siddique, R., Influence of rice husk ash (RHA) on the properties of self-compacting concrete: A review. *Construction and Building Materials*, 153, 2017, pp.751-764. <https://doi.org/10.1016/j.conbuildmat.2017.07.165>
- [10] Chen, R., Congress, S.S.C., Cai, G., Duan, W. and Liu, S., Sustainable utilization of biomass waste-rice husk ash as a new solidified material of soil in geotechnical engineering: A review. *Construction and Building Materials*, 292, 2021, p.123219. <https://doi.org/10.1016/j.conbuildmat.2021.123219>
- [11] Owino, A.O., Nahar, N., Hossain, Z. and Tamaki, N., Dimensional influence of basalt fiber reinforcements on the consolidation behaviour of rice husk ash stabilized soils. *Construction and Building Materials*, 339, 2022 pp.127686. <https://doi.org/10.1016/j.conbuildmat.2022.127686>
- [12] Abdi, M.R., Parsapazhouh, A. and Arjmand, M., "Effects of Random Fiber Inclusion on Consolidation, Hydraulic Conductivity, Swelling, Shrinkage Limit and Desiccation Cracking of Clays, 2008, pp.284-292.
- [13] Das, S. and Pal, S.K., Consolidation Characteristics of Silty-Clay Soil Mixed with Class F Indian Fly Ash. In *Indian Geotechnical Conference*, December 2012, pp. 13-45.
- [14] Kar, R. and Pradhan, P., Strength and compressibility characteristics of randomly distributed fiber-reinforced soil. *International Journal of Geotechnical Engineering*, 5(2), 2011, pp.235-243. <https://doi.org/10.3328/IJGE.2011.05.02.235-243>
- [15] Eberemu, A.O. and Sada, H., Compressibility characteristics of compacted black cotton soil treated with rice husk ash. *Nigerian Journal of Technology*, 32(3), 2013, pp.507-521.
- [16] Rao, D.K., Pranav, P.R.T. and Anusha, M., Stabilization of expansive soil with rice husk ash, lime and gypsum—an experimental study. *International Journal of Engineering Science and Technology*, 3(11), 2011, pp.8076-8085.

- [17] Sabat, A.K., Engineering properties of an expansive soil stabilized with rice husk ash and lime sludge. *International Journal of Engineering and Technology*, 5(6), 2013, pp.4826-4833.
- [18] Changizi, F. and Haddad, A., Strength properties of soft clay treated with mixture of nano-SiO<sub>2</sub> and recycled polyester fiber. *Journal of rock mechanics and Geotechnical Engineering*, 7(4), 2015, pp.367-378. <https://doi.org/10.1016/j.jrmge.2015.03.013>
- [19] Fatahi, B., Fatahi, B., Le, T.M. and Khabbaz, H., Small-strain properties of soft clay treated with fiber and cement. *Geosynthetics International*, 20(4), 2013, pp.286-300. <https://doi.org/10.1680/gein.13.00018>
- [20] Muñoz, Y.O., dos Santos Izzo, R.L., de Almeida, J.L., Baldovino, J.A. and Rose, J.L., The role of rice husk ash, cement and polypropylene fibers on the mechanical behavior of a soil from Guabirubota formation. *Transportation Geotechnics*, 31, 2021, pp.100673. <https://doi.org/10.1016/j.trgeo.2021.100673>
- [21] Hu, H. and Liu, Y., High modulus, high tenacity yarns. In *Technical textile yarns*, Woodhead Publishing, 2010, pp. 329-386. <https://doi.org/10.1533/9781845699475.2.329>
- [22] Dhand, V., Mittal, G., Rhee, K.Y., Park, S.J. and Hui, D., A short review on basalt fiber reinforced polymer composites. *Composites Part B: Engineering*, 73, 2015, pp.166-180. <https://doi.org/10.1016/j.compositesb.2014.12.011>
- [23] Sim, J. and Park, C., Characteristics of basalt fiber as a strengthening material for concrete structures. *Composites Part B: Engineering*, 36(6-7), 2005, pp.504-512. <https://doi.org/10.1016/j.compositesb.2005.02.002>
- [24] Sridharan, A. and Nagaraj, H.B., Coefficient of consolidation and its correlation with index properties of remolded soils. *Geotechnical testing journal*, 27(5), 2004, pp.469-474.
- [25] Ferrari, A., Favero, V. and Laloui, L., One-dimensional compression and consolidation of shales. *International Journal of Rock Mechanics and Mining Sciences*, 88, 2016, pp.286-300. <https://doi.org/10.1016/j.ijrmms.2016.07.030>
- [26] JIS A 1217, Test method for soil consolidation test. Japanese Industrial Standard, Guidance and Basic - Soil Test, The Jpn. Geotech. Soc. (in Japanese), (2010), pp.103-120.
- [27] JIS A 1227, Test method for soil consolidation test. Japanese Industrial Standard, Guidance and Basic - Soil Test, The Jpn. Geotech. Soc. (in Japanese), (2010), pp.215-227.
- [28] Yuan-qiang, C., Xu, L. and Shi-ming, W., One-dimensional consolidation of layered soils with impeded boundaries under time-dependent loadings. *Applied Mathematics and Mechanics*, 25(8), 2004, pp.937-944. <https://doi.org/10.1007/BF02438802>
- [29] Terzaghi K., *Theoretical Soil Mechanics*[M]. New York, N Y: John Wiley and Sons Inc, 1943.
- [30] Casagrande, A., and R.E. Fadum, Notes on Soil Testing for Engineering Purposes, Harvard University Graduate School Engineering Publication, Series No. 8, Massachusetts,1940.
- [31] Jain, A. and Puri, N., Consolidation characteristics of highly plastic clay stabilized with rice husk ash. *International Journal of Soft Computing and Engineering (IJSCE)*, 2, 2013, pp.413-418.
- [32] Ferrari, A., Favero, V. and Laloui, L., One-dimensional compression and consolidation of shales. *International Journal of Rock Mechanics and Mining Sciences*, 88, 2016, pp.286-300. <https://doi.org/10.1016/j.ijrmms.2016.07.030>
- [33] Robinson, R.G. and Allam, M.M., Effect of clay mineralogy on coefficient of consolidation. *Clays and clay minerals*, 46(5), 1998, pp.596-600.
- [34] Sridharan, A. and Nagaraj, H.B., Coefficient of consolidation and its correlation with index properties of remolded soils. *Geotechnical testing journal*, 27(5), 2004, pp.469-474.
- [35] Yeo, S.S., Shackelford, C.D. and Evans, J.C., Consolidation and hydraulic conductivity of nine model soil-bentonite backfills. *Journal of Geotechnical and Geoenvironmental Engineering*, 131(10), 2005, pp.1189-1198. [https://doi.org/10.1061/\(ASCE\)1090-0241\(2005\)131:10\(1189\)13](https://doi.org/10.1061/(ASCE)1090-0241(2005)131:10(1189)13)
- [36] Eberemu, A.O., Omajali, D.I. and Abdulhamid, Z., Effect of compactive effort and curing period on the compressibility characteristics of tropical black clay treated with rice husk ash. *Geotechnical and Geological Engineering*, 34(1), 2016, pp.313-322. <https://doi.org/10.1007/s10706-015-9946-9>
- [37] Santagata, M., Bobet, A., Johnston, C.T. and Hwang, J., One-dimensional compression behavior of a soil with high organic matter content. *Journal of geotechnical and geoenvironmental engineering*, 134(1), 2008, pp.1-13. [https://doi.org/10.1061/\(ASCE\)1090-0241\(2008\)134:1\(1\)13](https://doi.org/10.1061/(ASCE)1090-0241(2008)134:1(1)13)
- [38] Xu, D.S., Huang, M. and Zhou, Y., One-dimensional compression behavior of calcareous sand and marine clay mixtures. *International Journal of Geomechanics*, 20(9), 2020, p.04020137. [https://doi.org/10.1061/\(ASCE\)GM.1943-5622.0001763](https://doi.org/10.1061/(ASCE)GM.1943-5622.0001763)
- [39] Eberemu, A.O., Consolidation properties of compacted lateritic soil treated with rice husk ash. *Geomaterials*, 1(3), 2011, pp.70-78. <https://doi.org/10.4236/gm.2011.13011>

- [40] Laskar, A. and Pal, S.K., Effects of waste plastic fibers on compaction and consolidation behavior of reinforced soil. *EJGE*, 18, 2013, pp.1547-1558.
- [41] Onyelowe, K.C., Onyia, M.E., Bui Van, D., Baykara, H. and Ugwu, H.U., Pozzolanic reaction in clayey soils for stabilization purposes: a classical overview of sustainable transport geotechnics. *Advances in Materials Science and Engineering*, 2021. <https://doi.org/10.1007/s41204-021-00123-2>
- [42] Jamil, M., Kaish, A.B.M.A., Raman, S.N. and Zain, M.F.M., Pozzolanic contribution of rice husk ash in cementitious system. *Construction and Building Materials*, 47, 2013, pp.588-593. <https://doi.org/10.1016/j.conbuildmat.2013.05.088>
- [43] Gupta, D. and Kumar, A., Performance evaluation of cement-stabilized pond ash-rice husk ash-clay mixture as a highway construction material. *Journal of Rock Mechanics and Geotechnical Engineering*, 9(1), 2017, pp.159-169. <https://doi.org/10.1016/j.jrmge.2016.05.010>
- [44] Nshimiyimana, P., Miraucourt, D., Messan, A. and Courard, L., Calcium carbide residue and rice husk ash for improving the compressive strength of compressed earth blocks. *MRS Advances*, 3(34-35), 2018, pp.2009-2014. <https://doi.org/10.1557/adv.2018.147>
- [45] Cheng, G., Zhu, H.H., Wen, Y.N., Shi, B. and Gao, L., Experimental investigation of consolidation properties of nano-bentonite mixed clayey soil. *Sustainability*, 12(2), 2020, pp.459. <https://doi.org/10.3390/su12020459>
- [46] Abdi, M.R., Parsapazhouh, A. and Arjmand, M., Effects of Random Fiber Inclusion on Consolidation, Hydraulic Conductivity, Swelling, Shrinkage Limit and Desiccation Cracking of Clays, Vol 6, No. 4, 2008 pp.284-292.
- [47] Syed, M., GuhaRay, A., Agarwal, S. and Kar, A., Stabilization of expansive clays by combined effects of geopolymerization and fiber reinforcement. *Journal of The Institution of Engineers (India): Series A*, 101(1), 2020, pp.163-178. <https://doi.org/10.1007/s40030-019-00418-3>

## ***Construction Materials***

# PARAMETRIC MODELING OF RECYCLED BRICK AGGREGATE CONCRETE (RBAC) USING ARTIFICIAL NEURAL NETWORK (ANN) AND MULTIPLE LINEAR REGRESSION (MLR)

Albert A. Griño Jr<sup>1</sup>

<sup>1</sup>Faculty, Adamson University, Philippines

## ABSTRACT

This study aims to assess and compare the performance of Artificial Neural Network (ANN) and Multiple Linear Regression (MLR) model in predicting the compressive strength of concrete with recycled clay and brick tile. A proposed prediction model of artificial neural network (ANN) was generated using Matlab software for the compressive strength of Recycled Brick Aggregate Concrete (RBAC). The proposed model is tested, trained, and validated using the available test data of 147 concretes with various mixture proportions collected from different technical journals. The collected data is composed of eight input variables (parameters) and one output variable. The input parameters are the following: cement, water cement ratio, crushed tile ratio (fine), crushed tile ratio (coarse), crushed brick ratio (fine), crushed brick ratio (coarse), natural aggregate (fine), and natural aggregate (coarse) while the output parameter is the compressive strength. The result of the back-propagation algorithm in ANN model showed that Bayesian Regularization, with nine (9) neurons, is the best mathematical model with a Regression (R) and Mean Squared Error (MSE) values of 0.86499 and 0.007996756, respectively. Whereas, the correlation coefficient for the MLR model was 0.6508. The results clearly showed that the prediction using neural network model is more accurate than using multiple-linear regression model. Based on the result of the parametric study, the recommended amount for each material are in the following ranges: cement = 350 to 400 kg, water cement ratio = 0.3 to 0.4, recycled = 20 to 40 % and natural aggregates = 60 to 80 %.

*Keywords: parametric modeling, recycled brick aggregate, artificial neural network, multiple linear regression, compressive strength*

## INTRODUCTION

The construction industry plays a significant role to the growth and development of nation. Generally, construction industry uses three types of aggregates in construction projects (Ameri and Behnood, 2012; Behnood and Ameri, 2012): (a) virgin (natural), (b) artificial, and (c) recycled.

In recent years, a lot of attention has been given to the utilization of recycled aggregates to concrete due to depleting natural resources and in order to reduce environmental wastes. There are a lot of waste materials that can be generated from the construction activities which may include the following materials: concrete, tiles, metal, paper, wood, glass and mixed wastes such as trash and organic wastes. As such, these waste materials are considered as construction and demolition waste. Construction and demolition wastes (C&DW) are usually recognized as not dangerous, but their accumulation can generate serious environmental problems (Simion et al., 2013). It is interesting to note that around 90% of the construction waste can be reused and recycled. The construction waste is under the definition of a solid waste. Solid waste can be defined as all discarded household, commercial waste, non-hazardous institutional and industrial waste, street sweepings, construction debris, agricultural waste, and other non-

hazardous/non-toxic waste.

Concrete is considered as one of the commonly used materials in construction. It is composed of cement, water, and natural (fine and coarse) aggregates. Recycled aggregates can also be used to partially or completely replace the natural aggregates. In order to determine the optimum amount of recycled material there is a need to apply a numerical modelling such as artificial neural network that can simulate and generate a formula to predict the compressive strength of concrete with natural and recycled aggregates. Artificial neural network (ANN) had been widely used as a tool to create a numerical model for the experimental data. However, there are few literatures that focused on modelling the compressive strength of concrete with recycled aggregates. In that case, this study was established and focused on four (4) methods in the prediction of the compressive strength of Recycled Brick Aggregate Concrete (RBAC). The three methods in ANN are the following: (1) Levenberg-Marquardt, (2) Bayesian Regularization, (3) Scaled Conjugate Gradient and the fourth method is using Multiple Linear Regression (MLR) using Microsoft Excel.

This paper is an extension of the previous study of Sipos (2017) to further explore the applicability of using artificial neural network (ANN) and Multiple Linear Regression (MLR) with parametric study. This

study is significant since it can be used to determine the optimum amount of recycled tile/brick as partial/full replacement to natural aggregates in concrete mixture. An ANN model with one hidden layer is developed by using a MATLAB software to generate an appropriate model for predicting the compressive strength of Recycled Brick Aggregate Concrete (RBAC).

## METHODOLOGY

In this study, four different models have been developed using both ANN and MLR techniques. A total of 147 data sets were collected from 10 international published literatures to examine whether the ANN and MLR is better in predicting the compressive strength of Recycled Brick Aggregate Concrete (RBAC). The ANN training algorithms used are the following: (1) Levenberg-Marquardt (2) Bayesian Regularization and (3) Scaled Conjugate Gradient. A feed-forward back-propagation neural network model is developed to predict the compressive strength in 147 sets of experimental data. From these, 89 randomly selected data were used for training the network and the remaining 58 samples were equally divided for the ANN validation and testing processes (29 of them were selected as the testing data sets and the other 29 were used for validation of network).

A number of iterations with one hidden layer were tried in the ANN structure. The Regression (R) values were compared against various neurons (1,3,5,7,9 and 11) in the hidden layer in order to determine the most optimal topology (maximum R value) for the compressive strength.

The eight (8) input variables to be used in this study are the following: (a) cement (b)water/cement (c)Crushed Tile Ratio (CT) 0-4 (%) (d) Crushed Tile Ratio (CT) 4-16 (%) (e) Crushed Brick Ratio (CT) 0-4 (%) (f) Crushed Brick Ratio (CT) 4-16 (%) (g) Natural Aggregate 0-4 (%) and (h) Natural Aggregate 4-16 (%). The output parameter is the compressive strength, Fc28(MPa).

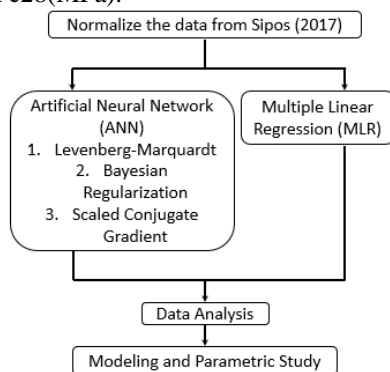


Fig. 1 Theoretical Framework

As seen in Figure 1 the theoretical framework of the study. All the data came from the author, Sipos (2017) were normalized using Equation 1 in order to standardized the input and output values ranging from zero to one. The normalized data were subjected to ANN and MLR.

$$x_{new} = \frac{x - x_{min}}{x_{max} - x_{min}} \quad (1)$$

Under the process of ANN, three algorithm methods were used such as Levenberg Marquardt, Bayesian Regularization and Scaled Conjugate Gradient using Matlab 2019a. For each method, all the data were trained, validated and tested. On the other hand, Multiple Linear Regression was also used in order to determine whether there is a linear relationship between the independent and dependent variables using Microsoft Excel. All the generated models from ANN and MLR were evaluated by comparing their regression values. The higher the value of regression (R) means that the model is a better representation among the generated models. The best model was subjected to parametric study in order to determine the effect of each independent variable to dependent variable by varying the amount of one independent variable while the other variables were held constant. Lastly, from the result of the parametric study a conclusion can be made by determining the optimum range of recycled brick/tile that can be added to the concrete matrix to attain a suitable compressive strength.

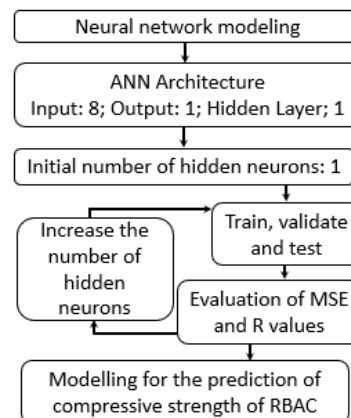


Fig. 2 Flowchart for optimizing the neural network model

It can be seen in Figure 2 the optimization for the three methods under the ANN. A number of hidden neurons were selected ranging from 1 to 11 with an increment of 2. For each iteration process, all the data were trained, validated and tested. The regression results of each algorithm were recorded and compared. The highest value of regression can be treated as the best model to predict the compressive strength of RBAC.



## RESULTS AND DISCUSSION

Table 1 Characteristics of the data set

Variables	Max	Min	Mean	Median	Standard Deviation	
Cement	527	250	374	400	66.42	
w/c	1.08	0.4	0.54	0.5	0.11	
CTR_0-4	100	0	17	0	24.44	
CTR_4-16	100	0	17	0	24.48	
CBR_0-4	100	0	23	25	28.41	
CBR_4-16	100	0	26	25	31.68	
NA_0-4	100	0	60	50	33.76	
NA_4-16	100	0	57	50	35.2	
output	fc'	81	9	30	27	13.12

It can be seen in Table 1 the statistical data of input and output variables. Statistical data includes the following parameters: maximum, minimum, mean, median and standard deviation. It can be observed that the water cement ratio has a range of 0.4 to 1.08 and relative to the other variables these values are very small. Thus, there is a need to normalize the data so that all the values in the variables are within the range of zero to one.

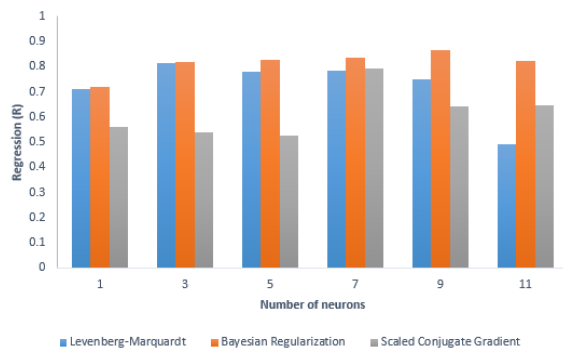


Fig. 4 Variation of Regression with respect to the number of neurons

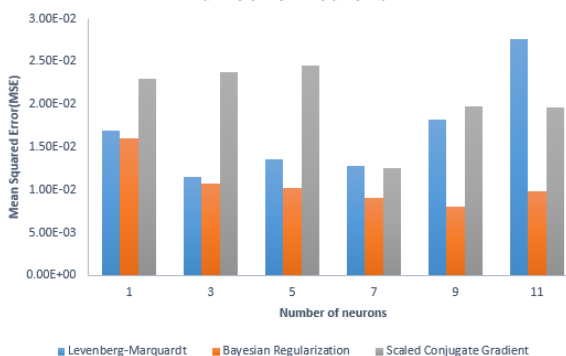


Fig. 5 Variation of Mean Squared Error (MSE) with respect to the number of neurons

It can be seen in Figure 4 and 5 the comparison of the regression and mean squared error for the three algorithms in ANN. It can be observed that BR\_9 model (with 9 neurons) gained the highest regression value (0.86499) and minimum MSE value of 0.007996756. For Bayesian Regularization algorithm, the ANN with 9 neurons in hidden layer appeared to

be the most optimal topology for compressive strength of RBAC.

Table 2 Multiple Linear Regression (MLR) Result

Regression Statistics	
Multiple R	0.650811271
R Square	0.423555311
Adjusted R Square	0.384564824
Standard Error	0.141686232
Observations	147

Using Microsoft Excel, the Multiple Linear Regression (MLR) was carried out and the result can be seen in Table 2 in which the regression value is 0.650811271.

Table 3 Regression Value of ANN and MLR models

Model	Regression Value
LM_3	0.81276
BR_9	0.86499
SCG_7	0.79114
MLR	0.65081

The comparison of the regression value from four models developed using both Artificial Neural Network and Multiple Regression Analysis in Microsoft Excel can be seen in Table 3. It can be observed that the goodness-of-fit of the ANN models is superior when compared to the regression model. The outcome is analogous to the result of Bingol et al. in 2013 which states the superiority of the ANN in predicting the compressive strength of concrete.

The higher values of R implies that the obtained data corresponds well to the experimental data. Comparing all the models, it can be concluded that the BR\_9 model (Bayesian Regularization with 9 neurons) is the best model among the generated models from ANN in Matlab and MLR using Microsoft Excel.

Table 4 Coefficients of all the input variables using Multiple Linear Regression (MLR)

Coefficients	
Intercept	0.130912093
Cement	0.35288032
Water/cement	-0.179805552
Crushed Tile Ratio (CT) 0-4	0.013143038
Crushed Tile Ratio (CT) 4-16	-0.182980652
Crushed Brick Ratio (CT) 0-4	0
Crushed Brick Ratio (CT) 4-16	0
Natural Aggregate 0-4	0.064598444
Natural Aggregate 4-16	0.057082633

From Table 4, it can be seen that the largest factor for the compressive strength of concrete is the cement followed by the natural aggregate and the crushed tile ratio 0-4. On the other hand, water/cement ratio and crushed tile ratio 4-16 have a negative effect to the strength of concrete while the crushed brick ratio does not have any significant effect to the strength.

The equation that can be generated using MLR in Excel is

$$f_c' = 0.3529X_1 - 0.1798X_2 + 0.01314X_3 - 0.1830X_4 + 0X_5 + 0X_6 + 0.06460X_7 + 0.05708X_8 + 0.1309 \quad (2)$$

### Parametric Study for the Components of Concrete

A parametric study was done in order to determine the effect of each independent variable to the compressive strength of concrete by varying the amount of one independent variable and setting the other independent variables to be a constant value. The constant value selected is the median value for each variable involved in the parametric study. The model adapted in the parametric study is the BR\_9 model (Bayesian Regularization with 9 neurons) since this is the best model among the generated models from ANN and MLR.

#### Cement

This component is generally used as a medium to bind all of the materials in concrete mixture through the process of hydration. Generally, increasing the cement content would increase the unit weight and workability of the concrete mixture. A simulation of cement type influence was carried out with a w/c ratio of 0.5, and the content of cement is varied from 250 to 550 kg with constant value of crushed brick and natural aggregate content.

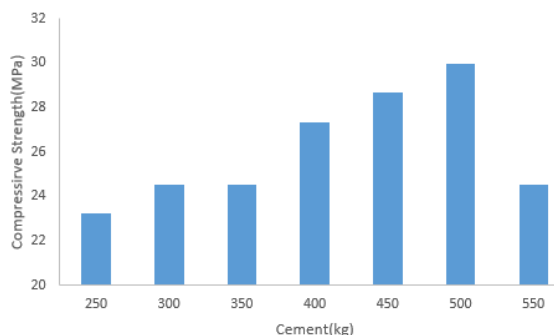


Fig. 6 Compressive strength of RBAC with varying amount of cement

The strength of concrete is independent to the cement content for a given w/c: increasing cement content does not affect strength (Wassermann et al.

2009; Dhir et al. 2004; Schulze 1999). An increase in the cement content results to an increase of strength in concrete for a given workability in a concrete matrix. Based on Figure 6, it can be seen that as the amount of cement increases, the compressive strength also increases up to 500 kg of cement. This shows that at 500 kg cement content, it is more likely that the mixture already reached its optimum workability, hence any cement added to the mixture would substantially decrease the concrete strength. A maximum compressive strength increase of 11.25% can be obtained within the range of 350 to 400 kg. This range reflect a suitable range to be used in order to obtain an optimum strength in concrete mixture.

#### Water Cement Ratio

This is defined as the mass of water divided by the mass of cement in the concrete mix and this is usually abbreviated as w/c. A simulation of water cement influence was carried out with a cement content of 400 kg, and the content of water cement ratio is varied from 0.4 to 1.2 with constant value of crushed brick and natural aggregate content.

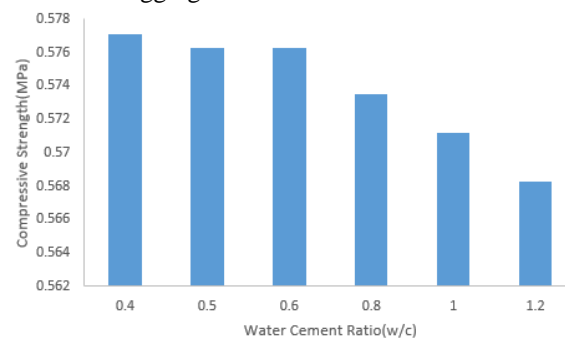


Fig. 7 Compressive strength of RBAC with varying amount of water cement ratio

Strength is primarily a function of w/c as long as there is sufficient paste to fill the voids between the aggregate particles and the mixture is adequately consolidated (Mindess et al. 2003; Kosmatka et al. 2002; Mehta and Monteiro, 1993). One theory that would relate water cement ratio to the strength of concrete is the Abrams' law. This law states that the strength of a concrete mix is inversely related to the mass ratio of water to cement (Punmia, 2003). As the water content increases in the concrete mix, the compressive strength of concrete decreases. It can be seen in Figure 7 that the compressive strength decreases as water cement ratio increases. The maximum decrease of strength can be observed from 1.0 to 1.2 with a 5% decrease. Thus, the maximum value of water cement ratio should be 0.4 only in order to obtain a desirable concrete mix. This value is also the recommended by Adnan (2007) in which the

authors states that Recycled Aggregate Concrete (RAC) with water-cement ratio 0.4 had the highest strength at the age of 28 days.

It can be noted that as the water-cement ratio increases, the porosity of the cement paste would also increase. Hence, the compressive strength will decrease because the porosity will increase as the void in the concrete matrix will be filled by the water or air.

#### *Recycled Fine/Coarse Aggregates*

Recycled concrete, or crushed waste concrete, is simply an old concrete that has been crushed to produce new aggregate. Concrete made with recycled coarse aggregates and conventional fine aggregate can obtain an adequate compressive strength (Kosmatka, 2011). A simulation of tile aggregate type influence was carried out with a concrete mixture of 400 kg cement and w/c ratio of 0.5, and the content of crushed tile aggregate is varied from 0 to 40% with decreasing crushed brick and natural aggregate content. Similarly, a simulation of brick aggregate type influence was carried out with a concrete mixture of 400 kg cement and w/c ratio of 0.5, and the content of crushed brick aggregate is varied from 0 to 44.4% with decreasing crushed brick and natural aggregate content.

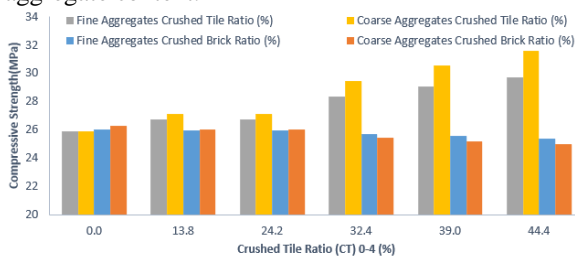


Fig. 8 Compressive Strength of RBAC with varying percentage of Recycled Aggregate

It can be observed in Figure 8 that the compressive strength increases as the percentage of recycled clay tile increases for both fine and coarse aggregates up to 40%. However, for brick tile there is a substantial decrease of strength after 24.2% percent and a constant value of compressive strength can be noticed in the same figure for the recycled brick tile within the range of 13.8 to 24.2 percent for both fine and coarse aggregates. The recommended percentage replacement of the recycled clay and brick tile is within the range of 15 to 25 percent. This is similar to the study made by Tsoumani (2014) which states that the optimal percentage is 25%.

#### *Natural (Fine/Coarse) Aggregates*

Around 50 to 60 percent in the concrete mixture made up of natural aggregates. The natural aggregate can be classified as fine or coarse. A simulation of

natural aggregate type influence was carried out with a concrete mixture of 400 kg cement and w/c ratio of 0.5, and the content of natural aggregate is varied from 0 to 50% with decreasing crushed brick(fine & coarse) and natural aggregate content.

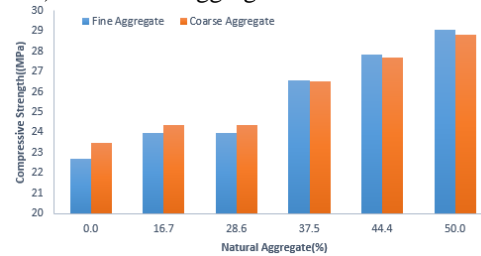


Fig. 9 Compressive Strength of RBAC with varying percentage of Natural Aggregate

The larger the aggregate percentage in concrete mix makes it to contribute a lot to its strength (Waziri et. al., 2011). Figure 9 shows the variation of the compressive strength with the natural aggregates. It can be noted that this is similar to Figure 8a for clay tile in which compressive strength increase as the percent of aggregates increases up to 50%. Also, the compressive strength of concrete with coarse aggregate is consistently higher than the concrete with fine aggregate for percentage up to 37.5% since aggregate size has a significant impact to the strength of concrete. The larger the size of the aggregates, the lesser will be the presence of voids in the concrete matrix which would increase the value of the compressive strength. This affirms the study made by Vilane(2016) that states the mean concrete compressive strength increased with increasing aggregates size.

Based on the result of the parametric study, the optimum amount for each material are as follows: cement = 400 kg, water cement ratio = 0.5, Recycled Tile (Fine) = 0%, Recycled Tile (Coarse) = 40%, Recycled Brick (Fine)=10%, Recycled Brick (Coarse) = 10%, NA (Fine) = 20%, NA (Coarse) = 20%. This is similar to the study made by Aliabdo et al. in 2014 in which they state that in order to avoid strength reduction, it is strongly recommended to limit the percentage of coarse aggregate replacement by recycled aggregate to 25% and 50% for concrete containing 350 and 250 kg/m<sup>3</sup>, respectively, of cement content.

## CONCLUSION

The compressive strength of RBAC can be predicted using ANN and MLR models with a regression value ranging from 0.53 to 0.86, and MSE values ranging between 0.008 to 0.02. The result of this study proved that Artificial Neural Network (ANN) models gave a more accurate prediction for the compressive strength of RBAC because of the

higher correlation value relative to the MLR in Excel. The ANN and MLR models developed in this study indicates an accurate prediction of compressive strength of RBAC. The best result for mathematical model belonged to BR\_9 model (Bayesian Regularization with nine (9) neurons) with a Regression(R) and Mean Squared Error (MSE) values of 0.86499 and 0.007996756, respectively. The best ANN for data training is BR\_7 model (Bayesian Regularization and 7 neurons). With this optimized network, Regression and Mean Squared Error (MSE) were 0.93918 and 0.0090454755, respectively.

The effect (weight factor) of each concrete components can be obtained from the generated ANN matrix function. From the MLR result, cement, and natural aggregates are the most significant contributor to the compressive strength of the RBAC. Meanwhile, the result of the parametric study revealed that in order to optimize the strength of concrete mixture with recycled brick/clay, it is recommended that the amount for each material are in the following ranges: cement=350 to 400 kg, water cement ratio=0.3 to 0.4, %recycled= 20 to 40 and %natural aggregates= 60 to 80 be adopted.

## REFERENCES

- [1] Ameri, M., Behnood, A., 2012. Laboratory studies to investigate the properties of CIR mixes containing steel slag as a substitute for virgin aggregates. *Constr. Build. Mater.* 26, 475e480. <https://doi.org/10.1016/j.conbuildmat.2011.06.047>.
- [2] Behnood, A., Ameri, M., 2012. Experimental investigation of stone matrix asphalt mixtures containing steel slag. *Sci. Iran.* 19 (5), 1214e1219. <https://doi.org/10.1016/j.scient.2012.07.007>.
- [3] Simion, Isabela Maria; Fortuna, Maria Emiliana; Bonoli, Alessandra; Gavrilescu, Maria (2013). Comparing environmental impacts of natural inert and recycled construction and demolition waste processing using LCA. *Journal of Environmental Engineering and Landscape Management*, 21(4), 273–287. doi:10.3846/16486897.2013.852558
- [4] Kalman Šipoš, Tanja; Miličević, Ivana; Siddique, Rafat (2017). Model for mix design of brick aggregate concrete based on neural network modelling. *Construction and Building Materials*, 148(), 757–769. doi:10.1016/j.conbuildmat.2017.05.111
- [5] Bingöl, A. F., Tortum, A., & Gül, R. (2013). Neural networks analysis of compressive strength of lightweight concrete after high temperatures. *Materials & Design* (1980-2015), 52, 258–264. doi:10.1016/j.matdes.2013.05.022.
- [6] Wassermann, R., Katz, A., and Bentur, A. (2009). Minimum cement content requirements: a must or a myth?. *Materials and Structures*, No. 42, 973–982.
- [7] Dhir, R. K., McCarthy, M. J., Zhou, S., and Tittle, P. A. J. (2004). Role of cement content in specifications for concrete durability: cement type influences. *Structures and Buildings*, No. 157, Institution of Civil Engineers, U.K., 113–127.
- [8] Schulze, J. (1999). Influence of water-cement ratio and cement content on the properties of polymer-modified mortars. *Cement and Concrete Research*, Vol. 29, 909–915.
- [9] Mindess, S., Young, J. F., and Darwin, D. (2003). *Concrete*. 2nd Ed., Prentice-Hall Inc., Englewood Cliffs, New Jersey.
- [10] Kosmatka, S., Kerkhoff, B., and Panarese, W.C. (2002). *Design and control of concrete mixtures*, 14th Ed., Portland Cement Association, Skokie, IL, USA.
- [11] Mehta, K. P., and Monteiro, P. J. M. (1993). *Concrete structure, properties, and materials*. 2nd Ed., Prentice Hall, New Jersey.
- [12] Punmia, Dr B. C.; Jain, Ashok Kumar; Jain, Arun Kr (2003-05-01). *Basic Civil Engineering*. Firewall Media. ISBN 9788170084037.
- [13] Adnan, Suraya Hani & Lee, Yee Loon & Abdul Rahman, Ismail & Mohd Saman, Hamidah & Wimala, Mia. (2007). Compressive strength of recycled aggregate concrete with various percentage of recycled aggregate.
- [14] Kosmatka, Steven H., , Kerkhof, Beatrix. (2011). *Design and control of concrete mixtures*. Portland Cement Association(PCA) USA.
- [15] Tsoumani, A. A., Matikas, T. E., Barkoula, N. M., (2014). Influence of recycled aggregates on compressive strength of concrete, *Proceedings of the 2nd International Conference on Sustainable Solid Waste Management*, Athens.
- [16] Waziri B. S.; Bukar, A. G and Gaji, Y. Z. (2011). Applicability of quarry sand as a fine aggregate. *Continental J. Engineering Science*.
- [17] Vilane, Bruce Roy. (2016). The Effect of Aggregate Size on the Compressive Strength of Concrete. *Journal of Agricultural Science and Engineering*. Vol. 2 (6). 66 - 69.

# RAW MATERIAL OPTIMIZATION WITH NEURAL NETWORK METHOD IN CONCRETE PRODUCTION ON PRECAST INDUSTRY

Ranti Hidayawanti<sup>1</sup>, Yusuf Latief<sup>2</sup>

<sup>1,2</sup>Faculty of Engineering, University of Indonesia, Indonesia

## ABSTRACT

The development of construction is presently experiencing rapid growth in Indonesia, leading to the requirement of the right materials for infrastructural enhancements, such as roads, bridges, high-rise residential buildings, and housing. From the existing infrastructure, concrete innovations such as precasts are needed with good quality materials, for the quick completion of constructions. This is because the need for good quality and smooth material helps to determine the success of a building project, with the use of technology through precast being a problem-solving process. Therefore, this study aims to analyze the patterns by which inventory procurement predictions produce precasts with good quality, using the readiness framework concept of the neural network through appropriate decision-making processes. It also focuses on innovating technological products used in the Indonesian precast industry. The Neural Network was used to produce the best target quality time and precast commodities. The result indicated two outputs from 2 neural network models, using five similar input-value variables. Based on the Adaline neural network, the outputs were observed as the highest sales-cost predictions for precast products, which often occurred in 1, 5, 6 and 9 months. Besides this, production activities were also normally operated at level (1), with profit optimization being highly considered before months 1, 5, 6 and 9. For the LVQ neural network, the result was a predictive classification of class intensity levels, where fast decision-making processes occurred in months 1, 6 and 9. Cost optimization was also carried out by ordering raw materials several months in advance, considering the trend in material prices and logistics.

*Keywords: Raw Material, Neural Network, Concrete, Precast.*

## INTRODUCTION

The Indonesian government has been undergoing massive infrastructural development since 2019, with an effect observed in the significant increase in precast products' demand in 2022. Based on these data, precast production was carried out by 76 registered factories, which were distributed throughout the country. Each factory had an increase in production, which varied between 210,000-500,000 tons yearly, to serve the increasing demand. This indicated that the average monthly production of each organization needs to reach 45,000 tons.

In Indonesia, efficiency is often measured from a cost and time perspective, showing that the use of precast concrete is more efficient than conventional methods [1]. Although this utilization is more efficient, technology-based precast supply chain parameters still need to become effective support. This supply chain is classified into various phases, namely planning, designing, manufacturing, transportation, installation, and construction. To achieve an integrated construction, the parties in these phases need to have efficient communication and effective collaboration in providing accurate and up-to-date information. According to the governmental data, the main problems in the precast supply chain phases began from the following, (1) poor planning, (2) ineffective communication between designers and manufacturers, (3) incompetent employees/workers,

(4) damage to raw materials, and (5) large sizes and heavy precast components and coordination in the bad project site. Besides these conditions, the key issues also contributed to negative consequences on the efficiency, productivity and effectiveness of precast delivery [2]. After procurement, the damages to raw materials are often found to affect the quality of the process and precast production during the inventory phase (initial stage). This explains that the procurement division needs to be able to provide the certainty of scheduling receipts for efficient project completion when ordering raw materials. Ordering of raw materials is carried out by considering the best price pattern for each item including cement, gravel and sand from several different vendors. Time Prediction of determining the peak sales pattern of precast products is carried out to find margins based on the difference in price patterns which will affect management's decision to choose the right vendor partner at the right time. Irrespective of these conditions, practical raw material orders and assembly time have still not been highly considered, leading to the probable effects and implications of excess inventory occurrences and additional project-financing increment, respectively. Therefore, a methodology should be determined for the effective, efficient, and economical control of precast plants' inventory management [3].

The utilization of technology has reportedly been implemented widely, to support the management of

raw materials during the inventory processes. This was in line with the raw material control for precast tunnelling projects in China [4], where many businesses were leveraging historical sales and demand data to implement intelligent inventory management systems. Demand forecasting involves predicting/ensuring the consumption/collection of precast raw materials. This plays an important role in the area of inventory control and supply chain, due to enabling production and distribution planning. It is also conditioned to reduce raw material delivery times and optimize decisions on the supply chain [5]. This is to help the developers and operators of inventory management systems in improving efficiency, maximizing productivity, and minimizing material losses [6].

Many studies have also evaluated smart inventory implementation, namely the dynamic brick-and-mortar supply chain analysis. This evaluated the benefits of implementing smart applications and systems to improve Vendor Managed Inventory (VMI) efficiency. In the supply chain mechanism, the manufacturer configured the production level and replenished the inventory at the retailer's store, where prices were set up to affect sales and inventory. In this condition, the company also shared the revenue and inventory costs through an agreement. This condition was very dynamic when inventory increased and decreased at production and sales levels respectively, with periodical variations observed according to several stochastic errors [7]. In this case, the need for accurate predictions led to a more effective and cheap supply chain, as well as allowed companies to provide quality, quantity, periodical, and low-production cost products [8]. Many studies also used other machine learning approaches to map prediction patterns, such as fuzzy subtractive clustering [9]. Therefore, this study aims to analyze the patterns by which inventory procurement predictions produce precast products with good quality, using the e-readiness framework concept of the neural network method through appropriate decision-making processes. In this condition, prediction modelling was prepared as part of the application of e-readiness in raw material management. The pattern of obtaining these materials was also used as the best test data, to assess the management model in smart inventory.

## LITERATURE REVIEW

### E-Readiness

Technology Readiness Index (TRI) 1.0 is constructed based on four-dimensional aspects, namely Optimism, Innovation, Discomfort, and Insecurity [10], as shown in Fig. 1. This is often applied to a company with the Strategic Alignment Maturity Model (SAMM), to determine the

utilization level of information systems in all business operations [11]. It is also one of the innovative references used in managing highly efficient logistics. In addition, TRI is related to the Global Competitiveness and Logistics Performance Indexes (GCI & LPI), as well as other similar supportive dimensions.

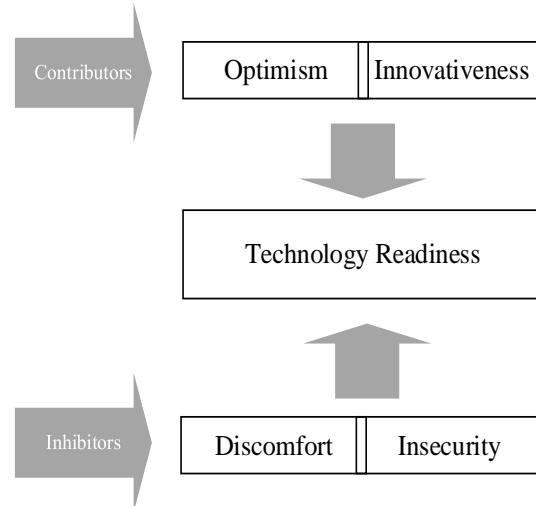


Fig. 1 E-Readiness Technology

In precast manufacturing companies, technology is also used in raw material management, by arranging and using a very suitable procedural schedule and method, respectively. Using linear programming methods, Markov models, and genetic algorithms, scheduling often emphasizes the management of time to handle and obtain raw materials [12]–[14]. In this condition, a good inventory receipt system is needed to provide more value during the prediction process, where efficient and periodical systematic performance is a function of operational activities. This helps to reduce time consumption in determining optimal operations in various parameters [15]. Additionally, process quality problems and production cost efficiency are adequately maintained [16]–[18].

### Neural Network Utilization

The amount of inventory is often related to the company's profit and the entire supply chain's survival. This indicates that prediction processes need to increase the company's ability to prevent risks, improve profits, and reduce losses during the acquisition of inventory, using the backpropagation neural network (BP) method [19]–[20]. Some reports were also observed based on the development of technology readiness, such as [21]–[22]. This emphasized determining the optimization value of material handling, using a neural network with 2 algorithm methods, namely ALN and LVQ (Adaptive Linear Neuron and Linear Vector Quantization). These methods led to the prediction of cost-benefit



into 3 categorical levels, namely high, medium, and low demand, as shown in Fig. 2.

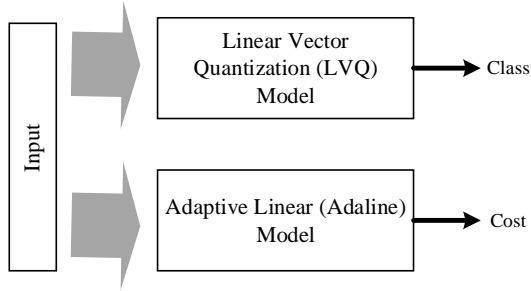


Fig. 2 Neural Network Model based on E Readiness

### Adaline

ADALINE (Adaptive Linear Neuron or later Adaptive Linear Element) is an early single-layer artificial neural network, which is implemented as an algorithm to predict outputs with an automatic controller. Although the accuracy obtained is not satisfactory, the value still changes and becomes highly precise during more data analyses [23]. In the following equation, an input vector ( $K$ ) is observed with the pattern.

$$X_k = [x_{0k}, x_{1k}, x_{2k}, \dots, x_{nk}]^T \quad (1)$$

Where  $X_k$  = the components of the weights and coefficients. Moreover, a weight vector ( $W_k$ ) is observed in the Eq. (2) as follows,

$$W_k = [wx_0, w_{1k}, w_{2k}, \dots, w_{nk}]^T \quad (2),$$

where  $y_K = W_K^T X_K$ .

$$\text{Output } y_k = \sum_{k=1}^n X_k W_k + \theta$$

Adaptive learning rule

Learning is also known as the Least Mean Square (LMS), whose rules in this process are observed as follows,

$$W \leftarrow W + \eta(d - o)x \quad (3)$$

### Linear Vector Quantization (LVQ) Model

This is one of the widely used ANN models (Artificial Neural Network), which emphasizes the prototype of a supervised learning classification algorithm and its network. These are trained through a competitive method similar to the Self-Organizing Map. The clustering technique is also used as a classifier to evaluate the deviations in the data sample through a random or specific density. This shows that performance remains the same with almost all combinations of training and testing [24]. Based on the following formula, learning is conducted by calculating the euclidian distance,

$$d(\vec{x}, \vec{w}_k) = \min d(\vec{x}, \vec{w}_k) \quad (4)$$

$W_k$  (weight improvement) is also used to determine the weight ( $w$ ) with the smallest distance value ( $d$ ) as follows,

$$w_k \leftarrow w_k + \eta.(x - w_k), \text{ when } c_m \neq y, \text{ it is close to each other or part of the set, respectively.}$$

### METHODOLOGY

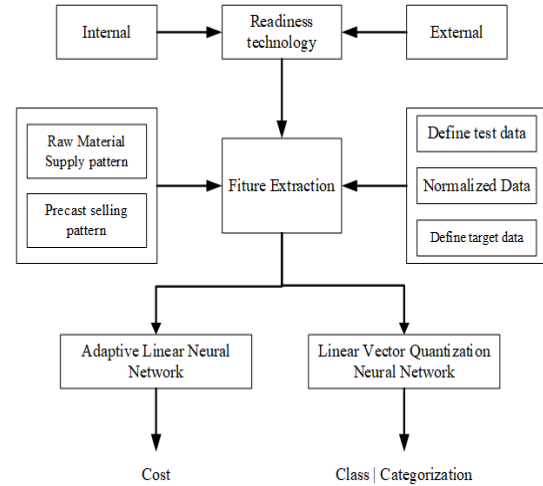


Fig. 3 Study Methodology

The e-readiness technology emphasized the following factors, (1) security, (2) technical issues, (3) software reliability, (4) digital operations for internet usage, and (5) technical skill utilization [25]. The concept of this technical influence also originated from internal and external organizations, as shown in Fig. 3.

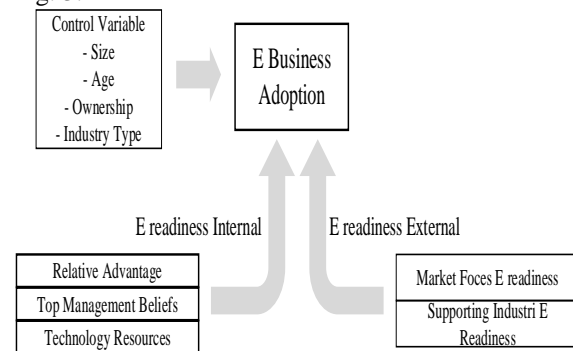


Fig. 4 The concept of e-readiness influence

Based on the external conditions, e-readiness emphasized many factors regarding the case perspective of each corporation in its respective business field. In this study, these factors were limited, including the IT technology infrastructure supporting the precast industry and the vendor market for raw materials. Meanwhile, the internal conditions of this technology focused on related technical

improvements, using neural network methods for prediction processes.

### Feature Extraction

The internal data sources were the direct measurement of the goods' receipts, regarding the yearly production of raw materials at precast organizations. In this condition, the raw material parameters included cement, sand, and gravel. In preparation for the precast products, a value extraction was also observed for the contributions of the materials and costs, as shown in Fig. 5. This showed that the cement and gravel costs and materials were the largest/lowest and smallest/highest contributions, respectively.

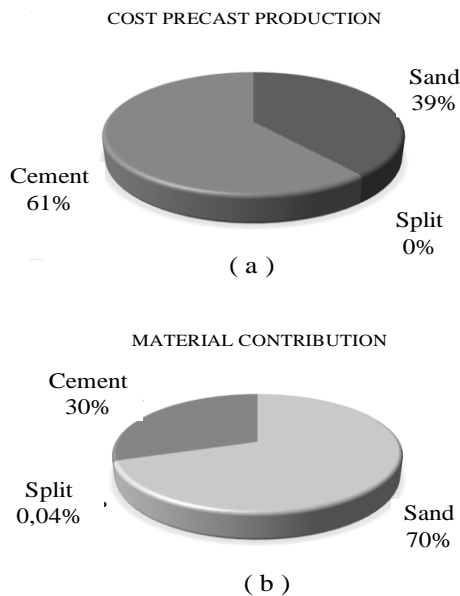


Fig. 5 Cost Contribution (a) production (m<sup>3</sup>) and material contribution (b) precast product

The second parameter focused on the monthly-supply behaviour pattern of each raw material for a year, as shown in Fig. 6.

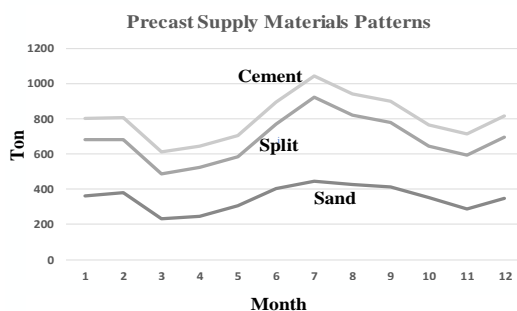


Fig. 6 Annual supply pattern of precast raw materials

### Data Test

This emphasized the data of sand, gravel and cement, which were mixed based on the best quality standard of Indonesian concrete category K 500-K 600. These data were obtained according to the order for 12 months, as shown in Table 1.

Table 1 Precast raw material cost

No	Materials	Cost IDR (m <sup>3</sup> )
1	Sand	242,000
2	Split	200,000
3	Cement	715,000

### Normalized data

The nominal unit of numeric data was normalized to facilitate data processing in the neural network architecture. This indicated that normalization was carried out by mapping into numbers between 0 and 1, as shown in the following formula,

$$X_{Map} = \frac{X_{Original} - X_{min}}{X_{max} - X_{min}} \quad (4)$$

Where :

$X_{map}$  = Normalization Value

$X_{Original}$  = Original Value

$X_{max}$  = Maksimum Value

$X_{Min}$  = Minimum Value

In 2021, the normalization of input variables were also carried out on the price of raw materials, frequency of intermediaries, and volume of transaction costs. Moreover, the target data originated from the average total sales of precast products in the same year.

### Target data

The target data contained three vectors, namely the minimum, maximum, and median sales values of the total cost, as shown in Fig. 7.

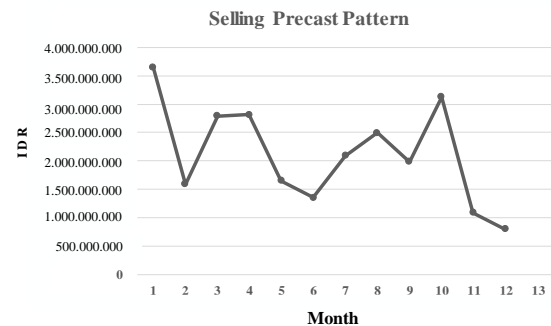


Fig.7 Total precast unit cost for the year.

Based on Fig 7, the optimization patterns of the raw material supply and sales profits were observed

when the production target need to achieve 45,000 tons monthly with a minimum unit cost of IDR800 million.

## DISCUSSION

Based on the external conditions, the system input parameters included the readiness of IT technology infrastructure, which supported the precast industry and market vendors providing raw materials. In this analysis, the final output was a value within a specified range. Meanwhile, the internal input factors included the monthly frequency of raw material supplies in a year (Tons). Table 2 shows the input and target variables of this analysis.

Table 2 Input Parameter Identification and Prediction

No	Input Parameter	Prediction Parameter	
		Adaline	LVQ
1.	IT Readiness Infrastructure		
2.	Level Market Vendor		
3.	Cement Contributions (monthly)	Monthly Precast Selling Patterns	Decision Classification Level
4.	Split Contributions (monthly)		
5.	Sand Contributions (monthly)		

## Architecture Neural Network Adaline

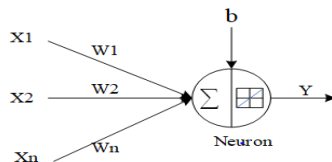


Fig. 8 Adaline Architecture

Based on Fig. 8, five defined input values were observed, indicating a linear activation function between 0 and 1.

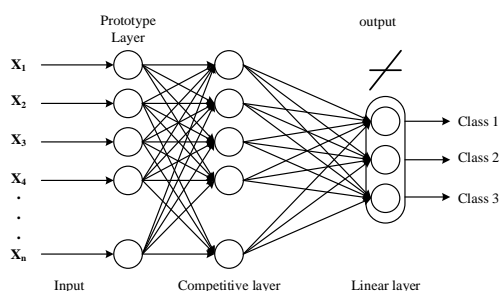


Fig. 9 Linear Vector Quantization Architecture

In Fig. 9, five defined input values were also observed, where a linear classification produced 3 cluster categories.

## Simulation Result

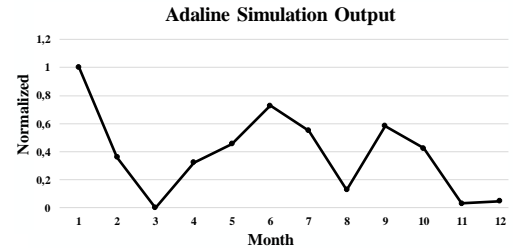


Fig. 10 Adaline Method simulation results

According to Fig. 10, the pattern of obtaining raw materials for precast products fluctuated based on the test data from 2020, through the Adaline method learning for a year. In this condition, the lowest orders were in the 3rd, 8th, 11th, and 12th months when 5 parameters were inputted into this method.

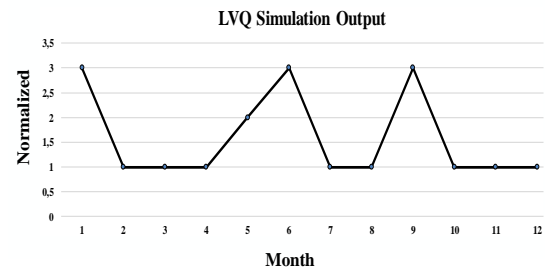


Fig. 11 LVQ Method Simulation Result

Based on Fig. 11, the pattern of obtaining raw materials for precast products also fluctuated regarding the test data from 2020, through the LVQ method learning for a year. This proved that the highest classes and the best values occurred in the 1st, 6th, and 9th months when 5 parameters were inputted into this method, with the lowest orders observed on the 2nd, 3rd, 4th, 7th, 8th, 10th, 11th, and 12th period. In the 5th month, the values obtained were also found not to be very high or low. These actions emphasized the option of maintaining existing raw materials or placing orders regarding the increment of the previous month.

Table 3. Class and Cost Relation

No.	Month	Classes	Cost (IDR)
1	Jan	3	3,644,810
2	Feb	1	1,829,060
3	Mar	1	804,661
4	Apr	1	1,724,870
5	May	2	2,097,578

6	Jun	3	2,872,875
7	Jul	1	2,370,019
8	Aug	1	1,170,018
9	Sep	3	2,464,231
10	Oct	1	2,010,972
11	Nov	1	895,467
12	Dec	1	942,555

According to Table 3, the second and third months had different advantages, although they were in class (1). This was in line with the eighth and eleventh months. The midpoint was also observed in class (2), which occurred in the 5th month. However, the 1st, 6th, and 9th months exhibited quite a large amount of transactions, leading to the significant effects on the order of raw materials and logistics financing considerations.

## CONCLUSIONS

Based on these results, cost optimization was conducted by accepting and creating new orders when the conditions were found in class (2). This action was often carried out by observing the trend of the previous month. Due to the high-order rate, the classes also showed that the level of operations need be accelerated and periodically limited when the conditions were categorized in class (3). For class (2), the order for raw materials was only performed by observing the Adaline method simulation, since a tendency was found for the market to absorb precast products in the following month. Furthermore, the application of the neural network method was appropriately implemented when supported by external e-readiness factors, including the which include infrastructure preparedness and many material vendor options. The implementation of this conceptual technology also used 2 neural network models for precast products. This involved the processing and production of similar input values and different decision model simulation, respectively. Irrespective of these differences, a strong correlation was still observed with the time efficiency of the decision-making process. Therefore, bother LVQ and Adaline contributed 50% to this decision approach.

## ACKNOWLEDGMENTS

The author is grateful to the Rector and LPPM IT PLN, for the experimental grant for Research Centre.

## REFERENCES

[1] D. H. Wisanggeni., Perbandingan Sistem Ditinjau Dari Segi Waktu dan Biaya Pada Proyek My Tower Apartement Surabaya, *Inst. Teknol.*

*Sepuluh Nop.*, 2017, pp 39 - 67

[2] M. Abedi, N. Rawai, M. S. Fathi, and A. K. Mirasa., Cloud Computing Information System Architecture for Precast Supply Chain Management Pelat Konvensional dan Precast Half Slab, *Appl. Mech. Mater.*, 2015, pp. 773–774.

[3] K. S. Im, S. H. Han, B. Koo, and D. Y. Jung., Formulation of a pull production system for optimal inventory control of temporary rebar assembly plants, *Can. J. Civ. Eng.*, vol. 36, no. 9, 2009, pp. 1444-1458.

[4] Z. Yu, Y. Wei, and Z. Cao., The Design and Application of Information Management System Based on IOT for Precast Concrete Segments, in *IOP Conference Series: Earth and Environmental Science*, vol. 371, no. 3, 2019, pp. 1-7.

[5] F. Z. Benhamida, O. Kaddouri, T. Ouhrouche, M. Benaichouche, D. Casado-Mansilla, and D. López-De-Ipiña., Demand forecasting tool for inventory control smart systems, *J. Commun. Softw. Syst.*, 2021, vol. 17, no. 2, pp. 185 - 196

[6] A. Alwadi, A. Gawanmeh, S. Parvin, and J. N. Al-Karaki., Smart solutions for RFID based inventory management systems: A survey, *Scalable Comput.*, vol. 18, no. 4, 2017, pp. 347 - 360.

[7] P. De Giovanni., Smart Supply Chains with vendor managed inventory, coordination, and environmental performance, *Eur. J. Oper. Res.*, vol. 292, no. 2, 2021, pp. 1-42.

[8] C. Ntakolia, C. Kokkotis, P. Karlsson, and S. Moustakidis., An explainable machine learning model for material backorder prediction in inventory management, *Sensors*, vol. 21, no. 23, 2021, pp. 1 - 12.

[9] I. Sangadji, Y. Arvio, and Indrianto., Dynamic Segmentation of Behavior Patterns Based On Quantity Value Movement Using Fuzzy Subtractive Clustering Method, *Journal of Physics: Conference Series*, 2018, vol. 974, no. 1, 2018, pp. 1-7.

[10] A. Parasuraman and C. L. Colby., An Updated and Streamlined Technology Readiness Index: TRI 2.0, *J. Serv. Res.*, vol. 18, no. 1, 2015, pp. 1-16.

[11] A. Wahyudin, R. Desmayanti, Munir, H. B. Santoso, and Z. A. Hasibuan., Business-information systems strategic alignment readiness maturity level: Corporate and business-technology driver perspective, *J. Eng. Sci. Technol.*, vol. 14, no. 3, 2019, pp. 1260 - 1270.

[12] C. F. Motta Toledo, L. De Oliveira, R. De Freitas Pereira, P. M. França, and R. Morabito., A genetic algorithm/mathematical programming approach to solve a two-level soft drink production problem, *Comput. Oper. Res.*, vol. 48, 2014, pp. 40-52.

[13] Z. Citra, B. Susetyo, and P. Wibowo., Optimasi Kinerja Proyek dengan Penerapan Metode

- Crashing dan Linear Programming pada Proyek Bulk Godown, *Rekayasa Sipil*, vol. 7, no. 2, 2019, pp. 106 - 113.
- [14] M. R. Bordón, J. M. Montagna, and G. Corsano., Mixed integer linear programming approaches for solving the raw material allocation, routing and scheduling problems in the forest industry, *Int. J. Ind. Eng. Comput.*, vol. 11, no. 4, 2020, pp. 525-548.
- [15] V. Subotić, M. Eibl, and C. Hochenauer., Artificial intelligence for time-efficient prediction and optimization of solid oxide fuel cell performances, *Energy Convers. Manag.*, vol. 230, 2021, pp. 1-14.
- [16] R. Hidayawanti, S. Legino, I. Sangadji, and R. P. A. Widodo., The efficiency of fly ash and cement slag to development building, *Int. J. GEOMATE*, vol. 16, Issue. 57, 2019, pp. 95-100.
- [17] R. Hidayawanti, Y. Latief, Y. Rahayu, F. I. Wachid, and R. P. A. Widodo., Utilization Of Ggbfs As Cement Substitute To Reduce Production Cost Of Construction Project, *Int. J. GEOMATE*, vol. 21, Issue. 86, 2021, pp 9-16.
- [18] R. Hidayawanti, D. D. Purnama, T. Iduwin, S. Legino, and F. I. Wachid., The impact aggregate quality material as a linear regression study on mixture concrete, *Int. J. GEOMATE*, vol. 18, Issue. 70, 2020, pp. 23-29.
- [19] L. Gu, Y. Han, C. Wang, G. Shu, J. Feng, and C. Wang., Inventory prediction based on backpropagation neural network,” *NeuroQuantology*, vol. 16, no. 6, 2018, pp. 664-673.
- [20] F. Bin Pan., Inventory prediction research based on the improved BP neural network algorithm, *Int. J. Grid Distrib. Comput.*, vol. 9, no. 9, 2016, pp. 307 - 316.
- [21] L. Gao and H. Dou., Inventory management of railway logistics park based on artificial neural network, *J. Eur. des Syst. Autom.*, vol. 53, no. 5, 2020, pp. 715 - 723.
- [22] M. Du, J. Luo, S. Wang, and S. Liu, Genetic algorithm combined with BP neural network in hospital drug inventory management system, *Neural Comput. Appl.*, vol. 32, no. 7, 2020, pp. 1-14.
- [23] P. C. Siswipraptini, R. N. Aziza, I. Sangadji, and I. Indrianto., The design of a smart home controller based on ADALINE, *Telkomnika (Telecommunication Comput. Electron. Control.*, vol. 18, no. 4, 2020, pp. 2177 - 2185.
- [24] S. Sahoo, S. Mishra, S. K. Mohapatra, and B. K. Mishra., Clustering deviation analysis on breast cancer using linear vector quantization technique, *Int. J. Control Theory Appl.*, vol. 9, no. 23, 2016, pp. 313 - 324.
- [25] M. O. M. Baeuo, N. Z. B. Nor Zairah, and A. A. M. Alaraibi., Technology factors influencing e-government readiness, *J. Theor. Appl. Inf. Technol.*, vol. 95, no. 8, 2017, pp. 1637 - 1645.

## EFFECT OF ADMIXED POLYPROPYLENE FIBERS ON CONCRETE PROPERTIES AND SHEAR STRENGTH OF REINFORCED CONCRETE BEAMS

Osama M. A. Daoud<sup>1</sup>, Reham Ibrahim Ahmed Ibrahim<sup>2</sup>  
<sup>1,2</sup> Department of Building and Roads Research Institute, University of Khartoum, Sudan<sup>2</sup>

### ABSTRACT

The main objective of this paper is to study the effects of adding various proportions of polypropylene fibers on the fresh and hardened properties of normal concrete. Also, the research aimed at investigating the effect of polypropylene fibers on shear strength of reinforced concrete beams. Compressive, flexural and split tensile strengths of concrete were investigated for grade 25 concrete for different ratios of polypropylene fiber/cement (0.0%, 0.25%, 0.35%, and 0.5% by weight). The mix without polypropylene fiber was considered as a control mix for comparison. Eight specimens of reinforced concrete beams (100mm×200mm in cross section and 1200mm in length) were investigated for ductility shear strength with and without polypropylene fibers. Regarding workability of concrete, results obtained have shown that the slump value was reduced with the increase of fiber content of the mix. The compressive strength of concrete had increased with about 50% for a fiber/cement content of 0.25% by weight, after that the increase in compressive strength had reduced to 20% compared to the control mix. For the mix with 0.5% of fiber/cement by weight the compressive strength slightly affected by addition of polypropylene fibers. For the split tensile strength, tests results have shown that tensile strength had increased gradually from 16% up to about 35% with the increase of fiber content. Similarly, the flexural strength had increased from 27% up to about 42%. Regarding the shear strength for the tested reinforced concrete beams, it was found that the polypropylene fiber didn't improve the shear strength. Slight reduction in the shear strength of the tested beams was noticed with the increase in fiber content more than 0.25%. Deflection of the tested beams had increased with the increase of fiber content for the same failure load which indicated that the fiber had improved the ductility of the beams. It was concluded that the polypropylene fiber clearly improved tensile and flexural strength of concrete, but the compressive strength slightly effected. Shear strength of the tested reinforced concrete beams didn't improved by the addition of polypropylene fiber but the ductility of the tested beams had increased according to the increase of deflection.

**Key words:** *Polypropylene fibers; Compressive strength; Tensile strength; Ductility; Shear strength.*

### INTRODUCTION

Concrete is a composite material containing hydraulic cement, water, coarse aggregate and fine aggregate. The resulting material is a stone like structure which is formed by the chemical reaction of the cement and water. This stone like material is a brittle material which is strong in compression but very weak in tension. This weakness in the concrete makes it crack under small loads, at the tensile end. These cracks gradually propagate to the compression end of the member and finally, the member breaks. The formation of cracks in the concrete may also occur due to the drying shrinkage. These cracks are basically micro cracks. These cracks increase in size and magnitude as the time elapses and the finally makes the concrete to fail. The formation of cracks is the main reason for the failure of the concrete. To increase the tensile

strength of concrete many attempts have been made. One of the successful and most commonly used methods is providing steel reinforcement. Steel bars, however, reinforce concrete against local tension

Only. Cracks in reinforced concrete members extend freely until encountering the bar. Thus, need for multidirectional and closely spaced steel reinforcement arises. That cannot be practically possible. Fiber reinforcement gives the solution for this problem so to increase the tensile strength of concrete a technique of introduction of fibers in concrete is being used. These fibers act as crack arrestors and prevent the propagation of the cracks. These fibers are uniformly distributed and randomly arranged. This concrete is named "fiber reinforced concrete [1].



## OBJECTIVES

The objective of this research is to study the effect of polypropylene plast fiber on mechanical properties of fresh (slump test) and hardened concrete (compressive, tensile, flexural strength) with variation of fiber content (0.25%, 0.35%, and 0.5%) as well as a control mix without fiber.

Another objective of the study is to explore the effect of fiber on the shear behavior and strength of reinforced concrete beam.

## PROBLEM STATEMENTS

Portland cement concrete is considered to be a relatively brittle material which is strong in compression but very weak in tension. This weakness in the concrete makes it crack under small loads so, use of fiber in concrete is to improve its properties and prevent the propagation of crack and enhance its compressive, tensile and flexural strength and Improves toughness and durability of concrete. The effect of fiber on the shear behavior and strength of concrete beams had not been covered in details in the literature.

## LITERATURE REVIEW

Mohamed R.A.S have presented results of experimental work on the effect of polypropylene fiber on compressive strength, flexural strength and split tensile strength. in the compressive strength increased upon 0.5% polypropylene fiber content in 1% polypropylene fiber content the compressive strength was reduced. in the flexural strength in 0.5 % the strength was reduced. In split tensile strength increased upon 0.5% of polypropylene fiber content, and in 1% the value of split tensile strength was reduced [2].

Thirumurgan and Siva Kumar used crimped polypropylene fibers for reinforcing high strength concrete, according to find the compressive strength index to this fiber reinforced concrete, their work reported that the workability of concrete decreased with the addition of polypropylene fibers, in their research they overcome this problem by addition of High Range Water Reducing Admixtures [3].

M.Marghani carried out an experimental study on the effects of adding polypropylene fiber on concrete properties. A mix of 0.0 fiber content had been set as control mix. polypropylene fiber were added to concrete in six different percentages of cement of weight as follows 0.25%, 0.5%, 0.75%, 1%, 1.25% and 1.5%. an experimental programme was carried out to investigate PP fiber

effects on fresh properties (workability) and hardened properties (Compressive, split tensile and flexural strength) the result of slump test indicated that workability of concrete is decreased with addition of polypropylene fibers. Reduction of 65% had been measured with the highest fiber content of 1.5% [4].

Anthony and Abimbola found from destructive compressive strength test results that it is observed that addition of polypropylene in low percentages, about 0.25%, increases the compressive strength by about 5% to 10%, while addition of 0.5% increases the compressive by about 3% to 5%. However, the compressive strength decreases by about 2% to 4% when 0.75% of polypropylene fibers are added and by 4 to 8% when 1% of polypropylene fibers are added. The results of the non-destructive tests follow the same pattern, a dosage of 0.25% increases the strength by 5 to 9%; dosage of 0.5% increased the strength from 3 to 5%. The strength decreases by about 2 to 4% when 0.75% of polypropylene fibers are added and by 4 to 8% when 1% of polypropylene fibers are added [5].

## MATERIALS

A Materials used

**Cement** The Portland Cement of 42 Grade was used in this study.

The initial and final setting times were 1:25 hr. and 4:33 hr. respectively, compressive strength 2 days and 28 days were 19.65 and 42.66 respectively.

**Fine Aggregate** uncrushed aggregate which obtained from Omdurman-Khartoum state Specific gravity 2.85, silt and clay content 0.98%, sieve analysis according to (B.S 882:1992)

**Coarse Aggregate** Crushed aggregate that was used has two size (10mm and 20 mm) were obtained from the local market (Torya mountain) specific gravity for 20mm and 10mm 2.88 and 2.85 respectively, sieve analysis according to (B.S 882:1992)

**Water** Ordinary portable water (tap water) was obtained from Khartoum area

**Fibre** Polypropylene Fibre was used. Density –bulk 900 kg/m<sup>3</sup>, Length 12mm, specific gravity 0.91, tensile strength 0.67Kn/mm<sup>2</sup>

## METHODOLOGY

The methodology adopted in this thesis to achieve the above objectives is divided into two parts; theoretical review and laboratory work.

### A. Theoretical review part:

1. Investigate topic area to define the thesis problem.
2. Study theoretical Background (Literature survey on basic requirements of PPFRC and properties of fresh and hardened PPFRC).

### B. Experimental work part:

1. Selection and preparation the suitable constituent materials.
2. Investigating the physical and mechanical properties of constituent materials (specific gravity, and sieve analysis for aggregates-initial, final setting time and compressive test for cement).
3. Developing a suitable mix design using local materials through conducting a series of trial mixes.
4. Slump flow test at fresh state of PPFRC concrete mixes to study the effect of increasing fiber content on workability.
5. Preparing, casting specimens, curing and testing after curing to get hardened state parameters; such as compressive, tensile, and flexural strengths, dynamic modulus of elasticity in addition shear behavior and strength of reinforced concrete beams
6. Analysis and discussion of experimental test's results. 15
7. Summary of all stages of research.

## RESULTS AND DISCUSSIONS

### Workability with addition of fibers (slump test):

The effect of fiber content on the slump of fresh concrete. It is clear from this Figure that the slump was decreased with the increase in fiber content. polypropylene fiber has hydrophilic property [6]. This property is attracting the moisture content. higher workability can be achieved with the addition of admixtures (super- plasticizer).

Table 1 The results of Slump test

Mix	Polypropylene fiber	Slump (mm)	Mix
G 25	0.0%	110	G 25
G25	0.25%	95	G25
G25	0.35%	75	G25

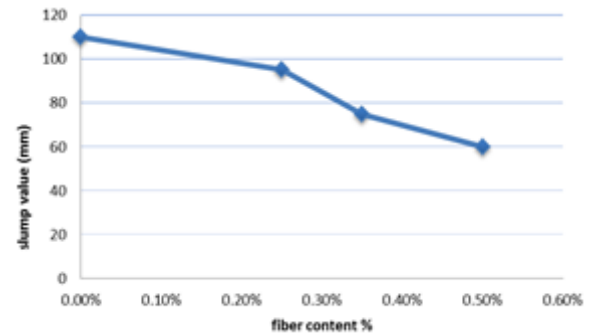


Fig. 1 Relation between Fiber content % and Slump in mm

### Compressive Strength

Compressive strength increases for all fiber reinforced mixes compared to the plain concrete. The optimum compressive strength was reached at a percentage of 0.25% polypropylene fiber. decreased the compressive strength due to the decrease of the cohesion of the concrete.

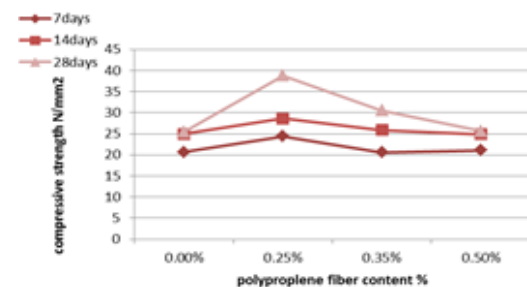


Fig. 2 Compressive strength Vs Fiber content

Table 2 Compressive strength results

Mix	7 days	14days	28 days
0.0%	21	25	26
0.25%	24	29	39
0.35%	21	26	31
0.5%	21	25	26

### Mode of failure for cubes:

Observation of the mode of failure of the cube in the control mix compared with the 0.25% fiber control mix.

In the control mix the standard shape of failure mode shown in Figure (3a) was easy to achieve. But for the 0.25% fiber content mix the shape of failure mode shown in Figure (3b), the standard shape of failure mode was not achieved.

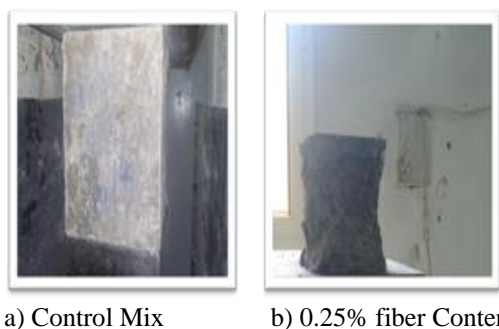


Fig. 3 Mode of Failure for Mixes

### Split tensile strength

The split tensile strength increased with the increase in polypropylene fiber content (tensile strength had increased gradually from 16% up to about 35%) and the mechanism of failure of concrete cylinders under split tensile strength was better in 0.25% and 0.35%, and 0.5% fiber content compared to the control mix.

Table 3 Split tensile strength results

Mix	Tensile strength 28 days (N/mm <sup>2</sup> )
0.0%	2.14
0.25%	2.48
0.35%	2.48
0.5%	2.84

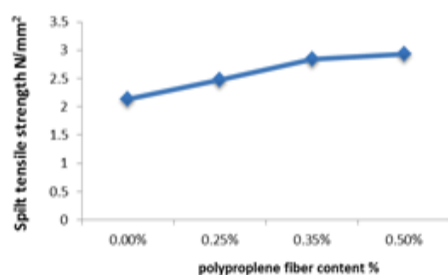


Fig. 4 Split tensile strength for different fiber content%

### Flexural strength

The flexural strength increases with the increase in polypropylene fiber content

Table 4 Flexural strength results

Mix	28 days
0.0%	7.41
0.25%	9.45
0.35%	9.78
0.5%	10.56

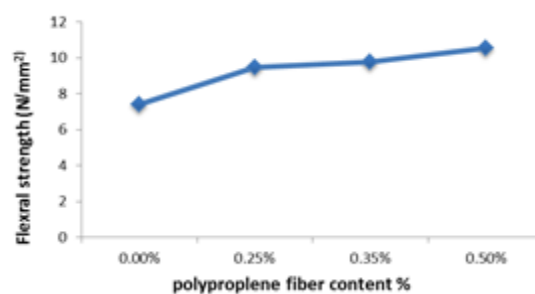


Fig. 5 Flexural strength for different fiber content%

### Modulus of elasticity

There is a slight variation in the results, but in overall, the addition of polypropylene fiber resulted in a decrease of the modulus of elasticity

Table 5 Modulus of elasticity results

Mix	Modulus of elasticity 28 days
0.0%	42.6
0.25%	40.8
0.35%	41.6
0.5%	39

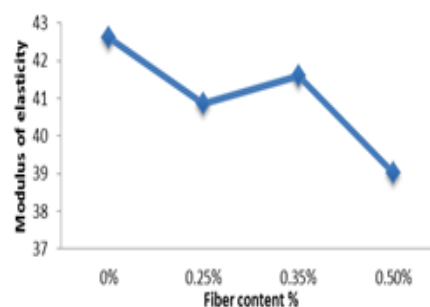


Fig. 6 Graph of modulus elasticity

### Shear strength for reinforced concrete beams

#### Failure load for shear strength

The shear strength for the tested reinforced beams, it was found that the polypropylene fiber didn't improve the shear strength. Slight reduction in the failure load of the tested beams

Table 6 Failure load for shear strength results

Mix	Failure load / 90 days(KN)
0.0%	90.73
0.25%	86
0.35%	69
0.5%	66

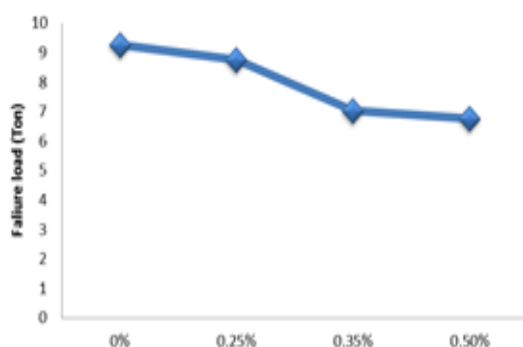


Fig. 7 Failure load for different fiber content

#### Mode of failure for reinforced beam concrete

The addition of polypropylene fibers does not change the crack pattern

Table 7 Type of failure for different fiber content%  
Failure load for shear strength results

Mix	Sample 1	Sample 2
0.0%	Shear tension	Shear tension
0.25%	Shear tension	Shear tension
0.35%	Shear tension	Shear tension
0.5%	Shear tension	Shear tension



Fig. 8 Shear behavior of beam 0.0% fiber content



Fig. 9 Shear behavior of beam 0.25% fiber content



Fig. 10 Shear behavior of beam 0.35% fiber content



Fig. 11 Shear behavior of beam 0.0% fiber Content

#### *Deflection of reinforced concrete beam for different fiber content*

Deflection of the tested beams had increased with the increase of fiber content for the same failure load which indicated that the fiber had improved the ductility of the beams. The maximum value for deflection at 0.35% polypropylene fiber content. But the reduction occurred in 0.5% polypropylene fiber content

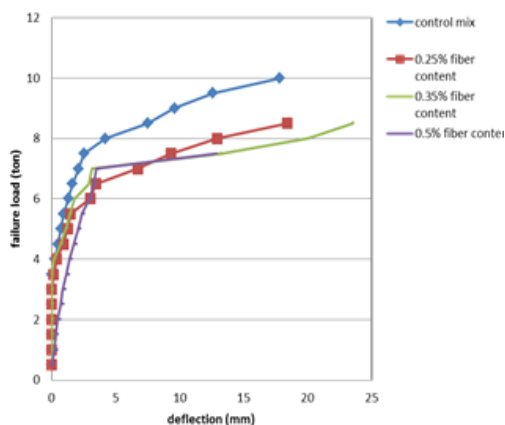


Fig. 12 load \_deflection diagram for mixes

## CONCLUSIONS

Based on the test results presented in this research in chapter four it can be concluded that,

- Polypropylene fibers reduced slump value. Workability of concrete decreases with the increase in polypropylene fiber.
- Proper feeding and mixing can virtually eliminate the problem of balling, the polypropylene fiber is added to the mixture to achieve a uniform distribution throughout the concrete, this helps to prevent balling.
- The polypropylene fibers are hydrophobic and therefore give poor bond characteristics with the cement matrix.
- Maximum compressive strength slightly increased with increasing the content of polypropylene fibers up to 0.5 vol. % in the tested concrete.
- PFRC shows improved tensile and flexural strength compared to conventionally reinforced( brittle concrete).
- Polypropylene fiber doesn't improve the concrete mix in the shear strength of reinforced concrete beams

## REFERENCES

- [1][http://www.grietinfo.in/projects/MAIN/CIVIL2013/cd-27-FRC PROJECT REPORT](http://www.grietinfo.in/projects/MAIN/CIVIL2013/cd-27-FRC%20PROJECT%20REPORT) (accessed 20-10-2014).
- [2] Mohamed R.A.S., "Effect of polypropylene fiber on the mechanical properties of Normal Concrete", Journal of Engineering sciences, Assiut university, Vol.43, No.4, pp.1049-1059, July 2006.
- [3] S. K. . Thirumurugan.S, "Compressive Strength Index of Crimped Polypropylene Fibers in High Strength Cementitious Matrix," World Appl. Sci. J., vol. 24, no. 6, pp. 698–702, 2013.
- [4] M.Marghni "Evaluation of fresh and hardened properties of polypropylene fiber reinforced concrete" thesis for MS.c of bulding technology in university of Khartoum , feb 2016
- [5] Anthony Nkem Ede and AbimbolaOluwabambi Ige, "Optimal Polypropylene Fiber Content for Improved Compressive and Flexural Strength of Concrete \n," IOSR J. Mech. Civ. Eng., vol. 11, no. 3, pp. 129–135, 2014.
- [6]<http://www.syntechfibres.com/polypropylene/properties-of-polypropylen-fibres/> (Accessed 21-9-2015).

## ADDITION OF SEWAGE SLUDGE ASH TO CONCRETE AS SUBSTITUTE FOR PORTLAND CEMENT

Jean-Frank Wagner

Geology Department, University of Trier, Germany

### ABSTRACT

Sewage sludge ash (SSA) is a waste product derived from the incineration of sewage sludge. Common management practices of sewage sludge ash are dumping into landfills and application on agricultural land. Based on the documented silica, alumina and iron contents of SSA, the present study investigates its pozzolanic potential by replacing cement with varying proportions of 2 different SSA in the production of mortar blocks. Rapid Hardening Cement (HRC) and Ordinary Portland Cement (OPC) respectively were replaced by 5, 10 and 15% by mass of SSA. The block units were cured for 7 and 28 days after which their compressive strength was determined. Results showed that SSA has a positive long-term effect on block shrinkage for both HRC and OPC. The block units cured for 28 days exhibit similar compressive strengths for HRC without SSA and with 5-15% of HRC substitution. Substitution of OPC by SSA showed a decrease in compressive strength of 20% for 5% and 40-60% for 15% OPC replacement.

*Keywords* Sewage sludge ash, Rapid Hardening Cement, Ordinary Portland Cement, Compressive strength

### INTRODUCTION

Sewage sludge incineration becomes more and more important. Sewage sludge ash (SSA) is the end product of incineration and there are large quantities which require disposal. However, as SSA has high concentrations of silica, alumina and iron, it can be used as pozzolan to replace cement in the production of cement-based blocks [1], [2]. The potential for SSA to be used as a pozzolan has become an important area of research in the last years because it may provide an adequate route for SSA recycling. The pozzolanicity of SSA has been shown by a number of authors [3], [4], [5]. In addition, replacing Portland cement by SSA will also reduce CO<sub>2</sub> emissions which are generated by the cement industry in huge quantities. One of the ways by which the pozzolanic potential of SSA is determined is by substituting different proportions of cement with SSA to make concrete or mortar blocks and testing these blocks for their mechanical performance. In some studies, it was observed that the compressive strength of SSA blended blocks were generally lower than the strength of the control and the compressive strength decreased with an increase in the amount of SSA [1], [6], [7], [8]. Pérez-Carrióna, et al. [9] reported a 25% increase and a 5% decrease of compressive strength for 10 and 20% SSA substitution respectively when compared to the control block. Tay & Show [10] reported similar results showing a 10% SSA concrete block to have the same compressive strength as the reference. Subsequent increase in SSA content by 20, 30 and 40% led to a successive decrease in

compressive strength. Only a few authors reported a slight increase of mortar strength by adding SSA [11], [12]. Pinarli & Kaymal [13] and Ing et al. [14] have shown a positive long-term effect, whereby the compressive strength of mortar at lower curing ages of 3, 7 and 14 days were lower than the reference mortar while at 28 days of curing the compressive strength was higher than the control strength. This suggests that a longer period of curing is required for the pozzolanic reaction to effectively take place.

The main objective of this study was to determine the compressive strengths of cement-based concrete blocks with different cements (Rapid Hardening Cement (HRC) and Ordinary Portland Cement (OPC)) and blended with different SSA. Testing with Rapid Hardening Cement (HRC) had been previously published by Wagner & Tabe Array Egbe [15].

### MATERIALS AND METHODS

#### Sewage sludge ashes

The SSA was collected from 2 wastewater treatment plants in Germany.

**SSAI:** Sludge is first drained by a screw press, conditioned with flocculation aids and dried to a dry matter content of over 85%. The dried sewage sludge is then fed continuously to a PYREG® double reactor and incompletely combusted at 650°C. By this processing Phosphorus in the sludge is normally concentrated to 10-20%.

The main chemical elements in the ash are SiO<sub>2</sub> (28.1%), Al<sub>2</sub>O<sub>3</sub> (8.7%), Fe<sub>2</sub>O<sub>3</sub> (25.3%) and P<sub>2</sub>O<sub>5</sub>



(18.2%).

**SSA2:** Here, too, a PYREG system is used to process the sewage sludge. After dewatering, the sludge runs through the PYREG® reactor, where it is mineralized at around 700 - 720 °C in the absence of oxygen.

The main chemical elements are SiO<sub>2</sub> (38.6%), Al<sub>2</sub>O<sub>3</sub> (15.3%), Fe<sub>2</sub>O<sub>3</sub> (12.7%) and P<sub>2</sub>O<sub>5</sub> (18.1%).

## Cements

The first cement used in the investigation is **Rapid Hardening Portland Cement (HRC)** bearing the trade name “Knaufschnellzement” produced by Knauf Bauprodukte GmbH & Co.KG. It is made from dry cement mortar, quarry sand and contains limestone powder as additive.

The second cement is “CEM I 42.5 R CE PM-CP2 NF” and comes from the company Cimalux. This is pure **Ordinary Portland Cement (OPC)** made from 100% Portland cement clinker without any secondary components.

## Cement-based block production process

The materials which were used in the production of the cement-based blocks were cement, SSA and water. SSA was dried at 105°C for 24 h.

Four sample categories of mortar blocks were produced. The reference sample contained no SSA (0%). In the other samples, 5, 10 and 15% by mass of cement was replaced successively by SSA. The amount of water used was kept constant for all samples with RHC and the water to cement ratio was 0.25. For the samples with OPC the water to cement ratio had to be increased to 0.35.

The mortar blocks were cured for 7 and 28 days at ambient temperature (20°C). Additionally, for OPC and both SSA further test series were cured at 40°C.

## Compressive strength testing

Compressive strength testing was conducted using a FHF Strassentest machine manufactured in accordance with DIN 51223. The machine is a point load machine, a 98 x 98 mm metal plate of weighing 1.4 kg was adapted to it to ensure uniform distribution of the pressure applied by the testing machine. The blocks (73x39x39 mm) were placed vertically upwards, and load was applied to the blocks by the equipment. The load was left to increase to block failure. The maximum load at which the blocks failed was recorded by the equipment.

## RESULTS AND DISCUSSION

### Block shrinkage

As shown by the results in Fig. 1 the reduction in

block lengths depends on the time of curing and most importantly on the concentration of SSA1 and RHC in the blocks. The blocks generally showed a lower shrinkage with an increase in SSA content; therefore, SSA significantly reduces the rate of block shrinkage.

The same pattern was consistent for mortar blocks with OPC and both SSA. Even a slight increase in volume was observed after 28 days of curing at 40°C.

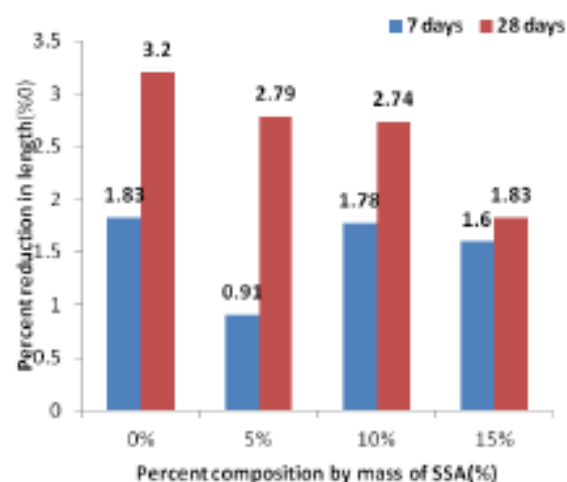


Fig. 1 Percent of shrinkage of the cement-based blocks at different % of SSA 1 substituting RHC and measured after 7 and 28 days of curing.

## Compressive strength

For RHC the control block exhibited a compressive strength of 27.06 MPa after 7 days of curing, while the block with the highest content by weight of SSA1 (15% SSA) showed the lowest compressive strength of 26.83 MPa. There was a very slight decrease in compressive strength of the blocks with an increase in SSA content (Fig. 2).

After 28 days of curing, the control block of RHC exhibited a compressive strength of 27.11 MPa. The compressive strength exhibited by the block with 5% ash was a little bit lower than the strength of the control block (0.67 %) but for the blocks containing 10% and 15% SSA1 the strength increased by 0.18% and 0.37% respectively.

The trend of decrease in strength with increase in SSA content exhibited by blocks cured for 7 days correlates with most of the studies found in literature [1], [6], [7], [8], [13].

The trend of a slight increase in compressive strength with an increase in the quantity of SSA amount in the blocks as exhibited by the blocks cured for 28 days in the present study is rarely observed in literature. However, this result correlates with studies by Monzó et al. [12] and Nazierah et al. [16].

All in all, the change in compressive strength is very low, so that it can be concluded that a substitution of RHC with SSA1 (up to 15%) has at

least no negative effect on the compressive strength.

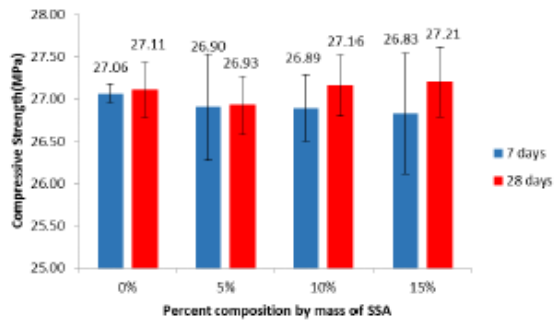


Fig. 2 Compressive strengths of blocks containing rapid hardening cement RHC and varying concentrations of sewage sludge ash SSA1 cured for 7 and 28 days.

For testing with OPC the compression strength of the reference mortar blocks (without SSA) was 20.5 and 31 MPa respectively after 7 and 28 days of curing. To better compare the strength decrease with the addition of SSA, these values are shown as 100% in Fig. 3 and 4.

With both sewage sludge ashes, a reduction in strength can be observed when replacing OPC by SSA, except for SSA1 with 5 and 10% substitution at 40°C and a curing time of 7 days. There is even a slight increase. After 28 days, however, a significant decrease is recorded in all samples.

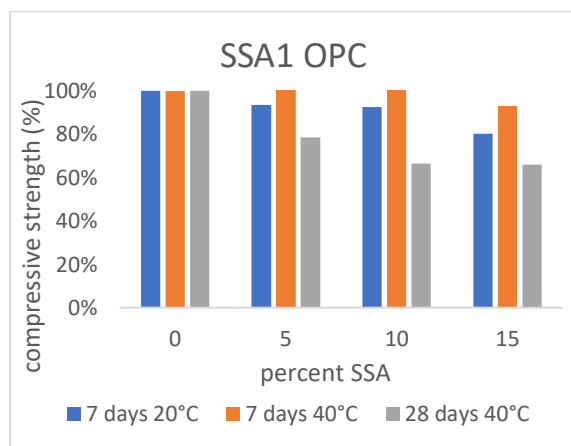


Fig. 3 Compressive strengths of blocks containing Ordinary Portland cement OPC and varying concentrations of sewage sludge ash SSA1 cured for 7 and 28 days.

If you look at the increase in curing temperature from 20° to 40°C, the positive effect (small decrease or even increase in strength) is more pronounced with SSA1 than with SSA2. The final strength after 28 days is similar for both ashes with 5% substitution (20% decrease in strength) and with 10% (37.5% decrease). For SSA1 with 15% replacement there is

only a slight further decrease, for SSA2 the strength is reduced significantly by 57%.

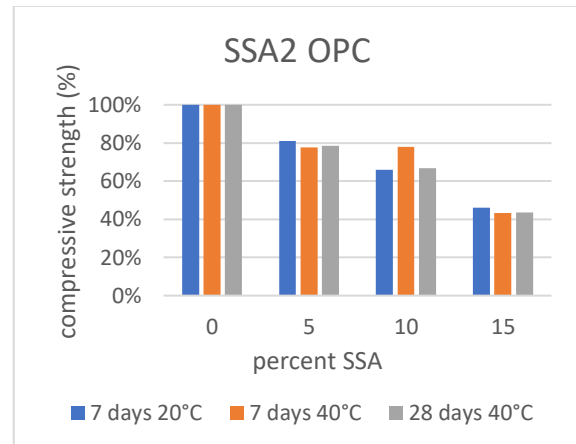


Fig. 4 Compressive strengths of blocks containing Ordinary Portland cement OPC and varying concentrations of sewage sludge ash SSA1 cured for 7 and 28 days.

## CONCLUSIONS

Mortar block shrinkage was found to correlate positively with the amount of SSA. A 15% substitution of rapid hardening cement as well as Portland cement by SSA significantly reduces the rate of block shrinkage.

The blocks containing SSA1 and substituting rapid hardening cement RHC exhibit similar compressive strengths after 28 days curing as the reference without SSA.

However, substitution of OPC by SSA showed a decrease in compressive strength of 20% for 5% substitution and 40-60% for 15% OPC replacement.

## REFERENCES

- [1] Halliday, J. E., Dyer, T. D., Jones, M. R., and Dhir, R. K., Potential use of UK sewage sludge ash in cement-based concrete. *Waste and resource management*, Vol. 165, 2012, pp. 57-66.
- [2] Donatello, S., and Cheeseman, C. R., Recycling and recovery routes for incinerated sewage sludge ash (ISSA): A review. *Waste Management*, Vol. 33, 2013, pp. 2328-2340.
- [3] Lin, K., Chiang, K., and Lin, C., Hydration characteristics of waste sludge ash that is reused in eco-cement clinkers. *Cement and Concrete Research*, Vol. 35, No. 6, 2005, pp. 1074-1081.
- [4] Lin, K.-L., Lin, D., and Luo, H., Influence of phosphate of the waste sludge on the hydration characteristics of eco-cement. *Journal of Hazardous Materials*, Vol. 168, Issue 2-3, 2009,

- pp. 1105–1110.
- [5] Tantawy, M. A., El-Roudi, A., Abdalla, E. M., and Abdelzaher, M. A., Evaluation of the Pozzolanic Activity of Sewage Sludge Ash. *ISRN Chemical Engineering*, 2012, pp. 1-3.
  - [6] Cyr, M., Coutand, M., and Clastres, P., Technological and environmental behavior of sewage sludge ash (SSA) in cement-based materials. *Cement and Concrete Research*, Vol. 37, 2007, pp. 1278–1289.
  - [7] Lisk, D. J., Compressive Strength of Cement Containing Ash from Municipal Refuse or Sewage Sludge Incinerators. *Bulletin of environmental contamination and toxicology*, Vol. 42, No. 4, 1989, pp. 540-543.
  - [8] Piasta, W., and Lukawska, M., The Effect of Sewage Sludge Ash on Properties of Cement Composites. *Procedia Engineering*, Vol. 161, 2016, pp. 1018-1024.
  - [9] Pérez-Carrióna, M., Baeza-Brotons, F., Payáb, J., Savala, J., Zornoza, E., and Borrachero, M., Potential use of sewage sludge ash (SSA) as a cement replacement in precast concrete blocks. *Materiales de Construcción*, Vol. 64, 2014, pp. 1-3.
  - [10] Tay, J.-H., and Show, K.-Y., Utilization of municipal wastewater sludge as building and construction materials. *Resources, Conservation and Recycling*, Vol. 6, 1992, pp. 191-204.
  - [11] Fontes, C., Barbosa, M., Filho, R. T., and Gonçalves, J., Potentiality of sewage sludge ash as mineral additive in cement mortar and high-performance concrete. *International RILEM conference on the use of recycled materials in buildings and structures*, Conference proceedings, 2004, pp. 797-806.
  - [12] Monzó, J., Paya, J., Borrachero, M., and Córcoles, A., Use of sewage sludge ash (SSA) cement admixtures in mortars. *Cement and Concrete Research*, Vol. 26, No. 9, 1996, pp. 1389-1398.
  - [13] Pinarli, V., and Kaymal, G., An innovative sludge disposal option-reuse of sludge ash by incorporation in construction materials. *Environmental Technology*, Vol. 15, No. 9, 1994, pp. 843-852.
  - [14] Ing, D. S., Chin, S. C., Guan, T. K., and Suil, A., The Use of Sewage Sludge Ash (SSA) as Partial Replacement of Cement in Concrete. *ARNP Journal of Engineering and Applied Sciences*, Vol. 11, No. 6, 2016, pp. 3371-3375.
  - [15] Wagner, J.-F. and Tabe Arrey Egbe, T., Sewage sludge ash as cement replacement in concrete blocks. *Proceedings SUM2018, Fourth Symposium on Urban Mining*, 2018, 6 p.
  - [16] Nazierah, M. Y., Kartini, R., Hamidah, M. S., and Nuraini, T., Compressive Strength and Water Absorption of Sewage Sludge Ash (SSA) Mortar. *CIEC*, 2015, pp.199-207.

# STUDY OF THE HEAT EQUATION AND THE EFFECT OF TEMPERATURE INSIDE AN ELECTRIC CABLE CONSISTING OF ALUMINUM AND COPPER METALS

\* Dalal Adnan Maturi <sup>1</sup>

<sup>1</sup>Departement of Mathematics, Faculty of Science, King Abdulaziz University, P.O.Box 42664, Jeddah 21551,  
Saudi Arabia

## ABSTRACT

In this paper, we study the mathematical physics model; partial discharge (PD) mapping and power cable fault location are approaches based on the principle of time domain reflection (TDR) measurement, influenced by the power cable's height Frequency wave propagation properties. Furthermore, power cables. They're increasingly being used to transmit electrical energy and communication signals simultaneously. Smart grids are an example of such technology. Power cables are exposed to a variety of temperatures when in use. Changes in the load current flowing through the cable cause differences. As a result, it is essential to Recognize how temperature affects the high-frequency characteristics of power wires. Temperature changes advance Errors in TDR measurements, according to simulations, and result in numerical solutions undertaken in this study. It's also shown that when the cable's temperature rises from 25°C to 60°C, the attenuation increases by 1° and the propagation velocity rises by 1°. a 4-percentage-point average The phase constant, on the other hand, drops by order of magnitude on average. The findings imply that temperature effects must be considered while making decisions. Communication channels in power cables are designed.

*Keywords: Heat Equation, Electric Cable, Aluminum, Copper, MATLAB.*

## INTRODUCTION

In the eighteenth century, the idea of electrical conductivity was developed, as were the first investigations on its temperature dependence. Although the German physicist Paul Karl Ludwig Drude (1863-1906) made the first serious theoretical advances on electrical conductivity of metals, The discovery of electricity as an imponderable elastic fluid transferable from one body to another by British scientist Stephen Gray (1666-1736) around one hundred and eighty years before, sweeping away the old idea of an electrical effluvia inseparably attached to a body in which they were excited [1-4]. Gray, a dyer by trade and an amateur naturalist by inclination, carried out a series of experiments using a hemp thread in 1720, inspired by the accounts of his physicist and compatriot Francis Hawksbee (1666-1713) [5,6], and after some related experiences as an assistant to the also British natural philosopher Jean Theophilus Desaguliers (1683-1744), Gray, a dyer by trade and an amateur naturalist by inclination, carried out a series. The early Gray's theories on electrical communication were practically ignored at first, but nine years later they returned to the fore and gained public domain with a fresh publication in 1731 [7,8]. No significant progress was made on this subject until 1734, when Charles Fran ciste Cisternay du Fay (1698-1739), a French scientist and Superintendent of the Jardins du Roi, proposed the existence of two types of electric fluid, vitreous and resinous, which

could be separated by friction and neutralized each other when combined [9]. The "two fluid" theory of electricity proposed by du Fay, which was based on experiments with the attraction and repulsion of different electrified substances, was later contrasted with the "one-fluid" theory proposed by American scientist Benjamin Franklin (1706-1790), which assumed only one fluid was present, either positively or negatively charged [10]. The basis for the behavior of the new property was established with the classification of substances as conductors or insulators and the establishment of the electrical flow direction from positive to negative.

## RATING FOR DYNAMIC CABLES

Due to the fluctuation of the conductor temperature during the useful life of the cable according to the inputs of the thermal models, the application of the steady-state current rating of cables may be cautious in some circumstances. As a result, throughout time, the assessment of a line's thermal stress has shifted from a steady-state thermal rating to a more general Dynamic Line Rating (DLR) or Dynamic Thermal Rating (DTR), which may better characterize thermal transients and their implications. The DLR is used to determine the line's actual current rating based on continuous measurements or the solution of the cable's thermal model. Assumptions on input variables that are conservative, such as those used in the steady-state model.

## THERMAL ANALYSIS OF POWER CABLES USING HEAT TRANSFER CONCEPTS

The current traveling through a power cable generates heat, which is released into the environment through the cable's metallic layers and insulation. In the presence of a temperature gradient, heat is an energy form that is transmitted from one system to another. Conduction, convection, and radiation are the three heat transfer mechanisms involved in this process. If the cable is buried, exposed to the air, or submerged in water, the conduction phenomena happens through the cable's metallic layers and insulation. From the cable surface to the outside world, convection and radiation occur. Convection is classified as natural convection or forced convection depending on the nature of the heat movement. Natural convection occurs when the flow is produced by buoyant forces caused by density differences in the air caused by temperature gradients. Forced convection is caused by external factors such as a pump, a fan, or the wind. In comparison to cables buried underground, heat transmission processes for cables deployed in open air or water are more complex due to interactions with the ambient environment. Electromagnetic waves, or photons, are referred to as radiation. Radiation does not require a medium and is greatly influenced by temperature [8]. Only for electrical cables located in air, heat is transported from the cable surface to its surroundings by convection and radiation. If the power wire in the air is exposed to solar radiation, it is considered an extra energy source [9].

## TEMPERATURE WITHIN AN ELECTRICAL CABLE

The temperature achieved within an electrical cable as a function of current and other parameters is required in the design of cable systems. Let us solve the nonhomogeneous heat equation in cylindrical coordinates with a radiation boundary condition to do this. The heat equation is derived from the law of conservation of energy

$$\text{Heat generated} = \text{heat dissipated} + \text{heat stored}$$

$$I^2 R N dt = -k \left[ 2\pi r \frac{\partial u}{\partial r} \Big|_r - 2\pi(r + \Delta r) \frac{\partial u}{\partial r} \Big|_{r+\Delta r} \right] dt + 2\pi r \Delta r c \rho du, \quad (1)$$

where  $I$  is the current through each wire,  $R$  is the resistance of each conductor,  $N$  is the number of conductors in the shell between radii  $r$  and  $r + \Delta r = 2\pi m \Delta r / (\pi b^2)$ ,  $b$  is the cable radius,  $m$  is the total number of conductors in the cable,  $\kappa$  is the thermal conductivity,  $c$  is the average specific heat, and  $u$  is the temperature. Equation (1) becomes in the limit of  $\Delta r \rightarrow 0$

$$\frac{\partial u}{\partial t} = A + \frac{a^2}{r} \frac{\partial}{\partial r} \left( r \frac{\partial u}{\partial r} \right), \quad 0 \leq r < b, \quad 0 < t \quad (2)$$

where  $A = I^2 R m / (\pi b^2 c \rho)$ ,

The nonhomogeneous heat equation for an infinitely long, axisymmetric cylinder is 8.3.139. We know that we must write the temperature as the sum of a steady-state and transient solution because of  $u(r, t) = w(r) + v(r, t)$ .

$$\frac{1}{r} \frac{d}{dr} \left( r \frac{dw}{dr} \right) = -\frac{A}{a^2} \quad (3)$$

or

$$w(r) = T_c - \frac{Ar^2}{4a^2}, \quad (4)$$

The steady-state solution  $w(r)$  meets the requirements.  $T_c$  is the (as-yet-unknown) temperature in the cable's center  $v(r, t)$  is a transient solution governed by

$$\frac{\partial v}{\partial t} = a^2 \frac{1}{r} \frac{\partial}{\partial r} \left( r \frac{\partial v}{\partial r} \right), \quad 0 \leq r < b, \quad 0 < t, \quad (5)$$

$u(r, 0) = T_c - Ar^2/(4a^2) + v(0, t) = 0$  is the initial condition.  $r = b$  at the surface

The boundary condition is  $u_r = -hu$ , where  $h$  is the surface conductance, because heat radiates to free space. Because after all transient effects pass away, the temperature equals the steady-state solution,  $w(r)$  must fulfill this radiation boundary condition independent of the temporary solution. This necessitates that

$$T_c = \frac{A}{a^2} \left( \frac{b^2}{4} + \frac{b}{2h} \right) \quad (6)$$

As a result, at  $r = b$ ,  $v(r, t)$  must satisfy

$$v_r(b, t) = -h v(b, t)$$

By separating the variables  $v(r, t) = R(r)T(t)$ , we can get the transient solution  $v(r, t)$  Using Equation (5) as a starting point

$$\frac{1}{rR} \frac{d}{dr} \left( r \frac{dR}{dr} \right) = \frac{1}{a^2 T} \frac{dT}{dt} = -k^2, \quad (7)$$

or

$$\frac{d}{dr} \left( r \frac{dR}{dr} \right) + k^2 r R = 0, \quad (8)$$

$$\frac{dT}{dt} + k^2 a^2 T = 0, \quad (9)$$

with  $R'(b) = -hR(b)$ .  $J_0(kr)$  where  $J_0$  is the zero-order Bessel function of the first kind, is the only solution to Equation (8) that stays finite at  $r = 0$  and satisfies the boundary condition. The transcendental equation I is obtained by substituting  $J_0(kr)$  into the boundary condition

$$kbJ_1(kb) - h b J_0(kb) = 0 \quad (10)$$

Equation (10) gives an infinite number of unique zeros  $k_n$  for a given value of  $h$  and  $b$ .

The problem's associated temporal solution

$$T_n(t) = A_n \exp(-a^2 k_n^2 t), \quad (11)$$

as a result, the total number of product solutions

$$v(r, t) = \sum_{n=1}^{\infty} A_n J_0(k_n r) \exp(-a^2 k_n^2 t). \quad (12)$$

The final challenge is to calculate  $A_n$ . Equation (12) is evaluated at  $t = 0$

$$v(r, 0) = \frac{Ar^2}{4a^2} - T_c = \sum_{n=1}^{\infty} A_n J_0(k_n r), \quad (13)$$

In  $J_0$ , there is a Fourier-Bessel series ( $k_n r$ ). We demonstrated how to compute the coefficient of a Fourier-Bessel series expanded in  $J_0(k_n r)$  with a boundary condition of the type we've arrived to the following conclusion

$$A_n = \frac{2k_n^2}{(k_n^2 b^2 + h^2) J_0^2(k_n b)} \int_0^b r \left( \frac{Ar^2}{4a^2} - T_c \right) J_0(k_n r) dr \quad (14)$$

Performing the integrations that have been specified

$$A_n = \frac{2}{(k_n^2 b^2 + h^2) J_0^2(k_n b)} \left[ \left( \frac{Ak_n b}{4a^2} - \frac{A}{k_n b a^2} - \frac{T_c k_n}{b} \right) J_1(k_n b) + \frac{A}{2a^2} J_0(k_n b) \right] \quad (15)$$

consider the following values:

$b = 4 \text{ cm}$ ,  $hb = 1$ ,  $a^2 = 1.14 \text{ cm}^2/\text{s}$ ,  $A = 2.2747 \text{ C/s}$ , and  $T_c = 23.94 \text{ C}$ . A represents 37 wires of #6 AWG copper wire in a cable providing a 22 amp current.

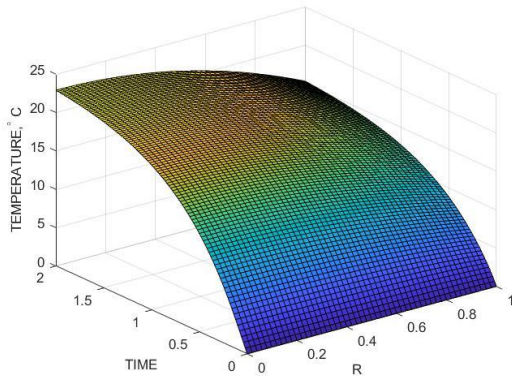


Fig. 1 At various points  $r/b$  and times  $a^2 t/b^2$  the temperature field (in degrees Celsius) within an electric copper cable with 37 wires and a current of 22 amperes. The temperature was initially set to zero, and then the cable was allowed to cool naturally as it was heated  $hb = 1$  is the value of the parameter, and the value of the parameter is the value of the parameter. The cable's radius is  $b = 4 \text{ cm}$ .

consider the following values:

$b = 4 \text{ cm}$ ,  $hb = 1$ ,  $a^2 = 0.86 \text{ cm}^2/\text{s}$ ,  $A =$

$2.2747 \text{ C/s}$ , and  $T_c = 23.94 \text{ C}$ . A represents 37 wires of #6 AWG aluminum wire in a cable providing a 22 amp current.

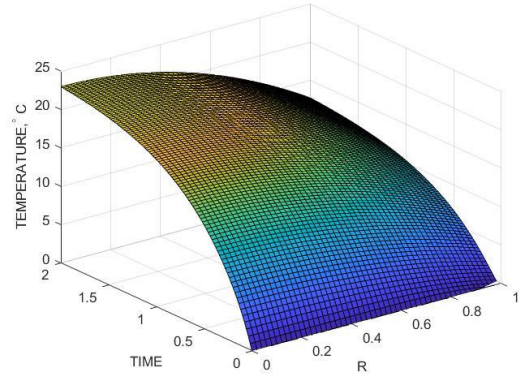


Fig. 2 At various points  $r/b$  and times  $a^2 t/b^2$  the temperature field (in degrees Celsius) within an electric aluminum cable with 37 wires and a current of 22 amperes. The temperature was initially set to zero, and then the cable was allowed to cool naturally as it was heated  $hb = 1$  is the value of the parameter, and the value of the parameter is the value of the parameter. The cable's radius is  $b = 4 \text{ cm}$ .

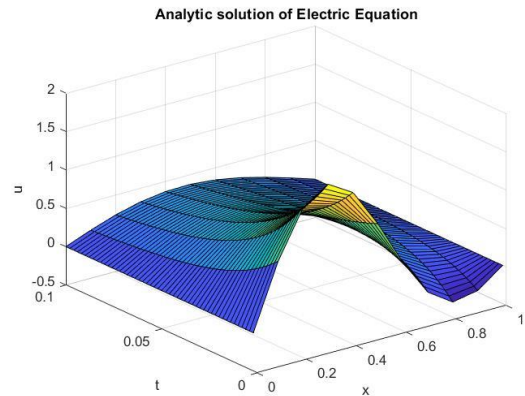


Fig. 3 Analytic solution of Electric Equation

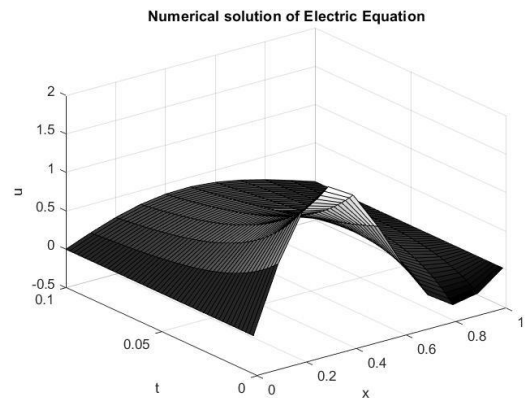


Fig. 4 Numerical solution of Electric Equation



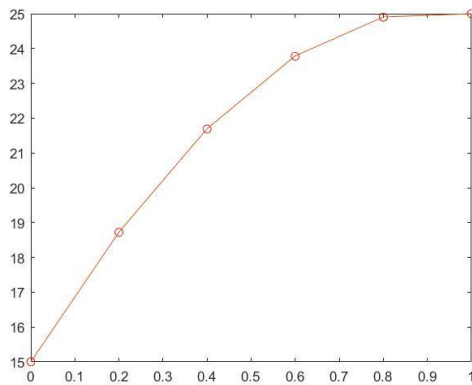


Fig. 4 Finite Element Method of Electric Equation

## CONCLUSIONS

The thermal models of subterranean cables were discussed in this study, starting with simple models with general hypotheses and progressing to more comprehensive specifications to meet practical instances. The heat transport concepts needed to derive an underground cable's thermal model have been summarized, and applications to specific scenarios have been defined (e.g., the non-infinite dimension of the soil, cable with a finite length). Furthermore, because the cable thermal model is commonly utilized in the sphere of power systems, the electrothermal analogy has been applied to it. To provide an overview of the primary contributions, the methodologies utilized to model heat transfer in the cables and in the external medium have been summarized. Finally, the cable thermal models have been used to calculate the cable current rating. Underground power cables have been widely investigated and modelled for decades, and as a result, there are several contributions in the literature. The historical components of this review paper have been presented, and the latest evolutions have been delineated. According to the literature assessment, there are a number of ongoing advancements that need to be improved. Due to the processing speed available, detailed FEM models of cables with the surrounding soil and ambient, including in 3D, are becoming feasible in non-uniform circumstances. However, there has been a fascinating development of improved and simplified models that can produce results that are comparable to FEM. The application of realistic thermal models of cables in the field of dynamic line rating, recognized as an activity that allows greater utilization of cable lines in various scenarios and is also useful for deferring expenditures

to upgrade the installed cables, is a topic that is becoming more appealing.

## ACKNOWLEDGMENTS

This paper was supported by the Deanship of Scientific Research (DSR), King Abdulaziz University, Jeddah.

## REFERENCES

- [1] Ben-Chaim M., The British Journal for the History of Science, Vol. 23, 3, 1990.
- [2] Clark D. H., and Murdin L., Vistas in Astronomy, Vol. 23, 351, 1979.
- [3] Chipman R.A., ISIS, Vol.45, 33, 1954.
- [4] Hauksbee F., Philosophical Transactions of the Royal Society of London 25, 2277, 2327, 2372 (1706-1707); 26, 87 (1708-1709); Physico-Mechanical Experiments on Various Subjects, 2nd ed. (Senex and Taylor, London, 1719).
- [5] Gray S., Philosophical Transactions of the Royal Society of London, Vol.31, 140, 1720.
- [6] Gray S., Philosophical Transactions of the Royal Society of London, Vol.37, 18, 1683-1775.
- [7] Franklin B. and Watson W., Philosophical Transactions of the Royal Society 47, 202, 1751-1752
- [8] Anders, G. Rating of Electric Power Cables in Unfavorable Thermal Environment; IEEE Press: Piscataway, NJ, USA, 2005
- [9] Lauria D., Pagano M., Petrarca C., Transient Thermal Modelling of HV XLPE Power Cables: Matrix approach and experimental validation, In Proceedings of the IEEE Power & Energy Society General Meeting (PESGM), Portland, OR, USA, 2018, pp. 5–10.
- [10] Wazwaz A.M., The variational iteration method; a reliable tool for solving linear and nonlinear wave equations, Comput. Math. Appl., 54 (2007) 926–932.
- [11] Wazwaz A.M., A First Course in Integral Equations, World Scientific, Singapore, (1997).
- [12] Wazwaz A.M., Suheil A. Khuri, The variational iteration method for solving the Volterra integrodifferential forms of the lane-Emden and the Emden-Fowler problems with initial and boundary value conditions, DE GRUYTER Open Eng. (2015);5:31-41.
- [13] Maturi A.D., Numerical Solution of System of Two Nonlinear Volterra Integral Equations, International Journal of Computers & Technology, Vol12, No.10, 2014, pp.3967-3975.
- [14] Maturi A.D., Bajamal. Z.A, AlGethami M.B., Numerical Solution of Volterra Integral Equation of Second Kind Using Implicit Trapezoidal, Journal of Advances In Mathematics, Vol8, No.2, 2014, pp.1540-1553.

- [15] Maturi A.D., Adomian Decomposition Method of Fredholm Integral Equation of the Second Kind Using Maple, Journal of Advances In Mathematics, Vol9, No.1, 2014, pp.1868-1875.
- [16] Maturi A.D., Application of Adomian Decomposition Method for Solving of Fredholm Integral Equation of the Second Kind, European Journal of Science and Engineering, Vol9, No.2, 2014, pp.1-9.
- [17] Sorkun H.H., Yalcinbas S., Approximate solutions of linear Volterra integral equation systems with variable coefficients, Applied Mathematical Modeling, 34(2010) 3451-3464.
- [18] Maturi A.D., Malaikah M.H., Numerical Solution of System of Three Nonlinear Volterra Integral Equation Using Implicit Trapezoidal, Journal of Mathematics Research; Vol. 10, No. 1; February 2018, ISSN 1916-9795 doi:10.5539/jmr.v10n1p44 URL: <https://doi.org/10.5539/jmr.v10n1p44>.
- [19] Maturi A.D., The Modified Decomposition Method for Solving Volterra Integral Equation Of The Second Kind Using Maple, International Journal of GEOMATE, Oct., Vol.17, Issue 62, 2019 pp. 23-28.
- [20] Maturi A.D., Aljedani I.A., Alaidarous S.E., Finite Difference Method For Solving Heat Conduction Equation Of The Granite, International Journal of GEOMATE, Sept., Vol.17, Issue 61, 2019 pp. 135 -140. ISSN: 2186-2982 (P), 2186-2990 (O), Japan.
- [21] Maturi A.D., Finite Difference Method For Solving Heat Conduction Equation Of The Brick, International Journal of GEOMATE, April, Vol.18, Issue 68, 2020, pp. 114-119.
- [22] Maturi A.D., Simbawa A.E., The Modified Decomposition Method For Solving Volterra Fredholm Integro-Differential Equation Using Maple, International Journal of GEOMATE, March Vol.18, Issue 67, 2020, pp. 84-89.

# ANALYSIS OF RESOURCE REQUIREMENTS IN A CONSTRUCTION SAFETY PROGRAM TO ESTIMATE COST OF ARCHITECTURAL WORK IN FLATS BUILDING

Rossy Armyn Machfudiyanto<sup>1</sup>, Yusuf Latief<sup>1</sup>, Ratih Fitriani<sup>1</sup> and Amira Syifa<sup>1</sup>

<sup>1</sup>Department of Civil and Environmental Engineering, Faculty of Engineering, Universitas Indonesia, Kampus Baru UI Depok, West Java - 16424

## ABSTRACT

According to the world meter's report in December 2020, Indonesia is ranked as the fourth most populated country globally. Previous reports also showed that the demand for basic human needs such as housing increases along with the population. Based on the Association of Indonesian Housing and Settlement Developers in 2021, the housing backlog reaches 8.2 million with an annual increase of approximately 500 thousand/year. To resolve this problem, The Ministry of Public Works and Housing in Indonesia implement the program "1000 Tower Project" to build vertical housing in form of flats building but several construction accidents occurred during its implementation. In this kind of flats building project, architectural works have the highest number of work items compared to other types, which makes further analysis necessary to mitigate construction accidents. Therefore, this study aimed to identify the list of architectural work, potential hazards, risk factors, and their controls for goals and programs to be drawn up with plans for resource needs. The method used was qualitative with secondary data or literature study, which involved the estimation of construction safety costs for architectural work in Flats projects by identifying resource requirements on safety programs.

**Keywords:** *Construction Safety Cost, Flats Building, Resource Requirement, Safety Program*

## INTRODUCTION

According to the International Labour Organization (ILO), the impact of work accidents is divided into 3 levels, namely the micro, mezzo, and macro. Accidents at the micro level will affect human safety, project delays, and the total project cost. At the mezzo level, it affects the company's performance and reputation, which negatively influence the competitiveness index of a country at the macro level [1]. The Ministry of Public Work and Public Housing (PUPR) stated that the impact of construction accidents will be felt by 5 subjects, namely labor, community, projects, companies, and the state (Construction 2020). The effect on the workforce can be in form of injury or death, causing doubts for other workers. The impact on the community includes injury, death, and feeling uncomfortable living around the project area. Meanwhile, the effect on the project is in form of a temporary halt in the project, delayed use of construction results, idle labor, and equipment, as well as decreased return on investment. The influence of the construction accident on the company is incompetence and a reduction in stock value. The wider impact is on the state, where there is an inability to carry out development safely. As in Indonesia, most of the construction work in the public sector in many countries uses a competitive tendering system. This is implemented to select contractors

with the lowest prices, which leads to low construction safety budgets [2]. According to a previous study [3], the most optimal construction safety cost for buildings is 1% of the total project budget. It was estimated [4] that construction safety costs on building projects are 1.92% of the total costs. Based on the calculation of the cost of each construction safety component in a building project, it was discovered that workers' training and PPE are the biggest [5]. Therefore, this study aims to conduct a resource analysis to estimate the cost of construction safety on the apartment building project.

## THEORETICAL STUDY

### Construction Safety Resource

Safety Resources in the Architectural Work of Flats Buildings is a potential capacity that can be used for construction activities. It requires a good management system for optimal use. Resources consist of the means that are necessary to carry out the project and achieve the goals and objectives efficiently and effectively. In the architectural work of high-rise flats buildings, safety resources are needed to achieve the project objectives. Based on a previous study [6], it was stated that the required resources are as follows:

Table 1. Construction Safety Resource Type

No	Construction	Safety	Resource Type
<b>Resource Component</b>			
	<b>Personal Equipment</b>	<b>Protective Equipment</b>	Equipment
1	Safety Helmet		Equipment
2	Goggles, Spectacles		Equipment
3	Face Shield		Equipment
4	Ear Plug, Ear Muff		Equipment
5	Masks		Equipment
6	Safety Gloves		Equipment
7	Safety Shoes		Equipment
8	Full Body Harness		Equipment
9	Safety Vest		Equipment
10	Fall Arrester		Equipment
<b>Safety Plan Development</b>			
11	Manufacture of Manuals, Procedures, Work Instructions, Work Permits and Forms	of	Labor
	Safety Socialization and Promotion		
12	Safety Briefing, Safety Meeting		Labor
13	Safety Simulation		
	Work Protective Equipment		
14	Safety Net		Equipment
15	Safety Rope		Equipment
16	Safety Deck		Equipment
17	Safety Fence		Equipment
	Insurance and Licensing		
18	Equipment Permit	Eligibility	Labor
19	Operator Permit		Labor
<b>Safety Personnel</b>			

20	Safety Expert and Safety Officer	Labor
<b>Signs</b>		
21	Hint Sign	Equipment
22	Prohibition Sign	Equipment
23	Warning sign	Equipment
24	Obligation Sign	Equipment
<b>Others Related to Risk Control</b>		
25	Light Fire Extinguisher	Equipment
<b>Additional (including Others Related to Risk Control)</b>		
1	Ear protector	Equipment
2	Noise measurement	Equipment
3	Material transport cart	Equipment

Based on the table, additional construction safety resources such as ear protectors and noise measurements are used only for Exposed Concrete Ceiling Finishing work. This is because the work uses a grinding tool with a loud sound in the intensity of a long duration compared to other jobs. There is also the provision of material transport carts that are only used for masonry and ceramic masonry, considering that the volume of work is significantly large and the load transported is also heavy. From the analysis of the need for the construction safety resource plan, the costs of each architectural work activity of high-rise buildings for the flats or apartment projects can be calculated.

## METHODOLOGY

Based on the flow of the study stages, the first step is to identify the targets and programs in each construction activity in the apartment building, specifically in the field of Architecture. The method used can be determined, namely expert validation with the Delphi approach, with approximately 3-5 experts. Subsequently, the analysis of experts' validation results is carried out to obtain the output of architectural work descriptions on the flats or apartment projects.

This is followed by a resource analysis using the needs matrix developed by the Minister of Public Works and Public Housing Regulation No. 10 of 2021, to estimate the safety cost in the apartment building.

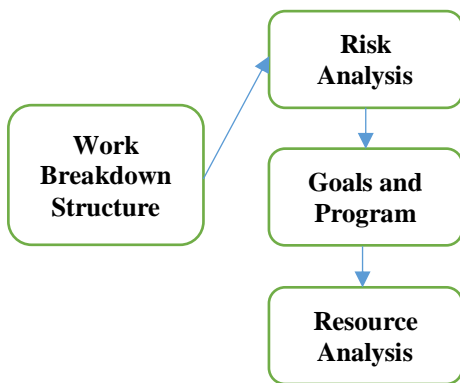


Fig. 1. Study Flow Methodology

## RESULT AND DISCUSSION

From previous studies on WBS standards for architectural work for rented flats [7], there were additional 16 to 258 activities (originally 242) including:

1. Installation of Moisture Resistant Gypsum on an Alternative Design of the Gypsum Wet Resistant Ceiling.
2. Practical Column Work on Alternative Designs for the Walls of Interior Paint Brick, Wet Area Ceramic Brick, Brick Parapet, Fire Rated Fire Stairs, and Pantry Ceramic.
3. Floor Screeding Work on an Alternative Floor Hardener Floor design.
4. Waterproofing and Testing Work on Alternative Designs for Wet Area Ceramic Floors.
5. Screed Leveling Coating Work on an Alternative Roll Carpet Floor Design.
6. Concrete Finishing Work on Alternative Concrete Embankment Designs.
7. The Work of Installing the Hanging Frame and Automatic Door Machine on the Alternative Design of the Automatic Entrance Glass Window Door.
8. Installation of Door Closers on Alternative Designs of Fire Ladder Doors.
9. Marking Work on Alternative Parking Marking Paint Designs.
10. Glass and Sealant Installation Work on Alternative Curtain Wall Designs.

The last stage of this study is to carry out the final validation of the WBS-based OHS cost components which are presented in the implementation of risk control. Therefore, a cost must be budgeted, consisting of the objectives and control programs for each activity. The WBS-based cost components that are compiled will increase the accuracy of safety cost calculations. They are also expected to increase the application of safety to reduce or eliminate the number of work accidents that occur in the flats

construction.

Based on the results of expert validation, 2 additional potential OHS hazards for architectural work in flats that were obtained include:

1. Fire, this potential risk can occur in alternative designs/methods of Waterproof Membrane Concrete Flooring, where it uses fire burning from a gas cylinder fire source.
2. Overload of Vertical Transport Equipment. This potential risk can occur in masonry work, considering the volume of wall work is significantly large with the load being transported and also heavy compared to other architectural work.

Therefore, the potential risks of safety hazards for architectural work in buildings are obtained, namely:

1. Fall from a height.
2. Hit, caused by objects that fall or move and others.
3. Collision, contact with sharp/hard objects from cuts, scratches, etc.
4. Inhalation/absorption of harmful substances into the body through inhalation or skin.
5. Slipping.
6. Exposed to electric current.
7. Movement beyond capacity (sprain).
8. Eyes exposed to/splashed with spray.
9. Caught on, in, and between objects (pinched, buried, drowned, etc.).
10. Exposure (temperature, air pressure, vibration, radiation, sound, light, etc.).
11. Fire.
12. Overload of Vertical Transport Equipment.

From the results of these potential hazards, the frequency and impact of risks for architectural work based on the WBS (Work Breakdown Structure) of the Construction Work of the Rental Flats Building Project are obtained. Based on the WBS architectural work standards, potential OHS risks were identified from each alternative design/method, and 52 risks were in the high-level category.

The resources needed for hazard control in the architectural work of flats are as follows:

1. Protective Hat
2. Eye Protection (Goggles, Spectacles)
3. Face Shield
4. Ear Protection (Ear Plug, Earmuff)
5. Respiratory and Mouth Protection (Masks)
6. Gloves (Safety Gloves)
7. Safety Shoes (Safety Shoes)
8. Full Body Harness
9. Safety Vest (Safety Vest)
10. Fall Arrestor
11. Preparation of Manuals, Procedures, Work

- Instructions, Work Permits and Forms
12. Safety Briefing (Safety Briefing),
  13. Safety Meeting (Safety Talk and/or Tool Box Meeting)
  14. OHS Simulation
  15. Safety Net
  16. Safety Line
  17. Fall Protection (Safety Deck)
  18. Safety Fence (Guard Railing)
  19. Equipment Eligibility Permit
  20. Operator Permit
  21. Safety Expert and/or Safety Officer
  22. Prohibition Sign
  23. Warning Sign
  24. Obligation Sign
  25. Information Sign
  26. Light Fire Extinguisher
  27. Procurement of Material Transport Carts
  28. Lighting
  29. Communication Tools/Handy Talkies
  30. Noise Measurement
  31. Manufacture of Work Benches/Platforms
  32. Create a Grounding Path
  33. Creating a special area for placing B3

Table 2 showed that the analysis results are carried out to calculate the need for construction safety resources in the construction of apartments, which will be used to estimate safety costs.

Table 2. Analysis of Construction Safety Resource

No	Construction Safety Resource	Items	Qty
1	Safety Plan Development	Construction Safety Plan document creation	Paper and Module 1 Ream of Paper 5 Volumes Module
		Preparation of work procedures and instructions	Paper and Module 1 Ream of Paper 1 Volume Module
		Preparation of reports on the implementation of Safety Management System	Paper and Module 2 Reams of Paper (how many times the compilation time) x Module
2	Socialization, Promotion and Training	Construction Safety Induction	Mineral Water and Snack Number of Workers + 10% (guests)
		Construction Safety Briefing (Safety Briefing)	The number of workers
		Meetings on safety (Safety Meeting, Safety Talk, and/or Tool Box Meeting)	The number of workers

3	Safety Equipment	Safety Patrol	(number of patrol times) x Number of Stakeholders
		Construction Safety Training	Instructor Seminar kit Consumption = Number of Workers
		HIV/AIDS outreach	
		Construction Safety Simulation	
		Banners (Banners)	Banners 4 pieces for each floor
		Poster	Poster 5 pieces for each floor
		OHS information board	Information boards 1 piece
		Safety Net	Safety Net Along the side of the project that is directly adjacent to the community
		Safety Rope (Life Line)	Lifeline 2 x building length
		Fall Protection (Safety Deck)	Wire mesh 3x2 m Iron Pipe Frames Along the longest side of the building
		Safety Fence (Guard Railing)	Guard Rail Length of building perimeter x Number of floors
		Restricted Area (Restricted Area)	Restricted Area Board 1 piece
		Fall arrester	Fall Arrester Number of workers working at height
		Disaster safety equipment	Stretcher Ambulance, Emergency Light, Flashlight, Body Bag Each Tool @ 2 pieces
		Protective Helmet (Safety Helmet)	Safety Helmet Number of Workers + 10% (guests)



		Eye Protection (Goggles, Spectacles)	Safety Goggles	The number of workers			Construction Safety Officer and/or Construction Safety Officer			
		Face Shield (Face Shield)	Face Shield	The number of workers			Emergency response officer	fireman	1 person	
		Diving Mask (Breathing Apparatus)	Breathing Apparatus	Min. 1 piece			First Aid Officer	First Aid Officer	1 person	
		Ear Protection (Ear Plug, Ear Muff)	Ear Plug	The number of workers						
		Respiratory and Mouth Protection (Masks)	Face Mask	Number of Workers per box + 30% (guests and in COVID-19 condition)			Traffic control officer/ coordinator/ flagman	Flagman	1 person	
		Gloves (Safety Gloves)	Safety Gloves	The number of workers			Medical and/or health personnel	Medical personnel	1 person	
		Safety Shoes (Safety Shoes)	Safety Shoes	Total Stakeholders + Workers	7		Environmental Management Officer	Janitor	2 persons	
		Safety Shoes (Rubber Safety Shoes and Toe Cap)	Rubber Shoes	The number of workers		Health Facilities	First aid kit	first aid	3 types of first aid packages: Package A: for 25 people Package B: for 50 people Package C: for 100 people	
		Full Body Harness	Safety Harness	Number of workers working at height			First aid room	First Aid Room	1 room	
		Life Jacket (Life Vest)	Life Vest				Fogging Equipment	Fogging Equipment	1 piece	
		Safety Vest (Safety Vest)	Safety Vest	Number of Workers + 10% (guests)			Cost of infectious outbreak health protocol (COVID-19)	Hand washing facilities	Handwashing place: 1 piece at the entrance gate Swab Antigen/PCR: number of workers and stakeholders per month Vitamins: number of workers and stakeholders	
		Aprons (Aprons/Coveralls)	Coverall Safety	A number of welding workers			Psychotropic and HIV examination	Medical check up	The number of workers	
		Fall protection (fall arrester)	Fall Arrester	Number of workers working at height			Adequate medical equipment for self-isolation	Patient's bed Oxygen tube Oximeter	Each item @ 3 pieces for the room area (± 16 m2)	
5	Insurance and Licensing	Insurance	Insurance Documents	The number of workers			Ambulance	Ambulance Car	1 piece	
		Checking or testing the fitness of the tool to get the license of the tool	Certificate/Permit Documents	A number of heavy equipment to be inspected/tested			Hint Sign	Hint Sign	1 piece	
6	Construction Safety Personnel	Construction Safety expert or construction safety expert	Safety Expert /Safety Officer	The Need for safety Experts/safety Officers (comparison of safety Experts/safety Officers with Workers) Low Risk = 1:60 Medium Risk = 1:50 High Risk = 1: 40	8	Signs				

		Prohibition Sign	Prohibition Sign	1 piece	Environmental inspection and testing/Sampling test	Report Document	1 inspection/test x per document
		Warning sign	Warning sign	1 piece	Making Worker Identity Card (KIP)	Worker Identity Card (KIP)	The number of workers
		Obligation Sign	Obligation Sign	1 piece	External audit	Report Document	1 audit x per document
		Information Sign	Information Sign	1 piece	CCTV	CCTV	4 pieces (gate, board of directors, field area and stockyard/warehouse)
		Temporary Job Sign	Temporary Job Sign	1 piece	<p>Based on the final validation, the results and discussions obtained are stated below:</p> <ol style="list-style-type: none"> <li>1. The cost components of ear protection and noise measurement are used only for Exposed Concrete Ceiling Finishing work. This is because the work uses a grinding tool with a loud sound in the intensity of a long duration compared to other jobs.</li> <li>2. The cost component for the procurement of material transport carts is only used for masonry and ceramic masonry, considering that the volume of work is significantly large and the load transported is also heavy.</li> <li>3. The vibration measurement component is omitted. This is because for architectural work, the intensity of the vibration generated is generally small and the duration of the work is not too long.</li> <li>4. The procurement component for fire sensing facilities is omitted because the work with the potential to be a fire hazard is only Waterproof Membrane Concrete Flooring, where at the time the work is carried out, electrical installations are not yet available.</li> </ol>		
		Evacuation route	Evacuation Route Sign	1 piece			
		Traffic Control Stick	Traffic Control Stick	1 x as much as the number of security			
		Traffic Cone (Traffic Cone)	Traffic Cone	10 pieces			
		Rotary Lamp	Rotary Lamp	1 piece			
		Temporary road equipment	Signs, markings and control devices	1 piece each			
9	Consultation with Experts related to safety	Environment expert	Experts	1 x consultation	<p>The table above is a recapitulation of the required safety cost components and arranged based on their control for each activity in the work of the superstructure of the building. The next stage can be arranged according to the format of the Circular Letter of the Minister of Public Works and Public Housing Number 66/SE/M/2015 concerning the Cost of Implementing an Occupational Health and Safety Management System Construction in the Public Works Sector.</p> <p>A previous investigation [8] stated that the safety cost component consists of several types of equipment such as personal protective materials, plans, training, work protective equipment, personnel, health facilities, signs, and security. It was also reported that the components of safety costs in building projects for all activities are personal protective equipment,</p>		
		Building engineer	Experts	1 x consultation			
10	Activities and equipment related to construction safety risk control	Work environment inspection	Report Document	1 x inspection per document			
		Light Fire Extinguisher	fire extinguisher	2 x per floor			
		siren	siren	1 piece			
		Lightning rod	Lightning rod	1 piece			
		Anemometer	Anemometer	1 piece			
		Safety flag	Safety flag	1 piece			
		Emergency lamp (Emergency Lamp)	Emergency Lamp	1 piece			

training, work protective equipment, personnel, health facilities, and security [9].

This study developed the safety cost component based on the component contained in the Circular of the Minister of Public Works and Public Housing Number 66/SE/M/2015 concerning the Cost of Implementing an Occupational Health and Safety Management System Construction in the Public Works Sector. During its application, not all equipment and components of safety costs are included in the preparation to avoid an increase in project cost. Before compiling the OHS costs on the project, there is a need to review the existing risk response to calculate the level of risk value to a low or acceptable level. After the implementation of the risk control response based on the review, it is discovered that the risk value has decreased from high or moderate to low and become acceptable. Therefore, the control and its components are sufficient. This is carried out to avoid the implementation of potential risk control which is feared to cost more than when the risk is accepted at an already low level.

## CONCLUSIONS

This study is expected to be used by project owners and contractors to understand and apply the flow of safety cost calculations in the construction of flats and implement regulations related to the location and height of the building. Resource analysis which is the most important process in estimating construction safety costs will also be a guide for job owners in assessing the fairness of the bid price submitted by bidders for safety costs in the process of selecting construction work service providers. This makes it necessary to develop a simpler method to calculate the safety cost in construction work, specifically flat projects, and focus more on its application in the field. Meanwhile, there is a need to develop an application for calculating construction safety costs for stakeholders to easily estimate safety costs, specifically in the construction of flats without losing any substance.

## ACKNOWLEDGMENTS

The authors are grateful for the financial support provided by the Ministry of Research and Technology/National Research and Innovation Agency through PDUPT Grant 2020 with contract number: NKB- 2875/UN2.RST/HKP.05.00/2020 managed by the Directorate for Research and

Community Engagement (DRPM) Ministry of Research and Technology/National Research and Innovation Agency.

## REFERENCES

- [1] Latief, Y., Machfudiyanto, R. A., Arifuddin, R., Setiawan, R. M. F., & Yogiswara, Y. (2017, July). Study of evaluation OSH management system policy based on safety culture dimensions in construction project. In *Journal of Physics: Conference Series* (Vol. 877, No. 1, p. 012028). IOP Publishing.
- [2] Choi, T. N., Chan, D. W., & Chan, A. P. (2011). Perceived benefits of applying Pay for Safety Scheme (PFSS) in construction—A factor analysis approach. *Safety Science*, 49(6), 813-823.
- [3] Shohet, I. M., Luzi, M., & Tarshish, M. (2018). Optimal allocation of resources in construction safety: Analytical-empirical model. *Safety science*, 104, 231-238.
- [4] Gurcanli, G. E., Bilir, S., & Sevim, M. (2015). Activity based risk assessment and safety cost estimation for residential building construction projects. *Safety Science*, 80, 1-12.
- [5] Hamid, A. R. A., Singh, B., & Mohd, A. S. (2014, April). Cost of compliance with health and safety management system among contractor in construction industry. In *National Seminar on Civil Engineering Research* (pp. 1-10).
- [6] Ferakhim, D., & Latief, Y. (2019). Development of safety cost for architectural works in rental apartments building construction project based on work breakdown structure. *International Journal of Engineering and Advanced Technology*, 8(5C), 16-27.
- [7] Rianty, M., Latief, Y., & Riantini, L. S. (2018). Development of risk-based standardized WBS (Work Breakdown Structure) for quality planning of high rise building architectural works. In *MATEC Web of Conferences* (Vol. 159, p. 01019). EDP Sciences.
- [8] Gunduz, M., & Ahsan, B. (2018). Construction safety factors assessment through frequency adjusted importance index. *International Journal of Industrial Ergonomics*, 64, 155-162.
- [9] Yilmaz, M., & Kanit, R. (2018). A practical tool for estimating compulsory OHS costs of residential building construction projects in Turkey. *Safety science*, 101, 326-331.

## EXPERIMENTAL STUDY ON SURFACE PROTECTION OF RESTORATIVE BRICK FOR CULTURAL PROPERTIES IN AYUTTHAYA

Yuko Ishida<sup>1</sup>, Masaru Koemoto<sup>2</sup>, Mika Yamada<sup>3</sup> and Hajime Ito<sup>4</sup>

<sup>1</sup>Department of technological systems, Kindai University Technical College, Japan;

<sup>2</sup> Osaka Bousui Construction Co., Ltd., Japan;

<sup>3</sup>Faculty of Science and Engineering, Waseda University, Japan;

<sup>4</sup>JIP Techno Science Corporation, Japan;

### ABSTRACT

Since early times, several bricks have been used as common building materials. Bricks deteriorate significantly in tropical climates because of high temperatures and humidity. Therefore, bricks used in historic structures are discussed to develop conservation measures. This study focuses on the bricks currently used for restoration at Ayutthaya in Thailand. These are locally hand-made and are sintered at low temperatures. The physical properties of the restorative bricks were investigated to consider better conservation measures. Moisture is a major cause of brick deterioration, and protection of the brick surface is expected to inhibit rainwater penetration into the interior. Therefore, an improved methodology of a protective coating to the bricks was provided, and its waterproofing performance was investigated. Water absorption characteristics were evaluated by wet-dry cycle tests. The specimens were immersed in water for 30 min before drying at 40°C for 23.5 h in one cycle. The cycle was designed to simulate the local rainy season. The coatings used were (1) plaster, (2) oil mixed plaster, and (3) silane-based surface impregnating material. The initial water adsorption ratio for the bricks with plaster was inhibited by approximately 1/3 compared to the uncoated bricks. Furthermore, the use of oil mixed with plaster can provide high waterproofing performance with less than 1% water absorption. However, the adhesive performance of the plaster to the bricks was decreased by mixing oil.

*Keywords: Historical brick building, Low-temperature sintering brick, Deterioration, Wet-dry cycle test, Plaster*

### INTRODUCTION

Bricks have long been used as a common building material in many parts of the world. Therefore, many old brick structures exist, as do many cultural buildings with heritage value. These historical brick buildings have problems such as weathering of the brick and peeling of the bond between individual bricks due to joint mortar expansion. Brick deterioration is often more severe in tropical climates because of temperature, moisture, high humidity, solar radiation, insects, micro-organisms, and salt effects [1]. In addition, biological deterioration due to the propagation of algae, lichen, and plants is a problem [2]. Some principles must be followed while repairing cultural properties, such as world heritage sites; the status quo will not be changed, original materials and construction methods will be used, and so on. Because of the individual uniqueness of each cultural property or differences in each surrounding environment, no established standardized repair method for historical brick buildings has been reported. From a global perspective, many cases of conservation and restoration of brick cultural properties exist [3]. However, it is often a method for replacing deteriorated bricks with new bricks from the viewpoint of preserving the structure, and there have been few cases where measures for preserving

bricks as materials have been considered. It is desirable to consider extending the life of material by removing the cause of deterioration, as a basic idea of preserving cultural properties, rather than strengthening the deteriorated and vulnerable parts [4]. Therefore, understanding the physical and chemical deterioration characteristics of brick and developing deterioration prevention measures for the material could help establish continuous maintenance methods for historical brick buildings.

### RESTORATION WORK OF WAT KRASAI PAGODA

The authors have studied the conservation of a brick-inclined pagoda at Wat Krasai temple in Ayutthaya, Thailand. This pagoda was restored in 2013 by covering the surface with new restorative bricks below the midsection and recreating the bottom base. In general, historic brick structures in Ayutthaya were stuccoed when they were first built. However, no surface protection was applied in this restoration. Therefore, the deterioration of the restorative bricks had already been confirmed by the time of the survey in August 2014 (Fig. 1). Based on our on-site investigation, we assumed the following causes of deterioration [5].

1. The bricks were stacked at an angle to match the

inclination of the pagoda, resulting in areas where rainwater collected and ran through the joint.

2. Rainwater is collected on the north and west faces, making drying difficult because of low sunlight.

3. Bricks on the part where rainwater collected deteriorate to soil and propagates plants on the soil, and plants also hold water.

It is desirable to protect the surface to prevent deterioration of the brick. However, applying a pure white stucco would drastically change the appearance, as the bricks are exposed in large areas of the pagoda. Changing the current situation requires discussion, in terms of cultural property protection. It is necessary to consider the actual status of originality, as well as a suitable protection method for restorative brick.



Fig.1 Deterioration of the restorative brick  
(Photograph taken in August 2014)

#### WATER ABSORPTION COEFFICIENT AND BULK DENSITY OF RESTORATIVE BRICKS

The restorative bricks for Ayutthaya's cultural properties used in the experiment were obtained from a local brick manufacturing plant in Ayutthaya in February 2020. The size of the bricks is approximately  $200 \times 100 \times 50$  mm, but the shape is distorted because of drying shrinkage and the surface is very uneven, making measurement difficult and allowing for large individual differences. A cracked cross-section is shown in Fig. 2. Many voids are found inside the brick, as well as organic matter.



Fig.2 Cross -section of the restorative brick

Water absorption and bulk density tests were performed on five specimens of  $50 \times 50 \times 20$  mm restorative bricks. The water absorption test was based on JIS R 1250. First, the specimens were oven-dried at  $105^{\circ}\text{C}$ – $120^{\circ}\text{C}$  for 24 h, and after being cooled to room temperature in a desiccator, the dry mass of  $m_1$  was measured. Second, the specimens were immersed in distilled water at  $20^{\circ}\text{C} \pm 5^{\circ}\text{C}$  for 24 h. After the surface water was wiped out, the saturated mass of  $m_2$  was immediately measured. The water absorption of restorative brick calculated using Eq. (1) is very high, exceeding 20% as shown in Table 1. However, according to previous studies [6], nearly 20% of water absorption is consistent with similar bricks in the Ayutthaya.

$$a = \frac{(m_2 - m_1)}{m_1} \times 100(\%) \quad (1)$$

The bulk density of restorative brick was calculated using the mass in the air-dried state and the volume. The volume of the specimens was measured using Archimedes' principle. After soaking the specimen in distilled water at  $20^{\circ}\text{C}$  until saturated, the mass was measured in a state of receiving buoyancy and was converted to volume. The results of bulk density in the air-dried state are shown in Table 2.

Table 1 Water absorption of restorative brick

Specimen No.	dry mass (g)	saturated mass (g)	Absorption (%)
1	83.58	101.19	21.07
2	77.38	94.50	22.12
3	79.27	96.93	22.28
4	82.28	100.07	21.62
5	88.55	106.98	20.81
Average	82.21	99.93	21.58

Table 2 Bulk density of restorative brick

Specimen No.	air-dried mass (g)	Volume (cm <sup>3</sup> )	Bulk density (g/cm <sup>3</sup> )
1	83.94	51.61	1.63
2	77.81	48.55	1.60
3	79.82	49.49	1.61
4	82.94	50.71	1.64
5	89.29	53.75	1.66
Average	82.76	50.82	1.63

#### COMPOSITION OF RESTORATIVE BRICKS AND IGNITION LOSS TEST

A scanning X-ray fluorescence spectrometer

(ZSX-Primus II) was used to provide the chemical composition of the bricks in terms of oxide. The main chemical composition, excluding trace elements, is shown in Table 3. The composition of the restorative bricks is mostly  $\text{SiO}_2$ ,  $\text{Al}_2\text{O}_3$ , and  $\text{Fe}_2\text{O}_3$ . Silica helps control shrinkage and excessive consolidation, whereas alumina provides moderate viscosity [7]. The silica content in bricks is typically 50%–60% and the alumina content is typically 20%–30%. Thus, the composition of restorative brick is within the standard range.

Table 3 Composition of the restorative brick

Chemical composition	Content ratio(%)
$\text{SiO}_2$	58.36
$\text{Al}_2\text{O}_3$	23.56
$\text{Fe}_2\text{O}_3$	8.92
$\text{CaO}$	1.31
$\text{MgO}$	0.99
$\text{SO}_3$	0.21
$\text{Na}_2\text{O}$	0.55
$\text{K}_2\text{O}$	4.42
$\text{TiO}_2$	1.23

Natthan et al. [6] analyzed the physical and engineering properties of ancient and substitution bricks for the preservation of historical buildings in Thailand. They obtained substitution bricks from restoration sites in Ayutthaya Province and ancient bricks from historic sites in Bangkok and Ayutthaya Province. They found that both ancient and substitution bricks contained  $\text{SiO}_2$  in the range of 60.3% to 68.2%,  $\text{Al}_2\text{O}_3$  in the range of 60.3% to 68.2%, and  $\text{Fe}_2\text{O}_3$  in the range of 7.25% to 8.74%. The restorative bricks we obtained contained slightly less  $\text{SiO}_2$  than in the previous study, and slightly higher  $\text{Al}_2\text{O}_3$  and  $\text{Fe}_2\text{O}_3$ . The component contents of the substitution (S) and restoration bricks (R) are shown in Fig. 3.

In addition, an ignition loss test was performed based on JIS A 1226. The organic matter content in restorative brick is very low (Table. 4).

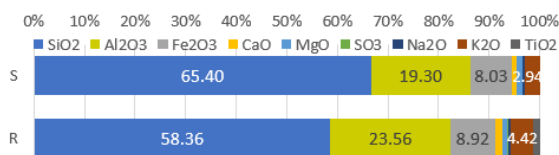


Fig.3 Chemical composition content ratio  
( The component of S is from reference value [6] )

Table 4 Ignition loss of the restorative brick

No.	ignition loss (%)
1	1.44
2	1.29
3	1.19
Average	1.31

## UNIAXIAL COMPRESSIVE STRENGTH TEST

According to a standard method for uniaxial compression test of ordinary fire brick based on JIS R 1250, the shape of the specimen is  $105 \times 100 \times 60$  mm, and the specimen is pressed until failure at a loading rate of 0.5 to 1.0  $\text{N/mm}^2$  per second with a surface of approximately  $105 \times 100$  mm as the pressing surface. However, two specimens of approximately  $10 \times 10 \times 20$  mm were used in this study for compression tests at axial strain rates of 0.01% to 0.1% per minute. The average uniaxial compressive strength was 11.74 MPa.

## ACCELERATED SLAKING TEST

An accelerated slaking test was performed based on JGS 2125-2020. First, the weight of specimens ( $m_1$ ) was measured, followed by air-drying for at least 24 h, and oven-drying at  $40^\circ\text{C} \pm 5^\circ\text{C}$  for 48 h. After cooling to room temperature, the mass ( $m_2$ ) was measured. The specimens were also photographed so that their shape, color, cracks, and voids could be confirmed. Moreover, the specimens were immersed in distilled water at approximately the same as room temperature, and the shape changes of the specimens were observed and photographed within 1 min of immersion, 30 min later, 1, 2, 4, 6, and 24 h later to determine each stage of slaking classification, from 0 to 4 (Fig. 4). After 24 h of immersion, the slaked material was drained, and its mass ( $m_3$ ) was measured. Finally, the slaked material was oven-dried at  $110^\circ\text{C} \pm 5^\circ\text{C}$  until its mass remained constant, and dried mass ( $m_4$ ) was measured. The preceding process was repeated thrice.

When the specimen is immersed in distilled water, large bubbles are ejected from the voids with great force immediately after immersion, and numerous fine bubbles are generated along with them (Fig. 5). The generation of fine bubbles decreased with time and continued until approximately 1.5 hours after immersion. The bubble generation was similar in all three slaking tests. In addition, when the specimens were immersed in distilled water, fine brick debris adhered to the surface fell into the water because of slight peeling or chipping. However, the amount of such debris decreased with each test pass. After completion of the test, the specimen did not slake and remained in the 0 categories for all three test cycles. The moisture content at each stage was calculated using  $m_1$ ,  $m_2$ ,  $m_3$ , and  $m_4$ . The variation in results was large, and clear trends such as increases, decreases, or correlations were not confirmed about changes in moisture contents.

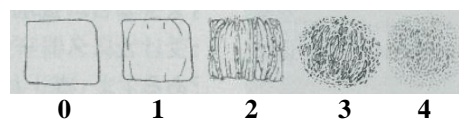




Fig.4 Classification of slaking level [8]



Fig.5 The generation of large and fine bubbles

## WET-DRY CYCLE TEST

### Purpose of the test

The existing historical brick buildings of the Ayutthaya Dynasty were covered with decorative stucco on the surface. However, much of the stucco has been peeled away, exposing the brick. Rainwater penetration through unprotected brick surfaces is a major factor in accelerated weathering. Therefore, a wet-dry cycle test was performed to investigate the effect of brick surface protection on rainwater infiltration.

### Preparation of the specimens

The size of the restoration brick used as the specimens was approximately  $200 \times 100 \times 50$  mm. Three types of protective materials were applied to one side of the  $200 \times 100$  mm specimens, and four cases were prepared (Table 5). Three specimens were prepared per case, and the averages were used for the results and discussion, except when special changes occurred in the specimens or an obvious defect in the experimental conditions. The plaster was mixed in a 1:1:1 ratio with Japanese commercial slaked lime, powder sanded from the restoration bricks and passed through a 0.15-mm sieve, and distilled water. An oil mixed plaster is prepared by mixing commercial salad oil, 1/4 of the total mass of slaked lime and brick powder, to the above plaster. The silane-based surface impregnating material using this experiment penetrates the capillaries of the bricks and forms a water-repellent layer inside the bricks. The impregnating material prevents water ingress, but water vapor passes through. The silane-based surface impregnating material was absorbed eight times the standard amount because of the high-water absorbency of the restorative brick.

The four sides of all specimens,  $100 \times 50$  mm  $\times$  2

and  $200 \times 50$  mm  $\times$  2 were covered with caulking material to prevent water absorption.

Table 5 Material of surface protection

	Surface protection
Case-1	None
Case-2	Plaster
Case-3	Oil mixed plaster
Case-4	Silane-based surface impregnant

### Experiment method

First, the initial mass of the specimen in the air-dried state was measured ( $m_0$ ). Then, the wet-dry cycle test was performed based on the following procedure.

1. Measure the mass of the specimen before water supply ( $m_1$ ).
2. Spread the felt on the tray and soak it in distilled water at  $20^\circ\text{C} \pm 5^\circ\text{C}$ .
3. Place the specimen with the protective material coated surface down on the felt, allow it to absorb water for  $30 \pm 5$  min, then measure the mass of the specimen ( $m_2$ ).
4. After drying at  $40^\circ\text{C} \pm 5^\circ\text{C}$  for  $23.5 \text{ h} \pm 10 \text{ min}$ , measure the mass of the specimen ( $m_3$ ).
5. Repeat wet and dry with 1 to 4 as one cycle.

The above experimental conditions were determined considering the local rainy season environment. A schematic of water absorption is shown in Fig. 6.

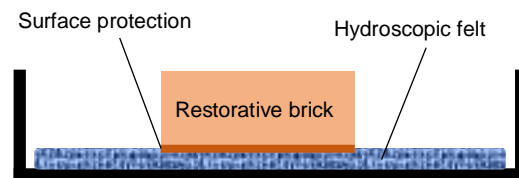


Fig.6 Schematic diagram of water supply

### Results and considerations

Twenty-six cycles of wetting and drying were performed. The average water absorption for the first time was 6.74% when the specimens were air-dried without surface protection and watered from one side for 30 min. The average water absorption was 21.58% after 24 h of immersion in the dry state, as mentioned in the previous section. Approximately 30% of the water-saturated state corresponds to 6.74% average water absorption. The water absorption during the first 30 min of water supply was very large, although the water content before water absorption, water absorption area, and water absorption conditions were different. Applying this result to the local situation, a reasonable amount of rainwater will permeate the bricks by a squall lasting 30 min, and the weight of the brick structure will increase by the amount of

rainwater that permeated. The increased weight acts as a compressive force on the lower bricks, which have absorbed water and become soft. Many vertical cracks were observed in the severely deteriorated areas of the bricks as shown in Fig.7. As cracks pass through the voids, water is likely to accumulate further in the voids due to infiltration.

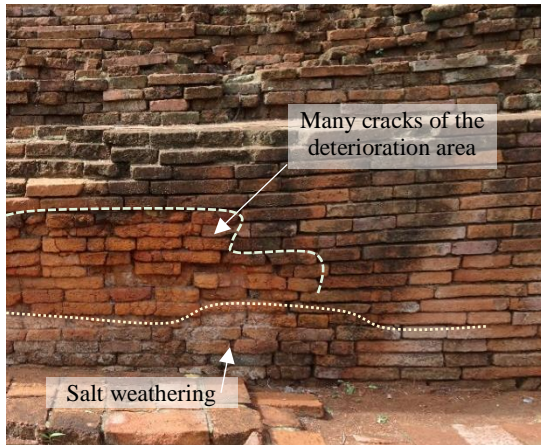


Fig. 7 Condition of the deterioration bricks

Figs.8–11 show the cycle variation in water absorption and a regression curve for each case. The vertical axis was set to range from 0% to 8% for Case-1 and 2, while the other cases were set to 0%–1% because of their low water absorption. The large variation in water absorption in each case depends on the error in water absorption time of 5 minutes in each experiment and the impregnation condition of the felt. When the surface was protected with plaster, the maximum water absorption was 2.27%, which was approximately 1/3 compared with the uncoated bricks. When the plaster was mixed with oil, the maximum water absorption was 0.66%, indicating a high penetration prevention effect. The silane-based surface impregnating material allowed almost no water to pass through, with a water absorption rate of less than 0.1%; additionally, its waterproofing performance did not deteriorate after 26 cycles. The water absorption rate decreased with each wet-dry cycle in Case1-3 and became almost stationary approximately after the 17th drying cycle. The bricks were relatively dry before the start of the experiment and initially absorbed a large amount of water, however, it was supposed that the bricks did not dry completely under the drying condition of 40°C for 23.5 hours. Therefore, the absorbed water gradually decreased as the non-drying water accumulated in the bricks through repeated wet and dry cycles. Finally, it is thought that the balance between the amount of water absorption for 30 minutes and the amount of dry water for 23.5 hours became constant.

The waterproofing effect after the plaster is peeling is discussed. The mass gain before and after water absorption of all specimens in each cycle is shown in

Fig. 12. One of the three specimens with oil mixed plaster peeled off from the brick after 12 cycles and another after 21 cycles. This could be due to the oil mixed with the plaster weakening the adhesion between the brick and plaster.

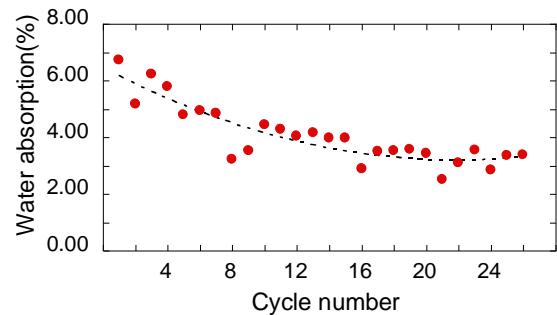


Fig. 8 Transition of water absorption (Case-1)  
-Without surface protection-

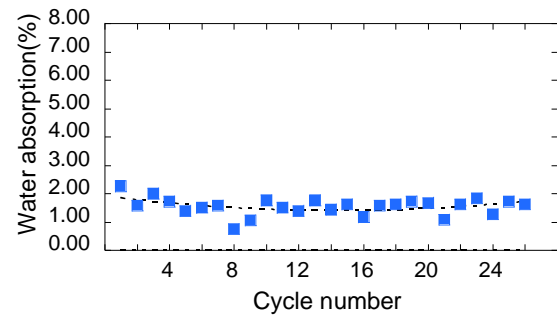


Fig. 9 Transition of water absorption (Case-2)  
-With plaster-

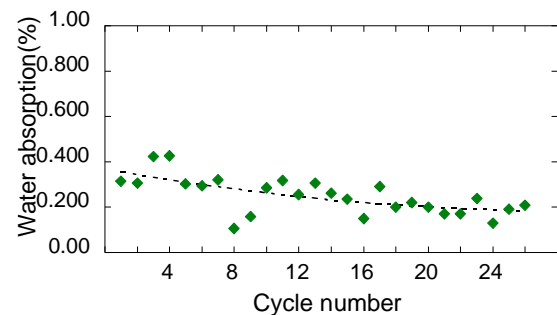


Fig. 10 Transition of water absorption (Case-3)  
-With oil mixed plaster.

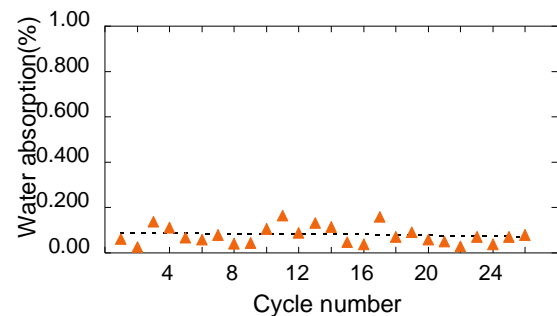


Fig. 11 Transition of water absorption (Case-4)  
-With silane-based surface impregnating material –  
By continuing the experiment after the loss of the oil mixed plaster, the amount of water absorption increased, but it was less than that in the Case-1 specimen without surface protection, implying that the waterproofing effect will last. There is a possibility of the oil mixed plaster adhered and remained in the microscopic voids on the brick surface.

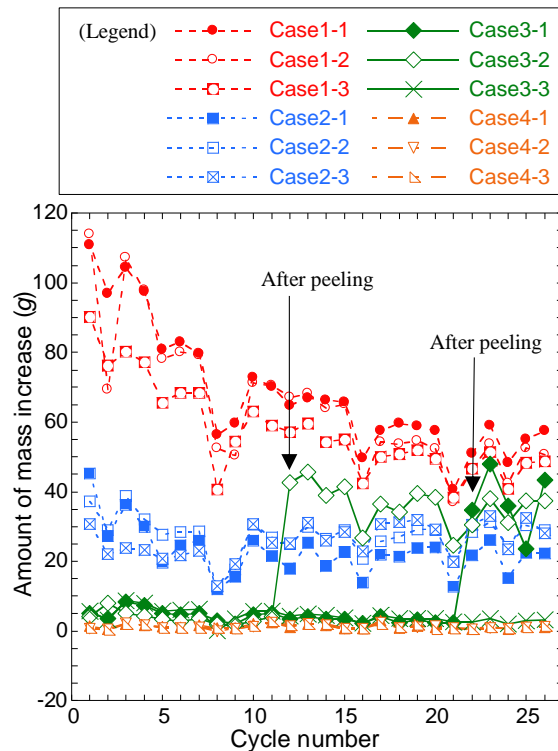


Fig. 12 Mass gain before and after water absorption in each cycle

## CONCLUSIONS

This study clarified the basic physical properties of restorative bricks used in historical brick structures in Ayutthaya. The restorative bricks sintered at low temperature is absorbed an amount of water by 30 min of water supply that cannot dry out in a rainy season day cycle. It is possible that moisture remains in the restorative brick due to daily squalls. The results of the wet-dry cycle test showed that the initial water absorption rate of the plastered bricks was reduced to about 1/3 of that of the uncoated bricks. It is desirable that the surface of restoration brick is covered with something to prevent water infiltration. The use of oil mixed with plaster can provide high waterproofing performance at a low cost; however, it

is necessary to improve the adhesion performance of the plaster with oil to the bricks as a future study issue.

## ACKNOWLEDGMENTS

We would like to thank Veerasak Sansaard belongings the Aytthaya historical park office for useful information about the restorative brick in Ayutthaya. The specimen preparation to apply this uniaxial compression test was supported by Prof. Hailong Wang in Faculty of Science and Engineering, Waseda University. ZSX-Primus II was the equipment shared in MEXT Project for promoting public utilization of advanced research infrastructure Grant Number JPMXS0440500021). The surface impregnating agents was supplied by Kinki Kabezai Co., Ltd., and we are also grateful to Mr. Junji Hamaoka CEO for his advice about plaster making.

## REFERENCES

- [1] Webb, T.L. and van Aardt, J.H.P., Deterioration of materials under tropical conditions, Proceedings of the symposium on design for tropical living, Durban, South Africa, 1957, p.620.
- [2] Yoshida Y., Hokoi S., and Ogura D., Degradation of a big buddha in Sukhothai ruins, Journal of Environ. Engineering AIJ, Vol.78, No.689,2013, pp.561-567. (in Japanese)
- [3] Warren J., Conservation of Brick, Oxford, butterworth-Heinemann,1999,p.294.
- [4] Kuchitsu N., Deterioration of bricks as a material of cultural properties, Materiaru Raifu Gakkaishi, Vol.17, No.1, 2005, pp.7-11. (in Japanese)
- [5] Ishida Y., Ito H. and Fukagawa R., Consideration on Conservation of the Wat Krasai Pagoda in Ayutthaya, Journal of Disaster Mitigation for Historical Cities, Vol.15,2021, pp.225-232. (in Japanese)
- [6] Natthan W., Chainarong A., Peerasit M., Weerachart T., Raktipong S. and Sutat L., Ancient materials and substitution materials used in Thai historical masonry structure preservation, Journal of renewable materials, Vol.9, No.2, 2021, pp.179-204.
- [7] Nishimura A., Fujii M., Minato T., Morikawa H. and Kagayama T, Latest Civil engineering material, Morikita Publishing Co., Ltd., 2014,p.225. (in Japanese)
- [8] The Japanese Geotechnical Society, Methods and Description of Geotechnical Materials Testing (1st Revised Edition), 2021, p.299.

## SELECTION OF RAILWAY BALLAST BASED ON CEMENTING POTENTIAL: A CASE STUDY IN THAILAND

Phitsanu Pholkainuwatra<sup>1</sup>, Sitthiphat Eua-apiwatch<sup>1</sup>, and Siam Yimsiri<sup>2</sup>

<sup>1</sup>Department of Civil Engineering, Faculty of Engineering, Burapha University, Thailand;

<sup>2</sup>Sustainable Civil Engineering and Infrastructure Research Unit, Burapha University, Thailand.

### ABSTRACT

Properties of fresh ballasts collected from five quarries around Thailand were investigated in the laboratory. The investigation includes properties specified by the State Railway of Thailand (SRT) for ballast, i.e. rock type, sieve analysis, flat and elongation, and Los Angeles abrasion. Furthermore, cementing value, water absorption, specific gravity, sulfate soundness, and petrographic analysis were also conducted. The obtained rock properties were then compared with the requirement for using as a ballast specified by various national standards, including the Australian Rail Track Corporation (ARTC), the American Railway Engineering and Maintenance of Way Association (AREMA), and the State Railway of Thailand (SRT). The results show that all rocks are more or less comply with all standards. However, Buriram basalt is considered as the best. Saraburi limestone has low abrasion resistance and high cementing value. The carbonate rock tends to give a higher cementing strength than igneous rock and metamorphic rock, and in terms of parent mineral, plagioclase usually found in igneous and metamorphic rock has poor cementation potential. The large abundance of plagioclase in igneous rock, such as Buriram basalt, Nakhon Sawan dacite, and Prachinburi andesite, resulting in lower cementing values. The large cementing value of Saraburi limestone may hinder its usage as a railway ballast. Therefore, the cementation properties of ballast by cementing value test, originally suggested by Raymond [1], is strongly recommended on the selection of ballast.

*Keywords: Ballast, Cementing, Rock, Railway*

### INTRODUCTION

In the past, cargo ships used stones as a ballast to weigh itself when empty ships travel. These stones had to be disposed of, so it was used as a substructure of railway. Until now, it is still called this stone a “ballast,” even though, in the later stage, stone has already been specifically produced for railway purpose [2]. Ballast is a selected material used to sprinkle and compact the top layer of a railway substructure in which the sleepers are embedded. Ballast can be subdivided into four zones as shown in Fig. 1, i.e. (i) crib - between sleepers, (ii) shoulder - beyond sleeper ends down to bottom of ballast layer, (iii) top ballast - upper portion of supporting ballast layer, and (iv) bottom ballast - lower portion of supporting ballast layer [3].

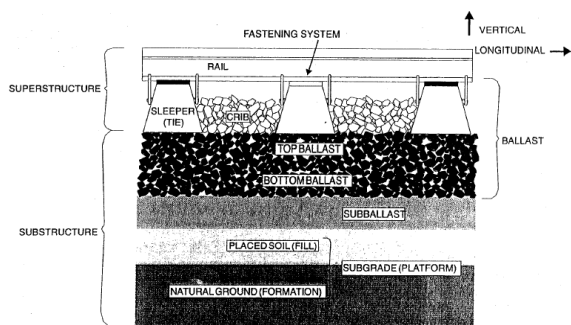


Fig. 1 Railway track structure components. [3]

Ballast is often made from hard rock, especially igneous rock, such as granite or even quartzite metamorphic rocks, because it is durable and has suitable drainage characteristics. Ballast should be (i) a non-porous and non-absorbent material, (ii) resistant to abrasion and corrosion, (iii) durable - will not crush or decompose under changing weather condition, and (iv) economically worthwhile. Federal Track Safety Standards (FTSS) classifies the most important functions of ballast as follows, (i) transmitting and distributing the load of the track and railroad rolling equipment to the subgrade, (ii) restraining the track laterally, longitudinally, and vertically under dynamic loads imposed by railroad rolling equipment and thermal stresses exerted by the rail, (iii) providing adequate drainage for the track, and (iv) maintaining proper track cross-level, surface, and alignment [4].

Moreover, the sub-ballast layer must be suitable for preventing an upward migration of fine particles from the sub-grade layer into the ballast layer's void. Ballast fouling is defined as a condition when finer particles in the ballast exceeds 2% by weight [5]. Ballast fouling may occur as a result of one or the combination of five different mechanisms, which include (i) fragmentation of ballast, (ii) migration of underlying sub-ballast materials, (iii) surface infiltration of weathered particles and coal droplets, (iv) upward migration of fines from subgrade formations, and (v) sleeper wearing [3].



The effect of ballast fouling is that the contaminated part prevents the ballast from performing its functions. Its severity depends on the amount and cause of contamination. Contamination caused by sedimentary and clay materials is mainly found in the field. Clay alone will not cause attrition; however, sediment particles can cause attrition. Both clay and sediment interfere with the drainage system of the tracks and, consequently, cause the deterioration of ballast due to the poor drainage of the railway tracks. Contamination from fine sand and gravel particles increases the shear strength and the stability of ballast but decrease drainage performance of ballast. Contamination of fine sand and gravel is not a significant problem in maintenance.

The basic properties of ballast are set by various countries. Australia standard is set by the Australian Rail Track Corporation (ARTC). US standard is set by the American Railway Engineering and Maintenance of Way Association (AREMA), and Thai standard is set by the State Railway of Thailand (SRT). The basic properties requirement consist of specific gravity, absorption, particle shape, flakiness index, Aggregate Compression Value (ACV), and Los Angeles Abrasion (LAA). Table 1 summarizes the properties of ballast specified by these standards.

Table 1 Comparison of ballast standards by different countries.

Properties	AREMA	ARTC	SRT
Specific Gravity	2.60-2.65	2.50	-
Absorption	1-2%	-	-
Particle shape	-	<30%	-
Flakiness Index	5%	<30%	<30%
ACV	-	25% max	-
LAA	25-40%	25% max	25% max

SRT also recommends ballast selection in Thailand to be made from hard rocks, including granite, rhyolite, quartzite, dacite, gabbro, basalt, andesite, diorite, and ballast. Ballast shall not contain any harmful chemicals and has no cementation force when powdered. This paper investigates cementing characteristics of ballasts collected from various quarries in Thailand.

## MATERIALS AND METHODS

### Physical and engineering properties

Ballasts collected from five quarries in Thailand are used in this study. Fig. 2 shows photos of ballasts, which are gneiss from Chonburi, andesite from Prachinburi, dacite from Nakhon Sawan, basalt from Buriram, and limestone from Saraburi. Table 2 shows testing program which includes Los Angeles abrasion, flat & elongation, absorption, specific

gravity, sulfate soundness, sieve analysis, and petrographic analysis.



Fig. 2 Ballast used in this study.

Table 2 Ballast testing program

Properties	Method
Los Angeles abrasion (LAA)	ASTM C535
Flat & elongation	ASTM D4791
Specific gravity & absorption	ASTM C127
Sulfate soundness	ASTM C88
Sieve analysis	ASTM D422, D1140
Rock type	Petrographic analysis

### Ballast cementing value

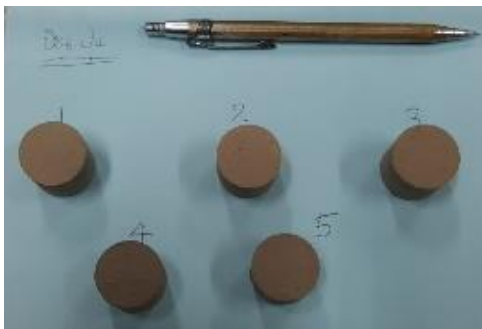
The ballast cementing value test is a test of coagulation of the formed rock due to degradation, originally suggested by Raymond [1]. Feng et al [6] explained the term "cemented ballast" as a condition where the ballast voids are filled with fine particles and bond the coarse aggregate together, resulting in a hard-to-break-up matrix of ballast particles fouling material. This condition can happen when a significant proportion of the fine particles are silt- or clay-size (<0.075 mm) and the ballast has become wet and then dried. This test has not been standardized; therefore, this study employed a ballast cementing

value test procedure as suggested by Boucher and Selig [7].

A ballast cementing value test can be conducted by crushing the rock using the LAA machine to obtain the fine particles passing #200 sieve. After that, the dough is formed using distilled water with a water content above the liquid limit and it is left overnight. A cylindrical briquette of 25 mm in diameter and 25 mm in height is prepared using a steel cylindrical mold. The pressure of 12.9 MPa is applied to the mold with a consolidation time is 10 min. The briquette is then extruded and left air-dried for 20 hours, then oven-dried for 4 hours. Fig. 3 shows photos of sample preparation. After that, the samples are placed in the desiccator until they are tested. Five samples of each rock are tested by an unconfined compression machine at the rate of 0.0335 in/min to obtain their maximum strength. The cementing value is an average of maximum strength of tested briquettes. Fig. 4 shows photos of unconfined compression test on tested briquettes.



(a) Apply pressure to a sample.



(b) Sample briquettes after extruded from the mold.

Fig. 3 Sample preparation for ballast cementing value test.



(a) Unconfined compression test.



(b) Failure of the sample.

Fig. 4 Unconfined compression test of a sample.

## RESULTS AND DISCUSSIONS

### Petrographic analysis

The purposes of petrographic examination is to classify and determine the relative amount of the constituent of the rock sample. A thin section of 0.03 mm thick of ballast from various sites is prepared and transmitted by light polarized microscope. The petrographic analysis results are shown in Table 3.

The predominant minerals in Chonburi gneiss are feldspar and quartz. Plagioclase is the main constituent in extrusive igneous, such as Prachinburi andesite, Nakhon Sawan decite, and Buriram basalt. Calcite, which is considered a carbonate mineral, is presented in Saraburi limestone.

### Physical and engineering properties

Sieve analyses are conducted to investigate the particle size distribution of ballast. Effective particles size corresponding to 10%, 30%, 50%, and 60% are obtained and the coefficient of uniformity ( $C_u$ ) and coefficient of curvature ( $C_c$ ) of ballast is then calculated. The sieve analysis result is presented in Fig. 5. The average particle sizes of the ballast are



presented in Table 4.

Sieve analysis results show that the nominal size of ballast ( $D_{50}$ ) varied from 40.1 to 45.0 mm. Chonburi gneiss contains more stones of larger diameter than other ballast. The coefficient of uniformity ranges from 1.3 to 1.6 and the coefficient of curvature ranges from 0.6 to 1.2. The grain size distribution of all ballasts can be classified as uniform ballasts (poorly graded gravel).

Table 3 Ballast petrographic analysis results

Ballast	Rock type	Predominant minerals	Percent (%)
Chonburi gneiss	Metamorphic	Feldspar	60
		Quartz	25
		Muscovite	10
		Chlorite	5
Prachinburi andesite	Extrusive igneous	Plagioclase	50
		Chlorite	30
		Olivine	15
		Pyroxene	5
Nakhon Sawan dacite	Extrusive igneous	Plagioclase	40
		Feldspar	25
		Amphibole	20
		Pyroxene	15
Buriram basalt	Extrusive igneous	Plagioclase	55
		Pyroxene	20
		Olivine	20
Saraburi limestone	Sedimentary	Calcite	100

Table 4 Average particle sizes of ballast.

Particle size (mm)	Gneiss	Andesite	Dacite	Basalt	Limestone
$D_{10}$	32.0	30.2	33.0	27.0	30.1
$D_{30}$	31.0	40.0	40.0	36.0	38.0
$D_{50}$	45.0	43.0	42.3	40.1	41.0
$D_{60}$	50.0	44.4	43.3	41.0	42.0
$C_u$	1.6	1.5	1.3	1.5	1.4
$C_c$	0.6	1.2	1.1	1.2	1.1

Table 5 presents physical and engineering properties of ballasts. LAA index of tested ballast ranged from 8.0 to 29.7% and most of the ballast comply with the ARTC (LAA<25%), AREMA (LAA 25-40%), and SRT (<25%), except Saraburi limestone with the LAA of 29.7%. ARTC and SRT recommended flat & elongation (1:3) values smaller than 30%, and only Nakhon Sawan dacite does not comply with these standards. AREMA required flat & elongation (1:2) value smaller than 5%, Nakhon Sawan dacite and Prachinburi andesite do not comply with AREMA requirement. AREMA required absorption smaller than 1 %, and the other two standards do not mention water absorption value. The result showed that all ballast comply with AREMA. The specific gravity of all the ballast varies from 2.68 to 2.87. The sulfate soundness values of all ballast pass the requirement of AREMA and SRT.

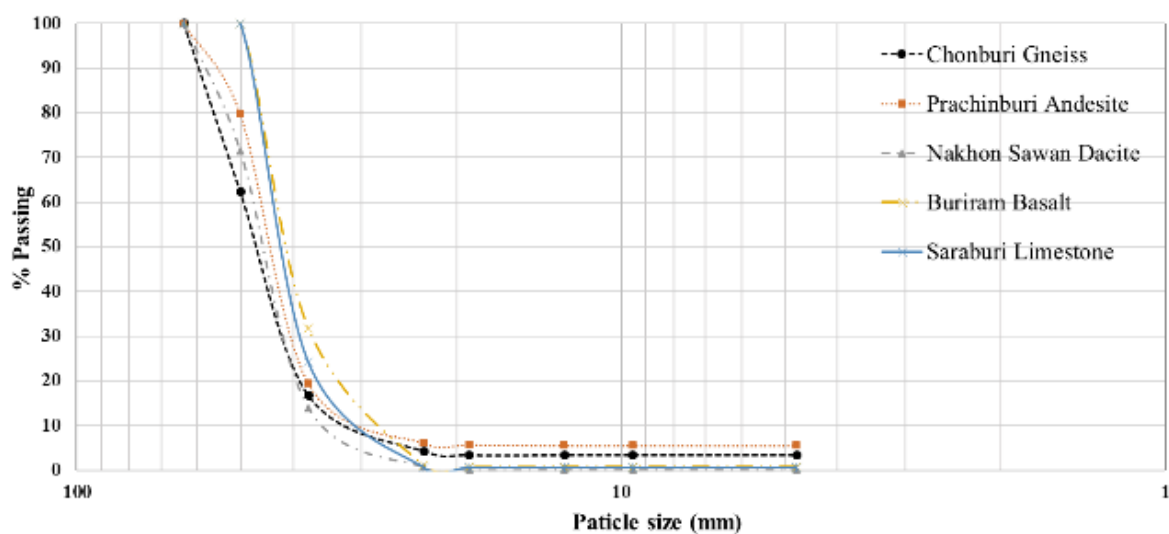


Fig. 5 Ballast particle size gradation results.

Table 5 Ballast basic properties.

Properties	Gneiss	Andesite	Dacite	Basalt	Limestone
LAA (%)	24.1	19.3	8.0	14.1	29.7
Flat & elong. (1:2) (%)	19.8	29.7	33.7	24.1	15.9
Flat & elong. (1:3) (%)	0.8	5.9	5.4	3.2	1.7
Absorption (%)	0.9	0.4	0.2	0.8	0.9
Gs	2.68	2.70	2.84	2.87	2.68
Sulfate soundness (%)	2.6	1.0	1.2	1.5	2.7

### Ballast cementing value test results

Table 6 summarizes ballast cementing value test results. Saraburi limestone has the greatest cementing strength compared to igneous rock and metamorphic rock. The higher strength may result from the rich in calcite which is a carbonate material. Plagioclase is usually found in igneous and metamorphic rock and has low cementation properties. The abundance of plagioclase in igneous rock, such as Buriram basalt, Nakhon Sawan dacite, and Prachinburi andesite, resulting in lower cementing strength. The lowest cementing strength of Chonburi gneiss may result from the appearance of quartz. Cementing strength of Saraburi limestone agrees well with the result from Raymond [1] who reported that the cementing strength of limestone varied from 1.0 to 2.8 MPa with an average of 1.7 MPa.

Table 6 Ballast cementing value.

Rock types	Cementing value (MPa)
Gneiss	0.2
Andesite	0.4
Dacite	0.4
Basalt	0.4
Limestone	2.5

### CONCLUSIONS

Ballasts collected from five quarries in Thailand are investigated in this study. The results show that all rocks are more or less comply with all standards. However, Buriram Basalt is considered as the best. Saraburi limestone has lower abrasion resistance and high cementing value. The carbonate rock tends to give a higher cementing strength than igneous rock and metamorphic rock, and in terms of parent mineral, plagioclase usually found in igneous and

metamorphic rock has low cementation potential. The large cementing value of Saraburi limestone may hinder its usage as a railway ballast.

Cementation properties of ballast by cementing value test, originally suggested by Raymond [1], is recommended on the selection of ballast. If this fine particle has the high cementation potential, it may bond the coarse aggregate and resulting in hard to break up the matrix of ballast. This hard spot cannot absorb the wheel/rail impact forces, and on wetting, the cemented fines may become soft and cause mud pumping.

### ACKNOWLEDGMENTS

This work was supported by Burapha University and Thailand Science Research and Innovation (TSRI) (Grant #63/2565) and by the Research and Development Fund of Burapha University to the Sustainable Civil Engineering and Infrastructure Research Unit.

### REFERENCES

- [1] Raymond R.P., Examination of Degraded Aggregate Cement Value Test, Transportation Engineering Journal of ASCE, Vol. 105, Issue 3, 1979, pp. 329-340.
- [2] Chantasorn N., Chapter 2 – Railway Track, Introduction to Railway Engineering and Modernization of Thailand's Rail Transportation and Related Industries, 3rd ed., The National Science and Technology Development Agency, 2016, pp. 31-62., in Thai.
- [3] Selig E.T. and Waters J.M., Chapter 2 – Track Components and Loading, Track Geotechnology and Substructure Management, Thomas Telford Publishing, 1994, pp. 2.1-2.15.
- [4] Federal Track Safety Standards (FTSS), Part 213, Subpart D, Office of Safety, FRA, U.S. Department of Transportation, 2014.
- [5] Indraratna B. and Salim W., Chapter 1 - Introduction, Mechanics of Ballasted Rail Tracks- A Geotechnical Perspective, Taylor and Francis, 2005, pp. 1-5.
- [6] Feng D.M., Boucher D.L. and Selig E.T., Laboratory Study of Ballast Cementing, Proceedings of 5th International Heavy Haul Railway Conference, 1993, pp. 207-214.
- [7] Boucher D.L. and Selig E.T., Application of Petrographic Analysis to Ballast Performance Evaluation, Transportation Research Record 1131, 1987, pp. 15-25
- [8] Bold R.D., Non-Destructive Evaluation of Railway Tracked Ballast, Ph.D. Thesis, Institute for Infrastructure and Environment, School of Engineering, University of Edinburgh, 2011, UK

## RECOVERY AND VALORIZATION OF DEMOLITION AND CONSTRUCTION WASTES SPREAD OVER ALL THE CITY OF CASABLANCA (MOROCCO)

Mourad MORSLI<sup>1</sup>, Mohamed TAHIRI<sup>1</sup>, Youssef HALIMI<sup>1</sup>, and Mehdi MAANANE<sup>2</sup>

<sup>1</sup> Organic Synthesis, Extraction and Valorization Laboratory, Ain Chock's Faculty of Sciences,  
Hassan II University of Casablanca, Morocco, email: [mourad.morsli@hotmail.fr](mailto:mourad.morsli@hotmail.fr);

<sup>2</sup> Geosciences Laboratory, Ain Chock Faculty of Sciences, Hassan II University of  
Casablanca, Morocco

### ABSTRACT

Morocco produces around 9 million tons per year of building waste (demolition and construction) [1]. The territorial network of recovery solutions for this waste is therefore crucial, but difficult to optimize because the waste disposal sites are temporary and present a great diversity of size and concentration. Waste collection centers must reconcile the needs of small players, the majority in the end-of-life quarry sector. It is not clear how this enormous amount of material can be obtained, especially as quarries are starting to suffer from excessive resource extraction; which results in a very negative impact on the environment

In this context, our project aims to recover and valorize this waste. In this present work, we present concrete results in recycling and exploitation of this abundant and permanent deposit and also the geolocation with GIS of the areas where are mainly deposited the demolition and construction wastes.

We have collected this waste by type and listed the elements that constitute it. After crushing and grinding the waste, we designed the representative sample. We characterized this sample by X-ray fluorescence and separated the different particle sizes by sieving. We have thus exploited each type of powder obtained to develop a suitable material.

We developed research works and obtained comforting results in particular in: The implementation of ecological and economical materials dedicated to sustainable buildings; Production from these lightweight cement materials requires only a new supplement to serve as an efficient and effective binder; The preparation of coatings, The remaining residue can finally be used in the inhibition of quarries and general construction work (Roads, bridges, rainwater storage basins, etc.)

The materials produced have been tested and characterized by X-ray fluorescence, specific surface area, resistance to compression and bending and crushing, etc. This work will be detailed in the article.

*Keywords: Demolition and construction waste materials, Recovery and recycling, lightweight cement, Coatings, ecological materials, Morocco.*

### INTRODUCTION

The building industry in general and the construction industry, in particular, are major consumers of natural resources and energy [2]. In addition, the construction sector generates unacceptable levels of waste. In recent years, the construction industry has become increasingly aware of the significant environmental impacts associated with waste generated during both the construction of new buildings and the demolition of old structures. The materials used in this study cover a wide range obtained from demolition and construction waste. Indeed, they can be classified as follows:

- Wastes from the total or partial demolition of buildings and/or civil engineering infrastructure.
- Waste resulting from the construction of buildings

and/or civil engineering infrastructure.

Construction waste management is a complex activity. There is no single recipe because such management varies from one case to another and from one trade to another. Moreover, the management of construction waste is extremely different depending on whether the work is new construction or conversion, rehabilitation, or renovation. Other decisive elements are the size of the construction site and its location (dense urban area or not, industrial area, rural area).

In this sense, we have realized the geolocation of the main sites of demolition and construction waste disposal. These wastes are crushed and then characterized and sifted to have a granular distribution of our sample on which we will base

ourselves to determine their way of valorization.

## MATERIALS ET METHODS

### Geographical location of demolition and construction waste depots in Casablanca

To have an idea of the quantity of demolition and construction waste, we have chosen the city of Casablanca, the largest city in Morocco, and taking into account different construction sites there, to make geolocation of the main sites where demolition and construction materials are thrown for a possible statistical study on this important deposit [3].

### Presentation of the materials studied

#### Demolition and construction waste

We have selected representative samples from different sites. These wastes (Figure 1) generally consist of cement blocks and rubble, sand, plaster, ceramic tiles, red bricks, and plaster, ... The limestone aggregates are substituted by deconstructed concrete aggregates to realize concrete formulations. A characterization study of the raw materials was carried out.



Fig. 1: representative samples of construction waste before crushing and grinding.

#### Cement used as an additional binder for concrete:

The cement used is portland cement (CPJ 45) by the Moroccan standard NM 10.1.004 [4] produced by the Société Ciment du Maroc.

#### The binder for coatings

Mortar is obtained by mixing a binder (lime or cement), sand, water, and possibly additives [5]. Multiple compositions of mortar can be obtained by playing on the different parameters: binder (type and dosage), additives, and water dosage.

As far as the binder is concerned, all cement and limes can be used; their choice and dosage depend on the work to be carried out and its environment. [5]

The purpose of this formulation is to highlight the possibility of using demolition and construction

waste for the preparation of mortars. In this sense, we conducted a series of tests, with variations in the rate of substitution of cement by these wastes ranging from 5 to 20% of the substituent.

The mechanical properties are analyzed and then compared with a control mortar.

## RESULTS AND DISCUSSION

### Geolocation

A motorized team with smartphones equipped with a mobile application of Geolocation was mobilized to crisscross the territory of the 8 prefectures of the municipality of Casablanca and to take note of the Cartesian coordinates (X, Y) with the insertion of the exact address, the photo of the point and the approximate estimate of the existing tonnage.

At the end of this mission, a global database of the spatial distribution of inert waste black spots in the municipality of Casablanca was generated with maps and Excel tables for each prefecture.



Fig. 2: Black spots of inert waste identified at the level of the City of Casablanca

Figure 2 shows the main sites where demolition and construction materials are discarded. Note:

- ❖ A large number of sites where demolition and construction waste are dumped, something that implies all stakeholders to give more interest to the recovery of these wastes.
- ❖ A concentration of these sites on the outskirts of the city, knowing that each site contains a very large quantity of waste.

### Physico-chemical characterization of demolition concrete waste and construction sites

After the collection of the demolition and construction waste, it was crushed and analyzed to define its physical and chemical properties. Tables 1 and 2 present the chemical composition by X-ray fluorescence and the analysis of heavy metals. A particle size analysis (Table 3) was performed on these samples to determine their recovery pathway.

Table 1 Chemical composition by FX

Elements	Waste concrete deconstruction%
SiO <sub>2</sub>	17,36
Al <sub>2</sub> O <sub>3</sub>	4,14
Fe <sub>2</sub> O <sub>3</sub>	2,16
CaO	58,94
MgO	0,89
K <sub>2</sub> O	0,47
Na <sub>2</sub> O	0,15
P <sub>2</sub> O <sub>5</sub>	0,08
MnO	0,02
SO <sub>3</sub>	2,33
TiO <sub>2</sub>	0,27
PAF	13

Table 2 Heavy metal analysis

Elements	Waste concrete deconstruction %
As	0,0006
Ba	0,0057
Cd	0
Co	0
Cr	0,0007
Cu	0,0005
Mn	0,0153
Mo	0,0001
Ni	0,0007
Pb	0,0008
Se	0,0001
Sr	0,0217
Zn	0,0024

Particle size analysis was carried out on the samples characterized to determine their recovery pathway.

#### Particle size analysis of raw materials

The dimensional analysis of the aggregates is essential to characterize the material and to know the performance of the concrete to be obtained. The test consists in classifying the different grains constituting the sample by using a series of sieves, nested one on the other, whose opening dimensions are decreasing from the top to the bottom [6].

The material studied is placed in the upper part of the sieves and the classification of the grains is obtained by the vibration of the sieve column.

Table 3 Dimensional analysis of aggregates

Sieve mesh in (mm)	Accumulated sieves	
	mass (g)	%
8	2110	22,35
5	1830	21,12

2,5	1760	20,31
1,25	1400	16,16
0,63	840	9,69
0,315	430	4,96
0,16	200	2,31
0,08	95	1,10

According to the dimensional analysis of the aggregates, we note that a great part of our sample (approximately 50%) contains aggregates with diameters (D) varying between 5 and 8mm.

To valorize this waste of BTP, we based ourselves according to the need for a granular distribution of our sample:

- ❖ D (mm) < 5 Lightweight cement
- ❖ 8 < D (mm) < 5 Coating

#### Recovery of demolition and construction waste: "Lean cement"

A large part of this experimental study was devoted to the selection of the appropriate mixing procedure. Samples were prepared by varying the proportion of demolition and construction waste into two substitution percentages of 20% and 40% which indicate the proportion of demolition and construction waste. For each formulation, we developed three specimens. In the first step, we determined the chemical composition by X-ray fluorescence (Table 4) and then analyzed the samples for heavy metals (Table 5). Density and compressive strength measurements were performed (Table 7).

Table 4 Chemical composition by FX

Elements	F 1 (20%)	F 2 (40%)
SiO <sub>2</sub>	19,25	22,29
Al <sub>2</sub> O <sub>3</sub>	4,37	4,52
Fe <sub>2</sub> O <sub>3</sub>	2,38	2,32
CaO	56,34	55,45
MgO	1,13	0,94
K <sub>2</sub> O	0,48	0,56
Na <sub>2</sub> O	0,17	0,16
P <sub>2</sub> O <sub>5</sub>	0,08	0,08
MnO	0,02	0,02
SO <sub>3</sub>	2,32	2,36
TiO <sub>2</sub>	0,30	0,32
PAF	12,56	10,79

Table 5 Heavy metal analysis

Elements	F 1 (20%)	F 2 (40%)
As	0,0003	0,0005
Ba	0,0068	0,0089
Cd	0	0

Co	0	0
Cr	0,0006	0,0008
Cu	0,0005	0,0004
Mn	0,0168	0,0144
Mo	0	0
Ni	0,0008	0,0007
Pb	0,0008	0,0005
Se	0,0002	0,0001
Sr	0,0223	0,0135
Zn	0,0019	0,0021

Table 6 Results of tests for the characterization of materials

	Natural aggregates		Construction waste	
	Crushed sand	GI gravel	GII gravel	Gravel
Granular class	0/5	8/16	14/20	0/20
Fine ratio (%) (case of sand)	13,1	***	***	***
Superficial cleanliness (%)	***	0,5	0,3	3,0
Flattening coefficient (%)	***	5	6	20
Bulk density (t/m <sup>3</sup> )	1,76	1,40	1,40	1,42
Actual density (t/m <sup>3</sup> )	2,74	2,71	2,71	2,69
Water absorption coefficient (%)	0,19	1,37	1,05	0,42

Table 7 Density and compressive strength

Formulations	Proof number	Density (g/cm <sup>3</sup> )		Compressive strength (MPa)			
		7 da	28 da	7 da	Average	28jrs	Average
F1 (20%)	1	2,37	2,38	21,5		27,5	
	2	2,37	2,38	21		27	
	3	2,37	2,39	22	21,5	28	27,5
F2 (40%)	1	2,37	2,38	19		24,5	
	2	2,36	2,38	18		23,5	
	3	2,36	2,37	18,5	18,5	24	24

Reference formulation : Rc28= 28 MPa. [NM 10.1.008: Rc7 = 19-20MPa; Rc28=28MPa]

- ❖ The densities of the F1 (2.39 g/cm<sup>3</sup>) and F2 (2.38 g/cm<sup>3</sup>) formulations at 28 days of age are similar to the density at 28 days of the reference formulation (2.39 g/cm<sup>3</sup>);
- ❖ The compressive strength at 28 days of the age of the F1 mix (20%) is acceptable compared to the NM 10.1.008 standard [7] for a class B25 concrete;
- ❖ When the substitution of natural aggregates by waste limestone aggregate concrete exceeds 20%, the compressive strength does not meet the requirement of the said standard.

#### Recovery of demolition and construction waste: "Coating"

#### Experimental program

A classical mortar should be composed of one part cement, three parts sand, and half a part water [8].

The cement, sand, water, and equipment must be at laboratory temperature for homogenization purposes.

Each batch is mixed mechanically in the mixer. The mixer is in running position.

For this experimental approach, 4 formulations with percentages of addition going from 0 to 20% of demolition waste were prepared.

The tests were carried out using specimens with dimensions of 40×40×160 mm (Figure 3).

The different compositions of the mortars are grouped in the table below:

Table 8 Composition of mortars

Mortars	Sand (g)	Cement (g)	Water (g)	Construction waste (g)
G1 (0%)	1350	450	225	0
G2 (5%)	1350	427.5	225	22,5
G3 (10%)	1350	405	225	45
G4 (20%)	1350	360	225	90

Fig. 3: Specimens of dimensions: 40×40×160 mm



The specimens emerged without delay, suitably, either horizontally or vertically, in water at 20°C±1°C and in suitable containers.

The age of the specimens is counted from the moment the cement and water are mixed until the beginning of the test.

#### Intake tests

The objective is to determine the start and end times of the setting of the dough using a Vicat device.

When the moving part is released the Vicat needle stops at a distance from the bottom of the mold such that  $d = 4 \text{ mm} \pm 1 \text{ mm}$ .

The end of the set corresponds to the moment when the dough has become a rigid block, the moment when the needle is only 0.5 mm deep in the dough [9].

The results are grouped in the following tables (9 and 10):

Table 9 Results tests start taking

Formulation	Start of taking (min)
G1 (0%)	205
G2 (5%)	199
G3 (10%)	201
G4 (20%)	195



Table 10 Results tests end of the intake

Formulation	End of taking (min)
G1 (0%)	275
G2 (5%)	263
G3 (10%)	272
G4 (20%)	260

According to the experimental results, the substitution of cement with construction waste has no considerable effect on the beginning or the end of the mortar.

### Specific surface

The mineral additives are currently among the most recent developments in the production of cement because their uses provide an improvement in the mechanical and chemical properties (durability) of cementitious materials (mortar and concrete) [10]. On the other hand, their use has the objective of reducing the consumption of clinker, contributing simply and economically to solving environmental problems.

The specific surface of the different formulations has been determined by the Blaine method (Blaine Permeabilities) [11]. This fineness is an important characteristic, during the mixing process, the greater the surface area of the cement in contact with the water, the faster and more complete the hydration. (Table 11)

Table 11 Results specific area measurement

Formulation	Specific area (cm <sup>2</sup> /g)
G1 (0%)	3565
G2 (5%)	3570
G3 (10%)	3567
G4 (20%)	3572

By comparing the specific surfaces of the formulations with different additions of the demolition waste, we can consider that the variation in the values of the specific surface is negligible, indeed the substitution of cement with construction waste does not have a remarkable influence on the specific surface.

### Laboratory testing

The mechanical properties of the prepared mortars are determined by the method of determining the compressive and flexural strengths of a cement mortar according to the Moroccan Standard NM 10.1.005 [12].

The half-prisms obtained in the bending test must be tested in compression on the lateral faces of the casting under a section of 40×40 mm.

The results of the flexural and compressive strength test at the ages of 2d and 7d are presented in the following table 12:

Table 12 Results of the flexural and compressive strength test

Mortars	2 days		7 days	
	Flexion (Pa)	Compression (MPa)	Flexion (Pa)	Compression (MPa)
G1(0%)	4,2	19,5	5,3	31,1
G2(5%)	3,9	17,4	5,7	27,3
G3(10%)	3,7	15,3	4,9	23,7
G4(20%)	2,7	12,8	3,9	18,9

Fig. 4: Graph of the flexural strength test at the ages of 2d and 7d

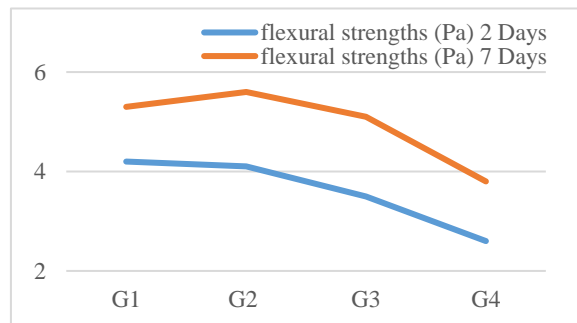
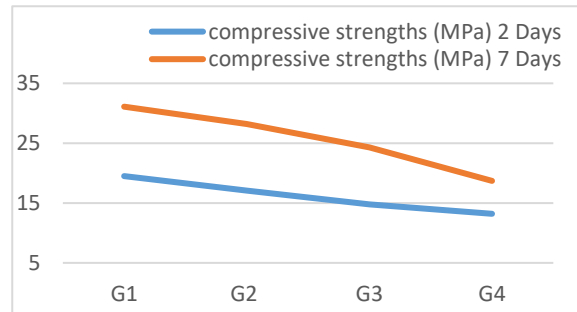


Fig. 5: Graph of the compressive strength test at ages 2d and 7d



Comparing the flexural and compressive strengths of mortars prepared with different additions of demolition waste, we can observe that the strengths drop considerably from the second day compared to the reference mortar without the addition of demolition waste.

Thus, the higher the substitution rate of demolition waste, the lower the strength.

To correct the revealed strength defects, a plasticizing admixture is used to improve the mechanical properties of the mortars [13].

Taking into account these results, tests with the addition of admixture estimated at 0.1% were carried out only on the reference formulations (G1: No addition) and on tone substitution of 20% of cement by demolition waste.

Since 20% substitution of demolition waste gives the lowest results, we believe that if the results with admixture are improved on this sample, they will also be improved for the other tests.

According to the datasheet of the admixture used,

it is a plasticizer that increases the mechanical resistance, reduces the cement dosage, and increases the setting time at 20°C (a delay in the setting of about 3 to 4 hours is obtained with 0.1%).

The results are grouped in the following table 13:

Table 13 The results of the flexural and compressive strength test at the ages of 2 and 7 ( with adjuvant addition)

Mortars	2 days		7 days	
	Flexion (Pa)	Compression (MPa)	Flexion (Pa)	Compression (MPa)
G1 (0%)	4.2	19,5	5,3	31,1
G2 (20%)	4,8	25,8	7,1	41,7

By comparing the results of the bending and compressive strengths of the different formulations with the reference formulation without demolition waste and adjuvant, we find that the use of adjuvant gives very beneficial and better results even than the strength of the reference mortar (without addition: G1).

## CONCLUSIONS

We proposed and compared different tests on concrete mortars. The first results show that for the manufacture of lean cement or coatings by the substitution of natural aggregates up to 20% of the concrete waste of limestone aggregates gives very conclusive consequences that can be further improved with the addition of admixtures.

## REFERENCES

- [1] CETEMCO. (2020). CETEMCO. Valorisation des déchets de déconstruction (V2D). <https://cetemco.org/rd/valorisation-des-dechets-de-deconstruction-v2d/>
- [2] Lieberherr-Gardiol, F. (2007). Durabilité urbaine et gouvernance, enjeux du xxie siècle. *Revue internationale des sciences sociales*, 193194 (3), 373-385.
- [3] Zarouali, M. J. E. (2014). Le Secteur des BTP au Maroc : Aspects économiques et Sociaux. *Dossiers de Recherches en Économie et Gestion*, 3(1), 31-46.
- [4] Institut Marocain de Normalisation (IMANOR), NM 10.1.004, Ciment et constituants des ciments, Partie 1 : composition, spécifications et critères de conformité, 2019.
- [5] Ahmed Abdo, A. E. (2017). Valorisation du déchet de marbre et de verre comme additif dans la production du mortier (Doctoral dissertation, Université Mohamed Boudiaf-M'sila).
- [6] Biryondeke, C. B., Ngapgue, F., & Musangi, G. O. (2016). Etude du coefficient d'absorption d'eau des

granulats d'origine volcanique de Goma et son influence dans la formulation du béton. *International journal of innovation and applied studies*, 15(1), 141.

[7] Institut Marocain de Normalisation (IMANOR), NM 10.1.008, Bétons - Spécification, performances, production et conformité, 2010.

[8] GUERBAS, T. (2015). Etude du comportement d'un mortier a base de sable mixte (sable de dune et sable concassé) armé de fibres synthétiques (Doctoral dissertation, university of M'sila).

[9],[10] Zeyneb, B. (2016). Influence de la surface spécifique des ciments aux ajouts minéraux (calcaire) sur le comportement mécanique du mortier (Doctoral dissertation, Université De Mohamed Boudiaf M'sila Faculté De Technologie).

[11] Blaine, R. L. (1941). Etudes de la mesure de surface spécifique par perméabilité à l'air. *Société américaine pour le matériel d'essai*.

[12] Institut Marocain de Normalisation (IMANOR), NM 10.1.005, Liants hydrauliques, techniques des essais, 2008.

[13] Belferrag, A. (2016). Contribution à l'amélioration des propriétés mécaniques et rhéologiques des bétons de sable de dunes (Doctoral dissertation, Université Mohamed Khider-Biskra).

## THE EFFECT OF LDPE PLASTIC WASTE ON THE COMPRESSIVE STRENGTH OF PAVING BLOCKS

Fauzan<sup>1</sup>, Rani Fahmi Zakaria<sup>1</sup>, Dyan Adhitya Nugraha M<sup>1</sup> and Zev Al Jauhari<sup>2</sup>

<sup>1</sup>Engineering Faculty, Andalas University, Indonesia

<sup>2</sup>Department of Civil Engineering, Bengkalis Polytechnic, Indonesia

### ABSTRACT

Plastic is one of the most common environmental problems in the world. One way to reduce plastic waste is by reusing it to produce other materials such as partial replacement of sand in paving blocks mixture. Paving block (concrete brick) is a building material made of a mixture of water, aggregate and portland cement. An experimental study was carried out to investigate the effect of LDPE and PET plastics as a substitute for fine aggregates on the compressive strength of paving blocks. In this study, paving blocks are planned to be of plan C quality with a minimum compressive strength of 12.5 MPa, which is usually used as a pedestrian facility. LDPE and PET plastics waste is used as partial replacement of fine aggregates, with variations of 0%, 5%, 10% and 15% of the fine aggregates volume. The compressive strength test was carried out on cylinder specimens of 150mm diameter and 300 mm length. The results shows that the use of LDPE and PET plastics waste as a partial replacement of fine aggregate decreased the compressive strength of paving blocks, in which the use of 5%, 10% and 15% of plastic reduced the compressive strength by 35.26%; 37.69%; 40.68% for LDPE, 34.15%; 52.22%; 56.53% for PET, and 23.14%; 18.01%; 24.65% for LDPEF, respectively. However, the compressive strength result of the tested paving blocks predominantly exceeds the minimum requirement for compressive strength of paving block quality C, which is 12.5 MPa.

*Keywords: Plastic waste, Paving block, Concrete bricks, Compressive strength, Fine aggregates*

### INTRODUCTION

Paving block or concrete brick is a composition of building materials made from a mixture of water, aggregate and Portland cement or similar hydraulic adhesive materials, with or without other additives that do not reduce the quality of paving blocks or concrete bricks [1].

To produce paving blocks that are more environmentally friendly and economical, other materials can be used as a substitute for paving block mixtures, one of which is plastic waste. Plastic is one of the most common environmental problems in the contemporary world. The disposal of this plastic is considered a major challenge due to its non-biodegradable nature and pollutant [2], [3].

According to the Central Pollution Control Board, the world produces nearly 150 million tons of plastic per year, equivalent to 4.8 tons per second [4]. Meanwhile, in Indonesia itself, according to the Secretary General of the Indonesian Olefin, Aromatic and Plastic Industry Association (Inaplas), plastic consumption has grown from 4.5 million tons in 2015 to 4.8 million tons in 2016, or grew by 5.2%. This increase in consumption is mainly driven by the growth of the food and beverage industry, where the industry uses a lot of plastic for its product packaging [5].

One alternative to reduce this plastic waste is the reuse of plastic to produce other materials [3]. In

addition to waste plastic, many other materials have been trialled as replacement materials in concrete mixes, including recycled electrical cable rubber [6] waste polystyrene [7], and scrap-tire rubber. The construction industry can use a large amount of solid waste, one of which is in the production of paving blocks [8]. The use of plastic in the manufacture of paving blocks can increase compressive strength and reduce the use of raw materials, the most important thing is that it is environmentally friendly and helps to reduce environmental problems [9], [10].

Currently, many studies are being carried out regarding the use of plastic waste as paving blocks. In each year 60million barrels of oil and another type of insulation would be safe by exploiting of plastic foam insulation in buildings [11]. The compressive strength value of using 10% LDPE plastic as a substitute for sand in paving blocks is greater than the 0% variant (without plastic waste mixture) which is 23.98 MPa and 23.68 Mpa, respectively [4]. The application of pavement blocks is perfect on pathways and street ways as it is a simple way of finishing and laying, also cost-effective compared to conservative paving blocks [12], [13].

Based on the background above and also the concern about the increasing amount of plastic day by day while decomposition takes a very long time, an experimental study was carried out to investigate the effect of using LDPE and PET plastic waste as a partial substitute for fine aggregates on the

compressive strength of paving blocks.

## MATERIALS AND METHODS

### Ingredients Used

#### Cement

The cement used in this study is Portland Composite Cement (PCC) produced by PT Semen Padang in Indonesia.

#### Fine aggregates

Fine aggregates in the form of locally available sand are used, with a maximum size of 4.75mm. the proportion of the fine aggregate can be seen in Table 1.

Table 1 Properties of fine aggregates

Characteristic	Value
<i>Fine modulus (FM)</i>	2.85
Rate of water	1.42%
Fill weight	1.41 kg/L
Specific gravity	2.50
Absorption	3.09%

#### Coarse aggregates

Locally available coarse aggregates of spilt are used Ø5-10 and Ø10-20. The properties of coarse aggregates can be seen in Table 2.

Table 2 Properties of coarse aggregates

Characteristic	Value	
	Ø5-10	Ø10-20
<i>Fine modulus (FM)</i>	5.34	6.94
Rate of water	1.32%	0.77%
Fill weight	1.33 kg/L	1.38 kg/L
Specific gravity	2.61	2.53
Absorption	3.20%	2.81%

#### Water

The water used for the mixture of paving blocks and curing is tap water that does not contain acids or organic substances.

#### PET plastic

The PET plastic used comes from plastic waste from mineral drink bottles, as shown in Fig. 1. This PET plastic is processed into fine aggregates by melting and then crushing a maximum of 4.75mm [14]. Table 3 shows the properties of PET Plastic

waste. The process of PET plastic waste to be fine aggregate is shown in Fig. 2.

Table 3 Properties of PET plastic

Characteristic	Value
Size	0.1 mm - 4.75 mm
Shape of PET	Irregular
Specific gravity	1.38 g/mL



Fig. 1 PET plastic.



Fig. 2 PET plastic processing.

#### LDPE plastic

Recycled LDPE plastic seeds are shown in Figs. 3 and 4. The properties of LDPE Plastic wastes is shown in Table 4.

Table 4 Proportions of LDPE plastic

Characteristic	Value
Size	(3.0 - 4.75) mm
Shape of LDPE	Pellets, Flattened round
Specific gravity	0.94 g/mL



Fig. 3 Shape of plastic LDPE pellet.



Fig. 4 Shape of plastic LDPE flattened round.

#### Fly ash

The fly ash used comes from the SBB Thamrin Nine Batching Plant, Jakarta, Indonesia.

#### Implementation Methods

##### Mix design

Mix design is calculated based on (American Concrete Institute) ACI-211.4R-93. Paving blocks are planned to be of plan C quality with a minimum compressive strength of 12.5 MPa. The ratio of cement volume : sand : split is (1 : 3.75 : 3.46) with w/c 0.681.

LDPE and PET plastic waste serves as a partial substitute for fine aggregates, where the amount of plastic added to the paving block mixture is based on the fine aggregate volume of concrete paving blocks (cement: quarry dust: sand = 1:1:2) by weight or volume were produced to serve as control having tested the compressive strength and water absorption properties [15].

There are three variations of paving blocks, namely PET paving blocks, LDPE paving blocks and LDPE fly ash (LDPEF) paving blocks. The fly ash

content used is 15% by replacing the weight of cement. The composition of the volume and weight of the material in 1m<sup>3</sup> mixture of paving blocks with PET, LDPE and LDPEF are shown in Tables 5 to 10.

Table 5 The composition of the material volume in 1m<sup>3</sup> mixture of paving blocks with LDPE

Material	Composition (%)			
	LDPE 0%	LDPE 5%	LDPE 10%	LDPE 15%
Cement	0.10	0.10	0.10	0.10
Sand	0.35	0.34	0.32	0.30
Split	0.33	0.33	0.33	0.33
Water	0.20	0.20	0.20	0.20
Air	0.02	0.02	0.02	0.02
LDPE	-	0.02	0.04	0.05

Table 6 The composition of the material weight in 1m<sup>3</sup> mixture of paving blocks with LDPE

Material	Composition (kg)			
	LDPE 0%	LDPE 5%	LDPE 10%	LDPE 15%
Cement	298.30	298.30	298.30	298.30
Sand	887.47	843.10	798.73	754.35
Split	836.96	836.96	836.96	836.96
Water	203.14	203.14	203.14	203.14
LDPE	-	16.68	33.37	50.05

Table 7 The composition of the material volume in 1m<sup>3</sup> mixture of paving blocks with PET

Material	Composition (%)			
	PET 0%	PET 5%	PET 10%	PET 15%
Cement	0.10	0.10	0.10	0.10
Sand	0.35	0.34	0.32	0.30
Split	0.33	0.33	0.33	0.33
Water	0.20	0.20	0.20	0.20
Air	0.02	0.02	0.02	0.02
PET	-	0.02	0.04	0.05

Table 8 The composition of the material weight in 1m<sup>3</sup> mixture of paving blocks with PET

Material	Composition (kg)			
	PET 0%	PET 5%	PET 10%	PET 15%
Cement	298.30	298.30	298.30	298.30
Sand	887.47	843.10	798.73	754.35
Split	836.96	836.96	836.96	836.96
Water	203.14	203.14	203.14	203.14
PET	-	24.49	48.99	73.48



Table 9 The composition of the material volume in 1m<sup>3</sup> mixture of paving blocks with LDPE fly ash (LDPEF)

Material	Composition (%)			
	LDPEF 0%	LDPEF 5%	LDPEF 10%	LDPEF 15%
Cement	0.08	0.08	0.08	0.08
Sand	0.35	0.34	0.32	0.30
Split	0.33	0.33	0.33	0.33
Water	0.20	0.20	0.20	0.20
LDPE	-	0.02	0.04	0.05
Fly Ash	0.01	0.01	0.01	0.01

Table 10 The composition of the material weight in 1m<sup>3</sup> mixture of paving blocks with LDPE fly ash (LDPEF)

Material	Composition (kg)			
	LDPEF 0%	LDPEF 5%	LDPEF 10%	LDPEF 15%
Cement	253.55	253.55	253.55	253.55
Sand	887.47	843.10	798.73	754.35
Split	836.96	836.96	836.96	836.96
Water	203.14	203.14	203.14	203.14
LDPE	-	16.68	33.37	50.05
Fly Ash	44.74	44.74	44.74	44.74

#### Manufacture of test specimen

Totally, 36 cylindrical specimens of 150mm diameter and 300mm were prepared for compressive strength tests, as shown in Table 11 and Fig. 5.

#### The curing of test specimens.

The curing of the test specimen is carried out in a water bath available at the Materials and Structural Laboratory of the Department of Civil Engineering, Andalas University, as shown in Fig. 6. The curing process used is to curing water for 28 days.

Table 11 The number of test specimens

Test specimen type	The number of test specimen
LDPEF	12
PET	12
LDPE	12



Fig. 5 The molding of test specimens.



Fig. 6 The curing of test specimens.

#### The testing of test specimens

Testing the compressive strength of the paving block was carried out using a Universal Testing Machine at the Material, Soil Mechanics and Highway Laboratory, Department of Civil Engineering, Padang State University, as shown in Fig. 7.



Fig. 7 Compressive strength test of cylinder test specimens.

## RESULTS AND DISCUSSION

The results of compressive tests performed on paving blocks with variations in the LDPE mixture are shown in Tables 12, 13 and Fig. 8.



Table 12 Compressive strength test results

LDPE (%)	Compressive strength (MPa)		
	LDPE	PET	LDPEF
0	19.32	19.32	15.36
5	12.51	12.72	13.55
10	12.04	9.23	14.46
15	11.46	8.40	13.29

Table 13 Percentage decreased of the compressive test results

LDPE (%)	Compressive strength (%)		
	LDPE	PET	LDPEF
0	-	-	-
5	35.26	34.15	23.14
10	37.69	52.22	18.01
15	40.68	56.53	24.65

As can be seen in Table 12, the result of the compressive strength of the cylinder test specimen without the addition of LDPE plastic waste is 19.32 MPa. The lowest compressive strength value is 11.46 MPa when replacing 15% of the sand volume with LDPE. Replacement of 5% and 10% volume of sand with LDPE results in the compressive strength of 12.51 MPa and 12.04 MPa, respectively. Meanwhile, for specimen without the PET plastic waste content, the compressive strength value is 19.32 MPa. The compressive strength results by replacing 5%, 10% and 15% of the volume of sand with PET is 12.72 MPa, 9.23 MPa and 8.40 MPa, respectively. For paving blocks containing combined LDPE and fly ash (LDPEF), on the other hand, the lowest compressive strength value is 13.29 MPa when replacing 15% of the volume of sand with LDPE, which is slightly decreased compared with the specimen without the addition of LDPE plastic waste content (15.36 MPa). The replacement of 5% and 10% of sand volume with LDPE results in the compressive strength of 13.55 MPa and 14.46 MPa, respectively.

The decrease in the lowest compressive strength value occurred when the LDPEF was 10% with a decrease of 18.01%, while the decrease in compressive strength value was greatest when PET was 15% with a large decrease of 56.53%.

Based on Fig. 8, it can be seen that the replacement of sand by LDPE and PET plastics causes a decrease in the compressive strength of paving blocks. The reason for this reduction in strength is associated with the smooth surface of the plastic that reduce the adhesion between plastic particles and cement paste [2], [16].

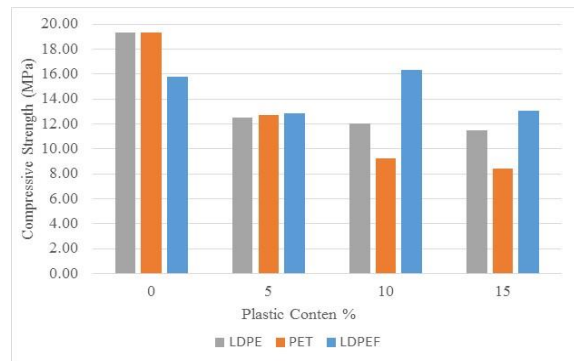


Fig. 8 Compressive strength of plastic use as a fine aggregate paving block.

## CONCLUSION

The use of LDPE and PET plastic waste as the partial replacement of fine aggregate decreased the compressive strength of paving blocks with the increase of plastic waste content. For paving blocks containing LDPE plastic waste, the use of 5%, 10% and 15% of the plastic waste, decrease the compressive strength by 35.26%, 37.69%, and 40.68%, respectively, while it decreased 34.15%, 52.22%, and 56.53%, respectively for paving blocks containing PET plastic waste. As for the use of combined fly ash and LDPE plastic waste (LDPEF) in paving block mixture, the decrease of the compressive strength was respectively 23.14%, 18.01%, and 24.65%. However, the compressive strength result of tested specimens predominantly exceeds the minimum requirement for compressive strength of paving block quality C, 12.5 MPa, so it can be used for pedestrian facilities.

## ACKNOWLEDGMENTS

The authors gratefully acknowledge the financial support from Andalas University. The author also would like to thank the staff of the Material and Structural Laboratory, of the Department of Civil Engineering, Andalas University for their help and support.

## REFERENCE

- [1] SNI 03-0691-1996, Concrete Bricks (Paving Block), Indonesian National Standardization Agency, pp.1-9, 1996.
- [2] Ohemeng. E. A., Yalley P. P. K., Dadzie J., and Djokoto S. D., Utilization of Waste Low Density Polyethylene in High Strengths Concrete Pavement Blocks Production, Civil and Environmental Research, Vol.6, No.5, 2014, pp.126-135.

- [3] Ghuge J., Surale S., Patil B.M. and Bhutekar S.B., Utilization of Waste Plastic in Manufacturing of Paver Blocks, System, International Research Journal of Engineering and Technology, Vol.6 No.4, 2019.
- [4] Ferreira L., Brito J. D., and Saikia N., Influence of curing conditions on the mechanical performance of concrete containing recycled plastic aggregate, Construction and Building Materials, Vol.36, 2012, pp.196-204.
- [5] Indrawijaya B., Wibisana A., Setyowati A. D., Iwadi D., Naufal D. P., and Pratiwi D., Utilization of LDPE Plastic Waste as a Substitute for Aggregates for The Manufacture of Concrete Paving Blocks, Jurnal Ilmiah Teknik Kimia, Vol.3, No.1, 2019.
- [6] Yildirim S. T. and Duygun N. P., Mechanical and physical performance of concrete including waste electrical cable rubber, IOP Conf. Ser. Mater. Sci. Eng. 245, 2017, 022054.
- [7] Herki B.A. and Khatib J.M., Valorisation of waste expanded polystyrene in concrete using a novel recycling technique, Eur. J. Environ. Civil Eng. 21, 2017, pp.1384–1402.
- [8] Mohan D.M.S., Vignesh J., Iyyappan P. and Suresh C., Utilization of plastic bags in pavement blocks. International Journal pure Application Mathematics, Vol.15 No.119, 2018, pp.1407-1415.
- [9] Ahmad N.F.A., Razali S. N. M., Sahat S., and Kaamin M, PET Concrete as Paver Block, AIP Conf. Proc., 2016, 020015-1 – 020015-6.
- [10] Gesoglu M., Güneyisi E., Hansu O., Etli S. and Alhassan M., Mechanical and fracture characteristics of self-compacting concretes containing different percentage of plastic waste powder, Constr. Build. Mater. 140, 2017, pp.562–569.
- [11] Mittal K., Agrawal S., Bhadoria, O.P.S. and Pandey M., Sustainability and limitation of Plastic Modified Bituminous Interlocked Paving Block, International Journal of Innovative Technology and Exploring Engineering, Vol.9, No.8, 2020.
- [12] Loganayagan, Keerthana, Abishek and Vetrivel A., Study on plastic PET bottles characteristic to develop eco-friendly plastic paver blocks, IOP Conference Series: Materials Science and Engineering, 1059, 2021, 012042.
- [13] Pandey A.N., Yadav A. and Chaudhary D, Waste Plastic Used in Paving Block, International Journal of Scientific Research and Review, Vol.7, No.4, 2019, pp.279-543.
- [14] Thorneycroft J., Orr J., Savoikar P., and Ball R. J., Performance of Structural Concrete with Recycled Plastic Waste as A Partial Replacement for Sand, Construction and Building Materials 161, 2018, pp.63-69.
- [15] Agyeman S., Obeng-Ahenkora N.K., Assiamah S. and Twumasi G, Exploiting recycled plastic waste as an alternative binder for paving blocks production, Case Studies in Construction Materials, Vol.11, 2019, 00246.
- [16] Ebrahim R., Mehdi D., Morteza H. B., Hamed A. and Iman M. N, On the mechanical properties of concrete containing waste PET particles, Construction and Building Material, Vol.47, 2013, pp.1302-1308.

# FRAGILITY CURVE DEVELOPMENT OF SCHOOL BUILDING IN PADANG CITY WITH AND WITHOUT RETROFITTING DUE TO EARTHQUAKE AND TSUNAMI LOADS

Fauzan<sup>1</sup>, Ruddy Kurniawan<sup>2</sup>, Nandaria Syahdiza<sup>3</sup> and Zev Al Jauhari<sup>4</sup>

<sup>1,2,3</sup>Engineering Faculty, Andalas University, Indonesia

<sup>4</sup>Department of Civil Engineering, Bengkalis Polytecnic, Indonesia

## ABSTRACT

SMPN 25 building in Padang City is a junior high school building that located in the high seismic zone and prone to tsunami. Based on the results of the initial analysis of the existing building using the current Indonesian building codes, this building have not been able to withstand the working earthquake and tsunami loads. In this study, the retrofitting of the building was designed using concrete jacketing that is with additional dimensions and reinforcement, aimed at making the building function as a vertical evacuation. The structural fragility curve of the building is determined for before and after retrofitting for both earthquake and tsunami loads. The fragility curve is determined from the ductility of the building for each variation of earthquake acceleration based on the Hazus standard. The first yield displacement was determined from the pushover analysis, and the ultimate displacement was determined from the time history analysis. The earthquake acceleration records used were the El-cento earthquake, the Northridge earthquake, the Kobe earthquake and the Padang earthquake. The results of the analysis show that the retrofit of the building structure using concrete jacketing reduce the probability of damage to the building structure by 42.06% at the level of extensive damage and by 4.42% at the level of complete damage at PGA 0.6g.

*Keywords: Fragility curves, School building, Tsunami loads, Earthquake, Retrofit*

## INTRODUCTION

The tsunami disaster hit West Sumatra in 1797 in Siberut and in 1833 in Sipora-Pagai, Mentawai Island, West Sumatra Province, Indonesia. These two tsunamis had different effects, both in terms of time to reach and inundation height [1].

Singh's (2008) research stated that the time interval between the occurrence of the first strong earthquake and the onset of the tsunami that hit the Padang coast was about 20-30 minutes. Judging from the map of the Padang city earthquake inundation, people must save themselves with a distance of 3-5 km to get to a safe area. With this data, it is estimated that the community does not have enough time to evacuate horizontally so that it will be more effective to evacuate vertically [2].

Vertical evacuation must be supported by a strong building structure that is resistant to earthquake and tsunami loads. In addition to the structure of the building must be strong enough to withstand earthquake loads that occur, the building must be able to withstand the load caused by the tsunami wave [2].

SMPN 25 Padang is an existing building in the Padang city which is located in the tsunami red zone area. An analysis of the existing building of SMPN 25 Padang based on the current Indonesian seismic standard (SNI 1726-2019) [3] and tsunami loads (FEMA P-646\_508) [4] had been carried out which aims to see the ability of the building structure to

withstand a combination of earthquake and tsunami loads. The results obtained from the structural analysis of the existing building shows that several structural elements are not able to withstand the tsunami loads acting on the building structure, so it is necessary to design the retrofit of the building structure so that the building can be used as a tsunami vertical evacuation.

In order to observe the probability of the occurrence structural damage of the building, a fragility curve of the school building with and without retrofitting due to earthquake loads and tsunami loads was developed.

## ANALYSIS OF THE STRUCTURE

### Structural Modelling

SMPN 25 building is an existing building in the Padang city which is located in a tsunami inundation area, around 0.97 km from the coastal line (Fig. 1). The building is located on Beringin Raya street, Lolong Belanti, North Padang, Padang City, West Sumatra, with coordinates latitude -0.919197 and longitude 100.357238. The building is four-story reinforced concrete structure with 15 m height.

In this study, the building structure was modeled with and without retrofitting using ETABS v.18. Plans and 3D modeling of building structures is shown in Figs. 2 and 3.

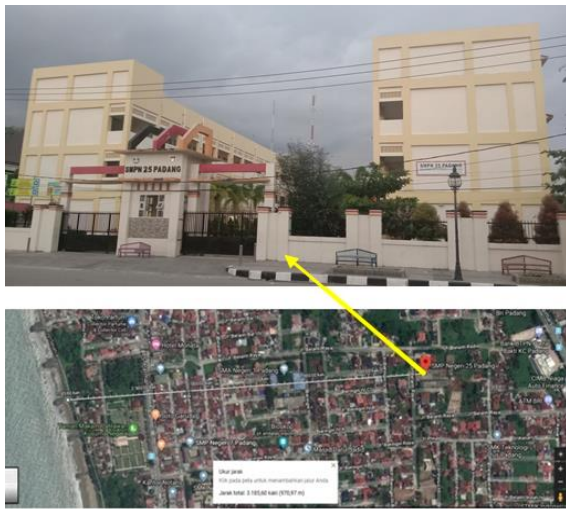


Fig. 1 The front view and the location of SMPN 25 building in Google Earth software.

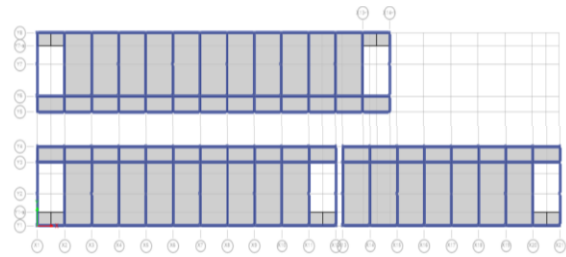


Fig. 2 The plan of SMPN 25 Padang building.

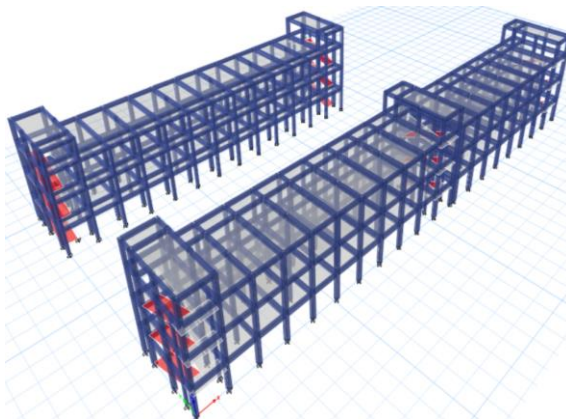


Fig. 3 The 3-D modeling of SMPN 25 building using ETABS.

### Earthquake Load

The earthquake load used in this study is the response spectrum based on SNI 1726-2019 for building analysis with and without retrofitting and ground motion earthquake data (time history) for non-linear time history analysis which is needed as an engineering demand parameter (EDP) in the calculation of the fragility curve. In this study, the

ground motion earthquake data uses 4 ground motion earthquake recording data, as shown in Table 1. Each ground motion earthquake data is matched with the earthquake characteristics of the Padang city for medium soil types using Seismomatch software. Each ground motion earthquake data is scaled with a variation of 0.2 to 2.0 with an interval of 0.2.

Table 1 Earthquake peak ground acceleration

Earthquake	Original PGA	PGA matched
El-Centro 1940	0.36 g	0.63 g
Northridge 1994	0.60 g	0.76 g
Kobe 1995	0.34 g	0.60 g
Padang 2009	0.60 g	0.60 g

### Tsunami Loads

The tsunami load was calculated based on the FEMAP-646-508 2012 with an inundation depth of 4.5 meters based on the inundation map of the Padang city. In this study, the calculation result of the tsunami loads on the building structure are hydrostatic force (49.166 kN), buoyant force (5.396 kN), hydrodynamic force (12.947 kN), impulse loads (19.421 kN), debris impact loads (401.431 kN), debris damming loads. (5244.426 kN), uplift load (0.001 kN) and extra gravity load (5.396 kN). These loads are applied to structural components such as columns and slabs.

### FRAGILITY CURVE DEVELOPMENT

In this study, an analytical method was carried out to obtain the fragility curve of the building with and without retrofitting due to earthquake and tsunami loads.

### Existing Building Analysis

The analysis of the existing building includes checking the cross-sectional capacity of the column and beam elements of the building against earthquake loads and combined earthquake and tsunami loads acting on the structure [5].

### Structural Retrofitting

An alternative design for retrofitting the building structure against tsunami loads is by using the concrete jacketing method, that is a method by enlarging the column cross section and adding flexural reinforcement and column shear around the old column [6]. In this study, retrofitting using concrete jacketing was designed for several structural elements in the building structure which have not been able to carry the load acting on the building structure due to the addition of the tsunami loads.

### Analytical Fragility Curve Development

The development of the fragility curve was carried out based on the Hazus standard [7], [8] and is developed using the Probabilistic Seismic Demand Model (PSDM) method with a cloud approach. The parameters used in the calculation of the fragility curve are obtained from the results of pushover analysis in the form of drift yield values and from the results of non-linear time history analysis in the form of maximum drift values [9].

## RESULTS AND DISCUSSION

### Load Bearing Capacities of Existing Building Structure

The analysis of the flexural cross-sectional capacity of the existing building structure can be seen in the axial-flexural (P-M) interaction diagram of the column (Fig. 7). Table 3 shows the shear capacity of the existing building column. The beam flexural cross-sectional capacity is shown in Table 4.

Based on the analysis of the existing building of SMPN 25 Padang against earthquake and tsunami loads, there are several structural elements that have not been able to withstand the tsunami loads such as the 2<sup>nd</sup> floor columns and the 1st floor beams. The structural elements that have not been able to withstand the tsunami loads is shown in Fig. 4.

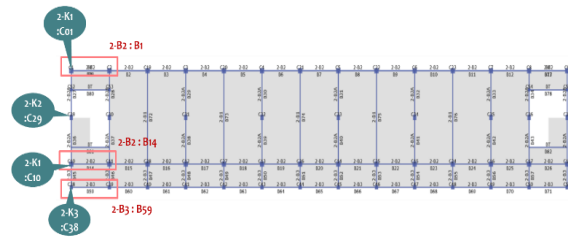


Fig. 4 Structural elements that have not been able to withstand the tsunami load.

### Concrete Jacketing Retrofit

Retrofitting design using concrete jacketing on weak structural elements was carried out based on the results of existing building analysis and the minimum requirements for adding dimensions and reinforcement for jacketing.

Dimensions details of the retrofitted structural elements is shown in Table 2 and Fig. 5. Fig. 6 shows the modeling of the retrofitted building structure.

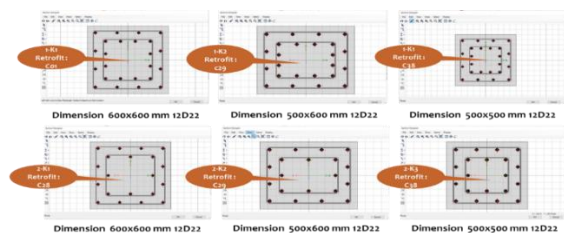


Fig. 5 Steel reinforcement details of the concrete jacketed columns.

Table 2 Concrete jacketing dimension of retrofitted SMPN 25 Padang building

Story	Existing columns				Concrete jacketed columns			
	Column type	Dimension (cm)	Ø (mm)	Number of rebar	Column type	Dimension (cm)	Ø (mm)	Number of jacket rebar
Story 1	1-K1 (C01)	45x45	22	12	1-K1 retrofit (C01)	60x60	22	12
	1-K2 (C29)	45x35	22	12	1-K2 retrofit (C29)	50x60	22	12
	1-K3 (C38)	35x35	22	12	1-K3 retrofit (C38)	50 x50	22	12
Story 2	2-K1 (C01)	45x45	22	8	2-K1 retrofit (C01)	60x60	22	12
	2-K2 (C29)	45x35	22	8	2-K2 retrofit (C29)	50x60	22	12
	1-K3 (C38)	35x35	22	8	2-K3 retrofit (C38)	50x50	22	12

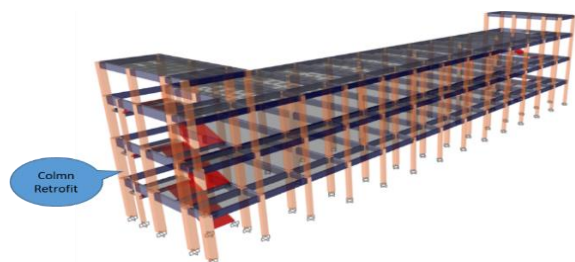


Fig. 6 The 3-D modeling of retrofitted SMPN 25 Padang building with concrete jacketing.

### Load Bearing Capacities of Structure With and Without Retrofitting

The P-M interaction diagram is used to describe the capacity of the column to withstand the working load. Figure 7 shows the comparison of the P-M interaction diagram obtained from the results of the structural analysis of the building with and without retrofitting. From the figure, it can be seen that retrofitting on columns improves the capacity of the building structure, in which columns of the retrofitted building have been able to withstand tsunami loads acting on the structure. The comparison of the shear



capacity of the column with and without retrofit is shown in Table 3. As can be seen from the table, the shear capacity of the columns improves after the retrofitting, in which the beam shear capacity of the retrofitted building can resist the applied working loads including tsunami loads.

The comparison of the flexural capacity of the beam with and without retrofit is shown in Table 4. As seen in the table that retrofitting on columns improves the capacity of the beam, so the beams are able to withstand the tsunami loads. The beam shear capacity is also able to withstand the tsunami loads.

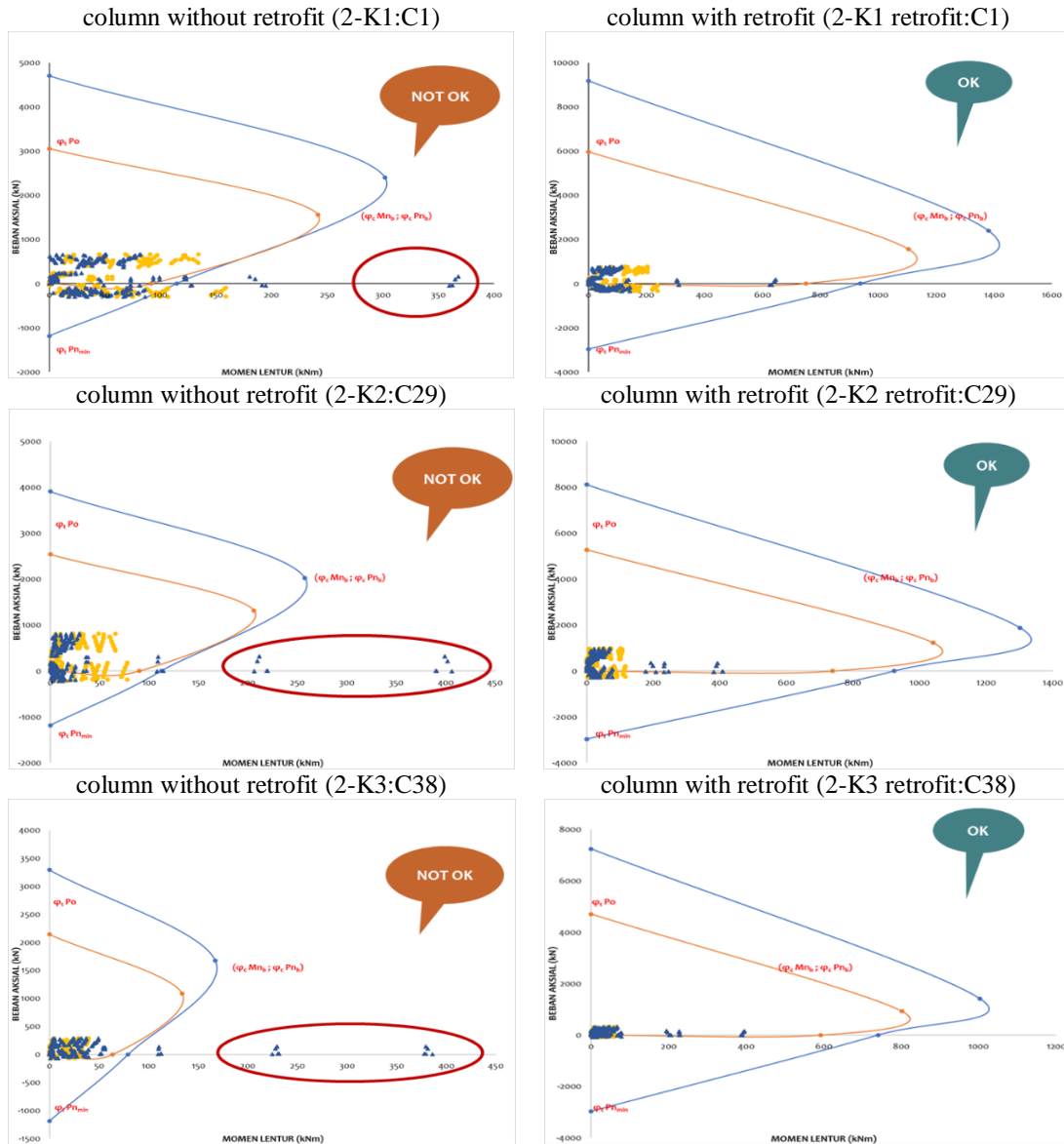


Fig. 7 P-M interaction diagram of the 2<sup>nd</sup> Floor column with and without retrofitting.

Table 3 Comparison of the shear capacity of the column with and without retrofitting

Column Section Code	Without retrofitting				Column Section Code	With retrofitting			
	Shear rebar	Vr (kN)	Vu' (kN)	Mu ≤ Mn		Shear rebar design	Vr (kN)	Vu' (kN)	Mu ≤ Mn
2-K1 (45x45) C01	Ø10-100 mm	293.43	1037.01	Not Ok	2-K1 retrofit (60x60) C01	Ø13-50 mm	1060.98	1037.01	Ok
2-K2 (45x35) C29	Ø10-100 mm	270.09	1180.61	Not Ok	2-K2 retrofit (60x50) C29	Ø16-50 mm	1476.79	1180.61	Ok
2-K3 (35x25) C38	Ø10-100 mm	204.21	1185.72	Not Ok	2-K3 retrofit (50x50) C38	Ø16-50 mm	1213.08	1185.72	Ok



Table 4 Comparison of the flexural capacity of the beam with and without retrofitting

Beam Section	Code	Number of rebar		$\phi M_n$ (kNm)	Without retrofitting			With retrofitting		
		Tens.	Comp.		$M_u$ (kNm)	$M_u \leq M_n$		$M_u$ (kNm)	$M_u \leq M_n$	
1-B2	B01	3D19	3D19	119.09	170.89	P	Not Ok	115.26	P	Ok
30/55		3D19	3D19	119.09	120.99	M	Ok	58.83	M	Ok
1-B2	B14	3D19	3D19	119.09	175.8	P	Not Ok	115.26	P	Ok
30/55		3D19	3D19	119.09	85.21	M	Ok	58.83	M	Ok
1-B3	B59	3D19	3D19	106.65	197.19	P	Not Ok	106.06	P	Ok
30/70		3D19	3D19	106.65	120.86	M	Ok	66.59	M	Ok

### Pushover Analysis Result

The capacity curve from the pushover analysis illustrates the relationship between base shear and rooftop displacement. In this study, the capacity curve from the pushover analysis is used to check the performance level of the existing structure and functions as an engineering demand parameter (EDP) in the calculation of the building fragility curve with and without retrofitting is given through the drift yield value.

There are 3 methods used to determine displacement yield; first yield is based on the first yield deviation that occurs, significant yield is based on the intersection between the elastic displacement and the equivalent load at the time of failure and based on the same energy absorption capacity between the elasto-plastic system with the actual structure at the same ultimate load. In this study, the determination of the displacement yield value for the development of the fragility curve uses a significant yield. The displacement yield value obtained for the existing building was 67.30mm and the displacement yield value for the retrofitted building was 38.98mm.

The drift yield value used in calculating the fragility curve is obtained from the comparison of the displacement yield value with the building height. So based on the results of the pushover analysis, the drift yield of the building structure is 0.45% for the existing structure and 0.26% for the retrofitted structure.

### Non-Linear Time History Result

In this study, the non-linear time history analysis uses 4 types of ground motions earthquake data (time history) which are scaled on a 0.2–2.0 scale with an interval of 0.2. So there are 40 ground motion data used in the calculation of the fragility curve. The Engineering Demand Parameter (EDP) value obtained from the non-linear time history analysis for this fragility curve calculation has 40 maximum displacement values per each fragility curve before and after retrofitting.

### Fragility Function and Fragility Curve

The fragility curve is a long normal function that

describes the probability of exceeding certain structural damage conditions by taking into account irregularities related to the capacity, demand and damage conditions (Hanus MH MR 5) [7]. The fragility curve depicts the relationship between the probability of the degree of structural damage and the hazard intensity measure (IM).

The general equation for the development of the fragility curve is shown in Eq. (1).

$$\text{Fragility} = P[\text{LS}|\text{IM}] = y \quad (1)$$

Where LS is the boundary condition or damage condition (DS), IM is a measure of ground motion intensity, and y is the state reached due to ground motion intensity (IM).

The equation is then idealized into a lognormal distribution, as shown in Eq. (2).

$$P(x) = \Phi \left[ \frac{\ln(x) - \lambda}{\zeta} \right] \quad (2)$$

Where  $P(x)$  is a probability function,  $x$  is a random variable,  $\zeta$  is the standard deviation value of  $\ln x$ ,  $\lambda$  is the mean value of  $\ln x$ ,  $\Phi$  and is the form of the cumulative normalized distribution. Lognormal is used because it is very suitable to determine various types of damage ranging from failure of structural components, non-structural components, building collapse, and the probability of zero on EDP equal to zero and below zero.

The fragility curve developed in this study is the fragility curve of the existing building (Fig. 8) and the fragility curve of the retrofitted building (Fig. 9).

The parameters for fragility functions obtained from the calculation results is used to describe the fragility curve for the building with and without retrofitting, as shown in Table 4.

Table 4 Parameters for fragility functions

Damage level	Without retrofit		With retrofit	
	$\lambda$	$\zeta$	$\lambda$	$\zeta$
Slight Damage	-2.55	0.28	-1.99	0.28
Moderate Damage	-1.83	0.28	-1.27	0.28
Extensive Damage	-0.69	0.50	-0.13	0.50
Complete Damage	0.32	0.50	0.89	0.50

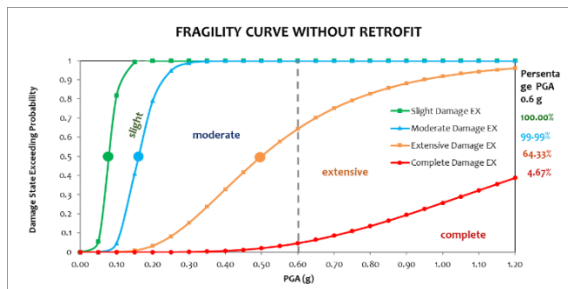


Fig. 8 Fragility curve of the existing building

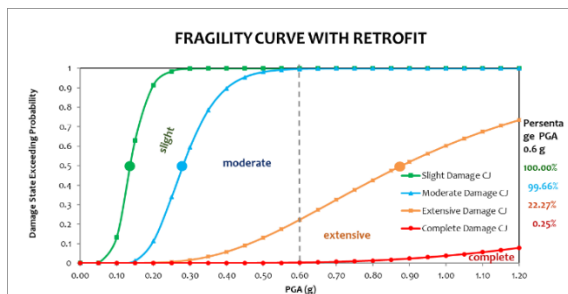


Fig. 9 Fragility curve of the retrofitted building

The probability of damage level to the building structure with and without retrofit during an earthquake with a PGA value of 0.6g is shown in Table 5.

Table 5 Comparison of structural damage level probability on the building with and without retrofit during an earthquake with a PGA value of 0.6 g

Damage level	Percentage of probability	
	Without retrofit	With retrofit
Slight Damage	100.00%	100.00%
Moderate Damage	99.99%	99.66%
Extensive Damage	64.33%	22.27%
Complete Damage	4.67%	0.25%

From the fragility curves of the building with and without retrofitting shown in Figs. 8 and 9 show that the percentage of the structural damage probability decreases after the structure was retrofitted. The retrofit of the building structure using concrete jacketing reduce the probability of damage to the building structure by 42.06% at the level of extensive damage and by 4.42% at the level of complete damage at PGA 0.6g.

## CONCLUSION

The structure of the SMPN 25 Padang building was modeled with and without retrofit against earthquake and tsunami loads. The results of the

existing building analysis show that several columns on the 2nd floor and several beams on the 1st floor have not been able to withstand the tsunami loads.

Retrofitting of the building using the concrete jacketing method on columns improves the capacity of the building structure, so the building are able to withstand the tsunami loads.

Based on the fragility curve developed, the percentage of the structural damage probability decreases after the structure was retrofitted. The retrofit of the building structure using concrete jacketing reduce the probability of damage to the building structure by 42.06% at the level of extensive damage and by 4.42% at the level of complete damage at PGA 0.6g.

## REFERENCES

- [1] Borrero, J.C., Tsunami Inundation Modeling for Western Sumatra. PNAS vol. 103 no. 52. 19677, 2006, pp. 19673–19677.
- [2] F. Ashar, D. Amaratunga, and R. Haigh, The Analysis of Tsunami Vertical Shelter in Padang City, 4th International Conference On Building Resilience, Salford Quays, United Kingdom, 2014, pp. 916-923.
- [3] Indonesian National Standardization Agency, Procedures for Planning Earthquake Resistance for Building and Non-Building Structures SNI 1726-2019, Jakarta, Indonesia, 2019, pp.1-248.
- [4] Federal Emergency Management Agency, FEMA P646: Guidelines for Design of Structure for Vertical Evacuation from Tsunami 2nd edition, Washington D.C, USA, 2012, pp.1-174.
- [5] Fauzan, Febrin A.I, and Zev A.J, Seismic Retrofitting Analysis Using Concrete Jacketing and Shear Wall on Dental Hospital Building of Andalas University, IOP Conf. Series: Materials Science and Engineering 602, 012108, 2019, pp.1-11.
- [6] Fauzan, Febrin A.I., Nurpadila S., and Zev A.J, The Effect of Tsunami Loads on Pasar Raya Inpres Block III Building in Padang City Based on FEMA P-646, MATEC Web of Conferences 258, 03020, SCESCM 2018, 2019, pp.1-9.
- [7] HAZUS, Earthquake Loss Estimation Methodology, Washington, D.C.: Federal Emergency Management Agency, 2002, pp.11-21.
- [8] HAZUS, Hazus Tsunami Model Technical Guidance, Washington, D.C.: Federal Emergency Management Agency, 2017, pp. 1-171.
- [9] A.C Utami, R Kurniawan and Fauzan, Analytical Fragility Curve Development of Maternity and Children's M. Djamil Hospital Building Padang due to Earthquake and Tsunami, IOP Conf. Series: Earth and Environmental Science 708, 012014, 2021, pp.1-10.

# REMEDICATION OF AL-QATIF EXPANSIVE CLAY USING CEMENT KILN DUST, INITIAL ASSESSMENT

Sultan Abdulaziz Almuaythir<sup>1</sup> and Mohamed Farid Abbas<sup>1,2</sup>

<sup>1</sup>College of Engineering, Prince Sattam Bin Abdulaziz University, Saudi Arabia; <sup>2</sup> Soil Mechanics and Geotechnical Engineering Research Institute, Housing and Building National Research Center (HBRC), Egypt

## ABSTRACT

Expansive soils exist naturally or may be used as a compacted material in different engineering projects. Uneven ground movements (heave) of expansive soils typically inflict damage to light structures, pavements, retaining structures and shallow tunnels. Given the high cost of damage inflicted to such structures, it is of a paramount importance to examine the probable approaches to reduce damage associated with its use. This study examines the feasibility of using Cement Kiln Dust (CKD) for Al-Qatif expansive clay stabilization. Geotechnical properties including compaction parameters, swell potential and unconfined compressive strength for different mixtures containing different doses of CKD were examined. The experimental results of the experimental program indicates that CKD be beneficially used to reduce the swell potential of Al-Qatif expansive clay as well as increase its strength.

*Keywords: Expansive soil, Cement Kiln Dust, Stabilization, Swell Potential, Unconfined Compressive Strength*

## INTRODUCTION

Expansive soils are extended worldwide especially in arid and semi-arid zones such as Saudi Arabia. Its nature in undergoing swelling and loss of shear strength, as a result of moisture change, results in structural damage that may cause huge economic losses as well as hampered development. In this regard, numerous studies have focused on stabilization of expansive soils by using additives such as lime [1]–[3] and cement [4]–[7]. However, stabilization of this soil with cement or lime admixture is effective but very costly and hence there is need for utilizing potentially cost-effective additives. Consequently, attention has been turned towards using industrial waste, such as fly ash [8]–[10], coal ash [11]–[13], husk ash [14]–[15] and Cement Kiln Dust [16]–[21], as a chemical stabilizer. Potential use of industrial waste as a chemical stabilizer will not only reduce the cost of disposal but also will reduce the environmental hazards caused by such wastes [19].

Cement Kiln Dust (CKD) is a waste by-product that is produced during manufacturing process of Portland cement. It is generated from burning the raw materials in a rotary kiln to produce clinker. CKD poses a storage trouble and considered a source of potential pollution. Consumption of such material in soil stabilization processes might solve some of these problems. However, researches that deal with use of CKD in expansive soil remediation is limited,

especially for treating expansive soil with high swell potential.

Several researchers examined the use of CKD in stabilization of expansive soils [16]–[21]. They reported an improvement in geotechnical properties with adding CKD and suggested use of CKD for expansive soil stabilization where it is more economical and is an environmental solution to other soil stabilizer agents such as lime and cement.

The main objective of this study is to experimentally examine the feasibility of using Cement Kiln Dust (CKD) for Al-Qatif expansive clay stabilization in view of deformation and shear strength aspects.

## MATERIALS

In this section, a brief description of the physical and chemical properties for the studied expansive soil and selected stabilizer are presented.

### Al-Qatif expansive soil

Al-Qatif expansive soil was selected for the current study since it is a typical expansive soil that are located in the Arabian Gulf coastal region, Saudi Arabia, where the main oil-industrial activities are located. Also, Al-Qatif expansive soil is considered to be a highly expansive soil and hence remediation of this issue will be more significant.

The sampled soil is a calcareous grayish silty clay

obtained from a field test pit at a depth of about three meters. Bulk disturbed specimens were air dried, then pulverized and screened through sieve No. 40. A summary of physical properties of selected soil are provided in Table 1.

Table 1 Physical properties of Al-Qatif soil

Physical Property	Value
Specific Gravity, $G_s$	2.74
Liquid Limit, LL (%)	140
Plastic Limit, PL (%)	45
Shrinkage Limit, SL (%)	18
Plasticity Index, PI (%)	95
% Finer than 200 $\mu\text{m}$	70
USCS Classification	CH

### Cement Kiln Dust (CKD)

In the current study the Cement Kiln Dust was used for stabilizing the Al-Qatif soil in order to reduce its swell potential and improve its shear strength. Current CKD is by product of Yamama cement plant, Riyadh, Saudi Arabia. Table 2 summarizes the average chemical composition of CKD, showing huge percentage of calcium oxide as well as high percentages of silica and aluminum oxides.

Table 2 Chemical composition of Cement Kiln Dust percent by weight of dry mass

Mineral	CaO	SiO <sub>2</sub>	Al <sub>2</sub> O <sub>3</sub>	K <sub>2</sub> O
%	67.47	14.37	4.21	2.54
Mineral	Fe <sub>2</sub> O <sub>3</sub>	SO <sub>3</sub>	Cr	Loss on Ignition
%	2.50	2.13	0.42	3.79

### METHODS

To study the feasibility of using CKD as a stabilizer of Al-Qatif soil, four percentages of CKD by dry weight (2.0, 4.0, 6.0 and 8.0 %) were used. Standard compaction tests, in accordance to ASTM D698 [22], were executed to determine the compaction characteristics of the selected mixtures. Fig. 1 shows the standard compaction test results for untreated and treated Al-Qatif soil. As CKD% increase, the maximum dry density decreases and optimum moisture content increase which is comparable with previous researches either for use of CKD [20] or other stabilizer.

As it is well known that characterization of any

geotechnical material is based on its deformation and stability properties, current experimental program involves oedometer (OED) and unconfined compressive (UCS) tests. Both testing groups were divided to subgroups based on the CKD% added. As well, Oedometer and UCS tests were executed for different curing periods (1, 7, 14 and 28 days). Actual curing period may slightly differ according to the availability of utilized devices and working days. Each tested sample has been labelled to infer the CKD% added and actual curing period.

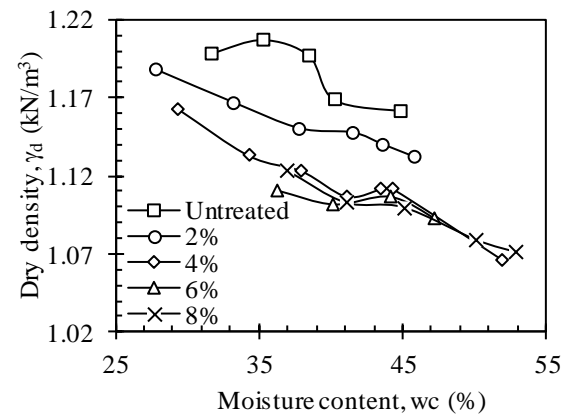


Fig. 1 Standard compaction tests for examined CKD %

In order to prepare OED specimens, dry soil was mixed with respective CKD% and optimum moisture content and thoroughly mixed. Thereafter, mixture was compacted in oedometer ring to the desired dry density (i.e., maximum dry density at selected CKD%), wrapped in thin plastic wrap and cured to the respected curing period in wet-desiccator. Same is adopted for UCS specimens, except that compacted specimen is dismantled after compaction instead of left in the compaction ring.

OED testing was adopted with respect to ASTM D4546-03 [23], method B. Once cured specimen was installed in oedometer device, 50 kPa applied stress (comparable to stress applied at foundation level of residential buildings) was applied in step loading and each load was left for five minutes, thereafter, specimen was inundated and deformation due to wetting was recorded for 24 hours. The final wetting strain was labelled as wetting potential ( $\epsilon_w$ ).

Specimens for the unconfined compressive strength test (38 mm in diameter and 78 mm in high) were constituted by statically compacting the mixture of Al-Qatif soil with specific CKD% with respect to compaction characteristics obtained from Fig.1. Strain rate of 0.25%/min. is selected for shearing tested specimens to ensure undrained condition and avoids probable moisture evaporation from cured specimens.

## RESULTS AND ANALYSIS

### Oedometer testing, OED

Table 3 shows that untreated specimens showed small swell ( $\varepsilon_w=6.60\%$ ) under 50 kPa applied stress. Fig. 2 shows that wetting strain ( $\varepsilon_w$ ) reduce with increase of CKD%. Fig. 3 depicts clearly the impact of CKD% on swell reduction. CKD%=6.0% is almost sufficient to remove the swell potential related to wetting. As well, it is seen that curing period is not an effective remediation factor of swell for all CKD% besides that curing period results in loss of remediation for 2.0% dose of CKD. This observation is more clearly seen in Fig. 4. As it is known from CKD properties, it has fast seating and 7 days curing is sufficient to ensure the mobilization of most stabilization.

Table 3 Summary of oedometer testing results

ID	Wetting strain, $\varepsilon_w$ (%)	Swell reduction (%)
CKD_0	6.60	0
CKD_2_1d	1.02	85
CKD_2_7d	1.47	78
CKD_2_15d	1.50	77
CKD_2_31d	2.53	62
CKD_4_1d	1.41	79
CKD_4_9d	0.75	89
CKD_4_15d	0.85	87
CKD_4_31d	0.59	91
CKD_6_1d	0.18	97
CKD_6_7d	0.45	93
CKD_6_15d	0.45	93
CKD_6_28d	0.39	94
CKD_8_7d	0.22	97
CKD_8_14d	0.19	97
CKD_8_28d	0.10	98

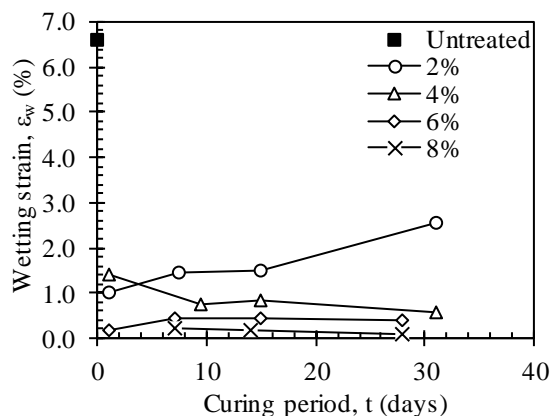


Fig. 2 Variation of wetting strain with curing period

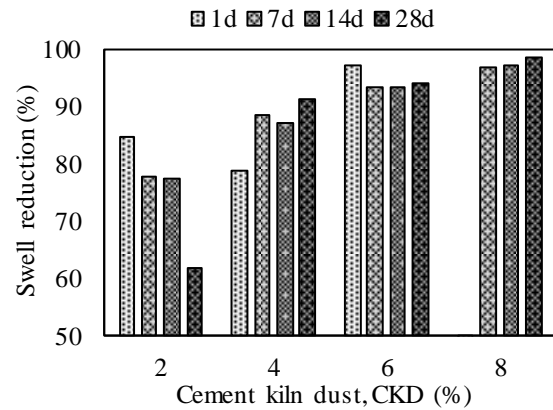


Fig. 3 Swell reduction versus CKD %

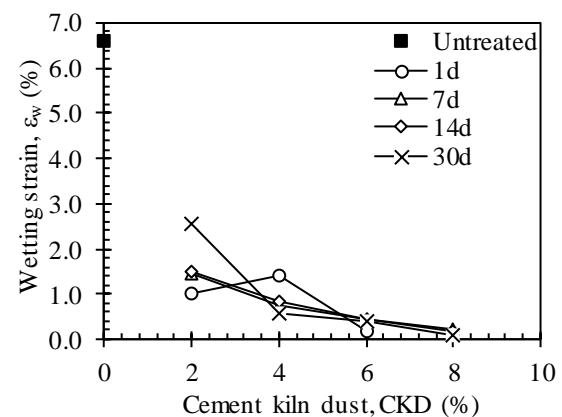


Fig. 4 Variation of wetting strain with CKD % for different curing periods

### Unconfined compressive strength, UCS

Evaluation of soil stability under undrained condition is often estimated in terms of unconfined compressive strength (UCS). The unconfined compressive strength is one of the key variable for estimating the undrained shear strength of fine grained soils. The obtained results, see Table 4 and Figs. 5 and 6, reveal that CKD addition is effective in improve stability of Al-Qatif soil. Moreover, curing period has a pronounced impact on UCS, Fig. 5, in contrast to its effect on swell reduction. Fig. 6 shows that CKD% greatly enhance the undrained strength of Al-Qatif soil.

Figure 7 shows the improvement percentage due to the addition of CKD and shows that UCS improvement continuously increase with CKD for examined CKD% and adding 8.0% of CKD increases the undrained stability by four times, indicating its improvement effectiveness.

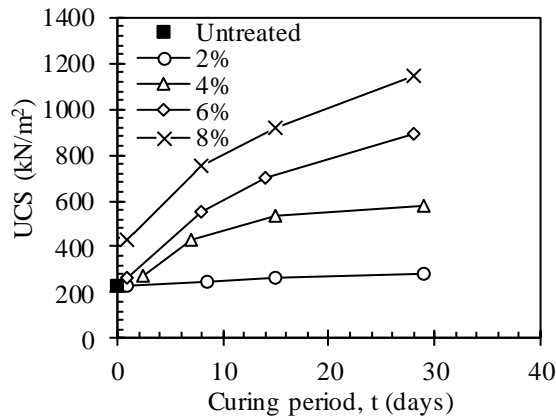


Fig. 5 Variation of UCS with curing time for examined CKD %

Table 4 Summary of unconfined compressive testing results

ID	UCS (kN/m <sup>2</sup> )	Strength Increase (%)
CKD_0	231.8	0.0
CKD_2_1d	231.6	0.0
CKD_2_8d	245.0	5.7
CKD_2_15d	265.0	14.3
CKD_2_29d	282.0	21.7
CKD_4_2d	273.9	18.2
CKD_4_7d	427.2	84.3
CKD_4_15d	535.0	130.8
CKD_4_29d	582.2	151.2
CKD_6_1d	261.4	12.8
CKD_6_8d	556.4	140.1
CKD_6_14d	698.4	201.3
CKD_6_28d	891.0	284.5
CKD_8_1d	427.1	84.3
CKD_8_8d	754.6	225.6
CKD_8_15d	923.0	298.3
CKD_8_28d	1148.2	395.4

## CONCLUSIONS

Expansive soils exist worldwide extensively in vadose zones such as Saudi Arabia. The structural damage accompanied with construction of light structure over such expansive soils cause huge economic losses as well as hampered development. Given the high cost of damage inflicted to such structures, it is of a very important to study most economic and effective approaches to reduce damage associated with its use.

Current study investigated experimentally the possibility of using Cement Kiln Dust (CKD) for Al-Qatif expansive clay stabilization, as a typical expansive soil encountered in region that embrace the main oil-industrial activates in Saudi Arabia. Evaluation of CKD performance is determined in view of deformation and shear strength aspects.

The results showed the fast efficiency of the reduction of swell potential related to wetting. On the other hand, CKD additive exhibited a continuously improve of undrained shear strength either with curing period or CKD%. In conclusion, use of CKD additive for Al-Qatif soil is recommended in view of deformation and strength aspects.

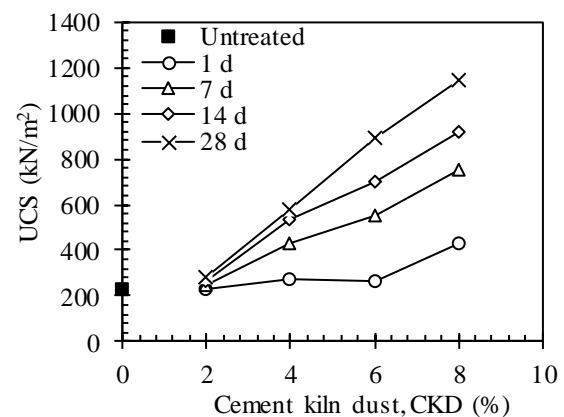


Fig. 6 Variation of UCS with CKD %

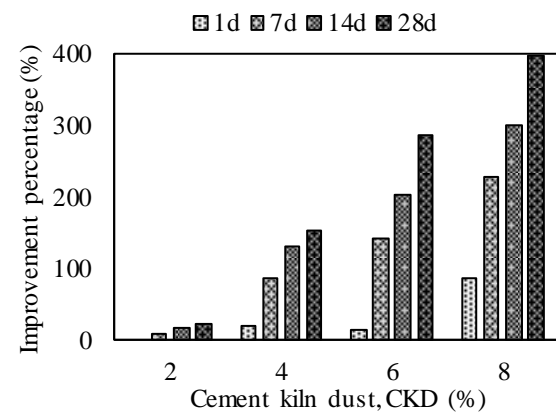


Fig. 7 UCS improvement versus CKD %

## ACKNOWLEDGMENTS

The authors extend their appreciation to the Deputyship for Research & Innovation, Ministry of Education in Saudi Arabia for funding this research work through the project number (IF-PSAU-2021/01/19009).



## REFERENCES

- [1] Khattab, S.I., Al-Mukhtar, M., and Fleureau, J.M., Long-Term Stability Characteristics of a Lime-Treated Plastic Soil. *Journal of Materials in Civil Engineering*, Vol. 19, 2007, pp. 358-366.
- [2] Ghobadi, M.H., Abdilor, Y., and Babazadeh, R., Stabilization of clay soils using lime and effect of pH variations on shear strength parameters. *Bulletin of Engineering Geology and the Environment*, Vol. 73, 2013, pp. 611-619.
- [3] Beetham, P., Dijkstra, T., Dixon, N., Fleming, P., Hutchison, R.V., and Bateman, J.C., Lime stabilization for earthworks: a UK perspective. *Proc. Inst. Civ. Eng. Ground Improv.* Vol. 168, Issue 2, 2015, pp.81–95.
- [4] Bhattacharja, S., and Bhatta J. I., Comparative performance of Portland cement and lime stabilization of moderate to high plasticity clay soils. Skokie, 2003, IL: Portland Cement Association.
- [5] Kim, W., Tam, N.M., and Jung, D.H., Experimental study on strength of cement stabilized clay. *Journal of Engineering, Design and Technology*, Vol. 3, 2005, pp. 116-126.
- [6] Al-Zoubi, M.S. Undrained Shear Strength and Swelling Characteristics of Cement Treated Soil. *Jordan Journal of Civil Engineering*, Vol. 2, 2008.
- [7] Yong-hui, S., Linrong, X., and Yu, C. Study on dynamic characteristics of cement-stabilized expansive soil subgrade of heavy-haul railway under immersed environment. *Rock and Soil Mechanics*, Vol. 41, 2020, pp. 2739.
- [8] Puppala, A.J., Hoyos, L.R., Viyanant, C., and Musenda, C., Fiber and fly ash stabilization methods to treat soft expansive soils. In *Soft ground technology*, Reston, VA: ASCE, 2001, pp. 136–145.
- [9] Hoyos, L.R., Puppala, A.J., and Ordóñez, C., Characterization of Cement-Fiber-Treated Reclaimed Asphalt Pavement Aggregates: Preliminary Investigation. *Journal of Materials in Civil Engineering*, Vol. 23, 2011, pp. 977-989.
- [10] Mahedi, M., and Cetin, B., Leaching of elements from cement activated fly ash and slag amended soils. *Chemosphere*, Vol. 235, 2019, pp. 565-574.
- [11] Modarres, A., and Nosoudy, Y.M., Clay stabilization using coal waste and lime – Technical and environmental impacts. *Applied Clay Science*, Vol. 116, 2015, pp. 281-288.
- [12] Afrakoti, M.T., Choobbasti, A.J., Ghadakpour, M., and Kutanaei, S.S., Investigation of the effect of the coal wastes on the mechanical properties of the cement-treated sandy soil. *Construction and Building Materials*, Vol. 239, 2020, pp.117848.
- [13] Mansouri, S., Nasiri, M., and Modarres, A., Technical and Environmental Impacts of Coal Waste Used as a Soil Stabilizer in Construction Projects of Forest Roads. *Croatian Journal of Forest Engineering*, Vol. 42, 2021.
- [14] Ali, F.H., Adnan, A., and Choy, C.K., Use of rice husk ash to enhance lime treatment of soil. *Canadian Geotechnical Journal*, Vol. 29, 1992, pp. 843-852.
- [15] Vattimalla, V., and Sandela, R., A comparative study of soil stabilization using fly ash and rice husk ash. *Int. J. of Innov. in Eng. Res. and Tech.*, Vol. 8, Issue 7, 2021, pp. 161–166.
- [16] Miller G.A., Azad S., Influence of soil type on stabilization with cement kiln dust. *J Constr Build Mater*, Vol. 14, Issue 2, 2000, pp. 89-97.
- [17] Hossain K.M.A., Mol L., Some engineering properties of stabilized clayey soils incorporating natural pozzolans and industrial wastes. *J Constr Build Mater*, Vol. 25, Issue 8, 2011, pp. 3495–3501.
- [18] Ismaiel H.A.H., Cement kiln dust chemical stabilization of expansive soil exposed at El-Kawther Quarter, Sohag Region, Egypt. *Int J Geosci*, Vol. 4, Issue 10, 2013, pp. 1416–1424.
- [19] Salahudeen, A.B., Eberemu, A.O., and Osinubi, K.J., Assessment of Cement Kiln Dust-Treated Expansive Soil for the Construction of Flexible Pavements. *Geotechnical and Geological Engineering*, Vol. 32, 2014, pp. 923-931.
- [20] Ismail A.I.M. and Belal Z.L., Use of cement kiln dust on the engineering modification of soil materials, Nile Delta, Egypt. *J Geotech Geol Eng*, Vol. 34, 2016, pp. 463–469.
- [21] Ogila, W.A., Effectiveness of fresh cement kiln dust as a soil stabilizer and stabilization mechanism of high swelling clays. *Environmental Earth Sciences*, Vol. 80, 2021, 1-24.
- [22] ASTM D698, Standard test methods for laboratory compaction characteristics of soil using standard effort (12,400 ft-lbf/ft<sup>3</sup> (600 kN-m/m<sup>3</sup>)). ASTM International, 2000, West Conshohocken, PA, USA.
- [23] ASTM D4546-03, Standard test methods for one-dimensional swell or settlement potential of cohesive soils. ASTM International, 2003, West Conshohocken, PA, USA.

# EFFECT OF MACRO-SYNTHETIC POLYPROPYLENE FIBER ON DRYING SHRINKAGE OF SELF-CONSOLIDATING CONCRETE

Aris Aryanto<sup>1</sup> and Andy Muliohardjo<sup>2</sup>

<sup>1,2</sup> Faculty of Civil and Environmental Engineering, Bandung Institute of Technology, Indonesia

## ABSTRACT

Development in the concrete industry led to an increasing need for faster construction, high performance, energy-saving, and eco-friendly concrete technology. Self-consolidating concrete (SCC) has become a promising concrete technology to shorten construction time and reduce labor needs. However, SCC has susceptible to shrinkage cracking due to high binder and low aggregate content. On the other hand, fiber has been used to control cracking and increase post-cracking behavior and toughness. Fiber addition into the SCC mix has become a common method to improve cracking resistance, even though it may reduce the workability. In this study, the effect of macro-synthetic fiber on the drying shrinkage of SCC is evaluated using free and restrained shrinkage tests. SCC mixtures include concrete containing different percentage of polypropylene fiber content (0.25, 0.5, 0.75 and 1.0% by volume). Besides that, compressive strength, splitting tensile strength, and workability in terms of Slump flow, J-Ring, and V-Funnel of fiber-reinforced SCC are also investigated. The results show that the addition of macro-synthetic fibers can delay crack formation due to drying shrinkage compared to plain SCC.

*Keywords: Self-consolidating concrete, Synthetic fiber, Workability, Shrinkage*

## INTRODUCTION

Self-consolidating concrete (SCC) has become more frequently used in concrete construction due to its better workability and efficiency in construction time and labor needs [1]. However, SCC is prone to shrinkage cracking due to high binder and low aggregate content [2],[3]. Shrinkage cracking on concrete structures may reduce structural performance and durability. On the other hand, introducing fiber into a concrete mixture has known to be used to control cracking and increase post-cracking behavior. At the same time, fibers may replace some minimum steel reinforcement. The addition of fiber into the SCC mixture is expected to improve cracking resistance and increase the hardened properties of concrete, such as tensile, flexural, and toughness. However, in high fiber content, it may also reduce the concrete workability, which may discard the beneficial factor of SCC. Hence, the effect of fibers on SCC, namely fiber-reinforced self-consolidating concrete (FRSCC), needs to be investigated to obtain an optimum dosage resulting in the best performance of FRSCC. The synergetic effect between fiber and SCC has also been investigated by several researchers [4],[5],[6]. However, the effect of the fiber content of macro-synthetic polypropylene fibers on drying shrinkage still needs to be investigated.

Various type of fiber has been used in the concrete mix, such as steel fiber, glass fiber, or synthetic fiber, e.g., polyester, polypropylene, polyethylene, or natural fiber. Among them, steel fiber is the most common and widely used. The fiber shape also varies,

such as straight monofilament, multifilament, crimped, embossed, or with an end-hook to improve its anchorage to concrete [7]. Fiber size can be categorized as macro- and micro-fiber depending on the aspect ratio, i.e., diameter to length ratio. In this study, only macro fibers with polypropylene materials are used.

This study investigated the effect of macro-synthetic polypropylene fibers to SCC on fresh and hardened properties, especially on drying shrinkage. Two drying shrinkage tests were carried out using free and restrained shrinkage tests according to ASTM C341 [8] and ASTM C1581 [9]. The main parameter is the variation in fiber content of 0, 0.5, 0.75, and 1.0% by volume. Based on the test results, the effect of fiber content on drying shrinkage cracking was confirmed.

## EXPERIMENTAL PROGRAM

### Material and Mixture Proportion

Type I cement of Portland cement composite (PCC) was used as a binder for the SCC mixture. To achieve the workability of SCC, a polycarboxylate high-range water reducer (HRWR) was added into the mixture without additional shrinkage reducing agent or mineral pozzolan. The maximum aggregate size was limited to 12.5 mm for coarse aggregate with a specific gravity of 2.73 and 1.09% of absorption. Natural sand finer than 2.4 mm was used with a specific gravity of 2.39 and 5.5% absorption as a fine aggregate. The mixture proportion was designed for specified concrete strength of 50 MPa, and a low

water-to-cement ratio of 0.32 was used to achieve higher concrete strength. The concrete mixture proportion is given in Table 1. The properties of polypropylene fibers used in this study are given in Table 2 and Fig.1. The fiber percentage of volume fractions of 0, 0.25, 0.5, 0.75, and 1.0. All concrete mixture parameters keep constant for all specimens, except for the coarse aggregate content adjusted to the fiber content.

Table 1 Concrete mix proportions

Mix No.	w/c	Cement (kg/m <sup>3</sup> )	Aggregate (kg/m <sup>3</sup> )		Fiber content (%)
			Coarse	Fine	
<b>NF</b>	0.32	618	781	801	0.0
<b>F0.5</b>	0.32	618	776	801	0.5
<b>F0.75</b>	0.32	618	774	801	0.75
<b>F1.0</b>	0.32	618	772	801	1.0

Table 2 Polypropylene fiber properties

Fiber shape	Monofilament with continuous embossed
Specific Gravity	0.92
Length, L (mm)	60
Diameter, d (mm)	0.4
Aspect ratio (L/d)	150
Modulus elasticity (GPa)	10
Tensile strength (MPa)	640



Fig. 1 Polypropylene fibers.

### Fresh Concrete Test

Workability is crucial in the fresh concrete properties, especially for self-consolidating concrete. As mentioned in the introduction, the fiber addition will affect the workability performance of SCC. There are three aspects of workability performances, i.e., filling ability, passing ability, and segregation resistance, that should be evaluated. The filling ability was measured by slump flow test according to ASTM

C1611 [10]. The filling ability or flowability is expressed in terms of the slump flow value of the diameter of 450-760 mm (18 – 30 inches). The passing ability test was conducted using the J-Ring test specified in ASTM C1621 [11]. The segregation resistance test was carried out using the V-funnel test according to EFNARC [12] and was also visually examined during the slump flow test.

### Mechanical Concrete Test

Compressive, splitting tensile, and modulus of elasticity tests were undertaken to measure the mechanical properties of concrete. The test procedures for compressive, splitting tensile, and modulus of elasticity tests follow the procedure as specified in ASTM C39 [13], ASTM C496 [14], and ASTM C469 [15], respectively. Compressive strength was tested at 3, 7, 14, 28, and 59 days. A concrete cylinder with a diameter of 150 mm and a height of 300 mm is used for compressive, splitting tensile, and modulus of elasticity tests. For each test result, an average of three samples were reported.

### Free and Restrained Shrinkage Test

This study carried out two types of shrinkage tests: free and restrained shrinkage ring tests. The main parameter of this study was the percentage of polypropylene fibers by volume (0.5%, 0.75%, and 1%), including plain concrete (0% fibers) as control specimens. Two specimens for each parameter were made for free drying and restrained shrinkage ring tests. The free drying shrinkage test procedures were specified in ASTM C 341 [8]. The specimen's size was 100 x 100 x 400 mm, and the embedded stud gauges were placed at two locations and the middle along the longitudinal direction of the specimens as reference points. The extensometer measured the length change or shrinkage strain between two reference points. The specimen and test setup are shown in Fig. 2 (a).

The restrained shrinkage test aims to examine the cracks that occur due to the drying shrinkage of concrete. The shrinkage ring test was conducted according to ASTM C1581 [9]. The test configuration of the shrinkage ring test is shown in Fig. 2(b). Shrinkage strain of concrete was measured from the stress that occurred at the inner steel ring determined by using four strain gauges attached to the internal steel ring. Strains in the steel rings are monitored at intervals of 30 minutes and recorded with the data acquisition system. The strain recording started on the second day after concrete casting and removing the outer steel mold. The top and bottom of the concrete ring surface were sealed with silicone rubber and a plastic base. Therefore, concrete drying only proceeds on the exposed surface, the outer circumferential surface of the concrete. The concrete

cracking was visually inspected every day, marked the time and the strain, and mapped the pattern.



(a) Free shrinkage test



(b) Ring restrained shrinkage test

Fig. 2 Test setup for shrinkage test

## RESULTS AND DISCUSSIONS

### Fresh Properties

Table 1 summarizes the test results of the fresh concrete properties of SCC with various polypropylene fiber content investigated in this study. Fiber addition from 0.5% to 1% by volume to the SCC mixture decreases the flowability of SCC, as shown in Fig. 3. Adding 0.75% fiber or more caused the slump flow value to be less than the minimum slump flow for SCC of 450 mm. These findings align with previous research by Nehdi M. and Ladanchuk J. D. [1]. As mentioned by Forgeron D. and Omer A. [16] in their study, the macro-synthetic fiber volume fraction below 0.5% still has an insignificant impact on the flowability of SCC. Besides fiber content, fiber length also plays a significant role in the flowability of SCC to move around or through obstacles [16]. As large macro-synthetic fibers with a length of 60 mm and aspect ratio of 150 were used in this study, the impact on flowability and passing ability will be significant.

Macro-synthetic fibers also decrease the passing ability of SCC through the J-Ring test, as shown in Fig. 4. Fiber increases passing resistance when the SCC mixture flows through the reinforcement gap.

Macro-synthetic fiber addition to SCC also causes blockage in the V-funnel test, as presented in Table 1. A blockage is found in the narrowed area in the V-funnel. This was also found by Forgeron D. and Omer A. [16] in their research. Usage of smaller fiber lengths or micro-synthetic fibers may reduce this blockage.

Table 3 Fresh properties of various FRSCC

Mix No.	Fresh concrete properties		
	Slump Flow (mm)	J-Ring (mm)	V-funnel (sec)
NF	626	575	5.43
F0.5	550	464	Blockage
F0.75	434	368	Blockage
F1.0	362.5	315	Blockage

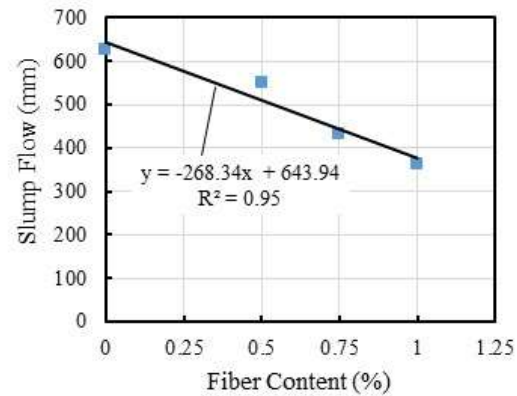


Fig. 3 Effect of Polypropylene fibers on slump flow

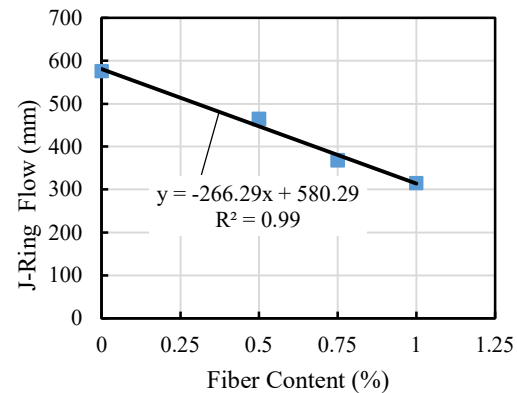


Fig. 4 Effect of Polypropylene fibers on J-ring flow

### Mechanical Properties

The compressive test results at 3, 7, 14, 28, and 59 days are given in Fig. 5. It was observed that the compressive strength of FRSCC is mostly lesser than that of the control specimens or plain concrete. As shown in Fig. 5, the compressive strength also slightly decreases by increasing the fiber volume, except for 28 days. A lower concrete strength is also found by others [17] and [1] when using polypropylene fibers.

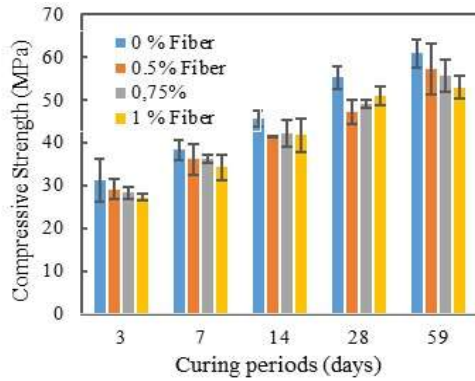


Fig. 5 Effect of Polypropylene fibers on compressive strength

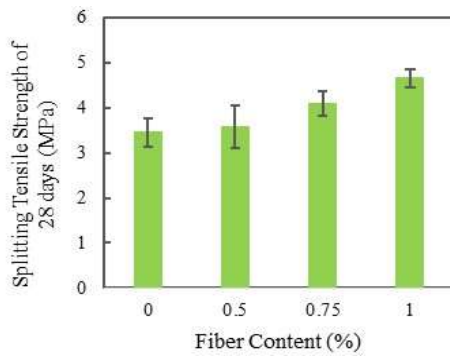


Fig. 6 Effect of Polypropylene fibers on splitting strength

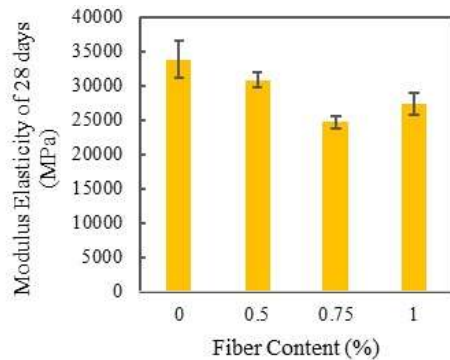


Fig. 7 Effect of Polypropylene fibers on the modulus of rupture

The splitting tensile test results for different fiber volume fractions are presented in Fig.6. The results indicate that adding the polypropylene fiber caused an increase in splitting tensile strength (3.2 to 34.6 %) compared to plain SCC. The maximum increase in tensile strength occurs at 1% of fiber volume fraction. As shown in Fig. 7, the addition of macro-synthetic fibers on the modulus of elasticity of SCC tends to decrease (9 to 19%). This is correlated to the small

modulus of elasticity of propylene fibers compared to the aggregate.

### Free Shrinkage

The effect of polypropylene fiber addition on free shrinkage can be seen in Fig. 8. It can be seen from the figure that the addition of polypropylene fiber slightly alters the free shrinkage strain of SCC. Similar behavior in that polypropylene fiber has an insignificant effect on free shrinkage strain reported by Grzybowski M. and Shah S. P. [18] and Sarigaphuti M., Shah S.P., and Vinson K.D. [19] for normal-weight concrete, and Daneti S. B., Wee T. and Thangayah T. [20] for lightweight concrete.

Compared with the steel fiber addition reported by Daneti S. B., Wee T., and Thangayah T. [20], the steel fiber contributes to a 12% reduction in free shrinkage strain. This could be due to the steel fiber having higher stiffness and strength than polypropylene fibers resulting in higher restraining against shrinkage. In Fig. 8, the polypropylene-FRSCC produces a higher free shrinkage strain than plain SCC. This attribute to aggregate content in mixture proportion was reduced with fiber's addition to having a constant cement to coarse aggregate ratio or filler content. Coarse aggregate content has a significant effect on shrinkage. Thus, the addition of fiber causes a decrease in shrinkage resistance when coarse aggregate content is reduced.

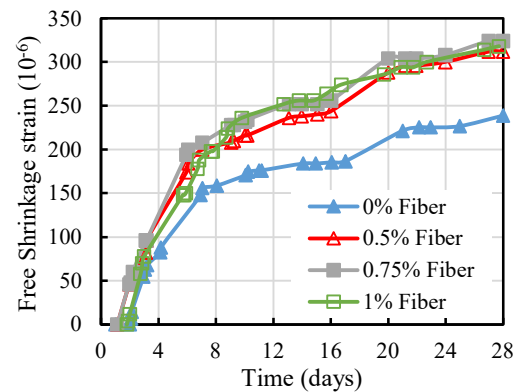


Fig. 8 Effect of Polypropylene fibers on free shrinkage

### Restrained Shrinkage

The deformation development obtained from the restrained shrinkage test measured in the steel ring is shown in Fig. 9. The time to cracking  $t_{cr}$  values in days are also indicated in the figure for each fiber volume fraction. When tensile stress resulting from the restrained shrinkage in the concrete exceeds the tensile strength, cracks can develop. As shown in Fig. 9, crack with a complete fracture or full-depth crack

are associated with a sudden drop or a compatible drop in the strain. Fiber addition to the SCC mixture can reduce cracking potential and delay crack formation, as indicated in Table 4 and Fig. 10. This agrees with previous findings comparing plain SCC and FR-SCC [21].

Table 4 Cracking age and measure strain

Mix No.	Time to cracking, $t_{cr}$ (days)	Measured strain at $t_{cr}$ ( $\times 10^{-6}$ )	Crack number
NF	3.25	38.39	1 to 2
F0.5	12.0	69.77	2
F0.75	4.0	72.87	2
F1.0	9.75	81.9	2

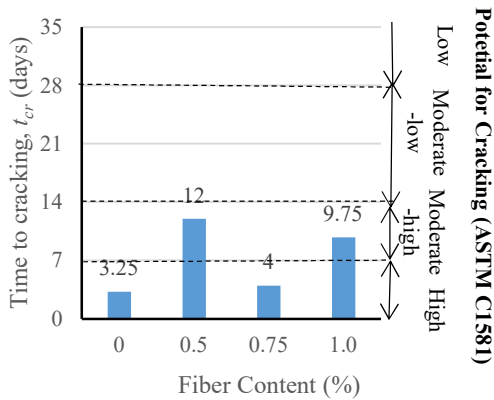


Fig. 10 Time to cracking of restrained shrinkage.

Cracking age for polypropylene fiber addition (0.5% to 1.0% fiber) increase from 4 to 12 days. The

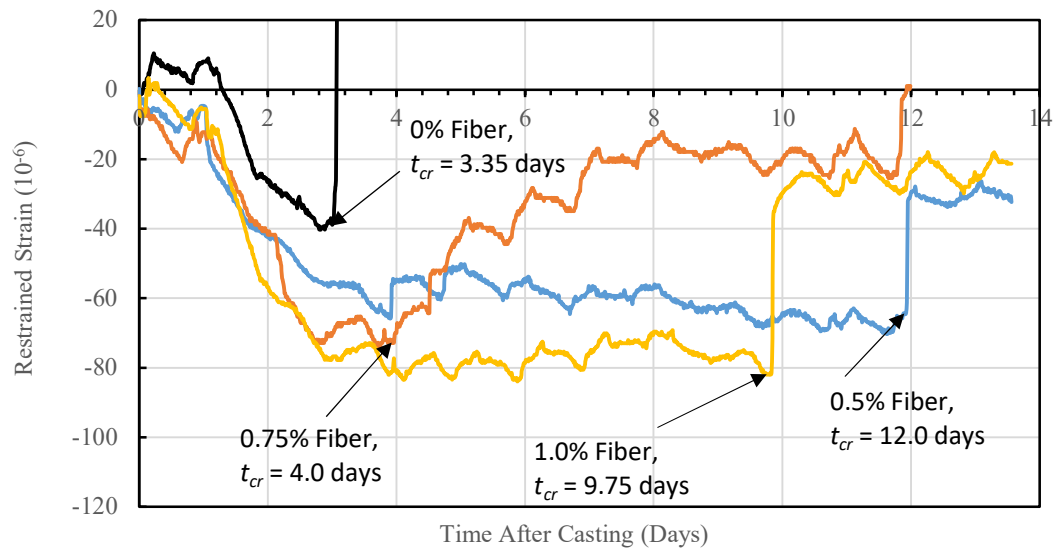


Fig. 9 Effect of Polypropylene fibers on restrained shrinkage

effect of fiber volume fraction on cracking time shows an unclear trend. However, the measured strain at cracking time increased with increasing fiber content, as shown in Table 4. Macro-synthetic polypropylene fiber addition also has smaller crack width than plain SCC, as shown in Fig. 11.



Fig. 11 Restrained shrinkage cracking (a) plain SCC (b) Fiber-Reinforced SCC.

## CONCLUSIONS

This study evaluated the effect of macro-synthetic polypropylene fibers on the fresh and hardened concrete properties, including drying shrinkage of self-consolidating concrete. The main parameters in this study are a variation of the volume fraction of fibers. The following conclusions can be drawn:

- Addition of macro-synthetic polypropylene fibers into the SCC mixture reduces the workability performance in terms of Slump flow, J-Ring, and V-Funnel values of SCC. The reduction increase with the increase in fiber volume fraction.
- Fiber's addition from 0.5 to 1% of volume fraction can increase the splitting tensile strength (3.2 to 34.6 %) and can decrease the compressive



strength (5.7 to 14.6%).and modulus of elasticity (9 to 19%) compared to plain SCC.

- From the restrained shrinkage test, adding 0.5 to 1% of polypropylene fibers in the SCC mixture can lower the cracking potential, with thin cracks appearing within 4 to 12 days.

## ACKNOWLEDGMENTS

The authors acknowledge the financial support from Bandung Institute of Technology (ITB), Indonesia to carry out the research under the Program Penelitian, Pengabdian pada Masyarakat dan Inovasi (P3MI). The authors are also thankful to PT Abel Grup Indonesia for supplying the polypropylene fibers used in this research.

## REFERENCES

- [1] Nehdi M. and Ladanchuk J. D., Fiber Synergy in Fiber-Reinforced Self-Consolidating Concrete. *ACI Materials Journal*, Vol. 101, No. 6, 2004, pp.508-517
- [2] Loser R. and Leemann A., Shrinkage and restrained shrinkage cracking of self-compacting concrete compared to conventionally vibrated concrete. *Mater. Struct.*, Vol.42 (1), 2009, pp. 71-82
- [3] Leemann, A., Lura P. and Loser R., Shrinkage and creep of SCC–The influence of paste volume and binder composition. *Constr. Build. Mater.*, Vol.25 (5), 2011, pp. 2283-2289
- [4] Wani T. A. and Ganesh S., Study on fresh properties, mechanical properties and microstructure behavior of fiber-reinforced self-compacting concrete: A review, *Materials Today: Proceedings*, 2022, pp.1-14
- [5] Li K.F., Yang C.Q., Wei Huang, Zhao Y.B., Yi Wang, Yong Pan, and Xu F. Effects of hybrid fibers on workability, mechanical, and time-dependent properties of high strength fiber-reinforced self-consolidating concrete, *Constr. and Build. Mater.* Vol.277 (3), 2021, pp.1-12
- [6] Drago S., Branko, B., Jakob Š., Jože, L. and Franc S., Shrinkage of polypropylene fiber reinforced high-performance concrete. *Journal of materials in civil engineering*, Vol. 23, Issue. 7, 2011, pp. 941-952.
- [7] Brown M. C., Ozyildirim H. C., and Duke W. L., Investigation of Steel and Polymer Fiber Reinforced Self-Consolidating Concrete, *ACI Symposium Paper*, Vol 274(5), 2010, pp.69-78
- [8] ASTM C 341/341M-06, Standard Practice for Length Change of Cast, Drilled, or Sawed Specimens of Hydraulic-Cement Mortar and Concrete, ASTM International, West Conshohocken, 2006.
- [9] ASTM C1581/1581M-09a, Standard Test Method for Determining Age at Cracking and Induced Tensile Stress Characteristic of Mortar and Concrete under Restrained Shrinkage, ASTM International, West Conshohocken, 2009.
- [10] ASTM, C1611/C1611M-14, Standard Test Method for Slump Flow of Self-Consolidating Concrete, ASTM International, West Conshohocken PA, 2014.
- [11] ASTM C1621/C1621M-09a, Standard Test Method for Passing Ability of Self-Consolidating Concrete by J-Ring, ASTM International, West Conshohocken PA, 2009.
- [12] EFNARC, The European Guidelines for Self-Compacting Concrete. Surrey, United Kingdom, 2005
- [13] ASTM C39/C39M-09a, Standard Test Method for Compressive Strength of Cylindrical Concrete Specimens, ASTM International, West Conshohocken PA, 2009.
- [14] ASTM C496/C496M-04, Standard Test Method for Splitting Tensile Strength of Cylindrical Concrete Specimens, ASTM International, West Conshohocken PA, 2004.
- [15] ASTM C469/C469M-02, Standard Test Method for Static Modulus of Elasticity and Poisson's ratio of Concrete in Compression, ASTM International, West Conshohocken PA, 2002.
- [16] Forgeron D. and Omer A., Flow Characteristics of Macro-Synthetic Fiber-Reinforced Self-Consolidating Concrete, *ACI Symposium Paper*, Vol 274(1), 2010, pp.1-14
- [17] Yao W., Li J., and Wu K., Mechanical Properties of Hybrid Fiber-Reinforced Concrete at Low Fiber Volume Fraction, *Cement and Concrete Research*, Vol. 33, No. 1, 2003, pp. 27-30
- [18] Grzybowski M., and Shah S. P., Shrinkage cracking of fiber reinforced concrete. *ACI Materials Journal*, Vol.87(2), 1990, pp.138-148.
- [19] Sarigaphuti M., Shah S.P., and Vinson K.D., Shrinkage cracking and durability characteristics of cellulose fiber reinforced concrete, *ACI Materials Journal*, Vol.90 (4), 1993, pp.309-318
- [20] Daneti S. B., Wee T. and Thangayah T., Effect of polypropylene fibers on the shrinkage cracking behaviour of lightweight concrete, *Magazine of Concrete Research*, Vol. 63(11), 2011, pp.871-881
- [21] Kassimi F. and Khayat K. H., Strategies to Mitigate Cracking of Self-Consolidating Concrete, *ACI Materials Journal*, Vol. 116, No. 3, 2019, pp.73-83.

## ACTIVATION ENERGIES OF CHLORIDE INDUCED CORROSION OF STEEL IN CONCRETE

Takahiro Nishida<sup>1</sup>, Keiyo Kawai<sup>2</sup> and Nobuaki Otsuki<sup>3</sup>

<sup>1</sup>Department of Civil Engineering, Shizuoka Institute of Science and Technology, Japan; <sup>2</sup>, Civil and Environmental Engineering, Ehime University, Japan; <sup>3</sup> Tokyo Institute of Technology, Japan

### ABSTRACT

The corrosion reaction of steel in concrete occurs sequentially, governed by elementary reactions such as the rate of dissolution of steel into the solution, the rate of diffusion of oxygen in Nernst diffusion layer, and the flow of electricity etc. Understanding and controlling the elementary reaction can reduce the rate of corrosion reaction induced by chloride attack in concrete. One way to understand the rate-limiting reactions of steel corrosion in concrete is to determine the activation energy of steel corrosion based on reaction kinetics and identify the rate-limiting process by figuring out which elementary reaction's activation energy is equal to the overall one. In this study, the activation energies related to chloride-induced corrosion in concrete, such as chloride ion/oxygen diffusion and micro-cell/macro-cell corrosion rates, were obtained from literature review and experiments to discuss the rate-limiting reaction of the corrosion reaction of steel in concrete based on reaction kinetics. As the results, the influence of temperature on deterioration due to chloride attack is explained by the Arrhenius theory from the viewpoint of practice and the activation energies are obtained. Also, the lifetime of structures in several cities in severe marine environment are estimated using obtained activation energies. And the lifetime of the structures in south Asian cities are estimated relatively short.

*Keywords: Temperature, Chloride induced corrosion, Activation energies, Diffusion, Steel corrosion*

### INTRODUCTION

Reinforced concrete is currently facing a major challenge in its maintenance worldwide due to the lack of supply of sufficient quality materials and limited construction budgets. Chloride induced corrosion of steel bars in concrete is one of the durability problems [1], [2], [3] especially in coastal and marine areas. Since concrete deterioration is based on diffusion and chemical reactions, the progressing speed of deterioration depends on temperature. It is generally known that the rate of material diffusions or the chemical reactions rises with the temperature elevation [4].

In developed countries such as the United States, the European Union, and Japan, standards for reinforced concrete construction materials and methods are set based on research and experience under mild temperature conditions (around 20°C). These standards are used and followed in some developing countries without sufficient local investigations. When conducting a survey using standards established in other countries, temperature is one of the most important parameters, as well as the materials used.

In above viewpoints, it is necessary to determine the influence of temperature on the deterioration process of reinforced concrete due to chloride attack and discuss the appropriate predicting or maintenance method under several temperature conditions. Especially Steel corrosion due to chloride in concrete

is one of the most serious deteriorations of reinforced concrete. The corrosion reaction of steel occurs sequentially, governed by elementary reactions such as the rate of dissolution of steel into the solution, the rate of diffusion of oxygen in Nernst diffusion layer, and the flow of electricity etc. Understanding and controlling the elementary reaction can reduce the rate of corrosion reaction induced by chloride attack in concrete. One way to understand the rate-limiting reactions of steel corrosion in concrete is to determine the activation energy of steel corrosion based on reaction kinetics and identify the rate-limiting process by figuring out which elementary reaction's activation energy is equal to the overall one. In this study, the activation energies related to chloride-induced corrosion in concrete, such as chloride ion/oxygen diffusion and micro-cell/macro-cell corrosion rates, were obtained from literature review and experiments to discuss the rate-limiting reaction of the corrosion reaction of steel in concrete based on reaction kinetics. Finally, temperature effects were introduced into the lifetime prediction of reinforced concrete members.

### METHODOLOGY

#### Materials Used and Environmental Conditions

Ordinary Portland cement (density: 3.16 g/cm<sup>3</sup>, specific surface area: 3 270 cm<sup>2</sup>/g) was used as binder. River sand (density (SSD): 2.60 g/cm<sup>3</sup>, F.M.: 2.59) and crashed stones (density (SSD): 2.64 g/cm<sup>3</sup>, F.M.:



diffusion or chemical reaction with the temperature elevation can be theoretically confirmed. During the process of chemical reactions, the reactants seem to shift to the products side through an active state with high energy. The difference energy between the active state and the reactant is called as the activation energy [4]. In the process, where multiple chemical reactions are sequentially generated, the activation energy follows the reaction which determines the rate of reaction.

On the other hand, by taking the logarithm of the given equation, equation (1) will be transformed into the following equation. From experimental results, the relationship between logarithm of the rate constant and the reciprocal of absolute temperature is generally called the Arrhenius plot.

$$\log k = \left( \frac{-\Delta E}{R} \cdot \log_{10} e \right) \left( \frac{1}{T} \right) + \log a \quad (2)$$

The activation energies reported in literatures as shown in Table 1.

#### Temperature Effect on Cl<sup>-</sup> Diffusivity in Concrete

The influence of temperature on diffusivity of Cl<sup>-</sup> in concrete is shown in Fig. 3. From this graph, the rate of Cl<sup>-</sup> diffusion in concrete rises up with the increase in temperature. Also, the Arrhenius plots of the Cl<sup>-</sup> diffusivity in concrete are shown in Fig. 4. From this, the relationship between logarithms of the diffusivity and the reciprocal of absolute temperature can be linearly distributed. It can be concluded that the diffusion of Cl<sup>-</sup> in concrete follows Arrhenius theory. Moreover, the apparent activation energies of the Cl<sup>-</sup> diffusivity in concrete obtained from Arrhenius plots are shown in Table 2. From this table, the apparent activation energies obtained in this study are a little high comparing with that obtained in literature survey [7]. This is because activation energies obtained in the literature survey are based on the data of cement paste. On the other hand, the Cl<sup>-</sup> diffusivities of minute test pieces taken from concrete containing interfacial transition zone between aggregate and cement matrix are used in this study. That is, it is considered that the pore structure of cement matrix, especially the property of the interfacial transition zone, influences on the apparent activation energy and diffusion phenomenon.

Fig. 5 shows the relationship between Cl<sup>-</sup> diffusivity of concrete and water cement ratio proposed by JSCE standard specification [8]. And the broken lines in the graph show the Cl<sup>-</sup> diffusivities considering with  $\pm 10$  °C difference against JSCE equation using obtained apparent activation energy. From this graph it is observed that the scattering of Cl<sup>-</sup> diffusivity in the literature data seems to be explained by temperature effect. Therefore, it can be concluded that the temperature profile is one of the

Table 1 Activation energies in literature.

Kinds	Authors	Activation Energy (kcal/mol)
Cl <sup>-</sup> Diffusivity in Cement Past	C. L. Page et al, 1981	7.7~10.0
Carbonation of Concrete	Uomoto et al, 1992	Around 5.1
O <sub>2</sub> Diffusivity in Cement Past	C. L. Page et al, 1987	3.6~5.3
Steel Corrosion in Cl <sup>-</sup> Solution	J. J. Podesta' et al, 1965	Around 11.5
Steel Corrosion in CO <sub>3</sub> Solution	C. De Waard C et al, 1975	Around 10.7

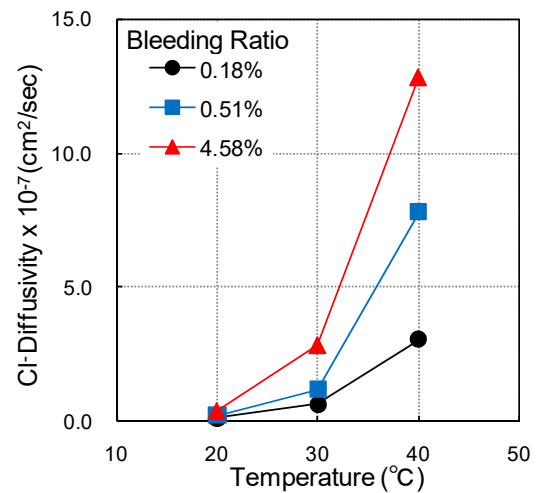


Fig. 3 Influence of temperature on Cl<sup>-</sup> diffusivity in concrete.

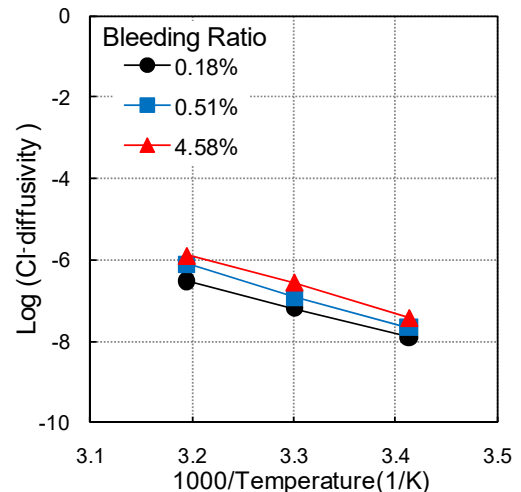


Fig. 4: Arrhenius plots of Cl<sup>-</sup> diffusivity in concrete

most important factors when we check the diffusion coefficient of Cl<sup>-</sup> in design stage.

Table 2 Apparent activation energies of Cl<sup>-</sup> diffusivity in concrete obtained from Arrhenius plots.

	Activation Energy (kcal/mol)
Present study: containing aggregate	16.8-32.2
Literature survey [7]: cement paste	7.7-10.0

### Temperature Effect on Corrosion in Concrete

The influences of temperature on macrocell and microcell corrosion rate in concrete are shown in Fig. 6. From these graphs, the macrocell and microcell corrosion rate in concrete rise with temperature

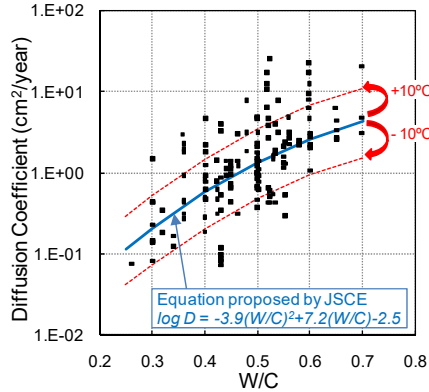
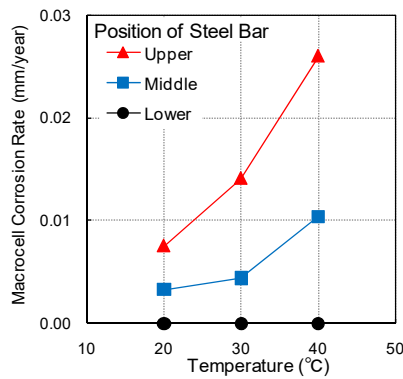
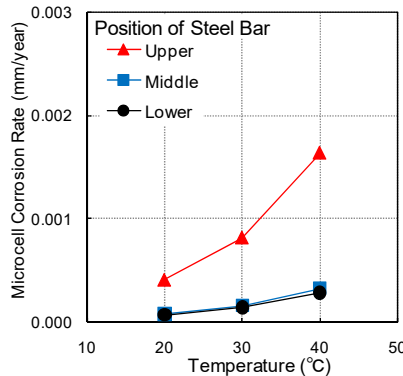


Fig. 5 Relationship between Cl<sup>-</sup> Diffusion Coefficient and W/C and temperature effect obtained in present study

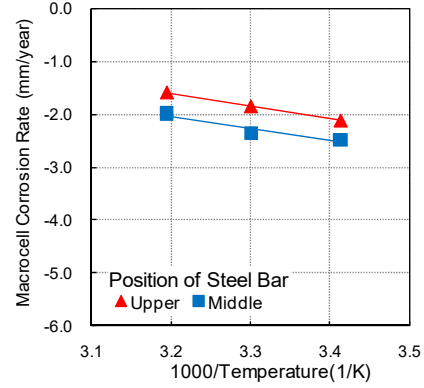


(a) Macrocell corrosion rate

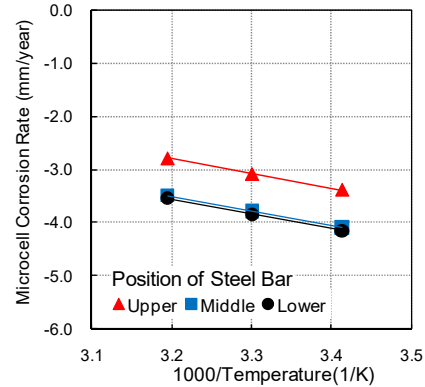


(b) Microcell corrosion rate

Fig. 6 Influence of temperature on corrosion rate of steel bars in concrete.



(a) Macrocell corrosion rate



(b) Microcell corrosion rate

Fig. 7: Arrhenius plots of corrosion rate of steel bars in concrete

elevation. Also, the Arrhenius plots of the corrosion rate in concrete are shown in Fig. 7. From these figures, the relationship between the logarithms of corrosion rate and the reciprocal of absolute temperature can be linearly distributed. Therefore, it can be concluded that the behavior of steel corrosion in concrete follows Arrhenius theory. Moreover, the apparent activation energies of macrocell and microcell corrosion in concrete obtained from Arrhenius plots are shown in Fig. 8. From these figures, macrocell and microcell corrosion in concrete has different temperature dependency. That is to say, the apparent activation energy of macrocell corrosion increases with the increase in specific concrete resistance. On the other hand, the apparent activation energy of microcell corrosion is constant regardless of the specific concrete resistance. The activation energy corresponds to ion diffusion phenomena in concrete, rather than O<sub>2</sub> diffusivity as shown in Table 1. Therefore, the corrosion rate of microcells in concrete was thought to be controlled by ion migration, such as Fe<sup>2+</sup>, when the steel was exposed to chloride attack in atmospheric condition.

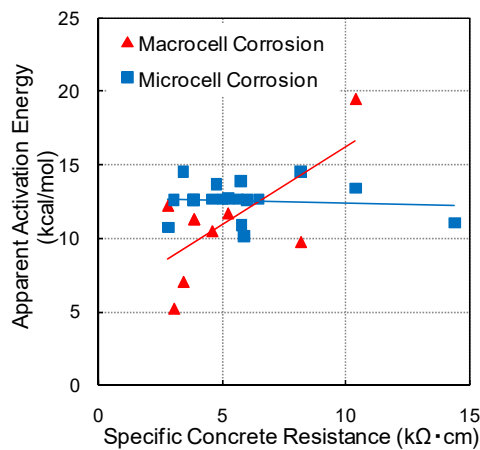


Fig. 8 Apparent activation energy of corrosion rate of steel bar.

## PREDICTION OF DETERIORATION PROCESS CONSIDERING TEMPERATURE EFFECT

### Lifetime of Reinforced Concrete due to Steel Corrosion

The determination of the lifetime of reinforced concrete is a difficult task because it includes many factors such as the importance of structures, part of the member or financial issue. However, it is important to discuss the lifetime of structures based on several assumptions from the engineering point of view. In this study, the lifetime was defined as the sum of the terms of prediction results of the incubation, propagation and acceleration period, and the influence of temperature on the lifetime of reinforced concrete was discussed.

The water cement ratio, water content in mixture proportion and concrete cover were set at 0.55, 175 kg/m<sup>3</sup> and 7.0 cm respectively. The environmental condition considered in this prediction was tidal zone which is considered as the most severe environment that induces chloride attack. Also, in this prediction, the data of temperatures for 55 cities around the world was used.

### Prediction of Incubation Periods

To predict the incubation periods, the rate of Cl<sup>-</sup> diffusion in reinforced concrete considering the temperature was investigated using a numerical analysis. In this numerical analysis, Nernst-Planck equation considering with Debye-Hückel equation and electro-neutrality condition was used. By considering these equation and condition, the influence of co-existing ions in pore solution of concrete could be simulated. The effectiveness of this numerical analysis was already confirmed in the literature survey done by authors [9]. In this study the above numerical analysis was modified to consider

the effect of the temperature.

The steel bar in concrete starts to corrode after the Cl<sup>-</sup> concentration over the certain value (threshold concentration). “Technical Standards and Commentaries for Port and Harbour Facilities in Japan” describes that the threshold concentration of Cl<sup>-</sup> can be set at around 2.0 kg/m<sup>3</sup> in port and harbour port concrete facilities. In this study, the period until the Cl<sup>-</sup> concentration around steel bar reaches to 2.0 kg/m<sup>3</sup> is calculated by numerical analysis as incubation period.

### Prediction of Propagation and Acceleration Periods

To predict the propagation and acceleration periods, the rate of steel corrosion in concrete considering temperature effect was investigated. The total quantity of corrosion was calculated by taking the sum of the quantity of corrosion in each period. The method of prediction for steel corrosion in concrete considering temperature effect is explained in the following.

Considering the influence of temperature on deterioration of reinforced concrete, the rate of corrosion of steel bar (macrocell and microcell) in concrete is different from each period. Especially it was confirmed that the influence of temperature on macrocell and microcell corrosion is different in previous chapters. Therefore, in case of predicting the propagation and acceleration period, it is necessary to consider the influence of temperature on macrocell and microcell corrosion rate separately. In this study the quantity of corrosion was calculated by integration of the rate of macrocell or microcell corrosion. The total quantity of corrosion was then calculated by the sum of the quantities of macrocell and microcell corrosion.

In the case of predicting the process of corrosion in concrete, it is necessary to know the basic rate of corrosion at a certain temperature. The data of corrosion rate at 20 °C in Table 3 were used as a reference for the basic rate of steel corrosion in concrete. In the case of corrosion rate of steel bar in concrete before cracking, the experimental results obtained in the previous section were used. On the other hand, in the case of the corrosion rate after cracking, the experimental results obtained by Otsuki [6] were used.

The total quantity of corrosion is calculated by taking the sum of the quantity of corrosion rates obtained in each period. Here it is reported that the total quantity of corrosion for crack propagation is equal to 10 mg/cm<sup>2</sup>. Also it is reported that the bending property of reinforced concrete becomes 70% of the initial property when 15 % of the steel bar decreases due to corrosion [9]. According to this literature survey the quantity of corrosion at 15 % degradation of strength in case of steel bar with 16mm



Table 3 Data of corrosion rate at 20 °C.

	Corrosion rate at 20 °C (mm/year)	
	Macrocell	Microcell
Before cracking	$5.5 \times 10^{-3}$	$2.6 \times 10^{-4}$
After cracking [6]	$2.0 \times 10^{-2}$	$6.0 \times 10^{-2}$

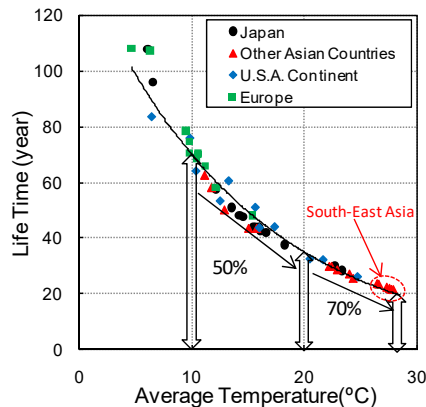


Fig. 9 Predicted results of lifetime of reinforced concrete using the 55 cities of temperature profile.

diameter is about 510 mg/cm<sup>2</sup> [10]. Therefore, the quantities of corrosion at 10 mg/cm<sup>2</sup> and 510 mg/cm<sup>2</sup> were used in order to determine the periods of cracking (end of propagation period) and structural deterioration (end of acceleration period) respectively.

### Predicted Results

Fig. 9 shows the relationship between the lifetime of reinforced concrete and the average temperature. From this figure it can be confirmed that the period of incubation, propagation and acceleration varied with the regional and seasonal temperature, and the lifetime of reinforced concrete exponentially decreased as the average temperature of the city. It is therefore necessary to consider temperature effect on the design and maintenance of reinforced concrete, especially in the key cities of South-East Asian countries, where deterioration was most severe as indicated by reinforced concrete having only 70 % of the lifetime compared to other countries with mild temperature environment (20 °C). Also it can be considered that the lifetime of the reinforced concrete decreases 50% with 10 °C increase of temperature.

### CONCLUSIONS

In present study, the influence of the temperature on the deterioration progress of RC due to chloride attack is theoretically and experimentally investigated. From the investigations the following conclusions are obtained.

- 1) The influence of temperature on deterioration

due to chloride attack is explained by the Arrhenius theory from the viewpoint of practice and the activation energies are obtained.

- 2) The lifetime of structures in several cities in severe marine environment are estimated using obtained activation energies. And the lifetime of the structures in south Asian cities are estimated relatively short.

### REFERENCES

- [1] Leeming, M. B., 1983. Corrosion of Steel Reinforcement in Off-shore Concrete Experience from the Concrete-in-the-Oceans Programme, Corrosion of Reinforcement in Concrete Construction, Edited by. A.P. Crane. Ellis Horwood Ltd., Chichester, UK, 59-78.
- [2] Sørensen, B., and Maahn, E., 1982. Penetration Rate of Chloride in Marine Concrete Structures, Nordic Concrete Research, Publication No.1, 24.
- [3] Popovics, S., Simeonov, Y., Boshinov, G., and Barovsky, N., 1983. Durability of Reinforced Concrete in Sea Water, Corrosion of Reinforcement in Concrete Construction, Edited by. A.P. Crane. Ellis Horwood Ltd., Chichester, UK, 19-38.
- [4] Ohki, M., Ohsawa, T., Tanaka, M., and Tihara, H., 1994. Chemical Dictionary, 275.
- [5] Otsuki, N., Yodsudjai, W., Nishida, T., and Yamane, H., 2004. New Test Methods for Measuring Strength and Chloride Ion Diffusion Coefficient of Minute Region in Concrete, ACI Materials Journal, V. 101, No. 2, 146-153.
- [6] Otsuki, N., Miyazato, S., Diola, N. B., and Suzuki, H., 2000. Influences of Bending Crack and Water-Cement Ratio on Chloride-Induced Corrosion of Main Reinforcing Bars and Stirrups, ACI Materials Journal, V. 97, No. 4, 454-464.
- [7] Page, C. L., Short, N. R., and Tarras, A. El, "Diffusion of chloride ions in hardened cement pastes." Chemical and Concrete Research, 11, 1981, pp.395-406.
- [8] Japan Society of Civil Engineers, 2001. Standard Specification for Concrete, Maintenance, 97-112.
- [9] Minagawa, H., Otsuki, N., Miyazato, S., and Nishida, T., 2002. Establishment of Numerical Analysis Method For the Prediction of Leaching of Calcium from Concrete Considering Migration of Multiple Ions, Concrete Library of JSCE, No.40, 253-268.
- [10] Maruya, T., Tangtermsirikul, S., Matsuoka, Y., 1992. Simulation of Chloride Movement in Hardened Concrete, Journal of Materials, Concrete Structures and Pavements, Japan Society of Civil Engineers, No.442/V-16, pp.81-90.

## APPLICATION OF DIGITAL IMAGE CORRELATION METHOD IN RC AND FRC BEAMS UNDER BENDING TEST

Messa Revolis<sup>1</sup>, Aris Aryanto<sup>2</sup>, Yuki Oribe<sup>3</sup> and Hibino Yo<sup>4</sup>

<sup>1,2</sup> Faculty of Civil and Environmental Engineering, Bandung Institute of Technology, Indonesia; <sup>3,4</sup> Graduate School of Engineering, Hiroshima University, Japan

### ABSTRACT

Techniques to monitor the strain field and crack development in the experimental testing are continuously improved. Digital Image Correlation (DIC) technique is recently developed and is a powerful tool for measuring object deformation. Using image correlation, this method can correlate the digital images of the undeformed and deformed objects to determine the displacement and strain field. Compared to conventional techniques (such as strain gauges), DIC has superiority due to computational accuracy, efficiency, and non-contact measurement. In this study, DIC is applied to analyze the mechanics of plain and fibrous concrete beams under the 4-point bending test in the laboratory. Four test specimens were cast: a plain and fibrous concrete with and without longitudinal reinforcement. Displacement and strain fields derived from digital image correlations are analyzed in crack detection, deflection, and curvature of beams. DIC analysis results show good agreement with experimental measurement and are suitable for early crack detection and measurement. Monitoring strain fields and cracks using DIC confirms the influence of fiber engagement on load resistance, cracking, and flexural behavior.

*Keywords: Digital Image Correlation (DIC), Concrete beams, Strain, Crack*

### INTRODUCTION

Reliable deformation measurement is essential for experimental test measurements in concrete structures. The most common conventional technique to measure deformation and strain field is strain gauges attached to the specimen's surface, e.g., concrete or steel reinforcements. However, measuring displacement and strain fields to capture the structural behavior requires many gages, which will be expensive.

Recently, a method known as Digital Image Correlation (DIC) has been developed to measure deformation and strain variation and crack patterns on an element's surface plane. This is based on advances in digital technology that capture high-resolution images supported by an advanced computation that can process the data from a digital image correlation [1]. DIC is relatively easy to operate, reduces research costs, and is considered more accurate in results than conventional measurements. It can also be performed for various potential applications and in different materials [2]. Several open-source and non-commercial DIC processing software are available nowadays [3].

The DIC technique is a non-contact optical measurement technique that can be applied to the test object's surface. It requires a continuous digital image that captures during the test. The displacement field is determined from the correlation between two images, undeformed and deformed images. This method can be applied from a small to a large-scale test. The accuracy of displacement measurement by

DIC is highly dependent on image texture or contrast [4], [5], and image resolution [6].

In concrete structural engineering, numerous concrete material and element testing is commonly carried out, e.g., compressive, tensile, flexure, and fracture tests. Those testing may utilize DIC technology to measure deformation and strain variation. For example, Sindu B. S. and Sasmal S. [7], Verbruggen S., DeSutter S., Iliopoulos S., Aggelis D.G., and Tysmans T. [8], and Lacidogna G., Piana G., Accornero F., and Carpinteri A. [9] use the DIC method for beam testing. Gali S. and Subramaniam K. V. L. [10] investigate the shear behavior of fiber-reinforced beams using the DIC technique. The application of the DIC method on fracture and crack was conducted by Fayyad T. M. and Lees J. M [11] and Bhosale A. B. and Prakash S.S. [12], Filho J, Xavier J, and Nunes L. [13], respectively. Meanwhile, Gentruck et al. [14] use DIC for full-scale testing of the prestressed concrete structures. Moreover, the extent of DIC's capabilities and the accuracy of results still need to be studied and verified.

In this study, the DIC method will be used in the 4-point bending testing of beams to evaluate deformation behavior and crack propagation by comparing the results from the strain gauge readings. Four concrete beams were cast using normal (plain) or fibrous concrete with or without longitudinal reinforcement. In addition, fiber's addition to concrete mixture has been known to change the post-cracking behavior of the concrete elements.

## EXPERIMENTAL PROGRAM

Four concrete beams were cast and tested to investigate load-deformation and crack behavior. All beams have similar dimensions, specified concrete strength, and loading arrangement but differ in fiber and longitudinal reinforcement addition. Polypropylene fiber with a 0.5% of volume fraction was used in this experiment. Specified concrete strength is 60 MPa, and the average measured concrete strength from compressive testing is 62 MPa for normal concrete (NC) and fiber concrete (FC).

Table 1 Specimen details

Specimen	Concrete type	Deformed steel bars
NC	Plain	No
FC	Fiber	No
NC-S	Plain	2D13
FC-S	Fiber	2D13

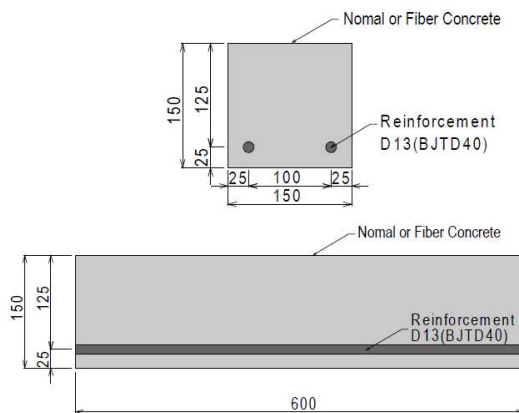


Fig. 1 Beam dimensions (in mm).

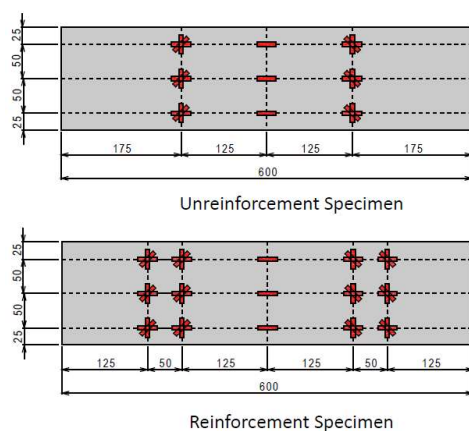


Fig. 2 Strain gages setup configurations.

This study uses a deformed steel bar with a nominal diameter of 13 mm with a specified yield

strength of 400 MPa (BJD40). All specimens tested in this study are summarized in Table 1. Fig.1 below shows the beam dimensions and reinforcement details.

To evaluate the strain and curvature in concrete beams, the strain gauges were attached to the surface of one side of the shaft, and another surface side was used as a surface object for DIC measurement. Strain gages configuration is shown in Fig. 2 for unreinforced and reinforced beam specimens.

## DIC Experimental Setup

All specimens were tested using a four-point bending test. Each beam was supported at both ends by two roller supports. The two-roller support was kept to have a clear distance of 450 mm. The load was applied at two-point that have a distance of 150 mm from each support. The beams were loaded using a universal testing machine (UTM) with displacement control. Three linear variable displacement transducers (LVDT) were installed under beams at 1/3, 1/2 (midspan), and 2/3 of the beam span to measure the deflection. A micro-camera with the crack width measurement was used to measure the crack opening.

A DLSR camera with a maximum image resolution of 5184 x 3456 pixels and a focal length of 55 mm was used to record the digital images under loading. The camera was put on a tripod and fixed away from the specimen and has a perpendicular axis to the surface of interest. Surface displacements were obtained by DIC using digital image cross-correlation. The image must have a particular texture from speckle patterns. To have speckle patterns, the one surface of beams was sprayed by applying a uniform white paint followed by a mist of black paint from the spray nozzle. The speckle patterns were created on the side without strain gauge attachment.

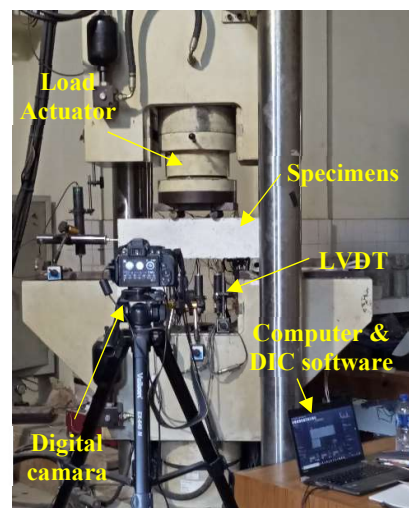


Fig. 3 DIC and loading test setup.

## RESULTS AND DISCUSSION

### Load-deflection Relationship

Beam's load-deflection responses are shown in Fig.4. Measured beam deflections shown in the figure are obtained at the midspan location. Beams' load capacity increases with the presence of fibers and longitudinal bars. The load response could not be controlled after the peak load in a beam without fibers and steel bars (NC), even with displacement control. With fiber addition in the concrete beams (FC and FC-S), there is an increase in load capacity indicated by the peak load. The peak load and corresponding deflections of all beams are listed in Table 2. The post-peak load response in fiber concrete beams showed a larger deflection than in non-fibers concrete beams. In FC specimens, beam with fibers and without longitudinal bars, there is a second peak load after the first peak or cracking load. This indicates that fibers significantly affect post-cracking behavior as crack-bridging increases deformation and toughness capacity. As shown in Fig.4(b) for FC-S specimens, there is no second peak load. However, there is a steady decrease, almost constant, in the load with increasing deflection. The effect of fibers is also noticed when comparing the peak load with the beam without fibers (NC-S).

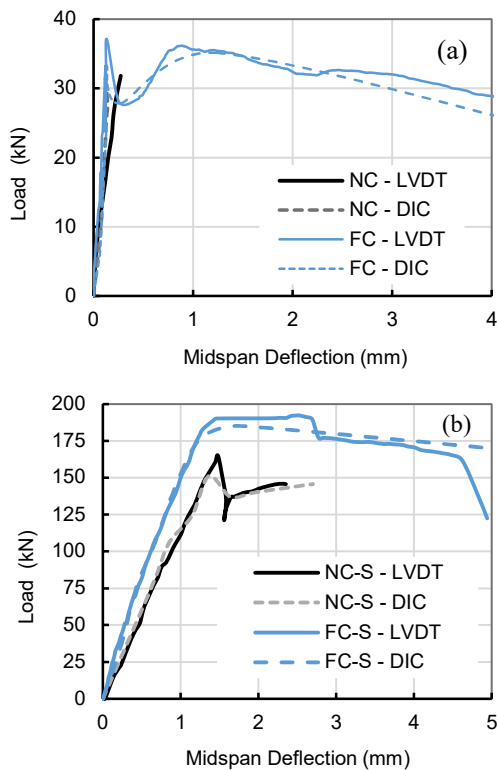


Fig. 4 Load-deflection responses of beams (a) NC

vs. FC (b) NC-S vs. FC-S.

Table 2 Summary of beams test

Specimen	Peak Load (kN)	Percent increase in peak load	Mode of failure
NC	31.8	-	Flexure
FC	35.12	27.6%	Flexure
NC-S	145.7	-	Shear
FC-S	185.08	27%	Shear

Note: comparison was made only between non-fiber and fiber concrete.

The images taken under different load conditions were analyzed using DIC software for each beam specimen using cross-image correlations. The displacement vectors of the DIC analysis results determined the beam deflection and crack opening. The displacement value from the DIC analysis was verified against the displacement from LVDTs. As shown in Fig. 4, the DIC approach effectively measures the displacement of beam elements.

### Crack pattern and crack progression

DIC was used to evaluate the beams' crack pattern and crack progression. Field strain measurement in the horizontal direction identifies the crack on the concrete beam surface. To identify cracks in the surface, a localized swarm of strain contours in a small region can indicate the crack. The crack pattern and the cracking sequence can be observed using this procedure. The DIC analysis results can have more accurate than visual observation.

The formation and progression of cracks in beams with fibers and longitudinal bars (FC-S) are shown in Fig. 5. Flexural crack was initiated in the middle of the beam at a load of 35.26 kN. Then, a shear crack located near the support was formed, as shown in Fig. 5(a). The shear crack was formed at approximately 45-degree of the height of the beam. Then another shear crack that originated from the flexural crack was also developed. This shear crack extended to the load point and became a primary failure mode. The shear failure mode of beams is due to longitudinal bars that increase the flexural capacity. All beams without longitudinal steel bars fail in flexure. Comparing FC-S and NC-S, a beam without fibers (NC-S) not only exhibits shear cracking but also experiences bond-splitting cracking, as shown in Fig. 6(c). This is also identified in the load-deflection response in Fig.4(b) that the beam exhibits small deflection. This also indicates that fibers significantly increase the bond splitting capacity of beams. DIC results can generally capture the crack pattern and progression, which is essential for evaluating structural behavior and mode of failure.



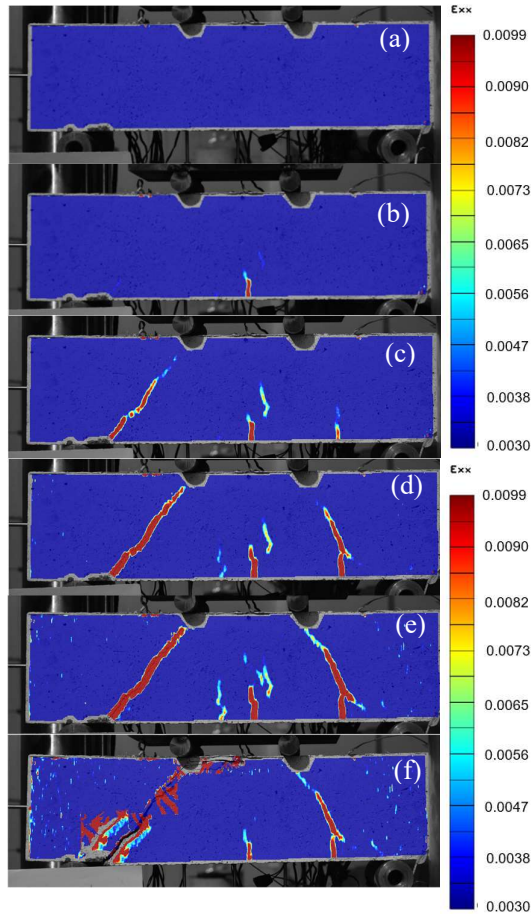


Fig. 5 Strain contours of FC-S beam at loads (a) 35.26 kN (b) 77.14 kN (c) 106.05 kN (d) 139.37 kN (e) 185.08 kN (f) failure.

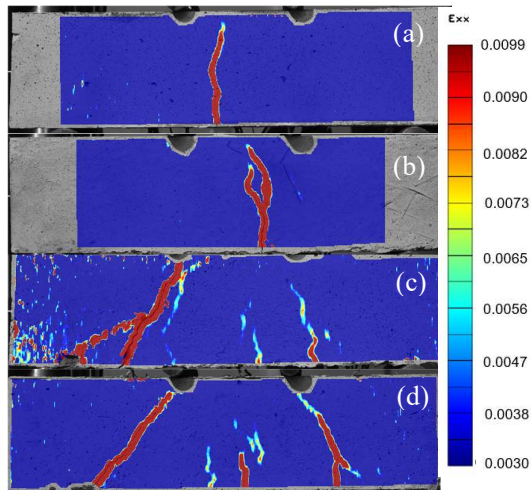


Fig. 6 Strain contours at peak load of beams: (a) NC (b) FC (c) NC-S (d) FC-S.

The crack patterns at the peak load for all beams are shown in Fig. 6. It is clearly demonstrated that the critical crack patterns, e.g., shear, flexure, and bond

splitting cracks that lead to failure, can be identified through DIC analysis.

### Crack opening measurement

Crack opening of shear and flexural cracks were measured at several locations in the primary crack, as shown in Fig. 7. Fig. 7 indicates the beams' crack opening calculated using DIC and crack meter methods under different loading rates. The crack opening was measured through field displacements from the DIC analysis. Cracks can be identified accurately from displacement contours after crack formation and can be observed much earlier than visual observation. A pair of gauge points were placed on either side of the crack to evaluate the displacement across the crack. The line joining the gauge points should be perpendicular to the crack. The gauge points should be set in fixed positions in processing digital images at different loads then the horizontal and vertical displacements will be obtained. The crack opening was obtained from relative displacement between two-gauge points across the crack.

The crack openings measured across the primary crack from all beams are shown in Fig. 7. With the addition of fibers in unreinforced beams, there is a delay in flexural crack formation indicated by a higher load when compared to a normal concrete beam (NC). It also shows an increase in crack opening throughout the load response. Fiber addition for reinforced beams that fail in shear affects the crack opening, which continues to open even in the post-peak as the load decreases. This indicates that fibers control the shear crack opening or dilatancy, which may lead to an alternate failure mode. A normal beam without fibers (NC-S) leads to bond splitting failure as a horizontal crack formed at the longitudinal bar axis near the support.

### CONCLUSIONS

Digital image correlation (DIC) in this study is used to observe deformation, crack patterns, crack progression and crack opening of all beam specimens under the bending test. From this limited investigation, some conclusions can be drawn.

- DIC produces a closely load-deflection curve compared to LVDT measurement. The beam's load-carrying capacity and ductility increase with fibers addition, indicated by peak load and post-peak displacement from load-deflection responses.
- The DIC method effectively determines the crack pattern and the crack progression in the bending test of unreinforced and reinforced concrete beams with or without fiber addition. Using the DIC method, the failure mode of beams can be captured from the crack pattern and crack

progression. Unreinforced beams (NC and FC) exhibit flexural failure, and reinforced beams (NC-S and FC-S) produce shear failure.

- The crack opening at selected locations in the beams extracted from DIC analysis was used to evaluate the effect of fiber addition and longitudinal bars as beam parameters. Fiber addition affects the crack opening, which can continue to grow even in the post-peak as the load decreases. Fibers in concrete seem to play a role in the crack progression and crack bridging.

## ACKNOWLEDGMENTS

This study is part of a research collaboration program between Bandung Institute of Technology (ITB), Indonesia, and Hiroshima University, Japan. Support from both institutions is acknowledged.

## REFERENCES

- [1] Supriya S. Gadhe S.S. and Navthar R. R., Digital Image Correlation Technique for Strain Measurement of Aluminium Plate, International Journal of Engineering Trends and Technology, Vol. 39, Issue. 6, 2016, pp.306-311.
- [2] McCormick N. and Lord J., Digital Image Correlation, Materials today, Vol.13, Issue. 12, 2010. pp.52-54.
- [3] Belloni V., Ravanelli R., Nascetti A., Di Rita M. Mattei D., and Crespi M., py2DIC: A New Free and OpenSource Software for Displacement and Strain Measurements in the Field of Experimental Mechanics, Sensors, Vo.19. 3832, 2019. pp. 1-19.
- [4] Mauroux T., Benboudjema F. Turcry P., Aït-Mokhtar A., and Deves O., Study of Cracking Due

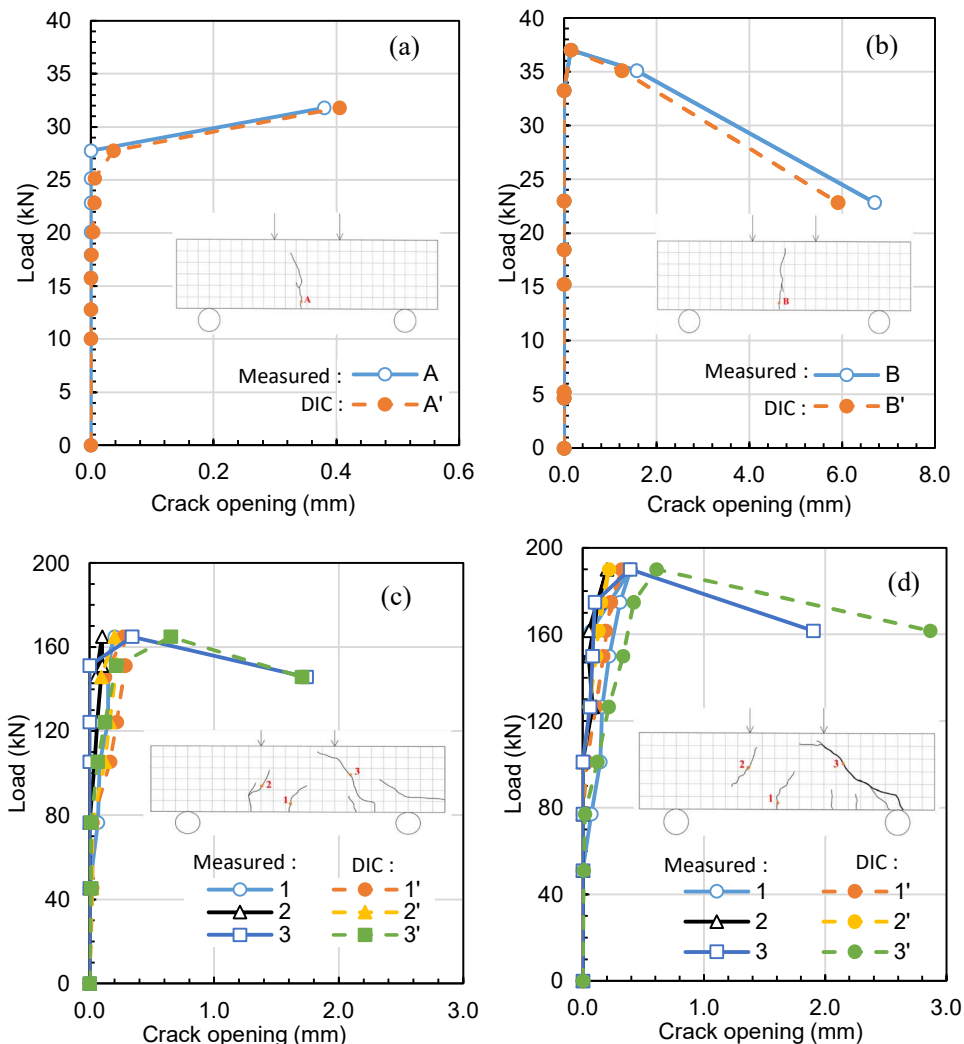


Fig. 7 Crack opening with manual and DIC measurement (a) NC (b) FC (c) NC-S (d) FC-S.



- to Drying in Coating Mortars by Digital Image Correlation, *Cement and Concrete Research*, Vol. 42, No. 7, 2012, pp. 1014-1023.
- [5] Lecompte D, Smits A., Bossuyt S., Sol H., Vantomme J., Van Hemelrijck D., Habraken A.M., Quality assessment of speckle patterns for digital image correlation, *Optics and Lasers in Engineering* Vol. 44, 2006, pp. 1132–1145.
- [6] Sun Z., Lyons J. S., and McNeill S. R., Measuring Microscopic Deformations with Digital Image Correlation, *Optic and Lasers in Engineering* Vol. 27, 1997, pp. 409-428
- [7] Sindu B. S., and Sasmal S., Multi-scale Abridged Cement Composite with Enhanced Mechanical Properties, *ACI Materials Journal*, Vol. 117, No. 4, 2020, pp.105-117
- [8] Verbruggen S., DeSutter S., Iliopoulos S., Aggelis D.G., and Tysmans T., Experimental structural analysis of hybrid composite-concrete beams by digital image correlation (DIC) and acoustic emission (AE), *J. Nondestruct. Eval.*, 35, 2016, pp. 1-10
- [9] Lacidogna G., Piana G., Accornero F., and Carpinteri A., Multi-technique damage monitoring of concrete beams: acoustic emission, digital image correlation, dynamic identification, *Constr. Build. Mater.*, 242, 2020. pp.1-18
- [10] Gali S. and Subramaniam K. V. L., Shear behavior of slender and Non-slender Steel Fiber-Reinforced Concrete Beams, *ACI Structural Journal*, Vol. 116, No. 3, 2019, pp.149-158.
- [11] Fayyad T. M. and Lees J. M., Application of Digital Image Correlation to reinforced concrete fracture, *Procedia Materials Science*, 20th European Conference on Fracture (ECF20), 2014, pp. 1585 – 1590
- [12] Bhosale A. B. and Prakash S.S., Crack Propagation Analysis of Synthetic vs. Steel vs. Hybrid Fibre-Reinforced Concrete Beams Using Digital Image Correlation Technique, *Int J Concr. Struct. Mater.*, Vol 14:57, 2020, pp.1-19
- [13] Filho J, Xavier J, and Nunes L., An alternative digital image correlation-based experimental approach to estimate fracture parameters in fibrous soft materials. *Materials*;15(7). 2022, pp.1-12
- [14] Genctrurk B., Hossain K., Kapadia A., Labib E., Mo Y. Use of digital image correlation technique in full-scale testing of prestressed concrete structures, *Measurement* Vol. 47, 2014, pp. 505-515

# A STUDY ON METHODS OF SELF-HEALING ASPHALT PAVEMENT

Enohmbey Chubisong Moses<sup>1</sup>, and Yoshitaka Kajita<sup>2</sup>

<sup>1</sup>Graduate School of Engineering, Tokai University, Japan <sup>2,3</sup>

## ABSTRACT

Asphalt is widely used in paving roads, parking lots, and other projects that require a smooth level surface. Asphalt is susceptible to cracking due to a variety of circumstances such as sun damage, water infiltration, etc. When a crack occurs on asphalt pavement, it gets widened by continuous wear and tear produced by automobiles leading to potholes and other defects, thereby preventing smooth traffic circulation. According to previous studies, researchers have discovered remarkable healing methods for asphalt in recent decades and suggested a variety of creative approaches to inspire and improve its self-healing capacity and extend the life cycle of asphalt pavement. The purpose of this study is to investigate the three main self-healing methods of asphalt pavement design. Which are Nanoparticles, Induction heating, and Rejuvenation. In summary, self-healing methods are techniques that investigate the properties of asphalt that has the potential to delay pavement cracking and increase its service life.

*Keywords: Self-healing, Asphalt pavement, Induction heating, Rejuvenation, Nanoparticles*

## INTRODUCTION

Rejuvenation and heating are two conventional techniques for achieving self-healing asphalt pavements. Typically, capsules, hollow fibers, or vascular fibers are used to integrate rejuvenators. When cracks occur, the healing agent flows out and heals the crack. Induction and microwave energy are usually used to heat the asphalt and heal the crack. While metallic additions are required for induction heating, no additives are necessary for microwave heating. Additives like nanoparticles, ionomers, supramolecular polymers, shape memory polymers, and other common polymer additives like crumb rubber are also being researched to provide asphalt intrinsic self-healing characteristics. Each of these technologies has advantages and disadvantages of its own [1]. This paper investigates the main self-healing methods available for asphalt pavement design.

## SELF-HEALING ASPHALT PAVEMENT

Erik Schlangen created a new kind of pavement called a "self-healing asphalt machine" that can repair itself over time. It is made of a porous material that enables water to drain through the surfaces and either go to the side of the road or toward collection equipment. Due to its shape, noise would disappear to the surface [1]. Erik Schlangen has used Five criteria to categorize the healing mechanism, or fatigue crack growth delay Plasticity-induced: during crack propagation, the material in the asphalt pavement is plastically deformed at the crack tip; once the load is removed, residual stresses in the matrix induce micro-closures and reduce the theoretical opening of the crack front.

- (i) Oxide-induced: deposit of debris oxide on freshly broken surfaces especially in humid conditions; the thickness of this oxide layer may be large enough

to prevent total closure changing the propagation kinetics of the crack.

- (ii) Roughness- induced: the irregularities and the micro-movements of the fracture surfaces prevent the total closure in absence of load
- (iii) Viscous fluid-induced: a viscous fluid penetrates within a growing fatigue crack affecting its propagation rate, and finally,
- (iv) Transformation-induced: phase transformations at the tip of the fatigue crack can delay the crack growth rate [2].

## Asphalt Pavement

Asphalt pavement is a Self-healing material. When asphalt is given rest intervals, it can restore its stiffness and strength by sealing the microcracks that excessive traffic loads and adverse weather have caused on the material. The wetting and inter-diffusion of material between two faces of a microcrack cause crack repair in asphalt pavement systems, which restores the original material's characteristics. When materials are moistened and mixed between two faces of a micro-crack, the crack in the asphalt pavement system is repaired and the original material's qualities are restored. To explain how asphalt materials heal, Little and Bhasin presented a three-step model: (i)wetting the two faces of a nano-crack. (ii)diffusion of the molecules from one face to the other; and (iii)randomization of the diffused molecules to restore the material's original strength [3].

## Types of Asphalt mix

There are three main types of asphalt mix: Hot Asphalt, MC Cold Mix, and UPM. Moreso, there are different varieties of these asphalts for summer and winter use [4]. When passing a construction site, we typically observe hot asphalt. Hot Asphalt, as its name

suggests, is mostly used for patching and paving. Practically it must be utilized immediately after purchase because it is easier to deal with while the asphalt is hot. As it becomes cooler, the more difficult it is to work with. MC Cold Mix is asphalt that can be used as a temporary fix. Since the asphalt is used at cold temperatures, it is slow to cure and is best used in areas that have little to no traffic. UPM is also a cold mix asphalt, but unlike MC Cold Mix, it can be used as a permanent fix to any asphalt or concrete problem, it is designed to work in any weather condition, UPM can be used to fix both wet and dry holes, allowing us to make any repair in any situation. Once it has been compacted, it is immediately ready to be tread upon.

### PREVIOUS STUDIES:

Researchers have recently discovered incredible healing potentials of asphalt and suggested several unique techniques to encourage and enhance the self-healing capacity of asphalt to increase its lifespan. using capsules containing waste oil. Their findings demonstrate that capsules can survive the mixing and compacting procedures and release the waste oils they contain when subjected to mechanical loads. Furthermore, it was discovered that samples of asphalt mastic with capsules showed self-healing levels that were 80% higher than samples without capsules, and the degree of self-healing was dependent on the ratio of capsules added to the mixtures and the curing temperature employed [5]. Tabacovic et al. 2022 investigated the impact of HealRoad capsules on the mechanical performance of 10 mm stone mastic asphalt mix and measured the damage repair (healing) effectiveness of the capsules in an asphalt mix. The results showed that HealRoad capsules do not negatively affect mix performance (indirect tensile strength and rutting resistance) when used in small amounts (>1 percent), and in certain circumstances, they even enhance it, as seen, for example, in the indirect tensile strength ratio (water sensitivity). However, because there are so few capsules in the mixture, the HealRoad capsules are unable to promote induction healing. Further research revealed that raising the capsule content to >5% of the mix can effectively activate induction heating [6]. Using molecular dynamics simulation, Zheng et al. 2022 examined the self-healing behaviour of recycled asphalt created by the liquefaction of straw oil. In their investigation, five ROSL contents designated as ROSL-2, ROSL-4, ROSL-6, ROSL-10, and ROSL-1, of 2 percent, 4 percent, 6 percent, 10 percent, and 15 percent respectively, were added to the aged asphalt to represent recycled asphalt. The molecular simulation was utilized to simulate the behaviour of Nanocracks during mending. They decided to make a three-layer structure with an outside layer of asphalt molecules and an inner layer of 30 vacuum molecules. The vacuum layer represented the asphalt's internal nanocracks. They discovered that the

elimination of cracks during the self-healing process was caused by the combined action of asphalt molecule stretching and model volume compression. Self-healing is greatly impacted by the van der Waals forces that exist between the molecules. Recycled asphalt's ability to self-heal is strongly linked to its ROSL content; the higher the ROSL concentration, the higher the diffusion coefficient, which is more suitable for self-healing. Recycled asphalt's ability to self-heal is strongly correlated with its ROSL content; the higher the ROSL concentration, the higher the diffusion coefficient, which is more conducive to self-healing. However, they suggest that the ideal ROSL content be set at 10% because ROSL-10 and ROSL-15 take roughly the same amounts of time to reach the equilibrium distribution of relative concentration and density stability, also because ROSL-10's diffusion coefficient is roughly equivalent to that of virgin asphalt [7].

### RESEARCH METHODOLOGY:

This paper studies some self-healing methods available for asphalt pavement design and will focus on three main types which are induction heating, rejuvenation, and nanoparticles

#### Types of Self-healing Agents

Healing agents mostly consist of softening additives with a high concentration of light components. Rheological and technical properties of hard binders are enhanced by the addition of these additives. Researchers have come out with self-healing methods where they employed sunflower oil, used vegetable oils, waste mineral oils, epoxy resins, waste oils from repair plants, and green bio-oils as healing agents. Asphalt has been utilized for self-healing using a few commercially available rejuvenators. The type of rejuvenator used has a big influence on how effectively the self-healing process works, so it's essential to choose one that can restore asphalt's lost properties and keep working after healing [8]

#### Induction Heating

Michael Faraday introduced the fundamental ideas behind electromagnetic induction in the 1930s. In induction heating, the material is placed in a magnetic field that has been created artificially, and as eddy currents pass through it, the substance is heated. According to researchers, temperature has a significant impact on the self-healing abilities of asphalt concrete. Raising the test temperature accelerates self-healing and simultaneously reduces the time required for complete healing. Induction heating improves asphalt concrete's potential for self-healing by raising the temperature. In this method, metallic fibers are heated by induced eddy currents and the heat energy diffuses into the bitumen to increase the temperature. The bitumen begins acting like

a Newtonian fluid when the asphalt mixture temperature exceeds the bitumen's softening point, allowing the asphalt mixture to mend quickly [9].

Some researchers have done experiments on the Preparation of asphalt concrete containing steel fibers where Conductive fibers were typically added to asphalt concrete to make it electrically conductive and suited for induction heating. Typically, without altering the mixture's graduation, steel fibers were added straight while mixing. The typical distribution of steel fibers in the mixture is depicted in Figure 1, where the steel fibers act as the heating elements and produce conductive routes. Long steel fibers are more efficient in improving asphalt mixture conductivity and induction heating speed, but they are very difficult to mix and have a propensity to form clusters that will absorb too much bitumen and reduce the mixture's mechanical qualities. Short and thick steel wool fibers with a diameter of 70–130  $\mu\text{m}$  and a length of 4.2 mm are recommended in the latest research. These steel wool fibers are relatively simple to blend using the standard mixing technique, and its ideal bitumen concentration is 6% by volume. The Marshall stability, residual Marshall stability ratio, water stability, raveling resistance, fatigue resistance, and low-temperature properties of the asphalt mixture can all be improved by the steel wool fiber. The induction heating speed, heating homogeneity, and therefore the induction healing ratio of the asphalt mixture can all be improved by using a composite of steel fibers and steel slag in place of some mineral aggregates [10]. Also, Induction Healing can be used to extend the fatigue life of asphalt concrete using three steps;

- (v) The first step entails fatigue testing at 15 °C, 10 Hz, and with 600 macrostrains perform on asphalt beams (380 mm  $\times$  63.5 mm  $\times$  50 mm) until the complex modulus drops to half of its initial value.
- (vi) The second step entails heating the fatigue-damaged beams to different temperatures, and
- (vii) finally, the heated beams are cooled to 15 °C and tested again under fatigue until the complex modulus drops to the same value as the first fatigue testing [9].

## Rejuvenation

Rejuvenation is the process of reviving the properties by restoring the ratio of asphaltenes and maltenes in the aged binder with the use of a rejuvenator. An asphalt rejuvenator penetrates the asphalt well below the surface to chemically revitalize and protect the asphalt binder by replacing the tar and oil lost due to oxidation. Waste cooking oil can be used as an asphalt rejuvenator. WCO should be treated and managed properly as it is considered harmful to human health and the environment when discarded by the users into kitchen sinks, waste bins, sewerage systems, or directly to land and water bodies. Many researchers have explored the opportunity of utilizing

WCO to rejuvenate the aged asphalt binder and improve its characteristics up to the scale of a virgin binder. The WCO can be applied directly to the asphalt binder (new or old), or after the suspension of pollutants has been filtered; in other cases, it is used following chemical treatment, which has shown improved results (Azahar et al., 2017). Unsaturated fatty acids, like the lower molecular weight components (maltenes) in the asphalt binder, are abundant in WCO. The asphalt binder experiences a loss of light oil components (maltenes) during its service life and an increase in the composition of heavy oil components (asphaltenes); the WCO replaces the lost maltenes in the aged binder (Azahar et al., 2016a). It is a good option for asphalt rejuvenation because of its copious availability. The risk of thermal cracking increases with the viscosity of the binder, while rutting and fatigue are increased by low viscosity. The addition of WCO to the binder softens the binder, enhances non-recoverable creep compliance, and reduces the resistance to permanent deformation. Accordingly, rutting resistance should be considered before adding WCO to the binder with caution depending on the site's climatic conditions. [11]. Microcapsules can also be used as asphalt rejuvenators. In the past, rejuvenators were spread onto the pavement surfaces and allowed to penetrate the pavement for healing. However, it was frequently challenging in the field to accomplish successful healing agent penetration for successful rejuvenation. Moreover, the pavements' ability to resist slipping was seriously affected, and the chemicals were bad for the environment. As a result, rejuvenator-containing microcapsules were made available. Later, further techniques for embedding the healing agents into the asphalt were created, including hollow fibers and the microvascular system. The crack is repaired when the healing agents solidify after being activated during cracking and being poured into the cracks by capillary action. [12]. The rheological characteristics of capsules containing asphalt binder were examined by Zhang et al [13]. The results of the DSR and bending beam rheometer (BBR) tests showed that the capsule integration marginally increases the high-temperature stability while slightly decreasing the asphalt's resistance to cracking at low temperatures. Additionally, it was discovered that self-healing asphalt has better anti-aging qualities than virgin asphalt. In terms of complex modulus and fatigue life, these capsules also considerably enhanced the asphalt binder's self-healing capabilities. Broken capsules are filled with the bitumen-rejuvenator mixture and do not leave any gap in the asphalt binder. The cracked capsules have no effect on the binder's mechanical characteristics. [12].

## Effect of capsules on the asphalt mix

The distribution of the capsules, their durability, and their strength can all be used to evaluate how well capsules operate in asphalt. It was discovered that the number of loading cycles used influenced how quickly



Fig. 1 Microcapsules made from Sunflower oil and calcium alginate.



Fig. 2 Materials used to produce homemade capsules from sunflower oil.

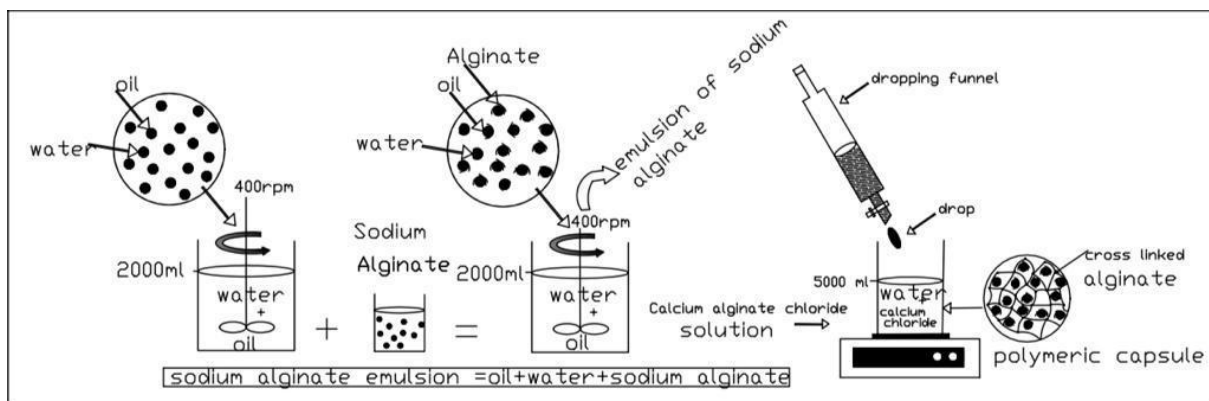


Figure 3 Manufacturing process of polymeric capsules by ionotropic gelation of alginate. [Adopted from Mansoori et al, 2018]

the healing agent was released under repeated loading [14]. Micaelo et al. [15] investigated the fatigue performance of asphalt mixtures containing sunflower oil encapsulated in calcium-alginate and coated with an epoxy-cement composite. Complex stiffness modulus and phase angle decreased because of the presence of capsules. Following a period of rest, the asphalt mixture with capsule inclusions showed increased rutting resistance. The fatigue performance, however, showed no obvious differences. Vegetable oil was employed by Mansoori et al. [12] as the self-healing agent with the same calcium alginate encapsulating medium. According to the performance studies, rutting and moisture damage showed positive results, however, stiffness modulus and fatigue parameters were affected negatively. Further, Mansoori et al. discovered that at temperatures above 40 °C, the healing in asphalt with and without self-healing chemicals is extremely comparable. Incorporating capsules in hot environments was not advised by the study. In-depth research was conducted by Garcia et al. [16] on the healing properties of several asphalt

combinations, including dense asphalt, stone matrix asphalt (SMA), and porous asphalt (PA). According to the study, porous asphalt has a slow release of healing chemicals, whereas denser mixes release them more quickly.

The capsules in fig 1 are home made using calcium lactate, Sodium Alginate, and sunflower oil. 1 teaspoon full of calcium lactate was put in a beaker containing 250ml of water it was stirred manually for about 5 mins and 1 teaspoon full of sodium Alginate was put in another beaker with 250ml of water and stirred for 5 minutes on a magnetic stir plate then we added one teaspoon full of sunflower oil in the sodium alginate mixture as it keep on stirring on the magnetic stir plate with the aid of a stir rod. We then added the calcium lactate solution into the sodium alginate containing the sunflower oil using a syringe. Capsules are seen to form as more calcium lactate solution is added with the syringe. The solution is later sieved, and capsules are selected. Some capsule sizes were larger than required so capsules of 2.5 mm and less were selected to be mixed with our Asphalt in

the laboratory. These capsules will serve as the rejuvenation agents in the asphalt.

### Nanoparticles.

Table 1. Shows a study on the advantages and disadvantages of asphalt self-healing techniques [11].

Techniques	Advantages	Disadvantages
Induction Heating	Can heat materials with low thermal conductivity.	No data about in situ progress.
	Transferable readily.	High manufacturing costs.
	Fast, selective, and uniform heating.	It has a limited recovery ratio.
	Fits environmental issues.	The heating mechanism is more complex than traditional methods.
Encapsulation	Multi-time recovery.	Depends on the electrical conductivity of the material.
	High recovery ratio.	Only work in the top layer. Helpful only once.
Ionomers	Good compatibility	Blend
	Multi-time recovery.	Only applies to early cracks
	Stable at high temperature. Good compatibility	

Note: From Benefits and drawbacks of asphalt self-healing techniques. Agzenai et al, 2015, University Carlos III de madrid e-Archivo

Nanoparticles are tiny particles with sizes between 1 and 100 nanometers. Undetectable by the human eye, nanoparticles can exhibit significantly different physical and chemical properties to their larger material counterparts. Nanomaterials can be categorized into four types [17] [7]

such as: (1) inorganic-based nanomaterials; (2) carbon-based nanomaterials; (3) organic-based nanomaterials; and (4) composite-based nanomaterials. Generally, inorganic-based nanomaterials include different metal and metal oxide nanomaterials.

The use of nanoparticles is an innovative and fascinating approach to creating self-healing materials to repair cracks, it does not involve the destruction and rebonding of polymer chains. If a crack develops, this method uses a dispersed particulate phase to fill it. Lee et al [18] created a hybrid nanoparticle that actively responded to injury and has the potential to cure itself several times. Tyagi et al. [19] indicated that nanoparticles may move toward the damaged area via a polymer-induced depletion attraction.

The tip of the surface notch may show a clear stress concentration, which may eventually cause cracks to spread throughout the system and degrade mechanical behaviour. The morphology obtained from the MD simulation serves as the input to the lattice spring model and determines the mechanical properties of the nanocomposite-coated surface. These nanocomposite coating nanocomposite coatings could produce flawless surfaces with improved mechanical qualities. The input for the lattice spring model, that establishes the mechanical characteristics of the nanocomposite coating surface, was the morphology modeled using MD. By applying this nanocomposite coating, we can create a surface devoid of flaws and improve the mechanical qualities. Experiments have been done to support certain features of the computer simulation. A multi-layered composite structure's fissures were used as a model by Gupta et al. [20] to show how embedded nanoparticles could migrate and cluster. The result showed that in the interfaces of the matrix and additive layer, the nanoparticles are evenly and preferentially separated.

### CONCLUSIONS

The methods discussed in this paper are a revolution in road construction and maintenance; they have been successfully implemented in the field, and it is anticipated that they will cut maintenance costs by doubling the lifespan of new pavements. Induction heating enhances local and rapid heating inside the material and increases the healing rates of bitumen. micro-encapsulation restores damage and increases durability, by reducing pavement rigidity and sealing cracks. However, there are still several issues that need to be resolved. The design of nanocapsules can withstand the high temperature and pressure during mixing and compaction processes, as well as obtain adequate dispersions of additives in the asphalt binder and asphalt concrete, which should provide homogenous qualities. Additionally, there are many models to measure binder (asphalt) healing, but more work is still required to model this process in asphalt composites.



## REFERENCES

- [1] A. Tabaković and E. Schlangen, “Self-Healing Technology for Asphalt Pavements,” *Springer Nature*, vol. Volume 273, p. 285–306, 2016.
- [2] D. Sun and et al, “A comprehensive review on self-healing of asphalt materials: Mechanism, model, characterization and enhancement,” *ScienceDirect*, Vols. 256,, pp. 65-93, June 2018,.
- [3] N. et, “Analysis of the scientific evolution of self-healing asphalt pavements: Toward sustainable road materials,” *Journal of Cleaner Production*, vol. 293, 15 April 2021.
- [4] X. e. al, “Self-Healing Asphalt Review: From Idea to Practice,” *Advanced materials interfaces*, 18 July 2018.
- [5] Y. al, “Self-healing of asphalt mastic using capsules containing waste oils,” *Construction materials*, 2020.
- [6] Tabakovic, “HealRoadCapsules MDPIApplied Sciences April2022,” *Applied science* 12(7), April 2022.
- [7] Z. 1. Xuewen, “Self-healing behavior of recycled asphalt prepared by residue oil of straw liquefaction based on molecular dynamics simulation,” *Scientific reports*, Xuewen Zheng 1, Wenyan Xu 2, Kai Cao 3, Keke Li 1.
- [8] A. Behnood, “Application of rejuvenators to improve the rheological and mechanical properties of asphalt binders and mixtures: A review,” *Journal of Cleaner Production*, vol. 231, pp. 171-182, 10 September 2019.
- [9] B. Anupam, U. Sahoo and A. Chandrappa, “A methodological review on self-healing asphalt pavements,” *Construction and Building Materials* 321 (2022) 126395, 2022.
- [10] A. García, “Uniformity and mechanical properties of dense asphalt concrete with steel wool fibers,” *Construction and Building Materials*, vol. 43, pp. 107-117, June 2013.
- [11] A. Y, “Advanced self-healing asphalt composites in the pavement performance field: mechanisms at the nano level and new repairing methodologies,” *Recent Pat Nanotechnol*, 2015.
- [12] T. Mansoori, “Self-healing of asphalt mastic by the action of polymeric capsules containing rejuvenators,” *Construction Materials*, vol. 161, pp. 330-339, 10 February 2018.
- [13] M. Baqersad, “Rheological and chemical characteristics of asphalt binders recycled using different recycling agents,” *Construction and building Materials*, vol. 228, 20 December 2019.
- [14] S. Bao, “Investigation of the Release and Self-Healing Properties of Calcium Alginate Capsules in Asphalt Concrete under Cyclic Compression Loading,” *Journal of Materials in Civil Engineering*, vol. 33, january 2021.
- [15] Micaelo, “Asphalt self-healing with encapsulated rejuvenators: effect of calcium-alginate capsules on stiffness, fatigue and rutting properties,” *Materials and Structures* 53, 2020.
- [16] H. A, “Self-healing of reflective cracks in asphalt mixtures by the action of encapsulated agents,” *Construction and Building Material*, vol. 252, 20 August 2020.
- [17] Y. Özge, “Self-healing of asphalt mastic using capsules containing waste oils,” *Construction Materials*, vol. 270, 8 February 2021.
- [18] L. Jae, “Using nanoparticles to create self - healing composites,” *PubMed*, 2004.
- [19] T. Sandeep, “Using Nanocomposite Coatings To Heal Surface Defects,” *ACS publication*, 2005.
- [20] G. Suresh, “Entropy-driven segregation of nanoparticles to cracks in multilayered composite polymer structures,” *Nature Materials* 5(3):229-233, 2006.
- [21] Micaelo, “Asphalt self-healing with encapsulated rejuvenators: effect of calcium-alginate capsules on stiffness, fatigue and rutting properties,” *Materials and Structures*, 2020.

## PRODUCING VALUABLE ‘SAND-LIKE’ MATERIAL FROM EXCAVATED MARINE CLAY USING MID-SIZED ROTARY KILN

Sathya Subramnian<sup>1</sup>, Juan Wei Koh<sup>1</sup> and Soon Hoe Chew<sup>1</sup>, Y. C. Tan<sup>2</sup>, C. S. Teo<sup>2</sup>, M. Y. C. Koh<sup>2</sup>, T. H. H. Cheung<sup>2</sup>, H.B. G. Foo<sup>2</sup>

<sup>1</sup>Department of Civil and Environmental Engineering, National University of Singapore, Singapore 117578;

<sup>2</sup> Building and Infrastructure Group, Housing and Development Board, Singapore 310480

### ABSTRACT

Traditional land reclamation relies heavily on sand. Since excessive extraction of sand may post environmental and ecological concerns, it is important to come up with a sustainable solution to reduce the reliance on sand. One of the sustainable solutions is to recycle and reuse the excavated marine clay obtained from excavation and underground constructions. However, this soft marine clay must be improved or treated before it can be used. ‘Sintering’ is a thermal process where a granulated clay is subject to heat treatment, causing an irreversible mineral change in the clay and thereby converting the soft marine clay to a useful ‘sand-like’ material. Preliminary laboratory research conducted on ‘clay sintering’ had been successful, which proved that the sintered product has ‘sand-like’ properties. This research aims to develop further into industry scale by using industry scale mid-sized rotary kiln to save on time and energy and thereby help in mass producing the sintered product. Parametric studies were conducted to identify the optimum operating conditions of the rotary kiln. Visual observations indicated that clay balls sintered at 800°C were uniformly sintered while clay balls sintered at 900°C had a well sintered surface with a black core. Further mineralogical studies were conducted to investigate the nature of this black core formation.

*Keywords: black core formation, land reclamation, rotary kiln, ‘sand-like’ material and sintering*

### INTRODUCTION

Sand is always a preferred filling material for land reclamation. Excessive extraction of sand from river or seabed always posed environmental and ecological concerns. Hence there is an urgent need to develop alternative filling materials which could be used for land reclamation. On the other hand, geology of Singapore indicates an abundant marine clay in the downtown area, where a lot of deep excavation and tunnelling works are under construction. Marine clay excavated during tunnelling or underground construction has poor engineering properties due to its low shear strength and high compressibility. In fact, in Singapore additional cost is needed to safely dispose the excavated marine clay. Furthermore, the need for finding a suitable dumping site for such marine clay is also challenging. One sustainable way of tackling the ‘no or low economic valued’ marine clay and the sand shortage problem is to convert the excavated marine to ‘sand-like’ material, thereby increasing economic value to the recycled and reused excavated clay. This would also reduce the reliance on imported sand. Singapore marine clay mineralogy predominantly consist of kaolinite. An irreversible mineralogical transformation is required for a successful conversion of soft marine clay to ‘sand-like’ material.

Sintering is a thermal process, which could be used to trigger the mineralogical change of kaolinite

at high temperature [1–3]. At a temperature of about 800–850°C, the kaolinite transforms to metakaolinite, and upon further heating to 1100°C, the metakaolinite is transformed into mullite [4–6]. Both the formation of metakaolinite and mullite are irreversible process. It was found that the formation of metakaolinite is sufficient for the current study, because laboratory scale testing conducted using a static furnace showed that this mineralogical change is possible and the strength & permeability was similar to granular material [7]. The static furnace is suitable for a controlled laboratory testing purpose, but a rotary kiln would be more suitable for industrial scale production. The clay balls in a static furnace are not subjected to any movement but in the case of rotary kiln with inclined axis, the heat required for sintering is delivered to the material by lifting and overturning each sample moving through the kiln. The sample in the kiln moves both radially and axially. The radial motion is controlled by rotational speed (rpm), the diameter of the kiln and the amount of sample inserted, while the axial motion is governed by the kiln’s inclination angle. Heat transfer to the material in the rotary kiln occurs in three different ways: (a) heat transfer to material by convection and gas radiation, (b) heat transfer to material by radiation, and (c) conductive heat transfer to material from kiln wall [8]. The more dynamic process of movement of clay balls and the multiple modes of heat transfer makes rotary kiln ideal for sintering process. Hence, it

is important to obtain the optimum operating conditions for the mid-sized industry scale rotary kiln to save energy. The end result of this production will then be tested from a mid-sized rotary kiln.

The objective of the current study is to use a mid-sized rotary kiln with 240mm in diameter and 2200mm long for the sintering process to obtain the optimum operating parameters and check the quality of the sintered product through visual observation and static compressive strength.

## MATERIALS AND METHODOLOGY

Soil containing marine clay obtained from excavation site is used in this study. The soil is sieved through 1mm sieve to remove shells, roots, and coarse sand particles. The liquid limit and plastic limit of the clay used in this study are 80% and 36%, respectively. The soil classifies as ‘CH’ clay of high plasticity according to Universal Soil Classification System (USCS).

### Methodology

The marine clay obtained after initial screening has a moisture content of 80-100%. The clay is dewatered to reduce the moisture content closer to plastic limit (~35%) to make it suitable for next stage, where the lumpy clay is turned into smaller clay balls. Low moisture content would result in formation of crack and high moisture content would make the clay balls sticky. The dewatered clay is then put inside an extruder with cutting blades to produce clay balls of 3mm size.

The moisture content of the clay balls is further reduced in the next pre-heating stage. The pre-heated clay balls are then sintered using mid-sized rotary kiln to produce the sintered product. The mid-sized rotary kiln used in this study has a rotary furnace which is 2.2m in length and 240 mm in diameter, as shown in Fig. 1.



Fig. 1 Mid-sized industry scale rotary kiln

Target sintering temperature ( $T$ ), kiln inclination

( $I$ ) and the kiln rotation frequency ( $R$ ) could be controlled by the user. The target sintering temperature based on literature review should be 800°C and higher for kaolinite to irreversibly convert to metakaolinite. The kiln inclination and rotation frequency are important parameters that control the amount of time the clay balls are retained in the rotary kiln. In other words, the parameters  $R$  and  $I$  control the retention time ( $t$ ) of the clay balls in the rotary kiln. It is important to find the optimum operating parameters for the rotary kiln to make the process energy efficient. The pictures of the end product at each stage is shown in Fig. 2.



Fig. 2 Pictures of end-product at each stage.

## RESULT AND DISCUSSION

### Target Sintering Temperature = 800°C

First series (series A) of testing was carried out by maintaining the target temperature at 800°C and varying the angle of inclination ( $I=2.0^\circ, 3.0^\circ, 3.6^\circ, 4.2^\circ$  &  $5.6^\circ$ ) and rotation frequency ( $R = 8, 10$  &  $12$  rpm). Table 1 summarizes the visual observation of the sintered product obtained from the parametric study.

Table 1. Summary of the parametric study (series A,  $T=800^\circ\text{C}$ )

Test No.	$I^\circ$	$R$ rpm	$t$ mins	Visual Inspection	S/U
A1	4.2	8	6.0		U
A2	3.6	8	7.67		U
A3	4.2	10	5.0		U
A4	3.6	10	6.0		U
A5	3.0	10	8.5		S
A6	5.2	12	3.0		U
A7	2.2	12	10.5		U

Note: S=Successful and U=Unsuccessful

The retention time ( $t$ ) defined here is the difference between the time of arrival of first sintered product and the time of arrival of last sintered product. In these series of testing, 50g of clay balls were used. For example, when the 50g of clay balls are put inside the rotary kiln, the stopwatch was started. The first sintered product would arrive at 2 mins elapsed time and the last sintered product would arrive at 12 mins elapsed time. Thereby the retention time would be 10 mins.

Comparing test A1 and A2, an increase in inclination angle ( $I$ ) reduces the retention time ( $t$ ) of clay balls in the kiln. Similar trends are observed while comparing A3, A4 and A5, where the increase in inclination angle reduced the retention time of the clay balls.

Similarly, higher kiln rotation frequency ( $R$ ) results in shorter retention time of clay balls in the rotary kiln (comparing A1 & A3 and A2 & A4). In some series of tests, there is a black core observed when the sintered product is cut open. It was thought in the beginning that this black core could be due to incomplete sintering process, where the clay balls did not have sufficient exposure to the heat energy. A more detailed analysis on the black core is carried out in the later section. It is important to find a suitable combination of inclination and rotation frequency thereby optimizing the retention time that produces well sintered clay. Shorter retention time would result in less energy consumption of the rotary kiln. Based on visual observations, Test A5 produces well-sintered clay.

#### Target Sintering Temperature = 900°C








Series A focusses on the importance of the retention time of the clay balls in the rotary kiln. Apart from retention time, the other way to achieve better sintering while keeping the retention time shorter is to increase the sintering temperature. Increasing sintering temperature would expose clay balls to more heat energy thereby reducing the time required for complete sintering. Series B testing is carried out with a sintering temperature of 900°C and the results are tabulated in Table 2.

The visual inspection of the 900°C sintered samples show black coring as well. Hence a detailed investigation of this black core is needed.

It is important to conduct a microscopic investigation to find the composition of the black core material. This could help conclude whether the ‘black core’ is acceptable (maybe a by-product of sintering) or unacceptable (unsintered product). Hence, microscopic investigations (TGA and XRD) are

needed to identify the black core in the sintered samples.

Table 2. Summary of the parametric study (series B,  $T=900^{\circ}\text{C}$ )

Test No.	$I^{\circ}$	$R$ rpm	$t$ mins	Visual Inspection	S/U
B1	4.2	6	6.67		U
B2	3.6	6	7.83		U
B3	3.0	6	10.50		U
B4	1.6	14	9.50		U
B5	1.6	8	13.16		U
B6	1.3	12	14.83		U
B7	1.0	10	>26		U

#### Microscopic Analysis

A new series of testing is carried out (Series C) to conduct the microscopic analysis. The parameters considered are summarized in Table 3.

Table 3. Summary of testing series C

Test No.	Mass g	$I^{\circ}$	$R$ rpm	$T^{\circ}\text{C}$	$t$ mins
C1	50	1.56	10	800	12.67
C2	100				14.67
C3	50	900			13.00
C4	100				15.00

Thermogravimetric analysis (TGA) and X-Ray diffraction (XRD) testing are conducted to study the mineralogical composition of the black core and the sintered product. The results obtained from TGA and XRD analysis are shown in Fig. 3 and Fig. 4 respectively.

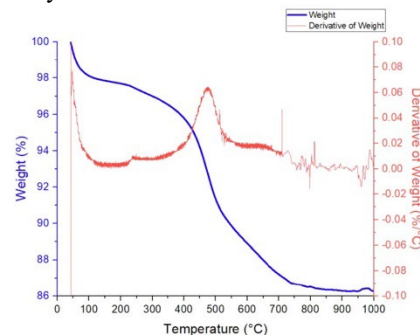


Fig. 3 TGA analysis on un-sintered marine clay

A rapid loss of weight occurs between 350°C - 700°C and a peak in the derivative of weight loss indicates that decomposition occurs at approximately 500°C (Fig. 3). The change in mass is attributed to the process of dehydroxylation, where evaporation of chemically bounded water occurs during the decomposition of kaolinite to metakaolinite. The reduction in mass stabilizes at 800°C, indicating the completion of dehydroxylation process. Since a complete dehydroxylation is necessary to prevent the potential disintegration of clay in water, a minimum temperature of 800°C must be used for sintering. Sintered clay without sufficient resistance against water would be unusable at land reclamation sites due to exposure to seawater and rain.

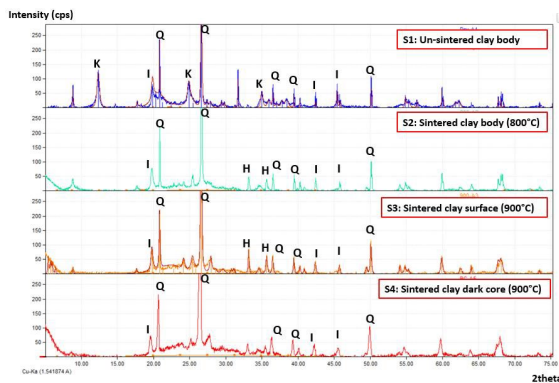


Fig. 4 XRD results on S1 sample (unsintered clay body), S2 sample (Sintered clay body at 800°C), S3 sample (Sintered clay surface at 900°C) and S4 sample (Black core at 900°C). (Note: Q=Quartz, I=Illite, K=Kaolinite and H=Hematite).

Fig. 4 (S2 & S3) shows that at sintering temperatures of 800°C and 900°C dehydroxylation has occurred, converting kaolinite into metakaolinite. Note that metakaolinite is undetectable by XRD due to it being an amorphous aluminosilicate. The absence of hematite in the black core in S4 and its presence in S2 and S3 samples validates that the hematite gives the red appearance in thermally treated clay. Furthermore, the absence of kaolinite in the black core in S4 sample indicates that a certain degree of heat treatment has occurred in the black core of the clay, bringing about the process of dehydroxylation. Therefore, the presence of a black core is not due to incomplete sintering. Even with the presence of black core the sintered product would not disintegrate in water (dehydroxylation has taken place).

The microscopic analysis through TGA and XRD has proved that the black core formation does not indicate unsintered product. Kaolinite has converted to metakaolinite in the black core, thereby resulting in a stable sintered product.

## Compressive Strength Testing

The compressive strength of individual sintered product was tested in a Zwick compression machine at a strain rate of 1mm/minute. Fig. 5 shows the compressive strength of individual sintered product. The strength of sintered product obtained from the rotary kiln is 7 MPa higher than that of sintered product obtained from static furnace. This could be the result of more effective heat transfer occurring in rotary kiln.

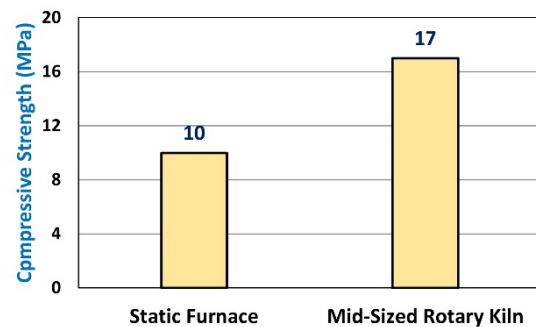


Fig. 5 Compressive strength of sintered product produced from static furnace and mid-sized rotary kiln.

## CONCLUSIONS

This study shows that the lumpy excavated soil containing marine clay can be converted to 'sand-like' material through sintering process using a mid-sized rotary kiln. TGA analysis showed that a minimum of 800°C is required for the marine clay to undergo complete dehydroxylation process, which results in evaporation of chemically bound water in kaolinite and conversion of kaolinite to metakaolinite occurs. This study also established, based on this particular rotary kiln model that;

- 1) The optimal retention time is achieved by a combination of kiln rotating frequency (10 rpm) and inclination angle (1.56°).
- 2) The red appearance of sintered product indicates the presence of metakaolinite with hematite, while the absence of hematite is responsible for the black core formation.
- 3) The black core formation at 900°C does not indicate that marine clay is un-sintered, through XRD analysis it was proved that the kaolinite had converted to metakaolinite.
- 4) The black core formed will not dissolve in water as the conversion of kaolinite has taken place, hence, it is considered as a stable sintered product.

## ACKNOWLEDGMENTS

This research is supported by the National Research Foundation, Singapore, and Ministry of National Development, Singapore, under its Cities of Tomorrow R&D Programme (CoT Award No. COT-V3-2019-2). Any opinions, findings, conclusions, or recommendations expressed in this material are those of the author(s) and do not reflect the views of National Research Foundation, Singapore, and Ministry of National Development, Singapore.

## REFERENCES

- [1] H. Katsuki, J. Kim, S.J. Kim, J.Y. Kim, J.H. Pee, W.S. Cho, Influence of alumina content in the raw clay on the sintering behavior of Karatsu ware, *J. Ceram. Soc. Japan*. 124 (2016) 833–837. <https://doi.org/10.2109/jcersj2.16014>.
- [2] Y.F. Chen, M.C. Wang, M.H. Hon, Phase transformation and growth of mullite in kaolin ceramics, *J. Eur. Ceram. Soc.* 24 (2004) 2389–2397. [https://doi.org/10.1016/S0955-2219\(03\)00631-9](https://doi.org/10.1016/S0955-2219(03)00631-9).
- [3] Y.F. Chen, M.C. Wang, M.H. Hon, Transformation kinetics for mullite in kaolin-Al<sub>2</sub>O<sub>3</sub> ceramics, *J. Mater. Res.* 18 (2003) 1355–1362. <https://doi.org/10.1557/JMR.2003.0186>.
- [4] F. Chargui, M. Hamidouche, H. Belhoucnet, Y. Jorand, R. Doufnoune, G. Fantozzi, Mullite fabrication from natural kaolin and aluminium slag, *Bol. La Soc. Esp. Ceram. y Vidr.* 57 (2018) 169–177. <https://doi.org/10.1016/j.bsecv.2018.01.001>.
- [5] J.W. Cogswell, H. Neff, M.D. Glascock, The effect of firing temperature on the elemental characterization of pottery, *J. Archaeol. Sci.* 23 (1996) 283–287. <https://doi.org/10.1006/jasc.1996.0026>.
- [6] K. Srikrishna, G. Thomas, R. Martinez, M.P. Corral, J.S. Moya, Kaolinite-mullite reaction series: a TEM study, *J. Mater. Sci.* 25 (1990) 607–612.
- [7] J.W. Koh, S. Subramanian, K.E. Low, S.H. Chew, K.E. Chua, T. Yeow Chong, S. Teo Cheng, L. Ji Mei Jamie, K. Meng Yang Charmaine, Laboratory-Scale Production of ‘Sand-like’ Material from Excavated Soft Soil, in: 7th Int. Conf. Geotech. Res. Eng., 2022.
- [8] S. Arad, Victor Arad, Heat Transfer in Rotary Kiln from Deva Cement Factory, in: SGEM2012 12th Int. Multidiscip. Sci. GeoConference, 2012. <https://doi.org/10.5593/sgem2012/s04.v2003>.



## ***Environment***

## MATERIAL SOURCE OF MUARAJAMBI TEMPLES, INDONESIA

Sondang Martini Siregar<sup>1</sup>, Edy Sutriyono<sup>2</sup>, Ari Siswanto<sup>3</sup>, Agus Aris Munandar<sup>4</sup>

<sup>1</sup>Environmental Science Faculty; <sup>2</sup>Geological Engineering; <sup>3</sup>Architectural Engineer, Sriwijaya University;

<sup>4</sup>Faculty of Cultural Sciences, Indonesia University, Indonesia

### ABSTRACT

The Muarajambi temples are on a fluvial landform, especially in a linear position along the Batanghari River. Inside the temples are the main building, the ancillary building, the fence, and the statue, which are made from various materials and remained the same as today. The problems are a) how is the regional location of the Muarajambi temple area? b) what are the types of building materials used for Muarajambi temples? c) where are the materials for the Muarajambi temples obtained? This study used a qualitative method with a petrographic analysis. The data collection was done by conducting a field survey, and then the samples were sent to the laboratory to determine the mineral content. The results showed that the Muarajambi temple area was on the rocks South Sumatra basin and in the Muara Enim formation. The materials used for building the temples are bricks (claystone), sandstones, and tuffs, while the materials used for the statues were tuffs, sandstone, and andesite stone. People used to have a policy of building temples on the riverbank by choosing bricks (claystone), tuffs, and sandstones as building materials because they were not waterproof and came from a local area. Meanwhile, the reason for using andesite stones for the statue material is that they are easy to be sculpted and more durable, even though the andesite materials are from outside the Muarajambi temple area.

*Keywords: Material, Source, Temple, Stone*

### INTRODUCTION

A temple is a building founded as a worship place for Hindus/Buddhists [1]. Inside the temples are the statues as the embodiment of deities worshipped by Hindus and Buddhists. So, the temple building is built from special materials. Manasara silpasastra mentioned that the temple materials are from 1 type, 2 types, or more than 2 material types [2].

In Indonesia, many temples are found in hilly places, mountains, or lowland areas near or far from a river [3]. In general, the temple material in Central Java is andesite stone, while the temples in East Java are from bricks (claystone) [4]. The temples in the Musirawas temple area are made from bricks (claystone); they are the materials found around the local [5]

The temple buildings are mostly found in South Sumatera, such as temples in Bumiayu, Telukking, Binginjungut, Lesungbatu, Tingkip, and Jepara that are found in the watershed [6]. The existence of those temples is indicated due to the previous trading contact with India. Along with the trading activity, it stimulates the arrival Hindu-Buddhist influence to develop in South Sumatra, particularly in the location near the river bank [7].

One of the temples in the Batanghari watershed is Muarajambi temple, particularly located on the north and the south side of Batanghari River [8]. The temples in a linear position against the Batanghari River are divided into some groups having a boundary with the channels or tributaries of Batanghari River. The temples have an area of 3,000 acres that has a boundary with the channels or tributaries of Batanghari River [9]. The Muarajambi

temples were from the 10<sup>th</sup> BC on the swamp landscape that is often swamped due to both the tides in a river and rainfall. The interesting point is that the temple building can remain up until now. The arising problems are a) how is the regional location of the Muarajambi temple area? b) what are the types of building materials used for Muarajambi temples? c) Where are the materials for the Muarajambi temples obtained? This study aimed to find out the location of Muarajambi temples, the stratigraphy of the rock formations in the Muarajambi temple area, and the source/location of Muarajambi temple materials.

### METHOD

#### Location Analysis

The method used here was conducting a survey and mapping by referring to the *ArcGIS* software, the BIG data of the geological map of the Lahat and Jambi quadrangles. The coordinate point is, then, placed on a basic geological mapping. Based on the map integration and the previous literature review, the name and the administrative boundary are adjusted. It becomes the baseline to make a map of feature placement in the research location.

#### Petrographic Analysis

A petrographic analysis is a branch of petrology as the study of rocks, especially rock contents and the texture relations. This analysis aimed to discover the name of each rock sample collected in the location based on the texture, structure, and the mineral content of rocks available in the research location.

The rock sample used in this study was a fresh rock because the rock sample needed to be prepared first until it became a thin incision that would be analyzed using a microscope. The name classification of sedimentary rocks was performed based on the classification by Pettijohn (1986) and Fisher (1966). At first, an observation survey on the rock exposure and the macroscopic description of hand specimen. The instrument used here was a polarizing microscope that can analyze the optical mineralogy of a thin incision in detail and the micro texture, and the structure were vital to know the origin of the rock.

### Material Source Analysis

The material source analysis is known by carrying out an interpretation of the relationship between the placement of artifacts/features and the stratigraphy of rock formation at a regional scale; therefore, it can indicate the material source of the temple building if it is from the inside or near the site location or the material taken from outside the location/region.

## RESULT AND DISCUSSION

### The Regional Location of Muarajambi Temple Area

The South Sumatra basin is a result of tectonic activities that are strongly related to Indo-Australian plate subduction that moves to the northern part to the northeastern part against the Eurasian plate that is relatively static. The plate subduction zone includes the western area of Sumatra Island and the eastern area of Java Island. Several microplates in between those zones also move and result in a convergence in various shapes and directions. The Indo-Australian plate subduction can affect the rock state, morphology, tectonic, and the structure in South Sumatra. The South Sumatra basin is a relatively large basin. The difference in the relief of bedrocks is due to the fault of bedrocks in blocks, it results in a bedrock elevation model and depression. Uneven relief and the reactivation of the block fault control the sedimentation and the fold in the tertiary layer in the basin. This basin consists of tertiary sediments unconformity located on the surface of metamorphic rocks and pre-tertiary igneous rocks. The South Sumatra basin is located elongating in an NWSE direction in the southern part of Sumatra Island. The area of this basin is around 85,670 km<sup>2</sup> consisting of 2 sub-basins, namely Jambi sub-basin and Palembang sub-basin. The research location was in the South Sumatra basin, specifically in Jambi sub-basin. The stratigraphy of South Sumatra basin consisted of the following formations: Kikim, Telisa, Lahat, Talang Akar, Gumai, Baturaja and the equivalent, Air Benakat, Muara Enim, Kasai and the equivalent, and the alluvial sediment on the upper surface [10]

Muara Enim formation was deposited at the Late Miocene to Pliocene in the form of the second regression cycle with a shallow marine deposition environment up to continental sands, delta, and claystone. The first (Air Benakat formation) and the second regression cycle are distinguished by their absence of glauconitic sandstone and the existence of a relatively thick coal layer in this Muara Enim formation. The precipitation is initiated in the swamp area of a coastal plain, and then it continues to the delta plain area with a local shale sequence development and thick sandstone. In this formation, there is iron-oxide in the form of concretions and silicified wood. Meanwhile, the coal available in this formation is generally in the form of lignite. The thickness in this formation is categorized as thin in the north part and the maximum is in the southern part with a thickness of 750 m [11]

The Kasai formation is deposited from the Pliocene to Pleistocene. This formation is the result of an erosion of lifting the Bukit Barisan and Tigapuluh mountain. The Kasai formation has a contact with Muara Enim formation that is marked by the lithology of tuffaceous sandstones. This formation is deposited in the third regression cycle marked by the occurrence of volcanic products. The Kasai formation is composed of continental sandstones, claystone, and pyroclastic materials (pumice tuff, tuffaceous sandstones, and tuffaceous claystone). This formation finalized the oceanic tide cycle. The lower part consists of tuffaceous sandstone with some variations of tuffaceous claystone and loose sandstone layers, and the upper part consists of a layer of tuffs, pumice that contains the remnant of plants and wood in a cross-bedding structure. There is also a lens-shaped lignite in sandstones containing tuffs. The deposition environment of this formation is fluvial with a thickness of >200 m. Alluvial sediment is a material deposit coming from a rock disintegration available in an area that is usually in either a lowland area or river. The alluvial sediment generally consists of blocks, pebbles or gravels, sands up to mud. [10]

The Muarajambi temple area in the line-up position above the stratigraphy of Muara Enim, Kasai, and Alluvial Sediment formations. The Muara Enim formation is marked green on the map. The stratigraphy of this formation contains iron-oxide in the form of concretions and silicified wood. In the western side, there is alluvial sediment containing blocks, pebbles, sands, and mud. The westernmost part of the temple area is located on the stratigraphy of Kasai formation that contains continental sandstones, claystone, and pyroclastic materials (pumice tuff, tuffaceous sandstones, and tuffaceous claystone).

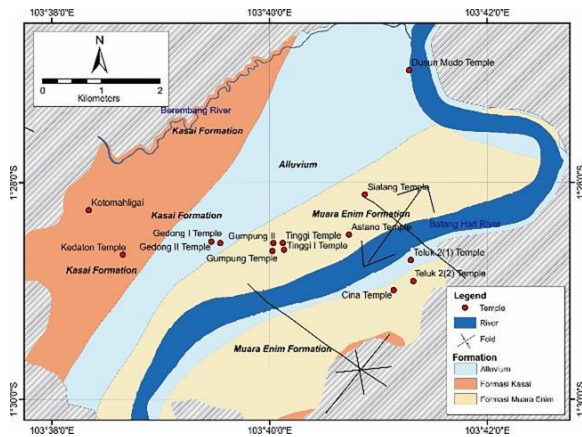


Fig.2 The Distribution of Muarajambi Temples (red) lining up above the stratigraphy of Muara Enim, Kasai, and Alluvial Sediment

### Types of Material for Temple Building

Nine samples were taken from the Muarajambi temple area, especially the samples from the temple building. Those samples were then analyzed using a petrographic analysis by cutting the stone to know the mineral content. After cutting the sample, the identification of rock sample was done by using a microscope at 40x magnification.

#### Claystone

Based on the analysis result, 3 samples taken from the Muarajambi temple area were known to be made from claystone, namely 1 sample from Kedaton temple and Teluk 1 temple. The material sample from Kedaton temple was brown-orange, gray, and brown. The rock composition consists of quartz and lithic/rock fragments of sedimentary rocks as a fragment and cement in the form of clay. The rock composition is 18% quartz, 12% lithics, and 70% clay cement. Therefore, the most rock content is clay.

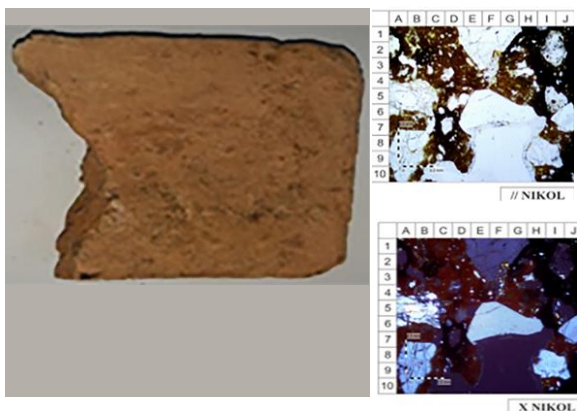


Fig 3. Brick Sample of Candi Kedaton containing 18% quartz, 12% lithics, and 70% clay cement

The brick sample of Candi Teluk temple is white and brown-orange. The rock composition consists of 30% quartz, 2% lithics, and 68% clay cement.

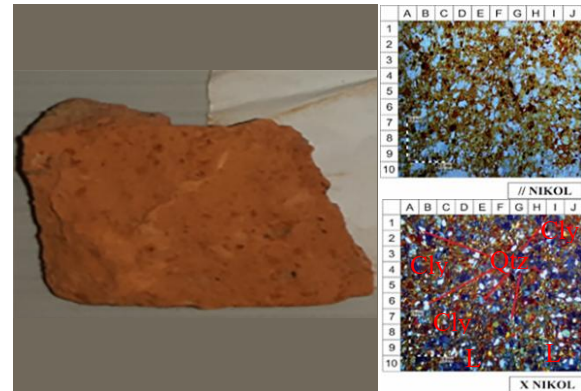


Fig.4 Brick Sample of Candi Teluk containing 30% quartz, 2% lithics, and 68% clay cement

#### Sandstone

The material sample of Kedaton temple showed dull white color from a group of colorless minerals. The rock composition consists of 90% monocrystalline quartz, 2% lithic fragments, and 8% feldspars. Through a calculation of rock content, the rock name can be determined as quartz arenite.

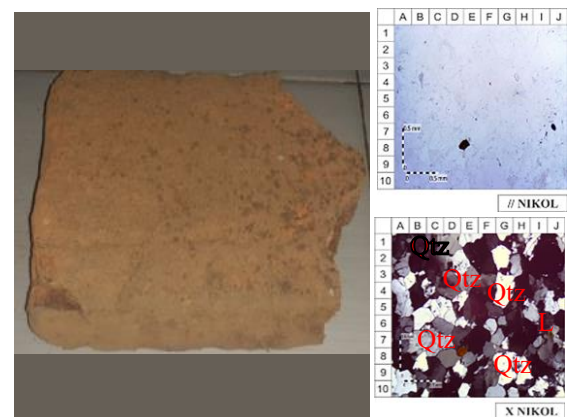


Fig.5 Sandstone Sample of Kedaton temple containing 90% quartz, 2% lithics, and 8% feldspars

The rock sample of Gedong temple 1 contains 92.3% quartz matrix, 5.1% feldspars, and 2.6% lithics (sediments). Through the calculation of rock content, the rock name can be known as *quartz arenite* [12]

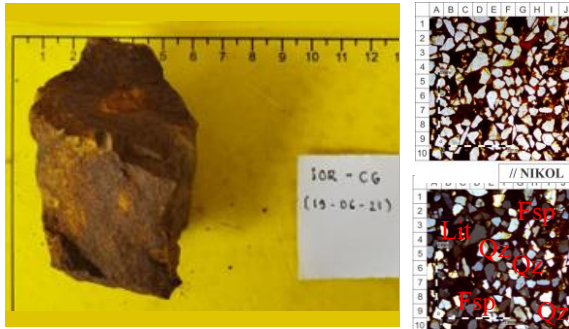


Fig.6 Sandstone Sample of Gedong 1 temple containing 92.3% quartz, 5.1% feldspars, and 2.6% lithics

#### Limestone

The sample of Kedaton temple is cream/white and pearly. The rock contains 100% colorless calcite. This sample is classified as carbonate rocks and known as Calcite Sandstone [13]

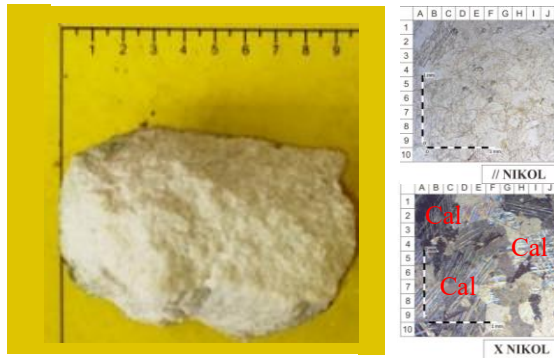


Fig.7 Limestone Sample of Kedaton temple containing 100% calcite sandstone

#### Tuffs

The rock sample of Gumpung temple is cloudy white and brownish cream. The rock contains 6% colorless quartz having 1% brown biotite, and 42% colorless lithics. The basic mass is in the form of 25% grayish cream and dark gray glass (PPL) and 26% porosity. Through the pyroclastic rock classification, the rock name is known as *Tuffaceous Sandstone/Vitric Tuff* [14]

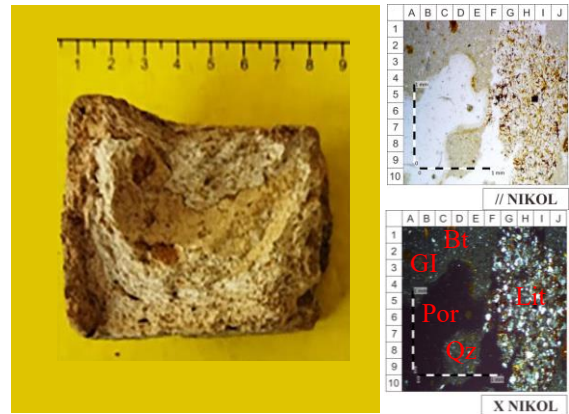


Fig.8 Tuff Sample of Gumpung temple containing 6% quartz, 1% biotite, 42% lithics, 25% glass, and 26% porosity

The rock sample of Kembarbatu temple is brown. This sample contains 10% colorless quartz fragments, 85% grayish cream and dark gray ground-glass mass (PPL), and 5% porous rocks. Based on the pyroclastic rock classification, then rock name is known as *Tuffaceous Sandstone/Vitric Tuff* [14]

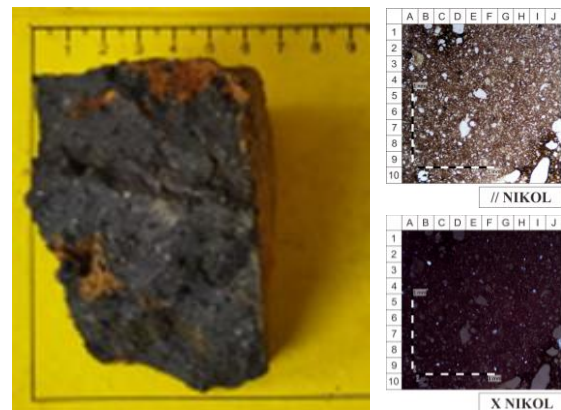


Fig.9 Tuff Sample of Kembarbatu temple containing 10% quartz, 85% ground-glass mass, and 5% porous rocks

#### Igneous Rocks

The igneous rock sample of Kedaton temple is cloudy white with yellowish and brownish gray spots. This rock contains 46.1% black quartz, 40.4% plagioclase, and 13.5% alkali feldspars. Based on the classification of intrusive igneous rock, the rock name is known as *Granodiorite*[15]



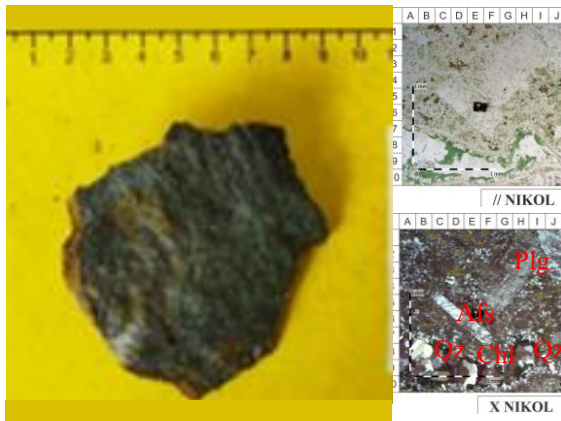


Fig.10 Igneous Rock Sample of Kedaton temple containing 46.1 %, 40.4% plagioclase, and 13.5% alkali feldspars

The rock sample of Gedong 1 temple is blackish gray with a hint of brown (XPL). The primary mineral consists of 32.3% colorless quartz, 12.9% colorless (cloudy) plagioclase, and 54.8% colorless alkali feldspars. Based on the classification of intrusive igneous rock, the rock name is known as Syenogranite [15]

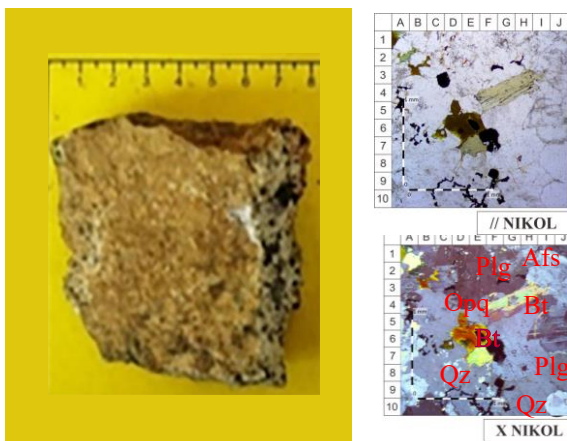


Fig.11 Andesite Rock Sample of Kutomahligai containing 40% quartz, 47.4% plagioclase, and 12.6% alkali feldspars.

The petrographic analysis result indicated that the Muarajambi temple materials consisted of claystone taken from Kedaton and Teluk temples, sandstones taken from Kedaton and Gedong 1 temples, tuffs taken from Kembarbatu and Gumpung temples, Limestone taken from Kedaton temple, and granite taken from Kedaton and Gedong 1 temples, and andesite rock taken from Kutomahlogai temple.

In South Sumatra, claystone generally becomes the temple material, such as Tingkip, Lesungbatu, and Binginjungut temples [16]. It also includes Bumiayu, Muarajambi, Bahal, and Padangroco temples [17]. The material of Batujaya temple is also claystone (bricks). The temples on a wetland, specifically around rice field areas [18]. Nalanda temples, Bihar

India, contains bricks (claystone). The temple in a lining-up position from the northern to the southern side is surrounded by a fence made from bricks (claystone) [19].

The Muarajambi temple area generally uses claystone as the material for the temple building and floor. It is because claystone is suitable for buildings established on a wetland as it is waterproof, heat absorbent, and durable [10].

Claystone used for temple buildings indicates that it is light and non-waterproof, so it is suitable for buildings established on a wetland [20]. The staircase and its balustrade are made from sandstone (the decoration on the balustrade tip). Sandstones and tuffs are used as statue material, such as Dualapara statue from Gedong temple that is made from sandstone, and Prajnaparamitha statue from Gumpung temple that is made from tuffs. The consideration of making statues from sandstone and tuffs is that those materials are easy to sculpt, indestructible, and durable [21].

Besides, there are temples that use 2 temple materials, such as Muaratakus temples that are made from the claystone of sandstone [14], Lesungbatu 1 temples that are made from bricks (claystone) and tuffs as well as Lesungbatu 2 temples that are made from tuffs and wood. Temples consist of a composition of big tuffs in a square shape, and there is a hole in between as a place to store the pegs of wooden poles. The wooden poles function to support the temple roof [22].

Wood is a natural material of tree trunks for human life needs as it is strong, able to support loads, durable, and easy to sculpt. The wooden material is used for building the construction, accessories, and tools. Since around the 665-57 BC, the wooden material has been used in Japan and Koreas as a material for building temples, Buddhist temples, and worship places for Shintoism [23].

Gravels and pebbles are the temple materials. The main room of Kedaton temples is made from gravels and pebbles in 2 meters height. Similarly, the gravels and pebbles are found after the height of 1,5 m after the Tuo Sumay temple excavation. The gravels and pebbles used as the temple materials aimed to maintain the stability of temple buildings [24].

### Material Sources of Muarajambi Temples

The Muarajambi temples are at the stratigraphy of Muara Enim, Kasai, and Alluvial Sediment formations. Based on the result of the petrographic analysis on the material sample, the Muarajambi temples are made from bricks (claystone). The relatively unique rocks are found in this area as no rock formation around the area, such as granite that is found in Kedaton and Gedong 1 temples, and andesite that is found in Astano and Kutomahligai temples. Besides, iron oxide rock is also found in Gedong 1



temple; the volcanic rock is found in Kembarbatu temple, and calcite sandstone found in Kedaton temple.

In general, the materials of Muarajambi temples, such as bricks (claystone), tuffs, sandstones, are collected from the local areas; they are the rock content obtained from the stratigraphy of Muara Enim and Kasai formations. The existence of other rocks, such as limestone, granites, and andesites, are taken from outside as they are the paramount materials for building statues, stupas, temple gates, and balustrade decorations.

Similarly, in Bumiayu temples, there are statues of 3 characters that are made from sandstones [25], Buddhist statues and Awalokiteswara statue that are made from andesite stones are found in Lesungbatu temple [16], and the Buddhist statue of Tingkip temple is made from sandstones [26]. The statue materials are not the rock constituents taken from local areas, but they are imported from outside the area for the worshipping purpose done inside the temple.

## CONCLUSION

The Muarajambi Temple area is located in the rock basin of South Sumatra, namely the Muara Enim formation. Generally, temple building materials are made of bricks (claystone) containing 8%-30% quartz, 2%-12% lithics, and 68%-70% clay cement. In addition, there are temples that use additional materials such as sandstone containing 90%-92.3% quartz, 5.1%-8% feldspars, 2%-2.6% lithics and tuff containing 6%-10% quartz, 1% biotite, 42% lithics, 25%-85% glass, and 5%-26% porosity. The material was obtained from the Muarajambi temple area.

The use of andesite, limestone, and calcite were considered important as they are used for making the god statues and the important components of the temples, so they are obtained from outside the Muarajambi temples.

## ACKNOWLEDGMENTS

The researchers would like to express gratitude to the South Sumatra Archeology Center, which has funded the research and petrographic analysis of rocks taken from the Muajambi temple areas. The researchers would also thank Dio Irawan who has helped analyze the rock samples and the locals who have granted us permission to conduct research and collect samples in the Muajambi temple areas.

## REFERENCES

- [1] Soekmono, *Candi Fungsi dan Pengertiannya*. Yogyakarta: Ombak, 2017.
- [2] A. A. Munandar, *Antarala Arkeologi*. Jakarta Selatan: Wedatama Widya Sastra, 2018.
- [3] V. Myriam and Y. Degroot, *Candi Space and Landscape: A Study on DIstribution, Orientation and Spatial Organization of Central Javanese Tmeple Remains*. 2009.
- [4] D. P. C. B. dan Permuseuman, *Candi Indonesia: Seri Sumatera Kalimantan Bali Sumbawa*. 2014.
- [5] S. M. Siregar, "Faktor-Faktor Penempatan Percandian di Lahan Basah (Studi Kasus Kawasan Percandian Muarajambi dan Bumiayu)," 2020.
- [6] S. M. Siregar, "Situs-Situs Klasik di Sumatera Selatan," *Siddhayatra*, vol. 8, no. 2, pp. 84–93, 2003.
- [7] S. M. Siregar, "Persebaran Situs-Situs Hindu-Buddha dan Jalur Perdagangan di Daerah Sumatera Selatan (Indikasi Jejak-Jejak Perdagangan di Daerah Aliran Sungai Musi)," *Kindai Etam*, vol. 2, no. 1, pp. 4–10, 2016.
- [8] E. Parwati and A. Suarasi, "Konsep Kosmologi Candi Empat Muarajambi sebagai Sumber Pembelajaran Sejarah," vol. 1, pp. 105–112, 2019.
- [9] C. N. Andarsih, Hamzah, and M. Safri, "Pemetaan Risiko Pemanfaatan Kawasan Cagar Budaya Nasional Muarajambi," *Siddhayatra*, vol. 26, no. 2, pp. 13–26, 2021.
- [10] G. L. De Coster, "The Geology of the Central and South Sumatra Basins," in *3rd Annual Convention Proceedings*, 1974, pp. 74–109, doi: 10.29118/ipa.670.77.110.
- [11] M. G. Bishop, "South Sumatra Basin Province, Indonesia: The Lahat/Talang Akar-Cenozoic Total Petroleum System," *USGS Open File Rep.*, no. 99-50-S, p. 22, 2001.
- [12] F. J. Pettijohn, *Sedimentary Rocks, Third Edition*, vol. 2, no. 4. 1975.
- [13] M. A. Perras and M. S. Diederichs, "The importance of classification for carbonates and mudrocks in engineering," in *Proceedings of the 2011 Pan-Am Canadian Geotechnical Conference*, 2011, no. January 2011, pp. 2668–2675.
- [14] R.V.Fisher and H.U.Schmincke, *Pyroclastic Rocks*, vol. 59. 1984.
- [15] M. J. Le Bas and A. L. Streckeisen, "The IUGS systematics of igneous rocks," *J. Geol. Soc. London.*, vol. 148, no. 5, pp. 825–833, 1991, doi: 10.1144/gsjgs.148.5.0825.
- [16] S. M. Siregar, M. E. Armanto, and L. R. Susanti, "Penempatan Bangunan Candi Tingkip, Lesung Batu dan Bingin Jungut pada Bentang Lahan Fluvial di Musi Rawas, Propinsi Sumatera Selatan," *Naditira Widya*, vol. 11, no. 1, pp. 31–46, 2017, doi: 10.24832/nw.v11i1.192.
- [17] A. Siswanto, A. Ardiansyah, and F. Farida, "Pendekatan Lingkungan Lokasi Candi-candi Masa Kerajaan Sriwijaya di Sumatera," in *Temu Ilmiah Ikatan Penenliti Lingkungan Binaan Indonesia (IPLBI)*, 2018, pp. H087–H093, doi: 10.32315/ti.7.h087.

- [18]M. Mansur, “Situs Percandian Batujaya di Karawang Jawa Barat: Analisis Manajemen Sumber Daya Arkeologi,” *Etnohistori*, vol. II, no. 2, pp. 175–184, 2015.
- [19]S. K. Tiwary, “Stucco Art of Nalanda Excavated Site, District Nalanda , Bihar : An Archaeological Overview,” *Ann. Archaeol.*, vol. 1, no. 1, pp. 13–21, 2018.
- [20]A. . Gde Bagus and H. Prihatmoko, “Kearifan Lokal Dalam Pembangunan Kompleks Candi Gunung Kawi,” *Forum Arkeol.*, vol. 29, no. 2, pp. 105–116, 2017, doi: 10.24832/fa.v29i2.186.
- [21]T. M. H. Lelono, “Bahan Dan Cara Pembuatan Arca Batu Sebagai Komponen Penting Candi-Candi Masa Klasik Di Jawa Material and Method of Making Stone Statue As a Key Component Classical Temple in Java,” *Berk. Arkeol.*, vol. 33, no. 1, pp. 93–108, 2013.
- [22]S. M. Siregar, “Faktor-Faktor Pertimbangan dalam Penempatan Bangunan Candi di Kawasan Musi Rawas,” in *Peradaban Masa Lalu di Sumatera Selatan*, 2015, pp. 57–76.
- [23]G. Suharjanto, “Bahan Bangunan dalam Peradaban Manusia: Sebuah Tinjauan dalam Sejarah Peradaban Manusia,” *Humaniora*, vol. 2, no. 1, p. 814, 2011, doi: 10.21512/humaniora.v2i1.3100.
- [24]S. M. Siregar, “Fondasi Bangunan Candi Tuo Sumay,” *Siddhayatra*, vol. 9, no. 2, pp. 64–68, 2004.
- [25]S. M. Siregar, “Candi Bumiayu: A Magical Touch from the Past,” in *Candi Bumiayu, Muaraenim*, 2012.
- [26]S. Widyawati and S. M. Siregar, “Candi Tingkip dan Lingkungannya,” *Siddhayatra*, vol. 23, no. 2, pp. 124–135, 2018.

# DESALINATION BEHAVIORS FROM SEAWATER USING NATURAL ZEOLITE AND CALCINED CA-Fe LAYERED DOUBLE HYDROXIDE FOR CULTIVATION

Takaaki Wajima<sup>1</sup> and Fumika Sekihata<sup>1</sup>

<sup>1</sup>Graduate School of Science and Engineering, Chiba University, Japan

## ABSTRACT

In recent years, it has been considered to secure water and food using seawater desalination technology, and a new simple desalination material for reducing high concentration sodium chloride in seawater is required. In this study, desalting agents were prepared from natural zeolite, obtained from Kagoshima prefecture, Japan, with addition of calcined Ca-Fe type layered double hydroxide (LDH), to desalinate seawater for cultivation. By treating with the mixture of natural zeolite and calcined Ca-Fe LDH at a mixing ratio of 5: 4, the salinity could be reduced from 3.61% in seawater to 0.97% by cation exchange reaction of natural zeolite and reconstruction reaction of calcined Ca-Fe LDH, and the pH of the obtained solution is 8.4-9.0. The desalination reaction using this mixture was almost same regardless of temperature. Radish sprouts, bean sprouts and mung bean could be harvested using seawater treated with a mixture of natural zeolite and calcined Ca-Fe LDH, while it was not possible to harvest using seawater.

*Keywords: Natural zeolite, Calcined Ca-Fe LDH, Desalination, Growth test*

## INTRODUCTION

Water is not only an essential material for human beings (70% of our bodies by weight) but also an important resource for human activities, such as agriculture, commerce, industry, domestic use and so on. In the 21st century, water scarcity is one of the most serious global challenges. Now, over one-third of the world's population lives in water-stressed countries, and, by 2025, this is predicted to rise to nearly two-thirds [1, 2]. The challenges of providing ample and safe water resources are further complicated by population growth, industrialization, contamination of available freshwater resources and climate change.

For water resource on earth, 70 % of Earth's surface is covered with water, and the total amount of water resources on the earth is about 1.3 billion km<sup>3</sup>. In water resources, seawater is about 97.5%, freshwater is about 2.5%, and human beings can only use about 0.01% of the total water resources, due to the most freshwater present as glacier, cloud, vapor and so on. According to the Food and Agriculture Organization (FAO) of the United Nation (UN), the annual water withdrawal worldwide from natural water bodies is estimated to be around 4250 km<sup>3</sup>, of which agricultural use is the largest consumer at around 71.7% of the total withdrawal [3]. This portion is even higher in arid and semi-arid countries. Therefore, the supply of agricultural water as freshwater resource is one of the important issue in the 21st century.

One way of supplying water resources is seawater desalination. Commercial desalination technologies

can be classified into two main categories. Thermal-based technologies, such as multi-stage flash (MSF) and multi-effect distillation (MED), and membrane-based technologies, such as reverse osmosis (RO), together constitute more than 80% of the global desalination capacity currently in operation worldwide [4]. However, these technologies are expensive for agricultural use because they produce high-quality fresh water for domestic or industrial use. Therefore, the development of technology for obtaining agricultural water from high-salinity water, such as seawater, is desired to secure food.

In previous studies, desalination behaviors of natural zeolite and synthetic zeolite in seawater were examined [4-7], and seawater was treated with calcined Mg-Al layered double hydroxide (LDH) and natural zeolite in two steps to obtain a solution that can be used for germination of radish sprouts from seawater [8-12]. Furthermore, we have succeeded in cultivating radish sprouts using seawater treated with a mixture of mordenite-type natural zeolite and calcined Ca-Fe LDH (calcination at 500 °C) (mixing ratio of zeolite to LDH = 5 : 4), which are cheap materials [13-16]. There is a possibility to develop a new desalination material that reduces the high salinity in seawater, causing salt damage to a level where crops can grow, using natural zeolite with calcined LDH. However, little information can be available on the desalination behaviors of natural zeolite with calcined Ca-Fe LDH.

In this study, the desalination behaviors of natural zeolite, calcined Ca-Fe LDH and the mixture of these in seawater were examined to produce the solution for plant growth from seawater.

## EXPERIMENTAL

### Samples

Mordenite-type natural zeolite obtained from Koriyama mine, Kagoshima Prefecture, Japan was used as a natural zeolite sample. The exchangeable cations (ECs) and cation exchange capacity (CEC) of natural zeolite were shown in Table 1. The sample was ground and sieved under 250  $\mu\text{m}$ , and dried to be used for the experiment.

Table 1 ECs and CEC of natural zeolite sample

EC (mmol/g)				CEC (mmol/g)
$\text{Na}^+$	$\text{K}^+$	$\text{Mg}^{2+}$	$\text{Ca}^{2+}$	
0.52	0.25	0.01	0.18	1.95

The calcined Ca-Fe LDH was prepared as follows. A mixed solution of  $\text{Ca}^{2+}$  and  $\text{Fe}^{3+}$  ( $\text{Ca/Fe} = 2$ ) (200 mL) was prepared from 0.2 M  $\text{CaCl}_2$  solution and 0.1 M  $\text{FeCl}_3$  solution, and dropwise to 0.3 M  $\text{NaCl}$  solution (100 mL) at 4 mL/min. The stirring was carried out for 1 h while bubbling nitrogen gas, and the pH of the  $\text{NaCl}$  solution was maintained at 12.5 by dropping  $\text{NaOH}$  solution during the stirring. After stirring, the mixture was filtered, dried, and calcined in an electric furnace at 500°C for 1 h to obtain calcined Ca-Fe LDH.

Seawater used in this study was collected from the surface layer of Imari Bay, Saga prefecture, Japan. Chemical composition, salinity and pH of seawater were shown in Table 2.

### Desalination treatment

The desalting abilities of natural zeolite, calcined Ca-Fe LDH, and the mixture of natural zeolite and calcined Ca-Fe LDH were evaluated as follows.

Natural zeolite sample (15 g), calcined Ca-Fe LDH (12 g) or the mixture of natural zeolite (15 g) and calcined Ca-Fe LDH (12 g) was added to seawater (40 mL) heated at 20, 50 and 80 °C, and stirred. After stirring for 0 - 60 min, the solution was filtered, the pH of the filtrate was measured by pH meter (Horiba, F-72), salinity was measured by salinity meter (LAQUA, ES-71), the concentrations of  $\text{SO}_4^{2-}$ ,  $\text{Cl}^-$ ,  $\text{Na}^+$ ,  $\text{K}^+$ ,  $\text{Mg}^{2+}$  and  $\text{Ca}^{2+}$  in the filtrate were measured with an ion chromatograph (Tosho, IC-2010) and those of  $\text{Fe}^{3+}$ ,  $\text{Si}^{4+}$  and  $\text{Al}^{3+}$  were determined using an atomic absorption spectrophotometer (Perkin Elmer, AAnalyst 200). The residue was dried, and the mineralogical structure of natural zeolite, Ca-Fe LDH and the residue obtained at each temperatures was confirmed by a powder X-ray diffraction apparatus (Rigaku, MiniFlex 600).

### Growth test

Radish sprouts, bean sprouts and mung bean were used for 10 days growth test. Tap water, seawater or seawater treated with the mixtures of natural zeolite and calcined Ca-Fe LDH was given by a spray every day, and germinations of radish sprouts, bean sprouts and mung bean were observed.

## RESULTS AND DISCUSSION

Figure 1 shows the salinity and pH of seawater treated with natural zeolite during the treatment at 20, 50 and 80 °C. Regardless of temperatures, the salinity rapidly decreased to be almost constant to about 2.4 %. With increasing the temperature, the time for salinity decrease to about 2.4 % was faster. At 20 °C and 50 °C, pH of seawater (8.0) decreased to about 7.5, while pH of seawater decreased to 5.8 at 80 °C.

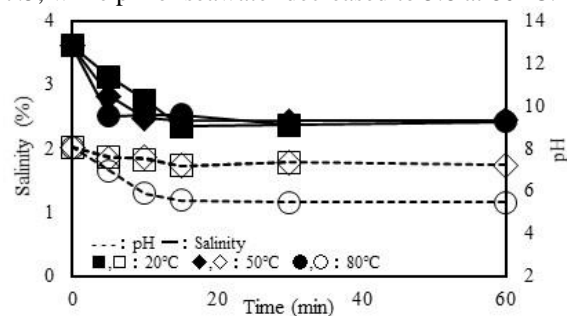


Fig. 1 Salinity and pH of seawater treated with natural zeolite during the treatment at 20, 50 and 80 °C

Figure 2 shows the salinity and pH of seawater treated with calcined Ca-Fe LDH during the treatment at 20, 50 and 80 °C. Regardless of temperatures, the behaviors of salinity decrease are almost same, and the salinity of seawater (3.61%) rapidly decreased to be almost constant to about 3.3 %. At 20 °C, pH of seawater increased to about 10.5, while pH of seawater increased to about 11 at 50 °C and 80 °C.

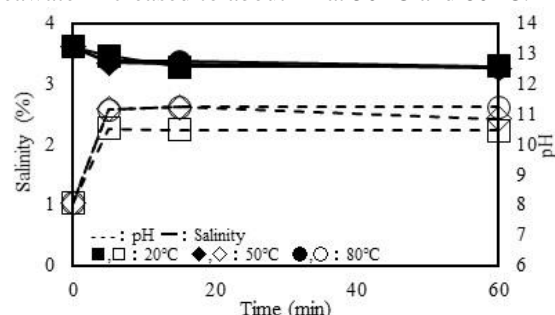


Fig. 2 Salinity and pH of seawater treated with calcined Ca-Fe LDH during the treatment at 20, 50 and 80 °C

From these results for natural zeolite and calcined Ca-Fe LDH, with increasing the temperature, the

change of solution pH was larger and the desalination reaction was faster.

Figure 3 shows the salinity and pH of seawater treated with the mixture of natural zeolite and calcined Ca-Fe LDH during the treatment at 20, 50 and 80 °C. Regardless of temperatures, the behaviors of salinity decrease are almost same, and the salinity of seawater gradually decreased to be 0.95 - 0.99 %, while pH of seawater were almost constant (8 - 9).

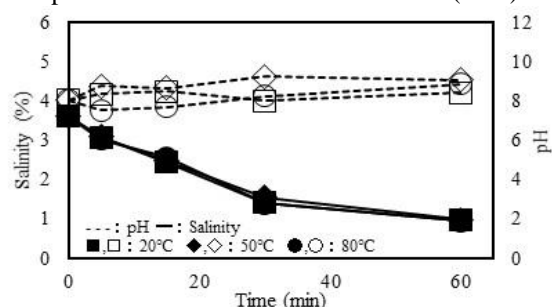


Fig. 3 Salinity and pH of seawater treated with the mixture of natural zeolite and calcined Ca-Fe LDH during the treatment at 20, 50 and 80 °C

Table 2 shows the salinities of seawater and the seawater treated with natural zeolite, calcined Ca-Fe LDH, and the mixture of natural zeolite and calcined Ca-Fe LDH at 20, 50 and 80 °C after 60 min treatment. Natural zeolite can reduce the salinity due to the cation exchange reaction, but the reaction causes pH decrease to increase  $H^+$ , which is competitor for cation exchange reaction, therefore the decrease of salinity stopped to be about 2.4% of salinity. Calcined Ca-Fe LDH can reduce the salinity due to the reconstruction reaction, but the reaction causes pH increase to increase  $OH^-$ , which is competitor for removal anions by reconstruction reaction of calcined Ca-Fe LDH, therefore the decrease of salinity stopped to be about 3.3 % of salinity. The mixture of natural zeolite and calcined Ca-Fe LDH can reduce the salinity due to the reactions of both cation exchange of natural zeolite and reconstruction of calcined Ca-Fe LDH, these reactions simultaneously supply  $H^+$  from natural zeolite and  $OH^-$  from calcined Ca-Fe LDH to be neutralized, and smoothly occurs to decrease the salinity of seawater.

Table 2 Salinities of seawater and the seawater treated with natural zeolite (NZ), calcined Ca-Fe LDH (CFL), and the mixture of natural zeolite and calcined Ca-Fe LDH (Mixture) at 20, 50 and 80 °C after 60 min treatment

Salinity (%)	Seawater	20°C	50°C	80°C
NZ	3.61	2.35	2.44	2.42
CFL		3.29	3.26	3.28

Mixture	0.97	0.99	0.95
---------	------	------	------

Figure 4 shows the concentrations of (a)  $SO_4^{2-}$ , (b)  $Cl^-$ , (c)  $Na^+$ , (d)  $K^+$ , (e)  $Mg^{2+}$ , (f)  $Ca^{2+}$ , (g)  $Fe^{3+}$ , (h)  $Si^{4+}$  and (i)  $Al^{3+}$  during the treatment with the mixture of natural zeolite and calcined Ca-Fe LDH at 20 °C, 50 °C and 80 °C. Regardless of temperatures, concentrations of  $Cl^-$ ,  $SO_4^{2-}$ ,  $Na^+$ ,  $K^+$  and  $Mg^{2+}$  decreased and those of  $Ca^{2+}$ ,  $Fe^{3+}$  and  $Si^{4+}$  increased by addition of the mixture. It was considered that the decreases of  $Cl^-$  and  $SO_4^{2-}$  was caused by calcined Ca-Fe LDH, those of  $Na^+$  and  $K^+$  and increase of  $Ca^{2+}$  by natural zeolite, and the increase of  $Fe^{3+}$  and  $Si^{4+}$  by the dissolution from calcined Ca-Fe LDH and natural zeolite, respectively. It is noted that Al concentration is almost zero without the dissolution from the mixture.

Table 3 shows the chemical compositions, salinities and pHs of seawater and the seawater treated with the mixture of natural zeolite and calcined Ca-Fe LDH at 20, 50 and 80 °C after 60 min treatment. Seawater used in this study indicate that chemical composition, salinity and pH are typical values of seawater [17, 18]. After treatment of seawater with the mixture of natural zeolite and calcined Ca-Fe LDH at 20, 50 and 80 °C, regardless of temperatures, the salinity decreased to lower than 1 % (0.95 - 0.99 %) and pH are 8.0 - 9.1, which can be used for plant cultivation. The contents of  $SO_4^{2-}$ ,  $Cl^-$ ,  $Na^+$ ,  $K^+$  and  $Mg^{2+}$  decreased, while that of  $Ca^{2+}$  increased.

Table 3 Chemical compositions, salinities and pHs of seawater and the seawater treated with the mixture of natural zeolite and calcined Ca-Fe LDH at 20, 50 and 80 °C after 60 min treatment

	Seawater	20°C	50°C	80°C
Content (mmol/L)				
$SO_4^{2-}$	42	5	4	7
$Cl^-$	904	222	219	221
$Na^+$	594	67	70	72
$K^+$	14	3	3	3
$Mg^{2+}$	75	2	0	0
$Ca^{2+}$	17	656	650	674
Salinity (%)	3.61	0.97	0.99	0.95
pH	8.0	8.44	9.08	8.88

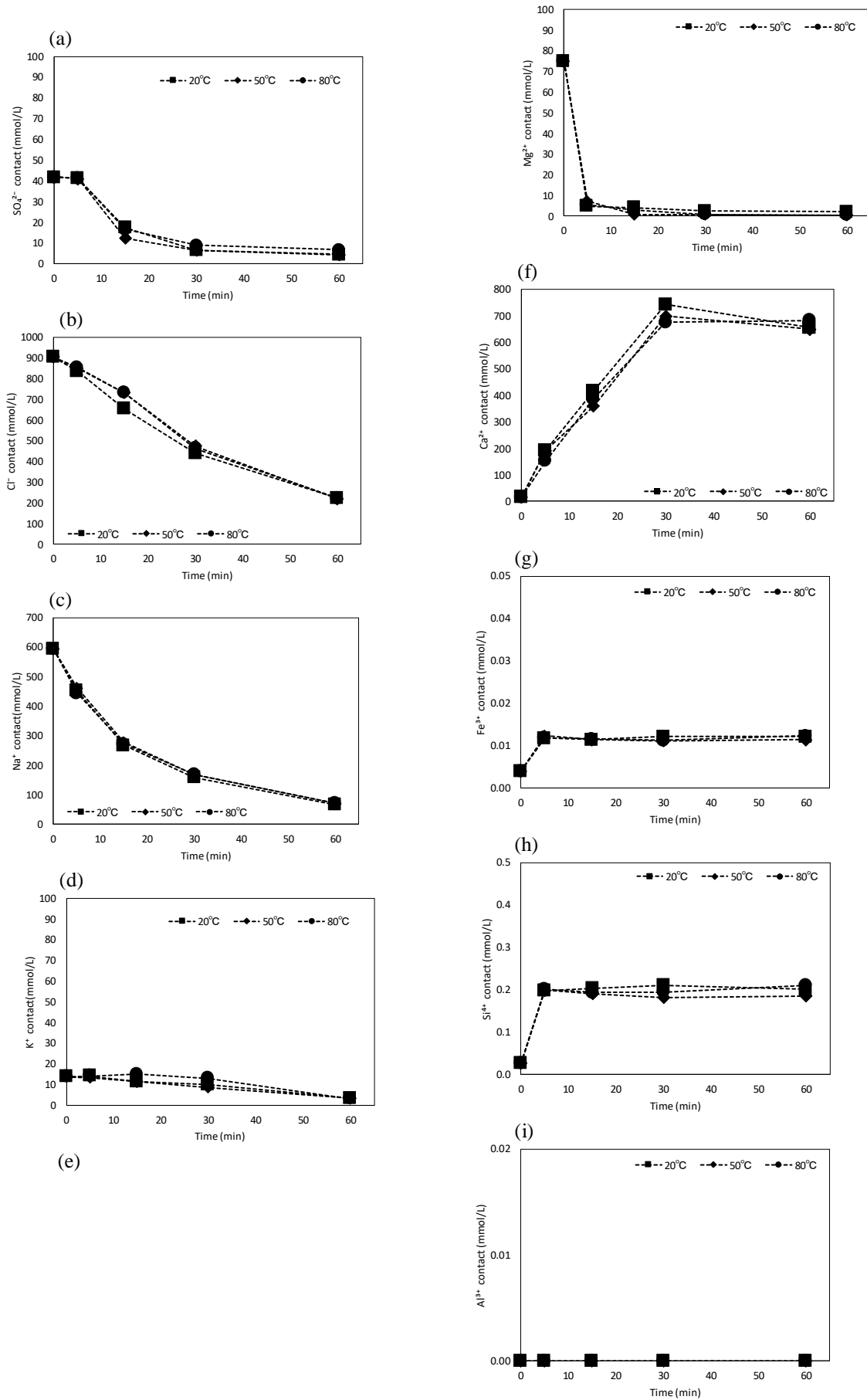




Fig. 4 concentrations of (a)  $\text{SO}_4^{2-}$ , (b)  $\text{Cl}^-$ , (c)  $\text{Na}^+$ , (d)  $\text{K}^+$ , (e)  $\text{Mg}^{2+}$ , (f)  $\text{Ca}^{2+}$ , (g)  $\text{Fe}^{3+}$ , (h)  $\text{Si}^{4+}$  and (i)  $\text{Al}^{3+}$  during the treatment with the mixture of natural zeolite and calcined Ca-Fe LDH at 20 °C, 50 °C and 80 °C

Figure 5 shows the XRD patterns of (a) Ca-Fe LDH, (b) calcined Ca-Fe LDH, (c) the mixture of natural zeolite and calcined Ca-Fe LDH, and the residue of the mixture of natural zeolite and calcined Ca-Fe LDH after 60 min treatment at (d) 20 °C, (e) 50 °C and (f) 80 °C. Ca-Fe LDH phase was transformed into amorphous and calcite phase (Fig. 5 (a), (b)). After desalination treatment, all residues have natural zeolite mineral phases, mordenite, and calcite, and Ca-Fe LDH phases which was formed from calcined Ca-Fe LDH by reconstruction reaction (Fig. 5 (c)-(f)). These results indicate that desalination of seawater by the mixture of natural zeolite and calcined Ca-Fe LDH was caused by cation exchange of zeolite and reconstruction of calcined Ca-Fe LDH.

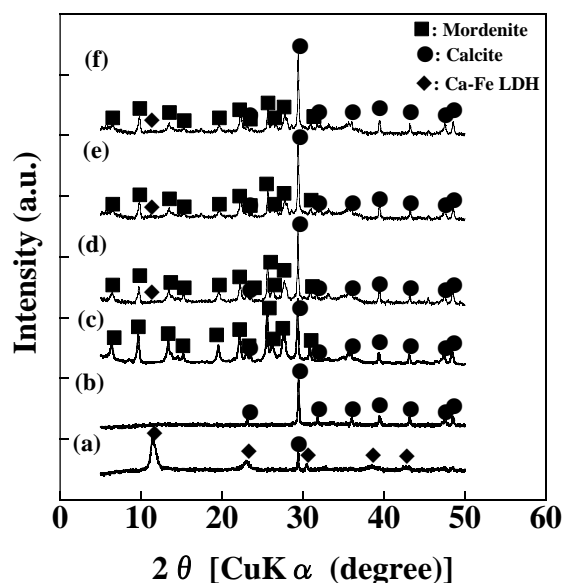
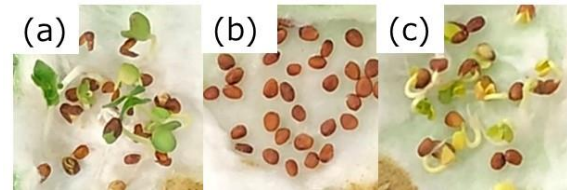


Fig. 5 XRD patterns of (a) Ca-Fe LDH, (b) calcined Ca-Fe LDH, (c) the mixture of natural zeolite and calcined Ca-Fe LDH, and the residue of the mixture of natural zeolite and calcined Ca-Fe LDH after 60 min treatment at (d) 20 °C, (e) 50 °C and (f) 80 °C.

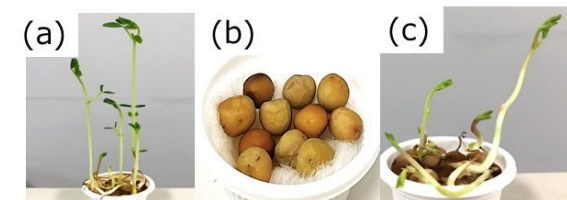
Figure 6 shows the observation of radish sprouts, bean sprouts and mung bean after 10 days' growth using (a) tap water, (b) seawater and (c) the seawater treated with the mixture of natural zeolite and

calcined Ca-Fe LDH. The germination of radish sprouts, bean sprouts and mung bean could be confirmed in tap water and the seawater treated with a mixture of natural zeolite and calcined Ca-Fe LDH (Fig. 6 (a), (c)), while these plants cannot be germinated in seawater (Fig. 6 (b)).

Radish sprouts



Bean sprouts



Mung bean

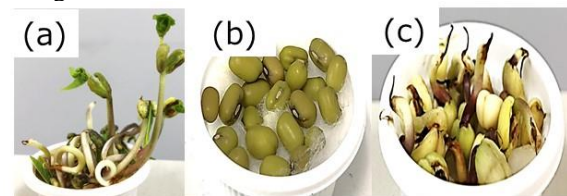


Fig. 6 Observation of radish sprouts, bean sprouts and mung bean after 10 days growth using (a) tap water, (b) seawater and (c) the seawater treated with the mixture of natural zeolite and calcined Ca-Fe LDH.

## CONCLUSIONS

For the development of desalination material to obtain agriculturally usable freshwater from seawater for stable supply of water resources, desalination behaviors of the mixture of natural zeolite and calcined Ca-Fe LDH in seawater were examined for producing cultivatin water from seawater.

Using natural zeolite, the salinity decreased from 3.5 % to about 2.5 %, and desalination speed was faster and pH was lower with increasing the temperature. Using calcined Ca-Fe LDH, salinity was little low (about 3.3%), and pH rises to about 10.5 - 11.0 from 8.0. Regardless of temperatures, when seawater were treated with the mixture of natural zeolite and calcined Ca-Fe LDH, the salinity decreased to 0.95 - 0.99% below the available salinity for agriculture (about 1.0%) and pH is neutral (8 - 9). When using the seawater treated with a mixture of

natural zeolite and calcined Ca-Fe LDH, the germination of radish sprouts, bean sprouts and mung bean was confirmed.

## ACKNOWLEDGMENTS

This study was performed under the Cooperative Research Program of the Institute of Ocean Energy, Saga University (22E03). This work partially supported by Japan Health Foundation.

## REFERENCES

- [1] Service R.F., Desalination freshens up, *Sci.* Vol. 313, 2006, pp. 1088.
- [2] Elimelech M., and Phillip P.W., The future of seawater desalination: Energy, technology, and the environment, *Sci.* Vol. 333, 2011, pp. 712-717.
- [3] FAO 2021, AQUASTAT data base.
- [4] Mezher T., Fath H., Abbas Z., and Khaled A., Techno-economic assessment and environmental impacts of desalination technologies, *Desalin.* Vol. 266, 2011, pp. 263-273.
- [5] Wajima T., Ion exchange properties of Japanese natural zeolite in seawater, *Anal. Sci.*, Vol. 29, 2013, pp. 139-141.
- [6] Wajima T., Shimizu T., Yamato T., and Ikegami Y., Effect of  $\text{HNO}_3$  and  $\text{H}_3\text{PO}_4$  on ion exchange of natural zeolite for making agricultural cultivation solution from seawater, *Int. J. Soc. Mater. Eng. Resour.*, Vol. 20, 2014, pp. 109-112.
- [7] Wajima T., Desalination of seawater using Ca-A zeolite for agricultural utilization, *Bull. Soc. Sea Water Sci. Jpn.*, Vol. 72, 2018, pp. 325-328.
- [8] Wajima T., Shimizu T., and Ikegami Y., New simple proceed of making agricultural cultivation solution from seawater, *Bull. Soc. Sea Water Sci. Jpn.*, Vol. 60, 2006, pp. 201-202.
- [9] Wajima T., Shimizu T., and Ikegami Y., Ion exchange properties of natural zeolite in the preparation of an agricultural cultivation solution from seawater, *J. Ion. Exch.*, Vol. 18, 2007, pp. 201-202.
- [10] Wajima T., Shimizu T., and Yamato T., Removal of NaCl from seawater using natural zeolite, *Int. J. Toxicol. and Environ. Chem.*, Vol. 91, Issue 1, 2010, pp. 21-26.
- [11] Wajima T., Shimizu T., Yamamoto T., and Ikegami Y., Simple two-step process for making agricultural cultivation solution from seawater using calcined hydrotalcite and natural zeolite, *Clay Sci.*, Vol. 14, 2008, pp. 7-12.
- [12] Wajima T., Desalination behavior of calcined hydrotalcite from seawater for preparation of agricultural cultivation solution using natural zeolite, *Energy Environ. Res.*, Vol. 4, 2014, pp. 3-10.
- [13] Sekihata F., and Wajima T., Preparation of desalination agent from Ca-type clay minerals, *Int. J. GEOMATE*, Vol. 19, 2020, pp. 123-129.
- [14] Tsutsui D., and Wajima T., Desalination property of various calcined layered double hydroxides from seawater, *Int. J. Environ. Agri. Res.*, Vol. 4, Issue 11, 2018, pp. 15-21.
- [15] Wajima T., Desalination of seawater using natural zeolite for agricultural utilization, *Int. J. GEOMATE*, Vol. 16, 2019, pp. 21-26.
- [16] Sekihata, F., and Wajima, T., Desalination behavior of natural zeolite in seawater, *Int. J. GEOMATE*, Vol. 20, 2021, pp. 82-88.
- [17] The society of Sea Water Science, Japan and The Salt Science Research Foundation, *Sea Water, its Property and Technology*, Tokai University Press, Tokyo, 1994.
- [18] Nakajima T., *Utilization of deep seawater*, Midori Shobo, Tokyo, 2002.

## MEASUREMENT OF CRACK DISPLACEMENT USING DIGITAL PHOTOGRAMMETRY

Afia S. Boney<sup>1</sup>, Satoshi Nishiyama<sup>1</sup> and Teruyuki Kikuchi<sup>2</sup>

<sup>1</sup> Graduate School of Environmental and Life Sciences, Okayama University, Japan; <sup>2</sup>J-POWER Design Co Ltd, Japan

### ABSTRACT

To evaluate the soundness of civil engineering structures constructed on rock slopes, new measurement techniques are needed to determine the relationship between structures and rock behaviour with high accuracy and accuracy. This paper describes an example of measuring the displacement of a structure related to a landslide on a slope. The proposed technique is measured by using two image processing, one is the computation of the target centroid with intensity value and the other one is perspective projection. Thus, it is possible to measure the displacement in an arbitrary camera position. For verifying the accuracy and precision of this technique, the experiments were performed, and the result indicated that the authors could measure approximately 0.1 mm of the displacement of the crack with high accuracy and precision when use the digital image taken from 0.5m of the target. In addition, the authors tried to apply this measurement system proposed herein to an actual tunnel for estimating the serviceability and it was concluded that the result of this measurement has relationship with the behaviour of the rock slope.

*Keywords: Digital Photogrammetry, Displacement, Image Processing, Reflective Targets*

### INTRODUCTION

Numerous civil engineering structures such as tunnels have been built on rock slopes. These infrastructures must be monitored to ascertain its safety. In the case of concrete structures such as dams and tunnels, width and patterns of cracks which occur on the surfaces of these, are critical to evaluate their soundness. This will determine whether countermeasures such as reinforcement, repair and reconstruction are required. Most existing methods employ manual inspection, with specific tools, to examine deficiencies in structures [1]. However, this traditional method is time-consuming, subjective and susceptible to human error. Furthermore, financial difficulties and worker shortages have become challenges in recent years, and it is necessary to establish a more affordable and versatile monitoring method. More recently, image-based methods of crack detection have been utilized. Although existing research has already proposed new, innovative methods, these utilize expensive equipment, complex experimental set up and image segmentation [2]. In this research, the authors propose a measurement technique which uses photogrammetry and digital image processing to measure the crack width. This method is fast, less expensive, reproducible and object. In addition, by using a Digital Single-lens Reflex (DSLR) camera, the author has control over the quality of the image.

### PRINCIPLE OF CRACK MEASUREMENT

In this section, the authors explain techniques and

principles for measuring cracks on a captured digital image [1]. This technique proposed herein measures the width and length of the crack without detecting the crack. Figure 1(a) shows the reflective target used in this research, and these targets consist of microscopic glass beads arranged in circles, to induce a strong diffused reflection of incident light. There are four circles on this target. The authors measure the distance of one pair of circles on both side of the crack. To measure the distance, a few processes were performed. Firstly, a pair of reflective targets is arranged around the crack as gauges and a digital image of the targets, taken from an arbitrary camera position, as shown in Fig. 1(b), is captured. Secondly, the centre of gravity in the two-dimensional coordinate is decided by calculating the centroid of the targets with its intensity value. Figure 2 shows an example of the distribution of the intensity value of the circle.

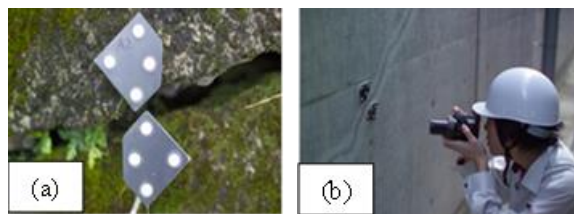


Fig. 1 Example photographs of (a) the reflective target installed on the crack surface and (b) camera position when taking an image of (a)

In this paper, the authors define intensity value as weight and calculate computation of the target centroid. The centre of gravity in the two-dimensional

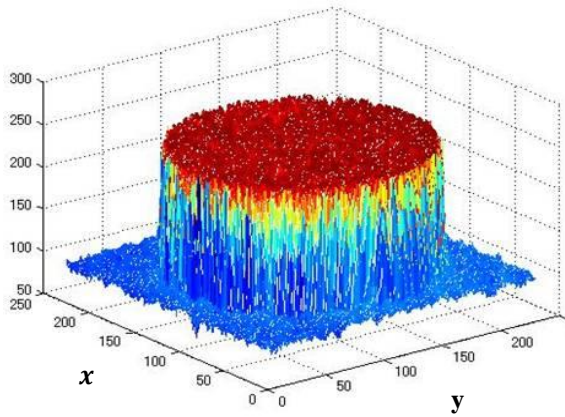


Fig. 2 An example of the distribution of the intensity value of the circle of the target. The vertical axis takes intensity value.

coordinate is defined by the origin of the image coordinate system  $x_0$  and  $y_0$ , the pixel size  $a_x$  and  $a_y$ , and the intensity value of the pixel  $(i, j)$   $q(i, j)$  as shown in Eq. (1).

$$x = x_0 + a_x \frac{\sum_{i=1}^n \sum_{j=1}^m (q(i, j) \times x_{ij})}{\sum_{i=1}^n \sum_{j=1}^m q(i, j)}$$

$$y = y_0 + a_y \frac{\sum_{i=1}^n \sum_{j=1}^m (q(i, j) \times y_{ij})}{\sum_{i=1}^n \sum_{j=1}^m q(i, j)} \quad (1)$$

After defining the centre of gravity of four circles, the perspective projection was adopted. This allowed the digital image, which was taken from an arbitrary camera position, to be converted to an image facing the target. It is then possible to measure the displacement of the crack. Additionally, the authors adopted collinearity condition as shown in Fig.3, which means that a measurement point, the camera (centre of lens) and the measurement point imagery which appears on the images taken, can be connected by a straight line. The perspective projection, as shown in Fig.4, is based on the collinearity condition and the authors defined  $z$  as constant in this study. Consequently, the perspective projection in a two-dimensional coordinate system is obtained. Furthermore, by calculating with the least-squares method, Eq. (2) is obtained, and the authors adopted perspective projection. Equation (2) has 8 unknowns in total:  $b_i$  ( $i=1\sim8$ ). This requires the establishment of one known point and the measurement of at least four known points to solve the equation. The residuals for the least square solutions were 0.10 to 0.05 of a pixel.

$$x_i b_1 + y_i b_2 + b_3 - x_i x'_i b_7 - y_i x'_i b_8 = x'_i$$

$$y_i b_4 + y_i b_5 + b_6 - x_i x'_i b_7 - y_i x'_i b_8 = y'_i \quad (2)$$

## EXPERIMENTS AND DISCUSSION

For evaluating the accuracy and the precision of this technique proposed, the authors performed experiments. The accuracy and precision are defined

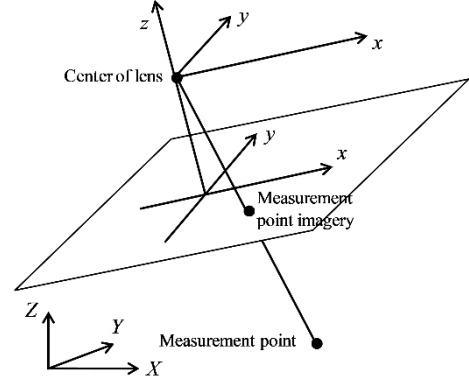


Fig. 3 Concept of the collinearity condition.

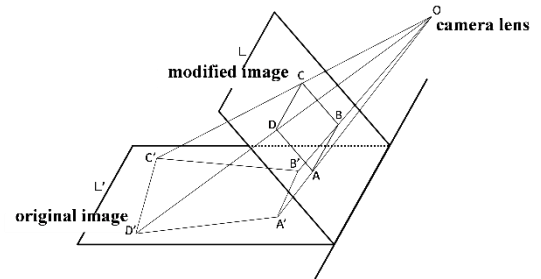


Fig. 4 Concept of the perspective projection.

in Eq. (3) and (4). Experimentally (Fig. 5(a)), one pair of reflective targets is attached at a fixed position, and another pair, to a micrometer as shown in Fig. 5(b).

$$\text{accuracy: } \sqrt{\frac{\sum (\text{measured value} - \text{true value})^2}{n}} \quad (3)$$

$$\text{precision: } \sqrt{\frac{\sum (\text{measured value} - (\sum_{i=1}^n \text{measured value})/n)^2}{n}} \quad (4)$$

To verify the influence of the camera position length, the micrometer was moved and that changed the displacement of the target. The image was taken from a different camera position and the displacement of the target was measured. The digital camera used had a resolution of 13 million pixels. The size of targets used in this experiment is 50mm by 50mm and focal length is 50mm. The result of the experiment is shown in Fig.6(a) and in Table 1. From the result of the experiment, the authors found that as  $L$  increases, the accuracy and precision of the measurement value deteriorates. Regardless of this result, it was also found that when the digital image was taken up to 1m away from the targets, the displacement was

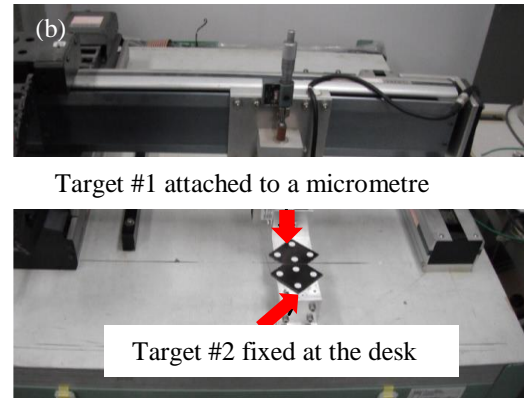
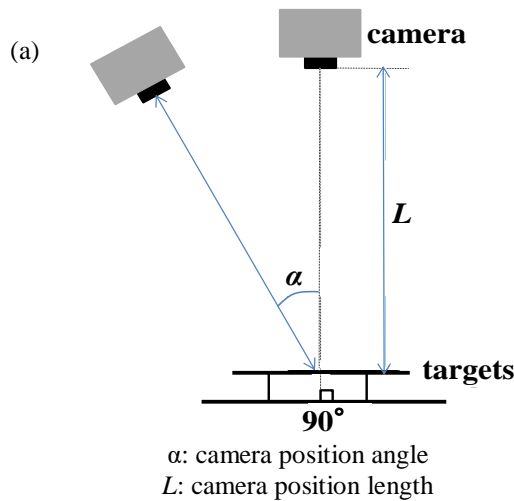


Fig. 5 (a) Schematic diagram of the small-scale laboratory experiment and (b) actual test set-up in the laboratory

measured with an accuracy and precision of less than 0.02mm.

Additionally, to evaluate the influence of the camera position angle, the digital images were taken from an arbitrary camera position and from the camera length 0.36m. Table 1 and Fig. 6(b) summarizes the results of the experiment. When the camera angle ( $\alpha$ ) is at less than 20°, the displacement of the targets can be detected with a good accuracy and precision of 0.01 mm. At 30° the accuracy decreased to 0.03 mm

Table 1 Influence of camera position length ( $L$ ) on crack width measurement

$L$	0.5m	1m
accuracy	0.02	0.04
precision	0.01	0.02

Table 2 Influence of camera position angle ( $\alpha$ ) on crack width measurement

$\alpha$	0°	10°	20°	30°
accuracy	0.01	0.01	0.01	0.03
precision	0.01	0.01	0.01	0.01

### EXAMPLE OF MEASUREMENT IN ACTUAL TUNNEL

To demonstrate the serviceability of this measurement system, the authors measured the displacement of the crack on an actual tunnel. This tunnel was selected as it was constructed twenty years ago, which makes it an ideal example tunnel that should be monitored for cracks, to prevent landslides occurring, from the groundwater in the slope. The purpose of this experiment is to investigate the soundness of this tunnel in a quantitative manner and to find the relationship between the landslide and the

displacement of the cracks. By using extensometers, the movement per year is observed to be 2-3mm. The diameter of the tunnel is 2m (Fig. 7).

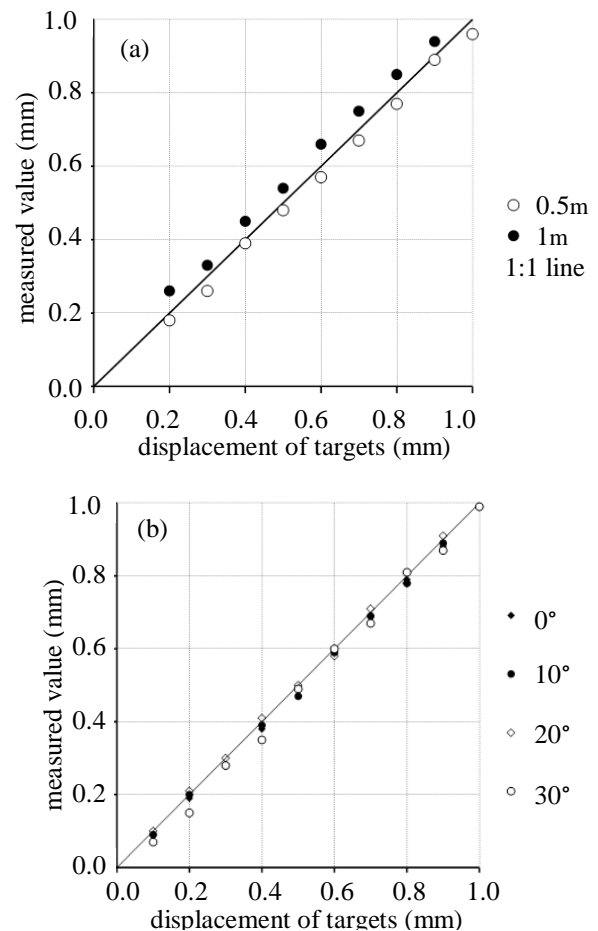


Fig. 6 (a) and (b) show the relationship between the displacement of targets and measured values. Figure (a) shows the result when  $L$  is changed and (b) shows the result when  $\alpha$  is changed.



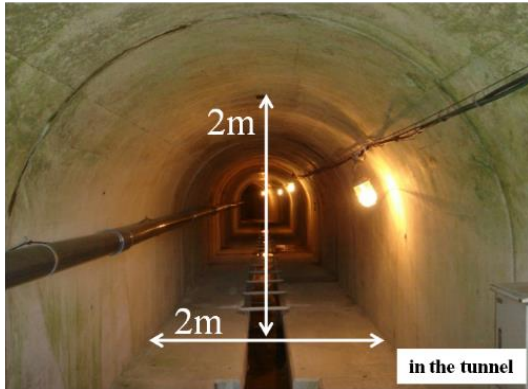


Fig. 7 Example photograph of the tunnel's interior

As a result of landslides in the tunnel, there are more than three hundred cracks present. The authors arranged thirty targets in the tunnel at various locations as shown in Fig. 8. For one year and nine months, the cracks were measured every two months and the result of the displacements of all the targets were recorded. It was found that the displacements per month were more than 0.2mm in 6 targets, though in most targets the displacements per month were less than 0.2mm. In addition, the displacements per month were more than 0.1mm in targets No.1, No.8 and No.11. Targets No.1 and No.11 were arranged in the shallow landslide and these targets measured the same crack in the tunnel. Target No.1 was in the side wall, target No.11 was located on the ceiling, and target No.8 was arranged in the deep sliding. As a result, the displacement of the targets arranged in the area with unsymmetrical earth pressure was less than 0.02mm per month.

In this paper, the authors focused on targets No.1, No. 8 and No.11 and compared the results by using

the other measurement system. At first, the authors showed the result of the measured values of targets No.1 and No.11 as summarized in Figure 10 (a) and found that the displacements of targets No.1 and No.11 agree with the displacement of the shallow landslide by using the electro-optical distance measurements. Figure 10 (b) shows the result of the measured values of target No.8 and ones of the inclinometer, and it was concluded that by the result of target No.8 the displacement was 2.14mm for 21 months. Therefore, the trend of the measured value of target No.8 also agrees with one of the measured values of the inclinometer. In addition, the displacement of target No.8 decomposed into the tensile displacement and the shear displacement. From the results, the movement of target No.8 corresponds with the direction of the landslide. In summary the authors can monitor the behavior of the deep sliding by measuring the displacement of target No.8 [3].

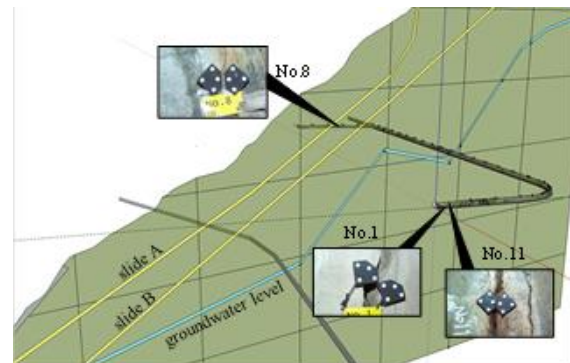


Fig. 9 The sketch of the tunnel and slope, and the image of the targets No.1, No.8 and No.11.

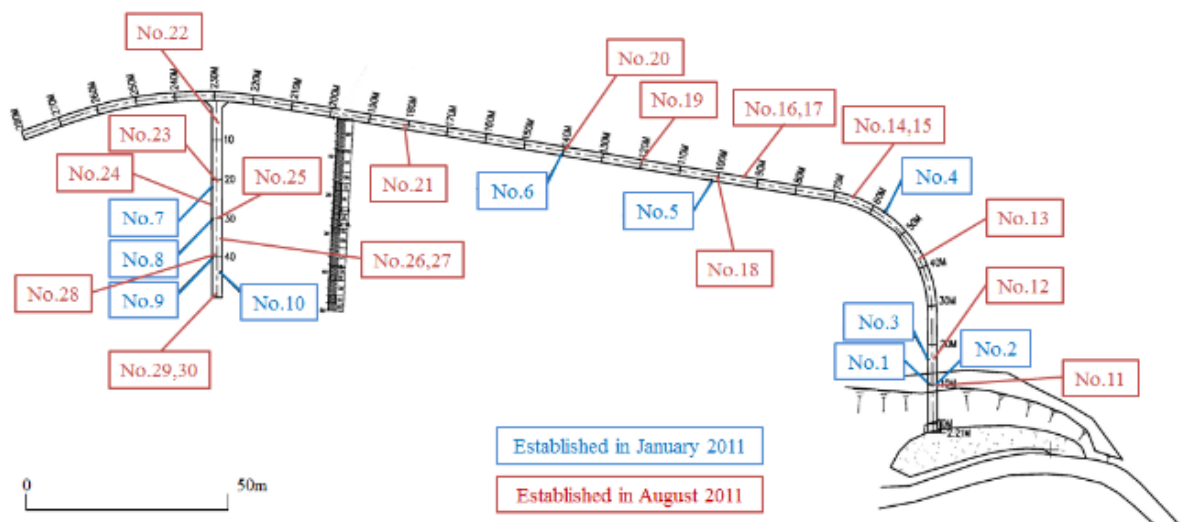


Fig.8 Schematic diagram of the tunnel alignment and the location and arrangement of the installed 30 targets



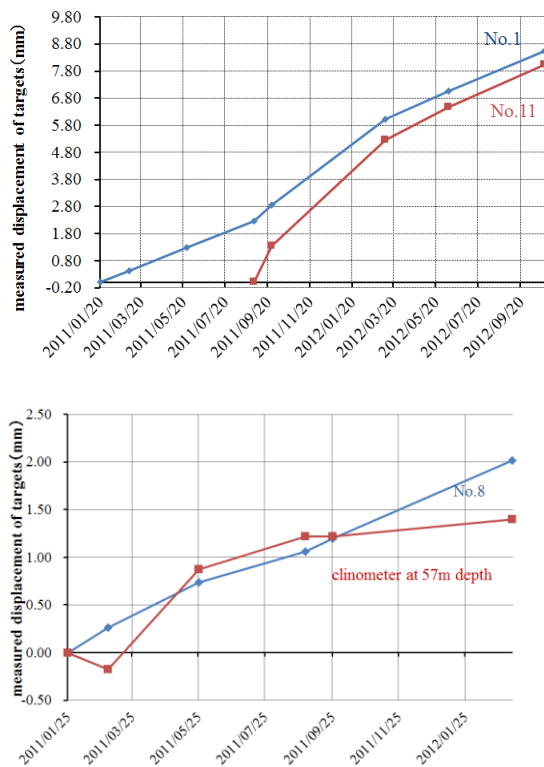


Fig. 10 (a) shows the values of the change of cracks' width and (b) shows the result of the displacement of No.8 and the measured value of the clinometer

## CONCLUSION

In this technique, the authors establish reflective targets around both sides of the crack as gauges and took a digital image of the reflective targets. The digital image adopted image processing, and the displacement of the targets was measured. From the result of the experiments, it was found that the accuracy and precision of the measurement technique are about 0.2mm. In addition, the authors demonstrated this measurement technique to a tunnel and measured the displacement of the cracks every two months. By comparing these results with the measurement system that uses extensometer, it was found that the trend of the displacement is consistent.

## REFERENCES

- [1] Munawar, H.S., Hammad, A.W.A., Haddad, A., Soares, C.A.P. and Waller, S.T., Image-Based Crack Detection Methods: A Review, *Infrastructures*, 2021, 6, 115.
- [2] Kaneko, S., Oka, S., and Matsumiya, N., Detection of Cracks in Concrete Structures from Digital Camera Images, *NTT Technical Review*, Vol. 10, No. 2, 2012.
- [3] Hattori, S., Akimoto, Y., Ohnishi, Y., and Miura, S., Semi-automated tunnel measurement by vision metrology using coded-targets, *Modern Tunneling Science and Technology*, 1: 285-288, 2001.

## STABILITY OF THE MUNICIPAL SOLID WASTE LANDFILL ON SLOPING LAND IN BATU CITY, EAST JAVA, INDONESIA

A Rachmansyah<sup>1</sup>, A P Putra<sup>2</sup>, A Darmawan<sup>3</sup>, Harimurti<sup>1</sup>

<sup>1</sup> Civil Engineering Department Brawijaya University Indonesia, [ariefftub@yahoo.com](mailto:ariefftub@yahoo.com)

<sup>2</sup> Magister Program, Civil Engineering Department, Brawijaya University, Indonesia

<sup>3</sup> Geocentris Consulting, Malang, Indonesia

### ABSTRACT

It is difficult to find a location for the final disposal site of municipal solid waste that meets the technical and environmental requirements. Due to this reason Government of Batu City Indonesia places final disposal facility on land with a steep slope, so the risk of landslides increases. This paper will be discussed the results of the slide hazard analysis of the landfill of municipal solid waste on sloping land and different condition. Slope stability analysis was used the Limit Equilibrium Method (LEM) also the Finite Element Method (FEM), where the results of the analysis were in the form of slope failure that be reflexed by value of the safety factor (SF). Furthermore, the stability analysis will be modeled into two conditions, namely conditions during the summer so that the groundwater level is normal and the rainy season conditions with very high rainfall, so that the groundwater level is assumed to increase to the middle part of waste landfill. Under normal conditions, the slope safety number in the LEM calculation is 0.8 and when the rainfall conditions are high it is 0.75. By using FEM, the average safety factor for normal conditions is 1.117 and for high rainfall conditions it is 1.021. The decreasing of safety factor value on high rainfall is 5% by the LEM and 10% by the FEM.

*Keywords: slope stability, solid waste, aerial survey, limit equilibrium, finite element*

### INTRODUCTION

Batu City, East Java Province, Indonesia which is located at the conjunction of three active volcanoes, is one of the most attractive tourist cities. In the city there are dozens of springs that emerge from the fissures of quaternary volcanic rocks. This condition makes it difficult to find a location for the processing facility of municipal solid waste that meets the technical and environmental requirements. Therefore, the city government places it on land with a steep slope which there are no aquifers or springs, but the risk of landslides increases.

Landfills are very susceptible to landslides because the shear angle is very small, it can become very extreme again if the rainy season arrives [1]. This paper will discuss the possibility of landslides in the landfill area. The analysis is carried out with the assumption that domestic waste is like soil material with certain characteristics. Thus, slope stability analysis was carried out on three layers of soil with different physical and mechanical properties [2].

The analysis of slope failure was carried out using the Limit Equilibrium Method (LEM) and Finite Element Method (FEM) whose results describe the value of safety factor (SF). Furthermore, the stability analysis will be modeled into two conditions, namely conditions during the dry season, where the groundwater level is normal. The second model is carried out during the wet

season with high rainfall, so that the groundwater level is assumed to rise to the bottom of the domestic waste heap.

Slope stability analysis most often uses the limit equilibrium method, because it is easy to understand and does not require a lot of data [3]. This method describes the ratio between the material force that will move and the resisting force. This comparison figure is known as the safety factor [4].

The general Limit Equilibrium Method (LEM) calculation formula for slope stability analysis requires several assumptions [5]. The first assumption is to form a slip plane. This method generally uses two types of slip planes, namely: circular and non-circular (can also be planar). The LEM calculation provides a Safety Factor value based on the calculation of the moment equilibrium ( $F_m$ ) and the horizontal force balance ( $F_f$ ). Morgenstern and Price proposed an equation to calculate the shear force between layers in the LEM that satisfies the balance between moments and forces. In calculating the safety factor, it is done by making an incision, only landslides that have a slip surface can be counted. Many experts propose a calculation formula with this calculation method, including Fellinius or Bishop [6].

Finite Element Method (FEM) is a calculation procedure used to get an approach to mathematical problems that often arise in engineering with various approaches and a series of algebraic equations involving values at discrete points in the part being evaluated. The finite element method equation is

created, and the solution is sought as well as possible to avoid errors in the result. The net consists of elements that are connected by nodes. Nodes are points on the net where the value of the primary variable is calculated. For example, for displacement analysis, the value of the primary variable is the value of displacement. Nodal displacement values are interpolated on the elements to obtain algebraic equations for displacement, and strain, through the nets formed [7].

## LOCATION AND METHOD

The modeling of the slope stability of the solid waste landfill was carried out at the Processing Facility of Municipal Waste in Tlekung Village, Junrejo District, Batu City. Landfill of solid waste is one of the facilities there.

The research that has been carried out is divided into several stages, namely:

1. Topographic survey by aerial method and slope profiling before and after the landfill
2. Sampling of soil that has not been contaminated and contaminated by leachate
3. Laboratory testing to determine the physical and mechanical properties of the soil
4. Analysis of slope stability of landfills using LEM and FEM. Slope stability analysis with FEM is used software Plaxis 2 dimensions.

For slope stability analysis, using either LEM or FEM a topographic profile is required [8]. The elevation contour map is made in conditions after there is a solid waste landfill, so the aerial method was used. This was done by considering the risk of accidents and the health of the surveyor. The topographic profiles before the landfilling was modeled from a topographic map that is published by the Indonesian Geospatial Information Agency.

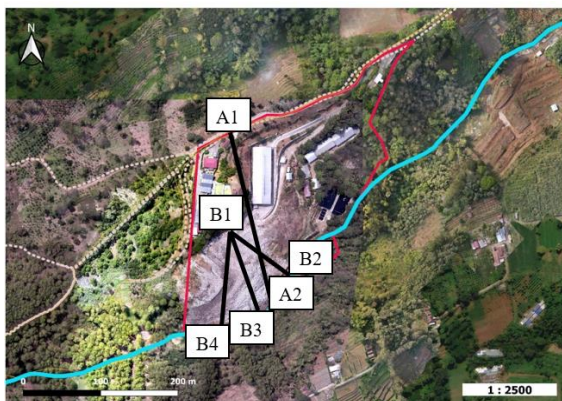


Fig 1. Aerial Photograph of the Processing Facility of Municipal Waste in Tlekung, Batu City

## RESULT AND DISCUSSION

### Geology and Topographic Profiles

The location of the Processing Facility of Municipal Waste on Tlekung Batu City is located on the slopes of Mount Butak which is part of the Panderman Volcano Complex. The rock around the landfill site is composed of tuff and andesite breccia. At the bottom of the landfill area there is an intermittent river.

In this study, three slope profile models were created that represent the condition of the landfill, symbolized by pieces B1-B2, B1-B3, and B1-B4. In addition, a slope profile is also needed when there is no waste pile symbolized by the A1-A2 slices (Figure 1 to Figure 5). These three profiles will be used for slope stability analysis of domestic waste piles.

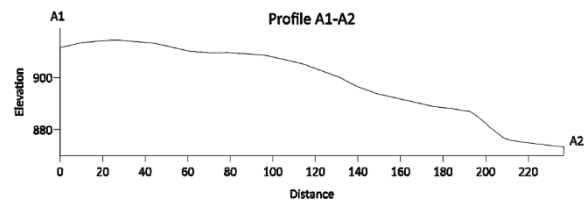


Fig. 2 Profil A1-A2 before solid waste landfilling

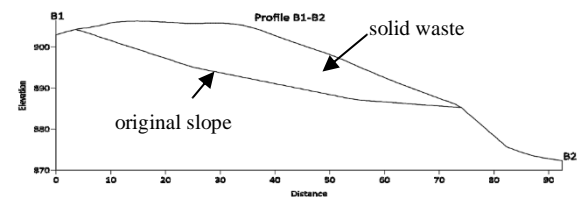


Fig. 2 Profil B1-B2 after solid waste landfilling

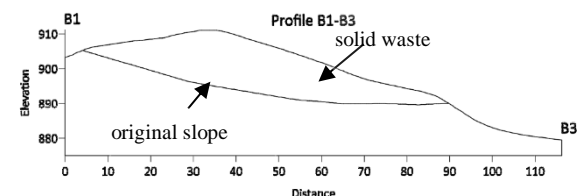


Fig. 3 Profil B1-B3 after solid waste landfilling

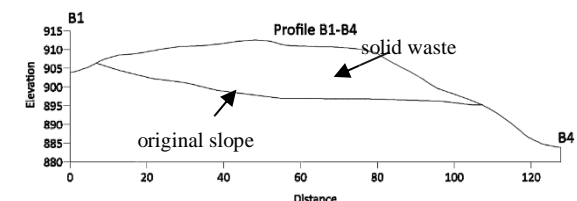


Fig. 4 Profil B1-B4 after solid waste landfilling

After these profiles the average height of solid waste landfill on the slopes is approximately 25 meters. This model is obtained from the height difference between the conditions before and after solid waste landfilling.

### Characteristic of Soil and Solid Waste

Physical and mechanical characteristics of soil and waste are important factors that must be known before modeling landslides, both with LEM and with FEM. Parameters to look for cohesion, internal friction angle, and unit weight.

#### Characteristic Of Soil

Soil samples were taken at 3 points. Two samples represent soil that has not been contaminated by leachate taken at the upper and lower of the landfill area. One sample represents contaminated soil is taken on a slope adjacent to the landfill. The mechanical properties of the soil were determined by direct shear test (Table 2).

Table 1. Characteristic of Soil Bedding

Sampel Tanah	Unit weight ( $\gamma_d$ ) gr/cm <sup>3</sup>	Cohesion (c) kg/cm <sup>2</sup>	Internal friction angle ( $\phi$ ) °
Upper landfill area	2,619	0,374	22
Contaminated soil	2,118	0,504	20
Lower landfill area	2,654	0,354	23

Based on these characteristics, the soil found is classified as sand, while the contaminated soil contains more organic and clay.

#### Characteristic of Solid Waste

Until now in Indonesia, there is no standardized method for testing the physical and mechanical properties of solid waste. Therefore, the physical characteristics of waste are based on previous research. Several researchers in Indonesia have tested the physical and mechanical properties of domestic waste, one of the results is presented in Table 3 [9].

Table 3. Physical and Mechanical Properties of Solid Waste

Parameter	Number	Unit
Internal friction angle ( $\phi$ )	15 - 20	°
Cohesion (c)	1,2	kg/cm <sup>2</sup>
Wet specific gravity ( $\gamma_{wet}$ )	3,16	gr/cm <sup>3</sup>

### Slope Stability Analysis by Using *Limit Equilibrium Method* (LEM)

#### Slope Stability before Solid Waste Landfilling

Slope stability analysis before domestic waste is piled up is needed as a comparison (Figure 6). From the analysis, the safety factor value is 1.734. This

shows that the slope before the landfill was stable.

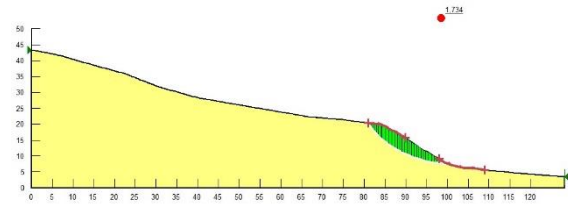


Fig. 6. Slope stability before solid waste landfilling

#### Slope Stability after Solid Waste landfilling

The slope stability after the landfilling is modeled by 3 layers of material, from top to bottom are: domestic waste layer, soil contaminated by leachate, and soil that has not been contaminated. This can happen, because before the garbage is stockpiled a geomembrane is not installed, so that leachate can seep into the ground.

Simulations are carried out in two conditions, namely during the dry season or normal conditions, and in the rainy season or the water level rises. Under normal conditions the thickness of polluted soil is 2 meters (Figure 7). During the rainy season, more leachate is formed, so that the thickness of the polluted zone increases to 3 meters (Figure 8).

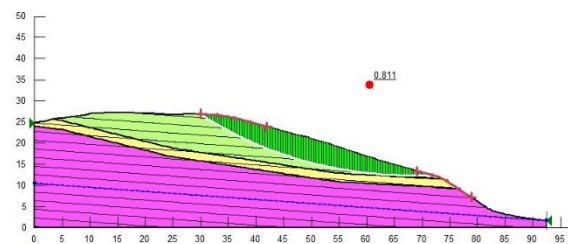


Fig. 7. Stabilitas lereng potongan B1-B2 kondisi normal

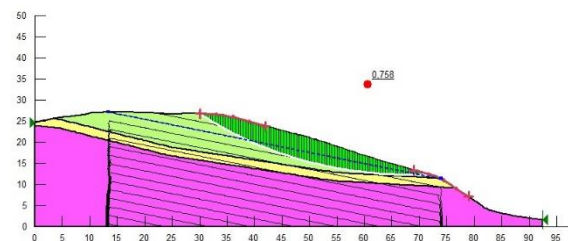


Fig 8. Stabilitas lereng potongan B1-B2 kondisi curah hujan tinggi

Slope stability analysis on profiles B1-B2 shows that the safety value is 0.818 on the normal condition, while it decreases to 0.774 when in the rainy season. The results of the slope stability analysis on other profile paths is shown in Table 4.

Based on the classification of the safety factor values [10], the slope stability of the landfill is in the critical category, because its value is less than 1.25. Based on this analysis, it shows that increasing water due to rain will reduce the value of the safety factor or stability. However, in all conditions, landslides only occur in domestic waste landfill.



Table 4. Value of safety factor that analyzed by LEM

Slope Profiles	Safety Factor		Stability
	Dry Season	Wet Season	
B1-B2	0,811	0,758	Critical
B1-B3	0,914	0,836	Critical
B1-B4	0,671	0,662	Critical

### Slope Stability Analysis by Using *Finite Element Method* (FEM)

Slope stability analysis of solid waste landfill using Finite Element Method (FEM) was conducted to determine the prominent differences from the analysis using the LEM method. Thus, the advantages and disadvantages of both methods for the analysis of domestic waste piles can be identified.

Table 5. Parameter of soil and solid waste for analyzing by FEM

Material	Unit weight (γd)	Cohesion (c)	Internal friction angle (φ)	Poisson Ratio (ν)	Modulus of Elasticity (E)
	kN/m <sup>3</sup>	kN/m <sup>2</sup>	°		MPa
Solid Waste	21,60	20,24	23	0,2	2000
Contaminated Soil	31,18	34,40	18	0,4	3000
Non-contaminated Soil	26,19	22,14	21	0,3	5500

### Slope Stability before Solid Waste Landfilling

Slope stability analysis before landfill is presented in Figures 9 and 10. The safety value of this analysis is 1.721 and is included in the safe category.

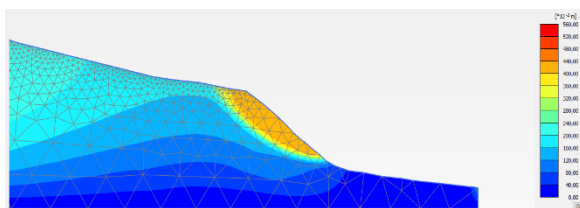


Fig. 10 Model of Slope failure before solid waste landfilling

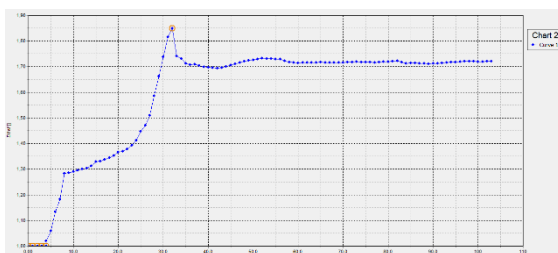


Fig. 11. Curve of safety factor value before solid waste landfilling

### Slope Stability after Solid Waste landfilling

Slope modeling after landfilling of solid waste using the finite element method was carried out under the same conditions as the limit equilibrium method. The slope model and the results of its analysis in the dry season are presented in Figures 12 and 13, while in the rainy season in Figures 14 and 15.

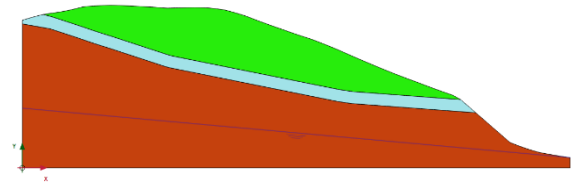


Fig. 12. Slope model on normal condition along B1-B2 profile

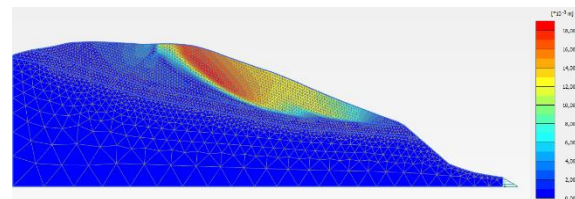


Fig. 13. Slope failure model on normal condition along B1-B2 profile

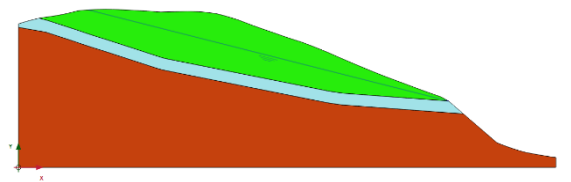


Fig. 14. Slope model on wet condition along B1-B2 profile

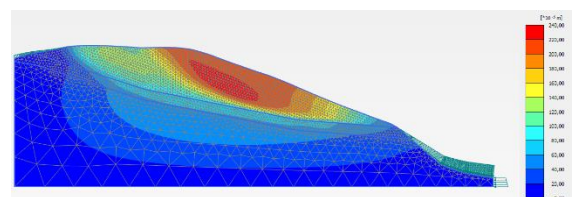


Fig. 15. Slope failure model on normal condition along B1-B2 profile

In Figure 12 and Figure 14 the waste landfill is depicted by a layer of green material, the soil contaminated with leachate is light blue, and the uncontaminated soil is represented by a brown layer. The blue line on the waste pile layer in Figure 14 represents the rise in ground water level during the rainy season. The two figures show that the slip plane

in both the dry and rainy seasons is located above the boundary between the soil and the waste heap. In other words, landslides occur only in domestic waste materials.

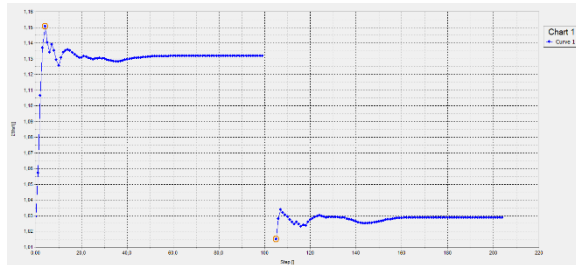


Fig 16. Curve of safety factor value of solid waste landfilling

On the Figure 16 the slope safety factor when under normal conditions is 1.132, while on the wet season decreased to 1.029. This results value of safety factor number, the slope can be categorized as critical. The analysis of safety factors on other slope profiles can be seen in Table 5.

Table 5. The value of safety factor by FEM analysis

Slope Profile	Safety Factor		Stability
	Dry season	Rainy season	
B1-B2	1,132	1,029	Critical
B1-B3	1,126	1,038	Critical
B1-B4	1,093	0,995	Critical

Based on the results of the analysis using FEM, slopes with waste piles in the dry season have a safety rating between 1.093 to 1.132 which is classified as critical. In the rainy season the value of the safety factor is between 0.995 to 1.029.

### Impact of Water on Slope Stability of Solid Waste Landfilling

Slope stability analysis with waste piles that have been carried out using the Limit Equilibrium Method (LEM) and the Finite Element Method (FEM) shows that the value of the safety factor is relatively small and can be classified in a critical condition. The increase in water in the landfill is reflected by a decrease in the value of the safety factor. This is probably caused by a decrease in the internal shear angle, while the cohesion is likely to be relatively constant. The percentage decrease in the stability of the landfill due to the influence of rainwater can be seen in Table 6. and Table 7.

Table 6. Decreasing percentage of slope stability by LEM analysis

Slope Profile	Safety Factor (SF)		Decreasing percentage of SF
	Dry season	Wet season	
B1-B2	0,811	0,758	5,3
B1-B3	0,914	0,836	7,8
B1-B4	0,671	0,662	0,9

Table 7. Decreasing percentage of slope stability by FEM analysis

Slope Profile	Safety Factor (SF)		Decreasing percentage of SF
	Dry season	Rainy season	
B1-B2	1,132	1,029	10,3
B1-B3	1,126	1,038	8,8
B1-B4	1,093	0,995	9,8

From the two tables, it can be concluded that the average decrease in slope safety in the LEM calculation is 5% and in the FEM calculation it is 10%.

### CONCLUSIONS

Based on the results of the analysis of the stability of the slopes of the waste heap at the TPA Tlekung, Batu City, it can be concluded that:

1. The slope before the landfill was classified as stable, as the number of safety factors generated from the analysis with LEM was 1.734 and analysis with FEM was 1.721. The two methods did not show a significant difference
2. When there is a pile of garbage on the slope, the value of the slope stability safety factor decreases. The calculation of the factor of safety with LEM is 0.799 during the dry season, and during the rainy season it decreases to 0.752. Analysis by FEM the average safety score under normal conditions is 1.117 and when conditions are high rainfall it is 1.021.
3. The presence of rainwater can reduce the value of the slope safety factor, so that the slope becomes critical or unstable. The decrease in the value of the safety factor is 5% in calculations with LEM and 10% with FEM.

Based on these conclusions, it can be recommended that to prevent landslides in domestic waste piles, it can be done by preventing water from entering the landfill or draining water as soon as possible to get it out of the landfill.

### ACKNOWLEDGMENTS

Acknowledgments were conveyed by the Head of the Faculty of Engineering, Universitas Brawijaya who provided in research and conference costs.



Thanks, are also conveyed to the Geotechnical Compartment of Civil Engineering Universitas Brawijaya for the input during the discussion.

## REFERENCES

- [1] Shi-Jin Feng, S J., Wu, S J., Fu, W D., Zheng, Q T., and Zhang, X L (2021): *Slope Stability Analysis Of A Landfill Subjected To Leachate Recirculation And Aeration Considering Bio-Hydro Coupled Processes*, Geoenvironmental Disasters, <https://doi.org/10.1186/s40677-021-00201-2>
- [2] Eid, H T., Timothy D. Stark, TD., Evans, W D., and Paul E. Sherry, (2000): *Municipal Solid Waste Slope Failure. I: Waste And Foundation Soil Properties*, Journal Of Geotechnical And Geoenvironmental Engineering, May 2000, p 397-407
- [3] Cheng, Y M and Lau, C K. (2014): *Slope Stability Analysis and Stabilization*, CRC Press
- [4] Huang, Y H (1983). *Stability Analysis of Earth Slopes*, Van Nostrand Reinhold Comp. Inc., NY. 8.
- [5] Rosenfarb, J.L and Chen, W.F. (1972), *Limit Analysis Solutions of Earth Pressure Problems*, Fritz Engineering Lab. Report, Lehigh University, 53 pp 11
- [6] Salhana Ismail, S., Taib, A M., Abd. Rahman, N., Hasbollah, D Z A., Ramli, A B., (2019): *Slope Stability of Landfill with Waste Degradation*, International Journal of Innovative Technology and Exploring Engineering, , Volume-9 Issue-1, p 2278-3075.
- [7] Das, Braja M (2011). *Principles Of Foundation Engineering, Seventh Editon*. Stamford: Cengage Learning.
- [8] Hardiyatmo, H. C., (2012). *Tanah Longsor dan Erosi - Kejadian dan Penanganan*. Yogyakarta: Gadjah Mada University Press.
- [9] Saman, 2018. *Penentuan Nilai Kohesi Dan Sudut Geser Sampah Kota Studi Kasus: Landfill Skala Laboratorium*. Jurnal, Seminar Nasional Teknologi dan Rekayasa (SENTRA), vol. II, halaman 82.
- [10] Bowles, Joseph (translated by Sinaban Pantur), (1999), “*Analisis dan Disain Pondasi*” edisi ke tiga jilid 2. Jakarta: Erlangga.

# **FACTORS INFLUENCING ANAEROBIC DIGESTION PROCESSES OF MARKET WASTE AND COW DUNG AS RAW MATERIAL FOR RENEWABLE ENERGY**

Ellina Sitepu Pandebesie, Susi Agustina Wilujeng and Trifena Karunia Marbun

Department of Environmental Engineering, Faculty of Civil, Environmental and Geo- Engineering,  
Institut Teknologi Sepuluh Nopember (ITS)

## **ABSTRACT:**

Activities in traditional markets produce organic waste that often consists of vegetable and fruit waste. This biomass has the potential to be used as raw material for renewable energy. One of the technologies that can be used is anaerobic digestion to produce biogas. Because market waste is organic material with high lignocellulose content, it is necessary to investigate what factors influence the process of utilizing market waste in the formation of biogas. The research was conducted on a laboratory scale by mixing market waste and cow dung. The study was carried out for 30 days. Parameters tested were lignocellulose content, Volatile Fatty Acid (VFA), Total Solid (TS), Volatile Solid (VS), C, N, and biogas production. The results obtained indicate that market waste has the potential to be used as raw material for biogas production if it is mixed with cow dung. Factors that affect biogas production were lignocellulose content, Volatile Fatty Acid, Total solid and Volatile Solid.

*Keywords: Anaerobic Digestion, Cow Dung, Lignocellulose, Market Waste, Volatile Solid*

## **INTRODUCTION**

Biomass has the potential to be used as a renewable and environmental friendly energy source. An Anaerobic Digestion (AD) technology can convert biomass into energy, by utilizing the activity of microorganisms [1], which will produce biogas. This technology is easy to implement and sustainable and can use a variety of wastes such as agricultural and livestock waste, household organic waste, and food as raw materials [2]. To obtain optimum results, anaerobic digestion operations must meet several requirements, among others the characteristics of raw material, Total Solid and Volatile Solid, the rate of VFA formation, and C/N ratio must be accordant with the growth conditions of microorganisms.

The characteristics of raw materials are determined by how easy they are to decompose by microorganisms. In particular, high-fiber raw materials such as vegetable residues and leaves are hard to degrade by their lignin content. According to [3], the higher the lignin content of organic material, the more difficult it is to decompose. The C/N ratio of the substrate should be around 20-30 [4]. If the C/N ratio is very high ( $>30$ ), it will inhibit the growth of bacteria, so that the biogas production rate is low. Meanwhile, if the C/N ratio is too low, it causes the accumulation of nitrogen which is toxic to microorganisms [1].

According to the Ministry of Environment and Forestry Indonesia, the composition of waste in Indonesia in 2020, consisting of 66,5% easily

biodegradable waste and 33,5% difficult to decompose. Meanwhile, based on the source, households contributed 38,3% of waste generation and the traditional market as much as 17,2%. Household and market activities generate waste that contains a lot of vegetable and food residue. The large volume of waste from households and markets can be used as raw material for renewable energy. This utilization will reduce the cost of waste management, especially the cost of transporting and processing waste. Market waste contains high lignocellulose and a C/N ratio of around 32,82 [5]. To process market waste containing high C content, it is necessary to mix it with materials containing high N, to obtain the optimum C/N ratio for anaerobic processes. One of the wastes that have not been treated properly in Surabaya is cow dung, where the production of cow dung reaches 5,26 tons/day and the C/N ratio is 16,6 [6]. In this research, market waste and cow dung will be mixed with a certain ratio to obtain the optimum C/N ratio in the anaerobic digestion process. The purpose of this research is to determine the potential of market waste as raw material for biogas production and the factors that influence the formation of biogas in the anaerobic digester process.

## **RESEARCH MATERIALS AND METHOD**

### **Materials**

The materials used are market waste from Pasar Keputih Surabaya and cow dung taken from the

Surabaya Slaughterhouse.

### Experimental Conditions

In this study, market waste was mixed with cow dung. For each experiment, the comparison of market waste and cow dung is R1 (0:100); R2 (30:70); R3 (50:50) and R4 (100:0). After mixing the composition, the acclimatization process was carried out in a 60 L drum before being divided into a 19 L reactor. This was done to obtain stable microorganisms that were able to adapt to the waste. To determine the stable condition, gases production volume measurements were carried out until the reactor has produced gases. After the acclimatization process, the substrate was transferred to a 19 L reactor. Each reactor was filled with 18 L of substrate (mixed waste). An intermittent process was carried out, in which a mixture of raw materials is added every 3 days, as much as 1.8 L. Sampling is done before adding the substrate. The intermittent operation consists of stopping the feeding process for some time, which allows a more optimal degradation of the accumulated substrate [7], because the contact time between microorganisms and the substrate is longer. The frequency of stirring was carried out 12 times a day, each for 5 minutes. The research was carried out for 30 days. The measured parameters are temperature, pH, volume of biogas, water content, lignin, cellulose, hemicellulose TS, VS, C, N, Alkalinity, and VFA. The parameter analysis method can be seen in Table 1.

Table 1 Parameters Analysis Method

Parameter	Sampling Time	Analysis Method
pH	Every 3 days	pH meter
Temperature	Every day	Thermometer
Biogas Volume	Every day	Volume Gas Gauge
Volatile Solid, Total Solid	Every 3 days	Gravimetres
Lignin, Cellulose, Hemicellulose	Every 3 days	Chesson-Datta
C-organic	Every 6 days	Walkey and Black
N-organic	Every 6 days	Kjeldahl
Alkalinity	Every 6 days	Titration
Volatile Fatty Acid	Every 6 days	Distillation

## RESULTS AND DISCUSSIONS

### Operation Conditions

#### Temperature

Temperature has an important role in the formation of biogas, where the higher the temperature, the better the methane gas yield. According to [3], temperatures between 25-35 °C are generally more optimum to support the rate of biological reactions. The temperature in each reactor is included in the mesophilic temperature range (25-35 °C). Based on observations, all reactors have the same pattern of temperature changes. On the 12th day, the temperature of the entire reactor rose to a temperature range of 30-32 °C. Then on the 16th day, the temperature of each reactor dropped to the range of 27-28 °C. On the 18th day, the temperature in all reactors increased to the range of 29-31,5 °C. After that, the temperature in the reactor was relatively stable, with a range of 28-31 °C. The temperature increase indicated micro-organisms growth rapidly and a process of decomposition of organic matter occurred by microorganisms [8].

#### pH

Based on Fig.2, only reactor with a composition of 100% cow feces (R2) was at the optimum pH (around 7) for the methanogenesis stage. While the other reactors pH below 6,5 are at the optimum pH for acidification. Therefore, methanogenic bacteria cannot optimally convert organic matter into methane. It is recommended that a buffer is needed to increase the pH to neutral so that the degradation process can run well. Intermittent treatment causes the pH value in each reactor to fluctuate. Because of the raw materials that are entered every three days with slightly different pH values. This can also be caused by the pH of market waste which tends to be acidic.

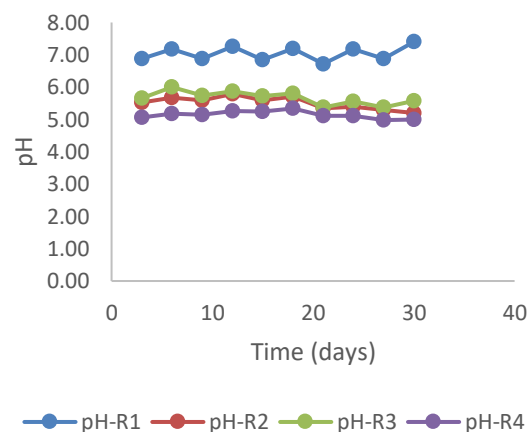


Fig 2. pH Conditions

### Alkalinity

Alkalinity is considered very important as it is related to the reactions that occur in AD. It indicates the ability of AD to neutralize the increase in acid, especially at the acetogenesis stage [9]. If the alkalinity increases, the population of methanogenic bacteria will also increase, while when the alkalinity concentration decreases, acidity will make volatile acid production faster than the ability of methanogenic bacteria to convert volatile acids into methane [10]. On the 12th day, the alkalinity value in almost all reactors increased or was the largest. It proves that at that time the ability of methanogens to convert volatile acids into methane was excellent. Simultaneously, the acidification process begins to occur, namely the process of formation of volatile acids by acidifying bacteria. Thus, the digester tries neutralizing the increase in acid that occurs. However, on the 18th to 30th days, the alkalinity of the entire reactor decreased. It proves that the production of volatile acids is faster than the ability of methane to convert volatile acids into methane. So the ability of AD to neutralize acid also decreases. However, reactor R1 on the 24th day started to increase again, until the alkalinity value decreased again on the 30th day. This could be due to the absence of the acid formation process.

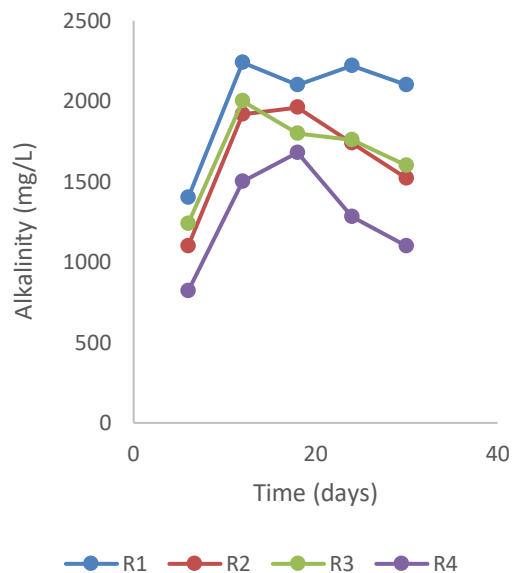


Fig. 3 Alkalinity

### C/N Ratio

It indicates the ability of AD to neutralize the increase in acid, especially at the acetogenesis. In the formation of biogas, the C/N ratio is a critical factor, because it determines the life and activity of microorganisms. Initial C/N ratio of each reactor

(R1, R2, R3 and R4) were 38,9; 33,05; 29,41 and 32,39 respectively. This value has met the optimum criteria for the anaerobic digestion process as can be seen in Fig. 4. The C/N ratio decreased in all reactors after 30 days of fermentation. This is caused by the element carbon and other organic materials have been decomposed by microorganism.

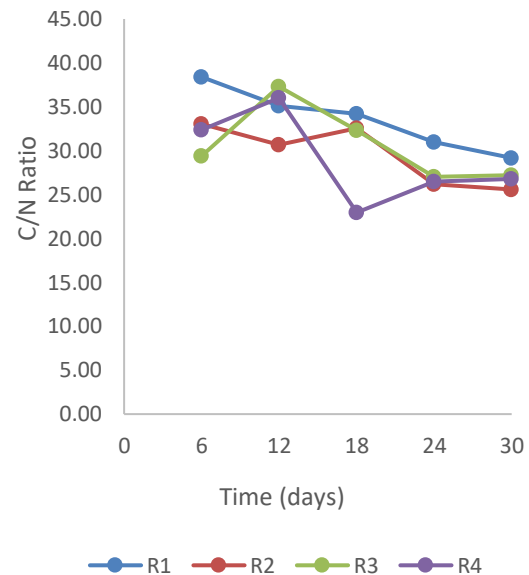


Fig. 4 C/N Ratio During Experiments

### Lignin, Hemicellulose and Cellulose Content influencing biogas produced

Based on Table 2, it concludes that lignin content fluctuated but decreased. This is because the polymer content in lignin has been converted into simpler components (monomers). This makes the degradation process easier. Lignin content on 6th days, R1 (2,94%) have the highest average lignin content compared to other reactors and has the highest overall lignin content degradation value (63,08%). The R4 reactor has the smallest average lignin content (2,55%). Hemicellulose content tends to rise, somehow may be due to the lack of enzymes needed for hemicellulose to be fully hydrolyzed into monomers. Reactor R4 with 100% Market Waste has the highest average hemicellulose content of 15,2% at the end of the process. The cellulose content showed an increase until the 30th day. The reactor with 100% Market Waste (R4) has the highest average cellulose content, where the initial content 23,51% increased to 25,88% at the end of the process.

Tabel 2 Lignin, Hemicellulose and Cellulose Content

Time (days)	Lignin (mg/L)				Hemicellulose (mg/L)				Cellulose (mg/L)			
	L-R1	L-R2	L-R3	L-R4	H-R1	H-R2	H-R3	H-R4	C-R1	C-R2	C-R3	C-R4
6	2,90	2,86	2,64	2,55	13,08	13,24	13,38	13,62	22,18	22,34	23,86	23,51
12	2,01	1,98	1,92	1,85	13,31	14,05	14,20	14,40	23,05	24,61	23,76	23,88
18	1,34	1,22	1,11	1,01	14,05	14,21	14,65	14,58	23,90	24,09	24,39	24,82
24	1,89	1,68	1,59	1,32	13,58	14,11	14,23	14,36	23,18	24,05	24,21	24,48
30	0,96	0,95	0,90	0,72	14,81	15,01	15,14	15,20	25,05	25,24	25,51	25,88

Note: L= lignin; H= hemicellulose; C= cellulose

The process of breaking down lignocellulose into lignin, hemicellulose, and cellulose biologically required the right types of microorganisms and takes a long time. Lignocellulose carries the structure of the plant biomass and is difficult substrate to degrade. Therefore, thermo-chemical and enzymatic pretreatments are necessary for lignocellulose degradation to make the monomers available for further processing [11]. After the hemicellulose and cellulose are formed, then a hydrolysis process occurs to form fructose and glucose. The next step is the process of asedogenesis, then the methane-forming microorganisms are active in forming biogas. With the addition of raw materials and sampling every three days, it seems that it is not enough time for microorganisms to move from the breakdown of lignocellulosic to biogas. The explanation above concludes that raw materials containing high lignocellulose are more difficult to

be metabolized by microorganisms to produce biogas.

#### Total Solid and Volatile Solid Influencing Biogas Produced

Total Solid (TS) and Volatile Solid (VS) are very influential on biogas production. The higher the TS and VS values, the higher the biogas formation that occurs [12]. decrease in TS and VS values indicates how much organic matter is converted into biogas. The role of the TS value on the work of AD is to determine the optimum gas production conditions. Research conducted by [13], showed that total methane production decreased with increasing TS value. Systems with high solid content are able to make the rate of methane production high [14]. Total solid and volatile solid content shown in Table 3.

Table 3. Total Solid and Volatile Solid Content

Time (days)	Volatile Solid (mg/L)				Total Solid (mg/L)			
	VS-R1	VS-R2	VS-R3	VS-R4	TS-R1	TS-R2	TS-R3	TS-R4
6	12.070	8.550	7.910	8.080	73.210	30.100	31.110	19.290
12	10.060	6.850	6.440	6.120	58.630	23.170	27.590	14.890
18	10.210	8.130	5.550	6.020	53.380	32.740	22.870	14.690
24	9.630	4.850	6.310	4.410	53.270	18.410	28.150	12.260
30	9.140	5.290	6.840	3.790	53.720	24.280	35.640	12.360

Note: VS=Volatile solid; TS = Total solid

Table 3 shows the total solid and volatile solid content of R1 is much higher than the other reactors. Raw materials with high solid content are able to increase the rate of methane production [14], because they generally have a high volatile solid content. This is shown by reactor R1 which can produce much higher biogas than other reactors. However, in the anaerobic digestion process, the optimum solid content is 22% in high rate digestion [3]. Total methane production decreases with increasing TS value which exceeds the optimum value [13]. In this study, the total solid cow dung was 19% while the market waste was 22%. At this solid content, the biogas formation process should be able to proceed well, but the measured biogas volume is not in accordance with the organic matter content in the reactor. This can occur due to leakage of gas pipes or other inhibiting factors, such as the fast VFA production rate, so that the rate of conversion of methane is hampered. It could also be because the raw material contains high lignocellulose, which takes longer in the decomposition process.

#### The effect of pH and VFA formation on biogas production

At the initial of the fermentation process, the addition of a large amount of material will cause a significant change in the digester environment and a temporary inhibition of microbial activity [15]. It is because hydrolysis/acidification microbes can produce many volatile fatty acids (VFA) due to excess substrate in a short time. The decreased pH value can also be caused by the formation of organic acids that accumulate due to the reaction of high organic content [16]. As a consequence, the pH will drop, and the methane-forming microbes are unable to convert much of the methane to acid [17]. The optimum pH value at the hydrolysis and acidification stages is 5,5-6,5 [18]. According to [19], the optimum pH value for the methanogenesis stage is 6,5-8,2. The best pH value for the digester process is 7,0, if the pH is below 6,5 the activity of methanogenic bacteria will decrease. Based on observations, only reactors with a composition of 100% cow feces were at the optimum pH (around 7) for the methanogenesis stage. From Fig. 5 it can be seen that pH and VFA formation affect gas production. The pH of R2, R3, and R4 did not meet the growth conditions of methanogenic microorganisms, so that biogas was not formed optimally. Mixing cow dung co-substrate can increase the pH of market waste so that microorganisms can still work even though they are not optimal.

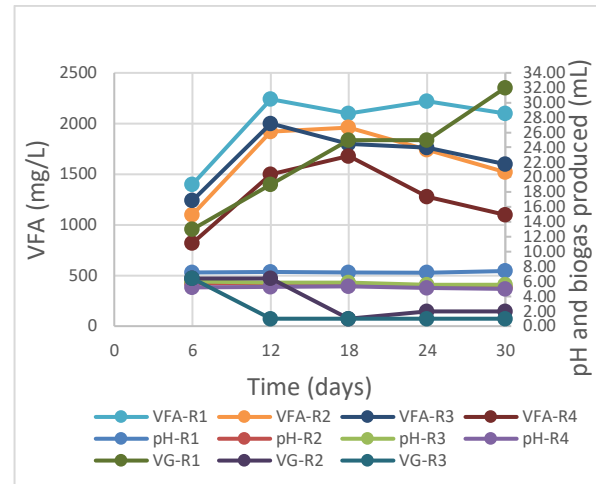


Fig. 5 pH and VFA influencing biogas production

#### CONCLUSION

The factors that influence the formation of biogas in the anaerobic digestion process in this study are the characteristics of the raw material (lignocellulose content), pH, Volatile Fatty Acid, Total Solid, and Volatile Solid. This research shows that market waste has the potential as raw material for biogas production, which can be done by adding co-substrates such as cow dung.

#### ACKNOWLEDGMENTS

This research was funded by the Directorate General of Higher Education of the Indonesian Ministry of Education and Culture and partly by the Institut Teknologi Sepuluh Nopember.

#### CONFLICT OF INTEREST

I declare that this publication has no conflict with any party and is the result of research by the author team.

#### REFERENCES

- [1] Zareei, S. and Khodaei, J. 2017. Modeling and Optimization of Biogas Production from Cow Manure and Maize Straw Using an Adaptive Neuro-Fuzzy Inference System. *Renewable Energy*. 114 (1) 423-427.
- [2] Cavinato, C., Ros, C. D., Pavan, P. and Bolzonella, D. 2016. Influence Of Temperature and Hydraulic Retention on The Production of Volatile Fatty Acids during Anaerobic Fermentation of Cow Manure and Maize Silage. *Bioresour Technol*. 223 (1): 59–64.
- [3] Tchobanoglous, G., Theisen, H. and Vigil, S.



1993. Integrated Solid Waste Management. Mc Graw Hill, Singapore.
- [4] Reisberg K., Sun L., Leven L., Horn S.J., and Schnurer A. 2013. Biogas Production from Wheat Straw And Manure –Impact of Pretreatment and Process Operating Parameters. *Bioresource Technology*. 149: 232-237.
- [5] Abdullah, N.O. and Pandebesie, E.S. 2018. The Influences of Stirring and Cow Manure Added on Biogas Production from Vegetable Waste Using Anaerobic Digester. *IOP Conf. Series: Earth and Environmental Science*. 135: 012005.
- [6] Trihadiningrum, Y., Ratnawati, R., Wulandari, R.A, Radita, D.R., Juliastuti, S.R. (2015). Comparison of Slaughterhouse Solid Waste Treatment Using Anaerobic-Anoxic-Oxic and Aerobic Composting Methods. The 5th Environmental Technology and Management Conference “Green Technology towards Sustainable Environment”. ISBN: 978-979-98278-5-2.
- [7] Nadais, H., Barbosa, M., Capela, I., Arroja, L., Ramos, C.G., Grilo, A., Sousa, S.A. and Leitao, J. H. 2011. Enhancing Wastewater Degradation and Biogas Production by Intermittent Operation of UASB Reactors. *Energy*. 2164-2168
- [8] Wellinger, J., Arthur, M. And Baxter, D. 2014. *The Biogas Handbook: Science, Production and Applications*. Woodhead Publishing, Cambridge.
- [9] Zhiying, Y. 2015. The Effects of Initial Substrate Concentration, C/N Ratio, and Temperature. *Bioresource Technology*. 17(1): 266-273.
- [10] Dong, X., Shao, L., Wang, Y., Kou, W., Cao, Y., Zhang D. 2015. Biogas By Two-Stage Microbial Anaerobic and Semi-Continuous Digestion of Chinese Cabbage Waste, *Chinese Journal of Chemical Engineering*. 23(5): 847-852.
- [11] Rozenfelde, L., Mâris, P., Irçna, K., Ieva, P., Nataïja, M., Nikolajs, V., and Alexander R. 2017. Enzymatic Hydrolysis Of Lignocellulose For Bioethanol Production. *Proceedings Of The Latvian Academy Of Sciences. Section B*, Vol.71, No. 4 (709): 275–279.
- [12] Zarkadas, I. S., Sofikiti, A. S., Voudrias, E. A., and Pilidis, G. A. 2015. Thermophilic Anaerobic Digestion of Pasteurised Food Wastes and Dairy Cattle Manure in Batch and Large Volume Laboratory Digesters: Focussing on Mixing Ratios. *Renewable Energy*. 24(2): 432-440.
- [13] Abbassi-Guendouz, A., Brockmann, D., Trably, E., Dumas, C. And Delgene`s, J.P. 2012. Total Solids Content Drives High Solid Anaerobic Digestion Via Mass Transfer Limitation. *Bioresource Technology*. 111: 55–61.
- [14] Duan, N., Dong, B., Wu, B. and Dai, X. 2012. High-Solid Anaerobic Digestion Of Sewage Sludge Under Mesophilic Conditions: Feasibility Study. *Bioresource Technology*. 104: 150–156.
- [15] Golueke, C. G., Oswald, W. J. and Gotaas, H. B. 1957. Anaerobic Digestion of Algae. *Applied Microbiology*. 5(1): 47–55.
- [16] Yang, L., Huang, Y., Zhao, M., Miao, H. and Ruan, W. 2015. Enhancing Biogas Generation Performance from Food Wastes by High-Solids Thermophilic Anaerobic Digestion: Effect of pH Adjustment. *International Biodeterioration and Biodegradation*. 26(1): 153-159.
- [17] Kwietniewska, E. and Tys, J. 2014. Process Characteristics, Inhibition Factors, and Methane Yields of Anaerobic Digestion Process, with Particular Focus on Microalgae Biomass Fermentation. *Renewable and Sustainable Energy Reviews*. 46(1): 491-500.
- [18] Kothari, R., Pandey, K., Kumar, S., and Tyagi, V. 2014. Different Aspects of Dry Anaerobic Digestion for Bio-Energy. *Renewable and Sustainable Energy Reviews*. 24(1): 174-195.
- [19] Lee, D. H., Behera, S. K., Kim, J. W., and Park, H. 2009. Methane Production Potential of Leachate Generated from Korean Food Waste Recycling Facilities: A Lab-Scale Study. *Waste Management*. 82(1): 876-882.

## TiO<sub>2</sub> PHOTOCATALYST SUPPORTED ON FLY ASH PARTICLES USED IN WASTEWATER TREATMENT LOADED WITH FOOD DYES

M. Visa<sup>1</sup>, I. Visa<sup>1</sup>

<sup>1</sup>Faculty of Product and Environmental Design, Transilvania University of Brasov, Romania

### ABSTRACT

The paper reports on a novel TiO<sub>2</sub>-fly ash (TiO<sub>2</sub>-FA) composite obtained through mild hydrothermal synthesis, as a possible adsorption and VIS-activated photocatalysis substrate able to simultaneously remove pollutants in advanced wastewater treatment processes. Combining FA with TiO<sub>2</sub> has the following advantages: (1) the TiO<sub>2</sub> crystallites grow on the alkaline activated FA forming a stable composite where photocatalytic VIS-active tandem systems can result by associating titania with semiconductor oxides from FA (2) the organic pollutant molecules migrate to the surface of TiO<sub>2</sub> and can be photo catalytically degraded and (3) activated fly ash substrates can adsorb inorganic (heavy metal) pollutants and organics, thus supporting photocatalysis and the *in situ* regeneration of the FA matrix.

The composites' surface properties were evaluated SEM, AFM and BET surface characterisation and PZC measurements, the phase composition and crystallinity by XRD and the optical band gap was estimated based UV-VIS spectroscopy. The adsorption and the UV - photocatalytic properties of the composites were evaluated in two – pollutants systems containing food dyes (Carmine 50% P-WSE-120 and FD&C Blue). Kinetic data allow the investigation of the simultaneous removal of both dyes in a stepwise mechanism. The kinetic studies were carried out at the optimum conditions and it was observed that the data were fitting pseudo-second order model. The adsorption efficiency of Brilliant Blue (BB) is over 73.67% and of Carmine (RC) dye is 82.07%.

*Keywords: Food dyes, photocatalytic, adsorption, wastewater*

### INTRODUCTION

It is believed that the addition of dyes to food took place in Egyptian cities as early as 1500 BC, when candy makers added natural extracts to give the appearance of the products and continued to the present day [1].

With the onset of the industrial revolution, people became dependent on foods including ketchup, mustard, jellies, candies and wine beautifully colored. Inorganic compounds were used to restore the color of the food. The red lead (Pb<sub>3</sub>O<sub>4</sub>) was routinely used to color cheese and confectionery, copper arsenite (CuHAsO<sub>3</sub>) was used to recolor used tea leaves for resale [2]. It also caused two deaths when used to color a dessert in 1860. The first food laws created in Augsburg, Germany, in 1531, concerned colorants and required saffron counterfeiters to be burned. In 1856, mauveine, the first synthetic color, was developed by Sir William Henry Perkin and by the turn of the century, unmonitored color additives had spread through Europe and the United States in all sorts of popular foods. Food coloring is used in commercial food production and domestic cooking, cosmetics, pharmaceuticals, home craft projects, and medical devices [3].

Synthetic dyes are often less costly and technically superior to natural dyes, but many synthesized dyes have been banned because of their adverse effects

(cancer, high blood pressure, hepatitis) on people and animals [4]. In 1962, the first EU directive (62/2645 /EEC) approved 36 dyes, of which 20 were naturally derived and 16 were synthetic. Each member state could designate where certain colors could and could not be used. Every year 7\*10<sup>5</sup> tones and over 10,000 different types of dyes and pigments are produced in the World [5] and are presented in the effluents of the food, textile, leather and dye industries.

Many processes have been applied to remove the harmful pollutants, including adsorption [6], [7], biosorption [8], electrochemical coagulation, electro flocculation and ozonation [9], photodegradation [10], photo-Fenton [11] or simultaneous methods [12]. The adsorption method is intensely used for removing soluble and insoluble pollutants from wastewater without the generation of hazardous by-products being inexpensive. Modified fly ash is a good adsorbent materials. Fly ash is one of the most known waste and it is used as raw material in many industries such as cement industry, but its negative effect on the environment cannot be completely neutralized by doing this, so reusing it as an adsorbent in the removal of different types of pollutants from wastewater solves two problems: water quality and waste management.

The aim of this work is to obtain a new composite starting from fly ash (FA) and a semiconductor photocatalysts(e.g.TiO<sub>2</sub>) which could thus represent

an efficient and environmentally friendly solution for to remove two food dyes: Carmine ( $C_{22}H_{20}O_{16}$ ), red color in water, notated (RC) and Brilliant Blue ( $C_{37}H_{34}N_2Na_2O_9S_3$ ) notated (BB). The chromophore groups are of anthraquinone type in Carmine and of methane triaryl group type in Brilliant Blue, both resistant to biodegradation.

## 2. EXPERIMENTAL

### 2.1. Materials and the Substrate's Preparation

Fly ash collected from CET power plant in Brasov, Romania is type F, according to the ASTM standard C-618-2a [13]. The total percentage of major oxides ( $SiO_2$ ,  $Al_2O_3$  and  $Fe_2O_3$ ) exceeds 70% and this type of fly ash FA will not aggregate during long contact with water, being suitable as substrate in adsorption of organic and inorganic pollutants [14]. The FA was washed in ultrapure water by stirring at room temperature (20–22°C) till constant pH=10.2 and conductivity values =1710  $\mu S$ .

The washed fly ash powder was further modified by 24 h contact with NaOH 2N (1g : 10mL) to activate the surface, as previously described [12]. The 40  $\mu m$  fractions were selected after sieving, and used to obtain a novel composite by mixing with the  $TiO_2$  photocatalyst (Degussa P25, 80% anatase, and 20% rutile). The new adsorbent (FLY-D) was obtained in an autoclave from the slurry of the powder mixture (mass ratio fly ash:  $TiO_2$ = 3:1) and NaOH 2N, under stirring (300 rpm) for 24 h, at 5 atm pressure and 150°C. After filtration, washing and drying at 105°C till constant mass, the dried FLY-D substrate was obtained and further used in photocatalytic and adsorption experiments.

### 2.2. Adsorption and Photocatalytic Experiments

#### 2.2.1 Adsorption process on FLY-D substrate

The pollutant systems were prepared using bidistilled water. Experiments were done on systems containing a dyes mix of RC 20 mg/L+ BB 20 mg/L. Two types of processes were investigated:

- Adsorption (A) on composite substrate (FLY-D under visible light, at room temperature (22°C), by mixing 0.5 g substrate with 50 mL solution under mechanical stirring;
- Photodegradation (F) investigations were done on FLY-D suspensions with the same composition as in the adsorption studies, with and without hydrogen peroxide (30%) addition, under UV irradiation.

The homemade photocatalytic reactor is equipped with three F18W/T8 black tubes (Philips), emitting UV-A light in the region of 340–400 nm and  $\lambda$  max emission =365 nm. During the kinetic studies, aliquots were taken at fixed moments (up to 180 min) when stirring was briefly interrupted and, after

filtration on 0.45mm filter, the supernatant was analysed. The dyes concentration before and after removal was evaluated based on absorbance spectra (PerkinElmer UV–VIS spectrophotometer, Lambda-950). In dye mixtures, the overlap with and a displacement of the peaks of a single dye is observed, and the concentrations were calculated after calibration, based on the first-order derivative of the absorption spectrum of each dye in the mixture, as previously described [15] at the maximum absorption of BB ( $\lambda$  BB = 630 nm) and RC ( $\lambda$  RC = 495nm). The adsorption and photodegradation efficiency of the dyes was evaluated using Eq. (1), where  $c_0$  is the initial concentration and  $c_t$  the pollutants concentration at moment t.

$$\eta = (c_0 - c_t) * 100 / c_0 [\%] \quad (1)$$

The results of pollutants, RC and BB dyes removal from solutions on substrate are presented in Fig1.

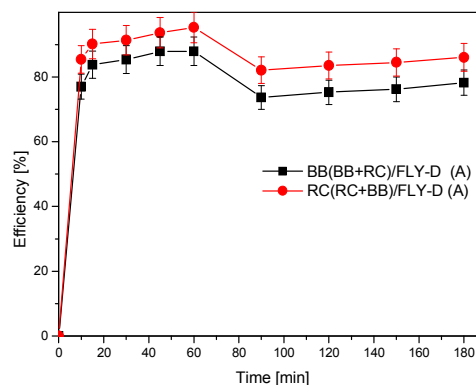


Fig.1. Adsorption efficiency vs. time for system RC +BB dyes

The optimal adsorption time can be estimated as 90min. when the adsorption equilibrium starts to settle for system. The adsorption efficiency of RC molecules (82.07%) and of BB molecules (73.67%) is very close and the adsorption/desorption increases in the same way, see Fig.1.

The lower bonding possibilities of RC prove that the adsorption on FLY-D runs on active sites of aluminosilicate and that the contribution of  $TiO_2$  in its adsorption is less important. Additionally, at the working alkaline pH (9.62) electrostatic interactions are less likely as the substrate is negatively charged and the anionic dyes cannot involve the  $-SO_3^-$  groups. During adsorption process the amount of active sites and their surface distribution is very important.

#### 2.2.2. Photocatalytic process on FLY-D substrate

The active species generated by photo-irradiation will attack the pollutant, if this is in the very close

vicinity of the substrate. Thus, adsorbed pollutant molecules will support an efficient photo-degradation process [16]. The most active photocatalytic component of the composite is  $\text{TiO}_2$  polymorphs have band gaps of 3.0 eV (rutile), 3.2 eV (anatase), thus are active under UV radiation with wavelengths lower than 413 nm for rutile and, respectively 387 nm for anatase. As the UV wavelength used in our experiments was 365 nm, we may conclude that only anatase and rutile are actually activated under irradiation and can exhibit the well-known coupling effect [17]. Once formed the electron-hole pair, the common mechanisms involves the holes for hydroxyl radical production. In alkaline media several other reactions are possible [18] [19], involving the  $\text{O}_2/\text{HO}^\cdot$ ,  $\text{O}_2/\text{HOO}^\cdot$  and the  $\text{O}_2/\text{H}_2\text{O}_2$  couples. The undesired process is the electron-hole recombination, and the photocatalytic efficiency strongly depends on the system's ability to limit this process.  $\text{H}_2\text{O}_2$  addition is expected to support electron trapping.

The results of pollutants, RC and BB dyes removal from solutions by photo-degradation are presented in Figs.2 and 3.

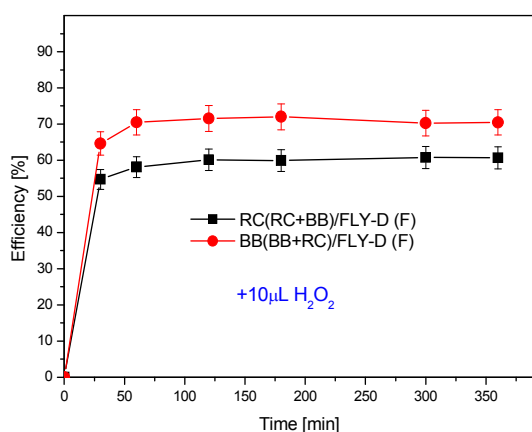


Fig.2. Photodegradation efficiency of RC and BB from dyes mixtures with 10  $\mu\text{L}$   $\text{H}_2\text{O}_2$  addition

In the working conditions, the  $\text{HO}^\cdot$  production from the direct hemolytic break of the  $\text{HO}-\text{OH}$  bond is unlikely, as higher energy is needed ( $\lambda < 254 \text{ nm}$ ). The substrate material can also interact with the electrons, contributing to the electron trapping mechanism. Once produced, the  $\text{HO}^\cdot$  radicals will attack the organic dye and several mechanisms are possible, [20]:

1. Hydrogen abstraction:  $\text{RH} + \text{HO}^\cdot \rightarrow \text{R}^\cdot + \text{H}_2\text{O}$
2. Redox reactions:  $\text{RH} + \text{HO}^\cdot \rightarrow \text{RH}^+ + \text{HO}^\cdot$
3. Addition to the  $\pi$ -bonds in the pollutant molecule

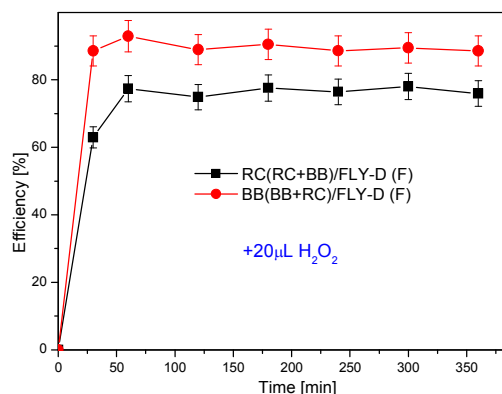


Fig.3. Photodegradation efficiency of RC and BB from dyes mixtures with 20  $\mu\text{L}$   $\text{H}_2\text{O}_2$  addition

### 3. RESULTS AND DISCUSSIONS

#### 3.1. The structure of the nano-composite material

The X-ray diffraction was used in order to investigate the crystal structures and phase composition of the composites, Fig4.

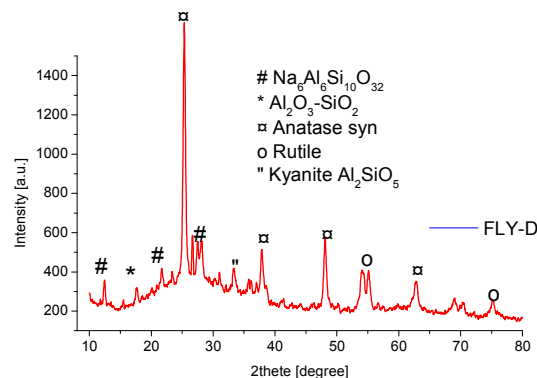


Fig.4. X-ray diffractogram of FLY-D

The XRD spectra, Fig.4, show overall crystalline percentages of 72% in FLY-D composite. As expected, the composite Fly-D contains large amounts of crystalline  $\text{TiO}_2$  polymorphs from Degussa P25 (anatase and rutile). Likewise, the composite shows new crystalline aluminosilicates important in adsorption process of dyes ( $\text{Na}_6\text{Al}_6\text{Si}_{10}\text{O}_{32}$ ,  $\text{Al}_2\text{O}_3-\text{SiO}_2$  and Kyanite ( $\text{AlSiO}_5$ )). The mainly processes are: re-precipitation or polymorph transformations spend in mild hydrothermal conditions:

1. The  $\text{TiO}_2$  crystallites grow on the alkaline activated FA forming a stable composite;
2. Tandem systems by associating titania oxide with semiconductor oxides from fly ash.

Information on the composite morphology/topography, respectively surface characteristics were obtained from the SEM micrographs, Fig.5 and AFM images.

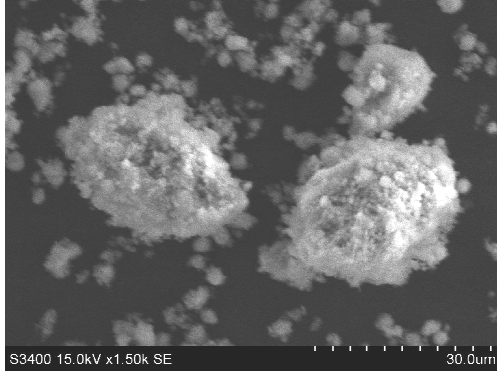


Fig.5. SEM images of the FLY-D composite

The SEM image of FLY-D shows a high degree of homogeneity of the particles. The  $\text{TiO}_2$  particles are embedded on fly ash particles. The elemental EDX analysis of the Fly-D shows a high intensity signal for the titanium atoms.

Table 1. Quantitative results of FLY-D particles

Element Line	Net Counts	Weight %	Atom %
O K	53	44.70	67.20
Na K	14	5.23	5.48
Al K	20	3.92	3.49
Si K	11	2.08	1.78
Ti K	86	42.90	21.54
Fe K	1	1.17	0.50
Total		100.00	100.00

The crystalline modifications are accompanied by a significant increase in the BET surface, from  $6.14\text{m}^2/\text{g}$  in FA to  $69.75\text{m}^2/\text{g}$  for FLY-D.

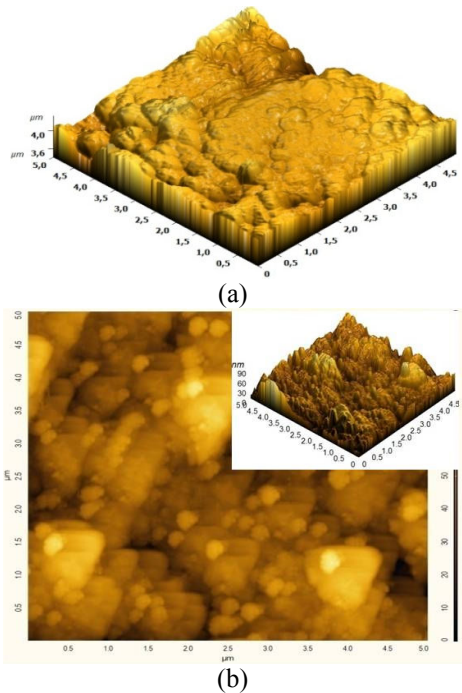


Fig.6. AFM topography of (a) washed FA; (b)FLYD

The re-organizing process is confirmed by the AFM pictures. The surface roughness increases from  $36.22\text{nm}$  to  $45.53\text{nm}$ , and the drop-shaped aggregates, Fig. 6b, are assembled into rough structures.

The surface charge depends on pH. The working pH values over  $\text{pH}_{\text{PZC}}$ , explain well the high adsorption efficiency of cationic dyes (crystal violet, methylene blue, etc.) [21].

When  $\text{pH} > \text{pH}_{\text{PZC}}$  the surface is negatively charged because in aqueous solution can exist the forms  $\text{Ti}^{\text{IV}} - \text{O}^-$  (Eq.2).



When working pH is over 7.97 values and the adsorbent surface is negative the dyes cations and other hydrated species or precipitate are adsorbed. Several PZC points were identified Fig.7 due to the complex composition of the substrate with more oxides,  $\text{SiO}_2$ , and  $\text{TiO}_2$  (anatase and rutile).

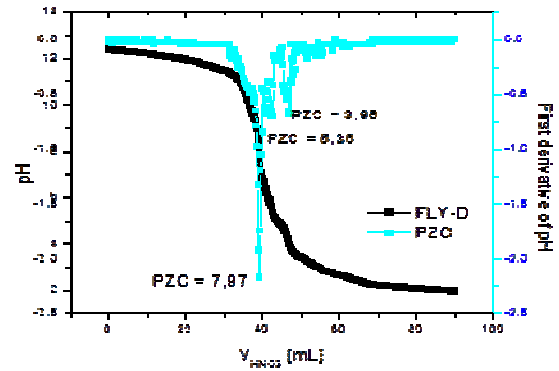


Fig.7. The isoelectric point of Fly-D composite

## 4. ADSORPTION KINETICS MODELING

### 4.1. Adsorption Kinetics Models Analysis

The amount of RC and BB dyes adsorbed at any time,  $q_t$  ( $\text{mg.g}^{-1}$ ), was calculated by Eq. (3):

$$q_t = (c_0 - c_t) \times V_{\text{sol}} / m_s \quad (3)$$

The kinetics models are fitted to experimental data by nonlinear regression analysis. To determine the uptake kinetic mechanisms of pollutants (RC and BB) from systems three kinetic models were investigated: pseudo-first order (Lagergren equation), pseudo-second order and intraparticle diffusion. The pseudo-second order kinetic (Eq.4) is the model which best describes the adsorption of the pollutants on the composite FLY-D.

$$\frac{t}{q_t} = \frac{1}{k_2 q_e^2} + \frac{t}{q_e} \quad (4)$$

Where:



$k_2$ - the equilibrium rate constant for the pseudo-second order adsorption ( $\text{g}\cdot\text{mg}^{-1}\cdot\text{min}^{-1}$ ),  $q_e$ - the adsorption capacity ( $\text{mg}\cdot\text{g}^{-1}$ ). The results are presented in table 2.

Table 2 Kinetic parameters of dyes removal in adsorption process

Pollutant	Pseudo-second order		
	$k_2$ [ $\text{g}\cdot\text{mg}^{-1}\cdot\text{min}^{-1}$ ]	$q_e$ [ $\text{mg}/\text{g}$ ]	$R^2$
RC(RC+BB)A	15.204	12.59	0.897
BB(BB+RC)A	17.492	20.56	0.972

#### 4.2. Photocatalytic Kinetics Models Analysis

For the photocatalysis process, the Langmuir-Hinshelwood mechanism simplified for low concentration as a pseudo first order kinetics was tested, Eq. (5):

$$\ln c/c_0 = -kt \quad (5)$$

The kinetic parameters and the correlation coefficients calculated from the linear form of the kinetic laws are given in Fig.8.

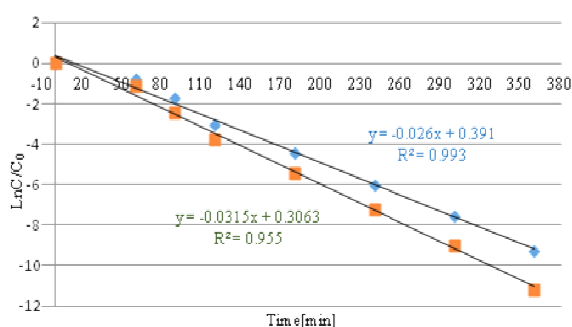


Fig.8. Pseudo-first order kinetics of dyes/FLY-D (Langmuir – Hinshelwood model)

The photo degradation efficiency with 20  $\mu\text{L}$   $\text{H}_2\text{O}_2$  addition is favorable for removal the food dyes (RC and BB).

Parallel kinetic mechanisms may occur, especially inter-particle scattering, due to bulky dyes adsorption in the pores of the substrate. As in previous cases, the adsorption capacity values of organic molecules are characterized by low values of maximum adsorption capacity.

#### 5. CONCLUSIONS

1. A novel nanocomposite with a large specific surface, high roughness, and high crystallinity was developed under mild conditions by hydrothermal process, starting from FA and  $\text{TiO}_2$ -Degussa P25.
2. The  $\text{TiO}_2$ -Degussa P25 imbedded on fly ash surface caused the new composite to be more

effective within the simultaneous processes of adsorption and photodegradation of food dyes.

3. The results show that the adsorption efficiency significantly depends on the surface properties.

4. Therefore, the data indicate that a large volume of food dyes are rapidly absorbed, leading to higher rate constants (15,204 and 17,492  $\text{g}\cdot\text{mg}^{-1}\cdot\text{min}^{-1}$ ).

5. The pseudo-second order kinetic is the model that governs the entire process of removing food dyes from mixed systems.

6. The addition of  $\text{H}_2\text{O}_2$  in the alkaline working conditions increased the efficiency of the pollutant removal process, but on the other hand would increase sustainability and cost issues.

#### Acknowledgements

This paper was supported by a grant of the Romanian National Authority for Scientific Research, CNCS – UEFISCDI, PNII -PT-PCCA-2013-4-0726-phase 2017. The structural funds project PRO-DD (ID 123, SMIS 2637, 11/2009) is acknowledged for providing the infrastructure used in this work.

#### REFERENCES

- [1] Downham A., Collins P., Colouring our foods in the last and next millennium, *Int. J. of Food Sci. and Technol.*, Vol.35, Issue 1, 2000, pp. 5-22.
- [2] Kobylewski S., Jacobson M.F., Toxicology of food dyes, *Int. J. Occup. Environ. Health*, Vol.18, Issue 3, 2012, pp. 220-246.
- [3] Rafii F., Hall J.D., Cerniglia C.E., Mutagenicity of azo dyes used in foods, drugs and cosmetics before and after reduction by *Clostridium* species from the human intestinal tract, *Food Chem Toxicol.*, Vol. 35, Issue 9, 1997, pp. 897–901.
- [4] Bonan S., Fedrizzi G., Menotta S., Caprai E., Simultaneous determination of synthetic dyes in foodstuffs and beverages by high-performance liquid chromatography coupled with diode-array detector, *Dyes and Pigments*, Vol 99, Issue 1, 2013, pp.36-40.
- [5] Kolodynska D., Halas P., Franus M., Hubicki Z., Zeolite properties improvement by chitosan modification Sorption studies, *Ind. Eng. Chem.*, Vol. 52, Issue 10, 2017, pp.187-196.
- [6] Visa M., Duta A., Advanced  $\text{Cd}^{2+}$  removal on dispersed  $\text{TiO}_2$ -fly ash, *Environmental Engineering and Management*, Vol. 7, Issue.4, 2008, pp.373-378.
- [7] Natarajan S., Bajaj H.C., Tayade R.J., Recent advances based on the synergetic effect of adsorption for removal of dyes from waste water using photocatalytic process, *J. Environ. Sci.*, Vol.65, 2018, pp. 201-222.
- [8] Kumar R., Ahmad R., Biosorption of hazardous crystal violet dye from aqueous solution onto treated ginger waste (TGW), *Desalination J.* Vol. 265, Issue 1-3, 2011, pp. 112-118.



- [9] Ciardelli G., Ranieri N., The treatment and reuse of wastewater in the textile industry by means of ozonation and electroflocculation, *Water Resources*, Vol. 35, Issue 2, 2001, pp. 567- 572.
- [10] Matos J., Cuevas S.M., Ruiz-Delgado A., Oller I., Malato S., Development of TiO<sub>2</sub>-C photocatalysts for solar treatment of polluted water, *Carbon J.*, Vol. 122, 2017, pp. 361-373.
- [11] Visa M., Duta A., Methyl-orange and cadmium simultaneous removal using fly ash and photo Fenton systems, *J. of Hazard Mater.*, Vol. 244, Issue 2, 2013, pp. 773-779.
- [12] Visa M., Andronic L., Lucaci D., Duta A., Concurrent dyes adsorption and photo-degradation on fly ash based substrates, *Adsorption Journal*, Vol.17, Issue 1, 2011, pp. 102-108.
- [13] Ramme B. W, Tharaniyil M. P, *Coal Combustion Products Utilization Handbook*, 2<sup>nd</sup> Ed., of America. 2005.
- [14] Duta A., Visa M., Simultaneous removal of two industrial dyes by adsorption and photocatalysis on a fly-ash-TiO<sub>2</sub> composite, *J. of Photochem. Photobiol*, Vol. 306, 2015, pp. 21-30.
- [15] Andronic L., Duta A., Photodegradation processes in two-dyes systems- simultaneous analysis by first-order spectra derivative method, *Chem. Eng. J.*, Vol. 198–199, 2012, pp. 468–475.
- [16] Irawatya W., Soetaredjoa F.E., Ayucitraa A., Understanding the relationship between organic structure and mineralization rate of TiO<sub>2</sub>-mediated photocatalysis, *Procedia Chem.*, Vol.9, 2014, pp. 131–138.
- [17] Jing L., Li S., Song S., Xue L., Fu H., Investigation on the electron transfer between anatase and rutile in nano-sized TiO<sub>2</sub> by means of surface photovoltage technique and its effects on the photocatalytic activity, *Sol. Energy Mater. Sol. Cells*, Vol. 92, Issue 9, 2008, pp. 1030–1036
- [18] Fujishima A., Rao T.N., Tryk D.A., Titanium dioxide photocatalysis, *J. Photochem. Photobiol. C*, Vol. 1, Issue 1, 2000, pp.1–21.
- [19] Forgacs E, Cserháti T, Oros G. Removal of synthetic dyes from wastewaters: a review. *Environment International J.*, Vol. 30, Issue 7, 2004, pp. 953- 971.
- [20] Ökte A.N., Karamanis D., Tuncel D., Dual functionality of TiO<sub>2</sub>–flyash nanocomposites: water vapor adsorption and photocatalysis, *Catal. Today*, Vol. 230, 2014, pp. 205–213.
- [21] Popa N, Visa M. New hydrothermal charcoal TiO<sub>2</sub> composite for sustainable treatment of wastewater with dyes and cadmium cations load.

# A NOVEL ROUGH FUZZY BASED DELPHI METHOD FOR HIGHWAY PROJECTS RISK ANALYSIS: THE SOE ASSIGNMENT SCHEME CASE STUDY

Gilang Ardi Pratama<sup>1,2</sup>, Yusuf Latief<sup>1</sup> and Lukas Beladi Sihombing<sup>3</sup>

<sup>1</sup>Department Of Civil And Environmental Engineering, Universitas Indonesia, Indonesia

<sup>2</sup>Department Of Industrial Engineering, Universitas Pamulang, Indonesia

<sup>3</sup>Department Of Civil Engineering, Universitas Pembangunan Jaya, Indonesia

## ABSTRACT

In accelerating the development of the area in Sumatra, the Indonesia Government assigned to PT. X to manage toll road concessions on 24 Sumatra toll roads. PT X is an enterprise with full ownership by the government. Because Sumatra toll roads Development are economically viable but not financially viable. This scheme was implemented to avoid abuse of authority and legal uncertainty issues from government administration administrators. Then, the Indonesian government was named it "The State-Owned Enterprise (SOE) Assignment Scheme." But this project has several technical problems and non-technical problems. The technical problems are Material, Geotechnical Condition, Equipment, and others. The non-technical problems are policy, financial, and others. Those problems may impact the time and cost of the Sumatran toll road development. This study aims to list the risks and evaluate each factor corresponding to the Sumatran toll roads development based on The Rough-Fuzzy of Delphi method. Questioners have been collected from 6 experts. There are 12 critical risk factors in this study that will impact the project. The proposed method can reduce the level of uncertainty and subjectivity that exists in the process of risk identification and analysis. The results of this study increase our understanding of the importance of the impact of each criterion which can be valuable for future studies on toll road projects with the SOE assignment scheme.

*Keywords: Rough Numbers, Fuzzy, Risk, Delphi, State-Owned Enterprise*

## INTRODUCTION

Based on Presidential Regulation No. 117 of 2015 on Amendments to Presidential Regulation No. 100 of 2014 on the Acceleration of Toll Road Development in Sumatra, TSTR (Trans-Sumatra Toll Road) is one of the National Strategic Projects (NSP). TSTR will connect Lampung Province to Aceh Province through 24 toll roads totaling 2,988 km, consisting of main corridors (backbone) with 2,069 km in length and support corridors with 919 km in length[1].

The construction of the trans-Sumatra toll road is not financially feasible, even though it is economically feasible. Consequently, no business entity is interested, which causes a business entity cannot realize the development of the toll road network. The government can take several actions in accordance with its authority because no Private business entity interested with this project, such as carrying out the construction of toll roads partially or entirely by itself, then delegating the operation and maintenance to a business entity selected through an auction process [1].

In the implementation of this SOE assignment, many problems affect the cost overrun and delay; when the issue limitation on this task was extremely limited, this paper, therefore, aimed to identify, evaluate, and rank the critical factors that affected the Sumatera toll road construction with this assignment scheme using the rough fuzzy Delphi method. This method is a

combination of rough set and fuzzy set numbers for the Delphi method application that is used for decreasing the ambiguous and subjectivity levels done by the experts who participated in the completion of this study.

## MATERIAL & METHODS

### BackGround of Case Study

In order to accelerate regional development in Sumatra, Presidential Regulation No. 100 of 2014 has been amended by Presidential Regulation No. 117 of 2015 concerning Amendments to Presidential Regulation No. 100 of 2015 concerning the Acceleration of Toll Road Development in Sumatra are using SOE assignment scheme [2].

Several studies have investigated issues related to the implementation of toll road projects and their performance. The initial step in risk management is to identify and categorize the risks.

According to Likhitrungsilp [3] risks in development projects are divided into two broad lines: general risks such as policy risks, financing risks, environmental risks, and stakeholder risks, and project-specific risks such as pre-construction, Construction Risk and operating risks

### Rough Number

The assumption from the response giver,  $r_{ij}^k$  can be expressed as lower limit  $\underline{Limit}(r_{ij}^l)$  and upper limit  $\overline{Limit}(r_{ij}^u)$  with the following formulation [4].

$$\underline{Limit}(r_{ij}^l) = \left( \prod_{k=1}^{n_{ijL}} x_{ij} \right)^{\frac{1}{n_{ijL}}} \quad (1)$$

$$\overline{Limit}(r_{ij}^u) = \left( \prod_{k=1}^{n_{ijU}} x_{ij} \right)^{\frac{1}{n_{ijU}}} \quad (2)$$

Thus, it can be expressed by the equation below  
 $RN(r_{ij}^k) = [\underline{Limit}(r_{ij}^k), \overline{Limit}(r_{ij}^k)] \quad (3)$

Therefore:

$$RN(r_{ij}^k) = ([r_{ij}^{1L}, r_{ij}^{1U}], [r_{ij}^{2L}, r_{ij}^{2U}], \dots, [r_{ij}^{ML}, r_{ij}^{MU}]) \quad (4)$$

### Fuzzy Number

Fuzzy set theory is a mathematical theory designed to model the ambiguity or imprecision of human[5]. A triangular fuzzy number is denoted as (l,m,u) whose membership function is  $F_{\tilde{a}}(X)$  as followst:

$$F_{\tilde{a}}(X) = \begin{cases} 0, & x < l \text{ or } x > u \\ \frac{x-l}{m-l}, & l \leq x \leq m \\ \frac{u-x}{u-m}, & m \leq x \leq u \end{cases} \quad (5)$$

### Proposed Rough Fuzzy Delphi Method

In this section a Rough Fuzzy Delphi method is proposed to obtain the objective of this study. Here are the steps:

Step 1. Form a group of n experts to evaluate risk factors. At least 5 experts for evaluation of the recommended criteria with minimum qualification of bachelor degree and 10 years of experience.

Step 2. In this step, the n expert team evaluates the criteria by means of the triangular fuzzy number values specified in the table below.

Table 1. Fuzzy Scales

No	Linguistic Term	Fuzzy Scales
1	Strongly Disagree	0,0,0.25
2	Disagree	0,0.25,0.5
3	Neutral	0.25,0.5,0.75
4	Agree	0.5,0.75,1
5	Strongly Agree	0.75,1,1

Step 3. The rough number formulation of  $RN(l_{ij}^k)$ ,  $RN(u_{ij}^k)$  and  $RN(r_{ij}^k)$  can be expressed with the following equation [4]:

$$RN(l_{ij}^k) = [\underline{Limit}(l_{ij}^k), \overline{Limit}(l_{ij}^k)] \quad (6)$$

$$RN(m_{ij}^k) = [\underline{Limit}(m_{ij}^k), \overline{Limit}(m_{ij}^k)] \quad (7)$$

$$RN(u_{ij}^k) = [\underline{Limit}(u_{ij}^k), \overline{Limit}(u_{ij}^k)] \quad (8)$$

Therefore, the average rough number of  $RN(l_{ij}^k)$ ,  $RN(u_{ij}^k)$  and  $RN(r_{ij}^k)$  can be written as follows [4]:

$$RN(\hat{l}_{ij}) = \left[ \left( \prod_{s=1}^R l_{ij}^{sl} \right)^{\frac{1}{R}}, \left( \prod_{s=1}^R l_{ij}^{su} \right)^{\frac{1}{R}} \right] \quad (9)$$

$$RN(\hat{m}_{ij}) = \left[ \left( \prod_{s=1}^R m_{ij}^{sl} \right)^{\frac{1}{R}}, \left( \prod_{s=1}^R m_{ij}^{su} \right)^{\frac{1}{R}} \right] \quad (10)$$

$$RN(\hat{u}_{ij}) = \left[ \left( \prod_{s=1}^R u_{ij}^{sl} \right)^{\frac{1}{R}}, \left( \prod_{s=1}^R u_{ij}^{su} \right)^{\frac{1}{R}} \right] \quad (11)$$

Thus, the rough triangular fuzzy number can be expressed with the following equation:

$$RN(\hat{z}_{ij}) = [\hat{z}_{ij}^l, \hat{z}_{ij}^u] \quad (11)$$

$$\hat{z}_{ij}^l = [l_{ij}^l, m_{ij}^l, u_{ij}^l], \text{ dan } \hat{z}_{ij}^u = [l_{ij}^u, m_{ij}^u, u_{ij}^u] \quad (12)$$

Step 4. Defuzzification of fuzzy numbers using the Best Non Fuzzy Performance (BNP) method, when  $\hat{z}_{ij}^l$  and  $\hat{z}_{ij}^u$  then defuzzcation can be performed with:

$$BNP(\hat{z}_{ij}^l) = \frac{(u_{ij}^l - l_{ij}^l) - (m_{ij}^l - l_{ij}^l)}{3} + l_{ij}^l \quad (13)$$

$$BNP(\hat{z}_{ij}^u) = \frac{(u_{ij}^u - l_{ij}^u) - (m_{ij}^u - l_{ij}^u)}{3} + l_{ij}^u \quad (14)$$

Step 5. Determining the crisp value of the rough number is done in a way according to normalization [6]:

$$\tilde{z}_i^l = (\tilde{z}_i^l - \min_i z_i^l) / \Delta_{Min}^{Max} \quad (15)$$

$$\tilde{z}_i^u = (\tilde{z}_i^u - \min_i z_i^l) / \Delta_{Min}^{Max} \quad (16)$$

$$\Delta_{Min}^{Max} = \max_i z_i^u - \min_i z_i^l \quad (17)$$

The determination of the total of crisp value with equation:

$$\beta_i = \frac{\tilde{z}_i^l \times (1 - \tilde{z}_i^l) + \tilde{z}_i^u \times \tilde{z}_i^u}{1 - \tilde{z}_i^l + \tilde{z}_i^u} \quad (18)$$

Then calculate with the crisp value for the last value.

$$\tilde{z}_i^{der} = \min_i z_i^l + \beta_i \Delta_{Min}^{Max} \quad (19)$$

Step 6. Determine whether the risk is important in the construction of the trans-Sumatra toll road with reference to the table below.

Table 2. Criteria Scale

No	Reference	Criteria
1	$0 \leq CV < 0.6$	Low
1	$0.6 \leq CV < 0.8$	Mild
1	$0.8 \leq CV < 1$	Critical

Step 7. Rank each risk for each indicator of the risk,

in order to determine the priority risk of each indicator according to expert opinion.

## RESULT AND DISCUSSION

By reviewing the previous studies on a case study on toll roads and an in-depth interview with experienced professionals, 104 risks were collected.

The common risk is divided into Policy, Financing, Environment, and stakeholders. The specific risks of the project are, furthermore, divided into the following categories: design and procurement, construction, and operation.

By distributing the questionnaire, seven experts who filled out the questionnaire had the following criteria.

Table 3. Respondent Criteria

No	Degree	Experience (Year)	Institution
1	Master Degree	17	Public
2	Master Degree	20	Public
3	Master Degree	37	SOE
4	Bachelor Degree	15	SOE
5	Bachelor Degree	11	SOE
6	Master Degree	40	Consultant
7	Doctoral Degree	30	Academic

The result of the Rough Fuzzy Delphi for Risk analysis can be seen in the table below:

Table.4 Result of Risk Analysis

No	Indicator[reference]	$\tilde{Z}_i^l$	$\tilde{Z}_i^u$	Crisp Value	Criteria	Rank
<b>X.1</b>	<b>POLICY FACTOR</b>					
1.1	Contract Terminated By Government [7]	0.54	0.74	0.59	Low	14
1.2	Change In Regulation [7-9]	0.71	0.79	0.75	Mild	3
1.3	Late on Project Permit And Approval [3, 10]	0.62	0.80	0.69	Mild	8
1.4	Asset Ownership [7, 10]	0.53	0.69	0.61	Mild	12
1.5	Lack Of Standard Contract Agreement [9]	0.58	0.74	0.68	Mild	9
1.6	Government Intervention [11]	0.68	0.74	0.70	Mild	5
1.7	Corruption [3, 12]	0.67	0.81	0.73	Mild	4
1.8	Lack Of Regulatory And Supervisory System [3, 12]	0.58	0.74	0.64	Mild	11
1.9	Domestic Political Situation [8, 10]	0.75	0.75	0.75	Mild	2
1.10	Bureaucratic of Tender System [3, 10]	0.45	0.69	0.54	Low	16
1.11	Concession Period [9, 13]	0.52	0.74	0.65	Mild	10
1.12	Lack Of Policy Support For Investors[9]	0.69	0.84	0.76	Mild	1
1.13	Nationalization Of Projects/Assets[8, 9]	0.49	0.69	0.53	Low	17
1.14	Strict Import-Export Permits[14]	0.37	0.63	0.45	Low	18
1.15	Wrong Decision By The Government[12]	0.49	0.67	0.54	Low	15
1.16	SPV Violate Policies[14]	0.68	0.74	0.70	Mild	5
1.17	Conflict On Contract[3, 7]	0.68	0.74	0.70	Mild	5
1.18	Difference Between Specification And Code[8]	0.48	0.72	0.61	Mild	13
<b>X.2</b>	<b>FINANCING FACTOR</b>					
2.1	Land Cost Increase [7, 8]	0.72	0.82	0.77	Mild	9
2.2	Inflation [3, 8, 10]	0.77	0.81	0.78	Mild	5
2.3	Financial Difficulties [7, 10, 13]	0.78	0.84	0.80	Critical	4
2.4	Interest Rate Fluctuation [3, 9]	0.66	0.77	0.71	Mild	12
2.5	Foreign Currency Fluctuation [3, 10]	0.64	0.75	0.68	Mild	14
2.6	Lack Of Investor Interest In Project Finance [15]	0.76	0.78	0.76	Mild	10
2.7	High Cost Of Funding [14]	0.64	0.75	0.68	Mild	14
2.8	Additional Tax Fee[10]	0.56	0.67	0.59	Low	19
2.9	Late Payments On Completed Work [9, 16]	0.84	0.89	0.85	Critical	2
2.10	Construction Cost Estimation Error [16]	0.87	0.90	0.92	Critical	1
2.11	Delay Financial Closure [10]	0.77	0.81	0.78	Mild	5
2.12	Difficulty Getting A Bank Loan [9]	0.77	0.81	0.78	Mild	5
2.13	Rising Material Costs [9]	0.66	0.77	0.71	Mild	12

No	Indicator[reference]	$\bar{z}_i^l$	$\bar{z}_i^u$	Crisp Value	Criteria	Rank
2.14	Financing Delays From The Government [8]	0.80	0.87	0.83	Critical	3
2.15	Government Credit Risk [12]	0.60	0.73	0.64	Mild	17
2.16	Spv Change [12]	0.47	0.66	0.49	Low	22
2.17	Profits That Are Not As Expected [9]	0.77	0.81	0.78	Mild	5
2.18	Devaluation [17]	0.64	0.75	0.68	Mild	16
2.19	Liquidity [17]	0.60	0.69	0.63	Mild	18
2.20	Changes In Discriminatory Tax On Projects [17]	0.55	0.68	0.58	Low	20
2.21	Financial Unclosed [in-depth interview]	0.70	0.76	0.73	Mild	11
2.22	World Economic Crisis [in-depth interview]	0.43	0.71	0.54	Low	21
<b>X.3</b>	<b>ENVIRONMENTAL FACTOR</b>					
3.1	Bad Weather[16]	0.47	0.69	0.58	Low	5
3.2	Natural Disasters[8]	0.68	0.74	0.70	Mild	3
3.3	There Are Important Things[15]	0.66	0.79	0.74	Mild	2
3.4	Unexpected Field Conditions[9]	0.71	0.79	0.75	Mild	1
3.5	Environmental Protection [13]	0.54	0.72	0.64	Mild	4
<b>X.4</b>	<b>STAKEHOLDER FACTOR</b>					
4.1	Political Agenda Related To Project Decision[18]	0.54	0.69	0.58	Low	6
4.2	Lack Of Information Dissemination [18]	0.60	0.69	0.63	Mild	4
4.3	Lack Of Attention From The Government [18]	0.53	0.72	0.56	Low	7
4.4	Lack Of Staff Capacity In Project Implementation [19]	0.71	0.79	0.74	Mild	3
4.5	Lack Of Efficient Conflict Management[18]	0.80	0.87	0.83	Critical	1
4.6	Difficulty In Assessing The Expectations Of Each Stakeholder [19]	0.58	0.70	0.62	Mild	5
4.7	Lack Of Coordination Between The Stakeholders Involved [19]	0.71	0.79	0.75	Mild	2
<b>X.5</b>	<b>PRE-CONSTRUCTRION FACTOR</b>					
5.1	Tender System Risk [10]	0.41	0.66	0.46	Low	16
5.2	Poor Feasibility Study [3, 10]	0.67	0.80	0.73	Mild	6
5.3	Not Good Risk Allocation [3, 9]	0.55	0.75	0.59	Low	14
5.4	Lack Of SPV Ability [3]	0.78	0.84	0.80	Critical	1
5.5	Late Land Acquisition [3, 10, 16]	0.78	0.84	0.80	Critical	1
5.6	Late Compensation Affected By The Project [3, 15]	0.77	0.81	0.78	Mild	4
5.7	Late Clearing And Rehabilitating Workplace [15]	0.44	0.66	0.55	Low	15
5.8	Government Breach Of Contract [3]	0.61	0.79	0.65	Mild	11
5.9	Many Of Land Brokers [8]	0.78	0.84	0.80	Critical	1
5.10	Conflicts On Design And Specifications [10]	0.66	0.79	0.67	Mild	9
5.11	Long Planning Time[14, 16]	0.63	0.76	0.67	Mild	10
5.12	Less Detailed Design [13]	0.55	0.75	0.63	Mild	13
5.13	Lack Of Consulting Experience [13]	0.71	0.79	0.75	Mild	5
5.14	Land Status [8]	0.66	0.77	0.71	Mild	7
5.15	Rejection By Project-Affected Communities [8]	0.54	0.77	0.63	Mild	12
5.16	Delay In Selecting Contractors During Tender Period[14]	0.64	0.75	0.68	Mild	8
<b>X.6</b>	<b>CONSTRUCTION FACTOR</b>					
6.1	Lack Of Contractor's Technical Ability[3, 10]	0.84	0.89	0.85	Critical	1
6.2	Lack Of Supporting Infrastructure[14]	0.76	0.78	0.76	Mild	5
6.3	Limited Amount Of Material [3, 10]	0.70	0.76	0.73	Mild	9
6.4	Limited Number Of Workers [10, 14]	0.70	0.76	0.73	Mild	9
6.5	Many Changes In The Scope Of Work[7, 15]	0.71	0.79	0.75	Mild	7
6.6	Problems Due To Differences Of Opinion In Practice[3]	0.54	0.72	0.64	Mild	15
6.7	Construction Price Escalation [9]	0.77	0.81	0.78	Mild	3
6.8	Material Procurement Delay [8]	0.79	0.84	0.81	Critical	2
6.9	Mismanagement By The Contractor [10]	0.76	0.78	0.76	Mild	5
6.10	Design Error [10]	0.64	0.76	0.68	Mild	13
6.11	Geotechnical Condition [13]	0.72	0.81	0.73	Mild	8

No	Indicator[reference]	$\bar{z}_i^l$	$\bar{z}_i^u$	Crisp Value	Criteria	Rank
6.12	Theft [9]	0.51	0.66	0.55	Low	21
6.13	Subcon Ability[9]	0.72	0.78	0.72	Mild	11
6.14	Construction Delay Risk [9, 13]	0.75	0.86	0.77	Mild	4
6.15	Lack Of equipment Capability [13]	0.57	0.74	0.63	Mild	16
6.16	Lack Of Construction Quality [14]	0.72	0.78	0.72	Mild	11
6.17	Lack Of Procurement Of Tools [8, 13]	0.57	0.74	0.63	Mild	16
6.18	Specification Change [12]	0.55	0.78	0.64	Mild	14
6.19	Lack Of Labor Productivity [9, 13]	0.57	0.74	0.63	Mild	16
6.20	Re-Work [13]	0.57	0.72	0.61	Mild	20
6.21	Contractor Change [in-depth interview]	0.57	0.74	0.63	Mild	16
<b>X.7</b>	<b>OPERATION FACTOR</b>					
7.1	Default Operators [3, 7]	0.57	0.74	0.63	Mild	16
7.2	Excess Operating Costs [7, 8, 15]	0.72	0.81	0.73	Mild	4
7.3	High Maintenance Cost [7]	0.73	0.84	0.75	Mild	3
7.4	Tariff Adjustment [7]	0.59	0.80	0.68	Mild	7
7.5	There Are Infrastructure Defects [3, 12]	0.72	0.81	0.73	Mild	4
7.6	Income Risk [3, 12]	0.76	0.89	0.80	Critical	1
7.7	Demand Risk [3, 10]	0.60	0.72	0.63	Mild	9
7.8	Lack Of Operator Ability[15]	0.48	0.69	0.55	Low	13
7.9	Lack Of Service Quality[12, 15]	0.57	0.72	0.61	Mild	10
7.10	Not Effective And Efficient During Operation And Maintenance[9, 14]	0.57	0.72	0.61	Mild	10
7.11	Many Traffic Accidents [8, 9]	0.52	0.69	0.57	Low	12
7.12	Toll Road Disruption Due To Demonstrations [8, 9]	0.49	0.67	0.54	Low	15
7.13	Overload Risk[8, 9]	0.62	0.76	0.70	Mild	6
7.14	Low Traffic Volume[8, 9]	0.71	0.87	0.80	Critical	2
7.15	Competitive Route [8, 9]	0.54	0.79	0.65	Mild	8
7.16	Vandalism [8, 9]	0.49	0.64	0.55	Low	14

The critical risks in the financing indicator are the error in construction estimation, Late Payments on Completed Work, dan Financing Delays from the Government. The State-Owned Corporation carried out the construction estimation in preparing the construction by coordinating with the government party[20], The late payments and financing delays happened because the assignment scheme financing for the equity part mostly relied on the State Equity Participation scheme; according to Fakhrin [20] it is important to find another financing scheme to prevent the financing delays. Then, there is a critical risk known as Lack of Efficient Conflict Management in the stakeholder indicator. It is because of many stakeholders are identified in the execution of the Sumatera toll road construction project. [20].

In the pre-construction factor, the critical risk is in the Lack of SPV Ability. Because the SPV recruitment in the State-Owned Corporate is extremely limited in this assignment scheme, not many other alternatives involve the private sectors. In addition, it is the first toll road construction project with the assignment scheme, so adaptation is needed. Moreover, Late Land Acquisition and Many Land Brokers also became the critical factors in the land clearing process that minimized the project performance, inhibiting the Sumatera toll road construction. This is because

the land clearing for toll areas is strongly different from other projects; in the toll road project, the area needed to be cleared quite large, and not all areas from the affected owners can be used or can only be used partially [3].The critical risks during the construction that hinders the TranSumatera toll road construction with the assignment scheme are the Lack of Contractor's Technical Ability and Material Procurement Delay. It is similar to the TransJawa toll road construction, specifically in Semarang – Solo, with the PPP scheme based on the owner's perception [16]. In the operational and risk factor maintenance period, the risk factors with the critical value were the income risk and the low traffic volume. It is interrelated as the small volume of the vehicles that crosses the Sumatra toll road will result in a low income for the toll road. The risk factors included in this group are crucial in the toll road construction project with the SOE assignment scheme and they must get a special attention.The failure in dealing with this risk is the main cause that results in adding a significant cost and the decrease in the targeted performance of the toll road construction with this State-Owned Corporate assignment scheme.



## CONCLUSIONS

From the research above, it can be concluded that :

1. The purpose of this paper was to identify the risk factors responsible for the excessive time and cost on the SOE assignment scheme-based toll road project and identify which of the factors above has a significant impact on excessive time and cost on the SOE assignment scheme-based toll road project.
2. The analysis of the survey result and the processing using the Rough Fuzzy Delphi reveals that 12 major risk factors significantly impact the SOE assignment scheme-based highway and toll road projects in terms of excessive time and cost.

## REFERENCES

- [1] BPJT-PU. Tahapan Makro Pengusahaan Jalan Tol. [cited 2020 02-08]; Available from: <http://bpjt.pu.go.id/konten/investasi/tahapan-makro-pengusahaan-jalan-tol>.
- [2] Indonesia, R., Peraturan Presiden tentang Perubahan atas Peraturan Presiden Nomor 100 Tahun 2014 Tentang Percepatan Pembangunan Jalan Tol Sumatera, Nomor Perpres Nomor 117 Tahun 2015. 2015.
- [3] Likhitrungsilp, V., S.T. Do, and M. Onishi, A comparative study on the risk perceptions of the public and private sectors in public-private partnership (PPP) transportation projects in Vietnam. *Engineering Journal*, 2017. 21(7): p. 213-231.
- [4] Chen, Z., et al., A rough-fuzzy DEMATEL-ANP method for evaluating sustainable value requirement of product service system. *Journal of Cleaner Production*, 2019. 228: p. 485-508.
- [5] Zadeh, L.A., Fuzzy sets. *Information and control*, 1965. 8(3): p. 338-353.
- [6] Song, W. and J. Cao, A rough DEMATEL-based approach for evaluating interaction between requirements of product-service system. *Computers & Industrial Engineering*, 2017. 110: p. 353-363.
- [7] Valipour, A., et al., A fuzzy analytic network process method for risk prioritization in freeway PPP projects: an Iranian case study. *Journal of Civil Engineering and Management*, 2015. 21(7): p. 933-947.
- [8] BPJT-PU, Analisis resiko investasi jalan tol, D.P. UMUM, Editor. 2005, Kementerian Pekerjaan Umum: Jakarta.
- [9] Wirahadikusumah, R.D., B. Susanti, and B.W. Soemardi, Risk in government's estimate for toll road: based on investors' perspective. *International Journal on Advanced Science, Engineering and Information Technology*, 2018. 8(2): p. 475-482.
- [10] Pai, S., et al., Identification of risks causing time and cost overrun in roads and highway projects in India. *International Journal of Civil Engineering and Technology*, 2018. 9(3): p. 683-697.
- [11] Castelblanco, G., et al., Risk allocation in unsolicited and solicited road public-private partnerships: Sustainability and management implications. *Sustainability*, 2020. 12(11): p. 4478.
- [12] Jokar, E., B. Aminnejad, and A. Lorak, Risk prioritization and selection of contractor participating in Public-Private Partnership (PPP) infrastructure project using Hybrid Fuzzy AHP and Fuzzy TOPSIS (Case Study: Saveh-Salafchegan Freeway Project). *Journal of Construction Engineering, Management & Innovation*, 2020. 3(1): p. 1-16.
- [13] Patel, T.D., T.C. Haupt, and T. Bhatt, Fuzzy probabilistic approach for risk assessment of BOT toll roads in Indian context. *Journal of Engineering, Design and Technology*, 2019.
- [14] Ahmadabadi, A.A. and G. Heravi, Risk assessment framework of PPP-megaprojects focusing on risk interaction and project success. *Transportation research part a: policy and practice*, 2019. 124: p. 169-188.
- [15] Deshpande, P. and S. Rokade, Prioritization and assessment of critical risks of public private partnership highway projects in India using analytical hierarchical process. *International Journal of Civil Engineering and Technology*, 2017. 8(6): p. 605-620.
- [16] Mochamad, A.W., Risk Management in Indonesia Construction Project: A Case Study of a Toll Road Project. 2018.
- [17] Suseno, Y.H., M.A. Wibowo, and B.H. Setiadji, Risk analysis of BOT scheme on post-construction toll road. *Procedia Engineering*, 2015. 125: p. 117-123.
- [18] Johnston, J. and A. Kouzmin, Addressing governance, accountability and performance monitoring issues in partnerships: can infrastructure Australia provide a strategic response? *Public administration quarterly*, 2010: p. 513-551.
- [19] De Schepper, S., M. Dooms, and E. Haezendonck, Stakeholder dynamics and responsibilities in Public-Private Partnerships: A mixed experience. *International Journal of Project Management*, 2014. 32(7): p. 1210-1222.
- [20] Fakhrin, M.R., L.S. Riantini, and Y. Latief, Risk-Based Institutional Evaluation of Trans Sumatera Toll Road Infrastructure Development to Improve Time Performance. in *International Conference on Global Optimization and Its Applications 2021*. 2021.

Copyright © Int. J. of GEOMATE All rights reserved, including making copies unless permission is obtained from the copyright properties.

## RESULTS OF RECOVERY PROJECT ON WETLANDS WITH LOST BIODIVERSITY

Michiko Masuda<sup>1</sup>, Koichi Nagarekawa<sup>2</sup> and Fumitake Nishimura<sup>3</sup>

<sup>1,2</sup> Faculty of Engineering, Nagoya Institute of Technology, Japan; <sup>3</sup> Faculty of Engineering, Kyoto University, Japan

### ABSTRACT

Many wetlands have been lost by vegetation succession and construction development. From the point of SDGs views, the disappearance of wetland ecosystem is a serious loss to the value of biodiversity. But all wetland will disappear due to vegetation succession before long. Until recently 20 century the new wetlands were born from slope collapse or flood ever. Now the phenomenon is prevented for safety people life. In order to maintain the wetland, we must protect the wetland from the vegetation succession. Wetland desiccation has changed the vegetation and led to a decrease in biodiversity. Therefore, in order to restore the wetland, we stripped the vegetation and investigated the flora and environmental factors that regenerate there. And we measured the environmental factors before stripping and after it. As a result, vegetation stripping restored the wetland flora over 5 times, and brought about a resurgence of biodiversity. In addition, vegetation stripping resulted in a decrease in nutrients, a decrease in pH, and a decrease in electro conductivity. To conserve the wetland biodiversity stripping method is very effective.

*Keywords: Vegetation succession, biodiversity, environmental condition, poor nutrition*

### INTRODUCTION

In Japan, wetlands are likely to the target of development such as reclamation and landfill. The result of that many wetlands have disappeared so far. According to the Geospatial Information Authority of Japan's Lake Wetland Survey 2000, 61.1% of wetland area has disappeared in Japan for 150 years [1]. In Aichi Prefecture with Tokai Group which contain argillaceous layer, wetlands used to exist everywhere in this area. But many spring wetlands are used as catchment areas for residential land development, agricultural land, road construction, etc. It has disappeared with the forest and its area has shrunk. In addition, many wetlands in Aichi Pref. are small size under 10 are, many of them disappeared due to vegetation succession. Furthermore, in recent years, new wetlands are rarely formed due to improvements in civil engineering technology and disaster prevention measures.

There are many conservationally important biological communities including endangered species in these declining spring wetlands. The spring wetlands in the Tokai region (that contains Aichi Pref.) grow mainly in the spring wetlands in the Zhou Ise Bay region. It is strongly associated with Tokai hill element plants, which are a classification group of endemic, quasi-indigenous and isolated plants, and academic research on relatively large number of spring wetlands has been carried out in the Tokai region [2]-[4].

Amid the problem of wetland reduction, a large-scale vegetation restoration operation was carried out

on a trial basis from 2013 in the Imou Wetland (3.2ha) located in Toyohashi City, Aichi Pref., in order to stop forestation and restore the good wetlands on the past. In this operation, organic matter was removed by cutting trees that were once wetlands and stripping the topsoil at a part of wetland. In this way, the purpose of removing organic matter is to suppress forestation to rescue sunshine and to suppress eutrophication to make it oligotrophic, thereby creating an ideal environment for spring wetlands. This is because the buried seeds in the soil can be used to regenerate the wetland. In facts some vanished species recovered from the soil. Though the recover method is very attractive for conservation, there are no analysis and survey. And we cannot know that all area with recovery method can be revived, then it is very danger to apply the method to small wetland.

Therefore, in this research, we focused on the following three points. First, how has the physical environment changed due to logging and stripping of topsoil? Second, How did the vegetation change before and after the recovery method? Third, are there enough buried seeds even in a wetland with a small area of about <10 area?

### MATERIALS AND METHODS

#### Study site

The two places of the investigation were located in Nagakute City, Aichi Pref. Site A is on the campus of Aichi University of Arts (35°16'73" north latitude, 137°16'97" east longitude) and site B is on

Yamanouchi (35°18'67" north latitude, 137°07'97" east longitude) at center of Japan (Fig. 1). Site A was a wetland that has begun to dry and shrubs have invaded. Site B was once a wetland, but vegetation succession has progressed and it has become forested. Although it gets a little damp, no spring water can be seen.

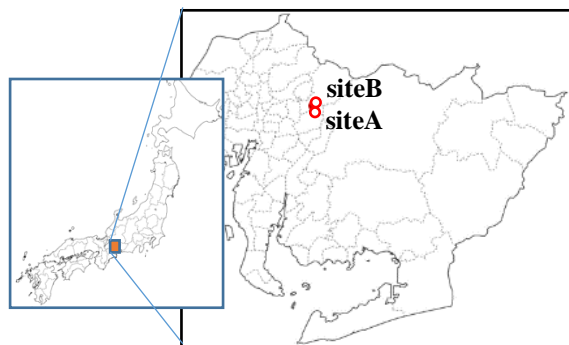


Fig. 1 The map of study site

At each site, eight 1m x1m quadrats were placed at 1m intervals along the contour lines in 2 row and 4 columns. The numbers are 1 to 4 from the left on the upper side of the slope and 5 to 8 from the left on the lower side of the slope. The following surveys were conducted on each of the installed quadrats.

In order to investigate the effect of the recovery method, logging and topsoil was stripped on 23th and 24th Jan. 2019.

### Vegetation survey

From April to December 2018, 2019 and 2020, the vegetation coverage area was calculated for each plant species that grows in quadrats once a month. To calculate the cover area, each quadrat was divided 5cm x 5cm and counting the number of mini squares with occupied each species at 3 levels (full, half, non).

### Environmental Factor Measurement

We measured each environmental factor at each quadrat once a month from January 2019 to December 2020. The first measurement is the condition before the recovery method. Four environmental parameters, loss on ignition (*IL*), pH (*ph*), electrical conductivity (*ec*) and soil hardness (*sh*) were measured. Loss on ignition was measured by sampling center and four corner at each quadrat. After sampling the materials was into an incubator at 120°C for 2days in order to loss the water. pH and electrical conductivity was measured 5 point at each quadrat (center and four corner) with mobile measurement machine (Eranear SZTZ2SET). Soil hardness were measured by Yamanaka method soil hardness meter(KamiyamaCo 401-0055) at each quadrat. And sky openness was measured at January, October 2019, June and October 2020 using by 360°

camera (Ricoh theta V) with CanopOn software.

### Statistical Analysis

Two-way ANOVA was performed to investigate the annual variation and homogeneity of each plant. There were 43 species of plants identified through the research time, but non wetland plants and woody plants that were not conservation targets, such as fern, *Rhododendron kaempferi*, *Pleioiblstus chino* var. *viridis*, *Ilex pedunculosa*, *I. crenata* var. *crenata*, *Almus japonica*, *Eurya japonica* var. *japonica*, *Akebia trifoliata*, *Rosa multiflora* etc...16 species combined into one as a non-conservation plant, and Tokai hill element plants, and wetland plants with a large number of samples are tested.

The dependent variable was the vegetation coverage area of each plant, and the two qualitative factors were the year and the quadrat, respectively. It is assumed that the population distribution of each group follows the normal distribution  $N(\mu, \sigma^2)$ , and the population variance  $\sigma^2$  is unknown, but all are equal. Null hypothesis: the mean value between each level is equal. Alternative hypothesis: at least one of the mean values between levels is not equal, the significance level is set to 0.05 and the rejection area  $R$  is set as follows.  $F_0$  is F distribution (normal), and  $\varphi_A$  is the difference between quadrats and  $\varphi_E$  is the difference between years,  $\alpha$  is a critical ratio ( $p < 0.05$ )

$$R: F_0 > F(\varphi_A, \varphi_E; \alpha) \quad (1)$$

If null hypothesis is in the rejection area  $R$ , it is judged to be not significant and null hypothesis is rejected. Analysis of variance shows that if significant, there is a difference between any one or more groups, but no information is available as to which group there is a difference.

We performed analysis using GLM (Generlized Linier Model, using quick-R: correspondence analysis program) to elucidate the cover area ratio of each plant species and its relationship to environmental factors between October 2019 and 2020. Since the probability distribution of the response variable follows the binomial distribution (ratio distribution so the binominal distribution), the link function is a logistic function.

$$\eta = \log\left(\frac{y}{1-y}\right) \quad (2)$$

$\eta$  is a function of the explanatory variable, and in the case of a generalized linear model, it is represented by a linear function of the explanatory variable.

The environmental factors are five types of measurement data obtained by measuring, loss on ignition (*hl*), pH (*ph*), electrical conductivity (*ec*), soil hardness (*sh*) and sky openness (*op*).

In this study, the variable reduction method is

adopted the method of selecting the variables used in the model. This is a method of inputting all variables into the model and excluding those with weak explanatory power. Akaike's Information Criterion (AIC) was used as a criterion for evaluating the fit of the model variables.

$$AIC = -2\ln L + 2k \quad (3)$$

$L$  is the maximum likelihood and  $k$  is the number of parameters. A model with the smallest AIC value was adopted.

## RESULTS

The stripped conservation method was shown surprising vegetation changes. Table 1 and 2 showed the change before and after topsoil stripping experiment. The structure of plant species was changing after the stripping, many wetland species emerged and some dry area species decreased.

Table 1 Total vegetation coverage of each species at each quadrat (cm<sup>2</sup>) in siteA

Speices	(siteA, 2018)	(siteA, 2019)	(siteA, 2020)
<i>Moliniopsis japonica</i>	486590	40170	27900
<i>Heloniopsis orientalis</i>	6410	20	350
<i>Rhynchospora chinensis</i>	111750	35700	94650
<i>Aster rugulosus</i>	550	3520	920
<i>Drosera rotundifolia</i>	770	210	60
<i>Drosera tokaiensis</i>	500	2180	1030
<i>Eriocaulon nudicuspe</i>	107270	26320	185250
<i>Hololeion krameri</i>	101260	4640	7200
<i>Metanartheicum luteoviride</i>	580		
<i>Gentiana thunbergii</i>	90	220	20
<i>Utricularia caerulea</i>	365	220	190
<i>Carex omiana</i>	123070	11590	5770
<i>Scirpus wichurae</i>	2460	1420	20550
<i>Imerata cylindrica</i>	9040	2110	400
<i>Pleioblastus chino</i>	12450	1140	620
<i>Alnus japonica</i>	3420	50	
<i>Fern spp.</i>	14760	2100	4080
<i>Toxicodendron trichocarpum</i>	5320		
<i>Rhododendron kaempferi</i>	1760	830	3700
<i>Akebia trifoliata</i>	300		
<i>Rosa multiflora</i>	4090		
<i>Ilex pedunculosa</i>	530		
<i>Eurya japonica</i>	30		
<i>Ilex crenata</i>	80		
<i>Hosta longissima</i>		30	80
<i>Gonocarpus micranthus</i>		30	10
<i>Scieria caricina</i>		8230	3640
<i>Scleria rugosa</i>		1870	3950
<i>Eleocharis wichurae</i>		1430	3460
<i>Juncus papillous</i>		2210	6250
<i>Utricularia bifida</i>		1840	1130
<i>Utricularia nipponica</i>		90	500
<i>Rhynchospora alba</i>			1150

Blue is a wetland species, and red is a non-wetland

Fig. 2, 3 and 4 showed the environmental factor changing after stripping. Fig 2 showed the ignition loss. Before the stripping the value of IL is very high, and after the experiment, seasonal change was observed but the value was not over 20%. Fig. 3 showed the value of pH. The value of pH was

changing seasonally, but the decline was observed. Fig.4 showed the electrical conductivity. This value showed the water dirt, so the value is high in winter and gradually decline to the summer. Fig. 5 showed the value of sky openness. The value of median was changing but there were not differences about the sky openness.

Table 2 Total vegetation coverage of each species at quadrat (cm<sup>2</sup>) in siteB

Speices	(siteB, 2018)	(siteB, 2019)	(siteB, 2020)
<i>Drosera rotundifolia</i>	200	9040	3350
<i>Drosera tokaiensis</i>			260
<i>Eriocaulon nudicuspe</i>	1260	11250	37890
<i>Carex omiana</i>			1910
<i>Scirpus wichurae</i>	11100	61000	160500
<i>Imerata cylindrica</i>		250	
<i>Pleioblastus chino</i>	35110		
<i>Alnus japonica</i>	30070		
<i>Fern spp.</i>	15460		
<i>Rosa multiflora</i>		1690	1820
<i>Ilex crenata</i>	112630	5570	5650
<i>Eleocharis wichurae</i>		4350	2550
<i>Juncus papillous</i>		27650	4850
<i>Ilex dentata</i>	1060	6550	8530
<i>Deutzia crenntata</i>	890		
<i>Alnus trabaculosa</i>	8460		
<i>Cryptomeria japonica</i>	1170		
<i>Osmunda japonica</i>	5060	4680	3650
<i>Dioscoreatokoro</i>	1370	720	
<i>Carex capillacea</i>		6250	99990
<i>Carex pudica</i>			80
<i>Ludwigia decurrens</i>			1660
<i>Monochoria vaginalis</i>			160

Blue is a wetland species, red is a forest species.

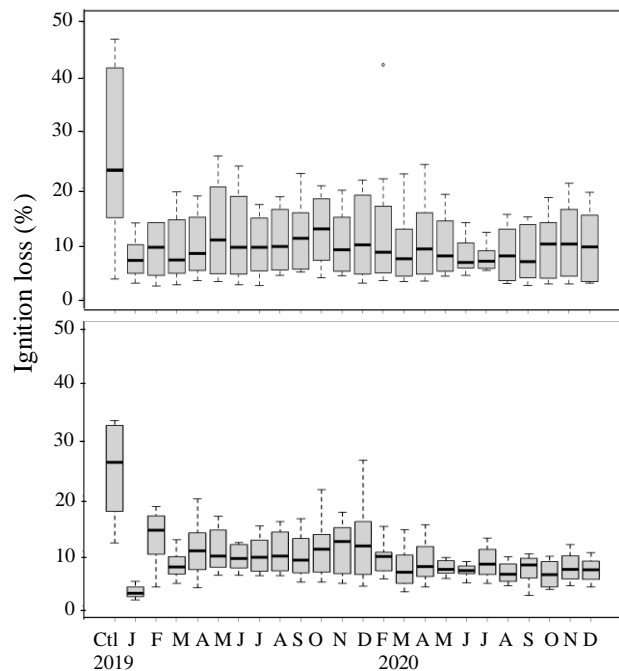


Fig. 2 The seasonally change of Ignition loss at site A and B

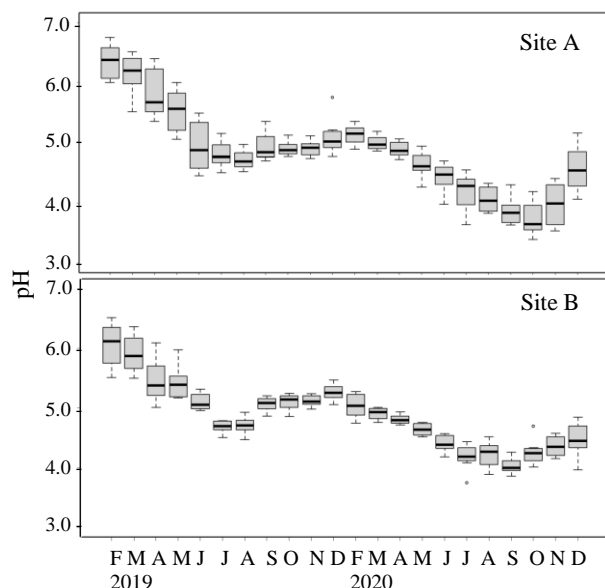


Fig. 3 Seasonal change of pH at each site

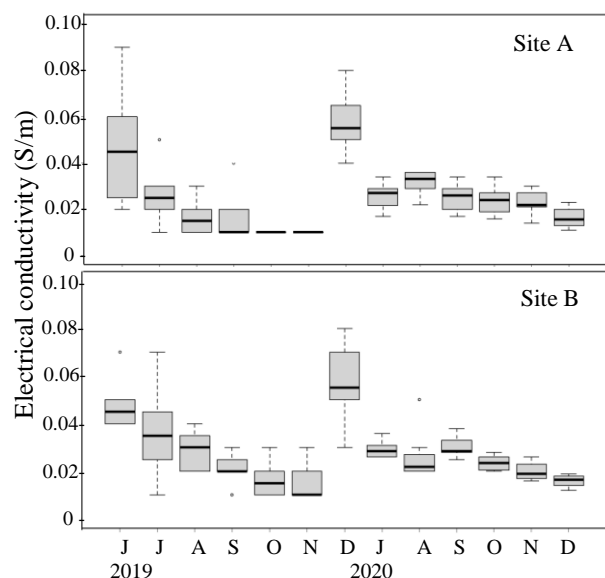


Fig. 4 The seasonal change of electrical conductivity at each site

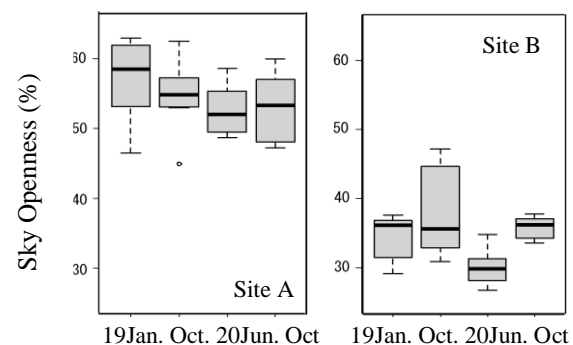


Fig. 5 The Sky openness at each site

Table 3 showed the soil hardness of each site. The value of the soil hardness was 0 to 17.63mm that showed the soil hardness enough for the plants to

grow. But the roots penetrate to the lower soil layer.

Table 3 Mean and SD of soil hardness at each site

	mean	SD
site A	6.212	3.185
site B	5.107	7.062

The result of ANOVA among the distribution of heterogeneity and years was shown in Table 4. The species of  $P < 0.05$  was shown in Table 5.

Table 4 The value of ANOVA test between quadrat and year

species	factor	F value	Pr(>F)	
<i>Moliniopsis japonica</i>	cordrat	23.72	<2e-16	***
	year	365.48	<2e-16	***
	cordrat:year	13.25	<2e-16	***
<i>Rhynchospora chinensis</i>	cordrat	3.896	1.36E-04	***
	year	3.51	3.17E-02	*
	cordrat:year	1.752	3.31E-02	*
<i>Carex omiana</i>	cordrat	4.357	4.62E-05	***
	year	41.567	7.87E-14	***
	cordrat:year	3.867	3.34E-06	***
<i>Scirpus wichurae</i>	cordrat	5.315	1.27E-06	***
	year	8.706	2.24E-04	***
	cordrat:year	1.556	7.25E-02	.
<i>Eleocharis wichurae</i>	cordrat	8.402	3.83E-07	***
	year	12.686	1.53E-05	***
	cordrat:year	5.391	1.07E-06	***
<i>Juncus papillous</i>	cordrat	7.7	7.59E-11	***
	year	29.21	1.03E-11	***
	cordrat:year	11.01	<2e-16	***
<i>Carex capillacea</i>	cordrat	4.155	3.67E-03	**
	year	37.835	4.50E-16	***
	cordrat:year	5.219	1.70E-05	***
<i>Utricularia bifida</i>	cordrat	1.196	3.20E-01	
	year	4.758	1.19E-02	*
	cordrat:year	0.648	7.93E-01	
<i>Utricularia nipponica</i>	cordrat	0.605	6.18E-01	
	year	1.873	1.76E-01	
	cordrat:year	0.811	5.72E-01	
<i>Doroseria tokaiensis</i>	cordrat	3.239	2.85E-03	**
	year	7.541	7.03E-04	***
	cordrat:year	3.57	3.05E-05	***
<i>Eriocaulon nudicuspe</i>	cordrat	14.83	<2e-16	***
	year	42.75	<2e-16	***
	cordrat:year	9.26	<2e-16	***
not wetland species	cordrat	2.872	5.98E-04	***
	year	10.339	4.39E-05	***
	cordrat:year	2.694	2.61E-05	***

\*\*\*  $p < 0.001$ , \*\*  $p < 0.01$ , \*  $p < 0.05$

From the data of field census, the number of 11 species was sufficient to create new models, one species non a wetland species *Ixeris dentata*, ten wetland species, *Moliniopsis japonica*, *Rhynchospora chinensis*, *Scirpus wichurae*, *Eleocharis wichurae*, *Juncus papillous*, *Carex capillacea*, *Utricularia bifida*, *Utricularia nipponica*,

*Doroseria tokaiensis* and *Eriocaulon nudicuspe*.

Table 5 The GLM model of 11 species of each parameter

	Parameter	Estimate	Std.Error	z value	P value
<i>M. japonica</i>	$\alpha$	-5.96519	-0.4429	-134.68	***
	ph	-0.2761	0.0248	-11.12	***
	hl	1.13614	0.0157	72.38	***
	ec	0.32967	0.0279	11.84	***
	op	2.01661	0.0448	45.02	***
<i>R. chinensis</i>	$\alpha$	-3.94588	0.0162	-243.55	***
	ph	-1.44274	0.0225	-64.243	***
	hl	-0.03098	0.0089	-3.469	***
	ec	-0.0651	0.0226	-2.887	***
	op	0.859059	0.0157	54.614	***
<i>S. wichurae</i>	$\alpha$	-2.71838	0.0113	-241.59	***
	ph	0.433861	0.0091	47.44	***
	hl	0.202669	0.0085	23.93	***
	ec	1.030462	0.0087	118.1	***
	op	-1.2311	0.0135	-91.24	***
<i>E. wichurae</i>	$\alpha$	-5.42382	0.0285	-190.27	***
	ph	-0.42105	0.0432	-9.753	***
	hl	0.12737	0.0264	4.82	***
	ec	0.20219	0.0448	4.511	***
	op	0.07077	0.0366	1.932	NS
<i>J. papillous</i>	$\alpha$	-4.47539	0.0183	-245.22	***
	ph	-0.85621	0.0322	-26.567	***
	hl	-0.03255	0.017	-1.914	NS
	ec	-0.30119	0.0329	-9.153	***
	op	-0.24823	0.0221	-11.214	***
<i>C. capillacea</i>	$\alpha$	-4.08307	0.0206	-198.33	***
	ph	0.43934	0.0152	28.91	***
	hl	0.1911	0.0139	13.76	***
	ec	0.92115	0.0144	64.15	***
	op	-1.18744	0.0236	-50.31	***
<i>U. bifida</i>	$\alpha$	-13.0903	0.463	-28.271	***
	ph	-5.23391	0.2896	-18.075	***
	hl	-1.46853	0.0901	16.296	***
	ec	0.64376	0.0958	6.723	NS
<i>U. nipponica</i>	$\alpha$	-9.0906	0.2444	-37.198	***
	ph	-2.16287	0.2382	-9.079	***
	hl	-0.02403	0.0804	-2.987	**
	ec	0.21293	0.1442	1.477	***
	op	0.59371	0.1292	4.595	***
<i>D. tokaiensis</i>	$\alpha$	-7.90888	0.1181	-66.983	***
	ph	-0.74351	0.1455	-5.111	***
	hl	1.0206	0.0526	19.413	***
	ec	-1.03555	0.1568	-6.604	***
	op	0.819059	0.1076	7.615	***
<i>E. nudicuspe</i>	$\alpha$	-1.73428	0.0058	-297.42	***
	ph	-0.88289	0.0096	-92.2	***
	hl	-0.1213	0.0054	-22.61	***
	ec	0.232448	0.0102	22.71	***
	op	0.542286	0.0071	76.8	***
<i>I. dentata</i>	$\alpha$	-5.28296	0.0282	-187.06	***
	ph	-0.51311	0.0396	-12.95	***
	hl	0.3522	0.0277	12.73	***
	ec	-0.5619	0.0372	-15.13	***
	op	-1.0708	0.034	-31.46	***

\*\*\* p<0.001, \*\* p<0.01, \* p<0.05, NS non-significant

$\alpha$  in Table 5 is initialization parameter.

The result of the GLM, six species, *M. japonica*, *S. wichurae*, *E. wichurae*, *C. capillacea*, *D. tokaiensis* and *I. dentata*, are easy to grow in an environment rich with large value of ignition loss (parameter hl). And among these species, low pH condition is harsh environment for plant roots, but four species, *M. japonica*, *E. wichurae*, *D. tokaiensis* and *I. dentata*, that prefer it.

## DISCUSSION

Many researchers worry about the extinction of endangered species [5]-[7]. The United Nation Summit calls for the protection of living organisms from the SDGs aim, but the rate of extinction has not decreased [8]. In Japan many endangered species that grow in wetlands have been reported, and it is required to propose a method for conserving species in wetlands [9]. It is very important to establish a method for wetland regeneration. Some people showed the experiment of recover wetland for logging and stripping top soil, there have been no examples analysis of changes in environmental condition or the quantitative status of restoration. This study is the first example of an analysis of the environmental effects of logging and topsoil removal, and the amount of emergence of what plant continuously.

According to the vegetation survey, the treatment of experiment restored the lost wetland plants and restored species that had not been reported in the last 20 years. Wetland restoration was shown to be possible regardless of the level of vegetation succession. However, the recovery of wetland plants has been shown to be significantly heterogeneous spatially and temporally. This showed that it is not always possible to restore all species in a small area. We must think about the amount of area in order to restore the wetland with high biodiversity.

When all ground cover removed, burial seeds emerged and make the population of wetland. And physical environment has also changed, in particular, ignition loss reduced. It was shown that once the organic matter is removed, ignition loss can be kept low, but pH and electro conductivity changed seasonally. Environmental factors change seasonally, it is difficult to find out the relationships between environmental factors and plant species. GLM is very convenient to find out the relationships [10]-[11]. The models show that some endangered species (*M. japonica*, *R. chinensis*, *J. papillous*, two *Utricularia* species, *D. tokaiensis*, *E. nudicuspe*) have low pH and low nutrient (electro conductivity) even with large ignition loss.

Four species, *M. japonica*, *S. wichurae*, *E. wichurae* and *C. capillacea*, that prefer a place with high ignition loss and abundant nutrients are considered to be able to grow even if the wetland



transitions. Because of these species with a high rate of population expansion form a patch community, we propose that these species preferentially removed as well as other no wetland species when the eutrophication of wetland progresses.

## CONCLUSIONS

The following conclusions are drawn from the study.

- 1) The physical environment changed to logging and stripping of topsoil, especially loss ignition. After stripping, loss ignition stable at low level, but pH and electro conductivity were changing seasonally. pH was high after stripping and gradually lower with high level observed in winter. Electro conductivity was high in winter because of the deciduous leaves.
- 2) Vegetation was changed after the recovery method. Especially half of non-wetland species was extinct from the wetland. And some endangered species restored in some quadrats.
- 3) In small wetland (under 10 area), there were enough burial seeds to restore the wetland, but the heterogeneity was observed among quadrats.
- 4) Wetland can be restored by recovery measures even if the vegetation succession progressed and wetland has already disappeared.

The logging and stripping top topsoil are useful to restore the wetland in small wetland. But the burial seeds are unevenly distributed, so it is necessary to consider the area to be restoration treatment.

## ACKNOWLEDGMENTS

We send thanks to Prof. T. Kitano who advised the analysis of statistical method. We also thank to the colleague at our laboratory, Nagakute city at Aichi Pref. and the group of 'the Nagakute wetland conservation group', they helped the field census.

## REFERENCES

- [1] Geospatial Information Authority of Japan., Survey results of changes in wetland area throughout Japan, 2000, <https://www.gsi.go.jp/kankyochiri/shicchimenseki2.html>.
- [2] Ueda K., Phytogeography of Tokai Hilly land element I. Definition, Acta Phytotaxonomy Geobotany, Vol. 10, 1989, pp. 190-202.
- [3] Nakamura T. and Ueda K., Phytogeography of Tokai Hilly land element II. Taxonomic study of *Drosera tokaiensis* (Komiya & C. Shibata) T. Nakamura & Ueda (Doroseraceae), Acta Phytotaxonomy Geobotany, Vol. 42, Issue 2, 1991, pp. 125-137.
- [4] Tomita K., How well have we understood the environment of the seepage marsh in the Tokai area of Japan?, Wetland Research, Vol. 8, 2018, pp. 63-79.
- [5] Dyke V.D. and Lamb R.L., Conservation Biology: Foundation, Concepts, Applications, Springer, 2020, pp. 11-58.
- [6] Primack R.B., Essentials of Conservation Biology, 6<sup>th</sup> edition, Sinauer, 2017, pp. 3-78.
- [7] Meffe G.K. and Carroll C.R., Principles of Conservation Biology, Sinauer, 1997, pp. 3-158.
- [8] IUCN, Summary Statistics, 2021, <https://www.iucnredlist.org/resources/summary-statistics>.
- [9] Washitani I., Floodplain wetland loss and regeneration: efforts to utilize paddy fields as wetland, Earth Environment, Vol 12, 2007, pp. 3-6.
- [10] Sugiyama Y., Nakamura M., Senda S, and Masuda M., Environmental parameters controlling the habitat of the brackish water clam *Corbicula japonica* identified by predictive modelling. International Journal of GEOMATE, Vol. 17, Issue 59, 2019, pp.68-73
- [11] Masuda M., Morioka T., and Nishimura F., The environmental parameters controlling the habitat of invasive alien species, *Spartina alterniflora* identified by predictive modeling. International Journal of GEOMATE, Vol. 20, Issue 79, 2021, pp. 62-67.

# PREPARATION OF GEOPOLYMER CEMENT FROM LUNAR ROCK SAND USING ALKALI FUSION, AND ITS EVALUATION OF RADIATION SHIELDING ABILITY

Osamu Toda<sup>1</sup>, Takaaki Wajima<sup>2</sup>

<sup>1,2</sup>Graduate School of Science and Engineering, Chiba University, Japan

## ABSTRACT

In this study, simulated lunar rock sand was converted into geopolymer cement by alkali fusion with sodium hydroxide, and its radiation shielding ability was estimated. Space development is currently being conducted in various countries. For construction on the moon, it is difficult to bring all the construction materials from the earth, and construction materials prepared from lunar resources are required. In addition, it is necessary to develop construction materials with radiation shielding ability since the lunar surface is directly affected by space radiation. In a previous study, it has succeeded in making geopolymer cement from simulated lunar rock sand using alkali fusion. Therefore, there is a possibility that geopolymer cement used for construction material can be prepared from lunar rock sand, abundantly present on the lunar surface.

In this experiment, geopolymer cement was prepared from simulated lunar rock sand by changing the mixing ratio of the sand, sodium hydroxide and water, and strength of the cement was examined to obtain high-strength geopolymer. In addition, the resulting high-strength geopolymer cement was subjected to radiation shielding tests to confirm its radiation shielding ability. As a result, it was found that the high-strength geopolymer cement with radiation shielding ability can be prepared from simulated lunar rock sand using alkali fusion with sodium hydroxide.

*Keywords: Simulant, Alkali fusion, Geopolymer cement, Radiation shielding, Maximum breaking load*

## INTRODUCTION

Space exploration with unmanned spacecraft for space development is currently active around the world. The moon is satellite of the planet earth, the nearest astronomical object, and development as a base for space development is planned. If all construction materials for the base construction were to be transported from the earth, the cost would be enormous (approximately 100 million yen/kg). Therefore, the development of construction materials made from lunar resources is required.

In this study, we focused on lunar rock sand (regolith) which is abundant on the lunar surface. Regolith is the sand that covers the surface of the moon with a thickness of several meters and is mainly composed of  $\text{SiO}_2$  and  $\text{Al}_2\text{O}_3$  in the form of aluminosilicate minerals, such as anorthite, albite and so on. In our previous study, the authors have succeeded in making geopolymer cements from lunar simulated sand (simulant) using alkali fusion [1]. Although ordinary Portland cement is mainly solidified by the formation of needle-like calcium silicate hydrate (C-S-H), geopolymer cement is mainly solidified by the polymerization of silicate ions bridged by metal ions, such as  $\text{Al}^{3+}$ ,  $\text{Fe}^{3+}$  and so on, which is similar to the reaction of zeolite synthesis [2, 3]. It is possible to make geopolymer cement which can be used as a building material from lunar rock sand abundantly

present on the moon by alkali fusion of lunar rock sand to supply silicate ions and metal ions.

Therefore, in this study, we attempted to convert simulated lunar rock sand into geopolymer cement by alkali fusion to be mixed with water setting in vacuum, and evaluated its strength and radiation shielding ability.

## EXPERIMENT

### *Sample*

Simulated lunar rock sand (Month soil simulation FJS-1, CSP Japan, Inc.) was used in this study. The chemical composition is mainly composed of 42% of  $\text{SiO}_2$ , 14% of  $\text{Al}_2\text{O}_3$ , 14% of  $\text{CaO}$ , 13% of  $\text{Fe}_2\text{O}_3$  and 3% of  $\text{MgO}$ .

### *Geopolymer preparation*

The precursor of geopolymer are made by mixing the sample with sodium hydroxide powder in a weight ratio of 6: 1 to 3: 1 (17%~33%), put in a platinum crucible, and heated up to setting temperature (500 °C) for 10 min in vacuum atmosphere. Thereafter, geopolymer cement are made by mixing the precursor of geopolymer with water in a weight ratio 6 : 1 to 3 : 1 (17%~33%), forming into a mold ( $\phi 5 \text{ mm} \times 20 \text{ mm}$ ), heating in

vacuum atmosphere at 120 °C for 1 to 24 h to obtain the product.

The precursor of geopolymer (1 g), which was subjected to alkali fusion at each mixing ratio of lunar simulated sand with sodium hydroxide, was put into 1 mol/L hydrochloric acid (20 mL) and shaken for 6 hours, followed by filtration. The concentrations of silicon, aluminum, iron, and calcium in the filtrate were analyzed by atomic absorption spectrophotometry (Perkin Elmer, AAnalyst 200) and the elution amounts ( $S$ ) (mg/g) were calculated using the following equation.

$$S = C \times V/w \quad (1)$$

where  $C$  is metal concentrations (mg/L),  $V$  is filtrate volume (L) and  $w$  is the weight for precursor of geopolymer (g).

#### Strength test

The maximum breaking load of the products was measured using a strength tester (ZT series ZTA-500 N, IMADA), referring to the compression test of the strength test method in JIS Z 8841[4]. Strength test method is shown in Fig. 1. The cross section after breaking was observed using SEM(JSM-6510A, JEOL) to analyzed the morphology of each sample.

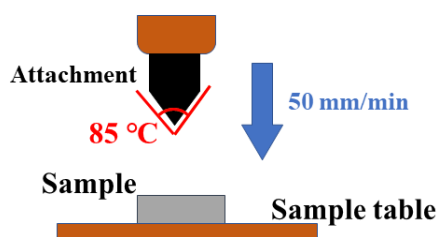


Fig. 1 Strength test method

#### Radiation shielding ability evaluation

The product for shielding test (5 cm × 5 cm × 5 mm) was prepared under the conditions to obtain the product with the highest strength, and its radiation shielding ability for  $\gamma$ -rays was evaluated using a radiation measuring instrument (KIND-pro, JSF) and a radiation source (uranium). Ordinary Portland cement (W/C = 50 %, 14 days) was used for comparison of radiation shielding performance. Radiation measurement method is shown in Fig. 2. A radiation source (uranium) is placed on a flat surface, and each shielding and measuring instrument is placed on a straight line. By moving the instrument,

the distance between the radiation source and the instrument is changed, and the radiation dose at each point is recorded.

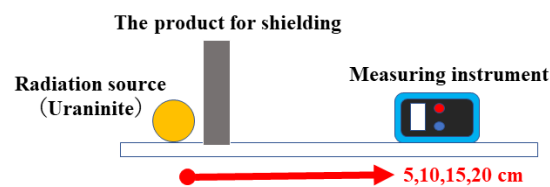


Fig. 2 Radiation shielding measurement method

## RESULTS AND DISCUSSION

#### Maximum breaking load

The maximum breaking loads for the products after 24 h heating on various conditions are shown in Table 1. The product with the highest breaking load was obtained when the weight ratio of lunar-simulated sand to sodium hydroxide was 4: 1 (25 %) and the weight ratio of the precursor to water was 5: 1 (20 %), indicating 584 N. It is noted that no brittle fracture can be observed on the conditions indicating N.D. As a comparison, the strength of ordinary Portland cement indicates higher than 1000 N. The product has a strength less than that of ordinary Portland cement.

When the water ratio is higher than 25 %, the strength is weak (lower than 150 N). It is considered that an increase in the amount of water in the mixture causes insufficient hardening by decreasing the bonding of silicates and metal ions due to the dilution, resulting in low strength.

Table1 The maximum breaking loads for the products after 24 h heating on various conditions

	Alkali ratio (NaOH/Simulant)				
	(%)	17	20	25	33
Water ratio (Water/Precursor)	17	421 N	310 N	363 N	319 N
	20	382 N	464 N	584 N	360 N
	25	N.D.	N.D.	N.D.	123 N
	33	N.D.	N.D.	N.D.	N.D.

N.D.: Not detected

The cross section of samples after strength test is shown in Fig.3. Samples with water ratios greater than 25% showed some large holes in the cross section, while those with water ratios less than 25% were almost filling overall.

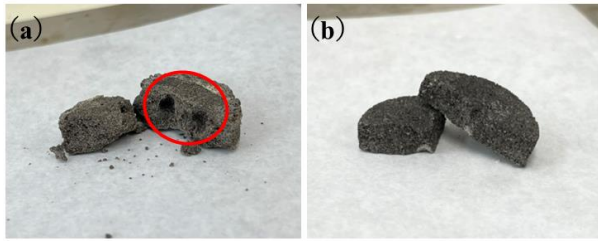


Fig.3 The cross section of samples after strength test; (a) water ratios greater than 25% and (b) water ratios less than 25%

Elution of Si, Al, Fe and Ca from precursor of geopolymer with various NaOH addition is shown in Fig.4. The amount of silicon elution increased as the addition of sodium hydroxide increased. The elution of aluminum and iron were nearly constant, while calcium was almost completely undissolved regardless of the addition of sodium hydroxide.

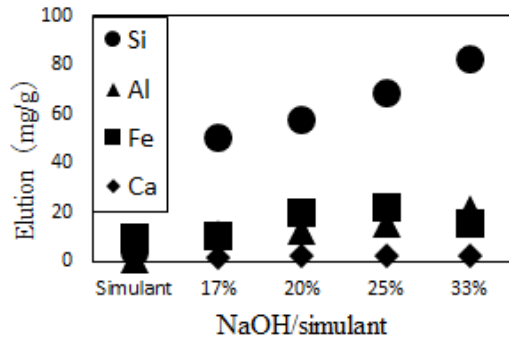


Fig.4 Elution of Si, Al, Fe and Ca from precursor of geopolymer with various NaOH addition

The ratio of the amount of metal dissolved from the precursor of geopolymer with various NaOH addition and the strength of their prepared products are shown in Fig.5. It is noted that calcium is not included in the metal ratio because very little calcium is dissolved from the precursor. The dissolution of aluminum and iron relative to the dissolution of silicon ( $\text{Si}/(\text{Al}+\text{Fe})$ ) is smaller, the strength is higher. This is because in the solidification of geopolymer cement, trivalent cations, such as iron and aluminum ions, react with silicate monomers to cross-link each other to form polymers, and when the ratio is smaller, more cross-linking promotes to form polymers to be harden.

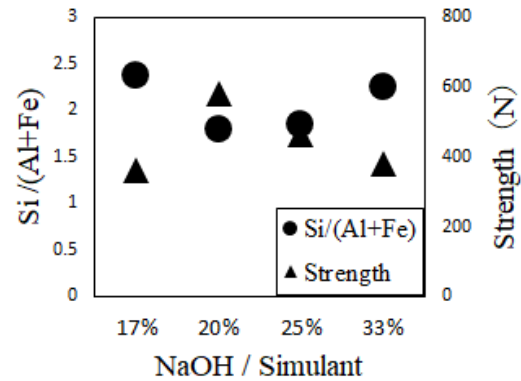


Fig.5 Ratio of the amount of metals dissolved from the precursor of geopolymer with various NaOH addition and the strength of their prepared products

The solidification of the samples was examined by heating the mixture of lunar-simulated sand and sodium hydroxide at a weight ratio of 4: 1 (25 %) and the precursor and water at a weight ratio of 5: 1 (20 %) under a vacuum atmosphere for 1 h to 3 h at 120 °C. It is noted that 120 °C is the average of surface temperature on the moon during the sunshine. The maximum breaking load of the prepared geopolymer cement as a function of heating time is shown in Fig.6. The strength is small from 0 to 2 h and increases to becomes constant (about 200 N) over 2 h.

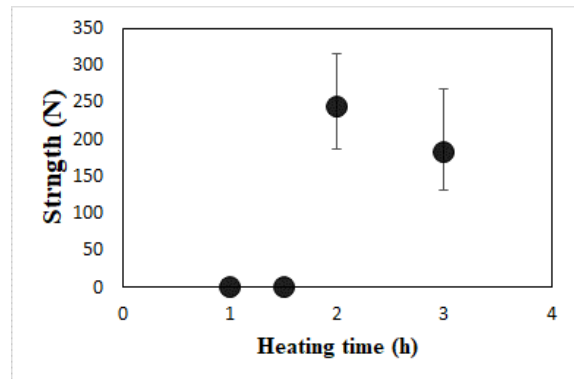


Fig.6 The maximum breaking load of the prepared geopolymer cement as a function of heating time

Furthermore, wet areas were observed on the surface of the sample after heating at lower than 2h, and the wooden needle pick was stuck on the surface of the sample, while the wooden needles was not stuck on the samples after heating over 2 h. It is considered that insufficient solidification occurred when the heating time was less than 2h due to insufficient dehydration reaction during the formation of the geopolymer, and solidified sufficiently after 2 h heating.

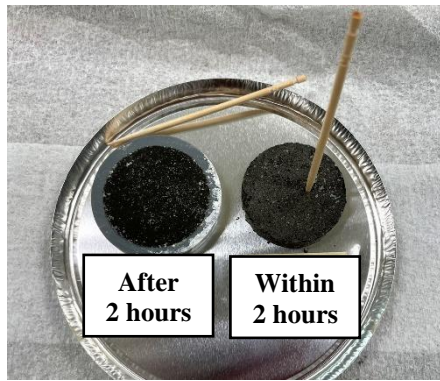


Fig.7 Photo after heating for 1 hour

SEM photos for cross sections of the product prepared by heating at 1 - 3 h are shown in Fig.8. At 1 h and 1.5 h, many gaps were observed in various places, while at 2 h and 3 h, no large gaps were observed, and the gaps were generally filled. It is considered that gaps were filled by the geopolymer due to the dehydration of water.

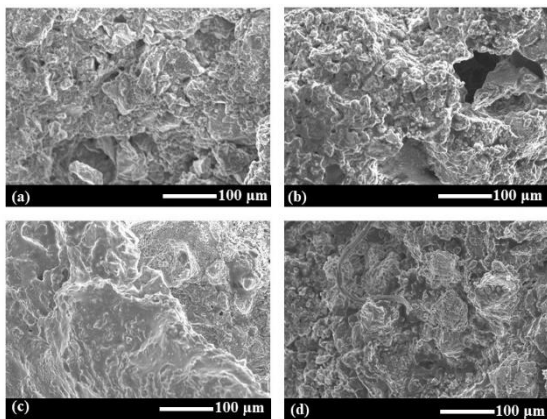


Fig.8 SEM photos for cross sections of products prepared by heating at (a) 1 h, (b) 1.5 h, (c) 2 h, and (d) 3 h

#### Radiation shielding ability

The radiation doses of the prepared geopolymer cement (GP) product, ordinary portland cement (PC), no shielding, and background (BG) are shown in Fig.9. Geopolymer cement has radiation shielding ability since it is lower than no shielding. The radiation shielding capacities of geopolymer cement product were almost same as those of portland cement.

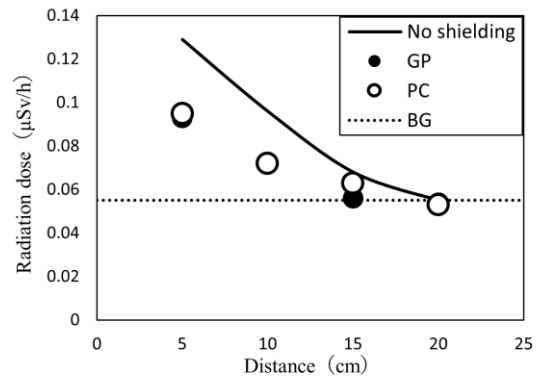


Fig.9 Radiation dose of the product and ordinary portland cement

## CONCLUSIONS

An attempt was made to prepare geopolymer cement by alkali fusion of simulated lunar rock sand with sodium hydroxide. The highest strength was found when the ratio of lunar simulated sand to sodium hydroxide and water was 4 : 1 : 1 (the mixture of lunar-simulated sand and sodium hydroxide at a weight ratio of 4: 1 (25 %) and the precursor and water at a weight ratio of 5: 1 (20 %)), and 2 h heating time in vacuum at 120 °C was found to be sufficient for the dehydration reaction in the formation of geopolymer.

The obtained geopolymer cement has the radiation shielding capacity and its capacity was found to be comparable to that of commercially available ordinary portland cement.

## REFERENCES

- [1] Sakamoto K. and Wajima T., Preparation of geopolymer cement from simulated lunar rock sand using alkali fusion, *International Journal of Geomate*, vol.18, 2020, pp.62-67.
- [2] Melkon T., Gunther M., and Stefan K. H., Relation of water adsorption capacities of zeolites with their structural properties, *Microporous and Mesoporous Materials*, vol.264, 2018, pp. 70–75.
- [3] Habbib G., Oliver S., Yvan M. and Philippe K., *The Reconstruction of Natural Zeolites*, Kluwer Academic Publishers, Dordrecht, 2003, pp. 1-5.
- [4] Sekiguchi I. Test methods for evaluating the strength of granules and agglomerates, 1994.



# PROPOSAL OF A FLOATING OFFSHORE BASE FOR DISASTER PREVENTION AND MULTIPURPOSE USE

Shinji Sato<sup>1</sup> and Kai Nagatomi<sup>2</sup>

<sup>1</sup> Department of Oceanic Architecture and Engineering, College of Science and Technology, Nihon University, Japan; <sup>2</sup> JR East Design Corporation, Japan

## ABSTRACT

To preserve sustainable environment, protect resources, and adhere to the basic rule of the international society in the marine environment, the installation of offshore floating fishery bases and the operation of such comprehensive facility are essential. Japan's exclusive economic zone is the 6<sup>th</sup> widest in the world. The most urgent issue is the Tokai earthquake that is predicted to occur within the next 30 years with a probability of 87% and associated tsunamis. Such tsunami damage is feared to impact not only Japan but many countries facing the Pacific Ocean. Thus, the installation of a survey base to accurately capture an occurrence and the scale of tsunami would be an effective measure. This facility is expected to be used for multiple purposes during regular times. One of the functions is a multipurpose harbor. By fishing, processing, and exporting all in fishing grounds in the ocean, work efficiency is improved and greenhouse gas emission is reduced. Furthermore, the present plan is based near the Ogasawara Islands, an area with limited tsunami impact, proposing to be an innovation base that incorporates exploration of various untapped ocean floor resources, ocean thermal energy conversion, and tidal power generation research.

*Keywords: floating base, tsunami monitoring, resource management, marine research, integrated research*

## BACKGROUND

### Reviewing Marine Resources and Promoting New Development

Use of marine resources has been mainly catching of fish and shellfish as part of fisheries. However, in recent years, wind over the sea is being utilized worldwide. With a goal of reducing greenhouse gas emissions to counter climate change, use of seawater itself is being promoted. In addition, there is worldwide research and development on power generation using ocean current and seawater temperature difference, and there is an urgent establishment of technologies and profitability for rare metals in seawater and minerals on the seafloor. As such, there are many marine resources that are not dependent of fish and shellfish, and their development is anticipated.

### Global Fisheries and Aquaculture Production

Global yield in fisheries has dramatically increased since 1990s. In 2000s, the yield continued to grow in China and other Asian countries. China, especially, accounted for 15% of the world's yield at about 14 million tons in 2010 to 2018. In terms of the aquaculture production, China and Indonesia showed most notable increase. China accounts for about 68 million tons while other Asian countries account for about 20 tons. The total accounts for over 70% of the world's yield (Fig. 1).

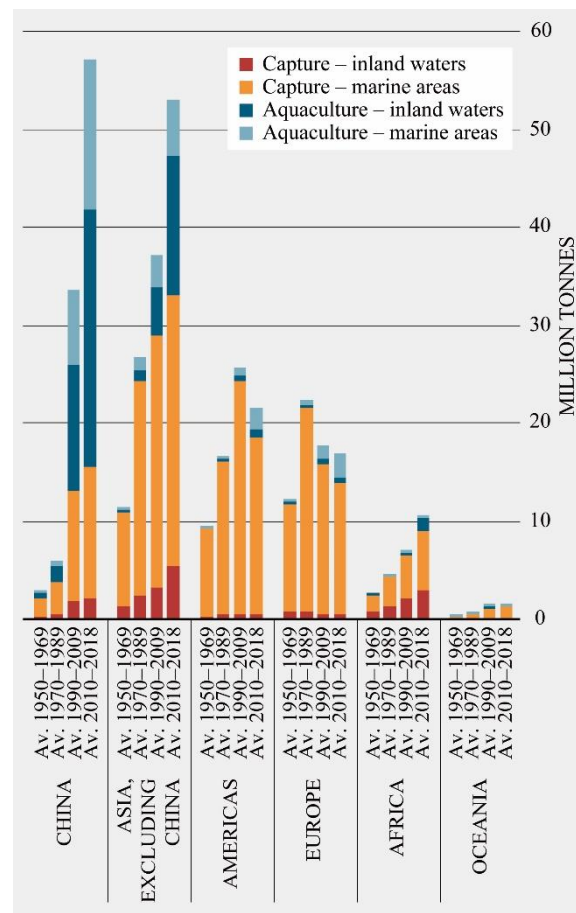


Fig. 1 Changes in the global yield and aquaculture production [1]



### Relationship Between Decreasing Yield and Decreasing Number of Fishery Workers in Japan

Around Japan, there are marine areas with high potential for fishing grounds, such as Northwest and Midwest Pacific Ocean. Furthermore, Japanese EEZ extends about 4.47 million km<sup>2</sup>, which is 12 times Japan's land area, which is the 6<sup>th</sup> widest in the world.

With such favorable fishing grounds, Japan has been operating diverse fishery work on open seas, offshore areas, and coastlines. However, number of fishery workers in Japan was about 152,000 in 2018: 14,000 reduction in the last 20 years. Thus, the average age of fisher workers is high, 56.9 years, clearing showing aging (Fig. 2).

A possible cause of this is the low productivity of the fishing industry. When compared to other countries (2013 fishery census by Ministry of Agriculture, Forestry and Fisheries and 2014 fisheries employment survey)—production per fishing boat of 791.7 (ton/boat) for Iceland, 637.9 (ton/boat) for Norway, and 404.2 (ton/boat) for New Zealand—Japan's production is about 20 times lower at 31.2 (ton/boat). As production per a fishery worker, the difference is about 10 folds as well. As such, this is linked to a decrease in the number of fishery workers.

### Consumption of Fish and Shellfish as Food in Japan

Changes in consumption of fish and shellfish as food per person per year in each major country and region (Fig. 3) shows that Japan is the only country that shows a decrease in the entire graph. In other words, in the last 30 years, the consumption of fish and shellfish in Japan has decreased and work environment for fishery workers has not improved. Hence, fishery workers cannot feel hopeful in the industry.

### Current Situation of the Fishing Industry and Distribution

One of the reasons the future of Japanese fishing industry is grim is the distribution style of fish and shellfish. It is part of Japanese culture to eat fish and shellfish raw, and the main style of distribution is to keep the products raw. This is because, in Japanese food culture, people consume fish and shellfish near the sea where such products are caught. However, today, the complex and diverse distribution structure suppresses profits for fishery workers, where products only arrive to consumers at a high price.

### PLAN POLICY

As such, Japan has considered marine life, such as fish and shellfish, as resources for a long time, but it has become difficult to continue in the same manner.

Under such a circumstance, in this Chapter, we propose the following five items as the plan policies. It means that it is time to stop considering the ocean as the biological resource only.

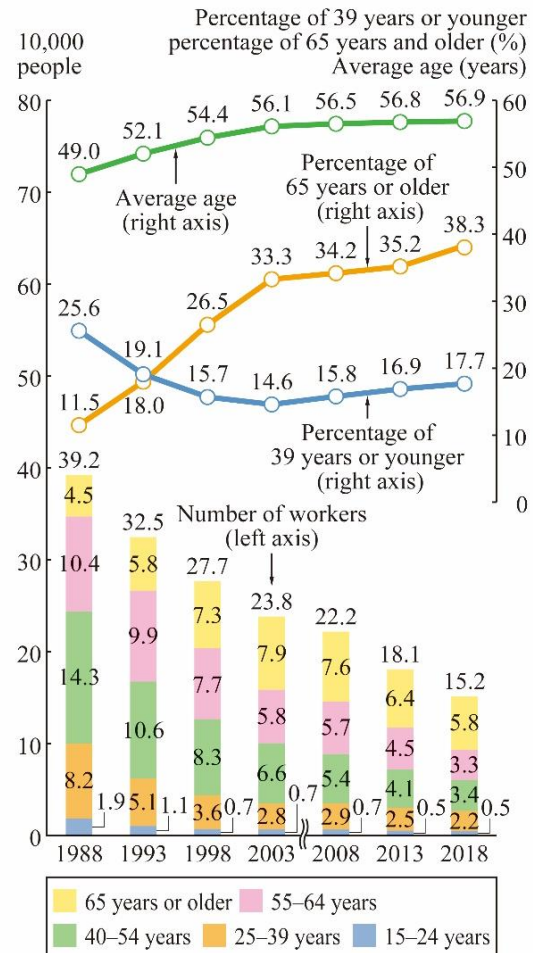


Fig. 2 Changes in the fishery workers [2]

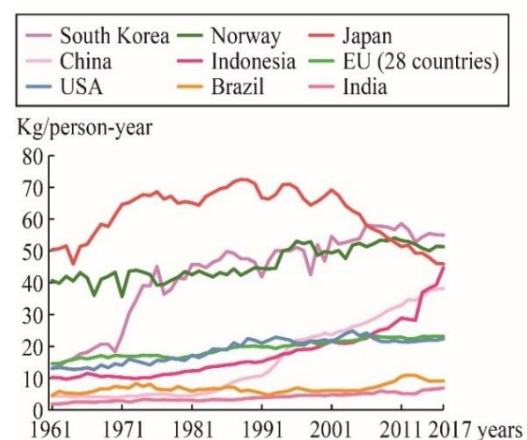


Fig. 3 Changes in the consumption of fish and shellfish per person per year in each major country and region [3]

### **Proposal to Consider the Ocean as a Place of Complex Resources and Use Such Resources Sustainably**

In this paper, we propose to consider diverse marine resources as comprehensive resources. We must build a sustainable system in a comprehensive manner.

As comprehensive marine resources, the energy potential of wind and current might be used. Recently, wind power is being used worldwide. Furthermore, tidal and ocean current power generations are being studied, and Japan's Mitsui O.S.K. Lines, Ltd. is planning to start an operation of an "ocean thermal energy conversion (ocean thermal energy conversion is a renewable power that generates power through a dramatic change in the seawater temperature between the surface and depth)" power plant with a 1,000-kW output by around 2025.

### **Toward Sustainable Fishery Environment**

We propose to change from the traditional fisheries that only caught fish and shellfish to fisheries that starts from production and ends with distribution. This is because wasteless use of fish and shellfish is needed in terms of resource protection. Thus, management based on Hazard Analysis and Critical Control Point (HACCP: A hygiene management in which food businesses understand the risk factors (hazards) such as contaminations and foreign objects and especially manage important processes to remove or minimize risk factors in the entire process from the procurement of raw materials to the shipment of products for securing the safety of products) as a highly hygienic system is needed for production, processing, and distribution. It aims to maintain the entire process as one, from sealed area for cargo handling, cooling, and freezing facilities. In addition, drones are used to shorten the duration of shipping process. In this manner, making the fisheries well managed, fisheries that were unstable due to weather becomes a routine task with stable income.

### **Centralized Management of Fishery Resources**

In the past 20 years, Asian countries have expanded fishing greatly. When comparing the production per fishery worker, large purse-seine, a type of offshore fishery, is about 200 (ton/person), while large fixed-net, a type of coast fishery, is only about 34 (ton/person). Thus, fishery workers appear to be working offshores. To make fisheries a sustainable industry, marine resources must be sustainably maximized, while evaluating resources based on science and appropriately managing the yield based on the evaluation.

In waters around Japan, foreign boats operate in the EEZ while many foreign boats operate in the

waters next to the EEZ based on bilateral agreements. A floating resource-management base for sustainable fishing industry that handles resource management and illegal operation on the sea is necessary.

### **Proposal for the Fishing Industry and Handling of Environmental Burden**

Many ships today were built when there was no environmental measure and have poor fuel efficiency.

International Maritime Organization (IMO) adopted "greenhouse gas reduction strategy" in April 2018. This strategy sets the following numerical goals with 2008 as the reference: (1) improve the fuel efficiency (greenhouse gas emission per amount transported) of the entire international marine transport by at least 40% by 2030, (2) reduce the total emission of greenhouse gases from international transport by at least 50% by 2050, and (3) achieve greenhouse gas emission of zero as early as possible in the present century.

However, demand for marine transport by ships is expected to increase further, where a challenge is how to reduce the environmental burden from ships. Meanwhile, about half (45%) of fishing boats of 5 to less than 9 tons are at least 30 years old as of 2018 (Fig. 4), associated with high environmental burden. In the future, new ships will be built as marine transport increases; thus, the use of small ships should be reduced and transitioned to large ships with less environmental burden.

### **Installation of a Research Base with a New Use on the Sea**

While considering the diverse marine resources as comprehensive resources and building a sustainable system, functions and facilities to research and develop such acquisitions are necessary. In the past marine research, surveys were conducted in field, but experiments were conducted and papers were prepared on land. When researchers and entrepreneurs are present in field, it would promote open innovation to develop marine resources.

For marine development, a facility that functions as a comprehensive center is desired. Some survey ships have such functions, but considering the livability, floating base would be effective.

### **BASIC PROPOSAL PLAN**

#### **Advantage of Integrating Functions (Environment, Safety, Disaster Prevention, and Securing of Resources)**

Going ahead, a place for open innovation by various countries and organizations is essential. To that end, not only diverse researchers and developers but sometimes tourists should also become involved

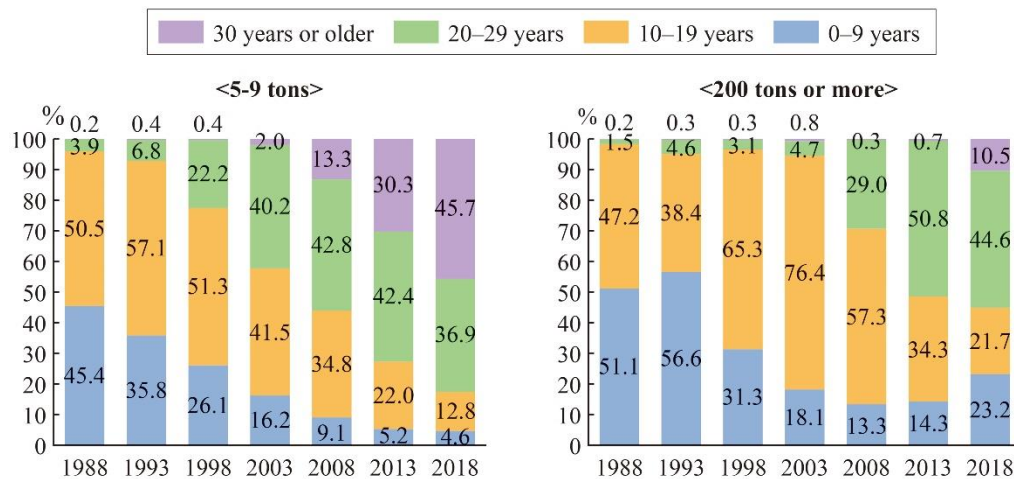


Fig. 4 Percentage of ships by age [4]

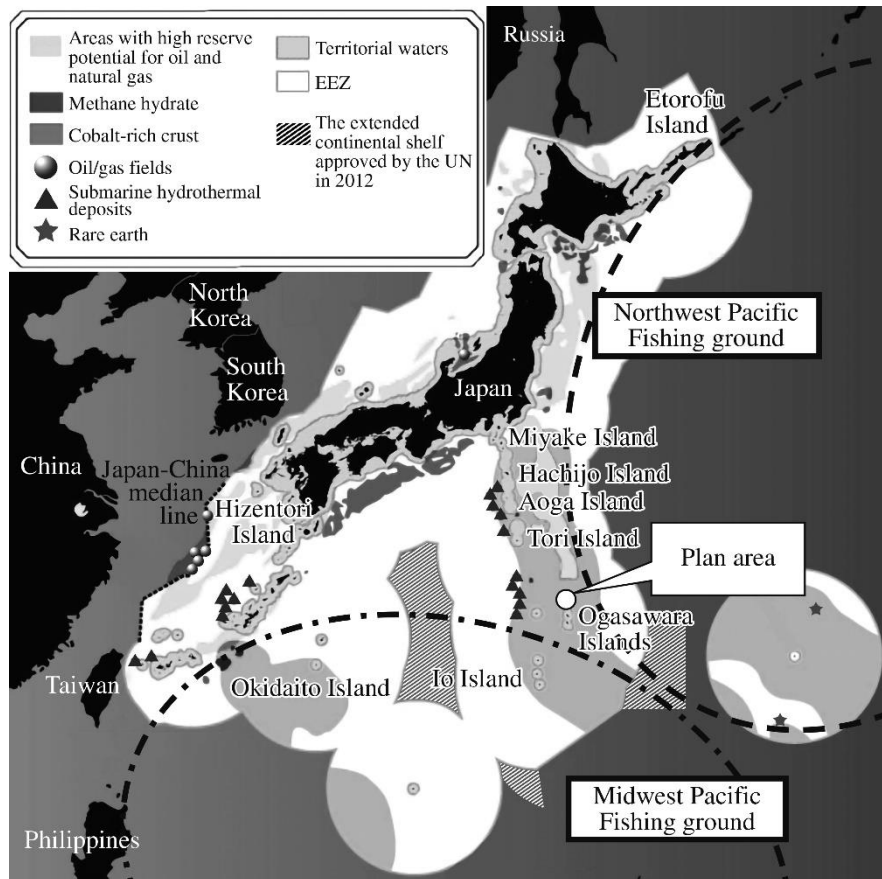


Fig. 5 Relationship between planned area, Japanese EEZ, and fishing grounds [7]

in discussions. The livability of the facility must be improved so that a wide variety of people can visit and stay at the facility

### Role as a Comprehensive Base That Connects the Northwest Pacific and Midwest Pacific Oceans

To manage and utilize the diverse resources of massive oceans, it is important to cooperate with the

fishing industry, which has been regarded as the core industry thus far. Functions should be integrated so that oceans are widely researched and research results are applied to the industry. To that end, we set the Ogasawara Islands and surrounding areas as the planned site to serve as the relay point connecting the Northwest Pacific and Midwest Pacific Oceans, so that people with various purposes can easily access the base (Fig. 5).

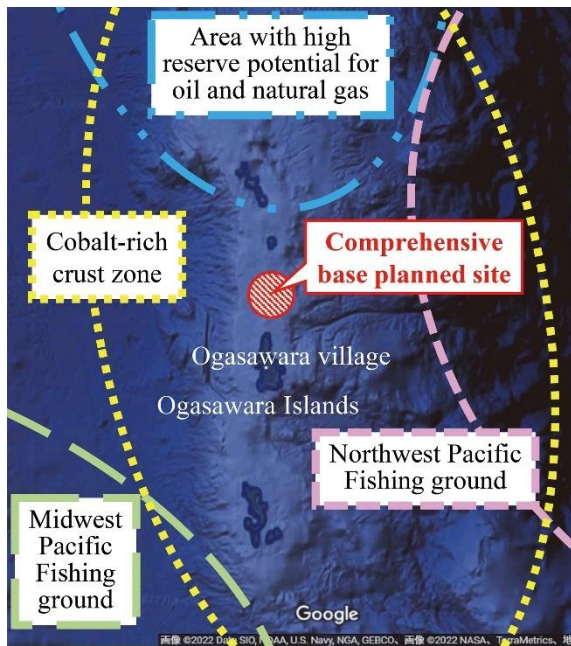


Fig. 6 Locations of ocean floor resources and comprehensive base

The fishing grounds around the Ogasawara Islands are scattered and distributed around the Mukojima Islands, Chichijima Islands, Hahajima Islands, and Ito Islands. These areas are blessed with rich fishing grounds, but there is inadequate infrastructure for the fishery industry. Furthermore, these areas are suited for marine renewable energy through ocean thermal energy conversion where the temperature difference between surface water and deep water remains at least 20°C. These areas also have a high reserve potential for ocean floor minerals and natural gas (Fig. 6).

To improve access to these areas, the access by air must be secured. To that end, runways for planes will be secured by connecting floating structures. In this manner, we aim to further expand the flow of people, items, energy, and information.

### Reusing Used Semisubmersible Rigs

Since the 2000s, the number of oil drilling rigs has dramatically increased with the rise in crude oil prices; however, in the 2010s, older types of drilling rigs have been replaced due to performance. We propose reusing such used drilling rigs. This would be advantageous in terms of the initial investment, leading to environmental considerations as well.

The total number of jack-up rigs, semisubmersible rigs, and drilling ships in operation in the world was 822 as of March 2020. Their operation rate has decreased in recent years due to the spread of COVID-19 and plunging oil prices. Among those, there are about 163 semisubmersible rigs [5].

The pontoon structure of semisubmersible rigs is

below the draft, which makes such rigs less susceptible to waves compared with other ships, providing structural stability. In particular, those built in the 1990s and later can accommodate water depths of 1,000 m or more, allowing for a comfortable living environment well above the surface of the water that is not impacted by waves. A good living environment is essential for attracting various people to the facility [6].

### Response to Typhoons, Earthquakes, and Other Disasters (Eruption of Submarine Volcanoes)

The planned area is close to the S-net (Seafloor observation network for earthquakes and tsunamis along the Japan Trench) and DONET (Dense Oceanfloor Network system for Earthquakes and Tsunamis), Japan's submarine earthquake survey systems. These are inline seafloor observation devices to monitor earthquakes and tsunamis in the Pacific Ocean. By working with such observation devices, the facility plays a role as a relay base to share information on submarine earthquakes, crustal movements, and water level changes to prevent disasters.

### Functions Introduced and Scale Calculation of the Facility

In addition to its main functions as a fishery base, this facility will be equipped with a marine resource management research wing, aquaculture research wing, and marine energy resource research wing as research functions. In addition, there will be an added salon function that connects these functions (Fig. 7).

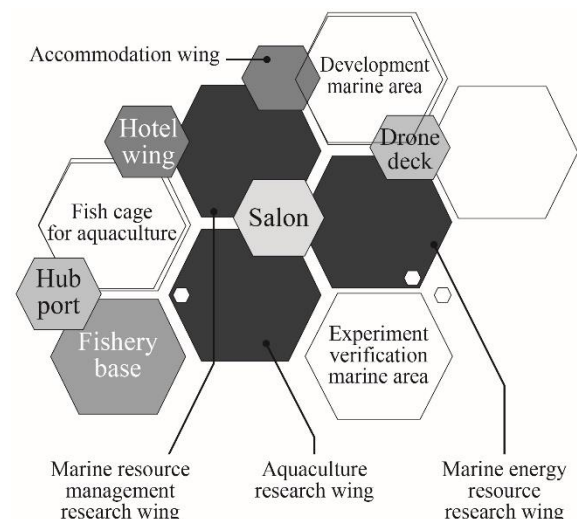


Fig. 7 Plan for the arrangement of introduced functions.



## CONCLUSIONS

1. When considering the issue of climate change as a contemporary challenge, as its impact is wide-ranging, it is necessary for various research results to be cross-sectionally analyzed and examined. By bringing together researchers from various fields and holding comprehensive discussions, the environmental impact can be understood from various aspects.
2. By opening a research venue and providing a place for more comprehensive discussions, joint research and development with various countries will become possible. This, in turn, will lead to the centralized protection of marine resources.
3. By reutilizing used semisubmersible rigs, the initial cost and disposal materials can be reduced. This will also reduce greenhouse gas emissions during the construction of new rigs, in consideration of the environmental issues.
4. By living in a comfortable environment directly connected to marine research areas for a long period of time, research will be further deepened. In addition, we will create a salon facility at the center where researchers from unfamiliar fields and other people can interact with each other, where such interaction with tourists and fishery workers might lead to new ideas.
5. In the future, a network will be created by building many offshore facilities similar to this one. In addition to its role as a fishery evacuation base, it will be possible for it to serve as a disaster response base against tsunamis.

## REFERENCES

- [1] The Food and Agriculture Organization (FAO), *The State of World Fisheries and Aquaculture 2020*, p. 5.
- [2] Fisheries Agency of Japan, *2019 White Paper on Fisheries Trends, Section 2, Changes in Fisheries Structure*, 2020, p. 51.
- [3] Fisheries Agency of Japan, *2019 White Paper on Fisheries Trends, Section 1, Transitions in Japan's Fishing Industry*, 2020, p. 17.
- [4] Fisheries Agency of Japan, *2019 White Paper on Fisheries Trends, Section 2, Changes in Fisheries Structure*, 2020, p. 56.
- [5] Maeda H., The technological history of offshore drilling rigs and the outlook of the future. *Journal of the Japanese Association for Petroleum Technology*. Vol.82, No.5, 2017, pp. 346-354.
- [6] Japan Oil, Gas and Metals National Corporation, *Marine Engineering Handbook* (5th ed.), 2010.
- [7] *Nikkei Business* November 12, 2012, Nikkei Business Publications, Inc., 2012, pp. 40-43.
- [8] Nagatomi K., Sato S., Proposal of floating fishery base for offshore fishery Design of logistics and tourism base off Chichijima in Ogasawara Islands, Summaries of design works of annual meeting, Architectural Institute of Japan, 2019, pp. 430-431.
- [9] Sato S., and Deyama R., Floating Automated Factory System for Effective Utilization of Seabed Resources and Reduction of Greenhouse Gas Emissions, *International Journal of GEOMATE*, In press.
- [10] Sato S., and Yamakage Y., Proposal of a Floating-Type Environmental Purification Facility Incorporating the Function of Tideland, *International Journal of GEOMATE*, Vol. 14, Issue 45, 2018, pp. 78-83.

## STUDY ON THE ALLEY IN THE CITY BASED ON PEDESTRIAN'S IMAGE

Shonosuke Kajita<sup>1</sup> and Kazunari Tanaka<sup>1</sup>

<sup>1</sup>Faculty of Engineer, Osaka Institute of Technology, Japan

### ABSTRACT

In recent years, the depopulation of local cities has become a serious problem. Depopulated areas are experiencing problems such as a decline in economic and social sustainability, stagnation of migration and interaction, and difficulties for tourists and residents to move around. However, due to the impact of the novel coronavirus pandemic since 2020, there is a growing interest in rural migration. Under these circumstances, it is necessary to propose the creation of spaces where people who have migrated to local areas can settle down. Therefore, our initial hypothesis is that a city with many places where people are easily attached would be easier to settle down. In this study, we focused on "streets" in the city and aimed to quantify some of the attachments that people have to the streets. As a research method, we conducted a factor analysis using the Semantic Differential (SD) method to find out what kind of psychology people have toward streets, where the factors that were considered to be related to the "attachment" were determined. In addition, to make the factors more concrete, we defined items that were thought to constitute the factors and conducted a path choice experiment using the one-to-one comparison method for these items. The items the number of people and wall irregularity revealed by the survey were analyzed and discussed, and attempts were made to quantify them.

*Keywords: road, attachment, rural depopulation, rural emigration*

### INTRODUCTION

In recent years, the depopulation of regional cities and their concentration in the Tokyo metropolitan area has become more serious. As a result, urban areas are experiencing various overcrowding phenomena, congestion, problems with waiting children, accidents during events and disasters, and the weakening of local communities. Conversely, depopulated areas are experiencing a decline in economic and social sustainability and difficulties in mobility for tourists and residents due to population outflow. However, the impact of the novel coronavirus infection since 2020 has increased interest in rural migration. By considering the local environment, we believe it is necessary to propose the creation of spaces that will encourage immigrants to settle in rural areas.

### PURPOSE AND METHODOLOGY OF RESEARCH

Creating cities that are attractive and livable for people and where they want to continue to live for a long time is a challenge in suppressing rural depopulation. To create a city that people want to settle in, we thought that "attachment" would be necessary. Attachment means something that people are deeply attracted to, and what they are familiar with. Our initial hypothesis is that a city with many places where people are easily attached would be

easier to settle in. In this study, we focused on the "streets" within the city, which "are the dominant element of the image for many people, and people observe the city as they move about, and other elements are placed and associated along their paths". And by focusing on the attachment that people have to the streets, we aimed to quantify some of the attachments that people have to the streets.

As a research method, we conducted a factor analysis using the Semantic Differential (SD) method to find out what kind of psychology people have toward streets, where the factors that were considered to be related to the "attachment" were determined. In addition, to make the factors more concrete, we defined items that were thought to constitute the factors and conducted a path choice experiment using the one-to-one comparison method for these entities. The items revealed by the survey were analyzed and quantified.

### RESEARCH USING FACTOR ANALYSIS

Using nine photographs of actual roads and eleven different rating scales, we conducted a factor analysis survey using the SD method on 97 university students attending the Osaka Institute of Technology. The rating scale used is shown in Table 1, and the factors got by varimax rotation are shown in Table 2.



Table 1 Rating scale

Narrow	-	Wide
Unapproachable	-	Approachable
Irritating	-	Fresh
Inconvenience	-	Convenience
Secular	-	Tasteful
Old	-	New
Local	-	Urban
Noisy	-	Quiet
Ugly	-	Beautiful
Pale	-	Dense
Feeble	-	Strong

Table 2 Factors obtained

	Functional ity	Emotional ity	Symbolis m
Convenience	0.738	0.288	0.200
Wide	0.705	0.159	0.195
Quiet	-0.481	0.391	-0.448
Beautiful	0.002	0.744	0.214
Fresh	0.155	0.683	-0.012
Tasteful	-0.464	0.490	-0.146
Approachable	-0.187	0.416	0.055
Strong	0.169	0.232	0.727
Dense	0.143	-0.030	0.600
Urban	0.568	0.135	0.570

Based on the structure of the rating scales for each factor, the first factor was "Functionality" because it asks about the convenience and ease of use of the road, the second factor was "Emotionality" because it asks about the aesthetics of the road, and the third factor was "Symbolism" because it is a sensory factor such as powerful and thick. In this study, we focused on "Symbolism" to quantify the emotions of the parts of human attachment that are not related to function or aesthetics.

We named the higher symbolism values as "independent symbolism" and the lower values as "relational symbolism". The reason for this is that in streets with high symbolism, the elements of the city are individually symbolic, while in streets with low

symbolism, the elements are related to each other. In this study, we focused on the relational symbolism and quantified the symbolism. The photos with high relational symbolism had four things in common: few people, plants, shade, and uneven walls, so we investigated these items.

## INVESTIGATION BY ROUTE SELECTION

For the four items identified from the discussion in the previous section, we conducted a route selection experiment using a pairwise comparison method. In this experiment, three different photos were prepared for each item, and for each photo, a contrasting photo was prepared. For example, for the number of people, we prepared three images with few people and high symbolism. Then, we increased the number of people and created contrasting photos with low relational symbolism using Photoshop. Figure 1, Figure 2, Figure 3, and Figure 4 show the results of the path selection process for these six photos.

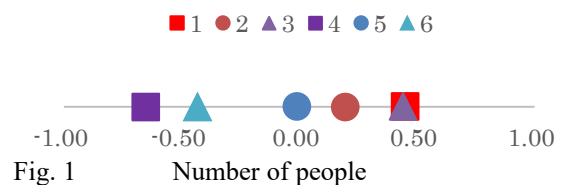


Fig. 1 Number of people

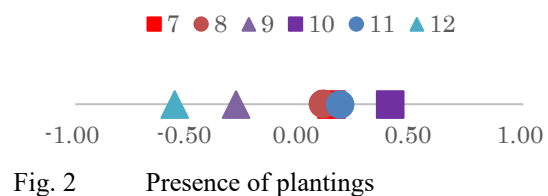


Fig. 2 Presence of plantings

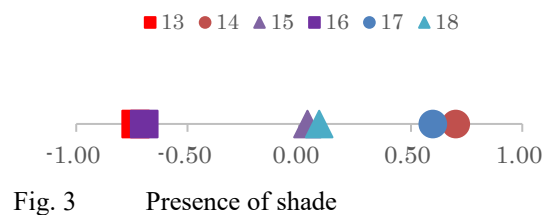


Fig. 3 Presence of shade

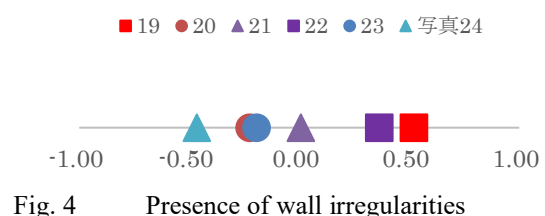


Fig. 4 Presence of wall irregularities

The first three photos in the first half of the six photos in each category were considered to have high relational symbolism before processing, and the latter three photos were contrasting. As a result, it was found that there are certain tendencies in the number of people and the unevenness of the wall. First, "the number of people" indicates that the fewer the number of people, the easier the path is to pass, and

the fewer the number of people in front of you, the easier the path is to pass. Secondly, the "presence/absence of uneven walls" was rated higher for the before and after photos, indicating that the path with uneven walls is more desirable.

For the "people" item, we found that the actual number of people and the percentage of people in the photo had nothing to do with the index we wanted to find. Therefore, we hypothesized that the "percentage of people on the street" might be related to relational symbolism. This time, as a "road" setting we searched for a correlation with a place that could be perceived as a "close space". The reason for this setting was because it was thought that the walls of the street space would be affected, and conversely, people present at the back in the picture would not be affected.

This time, I captured the location from a depression angle. The depression angle is the angle between the direction of gaze and the horizontal plane at eye level when looking down at an object. According to Higuchi, "the visual sense of unity with the harbor or lake is affected by whether or not the line of sight near the  $10^\circ$  angle of elevation stays on the water surface". From this, we hypothesized that the area below the  $10^\circ$  angle of depression could be regarded as a "close space" and examined the relationship between the percentage of people existing in the "close space" and the selection rate. In this study, "close space" is investigated in the range of  $10^\circ$  to  $30^\circ$  depression angle, which is defined as the lower limit of depression angle. In this study, the depression angle is defined as being equally spaced. Since the photograph used in this study had a vertical angle of view of  $57.6^\circ$ , we calculated the angle of elevation in the photograph. Figure 5 shows the relationship with the selection rate.

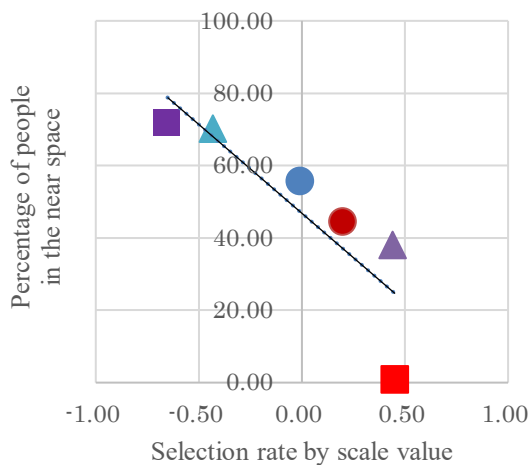


Fig. 5 Percentage of people and selection rate

As a result, there was a correlation between the "percentage of people who do not exist in the area below  $10^\circ$  angle of depression" and the "selection rate by scale value," indicating that the percentage of people who exist in the area below  $10^\circ$  angle of depression is related to relational symbolism. From this, we hypothesized that the simplicity of the ground in "close space" is related to relational symbolism.

Next, for the "unevenness of the wall", we thought that it would be better to have relative complexity above  $10^\circ$  angle of depression than "simplicity below  $10^\circ$  angle of depression". In other words, the more complex the wall was in relation to the ground, the higher the relational symbolism would be.

### EXPERIMENT ON WALL IRREGULARITIES

In the previous chapter, "wall irregularities" could be regarded as "the complexity of materials other than the ground". Next, we will clarify "people's perception of the unevenness of walls".

Wall irregularities can be expressed in various ways, such as color, texture, size, and proportion. In this experiment, we focused on proportion.

In this experiment, we used a video of road space with varying proportions of wall irregularities and asked the participants to stop the screen at the location where they felt the most change while moving around. The video was created so that the subjects would move through the area between the uneven walls, and the experimenter's eye level was set at the height of the center of the wall. Figure 6 shows a portion of the simulated video.

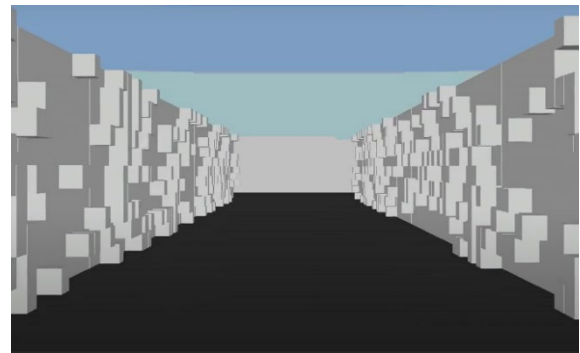


Fig. 6 Simulation for road space experiments

The length of one convex side is 10% of the height of the wall surface, and the number of convex sides within a unit of 10 convex sides and 10 convex sides are varied. The number of convexities was varied in five steps (5, 10, 15, 20, and 25). The positions of the convexities were determined by using random numbers.

Two types of paths were prepared, one with the same width as the wall height ( $D/H=1$ ) and the other with twice the width ( $D/H=2$ ), and the effect of the path width was also examined.

The results of the average and standard deviation of the percentage change in convexity are shown in Table 3 below.

Table 3 Percentage change in convexity

	D/H=1	D/H=2
Average	14.25%	15.50%
Standard Deviation	4.26	5.22

The results show that most people perceive the most change around 15% regardless of the width of the road.

Furthermore, when examining the position at which the video was stopped, it was found that most people (70%) stopped the video when the point of change had passed, that is when they were at the edge of their line of sight. It can be read that most people perceive the convexity to have changed by about 15% at their standing position.

## CONCLUSION

In this study, we used the SD method to analyze the images people have of roads, and three factors were used to express their feelings toward roads. Among them, we examined the attachment to symbolism. In order to quantify "relational symbolism" among the symbolism, we identified items that were considered to be related to it, and conducted a path selection experiment. We found that people were more likely to be attached to paths with fewer people and uneven walls.

In addition, the percentage of people with below the 10° angle of depression on the street was considered to be related to the relational symbolism, as was the complexity of the wall in relation to the ground when it was associated with the unevenness of the wall. In

addition, I would like to quantify the complexity of the wall by examining the photographs and the words of the questions in the one-to-one comparison method, and to quantify the relational symbolism more accurately.

## REFERENCES

- [1] Current regional and local conditions and issues  
[https://www.soumu.go.jp/main\\_content/000629037.pdf](https://www.soumu.go.jp/main_content/000629037.pdf)
- [2] Measures to correct the concentration of people in Tokyo,  
Ministry of Land, Infrastructure, Transport and Tourism  
<https://www.mlit.go.jp/policy/shingikai/content/001374933.pdf>
- [3] The Image of the City, Kevin Lynch, translated by Kenzo Tange and Reiko Tomita, Iwanami Shoten, 1968, pp.56
- [4] Evaluation experiment by SD method  
[http://lbm.ab.a.u-tokyo.ac.jp/~omori/sd\\_assess.html](http://lbm.ab.a.u-tokyo.ac.jp/~omori/sd_assess.html)
- [5] Table of Contents for Using SPSS  
<http://www2.kokugakuin.ac.jp/~ogiso/spss/index.html>
- [6] iid pair-wise comparison  
<https://www.iid.co.jp/service/tool/tool10.html>
- [7] pair-wise comparison  
Psychostatistics by Dr. Sirius  
[http://daas.la.coocan.jp/toukei\\_hosoku/paired\\_comparison.htm](http://daas.la.coocan.jp/toukei_hosoku/paired_comparison.htm)
- [8] Structure of Landscape, Tadahiko Higuchi, Gihodo Publishing, 1975, pp.48

## A STUDY ON THE THERMAL SENSATION OF SHORT-TERM RESIDENTS IN TROPICAL REGION

Kenta Fukagawa<sup>1</sup>, Yoshihito Kurazumi<sup>2</sup>, Ariya Aruninta<sup>3</sup> and Yoshiaki Yamato<sup>4</sup>

<sup>1</sup>Faculty of Science and Technology, Meijo University, Japan; <sup>2</sup>School of Life Studies, Sugiyama Jogakuen University, Japan; <sup>3</sup>Faculty of Architecture, Chulalongkorn University, Thailand; <sup>4</sup>Faculty of Architecture & Structural Engineering, Kure National College of Technology, Japan

### ABSTRACT

Climate change is one of the most serious issues in the recent world. Climate change is known as caused by the increase of carbon dioxide and many of the countries are forced to take measures. The first big measure was the Paris Agreement in 2015, and many countries joined the agreement. According to the agreement, many of the countries declared the major shifts, such as the shift to electric vehicle in the car industry. The biggest concern about the climate change for this moment is the rise of the temperature and it causes more death by heat stroke in summer. It also causes the more usage of air conditioning system and emits more carbon dioxide. It became a serious vicious circle. For that reason, it is important to analyze the mechanism of the human thermal sensation, which can be affected by the environmental history of the person, such as the residential area, the length of stay, and so on. In addition, it is expected that the effect of these histories especially appears strongly outdoors. For that reason, the outdoor experiment targeting the short-term residents was carried out in Bangkok. For the experiment, 5 measuring points were selected. As a result, a different tendency was grasped at one of the measuring points with open sky.

*Keywords: Global warming, Thermal sensation, Thermal discomfort, Image evaluation*

### INTRODUCTION

In recent years, high temperatures in urban areas have become a serious problem. Higher temperatures in urban areas are generally referred to as the heat island effect, and are said to be due to the effects of increased man-made land surfaces and increase of exhaust heat.

In addition, due to the effect of global warming, people in some urban areas are forced to live under extremely high temperature during the summer.

As a countermeasure to this worsening thermal environment, there is an urgent need to curb carbon dioxide emissions on a global scale.

Looking at measures by region, Singapore, for example, is promoting greening under the government's initiative. It is also considered mandating the installation of solar panels on new detached houses in Tokyo to decrease fossil fuel consumption. However, the clear effects of these measures are still expected to take time.

Focusing on the negative effects of this higher temperature in urban areas, the number of deaths due to heat stroke is on the rise and has become a serious problem, especially in Japan.

The death by the heat stroke is caused by losing the balance of body temperature. In addition, the balance of body temperature of human is mainly affected by the heat transfer between human body and the air. However, the thermal sensation of human is also important factor.

For instance, when the thermal sensation reaches to hot, the human body starts to sweat to control the body temperature, then the body temperature is to be adjusted. For that reason, to estimate the thermal sensation is important. However, the thermal sensation can be affected by both physical and psychological factors.

There are many researches targeted physical thermal factors. On the contrary, there are not many researches targeted the psychological factors.

Matsubara et al. [1] focused on sight sense as psychological effect and had experiment on hue-heat and clarified that the effect of visual stimulus causes 0.3 degree centigrade difference.

Kurazumi et al. [2] had research on the effect of artificial and non artificial visual stimulus on human thermal sensation, and mentioned the effect on human's neutral temperature.

Ohno et al. [3] had research on the composite environment of thermal and hue-heat impression, and grasped the interaction on the subject.

Ahmed [4] studied the thermal comfort for the tropical urban environments and showed the importance of development of outdoor comfort model.

According to those researches, it is important to clarify the evaluation tendency on outdoor thermal environment from the psychological aspect, which is human thermal sensation.

When considering the improvement of the

thermal environment, it is common to consider from the perspective of long-term residents. However, especially in a tourism-oriented country like Thailand, it is difficult to reduce accidents caused by heat stroke without considering the thermal environment of short-term residents. In addition, when the residents evaluate the outdoor thermal environment, it is said that the influence of the environmental record up to that point strongly appears.

For that reason, the purpose of this study is to clarify the evaluation tendency of the short-term residents on outdoor thermal environment in Bangkok.

## EXPERIMENT OVERVIEW

The research experiment took place on campus of Chulalongkorn university in 2016 (rainy/wet season) with a group of Japanese university students who just visited Bangkok as a first time as the subjects. The subjects were 11 males and 5 females, for a total of 16 subjects with the clo-value of between about 0.3 to 0.5.

The experiment performed on August 29<sup>th</sup> and 30<sup>th</sup>, which were sunny fine days, during the daytime only from before noon to afternoon. The observation points were selected in the university premises. 4 points were selected by considering surrounding environment such as surface ground condition and sky factors.

### Measurement Procedures

The observation points and route patterns are shown in Fig.1. The subject moved to these four observation points and filled out the declaration vote after staying for 10 minutes in each point. The movement patterns were the two patterns are as shown in Fig. 1. A total of four experiments were performed.

To analyze the sky factors of each observation points, all sky photos are taken in each point. The photos and the sky factors are shown in Fig.2. and Tab.1, and the outline of each measurement points are as follows.

The observation point No.0 is located the semi-outdoor space inside the university building and the sky ratio is very low. The point No.1 is located beside a pond where many trees around so the sky ratio is low but the green ratio is high.

The point No.2 is in the soccer field so the sky ratio is high. The point No.3 is located beside the engineer department building so the sky ratio is low. However, many trees are planted along the building so the green ratio is quite high.

The point No.4 is located near the auditorium where has an artificial square in front. For that reason, the ratio of green is low.



Figure1 Measuring points

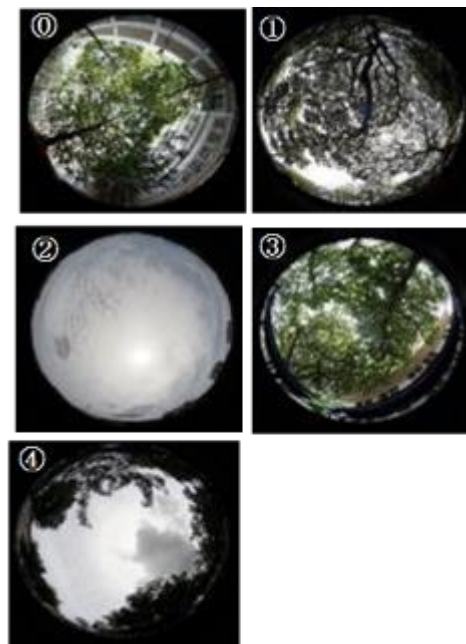


Figure 2 All sky photos of each observation points

Table 1 Ratio of sky factors

Measuring Point	Sky Factor		
	Sky	Non Sky	Green
①Building court	0.14	0.52	0.34
②Pond side	0.25	0.09	0.66
③North playfield	0.88	0.03	0.09
④Engineering bldg side	0.16	0.28	0.56
⑤Auditorium plaza	0.42	0.22	0.36

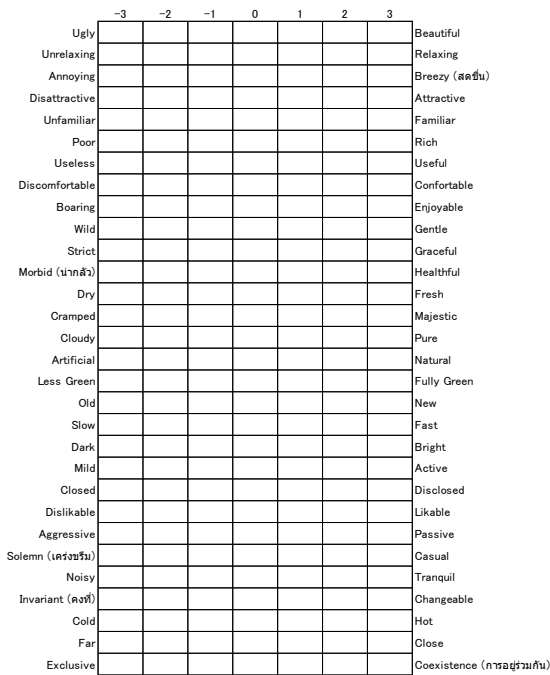


Figure 3 Declaration Vote

### Details of the declaration vote

The declaration vote was utilized for this experiment. The vote is composed of image evaluation part by using SD method and thermal sensation part. SD method part contains 30 adjective pairs with 7 level rating scales by giving the score of +3 to -3 as shown in Fig.3. Line rating scale was utilized for thermal sensation and thermal comfort parts.

### Thermal condition overview

For the experiment, temperature, wind speed, humidity, and ground surface temperature were measured as physical factors. All data were measured at 1 minute intervals. Fig.4 shows the averaged values of each measurement point.

Looking at the temperature data at the time of the measurement, although the highest value is shown at measurement point 2, the difference between the measurement points is extremely small.

Humidity data shows that there is a difference of up to 3% between the measurement points. However, like the temperature, the difference is extremely small.

The wind data of the point No. 2 marked the strongest value, where the sky factor was the largest.

Looking at the value of the ground surface temperature, at the observation point No. 2 was the highest, where the sky factor was the largest. Then followed by the highest value at the point No. 4 where located in the center of artificial square..

By the above results, it is clear that there is no extreme thermal environment at the observation points selected for this experiment.

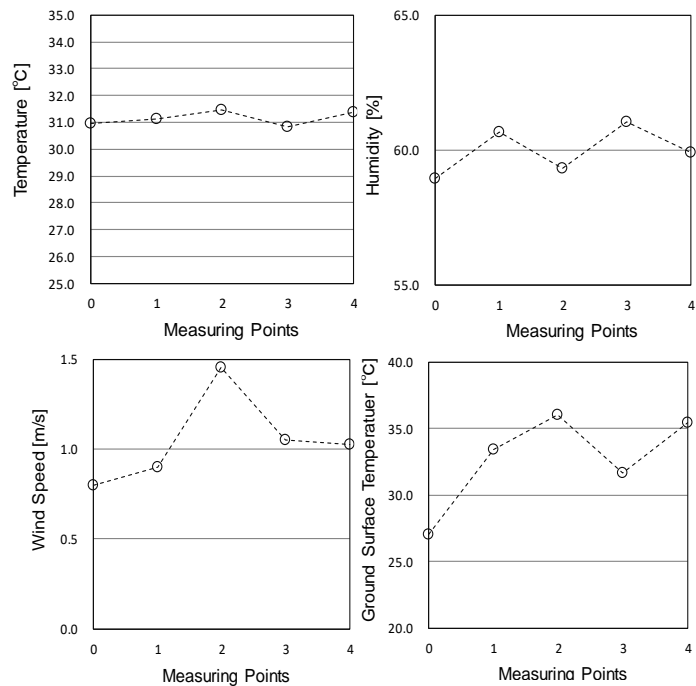


Figure 4 Thermal condition

## EXPERIMENT RESULTS

In this chapter, the results of image evaluation by the SD method and the evaluation results of thermal sensation and thermal discomfort are analyzed.

### Image evaluation result

The result of the image evaluation is shown in Fig.5. The image evaluation scores were aggregated and averaged for each observation point.

The observation point No. 2 shows characteristic results, especially for items such as Bright, Disclosed, and Hot that are presumed to affect the feeling of warmth and cold. This is estimated that the influence of the magnitude of the sky ratio which is the largest at the observation point No.2.

The Observation point No.3 also shows a different tendency from the other observation points in items such as Cramped, Dark, and Closed that express a feeling of openness in space. It is considered that this is due to the small sky factor and the low ability in the visual field range at that point.

The result of the image evaluation suggests that the sky factor, brightness, and the feeling of openness of the space at the time of evaluation may affect the evaluation results.

### Results of thermal sensation and thermal discomfort

The result of averaging the declared values of



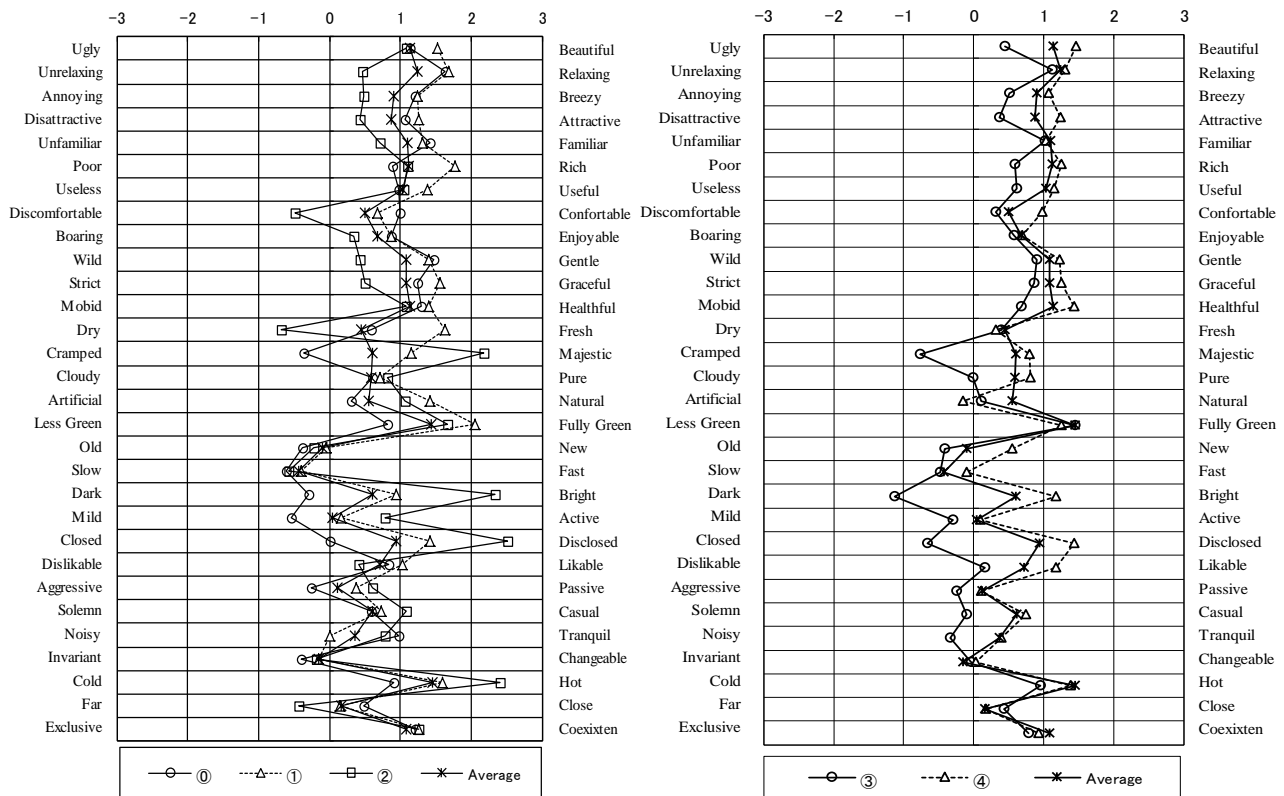


Figure 5 Results of image evaluation

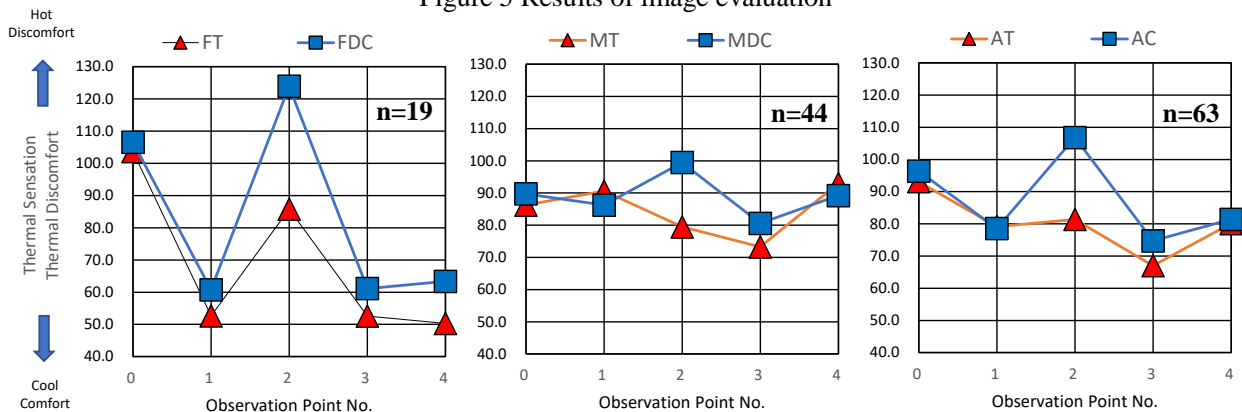


Figure 6 Results of thermal sensation and thermal discomfort vote

※F: Female, M: Male, A: Average, T: Thermal Sensation, DC: Thermal Discomfort

thermal sensation and thermal discomfort by gender and the overall average value is shown in Fig.6. Since the declaration method used in this measurement is the linear rating scale, the fluctuation tendency is more focused rather than the value itself.

Looking at the results declared by females, it can be seen that the results of Thermal sensation and discomfort are generally similar. However, the difference between those results get wider at observation point No.2.

Looking at the results declared by males, the tendency of thermal sensation and discomfort are generally similar.

The results of the male showed the similar tendency to that of female, except for observation point No.2. At this point, the thermal comfort

deteriorates, but the thermal sensation improves.

By the results shown in Fig. 4, there is no significant difference found in physical indicators such as temperature at observation point No. 2 compared to other points.

Therefore, it is considered that the difference of the image evaluation results is influenced by psychological factors rather than physical factors.

## ANALYSIS ON THE IMAGE EVALUATION STRUCTURE

To analyze the tendency of the image evaluation results by the subjects, factor analysis was taken. For the factor analysis, varimax rotation method was

Table 2 Factor loading matrix

Adjective Pairs	Factor	1st Comfort	2nd Sensation	3rd Impression
Unattractive - Attractive		0.83	0.18	0.23
Strict - Graceful		0.76	0.10	-0.02
Unrelaxing - Relaxing		0.72	-0.12	0.19
Annoying - Breezy		0.72	0.06	0.24
Unfamiliar - Familiar		0.72	0.12	0.19
Ugly - Beautiful		0.71	0.30	0.07
Poor - Rich		0.71	0.31	0.00
Wild - Gentle		0.70	-0.09	-0.17
Dislikable - Likable		0.68	0.25	0.20
Mobid - Healthful		0.67	0.30	-0.06
Discomfortable - Comfortable		0.67	-0.10	0.29
Boaring - Enjoyable		0.63	0.19	0.29
Useless - Useful		0.55	0.39	0.19
Cloudy - Pure		0.51	0.40	0.07
Dry - Fresh		0.50	-0.03	0.08
Exclusive - Coexistent		0.42	0.36	0.19
Old - New		0.36	0.20	0.29
Noisy - Tranquil		0.35	0.07	-0.19
Dark - Bright		0.06	0.85	0.10
Closed - Disclosed		0.09	0.84	0.00
Cramped - Majestic		0.17	0.82	-0.12
Mild - Active		-0.05	0.54	0.41
Aggressive - Passive		0.25	0.51	0.36
Cold - Hot		-0.03	0.51	0.00
Solemn - Casual		0.40	0.49	0.15
Less Green - Fully Green		0.37	0.39	-0.24
Slow - Fast		0.16	0.17	0.53
Invariant - Changeable		0.14	0.11	0.46
Far - Close		0.23	-0.23	0.38
Artificial - Natural		0.22	0.30	-0.37

\* Factor scores of higher than 0.37 are highlighted.

taken. Factor analysis was performed on the basis of an eigenvalue of 1.0 or higher, and 7 factors were extracted. Since there was a problem in the interpretation of the 7 factors, the number of factors was fixed at 3 to 6 and the factor analysis was performed again.

The most interpret result was obtained when the factor number is set as 3. The result of setting the factor number as 3 is shown in Tab.2. The factor scores of more than 0.37 are highlighted.

Focusing on the items marked high factor, the first factor is named as “Familiarity” because the items which are relating to comfort, such as “Unattractive - Attractive”, “Strict - Graceful” and “Unrelaxing - Relaxing”, are categorized.

The second factor is named as “Sensation” because the selected items, such as “Dark - Bright”, “Closed - Disclosed” and “Cramped -Majestic” which emphasize human sensation are relating.

The third factor is named as “Impression” because the items such as “Aggressive - Passive” “Slow - Fast”, and “Invariant - Changeable” are related.

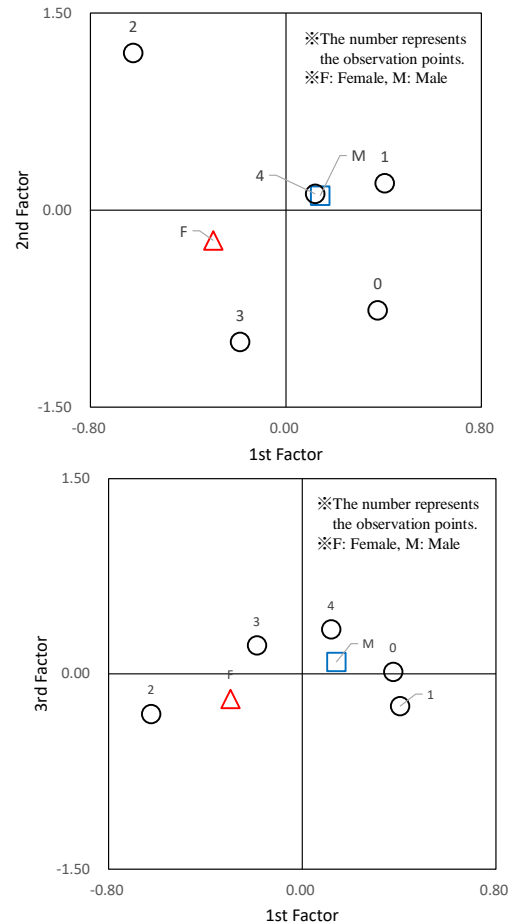


Figure 7 Average factor score by gender and observation point

#### Analysis on the average factor score

In order to analyze the tendency of each of the extracted factors by observation point and by gender, the average points were calculated and plotted.

The results are shown in Fig.7.

By this result, the observation point No. 2 tends to be different from the other points. Furthermore, the differences of the tendency are greater than those of the differences by the gender.

The difference between the items is more obvious between the 1st factor and the 2nd d factor.

In particular, the 2nd factor has a large tendency, suggesting that it may affect the thermal sensation and discomfort.

#### Analysis on the correlation of the image evaluation factors and the thermal discomfort and sensation

In the result of the average factor score, the difference at each point was larger than the gender difference. Therefore, in this chapter, the data is not classified by the gender, but use all the data to examine the relationship between each factor and the thermal discomfort and sensation.

Table 3 Result of correlation analysis

		Thermal Sensation	1st Factor	2nd Factor	3rd Factor
Thermal Discomfort	Pearson Correlation Coefficient	-.684**	-.158*	.358**	.041
	Sample Number	197	196	196	196
Thermal Sensation	Pearson Correlation Coefficient		.306**	-.204**	-.002
	Sample Number		193	193	193
1st Factor	Pearson Correlation Coefficient			-.080	-.231**
	Sample Number			201	201
2nd Factor	Pearson Correlation Coefficient				-.057
	Sample Number				201

\*\*shows advantage at 1 % level. \* shows advantage at 5% level.

The result is shown in Tab.3.

Focusing on Thermal discomfort, the 1st factor showed a significant negative correlation at the 5% level, and the 2nd factor showed a significant positive correlation at the 1% level.

The results of Thermal sensation showed significant results at the 1% level for both the 1<sup>st</sup> factor and the 2nd factor. In addition, the 1<sup>st</sup> factor showed the positive correlation and the second factor showed the negative correlation.

The 3rd factor did not show a significant correlation with thermal discomfort or thermal sensation.

## CONCLUSION

In this study, short time resident was targeted to clarify the evaluation tendency of thermal environment. The obtained results are as below.

- 1) Comparing the results of image evaluation of each measuring point, point “2” showed obviously different tendency.
- 2) By the factor analysis, 3 factors were obtained. In addition, the averaged factor scores of each measuring point, the measuring point “2” showed the highest value in the 2nd factor. Furthermore, the measuring point showed the lowest value in the 2nd factor.
- 3) By the correlation analysis between the obtained 3 factors and the thermal discomfort and sensation, the 1<sup>st</sup> and the 2<sup>nd</sup> factor showed significant correlation.

In summary of the above results, it is confirmed that by understanding the elements that affect the 2nd factor, it is possible to have some influence on thermal discomfort and thermal sensation of the short-term residents.

## ACKNOWLEDGEMENTS

I would like to show my gratitude to whom joined the experiment for your support.

## REFERENCES

- [1] N.Matsubara et al., Kyoto Prefecture University, The Japanese Psychological Association Conference pp.570-571, 2004,
- [2] Y.Kurazumi et al., Sugiyama Jogakuen University, Japanese society of Biometeorology Refereed Journal Vol.48-4 pp.129-144, Psychological effects of the environmental stimuli on thermal sense in outdoor spaces, 2011
- [3] H.Ohno H et al., Nagoyaeiyou college, Architectural Institute of Japan Refereed Journal No.374 pp. 8-18, The Interactions between Thermal Sensation and Hue-Heat Impression Under Various Thermal Conditions, 1987
- [4] K.Ahmed, University of Engineering and Technology of Dhaka, Energy and Buildings Vol 35, Issue 1, pp.103-110, Comfort in urban spaces: defining the boundaries of outdoor thermal comfort for the tropical urban environments, 2003
- [5] K.Fukagawa et al. Hiroshima International University, Architectural Institute of Japan Refereed Journal Vol. 605 pp.91-98, A study on the differences on the formation of the temperature among urban area, rural area and around irrigation ponds in a developing city, 2005
- [6] K.Fukagawa et al. Kyushu Sangyo University, Ecology Environment & Conservation International Journal Vol 23, Suppl. Issue pp. S31-S36, A study on the effect of visual stimuli on human thermal sensation – targeting water landscape, 2017

## THE RECYCLING BIOCHAR BASED-MUSHROOM GROWING MEDIA FOR SOIL ENRICHMENT IN CORN CULTIVATION

Ambar Pertiwinigrum<sup>1</sup>, Margaretha Arnita Wuri<sup>2</sup>, Alva Edy Tontowi<sup>3</sup> and Andang Widi Harto<sup>4</sup>

<sup>1</sup>Faculty of Animal Science, Universitas Gadjah Mada, Indonesia; <sup>2</sup>Center for Energy Studies, Universitas Gadjah Mada, Indonesia; <sup>3,4</sup>Faculty of Engineering, Universitas Gadjah Mada, Indonesia

### ABSTRACT

Climate change and global warming change new farming systems and technologies. Today, urban soil is amongst the most chemically contaminated soil and hence lacks fertility. Soil enrichment through the implementation of charcoal has been introduced for several years. This paper presented investigation results in the implementation of biochar from mushroom growing media for soil enrichment in corn cultivation. The aim of this study is to investigate the use of biochar as a substitute for inorganic fertilizer so that it can give a good long-term impact on the soil compared to inorganic fertilizer. The mushroom growing media was converted to biochar by pyrolysis at a temperature of 500°C for six hours. Biochar is used as soil enrichment with the different addition in soil: P1 (1%), P2 (2.5%), and P3 (5%). These compositions were carried out in polybags with a total mass of 6000 grams of soil for cultivating corn. The growth observation was carried out for 8 weeks until harvesting time. The stem length, root length, and the number of leaves were measured by every week. The addition of 1% of biochar shows the best performance in corn cultivation with a stem length of 125.3 cm or grows two times longer than without the addition of biochar. It's also the best performance in the root length and the number of leaves of 48 cm and 16 cm respectively (more than two times better than without the addition of biochar). It's related to the organic content and the characteristics of biochar in the growing media of corn cultivation.

*Keywords: Biochar, Recycle, Soil Enrichment, Cultivation.*

### INTRODUCTION

Approximately 40 to 50% of the Earth's land surface uses for agriculture activities (for production, cropland, managed grassland, and permanent crops including agroforestry and bio-energy crops). As we know, agriculture releases a significant amount of greenhouse gas emissions (GHG): (1) CO<sub>2</sub> is released from microbial decay or burning of plant litter and soil organic materials, (2) CH<sub>4</sub> is released when organic materials decompose in oxygen-deprived conditions, and (3) N<sub>2</sub>O is released by the microbial transformation in soils and manures. Agricultural land expanded during the last four decades and was driven by the increase in food demand and a growing population. Based on that fact, annual GHG emissions from agriculture are expected to increase in the coming decades. In 2005, agriculture contributed 10-12% of total global anthropogenic GHG emissions [1]. In addition, in 2030, agricultural emissions, especially N<sub>2</sub>O emissions are predicted to increase by 35-60% [1]. N-fertilizer application to intensive agricultural production causes the surplus N in soil and consequently increases N<sub>2</sub>O emissions. Via leaching, run-off, drainage, erosion, volatilization, and nutrients of fertilizer entering the groundwater and surface water that can endanger the ecosystems. Loss of soil particles and nutrients of fertilizer not only affects the quality of surface water and groundwater but also depletes soil fertility,

accelerates soil acidification [2], and climate change. Agricultural N<sub>2</sub>O emissions are predicted to increase up to 35-60% in 2030 due to the increase in nitrogen fertilizer use [3]. It means to prevent the impact of the increase in nitrogen fertilizer on the environment, a solution to overcome the problem must be required.

There are many technological developments to reduce GHG emissions in the agricultural sector, especially the use of nitrogen fertilizer, by environmentally friendly agriculture practices. Anthropogenic soil improvement by the implementation of charcoal has been introduced. The charcoal that is mixed with soil plays a very important role in the maintenance of soil fertility. Biochar, biologically active charcoal, is an environmentally friendly and low-cost porous material that has been widely applied as a soil amendment to increase soil fertility [4]. Compared to other soil amendments, biochar has a high surface area and porosity to absorb and retain nutrients and water and also provides beneficial habitat for microorganisms [5].

The aim of this study is to investigate the use of mushroom-growing media-based biochar as a biofertilizer and its impact. Converting biomass into biochar for land application has been purposed as a possible strategy for climate change mitigation due to the carbon present in the biomass being transformed into a more stable form, thereby resulting in lower CO<sub>2</sub> emissions [6].

In this study, recycling biomass by converting

mushroom-growing media into biochar also leads to a circular economy concept in agriculture. It's different from a linear economy that uses the concept "take-make-dispose", in a circular economy, the use of resources, energy, and waste can be minimized

## METHODOLOGY

This study was conducted in Centre for Innovation of Agrotechnology, Universitas Gadjah Mada. The material used in this study were the used baglog mushroom or mushroom growing media, *Zea mays* seeds, pyrolysis reactor, and polybags.

### The Converting Mushroom-Growing Media Into Biochar

The first, mushroom baglogs were separated from the packaging. Then mushroom-growing media was placed in the container and stirred until homogenous. The homogenous media was put in the pyrolysis reactor and converted into biochar at 500 °C for six hours.

### The Application Mushroom-Growing Media-Based Biochar as Soil Amendment

Samples were treated and divided into four groups media with three replications. Treatment P0 as control has a soil composition of 6000 grams of pure soil without the addition of biochar. Treatment P1, P2, P3 has soil composition by adding biochar 1% (60 grams), 2.5% (150 grams), and 5% (300 grams) of biochar respectively (Fig. 1). After that, *Zea mays* seeds (every three seeds) were grown on these soil samples. These samples were maintained by watering every 07.00 AM o'clock and 05.00 PM 0'clock for eight weeks. Observation by the measurement of root length and number of leaves was conducted every week. The measurement of water content, ash content, and C/N ratio of biochar also were carried out in this study. Total C-organic also was carried out by Walkey and Black method.

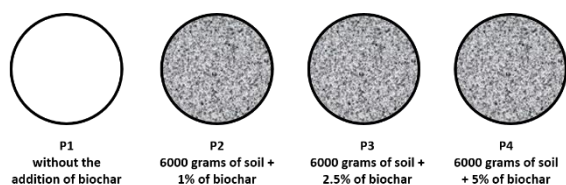


Fig. 1 The growing media samples

## RESULTS AND DISCUSSION

The conversion of mushroom-growing media into biochar by pyrolysis has been conducted at a

temperature of 500 °C for six hours. In this study, biochar was analyzed the water content because water and ash become a good habitat for microorganisms for plant growth. Based on the result of water content analysis, biochar has a water content and ash content of 14.85 and 5.01% respectively. Compared to the other report [7], there is no significant difference in which biochar usually has water and ash contents in the range of 25-65% and 1-13% respectively. Biochar also has a total C-organic of 41.02% where the value is equivalent to the standard compost for fertilizer. Although biochar is not a product of the composting process, its total C-organic is suitable as an additional fertilizer in the growing media [8]. It means that the addition of biochar in soil amendment has the potential to improve soil quality.

To investigate the impact of the addition of biochar on the plants, the experiment by the addition of biochar in soil for *Zea mays* growth was conducted. We maintained the growth of *Zea mays* by watering twice a day. Sirait [9] reported that *Zea mays* requires adequate amounts of water for the growth and development process. Observation has been done for two months to investigate the growth process represented by height, length of root, and the number of leaves [10]. The results in the height of *Zea mays* plants are shown in Table 1.

Table 1 The height of *Zea mays* plants in the different soil treatments

Week	P0	P1	P2	P3
1st	20.3	18.6	19.6	20.6
2st	30.6	34.3	30.6	28
3rd	47.3	55.6	54.3	48
4th	51.6	69.6	64.6	62
5th	53.6	82.6	68.3	66.6
6th	57	97	77.3	72.6
7th	61.3	111	86	81.3
8th	63	125.3	89.6	86

The height was measured from the butt of the stem to the internode of the last trunk before flowers. The data in Table 1 is then plotted in graphic in Fig. 2 so that the growth pattern is visible clearly. All samples show growth day by day for eight weeks. For P0, *Zea mays* that were applied with pure soil have the slowest growth compared to other samples. The growth of *Zea mays* underwent accelerating growth after applying biochar. The fastest and highest growth was performed by *Zea mays* that were applied to the soil with the addition of 1% of biochar. After eight weeks of growth time, *Zea mays* in P1 (with the addition of 1% biochar) grew up significantly with a length of 125.3 cm. The second fastest and highest growth was performed by sample P2 with a length of

89.6 cm after eight weeks of growth time. Almost the same pattern results also occurred in the sample P3 with a length of 86 cm after eight weeks.

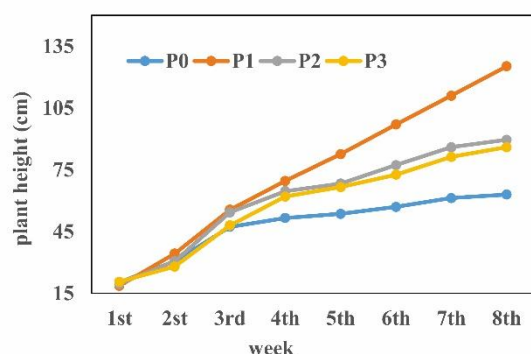


Fig. 2 The length of *Zea mays* plants in the different soil treatment

The measurement of the number of leaves and the length of the roots also was carried out in this study as an indicator of the positive impact of the addition of biochar. The results showed in Table 2.

Table 2 The number of leaves and length of roots of *Zea mays* plants in the different soil treatments after eight weeks of growth time

Growth indicator	P0	P1	P2	P3
Number of leaves	19	48	31	21
Length of roots	5	16	11	8

After eight weeks of growth time, samples P0, P1, P2, and P3 have 19, 48, 31, and 21 leaves respectively. The value is twice sampled P0. The same phenomenon also occurred in the length of roots. After eight weeks of growth time, samples P0, P1, P2, and P3 have lengths of the root of 5, 16, 11, and 8 cm respectively. Based on Table 2, the most leaves number and the longest root were found in sample P1 which was given the addition of 1% biochar. These values, both the number of leaves and the length of roots, are twice sampled P0.

The results showed that there is a correlation between the addition of biochar and the growth *Zea mays*. The addition of biochar in the soil has an important role to enhance soil fertility. Leila [11] analyzed the impact of biochar addition on enzymatic activities. Leila's report said that biochar increased the enzymatic activities due to the increase in organic C and/or total N. the increase in the enzymatic activities is an indicator of microbial biomass stimulation since most of the enzymes are produced by soil bacteria. It can also be concluded that the

addition of biochar composition impacted the microorganism abundance and community involved in enzyme synthesis [12]. It also can be explained due to biochar amendment contributes to the high carbon in soil composition and promotes enzyme synthesis and stimulates seed germination [13].

## CONCLUSIONS

In this study, the use of 1% biochar shows the best performance in the growth of *Zea mays* plants. But, with the addition of 2.5% and 5% biochar (P2 and P3) the growth capability reduced if the results were compared to P1. The addition of 2.5% and 5% shows results that are not quite different from each other even though it still showed better results than the control (P0).

The conversion of mushroom-growing media into biochar is a promising material to be used in agriculture, due to the possibility of biochar's properties to retain water, and nutrients, and give a beneficial impact on the growth rate of *Zea mays* plant. Despite the study being a preliminary study, the results concluded that the amendment soil strategy can be considered the use of waste-based biochar. The utilization of waste-based products as soil amendment also leads to accelerating circular economy implementation in agriculture. The impact of biochar on enzymatic activities in soil composition and crop yield must be investigated in further study.

## ACKNOWLEDGMENTS

In this study, it is impossible to thank everyone individually, so we give our thanks to many people and individuals who have assisted us over the years, and to the colleagues, students, and volunteers who have similarly offered their support. We also wish to express our sincere thanks to the Directorate General of Higher Education, Ministry of Education and Culture for its funding and support grant.

## REFERENCES

- [1] Pete S. and Daniel M., Agriculture in Climate Change 2007: Mitigation, 1st ed. Cambridge University Press, 2007, pp.499-540.
- [2] Chia-Hsing L., Chung-Chi W., Huan-Hsuan L., Sang S.L., Daniel C.W.T., Shih-Hao J., and Yong S.O., In-situ Biochar Application Conzss serves Nutrients while Simultaneously Mitigating Runoff and Erosion of a Fe-Oxide-Enriched Tropical Soil. Science of The Total Environment, Vol. 619-620, 2018, pp.665-671.
- [3] Food Agriculture Organization (FAO), World Agriculture: Towards 2015/2030 an FAO Perspective, 2003, pp.97.
- [4] Mao Y., Mingming S., Yanfang F., Jinzhong W.,



- Shanni X., Da T., Yu Z., Jun W., Huixin L., and Xi J., Effect of Biochar Amendment on The Control of Soil Sulfonamides, Antibiotic-Resistance Bacteria, and Gene Enrichment in Lettuce Tissues. *Journal of Hazardous Materials*, Vol. 309, 2016, pp.219-227.
- [5] Josiah H., Micahel D., Dwight S., and Andrew K., The Basics of Biochar: A Natural Soil Amendment. *Soil and Crop Management*, 2010, pp.1-6.
- [6] Fernanda R.O., Anil K.P., Deb P.J., Sushil A., Hui L., and Samir K.K., Environmental Application of Biochar: Current Status and Perspectives. *Bioresource Technology*, Vol. 246, 2017, pp.110-122.
- [7] Neneng L.N., Potency of Utilizing Biochar for Dryland Rehabilitation in Indonesia. *Journal of Land Resources Special Edition*, 2014, pp.57-68.
- [8] A. Soleymani, Safflower (*Carthamus tinctorius L.*) Seed Vigor Tests for The Prediction of Field Emergence. *Industrial Crops and Products*, Vol. 131, 2019, pp.378-386.
- [9] Juniar S. and Kriston S., A Selected *Stenotaphrum secundatum* as Superior Shade Tolerant Forage Resource. *Indonesian Bulletin of Animal and Veterinary Sciences*, Vol.30, Issue 2, 2020, pp.103-111.
- [10] Diah E. and Mochamad N., The Growth of Maize Crop (*Zea mays L.*) BISI-2 Variety on Non Rejected Sand at Pantai Trisik Kulon Progo. *Journal of Human and Environment*, Vol.18, Issue 3, 2011, pp.220-230.
- [11] Leila E., Ahmed A.A., Salah J., Hanene A., Evan A.N.M., Camelia M.G., and Mejdi J., Application of Olive Mill Waste-Based Biochar in Agriculture: Impact on Soil Properties, Enzymatic Activities and Tomato Growth. *Science of The Total Environment*, Vol. 755, 2021, pp.1-11.
- [12] Martin S., Andreas S., Kilian E.C.Smith., Moritz N., Martina R., and Joost T.V.D., Comparing Straw, Compost, and Biochar Regarding Their Suitability as Agricultural Soil Amendments to Affect Soil Structure, Nutrient Leaching, Microbial Communities, and The Fate of Pesticides. *Science of Total Environment*, Vol. 751, 2021, pp.1-19.
- [13] Sandeep K.V., Ashok K.D., Saikat G., Vinay K., and Ekrem G., Applications of Carbon Nanomaterials in The Plant System: A Perspective View on The Pros and Cons. *Science of The Total Environment*, Vol. 667, 2019, pp.485-499.

## STRATEGIES FOR INCREASING ACCESS TO WATER AND SANITATION IN A WATER-SENSITIVE AREA

Shella Zahrawani<sup>1</sup>, Ahmad Soleh Setiyawan<sup>1</sup>, Prasanti Widyasih Sarli<sup>1</sup>, Prayatni Soewondo<sup>1</sup>, and Dion Awfa<sup>2</sup>

<sup>1</sup>Faculty of Civil and Environmental Engineering, Institut Teknologi Bandung, Indonesia;

<sup>2</sup>Department of Environmental Engineering, Institut Teknologi Sumatera, Indonesia

### ABSTRACT

Manado city, Indonesia is a water-sensitive area because it is a disaster-prone area located on the riverside, seaside, and hills and has low access to water and sanitation. This study aims to develop a strategies to increase access to safe and sustainable water and sanitation in water-sensitive areas. The methods of EHRA (Environmental Health Risk Assessment) and SWOT (Strength, Weakness, Opportunity, and Threat) were used to analyze existing conditions and to develop strategies in the study area. As results, 76.33% of the community used refilled water for drinking, 37.67% of the community used portable water for bathing and washing, 73% of the community used latrine for feces collection, and 91% of the community managed solid waste by collecting and transporting it to the landfill. The results of the SWOT analysis show that the weights of strengths, weaknesses, opportunities, and threats were 3.632, 0.787, 1.756, and 1.594, respectively. Strategies to increase access to water and sanitation in a water-sensitive area were enforcing regulations, establishing a special supervisory, building facilities and infrastructure, and conducting socialization with the community. Implementing strategies based on strengths and opportunities is the best approach in increasing access to safe and sustainable water and sanitation in water-sensitive areas.

*Keywords: Increasing strategies, Water-sensitive area, Water, Sanitation*

### 1. INTRODUCTION

The high rate of urbanization, increasing population growth, and changes in water consumption patterns have resulted in a decrease of water quality and quantity [1] can threaten the sustainability of an area. This phenomenon will also have an impact on decreasing environmental sustainability. It is trigger the emergence of water-sensitive areas. Water-sensitive areas are characterized by areas sensitive to water sources, sanitation, disaster-prone areas, and densely populated communities with an informal economy [2]. This of course will have an impact on health.

Manado City is a disaster-prone area because it is located on the riverside, seaside, and hills. Data related to water and sanitation management in water-sensitive areas are relatively few, not up-to-date, and not discuss in detail. In 2019, the access to improved drinking water and sanitation were only 13.81% and 88.72% of households [3]. It is a challenge for Manado City Government to achieve SDGs 2030. One of the ways to achieve the target is to develop a strategies based on existing conditions.

One of the methods for developing strategies is the Strength, Weakness, Opportunity, and Threat (SWOT) analysis. SWOT analysis is the method most often used in formulating strategies. Therefore, this study will be carried out identification of the existing condition of water and sanitation in water-sensitive areas in Manado City as the basis for developing a strategy to increase access to water and sanitation.

### 2. STUDY AREA

The study was conducted in three water-sensitive areas in Manado City, namely (1) the Singkil Satu Area (Lingkungan 2) in Singkil Subdistrict is the hills area, thus, it is prone to erosion and is a densely populated, (2) the Wawonasa Area (Lingkungan 2) in Singkil Subdistrict is the riverside area of Tondano river, thus, it is prone to flooding and is a densely populated, and (3) the Titiwungen Utara Area (Lingkungan 2 and 3) in Sario Subdistrict is the seaside area of Sulawesi sea, thus, the potential for ROB flooding. The selection of the study areas are based on (1) the Decree of the Mayor of Manado Number 163/KEP/LT.02/Bappeda/2015, which are slum areas in Manado City, and (2) Deltares data where the areas are in a water-sensitive area.

### 3. METHODOLOGY

#### 3.1 Data Collection

Primary data was conducted using a random sampling. The secondary data was used to support the primary data, such as demographic and regulations. The questionnaire was adopted from the EHRA study [4] to describe water and sanitation management. Yamane formula was used to determine sample size:

$$n = \frac{N}{1 + Ne^2}$$

n = sample size (93 households)  
N = population size (1,345 households)  
e = margin of error (10%)

SWOT analysis was used to develop a strategy to increase access to water and sanitation. SWOT analysis was a management tool usually carried out in a corporate strategic plan to develop a company's strategic plan [5]. The SWOT analysis was used because this tool helps to identify the positive points or strengths, overcome weaknesses, increase opportunities, and check risks to avoid threats, therefore, allowing for better decision making [6]. SWOT analysis was carried out through a SWOT analysis questionnaire. Therefore, thirteen (13) stakeholders who responded were know about water and sanitation management in the study area. Strategy determination was obtained by assessing each strength and weakness which were included in the Internal Factor Analysis Summary (IFAS) matrix as well as opportunities and threats which were included in the External Factor Analysis Summary (EFAS) matrix. Assessment of each SWOT aspect was carried out by weighting of 1-5 and rating 1-4 for each IFAS and EFAS. The weight was the weight total of each aspects divided the weight total and the final total weight must be 1. The rating was the rating value of each aspects divided the respondents total. The total score for each factors was obtained by multiplying the weights and ratings. In the SWOT analysis diagram, there is an x-axis (IFAS) was the difference between the score of strengths and weaknesses, and a y-axis (EFAS) was the difference between the score of opportunities and threats. The coordinates of the x and y axes were plotted to a SWOT analysis diagram to know the quadrant position to formulate a strategy [7].

### 3.2 Data Analysis

Close-ended questions data and SWOT results were analyzed using descriptive statistics, processed, and illustrated using Microsoft Excel. The information gained, supported with documentation from direct observation, was used to describe the existing condition of water-sensitive areas.

## 4. RESULTS AND DISCUSSION

### 4.1 Clean Water and Drinking Water Management

The Joint Monitoring Program (JMP) divided water access into drinking water from improved sources or unimproved sources [8]. Improved water sources categories: (1) safely managed: "drinking water from an improved water source which was located on-premises, available when needed and free from fecal and priority chemical contamination", (2) basic: "drinking water from an improved source, the collection time was not more than 30 minutes", and (3) limited: "drinking water from an improved source, the collection time exceeds 30 minutes" [8]. The use

of clean water and drinking water sources in the study site can be seen in Figure 1 and Figure 2.

Figure 1, it shows that the main sources of clean water for hygiene (washing and bathing) were portable water in the hills area (49%) and riverside area (48%). Meanwhile, in the seaside area was bore well water (36%). However, in the riverside and seaside area, there were 4% and 3% of the community use unprotected dug well water. Figure 2, it shows that the main source of drinking water was refilled water (75%). However, in the seaside area, there was 3% of the community use unprotected dug well water.

Access to basic drinking water in hills, riverside, and seaside area were 90%, 95%, and 95%, respectively. Access to limited drinking water in hills, riverside, and seaside area were 10%, 5%, and 2%, respectively. In seaside area, there was 3% unimproved access to drinking water. The riverside and seaside areas has better basic access to drinking water. The community living on the riverside and seaside areas has easier access to get-and it is closer to the water sources. Meanwhile, the community in the hills area must try harder to get water sources. In addition, the soil structure of the hills area in the study site was dominated by rocks.

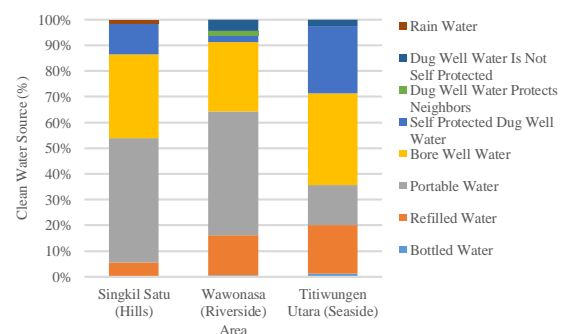


Fig. 1 Clean water sources in the study area

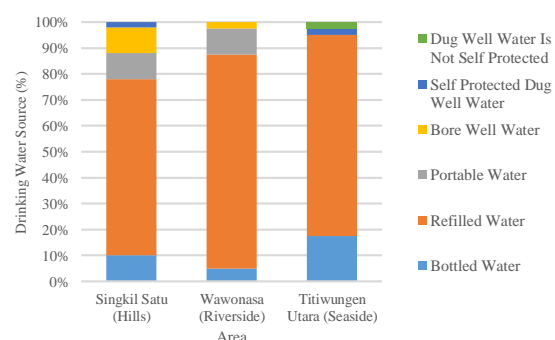


Fig. 2 Drinking water sources in the study area

### 4.2 Domestic Wastewater Management

Wastewater management that was inadequate and maintained can caused pollution of surface and groundwater with serious health impacts [9]. The

construction of toilets was not a solution to achieving the SDGs, but the strategy must focus on the collection and treatment of human feces to achieve a safe sanitation system [10]. When onsite sanitation technology was full, then there were several considerations: (1) emptying it, (2) stopping using the onsite sanitation technology, and (3) constructing a new onsite sanitation technology [10]. Domestic wastewater management can be seen in Table 1.

In the study site, more than 95% of the community had a private toilet. However, only 21-25% of the community who has self-construction septic tanks carried out periodic desludging. There were two ways of emptying, namely manual emptying and mechanical emptying [10]. In the study area, the emptying of fecal sludge using mechanical emptying from privately owned feces trucks. In the seaside area, there were 10% of the community discharged wastewater to the Wastewater Treatment Plant (WWTP), because the location was close to the WWTP in Megamas Area in Manado City. However, WWTP was also not functioning optimally. Access to basic sanitation in the hills, riverside, and seaside area were 96%, 95%, and 100%, respectively. In hills area, there was 4% unimproved access to sanitation and in

riverside area, there was 5% limited access or shared to sanitation. In general, fecal sludge management in the study site was unsafely managed sanitation.

#### 4.3 Solid Waste Management

The unsorted solid waste at the source, social taboo, citizen's attitude, poor assessment, inadequate potential strategies unorganized informal sector of waste, unplanned fiscal, and poor implementation of government policies were the challenges of municipal solid waste management (MSW) [11].

In general, the solid waste was managed by collecting and transporting it to the landfill (85-100%). However, in the hills area, there were 10% of the community burned solid waste and in the seaside area, there were 8% of the community disposed to the hospital because the location was very close to Pancaran Kasih Hospital. The frequency of solid waste transported was carried out every day (92.33%). The solid waste sorting was carried out in the hills area (20%) and the seaside area (7%). The solid waste retribution set by the Manado City government was IDR 20,000-50,000 per month according to the building type.

Table 1. Domestic wastewater management in the study area

Sanitation Chain	Criteria	Area		
		Singkil Satu (Hills)	Wawonasa (Riverside)	Titiwungen Utara (Seaside)
User interface	Toilet ownership	96% private toilet	95% private toilet	100% private toilet
	Toilet type	100% gooseneck		
	Defecation location	<ul style="list-style-type: none"> <li>96% private toilet</li> <li>4% neighbor/relative toilet</li> </ul>	<ul style="list-style-type: none"> <li>95% private toilet</li> <li>5% MCK/public toilet</li> </ul>	100% private toilet
Containment	Final disposal of feces	<ul style="list-style-type: none"> <li>92% latrine</li> <li>8% septic tank not impermeable</li> </ul>	<ul style="list-style-type: none"> <li>65% latrine</li> <li>35% septic tank not impermeable</li> </ul>	<ul style="list-style-type: none"> <li>58% latrine</li> <li>30% septic tank not impermeable</li> <li>10% WWTP</li> <li>2% unknown</li> </ul>
Emptying/Collection	Periodic desludging of feces	25%	21%	25%
Transport	-	Privately owned feces trucks on-call		
Treatment and Reuse/Disposal	-	Discharged into the ground or river without adequate treatment unit		

Table 2. Flood incidences in the study area

Criteria	Area		
	Singkil Satu (Hills)	Wawonasa (Riverside)	Titiwungen Utara (Seaside)
Flood incidences	98% never	60% several times a year	40% several times a year
Flood height	Adult heels	Adult knee	Adult heels
The flood dries up	1-3 hours	Half-day	1-3 hours

Table 3. IFAS matrix calculation in SWOT analysis in the study area

INTERNAL FACTORS		Weight	Rating	Score
<b>STRENGTHS</b>				
Clean Water and Drinking Water				
1	The community has access to water sources	0.129	3.615	0.465
2	There are regional regulations related to clean water/drinking water	0.158	3.692	0.583
Domestic Wastewater				
1	Almost the community (97%) has a private toilet	0.117	3.308	0.387
2	There are local regulations related to wastewater management	0.155	3.846	0.596
Solid Waste				
1	The community is willing to pay solid waste retribution	0.143	3.538	0.507
2	There are local regulations regarding solid waste management	0.167	3.769	0.628
Drainage				
1	Adequate drainage construction	0.132	3.538	0.466
<b>Total Strengths</b>				3.632
<b>WEAKNESSES</b>				
Clean Water and Drinking Water				
1	The water sources that are not pipelines are not protected	0.105	3.385	0.354
2	The community uses groundwater as the main source of water for hygiene	0.137	3.462	0.473
Domestic Wastewater				
1	The fecal sludge treatment system still uses latrine and self-constructed septic tanks that are not impermeable	0.121	3.077	0.371
2	Grey water is discharged into the drainage	0.129	3.231	0.416
Solid Waste				
1	All solid waste is directly transported to the TPA	0.115	3.385	0.390
2	There is no processing of solid waste before it is disposed into the TPA	0.129	3.308	0.426
Drainage				
1	Grey water mixes with rainwater runoff	0.139	3.308	0.461
2	Insufficient drainage capacity	0.126	3.308	0.417
<b>Total Weaknesses</b>				0.787
<b>Total Strengths-Weaknesses (x-axis)</b>				2.845

Table 4. EFAS matrix calculation in SWOT analysis in the study area

EXTERNAL FACTORS		Weight	Rating	Score
<b>OPPORTUNITIES</b>				
Clean Water and Drinking Water				
1	The community is willing to pay clean water fees	0.172	3.538	0.608
2	The community is willing to be given socialization and training	0.186	3.692	0.685
<b>OPPORTUNITIES</b>				
Domestic Wastewater				
1	The community knows the dangers of feces without proper management	0.155	3.538	0.547
2	Some communities have carried out feces desludging	0.155	3.385	0.523
Solid Waste				
1	Some communities do solid waste sorting	0.162	3.385	0.547
Drainage				
1	The WSUD urban planning concept integrates the sustainable water cycle	0.172	3.462	0.595
<b>Total Opportunities</b>				1.756

EXTERNAL FACTORS (Continued)		Weight	Rating	Score
<b>THREATS</b>				
Clean Water and Drinking Water				
1	Prone to floods and landslides	0.170	3.538	0.600
2	Water continuity is not guaranteed	0.159	3.385	0.539
Domestic Wastewater				
1	Limited land to build a septic tank	0.156	2.923	0.455
Solid Waste				
1	Difficult road access	0.156	3.154	0.491
2	Solid waste production continues to increase	0.187	3.385	0.632
Drainage				
1	Area contour	0.173	3.385	0.586
<b>Total Threats</b>				1.594
<b>Total Opportunities-Threats (y-axis)</b>				0.162

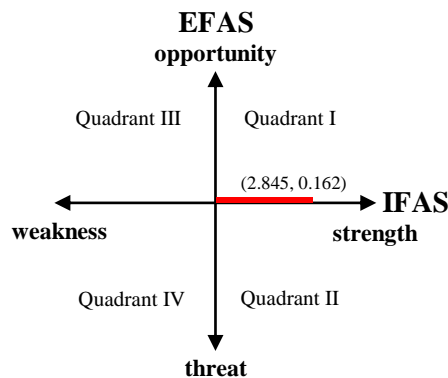


Fig. 3 The results of the SWOT analysis diagram

#### 4.4 Drainage Management

Urban water management was carried out by integrating water services, including water supply, sewerage, drainage and flood management, and environmental protection [2]. The drainage system in the study area was a mixed system. More than 90% of the community in the study site discharged grey water into the drainage, either through open or closed channels. Flood incidences in the study area can be seen in Table 2. In the riverside and seaside areas, flood incidences more often occurred several times a year. Meanwhile, in the hills area, landslides more often occurred during the rainy season.

#### 4.5 The Strategies to Increase Access to Water and Sanitation

The strategies to increase access to water and sanitation that applied in the study area was analyzed based on IFAS and EFAS matrix using SWOT analysis. IFAS and EFAS matrix calculations can be seen in Table 3 and Table 4. The total score of internal factors (x-axis) was 2.845 and the total value of external factors (y-axis) was 0.162. The results of the

calculation were plotted into a SWOT analysis diagram as shown in Figure 3.

The results of the SWOT analysis diagram show that the strategy for increasing access to water and sanitation in the study area was in quadrant I (progressive), thus, it can take advantage of all strengths and opportunities. The formulation of a strategy for increasing access to water and sanitation in water-sensitive areas was as follows:

1. Strategy 1, the enforcement of domestic wastewater regulations according to the Manado City Regional Regulation [12]. It has regulated increasing and developing access to domestic wastewater facilities and infrastructure, strengthening institutions and increasing management capacity, as well as increasing public awareness through triggering by providing economic benefits [13]. Domestic wastewater facilities and infrastructure can be started with the construction of a SNI septic tank and a fecal sludge treatment plant. Colouring project is also one possible strategy [14].
2. Strategy 2, create catchment areas and applied the concept of Water Sensitive Urban Design (WSUD) to reduce flooding. In Manado City Regional Regulation [15], it has planned to build infiltration ponds in flood-prone areas to control rainwater runoff.
3. Strategy 3, reducing solid waste by sorting it from the source, through a solid waste bank, TPS 3R or TPST. In Manado City Regional Regulation [16] stated that everyone who produce solid waste was obliged to reduce and handle solid waste in an environmentally manner, which is one way to change people's behavior [13].
4. Strategy 4, increasing water treatment capacity through PDAM Manado City. Manado City has Manado City Regional Regulation [17]. The aims to increase the productivity and performance of PDAMs in serving and increase the efficiency and effectiveness.



## 5. CONCLUSION

There were three specific areas in a water-sensitive area, namely hills, riverside, and seaside areas. The riverside and seaside areas has better access to water and sanitation with 95% access to improved drinking water, 95-100% access to basic sanitation, and 85-100% to the solid waste collecting and transporting. More than 90% of the community discharged grey water into the drainage. The riverside and seaside areas was more sensitive to flooding. The strategies for increasing access to water and sanitation were based on SWOT analysis, namely strengths (3.632), weaknesses (0.787), opportunities (1.756), and threats (1.594). therefore, the strategies to increase access to water and sanitation in water-sensitive areas were enforcing regulations, establishing a special supervisory, building facilities and infrastructure, and conducting socialization with the community. Implementing strategies based on strengths and opportunities is the best approach in increasing access to safe and sustainable water and sanitation in water-sensitive areas.

## 6. ACKNOWLEDGMENTS

This research was supported by Netherlands Organization for Scientific (NWO) and Indonesian Ministry of Education, Culture, Research, and Technology (KEMENDIKBUDRISTEK), and also Global Sanitation Graduate School (GSGS) program. This research was part of the Resilient Indonesia Slum Envisioned project (RISE).

## 7. REFERENCES

- [1] R. R. Rahmat and S. H. Djoeffan, "Penerapan Water Sensitive Urban Design Pada Permukiman DAS Cikapundung (Studi Kasus: Kelurahan Pasirluyu Kota Bandung)," *Jurnal Perencanaan Wilayah dan Kota*, vol. XVI, no. 1, p. 9, 2019.
- [2] T. H. F. Wong, B. C. Rogers, and R. R. Brown, "Transforming Cities through Water-Sensitive Principles and Practices," *One Earth*, vol. 3, no. 4, pp. 436–447, Oct. 2020, doi: 10.1016/j.oneear.2020.09.012.
- [3] Pemerintah Kota Manado, *Kajian Lingkungan Hidup Strategis RPJMD Kota Manado Tahun 2021-2026*. 2021.
- [4] Kelompok Kerja Perumahan, Permukiman, Air Minum, dan Sanitasi (Pokja PPAS), *Panduan Praktis Pelaksanaan EHRA (Environmental Health Risk Assessment/Penilaian Risiko Kesehatan Lingkungan)*. Kementerian Kesehatan Republik Indonesia, 2020.
- [5] M. M. Helms and J. Nixon, "Exploring SWOT analysis – where are we now?: A review of academic research from the last decade," *Journal of Strategy and Management*, vol. 3, no. 3, pp. 215–251, Aug. 2010, doi: 10.1108/17554251011064837.
- [6] T. J. Chermack and B. K. Kasshanna, "The Use and Misuse of SWOT Analysis and Implications for HRD Professionals," *Human Resource Development International*, vol. 10, no. 4, pp. 383–399, Dec. 2007, doi: 10.1080/13678860701718760.
- [7] Sardjito, E. B. Santoso, K. D. M. E Handayeni, and N. Farikha, "Quality improvement strategy of slum settlement in Kingking sub district, Tuban Regency," *IOP Conf. Ser.: Earth Environ. Sci.*, vol. 202, p. 012070, Nov. 2018, doi: 10.1088/1755-1315/202/1/012070.
- [8] WHO and UNICEF, "Progress on Drinking Water, Sanitation and Hygiene: 2017 Update and SDG Baselines," Geneva: WHO; New York: UNICEF, 2017.
- [9] W. Bank, "Improving On-site Sanitation and Connections to Sewers in Southeast Asia Insights from Indonesia and Vietnam [Research Brief].," 2022.
- [10] N. Chandana and B. Rao, "A critical review on sludge management from onsite sanitation systems: A knowledge to be revised in the current situation," *Environmental Research*, vol. 203, p. 111812, Jan. 2022, doi: 10.1016/j.envres.2021.111812.
- [11] A. Kumar and A. Agrawal, "Recent trends in solid waste management status, challenges, and potential for the future Indian cities – A review," *Current Research in Environmental Sustainability*, vol. 2, p. 100011, Dec. 2020, doi: 10.1016/j.crsust.2020.100011.
- [12] Manado City Regional Regulation, *Domestic Wastewater Management*, vol. 9 of 2016.
- [13] P. W. Sarli and P. Soewondo, "Strategic Thinking to Change Behavior and Improve Sanitation in Jodipan and Kesatrian, Malang, East Java, Indonesia," vol. 11, no. 10, p. 6, 2017.
- [14] P. Soewondo *et al.*, "Visual Improvement of Slum Areas to Accelerate Universal Access to Domestic Wastewater Treatment (Case study of Yogyakarta, Semarang and Manado)," *IOP Conf. Ser.: Earth Environ. Sci.*, vol. 409, no. 1, p. 012006, Jan. 2020, doi: 10.1088/1755-1315/409/1/012006.
- [15] Manado City Regional Regulation, *Manado City Spatial Plan for 2014-2034*, vol. 1 of 2014.
- [16] Manado City Regional Regulation, *Solid Waste Management*, vol. 1 of 2021.
- [17] Manado City Regional Regulation, *The Capital Investment of the Manado City government to PDAM Manado City*, vol. 6 of 2016.

## DETERMINATION FACTORS FOR SELLING LOCATIONS, GENDER, AND MIGRATION STATUS OF STREET VENDORS IN EAST JAKARTA IN ACHIEVING ECONOMIC RESILIENCE DURING THE COVID-19 PANDEMIC

Beti Nurbaiti<sup>1</sup>, Chotib<sup>2</sup>, Kemas Ridwan K<sup>3</sup>, Mia Siscawati<sup>4</sup> and Elisabeth Ratu Rante Allo<sup>5</sup>

<sup>1,2,3,4,5</sup> School of Strategic and Global Studies, University of Indonesia

### ABSTRACT

The purpose of this study was to analyze the economic resilience of street vendors (street vendors) households in East Jakarta in terms of selling locations, gender, and migration status. The selling locations are divided into 4 categories, namely local government-assisted location, temporary location, base /fixed location, and hawkers for both female and male street vendors with the status of lifetime migrant and non-lifetime migrant. The research method used is a quantitative approach by processing primary data for 420 street vendors in East Jakarta using logistic regression. The results show that street vendors selling in local government Assisted locations, female street vendors, and non-lifetime migrant street vendors tend to have high economic resilience, while the other groups are in base / fixed locations, male street vendors, and lifetime migrants are in moderate economic resilience. For street vendors who sell in temporary locations and lifetime migrants, they are in low economic resilience.

*Keywords: Street Vendors; Economic Resilience; Covid-19 pandemic; East Jakarta*

### I. INTRODUCTION

The COVID-19 pandemic has had a tremendous impact on all aspects of life, including social and health aspects, but the hardest hit is the economic aspect of all levels of world society (Safitri et.al, 2021). The impact of this pandemic is also felt by street vendors who work in the urban informal sector with a drastic decline in trade turnover. The decrease in street vendors' income has an impact on their ability to fulfill the basic aspects of daily life, health, and education. Most of the street vendors are migrants or newcomers who have lived and settled in Jakarta for a long time. The flow of rural-urban migration is unstoppable, especially with advances in transportation, technology, and community services in urban areas. These migrants argue that the city can provide a better life than when living in the village (Nurbaiti, 2017) and (Horiuchi and Takahashi, 2016). Migrants who are not ready with knowledge and capital will enter the informal sector, one of which is street vendors (Nurbaiti, 2016).

The informal sector has advantages in adapting flexibility and reducing poverty even though the income is uncertain (ILO, 2020) and (Priyono, 2015). Social capital often helps street vendors struggling and make a living in the city based on family and kinship relationships. Social capital also often helps market access, trading methods, to the ease of street vendors getting business capital without going through financial institutions (Nurbaiti and Chotib, 2020). Based on the phenomena mentioned above, the authors would like to examine the extent to which: (1) the correlation between trading locations and economic resilience; (2) gender with economic resilience street vendors;

and (3) recent migration status with economic resilience street vendors.

### II. LITERATURE REVIEW

Each individual has their reasons for being a migrant, moving from one place to another, between villages and cities to between countries. The biggest factor causing someone to become a migrant is to improve their standard of living (Nurbaiti, 2017). To become a migrant requires sacrifice to bear the risks of uncertainty and pressures of city life, being far away from family and relatives, especially in a metropolitan city like Jakarta (Chotib and Nurbaiti, 2018). The definition of migrant when referring to the explanation from the Central Statistics Agency (BPS, 2000) administratively can be divided into three, namely: (1) *lifetime migration*, where the current place of residence is different from the place of birth, has settled in the current place for more than five years. year; (2) *total migration*, where the current residence is different from the previous place of residence; and (3) recent migrants (*recent migration*), if a person.

The rural-urban wage gap is the main cause of the rapid flow of rural-urban migration and will continue to grow as long as migrants feel a positive impact (increased utility) in a new place. The main driving factor is the scarcity of jobs in the area of origin, but migration often occurs as a result of natural disasters, wars, conflicts, and the need for a better life. The attractiveness factor can also be the reason people migrate, including complete educational, health, and entertainment facilities (Todaro, 2000). Referring to the results of Nurbaiti and Chotib's research (2020), the informal sector develops because of financial and non-financial

benefits. In addition, the need for employment opportunities to generate income and reduce poverty by absorbing migrant workers is the main reason for entering the urban sector. Thus, it can be understood why the population continues to increase in cities, especially in DKI Jakarta as a result of urban-rural migration from year to year.

The existence of street vendors often uses space that is not intended to sell officially, most of which are in public spaces such as road shoulders, sidewalks, and even green open spaces. Street vendors produce urban social spaces that were originally abstract into real ones, which cannot be separated from social reality based on the control and domination of the parties involved (Lefebvre, 1991). The construction of entertainment facilities, as well as factories or offices, will produce a new social space, namely the rampant presence of street vendors around it. The phenomenon of street vendors refers to concrete spatial practices because in it there is a network of interaction and communication between individual street vendors daily. Space is formed by individuals with all their activities, and vice versa, humans act because they are formed by that space. Street vendors, through buying and selling activities, form space according to their wishes.

As time goes by, the process of socialization and interaction occurs between street vendors, thus forming a space zone. The socialization lasted a long time intensively so that a strong interaction was formed between street vendors. As a result, the previous street vendors' space zone was getting stronger, thus forming its *power or power*. Even though it looks abstract, the power of spatial domination by street vendors is real, and it can be seen that the local government/Satpol PP is making efforts to control street vendors. This can be understood as the abstract space of street vendors. The space production process by street vendors can also have obstacles such as permits for trading places, a small number of visitors, small capital, and competition between street vendors. The positive impact of street vendors from a social and economic point of view can be seen in terms of overcoming unemployment and poverty. On the other hand, it can be negative, are the city's social problems such as environmental cleanliness, conversion of public land, and congestion. However, the arrangement and empowerment of street vendors have been regulated in Governor Regulation No. 10 of 2015 where street vendors are divided into 4 selling locations, namely: (1) Local Government Assisted Locations; (2) Temporary Locations; (3) Base / Fixed Location; and (4) Hawkers.

Economic resilience is measured through 4 aspects, namely: (1) the condition of the family's place of residence; (2) family income (husband

and/or wife have a fixed income, primary needs are met such as clothing, food, and housing); (3) financing of children's education; and (4) family financial security. Resilience or family resilience must be considered as a concept that is 'created together' by all actors to be able to get through difficult times, especially when the Covid-19 pandemic hits parts of the world in various walks of life and increases the number of poverty rates (Lopez and Castro, 2021). Family resilience will be created if the family which generally consists of a husband, wife, and children carries out the eight family functions in a harmonious, harmonious, and balanced manner (REACH, 2021).

The eight functions of the family in question include: (1) the function of religion, where the family is a forum for introducing, teaching, and practicing religious values; (2) the function of affection, where affection is given from the time the child is born until an indefinite period of time; (3) protection function; (4) socio-cultural functions; (5) reproductive function; (6) socialization and education functions; (7) economic function; and (8) the function of environmental development. Therefore, family economic resilience is directly proportional to gender equality and justice applied in the family, where both husband and wife work hand in hand in domestic affairs and meet the needs of the family together (Aziz and Solikha, 2018).

### III. METHODS, HYPOTHESIS, AND RESEARCH RESULTS

Early research was conducted for 6 (six) months starting from November 30, 2021, to the end of May 27, 2022, using a questionnaire instrument for 420 street vendors in East Jakarta. The approach used is quantitative which includes: (1) descriptive analysis; (2) *bivariate* analysis; and (3) inferential analysis of logistic multinomial regression results to test the research hypothesis. Quantitative data analysis was performed using a multinomial logistic regression function with the following equation:

$$\ln\left(\frac{y=1}{y=0}\right) = \beta_0 + \beta_1 * KL04 + \beta_2 * KR08 + \beta_3 * KR12 + e \quad (1)$$

$$\ln\left(\frac{y=2}{y=0}\right) = \beta_0 + \beta_1 * KL04 + \beta_2 * KR08 + \beta_3 * KR12 + e \quad (2)$$

Where :

$y$  = street vendors' economic resilience, which are :

$\ln\left(\frac{y=1}{y=0}\right)$  is the probability of street vendors to have moderate economic resilience against street vendors who have low economic resilience

$\ln\left(\frac{y=2}{y=0}\right)$  is the probability of street vendors to have high economic resilience against street vendors who have low economic resilience  
 KL04 = types of street vendors at 4 locations

KR 08 = gender

KR12 = lifetime migration status

There are 3 research hypotheses, namely:

Hypothesis 1 (H1): street vendors who trade in local government-assisted locations have higher economic resilience than other selling locations;

Hypothesis 2 (H2): male street vendors have higher economic resilience than female street vendors;

Hypothesis 3 (H3): street vendors with lifetime migrant status have higher economic resilience than street vendors with non-lifetime migrants.

#### IV. DISCUSSION

The public space used by street vendors in trading and daily activities is 68% using pedestrians/sidewalks. There are 2 (two) types of sidewalks that are used, namely sidewalks with pedestrian, bicycle, or disabled lanes, as well as sidewalks specifically for pedestrians. As many as 28% of street vendors use the road area for selling, followed by the use of crossroads as much as 3%. There are as many as 1% of street vendors using green open spaces such as parks and or urban forests. For the respondents surveyed in this study, none of them sold using riverbanks, crossing bridges, and over waterways.

Table 4.1 Analysis of Economic Resilience by Selling Location

Variable	Group	Low (N %)	Moderate (N %)	High (N %)	Total (N %)
Selling Location	1. Local Government Assisted Location	9.3%	25.6%	65.1%	100.0%
	2. Temporary Location	41.1%	30.1%	28.8%	100.0%
	3. Base/Fixed Location	26.0%	57.7%	16.3%	100.0%
	4. Hawkers	27.8%	55.6%	16.7%	100.0%
Total		30.2%	43.6%	26.2%	100.0%

Source: processed by the author (2022)

Referring to Table 4.1 regarding the results of the cross-tabulation analysis of the category of economic resilience on the type of street vendors trading locations, it can be seen that low economic resilience tends to be in street vendors who trade in

Temporary Locations. Moderate economic resilience tends to be in Base/Fixed Locations and Hawkers, while high economic resilience is found in street vendors located in Local Government Assisted Locations.

Table 4.2 Analysis of Economic Resilience by Gender

Variable	Group	Low (N %)	Moderate (N %)	High (N %)	Total (N %)
Gender	1. Male	30.0%	50.2%	19.7%	100.0%
	2. Female	30.5%	35.3%	34.2%	100.0%
Total		30.2%	43.6%	26.2%	100.0%

Source: processed by the author (2022)

Based on the results of the cross-tabulation analysis of the categories of economic resilience in Table 4.2 associated with the sex of street vendors, it can be seen that low economic resilience can occur in male and female street vendors, there is no

significant difference. Moderate economic resilience tends to be in male street vendors, while those with low and high economic resilience are found in female street vendors.

Table 4.3 Analysis of Economic Resilience by Migration Status

Variable	Group	Low (N %)	Moderate (N %)	High (N %)	Total (N %)
Migration Status	1. Non-Life Time Migrants	25.5%	41.3%	33.2%	100.0%
	2. Life Time Migrants	33.9%	45.3%	20.8%	100.0%
Total		30.2%	43.6%	26.2%	100.0%

Source: processed by the author (2022)

Refer to the results of the cross-tabulation analysis of the categories of economic resilience in Table 4.3, that street vendors with non-lifetime migrants migration status have high economic

resilience. On the other hand, street vendors with the status of lifetime migrants have low to moderate economic resilience.

Table 4.4 Logistic Regression Multinomial Test Results on Economic Resilience

Independent Variable	Medium to Low		High to Low	
	Odds Ratio	Std. Error	Odds Ratio	Std. Error
Intercept		.964		.014
[KL04. Selling location = 1. Local Government Assisted Location ]	1.174	.823	6,901 **)	4.204
[KL04. Selling location = 2. Temporary Location ]	.328 *)	.622	.695	.201
[KL04. Selling location = 3. Base / Fixed Location ]	1.104	.584	.963	.002
[KL04. Selling location = 4. Hawkers	.	.	.	.
[KR08. 1=male]	1.009	.272	.591	2.877
[KR08. 3 = female]	.	.	.	.
[Non Life Time Migrant=.00]	1,810 **)	.266	1.963 **)	5.122
[Migrant Life Time=1.00]	.	.	.	.

Note: \*) Significant at = 10%; \*\*) Significant at = 5%; Source: processed by author (2022)

Based on Table 4.4, it can be explained the level of economic resilience of street vendors in each profile which will help answer the research hypothesis. There are two conditions analyzed based on multinomial logistic regression data processing, namely: (1) moderate economic resilience compared to low economic resilience, and (2) high economic resilience compared to low economic resilience. For the first condition, namely calculating the probability of moderate economic resilience against low economic resilience, the significant independent variables include the type of selling location and non-lifetime migrant status. Meanwhile, for the second condition, calculating the probability of high economic resilience against low economic resilience, the independent variables are significantly the same, namely selling location and non-lifetime migrant status.

The opportunity for economic resilience to occur for street vendors in temporary locations is 0.328 times lower than for street vendors who do not have locations/hawkers. In other words, street vendors who do not have a fixed location are more likely to have moderate economic survival than street vendors in temporary locations. As for the chance of moderate economic resilience, street vendors' non-lifetime migrants are 1,810 times higher than street vendors' lifetime migrants. Opportunities for high economic resilience occur in local government-assisted locations 6,901 times higher than hawkers, or in other words, street vendors in local government-assisted locations have higher economic resilience than hawkers. It can also be said that street vendors in local government-assisted locations have the opportunity to have high economic resilience than street vendors hawkers.

The same thing happened to street vendors as non-lifetime migrants who had a 1,963 times higher chance than street vendors as lifetime migrants. In other words, street vendors and non-lifetime migrants are more likely to have high economic resilience than lifetime migrants. For gender, there is no significant difference between the economic resilience of male and female street vendors.

## V. CONCLUSION

The first hypothesis states that street vendors who trade in local government-assisted locations have higher economic resilience than other selling locations, proven or accepted. This is because the street vendors at this location are more organized with trading facilities, as well as the availability of electricity, and clean water and are more comfortable with tables, chairs, and tents that have been arranged neatly as a contribution from the DKI Jakarta government to street vendors. Therefore, it is necessary to improve similar facilities for street vendors who sell in other locations so that they become organized/move to local government-assisted locations. It is hoped that later street vendors who do not stay and hawkers can be gradually facilitated to be able to sell in better locations.

The second hypothesis which states that male street vendors have higher economic resilience than women is not proven. Female street vendors have similar economic resilience to male street vendors, this shows that women can carry out their dual roles both in the domestic sphere (taking care of the household) and in the public domain (trading). Therefore, the empowerment program for street vendors, in general, has been carried out by the

relevant agencies, in this case, the Small and Medium Enterprises Cooperative Trade Industry Service (SME CTIS), so that it can be focused on female street vendors to maintain their economic resilience.

The third hypothesis which states that street vendors with the status of lifelong migrants have a higher economic resilience than non-migrant street vendors for life is not proven because the findings in the field are the opposite. This condition shows that non-migrants or local indigenous people already have sufficient capital accumulation, and a wider network than migrants/migrants, so they are better able to survive in difficult conditions such as during a pandemic like this.

### ACKNOWLEDGEMENTS

This research was supported by Department of Industry, Trade, Cooperatives, Small and Medium Enterprises, DKI Jakarta Province (DPPK UKM Provinsi DKI Jakarta).

### REFERENCES

- [1] Aziz, F. A., & Sholikha, A. F. (2018). Pengaruh Wanita dalam Ketahanan Ekonomi Keluarga Studi Kasus Pada Wanita Pengrajin Tikar Pandan di Desa Pesahangan Cimanggu Cilacap. *Yin Yang*, 13(1), 1–13.
- [2] Badan Pusat Statistik (BPS). 2000. Jakarta Dalam Angka. Badan Pusat Statistik (BPS), Provinsi DKI Jakarta.
- [3] Chotib & Nurbaiti, Beti. (2018). *Are Migrant Workers in DKI Jakarta More Welfare Than Non Migrants? A Data Analysis of SUSENAS 2013*. Journal of Strategic and Global Studies 1 (1), pp. 15-28.
- [4] Horiuchi, S. & Takashi T. (2016). *Globalization and Regional Revitalization in A Local University of Japan*. In : *Globalization , Economic, Political and Social Issues*. Nova Publisher, pp. 149 – 159.
- [5] International Labour Organization (ILO). (2020). *World Employment and Social Outlook-Trend 2020*. Geneva, International Labour Office.
- [6] Lopez, L. J. R., & Castro, A. I. G. (2021). Sustainability and Resilience in Smart City Planning: A Review. *Sustainability (Switzerland)*, 13(1), 1–25.
- [7] Nurbaiti, Beti. (2016). Pengaruh Status Migrasi Melalui Karakteristik Sociodemografi Terhadap Tingkat Kesejahteraan Pekerja di DKI Jakarta (Analisis Data Cross Sectional SUSENAS 2013). Disertasi. HAKI No : EC 00201816779, 3 Juli 2018.
- [8] Nurbaiti, Beti. (2017). Pengaruh Status Migrasi Melalui Karakteristik Sociodemografi Terhadap Tingkat Kesejahteraan Pekerja di DKI Jakarta (*The Influence of Migration Status through Sociodemographic Characteristics on the Welfare Level of Workers in DKI Jakarta*). *Jurnal Kajian Ilmiah Universitas Bhayangkara Jakarta Raya*, 17 (2).
- [9] Nurbaiti and Chotib. (2020). *The Impact of Social Capital On Welfare : The Evidence From Urban Informal Sector In East Flood Canal (BKT)*, Jakarta. IOP Conference Series : Earth and Environmental Science, 436012004.
- [10] Priyono, Edi. (2015). *Memahami Pasar Tenaga Kerja (Understanding the Labor Market)*. Pustaka Lentera, Jakarta.



# ON MOVEMENT OF PEDESTRIANS IN THE STATION SQUARE

Haru Kanda<sup>1</sup> and Kazunari Tanaka<sup>2</sup>

<sup>1</sup>Graduate School of Engineering, Osaka Institute of Technology, Japan; <sup>2</sup> Osaka Institute of Technology, Japan

## ABSTRACT

In Japan, the population is declining due to the declining birthrate and the increased proportion of elderly people, and so the idea of reconstructing cities into compact cities is being considered. By concentrating the main urban functions in a certain area, the travel distance is shortened, and some regions may become less dependent on automobiles. The mortality rate of pedestrian-to-vehicle accidents is the highest among accident categories. In this research, in order to make a basic town redevelopment plan and a design that is safe for pedestrians and to improve the value of an area, the characteristics of a pedestrian flow line will be clarified. Video was taken to acquire the flow line. The location and number of people were counted using animate software. We investigated the relationship with other transportation modes, focusing on the movement of automobiles. We analyzed the change by time and by day. As a result, it was found that there is a relationship between the amount of staying traffic and the impact of safety control.

*Keywords: Compact city, Traffic accident, Walkable*

## RESEARCH BACKGROUND

In 2021, 2,636 people died in Japanese road accidents [1]. Of the number of fatalities caused by traffic accidents, the number of fatalities by condition can be divided into walking, cars, motorcycles, and bicycles. In addition, the elderly (65+) account for the largest proportion of deaths while walking, exceeding 70% [1]. Of the pedestrian deaths, the percentage of pedestrians who violated laws and regulations when crossing exceeded 60%, including ignoring traffic lights, indicating that there are many problems on the pedestrian side as well. [1]

And in Japan's in the future, as the population declines and the birthrate declines and the population ages, the elderly will become the center of the city. In addition, although intensive urban structures have been studied in recent years, it is expected that walking and public transportation will be the main means of transportation. In other words, from these facts, there is a possibility that the occurrence of crossing violations and the mortality rate will be less likely to decrease as the number of pedestrians and the elderly increases.

One of the causes of crossing violations is that the conventional design methods have been planned to prioritize cars, making it difficult for pedestrians to use. Therefore, I thought it was important to focus on the case where the flow line of the pedestrian could not be controlled.

Therefore, as basic research for designing and planning a city that is safe for moving pedestrians, this research aims to predict the location of crossing violations, mainly focusing on the flow lines of pedestrians.

## RESEARCH METHOD

Table 1 Questionnaire survey question content

Questionnaire contents	
Attribute	Gender, age, place of residence
Examples of main survey questions	The most frequently used transportation when attending an event or using Eruto Sakurai (a complex facility adjacent to the station), whether you want to walk around Sakurai Station, or why you want to walk etc.

In order to observe changes in the staying population over a short period of time and obtain data, it is necessary to conduct the survey in areas where events are being held, etc. Also, public transportation and walking are the main modes of transportation in a compact city, and it is necessary to collect data at the points where they are concentrated. For these two reasons, the plaza in front of the station was chosen as the survey site. Specifically, the target was when an event was held in front of Sakurai Station in Sakurai City, Nara Prefecture. (October 29-31, 2021, November 20-21, 2021) This time, in order to extract the trajectory of pedestrians from the video data, we used a video camera installed in the plaza at 9 locations. Using the recorded video, the location and number of people passing through are counted for changes in the staying population and characteristic flow lines. All-day events are held during the above

period, but the 30th was the busiest day due to a special program. We observed changes in the pedestrian population over time and analyzed daily differences. The above is the survey method used in this survey, but at the same time, a simple questionnaire survey was also conducted as a preliminary survey for pedestrians in the plaza, and questions were asked about the basic attributes and main survey items as shown.

## RESULTS OF THE SURVEY

Figure 1 and Figure 2 show a day-by-day comparison of the 29th and 30th.

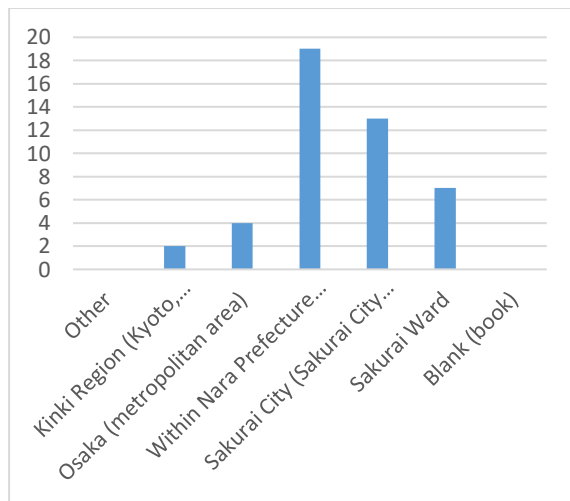


Fig. 1 Residence of participants on October 29

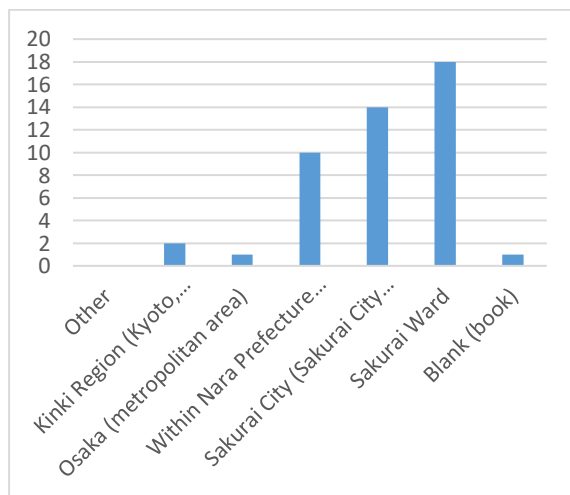


Fig. 2 Residence of participants on October 30

Preliminary survey results show that only on the 30th, the event attracted many participants from the local area, and the number of people was very large compared to the other survey days; on the other days, the number of people did not differ significantly from normal, and the survey results indicate that many

visitors came from outside Sakurai City.

Figures 3 and 4 show the trajectories (daily comparisons) taken from the video for the flow lines other than the sidewalks. The results of this study show that the flow lines on the 29th, which show the same level of retention and traffic as in normal times, have a fixed movement controlled by the design. On the other hand, on the 30th, when the number of trajectories is high, the movements are dispersed. Here, the percentage of people passing outside of the sidewalk on the 29th was 13.25% of the total and 4.65% on the 30th, indicating that the percentage of uncontrolled movement lines is smaller when there is a larger staying population. In addition, the 29th, which shows the same number of dwellings and traffic as in normal times, shows that the flow line has a fixed movement that is controlled by the design. Conversely, on the 30th, when it can be read that there are many trajectories, the movements are dispersed.

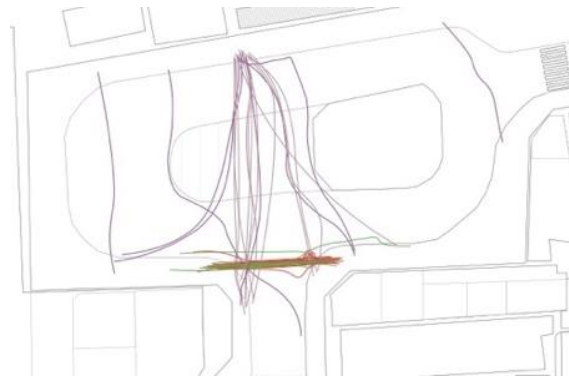


Fig. 3 Trajectory of crossing violators in October 29

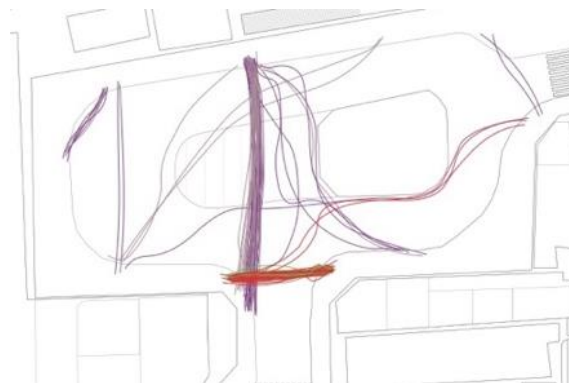


Fig. 4 Trajectory of crossing violators in October 30

## ANALYSIS

Two methods were used in the analysis of the results of this study, "Variable for Flexible Movement (VFM)" and "Density of Stores", respectively, were used to analyze simple predictions of the locations of crossing violators and the causes of their occurrence.

### Variable for Flexible Movement

In the analysis of the survey results, the focus was on the trajectories taken from the videos. The difference between the direction of the trajectory of the pedestrian's crossing violators and the direction of the shortest distance to a destination is the "Variable for Flexible Movement," (hereinafter referred to as VFM) and this value will be used in the evaluation. The larger VFM, the more likely it is that the sidewalk will not be able to control pedestrians, i.e., that crossing violations will occur from there if there are no guardrails, etc.

The analysis method involves fitting a virtual grid to the station square and calculating the trajectory of the pedestrian's crossing violators and the VFM of the applicable mesh. Figure 5 shows the results before, and Figure 6 shows the results after the projective transformation. In this case, the destination of shortest distance is the stairway leading to the station.

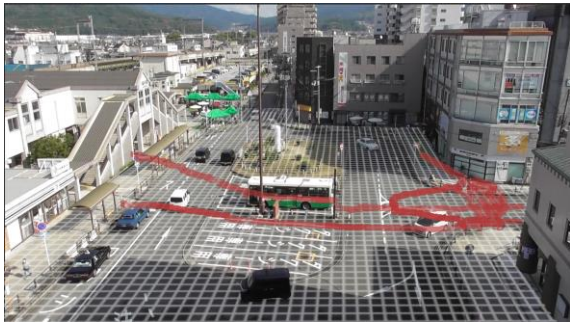


Fig. 5 Diagram showing locus and grid

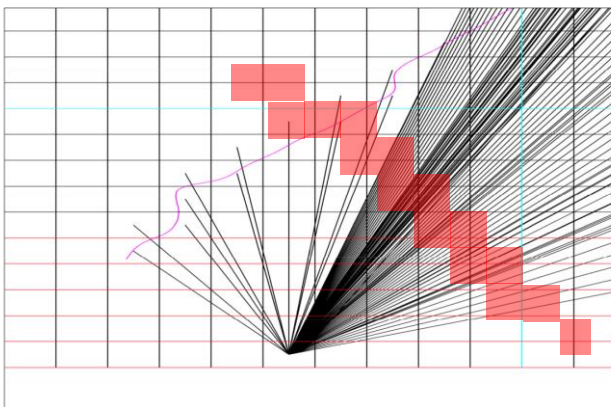


Fig. 6 Mesh for VFM

In order to easily visualize VFM, a three-dimensional representation was used in this study. Figure 7 shows a three-dimensional representation of VFM, calculated from the trajectories of crossing violators during a 10-minute period from 12:00 to 12:10 on October 31. The areas shown in Figure 8 are those where the VFM was actually higher and still coincide with the sidewalk. Figure 9 shows the

trajectories together, and it can be seen that the locations where crossing violations occurred coincide with the locations where VFM was high.

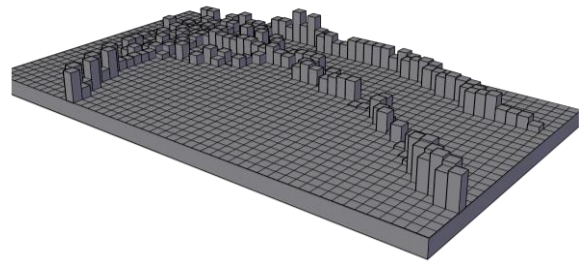


Fig. 7 Pedestrian VFM

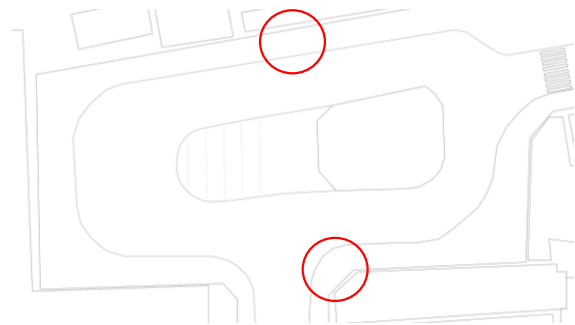


Fig. 8 Where VFM was high



Fig. 9 High VFM and trajectory

### Density of Stores

The density of the number of stores is calculated by Takahashi et al. for each street by multiplying the number of stores by the height influence ratio for each level of the hierarchy, summing them, and considering the effect of height on pedestrians. The number of stores divided by the length of each street is the density of stores, which is evaluated as the crowding of stores on the street [2]. This value is used to analyze the impact of the plaza on pedestrians in the direction of travel from the pedestrian flow line. The formulas used and the height impact ratios are shown below.

$$\text{Density of Stores} = X$$

$$X = \{\Sigma(p^n)(1/2)^{n-1} + \Sigma(q^m)(1/2)^{m-1}\}/d \quad (1)$$

Height Influence Ratio

Bn floor ratio、m floor ratio= $(1/2)^{(n-1),m}$

$p^n$ =Number of stores on n floors above ground

$q^m$ =Number of stores in basement n floor

d=Street Distance

As shown in Figure 10, the plazas on the west and east sides of the area where the most crossing violators occurred were designated as Plaza WEST and Plaza EAST, respectively, and the density of the number of stores in each was determined. The density of the number of stores was  $0.19 \times 10^{-3}$  and  $0.15 \times 10^{-3}$  for the WEST and EAST plazas, respectively, indicating that the density of stores was higher in the WEST plaza.



Fig. 10 Target square for density of stores

## DISCUSSION

The number of people who violated the crossing toward Plaza WEST are listed in Table 2 as east to west, and the number of people in the opposite direction are listed in Table 2 as west to east. On average, the density of stores is higher from east to west, possibly due to the higher number of stores and places to stop, and possibly due to VFM.

Table 3 shows the results of the t-test, which showed that the P-value was not very low, but since the sample size was small, we believe that if we increase the number of samples, we may obtain results with significant differences.

Table 2 Number of crossing violators by day

	10/29	10/31	11/20	11/21
East to West	16	28	7	31
West to East	17	15	13	25

Table 3 t-test

	East to west	West to east
average	20.5	17.5
t	0.724	
P(T<=t) one side	0.261	

## CONCLUSIONS

In this study, pedestrian movements were captured on video, and the characteristics of their trajectories were analyzed. As a result, the relationship between the staying population density and pedestrian flow lines was found. The VFM intensity, which is a value that controls or promotes pedestrian flow lines on the sidewalk itself, was visualized as a simple predictor of where pedestrian crossing violations would occur. In the future, we plan to increase the number of data samples and analyze the characteristics of the data over time and the relationship with other traffic in more detail, as is the case with the data on accidents involving people and vehicles.

## REFERENCE

- [1] National Police Agency (Traffic Bureau): Traffic Accidents in Japan in 2021, March 3, 2022
- [2] Takahashi H., Goto H., Sakuma Y., Saito R., Ishii T., The relationship between the moments of visitor's walking around and the density of stores on commercial area. – A case study on the area around Shimokitazawa-station –, Journal of the City Planning Institute of Japan, No. 40-3, October 2005
- [3] Mori K., Yokozeki T., Yano N., Road Crossing by Elderly People and People with Mobility Constraints in Disregard of Traffic Lights, Journal of Japan Society of Civil Engineers D3, Vol.73, No.5, I\_941-I\_947, 2017.
- [4] Kotaki S., Takayama J., Nakayama S., Rachi M., Study on Actual Situation and Planning Task for Environmental Space of Station Square – Case of Central Station Square in City –, Journal of Japan Society of Civil Engineers D3, Vol.71, No.5, I\_247-I\_259, 2015.
- [5] Matsui Y., Oikawa S., Hitosugi M., Cyclists Behavior and Mechanism of Traffic Accident Occurrence involving Cyclists, Journal of the Japanese Council of Traffic Science, Vol.15, No.3, 2015.
- [6] Ogawa K., Ishida N., Ahn Y., A Comparative Analysis of the Traffic Accident Probability of Bicycles by Running Position and Direction Considering Characteristics of Road Network and Trip Distance, Traffic science, Vol.51, No.1, 2020.

## CEMENT SOLIDIFICATION CHARACTERISTICS OF COAL CINDERS-MIXED SOIL

Shoji Kamao<sup>1</sup>, Kentaro Ishii<sup>1</sup>, Satoshi Shigemura and Yuta Murakami<sup>2</sup>

<sup>1</sup>Civil Engineering, Nihon University, Japan; <sup>2</sup> JR East Consultants Company, Japan

### ABSTRACT

Coal was used as fuel for steam locomotives, and coal cinders (coal waste) were buried underground for disposal. In recent years, redevelopment projects around train stations have been planned for the land where coal waste was once disposed of. In the redevelopment projects, buried coal waste is increasingly being excavated, and the disposal and treatment of the excavated coal waste are becoming an issue for developers. Excavated coal waste must be treated and disposed of as industrial waste, not as soil. In other words, even though the soil is excavated from the ground, it cannot, in principle, be used as backfill material to its original location (railroad sites) and is disposed of as industrial waste at a high disposal cost. Moreover, the high cost of disposal, along with the shortage of final disposal sites, has led to an increase in the project cost of redevelopment projects. For railroad operating companies such as East Japan Railways Company, the increase in development costs poses a major problem for the implementation of their projects in Japan. Therefore, the purpose of this study is to reuse coal cinders dumped underground with the backfill material. Laboratory solidification experiments were conducted to determine the initial water content, the cement added ratio, etc., as design parameters for the strength of backfill materials. From the experimental results, the strength characteristics of the improved soil mixed with coal cinders also changed as the various mixing ratios were varied- the possibility of applying the improved soil containing coal waste as backfill materials were clarified.

*Keywords: coal cinders, cement solidification, backfill material, unconfined compressive strength*

### INTRODUCTION

In Japan, the railroad network was extended throughout the country with the opening of the Shinagawa-Yokohama railroad in 1872 [1]. Coal-fired steam locomotives operated for about 100 years from the opening of the railroad until around 1975. Although coal cinders used for steam locomotives have been buried underground as land formation material for railroad sites, the extent, amount, and depth of coal cinders buried are unknown.

In recent years, coal cinders have been increasingly excavated as a result of the rebuilding of railroad facilities and the redevelopment of station areas. Basically, coal cinders, including mixed soil, excavated during construction cannot be backfilled as it is treated as waste (if backfilled, it violates Waste Management and Public Cleansing Act and constitutes illegal dumping) or disposed of as general residual soil (as it requiring disposal as industrial waste), which increases the cost of construction due to the high disposal cost [2] [3]. Further, most of the excavated coal cinders are landfilled at final disposal sites, and the environmental impact of their transportation and disposal is also significant. East Japan Railway Company is currently planning and implementing large-scale initiatives, including the redevelopment projects in various locations. However, the urgent issue is to reduce the cost of disposal of excavated coal cinders since the

excavation of huge amounts of coal cinders in the construction process puts pressure on the project budget.

Against this background, this study aims to make effective use of coal cinders buried underground as roadbeds for railway structures [4]. To be used as roadbeds, the unconfined compressive strength must be 1,000 kN/m<sup>2</sup> or more, so we set this as the target strength in our attempt to improve the excavated coal cinders mixed soil by cement solidification. The improved test samples were made by mixing several types of coal cinders collected in-situ with clay and cement in predetermined proportions and cured them for a predetermined period of time after setting several initial water content. Based on the measurement of unconfined compressive strength of the improved test samples, we attempted to understand the solidification (strength) characteristics of the samples by using water-cement ratios, amount of cement added, and water content ratios as parameters.

### THE MAIN CHARACTERISTIC VALUES OF THE SAMPLES

The coal cinder mixed soil (after this referred to as "coal cinders") used in this study was collected from the construction site of East Japan Railway Company and is classified as "coal cinders A" and "coal cinders B" based on the sampling point. The

coal cinder mixed soil was collected during excavation work for a redevelopment project in the station areas. The main physical characteristic values of coal cinders and clay are shown in Table 1. It was found that the density of soil particles in the coal cinder mixed soil (coal cinders A and B) decreased with the addition of coal cinders. The results also showed that the consistency properties and water content ratios varied significantly depending on the type of soil contained in the coal cinder mixed soil.

Table 1 Physical Properties of used coal cinders and clay

		Coal cinders A	Coal cinders B	Kasaoka clay
Soil particle density	$\rho_s$ (Mg/m <sup>3</sup> )	2.44	1.94	2.87
Liquid limit	$w_L$ (%)	NP	50.5	54.7
Plastic limit	$w_P$ (%)	NP	43.1	33.7
Plasticity index	$I_P$ (-)	NP	7.42	21.0
Natural water content	$w_n$ (%)	3.17	18.44	4.65
Ignition loss	$L_i$ (%)	16.71	8.83	5.85

## TEST PIECE PREPARATION METHOD

The test piece preparation method was based on the Japanese Geotechnical Society Standard (JGS 0821 [5]) without compaction of stabilized soil. Coal cinders that passed through a 2 mm sieve were used as samples. Commercially available Kasaoka clay (powder) and blast furnace cement type B were used as additional agents. The test piece was obtained by mixing Kasaoka clay, coal cinders, and blast furnace cement type B for about 10 minutes using a mixer to make the mixture uniform. An acrylic mold with a diameter of 3.5 cm and a height of 10 cm was used. The lower end was sealed with a rubber stopper, and the test piece was divided into five layers and tapped 100 times per layer to let the air out while filling the samples. After filling, the upper end was covered with plastic wrap and cured for a predetermined period of time. Cement and water were added to the dry mass of coal cinder mixed soil and Kasaoka clay at a predetermined ratio. The parameters used in this study (cement addition rate  $a_w$  and coal cinder addition rate  $D_w$ ) were defined as shown in formulas (1) and (2) below. The curing period of the test piece was 7 and 28 days ( $T_c=7$  days and  $T_c=28$  days, respectively), and they were cured in a constant-temperature room at 20 °C. The compositions of the test piece are shown in Table 2. For coal cinders A, the cement addition rates  $a_w$  were set to 10% and 35%, while the coal cinder addition rate  $D_w$  was set to only 50% to make the test piece. For coal cinders B, the cement addition rates  $a_w$  were set to 5%, 10%, 20%, and 35%, while the coal cinder addition rates  $D_w$  were set to 50%, 75%, and 100% to prepare the test piece.

For the initial water content  $w_0$ , it required water addition because the Kasaoka clay used was in a powdery state with a water content ratio of about 4.7%.  $w_0$  set below 30% makes uniform mixing difficult due to drying. On the contrary, if  $w_0$  exceeds 60% (near the liquid limit), the test piece is not strong enough to stand on its own after being cured, so in this experiment, the water content ratios were set within the 40-60% range.

$$a_w = \frac{m'_s}{m_g + m_s} \times 100 \text{ (%) } \dots (1)$$

$$D_w = \frac{m_g}{m_g + m_s} \times 100 \text{ (%) } \dots (2)$$

$m'_s$  : Mass of blast furnace cement type B

$m_s$  : Dry mass of Kasaoka clay

$m_g$  : Dry mass of coal cinder mixed soil

Table 2 Test programs of this study

		Cement addition rates $a_w$ (%)			
		5	10	20	35
Coal cinder addition rate $D_w$ (%)	50	40 coal cinders A	40-60 coal cinders A coal cinders B	40 coal cinders A	40-60 coal cinders A coal cinders B
	75	40 coal cinders A	40 coal cinders A	40 coal cinders A	40 coal cinders A
	100	40 coal cinders A	40 coal cinders A	40 coal cinders A	40 coal cinders A

## EXPERIMENTAL RESULTS AND DISCUSSION

### Relationship Between Unconfined Compressive Strength and Types of Samples

The relationship between unconfined compressive strength and cement addition rate for coal cinders A and B is shown in Fig. 1. The unconfined compressive strength was obtained under the following conditions: curing period  $T_c$  is 7 days, initial water content  $w_0$  are 40% and 50%, coal cinder addition rate  $D_w$  is 50%, cement addition rate  $a_w$  is 35%, and water-cement ratio  $w/c$  is 60%. The unconfined compressive strength was found to vary in the range of 350-4,000 kN/ m<sup>2</sup> depending on the cement addition rate. In both types of coal cinders, the unconfined compressive strength tended to increase linearly with increasing cement addition rate, and a comparison of coal cinders A and B showed that B had a greater value than A. The reason for the difference in strength between the two is considered to be due to the nature of the soil or the water content in the soil. In the same figure, the standard values for the roadbed are



compared, and it is found that the target value (1,000 kN/m<sup>2</sup>) is met with  $D_w = 50\%$  and cement addition rate of 15% or more for coal cinders A, and with  $a_w = 10\%$  or more for coal cinders B. The strength varies depending on the sample used. The observed differences in strength depending on the samples used suggest that unconfined compressive strength is closely related to the physical characteristic values of the samples.

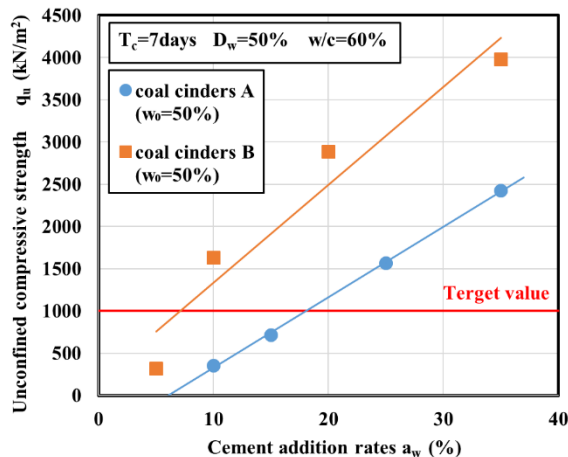


Fig. 1 Relationship between cement addition rates and unconfined compressive strength  
(Coal cinders A and B,  $w/c=60\%$ )

### Relationship between Initial Water Content and Unconfined Compressive Strength

The relationship between unconfined compressive strength and initial water content of coal cinders A is shown in Fig. 2. The unconfined compressive strength was obtained under the following conditions: curing period  $T_c$  is 7 days, initial water content  $w_0$  are 40-60%, coal cinder addition rate  $D_w$  is 50%, cement addition rate  $a_w$  is 35%, and water-cement ratios  $w/c$  are 60% and 100%. Comparing the water-cement ratio of  $w/c=100\%$  and  $w/c=60\%$ , the strength was greater at  $w/c=60\%$ . In terms of the change in the initial water content of the clay, the unconfined compressive strength tended to decrease with an increase in the water content ratio for both  $w/c$ , and a 20% increase in the water content ratio for  $w/c=60\%$  resulted in a decrease in the unconfined compressive strength by half. The same trend was observed at  $w/c=100\%$ . These results show how much water content affects the strength of cement solidification. It is thought that a higher water content facilitates uniform mixing of the samples and improves workability in the field. However, the strength decreases as water content increases, indicating that it is important to maintain an appropriate balance between water content ratio and strength.

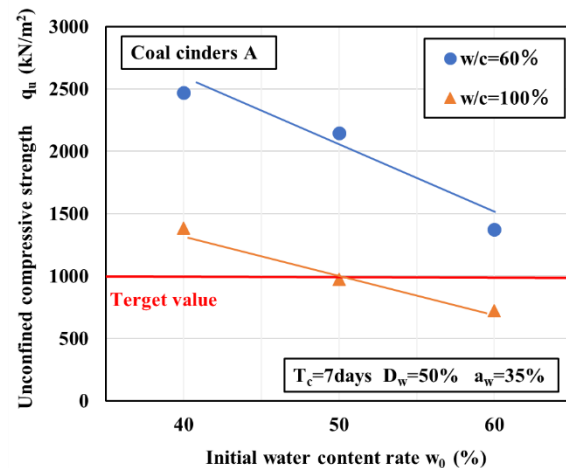


Fig. 2 Relationship between initial water content rate and unconfined compressive strength  
(Coal cinders A,  $w/c=60$  and  $100\%$ )

### Relationship between Water Content Ratio, Curing Period, and Unconfined Compressive Strength

Figs. 3 and 4 show the relationship between unconfined compressive strength and initial water content of coal cinders, and Fig. 3 shows the unconfined compressive strength obtained under the following conditions: curing period  $T_c$  are 7 and 28 days, initial water content  $w_0$  are 40-60%, coal cinder addition rate  $D_w$  is 50%, cement addition rate  $a_w$  is 35%, and water-cement ratio  $w/c$  is 100%. Fig. 4 shows the results obtained for a test piece by changing the water-cement ratio  $w/c$  to 60%. 7-day and 28-day strength comparison tests showed that unconfined compressive strength was greater at 28 days than at 7 days, although some cases could not be performed. For the 7-day strength, values were obtained by varying the initial water content, and a similar trend was observed for the 28-day strength. The 28-day strength decreased as the initial water content increased, as did the 7-day strength. Figs. 5 and 6 show the relationship between the rate of increase in unconfined compressive strength and the curing period from the results of Figs. 3 and 4 above, showing the percentage increase for each condition at  $T_c = 28$  days for the unconfined compressive strength  $q_u$  (28 days) when  $q_u$  (7 days) at  $T_c = 7$  days is used as a reference. Strength increases of 2.0-2.7 times and 1.8-1.9 times were observed for  $w/c=100\%$  and  $w/c=60\%$ , respectively. The increase in strength was not affected by changes in the initial water content or other conditions. The increase in strength was greater in " $w/c=100, w_0=50\%$ " compared to other conditions, but further study is planned with an increased number of samples.

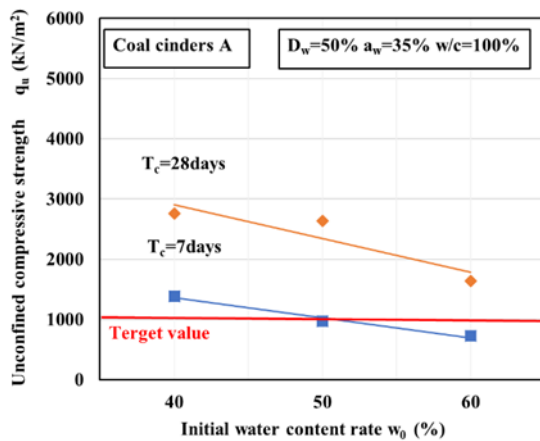


Fig. 3 Relationship between initial water content rate and unconfined compressive strength (Coal cinders A,  $w/c=100\%$ )

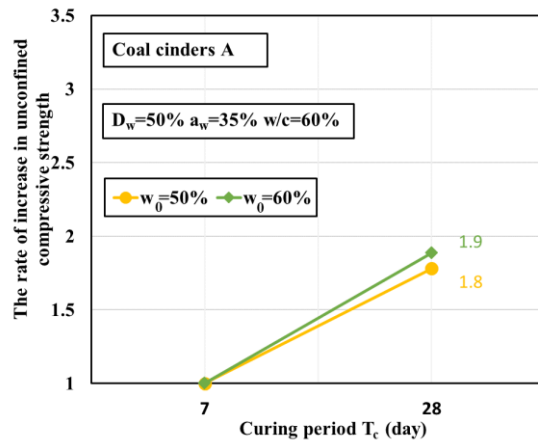


Fig. 6 Relationship between curing period and growth rate of unconfined compressive strength (Coal cinders A,  $w/c=60\%$ )

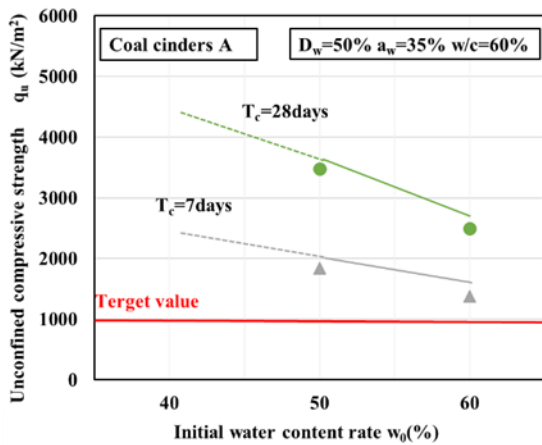


Fig. 4 Relationship between initial water content rate and unconfined compressive strength (Coal cinders A,  $w/c=60\%$ )

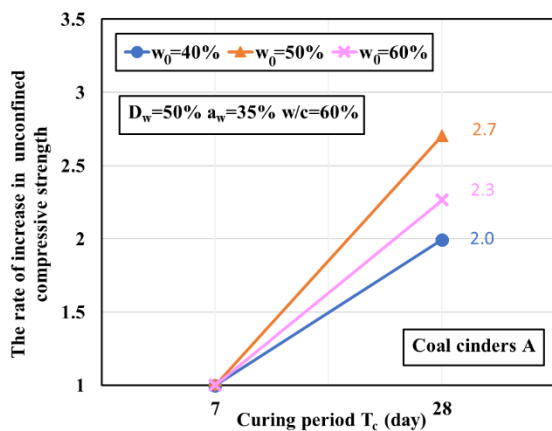


Fig. 5 Relationship between curing period and growth rate of unconfined compressive strength (Coal cinders A,  $w/c=60\%$ )

### Relationship between Coal Cinder Addition Rate and Unconfined Compressive Strength

The relationship between unconfined compressive strength and coal cinder addition rate for coal cinders A is shown in Fig. 7. The unconfined compressive strength was obtained under the following conditions: curing period  $T_c$  is 7 days, initial water content  $w_0$  is 50%, coal cinder addition rates  $D_w$  are 0%-71%, cement addition rates  $a_w$  are 15% and 35%, and water-cement ratio  $w/c$  is 60%. In the case of coal cinders A, the unconfined compressive strength of the improved soil reached a maximum at a coal cinder addition rate of about 13%, after which the 7-day strength of the improved soil decreased as the coal cinder addition rate increased.

The strength development of clay alone, i.e.  $D_w=0\%$ , was also observed, but the addition of coal cinders increased the strength, albeit slightly. The relationship between unconfined compressive strength and coal cinder addition rate for coal cinders B is shown in Fig. 8. For comparison, data for coal cinders A (curves in Fig.7) are also shown. The unconfined compressive strength was obtained under the following conditions: curing period  $T_c$  is 7 days, initial water content  $w_0$  is 40%, coal cinder addition rates  $D_w$  are 50%-100%, cement addition rates  $a_w$  are 5-20%, and water-cement ratio  $w/c$  is 60%. The data obtained for coal cinders B is only for those with the addition rate of 50% or more, but as with coal cinders A, the unconfined compressive strength decreased with increasing coal cinder addition rate, but unlike coal cinders A, the strength was found to be high even at 100% coal cinders content. The strength of the clay alone is lower than the maximum strength, which is considered to be due to the increase in strength caused by the coal cinders acting as fine aggregate. To increase the coal cinder addition

rate, it is important to understand the characteristics of the samples and to determine the composition based on the optimum water content ratio and cement addition rate.

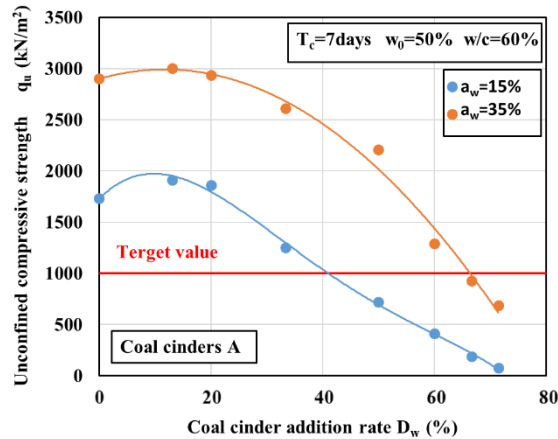


Fig. 7 Relationship between cement addition rate and unconfined compressive strength (Coal cinders A,  $w/c=60\%$ )

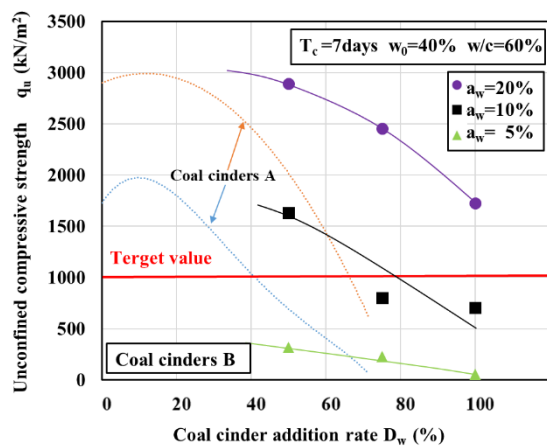


Fig. 8 Relationship between coal cinders addition rate and unconfined compressive strength (Coal cinders A and B,  $w/c=60\%$ )

## Results and Discussion on Coal Cinders A

Based on the results for coal cinders A as described above, the water-cement ratio  $w/c$  was fixed at 60% for easy mixing and expected strength, and the initial water content  $w_0$  was fixed at 40% for sufficient mixing and expected strength of the test piece. The cement addition rate was varied at 35% or less, while test pieces were prepared at coal cinders site B to compare each condition.

### Relationship between cement addition rate and unconfined compressive strength

The relationship between unconfined compressive strength and cement addition rate for coal cinders B is shown in Fig. 9. The unconfined compressive strength was obtained under the following conditions: curing period  $T_c$  is 7 days, initial water content  $w_0$  is 40%, coal cinder addition rates  $D_w$  are 50-100%, cement addition rates  $a_w$  are 5-35%, and water-cement ratio  $w/c$  is 60%. Although the unconfined compressive strength decreased as the coal cinder addition rate increased, it was found that the target value of 1,000 kN/m<sup>2</sup> could be exceeded by setting certain conditions. Moreover, it was found that the strength exceeding the target strength can be obtained by varying the amount of cement added. The target strength was not exceeded even when the coal cinder addition rate was varied at a cement addition rate of  $a_w=5\%$ , suggesting that a cement addition rate of 15% or more would be desirable.

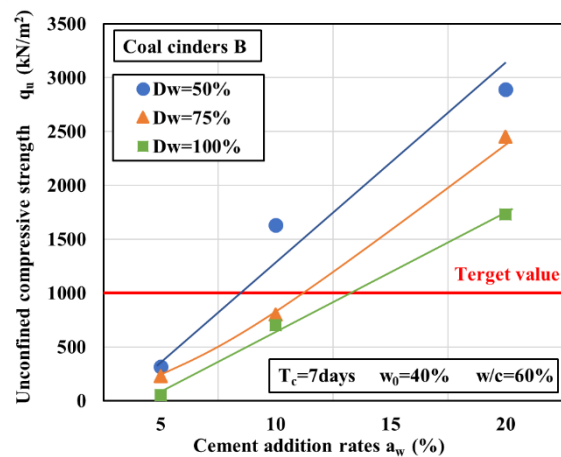


Fig. 9 Relationship between cement addition rate and unconfined compressive strength (Coal cinders A,  $w/c=60\%$ )

### Relationship between Coal Cinder Addition Rate and Unconfined Compressive Strength

The relationship between unconfined compressive strength and the coal cinder addition rate for coal cinders B is shown in Fig. 10. The unconfined compressive strength was obtained under the following conditions: curing period  $T_c$  is 7 days, initial water content  $w_0$  is 40%, coal cinder addition rates  $D_w$  are 50, 75 and 100%, cement addition rates  $a_w$  are 5, 10 and 20%, and water-cement ratio  $w/c$  is 60%.

As with coal cinders A, there was a tendency for the strength to decrease as the coal cinder addition rate  $D_w$  increases. A plot of the results under the same conditions as those of coal cinders A shows a graph indicating a greater decrease in strength with an increasing coal cinder addition rate compared to the graph for coal cinders B.

The reason for this is that unlike coal cinders A, coal cinders B contain not only coal cinders but also clay from the extraction site. Therefore, the coal cinders are considered to have a significant effect on the unconfined compressive strength.

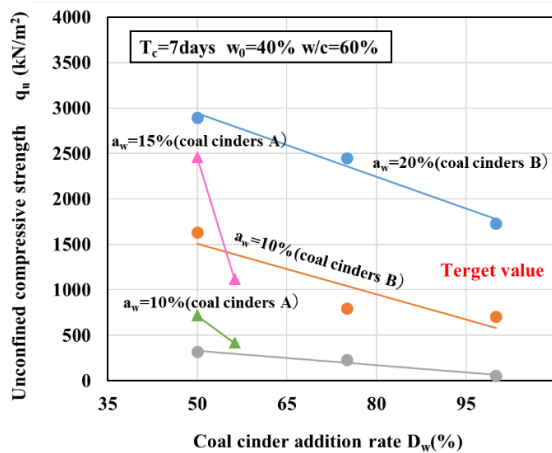


Fig. 10 Relationship between coal cinder addition rate and unconfined compressive strength (Coal cinders A and B,  $w/c=60\%$ )

### Comparison of Coal Cinders Used

The relationship between unconfined compressive strength and initial water content for coal cinders A and B is shown in Fig. 11. The unconfined compressive strength was obtained under the following conditions: curing period  $T_c$  is 7 days, initial water content  $w_0$  are 30-60%, coal cinder addition rate  $D_w$  is 50%, cement addition rate  $a_w$  is 35%, and water-cement ratio  $w/c$  is 60%. The strength of coal cinders B was about 1.8 times greater than that of coal cinders A. Although experiments with coal cinders B under the same conditions of initial water content  $w_0 = 50\%$  and  $60\%$  were not conducted, the trends of the coal cinder addition rate and cement addition rate are similar for both coal cinders A and B. Therefore, the unconfined compressive strength is considered to decrease with the increase of the initial water content, as in the case of coal cinders A.

### CONCLUSIONS

Based on the experimental results of this study, the following results were obtained:

- Understanding the characteristic values of the samples to be used is important, as they affect the unconfined compressive strength.
- The unconfined compressive strength decreases as the initial water content  $w_0$  and water-cement ratio increase.  $w_0$  of 40% or less is considered desirable.

- Unconfined compressive strength increases with a longer curing period.
- Cement addition rate  $a_w$  of 10% or more is considered desirable.

In order to reduce the cost of actual construction, it is considered necessary to find the most economical composition that meets the target strength of  $1,000 \text{ kN/m}^2$  by reducing the amount of cement and increasing the content of coal cinders, which are waste materials. The type of soil and water content ratio contained in coal cinders also affected the unconfined compressive strength. When the content of fine particles was small, the addition of fine particles increase in strength.

Coal contains many harmful substances. Among them, hazardous substances specified in the Soil Contamination Countermeasures Law are Benzene, lead, cadmium, mercury, cyanide, chromium, selenium, arsenic, fluorine, boron, etc. it is necessary to discuss detoxification when hazardous substances are included, too.

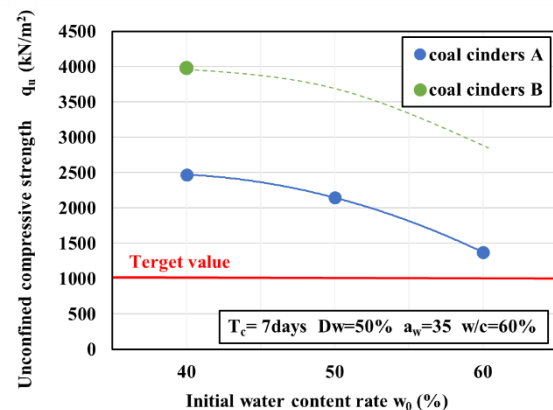


Fig. 11 Comparison of unconfined compressive strength and initial water content (Coal cinders A and B,  $w/c=60\%$ )

### REFERENCES

- [1] Japan's First Steam Engines: <http://steam.fan.coocan.jp/beginning/firstmodel.htm>
- [2] Waste Management and Public Cleansing Act: Act No. 137 of 1970, (In Japanese)
- [3] National Federation of Industrial Waste Management Associations: Industrial Waste Guidebook <http://www.haikibutu.net/img/PDF/guidebook2200.pdf>, 2009
- [4] Railway Technical Research Institute : Design standard for railway earth structures. p.242~p243, 2007. (In Japanese).
- [5] Japanese Geotechnical Society: JAPANESE GEOTECHNICAL SOCIETY STANDARD laboratory Testing Standards of Geomaterials Vol.1, p445~p453, 2020. (In Japanese).

# ROAD TRAFFIC EVALUATION FORCUSING ON VELOCITY AND FORM

Shion Muramoto<sup>1</sup> and Kazunari Tanaka<sup>2</sup>

<sup>1</sup>Faculty of Engineering, Osaka Institute of Technology, Japan

## ABSTRACT

In recent years, the proportion of traffic accident fatalities has increased despite the declining population. This is because the elderly constitute a high of the population. In order to reduce the number of deaths caused by traffic accidents, it is necessary to prevent accidents before they occur. We need to ensure safety by developing walking spaces that contribute to the safety of the elderly, disabled, etc. in our aging society. Therefore, we assume that the form and combination of road use affects each other and the ease of passage. The purpose of this study is to quantify the ease of passage using index values focusing on the velocity and the width of road usage patterns. The research method was to investigate the effect of sidewalk and roadside strip width on ease of passage from the pedestrian's perspective by means of a questionnaire, and to clarify the relationship between width and ease of passage. The index values were used to quantify the roads. The evaluation was compared with previous studies to analyze and discuss the effectiveness of the quantification.

*Keywords: road, pedestrian, velocity, passage*

## INTRODUCTION

In recent years, the number of traffic accident fatalities has decreased as the population has declined. However, as the population ages, the proportion of traffic fatalities among the elderly has increased. Looking at the causes of fatal accidents, the proportion of accidents caused by driver inattention and other factors is relatively high. For elderly drivers in particular, the percentage of accidents caused by mishandling of the steering wheel, brakes, etc. due to deterioration of physical functions, etc. is high. Under these circumstances, in order to reduce the number of fatalities from traffic accidents, it is important to prevent accidents before they occur and to mitigate the damage. In this aging society, it is necessary to ensure traffic safety on roads for daily life through the development of walking spaces and other facilities that contribute to the safety of the elderly, disabled, and other people. In addition, the ongoing development of public transportation in contemporary urban spaces and the continual urban change have resulted in different routes chosen by different people when they travel toward their destinations, even if the starting point is the same. To identify people's route choices, it is necessary to identify paths that are considered walkable. When considering walkability, people unconsciously choose paths that are safe and secure. In addition, we consider that people's perception of walkability may change depending on the type of use of the path and the traffic conditions. In other words, the ease of passage is considered to differ depending on the type of use. The purpose of this study is to quantify and evaluate how pedestrians, cars, and other

forms of transportation affect each other, and which combination of use patterns makes it easier to walk on a given road.

## RESEARCH METHODS

First, a questionnaire survey was conducted on the ease of passage provided by wide sidewalks and roadside strips, using photographs taken at pedestrian eye level, mainly among students attending the university.

Next, in order to quantify the ease of passage, we evaluated the ease of passage by using examples of roads that have been found to be walkable after road maintenance based on previous research questionnaires. To quantify the ease of passage, we focused on the moving velocity of pedestrians and automobiles, and the spacious width of the road, such as the occupied width. In this study, the value obtained by dividing the moving velocity by the occupied width is used as the index value. This index value is called the relative velocity index (RVI). The moving velocity of the road usage patterns was considered to be the average moving velocity, while the moving velocity of cars and motorcycles was considered to be the speed limit of the road. For the width occupied by cars, the road width defined by the Road Structure Ordinance was used. Road usage patterns and travel speeds, occupied widths, and RVI are shown in Tables 1 and 2.



Table 1 Usage patterns that mainly use the sidewalks

Usage patterns	Moving velocity (m/s)	Occupied width(m)	RVI (/s)
Wheelchair	1.19	1.00	1.19
Walking with umbrellas	1.30	1.00	1.30
Stroller	1.19	0.75	1.59
Pedestrian	1.30	0.75	1.73
Bicycle	4.17	1.00	4.17

Table 2 Usage patterns that mainly use the roadway

Usage patterns	Moving velocity (km/h)	Occupied width(m)	RVI (/s)
Car	20	2.75	2.02
	30	2.75	3.03
	40	3.00	3.70
	60	3.25	5.13
Motorcycle	20	1.30	4.27
	30	1.30	6.41
	40	1.30	8.55
	60	1.30	12.82

The evaluation using RVI is performed according to the procedure shown in Figure 1.

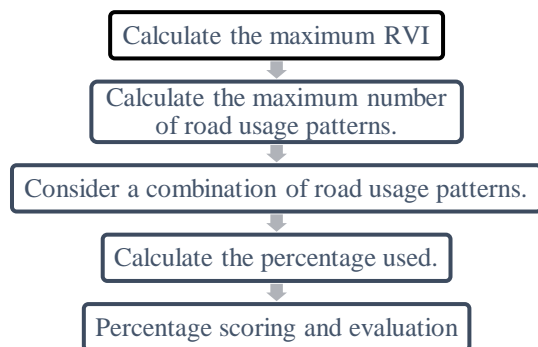


Fig.1 Evaluation Procedure

The maximum RVI is the RVI that can be allowed for the entire width of the road and is calculated by  $\{(RVI \text{ of pedestrians}) \times (\text{width of roadside strip or sidewalk}) + (RVI \text{ of regular vehicles}) \times (\text{width of roadway})\}$ . The maximum number of road usage patterns is calculated by finding the maximum value of  $\{(\text{width of roadway through each type of use})/(\text{occupied width of each type of use})\}$  and  $\{(\text{maximum index value through each type of$

use)/(index value for each type of use)\}. The street that a use form passes through is, for example, a sidewalk for pedestrians and a roadway for automobiles. The value that satisfies both of these maximum values is the maximum number that each usage form can pass through. Within this maximum number, combinations of usage patterns are considered. The percentages used are calculated according to Table 3.

Table 3 Calculation Method

Occupied width	(Sum of spacious widths of each type of use) / (width of the entire street)
RVI	(Sum of RVI for each type of use) / (Maximum RVI value for roads)
Area	(Total area of each type of use) / (Area of roads)

The area in Table 3 is obtained using the sum of the RVI and occupied width for each type of use. Starting with the usage form with the smallest RVI, plot the x-axis as the total occupied width and the y-axis as the RVI. And then, an approximate curve is drawn from the origin. The value obtained by integrating over this approximate curve by the road width from the origin is the area that can be allowed on the road. An example of the area for a car and a motorcycle with a speed limit of 40 (km/h) is shown in Figure 2.

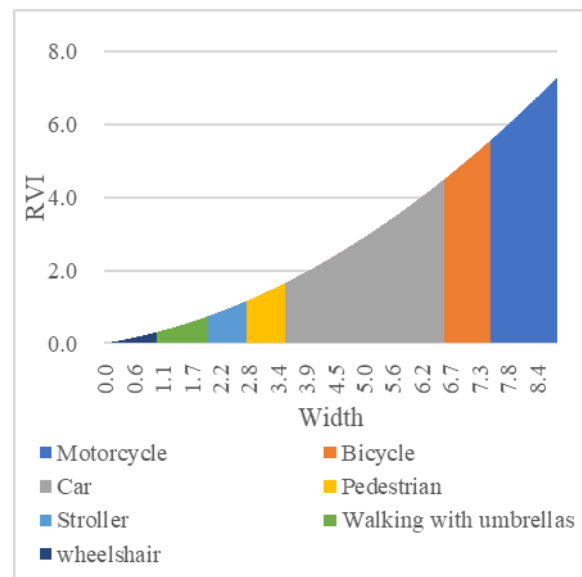


Fig.2 Example of area

The area of the color-coded portion of the graph is the area of the usage form.

Finally, we the percentage scoring and evaluation: will be discussed. A score of 18 was used as the maximum score. The relationship between percentages and scores is shown in Table 4.



Table 4 Relationship between evaluation score and percentage

6 points for 50% or less	5 points for 50% to 60	4 points for 60% to 70
3 points for 70% to 80	2 points for 80% to 90	1 point for 90% to 100

If there is a fence or other means between the sidewalk and the roadway, each road is differentiated and given an evaluation score. This average score was then used as the evaluation score for the road. If the percentage exceeded 100% of any one of the occupied width, RVI, or area, the evaluation score was evaluated as Z points. In this case, we considered the effect on the ease of passage.

### QUESTIONNAIRE SURVEY

The photographs used were processed for two types of sidewalk roads: wide and narrow sidewalks, and three types of roadside roads: wide, narrow, and no roadside roads. A questionnaire was used to evaluate these photographs on a 5-point Likert scale, with 5 being the easiest passage, and 1 being the most difficult.



Fig.2 Example of photo used

Tables 3 and 4 show results for cases with sidewalks and roadside strips on one side.

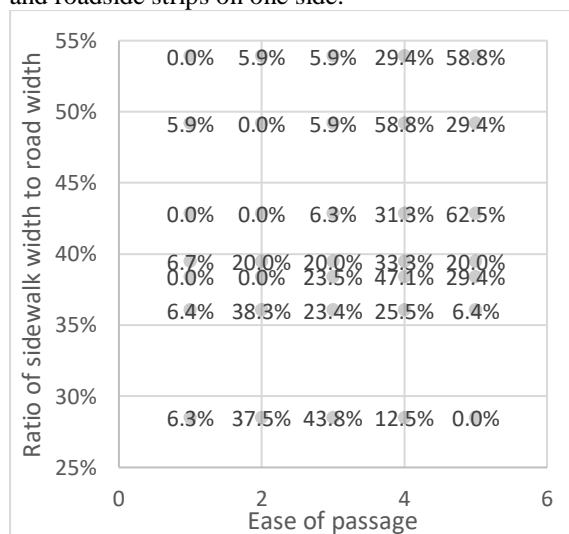


Fig.2 Relationship between percentage of sidewalks and ease of passage

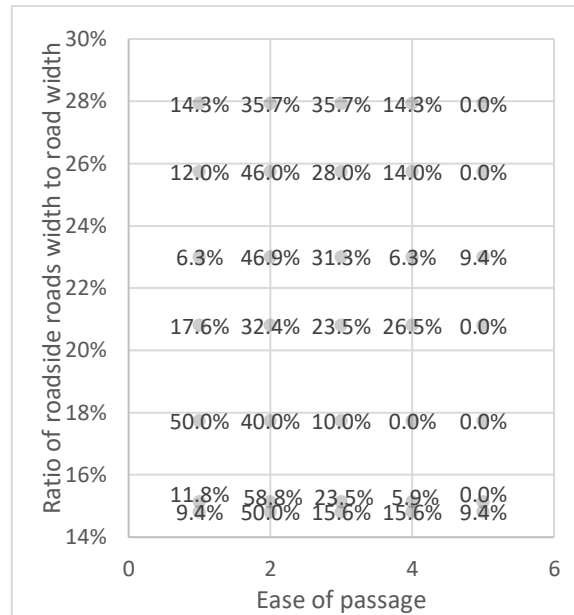


Fig.3 Relationship between percentage of roadside strip and ease of passage

The percentage of total scores of 4 and 5 for sidewalk photos was highest when the ratio was 42.9%. The maximum total score of 4 and 5 points was obtained for the roadside strip photo when the ratio was 20.8%. This means that the number of respondents who felt that the road was easy to pass did not continue to increase even when the percentage of the road width increased. This suggests that the width of sidewalks and roadside strips is not proportionally related to the ease of walking.

### VERIFICATION BY ROAD CASE STUDY

The results and evaluation patterns for the roadside and sidewalk road cases are shown in Tables 5 and 6. The improvement rate is the percentage within the evaluation pattern when the evaluation score improves by even one point.

Table 5 Results of Roadside Street Case Study

Evaluation Patterns		Rate of improvement
Walking form 1 person and vehicle		25%
	Car	20%
Walking form 2 persons	Motorcycle	0%
	Bicycle	10%
	Bicycle and Motorcycle	0%
Walking form 3 persons	Car	50%
	Motorcycle	20%
	Bicycle	20%

Table 6 Sidewalk road case results

Evaluation Patterns		Rate of improvement
Walking form 2 persons	Car	50%
	Motorcycle	50%
	2 cars	90%
	2 Motorcycles	90%
	Car and Motorcycle	50%
	Car and Bicycle	100%
	Motorcycle and Bicycle	100%
	2 cars and a bicycle	100%
	2 motorcycles and a bicycle	100%
	Car, Motorcycle and Bicycle	100%
Evaluation Patterns		Rate of improvement
Walking form 3 persons	Car	25%
	Motorcycle	25%
	2 cars	30%
	2 Motorcycles	35%
	Car and Motorcycle	25%
	Car and Bicycle	50%
	Motorcycle and Bicycle	50%
	2 cars and a bicycle	50%
	2 motorcycles and a bicycle	50%
	Car, Motorcycle and Bicycle	50%

In the road case of sidewalks, it is thought that the construction of bicycle lanes improved the evaluation

scores due to the change in the position of bicycles on the road. In addition, the improvement in scores in the evaluation using RVI is thought to be related to the ease of passage.

## CONCLUSION

In this study, the questionnaire survey revealed that the width of sidewalks and roadside strips are not proportionally related to the ease of passage. In addition, the RVI rating improves in road cases, which may be related to the ease of passage. In order to improve the reliability and accuracy of these results in the future, it is necessary to consider the relationship with the slope of the graph, etc., since the score increases with the width of the road when the same combination of usage patterns is used in the evaluation using RVI. In addition, as new personal mobility devices such as electric kickboards are being used, it is necessary to consider other forms of road use.

## CITATION AND REFERENCE LIST

- [1] Status of the Shijo Sidewalk Widening Project after Completion: Hiroshi Takahashi, Yasuo Shiromizu, Ryuzi Huziyoshi, Masaki Nkaya, Syo Wada, Tetuo Hayashi, Shinya Emoto and Katuhiro yamaguchi, 55th Annual Conference on Civil Engineering and Planning, Proceedings, 49-04 JSCE, 2017.6
- [2] Analysis on the Change of Bicycle User's Attitude and Route Selection Behavior with the Improvement of Bicycle Passage Environment: A Case Study of Bicycle Lane on Prefectural Road Higashi-Kanazawa taxi stand, Masahiro Rati, Michiaki Yama, Junichi Takayama, Masahiro Katagishi and Tatsuya Nakano, Journal of Civil Engineering Planning, Lecture Collection Vol.43 No.389 p.9, JSCE Society of Civil Engineering, 2011.5

## METHOD FOR EVALUATING URBAN COMFORT SPACES FOCUSING ON ENVIRONMENTAL SOUND USING EEG

Shotaro Otsuji<sup>1</sup> and Kazunari Tanaka<sup>2</sup>

<sup>1,2</sup>Faculty of Engineering, Osaka Institute of Technology, Japan

### ABSTRACT

Due to the rapid changes in the living environment caused by the Covid-19 pandemic, our quality of life has declined significantly. In many cases, it is difficult for individuals to restore the environment itself, and I thought it was necessary to find a way for anyone to easily reproduce a comfortable space. Focusing on sounds for which it is easy to secure a medium, in this study, we conducted an electroencephalogram measurement experiment aimed at clarifying the presence or absence of environmental sounds that listeners unconsciously feel comfortable with, and the tendency of preferred environments. In the experiment, the intensity values in the  $\alpha$ -waves frequency band were compared. As a result of grouping based on the appearance of EEG, it was found that there is a relationship between the preferred environmental sound and the difference in the tendency of EEG intensity. In addition, the electroencephalogram intensity values of the environmental sounds preferred by each group were Fourier-analyzed. As a result of these findings, it could be inferred that there are environmental sounds that many people unconsciously prefer, and that "Living room" tends to be the closest to them from the experimental results. However, there are many issues to be addressed in the experimental process, as there are large individual differences between subjects in analyzing the  $\alpha$ -waves frequency band. It is necessary to statistically handle more data. Future research includes verification with visual imagery and psychological response analysis to correctly assess how environmental sounds are heard.

*Keywords: The environment, Sound, EEG,  $\alpha$ -waves*

### INTRODUCTION

From 2020 to the present, the "Covid-19" virus have been spreading around the world, and their impact is immeasurable. As of July 2022, the number of infected people worldwide was 550 million and the number of deaths exceeded 6 million, and our lifestyles had drastically changed to cope with the explosive infectivity. As we were forced to refrain from most activities that involve going outside, the idea of using remote to improve our living environment attracted attention. According to Goto's research, the group that incorporated environmental music in their offices showed an average increase in mental and functional comfort. According to the "Annual Report of the Committee for the Adjustment of Pollution, etc., FY 2020" by the Ministry of Internal Affairs and Communications, "Noise" has the highest number of pollution complaints among the seven typical types of pollution. Therefore, I thought that if we could successfully control the surrounding sound environment, we could maintain a comfortable space. As part of this experiment, we focused on the relationship between  $\alpha$ -waves, which are closely related to comfort, and reproduced environmental sounds.

### PURPOSE AND METHOD OF RESEARCH

We aim to clarify the existence of a sound

environment that the person feels comfortable without being aware of it, and the tendency of that sound.

In this research we focused on sound. This is because of the variety of playback media available for listening to sound, their high prevalence, ease of location mobility and the fact that they are not restricted by location or time. We let the subjects listen to recordings of the original sound in each environment. To identify the classification of environmental sounds that tend to be preferred by the subjects and their individual differences, the  $\alpha$ -waves frequency band of the brain waves, which is a physiological response, was compared and analyzed.

### EEG MEASUREMENTS

The equipment used in the experiment was a PCM recorder (ZoomH2n), a simple EEG measuring instrument (EMOTIV EPOC X) and monitor earphones (SHURE SE215). The dedicated software EMOTIVPRO was used to measure EEG, and physiological response experiments were conducted to analyze the measured EEG. Fifteen students were used as subjects in this research. Each subject was allocated a letter of the alphabet from "A" to "O". The subjects were not told about the research.

In each environment, a sound source of 10 s of environmental sound plus 5 s of rest, for a total of 150 s, was created, which the subjects listened to with

their eyes closed. Ten environments were selected for recording for audio, which were of varying nature and conditions. The experiment also focused on the occipital potentials O1 and O2 based on the 10/20 method. Because this electrode is the most capable of detecting the  $\alpha$ -wave frequency band.

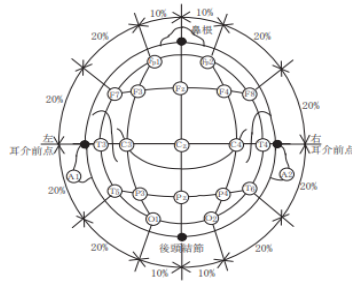


Fig. 1 Placement of electrodes using the 10/20 method.

Table 1 Order in which the audio was played and the name of each environment.

No	Environment Name
1	On the bridge (at night)
2	Classroom
3	Park square (in front of shops)
4	Station premises
5	Laboratory
6	Living room
7	Station square
8	Park square
9	Footsteps on the ground
10	Shopping mall outdoors



Fig. 2 Photograph of a subject undergoing EEG measurements.

The experimental results showed that all participants detected similar waveforms, albeit with

slight differences. It was also found that large individual differences occurred in the appearance of the  $\alpha$ -wave frequency band. Based on the results, the subjects were classified into two groups, Pattern-1 (high EEG intensity(B,H,I,J,O)) and Pattern-2 (low EEG intensity (A,C,D,E,F,G,K,L,M,N)). The classification method was based on whether the average value of Band power ( $\alpha$ -waves intensity) exceeded 10 or not. Band power is derived by performing an FFT on the  $\alpha$ -waves frequency band. There is a difference of approximately four times this value between Pattern-1 and Pattern-2.

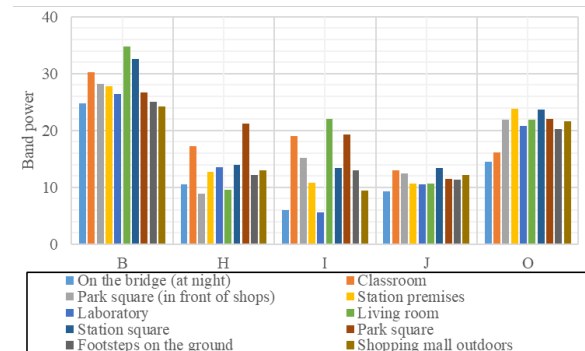


Fig. 3 Band power values of subjects in Pattern-1

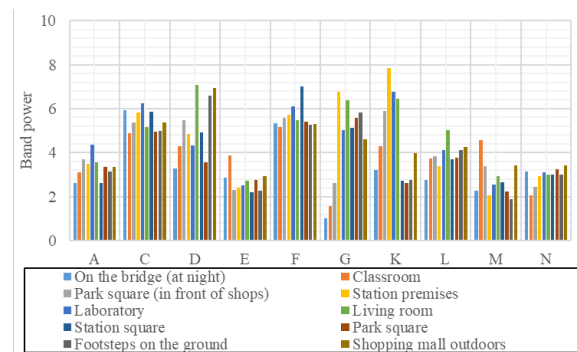


Fig. 4 Band power values of subjects in Pattern-2

A comparison of the characteristics of environments with high Band power values shows that Pattern-1 was dominated by lively environmental sounds associated with human activity and open spaces, while Pattern-2 was dominated by calm environments with relatively few people. Overall, the results show that "Living room" tends to be widely preferred and "On the bridge (at night)" is less favored.

Table 2 Classification of subjects in Pattern-1 and Pattern-2 and their Band power values.

Pattern-1	Pattern-2
Park square	Living room

Living room	Laboratory
Station premises	Station square
Classroom	Shopping mall outdoors
Park square	Park square
(in front of shops)	(in front of shops)
Station square	Footsteps on the ground
Footsteps on the ground	Station premises
Shopping mall outdoors	Classroom
Laboratory	Park square
On the bridge	On the bridge
(at night)	(at night)

Note: They are ordered from the top to the bottom by the Band power value.

However, there existed environmental sounds for which the tendency of the preferred environmental sound for each pattern was completely different. From the above, it can be considered that there is a relationship between the amount of detected  $\alpha$ -waves frequency bands and the preferred environmental sounds, although there are some individual differences among listeners.

#### FOURIER ANALYSIS

Fourier Analysis was used to compare the appearance of the  $\alpha$ -waves frequency band for different patterns. The data used were the high values of Band power and the time course, as determined in the EEG measurement experiment.

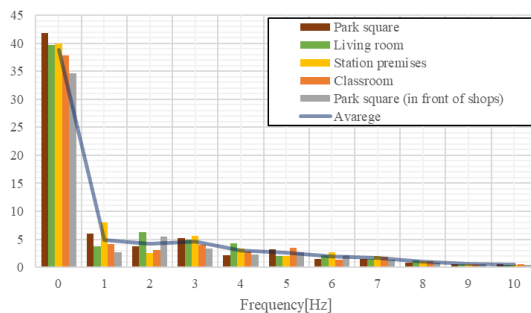


Fig. 5 In Pattern-1, after Fourier Analysis (top 5 Band power values).

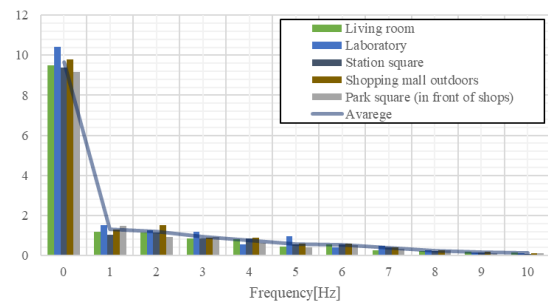


Fig. 6 In Pattern-2, after Fourier Analysis (top 5 Band power values).

The results showed that the waveform trends of both patterns were similar. In addition, only Pattern-1 showed variations for each environmental sound. This is the result of the individual differences of the subjects belonging to Pattern-1, which were largely reflected in the results.

Next, we compared the data from 'Park square' and 'Research room', which showed the most differences in the likelihood of each pattern being preferred in the EEG measurement experiment.

It can be read that the waveform transitions for both subjects were different. Despite the experiment being conducted under the same conditions, there are significant unconscious individual differences between subjects in the degree of their response to the environmental sounds.

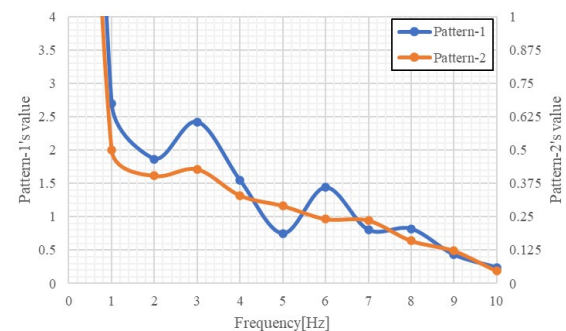


Fig. 7 Values after Fourier Analysis for each pattern ("Park square").

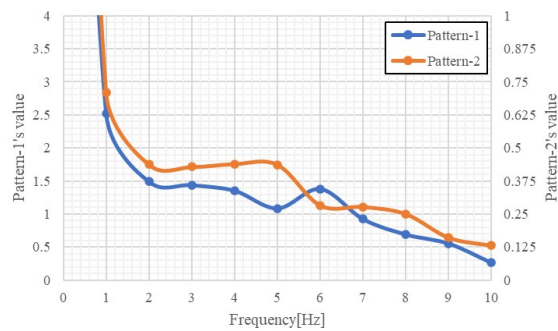


Fig. 8 Values after Fourier Analysis for each pattern ("Laboratory").

These results suggest that the characteristics of environmental sounds preferred by people can be divided into two main categories.

First, there are environmental sounds favored by many people, such as 'Living room' sounds. Calm sounds and familiar sounds may fall into this category. Second, there are environmental sounds such as 'Park square' and 'Research room', whose preference varies greatly depending on the amount of  $\alpha$ -waves frequency band detected. It is necessary to examine the relevance of these, together with various factors of the listeners, such as their preconceptions of environmental sounds, such as their preferences and experiences, visual images, and psychological responses.

## CONCLUSION

The experiment showed that, regardless of the appearance of the  $\alpha$ -waves frequency band, the sounds of daily life were the most preferred and the bridge was the least preferred. It was also found that there were several environmental sounds that showed significantly different results for each subject. The subjects with the highest frequency of appearance preferred lively environments such as Park square and Classrooms, while the subjects with the lowest frequency of appearance preferred calm environments such as Laboratories and Shopping mall outdoors. We hypothesized that the loudness of the environmental sounds may have a significant effect on the individual differences in the way subjects' brain waves appeared.

However, there are many challenges in the experimental process because of the large individual differences among subjects in the analysis of  $\alpha$ -waves frequency bands. In order to reduce bias due to subject characteristics, more data needs to be statistically handled. In the future, we will conduct validation using visual imagery and psychological response analysis in order to correctly assess how environmental sounds are heard.

## ACKNOWLEDGMENTS

We would like to express our sincere gratitude to all the subjects who cooperated with us in carrying out this research. We would like to thank Professor Kazunari Tanaka of the Department of Urban Design Engineering, Faculty of Engineering, Osaka Institute of Technology, for his guidance in all aspects, including providing us with the impetus for the research and the starting point for the research. I would also like to express my sincere gratitude to the members of the Spatial Design Laboratory who guided me from the very beginning in the handling of the machines used in the experiments, the composition of the thesis and other difficult questions at key points, and to the students who worked hard together on the research and supported each other in many ways.

## REFERENCES

- [1] Teruo Okuma Clinical Electroencephalography, 5th edition (Igaku Shoin) Kazuei Suenaga, Yasunori Okada Latest EEG Standard Text (Medical System Training Institute) P24
- [2] Ministry of Internal Affairs and Communications, "Annual Report of the Pollution Coordination Committee for FY 2020," p. 21
- [3] Goto, Hisaki, Research on Positive Environmental Effects in Office Environments and its Experimental Investigation.
- [4] Ministry of Internal Affairs and Communications, "Results of the 2020 Communications Usage Trends Survey".
- [5] Yoshida, Michiyuki, 'Objective Measurement and Evaluation of Comfort'.
- [6] Shimai, Tetsushi and Tanaka, Masatoshi, 'Relationship between pleasant and unpleasant evaluation of environmental sound and sound pressure'.
- [7] Hirai, Akiyasu, Koji Yoshida and Isao Miyaji, 'Comparative analysis of thought and memory during learning by simple electroencephalography'.
- [8] Shun Hirasawa, Tetsuya Watanabe and Motohachiro Tanaka, 'Comfort evaluation of environmental sound using EEG'.
- [9] Tahara, Kei, Tsuneo Harashima, Yuko Kobayashi and Akiyoshi Katada, Research on Auditory Imagery of Environmental Sounds in People with Hearing Impairment.



# APPLICATION OF THREE-DIMENSIONAL POINT CLOUDS FOR RIVER MANAGEMENT USING DRONE SURVEYING

Nanoka Akiyama<sup>1</sup>, Satoshi Nishiyama<sup>2</sup>

<sup>1,2</sup>Graduate School of Environmental and Life Science, Okayama University, Japan

## ABSTRACT

In recent years, record-breaking rainfall has been increasing due to effects such as global warming, which causes extensive damage in many parts of Japan every year. However, in the current river management, this is only determined by the results of visual inspections on foot or periodic longitudinal and cross-sectional surveys every 200 m. Therefore, we consider the use of three-dimensional laser point clouds acquired by ICT devices in river management recently. The 3D data obtained by laser point clouds can visualize the topography as a continuous "surface," thus improving the efficiency and sophistication of river management. Therefore, the purpose of this study is to investigate the application of 3D laser point clouds to river management using a drone survey equipped with a green laser scanner that can penetrate underwater. As a result, we can determine the underwater transmission capacity, and the depth that can be measured depends on the transparency, but we consider that it is effective to apply it to survey the underwater topography at shallower than about 2.0m. In addition, it was found that the surveying with an accuracy of 5 cm could be performed by using the adjustment points for measuring the height of river levees to identify overtopping hazard areas, which requires an accuracy of about 50 mm. Moreover, we demonstrated that it is possible to detect the deformation locations in real time by developing a method to superimpose the laser point clouds at two periods.

*Keywords: Three-dimensional point clouds, River management, Drone, ICP*

## INTRODUCTION

Recently, owing to factors, such as global warming and, frequent short duration heavy rains with hourly rainfall exceeding 50 mm and heavy rains with total rainfall exceeding several hundred to several thousand millimeters, causing large-scale disasters throughout Japan every year [1]. Additionally, considering the increasing tendency of factors, such as linear precipitation belts, to cause heavy rainfall, it is even more important to closely inspect rivers over vast distances. However, in the current river management system, only the results of visual inspections conducted on foot during the outflow period, typhoon season, and after the outflow, or periodic longitudinal and cross-sectional surveys conducted every 200 m are considered. Furthermore, the paucity of engineers and financial resources has become severe, and it is difficult to work for the detail and frequency of inspections. However, visual inspections rely on soundness judgments based on the experience of the engineer. Moreover, there is a lack of objective evidence to take measures at necessary places on a priority basis in the absence of quantitative data. Therefore, in recent year, we considered the application of three-dimensional (3D) point clouds acquired by Information and Communication Technology (ICT) devices in periodic longitudinal and cross-sectional surveying of rivers. In conventional surveying, the data is created by connecting "points" that surveyed point by point.

But this surveying allows visualization of the topography as a continuous "surface" that can be inspected and surveyed in detail. Including this advantage, the application of 3D point cloud data by ICT devices can improve the efficiency and sophistication of river management [2].

Among the various methods used in point cloud laser surveying systems, in this paper, we focus on drone surveying with a green laser scanner. It is equipped with a green laser scanner that penetrates underwater and measures the terrain on land and in the water from the ground level below 150 m with a high density of more than 100 points/m<sup>2</sup>. These features are garnering attention as promoting Digital Transformation (DX), and green laser drones are expected to be utilized for detailed surveying and inspecting of localized areas. Therefore, the purpose of this paper is to examine the application that can demonstrate the characteristics of green laser drone surveying, which is expected to be a method to realizing DX in the river sector.

## EXPERIMENTAL MEASUREMENT

### Used Equipment

As shown in Figure 1 and Table 1, we used a drone equipped with a green laser scanner of the wavelength of 532 nm, which penetrates underwater. The drone is equipped with a GNSS system with  $\pm 10$  mm horizontal and  $\pm 20$  mm altitude positioning

accuracy.



Fig. 1 Drone equipped with green laser scanner

Table 1 Specifications of the green laser scanner

Laser wavelength	532 ± 1 nm
Laser pulse rate	60,000 Hz
Scan speed	30 scan/s
Laser reflective angle	90°
Beam divergence	0.3 mrad
Weight (main body only)	2.6 kg

### Measurement Site And Experiment Overview

Figure 2 shows an overview of the measurement site. We measured in an approximately 1.2 km section from 14.6 to 15.8 km of Asahikawa River, Okayama Prefecture, as denoted by the red frame in Figure 2, in March 2020, October 2020, and April 2021 at three periods.



Fig. 2 Measurement site

Table 2 shows a summary of the measurement work. The ground altitude is the height above the water surface. The measurement method was varied at the third period in order to compare the effect of point cloud density.

Table 2 Measurement work

Period	First	Second	Third
Ground Altitude	50 m		100 m
Side lap	75 %		60 %
Flight speed	2.5 m/s		4 m/s

## ANALYSIS OF SYSTEM CHARACTERISTICS

### Point Density

Table 3 shows the point density at three periods. In addition, Figures 3 and 4 show the point density results obtained at first and third periods, respectively. The point densities in the first, second, and third periods are different because of the difference in ground altitude.

Table 3 Point density at three periods

Unit: points/m <sup>2</sup>	Point density
First period	100–1200
Second Period	100–1000
Third period	50–400

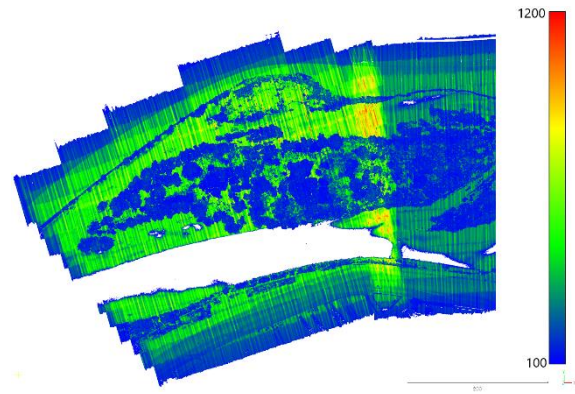


Fig. 3 Point density result at first period

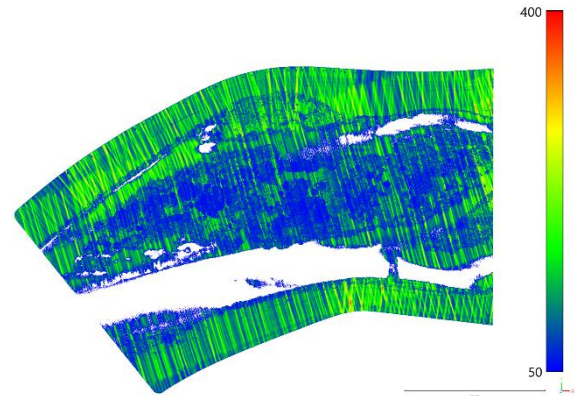


Fig. 4 Point density result at third period

### Accuracy Verification Results On Land

In the field, adjustment points were established to correct the data and verification points were set up to verify the accuracy of the survey. The accuracy was verified by comparing the surveying results using the Total Station (TS) with the drone surveying results. Table 4 shows the verification results of the surveying accuracy at three periods. In the table, X and Y refer to the horizontal directions whereas Z refers to the

elevation direction. The values in the table are the mean and Root Mean Squared Error (RMSE) of the difference between the coordinates values of the drone equipped with the green laser scanner and TS. In three periods, the mean and RMSE were below 50 mm in the plane and below 30 mm in the elevation, indicating that good measurements were possible. It was demonstrated that the desired accuracy of green laser drone surveying can be ensured by using

arbitrary adjustment points. In addition, the "Manual for Utilization of 3D Data for River Management (Draft)" states that a measurement accuracy of about 50 mm is required for grasping the height and shape of levees in order to extract overtopping hazard areas [2]. Therefore, it was found that it is possible to survey with an accuracy of 50 mm, which is necessary to grasp the height and shape of levees by using the adjustment points.

Table 4 Verification accuracy results at three periods

Unit: mm	First period			Second period			Third period		
Direction	X	Y	Z	Y	Y	Z	X	Y	Z
Average difference	0	13	8	8	-6	8	-4	-14	-1
RMSE	43	16	29	29	14	29	32	29	17

### Effect Of River Transparency On Riverbed Measurement

Table 5 shows the transparency measured in the field and the maximum water depths that could be measured. With the FTU turbidity of 0.8, a maximum water depth of 2.0 m could be measured, but with the FTU turbidity of 3.1, topographic surveying of water depths greater than 1.0 m was difficult. From these results, we consider that it is possible to apply to survey the water depth below 2.0 m when the FTU turbidity is below 1.0. In addition, cross-sectional views of the river channel for three periods are shown

in Figure 5 and 6. The point clouds at 1–3 periods are represented by green, red, and blue point clouds, respectively. At this location, the accumulation and erosion of approximately 20–70 cm was observed. It can be noticed that the high-density point clouds can reproduce the detailed topography of the riverbed.

Table 5 FTU turbidity and maximum water depths

Period	FTU turbidity	Maximum water depths
First	0.8	2.0 m
Second	3.12	1.0 m
Third	2.45	1.7 m

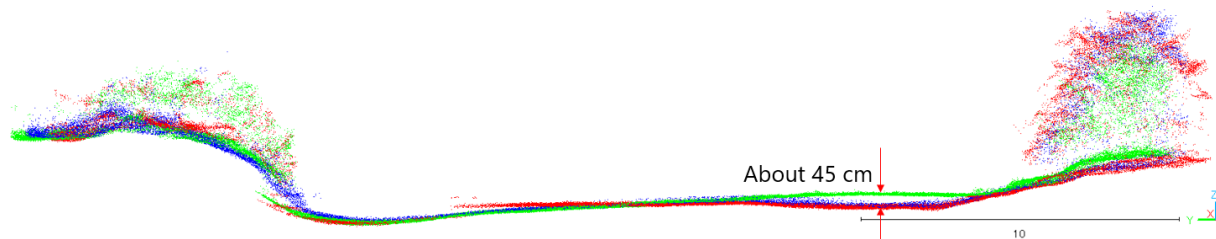


Fig. 5 Example of river cross-sections 1

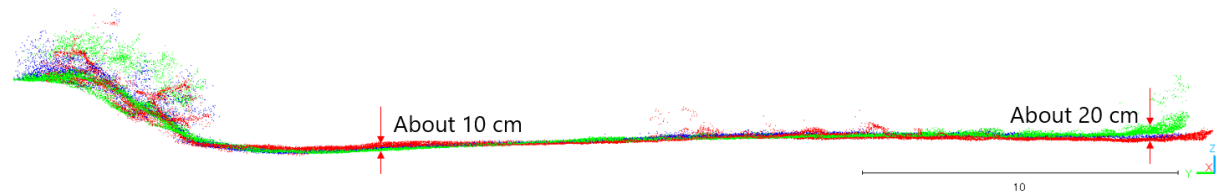


Fig. 6 Example of river cross-sections 2

### TECHNOLOGY FOR EXTRACTION OF DEFORMATION LOCATIONS

High density laser point clouds reproduce the topography of the measured section in detail by the green laser drone surveying. Therefore, the drone survey data is big data. In the long management

section, the number of point clouds can be more than several hundred thousands, and without data processing technology that can easily detect where deformations occur, the measurement results cannot be used effectively even if the detailed topography is reproduced. In this study, we developed laser point clouds analysis by applying Iterative Closet Points

(ICP) [3], [4]. ICP is a technology used to superimpose the figure made from the laser point clouds of the second period on the figure made from the laser point clouds of the first period, as shown in Figure 7. The displacement and direction of points can be regarded as displacement vectors, so that deformations can be expressed quantitatively and analyzed as point clouds. ICP is the process of directly superimposing the data of two periods without creating a TIN model from the point clouds data so that real-time analysis is possible.

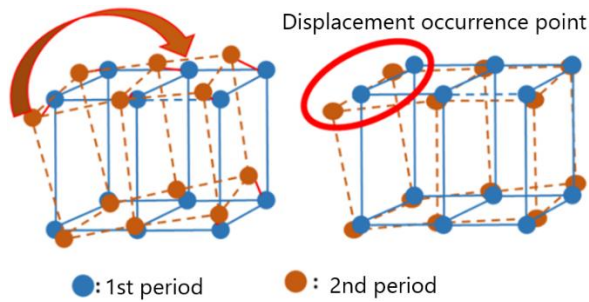


Fig. 7 Concept of data processing by ICP

Figures 8 and 9 shows the results of deformation extraction at the levee crown along the Z direction. Deformities are represented on a color scale. The result of the deformation extraction of the levee slope is shown in Figures 10 and 11. Figure 12 shows the point clouds for the first and second periods in green and blue, respectively. Slope deformations are represented by vectors. At the levee crown, since the deformation was within 5 cm, we considered that the levee has not settled. Slope deformations are represented by vectors. In addition, the displacement was more than 2 m on the levee slope. This is the vegetation growth during the two periods from Fig. 12. Thus, it is possible to obtain deformations in the local area. Furthermore, by filtering out vegetation, it is possible to capture changes in the ground surface itself.

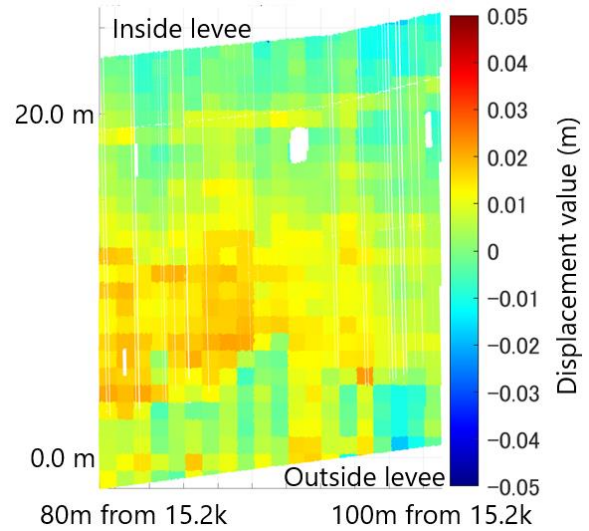


Fig. 8 Example of deformation extraction at the levee crown 1

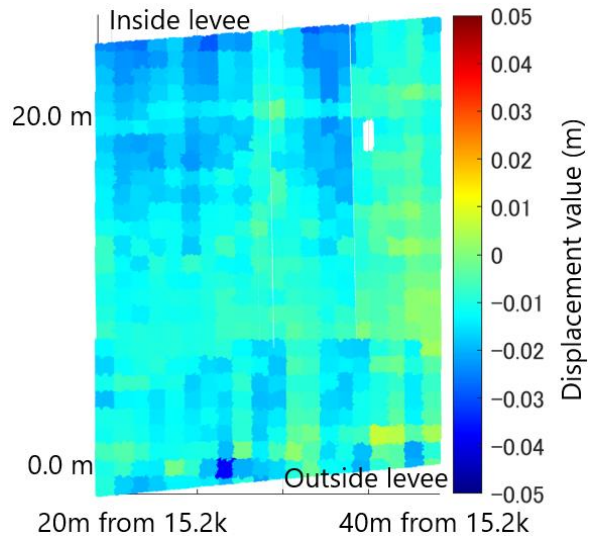


Fig. 9 Example of deformation extraction at the levee crown 2



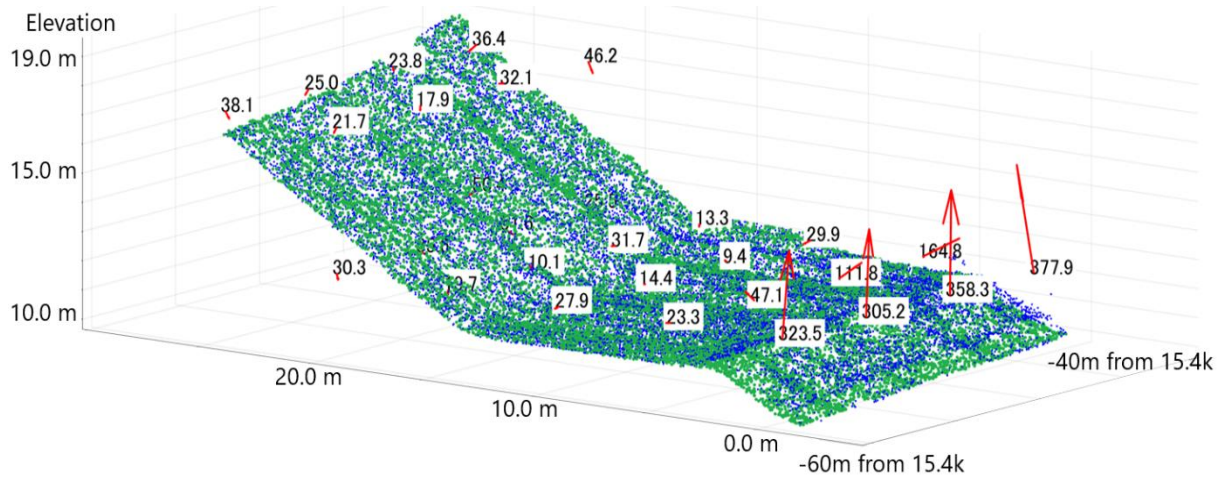


Fig. 10 Example of deformation extraction at the levee slope 1

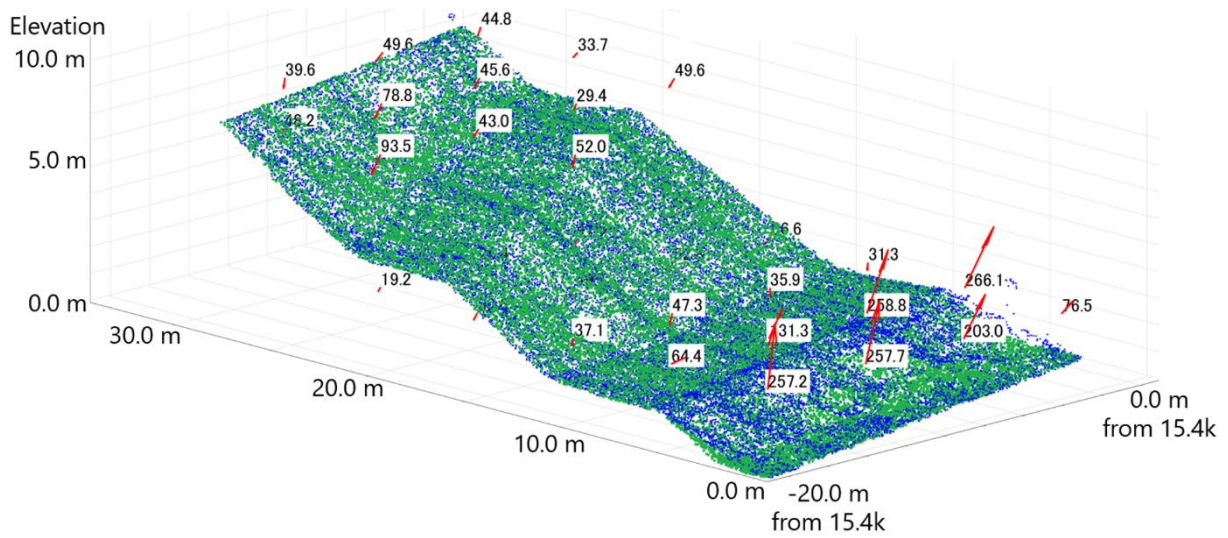


Fig. 11 Example of deformation extraction at the levee slope 2

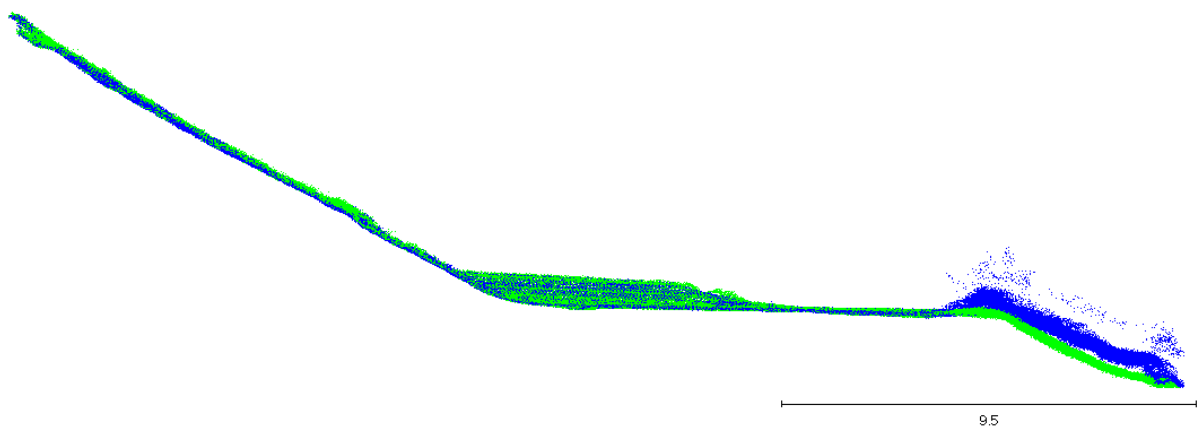


Fig. 12 Point clouds of levee slope in two periods

## CONCLUSIONS

In this paper, we examine the application that can demonstrate the characteristics of green laser drone surveying, which is expected to be a method to realizing DX in the river sector. The following summary shows applications for river management.

- 1) The point density obtained depends on the ground altitude. We need to change the ground altitude depending on the object to be measured.
- 2) It is possible to obtain the accuracy within 50 mm by using arbitrary adjustment points. Therefore, we can survey with an accuracy, which is necessary to grasp the height and shape of levees in order to extract overtopping hazard areas.
- 3) It is possible to determine underwater permeability with the FTU turbidity. It is useful for surveying topography at the FTU turbidity below 1.0 and water depths shallower than approximately 2.0 m.
- 4) Because the application of the ICP technology used in this study can quantitatively represent the deformation location, it has proven to be capable of deformation location in real time.

In the future, it is necessary to study the extracting deformations of riverbeds and the levees after vegetation removal by filtering. In addition, we need to study the effect of point density on deformation extraction.

## ACKNOWLEDGMENTS

This study was conducted under the project research of the Okayama Office of River, Ministry of Land, Infrastructure, Transport, and Tourism.

## REFERENCES

- [1] Nishimura S., Takeshita Y., Nishiyama S., Suzuki S., Shibata T., Shuku T., Komatsu M., and Kim B., Disaster report of 2018 July heavy rain for geo-structures and slopes in Okayama, Soils and Foundations, Vol. 60, Issue 1, 2020, pp.300-314.
- [2] Office of River Conservation Planning, River Environment Division, Water Management and Land Conservation Bureau, Ministry of Land, Infrastructure and Transport, Manual for Utilization of 3D Data for River Management (Draft), 2020.
- [3] Szymon R. and Marc L., Efficient Variants of the ICP Algorithm, Proceedings Third International Conference on 3-D Digital Imaging and Modeling, 2001, pp. 145–152.
- [4] Dirk H., Alexandru E. I., Federico T., Radu B., and Sven B., Registration with the Point Cloud Library, IEEE Robotics & Automation Magazine, Vol. 22, Issue 4, 2015, pp.110-124.



## ASSESSMENT OF DOMESTIC WASTEWATER MANAGEMENT PROGRAMS IN RIVERBANK SETTLEMENTS

Moch Zaelani Pebriansyah<sup>1</sup>, Ahmad Soleh Setiyawan<sup>2</sup>, Dyah Wulandari Putri<sup>3</sup> and Ken Aryu Ruska Yuniar<sup>4</sup>

<sup>1,4</sup> Water Supply and Sanitation Infrastructure Management, Institut Teknologi Bandung, Indonesia;

<sup>2,3</sup> Wastewater Engineering Research Group, Institut Teknologi Bandung, Indonesia

### ABSTRACT

Riverbanks areas have long been public settlements due to increasing population and economic problems. Bojong Village, Bandung Regency, Indonesia is one of the public settlements along the Cisungala river that has poor sanitation level. The purpose of this research was to select the most appropriate domestic wastewater management programs to be implemented in a riverbank area. Identification of domestic wastewater management practices was carried out by observation, interviews and questionnaires addressed to stakeholders and community. A pairwise comparison test was performed to assess the criteria on the selection of domestic wastewater management programs. The sanitation level in the riverbank area was mostly basic sanitation. Many residents discharged wastewater directly into river without any treatment process. There were various programs regarding domestic wastewater management, but they were not running effectively. A pairwise comparison test showed the weighting factors on the program selection criteria. The programs were selected based on various aspects, namely technical, social, institutional, financial, and regulatory aspects. The appropriate programs that increase public awareness regarding domestic wastewater management along with development onsite wastewater treatment facilities are needed to improve the level of sanitation and to create sustainable sanitation in riverbank settlements.

*Keywords: Assessment, Domestic wastewater, Management program, Riverbank area*

### 1. INTRODUCTION

A challenging area is an area that are difficult to build or apply affordable systems of sanitation services because of the geography and the climate condition, one of which is the riverbank [1]. These riverbanks areas also face social and economic problems, such as the illegal status of the sites and the low-level education and income of the inhabitants [2], [4]. The buildings along the rivers create numerous environmental problems, such as waste resulting from mining activities and household waste directly disposed to the river [3], [4].

Household wastewater management is classified into two categories: waste-wastewater (MCK) and kitchen wastewater [5]. According to the Regulation of the Governor of the Special Capital Region of Jakarta Number 41 of 2016 concerning the Master Plan for the Development of Domestic Wastewater Management Facilities and Infrastructure, wastewater is water that comes from the rest of the production process and other business activities that are not reused. Domestic wastewater, either grey water or black water, is wastewater derived from household, housing, apartments, offices, hospitals, malls, marketplaces, supermarkets, hotels, industry, and schools. By the regulation specified above, grey water includes kitchen-based non-toilet wastewater, waste-washing, and used bathing water, while black water is wastewater containing human waste **Error! Reference source not found..**

Sanitation infrastructure is critical for public

health and environment. Lack of sanitation is linked to reduced health and environmental degradation [7], [8], **Error! Reference source not found..** The importance of sanitation is reflected in Sustainable Development Goals (SDGs) 6. In slum areas, economic limitations, socio-cultural factors, and lack of knowledge cause low-income people to have a low level of concern for the quality of their housing, including water and sanitation [9], **Error! Reference source not found..** Fulfilling basic needs for clean water and sanitation is still a challenge faced by Indonesia in achieving SDGs targets [11], **Error! Reference source not found..** In 2019, national access to basic sanitation was 77.39%, where in West Java Province only 69.64% of its population has access to basic sanitation [12].

There is a gap between the government agenda and existing conditions in the field. This calls for a strategy for domestic wastewater management in the Bojong village riverbank, which is part of Majalaya subdistrict, reaching a target of adequate and safe sanitation access based on cooperation between municipal and provincial government. Not only may it be a physical infrastructure, but it may be a non-technical program associated with increasing access to domestic wastewater management facilities in the region. This study aims to develop strategies for sustainable domestic wastewater management in the riverbank area.

### 2. STUDY AREA

The research is conducted in Bojong Village, Majalaya District, Bandung Regency, Indonesia. The Cisungala River are located in Bojong Village, one of the sub-districts in Majalaya and its location can be seen in Figure 1.

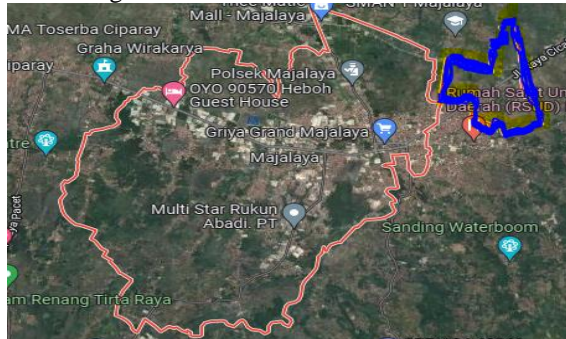


Fig. 1 Located of Bojong Village in Majalaya District, Bandung Regency



Fig. 2 Existing Condition of Cisungala River in Bojong Village

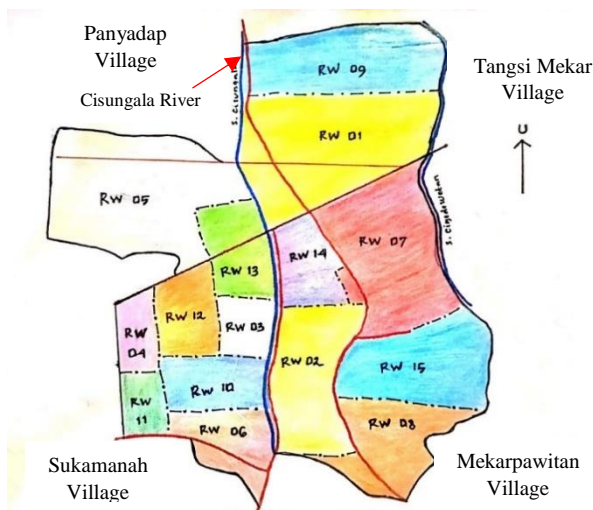


Fig. 3 Administrative map of Bojong Village

## 2.1 Area Description

Bojong Village is one of the villages in Majalaya District, Bandung Regency, Indonesia which has an area of 175.54 Ha. In 2020, the population of Bojong Village was 14,372 people. In 2019, the number of houses that have latrines was

2,709 units or 71.2% of the total houses and 11 units of public toilets. The Cisungala River is one of the tributaries of Citarum River, which passes through the administrative area of Bojong Village. The number of hamlets (RW) traversed by this river is 4 RW, namely RW 03, RW 06, RW 10 and RW 13. This research was carried out at those 4 hamlets. The distribution of each hamlets can be seen in Figure 3.

## 2.2 Domestic Wastewater Management Programs

Domestic Wastewater Management Programs is a list of programs regarding to the domestic wastewater management that have been implemented in various locations, precisely on the banks of rivers in Indonesia. In determining programs on the banks of the Cisungala river (Table 1), there are several stages in the program proposal, namely a longlist of program proposals, criteria for evaluating program proposals, and a shortlist of program proposals.

## 3. METHODOLOGY

This research was carried out in three stages, including problem formulation, program proposals, and program evaluation using pairwise comparison test. Primary data were obtained from questionnaire data on the community and experts in the field of domestic wastewater. Meanwhile, secondary data was obtained by searching for data related to the existing condition of the study area and the proposed program, and then conducted an assessment of the proposed program.

### 3.1 Identification of Problems

The components in the study were further detailed to focus more on problems in the study area regarding domestic wastewater management. A preliminary study was carried out by conducting brief interviews with residents around the study area regarding domestic wastewater management. A literature study was performed by searching for related problems from other areas. The problems found were then collected and matched with the conditions of the study area through a preliminary study.

### 3.2 Proposal of Programs

The program proposal is the stage of seeking information about domestic wastewater management programs that have been implemented by governments in other areas. There are several processes, namely longlist, assessment criteria and shortlist of program proposals.

#### 3.2.1 Longlist of Program Proposals

Longlists of proposed programs or long data on sanitation programs were obtained by studying literature from various sources such as research journals, reports on best practice programs for each

relevant domestic wastewater management programs from printed and online media. organization, and explored information on sanitation

Table 1 Shortlist of proposed domestic wastewater management programs in the Cisungala Riverbank area

No.	Aspect	Program
1	Technic	The Construction of Communal WWTP
		The Construction of communal Biofilter Septic Tanks
		The Construction of Individual Septic Tanks
		The Construction of piping network from Septic Tank to Communal WWTP
		Optimizing of Regional WWTP
		Optimizing of FSTP
2	Social Society	General MCK renovation
		Sosialization of Sanitasi Masyarakat dan Sekolah (SMS) programme
		Stop BABS Program
		Training of Technical and Practice Health Latrine
3	Institutions	Trisula's approaches to build awareness of people
		Institutional training for community self-help group
		Establish cooperation with other institutions build latrine and communal WWTP
4	Financial	Formation of the sanitation authority
		Private financial aid
		Periodic community fundraising
		Savings and loan money
5	Regulations	Savings and loan money from other members
		River Normalization regulatory
		River cleaning regulation
		Regulation for development at the river crossing

### 3.2.2 Assessment Criteria of Program Proposals

These criteria are recorded and assessed based on the existing conditions of the study area obtained from preliminary studies and literature studies. In determining the assessment criteria used, it must first be known the existing condition of the study area related to the criteria or factors obtained from each program. The criteria consist of the physical condition of the area, social, financial and economic conditions, as well as its institutions.

### 3.2.3 Shortlist of Program Proposals

Shortlist of program proposals is the result of sorting several programs that have been obtained from the longlist of program proposals through an assessment of several predetermined criteria. If the program passed at least half of the predetermined criteria, it is included in the shortlist of the proposed programs.

## 3.3 Assessment of Programs

In this stage, programs that have entered the shortlist of proposed programs were then assessed to determine the weight of the value of each program which was expected to be used as a reference in conducting a study of program implementation. For each aspect of domestic wastewater management, one program with the highest weight value was selected through the Pairwise Comparison test.

The Pairwise Comparison test is carried out

with the principle of Comparative Judgment. This principle is carried out by making an assessment of the relative importance of two elements at a certain level in relation to the level above it. The assessment affects the priority of the existing elements. The results of this assessment are written in a pairwise comparison matrix [13]. With pairwise comparisons, it can be seen the degree of relative importance between criteria. In the data processing, used Ms. excel 2013 and for data validation used SPSS vers. 25.

## 4. RESULTS AND DISCUSSION

### 4.1 Existing Condition of Domestic Wastewater Management

From figure 4, it can be seen that people in the area along the Cisungala River still use squat toilets as a user interface. However, there are still many people who do not have a septic tank and drain their domestic waste into the river. Thus, access to sanitation in this area is still relatively low and needs improvement.

Sanitation level of the community along Cisungala River was categorized as having basic sanitation 57.43%, access to proper sanitation 24.3%, access to safe sanitation 3.24% and no access to personal sanitation 15.03%. Figure 4 shows a diagram of domestic wastewater management in the area along

Cisungala River.

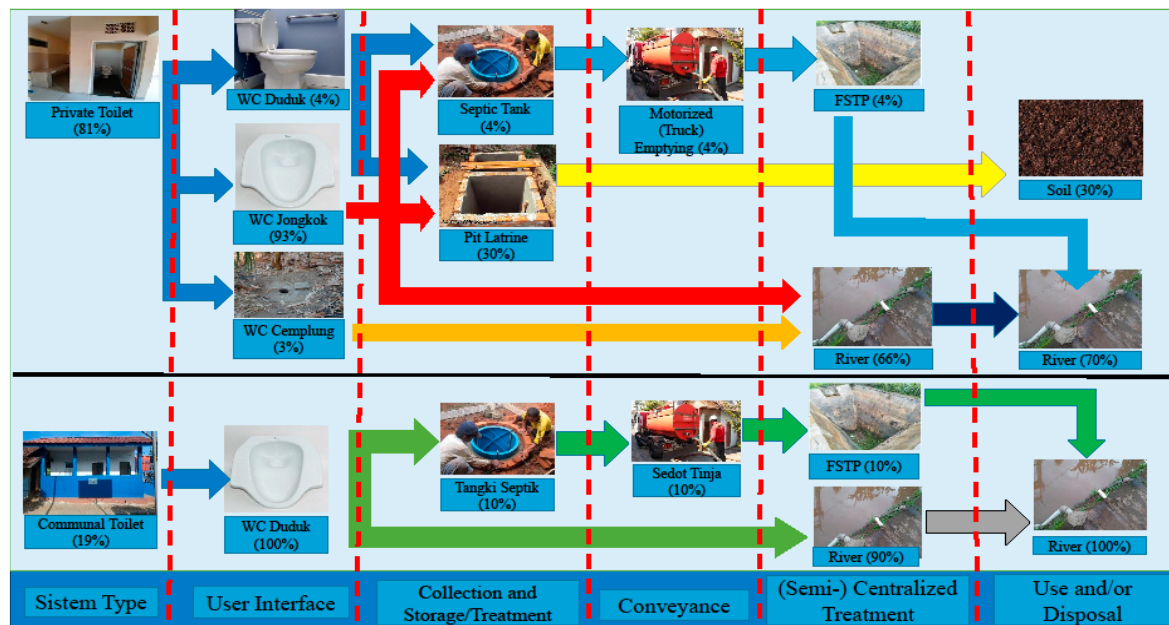


Fig. 4 Summary of the existing conditions of domestic wastewater management systems

#### 4.2 Evaluation of Existing Programs of Domestic Wastewater Management

In evaluating the existing domestic wastewater management program in the area along the Cisungala River, it was carried out by conducting literature studies and field observations with the results of community questionnaires. From the results of the community questionnaire, there are results regarding the residents' desire for toilet facilities and also aspects of community participation in evaluating the communal MCK development program.

Furthermore, in assessing community awareness, there are several parameters/sub-criteria that become questions to the community which consist of sub-criteria for community participation in the construction of MCK facilities, the form of community participation and community desires/initiatives in village activities. The results of the questionnaire can be seen in Figure 5.

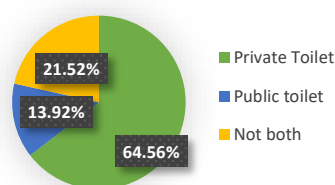


Fig. 5 Respondents' wishes for toilet facilities (n=79)

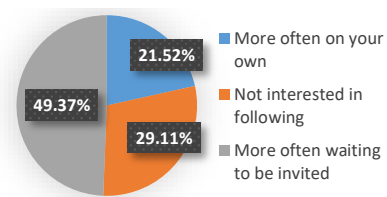


Fig. 6 Respondents' Initiative for participating in village activities (n=79)

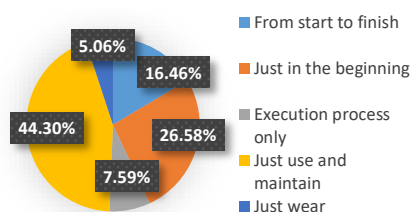


Fig. 7 Respondents' willingness in facility building activities (n=79)

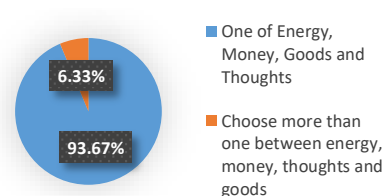


Fig. 8 Respondents' participation in the construction of facilities (n=79)

From the graph, it can be concluded that community participation in the Cisungala Riverbank area is still not too high, there is no community initiative/awareness to help in building facilities.

Tabel 2 shows evaluation of the existing program that has been carried out in the Cisungala riverbank area.

Table 2 Evaluation of existing programs in the area along the Cisungala River

No.	Programs	Existing Condition	Solution
1	Construction of Public MCK (Communal WC)	the majority is used for washing clothes for residents	the construction of private toilets is recommended in this area, because of privacy. Can be equipped with the construction of a septic tank for each private WC that has been built.
		the majority of bathing and latrine activities are carried out in private toilets	
		The majority have private toilets, but don't have a septic tank/similar	
		public toilet cleaning is still voluntary	
2	Citarum Harum Program	operational and maintenance activities are still a formality, after the handover O&M is not visible	if there is construction of a public toilet, it is necessary to carry out maintenance and operation, it can be handed over to residents for picket or a special officer designated for maintenance of the facility.
		Bojong Village is not included in the sanitation management area in this program	by submitting to related parties or being able to personally design sanitation activities by utilizing existing sanitation funds or submitting proposals to private parties
		there is still a pipeline that flows into the river	there is a need for socialization in the community to understand the surrounding residents
		there are still people who have doubts about this program	
		the availability of land in the area along the Cisungala river is limited	the willingness of residents to donate their land, but if necessary communal facilities can look for vacant land belonging to the village
		there are still few experts/facilitators related to sanitation	cooperation with other parties is needed to become a facilitator in the sanitation sector

Table 3 Recapitulation of the results of pairwise comparison testing for domestic wastewater management programs in the riverbank study area

No.	Aspect	Value Aspect	Programs	Value Program	Program Priority
1	Technical	0.243	The Construction of Communal WWTP	0.082	6
			The Construction of communal Biofilter Septic Tanks	0.125	5
			The Construction of Individual Septic Tanks	0.226	1
			The Construction of communal wastewater piping network from Septic Tank to Communal WWTP	0.175	2
			Optimazing of Regional WWTP	0.149	4
			Optimazing of FSTP	0.170	3
			General MCK renovation	0.073	7
2	Social Society	0.367	Sosialization of Sanitasi Masyarakat dan Sekolah (SMS) programme	0.239	2
			Stop BABS Programme	0.185	4
			Training of Technical and Practice Health Latrine	0.224	3
			Trisula's approaches to build awareness of people	0.352	1
3	Institutions	0.099	Institutional training for community self-help group	0.449	1
			Establish cooperation with other institutions build latrine and communal WWTP	0.346	2
			Formation of the sanitation authority	0.206	3
4	Financial	0.176	Private financial aid	0.422	1
			Periodic community fundraising	0.277	2
			Savings and loan money	0.125	4
			Savings and loan money from other members	0.176	3
5	Regulations	0.115	River Normalization regulatory	0.428	1
			River cleaning regulation	0.276	3
			Regulation for development at the river crossing	0.296	2

#### 4.3 Assessment of Domestic wastewater Management Program

Tabel 3 shows a recapitulation of the results of the Pairwise Comparison Testing for domestic wastewater management programs in the riverbank study area. The technical aspect of the priority program was the construction of individual septic tanks (0.226). In the socio-community aspect, the priority program was the Trisula Approach to Build Community Awareness (0.352). In the institutional aspect, the priority program was Institutional Training for community self-help group (0.449). In the financial-financial aspect, the priority program was financial assistance from the private sector (0.422), and for the regulatory aspect, the priority program was the river normalization program (0.428).

#### 5. CONCLUSION

This research was identified the sanitation condition and propose the most appropriate domestic wastewater management programs in a riverbank area. The sanitation level in the riverbank area was mostly basic sanitation 57,43% and public awareness about the importance of sanitation in that area was still lacking. Various programs based on technical, socio-community, institutional, financial, and regulatory aspects have been proposed. The recommended program by the technical aspect is building an individual treatment facility such as septic tank. The recommended program by the socio-community aspect is the Trisula Approach to build community awareness. The recommended program by institutional aspect is institutional training for community self-help group. The recommended program by financial aspects is financial assistance from the private sector. The recommended program by regulatory aspect is making regulation related to river normalization. The appropriate programs that increase public awareness regarding domestic wastewater management along with development onsite wastewater treatment facilities are needed to improve the level of sanitation and to create sustainable sanitation in riverbank settlements.

#### 6. ACKNOWLEDGMENTS

This research was supported by Riset ITB and the Global Sanitation Graduate School (GSGS) program.

#### 7. REFERENCES

- [1] E. R. Djonoputro, I. Blackett, J. W. Rosenboom, and A. Weitz, 'Understanding sanitation options in challenging environments', *Waterlines*, vol. 29, no. 3, Jul. 2010, doi: 0.3362/1756-3488.2010.020.
- [2] Sarwadi, A., Tohiguchi, M., Hashimoto, S., 2001. An analysis of the riverside settlement inhabitant's characteristics in relation to an urban situation, a case study in the musu urban riverside settlement, Palembang city, Sumatra, Indonesia. *J. Archit.Plan. Environ. Engin.*, AIJ 544, 225e231.
- [3] Prayitno, B., 2013. An analysis on spatial permeability and fluid dynamics of wind and thermal in tropical riverside residential areas of Banjarmasin city, Indonesia. *J. Manusia dan Lingkungan (J. Hum. Environ.)* 20 (2), 199e212.
- [4] M. V. Michiani and J. Asano, 'Physical upgrading plan for slum riverside settlement in traditional area: A case study in Kuin Utara, Banjarmasin, Indonesia', *Frontiers of Architectural Research*, vol. 8, no. 3, pp. 378–395, Sep. 2019, doi: 10.1016/j.foar.2019.03.005.
- [5] R. Iskandar, *Perilaku rumah tangga dalam pengelolaan limbah domestik - kasus desa-desa wilayah Jakarta, Depok dan Bogor sepanjang sungai Ciliwung*. Bogor: Institut Pertanian Bogor, 2010..
- [6] S. M. S. Wirawan, 'Community Preparation for Domestic Wastewater Management Development in Jakarta', vol. 5, no. 2, p. 11, 2020.
- [7] G. Hutton and M. Varughese, *The Costs of Meeting the 2030 Sustainable Development Goal Targets on Drinking Water, Sanitation, and Hygiene*. World Bank, Washington, DC, 2016.
- [8] M. Calver, A. Lymbery, J. McComb, and M. Bamford, *Environmental biology*. Open Oregon Educational Resources, 2009.
- [9] L. P. Defi, I. . Kusumayanti, Wika Maulany Fatimah, P. W. Sarli, and P. . Soewondo, "The The Rise Of Rainbow Village: Optimizing Aesthetical Program To Accelerate Sanitation Access", *International Journal Of Geomate*, vol. 22, no. 90, pp. 118–124, Apr. 2022.
- [10] B. Marx, T. Stoker, and T. Suri, 'The economics of slums in the developing world', *J. Econ. Perspect.*, vol. 27, no. 4, pp. 187–210, 2013.
- [11] *Badan Pusat Statistik, 'Survei Sanitasi Nasional'*, Jakarta, 2019.
- [12] R. Andiyanti, S. Mardiyah, W. S. Purba, and Y. Yunarsi, *Environment Statistics of Indonesia: Water and Environment 2020*. Jakarta, Indonesia: *Badan Pusat Statistik/BPS – Statistics Indonesia*, 2020.
- [13] Amalia, 'Analytical Hierarchy Process (AHP) : Multi-Attribute Decision Making (MADM)', 2016.



# THE IMPACT OF COVID 19 ON CHANGE OF MONTHLY INCOME IN INDONESIA

Aditya Maulana Mugiraharjo<sup>1</sup>, Chotib<sup>2</sup>

<sup>1</sup>School of Strategic and Global Studies, Universitas Indonesia, Indonesia;

<sup>2</sup> School of Strategic and Global Studies, Universitas Indonesia, Indonesia

## ABSTRACT

The COVID-19 pandemic has caused several changes and adjustments in various sectors of people's lives. One of the sectors affected is the employment sector. Various elements in the employment sector have also been affected by COVID 19, for example adjusting the number of hours worked. Furthermore, this paper wants to explain how the impact of COVID 19 affects the lost or reduced working hours and income of informal workers in Indonesia. This is important as an academic study because it is a new thing in the study of the urban field in the context of the impact of COVID 19, as well as an academic study in the discussion of the urban economy in Indonesia. The data analyzed is sourced from the 2021 Street Vendors Masterplan Survey, conducted by the Industrial, Commerce, and SME Agency of DKI Jakarta Province. The approach used is a quantitative approach, and uses a binary logistic regression analysis method. The independent variables in this study were employment status; reasons for working; work location; number of jobs; gender; age; marital status; household size; and household status.

*Keywords: COVID 19, Working hour, Job, Income, Informal Worker*

## INTRODUCTION

Urban is a space or a place for city residents to live, which consists of physical and non-physical elements. Urban areas have become one of the areas that have been heavily impacted by COVID 19 pandemic. This can be understood on the basis of the concentration of community activities, economy, entertainment, and services. Various steps were taken by the government in an effort to prevent the spread and transmission of the COVID-19, such as limiting community activities; work from home policy; efforts to encourage people mobilization with the concept of LIT (*light individual transport*) or non-motorized transportation, such as cycling and walking (International Transport Forum, 2020).

The economy is one of the sectors that has the biggest impact due to COVID 19, from the number of businesses experiencing a decline to bankruptcy, changes in the scheme of economic transactions in society, technological disruption in community activities, several matters related to the labor sector, such as the number of layoffs, reduced number of working hours (ILO, 2020; Ngadi and Purba 2020; Sobieralski, 2020; Spurr and Straub, 2020).

The number of layoffs and the reduction in the number of hours worked are the impact of the many workplace closures as a direct impact of the COVID 19 pandemic. The report of the International Labor Organization (ILO) 2929 revealed that there were several determinant variables led to a decrease in working hours, such as: *first*, working hours that are

shorter or the status of employee that employed but not working or temporarily laid off. *Second*, workers are forced to leave their active period of work and enter unemployment. The first half of 2020, it was found that around 5.4% of global working hours or the equivalent of 155 million full-time jobs have been lost due to COVID 19 (ILO, 2020; Ngadi and Purba, 2020).

In the case of several countries in the world, the opportunity to work remotely as a compromise to the COVID-19 pandemic is no more flexible due to the availability of more limited resources. In the Southeast Asia region, the percentage of lost working hours reached 2.1% or around 6 million equivalent full-time jobs in the first quarter of 2020. Meanwhile, in the second quarter of 2020, it was around 12.7% or the equivalent of 35 million time related to work. Loss or reduction in working hours occur in various ways, mainly as a result of existing labor market institutions and political decisions made, such as the implementation of large-scale social restriction policy (PSBB and PPKM) (ILO, 2020; Ngadi and Purba, 2020).

The nowcasting method proposed and used by the ILO identified four variations in cases of reduced or lost working hours: *first*, shorter working hours. What happened was a decrease in the average weekly working hours compared to the pre-COVID 19 situations; *second*, the employee status is employed but actually not working. The employee continues to have an attachment to the employment relationship, but is not involved in any work; *third*, unemployment, is the labor force available for and

looking for work; *fourth*, inactive is someone if out of the labor force (ILO, 2020).

In addition to formal workers whose changes can be seen after COVID 19, the weakest party are informal workers. According to Indonesia Central Statistics Agency, the number of informal workers in Indonesia in 2021 will amount to 70,91 million people. 1,81 million among them are informal workers who live or do their job in DKI Jakarta province. It can be understood because DKI Jakarta is the epicenter of community activities and economic cycles in Indonesia.

One of several type of informal workers is street vendors or Pedagang Kaki Lima in Bahasa Indonesia. According to dataindonesia.id, the number of street vendors Indonesia estimated in 22 million people. The challenge to get the exact amount of street vendors is they are mobile and tend to change where they do their business activity.

Based on this background explanation, this paper will explain the impact of COVID 19 on changes in working hours, as well as changes in income for informal workers especially street vendors in DKI Jakarta province.

## CONCEPT AND THEORY

### Change in Work

From the phenomenon of changes in the length of working hours in Indonesia, we can discuss using the conceptual framework of change in the context of working in a crisis situation. This concept can provide an understanding, such as crises can occur at anytime and can lead to unpredictable things. The Impact of the crisis can result in a decrease in the level of employment, and an increase in the unemployment rate (Beck, and Hensher, 2021)

Thus can be understood as the result of a damaged or disrupted supply chain system of production and distribution on a global scale. One of the root causes of the crisis that occurred in the middle of 2020-2022 was the COVID 19 pandemic which spread widely to several countries in the world.

The COVID 19 pandemic caused restrictions on community activities and which suppressed the community and of course disrupted the production supply chain system. Declining demand causes production to decline and leads to reduced financial transactions in various sectors.

Changes in work models that lead to increased layoffs and or reduced length of working hours for workers in Indonesia. Activity restrictions not only make some workers work from home but also restrictions for workers working in essential sectors who are still allow to operate, for example the limiting of employee who works in one day or one shift.

One of the keys for workers in the issue or transition period of the COVID 19 situation is how to use the time that is reduced due to restrictions on community activities. Community adaptation is needed and demands needed on the basis of changes in pattern of living and working in the community.

Changes from offline transaction patterns to online become a disruptor in community activities. People who are used to sell face to face directly between sellers and buyers are now forced to transform into online buying and selling activities.

Eichenbaum (2020) in his study revealed that policies that encourage restrictions on activities outside the home affect the number of deaths. Unfortunately, the enactment of this policy has an effect on the economy and recession. As stated earlier, the reduction in working hours was due to the COVID-19 recession (Beck, and Hensher, 2021)

The post COVID 19 situation may cause disruptions to the job market. The shift in the community service model and the form of the business model from offline to online has caused a lot of disruption to the existing business models. The offline form of store services has been reduced and replaced by online marketplace.

### Methods

The author uses data on the street vendor master plan 2021 DKI Jakarta Province. The variable used are as listed in table 1.

Tabel 1. Variables

No	Variable	Number of Question (in survey data)	Note
1	Change of Income	KR 16 and KR 17	The difference between KR 16-KR17
2	Street vendors type	KL 04	1. Lokbin 2. Loksem 3. Klaster Lapak 4. Mobile
3	Age	KR 07	Numerik
4	Sex	KR 08	1. Man 3. Woman
5	Education	KR 10	Recoding from KR 10, make 3 kategori
6	LT-Migrant	KR 11	1. migran, if was not born in DKI 0. non migran, if was born in DKI
7	R-Migran	KR 12	1. migran, if

			in last 5 years not live in DKI
8	Ownership Status	PU 02	0, non migran, if live in DKI in 5 years ago
10	Business Sector	PU 16	1. Owner 0. Others
11	Length of Business Hour	PU 21	1. Culinary 2. Non Culinary 3. Service
12	Sell in marketplace	BM 11	1. Full day 0. other
			1. Yes 3. No

## RESULT AND DISCUSSION

Based on data analysis based on the 2021 DKI Jakarta Street Vendor Masterplan data, accompanied by a discussion of the relationship between each independent variable and the dependent variable. In the context of the impact of COVID 19 on changes in the income of street vendors per month, there are several independent variables, namely: the type of street vendor; age, gender; level of education; type of population movement; business ownership status; business sector; length of trading in a day; join the online marketplace.

In the first variable, namely the age variable, it can be explained that the probability value is equal to 0.025. The basis for decision making is if the probability  $< 0.05$  then  $H_0$  is rejected. This means that the variable age of traders, there is no relationship with changes in income in a month. In this one variable, we can see that age is not a modifier or determinant of changes in traders' income

The next variable is the gender variable. Sex. Sex variables are divided into two, namely male and female. In traders, the sexes are male and female. The results of the analysis show that gender does not have a positive effect on changes in monthly income.

## CONCLUSIONS

Based on the description of the background of the problem, and looking at the discussion and discussion sections, it can be concluded that COVID 19 has a positive relationship in its influence on changes in the income of street vendors in DKI Jakarta every month.

Based on these conclusions, it can then be understood that groups of informal workers such as street vendors will experience the worst impact in the COVID 19 pandemic. The role of the Government is urgently needed in this regard, namely social assistance that can help reduce the burden on the general population.

## REFERENCES

- [1] International Transport Forum. COVID 19 Transport Brief: Analysis, Facts, and Figures for Transport Response to the Corona Virus: Re-spacing Our Cities for Resilience. 2020
- [2] Ruth Meilianna Ngadi, Yanti Astrellina Purba. Dampak Pandemi COVID 19 Terhadap PHK dan Pendapatan Pekerja di Indonesia. Jurnal Kependudukan Indonesia, Edisi Khusus Demografi dan COVID 19, 2020, pp 43-48.
- [3] Joseph B Sobieralski. COVID 19 and airline employment: Insights from Historical Uncertainty Shocks to the Industry. Transportation Research Interdisciplinary Perspectives, Vol 5, 2020.
- [4] Daniel Spurr, Caroline Straub. Flexible Employment Relationship and Careers in Times of the COVID 19 Pandemic. Journal of Vocational Behaviour, Vol 119, 2020.
- [5] DataIndonesia.id. Pekerja Informal di Indonesia Mencapai 70,91 Juta Jiwa Penduduk., 2021, Online, available: <https://dataindonesia.id/sektor-riil/detail/pekerja-informal-indonesia-capai-7791-juta-pada-2021>
- [6] Statistik.jakarta.go.id. Pekerja di DKI Jakarta pada Agustus. 2021, online, available: <https://statistik.jakarta.go.id/pekerja-di-dki-jakarta-pada-agustus-2021/>
- [7] International Labour Organization. ILO Glossary of Statistical Term, 2021, online, available: <https://www.ilo.org/ilostat-files/Documents/Statistical%20Glossary.pdf>
- [8] Matthew J Beck, David A Hensher. Australia 6 Months after COVID 19 Restrictions Part 2: The Impact of Working From Home. Transport Policy, 2021, online, available: <https://doi.org/10.1016/j.tranpol.2021.06.005>

# MULTIMODAL GOODS TRANSPORTATION POLICY MODEL: TRANSPORTATION POLICY ENHANCEMENT IN NORTH COAST LINE OF JAVA

Zony Yulfadli<sup>1</sup>, Achmad Wicaksono<sup>2</sup>, Ludfi Djakfar<sup>3</sup>, Muhammad Zainul Arifin<sup>4</sup>, and Moch. Abdillah Nafis<sup>5</sup>

<sup>1,2,3,4</sup>Civil Engineering, Faculty of Engineering, Universitas Brawijaya, Malang, Indonesia;

<sup>5</sup>Department of Technology Management, Institut Teknologi Sepuluh Nopember, Surabaya, Indonesia

## ABSTRACT

Logistics transportation in Java, especially in the North Coast Line of Java (Pantura), is still dominated by truck use. This situation burdened the capacity of roads, causing traffic problems and the inefficiency of the freight transportation from the production center to be distributed at Java Island. Likewise, both obstacles to implementing railroad transport between the ports and the global pandemic COVID-19 that made truck use in freight transportation increase by a good portion had significant impacts on the length of the freight transportation process and, therefore, logistics costs. This research will discuss public policy formulation of logistics transportation. Using the analytical hierarchy process to assess the best policy scenario by comparing some optimization assessment models done by previous studies helped make a policy prototype. Increasing taxes on trucks used to transport goods and spending more budgets on developing and enhancing advanced traffic management systems have significantly reduced traffic jams and damaged roads. It was also found that some policies about utilizing railways in goods distribution have a great potential to reduce overall costs.

*Keywords: Logistics, Multimodal, Pantura, Transportations Policy*

## 1. INTRODUCTION

Java is an island in Indonesia that is the center of the Indonesian economy. The development of the Economic Corridor on the island of Java is critical because the economy on the island of Java has the potential to develop various types of products. The connecting road on the island of Java is divided into a south lane and a north lane (Pantura). With social and economic development, the number of vehicles crossing the north lane has increased rapidly. In contrast, road capacity has remained so that the level of road service has gradually decreased [1]. Transportation problems in the form of congestion, delays, and queues are heterogeneous traffic problems [2]. The problems that arise are the increasing traffic volume during rush hour and conflicts between motorized and motorized vehicles [3].

The high growth of motorized vehicles, especially motorcycles in big cities, around 21% per year, has increased traffic flow on the roads. However, this increase was not followed by an increase in road capacity. In addition, land transportation is often faced with the problem of decreasing the quality and sustainability of land transportation infrastructure services (traffic congestion, high accident rates, pollution, energy wastage, and inadequate modes of transportation). Not to mention the added damage to infrastructure, which is not only caused by overload. Infrastructure and logistics have become even more important in

the recent COVID-19 pandemic. Sustainability of logistics services helps ensure the provision of food stocks, medical supplies, and all consumer goods. Finally, the monetization of this flow can be seen in the trade value of goods and shipping costs. In the same way, the concept of logistics refers to all the interrelated operations and activities required to distribute goods in a global commodity chain, thus their central location in a gear diagram [4].

One of the main problems on the Java northern coastline highway is over dimension & overload (ODOL). Over-dimension & overload (ODOL) cause losses ranging from road repair costs to frequent accidents on the north coast lane. The government is currently running an ATMS (Arterial Traffic Management System) project, which has several objectives, namely [5]:

1. Improve performance-based transportation services for traffic signal management on arterial and inter-city roads to improve planning, operation, and maintenance, resulting in increased safety, mobility, and efficiency for all user.
2. Supporting inter-city digital mobility improvement programs in every city and district in Indonesia
3. Designing the implementation of ATMS in Indonesia systematically, standardization and integration so that the implementation and management of transportation in Indonesia.
4. Building a culture of orderly traffic and the use of public transportation in Indonesian society

The following is an application of ATMS technology:

1. Advanced Traffic Light System  
Smart APILL that is integrated and coordinated across intersections and adaptive.
2. Traffic Data Collection  
Traffic flow and volume data are stored in a database and can be retrieved at any time for analysis and predictive models for better policy implementation.
3. Traffic Data Dissemination
4. Integrated Traffic Information System
5. Integrated Mobility
6. Integrated Punishment System  
It is integrated with an online ticketing system or other systems.

The other problem is traffic accidents which sometimes involve a truck. Figure 1 shows accident rate data in Indonesia from 2017 to 2021

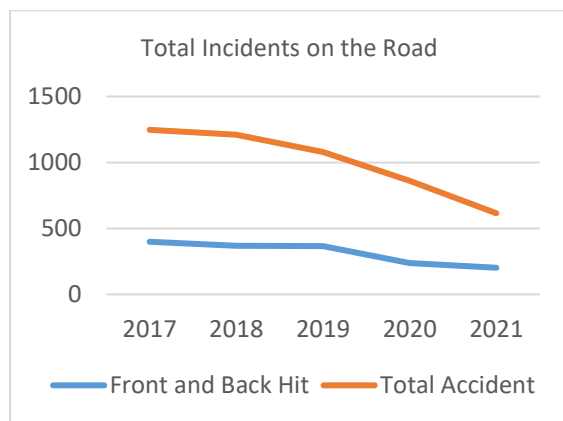


Fig. 1 Total Incident on the Road

Based on [Fig. 1](#), it is known that accidents in Indonesia from 2017 to 2021 have decreased successively. We can conclude, besides the effect of the Covid pandemic, that the ATMS program has also made good progress.

So in this study, we will discuss the formulation of public transportation logistics policies using the method of the Analytical Hierarchy Process to assess the best policy scenario by comparing several optimizations carried out by previous studies to assist in making policy prototypes. The resulting policy must be in accordance with the conditions and is not required to benefit all parties. So with the analytical hierarchy process method can find the best policy scenario in transportation optimization.

## 2. RESEARCH SIGNIFICANCE

The significance of this research is that the policies are expected to increase the optimization of land transportation so that unwanted things do not happen during the delivery of goods. Policies made using the analytical hierarchical process method produce three types of policy properties: policies that

are avoided, policies that are shifting, and policies that are providing new things (improve). The three types of policies are combined to find the combination of policies (scenarios) that best suit the scientific priorities obtained in the analytical hierarchy process method.

The scientific priorities used in this research are transportation, economic, social, and environmental systems. Priority determination is obtained based on the opinion of expert sources related to transportation and road infrastructure. The resource persons in this study were consultants, business development managers, and competent academicians related to land transportation policies.

## 3. METHODS

This research uses Analytic Hierarchy Process (AHP) for scenario decisions. AHP is a general theory of measurement used to derive ratio scales from discrete and continuous pairwise comparisons. AHP is concerned with deviations from consistency, i.e., measurement and dependencies within and between groups of structural elements. It has found its most comprehensive application in multi-criteria decision making, resource planning and allocation, and conflict resolution [\[6\]](#).

There are some ideas and principal to using the AHP method:

- a. Hierarchical Structures
- b. Criteria and Alternative Assessment
- c. Prioritization
- d. Logical Consistency

The AHP method is used in this study because it can parse problems with multi-factor and multi-criteria. AHP can be used to determine the best scenario according to the prioritized criteria based on AHP. To determine the score of each criterion using pairwise comparisons with the determination of the scoring criteria as follows at [Table 1](#).

Table 1 Pairwise Comparison Scale

Level of Importance	Definition
1	Both elements are equally important
3	One element is slightly more important than the others
5	One element is more important than other elements
7	One element is clearly more important than the other elements
9	One element is absolutely more important than the other elements
2,4,6,8	The middle value between two adjoining ratings

Source: Saaty, 1987

[Fig. 2](#) shows the general hierarchy structure of



Policy Scenario.

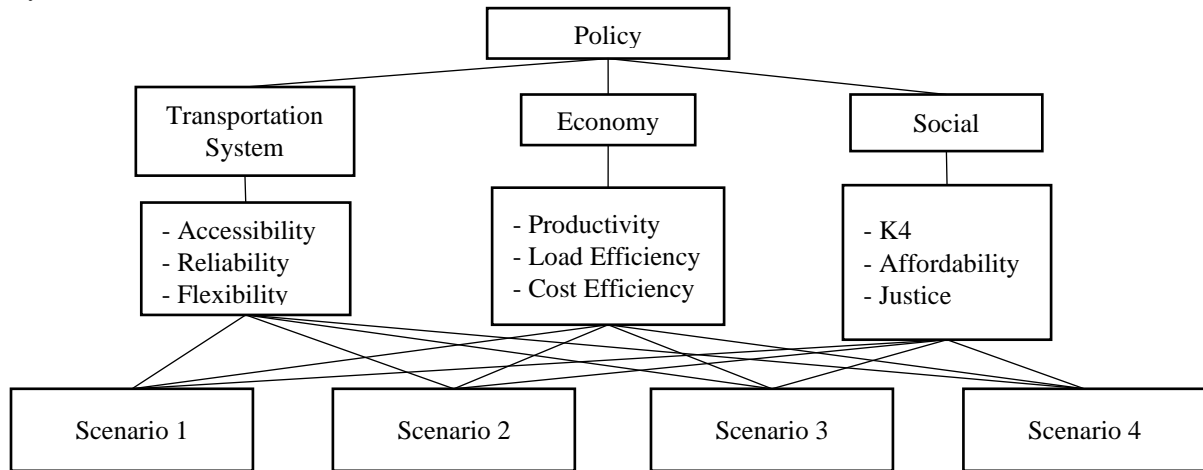


Fig. 2 General Hierarchy Structure of Policy Scenario.

Below is an analysis step using the AHP method:

### 3.1 Determining Local Priority Weight of The Three Factors

This procedure was adopted from the Saaty method, which was modified to fit the context of this study. The steps for the three individual factors are as follows:

1. Determining initial individual priority vectors.  
With three segments, which are three subsegments per segment. Priority vector  $V_s$  was gotten from average normalized original judgment ( $\frac{\alpha_{ij}}{s_j}$ ) matrix as shown in Eq. (1).

$$V_s = \begin{bmatrix} \frac{\alpha_{11}}{s_1} + \frac{\alpha_{12}}{s_2} + \frac{\alpha_{13}}{s_3}/3 \\ \frac{\alpha_{21}}{s_1} + \frac{\alpha_{22}}{s_2} + \frac{\alpha_{23}}{s_3}/3 \\ \frac{\alpha_{31}}{s_1} + \frac{\alpha_{32}}{s_2} + \frac{\alpha_{33}}{s_3}/3 \end{bmatrix} = \begin{bmatrix} V_1 \\ V_2 \\ V_3 \end{bmatrix} \quad (1)$$

2. Calculating consistency of judgment matrix per respondent with Consistency Ratio per segment ( $CR_s$ ) as shown in Eq. (2) and Eq. (3):

$$CR_s = \frac{(C_s - n^2)}{n(n-1)RI} \quad (2)$$

$$C_s = \begin{bmatrix} \alpha_{11} & \alpha_{12} & \alpha_{13} \\ \alpha_{21} & \alpha_{22} & \alpha_{23} \\ \alpha_{31} & \alpha_{32} & \alpha_{33} \end{bmatrix}_s \begin{bmatrix} V_1 \\ V_2 \\ V_3 \end{bmatrix}_s \quad (3)$$

Random Index (RI) with  $n=3$  is 0.58.

3. Generation of new judgment matrix labeled  $M_s$ , shown in Eq. (4).

$$M_s = \begin{cases} A_s, & CR \leq 0.10 \\ V_s \circ \left(\frac{2}{V_s}\right)^T, & CR > 0.10 \end{cases} \quad (4)$$

4. Determining priority vector per subsegment, as aggregated judgment matrix was based on Eq. (5):

$$W_s = \left( \sqrt[r]{\prod_1^r (m_{ij})_s} \right) \quad (5)$$

Where  $r$  is the total respondent.

5. Determining the priority vector of factors from the average aggregated judgment matrix, as shown in Eq. (6):

$$F_s = \begin{bmatrix} w_{11} + w_{12} + w_{13}/3 \\ w_{21} + w_{22} + w_{23}/3 \\ w_{31} + w_{32} + w_{33}/3 \end{bmatrix}_s = \begin{bmatrix} f_1 \\ f_2 \\ f_3 \end{bmatrix} \quad (6)$$

### 3.2 Determining Local Priority Weights of Scenario Per Factor

It has the same procedure in section 3.1, but all priority weights were consolidated in a  $3 \times 4$  matrix  $T_s$ , where the row represents each factor and the column for each scenario.

### 3.3 Determining Global Priority Weights of Scenario

From dot product from priority vector of factors and local priority weights of scenario per factor as shown at Eq. (7) and (8):

$$\Gamma_s = [F_s]^T T_s = [f_1 \ f_2 \ f_3] \begin{bmatrix} t_{11} & \dots & t_{14} \\ \vdots & \ddots & \vdots \\ t_{31} & \dots & t_{34} \end{bmatrix} \quad (7)$$

$$\Gamma_s = \begin{bmatrix} \gamma_1 \\ \vdots \\ \gamma_4 \end{bmatrix} \quad (8)$$

### 3.4 Determining Overall Ranking of Factors and Scenario

The sum of rankings from each segment was calculated to obtain the overall ranking for both factors and the scenario. The lowest sum denoted the highest rank, while the highest sum was given the lowest rank.

### 3.5 ASI (Avoid, Shift, and Improve) Policy



Providing additional road space may not solve the pressing problems of high congestion levels, declining air quality, and increasing greenhouse gas (GHG) emissions in cities. As a result, cities are becoming less livable, and mobility is far from being human-centered. Therefore, what is needed is a fundamental rethinking of the paradigms that guide mobility and urban planning. Inspired by sustainability principles, our alternative approach focuses on the mobility needs of people rather than car infrastructure. The approach, known as A-S-I (from Avoid/Reduce, Shift/Maintain, Improve), seeks to achieve significant GHG emission reductions, reduced energy consumption, and reduced congestion, with the ultimate goal of creating more livable cities.

Firstly, "avoid/reduce" refers to the need to improve the efficiency of the transport system as a whole. The need for motorized travel and the trip length. Second, the "shift/maintain" instrument seeks to improve individual travel efficiency. Third, the "improve" pillar focuses on vehicle and fuel efficiency and optimizing public transport's operational efficiency. Introducing renewable energy sources into the transportation sector should be a fundamental principle of motorized transportation [7].

#### 4. RESULT

All inconsistency values from the results of the AHP analysis shown in this study are less than 0.1. That is, all the answers to each question on the questionnaire proved consistent. The following are the criteria obtained from 3 respondents as follows.

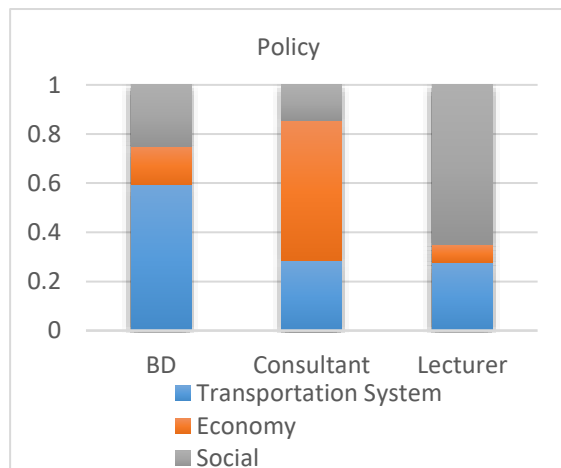


Fig. 3 Policy Criteria Weighting for Each Expert

From Fig. 3, each expert has a different perception of the importance of the policy criteria for the transfer of goods transportation modes by land. A BD Manager stated that the Transportation System was the most important, and a Consultant stated that

the Economic factor was the most influential. In contrast, a Lecturer stated that the most important factor in formulating policies was the Social factor. The following is the weighting for each criterion.

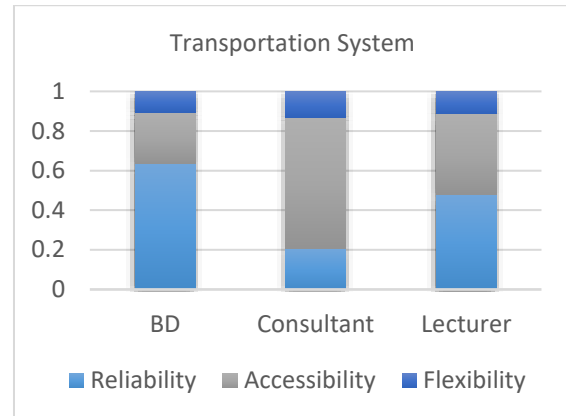


Fig. 4 Transportation System Criteria Weighting for Each Expert

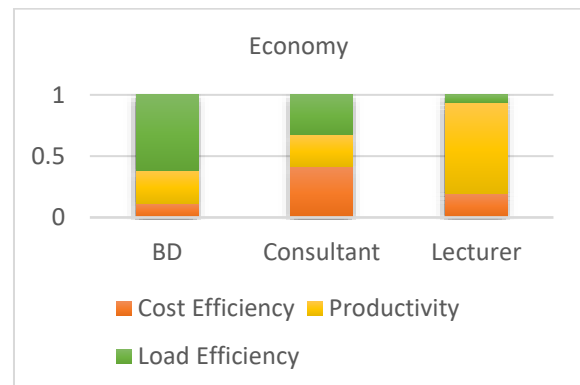


Fig. 5 Economy Criteria Weighting for Each Expert

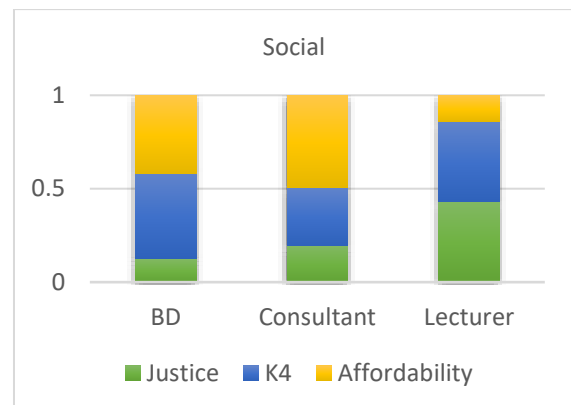


Fig. 6 Social Criteria Weighting for Each Expert

Fig. (4), (5), and (6) show that there appears to be a diversity of perceptions of experts regarding the importance of each sub-criteria in each policy factor. Each expert assigns a different weight to the most important sub-criteria for each policy criterion. The following statistics were obtained based on the combination of the three experts.



Fig. 7 Policy Criteria Combination Weighting



Fig. 8 Transportation System Criteria Combination Weighting (X1)



Fig. 9 Economy Criteria Combination Weighting (X2)



Fig. 10 Social Criteria Combination Weighting (X3)

From [Fig. 7](#), It was found that the Transportation System is a priority factor for formulating policies for transferring modes of transportation of goods by land, with an importance weight of almost 50%. The following is the combined weighting for each criterion. From [Fig. 8](#), the Accessibility sub-criteria is the most important, although there is a slight difference in Reliability. From [Fig. 9](#), the productivity sub-criteria is the most important. Meanwhile, from [Fig.10](#), the Security, Safety,

Health, and Sustainability (labeled by K4) sub-criteria is the most important. It should be noted that this does not mean that the other sub-criteria are not important because the nine sub-factors remain a reference in determining policy. The four scenarios based on the preparation of the A-S-I strategy will consider all the factors involved with the weighting of each sub-criteria at [Table 2](#).

Table 2. Policies Implemented for Each Scenario

Policies		Scenario I	Scenario II	Scenario III	Scenario IV
1	Increased tariffs for freight trucks arriving at their destination on different days	✓	✓		
2	Reducing the cost of shipping goods by rail with a journey of more than 600 km			✓	✓
3	Reducing the cost of shipping goods that fall into the category of perishable goods by train with a journey of more than 200 km	✓			
4	Implement punishment regulations in the form of fines for companies that often travel, as in points 1-4		✓	✓	
5	Provision of subsidies for switching modes to trains				✓
6	Promoting driver competency check procedures and completeness of vehicle facilities	✓		✓	
7	Promoting the use of information technology at ATMS in order to use information more effectively and efficiently		✓		✓

The following is the weighting for each respondent's policy scenario.

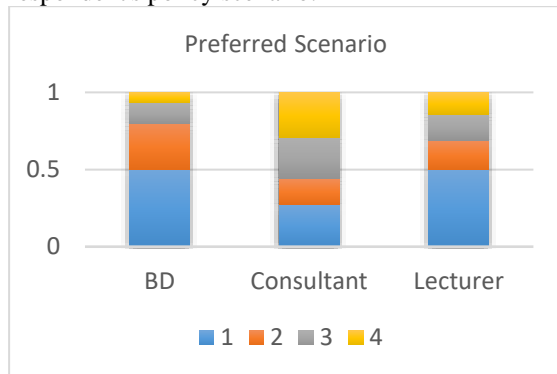


Fig. 11 Scenario Weighting Every Respondent

The priority weighting of the scenarios in Fig. (11) is carried out by considering the nine subfactor weights in Fig. (4), (5), and (6). Based on the results of the AHP analysis, a BD Manager and Lecturer considered that Scenario 1 was the most important and best scenario to be implemented immediately. A Consultant indicated that Scenarios 1 and 4 were equally important. Combining all the existing assessments will show a weighting pattern for each scenario based on the three existing factors.

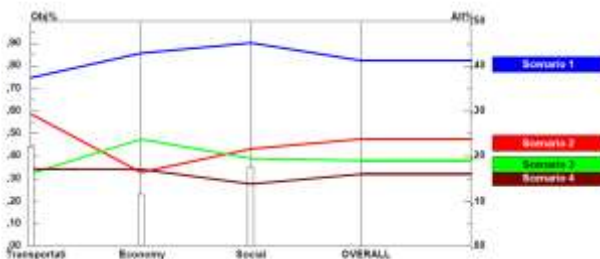


Fig. 12 Weighting of Each Scenario Based on The Three Factors

In the pattern shown in Fig. 12, all existing factors support that Scenario 1 is a priority Scenario that needs to be implemented immediately. The other scenarios still need to be reviewed because, in addition to their overall factor weights having a value below Scenario 1, these three scenarios are still complicated when viewed from economic factors versus other factors.

## 5. CONCLUSION

Based on the weighting of the policy criteria, the three respondents produced different opinions. The reason could be due to the interests and knowledge of each respondent, as well as different goals as well. It can be seen based on the weighting for each subsegment of each policy criterion which tends to

produce different weights for each respondent.

However, in the weighting of the scenarios, it is known that there are two respondents with the majority of the weighting who tend to agree with scenario 1. So that scenario one is chosen for the policy prototype, it is clarified by the weighting of each scenario based on the three factors, which show scenario 1 has the highest weight of the three other scenarios.

## 6. ACKNOWLEDGMENTS

We thank all those who participated in the completion of this research. Starting from the three respondents whose opinions were very helpful for us in completing this research, we learned many related policies that must meet various scientific aspects as well as supervisors who always provide direction to complete this research.

## 7. REFERENCE

- [1] Qu, Z., Xing, Y., Hu, H., Song, X., & Duan, Y. (2012). Study on the relationship between urban road network service level and capacity. *The Twelfth COTA International Conference of Transportation Professionals*. Beijing: American Society of Civil Engineers.
- [2] Lubis, A., Muis, Z., & Nasution, T. (2016). Relationship of Traffic Characteristics Parameters on the Belmera Toll Road. *CIVIL ENGINEERING COMMUNICATION MEDIA*, DOI:10.14710/MKTS.V22I2.12878.
- [3] Harahap, E., Suryadi, A., Ridwan, R., Darmawan, D., & Cecha, R. (2017). The Effectiveness of Load Balancing in Overcoming Traffic Congestion. *Journal of Theoretical And Applied Mathematics*, DOI: 10.29313/JMTM. V16I2. 3665.
- [4] Rivera, A. (2020). *The impact of COVID-19 on transport and logistics connectivity in the landlocked countries of South America*. Santiago: United Nations, Economic Commission for Latin America and the Caribbean (ECLAC).
- [5] Mulyana, C. (2021). *Law Enforcement in ODOL Enforcement and Arterial Traffic Management System*. Jakarta: Ministry of Transportation of the Republic of Indonesia.
- [6] Saaty, R. (1987). *The Analytic Hierarchy Process – What It Is and How It Is Used*. Pittsburgh: Pergamon Journal Ltd.
- [7] Bongardt, D., Stiller, L., Swart, A., & Wagner, A. (2019, March). Sustainable Urban Transport: Avoid-Shift-Improve (A-S-I). *iNUA #9: Implementing the New Urban Agenda*.

# SMART, INTEGRATED SUSTAINABLE, AND ENVIRONMENT-FRIENDLY TRANSPORTATION INFRASTRUCTURE CONNECTIVITY TO THE CAPITAL CITY OF NUSANTARA

Achmad Wicaksono<sup>1</sup>, Rosa Agustaniah<sup>2</sup> and Ludfi Djakfar<sup>3</sup>

<sup>1,2,3</sup> Department of Civil Engineering, Universitas Brawijaya, Indonesia

## ABSTRACT

The President of the Republic of Indonesia Joko Widodo issued a presidential decree regarding the stipulation of moving the capital city of Indonesia from Jakarta to North Penajam Paser and Kutai Kertanegara Regencies, East Kalimantan. The new state capital with the name Nusantara is stated in Law Number 3 of 2022 concerning the State Capital. The total area of the Capital of the Archipelago is planned at 256,142.74 hectares with a core city area of 56,180.87 hectares and a government center of 5,644 hectares. The transportation system of a connected road network to the Capital of the Archipelago and between supporting cities includes aspects of adaptation to integrated land use and preserving the ecosystem functions of watersheds. Good environmental quality with the concept of smart transportation infrastructure planning integrated sustainable and environmentally friendly with the application of a forest city to reduce the environmental footprint with 50 percent remaining green open space.

*Keywords: infrastructure, sustainable transportation, environment-friendly, road network*

## INTRODUCTION

The Government of Indonesia through President Joko Widodo on 26 August 2019 officially announced the move of the new State Capital, from Jakarta to Penajam Paser Utara and Kutai Kertanegara Regencies, East Kalimantan (Fig. 1). The planned area of the State Capital is 256,142.74 ha, with a core city area of 56,180.87 ha and a government center of 5,644 ha [14].



Fig. 1 Location of the State Capital in the Regencies of North Penajam Paser and Kutai Kertanegara, East Kalimantan.

Several reasons for choosing the location of the

State Capital in North Penajam Paser and Kutai Kertanegara Regencies, East Kalimantan is [14]; 1) strategic location, located in the central region of Indonesia; 2) location free from earthquake and tsunami disaster; 3) availability of state-owned land; 4) land slope and soil bearing capacity; 5) availability of water resources; 6) a location free from floods, forest, and land fires; 7) close to existing and developing cities; 8) socio-cultural carrying capacity, especially openness to immigrants; 9) meet the defense and security parameters.

The existence of a large-scale activity, namely the relocation of the capital city of Indonesia, to the Regencies of North Penajam Paser and Kutai Kertanegara, East Kalimantan, will have an environmental impact. The policy issue for developing transportation systems now and in the future is how each country plays its role in the framework of a sustainable transportation system [3]. This discourse originated from concerns about the interaction between transportation and the environment. The realization that the quality of the environment has been greatly affected by transportation activities, which continues to accumulate over time, has aroused the attention of many people to the "mistakes" that have been practiced so far in policy making and planning. The practice of managing transportation infrastructure on the one hand and the needs of the community to carry out their activities, on the other hand, cannot be continued as before, but needs to be observed with a different "glasses". The costs that must be borne by the community in traveling are not only out-of-pocket costs but also the impact on the environment. The

idea of developing sustainable transportation is an essential part of the problem of sustainable development. Experience in various countries shows that continuing to build the required infrastructure is not always the best solution. Every transportation infrastructure development brings environmental impacts, but the region has a certain environmental capacity limit to accept the impacts that arise. In addition, the construction of a road network, in particular, which only follows the demands of the needs tends to encourage an increase in the use of inefficient private vehicles. The growth of transportation needs (demand) needs to be controlled so that it is balanced with the ability of network supply and environmental constraints [17].

This paper discusses transportation issues related to transportation system development policies and strategies, sustainability development issues that need to be considered, especially those related to transportation infrastructure development, as well as proposed strategic steps to overcome transportation problems in the future.

## LITERATURE REVIEW

Put forward that the concept of sustainable development is trying to simultaneously realize the most basic needs, namely [9] (Fig.2); 1) the need for economic development to overcome poverty; 2) the need for environmental protection for air, water, soil, and biodiversity; 3) the need for social justice and cultural diversity to enable local communities to convey their values in solving these issues.

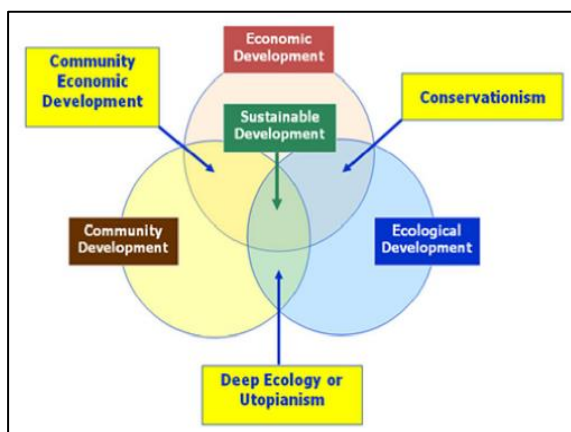


Fig. 2 Three development processes at the local level and the concept of sustainable development

More specifically for the transportation sector, a research institute based in Canada that focuses on the issue of sustainable transportation [3], formulates a definition that sustainable transportation is a system that; 1) enables the very basic access needs of individuals and communities to be met safely and in

a manner consistent with human health and ecosystems, and with equity within and between generations; 2) affordable, operate efficiently, provide a choice of transportation modes, and support economic development; 3) limiting emissions and wastes that are still within the earth's ability to absorb them, minimizing consumption of non-renewable sources, using and recycling their components, and minimizing land use and noise production.

The issue of sustainable development is an issue that every country is required to focus on this global agenda. Concerning transportation issues, the issue of sustainability is a logical consequence that is very directly related, because regional development and land use are fundamentally influenced by transportation networks. The evolution of the development of transportation systems provides the basic shape for land use characteristics, although the process is influenced by economic, social, and political considerations. Therefore, the policies implemented in managing the development of the transportation system become a central part of the context of sustainable development [3].

## METHODOLOGY

The research method is a scientific procedure or method to obtain data with a specific purpose [16] it is a scientific feature to obtain data with a specific purpose and use.

The research method on the concept of smart, integrated sustainable, and environment-friendly transportation infrastructure planning in the new capital city area uses the synthesis method, which is a complete article on summaries from various reference sources regarding understanding or opinions. The summary is compiled into a new article that contains a unit that is following the needs of the researcher. This presentation is obtained from various reference sources used by researchers in compiling a scientific work. The results of the synthesis can be in the form of data, facts, information, or new main ideas [13].

## RESULTS AND DISCUSSION

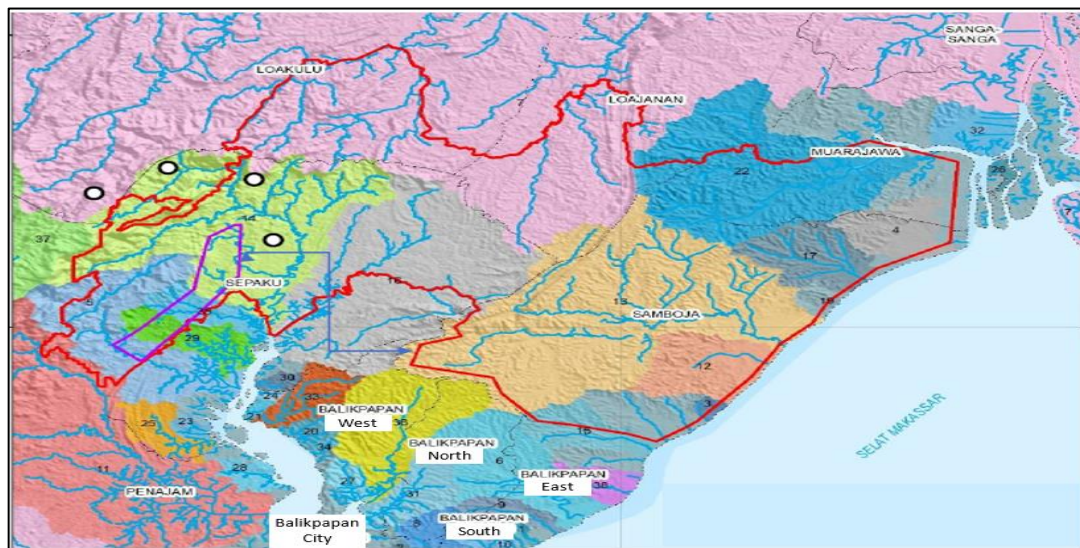
No State Capital has yet been moved from island to island, except in Indonesia. This is the first time because almost all of the world's eyes are on Indonesia. The vision of the State Capital 'Smart, Green, Beautiful, and Sustainable' is translated through the development of a city that is side by side with nature through the concept of a forest city and a smart and intelligent city.

The determination of the area of the State Capital area takes into account One River One Management, upstream-downstream integration, and the character of the Watershed, as well as the boundary of the Bukit Soeharto Grand Forest Park (Tahura) which will be developed and managed in an integrated manner into



a buffer area as well as a biodiversity conservation area ( Fig. 3). Infrastructure development including transportation must be able [15]; 1) maintain and protect catchment areas and water management regulators and their land cover in the form of the forest; 2) maintain and protect the karst area around the State Capital area; 3) maintain and protect buffer and riparian areas in the catchment areas and water sources (rivers, lakes and sea coasts); 4) support the implementation of rehabilitation, revegetation, and enrichment of green landscapes to improve the function of watersheds; 5) ensure that water consumption is carried out very efficiently; 6) maintain and protect the quality of surface water and groundwater.

Fig. 3 Map of the watershed boundaries of the



National Capital of the Archipelago

### Instruments for Environmental Protection and Management (Environmental Safeguards)

The application of environmental protection instruments (Environmental Safeguard) development of smart, integrated sustainable & environment-friendly transportation infrastructure planning concepts in the National Capital area to realize sustainable and environmentally friendly transportation infrastructure is carried out based on economic democracy with sustainable principles, with environmental insight. Various instruments of environmental protection and management must be implemented in an integrated manner based on; 1) strategic environmental studies; 2) spatial planning; 3) environmental quality standards; 4) standard criteria for environmental damage; 5) environmental impact analysis; 6) environmental management efforts and environmental monitoring efforts; 7) licensing; 8) environmental economic instruments; 9) environmental protection and management laws and

regulations; 10) environment-based budgeting; 11) environmental-based risk analysis; 12) environmental audit; 13) other instruments as needed.

### Roadmap Towards a Sustainable Transportation System

The development of sustainable transportation infrastructure is a comprehensive effort from various sectoral dimensions, regions, the involvement of actors, and their substance. (Fig. 4) Presents a proposed strategic step towards structuring a sustainable transport system. The development of transportation infrastructure is an integral part of every element of the realization of the necessary steps because this will greatly determine the efficiency and effectiveness of the utilization of the existing system.

Arrangements concerning aspects of technology, regulation, and user behavior need to be given priority. Implementation strategies need to be formulated to achieve more sustainable conditions in terms of operations, availability of more environmentally friendly systems, and use of resources.

### Recommendations for developing the concept of smart, integrated sustainable, and environment-friendly transportation infrastructure planning

#### a. Recommendation 1

Transport Infrastructure Development Should Consider a structured green space network (Fig. 5). To increase the carrying capacity, a network of protected spaces and areas that need careful treatment are needed that are connected to environmentally friendly corridors [15].



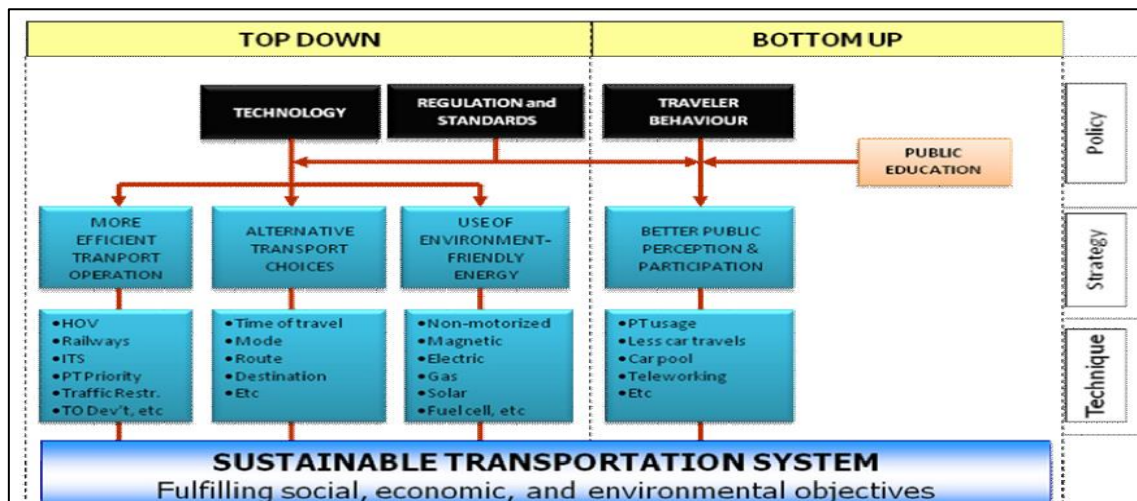


Fig. 4 Roadmap towards a sustainable transportation system

The primary green space network has a protection function; 1) conservation forest area (Tahura); 2) protected forest areas; 3) home range and main habitat for key animals. Secondary green space network that has a buffer and aesthetic function; 1) ecoriparian and coastal areas; 2) natural tourism areas; 3) botanical gardens and nurseries/nursery; 4) areas of high conservation value and carbon pools; 5) areas for enrichment/revitalization of a tropical rain forest ecosystem. A water-based open space network (blue space) functions to maintain water management and prevent landslides and floods; rivers, lakes, ponds, reservoirs, bays, and other water storage infrastructure..

#### b. Recommendation 2

Development of Transportation Infrastructure in the National Capital Region must be able to ensure the creation of good air quality and cool average air temperature [15] (Fig. 6)

#### c. Recommendation 3

The development of Transportation Infrastructure in the State Capital area must be able to protect wildlife habitats. Key wildlife habitats and home ranges should be protected by designating primary green spaces [15] (Fig. 7).

Green fingers are used as a green infrastructure to balance the city along with the growth of the city itself. Green fingers are also used as corridors for green mobility, habitat spaces, recreation areas, urban forests, water run-off management, urban agriculture, etc. Green Fingers also function as habitat corridors, where existing flora and fauna can still find their natural path of movement from one ecosystem to another [15] (Table 1).

Key wildlife habitat areas and home ranges must be protected, one of which is to be designated as primary green space managed by an approach (Fig. 8); 1) avoid clusters: areas/clusters that need to be avoided from physical development; 2) minimize cluster: this area/cluster can be physically developed by minimizing the impact (mitigation) on wildlife (green infrastructures); 3) restore cluster is an area/cluster that needs to be restored as wildlife habitat; 4) canopy bridges are indispensable for arboreal animals (a.l. gibbons, orangutans, civets). this solution is very vital for conservation areas that have arboreal species whose habitats are cut off by roads; 5) arboreal species don't like going down to the forest floor, so their movement is limited from tree to tree; 6) underpass-type crossings can be in the form of bridges, flyovers or box culvert tunnels [15].

Table 1. Existing flora and fauna

flora	fauna
▪ Meranti (Shorea spp.)	▪ Sambar Deer
▪ Tengawang (Shorea macrophylla)	▪ Proboscis monkey
▪ Keruing (Dipterocarpus retusus)	▪ Enggang Gading
▪ Api-api (Avicennia sp.)	▪ Orangutans
▪ Kijang Kuning	▪ Pesut Mahakam
▪ Beruang Madu	▪ Dugong
▪ Babi Berjanggut	▪ Estuary Crocodile
▪ Merak Kerdil Kalimantan	
▪ Kera Ekor Panjang	
▪ Macan Dahan	
▪ Perepat (Sonneratia sp.)	
▪ Mangroves (Rhizophora)	
▪ Black Orchid (Coelogyne pandurata)	

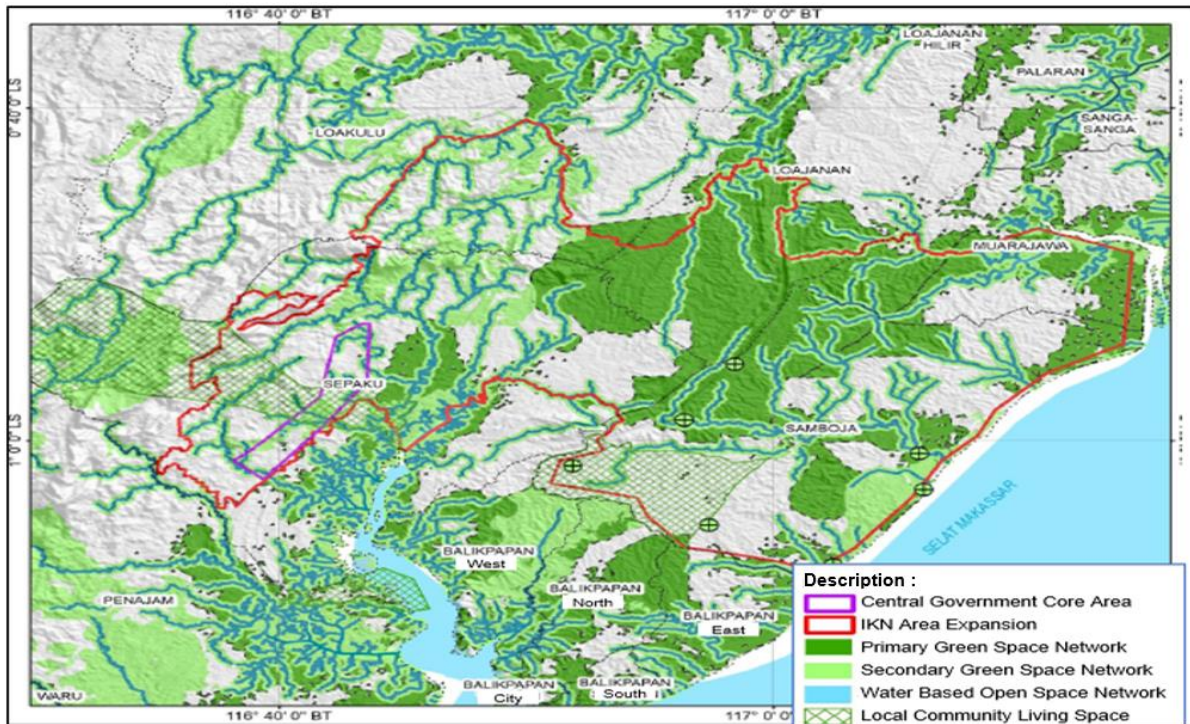


Fig. 5 The development of transportation infrastructure must consider a structured green space network.

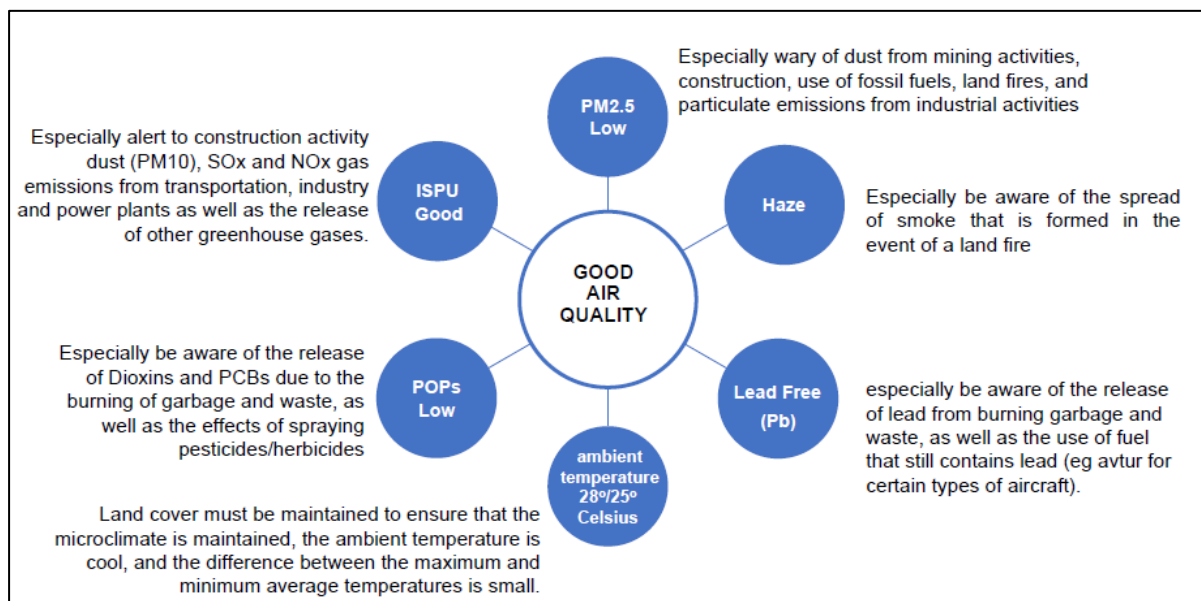


Fig. 6 The development of transportation infrastructure in the national capital area must be able to guarantee the creation of good air quality and cool average air temperature



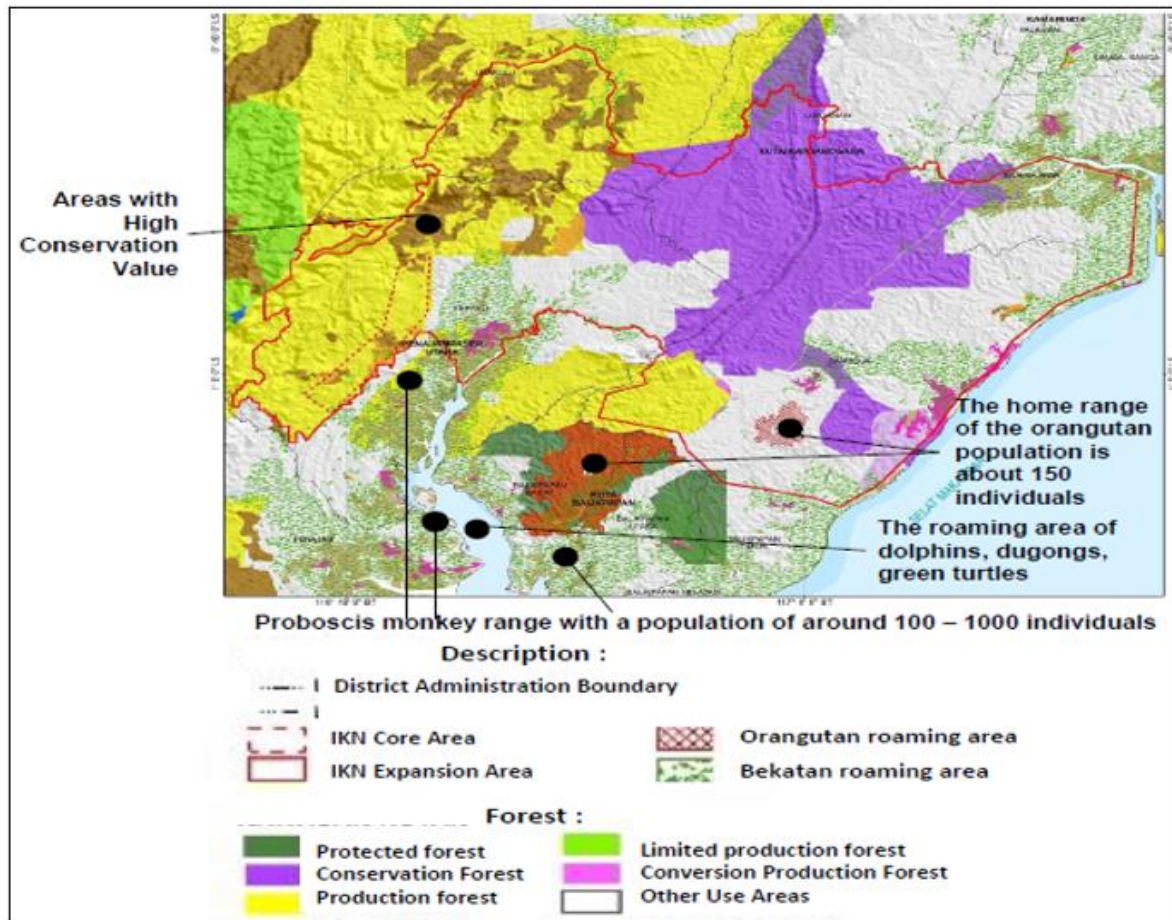


Fig. 7 The development of transportation infrastructure in the national capital area must be able to protect wildlife habitats.

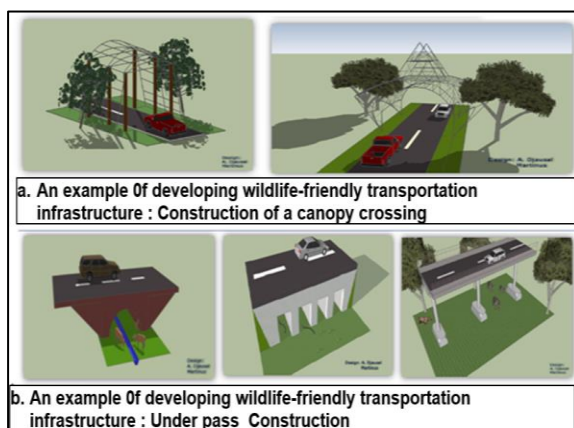


Fig. 8 The development of transportation infrastructure in the national capital area must be able to protect wildlife habitats.

#### d. Recommendation 4

The development of transportation infrastructure in the national capital region must be integrated with the application of smart city elements for environmental management [15] (Fig. 9)

#### e. Recommendation 5

The development of transportation infrastructure in the state capital area must be in line with efforts to control the physical expansion of satellite areas around the state capital area. The dominance of forest area space that has high environmental services, growth centers around the national capital must be controlled for physical expansion of its growth so as not to trigger deforestation, land conversion to activities that encourage damage and potentially marginalize communities who depend on forest sustainability [15] (Fig. 10).

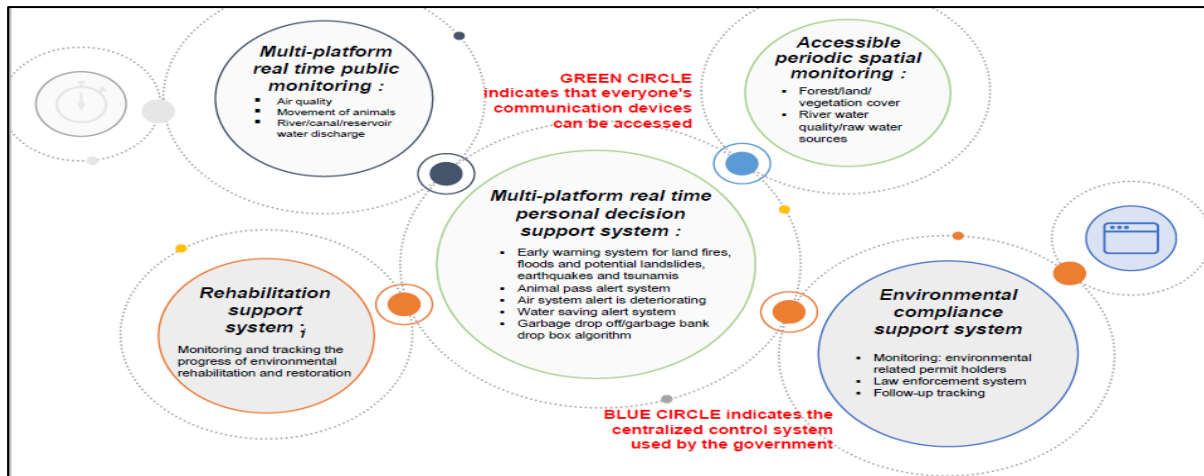


Fig. 9 The development of transportation infrastructure in the national capital area must be integrated with the application of smart city elements for environmental management

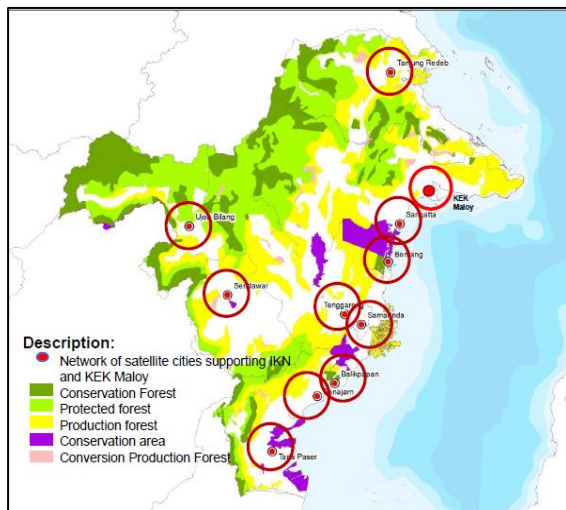


Fig. 10 The development of transportation infrastructure in the state capital area must be in line with efforts to control the physical expansion of satellite areas around the state capital area.

#### f. Recommendation 6

The development of transportation infrastructure in the national capital area must be in line with the refinement of the Island and Provincial Spatial Plans (RTRW). In addition to the regional spatial plan (RTRW) which will specifically regulate the nation's capital city, the Kalimantan Island regional spatial plan (RTRW) and the provincial spatial plan (RTRW) need to be refined to support efforts to maintain the continuity of the world's lungs and control physical expansion, which has the potential to cause deforestation [15] (Fig. 11).

#### g. Recommendation 7

Development of Smart, integrated and sustainable Transportation Infrastructure in the national capital region with the following planning concepts [15] (Fig. 12); 1) The concept of a compact city that minimizes travel; 2) Making public transportation the main choice; 3) Accessible for all community groups; 4) Encourage people to walk and cycle, with people friendly facilities; 5) Urban transportation is regulated by intelligent transport system; 6) Separation between the flow of pedestrians and unmotorized vehicles with motorized vehicles; 7) An integrated transport node between modes of transportation and land use (Transit Oriented Development) [1], [7]; 8) Radial corridor entering the center of government with Mass Rapid Transit underground, with a circular line combined underground and at grade.

#### h. Recommendation 8

The proposal for a smart, integrated sustainable & environment-friendly transportation infrastructure planning concept for the nation's capital city is as follows;

1. Traffic management system & public transport services (Fig. 13). It is integrated traffic management to ensure efficient and safe driving by presenting [18]; 1) smooth traffic flow; 2) improve the efficient transportation system; 3) intelligent mobility; 4) reduce travel time; 5) improve safety; 6) public information; 7) supporting facilities for transferring charging stations to the network (activity centers & transportation nodes).



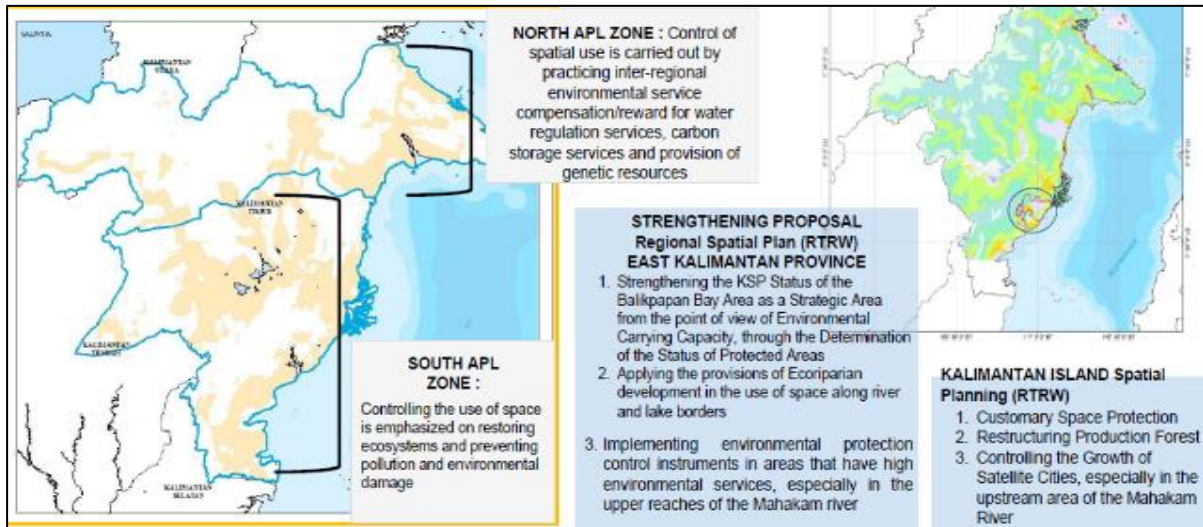


Fig. 11 Development of Transportation Infrastructure in the State Capital area must be in line with the refinement of the Island and Provincial Spatial Planning (RTRW)

Supported by reliable transportation (Light Rail Transit, toll roads, and bridges) connecting between airports, and from the airport to the nation's capital city; 3) an integrated intermodal transportation system that connects airports by land, sea, and rail 4) airport development carries the aerotropolis concept that is smart, integrated and pays attention to environmental ethics.

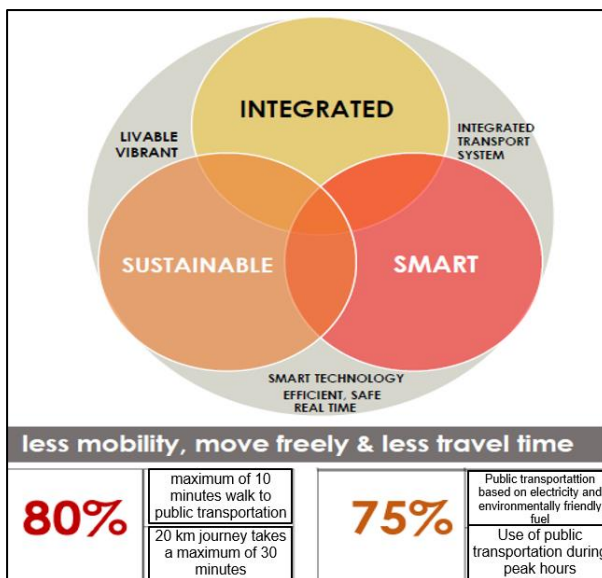


Fig. 12 The development of transportation infrastructure in the national capital area must be in line with the refinement of the Island and Provincial Spatial Planning (RTRW)

## CONCLUSIONS

- Policies in dealing with transportation problems in the State Capital area need to be approached both from the supply side and from the demand side. There is no "panacea" that with one particular action will be able to solve all transportation problems, but requires integrated and sustainable actions. Transportation Demand Management is a practice that needs to be pursued more intensively to optimize resource utilization.
- Methods that are proven to be effective in developed countries may not necessarily give the same results if applied in the State Capital region, given the different conditions of society, transportation systems, regions, and institutional readiness. Therefore, the implementation of policies taken in Indonesia needs to be adjusted to the existing conditions.
- Issues regarding sustainable development and especially sustainable transportation have become global issues for which each country is required to demonstrate its responsibilities following local problems and needs. Anticipatory measures are realized through the necessary preparations in the institutional, socio-cultural, regulatory, and law enforcement aspects, as well as human resource development, all of which are prepared through an integrated planning framework.

- The concept of future transportation in the nation's capital, as follows [18] (Fig. 14); 1) the farthest airport distance from the city center (the national capital can be reached in no more than 2 hours with the concept of a multi-airport system between Sultan Aji Muhammad Sulaiman Sepinggan International Airport (SAMS) Balikpapan, APT. Pranoto Samarinda and Very Very Important Person (VVIP) Airport; 2)

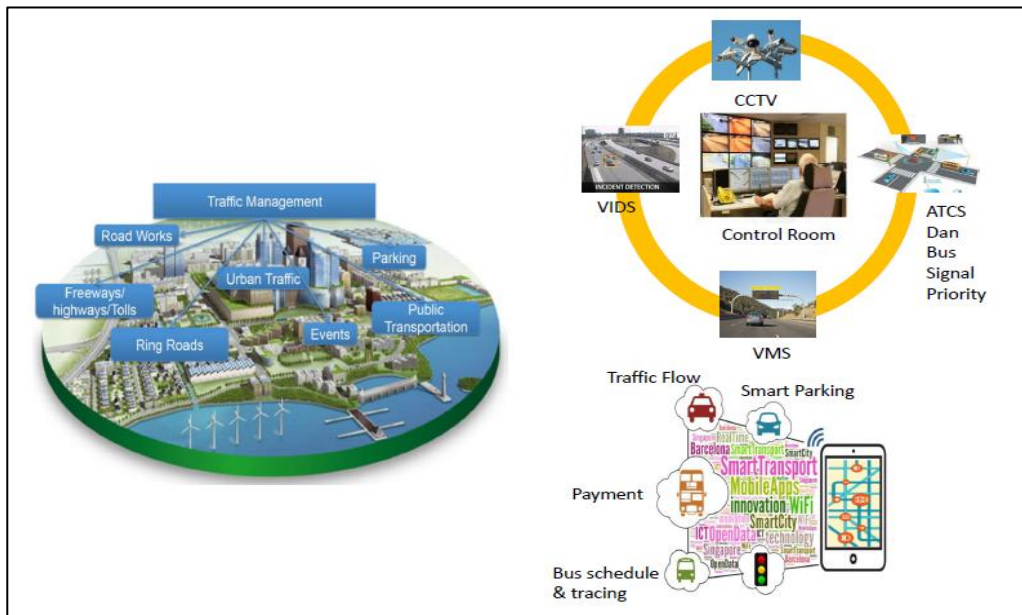


Fig. 13 Development of transportation infrastructure for traffic management systems and public transport services



Fig. 14 The concept of future transportation in the nation's capital



## REFERENCES

- [1] Ayuningtias, Sekar Hapsari; Karmilah, Mila. Application of Transit Oriented Development (TOD) as an Effort to Realize Sustainable Transportation. Foundation, 2019, 24.1:45-66.
- [2] Calthorpe, Peter. The next American metropolis: Ecology, community, and the American dream. Princeton architectural press, 1993.
- [3] Center For Sustainable Transportation. Definition and vision of sustainable transportation. 1997.
- [4] Cervero, Robert. Transit-oriented development in the United States: Experiences, challenges, and prospects. 2004.
- [5] Dikun, S. Main Thoughts on Urban Transport Policy Direction, MTI Seminar. Transport, 2000.
- [6] Sadly, Noer, et al. Development of Transportation Infrastructure and Spatial Structure with the Concept of Transit Oriented Development in Banda Aceh City. 2018.
- [7] Huang, Runjie, et al. "Measuring transit-oriented development (TOD) network complementarity based on TOD node typology." *Journal of transport and land use* 11.1 (2018): 305-324.
- [8] Isnaeni, Muhammad; Lubis, H. A. R. Environmental Effects of Interaction of Transport and Urban Spatial Planning. Bandung Institute of Technology, 2003.
- [9] Newman, Peter; Kenworthy, Jeffrey. Sustainability and cities: overcoming automobile dependence. Island Press, 1999.
- [10] Ohta, Katsutoshi. TDM measures sustainable mobility. IATSS Research, 1998.
- [11] Ministerial Regulation of ATR/BPN No. 16 of 2017 concerning Guidelines for the Development of Transit Oriented Areas
- [12] Rudi Azis, S. T.; Asrul, S. T. Introduction to Transportation Systems and Planning. Depublish, 2014.
- [13] Samin, Annisa Novianti; Chairul, Chairul; Mukhtar, Erizal. Analysis of coastal vegetation in the Pasir Jambak tourist area, Padang City. Biocolebes, 2016, 10.2.
- [14] The State Capital Infrastructure Development Planning Task Force of the Ministry of Public Works and Public Housing and the Planning Team (2021) Urban Design Development KIPP
- [15] Sigit, Hardwinarto, Development of integrated and environmentally friendly Transportation Infrastructure in the State Capital area, Director General of Forestry Planning and Environmental Management, Ministry of Environment and Forestry 2019.
- [16] Sugiyono, P. D. Business research methods: quantitative, qualitative, combined, and R&D approaches. CV Publisher. Alfabeta: Bandung, 2017, 225.
- [17] Syafruddin, A. D. Development of Transportation Infrastructure to Support Science-Based Sustainable Development. Unpublished papers. Faculty of Civil and Environmental Engineering. ITB, 2013.
- [18] The Secretariat Team of the Balitbang Task Force, Weaving the Connectivity of the State Capital Smart And Eco-Friendly Transportation System, Ministry of Transportation-Republic of Indonesia, 2019.

## EVALUATING IMPACTS OF OVER-DIMENSION AND OVERLOADING TRUCKS (Case Study in Arterial Roads)

Achmad Wicaksono<sup>1</sup>, Meriana Wahyu Nugroho<sup>2</sup>

<sup>1,2</sup> Faculty of Engineering Department of Civil Engineering, Brawijaya University, Indonesia; <sup>3</sup> Faculty of Engineering, Hasyim Asy'ari University, Indonesia

### ABSTRACT

The community increasingly needs logistics delivery services; therefore, trucks have an essential economic role. This situation has caused the volume of truck traffic also to increase. Trucks were the most significant contributor to accidents, some of which were caused by over-dimension and overloading trucks. The condition of trucks with loads that exceed the limit caused the speed of the trucks to decrease and caused congestion so that traffic flow became obstructed. Oversized and overloading trucks would block the view of drivers of other vehicles, thereby impairing visibility while driving. Collecting data in this study used a questionnaire method with a total of 194 respondents using a proportionate stratified random. Accident factors consisted of environmental factors, drivers, vehicles, and roads with analysis using a multinomial logistic regression method. The multinomial logistic regression analysis model used the backward stepwise method to obtain significant variables for accidents; then, significant variables were tested to get a suitable model. This study determined the factors that caused over-dimension and overloading truck accidents and produced a truck accident model on the Jombang arterial road. The modeling results of the factors causing the accident indicated that the significant variables for the occurrence of accidents are road surface conditions, traffic flow volume, accident history, vehicle load, vehicle size/dimensions, and speed limit signs. This research is expected to be a solution in determining transportation policies and providing recommendations for better and safer truck regulations.

*Keywords: Accident, Driver Socio-Economic, Over-dimension and Overloading, Regression Logistic Multinomial*

### 1. INTRODUCTION

The rapid development of transportation will indirectly increase the risk of the growth of traffic problems, including congestion and accidents. Traffic accidents according to Law of RI Number 22 of 2009 concerning Road Traffic and Transportation, namely an incident on a road that is unexpected and unintentional involving a vehicle with or without other road users resulting in human casualties and/or property loss [1].

The province of East Java is located on the island of Java, which has the largest population among the Indonesian islands. The province has 38 city and regency administrative areas. For several years, the number of traffic accidents has been the highest in Indonesia, but efforts to minimize the potential for accidents are still lacking. The difficulty has been increased not only by the behavior of the truck drivers but also because of some poor road geometry, poor road lighting, and the limited number of rest areas for drivers to rest [2]. Transporting goods by truck is the most popular because it has load flexibility and a long cruising range. So transportation is very dependent on the behavior of the driver, who can provide services in the form of punctuality and safety in driving [3].

Traffic accidents could not only cause property damage but also impact the incidence of fatalities which, in this case, were caused by interactions between vehicles and road users [4]. Efforts to reduce

the losses caused by truck accidents to fatal accidents were carried out by identifying risk factors and their impact on fatal accidents. The risk factors influencing the severity of an accident are so diverse and complex, as well as interact in complex ways; therefore, it is difficult to define the relationship among variables; for example, wet surface conditions are often seen during bad weather, and sharp turns, as well as steep slopes, often coincide along roads. Obtaining relevant risk factors and capturing the interactions among these variables from a comprehensive perspective would improve the understanding of accident mechanisms [5].

ODOL Truck Accidents were the most significant contributor to the negative impact on logistics delivery. The negative implications arise when an ODOL Truck with excess dimensions and loads. The ODOL Truck's condition with a load exceeding the limit caused the truck's speed to decrease and caused congestion, so traffic flow became obstructed. Over-dimension and overloading trucks would block the vision of other vehicle drivers, thereby interfering with driving distance. The problem of ODOL trucks for logistics delivery is important and requires handling by predicting and classifying accident fatalities and their causes. This study aimed to discover the characteristics and factors causing accidents involving transport truck vehicles in East Java Province.

## 2. TRAFFIC ACCIDENT

Traffic accidents involve environmental and human factors, so to reduce the number of accidents, these two factors need to be taken into account. Human factors are related to personality factors which are more or less permanent and temporary conditions of road users. Various personality traits that can invite danger on the road are a lack of sense of moral responsibility, ego-centricity, aggression, lack of emotional stability, and overconfidence. At the same time, temporary conditions that are dangerous are psychological conditions such as stress, anxiety, and boredom, as well as decreased physical conditions such as illness, fatigue, thirst, hunger, sleepiness, and drunkenness [6]. The factors influencing road traffic accidents can be distinguished into human, vehicle, road, and environmental factors. Socio-economic and demographic characteristics, land use regulations, and changing road network characteristics (design) could be applied to the transportation system to ensure better safety concerning truck accidents within the city [7].

Characteristics of respondents (duration of work, period of employment, duration of rest, travel time for one departure, and working hours), predisposing factors (level of knowledge), supporting factors (vehicle condition, weather conditions, and income), and driving factors (motivation/family support). Violations committed by employees due to work discipline problems were relatively high. This statement was evidenced by a survey that said 16% of employees in America were late for work in 2011 [8]. Driver's behavior (undisciplined, speeding, drunk), lack of sleep (sleep less), driver skill, work experience (old/new driver), as well as age and rest time of the driver were contributed. Two factors cause a decrease in a person's performance, namely individual factors, which include personality, attitude, physical characteristics, age, and experience, then situational factors, which include administrative regulations, work environment, work methods, and conditions of work equipment [9].

So every public transport driver must have a driving competency certificate, including safety driving, defense driving, and emergency response. Optimizing the function of the weighbridge to enforce the law for goods vehicles that are indicated to be carrying goods with overloading and over-dimension of the vehicle is not in accordance with the provisions [10].

However, several previous studies only considered the driver factor [11]-[12]-[13]-[14], and some considered only the driver and vehicle aspects

[15]-[16] as well as the addition to the characteristics of the driver. Traffic environmental factors could also be a factor causing traffic accidents; this was explained in a study conducted [17]-[18]-[3]. The combination of three factors was also considered; this combined driver, vehicle, and road characteristics [19]-[15].

In 2019 there were 1,376,956 traffic violations and only 136,470 (10%) committed ODOL violations. Every day an average of 378 goods transportation violates ODOL. ODOL violations were ranked 4th out of 11 types of traffic violations. The PUPR (Public Works and Housing) Ministry said state losses reached IDR 43 trillion for repairing national roads due to being passed by ODOL trucks. As for the performance of the weighbridge in 2019, as many as 1,246 trucks (40%) violated the most over dimensions. The number of Motor Vehicle Periodic Test Implementing Units (UPUBKB) in Indonesia is 468 (out of 514 regencies/cities), and 186 accredited units, 267 UPUBKB are still under the process of accreditation.

Table 1. Causes of Arterial Road Accidents

No	Year	Cause of Accident			
		Driver	Vehicle	Environment	Road
1	2016	854	93	13	28
2	2017	729	39	17	2
3	2018	935	30	13	17
4	2019	1153	0	0	21
5	2020	807	5	1	16

Based on the table above, it was known that accidents in 2016-2020, the incidence of traffic accidents on arterial roads was more dominantly caused by the driver factor with a percentage of 98%, while the difference in the number of accidents caused by environmental and road factors with a vehicle factor of 2%.

## 3. METHOD

### 3.1 Research location and object

The object of this research was trucks with over dimensions and loading (ODOL) in Jombang Regency that passed through arterial roads. In Jombang Regency, there were problems with the truck's dimensions and heaviest axle loads (MST), thus violating spatial regulations and conditions, disrupting goods transport traffic, and disturbing comfort, safety, and security can cause potential accidents.

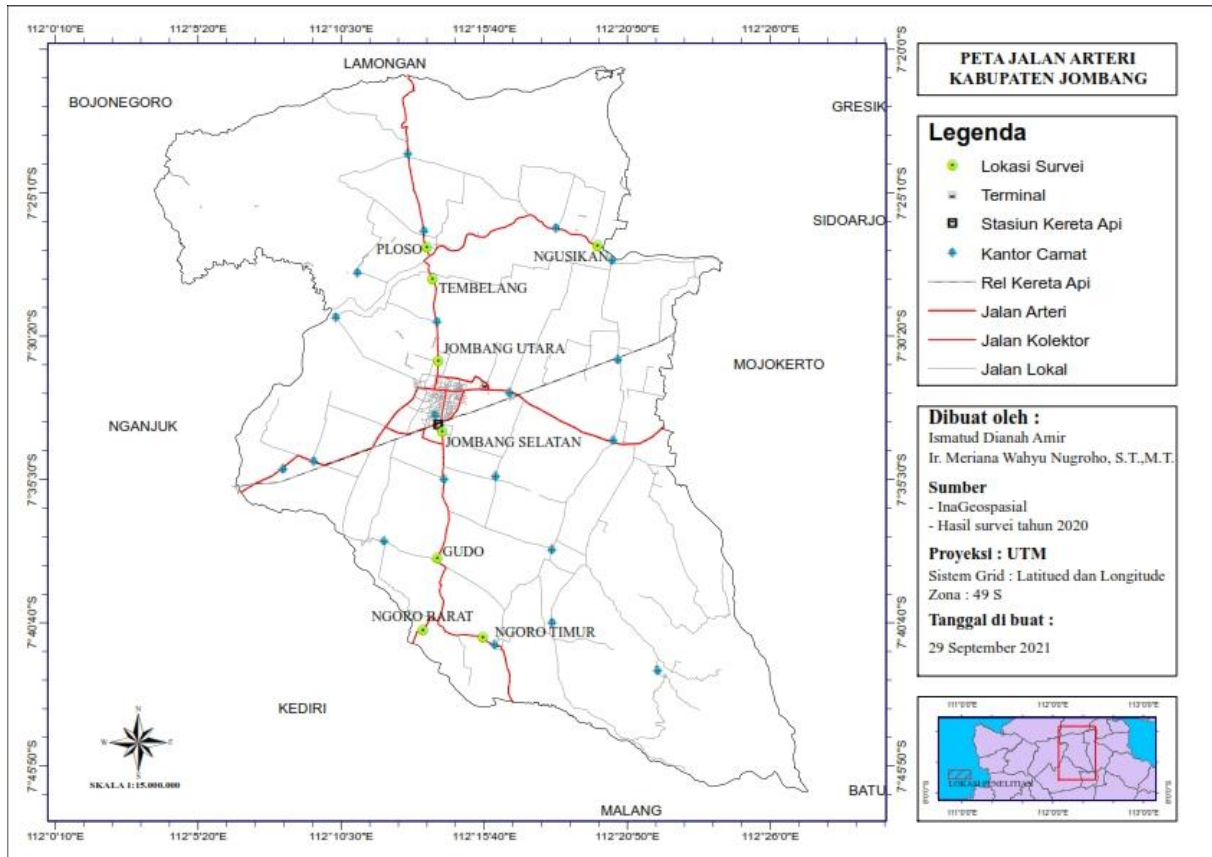


Figure 1. Research Location Map

The study was carried out at 8 points of the arterial road of Jombang city (Figure 2); data collection in the area was because the location was the main road connecting Jombang City with other cities, including Mojokerto, Lamongan, Gresik, Kediri, Tuban, and Nganjuk. The objects in this study included the following:

1. Over-dimension and overloading trucks (ODOL).
2. Truck driver.

The data for ODOL trucks consisted of the Indonesian Trucking Entrepreneurs Association (APTRINDO) East Java, Officers from the Department of Transportation of the Province of Jombang Regency, and Officers from the Traffic Directorate of the East Java Regional Police (Ditlantas Polda Jatim), Officers from the Public Works Department of Highways Jombang Regency.

Based on Figure 1, the number of ODOL truck accidents on each road section shows that the Ngusikan road section was 15 vehicles, the Ploso road section was 32 vehicles, the Tembelang road section was 69 vehicles, the Jombang road section was 262 vehicles, the road section was 35 vehicles, and the Ngoro road section was 106 vehicles.

### 3.2 Multinomial Logistic Regression

Multinomial logistic regression (polytomy logistic regression) is a logistic regression modeling used on response predictor data analysis with nominal non-binary categorical responses. For example, suppose the data you have is in the form of predictor-response data with a non-binary nominal scale response and has  $M$  categories. In that case, one baseline must be chosen. After that, compare the other categories with the predetermined baseline so that a logistics regression model would be obtained; if not specified, the baseline is the category with the lowest response value [20].

The triangulation validation test uses the Multinomial Logistics Regression method to determine the significant factors in accidents caused by oversized and overweight trucks. The sampling technique used was the Proportional Stratified Random Sampling technique on the driver/truck. The research variables used in the study are as follows.

Table 2. Predictor Variables

Predictor Variable	
Exogenous Factor	Indicator
X1.Road factor	X11.Road Type
	X12.Speed limit
	X13. Accident location
	X21.Weather
X2.Environmental factors	X22.Road Surface
	X23.Visibility
	X24.Time
	X25.Day
X3.Driver Health Factor	X31.Duration of driving
	X32. Driving Experience
	X33. Age
	X34. Bedtime
X4.Vehicle factor	X35. Distraction activity
	X36. Mindfulness
	X41.Vehicle tonnage
	X42. Vehicle Transmission
	X43. Vehicle type

The response variables with four indicators are presented in Table 3 below:

Table 3. Response Variables

Response Variable	
Endogenous Factor	Indicator
Y.ODOL Truck Accident Fatality	Y. Fatality rate
	1. Number of deaths
	2. Number of injured
	3. Number of vehicles involved
	4. Number of damaged vehicles

The steps taken to analyze this study are as follows.

1. Describe the characteristics of a freight vehicle accident with over-dimensions and overloading (ODOL) in the Jombang regency.
2. Conducting model analysis between freight vehicle accidents with over-dimensions and overloading with influencing factors with the following steps:
  - a. Test the independence of all predictor variables on the response variable.
  - b. Conduct multinomial logistic regression analysis.
  - c. Conduct simultaneous tests on predictor variables that have a relationship with the response variable and partial tests on predictor variables that have a relationship with the response variable.
  - d. Conduct model fit test
  - e. Calculating the accuracy of model classification

#### 4. RESULTS AND DISCUSSION

Estimated parameters of the research variables as shown in table 4. Below:

Table 4. Parameter Estimation and Odds Ratio

Logit	Predictor variable	B	Wald	P-Value	Odds Ratio
1	constants	-7.085	5.988	0.014	
	driving time[1]	-0.252	0.012	0.912	0.777
	Driver's age[1]	2.439	0.922	0.337	11.461
	Driver's age[2]	0.170	0.012	0.911	1.185
	Driver experience[2]	-1.089	0.194	0.660	0.336
	Certified training[2]	4.154	3.369	0.066	63.702
	Driving duration[1]	5.319	4.728	0.030	204.251
	Driving duration[2]	3.966	4.349	0.037	52.777
	Vehicle dimensions/size[2]	1.893	1.200	0.273	6.637
	Vehicle Age[1]	-1.810	0.506	0.477	0.164
	Vehicle Age[2]	0.067	0.001	0.971	1.069
	Accident location/hotspot[1]	-4.567	0.984	0.321	0.010
	Accident location/hotspot[2]	0.805	0.127	0.722	2.238
	constants	-2.322	16.174	0.000	
	driving time[1]	1.671	3.610	0.057	5.316
	driving time[2]	0.259	0.147	0.702	1.296
2	Driver's age[1]	4.706	9.799	0.002	110.555
	Driver's age[2]	0.656	1.384	0.239	1.927
	Driver experience[2]	0.456	0.655	0.419	1.578
	Certified training[2]	1.085	2.084	0.149	2.960
	Driving duration[1]	4.295	14.468	0.000	73.352
	Driving duration[2]	1.508	3.959	0.047	4.517
	Vehicle dimensions/size[1]	-3.038	2.802	0.094	0.048
	Vehicle dimensions/size[2]	-1.569	3.845	0.050	0.208
	Vehicle Age[1]	-3.665	10.244	0.001	0.026
	Vehicle Age[2]	1.002	2.531	0.112	2.724
	Accident location/hotspot[1]	4.371	9.909	0.002	79.153
	Accident location/hotspot[2]	1.224	2.325	0.127	3.402

Variables that were significant as a model, namely driver's age, duration of driving, vehicle dimensions/size, vehicle age, and the location of the accident (hotspot), could be obtained by two multinomial logistic regression functions as follows.

$$g_1(x) = -7.085 + 5.319X_{2,B}(1) + 3.966X_{2,B}(2) = 2.2 \quad (1)$$

$$g_2(x) = -2.322 + 4.706X_{2,I}(1) + 4.295X_{2,B}(1) - 1.569X_{3,I}(2) - 3.665X_{3,Z}(1) + 4.371X_{4,Z}(1) = 5.816 \quad (2)$$

Based on the logit 1 equation, the constant value was 7.085, where a negative value means that if the driver has high flying hours, the probability of an accident occurring is very low. Drivers who have high flying hours have the opportunity to increase the occurrence of accidents by 5.319.

The logit 2 equation had a constant value of -2.322, where a negative value means that if the driver has high flying hours, the probability of an accident occurring is very low. Older driver age has the opportunity to increase accidents by 4.295, smaller vehicle size has the opportunity to reduce accidents by 1.569, and newer vehicle age has the opportunity to reduce the chance of accidents by 3.665. Road conditions prone to accidents such as sharp turns could increase the probability of accidents amounted to 4.371.

The probability of over-dimensions and overloading trucks on the chance of an accident occurring with the categories of no accident, indirect accident, and accident occurring is shown in the following equation :

$$\pi_1(x) = \frac{\exp g_1(x)}{1 + \exp g_1(x) + \exp g_2(x)} = \frac{\exp(8.244)}{1 + \exp(8.244) + \exp(9.452)} = 0.026 \quad (3)$$

$$\pi_2(x) = \frac{\exp g_2(x)}{1 + \exp g_1(x) + \exp g_2(x)} = \frac{\exp(9.452)}{1 + \exp(8.244) + \exp(9.452)} = 0.971 \quad (4)$$

$$\pi_1(x) = \frac{1}{1 + \exp g_1(x) + \exp g_2(x)} = \frac{1}{1 + \exp(8.244) + \exp(9.452)} = 0.0029 \quad (5)$$

The odds ratio value at logit 1 (no accident category) for drivers with high flying hours was 204.251 less likely to have accidents than drivers with lower flight hours. Alternatively, it could be said that drivers with low flying hours were 52.777 times more likely to have no accidents than drivers with high flying hours.

The second logit explained that the indirect accident category for older drivers had an indirect accident probability of 110.555 compared to younger drivers. Drivers with high flying hours had 73.352 indirect accidents compared to drivers with lower flight hours. A truck with a larger size of 0.048 had an indirect chance of having an accident compared to a smaller truck, or it can be said that a truck with a smaller size of 0.208 had an indirect probability of having an accident compared to a truck with a larger size. Newer trucks were 0.026 less likely to have an indirect accident than older trucks. Accident-prone locations had an indirect accident probability of 79.153 compared to places that were not prone, or it can be said that locations that were not prone had 3.402 times the chance of indirect accidents compared to accident-prone locations.

Table 5. Model Classification Accuracy

Observation	Prediction			Accuracy (%)
	No accident	Indirect	Accident	
No accident	5	1	1	71.4%
Indirect	1	91	15	85.0%
Accident	0	11	69	86.2%
Overall accuracy	3.1%	53.1%	43.8%	85.1%

Table 5 showed the classification accuracy of the formed model was 85.1%, so it can be interpreted that the number of accuracy predictions was classified according to observations (actual conditions were 85.15 with a percentage of misclassification of 14.9%). The accuracy of the number of observations with no accident was 71.4%, indicating that the classification of the probability of not having an accident by 28.6 was incorrect. On the chance of an indirect accident having a classification accuracy of 85.0% and 15% of the indirect accident category was incorrect in its classification, as well as in the accident category classification accuracy of 86.2% indicated that 13.8% in the category of accidents was incorrect in its classification and was predicted to be in another category.

## 5. CONCLUSIONS AND SUGGESTIONS

The factors that cause the occurrence of over-dimension and overloading truck (ODOL) accidents are the driver's age, the duration of driving, the vehicle's dimensions/size, the vehicle's age, and the location of the accident (hotspot). The modeling for over-dimension and overloading (ODOL) truck accident on the primary arterial road in Jombang regency has two logit equations:

$$g_1(x) = -7.085 + 5.319X_{2.8}(1) + 3.966X_{2.8}(2) \quad (1)$$

$$g_2(x) = -2.322 + 4.706X_{2.1}(1) + 4.295X_{2.8}(1) - 1.569X_{3.1}(2) - 3.665X_{3.2}(1) + 4.371X_{4.2}(1) \quad (2)$$

The logit function above was used to generate the probability of each accident category as follows:

$$\pi_1(x) = \frac{\exp g_1(x)}{1 + \exp g_1(x) + \exp g_2(x)} = \frac{\exp(8.244)}{1 + \exp(8.244) + \exp(9.452)} = 0.026$$

$$\pi_2(x) = \frac{\exp g_2(x)}{1 + \exp g_1(x) + \exp g_2(x)} = \frac{\exp(9.452)}{1 + \exp(8.244) + \exp(9.452)} = 0.971$$

$$\pi_1(x) = \frac{1}{1 + \exp g_1(x) + \exp g_2(x)} = \frac{1}{1 + \exp(8.244) + \exp(9.452)} = 0.0029$$

The resulting model had a classification accuracy of 85.1%.

This research requires further research by calculating the Accident Equivalent Rate (AEK) on each road section and further research on toll roads. It is necessary to conduct a test method using binary logistic regression to determine the reliability of the resulting model.

## REFERENCES

- [1] Act No. 22 the year 2009 on Traffic and Road Transportation, Indonesian Government 2009.
- [2] Y. R. Utomo, M. Z. Arifin, and A. Wicaksono, "Analysis Descriptive of Logistic Vehicle Accident on Ngawi - Sidoarjo National Road," vol. 4, no. 4, pp. 257–262, 2019.
- [3] D. Yuniar, A. Wicaksono, L. Djakfar, and A. Efendi, "Effects of Coal Freight Road Policy Reforms on Transportation and Environmental Economics," *IOP Conf. Ser. Earth Environ. Sci.*, vol. 328, no. 1, 2019, DOI: 10.1088/1755-1315/328/1/012037.
- [4] M. of Transportation, *The Law on Road Traffic and Transport (Bahasa Indonesia)*. Indonesia: Secretariat General of The Ministry of Transportation, 2009.
- [5] Y. Yuan, M. Yang, Z. Gan, J. Wu, C. Xu, and D. Lei, "Analysis of the Risk Factors



- Affecting the Size of Fatal Accidents Involving Trucks Based on the Structural Equation Model,” *Transp. Res. Rec.*, vol. 2673, no. 8, pp. 112–124, 2019, DOI: 10.1177/0361198119841042.
- [6] A. Wicaksono, M. Z. Arifin, M. W. Nugroho, and Y. R. Utomo, “Truck Accident Risk Model for East Java, Indonesia,” pp. 828–835, 2021, doi: 10.1007/978-981-33-6311-3\_94.
- [7] N. Pasupuleti and S. S. Pulugurtha, “Spatial Extent and Modeling Intracity Truck Crashes,” *Procedia - Soc. Behav. Sci.*, vol. 104, pp. 1188–1197, 2013, DOI: 10.1016/j.sbspro.2013.11.215.
- [8] A. Galkin, N. Davidich, T. Melenchuk, Y. Kush, Y. Davidich, and O. Lobashov, “Modelling Truck’s Transportation Speed on the Route Considering Driver’s State,” *Transp. Res. Procedia*, vol. 30, pp. 207–215, 2018, doi: 10.1016/j.trpro.2018.09.023.
- [9] B. Naik, L. W. Tung, S. Zhao, and A. J. Khattak, “Weather impacts on single-vehicle truck crash injury severity,” *J. Safety Res.*, vol. 58, pp. 57–65, 2016, DOI: 10.1016/j.jsr.2016.06.005.
- [10] KNKT, “Traffic Accident Investigation and Road Transport Year 2007-2020 (In Bahasa Indonesia),” vol. 2020, no. 1, p. 6, 2021.
- [11] K. Landay, D. Wood, P. D. Harms, B. Ferrell, and S. Nambisan, “Relationships between personality facets and accident involvement among truck drivers,” *J. Res. Pers.*, vol. 84, p. 103889, 2020, DOI: 10.1016/j.jrp.2019.103889.
- [12] S. A. R. Shah, N. Ahmad, Y. Shen, A. Pirdavani, M. A. Basheer, and T. Brijs, “Road safety risk assessment: An analysis of transport policy and management for low-, middle-, and high-income Asian countries,” *Sustain.*, vol. 10, no. 2, 2018, DOI: 10.3390/su10020389.
- [13] A. H. Khoshakhlagh, S. Yazdanirad, F. Laal, and V. Sarsangi, “The relationship between illnesses and medical drug consumption with the occurrence of traffic accidents among truck and bus drivers in Tehran, Iran,” *Chinese J. Traumatol. - English Ed.*, vol. 22, no. 3, pp. 142–147, 2019, DOI: 10.1016/j.cjtee.2019.01.009.
- [14] Y. Sarwono, “Basic Understanding on Structural Equation Modeling (In Bahasa Indonesia),” *J. Ilm. Manaj. Bisnis Ukrida*, vol. 10, no. 3, p. 98528, 2010.
- [15] E. Rahimi, A. Shamshiripour, A. Samimi, and A. (Kouros) Mohammadian, “Investigating the Injury Severity of Single-Vehicle Truck Crashes in A Developing Country,” *Accid. Anal. Prev.*, vol. 137, no. 105444, 2020.
- [16] F. Saffanah Didin and H. Iridiastadi, “Risk factors for rear-end collision: A systematic literature review,” *IOP Conf. Ser. Mater. Sci. Eng.*, vol. 909, no. 1, 2020, DOI: 10.1088/1757-899X/909/1/012076.
- [17] M. Chen, P. Chen, X. Gao, and C. Yang, “Examining injury severity in truck-involved collisions using a cumulative link mixed model,” *J. Transp. Heal.*, vol. 19, no. September, p. 100942, 2020, doi: 10.1016/j.jth.2020.100942.
- [18] M. T. Haq, M. Zlatkovic, and K. Ksaibati, “Investigating Occupant Injury Severity of Truck-involved Crashes Based on Vehicle Types on A Mountainous Freeway,” *Accid. Anal. Prev.*, vol. 144, no. 105654, 2020.
- [19] Y. Wang, Y. Luo, and F. Chen, “Interpreting Risk Factors for Truck Crash Severity on Mountainous Freeways in Jiangxi and Shaanxi, China,” *Eur. Transp. Res. Rev.*, pp. 11–26, 2019.
- [20] J. Harlan, “Properties of AdeABC and AdeIJK efflux systems of *Acinetobacter baumannii* compared with those of the AcrAB-TolC system of *Escherichia coli*,” *J. Chem. Inf. Model.*, vol. 53, no. 9, pp. 1689–1699, 2013.

# APPLICATION OF THE IDEAL FLOW NETWORK (IFN) METHOD TO EVALUATE THE LEVEL OF SERVICE ARTERIAL ROADS

Susilowati<sup>1</sup>, Achmad Wicaksono<sup>1</sup>, Ludfi Djakfar<sup>1</sup> and Solimun<sup>2</sup>

<sup>1</sup> Civil Engineering Department, Faculty of Engineering, Universitas Brawijaya, Indonesia;

<sup>2</sup> Statistical Department, Faculty of Mathematics and Science, Brawijaya University, Indonesia

## ABSTRACT

The current government of Greater Malang continues to work hard to balance the density of land transport traffic to create better traffic flow and still encourage and improve its economy. Moreover, in recent years, INRIX has rated Malang as the third most congested city in Indonesia after Jakarta and Bandung. This study aims to identify factors and potential points of congestion on complex roads in the research object area. The research methodology uses literature studies, spatial databases, and data collection techniques by conducting surveys at each point of the research location with a daily traffic system (LHR) for a month. The research location is on the arterial road in the city of Malang. The road network system is variable to analyze using the IFN methodology; the working concept of the Ideal Flow Network (IFN) method uses pre-magic equilibrium as an ideal pattern, where all roads will have the same ideally congestion level. This study provides an alternative solution to overcoming congestion and determining when and where the congestion will occur in the city of Malang. Based on the analysis results, it is concluded that the smallest weighting of traffic volume is founded in alternative route three at each node, almost evenly and with a smaller dominant value. Then the value of the degree of saturation at each node is smaller so that the traffic flow becomes smoother.

*Keywords: Congestion, Ideal Flow Network (IFN), Modes of Transportation*

## 1. INTRODUCTION

Malang City is the second most traffic area in East Java after Surabaya, which is experiencing a high trend of motorized vehicle growth, both two-wheeled and four-wheeled vehicles. Malang City Government is currently trying hard to balance the balanced of land transportation traffic to create land traffic by encouraging its economy [1]. Moreover, INRIX had rated Malang City as the most congested city in Indonesia after Jakarta and Bandung [2].

Incorporating accurate intersection delays into route choice should make up for this difference in travel time calculations [2]. In addition, the research analyzes traditional mindsets related to road widening needed to overcome traffic congestion. This mindset occurs because the way of thinking is still locally in congested lanes in one corridor. In contrast, the Ideal Flow Network (IFN) invites transportation analysts to think globally across the road network, not just in one corridor. Using the pre-magic equilibrium benchmark as the ideal pattern, all roads will reach the same ideal congestion level; we redirect traffic from a congested route to a less congested one. Thus the difference between the maximum congestion and the average congestion of the entire network can be reduced. This research was conducted to know the structure of the road network in detail isn't only in one corridor but used to find alternative solutions to overcome congestion.

Several studies on road congestion include clear criteria between the two control systems, based on

vehicle delays when vehicle drivers join the queue until they cross the stop line, needs in decision-making [3]. Incorporating accurate intersection delays into route choice should make up for this difference in travel time calculations [2].

Traditional traffic assignment models use historical travel demand data, in this particular from Origin-Destination surveys, while cost more [4]. Traffic assignment can be seen from the supply side (road infrastructure) and the demand side rather than from the demand side only. The uniqueness and novelty of the IFN model [5]-[6] can be seen in Figure 1.

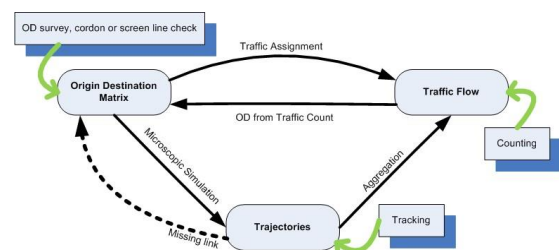


Figure 1. Missing Links in Transport Planning

Address resilience through three reliability measures, the Network Reserve Capacity, City Evacuation Capacity, and Network Vulnerability.

For Network Vulnerabilities, they note that the failure of some road sections can seriously consequence the overall performance of the intercity highway network. A network less prone to link failure is a strong network with vice versa [7].

## 2. DEFINITION

### 2.1 Traffic Congestion Theory

Congestion is a condition where the vehicle experiences various types of obstacles that result in a decrease in vehicle speed below usual conditions. Congestion will be very detrimental to the road user because it will hamper their travel time and increase the number of transportation costs. The word traffic jam has often been heard in big cities where mass transportation is still less attractive. Congestion occurs because road capacity is exceeded, as seen in the equation  $\text{Level of Service} = V/C$  (Volume/Capacity) close to 1, the ideal value of  $V/C < 0.75$ . (MKJI, 2017) [8]. Another cause of congestion is caused by many people who prefer private vehicles over public transportation.

Traffic jams have a negative impact, including the following:

1. Waste of time because the vehicle cannot go at normal speed.
2. Waste of energy because when stuck, the vehicle will continue to use fuel.
3. Increased air pollution because the energy consumption is higher at lower speeds, and the engine does not operate in optimal conditions.
4. Increased stress for road users.
5. Disrupt the smooth operation of emergency vehicles such as ambulances, fire engines, and the like.

Based on the causes of congestion described by the Federal Highway Administration (2005) [9], each cause has a different frequency level. The three biggest causes of congestion are physical bottlenecks with a percentage of 40%, traffic accidents with a percentage of 25%, and bad weather conditions with a percentage of 15%. Overall, the estimated number of each source of congestion can be seen in figure 2.

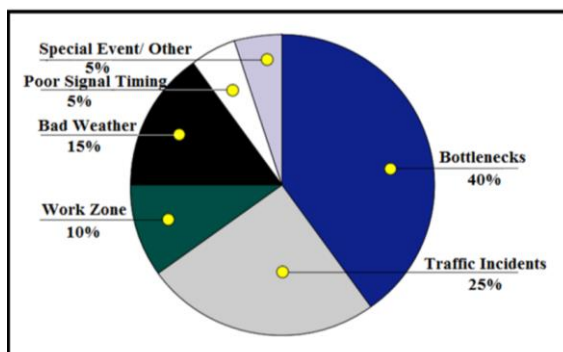


Figure 2. Causes and Percentage of Congestion

### 2.2 Road Service Level

Level Of Service (LOS) or road service level is a parameter that shows the condition of a road segment as a whole. The level of service of a road segment is determined based on quantitative values such as travel speed and degree of saturation and based on qualitative values such as freedom of the driver to choose the speed, degree of traffic resistance, and level of traffic comfort (Figure 3).

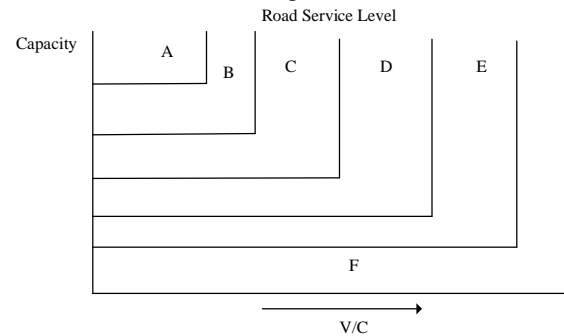


Figure 3. Relationship of Traffic Flow Service Level

The level of road service is determined on an interval scale of 6 levels. These levels are A, B, C, D, E, and F, where A is the highest level [8]. The higher the traffic volume on certain roads, the level of road service will decrease.

## 3. METHOD

### 3.1 Research sites

The research location is in Malang City, East Java Province following are alternative route maps of the arterial road, as shown in Figure 4.

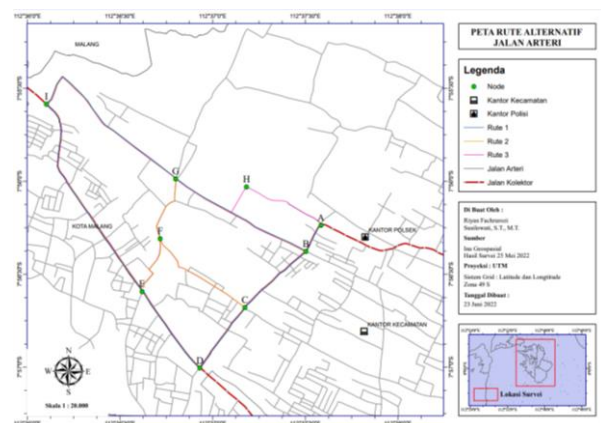


Figure 4. Alternative route map of arterial road

In the model, a directional graph represents a highway traffic network where Origin-Destination represents the origin, destination, and link intersections represent roads. Link weights, among others, represent travel time, distance, capacity, and traffic flow. This graphic representation is the traffic supply information (i.e., network structure) used to

make current traffic flow forecasts.

### 3.2 Ideal Flow Network (IFN)

Ideal Flow Network (IFN) is a special type of weighted directed (digraph) where two conditions are held. First, the digraphs are strongly related, and the weights must be positive, called flow. Second, at each node, the flow is balanced. The total inflow must equal the total outflow. Since network graphs are closely related to matrices, we can define the Ideal Flow matrix as a special matrix of the non-negative square matrix type, where the structure of the binary matrix (0,1) is fundamental, and the matrix is pre-magical [10].

#### 3.2.1 IFN As Aggregated Random Cycle

Ideal Flow is the constraint The relative link flow distribution of random walks in a strongly connected network with the probability distribution of outflows at each node. Since Random Walk is closely related to Markov Chain, we can also define Ideal Flow as the soft state equilibrium of link flow in a strongly connected network where current is conserved. Such an aggregation of random cycle paths over time is called a link stream, which will grow to infinity as time approaches infinity. However, because we divide the link flow by the flow statistics such as minimum, average, maximum or total flow, relative link flow is always combined with unique positive values, which we refer to as ideal flow.

#### 3.2.2 Axiom IFN

The four axioms of an ideal flow network are irreducibility, conservation flow, steady-state, and Markov property.

- Axiom 1: IFNs are strongly connected (ideal flow matrices are irreducible)
- Axiom 2: the flow in the IFN is maintained (the ideal flow matrix is pre-magic)
- Axiom 3: flow in IFN represents a steady-state equilibrium or constraining long-run distribution.
- Axiom 4: decisions at each IFN node follow the Markov property (based on local rather than global information).

#### 3.2.3 IFN based on Proportional Capacity

A capacity matrix is one of the simplest ideal flow model inputs to represent the maximum flow that can pass through the infrastructure. Link Capacity is the maximum flow the link can accommodate. The link capacity of a road network is closely related to the number of lanes or width of the road. The pattern (0,1) of the capacity matrix is the same as that of the fundamental adjacency matrix. Similarly, the

structure (0,1) of the ideal flow matrix is the same as the pattern (0,1) of the capacity matrix. Since the actual input of the ideal flow matrix is a stochastic transformation matrix of the capacity matrix, the relative proportion of each link capacity to the capacity of the other links is more important than the actual capacity. The proportion of capacity to absolute capacity in the real world will be a simple global scaling factor. Thus, the proportion of the capacity matrix can be simplified to the simple number of lanes in each link, where the capacity of each lane is assumed to be unchanged.

## 4. ANALYSIS AND DISCUSSION

In this study, we seek to provide an alternative solution using modern methods, namely by describing the level of traffic congestion on a node to other links by describing the traffic flow using the Ideal Flow Network (IFN) method. As in Figure 5.

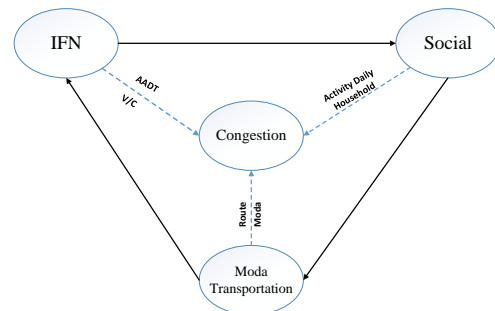


Figure 5. IFN Concept Framework

The Ideal Flow Network (IFN) method analyzes the entire road network globally, not just one corridor. With the policy of implementing the IFN model, the road network system impacts the socio-economic community in transportation. People's perceptions change towards the choice of transportation modes. This will reduce transportation costs so that the level of road service can be controlled.

Thinking simple that reducing conflict points at intersections can reduce congestion levels. Reducing conflict points at intersections can be done in various ways, including:

- arm reduction
- Lane reduction
- Controls of the amount of movement in each arm
- Systems engineering at the intersection

The absolute ideal flow network can be obtained through the scaling property of the ideal flow matrix. By limit ideal flow to absolute capacity will result in absolute link flow. Link speed and link delay can follow, as in figure 6.

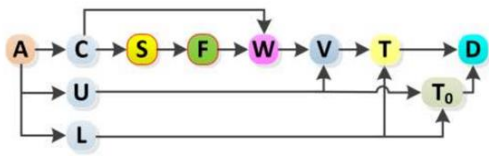


Figure 6. How IFN (Ideal Flow Network) works to analyze Traffic Assignment

In the Malang City area, several arterial roads experience congestion with a degree of saturation greater than the standard set. In this study, the location is along the Sukarno Hatta, MT. Haryono and Tlogomas Street.

Based on LHR survey data Tlogomas Street is 67,513 pcu/hour, MT. Haryono Street numbered 84,217 pcu/hour, and then Sukarno Hatta Street is a total of 91,073 pcu/hour, so the total vehicle on the three roads was 242,803 pcu/hour, equivalent to 242,800 pcu/hour. Then the capacity of the road segment is 2400 pcu/hour based on the provisions of the 1997 MKJI.

The road network structure can experience changes in terms of time that are permanent (long term) or temporary (short term) by changing links or nodes, either in structure or weight. Changes to the link can be made by subtracting the link weight from the path capacity matrix described with several alternatives. This analysis starts with breaking down the number of traffic flows on each link so that the number of departures and returns from the number of traffic flows is the same.

Alternative route 1 bypasses the main arterial route starting from the node A-B-C-D-E-A for one route from origin to destination. This alternative assumes that the capacity at the departure node is divided equally on each road network, where the number will equal the initial capacity (Figure 7).

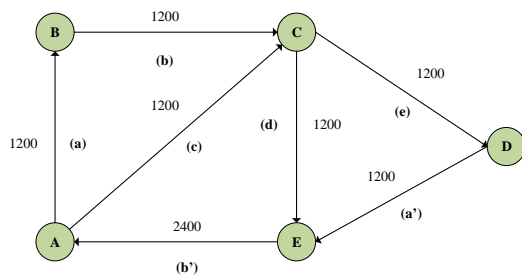


Figure 7. Alternative Route 1

symbols (a) as much as 1200 pcu/hour and node A – C with symbols (c) as much as 1200 pcu/hour, then from node B–C with the symbol (b) as many as 1200 pcu/hour, at node C is divided into two intersections, node C–D with a symbol (e) as much as 1200 pcu/hour and node C–E with the symbol (d) as much as 1200 pcu/hour. Then for the departure destination, starting from the node D–E with the symbol (a') of

1200 pcu/hour and the node E–A with the symbol (b') of 2400 pcu/hour.

Alternative route two bypasses the arterial route starting from the node A-B-C-D-E-F-G-A for route one from origin to destination. This alternative assumes that the amount of capacity at the node/departure node is divided equally on each road network whose number will equal the initial capacity, as shown in Figure 8.

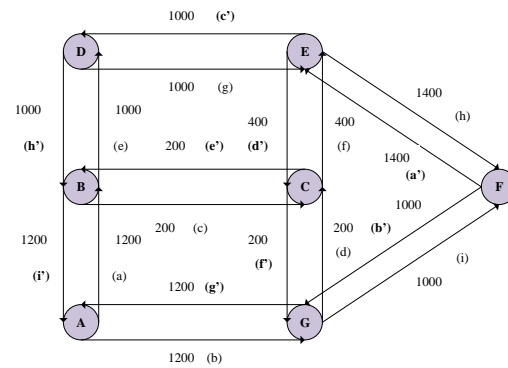


Figure 8. Alternative Route 2

The origin of the departure is shown from node A–B with symbols (a) as much as 1200 pcu/hour and node A–G with symbols (b) as much as 1200 pcu/hour, then from node B–C with the symbol (c) is 200 pcu/hour and node B–D with the symbol (e) is 1000 pcu/hour, at node G it is divided into two intersections, node G–C with the symbol (d) as many as 200 pcu/hour and node G–F with the symbol (i) as much as 1000 pcu/hour, node C–E with the symbol (f) as much as 400 pcu/hour, node D–E with the symbol (g) as much as 1000 pcu/hour. Furthermore, the node E–F with the symbol (h) has as many as 1400 pcu/hour.

Then the departure destination starts from the node F and is divided into two intersections, node F–E with the symbol (a') of 1400 pcu/hour and node F–G with the symbol (b') of 1000 pcu/hour, node E–C with the symbol (d') as much as 400 pcu/hour and node E–D with the symbol (c') as much as 1000 pcu/hour, on the node D–B with the symbol (h') as many as 1000 pcu/hour, the node of node C are divided into two intersections, node C–B with the symbol (e') as much as 200 pcu/hour and C–G with the symbol (f') as much as 200 pcu/hour, node G–A with symbol (g') are 1200 pcu/hour and node B–A with symbol (i') are 1200 pcu/hour.

Alternative route three by passing the arterial route starting from the node A-B-C-D-E-F-G-H-I-A for route one from the departure to the return journey (Origin-Destination) an assuming the amount of capacity at the departure node is divided equally on each road network whose number will be equal to the initial capacity. As in Figure 9.



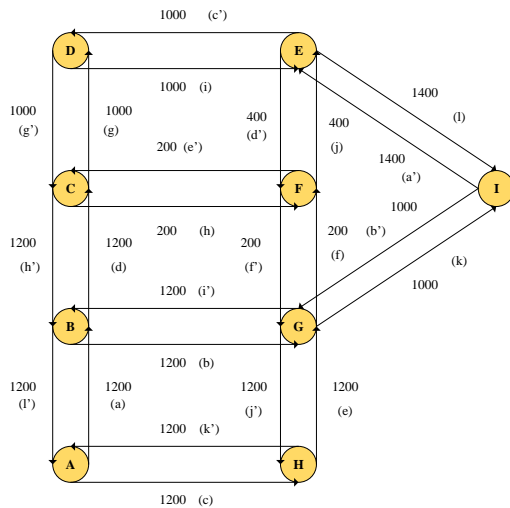


Figure 9. Alternative Route 3

The origin of the departure is shown from node A which is divided into two intersections, namely node A-B with the symbol (a) as much as 1200 pcu/hour and node A-H with the symbol (c) as much as 1200 pcu/hour, then from node B it is divided into two intersections, namely node B-C with the symbol (d) 600 pcu/hour and node B-G with a symbol (b) 600 pcu/hour, node H-G node points (e) as many as 1200 pcu/hour at node G are divided into two intersections, namely node G-I with the symbol (k) as many as 600 pcu/hour and node G-F with the symbol (f) as much as 1200 pcu/hour, node C is divided into two intersections, namely node C-D with the symbol (g) as much as 300 pcu/hour, node C-F with the symbol (h) as much as 300 pcu/hour. Node D-E with a symbol (i) is 300 pcu/hour, node F-E with a symbol (j) is 1500 pcu/hour, and node E-I with a symbol (l) is 1800 pcu/hour.

Then the departure destination starts from node I, divided into two intersextions: node I-E with a symbol (a) of 1200 pcu/hour and node I-G with a symbol (b') of 1200 pcu/hour. Node E is divided into two intersextions, namely node E-D with the symbol (c') as much as 600 pcu/hour and node E-F with the symbol (d') 600 pcu/hour, at node D-C with the symbol (g') as many as 600 pcu/hour. Node F is divided into two intersextions, namely node F-C with the symbol (e') as much as 300 pcu/hour and F-G with the symbol (f') is 200 pcu/hour, node C with the symbol (h') is 900 pcu/hour. Node G is divided into two intersextions: node G-B with the symbol (i') is 900 pcu /hour, and node G-H with the symbol (j') as many as 600 pcu/hour. The H-A node with the symbol (k') is 600 pcu/hour, and the B-A node with the symbol (l') is 1800 pcu/hour.

From the results of the breakdown of the traffic flow of the three routes, the results of the calculation of traffic volume and the degree of saturation (DS) on several arterial roads in the Malang City area were

obtained, as shown in Table 1. The traffic volume calculation is:

Table 1. Traffic Volume Calculation

Node Capacity (C) (pcu)		Volume (V) (pcu/hour)			Degree of Saturation (DS)		
		Route 1	Route 2	Route 3	Route 1	Route 2	Route 3
A-B	2400	30350	19164	14280	25.29	15.97	11.9
A-C	2400	30350	0	0	25.29	0	0
A-G	2400	0	19164	0	0	15.97	0
A-H	2400	0	0	14280	0	0	11.9
B-A	2400	0	19164	21420	0	15.97	14.87
B-C	2400	30350	3194	7140	12.65	15.97	14.87
B-D	2400	0	15970	0	0	15.97	0
B-G	2400	0	0	7140	0	0	14.87
C-B	2400	0	3194	10710	0	5.32	7.44
C-D	2400	30350	0	3570	25.29	0	7.44
C-E	2400	30350	6388	0	25.29	5.32	0
C-F	2400	0	0	3570	0	0	7.44
D-B	2400	0	5970	0	0	13.3	0
D-C	2400	0	0	7140	0	0	4.46
D-E	2400	30350	15970	3570	12.65	13.3	4.46
E-A	2400	60700	0	0	12.65	0	0
E-C	2400	0	6388	0	0	18.63	0
E-D	2400	0	15790	7140	0	18.63	14.87
E-F	2400	0	22358	7140	0	18.63	14.87
E-I	2400	0	0	21420	0	0	14.87
F-C	2400	0	0	3570	0	0	10.41
F-E	2400	0	22358	17850	0	15.97	10.41
F-G	2400	0	15970	3570	0	15.97	10.41
G-A	2400	0	19164	0	0	15.97	0
G-B	2400	0	0	10710	0	0	16.36
G-C	2400	0	3194	0	0	15.97	0
G-F	2400	0	15970	14280	0	15.97	16.36
G-H	2400	0	0	7140	0	0	16.36
G-I	2400	0	0	7140	0	0	16.36
H-A	2400	0	0	7140	0	0	8.9
H-G	2400	0	0	14280	0	0	8.9
I-E	2400	0	0	14280	0	0	11.9
I-G	2400	0	0	14280	0	0	11.9

Source: Survey, 2022

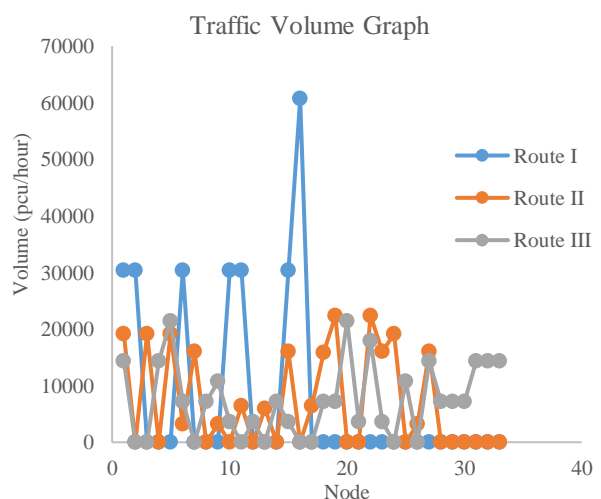


Figure 10. Traffic Volume Graph

Based on the analysis of each route on each road section, it was found that the highest volume of



vehicles on alternative route 1, the second-order alternative route 2, and alternative route 3 was in order 3.

After knowing the amount of traffic volume on each alternative route, and analyzed using the Ideal Flow Network (IFN), the value of the degree of saturation (DS) on each alternative route is shown in figure 11.

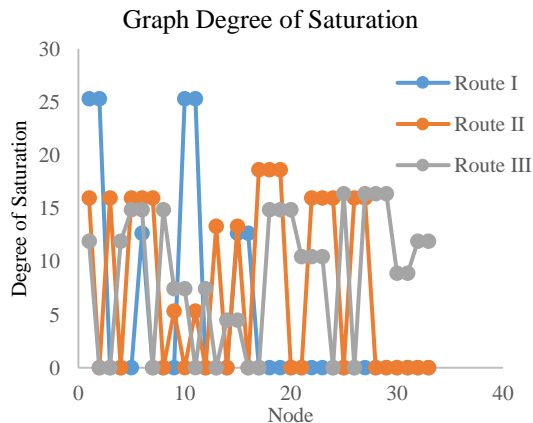


Figure 11. Saturation Degree Graph

The value of the degree of saturation (DS) on the three alternative routes, which has an ideal value based on the standard level of road services, is alternative route 3. The value of the degree of saturation from the third alternative route is 16.36; 14.87; 11.9; 10.41; 8.9; 7.44; 4.46.

## 5. CONCLUSION

Based on the analysis results, it is concluded that the smallest weighting of traffic volume is founded in alternative route three at each node, almost evenly and with a smaller dominant value. Then the value of the degree of saturation at each node is smaller so that the traffic flow becomes smoother.

## 6. ACKNOWLEDGMENTS

The authors thank Kardi Teknomo, Ph.D., who has provided direction and guidance regarding the Ideal Flow Network (IFN) method. And all of his colleagues who have helped during the implementation of this research.

## REFERENCES

- [1] Sari. Feby A. P., Policy Analysis of Handling Traffic Congestion On Teuku Umar Street, Jatingaleh Area, Semarang With The Process Hierarchy Analysis Method (AHP), p. 82, 2011.
- [2] Pishue. B. and T. Analyst, Global Traffic Scorecard,” *INRIX Res.*, 2020.
- [3] Koutsopoulos. H. N. and Habbal. M, Effect of Intersection Delay Modeling on The Performance of Traffic Equilibrium Models, *Transp. Res. Part A*, vol. 28, no. 2, pp. 133–149, 1994, doi: 10.1016/0965-8564(94)90034-5.
- [4] Al-Madani. H. M. N., Dynamic vehicular delay comparison between a police-controlled roundabout and a traffic signal, *Transp. Res. Part A*, vol. 37, no. 8, pp. 681–688, 2003, doi: 10.1016/S0965-8564(03)00024-7.
- [5] Teknomo. K, Gardon. R. W. and Saloma . C., Ideal flow traffic analysis: A case study on a campus road network, *Philipp. J. Sci.*, vol. 148, no. 1, pp. 51–62, 2019.
- [6] Teknomo . K and Gardon . R. W, Intersection analysis using the ideal flow model, *IEEE Conf. Intell. Transp. Syst. Proceedings, ITSC*, vol. 2018-March, pp. 1–6, 2018, doi: 10.1109/ITSC.2017.8317739.
- [7] Teknomo. K, Ideal relative flow distribution on directed network, *arXiv*, 2018, doi: 10.11175/easts.12.939.
- [8] Alexandra Maria Rios. C and Francisco de Sousa. R, Cluster analysis of the competitiveness of container ports in Brazil, *Transp. Res. Part A Policy Pract.*, vol. 69, pp. 423–431, 2014, doi: 10.1016/j.tra.2014.09.005.
- [9] T. Congestion, Final report of the safety assessment of methacrylate ester monomers used in nail enhancement products., *Int. J. Toxicol.*, vol. 24 Suppl 5, pp. 53–100, 2005, doi: 10.1080/10915810500434209.
- [10] Teknomo. K, Ideal flow of Markov Chain.pdf, *World Sci. Publ. Co.*, vol. 10, pp. 1–18, 2018, doi: 10.1142/S1793830918500738.

# THE EFFECT OF CHANGES IN LAND USE ON THE PREDICTION OF CRITICAL LAND DISTRIBUTION IN THE RAWAS WATERSHED (South Sumatra Province, Indonesia)

Zainuddin Muchtar<sup>1)</sup>, Dinar Dwi Anugerah Putranto <sup>2)\*</sup>,Febrian Hadinata <sup>2)</sup>, Lawin Bastian <sup>3)</sup>, Julian fikri<sup>4)</sup>

<sup>1)</sup>Doctoral Program in Engineering, Postgraduate Program, Faculty of Engineering, Sriwijaya University;

<sup>2)</sup>Department of Civil Engineering and Planning, Faculty of Engineering, Sriwijaya University, Indonesia

<sup>3)</sup> Ministry of Environment and Forestry of the Republic of Indonesia

<sup>4)</sup> Sriwijaya State Polytechnic

## ABSTRACT

The current regulation and monitoring of land degradation is an urgent need to increase national capacity in carrying out quantitative assessments and mapping critical land, as desired in the Sustainable Development Goals (SDGs). An innovative approach is needed to monitor critical land at the national, provincial, and district city scales. Sub-watershed scale analysis related to the distribution of degraded land by utilizing multi-temporal geospatial layers [1][2] is useful in providing a regionally consistent data set of required land distribution that can be used to support agendas aligned with sustainable development goals (SDGs). ) [3][4]. In the analysis of topographic conditions, types of land cover, duration and time of rain, the magnitude and distribution of erosivity based on soil type and slope, which is modeled using GIS techniques, can support data collection and predictive information on the distribution of critical land and potential environmental damage in the watershed area. The analysis was carried out using contour data from DEM NAS with contour intervals of 15 m, added with high points every 2.5 m, and analyzed using the Digital Elevation Model (DEM) technique so that the watershed boundary was obtained as the basic unit in morphometric analysis, river length, land slope, flow pattern, flow density, watershed shape, watershed area, to understand the hydrogeological behavior of the drainage basin and reveal the geological, geomorphological and flow direction conditions that occur in the area. Most of the land in the study area is located on the Alluvial plain. With such conditions, it can be concluded that the largest run-off coefficient value in the Rawas watershed area affects the condition of water availability and the carrying capacity of the soil's ability to absorb water; the run-off efficiency value is > 0.5.

*Keywords: Erosion, Coefficient infiltration, Land use, Sedimentation, Water balance*

## 1. INTRODUCTION

Pressure on land resources coupled with the effect of climate change on intensive rainfall, will result in a process of land degradation caused by rainfall that exceeds normal rainfall coupled with human activities, such as logging and inappropriate land development, which will increase the occurrence of run-off and soil erosion [5]. Therefore, to further preserve environmental quality and improve natural resource management and land planning, it is essential to monitor changes in land degradation that occur periodically [6].

Extreme rainfall events, especially at the beginning of the season, when the land surface does not have plant or plant cover, will cause significant run-off and exfoliation of the topsoil layer. Areas with steep slopes and non-composite soil structures will cause soil erosion. And if the soil structure is unstable, then the room with a steep slope will cause the cliff to collapse. Planting practices carried out by farmers on several types of land slopes, which are unsuitable, also cause a lot of erosion.

Meanwhile, during the dry season, land management that is not suitable will experience a water deficit. Such conditions will cause significant environmental damage in the watershed area. Based on data from the Musi Watershed Management Center (BPDAS MUSI) in 2011 [7], the site of critical land which is categorized as very essential in the Rawas watershed area is 5,810.909 Ha and a place of 499,399.042 Ha in the moderately critical category, Critical Potential is 443,737.122 Ha, while the rest is in non-critical condition, covering an area of 170.986,394 Ha.

### 1.1. Research significance

Optimization of land use arrangement is one of the critical activities that must be carried out if you want to reduce the essential distribution of land, as in the case of the Rawas watershed. The analysis of topographic conditions, types of land cover, duration and time of rain, and the magnitude and distribution of erosivity, which is modeled using GIS techniques, can support data collection on

predictions of critical land distribution and potential environmental damage in the Rawas watershed area.

The critical land analysis method discussed further in this paper combines land use distribution data and various additional data sets in a more flexible essential land estimation technique. Analysis of the sub-watershed scale related to the distribution of necessary land utilizing multi-temporal geospatial layers [6]. Multitemporal geospatial layers help provide a regionally consistent set of critical land distribution datasets that can be used to support agendas aligned with sustainable development goals (SDGs)[8]

## 2. METHODOLOGY

### 2.1 Study area

Rawas sub-watershed is one of the 36 water facilities in the South Sumatra Province Administrative Region and is also part of the Musi River Basin. This facility has a catchment area (DAS) of approximately 5,891 Km<sup>2</sup>, with a geographical location at variational coordinates of 102° 4' 4.8" – 103° 27' 36" east longitude and 2° 19' 15" – 3° 06' 36" south latitude. The boundary of the Rawas sub-watershed is also the administrative limit of North Musi Rawas Regency, which is the new Autonomous Region. The upstream area of this facility is at an altitude of 2,100 m above sea level, which is one of the highest peaks in the Kerinci Seblat National Park zone, partly included in the Administrative Region of North Musi Rawas Regency (1,884.61 Km<sup>2</sup> or 32%). Moreover, Kerinci Seblat National Park (TNKS) is part of the global warp, designated by UNESCO as a World Heritage Area, with more than 4000 species of primary forest flora and 115 species of ethnobotanical plants that are very beneficial for the preservation of forest resources. This focuses on the benefits of reducing global warming. In addition, two significant rivers or sub-river systems flow in the Rawas sub-watershed, namely the Rupit River, which fulfills and empties into the Rawas water body.

The water resources in the sub-systems of Rawas and Rupit rivers have benefited the residents in the watersheds. However, the licensing development for several lands utilized for plantation activities is increasing massively in this area. This indicates an imbalance in water availability during the rainy and dry seasons, as observed in other river systems within the Musi River Basin [9]-[10]. The provincial and district governments subsequently issued several permits for oil palm and rubber plantations, mining, infrastructure, and other economic developments, as well as many illegal operations in the hills and along Rawas River, based on the extraction of coal,

gold, sand, and Iron ore. Therefore, this problem is found to disrupt the raw water supply system. The mining activities in the hills and along the river basin of Rawas sub-watershed also affect the erosion magnitude and flooding volume in Tugu Mulyo District, Musi Rawas Regency.

### 2.2 Methods

Rainfall-run-off modeling using the RUSLE analysis technique [11] by utilizing GIS techniques to assess the criticality level of land based on the relationship between soil properties, slope diversity, land use patterns, and the amount of erosion. The physical parameters of the watershed are combined with time series parameters of high rainfall in the upstream and middle regions by calculating the amount of kinetic energy (annual Kinetic Energy) caused by rain intensity (precipitation) within 30 minutes for several return times variations. The amount of rainfall is the increase in the amount of Kinetic Energy (KE), soil vulnerability index (Kd), and the percentage of rainfall intercept (INT). Using the RUSLE model [12], all parameters in the watershed are analyzed to estimate the magnitude of detachment indexes or the amount of surface soil detachment, which has the potential to become a sediment solution, depending on the slope level soil structure and land cover.

Land cover data is used to redistribute the aggregate number of critical lands to increase the accuracy of the crucial land distribution data based on regional scale sizes [13]. In addition, various factors in the occurrence of environmental damage are known to correlate with how humans distribute land use activities in the landscape [14]. Therefore, a large number of land use groups can be used in the modeling to more effectively separate the distribution area of critical land within the watershed boundary unit and to better describe the distribution of degraded land [15].

#### 2.2.1 Extraction of Land use

The results of the Multispectral image classification are land cover maps used as the basis for multitemporal monitoring of land use and landform maps. Maps of landforms are generated through the visual interpretation of images. The relationship between land cover and landform is presented in a land use matrix, the result of which is the unit of land use class. For example, the relationship between an area with low-level vegetation land cover and plain fluvial landforms is a characteristic of paddy land use. Such linkages of land use can be determined. Other elements of interpretation, such as patterns, shapes, sizes, and associations, are also considered to identify land use objects. Processing is done digitally by recognizing objects and processing spectral values.

### 2.2.2 Extraction of drainage network

DEM (Digital Elevation Model) is digital data with x, y, and z values. The x and y values are the coordinates of the position/location, and the z values are the elevation values. DEM can be derived or used to generate new data that requires altitude information, for example; contour maps, elevation maps, land slope class maps, digital terrain models/Digital Terrain Model (DTM), hill shading, aspect maps, intervisibility (visible), slope length, watershed shape, watershed density, and so on [16]. In this study, the land slope class map was compiled using DEM processing. DEM data used is DEM Nas (Digital Elevation Model National Indonesia) data in the form of raster data with pixel values indicating location coordinates and altitude values. The DEM Nas data is interpolated to produce a contour map. The quality of the SRTM, which has a spatial resolution of 7.5 meters, is good enough to present altitude data on a scale of 1: 10,000.

Morphological parameters play an important role in watershed features and proper watershed management planning. Bharath [17] has discussed the importance of quantitative geomorphological evaluation in water resource management. Many geomorphologists improve watershed morphological methods [18]. Most watershed morphometric parameters are influenced by rock strata, lithology, and geological construction [16]. Likewise, geological, geomorphological, land cover, and hydrological information is beneficial for understanding watershed drainage patterns [16]. Presenting watershed morphometric conditions will provide a comprehensive picture of the drainage basin, which is very useful in research, including prioritizing watershed environmental management, hydrological modeling, conservation, and restoration [19].

### 2.2.3 Soil loss modeling

The soil loss determination method consists of two different base phases. The first one is the water phase; the second one is the sedimentation phase. At the water phase, the kinetic energy of rainfall, overland flow, and annual precipitation values and at the sedimentation phase rate of soil detachment by raindrop impact and transport capacity of overland flow values are calculated for every pixel by generating maps for each input data [20]. This predictive model for assessing soil erosion risk is called the Morgan model. The input parameters and operating functions of this model are given below. The strength of the energy generated from the volume of rainfall is half the mass of the particle times the square area of the soil surface. To calculate the amount of erosion used EI30, which was developed by Wischmeir and Smith, 1958 [20].

Model sediment transport flow is carried out by estimating mass conservation to simulate soil

erosion and deposition. The average change in soil loss is predicted through the RUSLE equation approach [11]:

$$E = R.K.L.S.C.P \quad (1)$$

where,

E = soil erosion rate (tonnes/ha/year)

R = Rain Erosivity Index

K = Soil erosion index

LS = Index of slope length and slope

C = Vegetation cover index

P = Index of tillage or soil conservation measures

The LS factor is calculated to predict the strength/erosivity of the run-off and is expressed as the ratio of slope-affected soil loss and slope length to soil loss under standard conditions at a slope of about 5o (9%) with a slope length of approximately 22.13 meters ( Wischmeter and Smith, 1958)[21]

$$LS = \left(\frac{\lambda}{22.13}\right)(65.4 \sin 2\beta + 4.56 \sin\beta + 0.0654) \quad (2)$$

The amount of rainfall (D) is a function of increasing kinetic energy (KE), soil vulnerability index (Kd), and the percentage of rain intercepts INT. Annual kinetic energy can be calculated from the rainfall station graph using an equation or estimated from rainfall data using an empirical equation. Soil vulnerability index is interpreted locally, but values are based on texture. For interception with sparse vegetation, it is estimated using the values obtained from the intercept loss measure [22].

$$D = Kd * (KE * e^{INT}) \quad (3)$$

Where,

$$KE = R * (11.9 + 8.7 * \log(10) I) \quad (4)$$

Kd = soil vulnerability index

INT = Interception (%)

I = Rainfall intensity (mm/hour)

### 2.2.4. Transport Sediment

The model's sediment transport capacity (T) is a function of the overland flow volume and slope (S) coverage factor. The importance of overland flow (Q) is the derivative of the annual rainfall (R), the ratio between soil moisture storage and the separation of yearly rainfall with the number of daily rains per year (n). Soil moisture storage (Rc) follows field capacity (ms), bulk density (Bd) and topsoil, root depth and topsoil, and the ratio of actual evapotranspiration (EPT). Plant factor (c) is obtained from the land cover sub-factor so that the

equation becomes

$$T = C * Q_2 * \sin(S) \text{ g/m}^2 \quad (5)$$

where,

S = Slope (radians)

C = land cover factor (0-1)

$$Q = R * e^{\frac{Rc}{Ro}} \text{ mm} \quad (6)$$

R = average annual precipitation mm

Rc =  $1000 * R_d * M_s * B_d * (E_a/E_p)^{0.5}$

where,

Rd = depth of root zone (m)

ms = soil moisture at field capacity (w/w)

Bd = bulk density on Top Soil (g/Cm<sup>2</sup>)

Ea/Ep = ratio of actual and potential evapotranspiration

Ro = R/n

where,

n = number of rainy days in a year

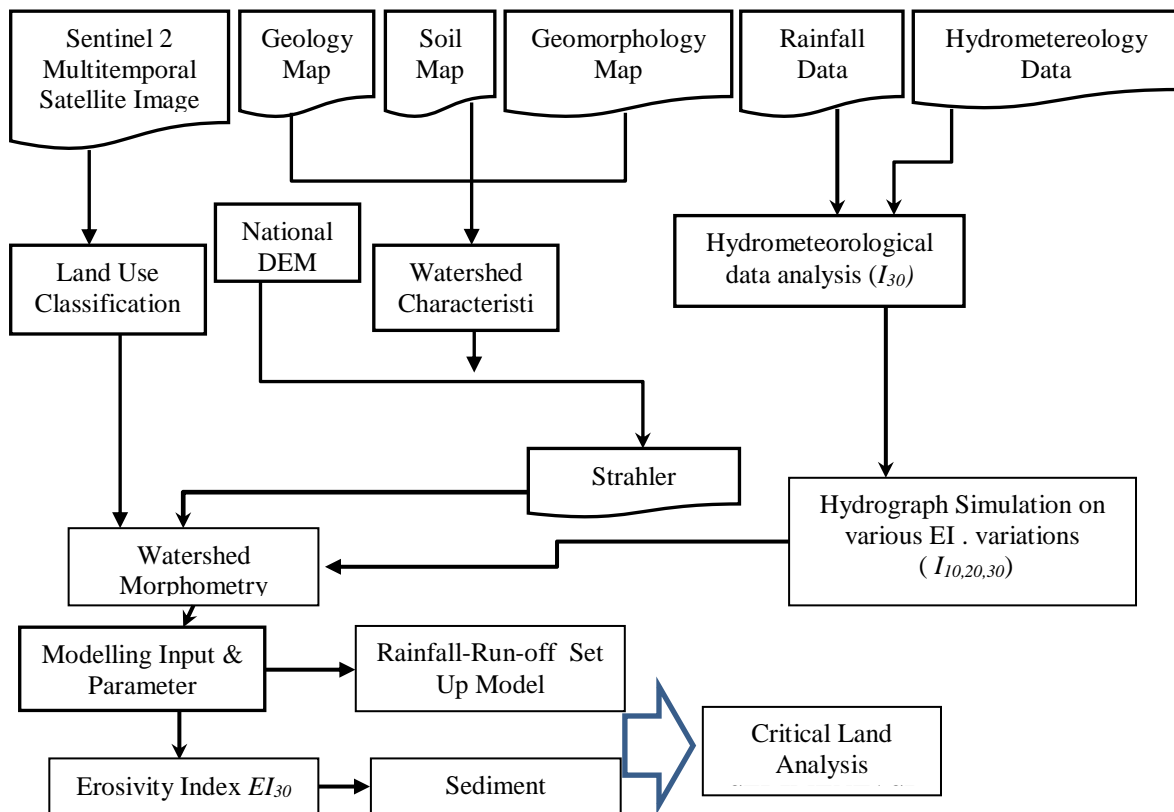


Fig. 1 Research Flowchart

### 3. EVALUATION OF MORPHOMETRIC PARAMETER

The morphometric analysis is based on data on the elevation of the watershed area, the aspect of the site, and the gradient and slope of the land that contributes to the drainage basin. Morphometric analysis to understand the hydrogeological behavior of drainage basins and reveal climatic, geological, geomorphological, and structural conditions that occur in the area.

#### 3.1. Watershed morphometric analysis

Drainage analysis in the watershed system will determine whether the flow pattern is good, the

inundation area, and the availability of water in the study area

##### 3.1.1 Flow Length

Flow length is one of the essential hydrological characteristics in a watershed area because it provides information about run-off characteristics. The size of the most extended river flow in the Rawas sub-watershed is 44.73 Km. And the shortest river length in the Rawas sub-watershed is 0.53 Km. All drainage channels in the river sub-system are elongated patterns, and there are not many river branches. Thus, it can be concluded that the Rawas sub-watershed is a basin with alluvial deposits of former sediment or river overflow.

### 3.1.2. Average flow length ( $L$ )

Average flow length is a dimensionless property that expresses the characteristic size of the drainage network and watershed surface components that contribute to the arrival time of water flow from upstream to downstream. For example, the average flow length in the Rawas watershed is 15.42 Km.

### 3.1.3. Basin area ( $A$ )

The Watershed area is another crucial parameter, such as the length of river drainage. The Rawas 8 watershed has the largest catchment area (484.96 Km<sup>2</sup>), and the smallest size is 0.75 Km.

### 3.1.4. Basin perimeter ( $P$ )

The basin's perimeter is the outermost boundary of the watershed, commonly called the circumference of the sub-watershed. Measured along the border between adjacent watersheds and used as an indicator of the size and shape of the watershed. The perimeter of the basin of the study area varies, with the largest circumference of 161.27 Km

### 3.1.5. Drainage pattern

In the basin, the drainage pattern reflects the influence of slope, lithology, and rock structure. Analysis of drainage patterns helps in identifying the stages of the erosion cycle. The drainage pattern presents several characteristics of the watershed through the drainage pattern and drainage texture. It is possible to infer the basin's geology, rock strike and deposition, the presence of faults, and other information about the geological structure of the drainage patterns. Texture drainage reflects climate, rock permeability, vegetation, and relief ratio by relating drainage patterns to geological data. The Rawas watershed has an elongated drainage pattern and trails. So it can be concluded that the research area is a flat and undulating area, with one extensive river system, a floodplain basin.

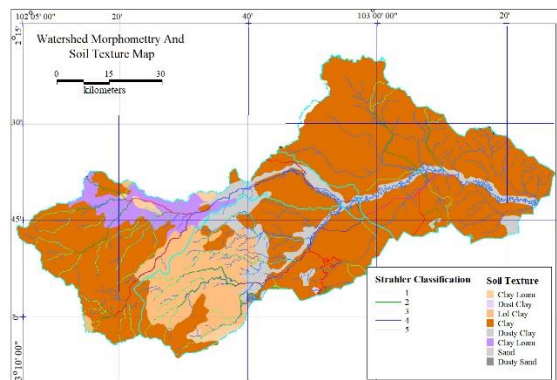


Fig. 2 Watershed morphometry and soil texture

### 3.1.6. Drainage density

Drainage density is the flow length per unit area of a basin or watershed and is another element of drainage analysis. Drainage density is a better quantitative expression for landform discretion and research. However, climate functions, lithology and structure, and the relief history of the area can be used as indirect indicators to explain these variables and landform morphogenesis. The drainage density of the Rawas basin is 0.197 Km/Km<sup>2</sup>.

## 3.2. Topography of the planning area

The planning area is one of the upper reaches of the Musi River Basin with an altitude of 2,100 m above sea level and the lowest area at an altitude of 25 m above sea level. The slope of the Rawas watershed varies, with a pitch of < 8% being the most expansive area and a hill of > 45% being the smallest area. The headwaters of the Rawas river is Mount Kerinci, which is part of the Kerinci Seblat National Park (TNKS) which has been designated as part of the lungs of the world and functions as a protected forest. The total economic value of the TNKS area is the direct use value and the residual water value for the water value. Indirect use value is the value of carbon sequestration, as well as the value of existence (existence) and inheritance (legacy).

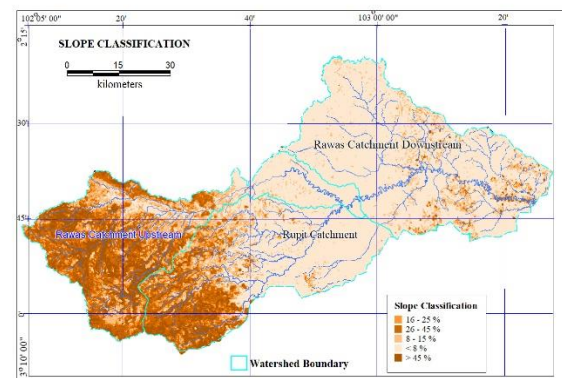


Fig. 3 Topography of the research area

### 3.2.1. Geology

The Rawas watershed has unconsolidated sediments from clay to sand sequences of different grades. Geologically, the Rawas watershed includes highlands and lowlands and is a quarter alluvial deposit from the Pleistocene to young age. Some parts of the basin have loamy sand formations due to silt deposits which are sometimes interspersed with sand. Shallow aquifers occur mainly in clay river deposits and meandering rivers. The bay has deep aquifers in thick sand layers and has good potential.



### 3.2.2. Geomorphology

The background of the Rawas river basin is quarterly alluvial deposits consisting of clay, silt, sand, and gravel of various grades. Based on the total dissolved solids, two groundwater samples in the field were deemed unfit for drinking, but all models were found helpful for irrigation.

### 3.2.3. Hydrology

A hydrogeological analysis is based on understanding the nature of the aquifer and the mode of occurrence. The availability of groundwater in the alluvial zone is controlled by the thickness of the sand and clay zone. Groundwater near the surface occurs under free aquifer conditions, while deeper aquifers arise under conditions of  $z$  (depth) limited to confined aquifer conditions. Rainfall is the primary source for replenishing groundwater in the basin. The water level shows a deteriorating trend in some parts of the study area due to rapid urbanization and intensive pumping. The average hydraulic gradient is 0.35 m/km, indicating the porous nature of the formation near the surface of the watershed.

The water yield of the Rawas watershed in the form of river flow is strongly influenced by the nature of the rain input and the physical parameters of the watershed. The characteristics of each watershed will result in different water production for the same amount of rain input and vice versa. Daily rainfall in the Rawas watershed is dominated by a classification of 24.00 - < 46 mm/day. The highest rainfall is 78.18 - < 121 mm/day. The lowest rainfall is 0 - < 18.91 mm/day. Based on the results of the monthly rainfall analysis for R 80, the highest average rainfall value occurred in November - March, with the maximum rainfall in December (176.97 mm/month), and the lowest rainfall occurred in September (30.29 mm/month).

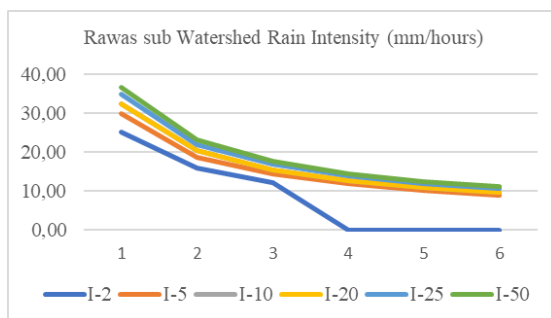


Fig. 4 1-6 Hour rain intensity design for 2 -50 years return period

## 3.6 Land use

Land use dramatically determines the magnitude of the soil loss index (F) and overland flow (Q). Each type of land use will be different

because it is influenced by a different coefficient of run-off (C) and the percentage of rainfall that enters the soil (A). From the land use map, the area and run-off coefficient values will be generated based on land use.

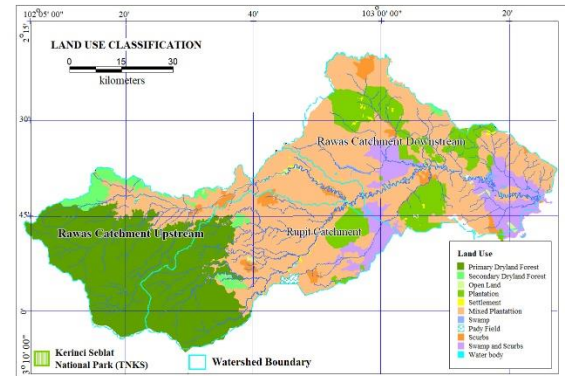


Fig. 5 Land use map of Rawas watersheds

From the map above, it can be seen that dense forest has the largest land use area in the Rawas watershed, which is 247120.77 Ha. Meanwhile, the minor land use is residential, with an area of 70.57 Ha.

## 4. RESULTS AND DISCUSSIONS

The formation of critical land is one indicator of ecological and environmental damage. Land that has been damaged will automatically reduce its function and role. The decline in this function is caused by land use patterns that do not pay attention to soil conservation techniques. Based on the results of the analysis of the amount of run-off and soil erosion that occurred in the last ten years (2010-2020), obtained an analysis of critical land in the Rawas sub-watershed covering an area of 221,530,294 Ha in the crucial category, 1,078,033 Ha in the introductory class, 62,930, 110 Ha in the moderately critical category, 225,692, 387 potentially critical and only 72,587,452 Ha, which is not critical (6.31%). The most prominent problem in the watershed is the damage to natural resources (soil, water, vegetation) caused by soil erosion, landslides, degradation of soil fertility, floods, and droughts.

General problems in the Rawas watershed environment can be grouped into 4 (four) parts according to their respective specifications, namely: (1) Physiographic problems (relief/mountainous and hilly topography, steep slopes), in the upstream area (Kerinci Seblat National Park/Mount Kerinci), there is a lot of illegal forest clearing by residents in search of gold ore, so the degree of erosion is high. In addition, high rainfall results in increased surface run-off, low soil stability, reduced soil fertility, and soil productivity will rapidly decline.

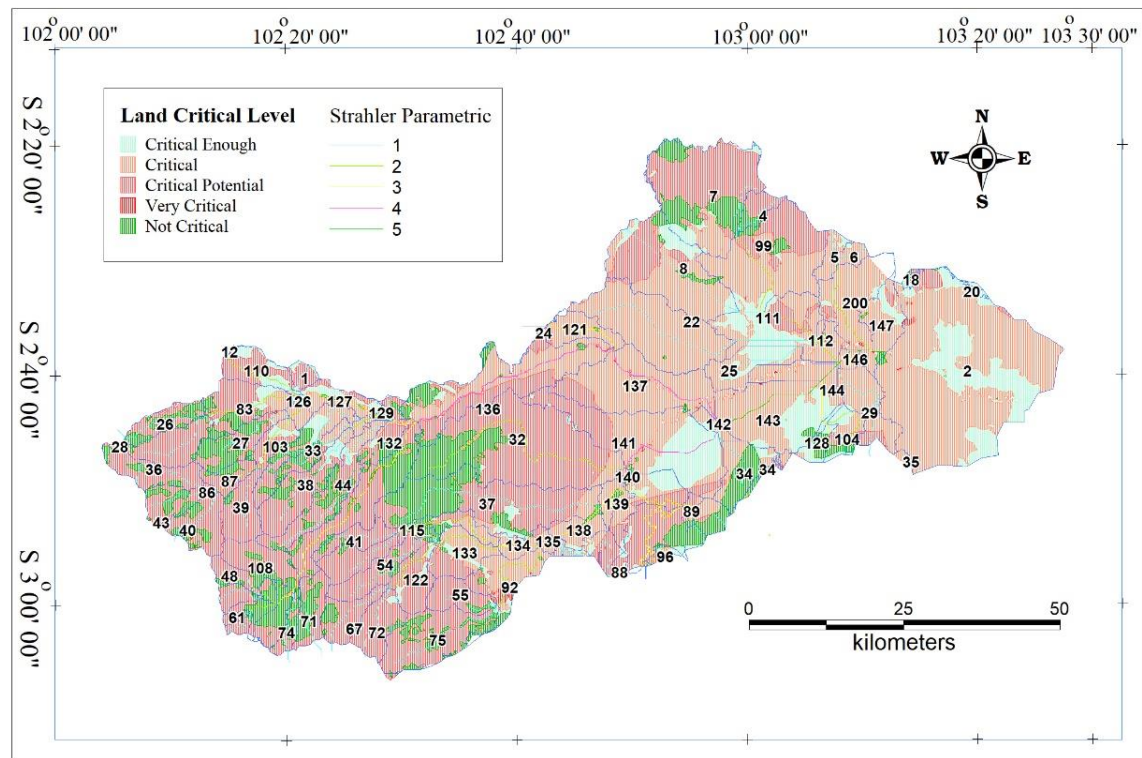
(2) Problems with the use of natural resources (destruction/burning of forests, shifting cultivation, grazing, illegal mining of uncontrolled gold ore), land clearing for land conversion for oil palm plantations, and so on.

(3) Problems with the final process or mechanism (erosion–high sedimentation, floods and droughts, water pollution or pollution, eutrophication, and so on.

(4) Socio-economic and population problems (illiteracy, underdevelopment, poverty, lack of trained or skilled workers, status or property rights to land, lack of facilities and infrastructure, and so on.

The four causes are interrelated. First, socioeconomic pressures and development

pressures can increase population pressure. The effect of population pressure can eventually increase the biophysical damage to the watershed (watershed criticality) due to an imbalance between population and land ownership (land carrying capacity has been exceeded). Third, departing from these problems, a new problem arises, which has become a common problem in Indonesia, namely the problem of spatial planning or land use resulting from land use that is not following the ability of the land. This fact or fact often hinders or becomes an obstacle in every arrangement of regional spatial planning because it involves various very complex problems. There is an overlap between status or property rights and community or development interests.



**Fig. 6** Morphometric condition and criticality level of Rawas watershed due to land use change

## 5. CONCLUSIONS

The main characteristics of critical land are bare, arid, and even appearing rocks on the ground surface.

The land's topography is generally hilly or steeply sloped [23]. Critical land is characterized by reeds vegetation that dominates it with the characteristics of grasslands having a relatively low soil pH of around 4.8-6.2. The largest area of critical land in the Rawas watershed area is dominated by Rawas Ulu and Muara Rupit sub-districts.

Classification is essential in areas with the allotment of Plantation and Production Forest space on a slope of 8% - 25%. Meanwhile, critical to moderately critical and potentially critical land are found in Rupit District on a hill of 8% - 25%. The land allocation in the area, based on the direction of the South Sumatra Province Spatial Plan (RTRWP), is for food crop agriculture, production forests, and plantations. The dominance of critical land in areas with slopes of 8% - 25% and >45% indicates that the erosion factor caused by high rainfall in the upstream region, and inappropriate land

management, is the leading cause of the discovery of many critical lands in the Rawas watershed.

## 6. ACKNOWLEDGMENTS

The authors are grateful to the Directorate of Research Technology and Community Service, Directorate General of Higher Education, Research and Technology, Ministry of Education, Culture, Research and Technology, the Republic of Indonesia, who has provided research funding through Doctoral Research grants based on No. SPPK : 142/E5/PG.02.00.PT/2022, Sriwijaya University College DIPA Date : November 17, 2021 with No. DIPA : SP DIPA-023.17.1.690523/2022. Acknowledgments are also given to the Doctoral Programs in Engineering, Faculty of Engineering, Sriwijaya University, for providing doctoral students with the performance of study activities in the Rawas sub-watershed area.

## 7. REFERENCES

- [1] C. O. Dumitru *et al.*, "Understanding satellite images: a data mining module for Sentinel images," *Big Earth Data*, vol. 00, no. 00, pp. 1–42, 2020.
- [2] L. Gigović, S. Drobnjak, and D. Pamučar, "The application of the hybrid GIS spatial multi-criteria decision analysis best–worst methodology for landslide susceptibility mapping," *ISPRS Int. J. Geo-Information*, vol. 8, no. 2, 2019.
- [3] G. Giuliani, B. Chatenoux, A. Benvenuti, P. Lacroix, M. Santoro, and P. Mazzetti, "Monitoring land degradation at the national level using satellite Earth Observation time-series data to support SDG15 – exploring the potential of the data cube," *Big Earth Data*, vol. 4, no. 1, pp. 3–22, 2020.
- [4] PBB, "Sustainable Development Goals," in *E-Handbook on SDG Indicator*, 2018, p. 15.
- [5] I. Chabay, *Land degradation, and restoration*. 2018.
- [6] M. Gonzalez-Roglich *et al.*, "Synergizing global tools to monitor progress towards land degradation neutrality: Trends.Earth and the World Overview of Conservation Approaches and Technologies sustainable land management database," *Environ. Sci. Policy*, vol. 93, no. November 2018, pp. 34–42, 2019.
- [7] Dinar DA Putranto, Yuono AL, Model Medan Digital untuk Pemodelan Rainfall-Runoff Analisis Sedimentasi secara Regional pada DAS Musi. South Sumatera Province, Indonesia: Lembaga Penelitian University of Sriwijaya, 2015.
- [8] N. C. Sims *et al.*, *Good Practice Guidance for Sustainable Development Goal (SDG) indicator 15.3.1*. 2021.
- [9] Putranto Dinar DA, Titis Pratami, "Assessment of Spatial Distribution of Land Based on Analysis of Slope and Water Conservation Programs", in *International Conference on sustainable agriculture (ICOSA)*, 2017, pp. 1–9.
- [10] A. L. Yuono, D. D. A. Putranto, and S. Tukirun, "Effect of land use changes of upstream Komerang subwatershed on declining water availability," *J. Ecol. Eng.*, vol. 21, no. 2, pp. 126–130, 2020.
- [11] P. Panagos *et al.*, "The new assessment of soil loss by water erosion in Europe," *Environ. Sci. Policy*, vol. 54, 2015.
- [12] N. Haregeweyn *et al.*, "Comprehensive assessment of soil erosion risk for better land use planning in river basins: A case study of the Upper Blue Nile River," *Sci. Total Environ.*, vol. 574, 2017.
- [13] F. Hu *et al.*, "Soil internal forces initiate aggregate breakdown and splash erosion," *Geoderma*, vol. 320, 2018.
- [14] M. Fernández-Raga *et al.*, "Splash erosion: A review with unanswered questions," *Earth-Science Reviews*, vol. 171. 2017.
- [15] N. Tayebzadeh Moghadam, K. C. Abbaspour, B. Malekmohammadi, M. Schirmer, and A. R. Yavari, "Spatiotemporal Modelling of Water Balance Components in Response to Climate and Landuse Changes in a Heterogeneous Mountainous Catchment," *Water Resour. Manag.*, vol. 35, no. 3, pp. 793–810, 2021.
- [16] P. K. Rai, P. Singh, V. N. Mishra, A. Singh, B. Sajan, and A. P. Shahi, "Geospatial approach for quantitative drainage morphometric analysis of Varuna river basin, India," *J. Landsc. Ecol. Republic*, vol. 12, no. 2, pp. 1–25, 2020.
- [17] A. Bharath, K. K. Kumar, R. Maddamsetty, M. Manjunatha, R. B. Tangadagi, and S. Preethi, "Drainage morphometry based sub-watershed prioritization of Kalinadi basin using geospatial technology," *Environ. Challenges*, vol. 5, no. June, p. 100277, 2021.
- [18] B. Niyazi, A. A. Khan, M. Masoud, A. Elfeki, J. Basahi, and S. Zaidi, "Morphological-hydrological relationships and the geomorphological instantaneous unit hydrograph of Makkah Al-Mukarramah watersheds," *Arab. J. Geosci.*, vol. 14, no. 9, p. 751, 2021.
- [19] H. Tansar, H.-F. Duan, and O. Mark, "Catchment-Scale and Local-Scale Based Evaluation of LID Effectiveness on Urban Drainage System Performance," *Water Resour. Manag.*, vol. 36, no. 2, pp. 507–526, 2022.
- [20] Y. Shinohara, K. Ichinose, M. Morimoto, T.

- Kubota, and K. Nanko, "Factors influencing the erosivity indices of raindrops in Japanese cypress plantations," *Catena*, vol. 171, 2018.
- [21] O. Articles, E. the L. F. for R. through I. S. L. P. of D. E. D. within A. Grid, R. D. Van Remortel, and R. S. & Supp, "Estimating the LS Factor for RUSLE through Iterative Slope Length Processing of Digital Elevation Data within ArcInfo GridNo Title," *Cartography*, vol. 30, no. 1, pp. 27–35, 2001.
- [22] C. Zheng and L. Jia, "Global canopy rainfall interception loss derived from satellite earth observations," *Ecohydrology*, vol. 13, no. 2, pp. 1–13, 2020.
- [23] W. Zhang, J. Zhou, G. Feng, D. C. Weindorf, G. Hu, and J. Sheng, "Characteristics of water erosion and conservation practice in arid regions of Central Asia: Xinjiang, China as an example," *Int. Soil Water Conserv. Res.*, vol. 3, no. 2, pp. 97–111, 2015.

# COPPER RECOVERY FROM WASTE WIRE HARNESS USING POTASSIUM HIDROXIDE

Koto Kagawa<sup>1</sup>, Takaaki Wajima<sup>2</sup>

<sup>1</sup>Graduate School of Science and Engineering, Chiba University, Japan

## ABSTRACT

This study aims to recover copper from waste wire harnesses by heating waste wire harnesses with potassium hydroxide (KOH) without releasing hydrogen chloride (HCl). Wire harnesses are mainly thin copper wires with diameter of a few mm coated with polyvinyl chloride (PVC). The demand of wire harnesses is increasing due to the development of electronic information equipment, such as home electric appliances, airplane, electric vehicles and so on, and the amount of waste wire harnesses will increase in future. Also, Japan relies on imports for 100% of its copper demand, and promotion of copper recycling is required. Therefore, copper recovery from waste wire harnesses is desired in Japan. Current copper recovery methods from waste wire harnesses include physical, chemical, and pyrolysis treatments, but these methods are difficult to apply thin wire harnesses, especially hydrogen chloride generated from PVC is a problem. In this study, waste wire harness was heated with KOH in an inert atmosphere to decompose PVC coating without releasing HCl by capturing with KOH, and copper cables were recovered. As a result, it was found that copper wire can be recovered by carbonizing PVC coating with KOH without releasing HCl gas, while it is difficult to recover copper wire by pyrolysis without KOH with releasing HCl gas.

*Keywords: Potassium Hydroxide, Wire Harness, Copper Recovery, PVC, Halogen Trap*

## INTRODUCTION

Wire harnesses are mainly thin copper wires of several hundred  $\mu\text{m}$  to several mm in diameter coated with polyvinyl chloride (PVC), and their use is increasing due to the shift to information technology. As a result, the amount of waste is expected to increase. In addition, since Japan relies on imports for 100% of its copper demand [1], copper recycling is required. Hence, recycling copper wire from wire harnesses has become an important issue in Japan.

Conventional treatments for waste wire harnesses can be roughly divided into three categories: physical, chemical, and pyrolysis treatment [2]. The physical treatment is mainly used to strip the coating, and the chemical treatment is mainly used to dissolve the coating in solvent, but the separated PVC coating and the large amount of leached liquid are problems. Thermal decomposition treatment is highly versatile, but the harmful hydrogen chloride gas was generated from the PVC coating.

Therefore, we focused on the recovery of copper wire from wire harnesses by heating with alkali hydroxide. In heating with alkali hydroxide, fuel gasification and carbonization of the PVC coating are accelerated, and the generated hydrogen chloride gas can be captured as alkali salt. The PVC coating is detached from the copper wire as fuel gas and carbonized powder, which enables effective utilization of the coated part as well as recovery of the copper fine wire.

In previous studies, by heating with wire

harnesses using sodium hydroxide (NaOH) as the alkali hydroxide under inert atmosphere, NaOH captures hydrogen chloride gas, increases gas production by accelerating the gasification of the PVC coating, and allows the effective separation of copper wire from the waste wire harness [3].

In this study, we attempted to recover copper wires by pyrolyzing the PVC coating of wire harnesses with potassium hydroxide (KOH), without releasing hydrogen chloride (HCl) gas.

## EXPERIMENT

### Sample

Waste wire harnesses provided by a domestic company were used in the experiment. Figure 1 shows the photo of the sample used and Table 1 shows their composition. It is noted that the diameter of this sample is 2 mm.



Figure 1 Photo of the sample

Table 1 The compositions of the sample

	Cu Wire	Covering					
		Cl	C	O	Al	Ca	Si
Content (wt.%)	40.5	5.1	38.9	11.3	0.7	2.7	0.6



### Experiment

The experiment was performed as follows (Figure 2, 3). 0 - 4 M KOH solution (5 mL) was placed in a reactor along with waste wire harness (3 g) and immersed in the solution. The reactor was heated up to 140 °C in 15 min and kept for 15 min to evaporate water to remain 0-20 mmol of KOH solid together with sample. Then, nitrogen gas was flowed into the reactor at 200 mL/min for 15 min to replace the inside of the reactor with nitrogen gas (Fig. 2). After the replacement, the flow rate of nitrogen gas was changed to 20 mL/min, and the temperature was raised to 500 °C in 45 min under a nitrogen atmosphere, followed by natural cooling for 30 min. Gases generated during heating were collected with 0.1 M NaOH solution (200 mL) for halogen gas by dissolving, and non-condensable gases ( $H_2$ ,  $CH_4$ ) were collected with a gas pack. The amount of halogen gas and non-condensable gas evolved was measured with a chlorine ion meter (CL-10Z, KRK) and gas chromatograph (GC-8A, Shimadzu), respectively, to be calculated. The residue after heating was removed from the reactor and stirred with 100 mL distilled water at 40 °C for 1 hour. After filtration and drying, the solid residue and copper wire were separated by sieving with a 2 mm hole diameter sieve. The filtrate was measured for chlorine concentration with a chlorine ion meter and pH with a pH meter (LAQUA, F-72)(Fig. 3).

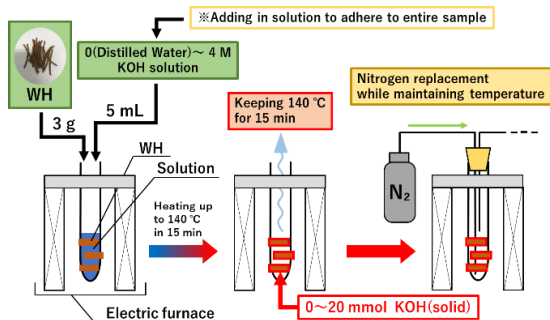


Figure 2 Coating treatment of potassium hydroxide for wire harnesses

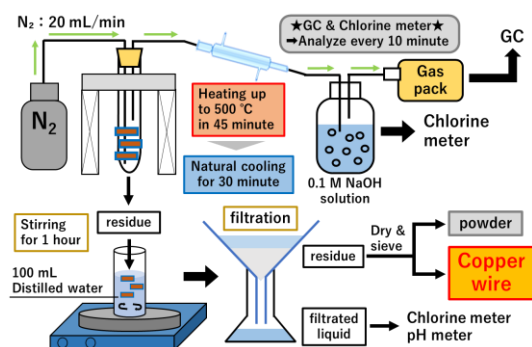


Figure 3 Experimental procedure for pyrolysis.

### RESULTS AND DISCUSSION

Figure 4 shows the amount of generated during heating with KOH of 0 - 20 mmol. Without KOH, hydrogen chloride gas was generated at around 300 °C. The amount of hydrogen chloride gas generated decreased with increasing KOH addition and was almost zero to 20 mmol.

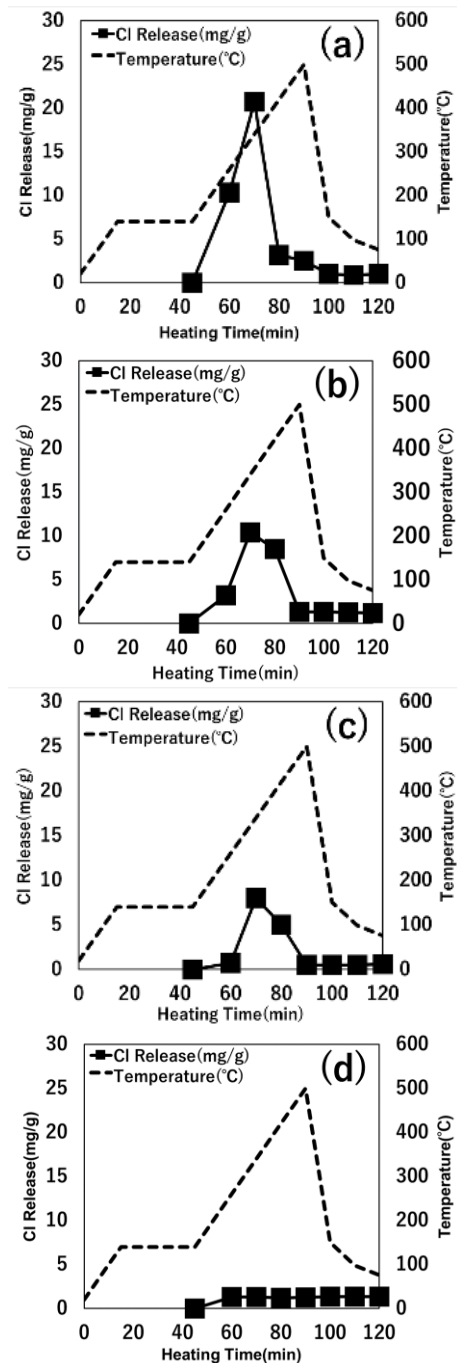


Figure 4 Hydrogen chloride gas generation during heating with KOH of (a) 0 mmol, (b) 5 mmol, (c) 10 mmol, and (d) 20 mmol



Figure 5 shows the amounts of hydrogen and methane generated during heating with KOH of 0 - 20 mmol. The amount of hydrogen and methane generated at around 500 °C. No significant change in the amount of hydrogen and methane was observed for the addition of 0 to 10 mmol, but the amount of hydrogen gas increased for the addition of 20 mmol. On the other hand, the amount of methane gas did not change significantly with increasing the amount of KOH added.

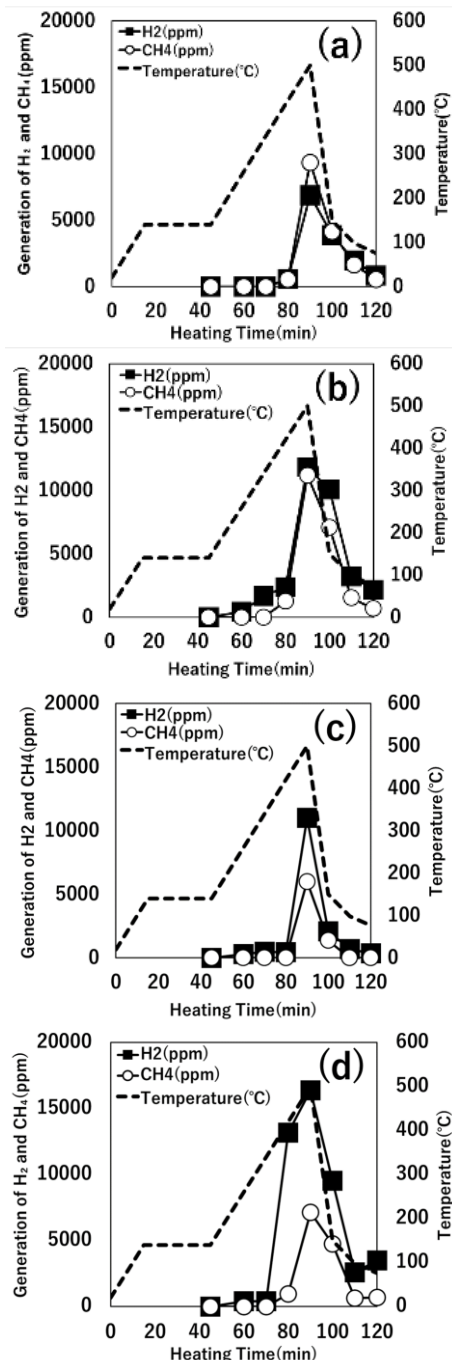


Figure 5 Amount of hydrogen and methane generated during heating with KOH of (a) 0 mmol, (b) 5 mmol, (c) 10 mmol, and (d) 20 mmol

Figure 6 shows the appearance of the residue after heating with KOH of 0 mmol and 20 mmol. Without KOH, the copper wire (indicated by red circles) was covered with black, fine-grained carbonized residue, while with 20 mmol KOH, a gray and dry residue covered the copper wire.

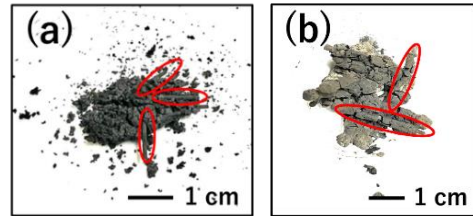


Figure 6 Residue after heating with KOH of (a) 0 mmol and (b) 20 mmol

Figure 7 shows the residue with 0 to 20 mmol KOH in distilled water after stirring for 10 minutes. The solution with residue without KOH addition was translucent because the residue was not completely dissolved, while the residue with KOH addition dissolved and the solution became black.

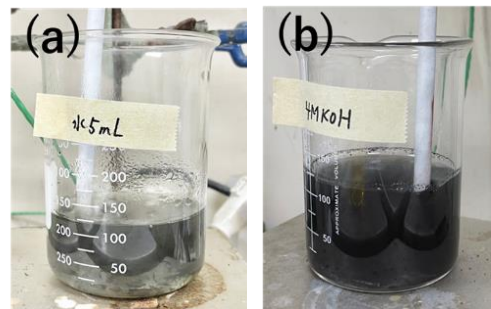


Figure 7 Residue in distilled water after stirring for 10 minutes with (a) 0 mmol and (b) 20 mmol KOH

Figure 8 shows the captured chlorine in the washing solution and pH of the solution obtained from washing the residue after pyrolysis. The amount of captured chlorine increased as the amount of KOH added increased. The pH did not change significantly (pH 8) until the addition of 10 mmol KOH residue, but increased to pH 10.5 with the addition of 20 mmol KOH. This is thought that 20 mmol KOH was reacted with HCl and the surplus unreacted KOH remained in the residue. It is noted that an increase in hydrogen generation was observed at 20 mmol (Fig. 4 (a)).

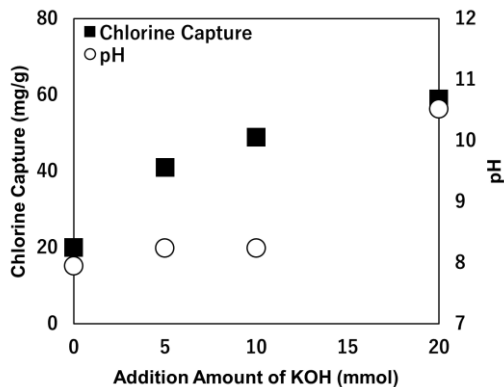


Figure 8 Captured chlorine and pH of filtrate at each addition amount.

Figure 9 shows the XRD pattern of the residue obtained by drying and sieving after stirring the residue obtained by pyrolysis with and without KOH. The residue obtained by 20 mmol KOH addition before washing showed the sylvite peak, while the XRD pattern after washing showed no sylvite (KCl) peaks, and the peaks of calcite ( $\text{CaCO}_3$ ) and corundum ( $\text{Al}_2\text{O}_3$ ) clearly appear. It is noted that the XRD pattern of the residue with and without KOH after washing are almost same. Potassium hydroxide captured hydrogen chloride gas to form potassium chloride, and the elution of potassium chloride occurred by stirring to appear the peaks of calcite and corundum.

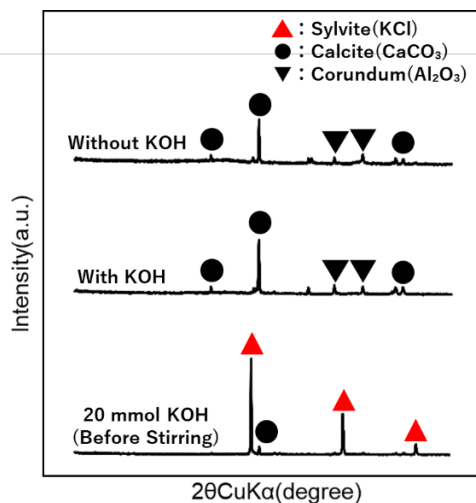


Figure 9 XRD pattern of the residue obtained by drying and sieving After stirring the residue obtained by pyrolysis with and without KOH.

Figure 10 shows the copper wire recovered from the residue with 0 and 20 mmol KOH by sieving after washing and drying. Without KOH addition, the recovered copper wire had a black surface without exfoliating the residue, while with KOH addition, the residue were exfoliated and the metallic luster of copper could be observed.

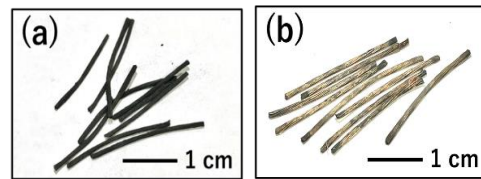


Figure 10 Copper wire recovered by sieving after drying of the residue with (a) 0 mmol, and (b) 20 mmol KOH

Figure 11 shows SEM images of the surface of the copper wire obtained by stirring, drying, and sieving the residue obtained from pyrolysis with and without KOH. The surface of the copper wire obtained with KOH addition had almost smooth without adhering the object, while that without KOH was covered with some objects.

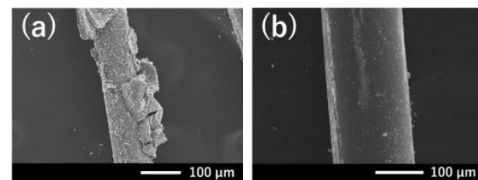


Figure 11 SEM images of the surface of copper wire obtained by drying and sieving : (a) 0 mmol, (b) 20 mmol

## CONCLUSIONS

In this study, we attempted to recycle PVC and recover copper wire while capturing hydrogen chloride by treating wire harnesses with potassium hydroxide coexistent heating.

The results showed that the addition of KOH improved the ability to capture hydrogen chloride gas, that the PVC gasified more efficiently, and that the separation of the copper wire from wire harness is more effectively using pyrolysis with KOH, compared to using pyrolysis without KOH.

These results suggested that thin copper wire can be recovered effectively using pyrolysis with KOH, without releasing HCl gas.

## REFERENCES

- [1] JOGMEC, Mineral Resources Material Flow 2020.
- [2] Li L., Liu G., Pan D., Wang W., Wu Y., Zuo T., Overview of the recycling technology for copper containing cables, Resources, Conservation and Recycling, Vol. 126, November 2017, pp. 132-140.
- [3] Wajima T, Pyrolysis Behavior of Polyvinyl Chloride with Sodium Hydroxide and Application to Copper Recovery from Multiwire Tinned Copper Cables, International Journal of the Society of Materials Engineering for Resources, Vol. 25, No.1, April 2022, pp. 70-77.

# INFLUENCE OF COMPOSITION ANALYSIS ON UNIT WEIGHT OF SYNTHETIC MUNICIPAL SOLID WASTE

Vidit Singh<sup>1</sup> and Prof.Taro Uchimura<sup>2</sup>

<sup>1,2</sup>Saitama University; Japan

## ABSTRACT

The Density of Municipal solid waste is a critical parameter in engineering analyses of landfills execution, design, and stability of landfills, but significant uncertainty as of now exists with respect to its value. By using synthetic municipal solid waste (SMSW) that replicates the typical composition of waste produced in India. To determine the relation between Maximum Dry Density (MDD) & Optimum Moisture Content (OMC) of fresh SMSW “Modified Proctor Test” has been performed. MSW is a very heterogeneous material, numerous efforts have been made in the past to generalize the density of MSW, but still, the effect of each material on the density is Obscure. In this paper, the variation in MDD & OMC has been provided depending on the varying percentage of each material (Paper, Plastic & Organic Content) present in it. As a result of regulations and shifting consumer habits, waste is continually changing. Engineers must therefore be mindful of the evolving mechanical characteristics of trash, and it's possible that prior findings may not be a reliable indicator of how waste will behave in the future. Therefore, Calculating the variation in unit weight can be useful in the design of engineered MSW landfills and also useful for future references.

*Keywords: Synthetic municipal solid waste, Density, Compaction, Maximum dry density, Optimum moisture content.*

## INTRODUCTION

The Municipal solid waste (MSW) landfills is an engineered geotechnical structure. The foundation's rainfall infiltration, leachate, and slope stability bearing capacity are some of the problems related to landfills. Therefore, based on the information available at the landfill site, a landfill design plan should be chosen based on the appropriate values of geotechnical Parameters of MSW such as density, shear strength, and permeability.

Specific guidelines on the likely range of MSW characteristics must be provided if the data are insufficient for analysis in order to evaluate the safety of MSW slopes and landfill design. The MSW exhibit a wide range of uncertainty related to unit weight depending upon the vulnerability related to the heterogeneity of waste, age of waste, different degrees of deterioration, filling method, construction practices, compaction method, and leachate levels [1]. Without taking into account, the variability in the geotechnical parameters, the design of the MSW landfill could result in stability or slope failure [18]. Even now, it is common practice to assess the stability of slopes using the little data that is currently accessible. Less reliability will be achieved by planning the landfill using the minimal information that is now available. The parameters density ( $\gamma$ ), cohesion ( $c$ ), and internal friction angle ( $\phi$ ) control the stability of an MSW landfill. Therefore, in this research paper efforts have been given to analyze the composition effect on the Unit Weight of MSW. Providing design parameters with a known range will

provide high-performance landfills with less possibility of failure [2], [3]. The rate of change could accelerate over the following years as many attempts are made to recycle and pretreat MSW using mechanical and biological methods. Additionally, it is anticipated that degradation changes a deposit's mechanical properties with time. Due to the heterogeneity of waste, it is impossible to fully characterize its engineering properties; however, it is crucial to understand basic behavior and to be aware of the likely ranges of the relevant engineering properties.

## UNIT WEIGHT

Laboratory results of MSW show the variation in Unit Weight of waste ranging from 8-10 kN/m<sup>3</sup> and 15 – 20 kN/m<sup>3</sup> for dry and degraded waste. Many of them have analyzed the effect of degradation on the unit weight of MSW [4], [5]. For fresh waste, the unit weight is mainly influenced by its composition calculated the unit weight of waste range from 3 - 18 kN/m<sup>3</sup> [6]. The unit weight of MSW landfills also varies with the depth performed test on bored samples which reported a range of 10 – 15 kN/m<sup>3</sup> [3].

It is quite surprising that there has been so little thorough research on unit weight because it is important information for landfill design. Due to the various waste types and dumping techniques, unit weight varies greatly. Common challenges in determining MSW unit weight include clearly separating out the contribution of daily soil cover, determining how unit weight changes over time and

with depth and assuming that the most of reported values correspond to waste that is close to the surface [6].

### Material Description

MSW is a collection of waste largely from household and commercial sources. The two primary categories of MSW are organic waste and inorganic garbage. Food trash, paper, garden waste, soil, and textiles are examples of organic waste, while plastic, metals, rubber, and glass are examples of inorganic waste. The content of waste varies greatly depending on the source of waste formation. The MSW has a vast array of particle sizes, from little soil fragments to large building stones. These materials' composition varies from location to location, site to site, and even from country to country.

It is necessary to have a classification system to characterize component qualities in both their initial state, or as they are brought to a landfill, and in any altered states. Due to physical forces including compaction, overburden, and degradation over time, dumping waste in a landfill alters component qualities like size and shape. Materials utilized in this investigation have been classified according to Dixon and Langer's proposed scheme from 2004 [7].

### Waste Mechanism

The current awareness of MSW/Waste behavior is relatively incomplete. Engineers and scholars have relied on the mechanics of soil for waste disposal [7]. Although this has been beneficial to some level, using soil behavior and designing the engineered landfill structure is not the best course of action. The landfill was designed using the principles of soil theory, and changes in the geotechnical properties of waste due to degradation over time haven't been considered much often, as well as since the lateral pressure of MSW hasn't been completely predicted the pressure analysis of MSW is also based on the principles of soil theory. Used for vertical extension of the landfill using retaining walls. The soil homogenous pressure hypothesis is highly challenging to apply because of the heterogeneity related to MSW.

Instead, MSW landfills should be designed using waste geotechnical properties and also considering the change in properties with respect to time in mind. While analyzing the similarities and differences of MSW with other soil materials will offer assistance to us to create and understand the engineering properties of MSW. It is always preferable to conduct tests on original materials in undisturbed conditions [8]. But it is not always possible to obtain the material in an undisturbed state and conduct the laboratory test on a real sample. Additionally, it can be challenging to generalize waste behavior due to the great variance in the sample.

### Factors Affecting Unit Weight of MSW

The unit weight of MSW changes due to numerous reasons a few of them are compaction effort, layer depth, layer thickness, and overburden pressure [9]. In contrast to soils, there are multiple materials present, and the state and level of deterioration affect the unit weight. According to this theory, the fresh waste density mostly depends on the waste composition, however, when the waste ages (degrades), the unit weight primarily depends on depth. It is extremely common to deposit the waste in the layer thickness of 2 to 3 m, which accomplishes moderate compaction and results in low poor density. The layer thickness is 0.5 - 1.0 m, which will achieve good compaction and therefore it exhibits high unit weight [4]. Depending on the level of compaction attained, a statistical analysis of the data is displayed in Table 1.

Table 1 Bulk unit weight of MSW for fresh waste [6]

Items (kN/m <sup>3</sup> )	Good Compaction	Moderate Compaction	Poor Compaction
Range	8.8-10.5	5.0-7.8	3-9
Average	9.6	7.0	5.3
Standard Deviation	0.8	0.5	2.5
COV (%)	8	8	48

### PURPOSE AND SCOPE OF THE CURRENT STUDY

The assessment of the literature demonstrates unequivocally that there is confusion surrounding the unit weight of MSW because of its heterogeneity, which demands a systematic investigation. It is currently unclear how the composition will affect the MSW unit weight. There have been numerous investigations into the engineering characteristics of MSW (Fassett et al., 1994; Dixon and Jones, 2005; Reddy et al., 2009); however, there have been few investigations into the effects of waste type (synthetic and natural), age, and waste material (fibrous, organic, and inorganic) on the shear strength behavior of MSW [9].

The current study suggested calculating the impact of paper, plastic, and organic material on the unit weight behavior of MSW. The magnitude of MSW unit weight is very heterogeneous based on the content of waste but the behavior with respect to the change in the composition will follow a trend. Calculating the influence of material composition on the unit weight of MSW will help us create a

generalized range of values of the unit weight and help us in further analysis and design of MSW landfills.

## MATERIAL CHARACTERIZATION AND METHODOLOGY

In total, nine distinct compositions of synthetic municipal solid waste were created in the lab. By doing a waste composition analysis on a sample taken from the Jawahar Nagar Landfill, Hyderabad India, it was possible to determine a reference classification for "typical" MSW. To choose synthetic waste elements that can mimic those found in MSW, this reference MSW has been employed. Following the construction of several synthetic wastes with a variety of categories (see Fig. 1) using these synthetic components, the relationship between classification and mechanical behavior was evaluated. Except for the components that represented the organic substance described below in Table 2. The composition of MSW is varied in such a way that it comprises the maximum range of each material. Ten different materials were used to make the Synthetic waste (Kitchen waste, paper, plastic metal, sand, cardboard, metals, textile, wood shaving, peat moss, and medium-grained soil) [10], [11].

The % of each material of the constituted synthetic waste sample obtained from landfill is presented below in Table 2. All the % of each test are also shown in Table 3, Table 4, and Table 5, which represent Paper, Plastic and Organic matter. To determine how various materials will affect the unit weight of MSW by considering various compositions. The ASTM D1557-91 Proctor test method has particle-size limitations. Thus, the synthetic MSW samples were produced according to particle-size limitations in the laboratory as shown in Table 2 below [12].

Table 2 Composition of Jawahar Nagar Dumping Yard, Hyderabad India

Material	Fraction %	Size (mm)
Sample	SW-1	
Metal	5.10	< 40
Paper	21.20	15 – 200
Yard- Trimming	2	50 - 100
Cardboard	4.10	50 - 100
Wood	6	10 - 150
Textile	3.65	10 - 100
Plastic	15.10	10 - 150
Sand	9	< 4.75 u
Peat moss	30	40 – 120
Soil	4	> 4.75 u
Total	100	

However, there are too many combinations of material and component sizes to realistically represent each with a synthetic alternative. Therefore, the component fractions had to be minimized in order to get a simpler but still representative synthetic waste. The sample of each composition has been made in Lab and testing. Components such as beverage cans, rigid and flexible plastic packaging paper/cardboard

Table 3 Composition used by keeping paper constant

Sample	SW-2	SW-3
Metal	6.34	4.13
Paper	10	30
Yard- Trimming	4.84	2.63
Cardboard	16.34	14.13
Wood	7.24	5.03
Textile	3.24	1.03
Plastic	5.24	3.03
Sand	10.24	8.03
Peat moss	31.24	29.03
Soil	5.24	3.03

Table 4 Composition used by keeping plastic constant

Sample	SW-4	SW-5	SW-6
Metal	5.67	4	3.45
Paper	21.77	20.10	19.55
Yard- Trimming	2.57	0.90	0.35
Cardboard	4.67	3.0	2.45
Wood	6.57	4.90	4.35
Textile	4.22	2.55	2.0
Plastic	10	25	35
Sand	9.57	7.90	7.35
Peat Moss	30.57	28.90	28.35
Soil	4.57	2.90	2.35

Table 5 Composition used by keeping Organic Matter Constant

Sample	SW-7	SW-8	SW-9
Metal	6.77	3.43	2.32
Paper	22.87	19.53	18.22
Yard- Trimming	3.67	0.33	0
Cardboard	5.67	2.33	1.22
Wood	7.67	4.33	3.12
Textile	5.27	1.93	0.82
Plastic	16.77	13.43	12.2
Sand	10.67	7.55	6.12
Peat Moss	15	45	55
Soil	5.64	2.33	1.18



and textiles can be employed provided that they are in an unsoiled state [13]. The maximum size of each material has been taken from the literature review, and each particle has been cut by hand using the cutting machine to keep the particle size in the given range. Mineral material was represented by sand, gravel, and soil. Synthetic waste components were selected based on consideration of both shape and size Table 2. Fig. 1 shows the different components used in this experiment. Each material has been cut and weighted in a particular fraction to simulate the waste composition as shown in Fig.1.



Fig. 1 Sample preparation of SMSW

From above Table 3, the composition of paper has been fixed for each sample (i.e., SW-2= Paper 10% and SW-3= paper 30%) and all the other material fractions have been calculated depending on the fixed fraction of paper. A similar, process was followed for calculating the composition fractions of plastic and organic matter as can be seen in Table 4 and Table 5. Some previous studies have also studied the engineering properties of MSW using SMSW. Table 4 shows the composition of SMSW used to find the influence of composition on Unit weight by a varying paper by 10%, 21.20%, and 30%. For Plastic the composition varies from 10%, 15%, 25%, and 35%. For Organic content, the composition varies from 15%, 30%, 45%, and 55%. By utilizing the above-mentioned composition, we have tried to analyze the unit weight of MSW by doing the standard proctor test as shown in Fig.2 and Fig.3.

The SMSW is filled in three layers inside the mold and each layer has been compacted with 25 blows from a constant height of 18 in. The water has been added in a range from 15% to 90% for every test. The testing mold dimensions are 15 cm inner diameter and

17.5 cm in height. The drop hammer used has a weight of 2.5 kg and a constant drop height of 45 cm as shown in Fig.2. Fig.3 shows the weighing of the sample after every compaction of testing material.



Fig. 2 Proctor Test Apparatus



Fig. 3 Sample weighing after Compaction

## RESULTS & DISCUSSION

The Unit weight of SMSW in each sample differs very much therefore it helped us in creating a range of values depending upon the material present on it. This laboratory-produced SMSW mix fraction was chosen to resemble the typical MSW composition of India. The maximum particle size tested in this investigation is 20 cm, and the average specific gravity was reported to be 1.52. One of the primary causes of a variation between MDD values is thought to be a difference in the maximum particle size [14]. As a result, this analysis takes into account the maximum size and composition of each material. The compaction curve for SMSW produced from the



conventional proctor test resembles the compaction curve for soils in general shape.

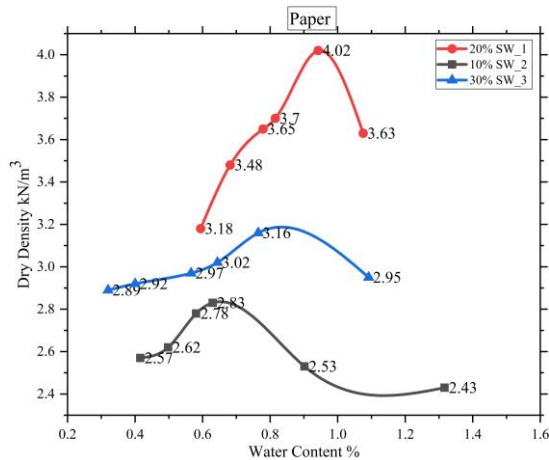


Fig. 4 Dry Density vs Water content for Paper

The dry unit weight of SMSW increased as the water content increased to its maximum and then began to drop as the water content increased further. Similar to soils, the additional increase in water solid content per unit volume was contributing to lubrication, which led to a denser arrangement of particles. Additionally, as the water content rises, solid materials become softer, which enhances deformation, compressibility, and rebound in response to compaction [1]. “However, compared to soils, waste does not show a significant decrease in dry unit weight at high moisture content, because the relative difference between the unit weight of “waste” and “solid” is lower for waste than for soils” [1].

The effect of increasing paper % on the unit weight of SMSW is in the range of 2.83 kN/m³ for 10%, 4.01 kN/m³ for 20%, and 3.162 kN/m³ for 30%. As for the paper, % increases the density increases reached its maximum and then started to decrease with the increase in paper %. With the inclusion of paper, the SMSW mix behaves denser than other mix proportions, unit weight tends to increase from 10 – 20 % from 2.83 to 4.01. Larger and lighter particle sizes make materials more compressible. Components deform at relatively low vertical stresses, with component rearrangement behavior predominating.

Similarly for Plastic, the % increases for the first two cases of unit weight, and with a further increase in % of plastic, the MDD tends to decrease. Plastic takes more volume compared to other materials in such as paper, metal, etc. Low unit weight is again caused by the inclusion of light and highly compressible material components deformed from the starting of the stress application while compacting. Plastic shows higher nature of compressibility and the SMSW mix with more plastic % tends easier to slip, therefore in the landfill if there

is more % of plastic than 15 – 20 % it will be more prone to slope failure.

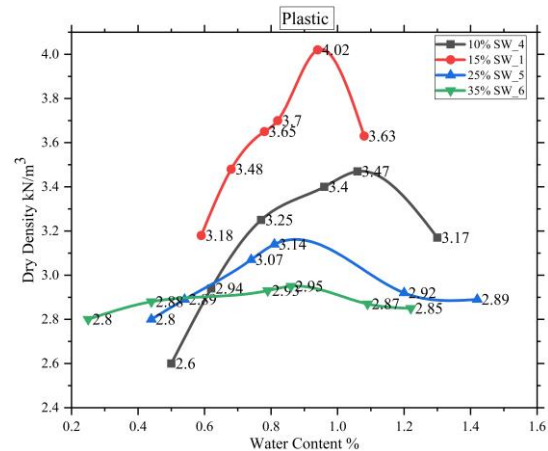


Fig. 5 Dry Density vs Water content for Plastic

For organic content, the effect on unit weight is calculated as follows 3.30 kN/m³ for 15% peat moss, 4.01 kN/m³ for 30%, 4.18 kN/m³ for 40%, and 3.28 kN/m³ for 50%. Similarly for plastic content 3.47 kN/m³ for 10%, 4.01 kN/m³ for 15%, 3.14 kN/m³ for 25%, and 2.95 kN/m³ for 35%. As can be seen above Fig. 6 shows the influence of material on the unit weight of SMSW for organic content, as the organic content increases the MDD also increases first three tests but with a further increase in % of organic matter the MDD decreases. The reason for this behavior is as organic material is very compressible and also it can break easily while compacting, due to the presence of water it tends to stick to other materials. Leading to greater interlocking of materials.

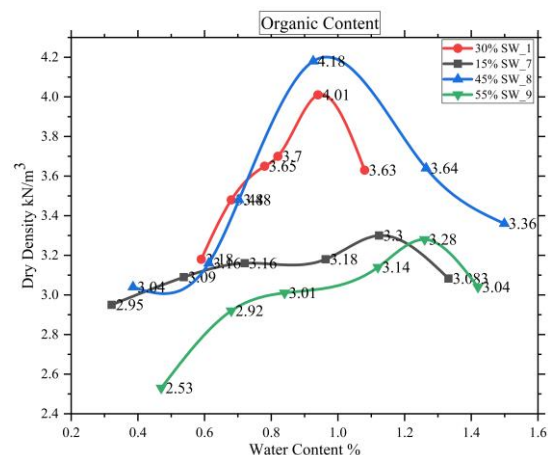


Fig. 6 Dry Density vs Water content for Peat Moss

A denser packing arrangement was achieved by increasing the solid content per unit volume, which assisted in lubricating the particles from the addition of water. Therefore, it exhibits less volume which

results in an increase in MDD reaching its peak at a certain point i.e., 30 – 35% of organic matter. Despite the difference in moisture content and overburden pressure between synthetic waste and real waste, it has been shown that SMSW used in this study has shown magnitude and trends that are comparable to real waste. The MSW is a heterogeneous material it also shows wide variation in magnitude, but the trends followed by the MSW are quite similar.

## CONCLUSION

This article presents the unit weight characteristics of SMSW of Hyderabad India. There are several failures of landfills happening around the world which have also caused loss of lives. Therefore, much more effort has to be given to analyze the MSW properties more efficiently and also to design the landfill in a more efficient way by utilizing the more elaborated waste properties. The relatively low unit weight of synthetic municipal solid waste is the result of the use of light components and minimal placement compaction forces. From the literature, it has been demonstrated that for the same landfill waste at field capacity, the dry unit weight of SMSW on the order of 2–4 kN/m<sup>3</sup> is equivalent to the bulk unit weight of 6–9 kN/m<sup>3</sup>. The following conclusions can be drawn from the present study:

- When the composition of the synthetic waste varies there are significant changes in the unit weight of the testing samples.
- When paper percent is increased from 10 to 20 %, the maximum dry density increases by 41.7 %, and when it is increased from 20 to 30 %, it lowers by 21.2 %.

For SW-1, SW-2, and SW-3

Paper %	10	20	30
MDD	2.83	4.01	3.16
OMC	0.62	0.92	0.76

- The maximum dry density increased by 15.56 % when the plastic percentage was increased from 10 to 15 %; from 15 to 25 %, it decreased by 22.69 %; and from 25 to 35 %, it decreased by 6.45 %.

For SW-4, SW-1, SW-5, and SW-6

Plastic %	10	15	25	35
MDD	3.47	4.01	3.1	2.9
OMC	1.05	0.92	0.80	0.85

The reason for this kind of density variation for paper and plastic is mainly due to the compressible nature of the material. The material tends to soften when water is added, which makes for a dense arrangement and also reduced the compaction rebound.

- The maximum dry density when Organic content % is increased 15 to 30% increased by 21.52% with further increase 30 to 45% increased by 4.24% and from 45 to 55% it decreased by 24.16% respectively.

For SW-1, SW-7, SW-8, and SW-9

Organic %	15	30	45	55
MDD	3.30	4.01	4.18	3.17
OMC	1.01	0.92	0.93	1.10

Nearly every step of landfill design and analysis uses knowledge of the unit weight of waste. In the beginning, factors such as waste composition, age, cover system, degree of compaction, and biodegradation have a greater impact on the unit weight of garbage. After a certain time, the landfill's depth primarily influences the unit weight. From the above discussion, it is clear that the effect of each individual material on MSW is very prominent and doing this composition analysis on fresh SMSW has provided us with a definite range of unit weight corresponding to the change in the composition of materials. The findings of this study showed that waste unit weight substantially relies on the composition of waste, hence a site-specific assessment is advised [15].

## ACKNOWLEDGMENTS

The author would like to acknowledge the contribution of Prof. Taro Uchimura Sensei, for his guidance. Additionally, I want to express my gratitude to JICA for giving me the opportunity to study in Japan and also providing a research grant to continue my research. The Department of Civil and Environmental Engineering at Saitama University in Japan provided the lab equipment for this study.

## REFERENCES

- [1] Oluwapelumi O. Ojuri and Peter K. Adegoke., Geotechnical characteristics of synthetic municipal solid waste for effective landfill design, *Int.J. of GEOMATE* Vol. 9, No. 1, 2015, pp. 1418-1427.
- [2] Hasan First pulat and Yeliz yukselen Aksoy., Factors affecting the shear strength behavior of municipal solid waste., *Waste Management*, Vol. 69, 2017, pp. 215-224.
- [3] Hossain M.Z. and Awal A.S.M.A., Experimental Validation of a Theoretical Model for Flexural Modulus of Elasticity of Thin Cement Composite, *Const. Build. Mat.*, Vol.25, No.3, 2011, pp.1460-1465.
- [4] Neil Dixon, and D. Russell V. Jones., Engineering properties of municipal solid waste, *Geotextiles & geomembranes*, Vol. 25, 2005, pp.

- 205-233.
- [5] Dixon N, Langer U, and Gotteland P., Classification and mechanical behavior relationships for municipal solid waste study using synthetic waste, *Journal Geotechnical Geo-Environmental Engineering*, ASCE, Vol. 134, 2008, pp. 79-90.
  - [6] Fassett J.B., Leonards, G.A Repetto, P.C., Geotechnical properties of municipal solid waste and their uses in landfill design, *Waste Technology*, 1994, pp. 1-31.
  - [7] Dixon N, Ng'ambi S, and Jones DRV., Structural performance of a steep slope landfill lining system, *Proceedings of the Institution of Civil Engineers Geotechnical Engineering*, Vol. 157, 2004, pp. 115–125.
  - [8] Langer U., Shear and compression behavior of undegraded municipal solid waste, Dissertation, Doctor of Philosophy, Loughborough University, 2005.
  - [9] Kavazanjian E., Mechanical properties of municipal solid waste., *Proceedings Sardinia, Eighth International Waste Management and Landfill Symposium*, Cagliari, Italy, Vol. 3, 2001, pp.415–424.
  - [10] Christopher A. Bareither, craig h. Benson and Tuncer B. Edil., Effect of waste composition and decomposition on shear strength of Municipal solid waste, *Journal of geotechnical and Geo-Environmental Engineering*, Vol. 138, No. 10, 2012, pp. 1161-1174.
  - [11] Hsin-yu and Tsuo-hsien Fan., In Situ test and slope stability analysis of municipal solid waste landfills, *Int.Symp. on Geoenvironmental Eng*, 2009, pp. 8-18.
  - [12] US.EPA., Municipal solid waste generation, recycling, and disposal in the United States, Facts and figures for 2006., <http://www.epa.gov/osw/nonhaz/municipal/pubs/msw06.pdf>, April 20, 2008.
  - [13] Manassero M, Van Impe WF, Bouazza A., Waste disposal and containment, *Proceedings Second International Congress on Environmental Geotechnics*”, Osaka, Vol. 3, 1996, pp.193–242.
  - [14] Krishna R. Reddy, Hiroshan Hettiarachchi, janardhanan Gangathulasi, Jean E. Bogner and Thomas lagier., Geotechnical properties of synthetic municipal solid waste, *International Journal of geotechnical Engineering* Vol.3, 2009, pp.429-438.
  - [15] Hisham T. Eid, Timothy D. Stark, W.Douglas Evans, and Paul E. Sherry., Municipal solid waste slope failure, *Journal of geotechnical and geo-environmental Engineering*, Vol. 126, No. 5, 2000, pp. 164.

# SPATIAL STATISTICS AND PERCOLATION PROBABILITY OF PORE-NETWORK IN POROUS MEDIA WITH AGGREGATE STRUCTURE

Junichiro Takeuchi<sup>1</sup>, Yu Song<sup>1</sup>, Yuto Takeuchi<sup>1</sup> and Masayuki Fujihara<sup>1</sup>

<sup>1</sup>Graduate School of Agriculture, Kyoto University, Japan

## ABSTRACT

Soil aggregates are clumps of relatively small soil particles bound each other by organic matter. Soil with aggregate structure possesses relatively large pores around the soil clumps, and it possesses relatively small pores in the clumps. This spatial arrangement of pores enables soil with aggregates to have a contradictory feature such as well drained but high water-retention. In this study, spatial autocorrelation of porous media with aggregates is evaluated with the global Moran's index, and the percolation probability, which shows the connectivity of a network, is also investigated. To compare those properties of porous media without aggregates, virtual porous media models with and without aggregates were generated from spherical grains variously sized by the discrete element method. The global Moran's index of porous media with aggregates showed around 0.36, which is more than double value of porous media without aggregates. This relatively high global Moran's index shows that porous media with aggregates have pore clusters formed by large and/or small pores, and the pore clusters by small pores get the media to retain water. Furthermore, it was shown that from the percolation threshold in porous media with aggregates is around 0.15, while those in porous media without aggregates are around 0.35. This quite small percolation probability threshold of porous media with aggregates asserts the existence of a sub-network formed by relatively large pores in the pore-network and this sub-network enables high drainability. Through the analyses of the spatial autocorrelation and the percolation probability, the properties of porous media with aggregates were shown quantitatively, and it leads to better understanding of soil features.

*Keywords: Soil aggregates, Spatial autocorrelation, Percolation probability, Water retention curve*

## INTRODUCTION

Soil aggregates play a critical role in growing plants, and those serve air and retained water with nutrients to roots. Such functionality and stability of soil aggregates have been studied so far [1], [2]. Recently, microscale 3D structure of soil aggregates is elucidated by microtomography. Peth et al. [3] investigated 3D structure of soil aggregates from different fields by synchrotron-radiation-based x-ray microtomography, and statistical properties are analyzed of the extracted pore-networks. Song et al. [4] investigated nanoscopic 3D structure of claystones and estimated permeability based on the Katz-Thompson equation. Jarvis et al. [5] evaluated connectivity or percolation probability, which is one of network properties in the percolation theory, of silt loam soil from 3D images by x-ray tomography. As discussed in [11], it is essential to investigate connectivity of pore-networks for elucidation of the constitutive relations of porous media such as the pressure-saturation curves, the hydraulic conductivity, air-permeability, and the air- and water-entry pressures.

In this study, properties of porous media with aggregates are investigated quantitatively from a point of view of a network in addition to spatial autocorrelation of pore arrangement in porous media.

Here, virtual porous media are generated, and pore-networks are extracted based on the watershed segmentation algorithm.

## POROUS MEDIA MODEL

Various virtual porous media are generated by using the discrete element method (DEM). In this study, three types of porous media are made: single particle size, uniform distribution of particle size, and aggregates. Here, these are referred to SIN, UNI, and AGG, respectively. The first and second media are made by packing particles with single size or various size randomly, and these do not have aggregate structure. The third one is made by packing aggregates of particles with single size, which are prepared according to the JKR (Johnson-Kendall-Roberts) model [6].

Pore-network models are extracted from each virtual porous medium based on the watershed segmentation algorithm, which separates voids in porous media into many parts like watersheds from 3D image of porous media [7]. In this study, the SNOW algorithm proposed by [8] is used to extract pore-networks. A pore-network consists of PBs (pore bodies) and PTs (pore throats). PBs are relatively large pores and PTs are relatively small pores that connect two PBs. Properties of PBs and PTs such as

volume, equivalent and inscribed diameters, coordinate, and length are obtained by the SNOW algorithm.

To ensure the REV (representative element volume) of porous media and the quality of pore-networks, the size of the container that packs particles (or the number of particles) and the resolution of the virtual porous media were examined in the previous study [9]. Pores at outer edge tend to be irregular because of a wall and especially pores in the top of media could be very large because a lid is not considered when particles are packed. To remove such irregular pores, about 30% of marginal pores are truncated from the extracted pore-networks. The inside pore-networks are used for the following analyses.

## ANALYSES

### Spatial Statistics

The spatial distribution of pores in porous media is analyzed by the spatial autocorrelation. Moran's  $I$  statistic is one of the statistical indexes that examine spatial autocorrelation of a certain property distributed spatially [10]. Here, pore size (PB's diameter) is a target, and it is examined if clusters of large and/or small pores exist in porous media.

The global Moran's  $I$  statistic shows the average level of spatial autocorrelation over the whole pore-network, and its value takes from -1 to 1.  $I$  is zero when pores distribute randomly,  $I$  is positive when some clusters exist, and  $I$  is negative when large and small pores distribute alternately.  $I$  is defined as follows.

$$I = \frac{\sum_{i=1}^n \sum_{j=1}^n w_{ij}(x_i - \bar{x})(x_j - \bar{x})}{m_2 S_0} \quad (1)$$

where  $n$  is the number of PBs,  $x_i$  is the attribute value (PB's diameter) of the  $i$ -th PB,  $\bar{x}$  is the average of  $x$ ,  $w_{ij}$  is the weight between  $i$ -th and  $j$ -th PBs. In this study,  $w_{ij} = 1$  when  $i$ -th and  $j$ -th PBs are adjacent, and  $w_{ij} = 0$  otherwise.  $m_2$  and  $S_0$  are defined as follows.

$$m_2 = \frac{1}{n} \sum_{i=1}^n (x_i - \bar{x})^2 \quad (2)$$

$$S_0 = \sum_{i=1}^n \sum_{j=1}^n w_{ij} \quad (3)$$

The statistical significance of the obtained Moran's  $I$  value is tested by the randomization test under the null hypothesis that there is no spatial

autocorrelation, where the obtained Moran's  $I$  value is compared with those of pore-networks whose attribute values are shuffled randomly [10].

### Percolation Probability

Percolation probability is an index of the connectivity of a network, and it shows how many elements of a network is open, how big 'open' clusters are formed in the network [11]. In this study, elements are pores (PTs and PBs) in a pore-network, and an 'open' element means that the target pore can be invaded by air if water-air interface reaches the pore satisfying the conditions described in the subsection of invasion percolation. Hence, it is determined whether a pore is open or not by comparing the capillary pressure and the air-entry pressure of the pore. Here the index is referred as invadability, and the invadability  $\alpha$  of each pore is calculated assuming the air-water interface reaches the target pore satisfying the condition.

$$\alpha = P_C - P_{AE} \quad (4)$$

where  $P_C$  is the capillary pressure,  $P_{AE}$  is the pore-air-entry pressure, and those are calculated as follows.

$$P_C = P_{air} - P_{water} \quad (5)$$

$$P_{water} = P_{btm} - \rho g \Delta z \quad (6)$$

$$P_{AE} = \rho g L \sigma \cos \theta / A \quad (7)$$

where  $P_{air}$  is the air pressure,  $P_{water}$  is the water pressure,  $P_{btm}$  is the pressure at the bottom of the pore-network,  $\rho$  and  $\sigma$  is the density and surface tension of water,  $g$  is the gravitational acceleration,  $L$  and  $A$  are the circumference and cross-section area of the pore,  $\theta$  is the contact angle, and  $\Delta z$  is the difference of the vertical coordinates between the pore and the bottom.

If  $\alpha$  is positive, the pore is 'open' or invadable. Otherwise, if  $\alpha$  is negative, the pore is not 'open' or uninadable. As the proportion of open pores increases by decreasing the water pressure imposed to the bottom in a case of the drainage process, open clusters also become large. As the open clusters grow, those begin to connect each other, and eventually one large open cluster is formed. The percolation probability of a finite network is evaluated by the percentage of pores in the maximum open cluster to the pores in the whole pore-network.

### Invaded Percolation Probability

The above two indexes, Moran's  $I$  and percolation probability, are static ones for a network

itself. In addition to the two indexes, water retention characteristics and invaded percolation probability, which were proposed by [12], are used to evaluate the property of porous media. The former is a conventional one that has been used to know the relation between the imposed water pressure and retained water in the medium. The latter also measures the relation between pressure and retained water, but it evaluates the relation in terms of probability in the same way with percolation probability. For a finite pore-network, the invaded percolation probability is evaluated by the percentage of pores that are invaded by air to the pores in the whole pore-network.

### Invasion Percolation

To simulate a drainage process, invasion percolation is employed. In the process, invading fluid invades into pores filled with invaded fluid if the invadability defined in Eq. (4) of the pores is positive. To ensure the physical process of drainage, the continuity rule for invading and invaded fluids needs to be satisfied when invading fluid invades into pores filled with invaded fluid. That is, the fluids on both sides on an interface that can shift need to connect to each other pool through other pores filled with the same type of fluid.

In the original invasion percolation [13], only one pore whose invadability is maximum among candidate pores, whose invadability is positive and satisfying the continuity rule, in one step. Takeuchi et al. (2018) showed that various invading regimes can be simulated by changing the number of invading pores in one step [12].

## RESULTS AND DISCUSSIONS

Three types of virtual porous media, SIN, UNI, AGG, are made by DEM, and each type has three samples to check fluctuation in properties. A sample of each type and extracted pore-networks after truncation of outer pores are shown in Fig. 1. Table 1 shows the parameters of the porous media and extracted pore-networks. Figure 2 shows the distributions of the coordinate number, which is the number of PTs that one PB connects with, of pore-networks and inscribed radius of PBs and PTs. Almost same distributions among three samples in each virtual porous media shows the volume employed in this study is enough for REV. There are no major differences in the distributions of the coordinate number among the virtual porous media.

Table 1 Parameters of porous media and extracted pore-networks

Items	SIN	UNI	AGG
Diameter (mm)	0.2	0.1-0.5	0.2
Mean num. of particles	3612	3318	2515
Num. of particles in one aggregate	-	-	120
Edge length of container bottom (mm×mm)	2.9×2.9	3.2×3.2	3.0×3.0
Mean num. of PBs	22122	17174	14951
Mean num. of PTs	6799	5510	4794

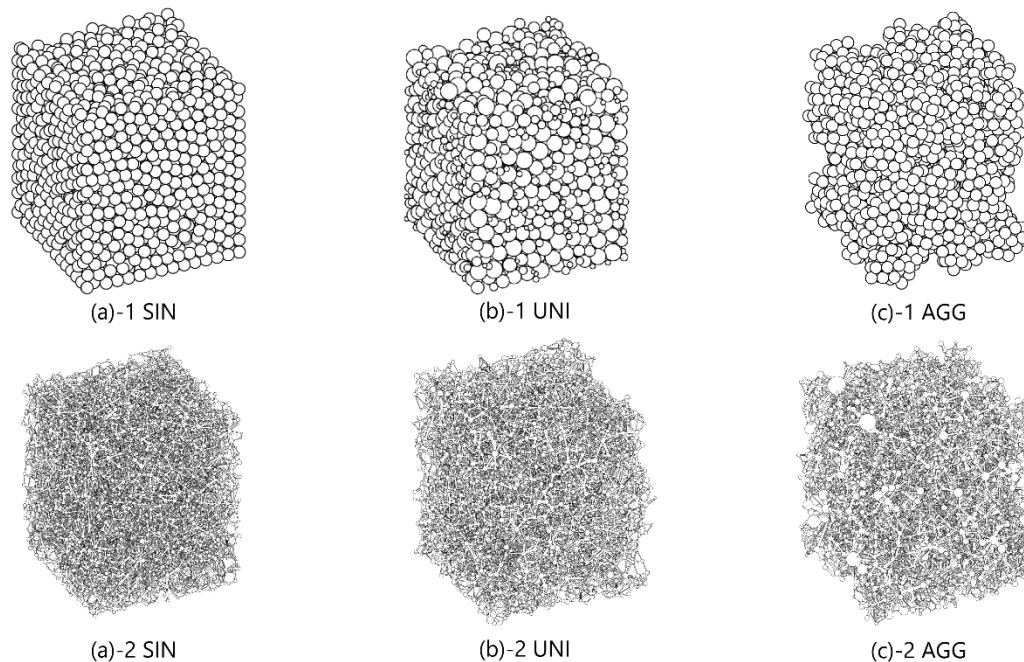


Fig. 1 Virtual porous media models (upper row) and extracted pore-networks (lower row): (a) single particle size, (b) uniform distribution, (c) aggregates.



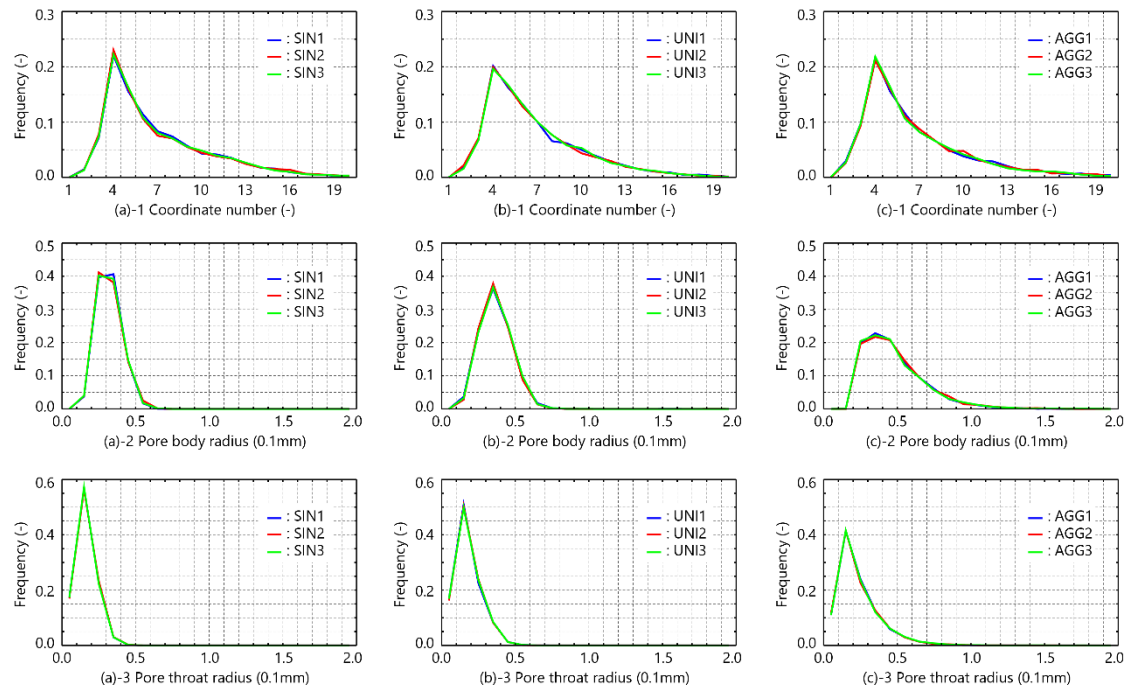


Fig. 2 Frequency of coordninate number (upper row), pore body radius (middle row), and pore throat radius (lower row): (a) single particle size, (b) uniform distribution, (c) aggregates.

With respect to the pore size, percentage of larger ones increases in UNI and AGG compared with SIN.

### Moran's $I$

Table 2 shows the calculated global Moran's  $I$  of each sample. The values of all samples are positive, which means that there are some clusters of larger and/or smaller pores in each pore-network. And  $p$ -values of all samples are quite small, which means that the realized spatial distribution of pores unlikely occurs by chance. SIN and UNI show almost same score, and that of AGG is more than twice as large as those of SIN and UNI. This shows that AGG tends to have larger clusters in pore-network.

### PP and IPP

Percolation probability and invaded percolation probability of each sample are shown in Figs. 3 and 4 with water retention property obtained from the simulation of the drainage process by the invasion percolation. Figure 3 is the result when the maximum number of pores invaded in one step is 1000, and this could reproduce uniform invasion if the imposed suction is sufficiently small. This can be considered a replication of the sand (soil) column method. Figure 4 is the one when the maximum number of pores invaded in one step is 10, and this can be considered a replication of the vacuum method in which suction is decreased gradually. This gradual invasion forms a fingering pattern, and this corresponds to the capillary fingering.

Almost same results among samples in each virtual medium except for IPP in Fig.4 also show that the porous media volume is sufficient to evaluate the objective properties, and that larger volume might be needed for IPP. When invasion is fingering, the invasion path strongly depends on the arrangement of pores. In a case of the drainage process, air proceeds selectively through larger pores, and about 40 to 50% of water, or about 75 to 82% of water, are left undrained in porous media.

Percolation probability and invaded percolation probability of SIN and UNI are almost same, and this means that the difference of particle size distribution does not affect the pore-network properties such as

Table 2 Global Moral's  $I$  of PBs

Items	Moran's $I$	Z-score	$p$ -value
SIN-1	0.132	6.56	$5.07 \times 10^{-11}$
SIN-2	0.137	6.76	$1.42 \times 10^{-11}$
SIN-3	0.143	7.10	$1.27 \times 10^{-12}$
average	0.137		
UNI-1	0.128	5.76	$8.45 \times 10^{-9}$
UNI-2	0.156	6.95	$3.68 \times 10^{-12}$
UNI-3	0.163	7.35	$2.04 \times 10^{-13}$
average	0.149		
AGG-1	0.351	13.54	$\cong 0$
AGG-2	0.367	13.99	$\cong 0$
AGG-3	0.355	13.29	$\cong 0$
average	0.358		

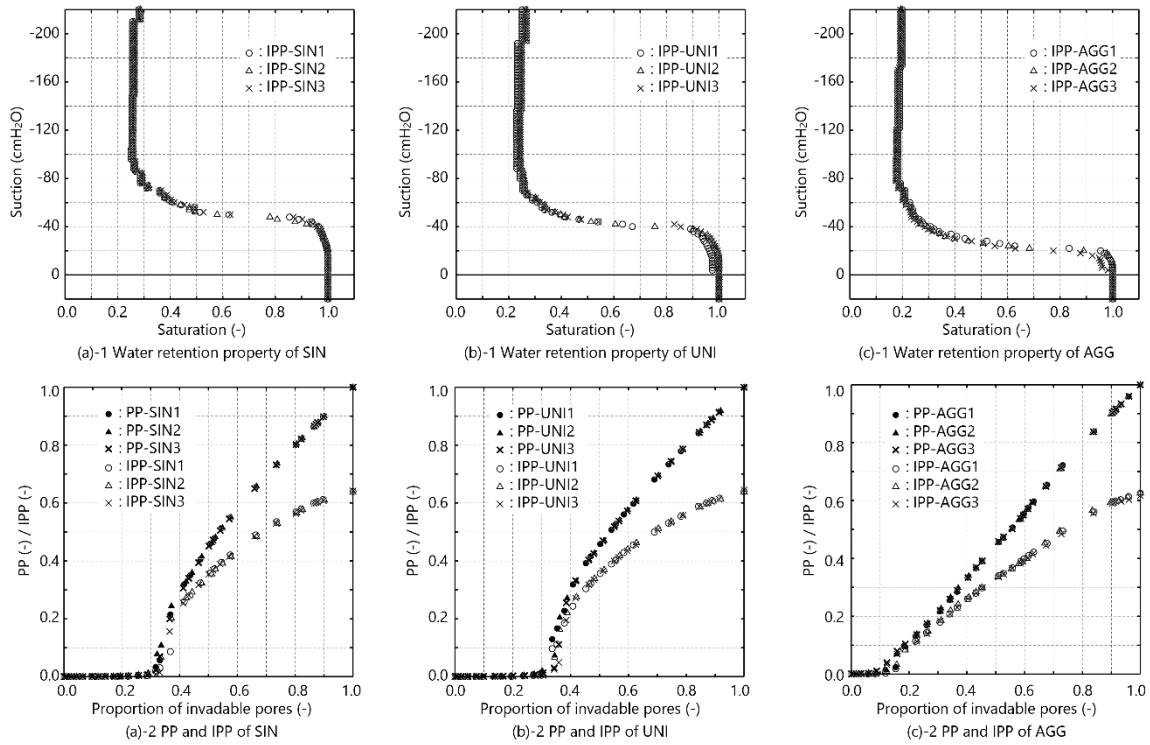


Fig. 3 Water retention property (upper row) and percolation probability and invaded percolation probability (lower row) in sand column method: (a) single particle size, (b) uniform distribution, (c) aggregates.

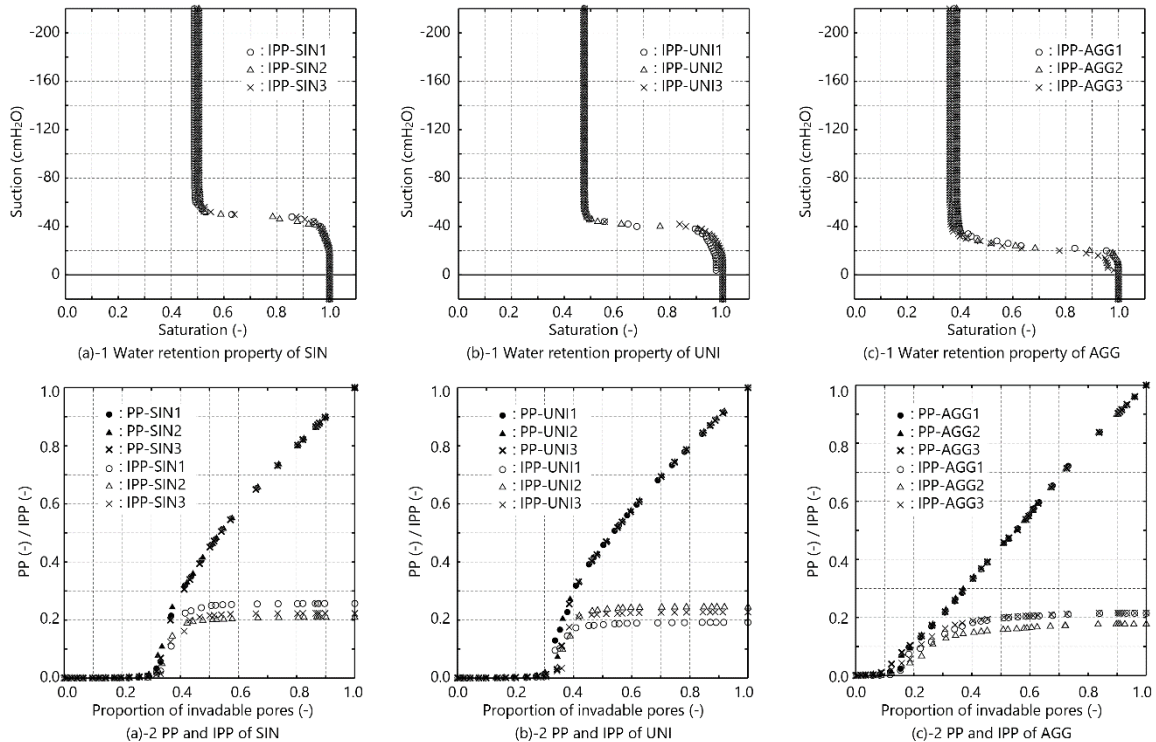


Fig. 4 Water retention property (upper row) and percolation probability and invaded percolation probability (lower row) in vacuum method: (a) single particle size, (b) uniform distribution, (c) aggregates.

connectivity and spatial autocorrelation. In addition, those graphs rise around 0.35 in all cases, and this means that at least one subnetwork that reaches from top to bottom is formed by 35% pores from the larger ones and that air begins to enter continuously. This

point is referred to as percolation threshold, and this corresponds to beginning of air-entry. Compared to the percolation threshold of SIN and UNI, that of AGG is about 0.15, which means that the top 15% of pores forms at least one subnetwork that connects

from top to bottom. This small percolation threshold is a notable feature of the porous media with aggregates structure.

## CONCLUSIONS

In this study, spatial autocorrelation and network property of virtually generated porous media with aggregate structure were investigated. To compare those of porous media without aggregate structure, porous media with single particle size and uniform distribution of particle size were generated. From each porous media model, pore-networks were extracted with the SNOW algorithm. For the spatial autocorrelation, global Moran's  $I$  was calculated. The global Moran's  $I$  of pores in the porous media with aggregates were more than twice of those without aggregates. This means that there are more clusters of relatively large and/or small pores in the porous media with aggregates than the porous media without aggregates. From the percolation probability and invaded percolation probability, it was shown that the percolation threshold of the porous media with aggregates is about 0.15, which is quite small compared with those (0.35) of the porous media without aggregates. This means that 15% pores from larger form subnetworks that spread through the whole porous media, and this gives porous media with aggregates high drainability.

## ACKNOWLEDGMENTS

This work was supported by JSPS KAKENHI Grant Number JP 20H03100.

## REFERENCES

- [1] Beare M. H., Cabrera M. L., Hendrix P. F., and Coleman D. C., Aggregate Protected and Unprotected Organic Matter Pools in Conventional and No-tillage Soils, *Soil Sci. Soc. Am. J.* Vol. 58, 1994, pp. 787-795.
- [2] Krull E. S., Skjemstad J. O., and Baldock J. A., Functions of Soil Organic Matter and the Effect on Soil Properties. Grain Research & Development Corporation Report Project No.CSO 00029, 2004, p. 129.
- [3] Peth S., Horn R., Beckmann F., Donath T., Fischer J., and Smucker A. J. M., Three-Dimensional Quantification of Intra-Aggregate Pore-Space Features Using Synchrotron-Radiation-Based Microtomography, *Soil Sci. Soc. Am. J.*, Vol. 72, doi:10.2136/sssaj007.0130, 2008, pp. 897-907.
- [4] Song Y., Davy C. A., Bertier P., and Troadec D., Understanding Fluid Transport through Claystones from Their 3D Nanoscopic Pore Network, *Microporous and Mesoporous Materials*, Vol. 228, 2016, pp. 64-85.
- [5] Jarvis N., Larsbo M., and Koesttel J., Connectivity and Percolation of Structural Pore Network in a Cultivated Silt Loam Soil Quantified by X-ray Tomography, *Geoderma*, Vol. 287, 2017, pp. 71-79.
- [6] Coetzee C., A Johnson-Kendall-Roberts (JKR) Contact Model, DOI:10.13140/RG.2.2.21772.54404, 2020, p. 20.
- [7] Rabbani A., Jamshidi S., and Salehi S., An Automated Simple Algorithm for Realistic Pore Network Extraction from Micro-tomography Images, *J. Pet. Sci. Eng.*, Vol. 123, 2014, pp. 164-171.
- [8] Gostic J. T., Versatile and Efficient Pore Network Extraction Metho Using Marker-based Watershed Segmentation, *Physical Review E*, Vol. 96, 2017, 203307.
- [9] Song Y., Takeuchi J., Takeuchi Y., and Fujihara M., Spatial Statistical Analysis of the Porous Medium Extracted from Virtual Packed Grains with Random Sizes, *Int. J. GEOMATE*, Vol. 21, pp. 68-74.
- [10] Okabe A. and Sugihara K., Network Spatial autocorrelation, *Spatial analysis along networks: statistical and computational methods*, John Wiley and Sons, 2012, pp.137-151.
- [11] Hunt A. and Ewing R., *Percolation Theory for Flow in Porous Media*, Springer, Heidelberg, 2009, p. 319.
- [12] Takeuchi J. and Fujihara M., Evaluation of Imbibition Process in Porous Media by Invaded Percolation Probability, *Int. J. GEOMATE*, Vol. 14, 2018, pp. 1-7.
- [13] Wilkinson D. and Willemsen J. F., Invasion Percolation: A New Form of Percolation", *J. Phys. A: Math. Gen.*, Vol. 16, 1983, pp. 3365-3376.

# NONLINEAR TIME SERIES ANALYSIS OF IRREGULAR OSCILLATION INDUCED BY SALINE INTRUSION IN GROUNDWATER WITH LAB-SCALE EXPERIMENT

Theara Seng<sup>1</sup>, Junichiro Takeuchi<sup>1</sup> and Masayuki Fujihara<sup>1</sup>

<sup>1</sup>Graduate School of Agriculture, Kyoto University, Japan

## ABSTRACT

Density-driven flow that arises in groundwater or saturated porous media is a challenging problem in protecting freshwater resources, because flow regimes would change depending on parameters such as density difference and permeability. Especially when a certain condition is satisfied, pollutant would spread widely on the convection currents induced by the density difference. In this study, the visualization experiment of saltwater intrusion into homogeneous porous media on a laboratory-scale and the nonlinear time series analysis of measured data were conducted. In the visualization experiments, it was shown that the flow regime changes from steady flow to oscillatory flow as the Rayleigh number increase, and that the measured EC data fluctuates erratically. To analyze the time series data produced by the visualization experiment, the phase space reconstruction, the Lyapunov exponent and the recurrence plot were conducted after the analyses by autocorrelation. The obtained results suggest that the irregular fluctuation of the salinity data could be chaotic, and that the series of analyses would help us to understand the dynamism of density-driven flow in groundwater.

*Keywords: Saltwater Intrusion, Density-driven Flow, Rayleigh Number, Nonlinear Time Series Analysis*

## INTRODUCTION

Density-driven flow that arises in groundwater or saturated porous media is a challenging problem in protecting freshwater resources, because flow regimes would change depending on parameters such as density difference and permeability. Certain pollutants are soluble in water and can leak into groundwater systems, such as seawater into coastal aquifers or wastewater leaks. Indeed, some pollutants can change the density of a fluid and induce density-driven flows within the aquifer. This causes faster propagation of the contamination due to convection. Especially when a certain condition is satisfied, pollutant would spread widely on the convection currents induced by the density difference. Accurate prediction of the movement of contamination in groundwater is essential. Thus, visualized experiment and numerical analysis of this density-driven flow play an important role in predicting how pollution can migrate through an aquifer [1]-[2].

In contrast to the transport of pollution by molecular diffusion, convection due to density-driven flow is an unstable process that can undergo quite complicated patterns of distribution. The Elder-problem is a simplified but comprehensive model that describes the intrusion of salt water from a top boundary into an aquifer [4]-[6]. Moreover, hydrogeological formations usually possess a heterogeneous and complicated structure, and geological condition may consist of layers of porous media with different porosities and permeability coefficients [7]-[8]. Difficulty in specifying hydrogeological parameters of the media, as well as

measuring the position and configuration of the layers, gives rise to certain errors. Typically, the averaged values of these quantities are used to overcome these uncertainties and many researches have been done mostly on homogenous porous media.

In both the Elder-problem and Benard-convection, flow dynamism is investigated through the state of high Rayleigh number ( $Ra$ ) [9]. Some research works were conducted to investigate density-driven flow phenomena which is typically associated with Rayleigh number [10]-[12]. From the extensive investigation of Kawabata [10], it revealed oscillatory flow and its variation associated with the Rayleigh number while periodic patterns appeared for the numerical model. In recent years, numerical analysis of instability of density-driven flow [13], and stability criterion of it in homogenous porous media [14]-[15] as well as chaos analysis [16] have been done. As the replication for Kawabata's work, Hashimoto [11] conducted visualization experiment and analyzed the time series data of this experiment by using the statistical tests methods. The patterns of time series data oscillated irregularly and seemed to be random which could be chaotic. Regarding irregular oscillation of saltwater data observed by [10] and [11], Theara et al. [12] estimated the oscillatory flow through designated Rayleigh number in which the dispersion coefficient kept varies. It is found that the oscillatory flow happened as a bifurcation with increase in  $Ra$ . However, the time series analysis wasn't conduct in this study.

To analysis the nonlinearity of time series data obtained from laboratory experiments, there were an

increasing number of studies which applied the concepts such as phase space reconstruction [17]-[18], the Lyapunov exponent [19]-[22] and [30], the recurrence plot [23]-[24], and the surrogate data test [25]-[29] by autocorrelation and Fast Fourier Transforms (FFT). Recent years, Regression (R) technique is widely used to analyze the nonlinear time series data in most fields including geophysics domain [31]-[32].

In this study, we aim to extent our investigation on irregular oscillation induced by density-driven flow in porous media through the visualization experiment of saltwater intrusion and conduct the nonlinear time series analysis of the measured EC data by employing the concepts of analysis mentioned above.

## VISUALIZED EXPERIMENT

In this study, we extended our investigation through visualization experiments on saltwater intrusion into homogeneous porous media on a laboratory-scale by prolonging the duration of the observation in order to obtain enough time series data for analyzing. The entire experimental times three hours were set in the previous study. For the experimental setup, the groundwater tank is filled by homogeneous glass beads and it has internal dimensions of 130 cm length, 45 cm height, and 5 cm width as shown in Fig. 1. Deaerated water is utilized as groundwater into the flow field. Commercial salt solution dyed with red food color is used as saltwater intrusion which is injected at the top left of aquifer model. Two cameras are installed to monitor saltwater behaviors at every step.

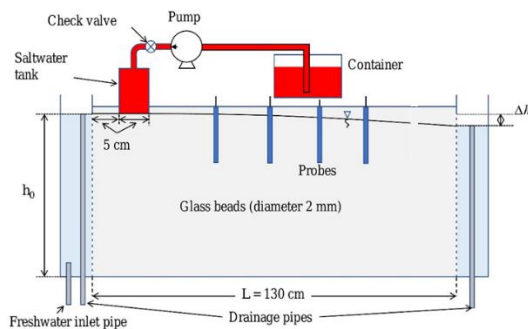


Fig. 1 Experimental setup of flow tank

The current experimental setting aims to measure time series data of salinity to analyze the irregular oscillation induced by the density-driven flow of saltwater intrusion. Hence, the portable electrical conductivity probes are inserted into the flow tank to measure the electrical conductivity time series data. At this time, the entire experimental time is extended up to 10 hours and the data is measured every 2

seconds. We give the name of the probes corresponding to their order from upstream to downstream as Cell1, Cell2, Cell3, and Cell4, respectively.

Two types of relative saltwater density are prepared: 1.0105 and 1.0210 to produce relatively low and high Rayleigh number flow regime. The hydraulic gradients ( $\Delta h$ ) are adjusted to 3.9 cm which generate high velocity flow of groundwater. The combinations of relative saltwater density and hydraulic gradients yields two kinds of the  $Ra$  from the lowest value of 25 to the highest value of 50. The  $Ra = 25$  is considered to be lower than threshold value (39.5) and  $Ra = 50$  is greater than the threshold one. Here,  $Ra$  is calculated based on the following formula.

$$Ra = \frac{(\gamma - 1)KH}{\alpha_L v} \quad (1)$$

where  $\gamma$  is the specific weight of saltwater,  $K$  is the hydraulic conductivity,  $H$  is the representative length,  $\alpha_L$  is the longitudinal dispersion length, and  $v$  is the groundwater velocity.

## NONLINEAR TIME SERIES ANALYSIS OF IRREGULAR OSCILLATION

In this study, two cases of time series salinity data were analyzed to confirm its nonlinearity. For nonlinear time series analysis, R language is used.

### Time Series Analysis

#### Autocorrelation

The autocorrelation for a periodic signal is also periodic and for deterministic chaotic systems the autocorrelation function decays exponentially with increasing lag [34]. When the autocorrelation function falls abruptly to zero, that indicates the lack of a deterministic component from the data; a slow fall to zero is a sign of stochastic or deterministic behavior; when the data slowly drops to zero and shows periodic behavior then the data is highly correlated and is either periodic or chaotic in nature. In this study, autocorrelation is conducted to observe these kinds of problem, especially to investigate the chaoticity.

### Determination of Embedding Dimension

#### False nearest-neighbors

This method is to determine the minimal sufficient embedding dimension  $m$  proposed by Kennel et al [35]. It is called the false nearest neighbor method. The idea is quite intuitive. Suppose the minimal embedding dimension for a given time series is  $m_0$ . This means that in a  $m_0$ -dimensional



delay space the reconstructed attractor is a one-to-one image of the attractor in the original phase space. Especially, the topological properties are preserved. Thus, the neighbors of a given point are mapped onto neighbors in the delay space. In this study, we set the maximum embedding dimension as 8.

## Nonlinearity Analysis

### Phase space reconstruction

Phase space or state space reconstruction is an abstract mathematical construction with important applications in statistical mechanics, where it allows the time evolution of a dynamical system to be represented in geometric form [31]. Phase space has as many dimensions as the number of variables to define the instantaneous state of the system. The R package *tsSeriesChaos* offers a family of codes for the analysis of nonlinear time series whose author and maintainer is Di Narzo [36]. In this study, the dynamics in a 3-D phase space is reconstructed from a single time series data, using a time delay, where a time series data is transformed into a trajectory in the 3-D phase space.

### Lyapunov exponent

Lyapunov exponents  $\lambda$  quantify the rate of separation of infinitesimally close trajectories. The largest Lyapunov exponent is a very useful quantity to calculate, since if it is positive, it indicates not simply nonlinearity, but chaos [19]-[22].

The first step of our approach involves reconstructing the attractor dynamics from a single time series. We use the method of delays since one goal of our work is to develop a fast and easily implemented algorithm. In practice of R, for each of the reference points, we look for  $k$  neighbors that are closer than radius of the ball inside ( $\varepsilon$ ) and have a temporal separation greater than Theiler window ( $t$ ). Then, we compute the log-average distance between the point and its  $k$  neighbors, and we follow it for a finite number ( $s$ ) of steps ahead in time. In our study, we consider 4,000 reference point, each with 100 neighbors inside a ball of radius 0.02. The evolution of the mean distance is monitored for 50 steps ahead in time and points separated by less than 5 from the reference point in the series are not considered as neighboring points.

### Recurrence plots

As our focus is on recurrences of states of a dynamical system, we define now the tool which measures recurrences of a trajectory  $\vec{x}_i \in \mathbb{R}^m$  in phase space. The RP efficiently visualizes recurrences and can be formally expressed by the matrix:

$$R_{i,j}(\varepsilon) = \theta\left(\varepsilon - \|\vec{x}_i - \vec{x}_j\|\right), \quad i, j = 1, \dots, n \quad (2)$$

where  $n$  is the number of measured points  $\vec{x}_i$ ,  $\varepsilon$  is a threshold distance,  $\theta(\cdot)$  the Heaviside function (i.e.,  $\theta(x) = 0$ , if  $x < 0$ , and  $\theta(x) = 1$  otherwise) and  $\|\cdot\|$  is a norm. Moreover, the RP is symmetric with respect to the main diagonal; that is,  $R_{i,j} \equiv R_{j,i}$ . If the series is periodic, with period  $T$ , then, for fixed  $i$ , there is a black dot every  $T - 1$  white circles. In our study, the number of measured points  $n = 4,000$ .

## VISUALIZED AND ANALYTICAL RESULTS

### Visualization Experiment

Figure 2 (a)-(b) shows the behavior of intruding salinity when the difference of water level is 3.9 cm. The time series data for the case  $\gamma = 1.0026$  shown in Fig. 3 ( $Ra=25$ ) indicated the relatively smooth pattern whereas those of the case  $\gamma = 1.0052$  highly fluctuated until the end. The cause of the large fluctuation of Cell3 and Cell4 in Fig. 3 ( $Ra=50$ ) is convection, which occurred mainly after Cell2 although it is difficult to recognize it in Fig. 2 (b). For the case  $\gamma = 1.0026$ , irregular fluctuation is observed in Fig. 3 ( $Ra=25$ ), although  $Ra$  is below the threshold value and no clear convection is observed.

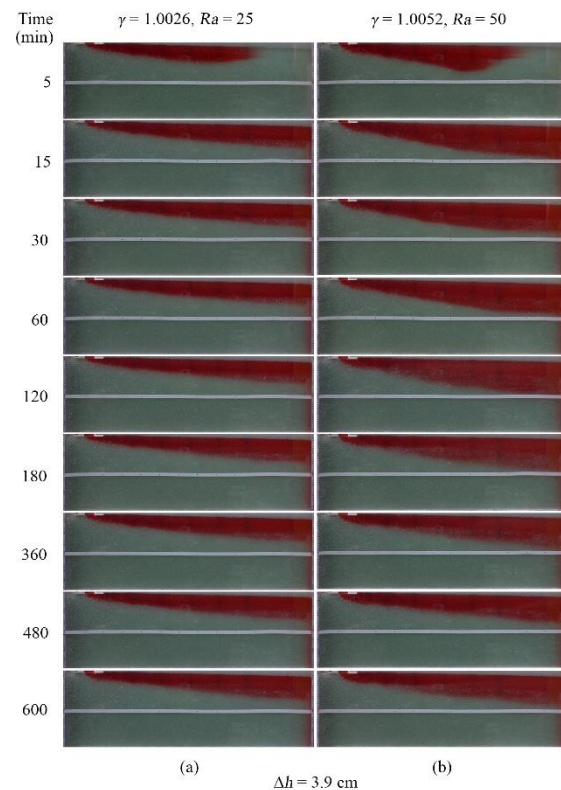


Fig. 2 Time variation of salinity distribution



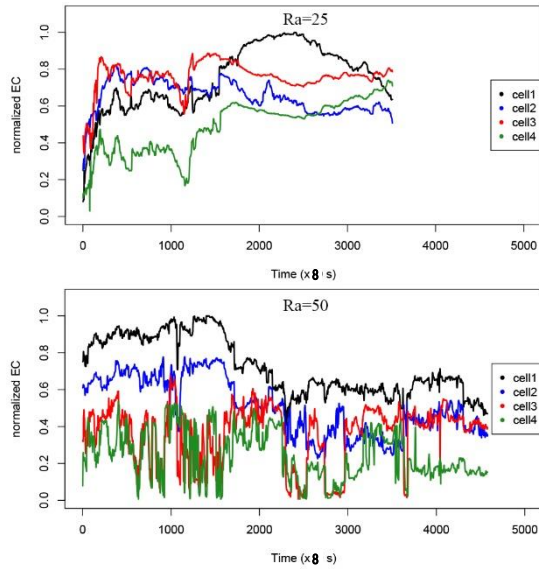


Fig. 3 Normalized salinity data under  $\Delta h = 3.9$  cm

In summary, in the visualization experiments, it was shown that the flow regime changes from steady flow to oscillatory flow as the Rayleigh number increase. However, most of the measured EC data fluctuates erratically which are contradictory to the result of Kawabata [10]. Particularly, the time series data in the high  $Ra$  flow regime are mostly considered that these irregular fluctuations are convection. Some reasons could be arisen. To analyze the time series data produced by this visualization experiment, the phase space reconstruction, the Lyapunov exponent, and the recurrence plot are used.

### Analytical Results

The results of autocorrelation plots show various patterns in Fig. 4 and Fig. 5. The autocorrelation functions for Cell1 to Cell2 decay slowly to zero (here only Cell1 is shown in Figs.4 and 5) which indicated a sign of stochastic or deterministic behaviors. However, the decays are slight faster on other two cells at downstream and they fluctuate around zero. Therefore, it could be considered a chaotic behavior. The nearest-neighbors analysis shown in Fig. 6 and Fig. 7 indicated that the average minimal sufficient embedding dimensions are more than 3. But we cannot draw figures more than 3 dimensions, 3D plot is used for phase space reconstruction.

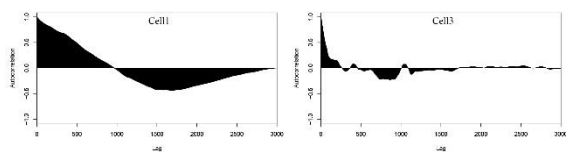


Fig. 4 Autocorrelation of  $Ra=25$  (Cell1 and Cell3)

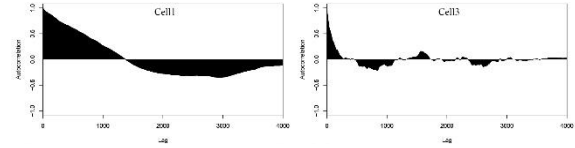


Fig. 5 Autocorrelation of  $Ra=50$  (Cell1 and Cell3)

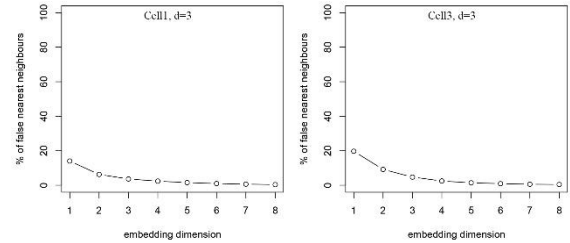


Fig. 6 Nearest neighbors of  $Ra=25$  (Cell1 and Cell3)

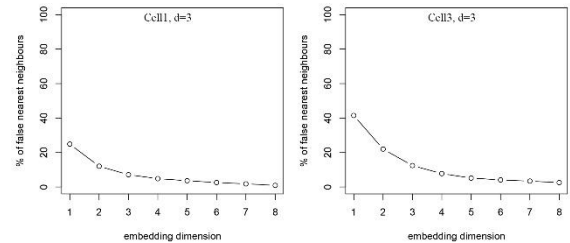


Fig. 7 Nearest neighbors of  $Ra=50$  (Cell1 and Cell3)

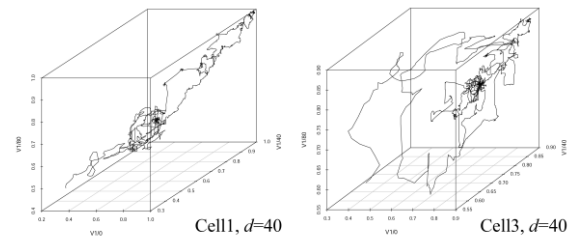


Fig. 8 Phase space reconstruction (time delay  $d = 40$ ) with  $Ra=25$  (Cell1 and Cell3)

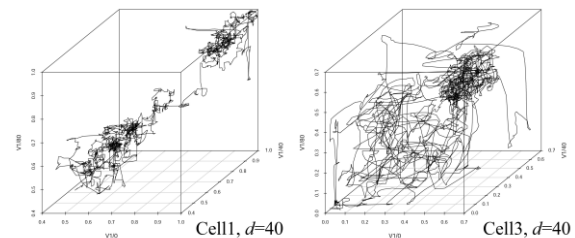


Fig. 9 Phase space reconstruction (time delay  $d = 40$ ) with  $Ra=50$  (Cell1 and Cell3)

The phase space reconstructions were analyzed by altering time delays in order to search for an optimal one. The value of time delay varies from 1 to 5. From the result of numerical experiments, the appropriate value of the delay is  $d = 40$  as shown in Fig. 8 and Fig.

9. This time delay corresponds to oscillations whose cycle are about 150-200 sampling times shown in Fig. 2. This time delay was applied to seek for the Lyapunov exponents (Figs. 10 and 11).

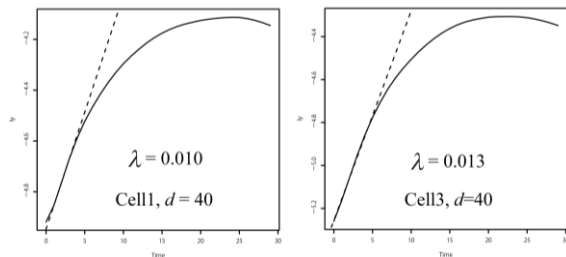


Fig. 10 Lyapunov exponent analysis  $Ra=25$

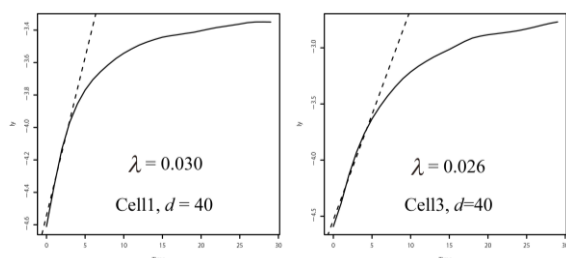


Fig. 11 Lyapunov exponent analysis  $Ra=50$

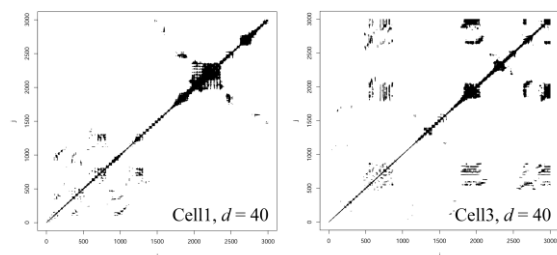


Fig. 12 Recurrence plot with  $Ra=25$

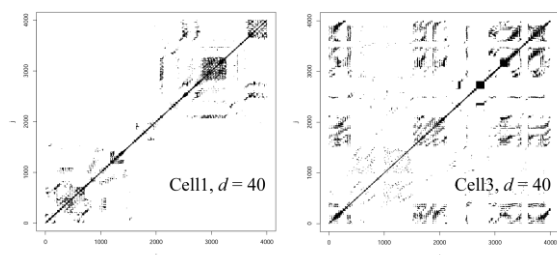


Fig. 13 Recurrence plot with  $Ra=50$

According to the results illustrate in Fig. 10 and Fig. 11, exponents (the slop of the dots line) are positive which indicate that the time series are not simply nonlinear but could be chaotic behavior. From the recurrence plots, it was shown that they repeatedly take the same value (Fig. 12 and Fig. 13). In conclusion, all the obtained results do not deny that

the irregular fluctuation of the salinity data is not chaotic.

## CONCLUSIONS

The visualization experiment of saltwater intrusion into homogeneous groundwater model and the nonlinear time series analysis of measured data were conducted in this study. The visualization experiments, it indicated that the flow regime changes from steady flow to oscillatory flow as the Rayleigh number increase. However, most of the measured EC data fluctuates erratically. According to analytical results of nonlinearity testing, the irregular fluctuation by the saltwater intrusion could be chaotic.

## ACKNOWLEDGMENTS

This research was partially funded by a Grant-in-Aid for Scientific Research(B) JP20H0310.

## REFERENCES

- [1] Kobus, H., Soil and groundwater contamination and remediation technology in Europe, In: Sato, K., Iwasa, Y. (eds.) Groundwater Updates, Springer, Tokyo, 2000, pp. 3–8.
- [2] Fan, Y., Duffy, C.J., Oliver, D.S., Density-driven groundwater flow in closed desert basins: field investigations and numerical experiments, J. Hydrol. 196, 1997, pp. 139–184. E
- [3] Ider, J.W., Steady free convection in a porous medium heated from below, J. Fluid Mech. 27, 1967, pp. 29–48.
- [4] Elder, J.W., Transient convection in a porous medium. J. Fluid Mech, 27, 1967, pp. 609–623.
- [5] Elder, J., Simmons, C., Diersch, H.-J., Frolkovič, P., Holzbecher, E., Johannsen, K., The Elder problem, Fluids 2(1), 11, 2017.
- [6] Voss, C.I., Souza, W.R., Variable density flow and solute transport simulation of regional aquifers containing a narrow freshwater-saltwater transition zone, Water Resour. Res., 23, 1987, pp. 1851–1866.
- [7] Schneider, A., Kröhn, K.-P., Püschel, A., Developing a modelling tool for density-driven flow in complex hydrogeological structures, Comput. Vis. Sci. 15, 2012, pp. 163–168.
- [8] Reiter, S., Logashenko, D., Vogel, A., Wittum, G., Mesh generation for thin layered domains and its application to parallel multigrid simulation of groundwater flow, Comput. Vis. Sci. 16, 2017, pp. 151–164.
- [9] Holzbecher, E., Modeling Density-Driven Flow in Porous Media, Springer, 1998, pp. 1-47.
- [10] Kawabata, M., Analysis and Verification of Density-driven Fluctuation Caused by Saltwater Intrusion into Groundwater, Master's Thesis,

- Kyoto University, 2017.
- [11] Hashimoto, H., Visualization Experiments of Bifurcation in Saltwater Intrusion to Groundwater and Chaotic Fluctuation Test for Salinity Data, Master's Thesis, Kyoto University, 2019.
  - [12] Seng, T., Takeuchi, J. and Fujihara, M., Identifying Impacts of Density-Driven Fluctuation to Groundwater Caused by Saltwater Intrusion, 6th Int. Conf. on Structure, Engineering & Environment (SEE), Kyoto, Japan, Nov.18-20, 2020, ISBN: 978-4-909106056 C3051.
  - [13] Shafabakhsh, P., Fahs, M., Ataie-Ashtiani, B., and Simmons, C. T., Unstable density-driven flow in fractured porous media: the fractured elder problem, *Fluids*, 4(3), 2019, p. 168.
  - [14] Musuuza J.L., Radu F.A., and Attinger S., The effect of dispersion on the stability of density-driven flows in saturated homogeneous porous media, *Advances in Water Resources*, 36(3), 2011, pp.417-432.
  - [15] Musuuza, J.L., Attinger S., and Radu F.A., An extended stability criterion for density-driven flows in homogeneous porous media, *Advances in water resources* 32(6), 2009, pp. 796-808.
  - [16] Kida, S., Analysis of Turbulence by Unstable Periodic Motion, Kyoto University, 2007.
  - [17] Takens, F., Detecting strange attractors in turbulence. In *Dynamical Systems and Turbulence*; Rand, D.A., Young, L.-S., Eds.; Springer: Berlin/Heidelberg, Germany, 1981, pp. 366–381.
  - [18] Kawabata, M., Junichiro T., and Masayuki F., Numerical analysis of density-driven fluctuation in groundwater caused by saltwater intrusion, *Jurnal Teknologi* 76, no. 15, 2015.
  - [19] Kantz, H. A robust method to estimate the maximal Lyapunov exponent of a time series, *Phys. Lett. A*, 185, 1994, pp. 77–87.
  - [20] Hazledine, S., Sun, J., Wysham, D., Downie, J. A., Oldroyd, G. E., and Morris, R. J., Nonlinear time series analysis of nodulation factor induced calcium oscillations: evidence for deterministic chaos?, *PLoS One*, 4(8), 2009, e6637.
  - [21] Falayi, E. O., Adewole, A. T., Adelaja, A. D., Ogundile, O. O., and Roy-Layinde, T. O., Study of nonlinear time series and wavelet power spectrum analysis using solar wind parameters and geomagnetic indices, *NRIAG Journal of Astronomy and Geophysics*, 9(1), 2020, pp. 226-237.
  - [22] Falayi, E. O., Adepiton, J. O., Adewole, A. T., and Roy-Layinde, T. O., Analysis of rainfall data of some West African countries using wavelet transform and nonlinear time series techniques, *Journal of Spatial Science*, 2022, pp. 1-12.
  - [23] Marwan, N., Romano, M. C., Thiel, M., and Kurths, J., Recurrence plots for the analysis of complex systems, *Physics reports*, 438(5-6), 2007, pp. 237-329.
  - [24] Zhao, Z. Q., Li, S. C., Gao, J. B., and Wang, Y. L., Identifying spatial patterns and dynamics of climate change using recurrence quantification analysis: a case study of qinghai-tibet plateau, *International Journal of Bifurcation and Chaos*, 21(04), 2011, pp. 1127-1139.
  - [25] Theiler, J., Eubank, S., Longtin, A., Galdrikian, B., and Farmer, J. D., Testing for nonlinearity in time series: the method of surrogate data, *Physica D: Nonlinear Phenomena*, 58(1-4), 1992, pp. 77-94.
  - [26] Schreiber, T., and Schmitz, A., Improved surrogate data for nonlinearity tests, *Physical review letters*, 77(4), 1996, pp. 635-638.
  - [27] Bartos, I., and János, I. M., Nonlinear correlations of daily temperature records over land, *Nonlinear Processes in Geophysics*, 13(5), 2006, pp. 571-576.
  - [28] Venema, V., Bachner, S., Rust, H. W., and Simmer, C., Statistical characteristics of surrogate data based on geophysical measurements, *Nonlinear processes in Geophysics*, 13(4), 2006, pp. 449-466.
  - [29] She, N., and Basketfield, D., Streamflow dynamics at the Puget Sound, Washington: application of a surrogate data method. *Nonlinear Processes in Geophysics*, 12(4), 2005, pp. 461-469.
  - [30] Rosenstein, M. T., Collins, J. J., and De Luca, C. J., A practical method for calculating largest Lyapunov exponents from small data sets. *Physica D: Nonlinear Phenomena*, 65(1-2), 1993, pp. 117-134.
  - [31] Huffaker, R. G., Huffaker, R., Bittelli, M., and Rosa, R., *Nonlinear time series analysis with R*, Oxford University Press, 2017.
  - [32] Cryer, J. D., and Chan, K. S., *Time series analysis: with applications in R (Vol. 2)*, New York: Springer, 2008.
  - [33] Dimitrova, Z. I., and Vitanov, N. K., Adaptation and its impact on the dynamics of a system of three competing populations, *Physica A: Statistical Mechanics and its Applications*, 300(1-2), 2001, pp. 91-115.
  - [34] Kennel, M. B., Brown, R., and Abarbanel, H. D., Determining embedding dimension for phase-space reconstruction using a geometrical construction. *Physical review A*, 45(6), 1992, 3403.
  - [35] Wallot, S., and Mønster, D., Calculation of average mutual information (AMI) and false-nearest neighbors (FNN) for the estimation of embedding parameters of multidimensional time series in matlab. *Frontiers in psychology*, 2018, 1679.
  - [36] Di Narzo, A. F., *Package tseriesChaos: Analysis of nonlinear time series*, 2015.

## MODELLING THE EFFECT OF CLIMATE CHANGES ON COASTAL AQUIFERS IN OMAN

Javed Akhtar<sup>1,3</sup>, Ahmad Sana<sup>2\*</sup>, Syed Mohammed Tauseef<sup>3,4</sup> and Shakila Javed<sup>1</sup>

<sup>1</sup> Civil & Architectural Engineering Section, Engineering Department, University of Technology and Applied Sciences, Muscat, Sultanate of Oman.

<sup>2</sup> Department of Civil and Architectural Engineering, Sultan Qaboos University, PO Box 33 Muscat, 123, Oman

<sup>3</sup> School of Engineering, University of Petroleum and Energy Studies, Dehradun, Uttarakhand, India Civil & Architectural Engineering Section, Engineering

<sup>4</sup> Centre for Interdisciplinary Research and Innovation (CIDRI), University of Petroleum and Energy Studies, Dehradun, Uttarakhand, India.

### ABSTRACT

In Sultanate of Oman, the only source of recharge for the aquifers, which have been overexploited over the past few decades, is rainfall, which is short in supply and varies with location and time. As a result, groundwater levels decreased, and seawater began to seep into coastal aquifers. The coastal aquifer of Wadi Al Jizi in Al Batinah region was chosen as the study area for modelling the groundwater levels and the solute transport using MODFLOW and MT3DMS, respectively. These models were calibrated and validated over a period of seventeen years using data collected from twenty monitoring wells under stable and transient conditions. Further, calibrated model was used to integrate future scenarios to simulate effect of climate changes considering two different parameters: Rainfall and Sea Level Rise (SLR). Ground water heads and salinity intrusion caused by altered rates of recharge and Sea level rise were simulated. According to these forecasts, if the base recharge rate will reduce by 10% and SLR considered to increase by + 0.50m from base SLR, salinity intrusion contains Total Dissolved Solids (TDS > 12800 mg/L) will encroach more than one km inland by the year 2040 when compared with 2016 intrusion. Groundwater resources in the Wadi Al-Jizi aquifer in Al Batinah region may be effectively managed with the use of the models and findings from the current study.

*Keywords: Numerical Modelling, Al Batinah, Sea Level Rise, Recharge Rate, Salinity Intrusion*

### INTRODUCTION

Sultanate of Oman is an arid country in the vast Arabian Peninsula suffering from insufficient freshwater supplies and extreme hot weather conditions. For the past few years, to meet with the increased water demand, coastal aquifers were overstressed, which leads to the depletion of water table, further, resulted in the saline intrusion. Moreover, large coastal area covered with fertile land become barren along with contaminated ground water resources.

Sultanate of Oman's seawater intrusion issue is especially severe in Salalah and the Al Batinah coast, both of which have extensive agricultural land. The priceless agricultural land has become unusable due to the seawater intrusion for more than two decades. The Sultanate is considered a dry region due to its 100 mm annual average rainfall. Continuous population growth, climate change, heavy urbanization, and changes in land use have increased the thrust on the conventional surface water source to the extent that it has forced groundwater extraction as an alternative to surface water to cope with water scarcity (Akhtar et al. 2022). Over 90% of the year, clear, bright skies and little wind are the "typical" weather conditions. The summer is hot and dry, while the winter is delightfully warm and dry. Rainfall serves as the primary supply of freshwater in the upper catchments, replenishing the aquifers in the process (Sana &

Shibli, 2003).

Al Batinah region, which makes up roughly 4% of the entire country's territory, is home to about one-third of the inhabitants of the nation. High evapotranspiration rates and a dry climate characterize the eastern coastal plain (Lakey et al., 1995). It is characterized by a warm, low-humidity winter, a hot, occasionally humid summer, and low, unpredictable amounts of precipitation. The average annual air temperature in the coastal region is 28.5° C, whereas it is 17.8° C in the highlands. High rainfall is reported in the southern high region compared to the coastal region (Weyhenmeyer et al., 2002). The quality of the groundwater is highly diverse along the Al Batinah region. Water quality in the hilly region is very good (less than 1500 mg/L) in the flat and low land regions; water quality reduces (1500 -6500 mg/L) as groundwater dissolves salts (primarily calcium carbonate) on its way to the ocean. Water quality in the Al Batinah region has significantly declined (Barwani and Helmi, 2006). This was shown by a 7 percent decline in the regions with suitable agricultural water (2,000–6,000 S/cm), which represented the loss of 2,714 hectares of irrigated land. The saline interface was also discovered 12 km inland in the Wadi Al Taww, Barka region in Al Batinah, Sultanate of Oman.

The main objective of the study is to simulate the groundwater flow with a numerical model to address

the seawater intrusion problem. The study is important and timely, considering the serious concern regarding water security in Sultanate of Oman (and in the world in general), and its significant influence on sustainable development of the country, that is exacerbated by the problem of seawater intrusion, climate change and population growth.

## LITERATURE REVIEW

Groundwater use and maintenance in arid and semi-arid environments are threatened by salinization, a global issue in coastal aquifers. Many of the coastal aquifers across the world have seen rapid declines in water quality over the last few centuries (Al Taani et al., 2013; Baalousha, 2016). Shammass & Jack, 2008 used GMS (Groundwater Modeling System) that included MODFLOW & MT3DMS to represent 3D groundwater flow and solute transport in Salalah, Oman. In order to replicate the intricate multi-layer aquifer found in the Wadi Samail watershed in the Al Batinah region, Al Hashmi et al. (2020) employed a 3D groundwater model (MODFLOW). In order to research the effects of climate change on the Sumail Lower Catchment (SLC) aquifer and the Jamma aquifer in the Al Batinah region of Oman, Maktoumi et al. (2018) employed MODFLOW and MT3DMS. The watershed seemed to continue groundwater flow in the direction of the sea despite seawater intrusion, although the Jamma aquifer was under stress, was negatively impacted, and was at risk. Using MODFLOW and MT3DMS, Chitrakar and Sana (2015) investigated the groundwater and seawater intrusion pattern in the Eastern Al Batinah coastal plain. Chun et al. (2018) used SUTRA (Saturated-Unsaturated Transport) to study the effect of climate change and SLR on the salinity intrusion in the coastal groundwater system of South Korea. Their findings revealed that for an accurate assessment of climate change impacts on seawater intrusion in coastal groundwater systems, both freshwater recharge rates and SLR should be taken into account. Ghazaw et al. (2014) used Visual MODFLOW to study the depleting level of groundwater of Saq aquifer located in the Qasim area in Saudi Arabia. Dibaj et al (2020) to investigate the combined consequences of over-abstraction and seawater intrusion in the Pingtung Plain coastal aquifer system in Taiwan used a three-dimensional variable-density finite element model. Seawater intrusion models are therefore a very effective instrument for managing and protecting coastal aquifers (El Hamidi et al. 2021)

## STUDY AREA

The Wadi Al-Jizi catchment located in Al Batinah region is selected as the study area (located between latitudes 2685288.72m N to 2702809.30m N and

longitudes 445120.53m E to 474236.85m E covered in topographic map (Fig.1). The study area is bounded by the Sea of Oman in the north, and Western Hajar mountain range in the south.

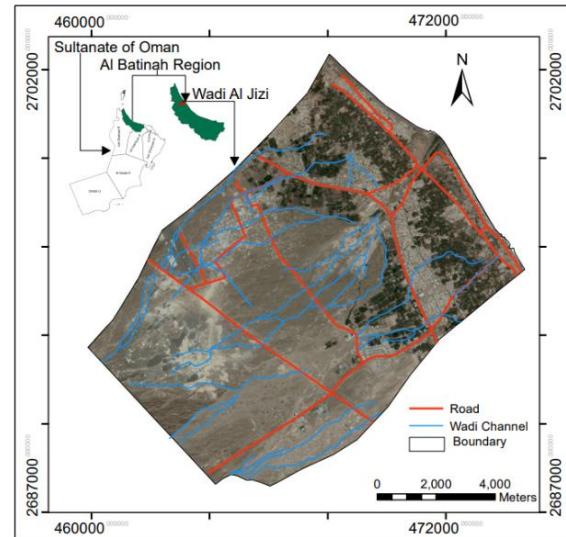


Fig.1 Study area of Wadi Al Jizi

The total area of Wadi Al-Jizi catchment area is 1,154 km<sup>2</sup>, including 519 km<sup>2</sup> of the eastern part. The eastern part of the aquifer system is studied that has an area of 123 km<sup>2</sup> approximately, extending from the sea towards the mountains. This part of the aquifer has been selected since most of the agricultural activities, pumping and observations wells and salinity monitoring wells are in this zone.

## METHODOLOGY

### Conceptual Model

A two-layered conceptual model (Fig.2) is considered which is a three-dimensional representation of the groundwater flow based on the available geological and hydrogeological data for the study area.

The next stage was model development, which was essentially the conversion of the conceptual model into the numerical model input files, and calibration is performed to demonstrate that the model can generate field determined heads and flows that are used as reference or calibration values or targets. The model is validated after calibration to predict water table fluctuations and salinity intrusion for a different set of data considering various scenarios

In the present study the extent of finite difference grid is 11903 m (x-direction) and 15285 m (y-direction), containing 356 columns and 357 rows. Since groundwater levels may change dramatically near pumping locations, a finer grid size 5.0 × 10.0 m was used for the areas where pumping wells are



located whereas a maximum grid size of  $40.0 \times 80.0$  m in other parts of the model domain was used.

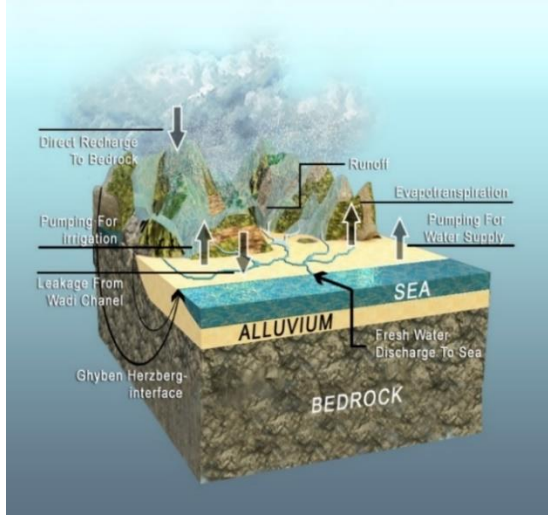


Fig. 2. Conceptual model of Wadi Al Jizi ground water flow system

The total number of grid cells are 254184 with 219916 active cells and the remaining as inactive. The boundary on the northeast side of the model domain (coastline) and the southwest boundary (upstream of the catchment) were set as specific head boundaries. Initial water heads of upstream boundaries were determined from water level records of observation wells located at or near the upper boundary. The east and west sides of the model domain have been oriented parallel to the wadi flow direction and therefore considered as no-flow boundaries. The inflow to the model was considered from recharge due to rainfall, while outflow was the discharge to the sea and from the existing pumping wells in Wadi-Al Jizi region.

### Numerical Model

In the present study the Groundwater Modeling System (GMS) is used that includes MODFLOW and MT3DMS for groundwater flow and solute transport processes, respectively. The governing equation in MODFLOW is shown as Eq. (1).

$$\frac{\partial}{\partial x} \left( K_{xx} \frac{\partial h}{\partial x} \right) + \frac{\partial}{\partial y} \left( K_{yy} \frac{\partial h}{\partial y} \right) + \frac{\partial}{\partial z} \left( K_{zz} \frac{\partial h}{\partial z} \right) + W = S_s \frac{\partial h}{\partial t} \quad (1)$$

where,  $K_{xx}$ ,  $K_{yy}$  and  $K_{zz}$  are values of hydraulic conductivity (L/T) along the x, y, and z coordinate axes (assumed to be parallel to the major axes of hydraulic conductivity); h is the potentiometric head (L); W is a volumetric flux per unit volume (1/T) representing sources and/or sinks of water, with  $W < 0.0$  for outflow from the ground-water system,

and  $W > 0.0$  for inflow;  $S_s$  is the specific storage of the porous material (1/L); and t is time (T). This equation combined with appropriate boundary and initial conditions, describes transient 3D groundwater flow in a heterogeneous and anisotropic medium, provided that the principal axes of hydraulic conductivity are aligned with the coordinate directions.

The detail about the model and information regarding the studies that utilized MODFLOW can be found in McDonald and Harbaugh (2000). The results obtained from MODFLOW for groundwater flow characteristics can be used to run MT3DMS which is an advanced version of 3D Mass Transport Model, MT3D developed by Zheng (1999). This model is capable of modelling advection in steady and transient flow fields, anisotropic dispersion, first-order decay and production reactions and linear and nonlinear sorption. This model is based on the general equation of mass transport as Eq. (2).

$$R \frac{\partial C}{\partial t} = D_{xx} \frac{\partial^2 C}{\partial x^2} + D_{yy} \frac{\partial^2 C}{\partial y^2} + D_{zz} \frac{\partial^2 C}{\partial z^2} - V \frac{\partial C}{\partial x} - \mu RC \quad (2)$$

where, C is the concentration of solute, and  $D_{xx}$ ,  $D_{yy}$  and  $D_{zz}$  are the dispersion coefficients in x, y, and z directions, respectively, V is the average pore water velocity, R, retardation factor, and  $\mu$  is decay coefficient. For seawater simulation by MT3DMS the decay constant is equal to zero, therefore,  $\mu RC = 0$ .

## RESULTS AND DISCUSSION

### Steady-State Groundwater Flow simulation

The model was initially calibrated in steady state for the year 2000. Trial and error adjustments of hydraulic conductivity values were carried out for the steady-state model until the observed and computed value matched in selected nine observation wells, distributed over the model domain. Hydraulic conductivity, one of the most important hydrogeological parameters of the aquifer, was calibrated manually using trial and error procedure. This input parameter was varied to determine the model response by conducting sensitivity analysis and calculating and plotting the groundwater fluctuations (Akhtar et al. 2022 -In Press)

Fig. 3 shows the calibrated values steady state results for the year 2000.

### Transient model calibration and validation

The steady-state result was used in the transient model simulation as the initial condition from 2000 to 2017. The transient simulation was divided into two



parts: Jan. 2000 to Dec. 2009 was used to calibrate the model and Jan. 2010 to Dec. 2017 was used to validate the model. The calibration target in the transient state model was the groundwater elevation in 9 observations wells.

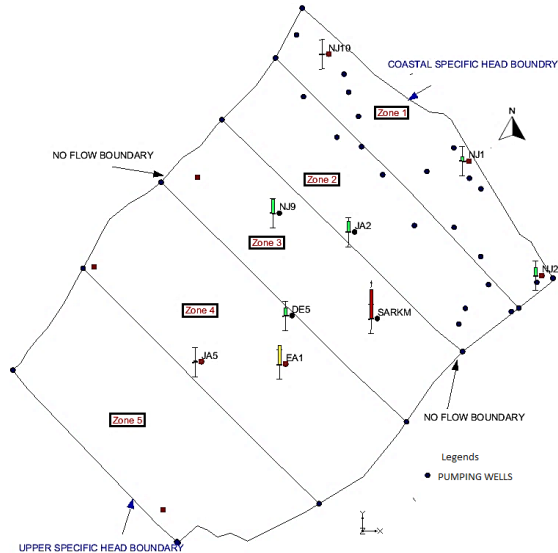


Fig.3 Model showing the zone distribution, boundary conditions & calibrated values in Steady State (Year 2000).

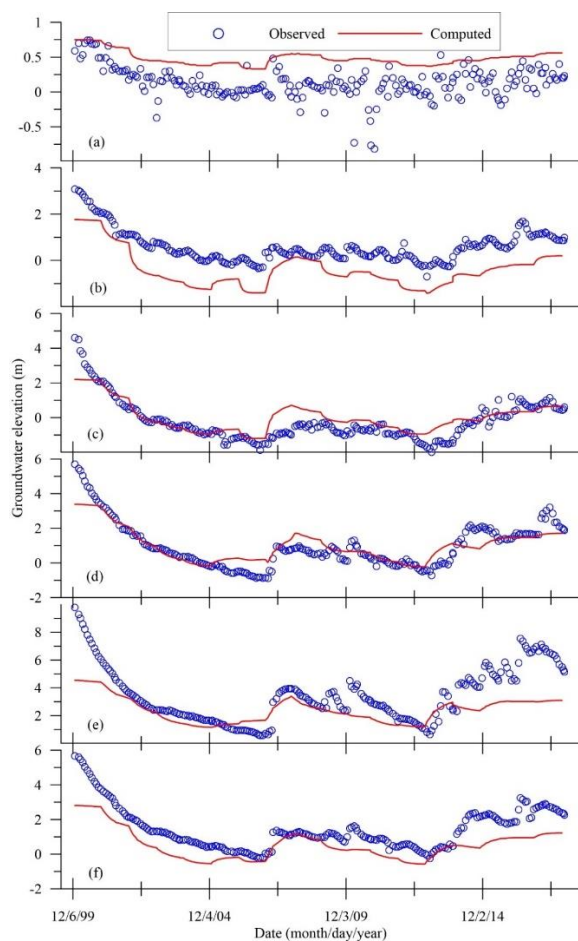


Fig.4 Time series plot of selected observation wells

(a) NJ-1, (b) JA-2, (c) NJ-9, (d) EA-1, (e) JA-5, and (f) DE-5

A total of 18 stress periods were used with 12-time steps in each month with a multiplier of 1 resulting in 6574 days. In the transient simulation the resultant hydraulic conductivity and vertical anisotropy from the steady state were used. For validation of the model, calibrated parameters like hydraulic conductivity, specific yield, and specific storage were used with a new set of pumping rates and recharge data for the period of 2010 to 2017. Fig.4 shows comparison of observed and computed groundwater elevation in the selected observation wells, namely, NJ-1, JA-2, NJ-9, EA-1, JA-5, and DE-5.

After the validation of the model, various management scenarios were studied to mitigate the seawater intrusion in Wadi Al-Jizi aquifer.

### Effect of Recharge rates on Seawater Intrusion

#### Scenario-1: Recharge rate reduction and increment

To study the recharge rates impact scenario, rainfall pattern which was followed from 2000 - 2017 was considered as baseline and an increment of recharge rates by 5% and 10% and reduction of recharge rates by 5% and 10% were considered in the baseline recharge rates of 2000- 2017 applied to the scenarios from 2018-2040. For this scenarios, base pumping rates and base sea level rise were considered and salinity intrusion contour (TDS > 12800 mg/L) which was taken as a standard measurement by the ministry was studied.

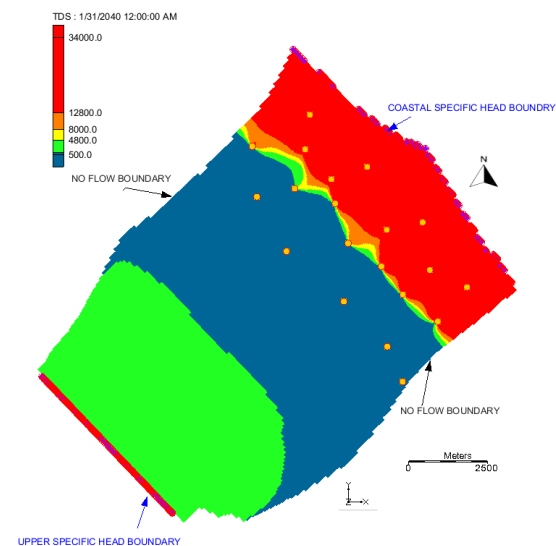


Fig.5 Salinity contours for Scenario-1 (Recharge increment by 5%) for the year 2040.

The salinity contours for the year 2040 was plotted to observe the impact of recharge rates in the study area

as shown in Fig. 5 & 6. The salinity intruded inland by an average distance of 2.71 km and 2.74 km in year 2040 by reducing the base recharge rate by 5% and 10% respectively. Similarly, having an increase in base recharge rates by 5% the salinity may retreat by 0.14 km (since the salinity intruded landward at an average distance of 2.60 km in 2040) respectively.

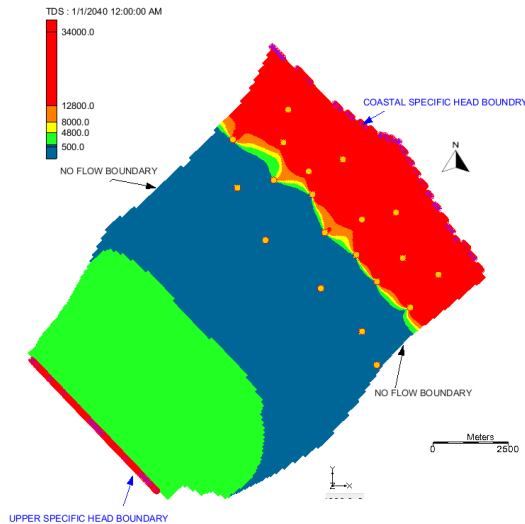


Fig.6 Salinity contours for Scenario-1(Recharge reduction by 10%) for the year 2040

#### Scenario-2: Recharge rate reduction and increment combines with Sea Level Rise

In this scenario, base pumping rates were considered, but the recharge rate has been reduced by 10% to from the base recharge rates and the Sea level rise of 0.25m and 0.50m were considered to study the impact of climate changes.

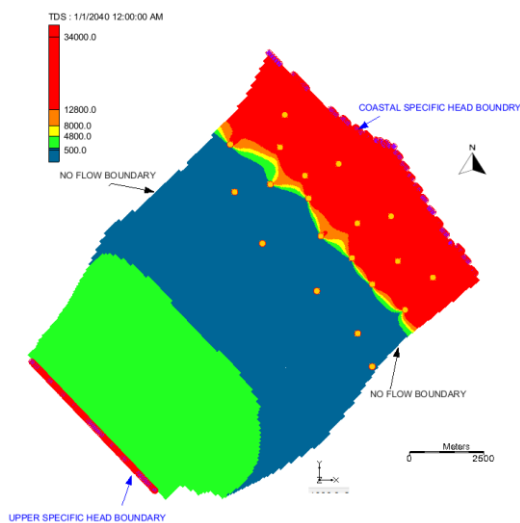


Fig. 7 Salinity contours for Scenario-2 (Recharge reduction by 10% & SLR +0.25m) for the year 2040

Fig. 7 shows the rise of 0.25 m above the baseline sea level (0.65m) combined with the reduced base

recharges rates by 10% showed that salinity intruded landward at an average distance of 2.67 km in the year 2040. A rise of 0.50 m added to the baseline sea level combined with the reduction of baseline recharge rates by 10% may result in salinity intrusion inland by 2.72 km as shown in Fig. 8.

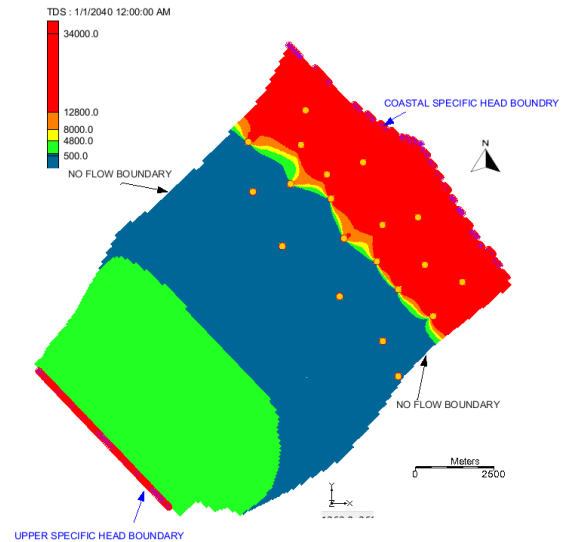


Fig. 8 Salinity contours for Scenario-3 (Recharge reduction by 10% & SLR +0.50m) for the year 2040

The distance by which the salinity may intrude inland for all the considered **eight** scenarios in the year 2040 is shown in Fig. 9.

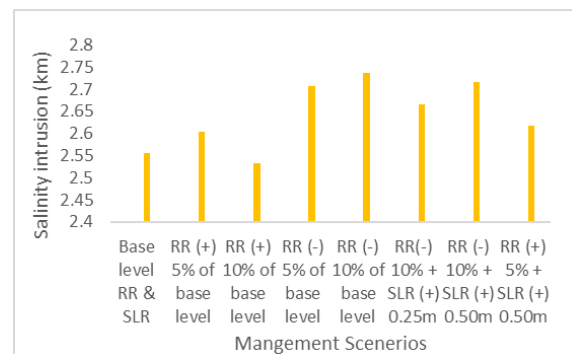


Fig. 9 Salinity intrusion distance (Year 2040) for all scenario

## CONCLUSIONS

If a numerical model is adequately calibrated using the measurements of head, pumping rates, and boundary conditions that are currently available, it can simulate and predict the head and quality of groundwater in coastal aquifers with a fair degree of accuracy and economy. A different set of measured data can then be utilized to evaluate the model using the calibrated geo-hydrological parameters. Finally, projections of groundwater quality and elevation can be produced for each future event that is anticipated. When compared to previous data, the ground water

salinity have been increased in majority of the salinity monitoring wells. Salinity intruded landward at an average distance of 2.67 km in the year 2040, as determined by a rise of 0.25 m over the baseline sea level (0.65 m) and the reduction of base recharge rates by 10%.

## ACKNOWLEDGMENTS

The authors acknowledge the Environment Authority, Sultanate of Oman for providing the groundwater elevations and quality data.

## REFERENCES

- [1] Akhtar J, Sana A, Tauseef S M, Chellaiah G, Kaliyaperumal P, Sarkar H, Ayyaperumal R, Evaluating the groundwater potential of wadi Al-Jizi, sultanate of Oman by intergrating Remote sensing & GIS techniques, Environmental Science and Pollution Research 2022, <https://doi.org/10.1007/s11356-021-17848-x>
- [2] Sana A and Al Shibli S H, Modelling of seawater intrusion into a coastal aquifer in the Sultanate of Oman”, Proceedings of 30th Congress of International Association for Hydro-Environment Research (IAHR 2003), Thessaloniki, Greece, pp.581-588.
- [3] Lakey R, Easton P, Hinai A H, Eastern Batinah Water Resources Assessment- The International Conference on Water Resources Management in Arid Countries Proceedings 1995. Muscat. Sultanate of Oman. The library of the General Directorate of Regional Municipality, Environment and Water Resources in North of Al Batinah, Sohar, Oman.
- [4] Weyhenmeyer C E, Stephen J B, Niklaus W H, Isotope study of moisture sources, recharge areas, and groundwater flow paths within the Eastern Batinah coastal plain, Sultanate of Oman, Water Resources Research 2002, Vol. 38, NO. 10, 1184, DOI: 10.1029/2000WR000149.
- [5] Al Barwani A. and Helmi T. (2006), Seawater intrusion in Coastal Aquifer: A case study for the area between As Seeb and As Suwaiq (1984–2005)”, International Conference on Economic Incentives and Water Demand Management, United Nations Education Scientific and Cultural Organization (UNESCO) 2006, France.
- [6] Al-Taani A A, Batayneh A , Mogren S , Nazzal Y, Ghrefat H, Zaman H, Elawadi E, Groundwater Quality of Coastal Aquifer Systems in the Eastern Coast of the Gulf of Aqaba, Saudi Arabia, Journal of Applied Science and Agriculture, 8(6) November 2013, Pages: 768-778.
- [7] Baalousha H M, Development of a groundwater flow model for the highly parameterized Qatar aquifers”, Model. Earth Syst. Environ. (2016) 2:67. DOI 10.1007/s40808-016-0124-8.
- [8] Shamma M. I and Jacks G., Seawater intrusion in the Salalah plain aquifer, Oman. Environmental Geological Journal 2008. DOI:10.1007/s00254-007-0673-2.
- [9] Al-Hashmi S, Gunawardhana I, Sana A, & Baawain M, Application of groundwater flow model in assessing aquifer layers interaction in arid catchment area, International Journal of Environmental Science and Technology, 2020 <https://doi.org/10.1007/s13762-020-02805-x>.
- [10] Al-Maktoumi A, Zekri S, El-Rawy M, Abdalla O, Al-Wardy M, Al-Rawas G. & Charabi Y, Assessment of the impact of climate change on coastal aquifers in Oman, Arabian Journal of Geosciences 11: 501. 2018. <https://doi.org/10.1007/s12517-018-3858-y>.
- [11] Chitrakar P and Sana A, Ground Water Flow and Solute Transport Simulation in Eastern Al Batinah Coastal Plain, Oman: Case Study”, Journal of Hydrologic Engineering, ASCE. ISSN: 1084-0699/050150020 (11).
- [12] Chun J A, Lim C, Kim D and Kim J S, Assessing Impacts of Climate Change and Sea-Level Rise on Seawater Intrusion in a Coastal Aquifer, Water 2018, 10, 357; doi:10.3390/w10040357
- [13] Ghazaw YM, Gumman A R, Al-Salamah I & Khan Q U Z, Investigations of Impact of Recharge Wells on Groundwater in Buraydah by Numerical Modeling, Arab J Sci Eng 2014, 39:713–724.DOI 10.1007/s13369-013-0690-2.
- [14] Dibaj M, Javadi A A, Akrami M, Ke K Y, Farmani R, Tan Y C & Albert S. Chen, Modelling seawater intrusion in the Pingtung coastal aquifer in Taiwan, under the influence of sea-level rise and changing abstraction regime, Hydrogeology Journal 2022.
- [15] EL Hamidi M.J., Larabi A and Faouzi M, Numerical Modeling of Saltwater Intrusion in the Rmel-Oulad Ogbane Coastal Aquifer (Larache, Morocco) in the Climate Change and Sea-Level Rise Context (2040), Water 2021, 13, 2167. <https://doi.org/10.3390/w13162167>.
- [16] McDonald M G and Harbaugh A W, A modular three-dimensional finite difference groundwater flow model technique of water resources investigations of United States geological survey (2000), Vol. 6, USGS, Denver, 586.
- [17] Zheng C, & Wang P P, MT3DMS:Transport Model for Simulation of Advection, Dispersion, and Chemical Reactions of Contaminants in Groundwater Systems; Documentation and User's Guide, 1999, Vicksburg, Mississippi: United State Army Corps of Engineers.
- [18] Akhtar, J., Sana, A. and Tauseef, S.M., Using MODFLOW to Investigate the Effect of Persistent Water Deficit in Al-Jizi Coastal Aquifer, Sultanate of Oman, Arabian Journal of Geosciences 2022. (In press)

# **SIMULATION OF SMOKE DISPERSION AND TEMPERATURE DISTRIBUTION ON KEBON MELATI SUB-DISTRICT FIRE USING COMPUTATIONAL FLUID DYNAMICS**

Deffi Ayu Puspito Sari<sup>1</sup>, Agnes Setioningrum<sup>1</sup>, Dani Harmanto<sup>2</sup>

<sup>1</sup>Environmental Engineering, Universitas Bakrie, Indonesia; <sup>2</sup> Aeronautical Engineering, De Montfort University, United Kingdom

## **ABSTRACT**

Kebon Melati sub-district is one of the most populous sub-district in DKI Jakarta with three cases of dense settlement fire the last twenty years. Those fire cause fire smoke dispersion and fire propagation as secondary impact. The aim of this research is to analyze fire smoke dispersion pattern and temperature distribution pattern around hotspots, also to analyze potential area that has to encounter those secondary impacts. Google Maps, AutoCAD 2015, Revit 2015, Autodesk Flow Design 2015, and Fire Dynamics Simulator are used in this research for modeling of fire and studying area geometry. Autodesk Flow Design 2015 simulation result wind flow in the west side of Kebon Melati sub-district is more stable than in the east and middle side which have wind flow turbulence as effect of wind flow separation by skyscraper buildings. On the outer west side of Kebon Melati sub-district, wind velocity increase up to 9 m/s as effect of wind flow separation by skyscraper buildings. Fire Dynamics Simulator simulation result, in 30 s simulation with 10.000 kW/m<sup>2</sup> Heat Release Rate per unit Area, fire smoke disperse up to 1.440 m in South direction. The south side of Kebon Melati sub-district is more vulnerable in degradation of visibility, fire smoke concentration enhancement, and fire propagation.

*Keywords: smoke dispersion, fire, CFD, temperature distribution, Fire Dynamics Simulator*

## **INTRODUCTION**

Jakarta, the Capital of Indonesia, has dense population that increase every year. One of problems appear from densely populated settlements is fire case. Cases of fire that occur on densely populated settlements can come from human error factors (human activities) (Ismawan, 2008).

Based on the fire history data by DKI Jakarta Province Fire and Rescue Service, many cases of fire in Jakarta caused by short-circuit electricity. One of the most densely populated areas that are prone to fire is Kebon Melati Sub-district, located in Tanah Abang District, Central Jakarta. In the last twenty years, there have been three cases of fire in Kebon Melati Sub-district.

In DKI Jakarta 2030 Regional Spatial Plan (RTRW), DKI Jakarta government maps Kebon Melati area as a middle-class vertical residence that combines inspection roads, green open spaces, and adequate transportation rates to Tanah Abang Market. That plan was formed because the government's target to make Tanah Abang a center for world trade (Transformasi, 2015).

## **OBJECTIVE**

The purpose of this study was to determine and explain smoke dispersion patterns and temperature distribution patterns in Kebon Melati Sub-district fire simulations using Computational Fluid Dynamics (CFD). In addition to knowing the smoke dispersion patterns and temperature distribution patterns in fire simulation, also determined factors related to smoke dispersion

patterns and temperature distribution patterns. So that it can be predicted in areas that will experience air pollution due to fire smoke dispersion and areas prone to fire propagation in Kebon Melati Sub-district.

## **METHODOLOGY**

In analyzing Kebon Melati fire case, the Computational Fluid Dynamics (CFD) method can be used to produce information about fluid flow and heat transfer patterns on fire conditions in Kebon Melati Sub-district. CFD is one of the numerical methods in fluid mechanics which basically uses the philosophy of discretization as an approach in solving mathematical equations. The use of CFD is very useful in virtual prototype analysis of a system or tool that will be analyzed by applying real conditions in the field (Pasha, 2011).

According to Tuakia (2008), Computational Fluid Dynamics/ CFD is the study of how to predict fluid flow, heat transfer, chemical reactions, and other phenomena by solving mathematical equations (mathematical models).

According to Mahan (2009), in general, the simulation process in CFD is divided into three stages, preprocessing, solving, and post processing. The previous step calculation results are interpreted into several forms including graphs, curves, animations, 2D and 3D images.

Preprocessing is the first step in a simulation that is making a preparation of building's geometry model in the form of CAD (Computer Aided Design), creating a grid or mesh, and determining

the boundary conditions of the geometry. Solving is the calculation process and the equations contained in the CFD model are solved using a computer program in accordance with the conditions that have been determined during preprocessing before.

Postprocessor displays visualizations including:

- 1.the results of geometry and cells that have been formed;
- 2.plots based on vectors;
- 3.contour based plots; and
- 4.plot based on the surface (two dimensions or three dimensions) (Marihot, 2015).

One of the CFD method modeling programs in fire simulation is Fire Dynamic Simulator (FDS). FDS is a CFD method modeling program for fluid flow with buoyancy style (McGrattan, Hostikka, McDermott, Floyd, Weinschenk, & Overholt, 2013).

FDS was developed by the National Institute of Standards and Technology (NIST) in collaboration with the VIT Technical Research Center of Finland, and other communities engaged in the field of fire safety. In visualizing the results of programming, FDS is continuous with the Smokeview program. Both programs are free and open-source accessible on the official NIST website.

FDS completes basic mass conservation, momentum equations, and energy for thermal expansion, as well as ideal gases with various mixture components. FDS applies the Large Eddy Simulation (LES) and Direct Numerical Simulation (DNS) turbulent models (Hu et al., 2011).

In its program, FDS requires a basic input line including building geometry, computational cell size, the location of the fire source, heat release rate (HRR) of the fire source, physical properties and thermal properties of the wall, as well as the size, location and time of ventilation. will affect the growth and spread of fire. (Barowy and Madrzykowski, 2012).

The study area in this simulation is Kebon Melati Sub-district, Tanah Abang District, Central Jakarta. The research methodology can be observed in Figure 1.1. The retrieval of meteorological data in the form of dominant wind direction and velocity data was carried out in November 2017. Three weeks of data collection was the dry season, and the last one week of data collection was the rainy season. The meteorological data obtained was validated with BMKG meteorological data (the Meteorology, Climatology and Geophysics Agency) in November 2017 which can be accessed through the official BMKG website. Data analysis techniques used are quantitative data analysis techniques by Computational Fluid Dynamics (CFD) simulation method.

The software used in this study includes Microsoft Office 2010, Microsoft Excel 2010, AutoCAD 2015, Revit 2015, Autodesk Flow

Design, Fire Dynamics Simulator. In this study, the AutoCAD 2015 license, Revit 2015, and Autodesk Flow Design were obtained by educational licenses that have 3 years of validity period.

Meteorological data analysis techniques were obtained using Microsoft Excel 2010 to determine the distribution of dominant wind direction and velocity in the form of tables and charts of Wind Rose. The analysis phase was also carried out to determine the flow pattern and temperature distribution and air rate around the fire simulation location. Analysis of flow patterns and temperature distribution and air velocity are obtained through CFD simulation methods.

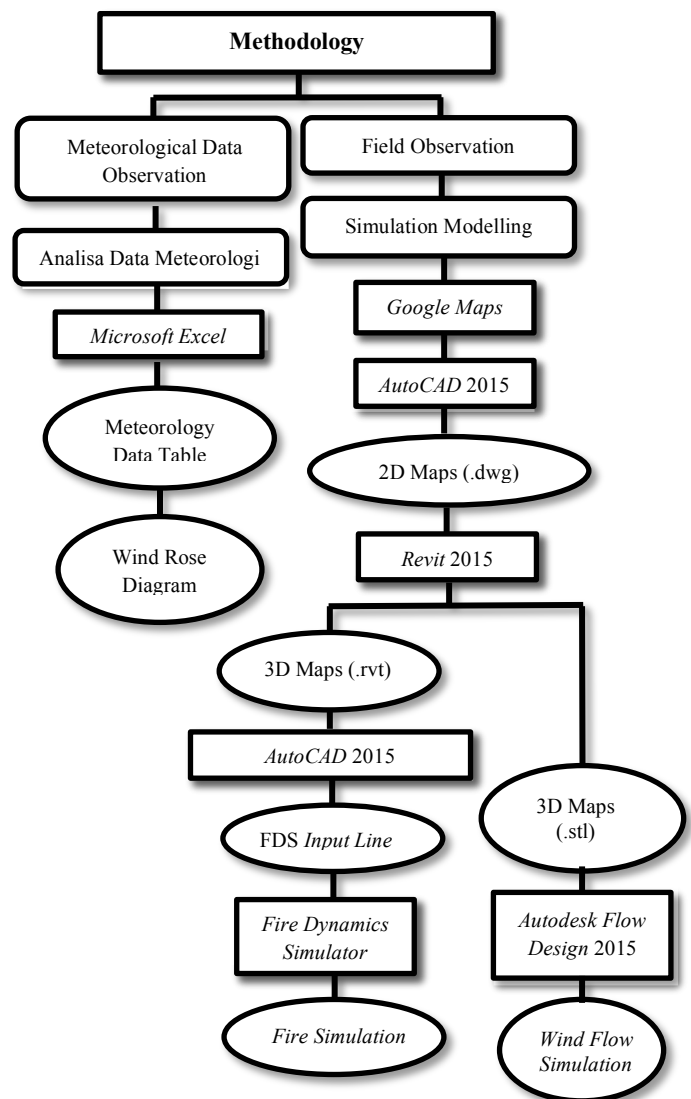


Figure 1.1 Research Methodology

The first stage in CFD simulation is the creation of location geometry obtained by Google Maps and converted in the form of two-dimensional (2D) line sketches using AutoCAD 2015 with 1:26 scale. The sketch of 2D lines was converted back into three-dimensional (3D) sketches using Revit 2015. The types of buildings in Revit 2015 modeling were divided into three types of building models, slums, simple houses, and high-rise buildings. The determination of the three types of buildings is based on field observations that have been carried out. Slum houses concentrated on the West side of Kebon Melati Sub-district. Multi floor buildings are concentrated in parts of the North and East sides, while simple houses are spread on the North, Central and South sides of Kebon Melati Sub-district.

At Revit 2015, building lines are converted into walls of varying types and heights. The walls of the slums are made of wood or plywood, while the walls of simple houses are made of brick material, and the walls of high-rise buildings are made of concrete.

The wall thickness of slums and simple houses in Revit 2015 software modeling is 0.1016 meters and the wall thickness of high rise buildings is 0.2032 meters. Variations in the type and thickness of the walls of the building can be arranged in the Properties column of each wall. In the case of slums, there is no variation in the number of floors of buildings, slum houses only have one floor of the building. Whereas a simple house building has a variety of building floors, one-floor building, and two-floors building. Multi floors building have variations in the number of floors, namely three floors to twenty floors. The height of each floor of the building is 3 meters and is set on the Revit 2015 leveling process.

After finishing 3D geometry, it exported into Fire Dynamics Simulator. In modeling FDS software, there are several input data that need to be prepared. The input data includes building property data in the form of building geometry and its constituent material, meteorological data in the form of wind direction and wind velocity, desired output parameters, ambient state of the environment in the simulation domain.

Setting the ambient state in the simulation domain includes mesh settings, wind velocity and wind direction, combustion reactions that will cause sparks in the simulation, starting point of fire and fire strength, and the desired simulation Mesh used has an X-axis that extends from the North side to the South side by 76 units, the Y-axis that extends from the Westside to the Eastside extends for 72 units, and 4 units of Z-axis. X and Y mesh axes have a unit value of 0.25 m, while the Z-axis has a unit value of 0.1667 m. So that the total dimensions of the mesh in this simulation are 18 m x 19 m x 4 m.

FDS operations require a very large computer storage capacity in large-scale geometry modeling.

Therefore the 3D sketches that have been formed are scaled down to a scale of 1: 12,000 using Revit 2015. Fire Dynamics Simulator will also obtained room scope fire simulation with fire-triggering specifications, the type and utilization of burned buildings.

Through Fire Dynamics Simulator, we can obtain temperature distribution patterns on burned objects and in the surrounding objects. In determining the fire smoke dispersion pattern, 3D geometry is exported to the Autodesk Flow Design program for further modeling with specifications of wind direction and velocity.

## RESULTS

Fire simulations were carried out at five different points in Kebon Melati Sub-district, as in Figure 1.2. The four points are determined with the assumption that they represent the four cardinal directions, namely North, East, South, West and one point in the middle of Kebon Melati Sub-district. Based on the field observations that have been carried out, the types and shapes of the buildings at the five points are divided into three types of buildings namely slum houses, simple houses, and high-rise buildings.

Point 1 on the north side and Point 3 on the south side of Kebon Melati Sub-district represents simple house buildings. Point 2 on the middle side and Point 4 on the east side of Kebon Melati Sub-district represents high-rise buildings, according to the observations that have been made. While Point 5 on the west side of Kebon Melati Sub-district represents slums.

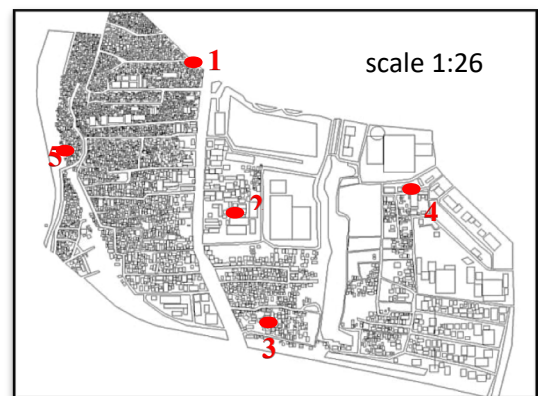


Figure 1.2 Meteorological Data Observation Points and Fire Simulation Points

Observation of meteorological data in the form of measurements of velocity and wind direction observations carried out for one month in November 2017, the first three weeks are the dry season and the last one week is the rainy season. Wind measurements carried out at five measurement points were analyzed using Microsoft Excel in the form of simple Wind Rose tables and diagrams formed from Radar type diagrams. Observations of meteorology data can be observed in Table 1.1.



Table 1 Meteorological Data of Five Observation Points

Date	Wind Velocity (m/s)					Wind Direction
	Location (Points)					
	1	2	3	4	5	
1	2.1	2.6	2.6	2.2	2.0	SBD
2	1.0	1.3	1.1	0.7	0.8	S
3	2.1	2.4	2.2	1.9	1.9	S
4	0.8	1.5	1.4	0.9	0.8	Ti
5	1.9	1.7	2.1	2.4	1.9	SBD
6	1.9	2.5	2.0	1.7	1.1	S
7	3.5	2.8	2.8	3.1	3.4	SBD
8	1.5	1.3	0.9	1.5	1.1	S
9	0.8	1.7	1.4	1.2	0.9	Te
10	2.4	2.2	2.4	1.9	1.9	S
11	1.5	1.8	2.0	1.7	1.5	S
12	2.0	1.9	2.1	2.4	1.9	ST
13	2.2	2.6	2.6	2.2	2.0	ST
14	1.5	2.5	2.1	1.7	1.1	Te
15	2.3	2.8	2.8	2.2	2.4	Ti
16	1.1	1.7	1.5	1.1	1.5	BD
17	2.2	2.3	2.1	1.7	1.8	TL
18	1.1	0.7	1.1	1.4	0.9	TT
19	0.8	0.8	0.8	1.1	1.0	SBD
20	2.2	2.2	2.5	1.9	1.9	ST
21	2.5	1.9	2.1	2.4	1.9	TTL
22	1.9	1.7	1.4	1.8	1.8	Ti
23	2.1	2.5	2.5	2.1	2.4	Te
24	3.6	3.6	3.2	2.6	2.9	TL
25	5.1	4.3	4.3	3.9	4.6	TTL
26	5.4	5.0	4.4	4.4	4.5	TTL
27	6.1	6.2	5.9	5.3	6.2	TL
28	5.5	5.5	4.8	5.1	5.4	TL
29	4.3	4.5	4.6	4.2	4.2	TTL
30	3.8	4.0	3.8	3.5	3.5	TTL
Av.	2.51	2.62	2.52	2.34	2.31	

Note:

BD = Southwest

S = South

SBD = South Southwest

ST = South Southeast

Te = Southeast

Ti = East

TL = Northeast

TT = East Southeast

TTL = East- Northeast

In the last week of measurement, there was an increase in wind velocity blowing in Kebon Melati Sub-district. This is caused by the transition of the season between the dry season to the rainy season

the following month. The measured wind velocity converted in the form of a simple Wind Rose diagram. The Wind Rose diagram in this study is a diagram that illustrates the distribution of wind velocity and wind direction distribution based on the number of events.

In the wind velocity conversion process of Wind Rose diagram data in Graph 1.1, wind velocity grouped and the frequency of occurrence calculated based on sixteen wind directions. The grouping of wind velocity is divided into six groups of velocity with a velocity range of each group of 1 m/s.

The wind group consists of groups with wind velocity range of 0 m/s to 1 m/s, groups with wind velocity range of 1 m/s to 2 m/s, groups with wind velocity range of 2 m/s to 3 m/s, groups with wind velocity range of 3 m/s to 4 m/s, groups with wind velocity range of 4 m/s to 5 m/s, and groups with wind velocity of more than 5 m/s.

Combined Wind Rose Diagram of five observation points in Graph 1.1 shows that in November 2017 the average wind observed at five observation points tends to blow towards the South with wind velocity of 1 m/s to 2 m/s. This trend is obtained from the observation of the number of events during November 2017, twenty incidents of wind gusts towards the South with wind velocity of 1 m/s to 2 m/s. So that is determined the wind flow modeling in Autodesk Flow Design is carried out with wind direction control to the South with 2 m/s wind velocity.

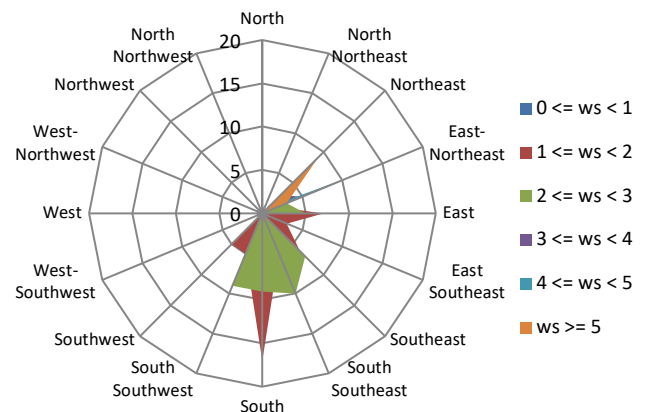


Fig. 1 Wind Rose Diagram of Five Observation Points

Note: ws = wind speed (m/s)

Kebon Melati Sub-district area modeling begins with a depiction of a line sketch map of Kebon Melati Sub-district area obtained from Google Maps. The map of area was redrawn with the Rectangle and Polyline commands in the AutoCAD 2015 so that the final results in the form of a line sketch map of the Kebon Melati Sub-district area, as in Figure 1.3. The sketch is then processed into a three-dimensional sketch with the help of Revit 2015.

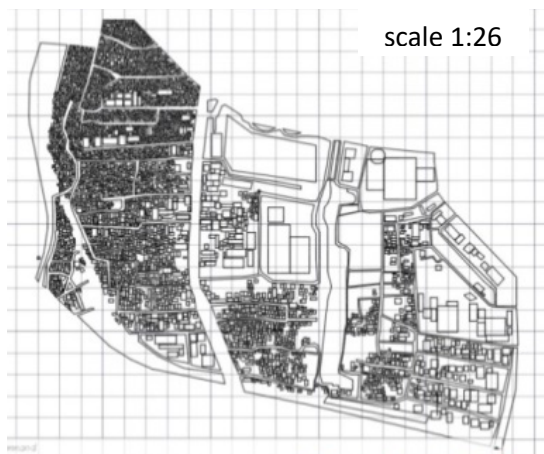


Figure 1.3 AutoCAD 2015 Results

In Revit 2015, building lines are converted into building's wall with varying types and heights. The walls of the slums are made of wood or plywood, while the walls of simple houses are made of brick material, and the walls of high-rise buildings are made of concrete. The height of each floor of the building is 3 meters and is set in Revit 2015 leveling process. The three-dimensional conversion results can be observed in Figure 1.4, as follows.

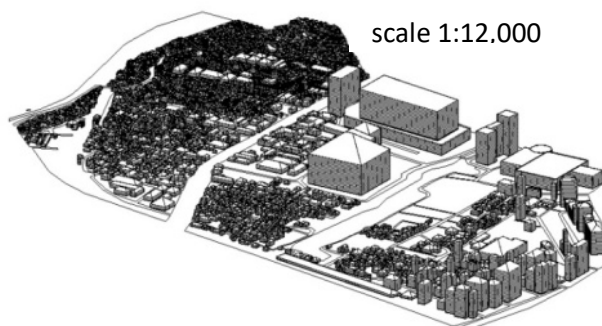


Figure 1.4 Revit 2015 Modeling Results

Autodesk Flow Design's modeling produces wind flow model with 2 m/s of velocity to the South. Modeling is limited to the observation of velocity and wind flow patterns. The fluid modeling used is the Flow Line model with fluid lines and tubes line type to facilitate the observation of the fluid flows pattern in the form of elongated lines.

Top side observation aims to observe the pattern of wind flow horizontally at different heights. Top side observation results can be observed in Figure 1.5 and Figure 1.6. Observation variations of height include wind flow at altitudes below 3 meters (low) and wind flow with altitudes more than 3 meters (high).

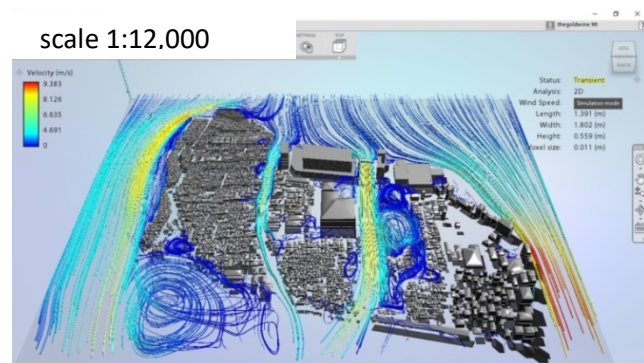


Figure 1.5 Low Wind Flow Modeling

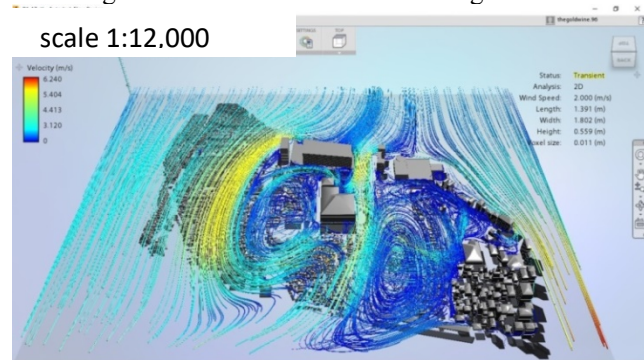


Figure 1.6 High Wind Flow Modeling

Based on these two modeling, several color lines can be observed. The difference in the color of the line illustrates the different of wind velocity. The red line shows the highest wind velocity while the dark blue line shows the lowest wind velocity, which is close to 0 m/s on the Southwest side of Kebon Melati Sub-district. Modeling with wind flow altitude variations caused differences of wind velocity range despite of equal initial wind velocity, which is 2 m/s. In modeling with low altitude, the largest wind velocity reached 9 m/s, which is on the eastern side of the Kebon Melati Sub-district. This velocity occurs as a result of the wind flow deflection in the area that has tight distance between buildings.

The largest wind velocity in modeling with high wind flow altitudes only reach 6 m/s, with the same flow location as low wind flow altitude modeling. The deceleration of wind velocity is due to the difference in building height in the area with the distance between buildings that are quite tight. The difference in height of the building causes a gap that allowed the wind to flow so that the wind flow hits the area is not completely deflected. The lowest wind velocity can be observed in the area surrounded by high-rise buildings on the Middle side of Kebon Melati Sub-district, with the turbulence of wind flow forming a circular flow pattern.

In accordance with Hosker analysis in Alamos et al. (2004), buildings can change wind flow fields and ward off wind flow, causing wind flow to rise and wind flow to fall, horizontal and vertical vortices between buildings, on street corners, and other places on the Urban Canopy Layer. The wind flow pattern produced is also in accordance with the research conducted by Oke (1988) and Grimmond (2002).

The wind flow around the building is broken down at the side of the building. In both models, turbulence can also be observed in the form of a circular flow pattern in an area that is lower than the height of the building. This turbulence occurs with lower wind velocity compared to deflected wind velocity. In accordance with the experiments conducted by Hoydysh in Alamos et al. (2004) wind flow on the street canyon forms a vertical vortex pattern paralleled with the axis to the street canyon and affects pollutant concentration on street canyon and ventilation outside the street canyon.

Side viewpoint modeling, the East side of Kebon Melati Sub-district, aims to observe the pattern of wind flow vertically in different building types. Variations in this modeling are carried out with variants of high-rise buildings, slums and simple buildings.

The largest wind velocity generated from two models has a slight difference. The largest wind velocity range in variants of high-rise buildings is higher than the variants of the slums and simple buildings. The largest wind velocity occurs when the coming wind hits the building so that the wind flow deflected toward the building.

In contrast to the research conducted by Ozmen, Baydar, and van Beeck (2016) on low-rise buildings, in this FDS simulation, the roofs of slums and simple buildings that have low building height are planar shaped so that the recirculation area produced due to the sharpness of the roof cannot be observed. clearly.

Figure 1.7 shows modeling with variants of building heights. In this modeling, turbulence can be observed in areas covered by buildings from wind exposure. Turbulence is in the form of a flow line that rolls up at a velocity lower than the velocity of the wind that hits building. This phenomenon is in accordance with the research conducted by Grimmond (2002), the wind flow pattern in the Urban Canopy Layer (low altitude area with several buildings as a barrier), will experience turbulence in the form of circular flow patterns due to interaction with the barrier. The circular flow pattern can increase pollutant concentration on the street canyon. The flow will be stable in the Inertial Sublayer that is above the Urban Canopy Layer area due to the absence of buildings that cause deflection interaction of wind flow.

scale 1:12.000

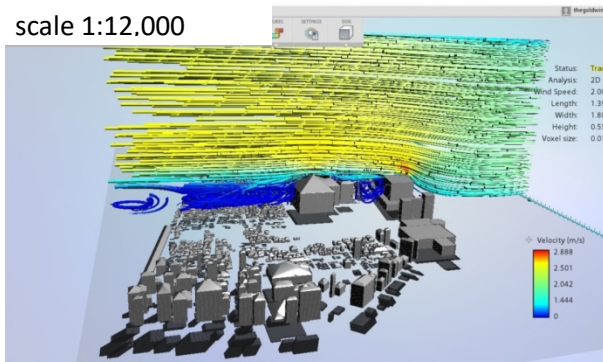


Figure 1.7 Wind Flow Modeling on Different Height of Building

In the high-rise buildings modeling, turbulence can be observed between its gaps. Turbulence forms a circular flow pattern with wind flow velocity up to 1 m/s. The turbulence of air flow can increase pollutant concentrations in street canyon. Increased flow velocities in streams with altitudes exceeding the height of high rise buildings occur due to the upward flow of wind flow by high rise buildings. The highest wind flow velocity reaches 2.8 m/s which is at the point of wind flow deflection by high-rise buildings, illustrated by the red line

Wind flow velocity and flow pattern in slums and simple house buildings modeling are more stable and constant than high-rise buildings modeling. This can be observed in Figure 1.8. The biggest velocity reaches 2.4 m/s on deflected wind flow after hit the outermost building from the direction of the wind coming. The velocity is represented by a red line. Wind velocity between slums and simple buildings is only between 0 m/s to 1.2 m/s. While the wind velocity at high altitude (more than 3 m) reaches 2.2 m/s which is depicted with a yellow line.

scale 1:12,000

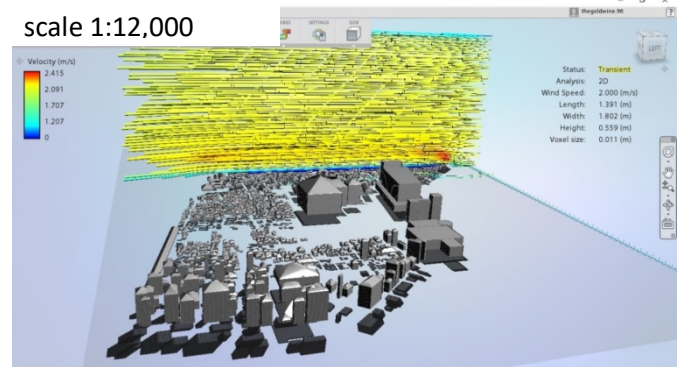


Figure 1.8 Slums and Simple Buildings Wind Flow Modeling

After obtaining Autodesk Flow Design modeling, the three-dimensional sketches generated from Revit 2015 software are also stored in drawing format (.dwg) that supported by AutoCAD 2015 software. These three-dimensional sketches are converted in the form of input lines that correspond to the Fire Dynamic Simulator (FDS) format. The conversion is done with the 3dsolid2fds command line in the AutoCAD 2015 software which was developed separately from the software.

In FDS modeling, there are several input data that need to be prepared. These input data includes building properties in the form of building geometry and its constituent material, meteorological data in the form of wind direction and wind velocity data, desired output parameters, ambient state of the environment in the simulation domain.

The mesh used has X dimension that extends from the North side to the South side for 72 units, the Y dimension extending from the Westside to the East side which extends along 76 units, and the



Z dimension representing mesh height for 4 units. The geometry of the building and its constituent material has been determined in the previous 3dsolid2fds conversion. The geometry of the simulation area can be observed in Figure 1.9.

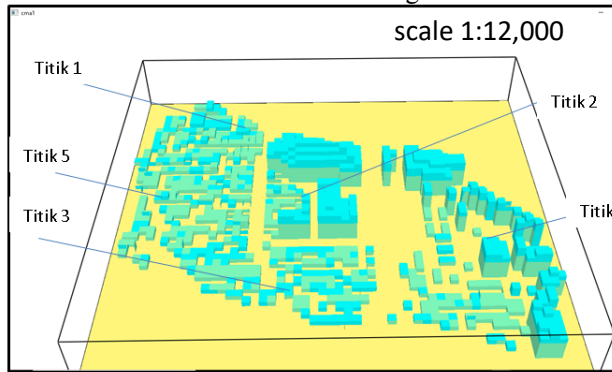


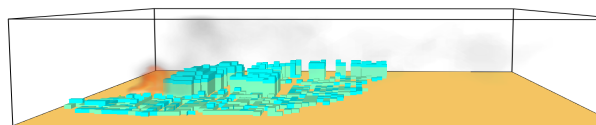
Figure 1.9 Five Observation Points Geometry

At Point 1, Point 3, and Point 5, the starting point of the fire (hotspots) is simulated on a flat plane located at the top of each building. Unlike the research conducted by Lin et al. (2016), hotspots in this simulation building are carried out on the roof of a building that has direct contact with the wind flow.

Based on Barowy and Madrzykowski (2012) complex physical and chemical modeling in electrical short circuit case occurs on smaller modeling scale than the computational cell size used in FDS simulations. So in this simulation, the source of the fire is from the planar plane on the top side of the building.

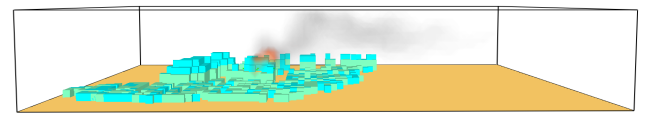
Fire simulations in FDS software can only be run on fire generated by a chemical reaction in each simulation. The reaction can only be processed on a flat plane that has been determined its surface constituent material. Results of five fire simulation points can be observed in Figure 1.10. Fire simulations are carried out within a period of 30 seconds. In this period of time, the smoke flow and radiation patterns around the simulation point can be clearly observed.

Fire and fire smoke parameters from time to time are then studied by FDS. In contrast a study conducted by Wahono (2008), with 700 kW/m<sup>2</sup> of Heat Release Rate per small area unit (HRRPUA) and ignition time of 35 seconds. The fire simulation in this study uses 10,000 kW/m<sup>2</sup> of HRRPUA. The amount of HRRPUA determines the magnitude of the starting point (hotpoint) of the simulated fire, and the period of time determining the duration of the burning time. The use of large HRRPUA is intended to facilitate visualization of the dispersion of smoke produced.



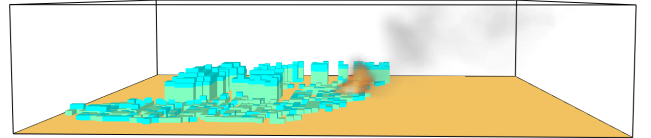
scale 1:12,000

(a) North Point



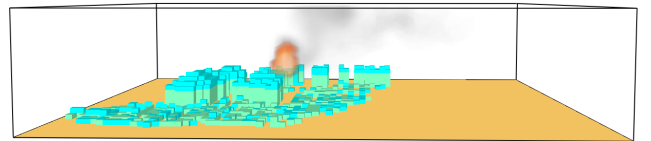
scale 1:12,000

(b) Middle Point



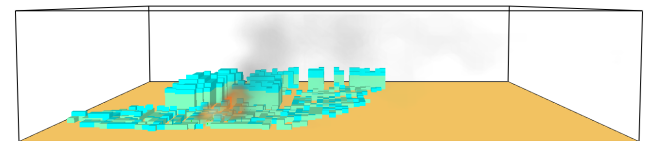
scale 1:12,000

(c) South Point



scale 1:12,000

(d) East Point



scale 1:12,000

(e) West Point

Figure 1.10 Five Points Fire Simulation Visualization

Based on the visualization of the five fire points, it can be observed that the resulting fire and the smoke produced are quite large. The resulting smoke interacts with the force produced by the wind flow that blows from the North to the South by 2 m/s. This is in accordance with previous research conducted by Sujatmiko et al. (2017), the continuity of combustion is determined by the availability of oxygen which is affected by openings or ventilation around the fire point.

These interactions cause fire smoke dispersions that are more likely disperse to the south side of the fire point. In accordance with the wind flow modeling in Autodesk Flow Design, the resulting fire smoke dispersion flow pattern is quite stable in areas with slums and simple houses. Fire smoke also tends to move upward, with altitude exceeding the height of the fire point. The fire smoke dispersion of the five simulation points reached a distance of 1,440 m to the south within 30 seconds of simulation.

This was also observed in the simulation of Point 2 and Point 4 above the high-rise building. Fire smoke does not experience turbulence as in

the Urban Canopy Layer, smoke tends to move up towards the south. So the potential dispersion of fire smoke concentrated in areas with high building density area on the south side of the fire point is not too significant.

In research conducted by Hu et al. (2011) scenario of fire with critical wind velocity, fire smoke will be circulated back to street canyon so that it can endanger pedestrians and potentially cause traffic accidents due to reduced visibility by smoke soot. However, these pollutant fumes can generally be released from street canyon with the help of buoyancy of smoke with strong fire source's buoyancy or at relatively weak wind velocity.

Visualizing the temperature distribution around the fire point, in Figure 1.11, it can be observed that the increase in temperature does not only occur at its hotspot, but also around the point of fire. The highest temperature in buildings in the North Point and the South Point reaches a temperature of  $307^{\circ}\text{C}$  and the wind that interacts with the fire produces a temperature distribution up to  $125^{\circ}\text{C}$  to the south of the fire point. The fire simulation of high-rise building in the Middle Point produced the highest temperature of  $570^{\circ}\text{C}$  and the wind that interacted with the fire caused a temperature distribution up to  $130^{\circ}\text{C}$  to the south of the fire point. The pattern of fire smoke dispersion at the Middle Point is more likely to move upwards so that the distribution of air temperature towards the south does not take a long period of time.

While the fire simulation at the East Point produces the highest temperature of  $770^{\circ}\text{C}$  with a temperature distribution up to  $170^{\circ}\text{C}$  to the south of the fire point. That was the highest temperature produced in all five fire simulations. The achievement of the temperature distribution is caused by the location of the hotspots above the upper floor of a high-rise building in high-rise buildings area. The wind flow that hit the hotspots has a constant flow because there is no turbulence produced on the Urban Canopy Layer. The highest temperature produced in the fire simulation West Point only reaches  $420^{\circ}\text{C}$  with  $140^{\circ}\text{C}$  to the south of the fire point.

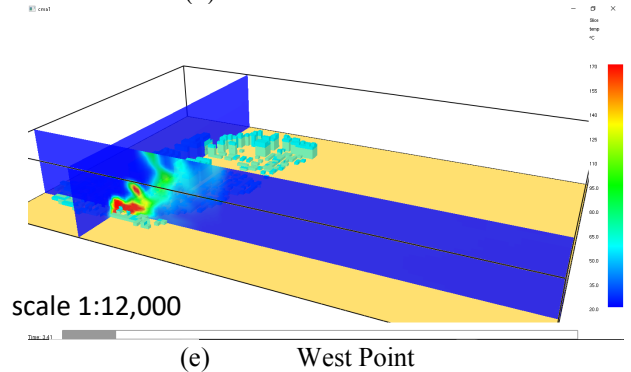
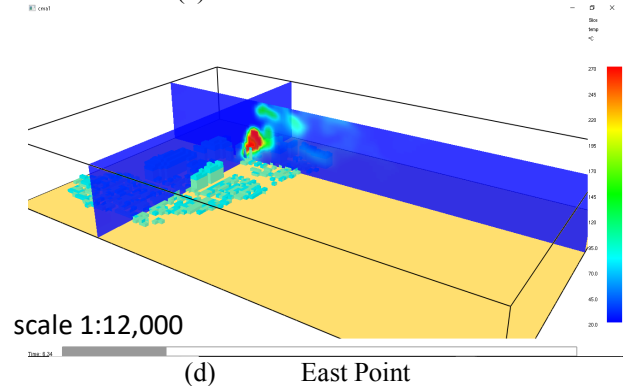
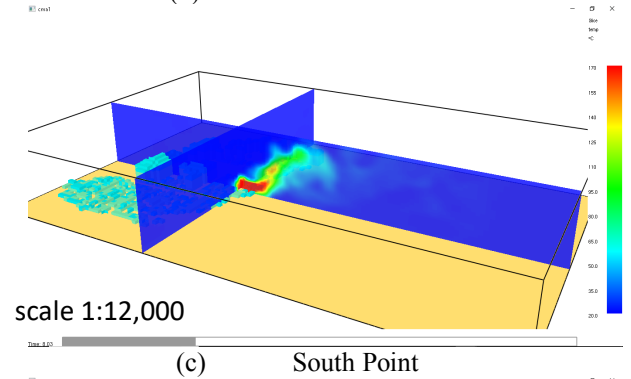
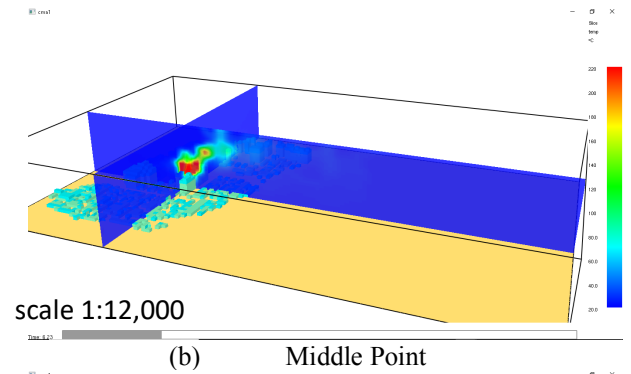
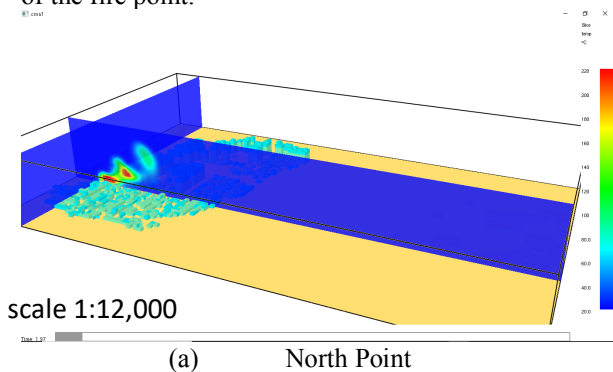
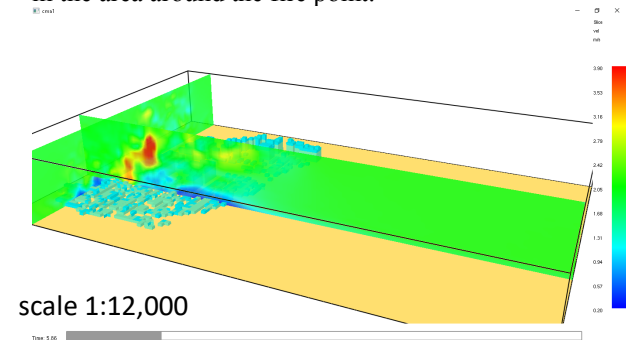


Figure 1.11 Temperature Distribution Visualization of Five Points Simulations

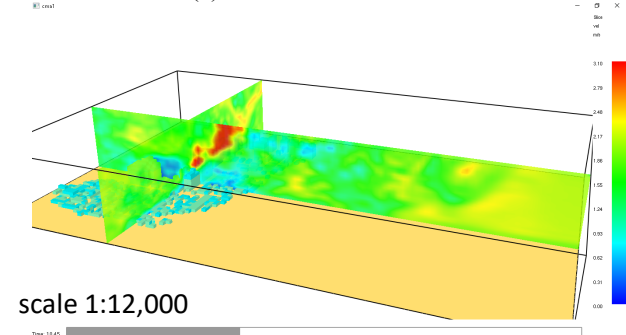
Visualization of wind velocities distribution around the focal point of the five fire simulations can be observed in Figure 1.12. In the simulation of the North Point and the West Point, there is an increase in wind velocity up to  $3.6\text{ m/s}$  with the distribution of wind velocity reaching  $2.2\text{ m/s}$  at the beginning of the simulation. Until the end of the simulation, there is a decrease in velocity up to  $0.45\text{ m/s}$ , high wind velocity are only distributed around the hotspots.

The increase in wind velocity at the South and Central Points only reached  $3.5\text{ m/s}$  with a wind

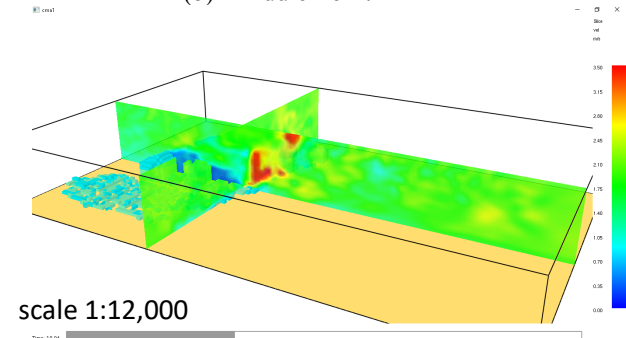
velocity distribution reaching 2.1 m/s. While the simulation at the East Point experienced an increase in velocity up to 3.0 m/s with a distribution of wind velocity reaching 1.8 m/s. There was no significant difference in the pattern of wind velocity distribution in the five simulations of the fire. The high wind distribution at the beginning of the simulation is caused by the initial wind velocity of 2 m/s used in the FDS simulation blowing at the beginning of the simulation. Until a certain time the wind exhaled has decreased velocity causing an increase in wind velocity only in the area around the fire point.



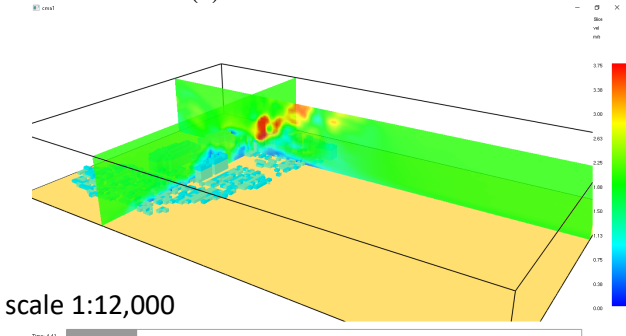
(a) North Point



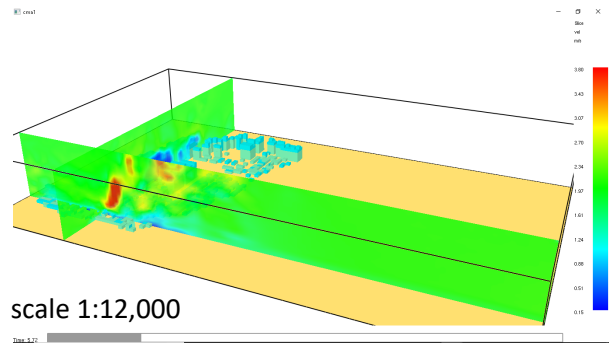
(b) Middle Point



(c) South Point



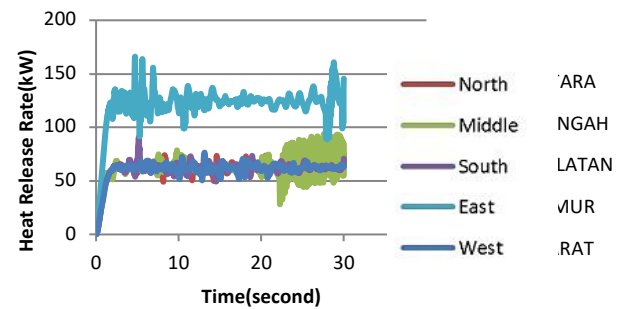
(d) East Point



(e) West Point

Figure 4.12 Wind Velocity Visualization around Five Simulation Points

Graph 1.2 shows the comparison of the rate of heat release at the North Point, Middle Point, South Point, East Point, and West Point of fire simulations. The graph shows the tendency of increasing the rate of heat release the same at the beginning of the fire. But after passing a certain time, the rate of combustion in the East Point increased more sharply than the other four points.



Graph 1.2 Heat Release Rate of Five Fire Simulations

In the research conducted by Sujatmiko et al. (2017) in Rusunami buildings, the higher the wind blows, the higher Heat Release Rate produced. East Point with fire simulation on the top floor of high rise buildings has a higher level of exposure to wind and oxygen than the other four points.

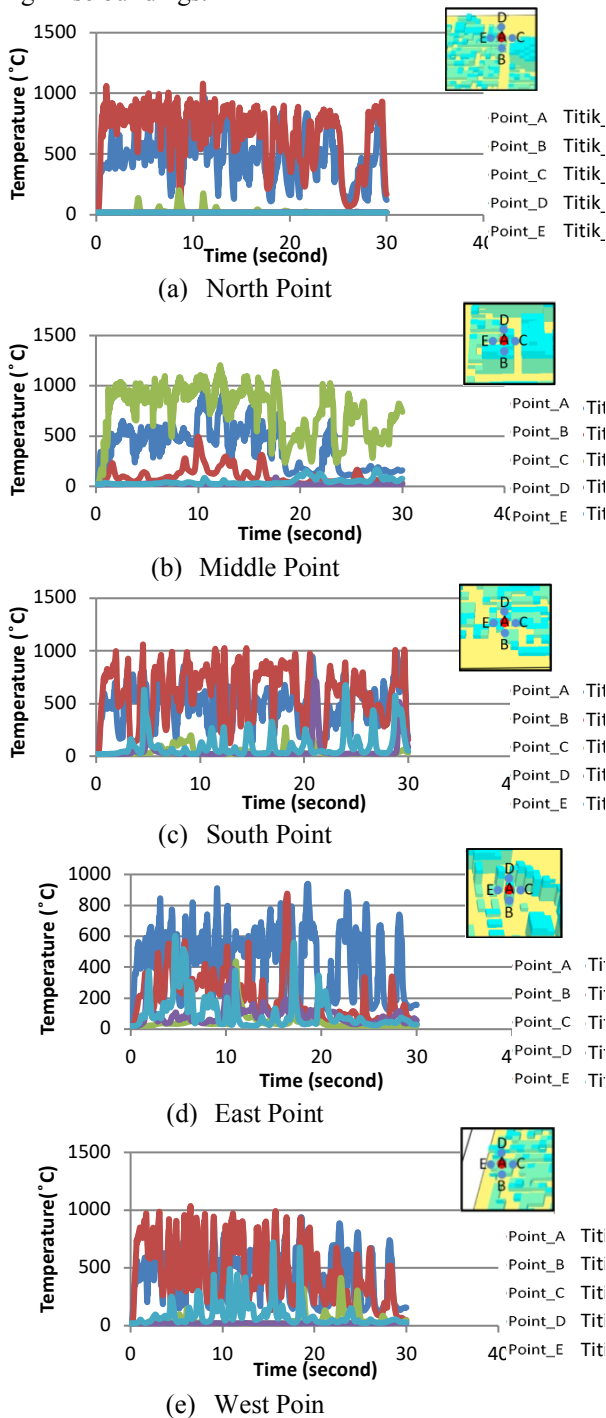
The Middle Point is also simulated in high-rise buildings, there is a large gap in the surrounding buildings, causing a turbulence flow at the hotspots. North Point, South Point, and West Point show stable heat release rate due to the steady flow of wind in the three points, according to the modeling in Autodesk Flow Design software.

Graph 1.3 showed the temperature distribution around the fire point at the five fire simulations. There was a sharp increase in temperature at Point A in the middle of the fire point and Point B which was on the south side of the fire point. The sharp increase in temperature at Point B shows the influence of wind power and wind direction that blows around the point of fire.

The high temperature produced by the fire will be distributed in the direction of the wind. In the Middle Point simulation, the highest temperature increase occurred at Point C on the East side of the fire point. This shows that the fire propagation



potential due to the air temperature distribution around the hotspot is not only influenced by the direction of the wind that blows but also the turbulence of the wind flow that occurs around high-rise buildings.

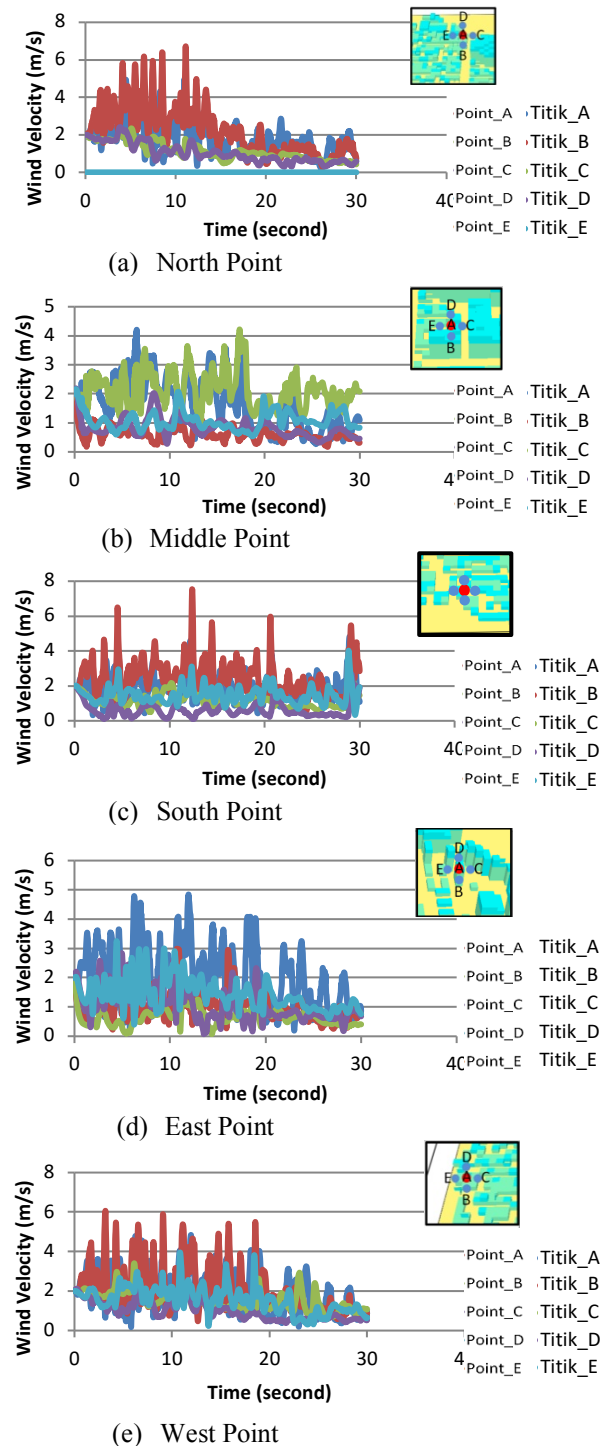


Graph 1.3 Temperature Distribution Around Hotspot of Five Fire Simulation

The distribution of wind velocity that occurs around each five fire points can be observed in Figure 1.4. At the beginning of the simulation, the highest increase rate of wind velocity occurs at the south side of the fire point, namely Point B. Increased wind velocity also occurs at Point A which is in the middle of the fire point. High wind velocity at Point B is caused by a wind flow deflection from a high rise building on the east side of the fire point. Whereas in the South Point

simulation, the increase in wind velocity at Point B is caused by the accumulation of wind flow velocities which are deflected by the building on the North side of the fire point with a constant velocity of wind flow on the West side of the fire point.

In the Middle Point simulation, an increase in wind velocity occurs at Points A and Point C. High wind velocity at Point A and Point C are affected by turbulence and deflection of air flow by high rise buildings on the North and East sides of the fire point.



Graph 1.4 Wind Velocity Distribution of Five Fire Simulation

Implicate with the evacuation process of the community around the fire location, the evacuation route used should not be on the south side of the fire point. The southern side of the fire point in the fire simulation Kebon Melati Sub-district has the greatest potential in reducing visibility and increasing the concentration of fire smoke pollution as a result of the phenomenon of smoke dispersion by the wind that is blowing dominantly towards the South. Increase of temperature on the south side of the fire point is also dangerous because it potentially cause fire propagation.

Decreasing visibility can jeopardize the activity of transportation users because it can increase the risk of accidents on the main road or small roads around the fire point. Fire smoke pollution concentrated due to air flow turbulence on street canyon can endanger the health of the respiratory and visual systems of the surrounding community. According to Alarie's (2002) study, when nitrogen-containing materials such as nylon and woolen cloth are burned, the smoke from the fire will contain hydrogen cyanide (HCN). Hydrogen cyanide can cause several health problems such as narrowing of the respiratory tract, headaches, vomiting, even death at high doses of exposure (Kompasiana, 2011).

The side that can be used as an evacuation route in this fire simulation is the Westside and the Middle side of Kebon Melati Sub-district. The Eastside which is dominated by high rise buildings has greater potential for the flow of fire smoke recirculation on street canyon due to turbulence flow by high rise buildings, compared to the West side which is dominated by slums and simple houses. Middle Side Kebon Melati Sub-district which is traversed by the main road can also reduce the concentration of fire smoke with high and stable wind flow velocity due to no buildings or objects that brush off the wind flow along the main road.

## Conclusion

Wind velocity and wind direction of Kebon Melati Sub-district that used in this study was obtained from meteorological observations in November 2017, with an average wind velocity of 2 m/s heading south.

Wind flow on the West side Kebon Melati Sub-district is more stable than the East side and Middle side which has turbulence in the flow of wind due to the bending of wind flow by high-rise buildings.

In Autodesk Flow Design wind flow simulation, wind velocity increase up to 9 m/s on the eastern side of the Kebon Melati Sub-district due to a wind flow deflection by high-rise buildings.

Wind flow velocities that experience turbulence on the East side and Middle side of Kebon Melati Sub-district only reach velocity of 2 m/s, according to the initial wind velocity.

Fire simulation using Fire Dynamics Simulator results five-point fire smoke dispersion pattern spreads towards the South side of the simulation

point, at an altitude of 3 m to 60 m according to the height of the fire point, until it reaches a certain time the smoke tends to move upwards.

Within 30 seconds, the dispersion of fire smoke with 10,000 kW/m<sup>2</sup> of Heat Release Rate per unit Area, reaches 1,440 m to the South of the five fire simulations.

The highest temperature generated in the five fire simulations reached 770° C in the East Point simulation with a temperature distribution of up to 170°C to the south of the fire point.

The highest wind velocity at five fire simulations reaches 3.6 m/s at North Point and West Point with the distribution of wind velocity reaching 2.2 m/s around hotspot.

The highest heat release rate produced in East Point simulation, reaches 160 kW due to the level of oxygen exposure that is greater than oxygen exposure at the North Point, Middle Point, South Point, and West Point.

Temperature distribution around hot point tends to increase at Point B which is on the South side of fires due to the influence of wind flow strength.

The distribution of wind velocity around hot point affected by turbulence of wind flow due to deflection of wind flow by high rise buildings on the North side and the East side of Kebon Melati Sub-district.

The South Side of Kebon Melati Sub-district has the greatest potential in reducing visibility and increasing the concentration of fire smoke pollution, as well as fire propagation potential.

The side that can be used as an evacuation route is the Westside and the Middle side of Kebon Melati Sub-district which has more stable wind flow than East side.

## Suggestion

Measurement of meteorological data in a longer period of observation so there will be comparison of simulation on dry season and rainy season.

Development of FDS software to be able to simulate the starting point of a fire that is caused by an electrical short circuit.

Simulation with other CFD software, such as Fluent and OpenFOAM to get a more accurate comparison of results.

## References

- Alamos, Los, Michael J. Brown, and Michael J. Brow. 2004. *Urban Dispersion- Challenges for Fast Response Modeling*. 5th AMS Symposium on the Urban Environment.
- Alarie, Yves. 2002. *Toxicity of Fire Smoke*. *Critical Reviews in Toxicology*, (vol. 32, page. 259–289).
- Barowy, Adam and Daniel Madrzykowski. 2012. *Simulation of the Dynamics of a Wind-Driven Fire in a Ranch-Style House - Texas*.

- Grimmond, CSB, T. R. Oke. 2002. *Turbulent Heat Fluxes in Urban Areas: Observations and a Local-Scale Urban Meteorological Parameterization Scheme (LUMPS)*. *Journal of Applied Meteorology* (vol. 41, hal.792-810).
- Hu, L. H. et al. 2011. *Large Eddy Simulation of Pollutant Gas Dispersion with Buoyancy Ejected from Building into an Urban Street Canyon*. *Journal of Hazardous Materials* (vol. 192, hal. 940–48).
- Lin, Cherng Shing, Meng Yin Chen, and Lung Sheng Pan. 2016. *Field Model Simulation and Analysis for a Residential Building Fire*. *Applied Mechanics and Materials* (vol. 851, hal. 810–15).
- Ismawan, D. A. 2008. *Kajian Kerentanan Kawasan Pemukiman Padat terhadap Bencana Kebakaran di Kecamatan Tambora - Jakarta Barat*. Semarang: Universitas Diponegoro.
- Mahan, V. 2009. *Simulasi Penyebaran Gas SO<sub>2</sub> dari Emisi Cerobong Menggunakan Computational Fluid Dynamics*. Bogor: Institut Pertanian Bogor.
- Marihot, L. 2015. *Pola Aliran dan Sebaran Suhu Udara di dalam Rumah Tanaman Tipe Modified Arch di Leuwikopo, Babakan, Dramaga, Bogor*. Bogor: Institut Pertanian Bogor.
- Oke, T. R. 1988. *Street Design and Urban Canopy Layer Climate*. *Energy and Buildings* 11(1–3):103–13.
- Ozmen, Y., E. Baydar, and J. P. A. J. van Beeck. 2016. *Wind Flow over the Low- Rise Building Models with Gabled Roofs Having Different Pitch Angles*. *Building and Environment* (vol. 95, hal. 63–74).
- Pasha, A. 2011. *Simulasi Dispersi Gas Karbon Monoksida (CO) dalam Gardu Tol Menggunakan Computational Fluid Dynamics (CFD) Studi Kasus : Gerbang Tol Bogor*. Bogor: Institut Pertanian Bogor.
- Racun Para Teroris Masa Kini (Hidrogen Sianida)*. 2015. Kompasiana, 26 Juni 2015.
- Sujatmiko, Wahyu, Hermawan K. Dipojono, F. X.Nugroho Soelami, and Soegijanto. 2017. *Study on Fire Dynamic Development in a Multistory Building Compartment*. *Procedia Engineering* (vol. 170, hal. 162–68).
- Saatnya Merevitalisasi Tanah Abang*. 2015. Transformasi, 9 Maret 2015. Diakses dari <http://www.transformasi.org/id/pusat-kajian/berita/umum/644-saatnya-merevitalisasi-tanah-abang>.
- Wahono, Edy. 2008. *Analisis Sistem Fire Roller Shutter terhadap Tingkat Keselamatan Bangunan Pasar dengan Simulasi Komputer* [tesis]. Depok: Universitas Indonesia.

## GEOMETRIC SHAPE FOR IRRIGATION SEDIMENT TRAPS VORTEX DESILTING BASIN

Muhammad Isnaeni<sup>1</sup>, Muhammad Syahril Badri Kusuma<sup>2</sup>, Joko Nugroho<sup>2</sup>, Mohammad Farid<sup>2</sup>, and  
Muhammad Cahyono<sup>2</sup>

<sup>1</sup>Doctoral Program of Water Resources Engineering, Faculty of Civil and Environmental Engineering,  
Institut Teknologi Bandung, Indonesia; <sup>2</sup>Water Resources Engineering Research Group, Faculty of Civil and  
Environmental Engineering, Institut Teknologi Bandung, Indonesia

### ABSTRACT

Modern irrigation schemes are increasingly demand-based, which means that the crop water requirements determine the water flow in a canal. The sediment transport aspect is a significant factor in irrigation development as it determines to a large extent the sustainability of an irrigation scheme, particularly in the case of unlined canals in alluvial soils, and as a trigger in reducing the wet capacity of the irrigation canal. The conventional sediment traps with a rectangular shape, rapidly advancing development, are challenging to construct because they require adequate space. The vortex desilting basin has proposed replacing the rectangular shape with more effectiveness considering the more concise area, deposition rate, removal efficiency, and minimum human resources as an operator. The method uses numerical methods with computational fluid dynamic (CFD) simulations by Ansys R.21 to acquire a geometric shape approach, then laboratory experiments with a model scale 1:40 prototype to an undistorted 3-D physical model. This study aims to develop a two-dimensional numerical model and the optimal regression equations for the determining settling basin dimension and then simulate and compare the deposition efficiency of the selected settling basins. The shape of the vortex desilting basin is slimmer at 42% than the conventional shape by optimising the slope orifice chamber in future research. In comparing the performance of rectangular sediment traps with the apple-to-apple hydraulic parameters and sediment variables, the results obtained based on deposition performance increased from 69.12% to 84.90% and flushing performance by leaving the minimum sediment fraction increased from 53.33% to 87.90%.

*Keywords: Irrigation, Vortex desilting basin, Sediment traps, 3-D physical model*

### INTRODUCTION

Land-use change on the main island in Indonesia is inevitably increased due to the demographic growth and regional development activity in the last two decades. Many areas have undergone relatively fast demographic, industrial and urban development [1], [2]. This intense land occupancy has affected the quality of surface waters, which became the receptacle of anthropogenic effluents from various origins. Irrigation modernisation is necessary for further efforts to overcome threats to the sustainability of irrigation countries. Indonesia is a developing archipelagic country where a land-use change of its most river catchment area has become a common predominant phenomenon for national agricultural, especially paddy, development policy. Land-use change tends to decrease the dependable flow for irrigation and increase the extreme discharge so that the annual yield of paddy fields tends to decrease [3].

River sediments are heterogeneous aggregates, composite structures composed of amorphous or poorly crystalline mineral particles, organic matter,

and biological matter (biofilms, bacteria, viruses, and biopolymers). While fresh sediment deposits are often close to fluid mud, older and deeper riverbed sediments tend to be consolidated, with the state of consolidation higher for deeper sediment. These vertical gradients complicate the modelling of sediment erosion, transport, and deposition [4], [5], [6]. A considerable effort is required to improve irrigation operations and modernise them. A desilting basin is a temporary sediment control structure to intercept sediment-laden runoff and retain the sediment. It aims to detain sediment-laden runoff from the disturbed area for sufficient time and allow most deposits to settle within the sediment trap [7].

Erosion occurring upstream of Citarum Watershed must be treated as necessary because the longer sediment accumulates, the more significant reduction in water capacity at Citarum. Soil erosion is a global environmental problem that threatens the lives of the majority of small farmers. Approximately 80% of agricultural land is degraded due to global soil erosion. The practice of sustainable agriculture is challenged by severe soil

erosion and reduced on-farm productivity of the soil, resulting in food insecurity. On land cultivation, soil conservation requires specific types of vegetation supported by an efficient strategy for controlling soil loss [5]. This phenomenon results in the flow of water for irrigation required that is diverted through the weir, resulting in a decreased supply of irrigation water.

Water flowing in the canal taking off from head works on such rivers also carries sediment load. The canal gets silted if it receives sediment load over its transporting capacity, and effective measures are not taken for its control. This results in a decrease in the discharge carrying capacity of the canal. Further, the canal slope is generally smaller than the main river; hence, sediment always tends to be deposited in the canal [8].

To address it, the weir as a head structure requires a sediment trap that can deposit non-cohesive type sediments and quickly flush out because the water required for irrigation is complicated to stop during the cropping pattern because farmers need it. This study examines and develops the modern shape of sediment traps as a proposed to replace sediment traps with conventional geometric shapes. In the present investigation, vortex settling chambers are studied.

The vortex settling chamber was investigated by Cecen and Bayazit (1975), Curi et al. (1975), Ogiwara and Sakaguchi (1984), Sanmuganathan (1985), Mashauri (1986), Paul et al. (1991), Athar (2000), Athar et al. (2002), Athar et al. (2005), Keshavarzi et al. (2006), Ansari (2008) and Ansari and Athar (2013). However, the development by the previous study is to deposit sediment in a power plant and electrical energy to avoid a larger diameter of non-cohesive sediment entering the turbine drive system. In irrigation, the sediment diameter allowed to enter the irrigation canal is cohesive type sediment whose diameter is  $< 0.06\text{mm}$ . It is challenging to deposit this type of sediment because it is suspension sediment that moves with the water flow.

Different types of ejecting devices are used to control sediment in the canal. These are tunnel-type ejectors, vortex tube types, settling basins, and vortex settling chambers. Settling chambers suffer two main disadvantages, i.e. requirement of large dimensions compared with other types and long residence time. Vortex settling chamber has overcome disadvantages of conventional settling chamber treating the same volume of sediment load. It is a continuous device that applies a certain fraction of flow for flushing sediment particles. The vortex settling chambers can also be used to separate solids from their transporting fluids, such as in treating sewage and industrial wastes [9].

This study improves the vortex desilting basin sediment traps that will gradually test their

hydraulic behaviour. Obtaining the nature of sediment rheology is very important because future research aims to find out the flushing force to flush non-cohesive sediment.

## RESEARCH SIGNIFICANCE

In Indonesia, irrigation scheme  $> 3,000\text{Ha}$  (Central Government Authority) = 2,871 units of weir, 64% = 1,834 units of weir built during the Colonial-Post-Independence period (1890 - 1960), and 71% of its 1,304 units did not have sediment traps, at that time the river flow has not much sediment transportation yet, because there was not much damage to the watershed. Meanwhile, the contribution of the assessment of the irrigation system's performance, 20% of which is the head structure (consisting of weir+sediment trap), the presence of sediment trap is an important constrain. Nowadays, when sediment traps are built, there is not sufficient space for hydraulic parameters. Could vortex settling basins with rounded geometric shapes improve deposition and desilting than conventional shapes?.

## METHODS

### Research Location

As a case study, this research takes an example of one weir which does not have a sediment trap. The location of the study on the contribution of this study is Macan weir, in Subang Regency, see Fig. 1 and Fig. 2. This weir services a technical irrigation area of 9,670 ha, where the current condition of the wet perimeter section area is reduced by  $\pm 35\%$ , caused by sedimentation. The existing conventional plan will construct rectangular sediment traps located right side of the head structure.



Fig. 1 Macan Weir, Located in West Java, Indonesia  
The flushing way outlet cross over the national bridge road. This case is an exciting point to



improve the shapes of sediment traps.

### Sediment Gradation Classified

Previously, research has been conducted for sediment deposition rate at this location by choosing a Fergusson-Church (2004) that resulted in 0.822cm/s for particles 0.07mm, see Fig. 4. The sedimentation deposition rate at the study site has been calculated at 52.66 m<sup>3</sup>/day, see Fig. 3 [3].

This research started by taking data on sediment properties obtained from primary data in 2019

tested at the Laboratory of Engineering Geology, Padjajaran University in Bandung, with the known sedimentation properties and physical properties. The sediment gradation was taken by comparing the data around the study site, such as on the Cibiet and Ciasem rivers, see Fig.3. The sediment properties in the Macan weir sediment trap were taken upstream (3 samples) and downstream (3 samples) sampling points, with laboratory test results at 20°C water temperatures summarised, see Table 1.



Fig. 2 a) Layout of Macan weir, 2 b) Propose of vortex desilting basins location at Macan weir

Table 1 Result of sediment laboratory test

No	Sample Location	Density $\rho_s = \text{kg/m}^3$	Sieve Analyzed #200 <0.007mm (%)	Mass Concentration S (kg/m <sup>3</sup> )	Consolidation Time (minute)	Volume Concentration C <sub>v</sub>	Mud Density $\rho_{s-k} = \text{kg/m}^3$
1	u/s S1	2672	33.1	910	5	0.37	1498
2	u/s S2	2681	34.3	654	5,10	0.29	1543
3	u/s S3	2699	34.5	577	5	0.22	1511
4	d/s S1	2710	35.6	1011	5	0.34	1412
5	d/s S2	2716	36.5	674	5	0.24	1432
6	d/s S3	2739	39.4	593	5	0.19	1411

(Laboratory of Engineering Geology, Padjajaran University, 2019)

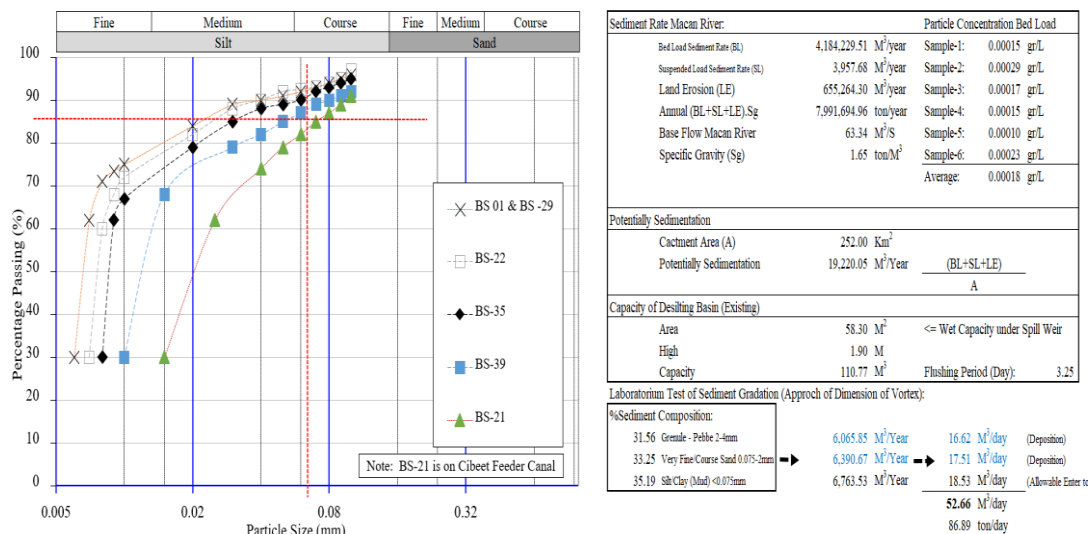


Fig. 3 Sediment gradation analysis/plot sediment size (left) and sediment transport rate (right)



From the sample data primary as collected, the following soil/sediment property index is obtained: a). Particle size analysis; b). Particle Concentration (Suspended and Bed Load); c). LL & PL obtained from Atterberg Limit; d). Water content obtains from Moisture Content; e). Dry density obtains from compaction test, and; f). Shear stress (Kg/cm<sup>2</sup>) was obtained from Mohr Circle-Triaxial Test. Therefore, the microstructure of mud samples in laboratory tests may significantly differ from that of the natural mud deposited in the riverbed.



Fig. 4 Laboratory activities to observe sediment properties in ITB

### Numerical Analysis by Computational Fluid Dynamic (CFD)

As a numerical approach, the method used in Computational Fluid Dynamics (CFD) to analyse the flow behaviours. This simulation will be carried out by modelling three fluid phases, namely air, water, and sediment or mud so that the sediment's flow characteristics can be obtained against time (transient). Because in this simulation, several fluids have different phases (air, water, and mud), multiphase modelling must be used. For flows with a clear separation between one phase and another, the Volume of Fluid (VoF) model is used. This model is also relatively simple and efficient compared to eulerian or mixture [7].

### Dimensional Analysis

Dimensional analysis is a process of formulating fluid mechanics problems in terms of non-dimensional variables and parameters. Dimensional analysis can be used in some cases to provide a complete set of dimensionless products constructed from the pertinent process variables. Similitude by dimensional analysis requires that the dimensionless products have the same value in the prototype as in the model [8].

Physical problems are described by relations, which are determined by quantities having a certain

dimension—length, time, mass, force, temperature, etc. These relations must be so structured that dependent and independent quantities are combined so as to yield dimensionally correct formulas [9]. The similarities that have been tested in this study are geometric, kinematic and dynamic.

### Experiment Set-up in Laboratory

Physical model tests are performed to investigate the hydraulic behaviour of the entire sediment trap or each component. Physical model tests often solve fluid mechanics and hydraulics problems to discover the hydraulic behaviour that is not obtained in numerical models with CFD [10].

This physical model test is intended to test or check the performance of sediment traps in the efficiency of deposition and desilting that have been previously tested in numerical analysis with CFD.

#### 3.5.1 Accessories of the Experimental Set-up

This test used a 3D speed meter programmable Electro-Magnetic Liquid Velocity Meter (PEMS). Acoustic Velocimeter (ADV) Doppler was designed to perform the speed of measurement points in water with scientific accuracy.

Simple ADV performance interface, enabling fast data collection by a data logger by a computer. Laboratory test used 2 unit Micro ADV 16MHz down and side-looking, 1 unit Probe Propeller Current Meter H33 with data logger and 8 unit Camera Highspeed DSLR.

#### 3.5.2 Schematic of Laboratory Test

A 3-D test of this physical model was carried out in the hydraulics laboratory of the Faculty of Civil and Environmental Engineering Institut Teknologi Bandung (ITB), see Fig. 5 and Fig. 6 conducted from February to May 2022.

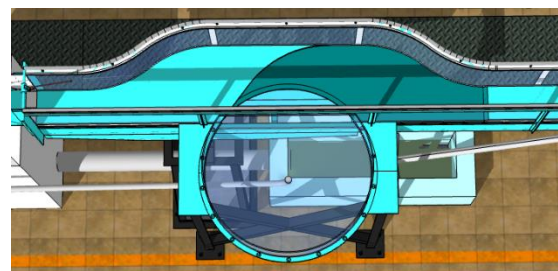


Fig. 5 Undistorted layout of 3-D physical model test

The determination of the scale model in the analysis of the relationship between scales prototype to model, as considering: Space in a laboratory; accuracy; facilities/accessories, and; Cost



Fig. 6 Visual view of the undistorted physical model with a scale of 1:40

### Experiment Procedure

The sediment removal efficiency of the vortex settling/desilting basin used was measured by systematically varying the inlet discharge, underflow flushing discharge, sediment size, underflow outlet orifice diameter and the width of the channel. The sediment trap efficiency is defined as the ratio of deposited sediment to the total sediment inflow for a given period within the sediment trap economic operation [11],[12].

### Limitations

In this study, the authors limited several variables so that the focus of the study became clear and not pseudo; here are the limitations of the research: a). Laboratory 3D Physical Model, Undistorted Scale 1: 40; b). Inlet Irrigation Main Canal length at Model: 5.5 m equal Prototype 220 m and static with 0.2m in model equal to 8.00 m at prototype; c). A circular cylindrical type of vortex settling basin having a diameter at model 1.00m equal to 40m at prototype was used for experimentation in the present study; d). Sediment to be deposited cohesionless type  $> 0.07\text{mm}$ , and  $< 0.07\text{mm}$  neglected and allowable enter to the main system; e). Water depth has variations based on Q 50%, 100% and 120% by NFR; f). The underflow outlet orifice static diameter is 0.025 m, equal to a diameter of 1.00m; g). Cohesion-less uniform sediments having sizes 0.008 mm to 0.825 mm were used, and; h). Suspended sediment concentration in the vortex settling basin varied from 11,200 ppm to 190,000 ppm by weight.

### RESULTS AND DISCUSSIONS

Decrease the flow velocity in the basin to assure the sediment particle remaining time longer than the settling time is the main design idea of the settling basin. To achieve this goal, the common procedures are widening the basin width and lowering the basin bottom. However, the same deposition efficiency

may be attained by different combinations of length, width, and depth [13]. The economic design of the settling basin with the specific efficiency is the focus of this study.

### Rectangular Shape Sediment Trap

The performance of a sediment trap is expressed in how effectively it is depositing and quickly flushing out the sediment fraction. As a comparison, in 2018, there was an undistorted 3-D of physical model of the rectangular shape of sediment traps in the Hydraulics Laboratory of PUSSAIR Bandung, see Fig. 7.

With a similar location and parameters. However, due to the Macan main canal's alignment in the irrigation system's direction, if it is built on a space with curved alignment is not optimal in terms of performance.



Fig. 7 Undistorted physical model test scaling 1:20 for conventional rectangular sediment trap

The results of physical modelling on conventional sediment trap forms with a model scale of 1:20 are not very optimal, the deposition efficiency is measured at 69.12%, and this sedimentary fraction that is deposited can only be flushed out by 53.33%, see Table 2. The alignment of sediment traps on the curved line leaves many sedimentary fractions in the inner curve, see Fig. 8.

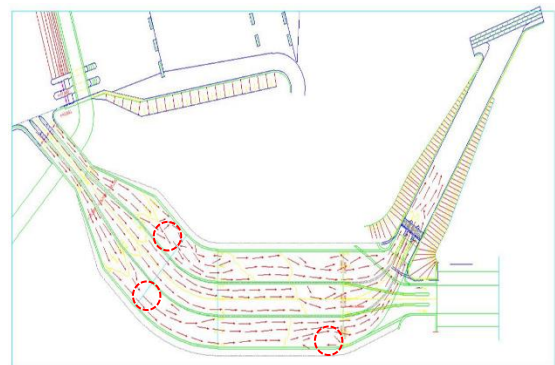


Fig. 8 Fraction of sediment on dashed line – break the red circle in rectangular sediment trap.

In the DC-04 design criteria issued by the Ministry of Public Works and Housing, sediments deposited in diameter > 0.07mm, for diameters <

0.07mm can be neglected and then allowed to enter the irrigation system with operational and routine and periodic maintenance conditions [14].

Table 2 Rectangular Conventional Sediment Trap, 2018

Result of 3-D Rectangular Conventional Sediment Trap, 2018

No	Parameters	Rectangular Conventional Sediment Trap	
		Prototype, Scale 1:1	3-D Physical Model, 1:20
a	Q 100%	10.64 m <sup>3</sup> /s	1.057 lt/s
b	Daily Sediment Transport	52.66 m <sup>3</sup> /day	5,367.80 cm <sup>3</sup> /day
c	Continue Settling Time	7 Days	24.63 Hours
d	Volume/Fraction Settled	37.50 m <sup>3</sup>	3,710.22 cm <sup>3</sup>
e	Desilting Time	1 Days	5.4 Hours
f	Volume/Fraction Desilted	21.08 m <sup>3</sup>	1,978.66 cm <sup>3</sup>
g	Velocity	1.261 m/s	20.430 cm/s
h	Froude Number	0.560 -	2.0151 -
i	Reynold Number	1.58.E+03 -	4.63E-01 -
j	Sediment Consentration	190,751 ppm	96,774 ppm
k	Trap Efficiency (TE)	<b>71.21%</b>	<b>69.12%</b>
l	Desilting Efficiency (η <sub>0</sub> )	<b>56.21%</b>	<b>53.33%</b>

#### Simulation for Approach Geometric Shape by CFD

For the approach of geometric shapes of sediment traps with the model of vortex settling/desilting basins, a numerical approach with the help of AnSys R.21 R.2 Student. Obtained previously developed shapes by Ansari (2008) and Ansari and Athar (2013). In all 22 runs were conducted for sediment removal efficiency of vortex settling/desilting basin by varying slope chamber of underflow outlet, whereas 44 runs were conducted for this study.

Here are the inputs used in boundary conditions: Mass-flow-Inlet: a). In the inlet section, it is defined as a mass flow inlet either for water or mud. b). Wall: On walls, it is defined as a wall with a no-slip condition to represent the friction between the fluid and the wall. c). Surface: At the top of the domain, the effects of wall friction are removed to represent atmospheric air, and d). Outlet: The outlet section is defined as a pressure outlet representing the flow's "exit" [7].

Computational Fluid Dynamics (CFD) is the art of transforming fluid dynamics set equations in the form of integrals and derivatives into discrete algebraic forms, which a computer can solve to obtain the values of the flow field at a particular discrete point or time. As for the regulatory equations in fluid dynamics: the continuity equation, the momentum equation and the energy equation [14], [15].

Here are the equations used in CFDs; Continuity equation of integral forms:

$$\frac{\partial}{\partial t} \iiint_V \rho dV + \iint_A \rho \vec{V} \cdot d\vec{A} = 0 \quad (1)$$

The continuity equation of the differential form:

$$\frac{\partial \rho}{\partial t} + \rho \vec{\nabla} \cdot \vec{V} = 0 \quad (2)$$

The equation of momentum in the direction of the x-axis:

$$\frac{\partial(\rho u)}{\partial t} + \vec{\nabla} \cdot (\rho u \vec{V}) = -\frac{\partial p}{\partial x} + \frac{\partial \tau_{xx}}{\partial x} + \frac{\partial \tau_{yx}}{\partial y} + \frac{\partial \tau_{zx}}{\partial z} + \rho f_x \quad (3)$$

The equation of momentum in the direction of the y-axis:

$$\frac{\partial(\rho v)}{\partial t} + \vec{\nabla} \cdot (\rho v \vec{V}) = -\frac{\partial p}{\partial y} + \frac{\partial \tau_{xy}}{\partial x} + \frac{\partial \tau_{yy}}{\partial y} + \frac{\partial \tau_{zy}}{\partial z} + \rho f_y \quad (4)$$

The equation of momentum in the direction of the z-axis:

$$\frac{\partial(\rho w)}{\partial t} + \vec{\nabla} \cdot (\rho w \vec{V}) = -\frac{\partial p}{\partial z} + \frac{\partial \tau_{xz}}{\partial x} + \frac{\partial \tau_{yz}}{\partial y} + \frac{\partial \tau_{zz}}{\partial z} + \rho f_z \quad (5)$$

The energy equation is written in the form of internal energy:

$$\frac{\partial}{\partial t} \left[ \rho \left( e + \frac{V^2}{2} \right) \right] + \vec{\nabla} \cdot \left[ \rho \left( e + \frac{V^2}{2} \right) \vec{V} \right] = \rho \dot{q} - \frac{\partial(\rho p)}{\partial x} - \frac{\partial(\rho p)}{\partial y} - \frac{\partial(\rho p)}{\partial z} + \rho \vec{f} \cdot \vec{V} \quad (6)$$

Where  $\rho$  is Liquid density ( $\text{kg m}^{-3}$ ),  $A$  is a mass area,  $\vec{V}$  is Velocity vector ( $\text{m s}^{-1}$ ) or velocity fluid parcel,  $e$  for internal energy, three velocity components are  $u, v, w$ ,  $\vec{V}$  vector,  $f$  any vector function [7],[10],[16]. The solution of a partial differential analytical equation results in a continuously closed-form dependent variable expression across domains. In contrast, the solution of numerical equations can only give values to discrete points in the domain, also called grid points. As a shaping approach to the vortex geometric shape settling/desilting basins proposed, as shown in Fig. 9, then input all the hydraulic variables and applying Eq.1 – Eq. 6 above in CFD resulted in shape as follows:

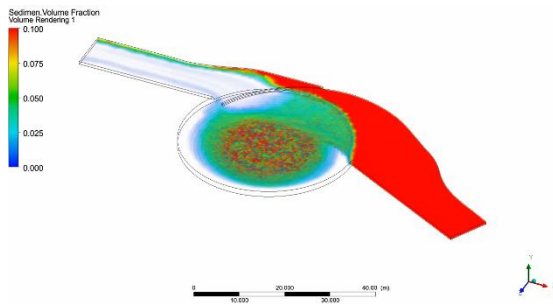


Fig. 9 Sediment volume fraction at settling time

As shown in Fig.9, it showed that the sediment fraction on the free vortex flow along the forced vortex flow side of the chamber is relatively high and states that sediment is well deposited, the percentage of sedimentary volume deposited from sediment transport within continues flow in 7 days of flow amounting to 82.11%. On the longitudinal section of this sediment trap is shown a fraction of sediment deposited present by the predominance of red in the following Fig.10 below:

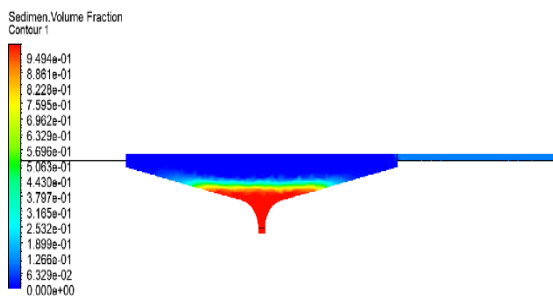


Fig. 10 Sediment volume fraction – longitudinal section view (deposition time)

This shape is also maximal at the time of desilting, although not all sediment fractions can be deposited because sediment diffusion exerts an influence.

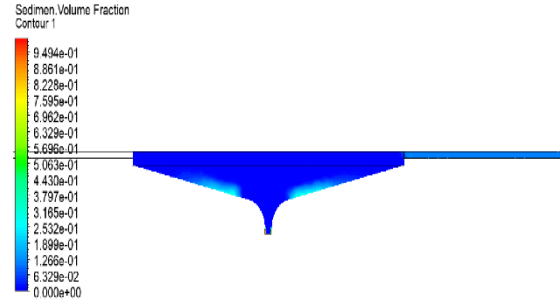


Fig. 11 Sediment volume fraction – longitudinal section view (desilting time)

In addition, the rheological process of sedimentary sediments also exerts an influence on the classification of this type of sediment. Of the 82.11% of sediment deposited, as shown in Fig. 10 and Fig. 11, a total of 69.31% of the sediment fraction can be drained. Leaving approximately 30.69% in cyan colour cannot be flushed out due to the position of the sediment in the transition of the free vortex flow to the forced vortex.

### Result Laboratory Undistorted 3-D Physical Model Test

The geometric approach of the vortex settling/desilting basin with a numerical approach to its results was tested with a physical model in the laboratory.

After the dimensional analysis, stages are carried out, and geometric, kinematic, and dynamic similarity tests and the available space, a model scale of 1:40 is determined. The following equation calculates the deposition efficiency value:

$$T_{ef} = \frac{V_{in} - V_{out}}{V_{in}} \times 100 \quad (7)$$

Where  $T_{ef}$  is trap efficiency (%),  $V_{in}$  is the volume of sediment entering the sediment trap,  $V_{out}$  is the volume of sediment as flushed at the outlet.

To calculate the efficiency of flushing-out/desilting, use the following equation:

$$\eta_0 = \frac{W_s \text{ flush} + W_s \text{ Settled}}{\text{Total } W_s \text{ Feeding}} \times 100 \quad (8)$$

Where  $\eta_0$  is flushing efficiency (%),  $W_s \text{ flush}$  is the flushed volume of a sediment chamber, and  $W_s \text{ Settled}$  as sediment deposited.  $W_s \text{ feeding}$  the total amount feeding of sediment transport rates [17], [18].



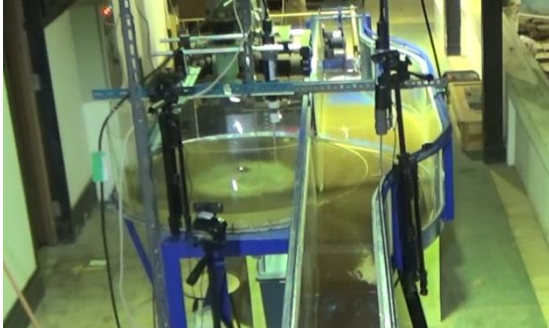


Fig. 12 Settled sediment volume



Fig. 14 Flushed – out of sediment fraction

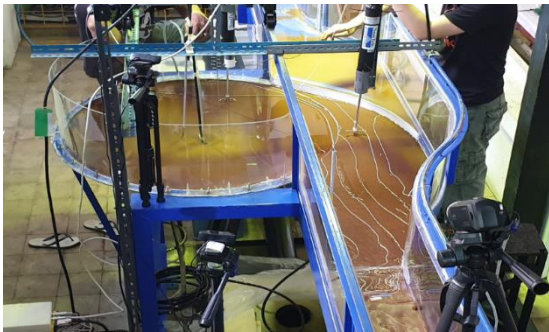


Fig. 13 Measurement of sediment fraction

As shown in Fig. 12, Fig. 13, and Fig.14, 11 runs were conducted for this study and feeding the sediment through a sediment feeder to determine the volume of deposition and the efficiency of flushing used the Eq equation. 7 and Eq.8. then the results obtained are tabulated in the following table:

Table 3 Comparison result of running for rectangular in 2018 and vortex settling/desilting basins in 2022

No	Parameters	Rectangular Conventional	Vortex Settling/Desilting Basins
		3-D Physical Model, 1:20	3-D Physical Model 1:40
a	Q 100%	1.057 lt/s	0.526 lt/s
b	Daily Sediment Transport	5,367.80 cm <sup>3</sup> /day	2,670.55 cm <sup>3</sup> /day
c	Continue Settling Time	24.63 Hours	12 Hours
d	Volume/Fraction Settled	3,710.22 cm <sup>3</sup>	2,267.29 cm <sup>3</sup>
e	Desilting Time	5.4 Hours	3 Hours
f	Volume/Fraction Desilted	1,978.66 cm <sup>3</sup>	1,992.95 cm <sup>3</sup>
g	Velocity	20.430 cm/s	8.158 m/s
h	Froude Number	2.0151 -	0.98 -
i	Reynold Number	4.63E-01 -	3.36E-01 -
j	Sediment Concentration	96,774 ppm	96,774 ppm
k	Trap Efficiency (TE)	<b>69.12%</b>	<b>84.90% ▲</b>
l	Desilting Efficiency ( $\eta_0$ )	<b>53.33%</b>	<b>87.90% ▲</b>

## CONCLUSION

Present research for steady, vortex, and open channel flows over smooth, rough, and movable beds, independent and based on Reynolds and Froude numbers. As a comparison of 2 different geometric shapes of sediment traps with hydraulic parameters such as discharge, the exact characteristics of sediments to deposition and flush out, the running results showed an increase in the number of volumes that could be settling from

69.12% to 84.90%. Meanwhile, for flushing, the sediment fraction of 53.33% increases to 87.90% from the deposited can be flushed out. For future research, it is optimising the geometric shape of the chamber to be optimum based on the diameter ratio chamber effect.

## ACKNOWLEDGMENTS

This study aims to develop a 3-D rectangular shape sediment trap for a vortex desilting/settling basin shape. The authors would like to thank the

Ministry of Public Works and Housing for their assistance regarding the data collection required for this paper. Furthermore, the authors would also like to express their gratitude to the research, Water Resources Engineering Research Group of the Faculty of Civil and Environmental Engineering Institut Teknologi Bandung, for supporting this publication.

## REFERENCES

- [1] M. S. Badri Kusuma, "EXPERIMENTAL MODEL OF DAM BREAK FLOW AROUND SEVERAL BLOCKAGES CONFIGURATIONS," *Int. J. GEOMATE*, vol. 16, no. 58, Jun. 2019, doi: 10.21660/2019.58.97684.
- [2] M. S. Badri Kusuma, "THE INFLUENCE OF THE NEW LRT PIER TO THE SEDIMENTATION PATTERN AROUND AMPERA BRIDGE IN MUSI RIVER, SOUTH SUMATERA, INDONESIA," *Int. J. GEOMATE*, vol. 18, no. 69, May 2020, doi: 10.21660/2020.69.13240.
- [3] M. Isnaeni, "RHEOLOGICAL RELATIONSHIP TO SEDIMENT DEPOSITION RATE IN MACAN WEIR SEDIMENT TRAPS," *Int. J. GEOMATE*, vol. 21, no. 87, Nov. 2021, doi: 10.21660/2021.87.j2370.
- [4] J. Lepesqueur, R. Hostache, N. Martínez-Carreras, E. Montargès-Pelletier, and C. Hissler, "Sediment transport modelling in riverine environments: on the importance of grain-size distribution, sediment density, and suspended sediment concentrations at the upstream boundary," *Hydrol. Earth Syst. Sci.*, vol. 23, no. 9, pp. 3901–3915, Sep. 2019, doi: 10.5194/hess-23-3901-2019.
- [5] A. A. Kuntoro, A. W. Putro, M. S. B. Kusuma, and S. Natasaputra, "The effect of land use change to maximum and minimum discharge in Cikapundung River Basin," Palembang, Indonesia, 2017, p. 100011. doi: 10.1063/1.5011621.
- [6] M. Cahyono, "The Development of Explicit Equations for Estimating Settling Velocity Based on Artificial Neural Networks Procedure," *Hydrology*, vol. 9, no. 6, p. 98, Jun. 2022, doi: 10.3390/hydrology9060098.
- [7] M. Isnaeni, "COMPARISON OF FOUR PARTICLE DEPOSITION RATE FORMULAE IN LAMINAR FLOW," *Int. J. GEOMATE*, vol. 21, no. 84, Aug. 2021, doi: 10.21660/2021.84.j2160.
- [8] M. A. Ansari and M. A. Khan, "Performance assessment of vortex settling chambers," *ISH J. Hydraul. Eng.*, vol. 20, no. 3, pp. 324–338, Sep. 2014, doi: 10.1080/09715010.2014.925330.
- [9] J. Chapokpour, "Turbulent Flow Measurement in Vortex Settling Basin," *Iran. J. Energy Environ.*, 2011, doi: 10.5829/idosi.ijee.2011.02.04.3098.
- [10] A. Bakker, "Lectures on Applied Computational Fluid Dynamics," *Ivy Leag. CFD Simul. Fluent Newsl. Fall 2003 Page 38*, vol. 2008, p. 612, 2008.
- [11] "Chapter-4 Physical Models and Laboratory Techniques in Coastal Engineering Downloaded from www.worldscientific.com.pdf."
- [12] K. Hutter, Y. Wang, and I. P. Chubarenko, "Dimensional Analysis, Similitude and Model Experiments," in *Physics of Lakes*, Cham: Springer International Publishing, 2014, pp. 307–396. doi: 10.1007/978-3-319-00473-0\_30.
- [13] "CFD-Post Tutorials," p. 82, 2021.
- [14] M. A. Ansari and M. Athar, "Design parameters of vortex settling basin," *Proc. Inst. Civ. Eng. - Water Manag.*, vol. 166, no. 5, pp. 262–271, May 2013, doi: 10.1680/wama.11.00098.
- [15] M. A. Eizel-Din *et al.*, "Trap efficiency of reservoirs on the Nile River," p. 7.
- [16] K.-C. Yeb and E.-T. Lin, "Efficiency Simulation and Design of Settling Basin," *Dep. Of Civil Eng. Natl. Chiao Tung University Hsinchu Taiwan*, p. 12, 2007.
- [17] M. S. Afzal, H. Bihs, and L. Kumar, "Computational fluid dynamics modeling of abutment scour under steady current using the level set method," *Int. J. Sediment Res.*, vol. 35, no. 4, pp. 355–364, Aug. 2020, doi: 10.1016/j.ijsrc.2020.03.003.
- [18] M. E. Mohammad, N. Al-Ansari, S. Knutsson, and J. Laue, "A Computational Fluid Dynamics Simulation Model of Sediment Deposition in a Storage Reservoir Subject to Water Withdrawal," *Water*, vol. 12, no. 4, p. 959, Mar. 2020, doi: 10.3390/w12040959.
- [19] T. M. Ravens and R. A. Jepsen, "Computational Fluid Dynamics Analysis of Flow in a Straight Flume for Sediment Erodibility Testing," *J. Waterw. Port Coast. Ocean Eng.*, vol. 132, no. 6, pp. 457–461, Nov. 2006, doi: 10.1061/(ASCE)0733-950X(2006)132:6(457).
- [20] R. A. Adhi and B. Ontowirjo, "Evaluation of the Sediment Trap Structure Performance in the Saddang Irrigation," *IOP Conf. Ser. Earth Environ. Sci.*, vol. 698, no. 1, p. 012026, Mar. 2021, doi: 10.1088/1755-1315/698/1/012026.
- [21] M. V. Estigoni, J. A. Vasquez, D. M. Robb, E. Wang, and F. F. Mauad, "2D NUMERICAL MODELLING OF SEDIMENT TRAP EFFICIENCY IN A MULTI-BASIN DESANDER," p. 10.



## PROFILING EXHALED VOLATILE ORGANIC COMPOUNDS FROM SEMERU ERUPTION REFUGEES BY USING E-NOSE

Arinto Yudi Ponco Wardoyo<sup>1</sup>, Eko Teguh Purwito Adi<sup>1</sup>, Hari Arief Dharmawan<sup>1</sup>, Susanthy Djajalaksana<sup>2</sup>, Arif Budianto<sup>3</sup>, Ngakan Putu Putra<sup>2</sup>, Aditya Sri Listyoko<sup>2</sup>, Fitri Indah Sari<sup>2</sup>, Raden Dicky<sup>2</sup>

<sup>1</sup> Department of Physics, Brawijaya University, Indonesia; <sup>2</sup> Pulmonology And Respiratory Medicine Department, Faculty Of Medicine, Brawijaya University, Indonesia; <sup>3</sup> Physic Study Program, University of Mataram, Indonesia

### ABSTRACT

Semeru Mountain was reported to erupt on December 4, 2021. The eruption caused more than 10.000 people to refuge from their homes. The refugee's health was reportedly affected by the volcanic eruption, especially by respiratory-related diseases. In this research, we tried to profile the exhaled breath content from the refugees by using an E-Nose-based system. The E-Nose named  $\mu Breath$  developed by Brawijaya University uses multi-array sensors to detect twenty parameters in terms of volatile organic compounds (VOCs) and other gases. Forty-four refugees were randomly selected by their capability to participate in this study. All of the participant's health was assessed for Chronically Obstructive Pulmonary Disease (COPD), tuberculosis, and asthma after a month of the eruption. Then, we build a profile that links the relationship between the measured exhaled content concentrations to the refugee's health condition. The profiling is established by using the K-Nearest Neighbor algorithm. We find that thirteen of the exhaled contents have a significant correlation to the refugee condition. The most distinguished profile is related to the refugee health condition of Chronically Obstructive Pulmonary Disease (COPD), tuberculosis, and asthma. In conclusion, it was found that the profiling of the exhaled content of the Mt. Semeru refugees has significant health impacts related to respiratory disease.

*Keywords: Breath, Exhaled, Profile, E-Nose*

### INTRODUCTION

Semeru Mountain is an active volcanic located at the latitude of 8° 06' 29" S and longitude of 112° 55' 12", East Java, Indonesia. The volcano was reported to erupt since 2014 and finally released a 15-km-high ash plume after the dome collapsed on December 4, 2021 [1]. During the eruption, the Center for Volcanology and Geological Hazard Mitigation, Department of Geology, Indonesian Ministry of Energy, and Mineral Resources reported a hot cloud avalanche up to 4 km in the direction of south-east from the summit [2]. TROPOMI instrument on the sentinel 5P-satellite captured the SO<sub>2</sub> emission spread west and north from the mountain three days after the eruption [3]. According to the Indonesian Agency for National Disaster Management, the eruption killed at least 50 people and forced more than 10.000 people to evacuate [4]. The agency also stated more than a thousand houses were heavily damaged by the eruption [5].

The volcanic eruption released a million chemical compounds when the eruption happened

[6,7]. Although the chemical characteristic of each mountain was different, the toxic nature of the component remains of concern [8–10]. Many respiratory diseases associated with exposure to volcanic emissions support this opinion [11]. In the case of Semeru, the mountain was reported to release a persistent concentration of SO<sub>2</sub> [12]. The gas was known to be fatal to humans along with the other gases or particulate [9,11,13,14].

Respiratory-related diseases can be detected through an analysis of the chemical components contained in the exhaled air. The presence of specific gases was related to diseases, especially volatile gas. Many studies found different gas components between healthy people and people with respiratory diseases [15–17]. An exhaled biomarker has been used to differentiate the human condition [18]. However, the study to profile exhaled breath of the people influenced by Volcanic Mountain has not been found up to now. This study is aimed to profile the exhaled breath of the Mt. Semeru refugees based on the measurement of the biomarker gases.

## METHOD

### Electrical Nose Design

Twenty parameters consisting of temperature, humidity, and eighteen chemical compounds were observed using sixteen sensors. The chemical compound consisted of Oxygen ( $O_2$ ) [19], Total Volatile Organic Compound (TVOC) [20], Carbon Monoxide ( $CO$ ) [21], Methane ( $CH_4$ ), Di-hydrogen Sulfide ( $H_2S$ ), Nitrogen Dioxide ( $NO_2$ ), Ammonia ( $NH_3$ ) [22], Ozone ( $O_3$ ), Ammonium ( $NH_4$ ) [23], Carbon Dioxide ( $CO_2$ ), Formaldehydes ( $CH_2O$ ) [24], Ethanol ( $C_2H_5OH$ ) [25], Propane ( $C_3H_8$ ) [26], Acetone ( $C_3H_6O$ ) [27], 1-Butanol ( $C_4H_9OH$ ), Hexane ( $C_6H_{14}$ ), Benzene ( $C_6H_6$ ), and Toluene ( $C_7H_8$ ) [28]. All of the gases were related to human exhaled breath [29]. The breath temperature and humidity were measured with SHT-11 sensor, TVOC and  $CO_2$  with CS-811 sensor,  $NO_2$  and  $CO$  with CJMCU-MICS-4541, and  $NH_4$  and  $H_2S$  with MQ-136 [30]. Meanwhile, the concentration of  $CH_2O$ ,  $C_6H_6$ , and  $C_7H_8$  was quantified with the MS-1100 sensor. The concentration of  $O_2$ ,  $O_3$ ,  $SO_2$ ,  $NH_3$ ,  $C_3H_6O$ ,  $C_6H_{14}$ ,  $C_4H_9OH$ ,  $C_3H_8$ ,  $CH_4$ , and  $C_2H_5OH$ , was conducted by using ME-2, ME-3, ME-4, CJMCU-MICS-6814, MQ-135, MQ-138, MQ-3, MQ-5, MQ-9, and TGS-2600 [30–32]. All of these sensors were applied in the  $\mu Breath$  breath analyzer device developed by the laboratory of Air Quality and Astro-imaging, Brawijaya University. The device was designed to save the measurement data in the form of a .csv file. All parameter was presented on the scale of ppm (part per million).

### Participant and measurement procedures

Forty-four refugees in the evacuation camps located on  $-8^\circ 12' 42.35''$  S and  $112^\circ 59' 6.04''$  ( $12.9$  km the peak of Mt.Semeru) were selected to participate on January 29, 2022, or fifty-six days after the large eruption. Before the test was conducted, all participants were assessed to classify their condition during the examination. Then, we instructed the participant to introduce their third exhalation breath to a 500 ml exhaled breath sample bag. The third breath was chosen to avoid the effects of breathing techniques, mouth odor, dead space air, or any other irrelevant factor [33–35]. The sample was measured immediately by an E-Nose device after breath collection procedure to evade the influence of the

environmental condition [29]. The measurement procedure was that exhaled breath was collected by blowing a sample bag. The bag was connected to Ubreath for the gas concentration measurement. During the measurement, the participant was asked to fill in the information about their current condition, consisting of age, gender, disease complaint, previous diagnosis, and symptoms. The information was used as a categorical parameter for further analysis.

### Data Evaluation

Eighteen gas concentrations were analyzed based on their correlation with the participant's condition. The classified condition consists of a health participant, the participant with a respiratory-related disease, and un-related diseases stated three different categories of the participants. Health participant was defined as people without any health problem or symptoms. The participant with respiratory-related and unrelated diseases was determined by using the previous diagnosis statement. As for the unknown disease, the participant with respiratory-related symptoms such as breathlessness, cough, dizziness, and chest pain was categorized into this classification [36–38]. Further, we also dropped the data of the participant with diseases unrelated to volcanic emissions e.g., tuberculosis.

The data were evaluated to find the correlation to respiratory-related diseases. Heat map analysis was performed to create a gas combination by using a correlation factor [39]. Then, we conducted Principal Component Analysis to cluster the selected gases combination. The PCA result was performed to reevaluate the data in order to assess the selected gas combination [40]. The final data combination was used as the reference data in the K-Nearest Neighbor (K-NN) [40,41]. In the K-NN, we evaluated the reference data to find the accuracy and Unknown diseases as test data.

## RESULT

Volcanic eruptions release a wide variety of gases that can cause damage to human tissue. In this study, we measure the various exhaled gases of the volcanic eruption refugees and relate them to the association with the diseases of asthma, chronic obstructive pulmonary disease (COPD), and pharyngeal abscess. The selection of the three diseases was based on the relationship between

tissue damage due to exposure to reactive substances and the disease suffered by the participants during the observation. As shown in Fig.1, the participants were categorized into 7 groups based on their disease. The observation showed that of the 44 selected participants, 9 participants did not show any health problems, 5 people were diagnosed with COPD, 2 people with tuberculosis, 5 people with asthma, 1 person with pharyngeal abscess, and 6 people with unrelated diseases. Meanwhile, 16 people were with the undiagnosed disease. For participants with undiagnosed disease, the results of the assessment showed that 5 people came with the symptoms of cough, 3 people had shortness of breath, 1 person was dizzy, 1 person had chest pain and fatigue, 4 people coughed with shortness of breath, and 1 person coughed with fever. For asthmatics, it was known that 1 person had symptoms of shortness of breath, 3 people had symptoms of shortness of breath accompanied by coughing, and 1 person had shortness of breath with chest pain. In COPD, 1 person has shortness of breath, 3 people have shortness of breath with cough, and 1 person is asymptomatic. For Pharyngeal Abscess, participants did not show any symptoms.

diseases, Health, Chronic Obstructive Pulmonary Disease, tuberculosis, Asthma, and represent Pharyngeal Abscess respectively. Each group has a specific distribution of gasses and concentration. As a sample: asthma, COPD, and a pharyngeal abscess had a significant concentration of  $C_3H_6O$  and TVOC. However,  $C_2H_5OH$  is found to have no significant difference among them, except the concentration is slightly high for asthma. In terms of  $O_2$ , it is generally found in each category, and the concentration is found at least the same. It is interesting that we find the  $O_2$  concentration of the females suffering from COPD higher than the asthma groups. Inversely, the  $CO_2$  concentration of COPD group is lower than the  $CO_2$  concentration of asthma. For the CO concentration, it can be seen in the male that the trend of the decreasing concentration in the order of COPD, Asthma, and Pharyngeal Abscess. On the other hand, the concentration of CO increases for the female. In the case of the concentration of  $NH_3$ ,  $CH_2O$ , and  $C_7H_8$ , there is no difference in the COPD, asthma, and pharyngeal abscess groups. The different concentration of those gasses is found in the case of COPD for the female and male participant. Tuberculosis has a similar characteristic based on the three gasses distribution concentration. Meanwhile, the concentration of the rest measured gasses is difficult to differ the group.

In order to differentiate each group, we analyze the concentration data using a heat map, as seen in Fig.2, to find the gas configuration based on the correlation value of  $C_v$  which is positive, showing an equivalent change, and is negative, indicating an oppositely change. The choice of the positive and negative values is based on the correlation of the chemical compound formation to the respiratory process.

The presence of oxygen in the air is important for the metabolism process. Based on this fact, we evaluate the correlation between oxygen and the rest of the gases. As a result, we obtain  $O_2$  to have a strong negative correlation with  $CO$  and a strong positive correlation with  $NH_3$ . On the other hand,  $O_2$  has a weak correlation with  $CO_2$ ,  $TVOC$ ,  $C_4H_9OH$ ,  $C_6H_6$ ,  $H_2S$ ,  $CH_2O$ , and  $C_7H_8$ . Meanwhile,  $O_2$  is found to have no correlation with  $C_3H_8$ ,  $C_6H_{14}$ ,  $O_3$ ,  $CH_4$ ,  $NO_2$ ,  $C_2H_5OH$ ,  $C_3H_6O$ , and  $NH_4$ .

In the case of TVOC, we find the gas to have a very strong positive correlation with CO, CO<sub>2</sub>, and C<sub>4</sub>H<sub>9</sub>OH. A very strong correlation is also obtained on CO with TVOC, C<sub>4</sub>H<sub>9</sub>OH, and CO<sub>2</sub>; CO<sub>2</sub> with

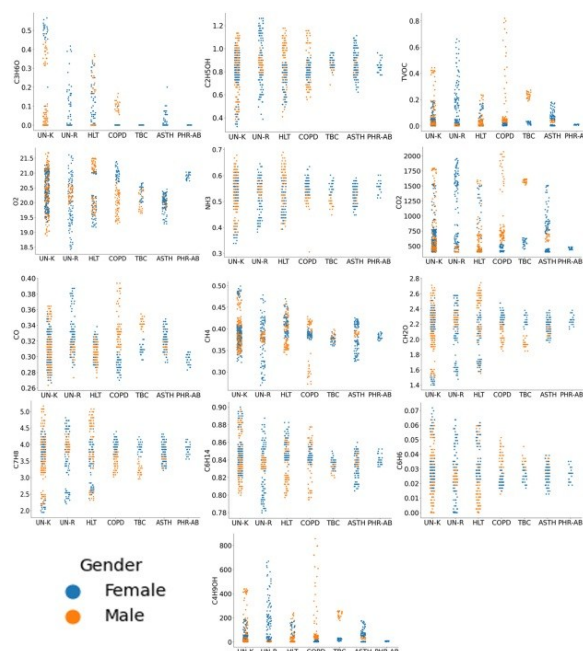


Fig.1 The profile of thirteen gases correlated with the diseases and the gender of the participant

Fig.1 shows the results of the measured gas component in each group, such as UN-K, UN-R, HLT, COPD, TBC, ASTH, and PHRAB represent Unrelated diseases, which represent Unknown

CO, TVOC, and C<sub>4</sub>H<sub>9</sub>OH; CH<sub>4</sub> with C<sub>3</sub>H<sub>6</sub>O, C<sub>6</sub>H<sub>6</sub>, and C<sub>6</sub>H<sub>14</sub>; C<sub>6</sub>H<sub>6</sub> with C<sub>7</sub>H<sub>8</sub>, CH<sub>2</sub>O, C<sub>2</sub>H<sub>5</sub>OH, NH<sub>3</sub>, C<sub>3</sub>H<sub>6</sub>O, CH<sub>4</sub>, and C<sub>6</sub>H<sub>14</sub>; C<sub>7</sub>H<sub>8</sub> with C<sub>6</sub>H<sub>6</sub>, C<sub>3</sub>H<sub>6</sub>O, C<sub>6</sub>H<sub>14</sub>, C<sub>2</sub>H<sub>5</sub>OH, CH<sub>4</sub>, NH<sub>3</sub>, and CH<sub>2</sub>O; C<sub>6</sub>H<sub>14</sub> with C<sub>2</sub>H<sub>5</sub>OH, C<sub>7</sub>H<sub>8</sub>, CH<sub>2</sub>O, C<sub>6</sub>H<sub>6</sub>, and CH<sub>4</sub>; C<sub>2</sub>H<sub>5</sub>OH with CH<sub>4</sub>, C<sub>6</sub>H<sub>14</sub>, C<sub>6</sub>H<sub>6</sub>, C<sub>3</sub>H<sub>6</sub>O, C<sub>7</sub>H<sub>8</sub>, and CH<sub>2</sub>O; C<sub>4</sub>H<sub>9</sub>OH with CO<sub>2</sub> and TVOC; C<sub>3</sub>H<sub>6</sub>O with CH<sub>2</sub>O, C<sub>7</sub>H<sub>8</sub>, NH<sub>3</sub>, C<sub>2</sub>H<sub>5</sub>OH, CH<sub>4</sub>, and C<sub>6</sub>H<sub>6</sub>; NO<sub>2</sub> with NH<sub>4</sub> and NO<sub>2</sub>; NH<sub>3</sub> with C<sub>6</sub>H<sub>6</sub>, C<sub>3</sub>H<sub>6</sub>O, CH<sub>2</sub>O, and C<sub>7</sub>H<sub>8</sub>; and NH<sub>4</sub> and NO<sub>2</sub>. Furthermore, a strong correlation is obtained between TVOC and CH<sub>4</sub>; CO with O<sub>2</sub> and CH<sub>4</sub>; CO<sub>2</sub> with CH<sub>4</sub>; CH<sub>4</sub> with NH<sub>3</sub>, TVOC, C<sub>4</sub>H<sub>9</sub>OH, CO, and CO<sub>2</sub>; C<sub>6</sub>H<sub>14</sub> with NH<sub>3</sub> and C<sub>3</sub>H<sub>6</sub>O; C<sub>2</sub>H<sub>5</sub>oh with NH<sub>3</sub>; C<sub>4</sub>H<sub>9</sub>OH with CH<sub>4</sub> and CO; C<sub>3</sub>H<sub>6</sub>O with C<sub>6</sub>H<sub>14</sub>; H<sub>2</sub>S with NO<sub>2</sub> and NH<sub>4</sub>; NH<sub>3</sub> with CH<sub>4</sub>, C<sub>6</sub>H<sub>14</sub>, O<sub>2</sub>, and C<sub>2</sub>H<sub>5</sub>OH; and NH<sub>4</sub> with H<sub>2</sub>S.

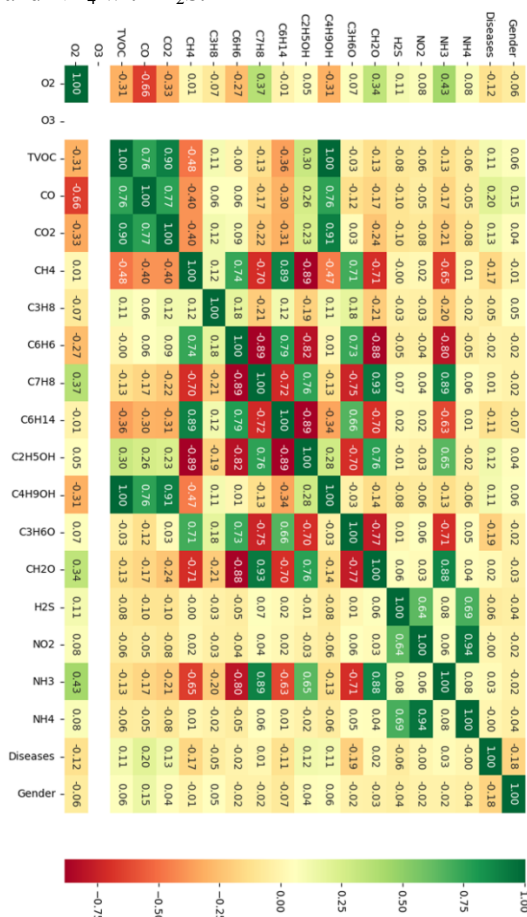


Fig.2 The correlation between the measured gases resulted in various relationship types consisting of very strong ( $C_v$  in the range of -1 to -0.7 and 0.7 to 1.0), strong ( $C_v$  in the range of -0.7 to -0.4 and 0.4 to -0.7), weak ( $C_v$  in the range of -0.4 to -0.1 and 0.1 to 0.4), and no correlation ( $C_v$  in the range of -0.1 to 0.1)

Based on the correlation value on the Fig.2, we configure the gases with three different categories consist of very strong correlation, strong correlation, and weak correlation. In the result, we categorize C<sub>2</sub>H<sub>5</sub>OH, C<sub>3</sub>H<sub>6</sub>O, C<sub>3</sub>H<sub>8</sub>, C<sub>4</sub>H<sub>9</sub>OH, C<sub>6</sub>H<sub>14</sub>, C<sub>6</sub>H<sub>6</sub>, C<sub>7</sub>H<sub>8</sub>, CH<sub>2</sub>O, CH<sub>4</sub>, CO, CO<sub>2</sub>, H<sub>2</sub>S, NH<sub>3</sub>, O<sub>2</sub>, and TVOC in the group of gases with the weak correlation. The gases of C<sub>3</sub>H<sub>6</sub>O, C<sub>6</sub>H<sub>14</sub>, CH<sub>4</sub>, CO, H<sub>2</sub>S, NH<sub>3</sub>, NO<sub>2</sub>, O<sub>2</sub>, C<sub>2</sub>H<sub>5</sub>OH, NH<sub>4</sub>, TVOC, C<sub>4</sub>H<sub>9</sub>OH, and CO<sub>2</sub> are classified as the gases with a strong correlation. Finally, the gases with a very strong correlation contain C<sub>2</sub>H<sub>5</sub>OH, C<sub>3</sub>H<sub>6</sub>O, C<sub>4</sub>H<sub>9</sub>OH, C<sub>6</sub>H<sub>14</sub>, C<sub>6</sub>H<sub>6</sub>, C<sub>7</sub>H<sub>8</sub>, CH<sub>2</sub>O, CH<sub>4</sub>, CO, CO<sub>2</sub>, NH<sub>3</sub>, NH<sub>4</sub>, TVOC, and NO<sub>2</sub>.

## DISCUSSION

Exposure to volcanic gases has been known to have a significant impact on humans. In the case of Mt.Semeru, the sulfur component was the main attention due to the concentration [12,42]. A sulfur component in volcanic eruptions has been related to the development of inflammation, tissue damage, and organ failure. In this study, those impacts are linked with asthma, COPD, and pharyngeal abscess [43–45].

In this study, we group a number of diseases consisted of unknown diseases, asthma, COPD, and a pharyngeal abscess that are related to tissue damage. Volcanic emission gases have been related to the activation of pro-inflammatory cytokine. The cytokine was responsible for the development of asthmatic allergy, COPD, and any other tissue damage [43–45]. Furthermore, the development of respiratory-related diseases is linked with the component of exhaled breath.

As shown in the result, thirteen gas concentrations are found differently depending on the participant condition. Fig.3 shows the concentration of the gases for COPD, asthma, and Pharyngeal Abscess. The different concentrations are related to a metabolism process causing disease [23]. In the case of the unknown disease group, the concentration distribution are similar to the group of COPD, asthmatic, and Pharyngeal Abscess.

For further analysis, we use a Principal Component Analysis (PCA) to find the data cluster for each correlation group as a result of the Heat Analysis. The results that the data cluster are clearly separated for the group of health, COPD, and asthma, as seen in Fig 3. However, the cluster

data still overlap for the group of COPD, tuberculosis, and unknown. Due to the overlapping data of tuberculosis and unknown group and we dismiss those groups from the PCA analysis. Another reason is that tuberculosis and respiratory-related disease are unrelated to volcanic exposures [46,47]. In the case of the Unknown group, we treat the data as the test data. After dropping the group of tuberculosis and unknown, the rest groups are reclassified again. The result is shown in Fig.3(d), where the cluster data are seen more clearly.

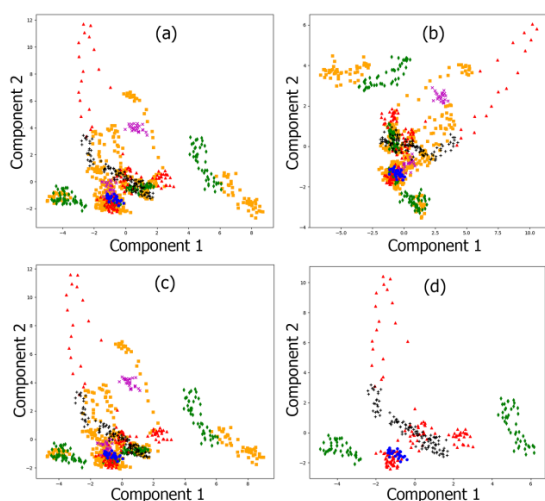


Fig.3 Principal Component Analysis shows the cluster of health participant (◆), COPD (▲), tuberculosis (✕), asthma (+), Pharyngeal Abscess (●), and Unknown disease (■)

Table 1 The results of the evaluation of unknown data using the K-Nearest neighbor method for healthy (HLTH), asthma (ASTH), COPD, and pharyngeal abscess (Phr-Ab)

ID	Pred	Hlth	Asth	COPD	Phr-Ab
1	COPD	0.20	0.16	0.64	0.00
2	Asthma	0.12	0.44	0.20	0.24
3	COPD	0.25	0.13	0.42	0.21
4	COPD	0.04	0.04	0.84	0.08
5	Asthma	0.16	0.36	0.20	0.28
6	COPD	0.00	0.12	0.69	0.19
7	phr-ab	0.08	0.12	0.00	0.80
8	COPD	0.04	0.04	0.80	0.12
9	Asthma	0.00	0.92	0.08	0.00
10	COPD	0.04	0.08	0.76	0.12
11	Health	0.63	0.25	0.08	0.04
12	COPD	0.12	0.32	0.56	0.00
13	COPD	0.00	0.56	0.44	0.00
14	Asthma/Health	0.42	0.42	0.17	0.00
15	COPD	0.08	0.00	0.92	0.00
16	COPD	0.00	0.08	0.71	0.21

We reevaluate the data using KNN and we obtain an accuracy more than 80%. The accuracy value can be trusted when compared to other similar E-Nose systems [35,48,49]. Furthermore, we evaluate the Unknown data with the K-NN approach to see the data categories based on the gas component. As a result, from the 16 participants from the unknown group, 4 participants have the same gas profile as the asthma group, 10 participants were in the COPD group, 1 participant in the Pharyngeal Abscess group, and 2 participants in the healthy group as presented in Table 1. The value of the categorized COPD group is the highest for the participant with an ID of 1, 3, 4, 6, 8, 10, 12, 13, 15, and 16. Meanwhile, the asthma group is found the highest value for the participant with the ID of 2, 5, 9, and 14. In the case of participant 14, the value is similar to the health group as well. The group of pharyngeal abscess and health has the highest value for participants 7 and 11. Finally, we obtain the profile of the exhaled breath related to volcanic-related diseases.

## CONCLUSION

In this study, we successfully profile the exhaled gas content of the Mt. Semeru refugees related to respiratory disease. We find the most possibility of related respiratory diseases are Chronically Obstructive Pulmonary Disease (COPD), tuberculosis, and asthma, with an accuracy more than 80 %.

## ACKNOWLEDGMENTS

This study was supported by Indonesian Ministry of Education, Culture, Research, and Technology. All authors would like to thank the support from Malang branch of The Indonesian Association of Pulmonologists. All authors also acknowledge the kind hand of Azarine A., Maria P.W.W., Ilham R., Anthony, Yokanan, Adrian Y., Muli Y., Juwita F., Silvy A., Naufal A.H., Rachmat S., Andrew S., and Uray R.

## REFERENCES

- [1] Global Volcanism Program. Report on Semeru (Indonesia) [Internet]. Vol. 47, Bulletin of the Global Volcanism Network. <https://volcano.si.edu/showre;> 2022. Available from:

- <https://volcano.si.edu/showreport.cfm?doi=10.5479/si.GVP.BGVN202201-263300>
- [2] Kementerian Energi dan Sumber Daya Mineral. Aktivitas Vulkanik Gunung Semeru, Jawa Timur 4 Desember 2021 [Internet]. Esdm.Go.Id. 2021 [cited 2022 May 14]. p. 1. Available from: <https://www.esdm.go.id/id/media-center/arsip-berita/aktivitas-vulkanik-gunung-semeru-jawa-timur-4-desember-2021>
- [3] NASA. SO<sub>2</sub> climatology from satellite instruments [Internet]. Global Sulfur Dioxide Monitoring Home Page. 2022 [cited 2022 May 14]. Available from: [https://so2.gsfc.nasa.gov/pix/daily/1221/java\\_tropomi\\_so2trm\\_20211208.png](https://so2.gsfc.nasa.gov/pix/daily/1221/java_tropomi_so2trm_20211208.png)
- [4] Muhari A. Korban Meninggal Paska Erupsi Semeru Bertambah Menjadi 51 Jiwa [Internet]. Badan Nasional Penanggulangan Bencana. 2021 [cited 2022 May 14]. p. 1. Available from: <https://bnpb.go.id/berita/korban-meninggal-paska-erupsi-semeru-bertambah-menjadi-51-jiwa>
- [5] Muhari A. Penanganan Paska Awan Panas Guguran Semeru Memasuki Status Transisi Darurat [Internet]. Badan Nasional Penanggulangan Bencana. 2021 [cited 2022 May 14]. p. 1. Available from: <https://bnpb.go.id/berita/penanganan-paska-awan-panas-guguran-semeru-memasuki-status-transisi-darurat>
- [6] Wallrabe-Adams H.J., Lackschewitz K.S., Chemical composition, distribution, and origin of silicic volcanic ash layers in the Greenland-Iceland-Norwegian Sea: Explosive volcanism from 10 to 300 ka as recorded in deep-sea sediments. *Mar Geol.* 2003;193(3–4):273–93.
- [7] Alraddadi S., Assaedi H., Characterization and potential applications of different powder volcanic ash. *J King Saud Univ - Sci* [Internet]. 2020;32(7):2969–75. Available from: <https://doi.org/10.1016/j.jksus.2020.07.019>
- [8] Candeias C., Ávila P.F., Sequeira C., and Manuel A, Rocha F., Potentially toxic elements dynamics in the soil rhizospheric-plant system in the active volcano of Fogo (Cape Verde) and interactions with human health. *Catena.* 2022;209(November 2021).
- [9] Horwell C.J., Baxter P.J., Hillman S.E., Calkins J.A., Damby D.E., Delmelle P., et al., Physicochemical and toxicological profiling of ash from the 2010 and 2011 eruptions of Eyjafjallajökull and Grímsvötn volcanoes, Iceland using a rapid respiratory hazard assessment protocol. *Environ Res* [Internet]. 2013;127:63–73. Available from: <http://dx.doi.org/10.1016/j.envres.2013.08.011>
- [10] Wardoyo A.Y.P., Noor J.A.E., Elbers G., Schmitz S., Flaig S.T., and Budianto A., Characterizing volcanic ash elements from the 2015 eruptions of bromo and raung volcanoes, Indonesia. *Polish J Environ Stud.* 2020;29(2):1899–907.
- [11] Carfora A., Campobasso C Pietro., Cassandro P., La Sala F., Maiellaro A., Perna A., et al., Fatal inhalation of volcanic gases in three tourists of a geothermal area. *Forensic Sci Int* [Internet]. 2019;297(2018):e1–7. Available from: <https://doi.org/10.1016/j.forsciint.2019.01.044>
- [12] Smekens JF, Clarke AB, Burton MR, Harijoko A, Wibowo HE., SO<sub>2</sub> emissions at Semeru volcano, Indonesia: Characterization and quantification of persistent and periodic explosive activity. *J Volcanol Geotherm Res* [Internet]. 2014;300:121–8. Available from: <http://dx.doi.org/10.1016/j.jvolgeores.2015.01.006>
- [13] Burhan E., Mukminin U., A systematic review of respiratory infection due to air pollution during natural disasters. *Med J Indones* [Internet]. 2020;29(1):11–8. Available from: <http://dx.doi.org/10.13181/mji.oa.204390>
- [14] Heaviside C., Witham C., and Vardoulakis S., Potential health impacts from sulphur dioxide and sulphate exposure in the UK resulting from an Icelandic effusive volcanic eruption. *Sci Total Environ* [Internet]. 2021;774:145549. Available from: <https://doi.org/10.1016/j.scitotenv.2021.145549>
- [15] MacNee W., Rennard SI., Hunt JF., Edwards LD., Miller BE., Locantore NW., et al., Evaluation of exhaled breath condensate pH as a biomarker for COPD. *Respir Med* [Internet]. 2011;105(7):1037–45. Available from: <http://dx.doi.org/10.1016/j.rmed.2011.02.009>
- [16] Saalberg Y., Wolff M., VOC breath biomarkers in lung cancer. *Clin Chim Acta* [Internet]. 2016;459:5–9. Available from: <http://dx.doi.org/10.1016/j.cca.2016.05.013>
- [17] Mazzone P.J., Wang X.F., Xu Y., Mekhail T., Beukemann M.C., Na J., et al., Exhaled breath analysis with a colorimetric sensor array for the identification and characterization of lung cancer. *J Thorac Oncol* [Internet]. 2012;7(1):137–42. Available from: <http://dx.doi.org/10.1097/JTO.0b013e318233d80f>



- [18] Navas M.J., Jiménez A.M., and Asuero A.G., Human biomarkers in breath by photoacoustic spectroscopy. *Clin Chim Acta* [Internet]. 2012;413(15–16):1171–8. Available from: <http://dx.doi.org/10.1016/j.cca.2012.04.008>
- [19] Maloča Vuljanko I., Turkalj M., Nogalo B., Bulat Lokas S., and Plavec D., Diagnostic value of a pattern of exhaled breath condensate biomarkers in asthmatic children. *Allergol Immunopathol (Madr)*. 2017;45(1):2–10.
- [20] Rodríguez-Aguilar M., Díaz de León-Martínez L., Gorocica-Rosete P., Pérez-Padilla R., Domínguez-Reyes C.A., Tenorio-Torres J.A., et al., Application of chemoresistive gas sensors and chemometric analysis to differentiate the fingerprints of global volatile organic compounds from diseases. Preliminary results of COPD, lung cancer and breast cancer. *Clin Chim Acta*. 2021;518(February):83–92.
- [21] Herath P., Wimalasekera S.W., Amarasekara T.D., Fernando M.S., and Turale S., Adverse effects of cigarette smoking on exhaled breath carbon monoxide, blood carboxyhemoglobin, and hematological parameters amongst Sri Lankan adult tobacco smokers: A descriptive study. *Popul Med*. 2021;3(Cvd):1–10.
- [22] Španěl P., Smith D., Quantification of volatile metabolites in exhaled breath by selected ion flow tube mass spectrometry, SIFT-MS. *Clin Mass Spectrom*. 2020;16:18–24.
- [23] Liang Y, Gai X.Y., Chang C., Zhang X., Wang J., and Li T.T., Metabolomic Profiling Differences among Asthma, COPD, and Healthy Subjects: A LC-MS-based Metabolomic Analysis. *Biomed Environ Sci* [Internet]. 2019;32(9):659–72. Available from: <http://dx.doi.org/10.3967/bes2019.085>
- [24] Aghaei S.M., Aasi A., Farhangdoust S., and Panchapakesan B., Graphene-like BC6N nanosheets are potential candidates for detection of volatile organic compounds (VOCs) in human breath: A DFT study. *Appl Surf Sci* [Internet]. 2021;536(August 2020):147756. Available from: <https://doi.org/10.1016/j.apsusc.2020.147756>
- [25] Castro M., Kumar B., Feller JF., Haddi Z., Amari A., and Bouchikhi B., Sensors and Actuators B : Chemical Novel e-nose for the discrimination of volatile organic biomarkers with an array of carbon nanotubes ( CNT ) conductive polymer nanocomposites ( CPC ) sensors. *Sensors Actuators B Chem* [Internet]. 2011;159(1):213–9. Available from: <http://dx.doi.org/10.1016/j.snb.2011.06.073>
- [26] Barker M., Hengst M., Schmid J., Buers H.J., Mittermaier B., Klemp D., et al., Volatile organic compounds in the exhaled breath of young patients with cystic fibrosis. *Eur Respir J*. 2006;27(5):929–36.
- [27] Chen H., Qi X., Ma J., Zhang C., Feng H., and Yao M., Breath-borne VOC biomarkers for COVID-19. *medRxiv*. 2020;
- [28] Chambers D.M., Ocariz J.M., McGuirk M.F., and Blount B.C., Impact of cigarette smoking on Volatile Organic Compound (VOC) blood levels in the U.S. Population: NHANES 2003-2004. *Environ Int* [Internet]. 2011;37(8):1321–8. Available from: <http://dx.doi.org/10.1016/j.envint.2011.05.016>
- [29] Beduk T., Durmus C., Hanoglu S.B., Beduk D., Salama K.N., Goksel T., et al., Breath as the mirror of our body is the answer really blowing in the wind? Recent technologies in exhaled breath analysis systems as non-invasive sensing platforms. *TrAC - Trends Anal Chem* [Internet]. 2021;143:116329. Available from: <https://doi.org/10.1016/j.trac.2021.116329>
- [30] Durán Acevedo C.M., Carrillo Gómez J.K., and Albarracín Rojas C.A., Academic stress detection on university students during COVID-19 outbreak by using an electronic nose and the galvanic skin response. *Biomed Signal Process Control*. 2021;68.
- [31] Saidi T., Zaim O., Moufid M., El Bari N., Ionescu R., and Bouchikhi B., Exhaled breath analysis using electronic nose and gas chromatography–mass spectrometry for non-invasive diagnosis of chronic kidney disease, diabetes mellitus and healthy subjects. *Sensors Actuators, B Chem* [Internet]. 2018;257:178–88. Available from: <http://dx.doi.org/10.1016/j.snb.2017.10.178>
- [32] Qian K., Bao Y., Zhu J., Wang J., and Wei Z., Development of a portable electronic nose based on a hybrid filter-wrapper method for identifying the Chinese dry-cured ham of different grades. *J Food Eng* [Internet]. 2021;290(October 2019):110250. Available from: <https://doi.org/10.1016/j.jfoodeng.2020.110250>
- [33] Charles M., Poinot P., Texier F., Arvisenet G., Vigneau E., Mehinagic E., et al., The “Mouth to Nose Merging System”: A novel approach to study the impact of odour on other sensory perceptions. *Food Qual Prefer* [Internet]. 2013;28(1):264–70. Available from:

- <http://dx.doi.org/10.1016/j.foodqual.2012.10.003>
- [34] Mule N.M., Patil D.D., and Kaur M., A comprehensive survey on investigation techniques of exhaled breath (EB) for diagnosis of diseases in human body. *Informatics Med Unlocked* [Internet]. 2021;26:100715. Available from: <https://doi.org/10.1016/j.imu.2021.100715>
- [35] Hidayat S.N., Julian T., Dharmawan A.B., Puspita M., Chandra L., Rohman A., et al., Hybrid learning method based on feature clustering and scoring for enhanced COVID-19 breath analysis by an electronic nose. *Artif Intell Med* [Internet]. 2022;129(May):102323. Available from: <https://doi.org/10.1016/j.artmed.2022.102323> %0Ahttps://linkinghub.elsevier.com/retrieve/pii/S0933365722000884
- [36] Maio S., Baldacci S., Carrozzi L., Pistelli F., Angino A., Simoni M., et al., Respiratory symptoms/diseases prevalence is still increasing: A 25-yr population study. *Respir Med* [Internet]. 2016;110:58–65. Available from: <http://dx.doi.org/10.1016/j.rmed.2015.11.006>
- [37] Molassiotis A., Lowe M., Blackhall F., and Lorigan P., A qualitative exploration of a respiratory distress symptom cluster in lung cancer: Cough, breathlessness and fatigue. *Lung Cancer* [Internet]. 2011;71(1):94–102. Available from: <http://dx.doi.org/10.1016/j.lungcan.2010.04.002>
- [38] Gulsvik A., Bakke P.S., Brøgger J., Nielsen R., and Stavem K., Respiratory symptoms and mortality in four general population cohorts over 45 years. *Respir Med* [Internet]. 2020;170:106060. Available from: <https://doi.org/10.1016/j.rmed.2020.106060>
- [39] Warncke G., Singer G., Windhaber J., Schabl L., Friehs E., Miekisch W., et al., Volatile Organic Compounds, Bacterial Airway Microbiome, Spirometry and Exercise Performance of Patients after Surgical Repair of Congenital Diaphragmatic Hernia. *Molecules*. 2021;26(3):645.
- [40] Xie Y., Meng W.Y., Li R.Z., Wang Y.W., Qian X., Chan C., et al., Early lung cancer diagnostic biomarker discovery by machine learning methods. *Transl Oncol*. 2021;14(1).
- [41] Scarlata S., Pennazza G., Santonico M., Pedone C., and Antonelli Incalzi R., Exhaled breath analysis by electronic nose in respiratory diseases. *Expert Rev Mol Diagn*. 2015;15(7):933–56.
- [42] Heggie T.W., Geotourism and volcanoes: Health hazards facing tourists at volcanic and geothermal destinations. *Travel Med Infect Dis* [Internet]. 2009;7(5):257–61. Available from: <http://dx.doi.org/10.1016/j.tmaid.2009.06.002>
- [43] Li R., Kou X., Tian J., Meng Z., Cai Z., Cheng F., et al., Chemosphere Effect of sulfur dioxide on inflammatory and immune regulation in asthmatic rats. *Chemosphere* [Internet]. 2014;112:296–304. Available from: <http://dx.doi.org/10.1016/j.chemosphere.2014.04.065>
- [44] Li X., Huang L., Wang N., Yi H., and Wang H., Sulfur dioxide exposure enhances Th2 inflammatory responses via activating STAT6 pathway in asthmatic mice. *Toxicol Lett* [Internet]. 2018;285(92):43–50. Available from: <https://doi.org/10.1016/j.toxlet.2017.12.020>
- [45] Wigenstam E., Elfsmark L., Bucht A., and Jonasson S., Inhaled sulfur dioxide causes pulmonary and systemic inflammation leading to fibrotic respiratory disease in a rat model of chemical-induced lung injury. *Toxicology*. 2016;368–369:28–36.
- [46] Ledesma J.R., Ma J., Vongpradith A., Maddison E.R., Novotney A., Biehl M.H., et al., Global, regional, and national sex differences in the global burden of tuberculosis by HIV status, 1990–2019: results from the Global Burden of Disease Study 2019. *Lancet Infect Dis*. 2022;22(2):222–41.
- [47] Moyo S., Ismail F., Van der Walt M., Ismail N., Mkhondo N., Dlamini S., et al., Prevalence of bacteriologically confirmed pulmonary tuberculosis in South Africa, 2017–19: a multistage, cluster-based, cross-sectional survey. *Lancet Infect Dis*. 2022;3099(22):1–9.
- [48] Binson V.A., Subramoniam M., and Mathew L., Detection of COPD and Lung Cancer with electronic nose using ensemble learning methods. *Clin Chim Acta* [Internet]. 2021;523(September):231–8. Available from: <https://doi.org/10.1016/j.cca.2021.10.005>
- [49] Zou Y., Wang Y., Jiang Z., Zhou Y., Chen Y., and Hu Y., Lung Cancer Breath profile as composite biomarkers for lung cancer diagnosis. *Lung Cancer* [Internet]. 2021;154(November 2020):206–13. Available from: <https://doi.org/10.1016/j.lungcan.2021.01.020>

# EFFECT OF DIATOMACEOUS EARTH ON DESICCATION CRACKING OF EXPANSIVE SOILS

Alemshet B. Tadesse<sup>1</sup>, Y. Fukubayashi<sup>2</sup>, A. Koyama<sup>3</sup>, and D. Suetsugu<sup>4</sup>

<sup>1</sup>Interdisciplinary Graduate School of Agri. and Eng., University of Miyazaki, Miyazaki, Japan

<sup>2,3,4</sup> Faculty of Engineering, University of Miyazaki, Japan

## ABSTRACT

Expansive soils shrink and swell are causing considerable density differences as the moisture content varies and cracks develop as the soil dries. This cracking condition has a detrimental effect on the stability of infrastructure built on expansive soil, such as road embankments. This paper investigates the influence of diatomaceous earth (at 5%, 10%, 15%, and 20% DE percent by mass) on the desiccation cracking of expansive soils. The report demonstrates an image analysis technique to describe soil surface cracking quantitatively. The geometric features of cracks such as surface crack area and crack connectivity were estimated and examined. The study considers soil crack area ratio and cracks index to investigate the effect of diatomaceous earth on expansive soil surface cracking. The crack area ratio and cracking index analysis results show that the expansive soil surface cracking is uneven and of significant size. The soil matrix containing 10% and 20% diatomaceous earth has reduced surface cracking and a homogenous radial cracking pattern. The image analysis approach, an essential method to quantitatively quantify soil desiccation cracking, revealed that diatomaceous earth substantially affects surface crack reduction.

**Keywords:** *Expansive Soil, Desiccation Cracking, Diatomaceous Earth (DE), Image Analysis*

## 1. INTRODUCTION

Expansive soils tend to swell as they absorb moisture, whereas they shrink when they lose moisture which encounters volume change because of the dry and wet seasons in the year. In the dry season, desiccation cracking develops due to the loss of water [1]. Desiccation cracks are more common in tropical countries such as Ethiopia due to the prevalent occurrence of expansive soils (i.e., vertisols that account for 10% of the soil distribution), as illustrated in Fig. 1. This natural phenomenon covers a wide variety of scales, from a fraction of smaller sizes to a larger scale of sizes. As a result, soil desiccation cracking is getting massive attention in geotechnical engineering and other related disciplines.

Desiccation cracks illustrated in Fig. 2 are mainly caused by shrinkage due to rapid water evaporation from the soil surface. These desiccation cracks induce an interparticle tension and volume change, increasing cracking permeability and reducing soil stability due to the generated flow paths. It has been noted that the temperature in Ethiopia ranges from 27°C to 50°C; because of climatic changes, rapid water evaporation occurs, leading to desiccation cracking [2]. In general, rainfall assists in the partial or full self-recovery of cracks during the wet season, as shown in Fig. 3 on the surface in shallow and narrower cracks [3]. Whereas heavy rainfall in combination with hot weather contributes to desiccation cracking.

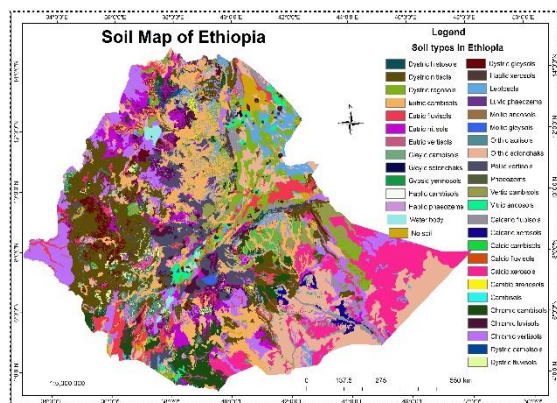


Fig. 1 Soil map of Ethiopia



Fig. 2 Desiccation cracking in expansive natural soil  
(Source: <http://geophilous.blogspot.com>)

The resulting formation of cracking networks negatively alters the soil properties and compromises the integrity of soil structures [3].

Mechanical properties of soils subjected to desiccation cracking are highly influenced by increased compressibility, excessive deformation, and weakened strength. The ultimate reduction of performance and failure of civil infrastructures are due to the combined effects of desiccation cracking influence parameters [4]. A critical influence on the performance of geotechnical engineering structures such as road embankments occurs due to desiccation cracking dictating remedial or eradication solutions such as altering soil property and providing moisture barrier.

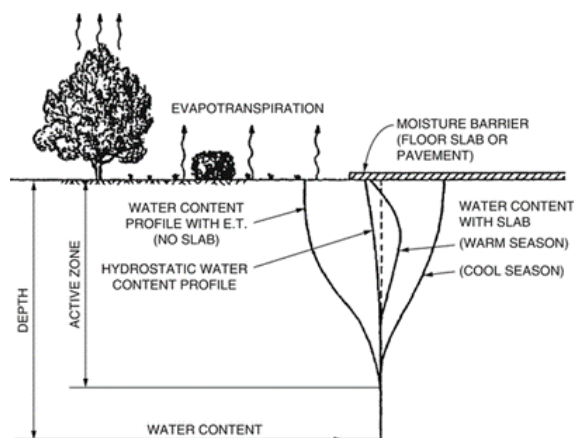


Fig. 3 Water content profiles inactive zones

Different research have been investigated mitigating desiccation cracking by the influence of additives such as cement, lime, sand, fibers, and bio-enzymes [3],[5]. These studies focus on hydraulic conductivity and volumetric shrinkage of clay soil. These additives can reduce shrinkage but sometimes increment in permeability might be observed. For example, Ahmed F. et al. (2021) [6], studied the polypropylene fiber effect on desiccation cracking under multiple wetting-drying cycles on kaolin clay, and the reinforcement reduces cracking.

Very recently, Yaxing et al. (2021) [5] studied the use of fibers (i.e., jute fiber and polyvinyl alcohol fiber (PVA)) and illustrated the evolution of desiccation cracking by applying the digital image correlation (DIC) method. Experimental results showed that the presence of fibers significantly affects the crack evolution and the reinforced soil's length and area during shrinkage.

Furthermore, many other studies have also been conducted on reducing desiccation cracking by utilizing multiple additives. So that in the form of fiber or chemicals to improve shrinkage limits, tensile strength, shear strength, and hydraulic conductivity. However, adding those additives does not significantly affect the mechanical behavior of clay

soils. Hence, further examinations are required to comprehensively understand, quantitatively analyze, and express treated soils. Besides, very few studies have been conducted on the effect of diatomaceous earth (DE) on desiccation cracking reduction. Diatomaceous earth is preferred in this study due to its rich content of silica ( $\text{SiO}_2$ ). It is hypothetically assumed that the silica and other chemical elements in the additive will remove and replace the water molecules of the expansive clay surface and reduce shrinkage and swelling.

Therefore, the objective of this study is to investigate the effect of diatomaceous earth on desiccation cracking of expansive soil by using image analysis techniques to capture the crack morphology, mode of cracking, and crack connectivity. The diatomaceous earth is mixed at 5%, 10%, 15%, and 20% by mass, and the desiccation cracking experimental parameters were examined during drying.

## 2. MATERIALS AND METHODS

Locally available natural expansive soil was used from the Yanaizu area, Fukushima prefecture, Japan, and diatomaceous earth was purchased from the market.

### 2.1 Materials

#### 2.1.1 Expansive Soil

Pertinent characteristics of the soil are shown in Table 1. The soil that passes through a 425 $\mu\text{m}$  sieve was subjected to the free swell index test. The result was categorized under extremely high expansive soil as per the Indian Standard. The chemical composition of materials from energy dispersive spectrometry (EDAX) is presented in Table 2, and the chemical element composition of the soil of Japan.

Table 1. Physical Properties of Yanaizu expansive soil

Soil Property		Value	Standard
Liquid Limit, LL (%)		134.3	ASTM D4318
Plastic Limit, PL (%)		42.3	
Plastic Index, PI (%)		92	
Particle Size Distribution	Gravel (%)	13.5	JGS0131
	Sand (%)	32.2	
	Silt (%)	0.3	
	Clay (%)	54	
Free Swell Index, FSI (%)		134	IS 2720-40
Specific Gravity ( $\rho_s$ , g/cm <sup>3</sup> )		2.55	JGS0111
Soil Class	USCS	CH	ASTM D2487
	AASHTO	Clay	AASHTOM145

AASHTO: American Association of Highway & Transport Office  
ASTM: American Standard Testing Method

IS.: Indian Standard; USCS.: Universal Soil Classification System

Table 2. Chemical Composition of Materials

SiO <sub>2</sub>	Al <sub>2</sub> O <sub>3</sub>	Fe <sub>2</sub> O <sub>3</sub>	CaO	MgO	K <sub>2</sub> O	Na <sub>2</sub> O
* 72.88	14.86	5.98	-	2.55	2.4	1.33
**90.33	5.97	2.5	0.69	0.25	0.26	1.26

\* - Expansive soil, \*\* - Diatomaceous earth

### 2.1.2 Diatomaceous Earth

Filter grade diatomaceous earth was used as an additive in experimental desiccation tests. The fixed point of the study was to utilize brewery silage diatomaceous obtained from beer filtration waste. However, it is not easy to get the waste here in Japan; therefore, we were looking for a commercially available filter grade DE and purchased it from the Showa Chemical Industry Co., Ltd of Japan. Diatomaceous earth was preferred because of its reach silica content (see Table 2) with a hypothesis that the water molecules will be replaced by highly Si, or Al, Fe, and Ca cations due to cation exchange. These ion exchanges will influence the capillary suction and tensile strength and later reflect on desiccation cracking reduction.

## 2.2 Methods

### 2.2.1 Mix Design and Sample Preparation

This study examined five mix designs of one control (natural soil) and four diatomaceous earth-treated blends, as shown in Table 3 below. Therefore, the designation coding system herein, shown in Table 3, is adopted.

Table 3 Soil mix design of the experiment

Mix Group	Designation	DE, %
Control <sup>1</sup>	ES + 0%DE	0
DE Treated	ES + 05%DE	5
	ES + 10%DE	10
	ES + 15%DE	15
	ES + 20%DE	20

<sup>1</sup>Natural Soil, DE: Diatomaceous Earth

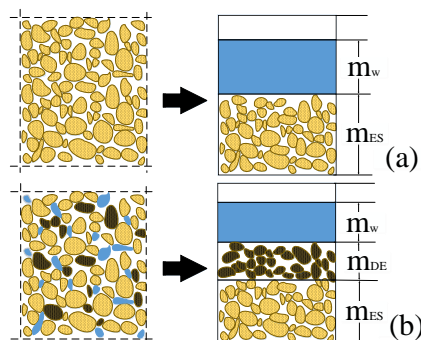


Fig. 4 Untreated and treated soil specimen phases

The diatomaceous earth and water contents percentages are defined in Equation. (1) and (2) according to the phase diagram illustrated in Fig. 4 below:

$$\% \text{ DE} = \frac{m_{\text{DE}}}{m_{\text{BE}} + m_{\text{ES}}} \times 100 \quad (1)$$

$$\% \omega_c = \frac{m_{\text{DE}}}{m_{\text{BE}} + m_{\text{ES}}} \times 100 \quad (2)$$

where DE= DE content,  $\omega_c$  = water content;  $m_{\text{DE}}$ = mass of DE,  $m_{\text{ES}}$  = mass of expansive soil, and  $m_w$  = mass of water.

Sample preparation was done from the collected natural soil was cautiously crushed, air-dried, and sieved through a 2mm and 425 $\mu$ m sieve. Next, the saturated slurry samples were prepared thoroughly by dry mixing of the expansive soil and diatomaceous earth as per the mix design (see Table 3). Then, distilled water close to the liquid limit (LL=134.3%) amount is added to the dry mix, and great care was taken to pulverize lumped particles while mixing and targeting the homogeneity of mixtures. The slurry was then poured into 92mm diameter, 17mm height, and 2mm thickness size greased glass containers and de-aired on a horizontal shaking plate to remove the air bubbles and ensure full saturation. Then, the slurry was sealed by a plastic cover and kept for 24 hours to have a homogenous water distribution before the desiccation experiment started.

### 2.3 Desiccation Cracking Experimental Test

The desiccation cracking experiments were carried out on five saturated slurry state specimens in the laboratory. Samples were subjected to indoor real-time temperature and relative humidity conditions from 3<sup>rd</sup> to 13<sup>th</sup> October 2021 G.C. The sample was desiccated in the laboratory at room temperature of 25  $\pm$  2°C and relative humidity of 85  $\pm$  5% in warm environmental conditions. Digital images were taken at 135mm height above the soil sample, and their respective soil mass was measured every 24hr. The experiment lasted for 12 drying days, and stabilized mass and cracked morphology were observed. Obtained cracked images were analyzed using a digital image analysis tool called ImageJ.

### 2.4 Image-based crack analysis

Digital images were analyzed using an image analysis technique and Fiji (ImageJ) software. The Schematic diagram of the image analysis technique is illustrated as shown in Fig. 5. Crack parameters such as area, crack intensity (D<sub>c</sub>), and crack index (r) were used and computed to characterize the desiccation



cracking of untreated and treated soil specimens [7]. The intensity of soil crack and cracking index are the parameters to describe the soil cracking process, and they are expressed using the linear surface areas of the formula specified in Equation. (3) and (4).

$$D_c = \sum_{i=1}^n \left( \frac{a_{ci}}{A} \right) * 100\% \quad (3)$$

Where  $D_c$  is soil crack area density,  $a_{ci}$  is the sum of all soil crack areas in the typical cracked soil ( $\text{mm}^2$ ), and  $A$  is the total surface area of the ordinary cracked soil ( $\text{mm}^2$ ).

The soil cracks spatial morphological property is expressed in terms of connectivity which is the connection between crack topologies.

$$r = \frac{L}{L_m} = \frac{L}{3(v-2)} \quad (4)$$

Where  $r$  is the connectivity index,  $L$  is the number of connected cracks,  $L_m$  is the number of maximum possible interconnected cracks, and  $v$  is the number of crack nodes. The cracking index  $r$  ranges from 0 to 1, and the greater value indicates higher crack connectivity.

The characterization method preferred here considers the mode of cracking observed from the untreated and treated soil specimens. Among the soil specimens tested, two specific cases are observed; the first case is the irregular desiccated samples in soil matrices (i.e., DE+0%DE, DE+5%DE, and DE+15%DE), and a regular uniform radial cracking observed in (i.e., DE+10%DE and DE+20%DE). Hence, the two cases are exemplified schematically shown in Fig. 6.

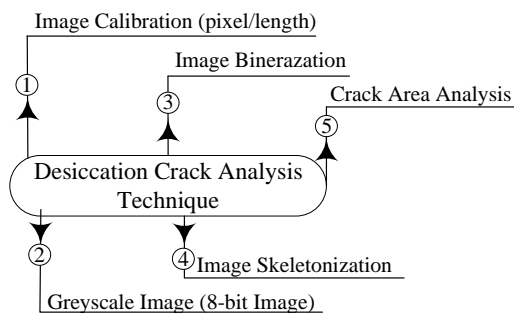


Fig. 5 Schematics of Crack Analysis Technique

Fig. 6 presents the designation for the spatial distribution of surface desiccation cracking area and cracking parameters utilized using the image analysis technique. The crack area denotation described here is for two categories depending on cracking modes (see Fig. 6 a. irregular mode of cracking and b. for uniform radial desiccation cracking). The shrunk (clod) area is the final area of the soil shrink part,

while cracking in between the clod areas is designated as the cracked part. The second mode has two crack area parts, the shrunk area and the uniform cracked part designated as shrunk part. Also, the crack connectivity and index parameters are illustrated in the irregular mode of cracking. The crack segment which connects the nodes (i.e., crack intersection point) is labeled as a crack.

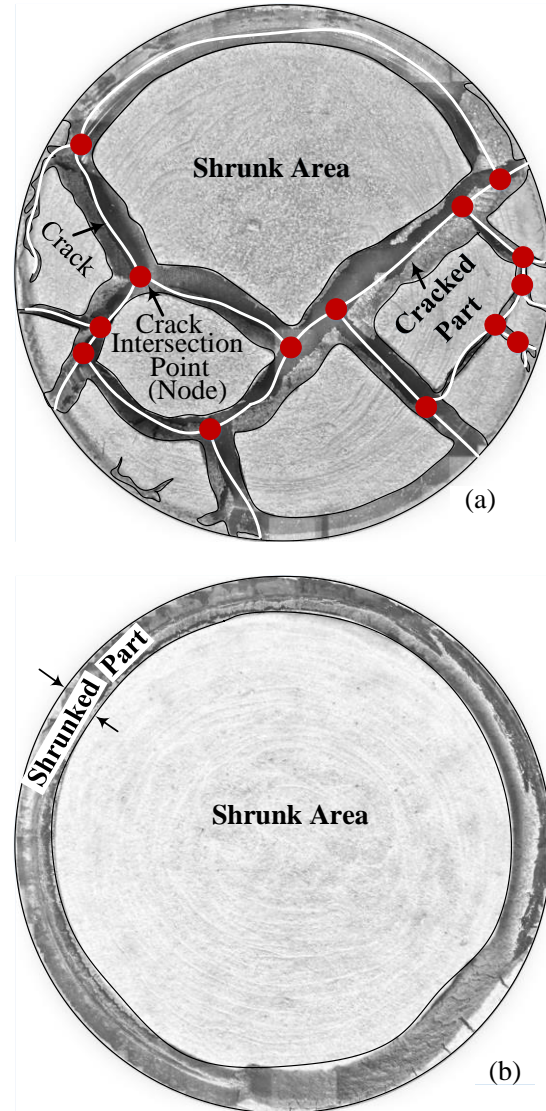


Fig. 6 Crack image processing and geometrical description of the areas a. irregular cracking scenario and b. uniform radial shrinkage scenario of soil specimens

Crack networks on the surface of soil specimens are highly irregular and difficult to measure with a manual measurement technique using a ruler or other conventional method, which brings an error. These errors can be reduced with the digital image analysis method, and reliable, realistic data can be obtained. The image analysis technique is currently utilized by various studies to characterize desiccation cracking in expansive soils quantitatively [7]. The schematics



depicted in Fig. 5 are used in this study. Color images of the cracked samples are converted into greyscale images and later changed into binary black and white photos. Proper engineering judgment needs to be considered to refine the cracks and shrunk areas. It should be scaled, reduced to a greyscale image, binarized and skeletonized to identify and quantify the cracked and shrunk areas analysis using Equation (5).

$$SA = OA - \left( SP + \sum_{i=1}^n CP \right) \quad (5)$$

Where SA is shrunk (clod) area; OA is the original uncracked area; SP area of the shrunk part, and CP area of the cracked part. For irregular cracking mode shrunk part area will be zero; in the nonuniform cracking manner cracked part of the area in Equation **Error! Reference source not found.** will be zero.

### 3. RESULTS AND DISCUSSION

#### 3.1 Mechanism of desiccation cracking

The drying test series in an open indoor laboratory atmosphere and the test results include the evolution of cracking parameters (i.e., expressed in crack area ratio, crack connectivity, and cracking index) and water evaporation rate. In this context, Fig. 7 shows the overall mechanism of desiccation cracking in clay soil. The schematics briefly illustrate and explains the stages of cracking and contributing factors for desiccation cracking. The saturated soil subjected to drying conditions experiences atmospheric air contact at the specimen's top surface. Later water-vapor exchange occurs at the topmost surface, and water-air menisci happen.

Eventually, at a macroscopic level, the suction value (i.e., the difference between air pressure and water pressure) at the beginning of the desaturation point is referred to as the air entry value. This suggests that the negative water pressure plays a critical role in determining when the gas phase intrudes the saturated porous soil body [8]. Hence, capillary suction in the upper layer is developed, which affects the arrangement of soil particles leading to a volume change due to rearrangement. The subsequent process includes an interphase transfer of liquid water, and water vapor develops following several scenarios [9].

With the complexity of pore size distribution, it can be viewed that the air intrusion is an under-surface cavity occurring in the liquid water when a constant temperature is brought to evaporation through an evolution of the suction (negative) pressure. As schematically shown in Fig. 7, water vaporizes in the soil pores and is diffused from the interior consisting of tiny pores to a larger pore extending upwards and being exposed to the

specimen's top surface. With gradual drying of the soil specimens, the water is vaporized at deeper depths in the soil, with the vapor passing through the dry surface layer to the atmosphere, which will, in turn, affect the interparticle tensile strength [9].

Once the tensile stress is developed within the soil particles and exceeds the strength of the soil, desiccation cracks occur with the increment of suction. In addition, soil microstructure usually shows heterogeneity in soil particle arrangements, even for slurry specimens signifying that the tensile bonding strength between the soil particles is not uniform [9]-[10]-[11]. Under this effect of the tensile stress, the weak part of the lower bonded strength fails first, leading us to observe a surface crack at the top surface of the soil specimens. Hence, at the macroscopic level, the tensile strength of the soil is critical in reflecting the soil's mechanical property at the weakest zone. Furthermore, with the gradual change of liquid water to vapor water and later evaporation via macropores by a diffusion, at some point, there will be residual water at the shrinkage potential limit, which the temperature might not remove at that experimental condition time[12]-[13]-[14].

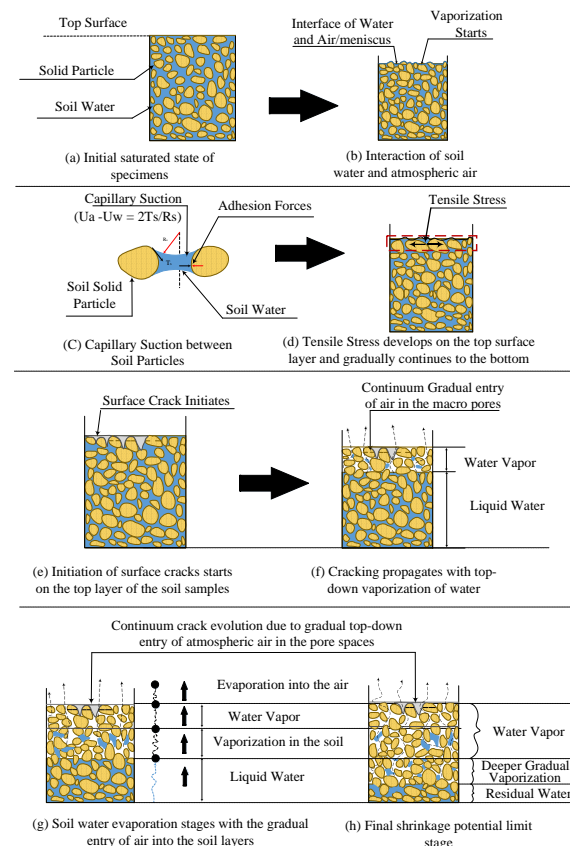


Fig. 7 Mechanism of desiccation cracking schematics

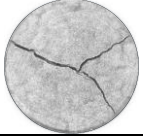





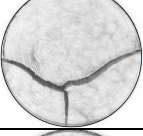



It has been observed that the crack networks in the natural soil, ES+5%DE, and ES+15%DE, have irregularly desiccated segments of cracks. The propagation of desiccation cracks gradually develops

by widening from the preexisting cracks until final consolidation is observed in consecutive mass measurements, while ES+10%DE and ES+20% DE have a uniform radial deformation on the soil blend, resistance in tensile strength has been kept, which needs to be quantified.

### 3.2 Cracking Initiation Pattern Observation

From the desiccation crack, experimental tests resulted in those irregular predominant cracks being developed on the control (natural soil) and soil slurries blended with 5% and 15 % DE. However, soil slurry specimens combined with 15% and 20% DE have uniform regular radial shrinkages.

Table 4. Crack Propagation and End of Dried State of Untreated and Treated Samples

Soil Matrix	Crack Initiation State (START)	Complete Dried State (END)
ES + 0% DE		
ES + 5% DE		
ES + 10% DE		
ES + 15% DE		
ES + 20% DE		

### 3.3 Quantitative characterization of crack area

The surface crack area ratio, crack connectivity, and cracking index parameters were considered to characterize the desiccation cracking in the soil matrices. The crack area ratio of the soil specimen can be evaluated using Equation (6).

$$R_s = \frac{A_{sf}}{A_{si}} \quad (6)$$

Where  $R_s$  = Area ratio of soil specimens

$A_{sf}$  = Area of the final surface area of soil specimen

after shrinkage ( $\text{mm}^2$ ),  $A_{si}$  = Area of the initial surface area of soil specimen before shrinkage ( $\text{mm}^2$ ).

The spatial soil connectivity is calculated using the connectivity index parameter  $r$  among the soil specimens. Fig. 8 illustrates the soil specimens' soil crack morphology intensity and connectivity index. It shows the crack intensity and index from the beginning of the crack initiation, starting from the 3<sup>rd</sup> day to the stability of cracking from the 7<sup>th</sup> to 11<sup>th</sup> day of the desiccation cracking experiment. The cracking index indicates that the natural soil, ES+5%DE, and ES+15%DE have effective connectivity. However, the soil blend ES+10%DE and ES+20%DE doesn't have a significant cracking index. Notably, ES+20%DE significantly reduces desiccation cracking intensity and spatial crack connectivity.

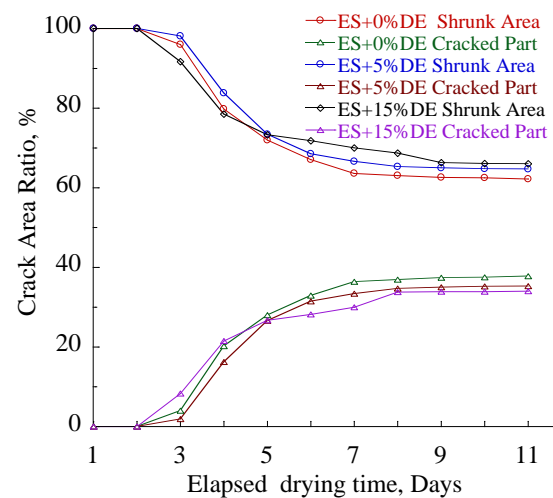


Fig. 8 Crack area ratio comparison of the irregular desiccated soil specimens

Fig 8 illustrates the cracking intensity among the soil matrices, that have irregular cracking modes. The addition of 5% DE and 15% DE does not influence the desiccation cracking of the expansive soil. However, the soil blends at 10%DE and 20%DE have significantly reduced the morphology of crack density and crack connectivity. But as it is already cited in Fig. 7, which clearly illustrates the mechanism of desiccation cracking and associated parameters related to that. Therefore, the capillary suction, which is dependent on cation exchange capacity, tensile stress in the soil mass which emanates from the suction development, and shear strength of the soil, needs to be addressed to comprehensively understand and reduce desiccation cracking in expansive soil.

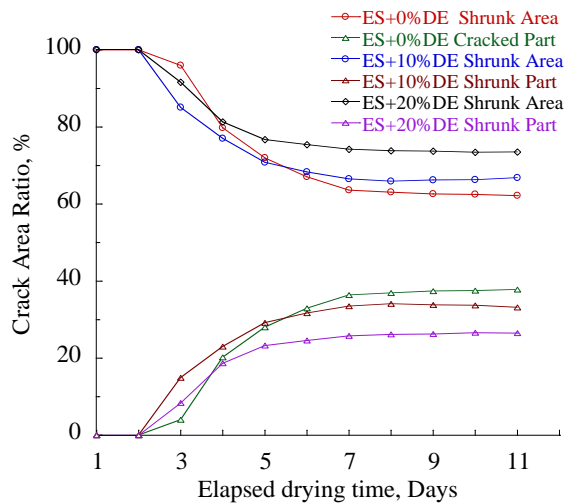


Fig. 9 Crack area ratio comparison of the regular desiccated soil specimens

The result in Fig. 9 presents the crack area ratio comparison between the natural soil and soil matrices at 10% and 20% diatomaceous earth-treated samples. It is observed that the DE at 10% and 20% mix has significantly reduced the desiccation cracking. The maximum crack area ratio resistance observed is at 20% DE mixture, which is about a 16% reduction from the other soil matrices.

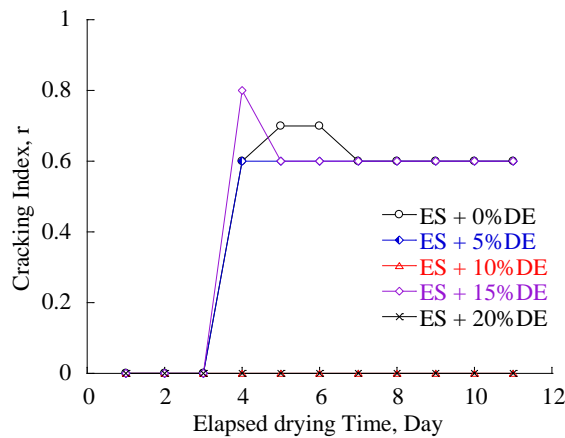


Fig. 10 Soil crack connectivity index

Fig. 10 expresses the cracking index comparison; it is observed that the crack connectivity in 10% and 20% DE mixed specimens are null. However, the natural soil, 5% and 15% DE mixed soils cracking index result ranges from 0.6 to 0.8. The cracking index results in the natural soil, 5% and 15% DE has shown that there is a significant number of interconnected cracks. Thus, such a scenario has an implication for the expansive soil in terms of permeability of water during wet seasons and loss of strength to bear the self-weight as well as external loads.

### 3.4 Soil water evaporation

Initially, under the saturated condition, the soil specimens have enough water in the soil pore spaces. During the drying state of the soil specimens, the soil water at the topmost surface of the specimen changes to water vapor and is continuously removed from the soil pores, which start from the topmost surface and get deeper. Thus, the upward diffusion of vapor exceeds the vaporization within the soil and the diffusion of vapor from the underlying layer [15].

When the soil gets dry over the experimental dates, the evaporation rate calculation in Equation (7) below is adapted from reference [15]:

$$E = \frac{\Delta m}{\rho_w A \Delta t} \quad (7)$$

Where  $E$  (mm/h) is the evaporation rate;  $\Delta m$  (g) refers to the mass change of the tested soil under evaporation within the time interval  $\Delta t$  (h);  $\rho$  corresponds to the water density ( $0.001\text{g/mm}^3$ ), and  $A(\text{mm}^2)$  is the area of the magnitude of the bottom surface of the container obtained from the image analysis.

From Fig. 11, it can be observed that the evaporation rate evolution in the soil specimen under the drying desiccation experiment elapsed time and temperature difference between two consecutive days. When the desiccation drying process continues, the temperature difference increases, but on the third day of the test, the temperature difference will drop, and crack initiation starts. Eventually, the evaporation rate decreases with different temperatures. According to Table 4 and Fig. 11, the soil matrices experience a sudden evaporation rate increment at the temperature difference drop point and gradually decrease in rate, but cracks gradually develop and keep a stable crack evolution.

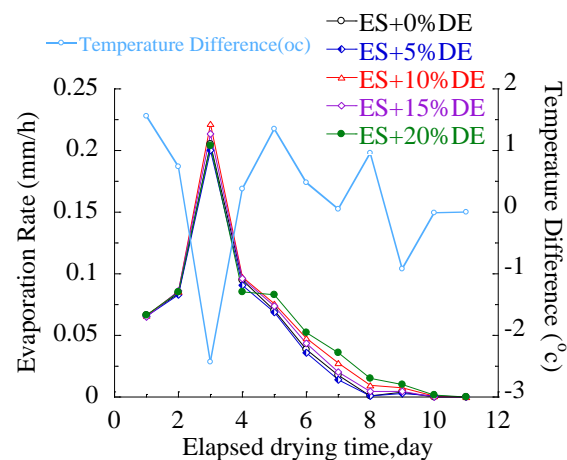


Fig. 11 Evaporation rate of tested soil specimens

#### 4. CONCLUSIONS

In conclusion, the experimental results showed that diatomaceous earth could be used as an additive to reduce desiccation cracking of expansive soil. The results show that the addition of diatomaceous earth affects the desiccation cracking, which in turn has an implication on the physical, mechanical, and chemical properties of expansive soil. The DE-expansive soil matrix with higher DE content spatial distribution in a desiccation cracking manner. Particularly, the observed reduction in desiccation cracking at a mixture of 20% diatomaceous earth decreased the crack spatial distribution by 16%. Also, with an increase in diatomaceous content, the cracking connectivity at 10% and 20% diatomaceous earth soil matrix manifested a maximum removal of crack connectivity. However, it was assumed that the water would be absorbed with the addition of diatomaceous earth, but the experimental results didn't reflect that. This result was due to the high pore size distribution, resulting in a high evaporation rate.

#### 5. FURTHER STUDY

The authors will further study additional experimental parameters to comprehensively comprehend and explain the effectiveness of diatomaceous earth on desiccation cracking of expansive soil. Further experiments such as cation exchange capacity, soil suction, tensile strength test, shear strength, and pore distribution will be tested.

#### 6. ACKNOWLEDGMENTS

This work was supported by JST-JICA, SATREPS, grant number JPMJSA1807. I would like to extend my sincere gratitude to my immediate supervisors Pr. Daisuke Suetsugu and Dr. Fukubayashi Yoshinori for their relentless guidance and support.

#### 7. REFERENCES

1. Tang, C.S.; Zhu, C.; Cheng, Q.; Zeng, H.; Xu, J.J.; Tian, B.G.; Shi, B. Desiccation Cracking of Soils: A Review of Investigation Approaches, Underlying Mechanisms, and Influencing Factors. *Earth-Science Rev.* **2021**, *216*, 103586, doi:10.1016/j.earscirev.2021.103586.
2. Walke, B. Seasonal Weather Assessment for Ethiopia. **2016**, *3*.
3. Kim, S.; Xue, J.; Xie, Y.; Zhou, L. Controlling Desiccation Cracks in Clay with Fibre and Enzyme. *Proc. 2nd Symp. Coupled Phenom. Environ. Geotech.* **2017**.
4. Costa, S.; Kodikara, J.; Barbour, S.L.; Fredlund, D.G. Theoretical Analysis of Desiccation Crack Spacing of a Thin, Long Soil Layer. *Acta Geotech.* **2018**, *13*, 39–49, doi:10.1007/s11440-017-0602-9.
5. Xu, Y.; Yao, X.; Zhuang, Y.; Duan, W.; Zhang, X.; Hu, S.; Dong, X. The Effects of Fiber Inclusion on the Evolution of Desiccation Cracking in Soil-Cement. *Materials (Basel)*. **2021**, *14*, 1–13, doi:10.3390/ma14174974.
6. KHALIFA, A.; Galaa, A.; mohamed, M. Effect of Polypropylene Fibers Length and Content on Cracks Development in Clay Lining. *J. Al-Azhar Univ. Eng. Sect.* **2022**, *17*, 65–82, doi:10.21608/aej.2022.216585.
7. Shit, P.K.; Bhunia, G.S.; Maiti, R. Soil Crack Morphology Analysis Using Image Processing Techniques. *Model. Earth Syst. Environ.* **2015**, *1*, 1–7, doi:10.1007/s40808-015-0036-z.
8. Hu, L.B.; Hueckel, T.; Péron, H.; Laloui, L. Modeling Evaporation, Shrinkage and Cracking of Desiccating Soils. *12th Int. Conf. Comput. Methods Adv. Geomech. 2008* **2008**, *2*, 1083–1090.
9. Tang, C.S.; Cui, Y.J.; Tang, A.M.; Shi, B. Experiment Evidence on the Temperature Dependence of Desiccation Cracking Behavior of Clayey Soils. *Eng. Geol.* **2010**, *114*, 261–266, doi:10.1016/j.enggeo.2010.05.003.
10. Hamza, O.; Ikin, J. Electrokinetic Treatment of Desiccated Expansive Clay. *Geotechnique* **2020**, *70*, 421–431, doi:10.1680/jgeot.18.P.266.
11. Abbaszadeh, S.; Houston, S.L.; Zapata, C.E. Effect of Desiccation Cracking on the Swell and Swell Pressure of Expansive Clay. *Geotech. Struct. Eng. Congr. 2016 - Proc. Jt. Geotech. Struct. Eng. Congr. 2016* **2016**, 2054–2065, doi:10.1061/9780784479742.176.
12. Merlin, O.; Al Bitar, A.; Rivalland, V.; Béziat, P.; Ceschia, E.; Dedieu, G. An Analytical Model of Evaporation Efficiency for Unsaturated Soil Surfaces with an Arbitrary Thickness. *J. Appl. Meteorol. Climatol.* **2011**, *50*, 457–471, doi:10.1175/2010JAMC2418.1.
13. Tang, C.S.; Shi, B.; Liu, C.; Suo, W. Bin; Gao, L. Experimental Characterization of Shrinkage and Desiccation Cracking in Thin Clay Layer. *Appl. Clay Sci.* **2011**, *52*, 69–77, Doi:10.1016/j.clay.2011.01.032.
14. Al-Dakheeli, H.; Bulut, R. Interpretation of Desiccation Soil Cracking in the Framework of Unsaturated Soil Mechanics. *Geotech. Eng.* **2019**, *50*, 74–80.
15. Zeng, H.; Tang, C.S.; Zhu, C.; Cheng, Q.; Lin, Z. ze; Shi, B. Investigating Soil Desiccation Cracking Using an Infrared Thermal Imaging Technique. *Water Resour. Res.* **2022**, *58*, 1–22, doi:10.1029/2021WR030916.

# URBAN HEAT HAZARD MODEL BASED ON LOCAL CLIMATE ZONE

Adi Wibowo<sup>1</sup>, Nadira Retno Abisha<sup>2</sup>, Eko Kusratmoko<sup>3</sup> and Ratna Saraswati<sup>4</sup>

<sup>1,2,3</sup> Department Geography, Faculty Mathematics and Natural Sciences, University of Indonesia, Indonesia.

## ABSTRACT

Urban heat hazard is the temperature in an urban area of more than 30°C and impacts humans. The local climate zone (LCZ) is an area within 100 x100 meters and has a specified climate type. The LCZ is based on the composition of developed and vegetated areas. The value of LCZ represents air surface temperature as an effect of land surface temperature on the environment. The study aims to develop an urban heat hazard model based on the local climate zone. The study used high-resolution multi-spectral imagery collected from remote sensing using Google Earth Engine, and the result uses to develop LCZ and Land Surface temperatures (LST). Local Climate Zone in the study area with 1.000 x1.000 m<sup>2</sup> generated from 100 x 100 meters based on band thermal Landsat data. The LST value uses an algorithm to determine the effect on the environment as air surface temperature and the impact on humans based on the Universal Thermal Climate Index. This study concluded that a local climate zone determines the urban heat hazard in the city regarding urban heat signature. The urban heat hazard affects the environment, with air surface temperature getting more than 32°C, which impacts a human with head headache, sweat, and heatstroke.

*Keywords: Land surface temperature, Urban Heat Signature, air surface temperature, local climate zone, urban heat hazard*

## 1. INTRODUCTION

The Changes in land cover impact two aspects, natural variations of the earth system and human activities [1]. Some examples of land cover changes caused by human activities include bare land surfaces and vegetation converted into impermeable surfaces such as asphalt, concrete, and cement or changing urban morphology such as building areas with varying heights and densities [2]. This land cover change causes the temperature on the earth's surface to change [3].

Land cover change is a global environmental problem, especially in developing countries [4]. Changes in land cover from vegetation to urban land cause a break in the carbon and water cycle and energy fluxes between the soil and the atmosphere [5]. Land Surface Temperature (LST) derived from remote-sensed Thermal Infrared (TIR) satellite imagery is a crucial variable in understanding the impact of land use and land cover change (LULC), which has been linked to urban thermal patterns in various ways (Soydan, 2020) [6]. LST is also an important variable related to climate change in urban areas and indicates ground-level energy balance [7].

Air temperature is essential in explaining the conditions of the terrestrial environment on earth [8]. Land cover types with high vegetation cover are associated with low temperatures, and conversely, land cover types with low vegetation cover are associated with high temperatures [9]. As a consequence of changes in the heat balance and

Urban Heat Island (UHI) [10], the air temperature in urban areas with dense buildings/populations is higher than the temperature in the surrounding areas/outskirts of the city [11]. This explanation provides an overview of existing research that has not yet produced a local climate map based on changes in ground cover, land surface temperature and air temperature.

Spatial-temporal analysis of land use can be carried out with the help of Google Earth Data [12] which deals with land cover changes related to soil surface heat [13]. Hot temperatures can impact the environment [14] [15], that research has been carried-out on the relationship between changes in ground cover and land surface temperature and air temperature.

Climate is the weather conditions in an area over a long period [16] [17]. The current climate classifications made for macro-scale (> 10,000 km) and mesoscale (100 – 1000 km) [18]. Microclimate classification is not widely used [19]. The division of climate into smaller scales, such as in urban areas, was not widely applied until the emergence of the theory of Local Climate Zones (LCZ). LCZ is an urban land classification system based on the morphological characteristics of the city, including buildings and types of land cover [20]. The Local Climate Zone describes an area with uniform land cover, structure, building materials and human activities within 100 meters to several kilometres [21]. Local climate zones are currently widely used as a reference in studies related to UHI because their



typology is universal and can classify urban areas worldwide with the same standard [22]. Local Climate Zone is the latest method in climate classification for an urban scale.

The heat effect on an urban area is called an urban heat hazard based on a threshold. The threshold used the Universal Temperature Climate Index [14] [15] for assessing the Urban Heat Hazard (UHH). It will become an urban heat hazard threat whenever urban heat signatures are above their threshold [13]. The urban heat hazard could threaten the sustainable urban environmental quality and human well-being.

## 2. METHOD

The study uses Landsat 8 OLI-TIRS medium resolution to extract land cover features and generate temporal LST. Remote sensing data processing, including land cover classification and LST processing. The satellite image used in this study is the Landsat 8 OLI/TIRS Satellite Imagery which was taken in the month with the lowest rainfall with more than 20% cloud cover. The nomenclature used is the 2010 National Standardization Agency nomenclature which is generalized to land cover. The classification is divided into five classes: water bodies, built-up land, open land, non-agricultural vegetation, and agricultural vegetation. The area of each class calculates every year to determine the changing area. The Khat Kappa method is a statistical calculation method used in research to test the accuracy of the data between land cover classification resulting from satellite imagery processing and the results of Google Earth validation and field surveys. The land surface temperature was obtained from calculating the satellite brightness value in identifying the land surface temperature, namely band 10 on the Landsat 8 OLI/TIRS image, with the formula in Eq. 1.

$$L\lambda = (M \times DN) + A \quad (1)$$

The first step is to change the image pixel value (DN) to spectral radiance, where  $L\lambda$  is the spectral radiance ( $Wm^{-2}SR^{-1}\mu m^{-1}$ ),  $M$  is the multiplicative digital number in band 10, and  $DN$  is the digital number in band 10. Moreover,  $A$  is the additive value in band 10. After the spectral radiance value is obtained, it is changed to estimate the soil surface temperature value with the formula in Eq. 2.

$$T = \frac{K2}{\ln\left(\frac{K1}{L\lambda} + 1\right)} \quad (2)$$

Where  $T$  is the temperature of the satellite sensor (Kelvin),  $K1$  is the calibration constant 1 for Landsat OLI (774853 K),  $K2$  is the calibration constant 2 for Landsat OLI (1321.0789 K), and  $L\lambda$  is the spectral radiance band 10. Kelvin temperature value converted to Celsius with the following algorithm in Eq. 3.

$$LST(Celcius) = T - 272,15 \quad (3)$$

Temp-Kelvin is the estimated land surface temperature from satellite sensors in Kelvin units.

The result of air surface temperature modelling will create a surface air temperature map by applying the existing model using a raster calculator on the ArcGISPro device.

The study area is Bogor City, located in the western part of West Java Province, Indonesia, at  $106^{\circ}43'30''$  -  $106^{\circ}51'00''$ E and  $6^{\circ}30'30''$  -  $6^{\circ}41'00''$  S (Fig. 1). The result used to develop LCZ and Land Surface temperatures (LST). Local Climate Zone in the study area with  $1.000 \times 1.000 \text{ m}^2$  generated from  $100 \times 100$  meters based on band thermal Landsat data and Land Cover Type. The LST value uses an algorithm to determine the effect on the environment as air surface temperature and the impact on humans based on the Universal Thermal Climate Index.

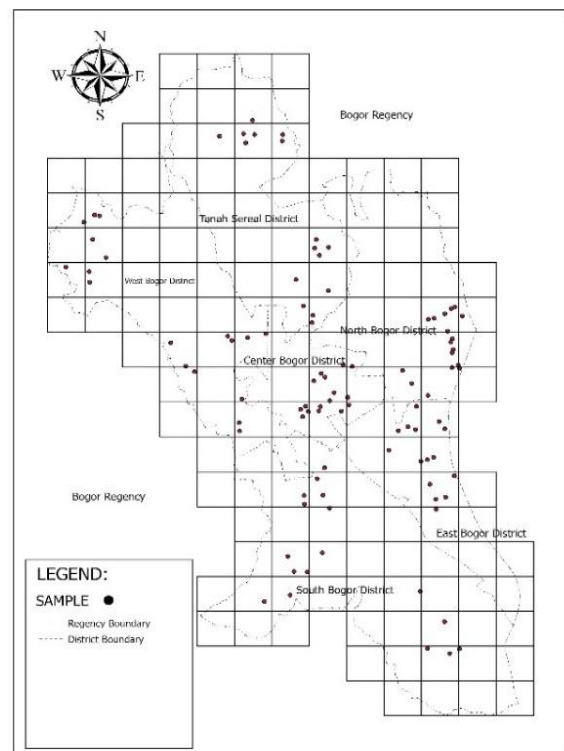


Fig. 1 The study area and Sample Location.

The threshold becomes a hazard whenever the temperature of land cover types is above  $32^{\circ}\text{C}$  with category intense heat stress [14]. The threshold is based on the Universal Temperature Climate Index [14] [15] for assessing the Urban Heat Hazard (UHH). The UHH uses spatial analysis (spatial pattern) and overlays between landcover types, LST and Air Surface temperature (AST). Thus all generated spatial models of Urban Heat Hazard based on the Local Climate Zone in Bogor City in 2022.

## 3. RESULT AND DISCUSSION

### 3.1. Green Open Space

Based on the results of Landsat 8 OLI image processing in 2022 (Fig. 2), it has known that the total green open space area is 4,577 ha or 39% of the area of Bogor City. The area consists of public green open



space and private green open space. If it is reviewed based on Law No. 26 of 2007 concerning spatial planning, which regulates the area of green open space in urban areas, it must be at least 30% of the total city area. The sub-district with the most significant total green open space is the South Bogor District, with an area of 1,745 ha of green open space whose territory has a hilly area. Meanwhile, the district with the slightest green open space is in Central Bogor District, with an area of 260 ha.

Table 1 Green Open Space in Bogor City, 2022

Green Open Space	Area (m <sup>2</sup> )	Per cent (%)
Public	2	5
Private	1	6

Source: Data Processing, 2022

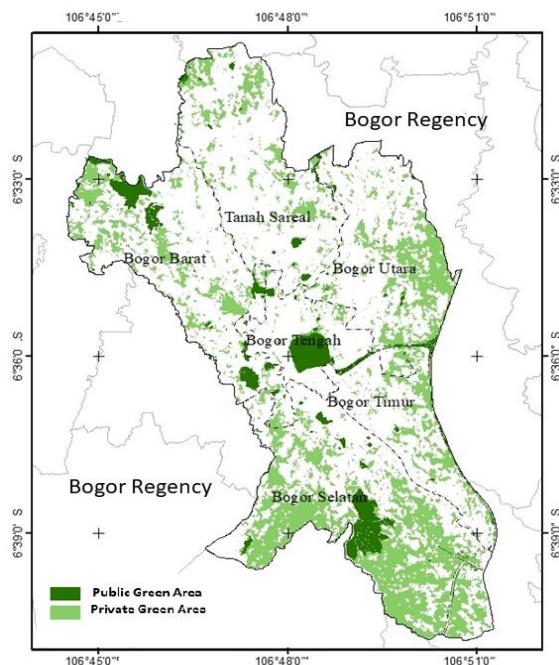


Fig. 2 The Green Open Space in Bogor City, 2022

### 3.2. Local Climate Zone

The land cover map for 2018 and 2022 was generated from processing Landsat 8 OLI satellite imagery data recorded on 1st April 2018 and 4<sup>th</sup> April 2022. Land cover in the form of built-up land occupies about 6,459 hectares, or 55% of the area of Bogor City. Meanwhile, for land cover in the form of open land and water bodies, each occupies an area of 1% and 4% of the total area of Bogor City. The built-up land area dominates the Bogor City area with a percentage of 57% or around 6,782 Ha. This increase was caused by a change in land cover, initially in the form of open land or vegetated land into built-up land. The area of vegetated land is decreasing over time because various developments in the city area replace it. Meanwhile, open land occupies the smallest area of 83 hectares or 1% of the total area. Meanwhile, the

water body has an area of 408 hectares or 3% of the total area of Bogor City (Table 2).

Table 2 The Land Cover Change Between 2018 and 2022 in Bogor City

Land Cover	2018	2022
Green Open Space	4.876	4.577
Build-up Area	6.459	6.782
Open Space	72	83
Water Body	443	408
Total Area	11.850	11.850

Sources: Data Analysis

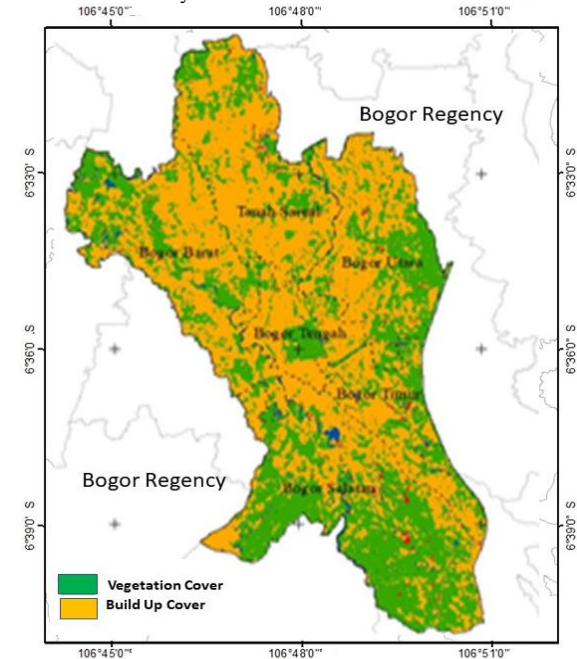


Fig. 3 The Land Cover in Bogor City, 2022

Based on the results of the 2018 Landsat 8 OLI image analysis, Bogor City's Land Surface Temperature (LST) ranges from 15 - 35 °C (Fig. 4). Bogor City during 2018 dominated LST with 26 – 30°C an area of 7646.26 Ha or 64.5% of the area of Bogor City. The LST with 15 – 20°C with an area of 29.69 or 2% based on Bogor City (Table 3).

Table 3 The Land Surface Temperature Between 2018 and 2022 in Bogor City

LST (°C)	2018 (m <sup>2</sup> )	2022 (m <sup>2</sup> )
15 - 20	29.69	0
21 - 25	2,714.15	0
26 - 30	7,646.26	2,640.84
31 – 35	1,459.91	8.882.01
> 35	0	363.15

Sources: Data Analysis

Areas with high-class LST in 2018 in Bogor City spread over land cover areas with the built-up area. Areas with high-temperature LST spread in the northern part of Tanah Sareal District, the southern

part of North Bogor District, southeast and north of North Bogor District, the northern part of South Bogor, the northeastern part of Central Bogor, and West Bogor District (Fig. 4).

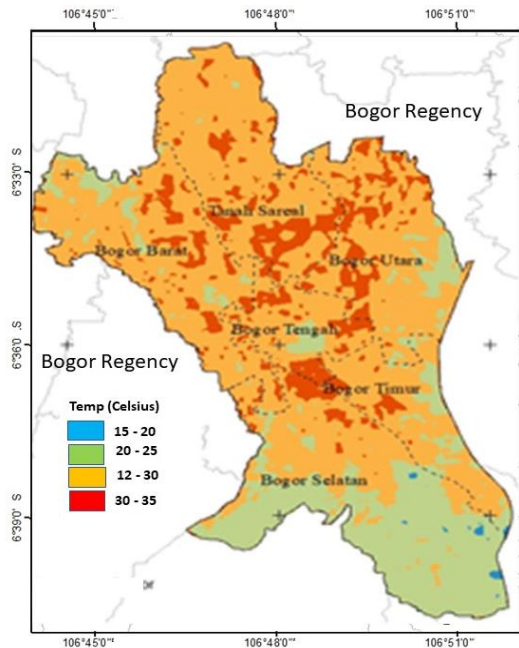


Fig. 4 The Land Surface Temperature in Bogor City, 2018

Based on the results of the Landsat 8 OLI image conversion recorded in 2022, the Land Surface Temperature (LST) of Bogor City is between 25°C–more than 35°C, including in the medium – very high class (Fig. 5). LST Bogor City in 2022 domination by high temperature, with an area of 8,882.01 ha or 74.9%, LST with a medium temperature laid on 2,640.84 ha or 22.6%, and very high-temperature is 363.15 ha or 3% (Table 3).

Areas with high-class LST in 2022 in Bogor City are spread over areas with various land covers, including vegetated land, built-up land, and open land, except for water bodies. Areas with very high-class LST are spread out in the centre of Bogor City with land cover, namely built-up land. Areas with moderate LST in 2022 in Bogor City spread over areas with land cover, namely vegetated land spread across the south and northwest of Bogor City (Fig. 5).

Based on Land Cover and Land Surface Temperature, both of them generate a Local Climate Zone (LCZ) within 1,000 x 1,000 meters. The type of LCZ is separated into five classes (Fig. 6). LCZ 1 is a type of land cover with 100 % vegetation, LCZ 2 with 80 % is vegetation-covered, LCZ 3 covers with 60 %, LCZ 4 covers with 40 % vegetation covered and LCZ 5 covers similar or less than 20 % covered by vegetation (Table 4).

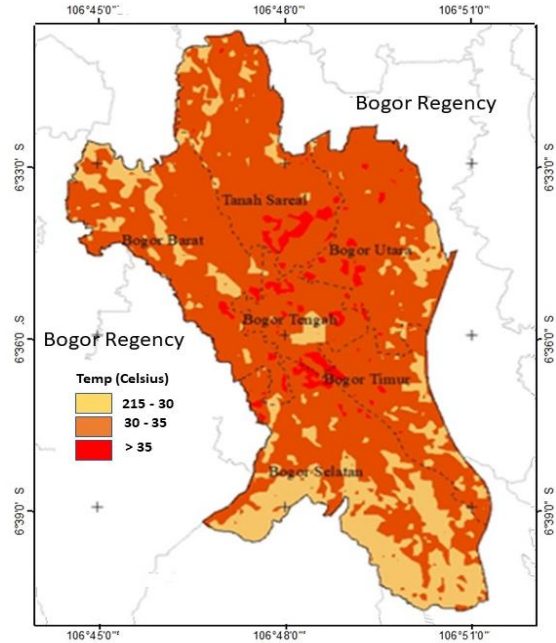


Fig. 5 The Land Surface Temperature in Bogor City, 2022

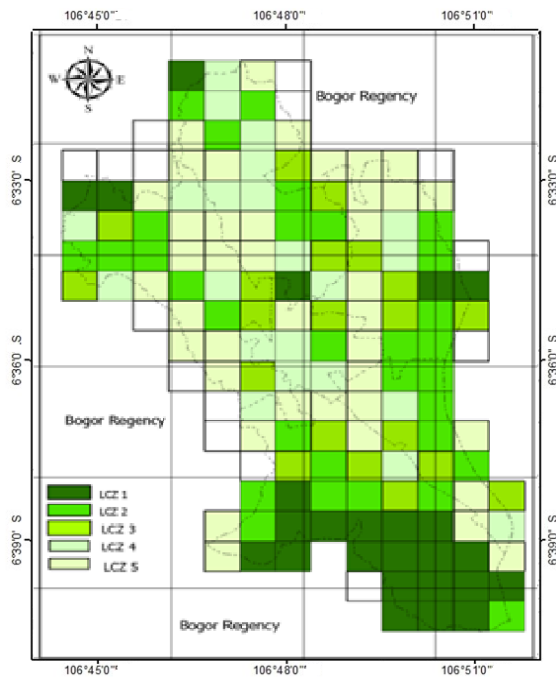


Fig. 6 Local Climate Zone In Bogor City, 2022

Table 4 Local Climate Zone in Bogor City, 2022

LCZ	Total Grid	Area (m <sup>2</sup> )	Percentage (%)
LCZ 1	25	25.000	20
LCZ 2	31	31.000	24
LCZ 3	21	21.000	16
LCZ 4	35	35.000	25
LCZ 5	20	20.000	15

Sources; Data Analysis

### 3.3. Urban Heat Hazard

Based on Land Surface Temperature on Universal temperature Index, Urban Heat Hazard in 2018 only maximum with Moderate Hazard, and on the other hand in 2022, the Urban Heat Hazard getting High Heat Hazard caused the temperature upper than 35°C (Table 5). The impact of high heat hazards on the human body is getting sweat and head Headaches until heat stroke. Moreover, the distribution of Urban Heat Hazard spreads around Bogor City (Fig. 7).

A previous study by Ali and Patnaik concluded that residents in summer could improve the urban climatic condition through shading and transpiration. In contrast, plants release water vapour into the surroundings, increasing relative humidity and decreasing air temperature [23]. The Urban Heat will not impact humans if the temperature is lowest, caused by vegetation-covered (plants) dominant in that areas. This result had similar to Ali and Patnaik, where the dense vegetation covered was the lowest temperature due to urban heat hazards.

Table 5 The Urban Heat Hazard Between 2018 and 2022 in Bogor City

LST (°C)	2018	2022
15 - 20	No Hazard	0
21 - 25	No Hazard	0
26 - 30	Low	Low
31 – 35	Moderate	Moderate
> 35	0	High

Sources: Data Analysis

Threatening the natural ecosystem creates vulnerability to an environmental hazard [24]. The research agrees with Bekele et al., which explained the land cover changes in Bogor City. These changes will generate the heat hazard in Bogor City as Urban Heat Hazard Threat.

Generally, cities face specific urban events due to the urban setting that can alter the local microclimate with higher impacts [25]. Urbanization increases the risk of extreme heat episodes in Europe's cities due to the loss of urban green space [26]. That spatial-temporal detecting land cover changed much importance [27]. This research agrees with Ashaolu et al. to detect the land cover change. The research detecting land cover changed the effect on urban heat and impact on air surface temperature as thermal comfort.

Finally, the novelty of the result is that the research improved the Local Climate Zone could detect urban heat hazards based on a combination of vegetation covered and build-up area.

## CONCLUSIONS

The LST value uses an algorithm to determine the effect on the environment as air surface temperature and the impact on humans based on the Universal Thermal Climate Index. This study concluded that a local climate zone determines the urban heat hazard in the city regarding urban heat

signature. The urban heat hazard affects the environment, with air surface temperature getting more than 32°C, which impacts a human with head headache, sweat, and heatstroke.

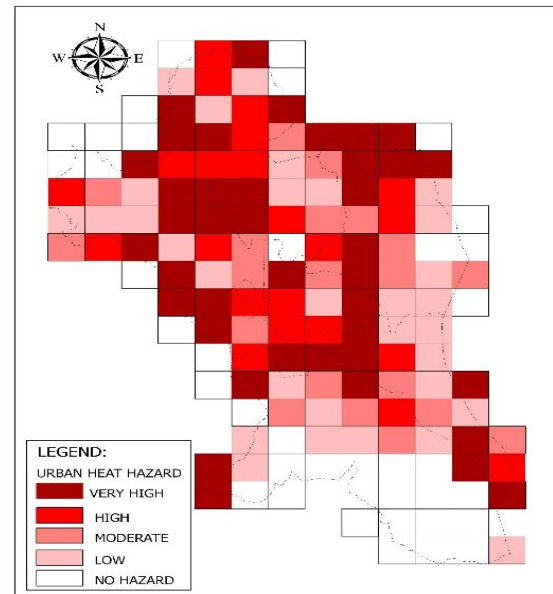


Fig. 7 Spatial Model of Urban Heat Hazard in Bogor City, 2022

## REFERENCES

- [1] Dong S., Yan X., and Xiong Z., Varying Responses in Mean Surface Air Temperature from Land Use/Cover Change in different seasons over northern China. *Acta Ecologica Sinica*, Vol. 33, Issue 3, 2013, pp.167–171.
- [2] Adulkongkaew T., Satapanajaru T., Charoenhirunyingyos S., and Singhirunnusorn W., Effect of Land Cover Composition and Building Configuration on Land Surface Temperature in an Urban-Sprawl City, Case Study in Bangkok Metropolitan Area, Thailand. *Heliyon*, Vol. 6, Issue 8, 2020, e04485.
- [3] Wang L., Tian F., Wang X., Yang Y., and Wei Z., Attribution of The Land Surface Temperature Response to Land-Use Conversions from Bare Land. *Global and Planetary Change*, Vol. 193, 2020, p103268.
- [4] Li J Juan, Wang X Rong, Wang X Jun, Ma W Chun and Zhang H., Remote sensing evaluation of urban heat island and its spatial pattern of the Shanghai metropolitan area, China. *Ecological Complexity*, 6(4), 2009, pp.413-420.
- [5] Lejeune Q., Davin E. L., Guillod B. P., and Seneviratne S. I., Influence of Amazonian Deforestation on The Future Evolution of Regional Surface Fluxes, Circulation, Surface Temperature and Precipitation. *Climate Dynamics*, Vol. 44, Issue 9-10, 2015, pp.2769-2786.
- [6] Kimura Soydan O., Effects of Landscape Composition and Patterns on Land Surface

- Temperature: Urban Heat Island Case Study for Nigde, Turkey. *Urban Climate*, Vol. 34, Issue August 2020, pp.100688.
- [7] Islam Gohain K. J., Mohammad P., and Goswami, A., Assessing the Impact of Land Use Land Cover Changes on Land Surface Temperature Over Pune City, India. *Quaternary International*, April 2020, pp. 0–1.
- [8] Madakarah N. Y., Supriatna, Wibowo A., Manessa M. D. M., and Ristya Y., Variations of Land Surface Temperature and Its Relationship with Land Cover and Changes in IPB Campus, Dramaga Bogor 2013-2018. *E3S Web of Conferences*, Vol. 125 Issue 2019, pp.
- [9] Wibowo A., Yusoff M. M., and Salleh K. O., Monitoring Urban Heat Signature and Profiles of Localized Urban Environment in The University of Malaya. *IOP Conference Series: Earth and Environmental Science*, Vol 481, Issue 1, 2020.
- [10] Wong N. H., and Yu C., Study of Green Areas and Urban Heat Island in a Tropical City. *Habitat International*, Vol. 29, Issue 3, 2005, pp.547–558.
- [11] Priyadarsini R., and Hien W. N., Causes of Urban Heat Island in Singapore: An investigation using Computational Fluid Dynamics (CFD). *PLEA 2009-Architecture Energy and the Occupant's Perspective: Proceedings of the 26th International Conference on Passive and Low Energy Architecture*, 2009, pp. 22-24.
- [12] Wibowo A., Salleh K.O., Frans FTRS and Samed J. M., Spatial Temporal Land Use Change Detection using Google Earth Data. *IOP Conference Series: Earth and Environmental Science*, Vol. 47, Issue. 1, 2016, pp.012031.
- [13] Wibowo A., and Salleh K. O., Land Cover Types and Their Effect on the Urban Heat Signature of University Campuses Using Remote Sensing. *International Journal of Technology*, Vol. 9, Issue 3, 2018, pp.479–490
- [14] Wibowo A., and Khairulmaini O.S., Landscape features and potential heat hazard threat: a spatial-temporal analysis of two urban universities. *Natural Hazards*, Vol. 92, Issue 3, 2018, pp.1267-1286.
- [15] Wibowo A., Yusoff M. M., and Shidiq I. P. A., Urban Heat Hazard Threat on University Campus (the University of Indonesia and the University of Malaya). *GEOMATE Journal*, Vol. 19, Issue 76, 2020, pp.141-148.
- [16] Chapman L., and Thornes J. E., The use of geographical information systems in climatology and meteorology. *Progress in Physical Geography*, Vol. 27, Issue 3, 2003, pp.313–330.
- [17] Oke T. R., The Energetic Basis of the Urban Heat Island. *Quarterly Journal, Royal Meteorological Society*, Vol. 108, Issue 455, 1982, pp.1–24.
- [18] Aslam, A., and Rana I. A., The Use of Local Climate Zones in The Urban Environment: A Systematic Review of Data Sources, Methods, and Themes. *Urban Climate*, Vol. 42, 2022, pp.101120.
- [19] Li Y., Song Y., Cho D., and Han Z., Zonal classification of microclimates and their relationship with landscape design parameters in an urban park. *Landscape and Ecological Engineering*, Vol. 15, Issue 3, 2019, pp.265–276.
- [20] Cardoso R. Dos S., Amorim M. C. C. T., Liu D., and Montenegro A., Using High-Resolution Satellite Imagery To Characterize Local Climate Zones in Presidente Prudente, Brazil. In *10th International Conference on Urban Climate (ICUC 10)*, 2013, pp. 156-162.
- [21] Stewart I. D., and Oke T. R., Local Climate Zones for Urban Temperature Studies. *Bulletin of the American Meteorological Society*, Vol. 93, Issue 12, 2012, pp.1879-1900.
- [22] Collins J., and Dronova I. Urban Landscape Change Analysis Using Local Climate Zones and Object-Based Classification in the Salt Lake Metro Region, Utah, USA. *Remote Sensing*, Vol. 11, Issue 13, 2019, pp.1615-1642.
- [23] Ali S.B., and Patnaik S., Assessment of the impact of urban tree canopy on microclimate in Bhopal: A devised low-cost traverse methodology. *Urban Climate*, Vol 27, 2019, pp.430-445.
- [24] Bekele D., Alamirew T., Kebede A., Zeleke G., and Melesse A.M., Land use and land cover dynamics in the Keleta watershed, Awash River basin, Ethiopia. *Environmental Hazards*, Vol. 18, Issue 3, 2019, pp.246-265.
- [25] Aprea C., D'Ambrosio V., and Di Martino F., A climate vulnerability and impact assessment model for complex urban systems. *Environmental science & policy*, Vol. 93, 2019, pp.11-26.
- [26] Davies H.J., Doick K.J., Hudson M.D., and Schreckenberg K., Challenges for tree officers to enhance the provision of regulating ecosystem services from urban forests. *Environmental Research*, Vol. 156, 2017, pp.97-107.
- [27] Ashaolu E.D., Olorunfemi J. F., and Ifabiye I. P. Assessing the Spatio-Temporal Pattern of Land Use and Land Cover Changes in Osun Drainage Basin, Nigeria. *Journal of Environmental Geography*, Vol. 12, Issue 1, 2019, pp.41-50.



## URBAN HEAT SIGNATURE AS MONITORING OF ENVIRONMENTAL HEALTH

Adi Wibowo<sup>1</sup>, Iqbal Putut Ash Sidiq<sup>2</sup>, Mariney Binti Mohd Yusoff<sup>3</sup> and Tengku Adeline Adura Binti  
Tengku Hamzah<sup>4</sup>

<sup>1,2</sup>Department Geography, Faculty Mathematics and Natural Sciences, University of Indonesia, Indonesia.

<sup>3,4</sup>Department Geography, Faculty Arts and Social Sciences, University of Malaya, Malaysia.

### ABSTRACT

The urban area has a variety of land cover with varying surface temperatures. Urban heat signature is a representation of the temperature of land cover. Sun heating on land cover affects the urban environment, and its effect on the Urban Heat Signature (UHS) is essential to assess UHS-related environmental health. Even though the increased temperature is a natural phenomenon in urban areas, it could be a threat in tropical cities when it is higher than 30°C, such as increased temperatures will impact human life. The method used Landsat TIRS (100 m) ground resolution to estimate land and air surface temperature. Environmental health monitoring uses Universal Temperature Climate Index (UTCI) dan Effective Temperature Index (ETI). The result of UHS profiles related to vegetation cover of 25-33°C, with a mean of 28°C as the lowest temperature, and building cover with a profile of 33-39°C, with a mean of 35°C as the highest temperatures based on land cover types. The Urban Heat Signature between 30-33.0°C affect air temperature with a max >33.0°C. The temperature will impact humans with uncomfortable sensations, and then it will decrease capacity and achievement of work. This result concluded that UHS's effect on the air temperature and heat intensity impacts human health, indicating that the environmental condition is unhealthy.

*Keywords: Land cover, land surface temperature, air surface temperature, urban heat signature, environmental health*

### 1. INTRODUCTION

Land cover types and sun radiation will generate a direct heat signature. Various types of land cover, as a representation of land uses [1], [2], could absorb and radiate sun radiations to generate urban heat [3] [4]. According to Taha (1997), heat signature depends on local climate characteristics, land use, and land cover types [5]. Therefore, the information on temperature and land use cover, which provides for monitoring the urban environment and human activities, will enhance our understanding of the urban environment [6].

The Changes in land cover impact two aspects, natural variations of the earth system and human activities [7]. Some examples of land cover changes caused by human activities include bare land surfaces and vegetation converted into impermeable surfaces such as asphalt, concrete, and cement or changing urban morphology such as building areas with varying heights and densities [8]. This land cover change causes the temperature on the earth's surface to change [9].

Land cover change is a global environmental problem, especially in developing countries [10]. Changes from vegetation to urban land cover cause a break in the carbon and water cycle and energy fluxes between the soil and the atmosphere [11]. Land Surface Temperature (LST) derived from remote-sensed Thermal Infrared (TIR) satellite imagery is a

crucial variable in understanding the impact of land use and land cover change (LULC), which has been linked to urban thermal patterns in various ways [12]. LST is also an important variable related to climate change in urban areas and indicates ground-level energy balance [13].

Air temperature is essential in explaining the conditions of the terrestrial environment on earth [14]. Land cover types with high vegetation cover are associated with low temperatures, and conversely, land cover types with low vegetation cover are associated with high temperatures [15]. As a consequence of changes in the heat balance and Urban Heat Island (UHI) [16], the air temperature in urban areas with dense buildings/populations is higher than the temperature in the surrounding areas/outskirts of the city [17]. This explanation provides an overview of existing research that has not yet produced a local climate map based on changes in ground cover, land surface temperature and air temperature.

Spatial-temporal analysis of land use can be carried out with the help of Google Earth Data [18] which deals with land cover changes related to soil surface heat [19]. Hot temperatures can impact the environment [20] [21], that research has been carried-out on the relationship between changes in ground cover and land surface temperature and air temperature.

Temperature information provides a powerful way to monitor the urban environment [6]. Hence, from a satellite image, the thermal infrared (TIR) band generated land surface temperature by gathering Land Surface Temperature (LST) or UHS [22] [23] [24]. The variation of UHS has used spatial-temporal analysis to generate a spatial pattern related to the highest vegetation cover with low temperature and without vegetation cover with the highest temperature [4]. The daily pattern of UHS during the daytime is characteristic of heat signature behaviour related to greenery areas, which behave as a cooler ambient temp [25].

## 2. METHOD

The study uses Landsat 8 OLI-TIRS medium resolution to extract land cover features and generate temporal LST. Remote sensing data processing, including land cover classification and LST processing. The satellite image used in this study is the Landsat 8 OLI/TIRS Satellite Imagery which was taken in the month with the lowest rainfall with more than 20% cloud cover. The nomenclature used is the 2010 National Standardization Agency nomenclature which is generalized to land cover. The classification is divided into five classes: water bodies, built-up land, open land, non-agricultural vegetation, and agricultural vegetation. The area of each class calculates every year to determine the changing area. The Khat Kappa method is a statistical calculation method used in research to test the accuracy of the data between land cover classification resulting from satellite imagery processing and the results of Google Earth validation and field surveys. The land surface temperature was obtained from calculating the satellite brightness value in identifying the land surface temperature, namely band 10 on the Landsat 8 OLI/TIRS image, with the formula in Eq. 1.

$$L\lambda = (M \times DN) + A \quad (1)$$

The first step is to change the image pixel value (DN) to spectral radiance, where  $L\lambda$  is the spectral radiance (wm-2SR-m), M is the multiplicative digital number in band 10, and DN is the digital number in band 10. Moreover, A is the additive value in band 10. After the spectral radiance value is obtained, it is changed to estimate the soil surface temperature value with the formula in Eq. 2.

$$T = \frac{K2}{\ln\left(\frac{K1}{L\lambda} + 1\right)} \quad (2)$$

Where T is the temperature of the satellite sensor (Kelvin), K1 is the calibration constant 1 for Landsat OLI (774853 K), K2 is the calibration constant 2 for Landsat OLI (1321.0789 K), and  $L\lambda$  is the spectral radiance band 10. Kelvin temperature value converted to Celsius with the following algorithm in Eq. 3.

$$LST(Celcius) = T - 272,15 \quad (3)$$

Temp-Kelvin is the estimated land surface temperature from satellite sensors in Kelvin units. The result of surface air temperature modelling will create a surface air temperature map by applying the existing model using a raster calculator on the ArcGISPro device.

The study area is The Bogor Agriculture University (BAU) campus. BAU laid in the Bogor Regency area, Dramaga District. BAU campus is geographically between 06°32'41"-06°33'58" S and 106°42'47"-106°44'07" E, which includes the fort village on the north end, Babakan village into the East End and most of the rest area located in the Cibanteng Village. The total campus area is about ±250 Ha.

## 3. RESULT AND DISCUSSION

### 3.1. Land Cover

The Bogor Agriculture University (BAU) campus had a total percentage of areas of these features for greenery area with 75.3% and a no-greenery area of 24.7% in 2018. The BAU campus was 16.9% covered by building cover and 57.3% covered by the densely vegetated surface in 2018. The rest of the landscape is presented in Table 1. The Land cover maps show in Figure 1.

Table 1 Land Cover in BAU Campus, 2018

Land Cover	Area (hectare)	Percentage (%)
Paved Open Space	19.34	7.8
Build-up Covered	41.53	16.9
Open Vegetated	41.61	17.0
Water Body	2.38	1.0
Dense Vegetated	140.71	57.3

Sources: Data Analysis

Land cover from the BAU campus from Google Earth digitization processing in 2013 and 2018. The resulting land cover classifications were water bodies, vegetation, built-up land, agricultural land and open land. The result is that the built-up area is increasing, followed by a decrease in the area of vegetation. Table 2 shows the land cover area at the BAU campus.

Table 2 The Land Cover 2013 and 2018 on the BAU

Land Cover	2013	2018
Green Open Space	152.44	145.46
Build-up Area	45.70	50.48
Open Space	2.82	4.50
Water Body	1.04	1.04
Open Vegetated	37.73	38.25

Sources: Data Analysis



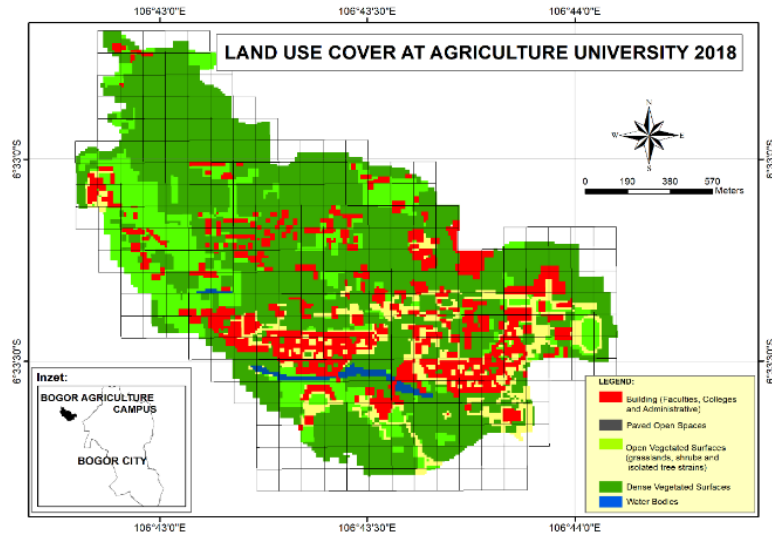


Fig. 2. The Land Cover in Bogor Agriculture University

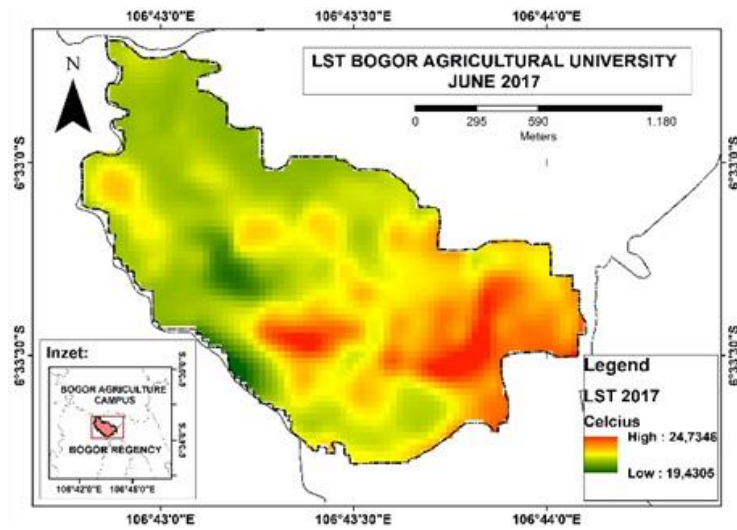


Fig. 3 The Land Surface Temperature in BAU, 2017

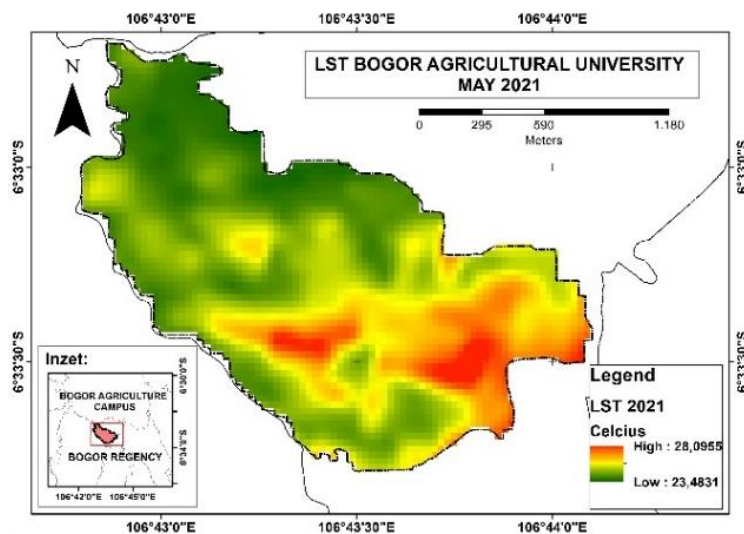


Fig. 4 The Land Surface Temperature in BAU, 2021

### 3.2. Urban Heta Signature

The finding gives a new understanding of urban heat signature, and urban heat signature behaviour and its effect and impact become urban heat hazard in another university. The relation between UHS and land cover types in 2013-2015 (Table 3) had min temp 25.7°C relationship with Paved Open Space, UHS min temp 23.5°C relation with Open Vegetated Covered, Dense Vegetated Covered relations with min temp 23.1°C. UHS with max temp 32.4°C relation with all land use cover types. UHS with the highest mean temperature is Paved Open Space, and the lowest is Water Bodies with a mean temp 24.6°C.

Table 3 The Land Cover and Urban Heat Signature

Land Cover	2013	2015	2018
Dense vegetated	26.5	25.9	28.9
Build-up Area	27.5	26.8	30.4
Paved Open Space	28.1	27.3	31.1
Water Bodies	25.5	25.9	30.2
Open Vegetated	26.8	11.850	11.850

Sources: Data Analysis

This research used north to south cross-section directions to describe the dynamic change of surface temperature across different land-use and land-cover types (or the UHS). The urban heat signature in 2017 is seen in Fig. 3, and the UHS in 2021 is seen in Fig. 4). The minimum land surface temperature in 2017 was 19.8 °C, rising to 23 °C. Similar to the minimum, the maximum temperature rises to 27.5 in 2021 from 22.5 in 2017.

The relation between UHS and land use cover types in 2013-2018 (Table 4) had a mean temp 27.0°C relationship with Dense Vegetated Covered. UHS with max temp 32.2°C relation with all land use cover types. UHS with the highest mean average temperature is Paved Open Space, and the lowest is Dense Vegetated Covered. The index is 1-5 for high and low temperatures, the Paved Open Space has the highest index, and the lowest is Dense Vegetated Covered.

Table 4 The Urban Heat Signature on Land Cover in BAU Campus

Land Cover	Max	Mean	Index
Paved Open Space	32.4	28.3	5
Building Covered	32.4	27.9	4
Open Veg. Covered	32.4	27.2	3
Water Bodies	32.4	27.9	2
Dense Veg. Covered	32.4	27.0	1

Sources: Data Analysis

### 3.3. Environmental Health based on Urban Head Hazard

The relation between AST and land use cover types in 2018 had a min temp 21.5°C relationship with

Dense Vegetated Covered. UHS with max temp 32.2°C relation with all land use cover types. UHS with the highest mean average temperature is Paved Open Space, and the lowest is Dense Vegetated Covered. The index is 1- 5 for high and low temperatures, the Paved Open Space is the highest, and the lowest index is Dense Vegetated Covered.

Based on the Universal temperature Index, Urban Heat Hazard in 2018 only maximum with Moderate Hazard, and on the other hand, in 2021, the Urban Heat Hazard getting High Heat Hazard caused a temperature higher than 35°C. The impact of high heat hazards on the human body is getting sweat and head Headaches until heat stroke.

Table 5 The Air Surface Temperature and Urban Heat Hazard in BAU Campus

Land Cover	AST(°C)	Hazard
Paved Open Space	5	Very High
Building Covered	4	High
Open Veg. Covered	3	Moderate
Water Bodies	2	Low
Dense Veg. Covered	1	Verry Low

Sources: Data Analysis

The urban climatic condition through shading and transpiration, whereas plants release water vapour into the surroundings, increasing relative humidity and decreasing air temperature [26]. The temperature of the narrow green alleys is lower than that of their counterparts. The research had similar results to Ali and Patnaik, where the dense vegetation covered was the lowest temperature due to urban heat signature, air surface temperature, and perception study. That condition threatens the natural ecosystem and creates vulnerability to an environmental hazard [27]. The research agrees with Bekele et al., explaining that land cover changes will generate the heat hazard on the university campus as Urban Heat Hazard Threat.

Generally, cities face specific urban events due to the urban setting that can alter the local microclimate with higher impacts [28]. Urbanization increases the risk of extreme heat episodes in Europe's cities due to the loss of urban green space [29]. That spatial-temporal detecting land cover changed much importance [30]. This research agrees with Ashaolu et al. to detect the land cover changed. Urban outdoor environments, including university campuses, particularly in the tropics, largely depend on their frequency of use, which can be profoundly altered by the level of outdoor thermal comfort [31]. This research agreed with Ghaffarianhoseini et al. The research detecting land cover changed the effect on urban heat and impact on air surface temperature as monitoring environmental health on a university campus.

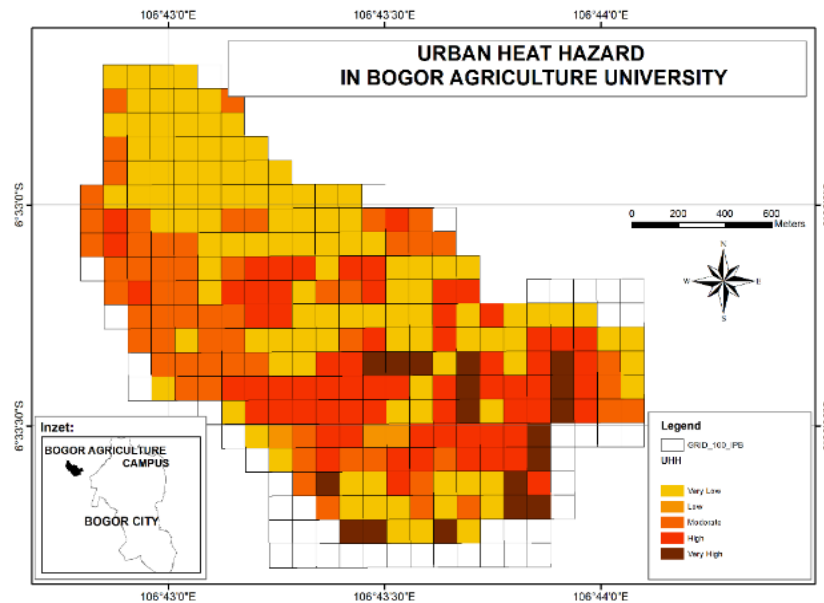


Fig. 5 Urban Heat Hazard in BAU Campus, 2021

## CONCLUSIONS

The result of UHS profiles related to vegetation cover of 25-33°C, with a mean of 28°C as the lowest temperature, and building cover with a profile of 33-39°C, with a mean of 35°C as the highest temperatures based on land cover types. The Urban Heat Signature between 30-33.0°C affect air temperature with a max >33.0°C. The temperature will impact humans with uncomfortable sensations, and then it will decrease capacity and achievement of work. This result concluded that UHS's effect on the air temperature and heat intensity impacts human health, indicating that the environmental condition is unhealthy.

## REFERENCES

- [1] Ren C., Spit T., Lenzholzer S., Yim H.L.S., Heusinkveld B., van Hove B., Chen L., Kupski S., Burghardt R., Katschner L., Urban climate map system for Dutch spatial planning. *Int J Appl Earth Obs Geoinf*, Vol. 18, 2012, pp.207–221.
- [2] Steeneveld G.J., Koopmans S., Heusinkveld B.G., Theeuwes N.E., (2014) Refreshing the role of open water surfaces on mitigating the maximum urban heat island effect. *Landsc Urban Plan* Vol. 121, 2012, pp.92–96.
- [3] Wong N.H., and Yu C., Study of Green Areas and Urban Heat Island in a Tropical City. *Habitat International*, Vol. 29, Issue 3, 2005, pp.547-558.
- [4] Srivanit M., and Hokao K., Evaluating the Cooling Effects of Greening for Improving the Outdoor Thermal Environment at an Institutional Campus in the Summer. *Building and Environment*, Vol. 66, 2013, pp.158-172.
- [5] Taha, Haider. (1997). Urban Climates and Heat Islands: Albedo, Evapotranspiration, and Anthropogenic Heat. *Energy and Buildings*, Vol. 25, Issue 2, 1997, pp.99-103.
- [6] Asmat A., Mansor S., and Hong W. T., Rule-Based Classification for Urban Heat Island Mapping. 2nd Fig Regional Conference Marrakech, Morocco, 2003, p5.
- [7] Dong S., Yan X., and Xiong Z., Varying Responses in Mean Surface Air Temperature from Land Use/Cover Change in different seasons over northern China. *Acta Ecologica Sinica*, Vol. 33, Issue 3, 2013, pp.167–171.
- [8] Adulkongkaew T., Satapanajaru T., Charoenhirunyingyos S., and Singhirunnusorn W., Effect of Land Cover Composition and Building Configuration on Land Surface Temperature in an Urban-Sprawl City, Case Study in Bangkok Metropolitan Area, Thailand. *Heliyon*, Vol. 6, Issue 8, 2020, e04485.
- [9] Wang L., Tian F., Wang X., Yang Y., and Wei Z., Attribution of The Land Surface Temperature Response to Land-Use Conversions from Bare Land. *Global and Planetary Change*, Vol. 193, 2020, p103268.
- [10] Li J Juan, Wang X Rong, Wang X Jun, Ma W Chun and Zhang H., Remote sensing evaluation of urban heat island and its spatial pattern of the Shanghai metropolitan area, China. *Ecological Complexity*, 6(4), 2009, pp.413-420.
- [11] Lejeune Q., Davin E. L., Guillod B. P., and Seneviratne S. I., Influence of Amazonian Deforestation on The Future Evolution of Regional Surface Fluxes, Circulation, Surface Temperature and Precipitation. *Climate Dynamics*, Vol. 44, Issue 9-10, 2015, pp.2769-2786.
- [12] Kimura Soydan O., Effects of Landscape Composition and Patterns on Land Surface Temperature: Urban Heat Island Case Study for

- Nigde, Turkey. *Urban Climate*, Vol. 34, Issue August 2020, pp.100688.
- [13] Islam Gohain K. J., Mohammad P., and Goswami, A., Assessing the Impact of Land Use Land Cover Changes on Land Surface Temperature Over Pune City, India. *Quaternary International*, April 2020, pp. 0–1.
- [14] Madakarah N. Y., Supriatna, Wibowo A., Manessa M. D. M., and Ristya Y., Variations of Land Surface Temperature and Its Relationship with Land Cover and Changes in IPB Campus, Dramaga Bogor 2013-2018. *E3S Web of Conferences*, Vol. 125 Issue 2019, pp.
- [15] Wibowo A., Yusoff M. M., and Salleh K. O., Monitoring Urban Heat Signature and Profiles of Localized Urban Environment in The University of Malaya. *IOP Conference Series: Earth and Environmental Science*, Vol 481, Issue 1, 2020.
- [16] Priyadarsini R., and Hien W. N., Causes of Urban Heat Island in Singapore: An investigation using Computational Fluid Dynamics (CFD). *PLEA 2009-Architecture Energy and the Occupant's Perspective: Proceedings of the 26th International Conference on Passive and Low Energy Architecture*, 2009, pp. 22-24.
- [17] Wibowo A., Salleh K.O., Frans FTRS and Samedi J. M., Spatial Temporal Land Use Change Detection using Google Earth Data. *IOP Conference Series: Earth and Environmental Science*, Vol. 47, Issue. 1, 2016, pp.012031.
- [18] Wibowo A., and Salleh K. O., Land Cover Types and Their Effect on the Urban Heat Signature of University Campuses Using Remote Sensing. *International Journal of Technology*, Vol. 9, Issue 3, 2018, pp.479–490
- [19] Wibowo A., and Khairulmaini O.S., Landscape features and potential heat hazard threat: a spatial-temporal analysis of two urban universities. *Natural Hazards*, Vol. 92, Issue 3, 2018, pp.1267-1286.
- [20] Wibowo A., Yusoff M. M., and Shidiq I. P. A., Urban Heat Hazard Threat on University Campus (the University of Indonesia and the University of Malaya). *GEOMATE Journal*, Vol. 19, Issue 76, 2020, pp.141-148.
- [21] Allam M., Bakr N., and Elbably W., Multi-temporal assessment of land use/land cover change in an arid region based on Landsat satellite imagery: A case study in Fayoum Region, Egypt. *Remote Sensing Applications: Society and Environment*, Vol. 14, 2019, pp.8-19.
- [22] Wibowo A., Andry R., and Iqbal P. A., Spatial-Temporal Analysis of Urban Heat Island in Tangerang City. *Indonesian Journal of Geography*, Vol. 45, Issue 2, 2013, pp.101- 112.
- [23] Weng Q., Fu P., and Gao F. Generating daily land surface temperature at Landsat resolution by fusing Landsat and MODIS data. *Remote Sensing of Environment*, Vol 145, 2014, pp.55-67.
- [24] Rozenstein O., Qin Z., Derimian Y., and Karnieli, A., Derivation of land surface temperature for Landsat-8 TIRS using a split window algorithm. *Sensors*, 14(4), 2014, pp. 5768-5780.
- [25] Wong N. H., Jusuf S. K., Aung A. L. W., Htun Kyaw Thu, To Syatia, and Wu Xuchou., Environmental study of the impact of greenery on an institutional campus in the tropics. *Journal of Building and Environment*, Vol. 42, 2007, pp.2449-2970.
- [26] Ali S.B., and Patnaik S., Assessment of the impact of urban tree canopy on microclimate in Bhopal: A devised low-cost traverse methodology. *Urban Climate*, Vol 27, 2019, pp.430-445.
- [27] Bekele D., Alamirew T., Kebede A., Zeleke G., and Melesse A.M., Land use and land cover dynamics in the Keleta watershed, Awash River basin, Ethiopia. *Environmental Hazards*, Vol. 18, Issue 3, 2019, pp.246-265.
- [28] Apreda C., D'Ambrosio V., and Di Martino F., A climate vulnerability and impact assessment model for complex urban systems. *Environmental science & policy*, Vol. 93, 2019, pp.11-26
- [29] Davies H.J., Doick K.J., Hudson M.D., and Schreckenberg K., Challenges for tree officers to enhance the provision of regulating ecosystem services from urban forests. *Environmental Research*, Vol. 156, 2017, pp.97-107.
- [30] Ashaolu E.D., Olorunfemi J.F., and Ifabiyi I.P. Assessing the Spatio-Temporal Pattern of Land Use and Land Cover Changes in Osun Drainage Basin, Nigeria. *Journal of Environmental Geography*, Vol. 12, Issue 1, 2019, pp.41-50.
- [31] Ghaffarianhoseini A., Berardi U., Ghaffarianhoseini A., and Al-Obaidi K., Analyzing the thermal comfort conditions of outdoor spaces in a university campus in Kuala Lumpur, Malaysia. *Science of the total environment*, Vol 666, 2019, pp.1327-1345

# STUDY ON THE TEMPERATURE MITIGATION EFFECT BY A CULTURAL HERITAGE IN JAPAN -TARGETING A SHRINE LOCATED NEAR THE CENTER OF FUKUOKA CITY

Kenta Fukagawa<sup>1</sup>, Yoshihito Kurazumi<sup>2</sup> Ariya Aruninta<sup>3</sup> and Yoshiaki Yamato<sup>4</sup>

<sup>1</sup>Faculty of Science and Technology, Meijo University, Japan; <sup>2</sup>School of Life Studies, Sugiyama Jogakuen University, Japan; <sup>3</sup>Faculty of Architecture, Chulalongkorn University, Thailand; <sup>4</sup>Faculty of Architecture & Structural Engineering, Kure National College of Technology, Japan

## ABSTRACT

In recent years, many researchers have focused on the urban heat island, caused mainly by the increase in the artificial ground due to the development in urban areas. Several mitigation techniques have been utilized to reduce the temperature of the surrounding microclimate by installing green spaces in urban areas. To obtain more significant benefits, the establishment of large-scale green spaces such as urban parks is more effective. However, designing urban parks in a big city is economically not efficient according to the limited land area and its high price. For that reason, roof and wall greening are one of the alternatives. Looking at the conditions in Japan, some areas with greens exist in the city, not parks but shrines. Shrines are religious landmarks based on the religion called Shinto. Shrines are often religiously and publicly protected and preserved in Japan. However, according to the lack of successors or decrease in the surrounding population, or financial difficulties, the number is decreasing. The purpose of this study is to clarify the temperature mitigating effect of the greens in a shrine and reevaluate it by the aspects of both cultural and environmental sides for future preservation. For this study, a shrine called Hakozaki shrine was targeted. It is a cultural heritage and the huge green area which connects the seashore and the city center. The measurement was carried out in the summer, of 2021. As a result, the mechanism of the temperature mitigating effect by the shrine was clarified.

*Keywords: Land use, Urban Heat Island, Green space, Temperature Mitigating effect*

## INTRODUCTION

In recent years, UHI has become a global problem. Therefore, as a countermeasure, installing green spaces in urban areas is being taken worldwide. A typical example is Singapore's national-level greening policy. Singapore is focusing on wall greening and the expansion of urban parks.

Typical examples of green spaces in urban areas of Japan, on the other hand, include parks and religious facilities, such as shrines and temples. Shrines generally have large-scale green spaces, so they are often traditionally used for festivals and other events, and so on. They are also utilized as a place for local gatherings and parks. Therefore, it can be said that those shrines play many roles other than religious symbols. A typical example of a shrine is Meiji Jingu, which is located in Tokyo. The satellite photo is shown in Fig.1.

In addition to playing a role as a vast green space in the city center, it also plays a role as a representative religious facility in Japan, with 3.1 million people visiting for worship every year.

Due to changes in the times and the declining population, some of the shrines have ended their role and have been abolished or merged, and the number is decreasing. However, shrines are not only historical and cultural heritages but also works as

green spaces which mitigate the temperature of the surroundings in a city.

There are many studies relating to the temperature mitigating effect of natural resources.

Yokohari et al. [1] studied the effect of reducing the temperature of rice paddies located in residential areas in summer. Furthermore, Fukagawa et al. [2] surveyed several land-use types including rice paddies to determine the effect on microclimate in four seasons in developing areas in Japan. Therefore, to obtain greater efficacy, it is estimated that the existence of large-scale green spaces is more effective.

Related examples of studies that examined the effect of temperature mitigation by urban green areas, such as parks, are as followings.



Fig.1 Satellite photo of Meiji Jingu in Tokyo





Fig. 2 Location of Fukuoka city



Fig. 3 Satellite photo of Hakozaiki shrine

Feyisa et al. [3] examined the temperature mitigating effect of a park located in Addis Ababa and showed its influences. Kong et al. [4] examined the pattern of heat islands and the effects of green space inside a park in the eastern part of China. Brown et al. [5] examined the mitigating effect of climate change by studying an urban park and clarified its effects.

Fukagawa et al. [6] examined the temperature mitigation effect of an urban park, built in recent years, with rainwater storage functions.

According to the studies, the occurrence prediction of heat islands and the temperature mitigating effect of green areas such as parks were confirmed as appropriate case studies. However, since the appearance pattern of heat islands differs depending on various influences such as city size, traffic conditions, and climate zones, further investigation is necessary. It is important to develop a quantitative understanding of the climate mitigation effect of green spaces, especially as a heat island mitigation measure.

Therefore, the purpose of this study is to examine the impact of the green areas of shrines located in urban areas on the surrounding microclimate and to re-evaluate the value of the shrine as an environmental resource.

## RESEARCH OVERVIEW

This research was conducted at Hakozaiki Shrine located in Fukuoka City. Fukuoka City is the largest city in Kyushu, located in the southern part of Japan as shown in Fig.2. Fukuoka city has a population of about 1.5 million, one of the cities with the highest population growth rate in recent years in Japan. Therefore, urban redevelopment is being actively carried out.

Hakozaiki Shrine, the site of the survey, was established in 923 and has been a symbol of the region to this day. The satellite photo is shown in Fig.3.

The site is arranged linearly from the torii gate on the sandy beach to the main road near the city center. Most of the site is always open to residents and

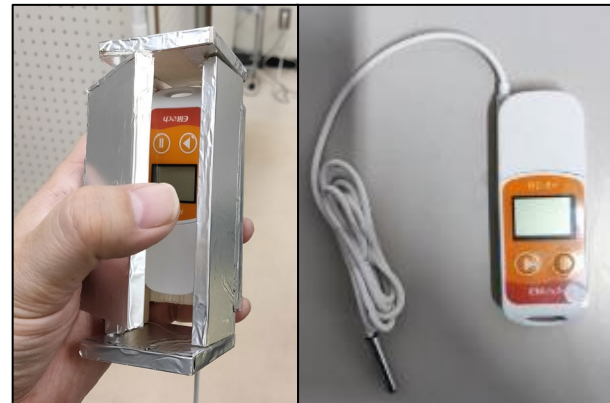


Fig. 4 Measurement instrument

worshippers, and in addition to its religious role, it also plays a park-like role.

Before the Covid, a festival called “Hojoya” was held at the shrine in September every year. “Hojoya” is known as one of the most famous festivals in Fukuoka City.

For that reason, it can be said that Hakozaiki Shrine has great value as a religious, environmental, and tourism resource.

However, due to the influence of the redevelopment plan as a commercial facility on the site due to the relocation of Kyushu University, which was located nearby, the redevelopment of the surrounding area is progressing rapidly. It is presumed that it is also effective as a wind path because there are abundant trees on the site and the site is open straight from the coastline to the city area.

Therefore, it is important to understand the impact on the surrounding microclimate when considering the conservation of Hakozaiki Shrine.

## Measurement Procedures

The measurement was carried out at 10-minute intervals by installing temperature loggers (Elitech-5+) in and around Hakozaiki Shrine for a total of 27 days from July 9 to August 4, 2021.

For temperature measurement, a simple wooden Stevenson screen was installed at each measurement



point. The photo of the measurement instrument is shown in Fig. 4.

For meteorological data other than temperature, measurement data by the Japan Meteorological Agency was used.

### Overview of Measurement Points

The locations of the measurement point are shown in Fig. 5, and the sky photos of the measurement point are shown in Fig. 6. A total of 23 measurement points were set up in and around the shrine premises. However, ④, ⑤ and ⑬ are lost during the measurement. For that reason, data from a total of 19 measurement points were used in this study.

The sky factor of each measurement point is shown in Tab. 1.

Measurement points ① to ⑨ are located at the location that leads to the city area ⑨ from the coastline of ① through the shrine grounds. Therefore, it is expected to function as a sea breeze road. In addition, the amount of greenery in ② to ⑧ located on the shrine site is larger than at other points.

Measurement points ⑩ to ⑬ It is installed along a narrow road in the northern part of the shrine. Therefore, the sky factor is low. However, because it is located near the shrine, the proportion of greenery is relatively high except for ⑮ and ⑯, which are close to the city area.

Measurement points ⑰ to ⑳ are installed along a two-lane road with quite heavy traffic in the southern part of the shrine. Therefore, the ratio of artificial structures is high. On the other hand, the amount of green is small.



Fig. 5 Location of each measurement point

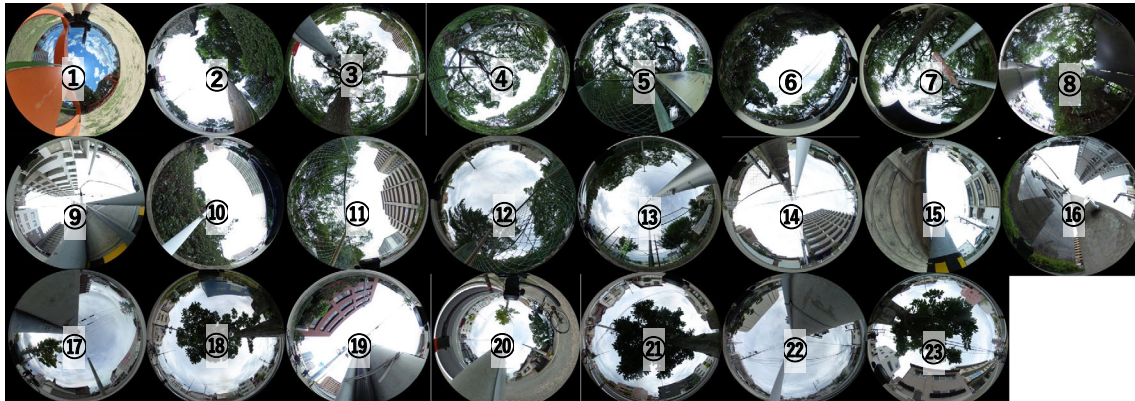


Fig. 6 Sky photos of each measurement point

Table 1 Sky factor at each measurement point

	Green	Sky	Artificial structure	Others	Total		Green	Sky	Artificial structure	Others	Total
①	9.6	28.7	30.9	30.8	100.0	⑬	43.8	23.5	22.9	9.8	100.0
②	47.8	22.0	30.2	0.0	100.0	⑭	3.4	28.9	67.7	0.0	100.0
③	70.3	15.1	14.6	0.0	100.0	⑮	0.7	14.8	84.5	0.0	100.0
④	78.5	18.0	3.5	0.0	100.0	⑯	13.6	12.1	74.3	0.0	100.0
⑤	32.7	5.8	61.5	0.0	100.0	⑰	7.3	26.6	66.1	0.0	100.0
⑥	55.3	14.6	4.0	26.1	100.0	⑱	14.7	32.8	52.5	0.0	100.0
⑦	61.3	4.5	16.5	17.7	100.0	⑲	6.3	26.1	67.6	0.0	100.0
⑧	54.8	3.2	34.4	7.6	100.0	⑳	16.8	23.1	60.1	0.0	100.0
⑨	0.0	12.0	82.7	5.3	100.0	㉑	28.6	19.1	52.3	0.0	100.0
⑩	24.7	20.7	54.3	0.3	100.0	㉒	31.1	16.7	52.2	0.0	100.0
⑪	42.5	14.8	42.6	0.1	100.0	㉓	9.5	24.0	65.7	0.8	100.0
⑫	44.5	21.9	26.4	7.2	100.0						

\*Gray shadings are lost measuring instruments

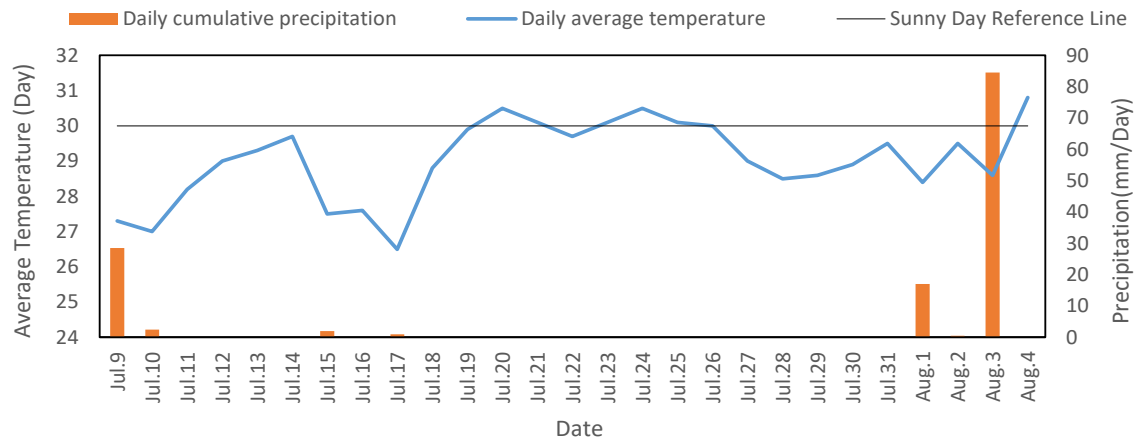


Fig. 7 Weather overview during the measurement period

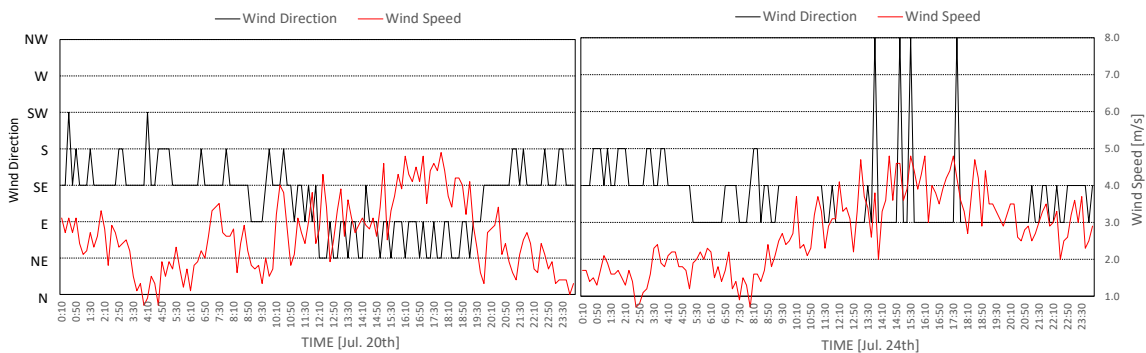


Fig. 8 Weather overview during the measurement period

## MEASUREMENT RESULT

Fig. 7 shows the results of the weather conditions during the measurement period based on the measurement data of the Fukuoka Meteorological Observatory where locates about 6 km away from the shrine. There was only a little rainfall during most of the measurement period, and the average daily temperature remained high.

### Setting the Representative days

In this study, for the purpose of grasping the influence of land use at each measurement point, the temperature data on the days when the daily cumulative precipitation is 0 mm for 4 consecutive days or more and the daily average temperature exceeds 30 °C is used.

Then, the above conditions were met for a total of 6 days, July 20, 21 and July 23-26. Of these, the longest sunshine hours were 12.4 hours on July 20, followed by 12.1 hours on July 24, so in this study, these two days were considered as representatives.

### Wind Direction and Wind Speed

Fig. 8 shows the time fluctuations of the wind speed and direction on July 20 and July 24, which are set as representative days.

Looking at the wind speed results, the average is about 3 m / s.

On the other hand, in terms of wind direction, the wind is southward at night and eastward during the day. Even though the measurement points are located near the coast, the influence of the sea breeze was small during the selected two representative days.

### Temperature Fluctuations at each Measurement Point

The time fluctuations of each measurement point on the representative days are shown in Fig. 9 and 10.

In the legend in the figure, ○ indicates the premises of the shrine, △ indicates the northern part of the shrine, and □ indicates the southern part of the shrine.

Looking at the daytime data, the temperature was high at ① which is the closest to the coast, ② which is close to the highway with heavy traffic, and ⑥, which is located at a relatively open point in the shrine.

On the other hand, the temperature was low at ⑦ and ⑧, where the amount of green was large among all the measurement points. In addition, the temperature tends to be low even in ⑨, which is surrounded by artificial structures and has a low sky factor.

Looking at the results at night, when looking at the data on the premises of the shrine, the temperature tends to be low in ⑦ and ⑧, like the results during the day. On the other hand, in ①, where the

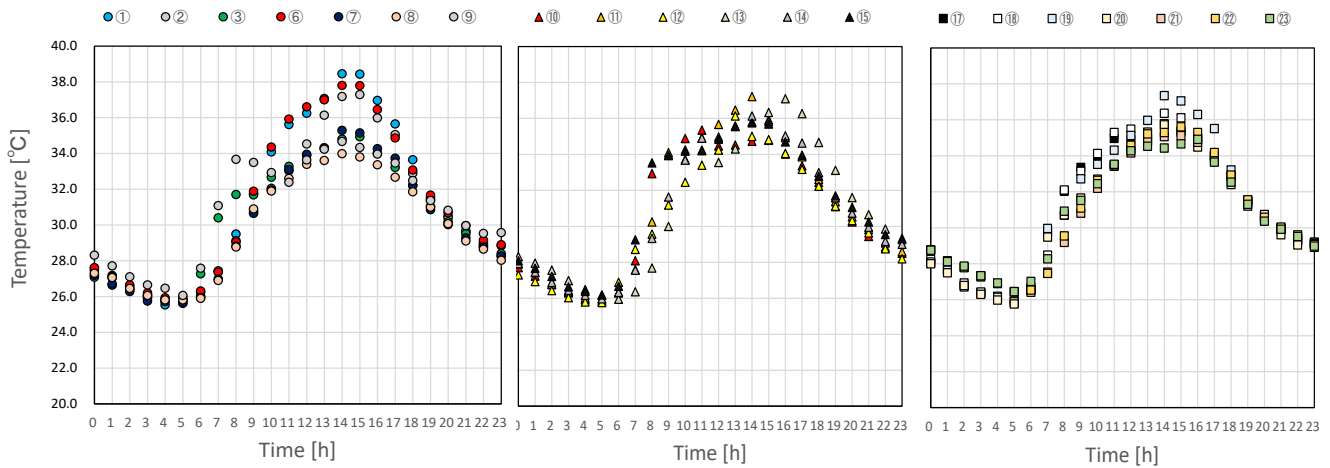


Fig. 9 Hourly Temperature Fluctuation on August 20th

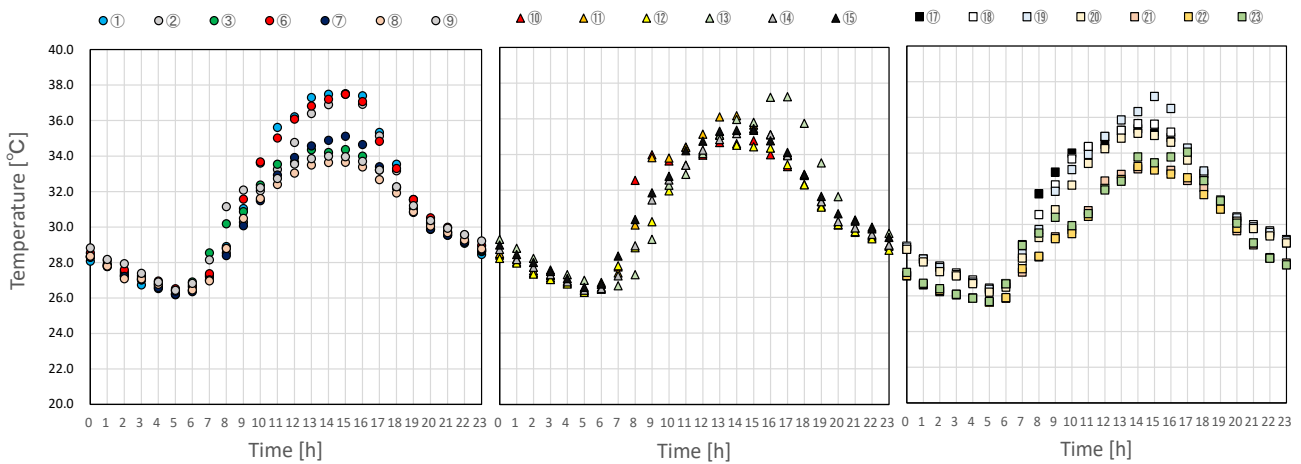


Fig. 10 Hourly Temperature Fluctuation on August 24th

temperature was high during the day, the temperature was low at night. Looking at the entire measurement points, the results were low at 12, 20 and 23.

From this result, the daytime results are strongly influenced by solar radiation, artificial waste heat, and the green space in the shrine. On the other hand, at night when the atmosphere is stable, it is presumed that the outflow of cold air from the green space in the shrine to the surrounding area and the influence of the sea breeze appear in the temperature formation.

#### Analysis of Temperature Formation Tendency in the Measurement Area

Fig. 11 and 12 show the results created using the data at 14:00 when the temperature was the highest in the daytime, and at 2:00 am, when the atmosphere is relatively stable 12 hours after that, and the influence of the surrounding environment is expected to appear strongly.

Looking at the results of the daytime temperature formation tendency in Fig. 11, the temperature is high

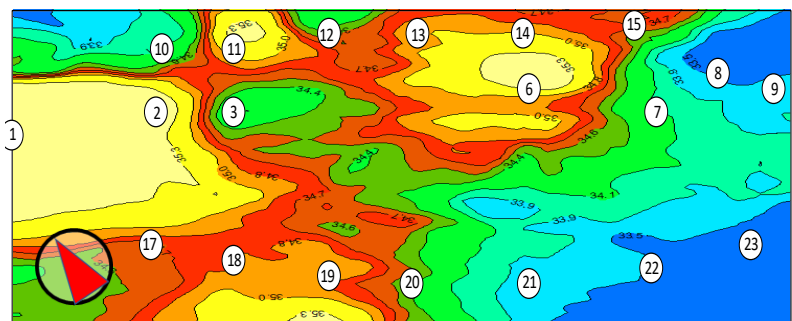


Fig. 11 Temperature Contour Map at 14

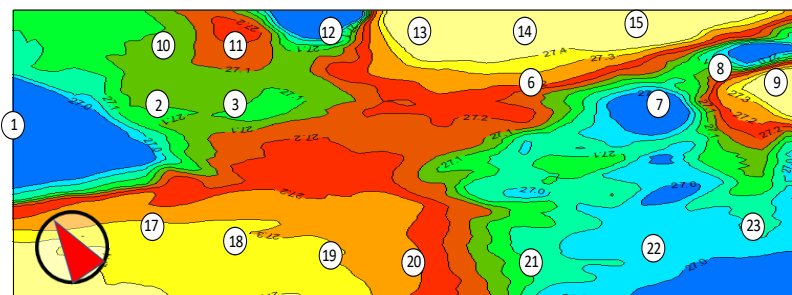


Fig. 12 Temperature Contour Map at 2

on the seaside and along the main road with heavy traffic. In addition, the temperature in the green area of the shrine and its eastern side is decreasing.

Looking at the nighttime temperature formation results shown in Fig. 12, a small low-temperature area

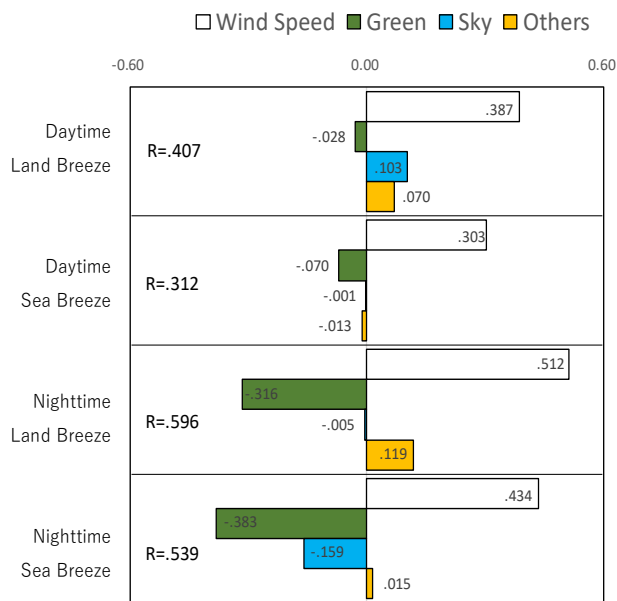


Fig. 13 Result of Multiple Regression Analysis

can be confirmed from the seaside to the main road. In addition, it seems that the low-temperature area confirmed during the day on the shrine site is moving to the inland side. It is presumed that this is because the influence of sea breeze and green space appears clearly at night when the atmosphere is stable, and at the same time, it affects the temperature formation in the surrounding area.

#### Analysis of Factors Contributing to Temperature by Multiple Regression Analysis

To analyze the factors affecting the temperature in the measurement area centered on the shrine were examined using multiple regression analysis. The dependent variable is the 6 days on a clear day shown in the previous chapter, and the independent variables are wind speed, green amount, sky factor, and other sky factors. A total of 4 patterns were analyzed. The results are shown in Fig. 13.

From this, the temperature reduction effect due to the number of green increases at night when the atmosphere is stable. On the other hand, the temperature tends to rise by the wind speed increases. However, in the case of sea breeze, the effect of raising the temperature due to the wind speed is reduced, and the effect of reducing the temperature due to the amount of green is expanding as compared with the case of la and breeze.

From the above, it can be interpreted that the temperature reduction effect of the site of the shrine, which has most of the green space in the measurement target area, has appeared. In addition, it is presumed that the effect spreads to the eastern area of the shrine during the sea breeze and that the most remarkable effect appears at night.

## CONCLUSION

The findings obtained in this study are shown followings.

- 1) In the survey area, the effects of artificial waste heat centered on the arterial road and high temperature due to the artificial covering surface appear strongly during the daytime. Also, even within the shrine premises, the temperature tends to be high when the sky factor is high.
- 2) At night, the effects of greens in the shrine are clearly visible, and when affected by the sea breeze, it seems that the temperature reduction effect is spreading to the surrounding areas.

As mentioned above, it was shown that in addition to the traditional cultural and historical value of this shrine that was the subject of this study, this paper proved the effect of mitigating the surrounding temperature as wind paths at night.

## ACKNOWLEDGEMENTS

We would show gratitude to everyone at Hakozaki Shrine for their cooperation in this research and Johnson Controls Co., Ltd. for providing the scholarship donation.

- [1] Yokohari, M., Brown, R. D., Kato, Y. and Yamamoto, S. 2001. The cooling effect of paddy Fields on summertime air temperature in residential Tokyo, Japan. *Landscape and Urban Planning*, 53: 17-27.
- [2] Fukagawa, K., Shimazawa, T., Murakawa, S., Koshikawa, Y. and Ando, G. 2006. A study of the differences on the formation of temperature among urban areas, rural areas, and around irrigation ponds in a developing city. *Architectural Institute of Japan Refereed Journal*. 605: 95-102.
- [3] Feyisa, G. L., Dons, K. and Meilby, H. 2014. Efficiency of parks in mitigating urban heat island effect: An example from Addis Ababa. *Landscape and Urban Planning*. 123: 87-95.
- [4] Kong, F., Yin, H., James., Hutyra, L. R. and S.He, H. 2014. Effects of spatial pattern of greenspace on urban cooling in a large metropolitan area of eastern China. *Landscape and Urban Planning*. 128: 35-47.
- [5] Brown, D.R., Vanos, J., Kenny, N. and Lenzholzer, S. 2015. Designing urban parks that ameliorate the effects of climate change, *Landscape and Urban Planning*, 138: 118-131.
- [6] Fukagawa, K., Aruninta, A., 2014. A Study on the Efficiency of De-signing Urban Park as Cooling Spot in the Center of Bangkok - Targeting Raining Season - Ecology, Environment, and conservation.



## SOME QUESTIONS ABOUT GEORGIA'S LANDSCAPES DYNAMICS (ON THE EXAMPLE OF SAMTSKHE-JAVAKHETI)

Maia Tskhavadze<sup>1,2</sup>, Dali Nikolaishvili<sup>1</sup>, Lia Matchavariani<sup>1</sup>, Lamzira Lagidze<sup>1</sup>, Vazha Trapaidze<sup>1</sup>

<sup>1</sup>Faculty of Exact and Natural Sciences, Ivane Javakhishvili Tbilisi State University, Georgia;

<sup>2</sup>Climate Change Division, Ministry of Environmental Protection and Agriculture, Georgia

### ABSTRACT

The given paper was based on the concept of spatial-temporal analysis and synthesis of natural territorial complexes (NTCs) enabling to study of nature components by applying the unified methodology. Daily condition of landscapes based on meteorological parameters (air temperature, precipitation, snow cover, etc.) applied to determine the changes in the structure of landscapes. This point is very important for forecast trends of physical-geographical processes in landscapes. Such issues can help to clarify the following basic questions: which natural or natural-anthropogenic processes are more obvious? In which landscapes are these processes more intensive and which ones will be changed considerably? How much is rejected last year's annual dynamics of the NTC from long-term dynamics? All of these issues are very important for determining the resource potential of landscapes and their changes. This issue was investigated according to two stages: I stage – determine season dynamic of landscapes; II stage – comparing data of two periods (past and nowadays). To achieve the main purpose of research a great number of meteorological data were analyzed and all data were processed employing GIS technologies. Thus, according to these data, the degree of landscape changes and its spatial distribution was revealed.

*Keywords: Landscapes Dynamics, Landscape ethology, Samtskhe-Javakheti, Georgia*

### INTRODUCTION

Landscape ethology is a relatively new field of landscape science that allows us to identify current trends in the geographical environment through the study of elementary parts (geomasses), vertical structure, and function. Its practical significance lies primarily in the fact that it forms the theoretical basis for the spatial-temporal analysis of landscapes and physical-geographical regions, focusing on the provision of information on the average annual and potential status of NTCs, and most importantly in the development of environmental management systems [1].

The study of landscape dynamics issues is of great theoretical and practical importance. It can be used to determine the physical-geographical or anthropogenic processes taking place in landscapes and in the geographical environment in general. Their identification plays a certain role in identifying current trends in the environment and in revealing the main directions of spatial planning.

The dynamic of landscapes as a whole has been repeatedly studied in the world. For example, the books [2, 3, 4] provides an overview of the ecological indicators of landscape dynamics in the context of geographical landscape integration. The landscape dynamic in Georgia, both in a single context and against the background of separate regions has been studied as well [1, 5, 6, 7, 8], etc. In these papers, the issues of landscape dynamics are analyzed according

to the data of landscape types, subtypes, and basic meteorological stations. Based on this, a fairly clear and complete picture of the annual dynamics of landscapes was created. However, it should be also noted that landscape types/subtypes combine landscapes that differ from each other in terms of thermal and hydration conditions. Accordingly, it is necessary to study these differences as well. Particularly, it is insufficient to study the issues of dynamics by low-ranking landscape units. It requires the selection and analysis of not only the base but also several meteorological stations/substations. This will allow us to move to a more detailed stage after the study – to study the issues of dynamics at the level of landscape genera, species, and types of NTCs.

For our research, in particular, much more accurate data is needed to detect climate change – both in terms of time and the abundance of meteorological stations/checkpoints. This is also due to the spatial stretching factor of landscapes (some landscapes that follow orthographic structures are of elongated configuration) and 1 meteorological station often does not present a complete picture. Therefore, data from 12 meteorological stations/checkpoints are used for the Samtskhe-Javakheti landscape analysis. Thus, the analysis of the climatic characteristics of the landscapes was carried out based on data from several stations.

Landscape dynamics for the whole Caucasus are discussed in N. Beruchashvili's monograph [9], where based on computer modeling scenarios of the development of landscape-ethological situations under different physical-geographical or anthropogenic impacts are developed. In particular, what shifts can occur in the landscape structure during the development of various scenarios of environmental change (global climate change, deforestation, forestation, or minor glaciation)? This is a general model that can be developed as a result of natural or anthropogenic impacts on the landscapes of the Caucasus, including Georgia. However, these impacts may not even be real, at least in the recent past, for example, deforestation of the entire Caucasus, or, conversely, complete forestation of landscapes, minor glaciation, etc. [6]. Because of the above, it is also relevant not only to study the changes caused by the actual (experimental) processes but also the actual changes in the landscape.

## RESEARCH METHODS AND DATA

Determining the issues of landscape dynamics requires the analysis of average multi-year data of meteorological parameters. Of particular importance in this regard is the determination of air temperature, atmospheric precipitation, and snow cover. They showed what changes have taken place in the phytogenic, pedogenic, or nival structures of landscapes. The present study is based on the analysis of these parameters.

For this purpose, data from meteorological stations related to Georgian landscape genera were used, which was carried out using GIS technologies. However, it is also clear that there is a shortage of data – not all landscapes are equally secure in meteorological data. Accordingly, in the absence of meteorological stations in a certain landscape, we resorted to extrapolation and interpolation methods.

In Samtskhe-Javakheti, the data of meteorological stations, which exist throughout the period of their operation, are used to study climate change. The data for some stations is continuous, though for some stations it is discrete, or in some cases up to the modern period. For some landscapes, we have an almost continuous chain of data. This applies to meteorological stations in Akhaltsikhe, Bakuriani, and Borjomi (landscape: lower mountain erosion-accumulation landscape with hornbeam-oak, oak-pine, and pine forests, rarely with shibliak; Denudation-erosion-accumulation landscape of mountain depression with steppe, dry shrub (phrygana), shibliak and rarely mountain semi-desert vegetation; Erosion-denudation landscape of the middle mountain with beech-oak, in some places pine. The shortest periodic data contains information on the years 1944-1963. Such is the Arali meteorological station (Denudation-erosion-accumulation landscape of mountain

depression with steppe, dry shrub (phrygana), shibliak, and rarely mountain semi-desert vegetation).

The process of climate change in Samtskhe-Javakheti and its impact on environmental conditions were assessed by analyzing the following parameters: daily average air temperature, frequency of atmospheric precipitation, wind speed, and height of sustainable snow cover. Based on the multi-year daily data provided by the National Environment Agency, the trends of annual, seasonal, and monthly changes in these parameters were analyzed and evaluated. Data from 12 meteorological stations are used for this purpose: Abastumani, Akhalkalaki, Akhaltsikhe, Bakuriani, Borjomi, Goderdzi, Paravani, and Tsalka, Aspindza, Jvari, Minadze, and Arali. However, the available data can be assessed as partially deficient, since: first, meteorological stations do not function in the whole area of the study area (in all landscapes); Second, we do not have complete meteorological data for the existing stations either. Due to the created situation, we considered it expedient to use extrapolation and interpolation methods, as well as temperature and plivial gradients. This approach was based on general geographical regularities, which took into account the natural conditions of neighboring landscapes. To reveal a broad picture/trend, multi-year data were calculated: initially the average indicators of each year/month, autumn – 10-year periods. Based on the analysis of these periods, the tendency of changes in the climatic indicators of each station (average, absolute maximum, absolute minimum) was determined. In addition, differences between the first and last decades have been identified. Seasonal data (spring, summer, autumn, winter) were also analyzed and trends were identified, as well as the frequency of extremes.

The study was conducted in 2 stages. Dynamics of daily conditions of landscapes in the first stage based on average multival annual data. This creates a general background and gives us an idea of what features characterize this or that Landscape in general. The second stage is based on a comparison of specific periods of time (earlier and later).

## RESULTS AND DISCUSSION

### Major Landscapes

The territorial distribution of Samtskhe-Javakheti landscapes is determined by a whole set of factors. This complex includes oroclimatic barriers, heat and moisture distribution, vegetation, paleogeographical development features of the area, and the degree of anthropogenic transformation. All of them are important and affect the territorial distribution of landscapes, and their physical-geographical features. Absolute height plays an important role in the differentiation of Samtskhe-Javakheti landscapes. In particular, the 2600 m altitude range generates great



contrasts in terms of landscape, which is related to the sharply defined vertical plane.

The area of Samtskhe-Javakheti is represented by diverse landscapes: 5 types, 9 subtypes, and 13 genera. These landscapes are: 1. Mountainous Thermo-moderate Humid (Subtypes: Low-mountain forests Colchik & middle mountain forest); 2. Mountain Thermo-moderate Semi-humid/Mountainous Thermo-moderate Semiarid (Subtype: Transitional to thermo-moderate mountainous depression with steppes, meadow-steppes, dry shrub “frigana” and “shibliak”); 3. Mountainous Thermo-moderate Semiarid (Subtype: Transitional to thermo-moderate mountainous depression with steppes, meadow-steppes, “frigana” and “shibliak”); 4. The Mountainous Moderately Cold (Subtype: Middle mountain coniferous forest); 5. High Mountain Meadow (Subtype: High mountain subalpine forest-shrubland-meadow).

### Multi-year dynamics of air temperature

The meteorological data given below is mainly based on the database of the National Environment Agency, as well as on Georgia's UNFCCC [10], [8], etc.

Analysis of data from 1986-2015 showed that the average annual air is highest in the lower mountain forest and mountain hollow landscapes. The average temperature increased by 0.47°C compared to 1956-1986. Temperature increases were also recorded by season (Table 1). Separate months analysis showed that warming is in progress mostly during the summer months. Maximum warming was recorded in August – at 1.24°C also warming trend is quite high in September-October at 0.83°C and 0.95°C. The absolute minimum temperature was recorded on December 7, 2016 (-20.7°C), and the maximum temperature was recorded on July 25, 2018 (36.4°C). In 2016-2020, compared to previous years, there is a noticeable increase in temperature in all seasons.

Table 1 Air temperature dynamics at certain time intervals (Mountain depression Landscape)

Seasons	1986-2005	Increase compared to 1956-1986
Spring	-8	0.21
Summer	19.7	0.88
Autumn	10.2	0.57
Winter	-1.8	0.2

On the High Mountain Plateau increased by 0.47° in 1986-2015 compared to 1986-2015. Here, the place has an increase in temperature for all seasons. Here, also the warming takes place mainly in late summer and early autumn, namely in August the increase is 1.24°C, and in September-October – 0.9°C. The increase in temperature is noticeable in all seasons, especially in winter. The absolute minimum temperature was recorded in December 2016 (-28°C); The maximum temperature was 34.3°C in August 2019.

Approximately the same trend will be observed in other landscapes. There is an increase in temperature everywhere, but with different intensities (Table 2). The rise in temperature occurs mainly in the summer and subsequent months – July, Aug., Sept., October.

Table 2. Dynamics of air temperature (°C) according to landscapes

Landscapes	1951-1980	1981-2010	Increase in air temperature
Lower Mountain	9.3	10	0.77
Middle Mountain Forest	4.71	5.19	0.48
Mountain depression	8.85	9.02	0.17
High Plateau	5.6	6.36	0.7
High Mountain	2.39	3	0.6
Subalpine & Alpine			

### Perennial dynamics of atmospheric precipitation

Quite significant changes took place in the annual amount of atmospheric precipitation and its seasonal distribution. For this purpose, we have considered the data series in 4 periods: I (1937-1976), II (1977-1986), III (1987-1996), and IV (1997-2006).

The total amount of atmospheric precipitation on the high mountain plateaus has increased by almost 900 mm (from 5600 mm to 6530 mm), although in periods II and III its amount has slightly decreased compared to the period I, although in 1997-2006 – increased. Precipitation during the first period – increased from 245 mm to 1004 mm: in winter – from 245 mm to 274 mm, in spring from 275 mm to 859 mm, in summer from 516 to 1.004 mm, in autumn – from 349 mm to 419 mm. The total precipitation of this period is 5633 mm. The same happened in other periods, but one important feature was revealed: we have a min. amount of precipitation in winter in period II – 190 mm, and a max. in the period I – 1004 mm. In spring the min. amount of precipitation is in period III – 265 mm, and the max. in period IV – 901 mm. In summer, the min. value is 441 mm in period III, and the max. is 1004 mm in the period I. The min. magnitude in autumn is 310 mm in the IV period and the max. is 512 mm in the IV period.

Atmospheric precipitation tends to decrease in high mountain subalpine and alpine meadow landscapes. Precipitation during the 30-year period (1963-1992) During the periods I (1963-1972) and II (1973-1992) the amount of precipitation decreased by 3,789 mm, from II to III the period increased by 770 mm.

The situation is similar in the high mountain plateau landscapes, where there is also a tendency for precipitation to decrease, namely that over 40 years the total precipitation has decreased by 1808 mm. However, during periods I (1967-1976) and II (1977-1986) the amount of precipitation decreased by 450 mm, from II to III (1987-1996) it decreased by 1680 mm. The only exception is the period from III to IV (1997-2006) when precipitation increased by 318 mm.

### Multi-year dynamics of wind regime

On the territory of Samtskhe-Javakheti winds of different directions prevail. The peculiar conditions of the terrain have a great influence. Here the main wind directions coincide with the direction of the river valleys. The recurrence of winds in the other directions is negligible. For example, the recurrence of the west direction is only 1%. Akhaltsikhe basin and Javakheti plateau are distinguished by the peculiarity of the relief; The first is closed by ridges, and the second is relatively wide, which gives a special character to the wind regime.

The average annual wind speed in Samtskhe-Javakheti is not the same everywhere, in mountain depressions, it is relatively small and in most parts of the area does not exceed 2.0-2.5 m/sec. As for the high mountain plateau, the wind speed here is relatively high. According to the observation, materials reaches 4 m/sec. The latter, in its central and southern part, is dominated by winds from the south-east (28%) and north-west (20-24%) during the year, and from the south (32%) and east (18%). South-east winds are also relatively frequent in this part of the plateau.

The average wind speed is a significant part of the area is maximum in the winter months, especially during the winter, with relatively weak winds in the spring and summer months.

Strong winds (wind speed 15 m/s and more) are small compared to other regions of Georgia. The average number of strong windy days is relatively common in the high plateau landscapes, where it reaches 14 days a year. Such a high number can be explained by its location on the open ground. In the central part of the mentioned plateau, the number of strong windy days is much higher in some years. The maximum number of strong windy days here is 49.

### Analysis of daily conditions

Each landscape is characterized by a certain set of daily conditions. However, they are distinguished by the recurrence and duration of daily conditions. In some landscapes, we find only typical conditions for it. However, conditions that are identical for different landscapes are quite long. It is very important to determine the duration and recurrence of this or that condition of the NTCs for each landscape.

In most landscapes, most of the time of the year falls on summer and winter conditions, while the daily conditions of spring and autumn are of negligible duration. This will be observed in almost all landscapes of Georgia. It is logical that the duration of the winter, namely the nival states, increases according to the absolute height, while the duration of the pluvial daily states extends from east to west.

Sustainable snow cover in western Georgia is falling relatively slowly. Because of this, the onset and completion of complications of spring

phytogenic structure are delayed by 5-15 days. It turns out that in several landscapes in eastern Georgia, including Samtskhe-Javakheti, spring conditions are longer than in western Georgia.

Middle mountain forest landscapes, which unite 12 genera of landscapes in Georgia, are spread in the range of 800-2000m altitude above sea level, -both in western as well as eastern Georgia – in the Caucasus as well as the Lesser Caucasus-. Accordingly, the dynamics of the daily states of landscapes proceed differently in each of the above-named classification units. In general, it can be said that in the middle mountain forest landscapes there are 30 types of the daily condition of landscapes, 17 of which are dominant and are found every year.

In Samtskhe-Javakheti, in the middle mountain forest landscapes of 1936-2014, there is a tendency for a sharp increase in atmospheric precipitation. This was also reflected in the increase in pluvial states. Significant growth was observed from 1998-2004. This increase was also reflected in the increase in nival conditions (Fig. 1).

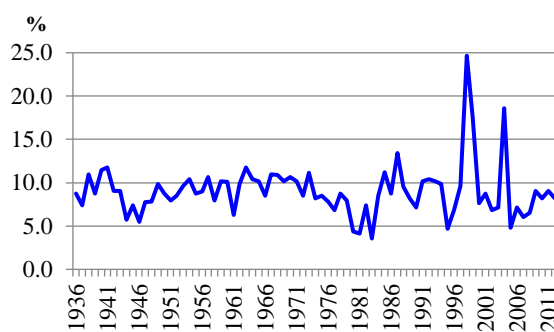


Fig. 1. Trend of nival daily conditions (1936-2013)

If we compare different periods, we will see that the situation of atmospheric precipitation sums is very different. There is an increase in precipitation, in some years – on the contrary, a decrease. However one important trend has been observed, during the period 1972-1991, the amount of precipitation increased sharply during the spring and partly during the summer. This difference was 200-250 m per year. Due to the lack of observational data from the 1990s, it is impossible to judge the trends of the last decades. During the same periods, there was no sharp change in air temperature.

It is interesting to note that against the background of the increase in pluripotent and nival conditions, there is also a tendency for the growth of semiarid conditions. This seems like an unusual situation. On the contrary, the share of humid states is narrowed. This is due to the circumstances of the summer period.

The longest period of the year, about 1/2 comes in the stabilization of the winter structure, about 1/3 – in the stable conditions of the summer phytogenic structure. Compared to the lower mountain forest

landscapes, there are few summer phytogenic structure stabilization conditions Longevity, which is -logical, since the increase in absolute height decreases the length of summer, hence the amount of heat. The most deficient in duration are the – phytogenic structural conditions of spring and autumn (-5-5-%). The plural position is -based -on the total longevity of the year  $\frac{1}{4}$  [6]. There is, however, a significant difference according to the genera of the landscapes. In some landscapes of western Georgia, where the annual amount of precipitation is significantly higher than the corresponding rate in eastern Georgia, the duration of these conditions is 34%.

In the lower mountain forest landscapes, the trend of decreasing semiarid conditions is observed in the period 1936-2013, although in some years it has also increased. The duration of semiarid conditions increased significantly between 1990-2004, although it declined sharply in the mid-2000s after the mid-period. The sharp downward trend is characterized by the trend of cryo-thermal conditions, although there is a pronounced upward trend in the period from the mid 1980s to the early 1990s (Fig. 2).

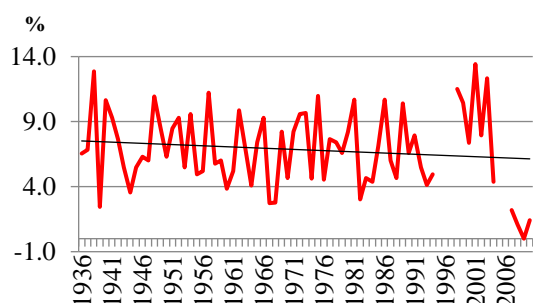


Fig. 2 Trend of semiarid conditions (1936-2013)

The trend of increasing semiarid states in mountain depression landscapes from 1936 to 2013 is characterized by several features: 1. The general trend throughout this period is a slight decrease in semiarid conditions, although it varies greatly from period to period; 2. Aridity was highest during 1995-2001 and lowest during 1981-1985 (Fig. 3). Also, during 1936-2013, the duration of nival states varied at a fairly large interval (Fig. 4). It was maximal in 1938-1940, 1962-1933 and 1987. However, the general trend is declining. Thus, it is true that the share of semiarid states is not increased, although the duration of nival states is reduced at the expense of humidification.

Landscape-geophysical indicators also change according to the change in the daily conditions of the landscapes. In particular, the strength and structure of the vertical structure, and the number of geomasses (especially phytomasses and hydromassages) undergo significant changes. Here are some examples.

In mid-montane forest landscapes, soil moisture varies with changing daily conditions. It is maximum in May and October, and minimum in the summer

months. This rate is high in western Georgia. The same can be said for other landscapes, which suggests that there is no direct link between soil moisture and daily conditions. In addition, the duration of this or that daily conditions and the number of days before the pluvial state should be taken into account.

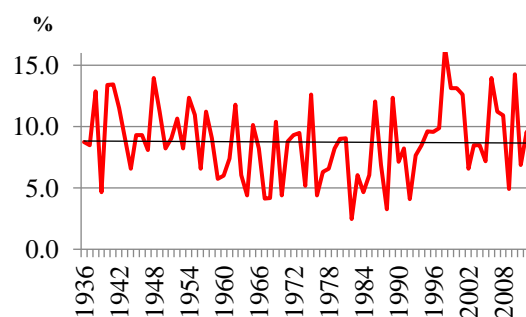


Fig. 3 Trend of semiarid conditions (1936-2013)

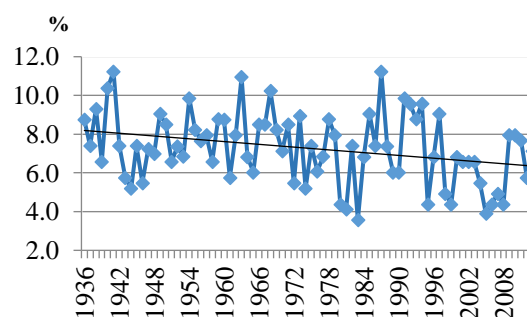


Fig. 4 Trend of nival states (1936-2013)

In winter, due to the dominance of winter structure stabilization (1H), snowmelt and water leakage in the soil is delayed until the second decade of May, so the soil moisture is also low.

In the case of simplification of winter nival structure and complication of spring phytogenic structure, due to snowmelt, soil moisture increases to 37-42% (in 0-50 cm layer). Therefore, from the end of winter to mid-June, high soil moisture is maintained [6].

A significant correlation was found between the number of phytomasses and the average soil moisture. In most of the Georgian landscapes (with the exception of the -high mountain subnival, nival and semi-arid landscapes of eastern Georgia) the amount of phytomasses reaches a maximum when the soil moisture is maintained not only in the topsoil but also deeper. In particular, when the 30% isoline passes at 25-35 cm, and the 20% isoline – at a depth of 20-25 cm and deeper.

This, obviously, is due to the frequency and duration of humid and pluvial conditions. For example, in the lower and middle mountain forest landscapes of Georgia, the amount of phytomass over 250-300 t/ha is observed where the 30% isoline of soil

moisture passes at a depth of 30 cm, and the 20% isoline is deeper than 80 cm. [7]. It turned out that it does not really matter where the 30 cm isoline of soil moisture passes deeper than 30 cm, since the amount of phytomass in such conditions is quite large almost everywhere (300-500 t/ha and more).

Different features were revealed in those landscapes where the duration of semi-humid, semi-arid, and arid conditions is much longer. In this way, the foothills landscapes of Eastern Georgia can be inhabited. The maximum of phytomass is observed here where the 30% isoline of the soil passes closer to the surface – at a depth of 15-20 cm, and the 40% isoline should not be close to the surface and it should go much deeper than 15 cm. Where the 30% isoline passes at a depth of 0-15 m from the surface, the amount of phytomass is only 20-25 t/ha on average.

The capacity of the vertical structure varies significantly in some landscapes, and slightly in others. It has to do with what form of life is dominant in this or that landscape layer. If trees predominate, this change is minimal (up to about 1 m) and is mainly due to changes due to tree pollination and defoliation. In forestless NTCs, on meadows, on steppes, the capacity can change 2-3 times and even more.

Among the landscapes of Georgia, the power of the vertical structure of BTCs is especially significantly reduced in the high mountain subalpine meadow landscapes. The degree of reduction here can be 10 or more. Among non-forested BTUs, capacity varies least in those landscapes (excluding high mountain subnival and nival landscapes) dominated by semi-desert vegetation [6].

The complexity of the vertical structure of NTCs in the average mountain forest landscapes of Georgia is also maximum in summer and minimum in winter. The difficulty becomes particularly easy in forestless NTCs, where only 2-3 of the 4-7 geo-horizons present in the summer season may remain. As for forest NTCs, here the reduction has a very different character. The change is particularly significant in the lower and upper mountain forest landscapes. In the middle part of the hypsometric distribution of middle mountain forest landscapes, it is relatively small. However, it is important to consider -which types of the vertical structure of NTCs (forest or non-forest) predominate. The least change is observed in forest NTCs with dead cover, or Colchic undergrowth, and the most – in forest NTCs with grassy or deciduous shrubs.

## CONCLUSION

- The study identified some of the dynamic features of landscapes not only by average perennials but also by individual years. This has allowed us to identify some of the trends that are taking place in this or that landscape, as well as the tendency of humidification or aridization, temperature increase or decrease, and in

which landscapes these processes are more pronounced and which of them are threatened by fundamental structural changes. In addition, it became possible to determine what changes are expected according to the landscape-geophysical characteristics (number of geomasses, strength, and complexity of the vertical structure). This, in the end, allowed us to identify trends in the resource potential of landscapes.

- In Samtskhe-Javakheti a diverse picture of changes in temperature and atmospheric precipitation was revealed, in particular, there is a sharp variability of air temperature and atmospheric precipitation, with a kind of alternation of warming and cooling.
- Observable The increase in average annual temperatures during the period was observed in the central and northern parts of the High Mountain Plateau landscapes, while the decrease was observed in its southern part. Air temperatures remained almost unchanged in the lower mountain or middle mountain forest landscapes from 1962-2004. As for atmospheric precipitation, their size in recent years has been particularly pronounced in high-mountain plateaus, while diminishing in mountain depression landscapes.

## REFERENCES

- [1] Beruchashvili N.L. Ethology of the Landscape and Mapping of the Natural Environment State. Tb., TSU, 1989, 198 p.
- [2] Sahdev S., Singh, R.B., Kumar, M. Geoecology of Landscape Dynamics. Springer, 2020, 379 p.
- [3] Feranec J. European Landscape Dynamics: Corine Land Cover Data, 2016, 337p.
- [4] Farina A. Landscape Dynamics. Oxford Bibliographies, 2017.
- [5] Beruchashvili N.L. Four Dimensions of the Landscape. M., Mysl, 1986. 182 p.
- [6] Nikolaishvili D. Spatial-Temporal Analysis of the Landscapes of Georgia. Tb., TSU, 2009, 431 p.
- [7] Nikolaishvili D., Lagidze L., Tsitsagi M., Tskhvaradze M., Kubetsia M. Climate Change Trends in Landscapes of Samtkhe-Javakheti. Proceedings of the 18th International Multidisciplinary Scientific GeoConference SGEM2018, vol.18(3.2), 2018, Bulgaria, 765-772.
- [8] Lagidze L., Matchavariani L., Paichadze N. The Influence of Circular Processes on Change in Precipitation in the Scope of Climate Change. International Journal of GEOMATE, Japan, 2017, 13(39), 213-219.
- [9] Beruchashvili N.L. Caucasus: Landscapes, Models, Experiments. Tb., UNEP, GRID, 1995, 310 p.
- [10] Georgia's Third National Communication to the United Nations Framework Convention on Climate Change. National Climate Research Centre, Tbilisi, 2015

## STRENGTH PARAMETERS AND THE RATE PROCESS THEORY APPLIED TO COMPACTED FADAMA SOILS

Ola, Samuel Akinlabi<sup>1</sup>, Fadugba, Olaolu George<sup>2</sup> and \*Nnochiri, Emeka Segun<sup>3</sup>

<sup>1,3</sup> College of Engineering, Afe Babalola University, Ado-Ekiti, Nigeria

<sup>2</sup>School of Engineering and Engineering Technology, Federal University of Technology Akure, Nigeria.

### ABSTRACT

Fadama soils of Northern Nigeria is generally a problem soil for highway and geotechnical engineers. There has been no consistent conclusion on the effect of the strain rate on shear strength of soils, thus necessitating the need to clarify this issue with various types of soil. Consolidated undrained tests with pore pressure measurements were conducted at optimum moisture content and maximum dry density using standard proctor compaction. Back pressures were applied to saturate the soil. The shear strength parameters were determined. Analyzing the results and model studies using the Rate Process Theory, functional relationships between the deviator stress and strain rate were determined and expressed mathematically as: deviator stress =  $\beta_0 + \beta_1 \log(\text{strain rate})$  at each cell pressure where  $\beta_0$  and  $\beta_1$  are constants. Also, functional relationships between the pore pressure coefficient  $\bar{A}_f$  and the time to failure were determined and expressed mathematically as: pore pressure coefficient,  $\bar{A}_f = \psi_0 + \psi_1 \log(\text{time to failure})$  where  $\psi_0$  and  $\psi_1$  are constants. For cell pressure between 69 – 310 kN/m<sup>2</sup> (10 - 45psi) the constant found for Fadama soil in this study are:  $\psi_0=0.17$  and  $\psi_1=0.18$ . The study also shows the dependence of the angle of friction ( $\phi$ ) on rate of strain as it increases from 22° to 25° for increase in rate of strain from 0.08%/min to 1.0%/min. Conclusively, the study also shows that within the strain rate utilized in the research, the deviator strength increased with strain rate while the excess pore water pressure decreased with increase in rate of strain.

*Keywords: Fadama soils; Rate process; Deviator stress; Pore pressure coefficient; Rate of strain.*

### INTRODUCTION

Fadama soils occur in most of the Savannah zones of Northern Nigeria either at the banks of rivers or in depressions along the Savannah plains. It is the best agricultural land in this areas and it is consequently intensively cultivated. However, although the Fadama soil is a blessing to the farmers and Agricultural Engineers, it is a problem soil for Highway and Geotechnical Engineers. In this study, the effect of the rate of strain on the shear strength of the soil has been studied. According to [1], there has been no consistent conclusion on the effect of strain rate on the shear strength of soils. For example, [2] discovered that when strain rate was lower than a critical value, peak strength increased with strain rate, and above that, it decreased. [3] found that the non-drainage shear strength and the elastic modulus of clayey soils were increased with increased strain rates. [4] revealed a positive correlation between the ultimate strength of clayey soil and strain rate. [5] investigated the effect of strain rate on non-drainage shear strength and found that non-drainage shear strength was proportional to strain rate, regardless of the consolidation and soil test type employed. [6] working on the red clay soil of Addis Ababa showed that as the strain increases the strength of the soil also increases. In this study, computerization and analysis

of the test results gives the constants in the Rate Process Theory for the Fadama soil.

### The Geology of Site

The clay known as Fadama soil from Shika, Samaru, Zaria Nigeria used in this study was located at a distance of about a kilometre off the main Zaria-Sokoto road at 14 kilometre from Zaria (Fig. 1). Samples were taken during the wet season in July at a depth of one metre and below. The water table was at 0.61 metre below the ground surface.

The soil is greyish brown clay, and silts with little fine sand, and is the product of the most recent erosion cycle formed from alluvial deposits left by flowing water. These alluvial deposits are known to contain substantial Aeolian components due to large quantities of dust spread over the country annually by the seasonal harmattan winds. Based on the Pleistocene sequence of alternating humid and arid climatic periods, these aeolian deposits are known to be about 7,000 years old [7].

Fadama fall under the classification of mineral hydromorphic soils whose development and characteristics are influenced by permanent or seasonal water logging [8]. This also corroborates the assertion of [9] that the occurrence and distribution of soils in nature varies from location to location, also, the type of soil depends on the rock type, its mineral



constituents and the climatic regime of the area. Variations in the drainage of Fadamas occur because of the variations in soil structure, organic matter content as well as the heights of water table. Generally, these soils have a weak to moderate, fine to medium sub-angular blocky structure except for the flood plain soils which are often structureless, especially if recently deposited. The soil sample was taken in an area where the main rainfall is about 1100mm. and this comes mainly between April and October and open water evaporation is about 1880mm per annum [10].

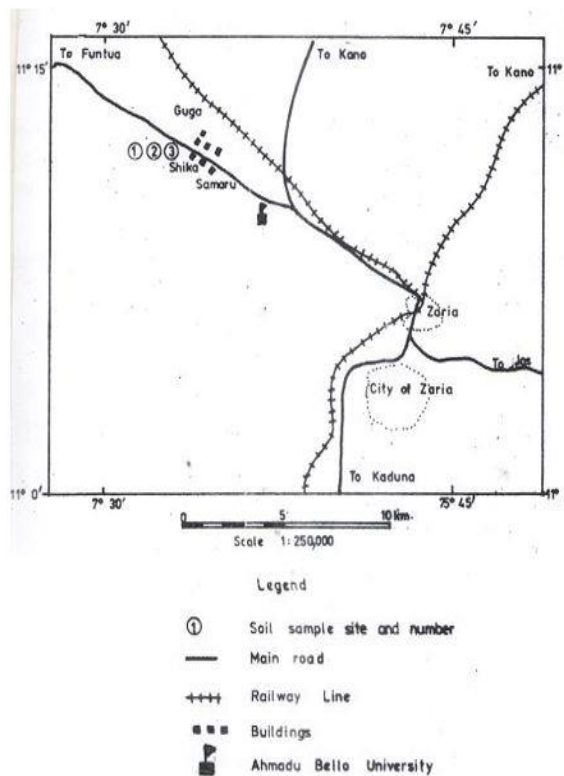


Fig. 1: Map of Zaria showing location of soil samples

## GEOTECHNICAL PROPERTIES

### Physical Properties

Methods of Testing Soils for Civil Engineering Purposes B.S.1377 (1990) was used. The Unified Soil Classification System (USCS) was used to classify the soils. The results of the grain size analysis for all the three sites investigated are shown in Figure 2. The results from the three sites are consistent and show that the soil contains about 46.0 to 47.0% clay, 36.0 to 37.5% silt and 15.5 to 17.0% fine sand. This is also shown in Table 1.0 where summary of the physical properties are given.

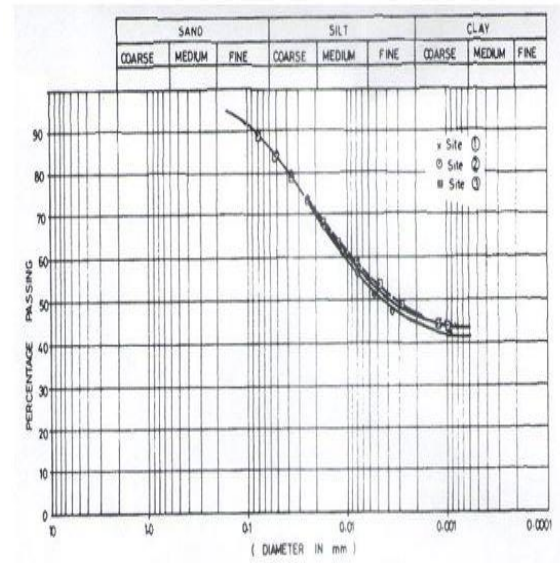


Fig 2: Particle size distribution of Fadama soils

Table 1 Physical properties of Shika Fadama soil.

Clay (< 0.002mm.),%	46.0 to 47.0
Silt(0.06 – 0.002mm.),%	36.0 to 37.5
Sand (2- 0.06mm.),%	15.5 to 17.0
Natural water content	42%
Liquid limit, %	46%
Plastic limit, %	20%
Plasticity index, %	26%
Specific gravity	2.60
Activity (P.I./% of clay)	0.556
Maximum dry density, kg/m <sup>3</sup> (pcf)	
1660- 1692(104-106)	
Optimum moisture content, %	19.5-19.7%

The natural water content is 42%, the liquid limit is 46%, plasticity index is 26%, and specific gravity is 2.6. The results of the Atterberg limits show the soil to be inorganic clays of medium plasticity.

### Mineralogy

In order to determine the mineralogy of the soil, x-ray diffraction analysis was used to identify the various minerals. The method was supplemented with the Differential Thermal Analysis (D.T.A) method, Cation Exchange Capacity (C.E.C) and Glycol retention.

Figure 3 shows the x-ray diffraction analysis on the fraction of the soil passing No 200 sieve. The presence of kaolinite was identified by the 7.2 Å<sup>0</sup> peak in the Air Dry Preferred Orientation (ADPO).

The presence of quartz was confirmed by the  $4.27\text{\AA}^\circ$  reflection and by a narrow characteristics peak at  $3.36\text{\AA}^\circ$ .

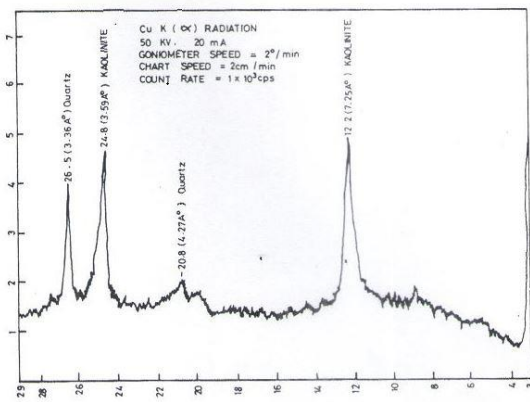


Fig. 3: X-Ray Diffraction for Fadama soils

The results of the x-ray were confirmed by the DTA shown in Figure 4. At  $600^\circ\text{C}$ , the slope ratio was found to be 1.60 thus placing the sample within the range of 0.78 and 2.34 suggested for kaolinite by [11]. The C.E.C was 4.5 meq/100g for the sample. [12] suggested a range of 3 to 15 meq/100g for kaolinites. Ethylene glycol retention of 17.1 mg/g was obtained.

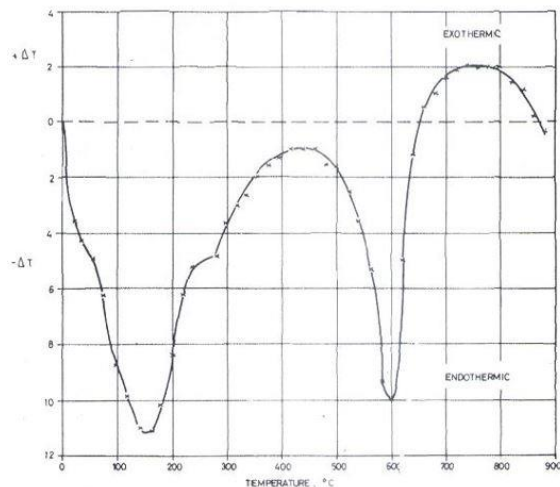


Fig 4: Differential thermal analysis for Fadama soils

### Shear Strength

The moisture density relationship was determined by the use of standard proctor method. Fig.5 illustrates the results obtained for three different sites where samples were collected. The maximum dry density varied from 1660 to 1692  $\text{kg}/\text{m}^3$  (104-106 pcf) and the optimum moisture content varied from 19.5 to 19.7% (Table 1). All the shear tests were conducted at this optimum moisture content and maximum dry density using the standard proctor compaction.

Because Fadamas are generally found in low-lying areas, large quantities of fill materials are

normally required for construction of embankments when a highway is to pass through these areas. Hence the shear strength properties of these compacted soils are of great importance for construction. Also important for these embankments are the rate of pore pressure dissipation and the effect of the rate of loading on the shear strength characteristics of the soil.

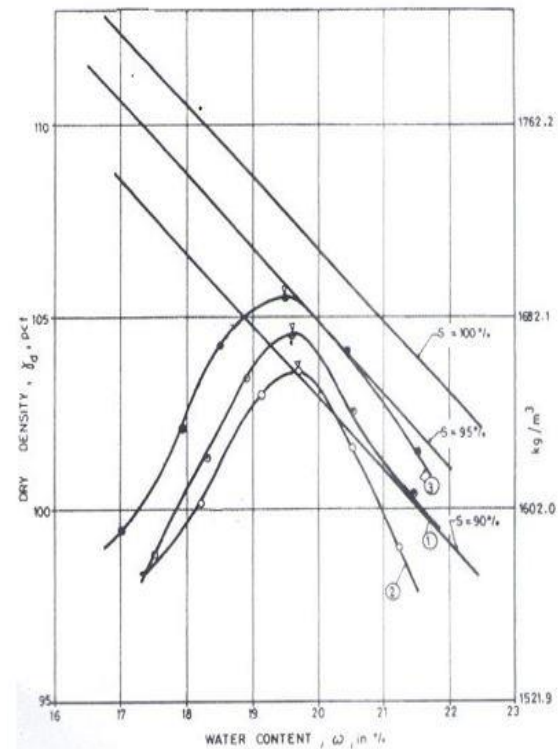


Fig. 5: Moisture/Density relationship for Fadama soils

Consolidated undrained triaxial tests were performed at cell pressures of 69, 207, and 310  $\text{kN}/\text{m}^2$  (10, 30 and 45 psi). The loading rates utilized were 0.08, 0.2, 0.4 and 1.0%/min. (0.0024, 0.006, 0.012 and 0.03 in/min) respectively. Also some back pressures were applied to saturate the soil. In analyzing the shear strength of the soil, it was found that the total stress criterion using the maximum deviator stress  $(\sigma_1 - \sigma_3)_{\text{max}}$  and the effective stress criterion using the maximum effective principal stress ratio  $(\sigma'_1 / \sigma'_3)$  gave almost identical results since the compacted soil was relatively insensitive and consequently, the maximum deviator stress was used in the analysis of the shear strength characteristics in this study.

### RATE PROCESS THEORY

The relationship derived from the rate of strain  $\epsilon_R$  under constant shear force considering the net

activation frequency in the direction of distorting forces was obtained as follows using [13] on Rate Process Theory.

$$\epsilon_R = 2X \frac{KT}{h} \exp(-\Delta F/RT) \sinh(f\lambda/2KT) \quad (1)$$

Where: X = function of the number of flow units in the direction of deformation and the average component of displacement in the same direction due to a single surmounting of the energy barrier.

k=Boltzmann's constant =  $1.38 \times 10^{-16}$  erg

$K^{-1} = 3.29 \times 10^{-24}$  cal° K<sup>-1</sup>

h= Planck's constant =  $1.38 \times 10^{-16}$  erg

R = universal gas constant =  $1.98$  cal°k erg sec<sup>-1</sup>

T = absolute temperature °k

f = average shear force acting on each flow unit, dynes

$\lambda$  = separation distance between successive equilibrium position, cm

$\epsilon_R$  = rate of strain

The following functions are treated constant with its equivalent symbols.

$$a = 2X \frac{KT}{h} \exp(-\Delta F/RT) \quad (2)$$

$$b = \frac{\lambda}{2KT} \quad (3)$$

Hence, Eq. (1) becomes

$$\epsilon_R = a \sinh fb \quad (4)$$

To obtain a significant creep rates in soil, the shear stresses must be large enough, that is stress level of above 25% of the strength or more. Then the value of the term (f $\lambda$ /2 KT) is greater than 1.0. In this case the hyperbolic sine in Eq. (4) can be replaced by a simple exponential equation:

$$\epsilon_R = a \exp fb \quad (5)$$

If the maximum shear stress is D/2, where D is the principal stress difference (deviator stress), the relationship between the average shear force per flow unit and the deviator stress on the plane of maximum shear stress is approximated by:

f = D/2S, where S is the bonds per unit area acted on by the sustained shear stress. Thus Eq. (5) becomes:

$$\epsilon_R = a \exp Db/2S \quad (6)$$

i.e.  $\ln \epsilon_R = \ln a + Db/2S$

$$D = \frac{2S}{b} (\ln \epsilon_R - \ln a)$$

$$D = -\frac{2S}{b} \ln a + \frac{2S}{b} \ln \epsilon_R$$

$$D = C + \frac{2S}{b} \ln \epsilon_R \quad (7)$$

In this study, computerization and analysis of the test results gives the constants in Eq. (7).

The experimental results showing the influence of rate of strain on maximum deviator stress for compacted Fadama soils is presented in Table 2 and Fig. 6. When the results are fitted into several models including linear regression, Quadratic Logarithm, Reciprocal and Square root models. The Logarithmic model gives the best fit equation as shown in Table 3. The constants, C and 2S/b are presented in Table 3 for the various cell pressures of 68.95, 206.85 and 310.28 kN/m<sup>2</sup> (10, 30 and 45 psi). The experimental results showing the influence of rate of strain on the excess pore water pressure, pore pressure coefficient  $A_f$  and time to failure for compacted Fadama soils is presented in Table 4. When the results are fitted into several models including Linear Regression, Quadratic, Logarithmic, Reciprocal and Square root models, the Logarithmic model gives the best fit equation as shown in Table 5 for pore pressure coefficient and time to failure with the equation  $A_f = 0.17 + 0.18 \log t_f$  for 68.95 and 206.85 kN/m<sup>2</sup> (10 psi and 30 psi) and  $A_f = 0.17 + 0.2 \log t_f$  for 310.28 kN/m<sup>2</sup> (45psi). Fig. 7 shows the influence of rate of strain on excess pore water pressure at failure for compacted Fadama soils.

From the model derived in this study the following conclusions can be made

- Deviator stress =  $\beta_0 + \beta_1 \log$  (strain rate)

where  $\beta_0$  is a constant and  $\beta_1$  is the coefficient of the log term

- pore pressure coefficient ,  $\bar{A}_f = \psi_0 + \psi_1 \log$  (time to failure)

where  $\psi_0$  is a constant and  $\psi_1$  is the coefficient of the log term

Table 2. Relationship between Deviator Stress and Rate of Strain.

Cell pressure $\sigma_3$ kN/m <sup>2</sup> (psi)	Rate of strain $\epsilon_R$ %/min	Time to failure $t_f$ (min.)	Deviator stress at failure ( $\sigma_1 - \sigma_3$ ) kN/m <sup>2</sup>	Failure strain $\epsilon_f$ %
69 (10)	0.08	200	200	16.0
	0.2	83	203	16.6
	0.4	43	210	17.2
	1.0	19.4	221	19.4
207 (30)	0.08	230	321	18.4
	0.2	97	329	19.2
	0.4	50	332	20.0
	1.0	23.2	352	23.2
310 (45)	0.08	285	407	22.8
	0.2	115	421	23.0
	0.4	58	431	23.2
	1.0	24	476	24.0

Table 3. Equations Representing the Relationship between Deviator Stress and Rate of Strain

Model	Cell Pressure, $\sigma_3$ (psi)					
	10		20		45	
	R <sup>2</sup>	%Fit	R <sup>2</sup>	%Fit	R <sup>2</sup>	%Fit
<b>Linear</b>	0.8767	87.7	0.7998	79.98	0.8877	88.8
<b>Quadratic</b>	0.8617	86.2	0.7789	77.89	0.8917	89.2
<b>Logarithmic</b>	0.9931	99.3	0.9603	96.03	0.7228	72.3
<b>Reciprocal</b>	0.7446	94.5	0.7579	75.79	0.4313	43.1
<b>Square Root</b>	0.9216	92.2	0.8573	85.73	0.8526	85.3
<b>Best Fit Equation</b>	$D=32.8+1.4 \log \epsilon_R$		$D=51.9+2.2 \log \epsilon_R$		$D=71.5+4.8 \log \epsilon_R$	

R<sup>2</sup> indicates the proportion of variation of deviator stress explained by the rate strain.

Table 4 Relationship between Rate of Strain, Pore Pressure Coefficient, Excess Pore Water Pressure and Time to Failure

Cell Pressure $\sigma_3$ (psi)	Rate of Strain in/min	Pore Pressure Coefficient $\bar{A}_f = \Delta u / (\sigma_1 - \sigma_3)_f$	Excess Pore Water Pressure $\Delta u$ , (psi)	Time to Failure $t_f$ (min)
<b>10</b>	0.0024	0.195	5.7	200
	0.006	0.188	5.6	83
	0.012	0.180	5.5	43
	0.03	0.169	5.4	19.4
<b>30</b>	0.0024	0.209	9.4	230
	0.006	0.199	9.5	97
	0.012	0.195	9.4	50
	0.03	0.172	8.8	23.2
<b>45</b>	0.0024	0.220	13.0	285
	0.006	0.211	12.9	115
	0.012	0.202	12.6	58
	0.03	0.177	12.2	24

TABLE 5: Equations Representing the Relationship between Pore Pressure Coefficient and Time to Failure

Model	Cell Pressure, $\sigma_3$ (psi)					
	10		30		45	
	R <sup>2</sup>	%Fit	R <sup>2</sup>	%Fit	R <sup>2</sup>	%Fit
<b>Linear</b>	0.8649	86.5	0.7659	76.6	0.7482	74.8
<b>Quadratic</b>	0.6550	65.5	0.5451	54.5	0.5194	51.9
<b>Logarithmic</b>	0.9298	93.0	0.9921	99.2	0.9914	99.1
<b>Reciprocal</b>	0.757	72.6	0.8777	87.8	0.8621	86.2
<b>Square Root</b>	0.9807	98.0	0.9397	94.0	0.9358	93.6
<b>Best Fit Equation</b>	$A_f = 0.17 + 0.18 \log t_f$		$A_f = 0.17 + 0.18 \log t_f$		$A_f = 0.17 + 0.2 \log t_f$	

R<sup>2</sup> indicates the proportion of variation of deviator stress explained by the time to failure

## General Discussion

### Deviator stress

Table 2 as well as Fig. 6 shows the effect of rate of strain on the deviator stress of the Fadama soil. The deviator stress at failure increases with the increase in the rate of strain and also with increasing cell pressure. Shown in Table 2 are the failure strain  $\epsilon_f$ , and time to failure,  $t_f$ . The failure strain increases with increase in rate of strain and also with increasing cell pressure. The percentage increase in deviator stress between the two extreme rates of strain (0.08 and 1.0%/min) for cell pressure of 69 and 207kN/m<sup>2</sup> (10 and 30 psi) is about 10% each

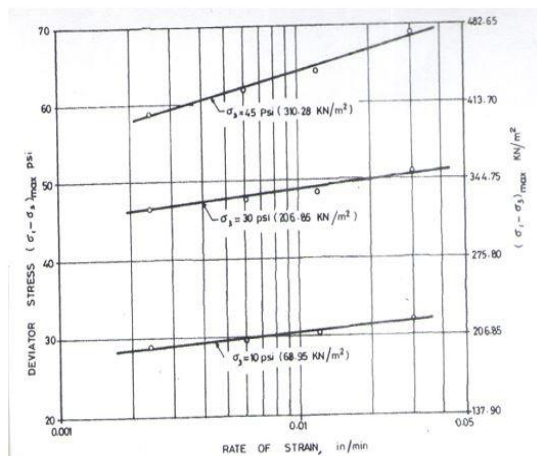


Fig. 6: Influence of the rate of strain on maximum deviator stress for compacted Fadama soils

### Excess Pore Water Pressure

The influence of rate of strain on the excess porewater pressure at failure is shown in Fig 7. As the rate of strain increases, there is a consistent decrease in the pore water pressure. Similarly, there is a consistent increase in the excess pore water pressure at failure for increasing cell pressures

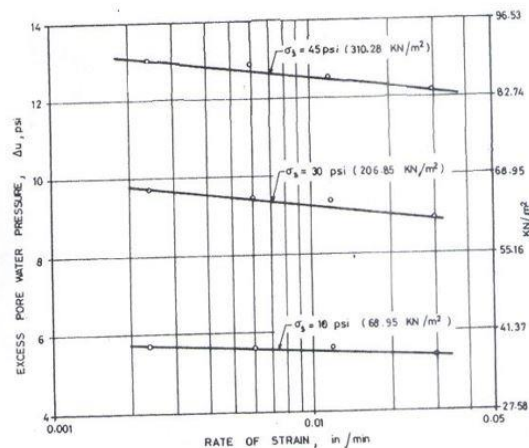


Fig. 7: Influence of the rate of strain on excess pore water pressure at failure for compacted Fadama soils

### Strength Parameters $c'$ and $\phi'$

A summary of the shear strength parameters are given in Table 3 and there is a definite trend of an increase in the effective angle of internal friction for increasing rate of strain.

Table 6. Effect of Rate of Strain on Shear Strength Parameters of Fadama Soils.

Rate of Strain $\epsilon_R$ %/min. ( in/min.)	Effective Cohesion $c'$ , kN/m <sup>2</sup> (psi)	Effective Angle of Internal Friction, $\phi'$ degree
0.08 (0.0024)	58.6 (8.5)	22
0.20 (0.0060)	55.2 (8.0)	23
0.40 (0.0120)	56.5 (8.2)	24
1.0 (0.030)	57.2 (8.3)	25

No such trend could be observed for cohesion. The effective angle of internal friction increased from 22° at 0.08%/min. (0.0024 in/min) strain to 25° at 1.0%/min (0.03 in/min) strain.

## CONCLUSION

The Fadama soil is a greyish brown CLAY and SILT with little fine sand formed from alluvial deposit. The mineralogy consists mainly of kaolinite and quartz [14]. From the analysis of the results and model studies carried out using the Rate Process theory the following conclusions can be made for the Fadama soils.

- Model studies have shown that there is a functional relationship between the deviator stress and strain rate which can be expressed mathematically as follows:
- Deviator stress =  $\beta_0 + \beta_1 \log(\text{strain rate})$  at each cell pressure where  $\beta_0$  and  $\beta_1$  are constants.
- Model studies have also shown that there is a functional relationship between the pore pressure coefficient  $\bar{A}_f$  and time to failure which can be expressed mathematically as follows:
- Pore Pressure Coefficient,  $\bar{A}_f = \psi_0 + \psi_1 \log(\text{time to failure})$

Where  $\psi_0$  and  $\psi_1$  are constants.

For cell pressures between 69 – 310 kN/m<sup>2</sup> (10-45psi) the constants found for Fadama soils in this study are:  $\psi_0 = 0.17$ , and  $\psi_1 = 0.18$

The study also shows the dependence of the angle of friction ( $\phi'$ ) on the strain rate. For the Fadama soils,  $\phi'$  increases from 22° to 25° for increase in rate of strain from 0.08%/min to 1.0%/min.

## REFERENCES

- [1] Tianfei Hu, Dawei Liu, and Jian Change (2020). Experimental study on strain rate effect of strength characteristics of unsaturated silty clay. *Case Studies in Construction Materials* 12. (<https://doi.org/10.1016/j.cscm.2020.>)
- [2] Chen, T.L., Zhou, C., Shen, Z.J.(2004). Compression and shear test of structured clay. *Chin. J. Geotech. Eng.*, 26(1), pg. 31-35.
- [3] Zhu, J. G., and Yin, J.H. (2000). Strain – rate dependent stress strain behaviour of over-consolidated Hong Kong marine clay. *Can. Geotech. J.* ,37(6) pg. 1272 – 1282.
- [4] Sheahan, T.C., Ladd, J.T., and Germaine (1996). Rate-dependent undrained shear behaviour of a resedimented clay. *J. Geotech. Eng., ASCE*, 122 (2)(1996), pg. 90 - 395.
- [6] Gao, Y.B., and Wang, Z.W. (2005). Effect of strain rate on undrained shear strength of clays. *Chin. J. Rock Mech. Eng.*, 24 (52)pg. 5779 – 5783.
- [7] Admassu, T. (2011). <http://etd.aau.edu.et/handle/123456789/15830>.
- [8] Mortimore , (1970). Zaria and its region. Occasional paper No.4, Department of Geography, Ahmadu Bello University, published for the annual conference of the Nigerian geographical association, Zaria.
- [9] Klinkengerg, D., and Higgins, G.M. (1968). An outline of Northern Nigeria soils. *Nigerian journal of science*, 2(2): 91-115
- [10] Surendra, R. and Sanjeev, K. B., (2017). Role of Geotechnical Properties of Soil on Civil Engineering Structures, *Resources and Environment*, Vol.7No. 4, pg. 103-109.doi: 10.5923/j.re.20170704.03.
- [11] Ipinmidun, W.B. (1972). A preliminary survey of the agriculture potentials of some valleys around Zaria, Nigeria. *Samaru Research Bulletin* 175, I.A.R., Ahmadu Bello University, Zaria, Nigeria.
- [12] Bramao, L; Cady, J.G.; Hendricks, S. B; and Swerdlow, M. (1952). Characterization of kaolin minerals. *Soil science* 73, pg. 273-287.
- [13] Grim, R.E. (1968). Clay mineralogy. 2<sup>nd</sup> edition, McGraw Hill, New York. [13]Scott, R.F., and Ko Hon-Yim (1969). Stress-Deformation and Strength Characteristics –State of the Art Report, 7<sup>th</sup> I.C.S.M.F.E, Mexico, 1969 pg. 1-47.
- [14] De Castro, L.C., and Ola, S.A., (1983). Geotechnical properties of compacted soils in Tropical soils of Nigeria in *Engineering practice* (Ola,S.A Ed) A.A. Balkema/Rotterdam pg. 145-154.



# AN EMPIRICAL STUDY OF FLEXURAL STRENGTH OF BEAMS MADE OF RECYCLED AGGREGATE CONCRETE FROM CONSTRUCTION AND DEMOLITION WASTE IN HANOI, VIETNAM

Ha Tan NGHIEM<sup>1</sup>, Tran Viet CUONG<sup>1</sup>, Nguyen Ngoc TAN<sup>1</sup>, Phan Quang MINH<sup>1</sup>, Nguyen Tien DUNG<sup>1</sup>,  
Ken KAWAMOTO<sup>2</sup>, and Nguyen Hoang GIANG<sup>\*1</sup>

<sup>1</sup> Hanoi University of Civil Engineering, 55 Giai Phong Rd., Hanoi, Vietnam; <sup>2</sup> Graduate School of Science  
and Engineering, Saitama University, 225 Shimo-okubo Sakura-ku Saitama, Japan

## ABSTRACT

The employment of recycled materials from construction and demolition waste (CDW) for mixing recycled aggregate concrete (RAC) is widely practiced in developed countries. In Vietnam however, being a developing country with rapid rate of urbanization, especially in major cities such as Hanoi, the substantial amount of CDW generated (2,100-2,300 tons/day [1]) is still mainly treated by landfilling. To promote the recycling of CDW, it is crucial that studies of the performance of recycled products, which is RAC in this paper, are conducted. Adopting a standard experiment set up of reinforced beams, the authors employed local recycled coarse aggregates (RCA) in Hanoi, Vietnam produced from crushed concrete (CC) and crushed brick (CB – mixed with CC at controlled percentages) to conduct experiments to observe flexural behaviors with reference to equivalent natural aggregate concrete (NAC) such as: cracking load, ultimate load, crack pattern, crack width, etc. Initial results show that RAC beams using 100% RCA from CC have their cracking loads reduced by 17.69%, while the ultimate loads only reduce by 3.70% (on average – in comparison with NAC beams). Cracking load continues its trend of increasing reduction with the increasing amount of mixed RCA from CB: with 30% CB and 70% CB, the reductions are 36.46% and 49.87% (in comparison with NAC beams), respectively. Ultimate load experiences a surprising phenomenon: while  $P_{ult}$  of RAC-30B still follows the trend of increasing reduction (9.00% – in comparison with 3.70% of RAC-0B), that of RAC-70B is as strong as NAC.

*Keywords: Construction and demolition waste, Recycled aggregate concrete, Flexural strength, Reinforced concrete beam*

## INTRODUCTION

Studies of RAC employing coarse and/or fine aggregates produced from recycling CDW in various countries have shown that given sufficient quality control, this type of concrete is capable of being applied in casting structural members. Naturally, RAC has lower values of mechanical properties (compressive strength, modulus of elasticity, or flexural strength) than that of NAC. Take compressive strength for example, studies since the 1970s of the past century up until now generally report an average reduction of 15-20% of this property when replacing 100% natural coarse aggregate (NCA) with RCA produced from CC ([2]–[8]). However, with such reduction, the strength of RAC in these studies is still adequate for different applications in construction. As a result, further experiments on behavior of RAC beams have been designed and conducted. For such experiments, there are considerations of the type of recycled aggregates to be employed (coarse and/or fine), as well as the type of source CDW (CC and/or CB).

In Poland, the authors [9] set up a 4-point flexural test apparatus for rectangular beams of cross-sectional dimensions of  $B \times H = 200\text{mm} \times 300\text{mm}$ . The

beams were 2,400-mm long, and were loaded at equal intervals of 800mm. Values of ultimate load and deflection, together with observations of crack formation were recorded. It was found out that the ultimate load of RAC beam did not reduce much (only by 3.5%) in comparison with that of reference NAC beam. However, the instantaneous deflection of RAC beam was always larger by 18-100% (i.e., double). In this experiment, the authors employed RCA produced from CC to replace NCA with the replacement rate of 100%, all other materials remained natural.

With a similar choice of recycled aggregates to the previous authors, Arezoumandi et al. [10] conducted experiments on RAC and NAC beams in the United States in 2015. Test results showed that the reduction of ultimate load of RAC beam was negligible (less than 1%) compared with equivalent NAC beam. This behavior was also reported by Zhao and Sun [11] in China in 2013. In their experiments employing RCA produced from CC, ultimate loads of RAC beams were lower by 2.6-4.1% with increasing replacement rate from 30-75%.

A number of other publications over the years shared the same conclusion of ultimate load. However, it was also observed that the cracking load

of RAC beam was much lower than that of NAC beam – with a maximum reduction of up to 46.3% [12]. Table 1 summarizes these reduction rates.

Table 1 Reduction rate of cracking load and ultimate load in a number of papers on RAC beams

Authors	Replacement rate of RCA (%)	Reduction rate of cracking load (%)	Reduction rate of ultimate load (%)
[13]	50	20	4.8
	100	20	5.5
[10]	100	8-18	<1
[12]	20	10.5-10.9	<1
	50	20.3-45.6	<1
	100	26.4-46.3	<5
[8]	50	14.3	1.5
	100	14.3	3.8

Note: all studies only employed RCA produced from CC with various replacement rates of NCA.

It can be clearly seen that in most previous studies of RAC beams, the authors opted for RCA produced from CC – which is the best type of source material in terms of strength and conformity. The quality of RCA is also much easier to control in comparison with recycled fine aggregate. Experimental results of RAC beams employing materials with less conformity (i.e., containing a certain content of CB) are very much desirable. This issue is even more relevant in developing countries such as Vietnam, where an effective management system of CDW is still lacking, hence the major amount of CDW is mixed CC-CB.

To address this need, the authors adopted an empirical method to study the flexural behavior of RAC beams, in which 100% NCA was replaced by RCA. The RCA in these experiments consisted of CC and CB at controlled percentages. Results of cracking load and ultimate load, together with observations of crack patterns shall be reported.

## PRODUCTION OF RCA FROM CDW

The source material selected in this study is CDW from the demolition of Tan Mai Primary School, Hanoi, Vietnam. Figure 1 shows the concrete boulders resulted from the process of crushing and separating all reinforcing steel bars. CDW was collected to a recycling facility, and would go through a stationary production line to be crushed and sieved (Fig. 2).

The RCA collected from this production line was then further sieved into the sizes of 10-20mm, and of 5-10mm. Figure 3 presents the final product of RCA from CC. RCA from CB was produced in a similar

procedure, with the source material being crushed brick wall segments from the same demolition site.



Fig. 1 Source CC from the demolition of Tan Mai Primary School, Hanoi, Vietnam



Fig. 2 Stationary CDW crushing machine in Hanoi



Fig. 3 RCA from CC of size 10-20mm (left), and 5-10mm (right)

## EXPERIMENT DESIGN

### Mix Design of Concrete

NAC and RAC in these experiments were mixed

at a constant water/cement ratio of 0.55. The target cube strength of concrete was  $f_{cu} = 30\text{MPa}$  for all mix proportions. A total of four mix proportions were adopted, denoted by numbers as follows:

- (1) NAC (100% natural aggregates);
- (2) 100% RCA from CC, 100% natural sand as fine aggregates;
- (3) 70% RCA from CC, 30% RCA from CB, 100% sand as fine aggregates; and
- (4) 30% RCA from CC, 70% RCA from CB, 100% sand as fine aggregates.

Mix proportion details are presented in Table 2.

Table 2 Mix design of  $1\text{m}^3$  concrete

Mix Mat.	(1)	(2)	(3)	(4)
C	300	300	300	300
S	850	850	850	850
G1	275	–	–	–
G2	825	–	–	–
C1	–	275	192.5	82.5
C2	–	825	577.5	247.5
B1	–	–	82.5	192.5
B2	–	–	247.5	577.5
W	165	165	165	165
A	3	3	3	3

Note: C – cement; S – sand; G1 – NCA size 5-10mm; G2 – NCA size 10-20mm; C1 – RCA from CC size 5-10mm; C2 – RCA from CC size 10-20mm; B1 – RCA from CB size 5-10mm; B2 – RCA from CB size 10-20mm; W – water; A – additives; all units are in kilogram (kg).

To enhance the final quality of RAC, the two-stage mixing approach (TSMA) was adopted. This process of concrete mixing was proposed by Tam et al. in 2005 [14], and was reported to be able to improve the instantaneous strength and microstructure of RAC, as well as its long-term behaviors such as shrinkage or creep [15]. Figure 4 displays the difference between TSMA and the normal mixing approach (NMA).

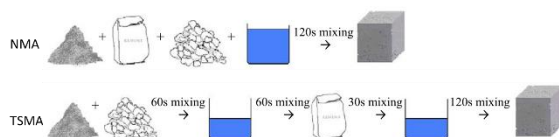


Fig. 4 NMA and TSMA  
Source: Tam et al. (2005) [14]

## Beam Model and Configuration

### Beam details and setup of sensors

12 reinforced concrete beams of rectangular cross-section (3 for each concrete mix proportion) were casted for conducting 4-point flexural

experiments. The cross-sectional area of all beams is  $B \times H = 150\text{mm} \times 200\text{mm}$ , and the length is 1,800mm. Steel reinforcements are arranged as follows ( $\Phi$  – diameter of rebar):

- Longitudinal reinforcements:  $2\Phi 8$  (deformed bar) top reinforcements;  $2\Phi 16$  (deformed bar) bottom reinforcements.
- Stirrup:  $\Phi 6@100\text{mm}$  (plain bar) throughout, skip at midspan.

Beams are situated on two supports at a distance of 1,300mm. The pure bending length is 300mm. Each beam was arranged with the following sensors (Fig. 5):

- 03 linear variable differential transformer (LVDT) sensors  $D_{1,2,3}$  for measuring deflection at designated points (one at midspan, and two at supports).
- 02 resistance strain gauges  $D_{C1,C2}$  for measuring strains at top and bottom layers of concrete.
- 02 resistance strain gauges  $D_{S1,S2}$  for measuring strains in bottom rebars.
- 01 resistance strain gauge  $D_{S3}$  for measuring strain in one of the two top rebars.

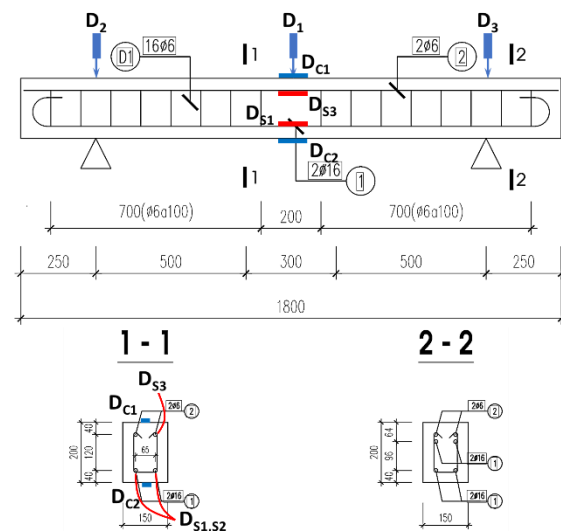


Fig. 5 Beam detail and sensors arrangement

### Experiment procedure and apparatus

Experimental beams were cast by the TSMA as shown in Fig. 6. At 3-day old, formworks were removed and the beams were allowed to be cured at room temperature. Final products with all strain gauges installed are presented in Fig. 7. Each beam was fixed onto the apparatus as shown in Fig. 8.

All results of loading, deflection, and deformation were recorded by a 30-channel data-logger. Throughout each experiment, the crack formation was closely observed. By the end, all crack patterns were marked on every beam.





Fig. 6 Casting of experimental beams



Fig. 7 Beams with installed sensors

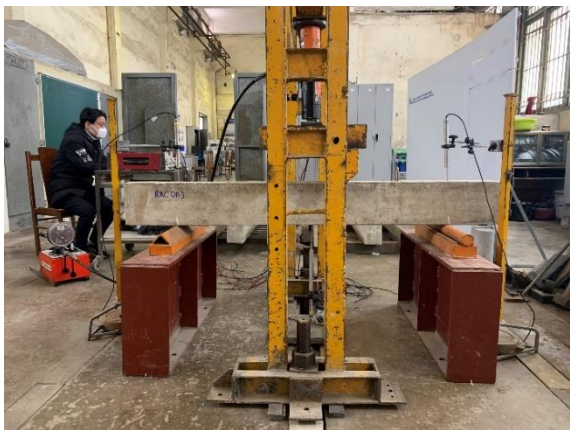


Fig. 8 4-point flexural test apparatus

## RESULTS AND DISCUSSIONS

Monitoring the experiment process, values of cracking load and ultimate load of each beam were recorded. These results are presented in Tables 3 and 4, respectively. In these tables, the designation (1)<sub>1</sub> stands for concrete mix proportion (1) – beam number 1, and so on.

Concerning the mix proportion (2) whereby 100% NCA were replaced by RCA produced from CC, the cracking load is reduced by an average of 17.69% in comparison with the reference NAC beam, while the ultimate load is reduced by an average of only 3.7%. This behavior agrees with previous conclusions of published papers which suggests that cracks would appear much sooner in RAC beams than in reference NAC beams, but with the same mix design, their load-bearing capacity are almost identical.

Table 3 Cracking load of experiment beams

Beam	Cracking load (T)		Reduction (%)	
	Value	Ave.	Value	Ave.
(1) <sub>1</sub>	3.9			
(1) <sub>2</sub>	3.8	3.73	–	–
(1) <sub>3</sub>	3.5			
(2) <sub>1</sub>	3.3		11.53	
(2) <sub>2</sub>	2.9	3.07	22.25	17.69
(2) <sub>3</sub>	3.0		19.57	
(3) <sub>1</sub>	2.3		38.34	
(3) <sub>2</sub>	2.4	2.37	35.66	36.46
(3) <sub>3</sub>	2.4		35.66	
(4) <sub>1</sub>	1.8		51.74	
(4) <sub>2</sub>	1.8	1.87	51.74	49.87
(4) <sub>3</sub>	2.0		46.38	

Table 4 Ultimate load of experiment beams

Beam	Ultimate load (T)		Reduction (%)	
	Value	Ave.	Value	Ave.
(1) <sub>1</sub>	10.0			
(1) <sub>2</sub>	10.3	10.0	–	–
(1) <sub>3</sub>	9.8			
(2) <sub>1</sub>	9.7		3.00	
(2) <sub>2</sub>	9.5	9.63	5.00	3.70
(2) <sub>3</sub>	9.7		3.00	
(3) <sub>1</sub>	9.1		9.00	
(3) <sub>2</sub>	9.2	9.10	8.00	9.00
(3) <sub>3</sub>	9.0		10.00	
(4) <sub>1</sub>	10.1		-1.00	
(4) <sub>2</sub>	10.0	10.10	0.00	-1.00
(4) <sub>3</sub>	10.2		-2.00	

It is clearly observed that the cracking load exhibits a general decrease with increasing percentage of CB in the mix. A contribution of 70% CB in RCA results in halving the cracking load. It can also be said that this observation is expected as CB is a much weaker material in terms of strength compared with natural aggregates or CC.

For the ultimate load, however, there was an unusual point of interest at the 70% CB content in RCA. The load-bearing capacity of these three beams

is as high as the reference NAC beams (value of  $P_{ult}$  of around 10 tons). This might be due to the significant amount of brick and attached mortar absorbs a lot of water right at the moment of concrete mixing – which results in a reduction in W/C ratio. Nevertheless, this explanation still needs further confirmation through other means of observation, the determination of compressive strength and elastic modulus, and even through additional experiments.

Crack patterns of beams are as presented in Fig. 9. It can be seen that most cracks are vertical, and are concentrated around the segment of pure bending. Therefore, it can be safely deduced that all experiment beams fail by flexure, not by shear.

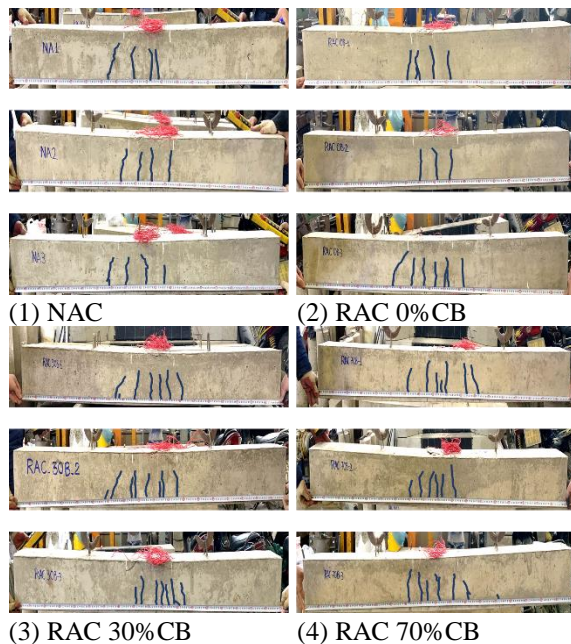


Fig. 9 Crack patterns of experiment beams

## CONCLUSIONS

In this paper, experiments of reinforced beams were set up to observe flexural behavior of RAC with reference to equivalent NAC, including: cracking load, ultimate load, and crack pattern. Results obtained generally agree with previous studies, whereby RAC beams cast with 100% RCA produced from CC would be almost as strong as reference NAC beams, but cracks would also appear much sooner. Hence, it is advisable that when designing with RAC, the serviceability limit state should be considered carefully. Revisions of design standards may as well be needed in order to facilitate the application of RAC in various structures (in this particular case, flexural members).

The ultimate load of RAC beams cast with RCA having high content of CB should be further studied as it displayed a strange behavior that was not totally consistent with common predictions. A look into the

microstructure of concrete might reveal more explanations. More experiments may also be conducted on RAC beams cast with RCA having intermediate percentages of CB (40%, 50%, or 60%) in order to provide a better view on the variation of the ultimate load.

## ACKNOWLEDGMENTS

This research was supported by JST–JICA Science and Technology Research Partnership for Sustainable Development Program (SATREPS) project (No. JPMJSA1701).

## REFERENCES

- [1] Ministry of Natural Resources and Environment, 2016 Report on National Environment: Urban Environment, Natural Resources and Environment Publishing House, 2016.
- [2] Nixon, P.J., Recycled concrete as an aggregate for concrete – A review. *Mater. Struct.*, Vol.11, No.5, 1978, pp.371-378.
- [3] Ravindrarajah, R.S. and Tam, C.T., Properties of concrete made with crushed concrete as coarse aggregate. *Mag. Concrete Res.*, Vol.37, No.130, 1985, pp.29-38.
- [4] de Oliveira, M.B. and Vazquez, E., The influence of retained moisture in aggregate from recycling on the properties of new hardened concrete. *Waste Manag.*, Vol.16, 1996, pp.113-117.
- [5] Topçu, I.B. and Sengel, S., Properties of concretes produced with waste concrete aggregate. *Cem. Concr. Res.*, Vol.34, 2004, pp.1307-1312.
- [6] Kou, S.C., Reusing recycled aggregates in structural concrete (PhD Thesis), The Hong Kong Polytechnic University, 2006.
- [7] Tong, T.K., Nghiên cứu sử dụng phế thải xây dựng trong chế tạo bê tông (PhD Thesis, in Vietnamese), Hanoi University of Civil Engineering, 2017.
- [8] Xiao, J.Z., *Recycled Aggregate Concrete Structures*, Springer-Verlag GmbH Germany, 2018.
- [9] Ajdukiewicz, A.B. and Kliszczewicz, A.T., Comparative Tests of Beams and Columns Made of Recycled Aggregate Concrete and Natural Aggregate Concrete. *J. Adv. Concr. Technol.*, Vol.5, No.2, 2007, pp.259-273.
- [10] Arezoumandi, M., Smith, A., Volz, J.S., Khayat, K.H., An experimental study on flexural strength of reinforced concrete beams with 100% recycled concrete aggregate. *Eng. Struct.* Vol.88, 2015, pp.154-162.
- [11] Zhao, S. and Sun, C., Experimental Study of the Recycled Aggregate Concrete Beam Flexural Performance. *Appl. Mech. Mater.*, Vol.368-370, 2013, pp.1074-1079.

- [12] Seara-Paz, S., González-Fontebao, B., Martínez-Abella, F., Eiras-López, J., Flexural performance of reinforced concrete beams made with recycled concrete coarse aggregate. *Eng. Struct.*, Vol.156, 2018, pp.32-45.
- [13] Ignjatovic, I.S., Marinkovic, S.B., Miskovic, Z.M., Savic, A.R., Flexural behavior of reinforced recycled aggregate concrete beams under short-term loading. *Mater. Struct.*, Vol.46, 2013, pp.1045-1059.
- [14] Tam, V.W.Y., Gao, X.F., Tam, C.M., Microstructural analysis of recycled aggregate concrete produced from two-stage mixing approach. *Cem. Concr. Res.*, Vol.35, 2005, pp.1195-1203.
- [15] Tam, V.W.Y. and Tam, C.M., Assessment of durability of recycled aggregate concrete produced by two-stage mixing approach. *J. Mater. Sci.*, Vol.42, 2007, pp.3592-3602



# LEGALIZATION OF THE USE OF MEDICAL MARIJUANA AS A TREATMENT IN THE EFFORT OF RENEWING THE NATIONAL HEALTH LAW IN INDONESIA

Siska Elvandari<sup>1</sup>, Yandrizza, A.<sup>1</sup> Irzal Rias<sup>1</sup>, Tenofrimer<sup>1</sup> and Ansiha Nur<sup>2</sup>

<sup>1</sup>Faculty of Law, Universitas Andalas, Indonesia; <sup>2</sup> Faculty of Engineering, Universitas Andalas, Indonesia

## ABSTRACT

This study focuses on finding an ideal concept regarding the criteria for legalizing the use of medical marijuana as a treatment in an effort to reform the national health law in Indonesia, and being able to find an ideal concept of criminal law policy in an effort to minimize the misuse of medical marijuana use as a treatment in an effort to reform the law health in the future (*Ius Constituendum*), so that various criminal law policies must be carried out. Criminal Law Policy in an effort to minimize cases of medical marijuana abuse as an effort to renew health law in the future (*Ius Constituendum*). Recommendations to several relevant agencies, legal practitioners, and health practitioners are expected to be able to know, review and find a concept regarding the criteria for legalizing the use of medical marijuana as a treatment in an effort to reform national health law in Indonesia, and how criminal law policies are in an effort to minimize the misuse of medical marijuana use. as a treatment in an effort to renew health law in the future (*Ius Constituendum*). By conducting a normative juridical analysis, using the principles of law and legislation as well as several legal principles in the field of health law, in the form of the principles of "For Life" (*Pro-Life*), "For Choice" (*Pro-Choice*), in efforts to reform the national health law.

*Keywords: Health, Legalization, Medical marijuana, Treatment*

## INTRODUCTION

Every human being who is born and lives has inherent rights as a form of God's gift which is natural and fundamental. These rights exist since humans are born, because every person, society, and state must maintain, protect, and respect each other, these rights are human rights (HAM). Human rights must be upheld and protected by the rule of law, so that other people, or the state, are not arbitrary about these inherent rights. The ratification of the Universal Declaration of Human Rights by the United Nations is a real form of awareness of the nations of the world legally to protect the human rights of every human being. Indonesia as a concrete form of protecting the rights of every human being has been stated in the 1945 Constitution and the Government has also ratified Law Number 39 of 1999 concerning Human Rights (HAM) [1].

One form of human rights protection that must be realized is the right to health. The right to health is part of the welfare element of every human being, so that every human being who lives does not expect to get sick, so health is always well taken care of. Quality development in the health sector is a very important national development investment and must be continuously improved. If the health of the community is disrupted, it will have a large economic loss for the country. Without the fulfillment of the right to health, development in the health sector automatically cannot be realized [2]. In the 2009 National Health System, it is stated that health

development is an effort carried out by all components of the nation that aims to increase awareness and the ability to live healthy for everyone so that the highest level of public health can be realized [3].

In order to increase the degree of public health which can be realized as high as possible starting from the improvement of human resources, which needs to be done in order to realize the welfare of the people, it is necessary to make efforts to improve in the field of medicine and health services, among others by seeking the availability of certain types of narcotics which are very much needed as a substitute for drugs. drugs and to prevent and eradicate the dangers of narcotics and narcotic precursors, so that the Government forms a law, namely Law Number 35 of 2009 concerning Narcotics. In the Consideration of Law Number 35 of 2009 concerning Narcotics, states that [4]: a. to realize a prosperous, just and prosperous Indonesian society that is materially and spiritually evenly distributed based on Pancasila and the 1945 Constitution of the Republic of Indonesia, the quality of Indonesian human resources as one of the national development capital needs to be maintained and improved continuously, including the degree of health; b. In order to improve the health status of Indonesian human resources in the context of realizing the welfare of the people, it is necessary to make efforts to improve the field of treatment and health services, among others by seeking the availability of certain types of Narcotics which are urgently needed as drugs as well as preventing and

eradicating the dangers of abuse and illicit trafficking of Narcotics and Narcotics Precursors; c. Narcotics on the one hand are drugs or materials that are useful in the field of treatment or health services and the development of science and on the other hand can also cause very detrimental dependence if misused or used without strict and careful control and supervision; d. importing, exporting, producing, planting, storing, distributing, and/or using Narcotics without strict and thorough control and supervision and contrary to laws and regulations is a Narcotics crime because it is very detrimental and is a very big danger to human life, society, nation and state. and Indonesia's national security; e. Narcotics crime has been transnational in nature which is carried out using high modus operandi, advanced technology, supported by an extensive network of organizations, and has caused many victims, especially among the nation's young generation which is very dangerous to the life of the community, nation and state so that the Law Number 22 of 1997 concerning Narcotics is no longer in accordance with the development of the situation and conditions that develop to overcome and eradicate these criminal acts; f. that based on the considerations as referred to in letter a, letter b, letter c, letter d, and letter e, it is necessary to establish a Law on Narcotics.

In Law Number 35 of 2009 concerning Narcotics, it is stated that: narcotics can only be used for the benefit of health services and/or scientific development, but not all types and classes of narcotics are used for health purposes, especially for class I narcotics which are in large quantities. Even if it is limited, it can only be used for the benefit of developing science and technology, in addition to its benefits in the world of medicine, if misused or misused, narcotics can cause harmful consequences for the life and values or patterns of the Indonesian nation which serve as the philosophical basis, namely Pancasila and the 1945 Constitution which in the final stage leads to a criminal act.

The rampant circulation of narcotics in several regions in Indonesia shows that there have been deviations from the use of narcotics, which are usually used by doctors and health professionals for medical purposes because they have substances that are able to help the patient's healing process. However, because the substances contained in these drugs can cause addiction or addiction or other negative effects, the use of which is beyond the dosage limit has now been discontinued for several reasons. One of the effects it causes is not light, such as causing excessive addiction and always wanting to consume it continuously, even though increasing the dose of its use causes one's own health to be threatened, such as the death of a drug user.

Another phenomenon that has caught the public's attention is not only the use of narcotics that leads to narcotics abuse, such as several cases that the author

has described in the previous section, but there is also a case that has greatly attracted public attention when using narcotics for the purpose of medical treatment, namely the case of Fidelis Ari. , with the following position cases: On February 19, 2017 Fidelis Ari was arrested by the National Narcotics Agency, for planting marijuana to treat his wife who had a spinal cyst, and a month after Fidelis Ari was arrested his wife was declared dead. The death of his wife because his wife could not access the medicine he needed to maintain life in the form of a potion or concoction of marijuana leaves that Fidelis Ari made himself. This can be seen from a number of Non-Governmental Organizations (hereinafter referred to as NGO) regretting the steps taken by the National Narcotics Agency (hereinafter abbreviated as BNN) to arrest and detain Fidelis Ari. They considered that Fidelis should not have been arrested for growing marijuana for his wife's treatment.

This case is one that is said to be contrary to human values, so it is felt that it needs to get attention from various groups, such as the Government, Law Enforcement Agencies, and several other related agencies. This can be seen from the various reactions that were born from various circles, such as: Chairman of the Nusantara Maritime Circle (hereinafter abbreviated as LGN) Dhira Narayana said, this is not the first case where someone uses marijuana as a drug. Since 2010, LGN has documented many people using marijuana as a treatment and some of them are still in prison [4]. This does not mean that if BNN does not investigate this case, then they violate the law. The termination of the investigation can still be carried out as stipulated in article 109 paragraph 2 of the Criminal Procedure Code [5].

For comparison, at the beginning of 2022 a similar case was repeated, where the figure of Santi Warastuti was in the spotlight after uploading a photo of his action in the Car Free Day (CFD) of the Jakarta HI Roundabout on Sunday (26 June 2022) which went viral on social media. Through his personal Twitter account, singer Andien Aisyah uploaded a photo of Santi carrying a large poster that reads "Please, my son needs medical marijuana" in a crowd of residents. In the action, Santi was seen accompanied by a middle-aged man with a child lying weakly in the stroller. Apparently, the child is Pika, the baby of Santi and her husband who suffers from cerebral palsy or a disorder that affects one's muscle ability, movement, and body coordination [6].

Investigate, this action aims to urge the judges of the Constitutional Court (hereinafter abbreviated as MK) to immediately decide on a judicial review lawsuit against Law Number 35 of 2009 concerning Narcotics which he requested. Santi with her husband Sunarta and their son Pika came from Yogyakarta to Jakarta to deliver a letter of hope to the Constitutional Court regarding this. The reason is that it has been

almost two years since the Court has not decided on the matter of judicial review. In fact, Pika who suffers from cerebral palsy requires cannabis seed oil or CBD oil therapy to seek his recovery. Santi filed a lawsuit for judicial review of Law Number 35 of 2009 concerning Narcotics to the Constitutional Court along with two other mothers in November 2020. The children of the two mothers are also not in good health because they suffer from pneumonia and epilepsy respectively.

In their lawsuit to the Constitutional Court, the three mothers questioned the explanation of Article 6 Paragraph (1) letter a and Article 8 Paragraph (1) of the Narcotics Law which prohibits the use of marijuana for health services. This article is considered detrimental to the constitutional rights of the applicant because it prevents them from getting treatment for the baby. Therefore, the three wanted the Court to legalize the use of class I narcotics so that their children could receive treatment. In addition to the three women, several other institutions also became plaintiffs in this case, namely ICJR, LBH Masyarakat, IJRS, Yakeba, and EJA. Almost two years since the lawsuit was filed, the Court has yet to decide this case. However, since November 2020, the Constitutional Court has asked the applicant for information from a number of experts through a series of trials. The spokesman for the Constitutional Court, Fajar Laksono, said that the trial of this case was quite long because it brought many experts from the litigants. "Currently, his position is under internal discussion by a constitutional judge [6].

Based on the explanation above, it caused reactions from various groups. LBH Community Narcotics Policy Analyst Yohan Misero said the current Narcotics Law does not accommodate the use of marijuana for medical purposes, so Law Number 35 of 2009 concerning Health must be revised immediately. This law does not accommodate the use of marijuana for health, even Article 8 of the Narcotics Law prohibits the use of narcotics class I for health. The Narcotics Law should not prohibit the use of any substance or plant for health, and Yohan also encourages the Government to conduct research to prove the health benefits of cannabis leaves, and believes that current technology and human resources are capable of producing quality research.

The above phenomenon strongly indicates that the community's sense of legal awareness is decreasing in achieving the right to health in the form of efforts to achieve optimal health degrees which are based on respect for and protection of human rights, namely the right to life. Based on Article 28 a of the 1945 Constitution, it is stated that the right to live and maintain life and life is the right of every person, while according to Article 4 of Law no. 39 of 1999 concerning Human Rights, states that: The right to life is a human right that cannot be reduced under any circumstances and by anyone. The right to life based

on Article 29 in conjunction with Article 1 Paragraph 3 of the Third Amendment of the 1945 Constitution states that life does not belong to humans. Life is a gift from God to everyone that must be guarded and maintained from the beginning to the end (when it is taken back) not indefinitely.

The reactions carried out by the various agencies above, according to the author, are not the right solution. This is because we should look at the phenomena above as a whole which are closely related in various aspects of life, not see the phenomena above based on the presence or absence of something to get further regulation in laws and regulations, because the phenomenon is not only limited to the right to choose or the right to choose to do something or Pro Choice, but view the above phenomenon as the right to live and maintain life or Pro Life as an effort to continue to view humans as whole humans as an effort to dignify humans and humanity itself. Based on the foregoing, it is critical to discuss the legalization of the use of medical marijuana as a treatment in the effort of renewing the national health law in Indonesia. The problems that will be discussed are 1) the criteria for legalizing the use of medical marijuana as a treatment in an effort to reform the national health law in Indonesia, and 2) the criminal law policy in an effort to minimize the misuse of medical marijuana use as a treatment an an effort to reform health law in the future (Ius Constituendum)

## METHODOLOGY

### 1. Research Approach.

The method of approach in this research is a normative juridical research. Normative juridical research is a legal research conducted by researching and reviewing the literature. According to Soekanto and Mamudji [7], normative legal research includes research on legal principles, legal systems, vertical and horizontal level of synchronization, comparative law and legal history.

### 2. Research Specification

The type and specification of this research is descriptive analytical research. This approach is used because this research analyzes the judge's decisions. The implementation of this method is not limited only to data collection and compilation of data, but also includes the analysis and interpretation of the meaning of the data [8].

### 3. Research Phase is performed through 2 stages, namely:

- a. The literature study phase begins by collecting secondary data needed in the research, namely basic materials of normative legal research (literatures), used literature research methods that include: First, primary legal materials consisting of Basic Norms or Basic Rules of the Constitution, Basic Regulations: The Body

of the Constitution, Congress Decrees, Laws and Regulations, namely: Act, Government Regulations, Presidential Decrees, and Other Regulations related to narcotics abuse cases, and existing jurisprudence relevant to the writing in this study. Second, secondary legal materials provide explanations about primary legal materials, such as: papers, workshops, seminars, symposia, discussions, and research results, magazines or newspapers that are related to this research object. Third, tertiary legal materials that provide guidance and explanation of primary and secondary legal materials, for example dictionaries, encyclopedias, and so on.

- b. The field study phase is obtained directly from the source of information through interview, using the structured questionnaire about the criteria of narcotics use that could be categorized for medical treatment, and the condition in which the narcotics use could be categorized as narcotics abuse, in perspective of health law in West Sumatra; and to know the Criminal law policy's effort to minimize the narcotics abuse case, as reformation effort for the law of health in the future (Ius Constituendum).

#### 4. Data collection technique

Based on the problems and the approaches as described in the previous section, this study uses two types of tools for data collection, i.e. document studies and interviews. The documents studies were used to collect secondary data, in forms of legal materials as described above; while interviews were used to collect primary data, both from respondents and from informants, because the expected data from this interview method was an in-depth data. Then, the interview guidance used is the free guidance interview (unstructured interview guidance).

## RESULTS AND DISCUSSION

### The criteria for legalizing the use of medical marijuana as a treatment in an effort to reform the national health law in Indonesia.

The criteria that become the benchmark of the use of medical marijuana as a treatment in an effort to reform the national health law in Indonesia include Supervision, Age Limits, Number and Place Limits. Supervision is carried out by the Minister of Health, the Food and Drug Monitoring Agency (BPOM), the National Police/BNN, and the Health Professionals. The inclusion of the National Police, BNN, and the Health Profession as an effort to achieve legal certainty with full principles of legal protection based on the existence of duties, principals, functions and authorities that are closely related to the investigation process in finding the basis for the start of the criminal

justice system process, namely seeking at least 2 (two) two) sufficient evidence and to meet the requirements of sufficient initial evidence.

The age limit and the number limit must be adjusted to the adage in health law, must pay attention and consider the same situation and conditions that are the basis for consideration in determining the right dose and will be used in narcotics users for medical purposes. This is because the human condition is basically not the same because many factors influence it. Place is also an important factor for the Government to monitor the situation and condition of its people.

Table 1. Data of revealed crime cases of drug abused in West Sumatera Regional Police Corps year 2020-2021

No	Regional Unit	Result for Revealed Case of Drug Abused Crime				Trend
		2020 (Jan-Jun)		2021 (Jan-Jun)		
		Case	Suspect	Case	Suspect	
1	Ditres Narkoba	56	67	67	89	Case increase by 18 (4%)
2	Polresta Padang	131	178	132	156	
3	Polres Bukittinggi	27	40	29	36	
4	Polres Pasaman	10	16	19	24	
5	Polres 50 Kota	11	15	17	21	
6	Polres Pessel	10	11	14	20	
7	Polres Padang Pariaman	24	36	15	21	
8	Polres Sawahlunto	9	15	10	12	
9	Polres Tanah Datar	7	12	14	23	
10	Polres Solok	5	5	6	8	
11	Polres Agam	14	15	15	15	
12	Polres Padang Panjang	14	15	15	15	
13	Polres Solsel	4	4	8	9	
14	Polres Payakumbuh	29	33	32	44	
15	Polres Solok Kota	23	32	19	29	
16	Polres Dhamasraya	16	28	11	14	
17	Polres Mentawai	1	1	2	2	
18	Polres Sijunjung	9	14	9	12	
19	Polres Pariaman	21	24	14	21	
20	Polres Pasbar	27	32	17	22	
	Total	442	587	460	593	

Notes : Polres = Resort police



Table 1 and Table 2 shows the success of the Narcotics Directorate of Regional Police of West Sumatra and the society, to minimize the occurrence of narcotics abuse cases. In the future, it will required cooperation with several relevant agencies as the responsible parties, such as: National Agency for Drugs and Food Control (BPOM), Commission III of the House of Representatives, Indonesian Doctors Association (IDI), Pharmacy Experts, and the Ministry of Health, in formulating various policies as the institutions who have its main duties, functions and authority, and also as reminder for re-align the public's understanding on narcotic use, and to define the criteria between narcotic usage as a narcotics abuse or as a series of processes in medical treatment.

Table 2. Comparison in Evidence Revealed on the Year 2020-2021

No	Type of evidence	Result of evidence revealed	
		2020 Jan-Jun	2021 Jan-Jun
1	Marijuana	134.14 Kg	231,78 Kg
2	Marijuana Plant	70 Plant	60 Plant
3	Methamphetamine	2.017,3 Gr	2.266,39 Gr
4	Ecstasy	28 pills	18 pills
5	Class. IV Psychotropics	-	40.000 pills of Hexymer brand + 600 pills of Alpozolam brand + 47 pills Erimin brand.

**The criminal law policy in an effort to minimize the misuse of medical marijuana use as a treatment in an effort to reform health law in the future (Ius Constituendum)**

Figure 1 shows criminal law policy in Indonesia. The criminal law policy in an effort to minimize the misuse of medical marijuana use as a treatment in an effort to reform health law in the future (Ius Constituendum) is closely related to the 4 (four) criteria mentioned above. Supervision is carried out by the Minister of Health, the Food and Drug Monitoring Agency (BPOM), the National Police/BNN, and Health Professionals. The inclusion of the National Police, BNN, and the Health Profession as an effort to achieve legal certainty with full principles of legal protection based on the existence of duties, principals, functions and authorities that are closely related to the investigation process in finding the basis for the start of the criminal justice system process, namely seeking at least 2 (two) two) sufficient evidence and to meet the requirements of sufficient initial evidence.

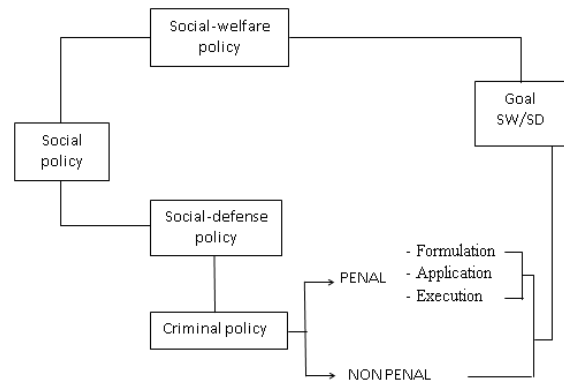


Fig. 1 Criminal law policy as part of criminal policy and social policy

Figure 2 shows a comparison Scheme of Criminal Policy Scope. It is shown that crime prevention efforts could be pursued by: a. criminal law application; b. Prevention without punishment; and c. influencing the public's view on crime and punishment/mass media. Criminal eradication is divided into two mainlines; "penal" (criminal law) and "non-penal" (non/outside of criminal law). In the divisions by G. Peter Hoefnagels above, the efforts mentioned in points (b) and (c) may be included in the "non penal" effort group.

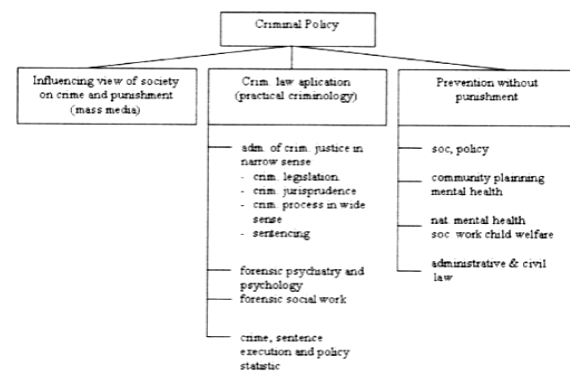


Fig. 2 Scheme of the criminal policy scope

In comparison with the author's case, this case should be a momentum to review existing policies so that they can be accustomed according to the current situation and social condition. These policies at once become the answer for the criteria that will be used as a benchmark on the use of narcotics in medical treatment and narcotics abused, as described in Table 3. It shows that the formulation policy in the future will closely related to the four (4) criteria above. Supervision will be conducted by the Minister of Health, National Agency for Drugs and Food Control (BPOM), Police / BNN, and Health Professionals. Inclusion of the Police, BNN, and Health Professionals, who act as an effort to achieve legal



certainty within the principle of legal protection. It was based on the existence of duties, principals, functions and authority which are closely related to the process of investigation, searching for basic start-up in the process of criminal justice system, by searching two sufficient evidence, to meet requirements for sufficient initial proof.

This health profession is aimed at carrying out medical actions that are still based on 3 (three) standard actions, such as: Standard Operational Procedure (SOP), Service Standards, and Professional Standards. This is necessary considering the health profession in general, and the medical profession as a noble or honorable profession (*Officium Nobile*), by placing humans as objects.

Furthermore, it must pay attention and take into account the same situations and conditions that are the basis for consideration in determining the right dose and will be used in medical marijuana users for medical purposes. This is due to the fact that the human condition is not uniform, as many factors influence it. The location is also an important factor for the government to monitor the health of its citizens.

## CONCLUSIONS

The use of medical marijuana can be regarded as a new breakthrough in treatment in an effort to reform national health laws in Indonesia. This is enforced in an effort to defend the right to life and the right to defend one's life. This effort is carried out by improving the medical rehabilitation system, where patients who use medical marijuana are allowed with

various conditions as long as it is determined by the law which is the core of health services, with the ultimate aim of dignifying patients as whole human beings, to reduce suffering, prolong life, and accompany the patient until the end of his life.

## ACKNOWLEDGMENTS

This research is supported by the funding of LPPM Universitas Andalas.

## REFERENCES

- [1] Riyanto, S., *Establishment of a Special Medical Court*, Yogyakarta: Deepublish, 2012, p. 1.
- [2] Riyanto, S., *Establishment of a Special Medical Court*, Yogyakarta: Deepublish, 2012, p. 3.
- [3] Hartini, Y. S., *Pharmacy Practice Review of Regulations on Pharmacists Occupation*, Yogyakarta, Sanata Dharma, 2010, p. 3.
- [4] Law Number 35 of 2009 concerning Narcotics.
- [5] Ihsanuddin, Fidelis Case Becomes Momentum to Legalize Marijuana for Medicine, accessed at <http://www.kompas.com>, on July 8, 2022.
- [6] Elvandari, S., *Medical Dispute Resolution Law*, Depok, Rajawali Pers, 2021, p. 3.
- [7] Soekanto, S, and Mamudji, S., *Research on Normative Law, A Brief Review*, Jakarta, Rajawali Press, 1985, p. 13.
- [8] Moerad, P., *Law Formation through Court Ruling Criminal Case, Bandung, Disertation on Doctoral Program in Science of Law*, Padjajaran University, 2004, p. 43.

# FLASH CALCINATED SEDIMENT USED IN THE CEM III CEMENT PRODUCTION AND THE POTENTIAL PRODUCTION OF HYDRAULIC BINDER FOR THE ROAD CONSTRUCTION – PART I: CHARACTERIZATION OF CEM III CEMENTS

Mahfoud BENZERZOUR<sup>(1)</sup>, Duc Chinh CHU<sup>(1)</sup>, Joelle KLEIB<sup>(1)</sup>, Mouhamadou AMAR<sup>(1)</sup>, Nor-Edine ABRIAK<sup>(1)</sup>, Jaouad NADAH<sup>(2)</sup>.

<sup>(1)</sup> Univ.Lille, IMT Nord Europe, Univ.Artois, Yncrea Hauts-de-France, ULR 4515-LGCgE, Laboratoire de Génie civil et géo-Environnement, F-59000, Lille, France.

<sup>(2)</sup> EQIOM Le LAB, CRT 1 Parc Vendôme – 460 Allée de l'Innovation, 59810 LESQUIN, France.

## ABSTRACT

The maintenance operation of waterway generates about of 300 Mt of sediments every year in Europe and provokes a real problem for the environment. The dredged sediments have been used in several application such as the cement production, the road construction and the supplementary cementitious materials (SCMs) in the concrete. Knowing that about of 4.6 billion tons of cement are produced every year in the world and the cement industry releases about of 8% of CO<sub>2</sub> global emission. The reduction of CO<sub>2</sub> emission amount as well as the reservation of natural resource becomes a challenge in the 21<sup>st</sup> century. Consequently, in this study, a fluvial sediment was used to replace a part of traditional raw materials in the clinker production and another fluvial sediment treated by flash calcination was used to substitute a part of slag for the CEM III production. The CEM III cements produced can be used as a hydraulic binder in order to treat the soil in the geotechnical application. The characterization results indicated that the raw materials replacement by sediment did not modify the cement's properties compared to the CEM III reference. However, a substitution rate of 25% wt slag by the flash calcination sediment promoted the cement reactivity as well as the mechanical and microstructural properties of hydrated cement.

*Keywords: Flash calcined sediment, Cement, Hydration, Slag, Compressive strength, Microstructure.*

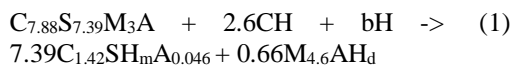
## INTRODUCTION

The cement industry produces about 4.6 billion tons of cement every year, which is an essential component for the concrete production. However, this production activity also contributes approximately 8% of CO<sub>2</sub> global emission in the world. In addition, the extraction and transport operations of raw materials have the negative impacts on the environment. The need to limit the CO<sub>2</sub> emission and reservation of natural resources has become the veritable challenge for the cement industry in 21<sup>st</sup> century. Several previous studies have proven the feasibility of waste recycling to replace a part of traditional raw materials in the clinker production such as the municipal solid waste incineration [1], steel slag [2], civil construction waste [3] or dredged sediment [4, 5]. Although the characterization results of clinker made from the traditional raw materials replacement by the waste in the raw meal showed that all the four typical phases were identified, but the cement quality were very variant along with the substitution rate and type of waste used. In a previous study [6], the content increase of municipal sewage sludge incorporated in the raw meal led a longer initial setting time, final setting time and a slight decrease of compressive

strength of hydrated cement. These results can be explained by the presence of minor elements in the waste which can modify the polymorphs of mineral phases in the produced clinker. For example, MgO promotes the formation of M3 polymorph in C<sub>3</sub>S phase, which is well known to be less reactive compared to the M1 polymorph [4]. Consequently, the waste recycling in the clinker production must be performed with caution to ensure the cement quality. However, this solution can only limit the consumption of traditional raw materials while not reduce the CO<sub>2</sub> emission during the clinkering process. To solve this problem, several previous studies attempted to reduce the clinker content in the cement by partially or totally the clinker with supplementary cementitious materials (SCMs). From the environmental point of view, the SCMs use not only reduces the quantity of CO<sub>2</sub> emission due to the clinker production, it also eliminates the need of disposal for the storage of some residual products of industry as granulated blast furnace slag from the iron production, fly ash from the coal combustion or silica fume generated from the silicon and ferrosilicon alloy production. In addition, from the technical point of view, the SCMs incorporated in the concrete can improve the durability against corrosion, sulfate attack [7] or alkali – silicate

reaction [8] as well as the mechanical performance and the microstructure at long –term. Depending on the chemical – mineral compositions as well as the physical properties of SCMs, the hydration reactions of cement containing the SCMs are very different than those of pure cement hydration. The principal change are from the products formed as the lower Ca/Si ratio in the C-S-H hydrate or the consumption level of  $\text{Ca}(\text{OH})_2$  by the SCMs [9].

The slag has successfully been used with the Portland cement to produce the cement blends that are more economical, more environmentally friendly and have performance advantages. The replacement level of slag can reach 65 wt% in the cement CEM III/A described in the NF EN 197-1 standard [10]. In a previous study, a slag containing  $\text{CaO}$  (noted C),  $\text{SiO}_2$  (noted S),  $\text{MgO}$  (noted M), and  $\text{Al}_2\text{O}_3$  (noted A) with molar proportions of 7.88 : 7.39 : 3 : 1 was used to study the chemical reaction of slag in the presence of calcium hydroxide (noted CH). The result showed that the chemical reaction for the slag/CH could be written as follows:



with  $b = 7.39m + 0.66d$ .

Generally, the C-(A)-S-H gel formed in the Portland cement –slag blends has a lower Ca/Si ratio and a higher Al/Si ratio than pure Portland cement. Although, the CEM III cement – slag has demonstrated good economical – environmental – mechanical performance, but the worldwide slag supply is relatively limited when compared to the annual demand for concrete for new construction and repair [11]. For example, the slag production in France has gradually decreased due to the deindustrialization of the steel industry. Consequently, all the potential materials must be study in earnest to reduce the cement content as well as the conventional mineral admixtures.

One potential material that has been investigated in the recent years to substitute a cement part in the concrete, is the sediment that generate from the dredging operation at ports and waterways with approximately of 300 Mt of sediments dredged every year in Europe. Several previous studies [4, 12, 13] indicated that the dredged sediments could be used as the raw material in the clinker production [4, 5, 14], as the alternative material in the road construction [15, 16]. In addition, the sediments treated by the thermal treatment also present the

pozzolanic activity and can be used as SMCs in order to replace a cement part in the mortar or concrete.

The aims of this research were twofold: the reuse of sediment in the raw meal for the clinker production at the laboratory was firstly performed, and then the sediment treated by flash calcination method was used to replace a slag part in the CEM III cement production. The properties of clinkers including the free lime content, the mineral phases contents, as well as of the water demand and the setting time of CEM III cements, the compressive strength and the porosity of mortars were analyzed.

## MATERIALS AND METHOD

### Materials in the clinker/cement production

In this research, the sediment used in the clinker production is a fluvial sediment collected at the Air sur Lys region (referenced ASL) in the North of France, France. The other raw materials, such as the limestone, clay, sand and iron oxide were extracted from the natural quarries. All the raw materials were dried to constant mass at 105 °C and ground to reach the particle size smaller than 200  $\mu\text{m}$  according to the requirement in the cement industry. Based on the chemical composition analysis of all the raw materials and the viscosity analysis of the raw meal containing the ASL sediment, the content of ASL sediment in the raw meal was limited to 2 wt% to assure the viscosity requirement. In this part, two different formulations of clinker were established using the moduli values habitually used in the cement industry: Lime Saturation Factor (LSF), Silica Ratio (SR) and Alumina Ratio (AR). The first is the reference clinker (referenced OPC TM) made from the limestone, the clays and iron oxide only. The second clinker, named OPC 2%ASL corresponds to a sediment substitution rate of 2 wt% in the raw meal. The proportion of each raw materials in the formulation was calculated using the values as follows:  $\text{LSF} = 98$ ,  $\text{SR} = 2.5$  and  $\text{AR} = 1.65$  respectively. The sample preparation and clinkering process used in this research was similar than that used in a previous study [4]. The free lime content and mineral phases content of both clinkers was obtained using two different methods: Schläfer-Bukolowki method and the Bogue formula, the Rietveld method based on the XRD analysis. The results were given in Table 1.

Table 1 Free lime content and mineral phases content in both clinkers.

Method	Clinker	$\text{C}_3\text{S}$ (wt.%)	$\text{C}_2\text{S}$ (wt.%)	$\text{C}_3\text{A}$ (wt.%)	$\text{C}_4\text{AF}$ (wt.%)	$\text{CaO}$ free (wt.%)
	Clinker TM	61.63	15.76	9.14	9.18	1.60

Schlafer-Bukolowki method –Bogue formula	Clinker ASL	2%	63.98	12.23	10.06	9.25	1.65
Rietveld method	Clinker TM		64.87	12.47	8.83	9.04	1.19
	Clinker 2% ASL		66.23	12.90	9.61	8.64	1.48

From the results obtained, some conclusion can be made as follows:

- The clinkering process was complete and the cooling process did not lead the decomposition of  $C_3S$  into  $C_2S$  and  $CaO_{free}$ .
- The ASL sediment can be used to replace a part of traditional raw materials and it did not change the formation of four typical mineral phases.

In next part of this research, a other sediment collected from the Noyelle – Sous –Lens region

(referenced RS), in the North of France, France. The RS sediment was firstly dried at 105 °C to constant mass, then ground to reach the particle size smaller than 250 µm. Finally, it was calcined at 750 °C (named SF) in the flash furnace. The slag used in the CEM III cement production was provided by EQIOM Company. The chemical composition of sediment before and after the flash calcination as well as the slag obtained by XRF analysis was presented in Table 2.

Table 2 Chemical composition of sediment before and after the flash calcination and slag obtained by XRF analysis.

Oxide (wt.%)	CaO	SiO <sub>2</sub>	Al <sub>2</sub> O <sub>3</sub>	Fe <sub>2</sub> O <sub>3</sub>	SO <sub>3</sub>	Na <sub>2</sub> O	K <sub>2</sub> O	MgO	ZnO	P <sub>2</sub> O <sub>5</sub>	LOI	Total
RS	10.57	39.62	9.64	5.12	0.22	0.69	1.84	0.88	0.27	2.1	27.63	99.17
SF	11.21	49.71	12.00	5.33	0.18	0.74	2.25	1.12	0.31	2.26	13.70	99.49
Slag	40.98	34.27	10.95	0.27	0.43	0.17	0.49	6.56	ND	ND	4.7	99.40

The XRF result indicates that: the flash calcination did not modify the chemical composition of sediment. In addition, the molar proportion of principal oxides of slag as  $CaO : SiO_2 : MgO : Al_2O_3 = 6.8 : 5.3 : 1.5 : 1$  which is lower than that of slag

used in Eq.(1). It can modify the chemical reaction of slag with the portlandite described in the Eq. (1). In next stage, three different CEM III cements were produced blending the clinker, gypsum, slag and SF sediment to achieve a  $SO_3$  content of 2.4 %wt. The proportion of each component in the three CEM III cements was shown in Table 3.

Table 3 Proportion of each component in the three CEM III cements.

Cement	OPC TM (wt.%)	OPC 2%ASL (wt.%)	SLAG (wt.%)	GYP (wt.%)	SF (wt.%)
CEM III TM	56.55	-	37.70	5.76	-
CEM III 2%ASL	-	56.52	37.68	5.80	-
CEM III SF	56.48	-	28.24	5.86	9.41

### 1.1. Cement characterization

Numerous analyses were performed in order to characterize the properties of CEM III cement anhydrous as well as the cement hydrated. The

specific density of all the cements was measured using the helium pycnometer Accupyc 1330 device according to the NF EN 1097-7 standard. The specific surface area was obtained by using the

Blaine surface method [17] and the Brunauer – Emmett – Teller (BET surface area) method. The initial setting time of all the cements was measured using the Vicat needle according to the NF EN 196 – 6 standard [18] after the determination of water demand.

Cement pastes were prepared with a W/C ratio of 0.5 in order to study the hydrates formed from the cement hydration reaction. The XRD analysis using the Bruker D2 Advance type device equipped with a Cu anode,  $\lambda = 1.5406 \text{ \AA}$  and the angle acquired  $2\theta$  from  $5^\circ$  to  $80^\circ$  was used to identify the hydrates after 28 days of curing.

The mechanical performance is an important index to investigate the cement quality. In this research, the compressive strength was measured on prismatic mortar samples ( $4 * 4 * 16 \text{ cm}^3$ ) that were previously prepared in accordance with standard NF EN 196-1 [19]. The mechanical test was carried out with an INSTRON 5500R (loading capacity of 150 KN) after being cured for 2, 7 and 28 days respectively in the water. The test result is used to determine the cement class according to the standard NF EN 197-1 [10].

The porosity and the pore size distribution of mortars were measured using the Mercury Intrusion Porosimetry (MIP) technique (Micromeritics

Autopore IV device). Based on a previous research [20], the mortar specimen of  $1 * 1 * 1 \text{ cm}^3$  was firstly immersed in a solvent solution for 3 days to stop the hydration, then dried at  $40^\circ \text{C}$  to a constant mass before the analysis.

## RESULTS AND DISCUSSIONS

### Cements characteristics

The physical properties of three cements were presented in Table 4. The results indicate that the CEM III 2%ASL possesses the properties very similar to those of reference cement CEM III TM. It confirms that a sediment substitution ratio of 2 wt% in the raw meal did not modify the characteristics of final cement. However, a slag replacement by the flash calcined sediment ratio of 25 wt% changes all the properties of cement. For example, the specific density of CEM III SF is lower than that of CEM III TM. It can be explained by a less specific density of SF sediment compared to the slag ( $2.65 \text{ g/cm}^3$  for SF sediment and  $2.88 \text{ g/cm}^3$  for the slag). The water demand of CEM III SF as well as the initial setting time of CEM III SF are higher than those of both cements CEM III TM and CEM III 2% ASL. It can be due to a higher BET specific surface area of CEM III SF that leads to a more significant water demand.

Table 4 Physical characteristics of CEM III TM, CEM III 2%ASL and CEM III 10%SF cements

Properties	CEM III TM	CEM III 2%ASL	CEM III SF
Density ( $\text{g/cm}^3$ )	3.02	3.02	2.98
Blaine specific surface ( $\text{cm}^2/\text{g}$ )	3860	3840	3980
BET specific surface ( $\text{m}^2/\text{g}$ )	1.37	1.36	1.90
Water demand (%)	33.33	33.33	35.00
Initial setting time (minutes)	255	255	280

### Hydrates formed from the hydrated cement pastes

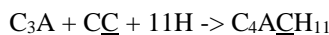
The result of XRD analysis performed on the cement paste specimen after 28 days of hydration was presented in Fig.1. From the XRD patterns, some observations can be made as follows:

- The XRD patterns were nearly identical for the CEM III TM and CEM III 2% ASL cement pastes. The main hydrates identified were Ettringite (Aft), Monosulfate (AFm), Monocarbonate, Hydrotalcite and portlandite (CH). Although, C-S-H is a main hydration product of Portland – slag cement [21], but it's very difficult in order to

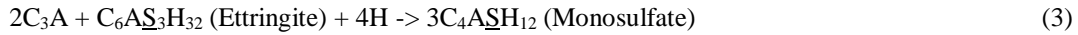
identify by XRD analysis due to amorphous nature of C-S-H.

- The main difference in the XRD pattern of CEM III SF cement paste compared to that of CEM III TM and CEM III 2% ASL was the transformation of ettringite ( $9.1^\circ 2\theta$ ) into monosulfate ( $9.8^\circ 2\theta$ ). This result can be explained by a higher content of  $\text{CaCO}_3$  in the SF sediment which will react with the remaining aluminates to form the monocarbonate ( $11.7^\circ 2\theta$ ) according to the Eq (2) [22]. It prevents the reaction of remaining aluminate with ettringite to form the monosulfate in accordance to the Eq (3).

(2)







- In addition, the quartz ( $SiO_2$ ) was also identified in the XRD pattern of CEM III SF cement

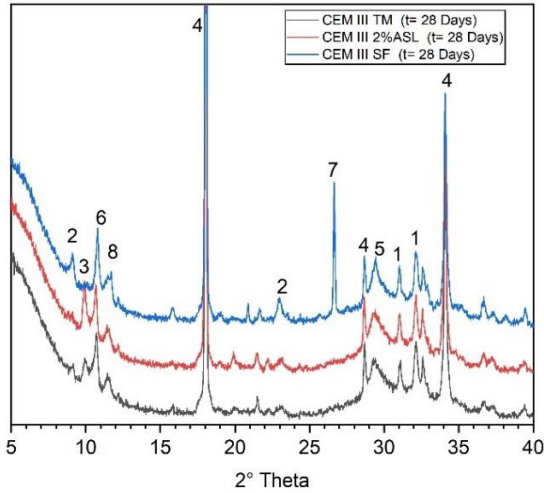


Fig. 1 XRD patterns of all the three cement pastes with E/C = 0.5 after 28 days of curing. (1) :  $C_3S + C_2S$ , (2) : Ettringite, (3) : Monosulfate, (4) : Portlandite, (6) : Hydrotalcite, (7) Quartz, (8) : Monocarbonate.

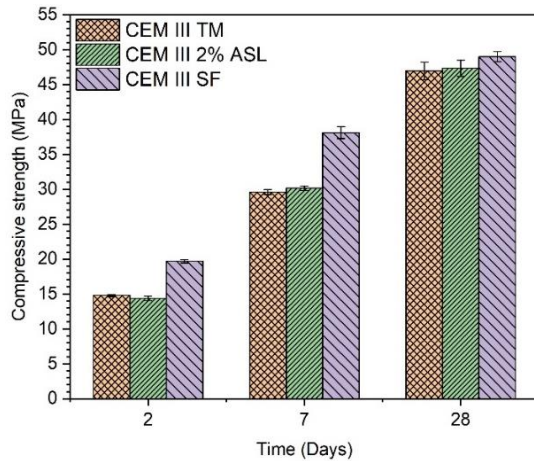


Fig. 2 Compressive strength of mortars over time of hydration.

### Compressive strength of mortars

The compressive strength of all the mortars over time of hydration was shown in Fig. 2. As the previous analysis results, the mechanical performance of CEM III 2%ASL was nearly identical to that of CEM III TM at early ages and long term. This result confirms that the cement quality made from the sediment substitution in the raw meal was similar to that of cement made from the traditional raw materials. However, this result also indicates that the CEM III SF has a higher

paste. It was from the presence of quartz in the SF sediment, which was generally considered as inert. mechanical performance compared to that of CEM III TM and CEM III 2%ASL at early ages as well as in the long term. Indeed, it can be explained by the higher specific surface area of CEM III SF, which improves the cement reactivity. This result also demonstrates the interest of slag replacement by the SF sediment in the mechanical development of mortar. According to standard NF EN 197-1 [10], all three cements are classified as CEM III 42.5 class.

### Porosity of mortars

Fig. 3 presented the relationship between the compressive strength and the total porosity obtained by the MIP technique after 2 and 28 days of curing. The result indicated that:

- The evolution of microstructure as well as compressive strength of mortar confectioned from the CEM III 2%ASL was nearly identical to that of mortar based on CEM III TM.
- As the mechanical test result, the mortar made from the CEM III SF also exhibited a lower porosity compared to that of the CEM III TM and CEM III 2% ASL. This result can suggest that the hydrate amount produced from the CEM III SF hydration is higher than that formed from the CEM III TM and CEM III 2% ASL hydration as the law described in a previous study [23] which established the dependence of compressive strength on the hydrate amount formed.

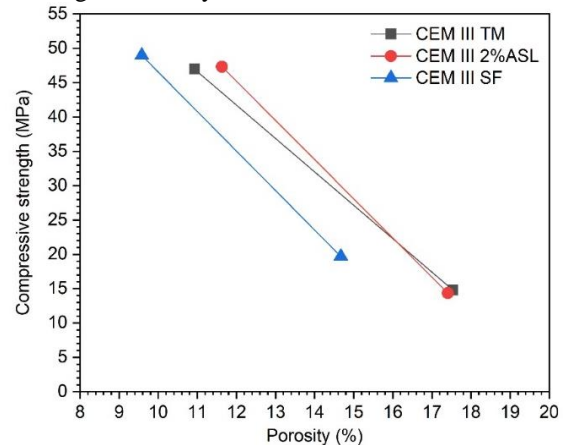


Fig. 3 : Relationship between the compressive strength and the porosity measured by MIP technique of all the mortars.

### CONCLUSION

The research focus to investigate the feasibility of dredged sediment recycling as a raw material in the clinker production as well as SCMs for the slag

replacement in the CEM III cement. The main results obtained were as follows:

- The dredged sediment can replace a part of traditional raw materials in the clinker production. The properties of clinker and cement made from the sediment substitution were identical compared to those of CEM III TM.
- The evolution of microstructure as well as the compressive strength development of CEM III 2% ASL mortar were nearly similar to those of CEM III TM mortar.
- The slag replacement by the flash calcined sediment improved the mechanical performance and the microstructure of mortar at early ages and long term compared to the CEM III TM and CEM III 2% ASL cement.
- The flash calcined sediment incorporation produced a higher amount of hydration compared to that formed from the Portland – slag cement only.
- All three cements are classified as CEM III 42.5 class according to standard NF EN 197-1.

#### AUTHOR STATEMENT

**Mahfoud BENZERZOUR:** Methodology, Conceptualization, Supervision, Validation, Writing-review & Editing, Resources.

**Duc Chinh CHU:** Conceptualization, Methodology, Investigation, Visualization, Writing-original draft

**Joelle KLEIB:** Supervision, Validation, Writing-review & Editing.

**Mouhamadou AMAR:** Supervision, Validation, Writing-review & Editing

**Jaouad NADAH:** Supervision, Validation.

**Nor-Edine ABRIAK:** Supervision, Validation, Resources.

#### Funding

No applicable

#### DECLARATIONS OF COMPETING INTEREST

The authors declare that they have no known competing financial interests or personal relationships that could have appeared to influence the work reported in this paper.

#### AVAILABILITY OF DATA AND MATERIAL:

We confirm that all results are available in the database. If necessary, please contact us at the address: **mahfoud.benzerzour@imt-nord-europe.fr**

#### ACKNOWLEDGMENTS

The authors wish to acknowledge the SEDICIM project and the FEDER funds.

#### REFERENCE

- [1] 1. Pan, J.R., Huang, C., Kuo, J.J., Lin, S.H.: Recycling MSWI bottom and fly ash as raw materials for Portland cement. *Waste Manag.* 28, 1113–1118 (2008). <https://doi.org/10.1016/j.wasman.2007.04.009>
- [2] 2. Tsakiridis, P.E., Papadimitriou, G.D., Tsivilis, S., Koroneos, C.: Utilization of steel slag for Portland cement clinker production. *J. Hazard. Mater.* 152, 805–811 (2008). <https://doi.org/10.1016/j.jhazmat.2007.07.093>
- [3] 3. Costa, F.N., Ribeiro, D. V: Reduction in CO<sub>2</sub> emissions during production of cement, with partial replacement of traditional raw materials with civil construction waste (CCW). *J. Clean. Prod.* 123302 (2020). <https://doi.org/10.1016/j.jclepro.2020.123302>
- [4] 4. Chu, D.C., Kleib, J., Amar, M., Benzerzour, M., Abriak, N.: Recycling of dredged sediment as a raw material for the manufacture of Portland cement – Numerical modeling of the hydration of synthesized cement using the CEMHYD3D code. *J. Build. Eng.* 48, 103871 (2022). <https://doi.org/10.1016/j.jobbe.2021.103871>
- [5] 5. Aouad, G., Laboudigue, A., Gineys, N., Abriak, N.E.: Dredged sediments used as novel supply of raw material to produce Portland cement clinker. *Cem. Concr. Compos.* 34, 788–793 (2012). <https://doi.org/10.1016/j.cemconcomp.2012.02.008>
- [6] 6. Lin, Y., Zhou, S., Li, F., Lin, Y.: Utilization of municipal sewage sludge as additives for the production of eco-cement. *J. Hazard. Mater.* 213–214, 457–465 (2012). <https://doi.org/10.1016/j.jhazmat.2012.02.020>
- [7] 7. Yu, C., Sun, W., Scrivener, K.: Degradation mechanism of slag blended mortars immersed in sodium sulfate solution. *Cem. Concr. Res.* 72, 37–47 (2015). <https://doi.org/10.1016/j.cemconres.2015.02.015>
- [8] 8. Boddy, A.M., Hooton, R.D., Thomas, M.D.A.: The effect of the silica content of silica fume on its ability to control alkali-silica reaction. *Cem. Concr. Res.* 33, 1263–1268 (2003). [https://doi.org/10.1016/S0008-8846\(03\)00058-9](https://doi.org/10.1016/S0008-8846(03)00058-9)
- [9] 9. Lothenbach, B., Scrivener, K., Hooton, R.D.: Supplementary cementitious materials. *Cem. Concr. Res.* 41, 1244–1256 (2011). <https://doi.org/10.1016/j.cemconres.2010.12.001>
- [10] 10. Association Française de Normalisation (AFNOR): NF EN 197-1: Composition, spécifications et critères de conformité des ciment courant.
- [11] 11. Bentz, D.P., Ferraris, C.F., Jones, S.Z., Lootens, D., Zunino, F.: Limestone and silica powder replacements for cement: Early-age performance. *Cem. Concr. Compos.* 78, 43–56 (2017). <https://doi.org/10.1016/j.cemconcomp.2017.01.000>

1

- [12] 12. Chu, D.C., Amar, M., Kleib, J., BENZERZOUR, M., Damien, B., ABRIAK, N.-E., NADAH, J.: The Pozzolan Activity of the Sediment Treated by the Flash Calcination Method. Prepr. (Version 1) available Res. Sq. (2021). <https://doi.org/10.1007/s12649-022-01789-8>
- [13] 13. Amar, M., Benzerzour, M., Kleib, J., Abriak, N.E.: From dredged sediment to supplementary cementitious material: characterization, treatment, and reuse. *Int. J. Sediment Res.* (2020). <https://doi.org/10.1016/j.ijsrc.2020.06.002>
- [14] 14. Faure, A., Coudray, C., Anger, B., Moulin, I., Colina, H., Izoret, L., Théry, F., Smith, A.: Beneficial reuse of dam fine sediments as clinker raw material. *Constr. Build. Mater.* 218, 365–384 (2019). <https://doi.org/10.1016/j.conbuildmat.2019.05.047>
- [15] 15. Siham, K., Fabrice, B., Edine, A.N., Patrick, D.: Marine dredged sediments as new materials resource for road construction. *Waste Manag.* 28, 919–928 (2008). <https://doi.org/10.1016/j.wasman.2007.03.027>
- [16] 16. Tran, N.T.: Valorisation de sédiments marins et fluviaux en technique routière, (2009)
- [17] 17. Association Française de Normalisation (AFNOR): NF EN 196-6 : Méthodes d’essai des ciments - Détermination de la finesse. (2018)
- [18] 18. AFNOR: NF EN 196-3. Methods of testing cements. Part 3 – Determination of setting times and soundness, 2017.
- [19] 19. NF EN 196-1: Méthode d’essai des ciments- Partie 1 : Détermination des résistance. (2016)
- [20] 20. Elkarim, M., Bulteel, D., Potier, G., Michel, F., Zhao, Z., Courard, L.: Use of grinded hardened cement pastes as mineral addition for mortars. (2020). <https://doi.org/10.1016/j.job.2020.101863>
- [21] 21. Durdziński, P.T., Ben Haha, M., Zajac, M., Scrivener, K.L.: Phase assemblage of composite cements. *Cem. Concr. Res.* 99, 172–182 (2017). <https://doi.org/10.1016/j.cemconres.2017.05.009>
- [22] 22. De Weerd, K., Haha, M. Ben, Le Saout, G., Kjellsen, K.O., Justnes, H., Lothenbach, B.: Hydration mechanisms of ternary Portland cements containing limestone powder and fly ash. *Cem. Concr. Res.* 41, 279–291 (2011). <https://doi.org/10.1016/j.cemconres.2010.11.014>
- [23] 23. T.C. Powers: Structure and Physical Properties of Hardened Portland Cement Paste Authorized Reprint from American Ceramic Society. *J. Am. Ceram. Soc.* 41, 7 (1958)

## MICROSCOPIC INVESTIGATION ON ATMOSPHERIC PARTICLES IN CHELYABINSK, SOUTH URAL REGION, RUSSIA

Olga V. Rakova<sup>1</sup>, Tatyana G. Krupnova<sup>1</sup>, Kirill A. Bondarenko<sup>1</sup>, Svetlana V. Gavrilkina<sup>2</sup> and Valerii N. Udachin<sup>2</sup>

<sup>1</sup>Institute of Natural Sciences and Mathematics, South Ural State University, Russia; <sup>2</sup>Ilmen reserve, South Urals Federal Research Center of Mineralogy and Geoecology of the Urals Branch of the Russian Academy of Sciences, Russia

### ABSTRACT

Fine atmospheric particles have physiological toxicity affecting human health. This study investigates the compositional and morphological properties of the particulate matter smaller than 10  $\mu\text{m}$  ( $\text{PM}_{10}$ ) collected in the winter season from five different monitoring stations in Chelyabinsk, Russia. The concentration of 20 elements (Al, B, C, Ca, Cl, Cr, Cu, Fe, K, Mg, Mn, N, Na, Ni, O, Pb, S, Si, Ti and Zn) were determined by scanning electron microscopy-energy dispersive X-ray spectroscopy (SEM-EDS). In order to determine the possible sources of emissions of atmospheric particulate matter, a principal component analysis (PCA) was performed. The results revealed the presence atmospheric  $\text{PM}_{10}$  such as aluminosilicates, calcium particles, sulphates, and metallic particles differentiated on the basis of the chemical composition and morphological parameters. Fe-Mg-rich fine particles and aluminosilicates were observed at all sites and showed a similar nature due to their mainly natural origin. The metal-containing particles showed a more heterogeneous composition mainly related to human activity. The major metal particles were Fe and Zn, Pb, Cu, Mn, Ni and Cr, which were likely emitted from various industries and coal-fired power plants at high temperatures. S-rich particles originated from incomplete diesel combustion. Sulfate  $\text{PM}_{10}$  with metal inclusions contain Mn, Ti, Zn, Cu, and Cr. The higher content of potentially toxic elements in traffic-related S-rich particles compare with industrial-related PM and were the result of the solubilization of metals in airborne particles and increased their toxicity.

**Keywords:**  $\text{PM}_{10}$ , scanning electron microscopy, individual characterization, elemental composition, anthropogenic sources

### INTRODUCTION

Control over air pollution in Russian cities is increasing every year, as residents are worried about the increase in haze or smog driven by elevations in atmospheric particulate matter (PM), especially particles with aerodynamic diameters  $<2.5 \mu\text{m}$  ( $\text{PM}_{2.5}$ ) and  $10 \mu\text{m}$  ( $\text{PM}_{10}$ ). By entering the body and penetrating deep into the respiratory tract, small airborne particles cause significant harm to health.

In 2010, Russia set maximum permissible concentrations of  $\text{PM}_{2.5}$  and  $\text{PM}_{10}$  (35 and 60  $\mu\text{g}/\text{m}^3$  (24-hour mean concentrations), 25 and 40  $\mu\text{g}/\text{m}^3$  (annual mean concentrations), respectively) [1]. Since then, the number of automatic air monitoring posts has grown in Russian cities. However, these concentrations are higher than  $\text{PM}_{2.5}$  and  $\text{PM}_{10}$  concentrations recommended by WHO (25 and 50  $\mu\text{g}/\text{m}^3$  (24-hour mean concentrations), 10 and 20  $\mu\text{g}/\text{m}^3$  (annual mean concentrations), respectively [2].

Industry is one of the main sources of PM pollution in Russian industrial cities. The presence of fine particles in the emissions of various industries has been confirmed: in mechanical engineering-up to 13%  $\text{PM}_{2.5}$  and up to 40%  $\text{PM}_{10}$ ; in ferrous

metallurgy-up to 79%  $\text{PM}_{2.5}$  and up to 84%  $\text{PM}_{10}$  [3]. Another major source of air pollution in the urban environment is vehicular transport and it is important to identify the sources of PM air pollution.

Various factors contribute to the formation of airborne pollutants, the spatiotemporal variability of such pollutants is expected to be significant depending on the processes of pollutant formation and local meteorological conditions. The road dust and PM collected from the industrial city area is enriched with trace elements [4-6]. It seems reasonable, therefore, to assess potential health risks associated with the exposure of inhabitants of large cities.

Scanning electron microscopy analysis is a useful tool for the characterization of aerosol samples at the level of individual particles [7]. Scanning electron microscopy-energy dispersive X-ray spectroscopy (SEM-EDS) examines particles which are too small to be studied with conventional optical microscopes and gives information on the nature and origin of the particles.

Using SEM-EDS, this work identifies and characterizes the morphology and chemical composition of particles present in samples of  $\text{PM}_{10}$  collected from the Chelyabinsk urban area. With the

data obtained from the characterization, a principal component analysis (PCA) was carried out, from which it was possible to identify some of the potential emitting sources of PM<sub>10</sub> in the region.

## MATERIALS AND METHODS

### Study area, data, and sample collection

The sampling stations were located in Chelyabinsk (55°09'14"N, 61°25'44" E, Elevation: 219 meters) (Fig. 1). Chelyabinsk is located on the eastern slope of the Southern Urals. The city has a humid continental climate. The average temperature in January is -14°C/6.6 °F. July has a relatively cool average of 19°C/66.7 °F, while the annual average is 3°C/37.8 °F. The results of long-term observations show that the prevailing winds are from the south, southwest, west, and northwest. In Chelyabinsk, the lowest frequency is recorded for east, southeast, and northeast winds. Wind directions vary slightly throughout the year. The population of Chelyabinsk was 1,130,132 in 2010. The city has a land area of roughly 530 km<sup>2</sup>.

Chelyabinsk is one of the most air-polluted cities in Russia. According to a report by the Ministry of Ecology of the Chelyabinsk Region, Chelyabinsk showed heavy air pollution, having about 110 days per year when pollution is above the national standards [8].

The five sampling sites were located in urban residential areas and the sampling locations are illustrated in Fig. 1. PM<sub>10</sub> sample collection was performed using cascade impactor samplers (Fig. 2). Impactors were operated at a flow rate of 16 L min<sup>-1</sup> for 24 hours.



Fig. 1 The study area, the location of the five sampling sites and prevailing winds

### Scanning electron microscopy

The samples were characterized by SEM-EDS. SEM analysis was performed on a Jeol JSM-7001F Scanning Electron Microscopy Complex. SEM-EDS is a non-destructive analytical method for surface elemental analysis, with a potential detection limit of 0.1–0.5 wt.% for most elements.

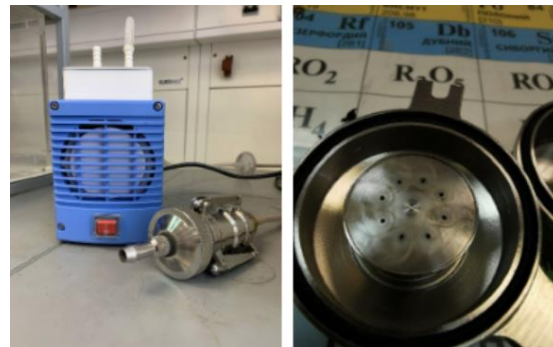


Fig. 2 The aerosol cascade impactor sampler

For SEM-EDS analyses, PM<sub>10</sub> samples were mounted with double-sided tape on an aluminum SEM stub for analysis. With the help of a vacuum coating unit (Gold Sputter Coater, SPI-MODULE, US), a very thin layer of gold was deposited on the surface of each sample in order to achieve better conductivity and less electron charge. 300 particles were manually analyzed 60 particles selected randomly from each of the 5 samples.

## RESULTS AND DISCUSSION

### Overall chemical composition of PM<sub>10</sub>

According to the characteristic SEM-EDX analysis, atmospheric particles collected in winter from Chelyabinsk urban area contained 20 elements (Al, B, C, Ca, Cl, Cr, Cu, Fe, K, Mg, Mn, N, Na, Ni, O, Pb, S, Si, Ti and Zn). The single particles were grouped and labeled as: Fe-containing Fe-Mg-containing, aluminosilicates, particles containing and rich in S, particles containing C and N, metal particles including Fe and Zn, Pb, Cu, Mn, Ni and Cr.

The most abundant elements detected in PM<sub>10</sub> were Fe and Mg which were present in 80–100% of the particles. It could be assumed that Fe-Mg-complexes were included in the composition of natural aluminosilicates. Chelyabinsk stands on sedimentary rocks and granite, typical for the Urals, consisting of oxides Al<sub>2</sub>O<sub>3</sub> (14–15%), SiO<sub>2</sub> (70–72%), Fe<sub>2</sub>O<sub>3</sub> (0.7–1.1%), MgO (0.6–1.1%) [9]. Such particles were found at all sites.

### Characteristic PM<sub>10</sub> collected from Site 1

Fig. 3a shows the predominant morphologies of C-rich particles collected at Site 1. They were regular spherical and spheroidal shapes, with some presenting surface defects such as porosity.



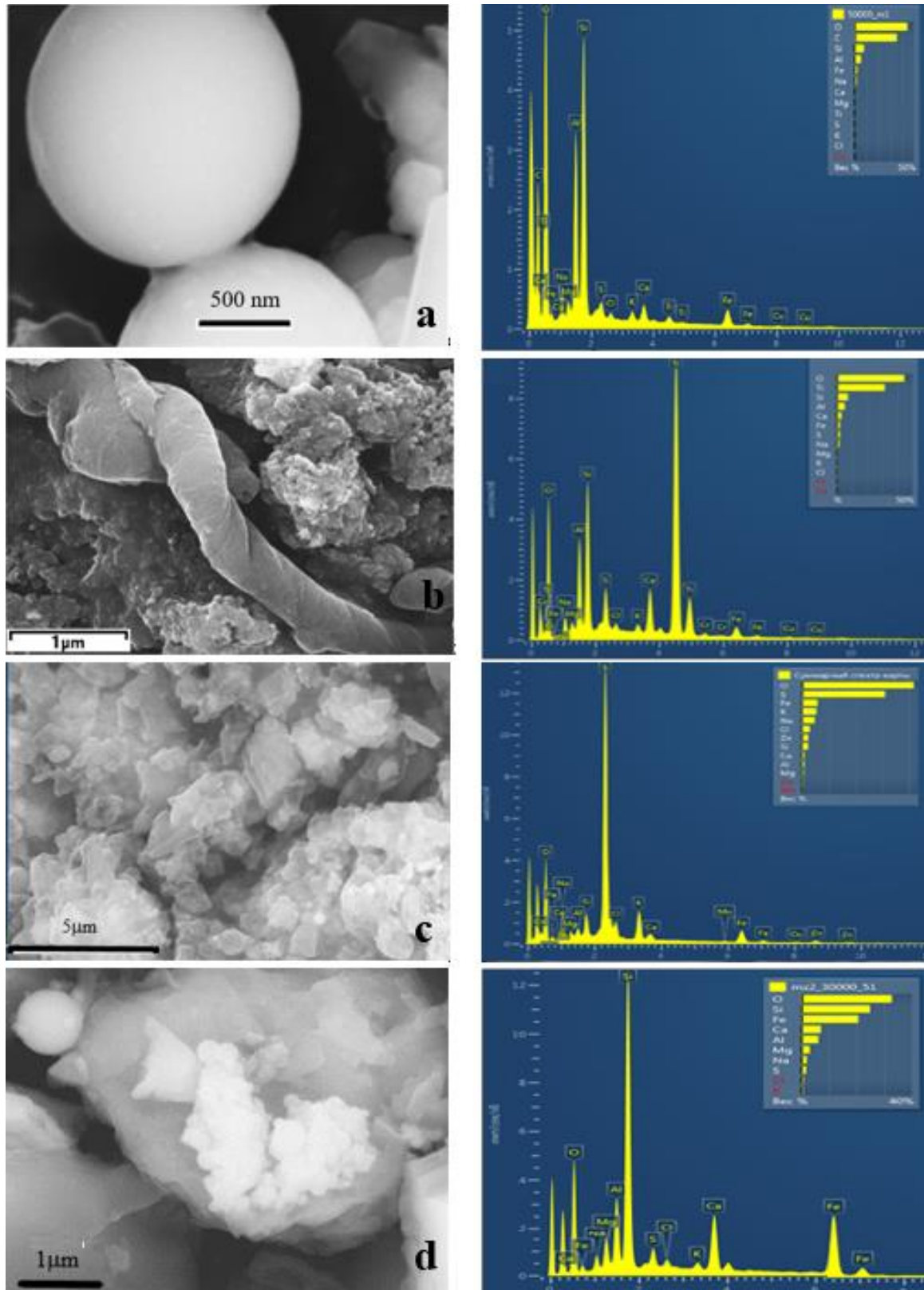


Fig. 3 a) SEM micrograph (magnification 10,000X) C-rich particles collected in Site 1 and their EDX spectrum b) SEM micrograph (magnification 5,000X) Ti-rich aluminosilicate particles collected in Site 1 and their EDX spectrum c) SEM micrograph (magnification 1,000X) S-rich particles collected in Site 2 and their EDX spectrum d) SEM micrograph (magnification 5,000X) Fe-rich aluminosilicate particles collected in Site 5 and their EDX spectrum

The spheres contained sulfur and nitrogen oxides. The particle size of this type varied in the range of 1–5  $\mu\text{m}$ . These particles are observed in cities with a large vehicular traffic and are associated with exhaust emissions from automobiles using gasoline or diesel combustibles [10].

Particles in the form of filaments containing aluminosilicate particles enriched with oxides of titanium and other metals were also found (Fig. 3b). They were characteristic of the rock wool production plant located near Site 1.

### Characteristic PM<sub>10</sub> collected from Site 2

Site 2 had the largest number of S-rich particles, with more than half of them containing more than 3 % sulfur. Sulfate PM<sub>10</sub> is commonly identified as markers of secondary aerosols related to long-distance transport [11]. The majority of the sulfate particles had one or more potentially toxic metal inclusions. Figure 3c shows typical rod-shaped, crystalline, and spherical particles. The size of metal-containing S-rich particles was about 1  $\mu\text{m}$ . Most metal particles were classified as Fe-rich (e.g., hematite), Zn-rich (e.g., zinc sulfate and zinc oxide), Pb-rich (e.g., anglesite), Mn-, Ti-, Cu-, Cr- or W-rich, which were likely emitted from road traffic (exhaust and tire, brake, car body or road surface abrasions) [12]. Site 2 had the highest traffic volume. Zn, Cu, and Ti are often related to brake-pad erosion; Fe, Cu, Pb, and Zn from brake-disc wear. To identify PM from tire abrasion, Cd, Cu, Pb, and Zn can be monitored. Metals such as Fe and Zn are also linked to the corrosion of car-body parts. Road dust and roadside soil often contain metals, including Pb, Cu, Cd, and Zn, indicative of contamination by road traffic emissions and the abrasion of road surfaces. It has been shown that sulfates from aqueous SO<sub>2</sub> (S(IV)) oxidation catalyzed by transition metals are an important atmospheric process during winter, an alternative to the photochemical pathway that is highly unlikely because of the ultralow O<sub>3</sub> concentrations [13]. Metal catalysis can promote the conversion of SO<sub>2</sub> to sulfates in fog droplets [14]. The internal mixing of metals and acidic constituents solubilize metals and modify metal inclusion shapes. The solubilization of metals in airborne particles can increase their toxicity in the particles [15].

### Characteristic PM<sub>10</sub> collected from Site 3 and 4

At Sites 3 and 4, the morphological characterization results allowed us to classify most of the observed particles as soot due to the presence of large amounts of carbon in the collected sample; the elemental composition spectra were only qualitative and semiquantitative.

The soot particles had a spongy aspect and formed spheres of a size in the order of nanometers; they are united in chains, forming a mass of amorphous agglomerates, which give rise to larger particles. They had the structural complexity of these particles, and their composition is dominated by carbon (C) and oxygen (O). The soot particles appeared as large clusters of small spheres united by chains and were found to be similar to those in studies of urban regions in Brazil [16]. Such particles are known to be produced by anthropogenic sources such as vehicular emissions, and coal burning. At Site 3 the source of the soot is the heavy traffic of trucks that run on a highway through the city. At Site 4 the source of soot is the burning of coal at a thermal power plant.

### Characteristic PM<sub>10</sub> collected from Site 5

Fig. 3d shows spherical Fe-rich PM<sub>10</sub> found at Site 5. These particles consisted of iron oxide. They could be steel dust emitted by the metallurgical enterprises and placed in numerous slag dumps. Their size ranges between 0.5 and 2  $\mu\text{m}$  and they present a peculiar morphology; they are characterized by a perfect sphericity indicating their smelting iron origin or metallurgical activities in general.

### Sources implied by PCA

To increase the plausibility of the found sources of aerosol particles, a PCA was performed by the Varimax Rotated Factor Matrix method. Total 12 principle components (PCs) were extracted (eigenvalue>1) as that explained the 72% of the variance of the data (Table 1). A large number of PCs is explained by the large number of different sources because various industrial enterprises are located in Chelyabinsk. Atmospheric particles can interact with each other. PC1 explained 11 % variance and was loaded with C, O, Na, Si, S, K, Cl, Fe. It indicated that PM<sub>10</sub> contained carbonates, silicates and chlorides of sodium, potassium and iron which were mainly from natural sources. The same can be tell about PC6, PC8 and PC9 explained 6, 4 and 4% of variance, respectively. They were loaded with aluminosilicates, chlorides and carbonates indicating also natural sources. PC2 titled industrial emission (9% of the total variance) exhibits high loadings of Fe and may be associated with steel production activities. PC4, PC5 and PC10 explains 7, 7 and 4 % of the total variance, respectively, and have high loadings of B, C, O and Fe. They mainly arose from anthropogenic sources such as burning of coal (B, C and O contained soot PM corresponding to PC4 and PC5) or various transportation fuels (PC10 which has additional Fe loading).

Table 1. Results of principal component analysis (varimax rotation with kaiser normalization) at the five study sites, only factor loadings  $\geq 0.25$  are shown, the highest loadings are in bold

Element	PC1	PC2	PC3	PC4	PC5	PC6	PC7	PC8	PC9	PC10	PC11	PC12
Al						<b>0.91</b>			0.30			
B				<b>0.91</b>	0.33							
C	-0.50			-0.28	<b>-0.70</b>		-0.53		0.30	-0.47	-0.43	-0.55
Ca								<b>0.94</b>				
Cl	<b>0.56</b>					<b>-0.32</b>						
Cr												0.27
Cu											<b>0.35</b>	0.29
Fe	-0.25	<b>0.96</b>					-0.47			-0.26		-0.37
K	<b>0.25</b>											
Mg							<b>0.60</b>					
Mn											<b>0.80</b>	
N										<b>0.89</b>		
Na	0.27						-0.30					<b>-0.31</b>
Ni												<b>0.28</b>
O	-0.28		-0.33		<b>0.67</b>	-0.34	-0.53	-0.31	0.35	-0.41	-0.36	-0.45
Pb												<b>0.29</b>
S	-0.42		<b>0.89</b>				-0.26	-0.27			-0.31	-0.45
Si	-0.26					-0.34	-0.26		<b>-0.98</b>		-0.25	-0.33
Ti												<b>0.82</b>
Zn							<b>0.37</b>					<b>0.31</b>
Eigenvalue	3.1	2.5	2.1	2.0	1.9	1.6	1.4	1.2	1.2	1.1	1.0	1.0
Variance contribution rate (%)	11	9	8	7	7	6	5	4	4	4	4	4
Cumulative variance contribution rate (%)	11	20	28	35	42	47	52	56	61	64	68	72

PC7 was responsible for 5% of the total variance includes C, O, Na, Mg, Si, S, Fe and Zn and may be linked to slag dumps dust. PC11 was responsible for 4% of the total variance and high loadings of C, O, Si, S, Fe and Mn. This source was characterized as ferromanganese production. PC3 and PC12 were responsible for 8 and 4 % of the total variance respectively. They included S and O, besides PC12 was also represented by Na, Si, C, Cr, Ti, Fe, Cu, Ni, Pb and Zn. They were traffic-related S-rich particles.

## CONCLUSIONS

This work studied the morphological and chemical characteristics of metal-containing atmospheric particles collected in winter season from 5 sites in the Chelyabinsk urban area. Different magnifications have been selected for SEM-EDS analysis to classify the size range of the particles. SEM-EDS allowed us to provide information about the sources of PM and to highlight differences and similitudes among the sites. Single particle studies gave information for understanding the formation of PM and their potential toxic characteristics. The five sites are mainly characterized by traffic related pollution and metallurgical activity. Metal particles were mainly characterized by iron. S-enriched

particles included potentially toxic elements from traffic related sources. Additionally it should be noted that PM<sub>10</sub> nature vary depending on the weather and in future studies it would be useful to compare the obtained results with, for example, a summer sampling.

## ACKNOWLEDGMENTS

The research was found by the Russian Science Foundation (RSF), project number 22-17-20006 (<https://rscf.ru/en/project/22-17-20006/>) and Chelyabinsk region.

The authors wish to thank Ekaterina Yudina for SEM measurements.

## REFERENCES

- [1] GN 2.1.6.2604-10, 2010. Hygienic norms Supplement No. 8 to GN 2.1.6.1338-03. Maximum permissible concentrations (MPC) of pollutants in atmospheric air of populated areas. (Rus).
- [2] World Health Organization, Occupational and Environmental Health (2005). "WHO Air quality guidelines for particulate matter, ozone, nitrogen dioxide and sulfur dioxide: Global update 2005: Summary of Risk Assessment".
- [3] Zagorodnov S.Yu., May I.V. and Kokoulina A.A.,

- Fine-disperse particles (PM<sub>2.5</sub> and PM<sub>10</sub>) in atmospheric air of a large industrial region: issues related to monitoring and standardization of suspended particles in industrial emissions, *Hygiene & Sanitation*, No.98, 2019, pp.142-147.
- [4] Krupnova T.G., Rakova O.V., Gavrilkina S.V., Antoshkina E.G., Baranov E.O. and Yakimova O.N., Road dust trace elements contamination, sources, dispersed composition, and human health risk in Chelyabinsk, Russia, *Chemosphere*, 2020, p.261.
- [5] Krupnova T.G., Rakova O.V., Bondarenko K.A., Potgieter-Vermaak S. and Godoi R.H.M., Elemental composition of PM<sub>2.5</sub> and PM<sub>10</sub> and health risks assessment in the industrial districts of chelyabinsk, south ural region, Russia *International Journal of Environmental Research and Public Health*, Vol. 18, No.23, 2021, p.12354.
- [6] Krupnova T.G., Rakova O.V., Mashkova I.V., Artyukov E.V. and Vlasov N.E., Health risk assessment of metal(loid)s exposure via indoor dust from urban area in Chelyabinsk, Russia, *International Journal of GEOMATE*, Vol.16, No.55, 2019, pp.1-7.
- [7] Ramirez-Leal R., Valle-Martinez M. and Cruz-Campas M., Chemical and Morphological Study of PM<sub>10</sub> Analysed by SEM-EDS, *OJAP*, No.3, 2014, pp.121-129.
- [8] Krupnova T.G., Rakova O.V., Plaksina A.L., Gavrilkina S.V., Baranov E.O. and Abramyan A.D., Short Communication: Effect of urban greening and land use on air pollution in Chelyabinsk, Russia, *Biodiversitas*, no.21, 2020, pp.2716-2720.
- [9] Baranovsky A.G. Analysis of the variability of the composition, structure and physical and mechanical properties of eluvial clay soils and the possibility of their prediction: on the example of Chelyabinsk. Dissertation for the degree of Ph.D., Moscow, 2017.
- [10] González L.T., Longoria Rodríguez F.E., Sánchez-Domínguez M., Leyva-Porras C., Silva-Vidaurre L.G., Acuna-Askar K., Kharisov, B.I., and Alfaro Barbosa J.M., Chemical and morphological characterization of TSP and PM<sub>2.5</sub> by SEM-EDS, XPS and XRD collected in the metropolitan area of Monterrey, Mexico, *Atmospheric Environment*, No.143, 2016, pp.249-260.
- [11] Cozzi F., Pellegrini I., Adami G., Reisenhofer E., Bovenzi M. and Barbieri P., Sulphur speciation of PM<sub>10</sub> samples by XANES spectroscopy, *Central European Journal of Chemistry*, Vol.7, No.3, 2009, pp.395-401.
- [12] Penkała M., Ogrodnik P. and Rogula-Kozłowska W., Particulate Matter from the Road Surface Abrasion as a Problem of Non-Exhaust Emission Control, *Environments*, Vol. 5, No.1, 2018, p.9.
- [13] Li W., Zhou S., Wang X., Xu Z., Yuan C., Yu Ya., Zhang Q. and Wang W., Integrated evaluation of aerosols from regional brown hazes over northern China in winter: Concentrations, sources, transformation, and mixing states, *Journal of Geophysical Research*, No.116, 2001, D09301.
- [14] Desboeufs K.V., Sofikitis A., Losno R., Colin J.L. and Ausset P., Dissolution and solubility of trace metals from natural and anthropogenic aerosol particulate matter, *Chemosphere*, Vol.58, No.2, 2005, pp.195-203.
- [15] Li W., Wang T., Zhou S., Lee S., Huang Y., Gao Y. and Wang W., Microscopic Observation of Metal-Containing Particles from Chinese Continental Outflow Observed from a Non-Industrial Site, *Environmental Science and Technology*, Vol.47, No.16, 2013, pp.9124-9131.
- [16] Ferreira T.M., Forti M.C. and Alcaide R.L.M., Inhalable particulate matter characterization in a medium-sized urban region in Brazil (São José dos Campos Town) - Part I: Morphology, *Química Nova*, Vol.36, No.9, 2013, pp.1380-1387.

## CAN TREES HELP REDUCE LEAD IN URBAN AIR? A CASE STUDY OF GREENING IN A RUSSIAN INDUSTRIAL CITY

Tatyana G. Krupnova<sup>1</sup>, Olga V. Rakova<sup>1</sup>, Susanna V. Berentseva<sup>1</sup>, Svetlana V. Gavrilkina<sup>2</sup> and Valerii N. Udachin<sup>2</sup>

<sup>1</sup>Institute of Natural Sciences and Mathematics, South Ural State University, Russia; <sup>2</sup>Ilmen reserve, South Urals Federal Research Center of Mineralogy and Geoecology of the Urals Branch of the Russian Academy of Sciences, Russia

### ABSTRACT

Urban trees can be effectively used as a biomonitor and phytoremediator of air pollution, but not all species are equally capable of filtering the air. Lead-containing PM<sub>2.5</sub> has raised severe public health concerns in industrial cities. PM<sub>2.5</sub> pollution episodes occur in Chelyabinsk (Russia) because of a zinc production plant located in the urban area. During zinc production from lead-zinc concentrates, the environment around the enterprise may become contaminated with lead. We measured the amount of Pb in PM<sub>2.5</sub> and Pb accumulated by the leaves of *Betula pubescens*, *Populus nigra* L., *Acer negundo* L. and *Pinus silvestris* L. from the 32 sites. The lowest value of Spearman's coefficient was found for pine needles. The stomata of the needles were clogged with anti-icing agents that had accumulated over the winter. Pb found in the tree leaves correlated significantly with that found in the PM<sub>2.5</sub>. The correlations of Pb concentration were maximal for birch tree leaves. The leaves of all three species studied – *B. pubescens*, *P. nigra*, *A. negundo* – can be used as phytoremediators of Pb air pollution in the Chelyabinsk urban area.

**Keywords:** PM<sub>2.5</sub>, air pollution, lead, vegetation, phytoremediation

### INTRODUCTION

The world's population is expected to increase by 2 billion by 2050 – from 7.7 billion to 9.7 billion – and by the end of the century, despite continuing declines in fertility, it will peak at nearly 11 billion. Until 2009, more people lived in rural areas than in urban areas. Today, cities and towns are home to about 55 percent of the world's population, with urbanization projected to reach almost 70 percent by 2050 [1].

Russian cities are traditionally well greened. Chelyabinsk is a typical Russian industrial city with over a million inhabitants. Its urban area is characterized by the concentration in a relatively small space of a large number of ferrous and non-ferrous metallurgical industries, a developed transport network, and rapid growth in urban construction. All this has led to residents of the city worrying about “black sky regimes” and the uncontrolled removal of green spaces. Despite the clear contribution of urban greening to improving urban quality of life and the existence of demands for urban sustainability, there is a methodological gap in evaluating the effectiveness of urban greening in Russian industrial cities. We used physical and chemical analysis to search for solutions and recommendations for the modern organization of urban greening for city authorities. It is also useful because urban greenery shows positive associations with human health and mortality [2]. Green spaces play an important role in preserving the health of the population in cities. One of the modern solutions for

the sustainability of the urban space is the use of urban greening. Trees can give a good spatial coverage and their leaves are excellent air pollutants collectors, they are frequently used for air quality assessments. According to the deposition of the atmospheric particulate matter (PM), especially particles with aerodynamic diameters <2.5 μm (PM<sub>2.5</sub>), on the leaf surface, metals cations are bound by extracellular ligands. The number of studies rose in this field, but the species responded differently to the atmospheric pollution. This is connected with the ability of trees to capture heavy-metal, which has a serious impact on human health [3]. In the present paper we studied the role of tree leaves and needles in the remove of lead-containing PM<sub>2.5</sub> from the atmosphere. The foliar transfer of metals and metalloids in plant leaves and needles as a way of urban air purification remain under-studied. This study focused on the foliar uptake of metals from enriched PM<sub>2.5</sub> resulting from the different urban anthropogenic emissions including emissions from a zinc production plant located in Chelyabinsk. We chose lead (Pb) as a model element. Worldwide lead pollution is on the rise; lead was responsible 900 000 premature deaths [4]. During zinc production from lead-zinc concentrates, the environment around the enterprise may become contaminated with Pb. Pb is known to have many toxic effects in humans and is ranked second in the priority list of hazardous substances compiled by the US Environmental Protection Agency (USEPA) [5]. Lead exposure may cause changes in the neurologic system, leading to loss of neurological function [6].



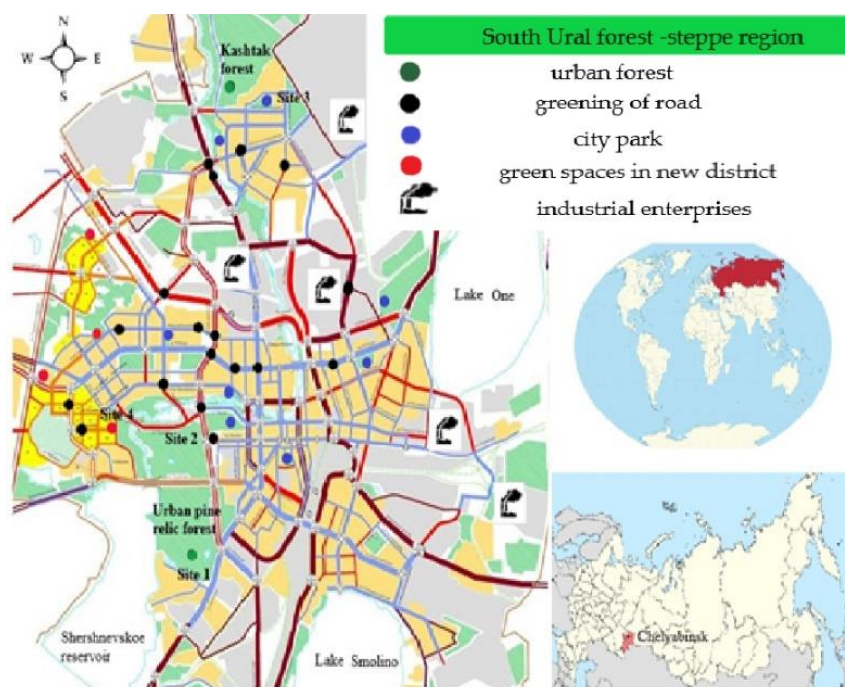


Fig. 1 Map of Chelyabinsk and location of the research sites

The Pb-containing PM present on and inside leaves were investigated by scanning electron microscopy coupled with energy dispersive X-ray microanalysis (SEM-EDX).

The study addresses the following two research questions:

- 1) Can trees help reduce lead in Chelyabinsk urban air?
- 2) What tree species are the best Pb accumulators?

## MATERIALS AND METHODS

### Study area

The present research studies Chelyabinsk urban greening. Chelyabinsk is the capital of the South Urals region. Chelyabinsk is one of the largest industrial cities in Russia, with a population of more than 1 million people. The city has an unfavourable situation with air pollution and is included in the project "Clean Air".

We chose four types of green area (Fig. 1): urban forest (two sites), the greening of roads (18 sites), established city parks (eight sites) and public residential green spaces in new districts (four sites).

### Sampling and analysis of PM<sub>2.5</sub>

The PM<sub>2.5</sub> samples were collected on 37 mm polycarbonate filters using low volume cascade impactor samplers operated at a flow rate of 16 l·min<sup>-1</sup> at a height of 2 m (72 h of sampling). These PM<sub>2.5</sub> samples were collected at each station in July 2022. The loaded PM<sub>2.5</sub> filters were placed in a PTFE digestion vessel for acid treatment (2 ml

hydrofluoric acid and 6 mL nitric acid), then microwave digested (MWS 4 Speedwave, Berghof, Germany) for 2 h after the setup routine for Pb analysis [7]. After digestion, the extracts were filtered using a blue-ribbon filter, and distilled water was added so that the total volume was 25 ml. Pb was analysed using Perkin Elmer ELAN 9000 Inductively Coupled Plasma Mass Spectrometry (ICP-MS). Certified reference material GSO 10413-2014 CO cespitose and podsolc srednesuglinisty soil (I BEND Rosselkhozakademii's VNIIA, Russia) was used for quality control. The range of recovery efficiency was 119%. The Pb limit of detection was estimated considering the standard deviation of 10 blank measurements (three times the standard deviation was used). The limit of detection of atmospheric concentrations obtained for Pb in PM<sub>2.5</sub> samples was 4.2 ng m<sup>-3</sup>.

### Selection of tree types and sampling of leaves and needles

Objects of research were tree species widely found in Chelyabinsk: *Betula pubescens*, *Populus nigra* L., *Acer negundo* L. and *Pinus silvestris* L. Selected tree species are most widely used for landscaping the city. We collected tree leaves and pine needles from 2–3 trees at each site, 20 leaves or 30–40 pine needles from each tree. We collected samples from the maximum number of branches available evenly around the tree from the lower part of the crown. Visibly damaged leaves or pine needles were not used for the analysis. The details of sample

collection and preparing for analysis were given in our previous work [8].

We washed the leaves and pine needles in running distilled water and air-dried them. All samples (leaf powder and pine needles) were digested separately into 10 ml of aqua-regia solution (HNO<sub>3</sub>: HCl v/v 3:1) on a hot plate at 120°C for 2 h. After cooling, the solution was filtered through blue ribbon filter paper and deionized water was added to make up a volume of 50 ml. The solutions were analysed for Pb content by mass spectrometry with inductively coupled plasma ICP-MS using Perkin Elmer ELAN 9000. The analyses were performed in triplicate. All reagents were of analytical grade. The Russian national state standard samples (Vinogradov Institute of Geochemistry SB RAS, Russia) of birch leaves (GSO 8923-2007) and a mixture of herbs (GSO 8922-2007) were used to check the accuracy of the Pb content in the leaves and needles. The ranges of recovery efficiency were 98–105 %. The limit of detection of concentrations obtained for Pb in leaves was 0.1 mg kg<sup>-1</sup> of dry weight (dw).

Small leaf strips or needles (washed with chloroform for top-part epicuticular wax removal before SEM analysis) were cut out from the area between the margin and midrib of leaves. Each sample was fixed on a metallic pin stub, using conductive double-sided tape, and left to dry at room temperature for at least three days. This dehydration is required to avoid sample damage, as water would evaporate too fast at low pressure. Before the microscopic analysis, samples were vacuum-coated with Au to make them conductive in order to prevent a charge build-up. SEM analyses were performed on a Jeol JSM-7001F Scanning Electron Microscopy Complex. Photographs were taken of randomly chosen spots at 500× magnification, at 5 kV.

### Data processing

Microsoft Excel 2013 and SPSS 24.0 software were used to organize and analyse the data. The Kolmogorov-Smirnov test was used to test data normality. The relationship between the data was determined using Spearman's test. MapInfo Pro 2019 was used to build the spatial distribution maps of Pb concentrations.

## RESULTS AND DISCUSSION

### Lead concentrations in PM<sub>2.5</sub>, pine needles and tree leaves

The concentrations of Pb were identified in PM<sub>2.5</sub>, pine needles, and tree leaves of three species. The Pb concentrations are shown in Table 1.

Table 1. Atmospheric concentrations (ng·m<sup>-3</sup>) obtained for Pb in PM<sub>2.5</sub> samples and concentration (mg·kg<sup>-1</sup> dw) obtained for Pb in pine needles and tree leaves collected in the Chelyabinsk urban area (n = 32)

Environmental object	Max	Mini	Mean	SD
PM <sub>2.5</sub>	35.0	5.0	18.0	0.5
Pb in pine needles	6.10	0.10	2.80	0.05
Pb in poplar leaves	12.30	0.20	5.50	0.05
Pb in maple leaves	9.50	0.20	4.20	0.05
Pb in birch leaves	15.0	0.3	7.1	0.1
Pb in birch leaves	15.0	0.3	7.1	0.1

Note: SD- Standard deviation. It was the amount of variation or dispersion of a values set.

It is known that the foliar pathway for metal uptake may be predominantly the soil–root pathway in urban and industrial environments [8]. In the present study, some PM are ultrafine, i.e., sub-micronic and nanoparticles were observed by SEM-EDX in leaf surfaces.

The mean concentrations of Pb in different tree leaves, ranging from 2.8-7.1 mg·kg<sup>-1</sup> dw. It is well known that there is a well-recognized definition of "phytoremediator" of Pb from soils which the Pb concentration in plant leaves is higher than 1000 mg·kg<sup>-1</sup> dw [9]. In this study, the deposition of lead from air is studied, so these approaches are not applicable. Rachmadiarti et al. [10] showed that *Wedelia triloba* (L.) Hitchc. and *Syzigium* sp. grown on the main roads absorbed 0.146-0.288 µg·g<sup>-1</sup> of Pb by leaf surface area and Pb content of both the plants was within the normal range, as the accepted Pb content for many plant species range from 1.0-3.5 µg·g<sup>-1</sup>. In our study Pb content in tree leaves was higher than for many plant species.

The Pb content detected in leaf samples (mg·kg<sup>-1</sup> dw.) from urban trees in Chelyabinsk differed by tree species and location (Fig. 2). The highest Pb content was found in birch leaves collected near the zinc production plant, followed by the leaves of same species collected from the urban area near the steel plant. Poplar leaves collected from the Kashtak forest located in the north of the city showed the lowest Pb content, but samples of the same species collected from locations with similarly busy traffic showed intermediate values of Pb content.

Foliar uptake is likely favoured by these PM morphologies. Comparing the capacity of the leaves to adsorb Pb particles across the deciduous tree species investigated, we can state that the most efficient species was the birch followed by the maple and then the poplar (see Table 1). Birch tree (accumulated the most PM compared to other tree species because its leaves contain high amounts of cuticular wax.

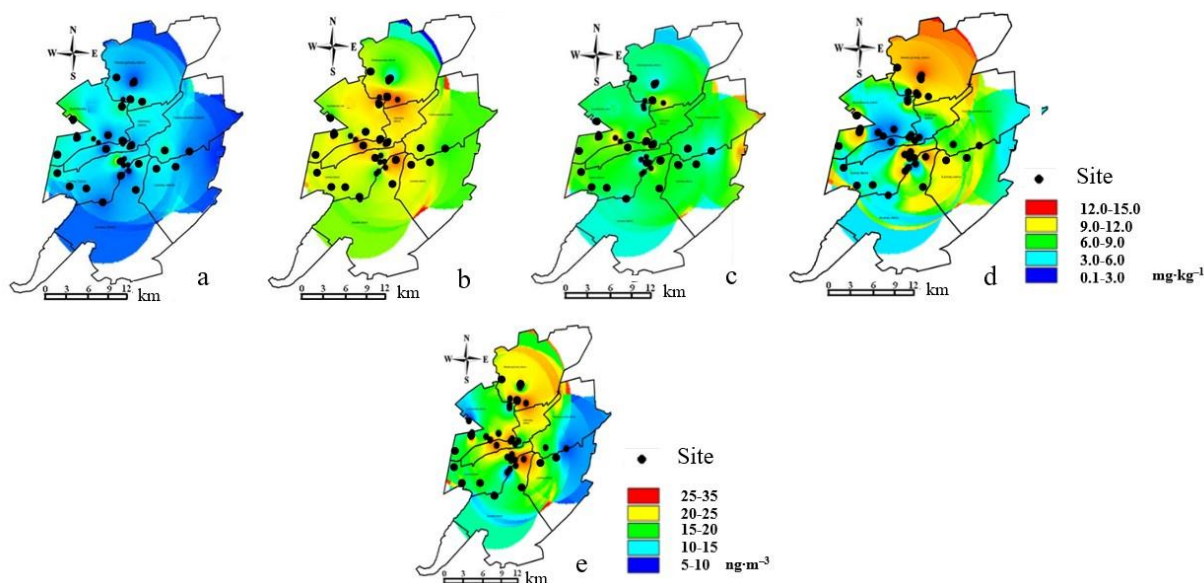


Fig. 2 Spatial distribution maps of the Pb concentrations in (a) pine needles, (b) poplar, (c) maple, and (d) birch leaves, and (e) Pb in  $PM_{2.5}$  from all sampling sites. The red and yellow colors on each small map represent relatively high concentration of Pb, while the green and blue colors represent relatively low concentrations, respectively.

Our results confirm Hrotko et al. [11] who reported large differences between tree species in heavy metal retaining capacity in foliar dust. Schreck et al. [12] reported that many factors may affect the air-vegetation transfer including plant characteristics such as functional type, leaf surface area, cuticular structure, and leaf longevity. Rough and hairy leaves accumulate significantly more lead (e.g. birch leaves) than smooth leaves (e.g. poplar leaves). Maple leaves occupy an intermediate position, they have a larger leaf surface than birch, but more rare and narrow stomata. Compared to poplar, maple has a rougher surface that better holds particles.

It is known that the foliar pathway for metal uptake may be predominantly the soil-root pathway in urban and industrial environments [8]. In the present study, some PM are ultrafine, i.e., sub-micronic and nanoparticles were observed by SEM-EDX in leaf surfaces.

Morphological factors such as stomatal index, trichome density, and leaf length affect the efficiency of dust collection by plants. These hypotheses of surface structure were confirmed by scanning electron microscopy (SEM) images of plant surfaces (Fig. 3).

Fig. 3a shows that the lowest concentration of lead is recorded in pine needles. This is because the absorption of any substances from the surrounding air by pine needles is significantly reduced due to clogging of the stomata with crystals of anti-icing agents that accumulate during the winter. This is in good agreement with the images presented in Fig. 3.

The stomata of needles taken further from major roads are less clogged (Fig. 3d).

#### Correlation of lead in $PM_{2.5}$ with lead content in leaves and needles

We studied the correlations of Pb in  $PM_{2.5}$  with Pb concentrations in pine needles and poplar, maple, and birch leaves. Table 2 presents Spearman's correlation coefficients.

Table 2. Spearman's correlation coefficients between lead in  $PM_{2.5}$  and lead content in leaves and needles (n=32)

Environmental factor/ object	Spearman's coefficient value
Pb in pine needles	0.31
Pb in poplar leaves	0.58*
Pb in maple leaves	0.63*
Pb in birch leaves	0.71*

Note: \* Correlation is significant at 0.001 (two-tailed)

The lowest value of Spearman's coefficient was found for pine needles with Pb in  $PM_{2.5}$ . The reason for the absence of a significant correlation was fact that the stomata of the needles were clogged with anti-icing agents that had accumulated over the winter. The correlation coefficients for the leaves fall within the range of 0.58–0.71. Table 2 indicates that Pb concentrations in  $PM_{2.5}$  correlate significantly with those found in the tree leaves at the 0.001 level of significance.

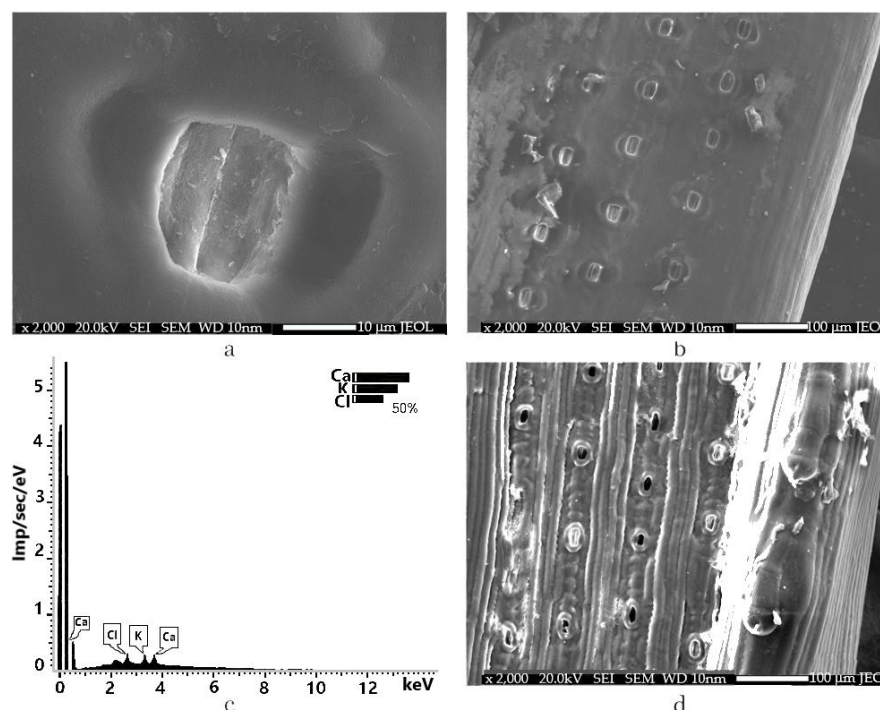


Fig. 3 SEM-images of plant surfaces: (a) salt crystal in the stoma of *P. silvestris*; (b) stomata of pine needles clogged with reagents; (c) spectrum of the composition of salt crystals in stomata of *P. silvestris*; (d) the state of stomata of pine needles collected at a distance from the roads.

The correlation coefficients of Pb concentration in leaves and in  $PM_{2.5}$  was the highest for birch trees because the birch leaf surface has hairs, and it might favor its metal tolerance and adsorption of fine atmospheric  $PM_{2.5}$ . Specific leaf surface areas could explain differences in rates of uptake between tree species. Maple leaves exhibit a dissected shape of its leaves with a folded structure. This leads to the formation of more reliable correlations for maple compared to poplar. However, the correlation is also high for poplar because the leaves have a high wax content [13].

## CONCLUSIONS

This study showed that tree leaves play an important role in the absorption of Pb-containing  $PM_{2.5}$  from the air. Birch leaves have the best phytoremediation properties of Pb-rich  $PM_{2.5}$  air contamination. Despite the summer period of sampling, the stomata of pine needles taken on the roadside were clogged with anti-icing agents, which prevents the pines from fulfilling their phytoremediation effects. It shows critical need to reduce use of road salt in winter.

In general, urban greening has various functions. It not only forms the urban-ecological framework of the city, but also regulates the urban microclimate, purifying the air in an industrial city, and having an aesthetic, educational, and cultural-historical function. Urban greenery needs to be maintained,

protected, and improved. The local city authorities of Chelyabinsk are not making enough efforts to increase the urban green cover. It should also be noted that in the last two years there has been a negative trend in the era of universal urbanization – population decline. Among other things, it can be assumed that it is associated with poor ecology and poor quality of life in the city. Therefore, work towards effective greening of the city could improve the situation. The government and the public should be aware of the scope and function of green spaces and protect them by collecting more data on green cover to enforce laws, increase the role of public organizations and enterprises, and use modern landscaping methods. Such approaches are urgently needed before more green spaces disappear from the cityscape. The loss of green cover may exacerbate the city's environmental problems, which are already chronic, negatively affecting the image and viability of Chelyabinsk.

## ACKNOWLEDGMENTS

The research was found by the Russian Science Foundation (RSF), project number 22-17-20006 (<https://rscf.ru/en/project/22-17-20006/>) and Chelyabinsk region.

## REFERENCES

- [1] United Nations. Shifting Demographics, 2020. Available: <https://www.un.org/en/un75/shifting-demographics> (accessed on 01 October 2022).
- [2] Van den Berg M., Wendel-Vos W., Van Poppel M., Kemper H., Van Mechelen W. and Maas J. Health benefits of green spaces in the living environment: A systematic review of epidemiological studies, *Urban Forestry and Urban Greening*, Vol.14, No. 4, 2015, pp.806-816.
- [3] Krupnova T.G., Rakova O.V., Mashkova I.V., Artyukov E.V. and Vlasov N.E., Health risk assessment of metal(loid)s exposure via indoor dust from urban area in Chelyabinsk, Russia, *International Journal of GEOMATE*, Vol.16, No.55, 2019, pp.1–7.
- [4] Fuller R., Landrigan P.J., Balakrishnan K., Bathan G. et al., Pollution and health: a progress update. *Lancet*, Vol.391, No.10119, 2018, pp.462-512.
- [5] Agency for Toxic Substances and Disease Registry, 2019. Priority List of Hazardous Substances that Will be the Subject of Toxicological Profiles. Available online: <https://www.atsdr.cdc.gov/spl/index.html#2019spl> (accessed on 01 October 2022).
- [6] Agency for Toxic Substances and Disease Registry, 2020. Toxicological Profile for Lead. Available online: <https://www.atsdr.cdc.gov/ToxProfiles/tp13.pdf> (accessed on 01 October 2022).
- [7] Krupnova T.G., Rakova O.V., Bondarenko K.A., Potgieter-Vermaak S. and Godoi R.H.M., Elemental composition of PM<sub>2.5</sub> and PM<sub>10</sub> and health risks assessment in the industrial districts of chelyabinsk, south ural region, Russia *International Journal of Environmental Research and Public Health*, Vol. 18, No.23, 2021, p.12354.
- [8] Krupnova T.G., Rakova O.V., Gavrilkina S.V., Antoshkina E.G., Baranov E.O., Dmitrieva A.P. and Somova A.V., Extremely high concentrations of zinc in birch tree leaves collected in Chelyabinsk, Russia, *Environmental Geochemistry and Health*, No. 43, 2021, pp.2551-2570.
- [9] Egendorf S.P., Groffman P., Moore G. and Cheng Z., The limits of lead (Pb) phytoextraction and possibilities of phytostabilization in contaminated soil: a critical review, *International Journal of Phytoremediation*, Vol. 22, No.9, 2020, pp.916-930.
- [10] Rachmadiarti F., Purnomo T., Azizah D.N. and Fascavitri A., Syzigium Oleina and Wedelia Trilobata for Phytoremediation of Lead Pollution in the Atmosphere, *Nature Environment and Pollution Technology*, Vol.18, No.1, 2019, pp.157-162.
- [11] Hrotkó K., Gyeveiki M., Sütöriné D.M., Magyar L., Mészáros R., Honfi P. and Kardos L., Foliar dust and heavy metal deposit on leaves of urban trees in Budapest (Hungary), *Environmental Geochemistry and Health*, No.43, 2021, pp.1927-1940.
- [12] Schreck E., Foucault Y., Sarret G., Sobanska S., Cécillon L., Castrec-Rouelle M., Uzu G. and Dumat C., Metal and metalloid foliar uptake by various plant species exposed to atmospheric industrial fallout: Mechanisms involved for lead, *Science of the Total Environment*, Vol.15, No.427-428, 2012, pp.253-262.
- [13] Wei X., Lyu S., Yu Y., Wang Z., Liu H., Pan D. and Chen J., Phylloremediation of Air Pollutants: Exploiting the Potential of Plant Leaves and Leaf-Associated Microbes, *Frontiers in Plant Science*, No.8, 2017, p.1318.



# GEOMATE 2023

The 13th International Conference on


## Geotechnique, Construction Materials & Environment

November 2023

Mie, Japan

- The "International Journal of GEOMATE" is a Scientific Journal of the GEOMATE International Society that encompasses a broad area in Geotechnique, Construction Materials and Environment.
- The key objective of this journal is to promote interdisciplinary research from various regions of the globe.
- The editorial board of the journal is comprised of extensively qualified researchers, academicians, scientists from Japan and other countries of the world.
- It is peer-reviewed Journal that is published quarterly till 2015 and now monthly. All articles published in this journal are available online.
- Contributors may download the manuscript preparation template for submitting paper or contact to the Editors-in-Chief

[[editor@geomatejournal.com](mailto:editor@geomatejournal.com)].



ISSN: 2186-2982 (Print) 2186-2990 (Online)


Scopus  
EBSCO

doi crossref

CENGAGE Learning

GIF GLOBAL IMPACT FACTOR

**International Journal of GEOMATE**  
(Geotechnique, Construction Materials and Environment)

 THE GEOMATE INTERNATIONAL SOCIETY  
Tsu, Japan

<https://geomate.org/index.html>

## FUNDAMENTAL PROPERTIES OF SOIL AND RICE HUSK ASH COMPOSITE FOR GROUND IMPROVEMENT – A REVIEW

Abd Elmageed Atef<sup>1</sup>, Alex Otieno Owino<sup>1</sup>, Md. Yachin Islam<sup>1</sup>, Md. Mahabub Alan<sup>2</sup>,  
Md. Soybur Rahman<sup>3</sup> and Zakaria Hossian<sup>1</sup>

<sup>1</sup>Graduate School of Bioresources, Mie University, Japan.

### ABSTRACT

Nearly 170 million tons per year of waste rice husks are produced worldwide, which pollutes the environment and poses health risks. RHA has become a potential threat to the ecosystem and needs real solutions. The direct disposal of RHA into open land or water bodies causes environmental pollution. One of the possible solutions is to utilize RHA additive to cement, lime, basalt fibers, Carbide slag, etc. This paper summarized the fundamental properties of soil and rice husk ash and its application in ground improvement and environmental protection. A comprehensive review of the literature available on RHA-soil mixture was performed to identify the gaps in understanding the behavior of the mix in terms of mechanical properties, durability, environmental impact, and internal mechanism. The results showed that adding RHA may significantly improve the soil's compressive strength, shear strength, and CBR value, which would be advantageous for both the economy and the environment. Additionally, it can significantly enhance soil performance in terms of shrinkage cracking. Generally, the full use of RHA as an addition for cement/lime, etc., in-ground improvement is promising since it can result in energy savings, low carbon emissions, and sustainable development. However, using control burned RHA with high amorphous silica content, conducting soaked CBR tests, consolidation tests, and freezing/thawing tests to analyze the effects of RHA on the geotechnical properties of soil still need to be studied further.

**Keywords:** Rice husk ash, Environmental impact, Ground improvement, Properties of soil

### INTRODUCTION

Soil comprises minerals, soil organic matter (SOM), water, and air. The composition and proportion of these components greatly influence soil physical properties, including texture, structure, and porosity, the fraction of pore space in the soil. In turn, these properties affect air and water movement in the soil, thus the soil's ability to function [1]. Ground improvement techniques are often used to increase the soil strength, lessen the compressibility, enhance the performance under the load and improve the soil properties in terms of their bearing capacity, shear strength, settlement characteristic, and drainage [2]. These techniques are widely used in an enormous scope of construction, such as industrial, commercial, and housing projects and infrastructure construction for dams, tunnels, ports, roadways, and barriers. Ground improvement is an alteration or stabilization technique to modify the soil's geotechnical properties, improving the soil's strength and stability. It reduces the permeability and compressibility of soil [2].



Fig. 1: Raw Rice to RHA and Synthesized Silica[2].

Rice is one of the most consumed food items worldwide; during the paddy milling process, 78% of the weight represents rice, broken rice, and bran 22% of the weight means husk. In this process, 17% to

25% ash is produced from the whole rice husk when it is burnt fig. 1 The paddy rice production was 782 million tons worldwide in 2018 (FAOSTAT,2020) Fig 2, and about 172 million tons of rice husk and 34 million tons of RHA were produced from the paddy rice in that year. The content of SiO<sub>2</sub> in RHA is more than 70% and can also go up to more than 90%, especially under controlled combustion temperature conditions[2].

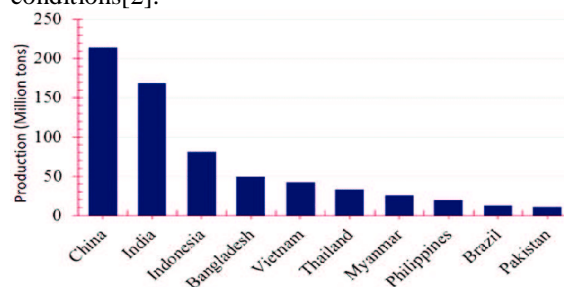


Fig. 2 Leading rice (paddy) producing countries worldwide (FAOSTAT2018).

### LITERATURE REVIEW

Many studies have shown that RHA has abundant nanopores (including many closed pores). The porous structure contributes to low dry weight, large specific surface area, and excellent thermal insulation properties [3]. In a wide range of building projects, including those involving industry, commerce, housing, and infrastructure development for dams, tunnels, ports, roads, and embankments, stabilized soil employing additives can be operated successfully.

Table 1 literature review

Author(s)	Soil type	Materials additives	and	Results
Musa, Alhaji. (2007) [4]	Laterite soil	RHA+ Cement		Under the specific cement content, CBR and UCS increased with the increase in RHA content, and the optimum RHA content is between 4-6%.
Arabani, et al. (2017) [5]	Asphaltic soil	RHA		RHA reduced the permeability and thermal sensitivity and improved the mixture's stability, rutting resistance, and fatigue life. The optimum RHA dosage is 15%.
Kabubo, et al. (2017) [6]	expansive soil	RHA + Lime		The combination of 20% RHA and 2% lime can improve CBR by 800% and reduce the free expansion rate by 70%.
Kofi, et al. (2017) [7]	sea sand	RHA+ Cement		The optimum strength of the pit sand-cement mortar prisms after 1, 2, 7, and 28 days was recorded at 11.11% RHA by the mass of the cement.
Ahmad et al. (2018) [8]	Clay soil	RHA + Cement		It is recommended that 8% of RHA content with 2% cement is the optimum amount for practical purposes.
Daud, et al. (2018) [9]	peat soil	RHA+Cement		The results show that the modified soil of MDD and OMC values are increased due to the increment amount of binder material.
Ghorbani, et al. (2018) [10]	Sand-clay	RHA+Fibre Polypropylene +cement		The optimum combination is 8% RHA, 8% cement, and 6mm polypropylene fiber.
Phanikumar, et al. (2018) [11]	Expansive soil	RHA+ Fly ash		The combination of fly ash and RHA significantly reduced the free expansion index and increased the UCS value.
Pornkasem, et al. (2018) [12]	Soft clay	RHA + Cement		The content of cement in the mixture is more than 10%, and adding 35%, RHA contributed to improving the strength.
Rahgozar, et al. (2018) [13]	Clyey soil- sand	RHA + Cement		The UCS value of the treated sample with 6% RHA and 8% cement cured for 28 days can reach up to 2900 kPa.
Jafer, et al. (2018) [14]	Soft clay	RHA+Flyash+palm oil fuel ash		The UCS of treated soil increased an additional 200 kPa to 923 KPa compared to that of untreated soil.
Janbuala, et al. (2018) [15]	Expansive soil	RhA + Bagasse ash		The optimum content of rice husk ash or bagasse ash is 30%.
J. Idrus, et al. (2018) [16]	sand	RHA		the best percentage mixture potentially considered to be used for the subbase is (90% - 10%) sand and RHA.
Arpit Jain. (2019) [17]	Black cotton soil	RHA		RHA reduced the plasticity index and sensitivity to moisture change, improved CBR, secant modulus, and cohesion of the parent soil.

Hamzah N, et al. (2019) [18]	Peat soil	RHA+ lime	Sawdust +	It can deduce a promising and improving result in stabilizing the soil with sawdust and Rice Husk Ash in both economic and strength capacity. The optimum combination is 7.5% RHA and 2% lime, at which the UCS can reach the maximum value.
Liu, et al. (2019) [19]	expansive soil	RHA+Lime		RHA-lime can inhibit expansion and reduce compression index. The optimum combination is 16% RHA and 4% lime.
Philbert, et al. (2019) [20]	clayey soil	RhA + Carbide slag		The addition of RHA accelerated the curing process and increased the UCS of the mixture.
Tonmoy, et al. (2019) [21]	Weak organic soil	RHA + Nylon fiber		The optimum combination is 15% RHA and 1.0% nylon fiber. Compared with untreated organic soil, the UCS value increased by 252.48%.
Y.Y.liu, et al. (2019) [22]	Expansive soil	RHA+ Carbide slag		The optimum combination is 10%RHA and 5% calcium carbide. The 7-day UCS value is close to 2MPa.
Hu et al. (2020) [23]	-	RHA + Cement		Indicated that paste with 15% rice husk ash improved sulfate resistance by stabilization of CeSeH and the refinement of pore structure.
Ramesh, Manjunatha. (2020) [24]	Black cotton soil	RHA + lime		The optimum dosage of RHA and CL was found to be 20% and 8%, respectively.
Yu, et al. (2020) [25]	Clay	RHA		RHA can increase the axial failure stress of soil at an optimum RHA content of 15%.
Nahar, et al. (2021) [26]	silty gravel and sand	RHA + Cement		The mixture of soil with RHA 5% and cement 6% showed the highest CBR value and second-highest permeability in this study.
Sharma, et al. (2021) [27]	clayey soil	RHA+Lime		The addition of RHA reduced DFS. RHA increased the OMC and reduced the MDD of the soil. RHA (12%) and lime (5%) increased the CBR value. C&D waste + lime improved the UCS, CBR and resilient modulus of clayey soil.
Owino, et al. (2022) [28]	Clay soil	RHA + Cement + basalt fibers		It is demonstrated that a reconstitute clay soil combination of 12 mm basalt fibers, 5% RHA, and 3% cement, enhanced the ultimate yield pressures and the resistance to excessive swelling.



The addition of RHA can significantly increase red clay soil CBR value, according to research examining the effectiveness of RHA treatment on red clay soil through compaction and unconfined compression. CBR tests. The results showed that the optimal content of RHA is 6%, and the UCS of laterite soils treated with 6% RHA and 4% lime and cured for seven days can reach up to 1.15 MPa. Musa et al. [4]

The maximum dry density of the treated laterite declined and stabilized as the RHA content rose. Still, the ideal moisture content increased over time, which may be connected to the unique pore structure and substantial specific surface area of RHA particles.

Additionally, with the particular cement composition, the CBR and UCS rose and subsequently fell as the RHA concentration rose. Between 4 and 6% was discovered to be the ideal RHA level.

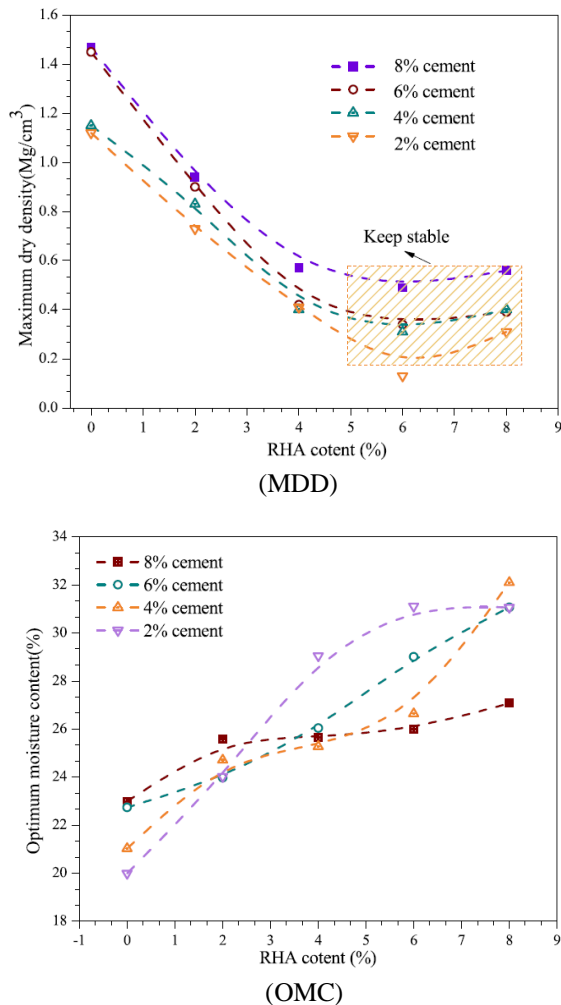


Fig. 3 Effect of RHA content on compaction characteristics of red clay: (Mdd) maximum dry density (b) Optimum moisture content [4].

RHA has also made some progress in its exploration of the strengthening of soft soil. Specifically, Pornkasem [12] used biomass waste ash to partially replace Portland cement in a deep mixing pile to treat soft clay and analyzed the influence of RHA content, cement content, curing age, and initial moisture content and achieved good results.

Fig. 4 shows the stress-strain relationship of treated soft soil under different RHA contents. It can be observed that the addition of RHA did not change the stress-strain relationship of soft soil, but an appropriate amount of RHA can significantly enhance the stress that the soft soil can endure.

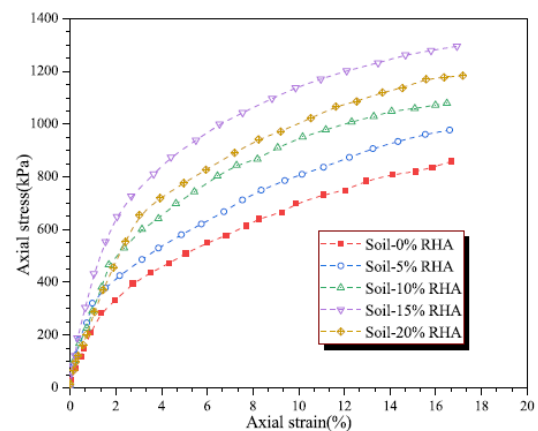


Fig 4. Stress-strain relationship of RHA-treated soft soil [25].

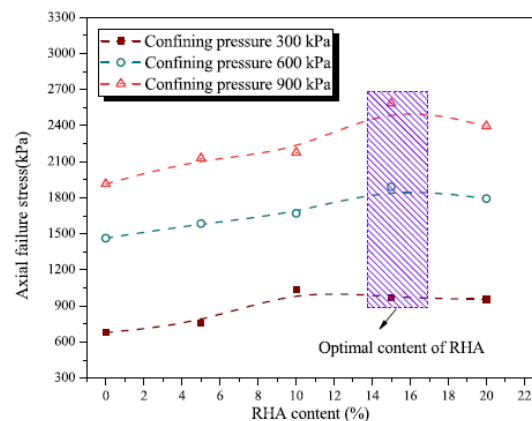


Fig 5. Axial failure stress of RHA-treated soft soil[25].

The optimal dosage of RHA is recommended to be 15%. RHA can solidify problematic soil, subgrade, and pavement components individually or jointly. The content of RHA is widely dispersed between 6% and 40%. This may be attributed to the different types of soil.



The research methods of RHA-reinforced soil are mainly focused on the basic physical and mechanical properties. Yet, in-depth research on the permeability characteristics, dynamic characteristics, durability, and environmental impact under complex environments of RHA-treated soil was hardly reported. The results showed that adding RHA can effectively improve the performance of soil related to shrinkage cracking and significantly enhance the compressive strength, shear strength, and CBR value of the soil, indicating economic and environmental benefits.

## CONCLUSION

In this study, the research status of fundamental properties of soil and rice husk ash composite for ground improvement was introduced from the aspects of production, physical characteristics, chemical composition, and microstructure. RHA has a low specific gravity, large pores, and a large specific surface area and contains more than 70% SiO<sub>2</sub>. Its essential characteristics are related to many factors, such as rice husk source, ash production equipment, combustion temperature, combustion time, and modification treatment.

It is necessary to study durability, micro mechanism, the environmental impact of RHA-treated soil, and degradation rule, the mechanism in a complex environment, to guide the sustainable utilization of RHA in fundamental properties of soil, achieving the double benefits in terms of economy and environment.

Overall, the comprehensive utilization of RHA composite for ground improvement as a partial alternative to cement/lime is promising as it can contribute to energy savings, low carbon emissions, and sustainable development. However, acquiring higher active RHA, micro mechanism of RHA-soil, and in a complex environment, the durability, deterioration mechanism, and environmental impact of RHA treatment on soil mixtures still need to be studied further.

In general, the appropriate amount of RHA can reduce the maximum dry density, increase the optimal moisture content, and enhance the UCS, shear strength, and CBR value of soil, exhibiting a significant improvement in the performance of problematic soils.

## FUTURE RESEARCH

To use control burned RHA with high amorphous

silica content.

To conduct soaked CBR tests, triaxial test, UCS test, direct shear test, compaction test, consolidation test, and freezing/thawing tests to analyze the effects of RHA on the geotechnical properties of soil.

## ACKNOWLEDGMENTS

The authors would like to thank Mie University Graduate School Doctoral Student Development Support for their financial assistance and advice.

## REFERENCES

- [1] Alhassan M., Alhaji M. M., Utilisation of rice husk ash for improvement of deficient soils in Nigeria: a review. *Nigerian Journal of Technology*, Vol. 36, Issu 2, 2017, pp. 386–394.
- [2] Kunchariyakun K., Asavapisit S., Sinyoung S., Influence of partial sand replacement by black rice husk ash and bagasse ash on properties of autoclaved aerated concrete under different temperatures and times [J]. *Construction Building Materials*, vol. 173, 2018, pp. 220-227.
- [3] Noaman Md. Abu., Karim Md. Rezul., Islam Md. Nazrul., Comparative study of pozzolanic and filler effect of rice husk ash on the mechanical properties and microstructure of brick aggregate concrete. *Heliyon*, Vol. 5, Issu 6, 2019, pp.e01926.
- [4] Musa A., Alhaji M., Effect of Rice Husk Ash on cement Stabilized Laterite, *Leonardo Electronic Journal of Practices and technologies*, 2007, 11: 47-58
- [5] Arabani, M., Tahami S. A., Assessment of mechanical properties of rice husk ash modified asphalt mixture[J]. *Construction and Building Materials*, Vol. 149, Issu 15, 2017, pp. 350–358.
- [6] Karatai T. R., Kaluli J. W., Kabubo C., Thiongo G., Soil stabilization using rice husk ash and natural Lime as an alternative to cutting and filling in road construction. *Journal of Construction Engineering and Management*, Vol. 143, Issu 5, 2017, pp. 04016127.
- [7] Tulashie S. K., Kotoka F., Mensah D., Kwablah A. K., Investigation of the compressive strength of pit sand, and sea sand mortar prisms produced with rice husk ash as additive. *Construction and Building Materials*, Vol. 151, 2017, pp. 383-387.
- [8] Ahmad J., Rosli M. I. F., Rahman A. S. A., The Effect of Rice Husk Ash (RHA) Mixtures on Geotechnical Properties of Soil. In *Regional Conference on Science, Technology and Social Sciences*, 2018, pp. 345–352.
- [9] Daud N. N. N., Daud M. N. M., Muhammed A. S., Rice husk ash (RHA) as a partial cement replacement in modifying peat soil properties. In *AIP Conference Proceedings*, Vol. 1930, Issu 1, 2018, pp. 020046.

- [10] Ghorbani A., Salimzadehshooili M., Medzvieckas J., Kliukas S., Strength characteristics of cement-rice husk ash stabilised sand-clay mixture reinforced with polypropylene fibers. *Baltic Journal of Road and Bridge Engineering*. Vol. 13, Issu 4, 2018, pp. 447–474.
- [11] Phanikumar B. R., Nagaraju T. V., Effect of Fly Ash and Rice Husk Ash on Index and Engineering Properties of Expansive Clays [J]. *Geotechnical and Geological Engineering*, Vol. 36, Issu 6, 2018, pp. 3425–3436.
- [12] Jongpradist P., Homtragoon W., Sukkarak R., Kongkitkul W., Jamsawang P., Efficiency of Rice Husk Ash as Cementitious Material in High-Strength Cement-Admixed Clay [J]. *Advances in Civil Engineering*, 2018, pp. 1–11.
- [13] Rahgozar M. A., Saberian M., Li J., Soilstabilization with non-conventional ecofriendly agricultural waste materials: An experimental study. *Transportation Geotechnics*, Vol. 14, 2018, pp. 52–60.
- [14] Jafer H. M., Atherton W., Sadique M., Ruddock F., Loffill E., Development of a new ternary blended cementitious binder produced from waste materials for use in soft soil stabilisation. *Journal of cleaner production*, Vol. 172, 2018, pp. 516–528.
- [15] Janbuala S., Eambuala M., Ardpasa A., Effects of rice husk ash and bagasse ash on properties of expanded clay. In *AIP Conference Proceedings*, Vol. 1973, Issu 1, 2018, pp. 020014.
- [16] Idrus J., Mahirah A. L. N., Masyitah M. N., Shafieza A. N., Fatimah S., The suitability of sand-rice husk ash (RHA) blends for subbase applications. In *AIP Conference Proceedings*. Vol. 2020, Issu 1, 2018, pp. 020020.
- [17] Jain A., Choudhary A. K., Jha J. N., Influence of rice husk ash on the swelling and strength characteristics of expansive soil. *Geotechnical and Geological Engineering*, Vol. 38, Issu 2, 2020, pp. 2293–2302.
- [18] Hamzah N., Yusof N. A. M., Rahimi M. I. H. M., Assessment of compressive strength of peat soil with sawdust and Rice Husk Ash (RHA) with hydrated lime as additive. In *MATEC Web of Conferences*, Vol. 258, 2019, pp. 01014.
- [19] Liu Y., Su Y., Namdar A., Zhou G., She Y., Yang Q., Utilization of cementitious material from residual rice husk ash and lime in stabilization of expansive soil. *Advances in Civil Engineering*, 2019.
- [20] Nshimiyimana P., Messan A., Zhao Z., Courard L., Chemico-microstructural changes in earthen building materials containing calcium carbide residue and rice husk ash. *Construction and Building Materials*, Vol. 216, 2019, pp. 622–631.
- [21] Brahmachary T. K., Ahsan M., Rokonzaman M., Impact of rice husk ash (RHA) and nylon fiber on the bearing capacity of organic soil. *SN Applied sciences*, Vol. 1, Issu 3, 2019, pp. 1–13.
- [22] Liu Y., Chang C. W., Namdar A., She Y., Lin C. H., Yuan X., Yang Q., Stabilization of expansive soil using cementing material from rice husk ash and calcium carbide residue. *Construction and Building Materials*, Vol. 221, 2019, pp. 1–11.
- [23] Hu L., He Z., Zhang S., Sustainable use of rice husk ash in cement-based materials: Environmental evaluation and performance improvement. *Journal of Cleaner Production*, Vol. 264, 2020, pp. 121744.
- [24] Ramesh H. N., Manjunatha B. V., Justification of strength properties of microstructural changes in the black cotton soil stabilized with rice husk ash and carbide lime in the presence of sodium salts. *SN Applied Sciences*, Vol. 2, Issu 3, 2020, pp. 1–12.
- [25] Lihua L. I., Xiao-ting Y. U., Mechanical properties of reinforcement about rice husk ash mixed soil [J]. *Rock and Soil Mechanics*, Vol. 41, Issu 7, 2020, pp. 2168–2178.
- [26] Nahar N., Hossain Z., Tamaki N., Optimum utilization of rice husk ash waste for ground improvement. *Int Agric Eng*, Vol. J30, 2021, pp. 1–10.
- [27] Sharma A., Sharma R. K., Sub-grade characteristics of soil stabilized with agricultural waste, constructional waste, and Lime. *Bulletin of Engineering Geology and the Environment*. Vol. 80, Issu 3, 2021, pp. 2473–2484.
- [28] Owino A. O., Nahar N., Hossain Z., Tamaki N., Dimensional influence of basalt fiber reinforcements on the consolidation behaviour of rice husk ash stabilized soils. *Construction and Building Materials*, Vol. 339, 2022, pp. 127686.

# GEOMATE 2023

The 13th International Conference on


## Geotechnique, Construction Materials & Environment

November 2023

Mie, Japan

- The "International Journal of GEOMATE" is a Scientific Journal of the GEOMATE International Society that encompasses a broad area in Geotechnique, Construction Materials and Environment.
- The key objective of this journal is to promote interdisciplinary research from various regions of the globe.
- The editorial board of the journal is comprised of extensively qualified researchers, academicians, scientists from Japan and other countries of the world.
- It is peer-reviewed Journal that is published quarterly till 2015 and now monthly. All articles published in this journal are available online.
- Contributors may download the manuscript preparation template for submitting paper or contact to the Editors-in-Chief

[[editor@geomatejournal.com](mailto:editor@geomatejournal.com)].



ISSN: 2186-2982 (Print) 2186-2990 (Online)

Scopus  
EBSCO


doi crossref

CENGAGE Learning

GIF GLOBAL IMPACT FACTOR

Clayey soils

**International Journal of GEOMATE**  
(Geotechnique, Construction Materials and Environment)

 THE GEOMATE INTERNATIONAL SOCIETY  
Tsu, Japan

<https://geomate.org/index.html>